Journal of Computational Methods in Sciences and Engineering 10 (2010) 91–94
DOI 10.3233/JCM-2010-0351
IOS Press

In Memoriam

Memories to Stanisław Kielich: My teacher, my mentor and my friend

Tadeusz Bancewicz*
Nonlinear Optics Division, Faculty of Physics, Adam Mickiewicz University, Umultowska 85, 61-614 Poznań, Poland

1. Kielich's style

There is no doubt that Kielich wrote his papers in his own elegant and specific style. He invented and introduced a special formalism suitable for molecular and nonlinear physics based on Cartesian tensors in which he made use of his deep knowledge of achievements of the old masters of molecular physics. In his scientific work he has shown his great involvement in molecular physics. In the peak of his carrier he wrote his papers fast and efficiently. In the nineteen sixties after construction of the laser, a lot of new optical (linear and nonlinear) effects were discovered. Several of them Kielich had already on his mind. His colleges remember that at a few occasions on the day following their discussions of a new physical effect Kielich would come to the Institute with his paper on the subject almost ready for publication. He mastered tensor calculus, so nonlinear optics was the area he admired. He learned tensor calculus while working with Piekara [1] and then he extended this formalism. From the early years of his scientific carrier he strongly admired works of Buckingham [2,3]. He liked to generalize every problem he worked on.

2. Light scattering

Kielich was especially interested in the theory of light scattering (linear and nonlinear). One of his first single-handed papers was devoted to the light scattering problems [4–7]. Moreover, from the beginning of his research work he was strongly involved in several subjects of nonlinear optics [8]. It is interesting to note that the laser had yet not been constructed at this time! Invention of the laser was a great stimulation in the area of nonlinear physics research. Already in 1961 Kielich wrote a paper on the nonlinear light scattering [9]. Several works followed this study [10–17]. Kielich is recognized [10,12] for having predicted for the first time the phenomenon of the hyper-Rayleigh scattering of intense laser

*Corresponding author. E-mail: tbancewi@zon12.physd.amu.edu.pl.

Fig. 1. Professor Kielich with Professor Bloembergen in Fontevrault.

Fig. 2. Professor Kielich with Professor Davies working in Poznañ.

light. Parallel studies were performed by Li [18] and Cyvin, Rauch and Decius [19]. This effect was experimentally detected for the first time in 1965 by Terhune, Maker and Savage [20].

Studying light scattering process Kielich paid special attention to the role of intermolecular interactions in nonlinear phenomena [17,21–23]. He studied intermolecular interactions in his very elegant and efficient statistical-molecular tensor based style [24]. In 1968 the monomer forbidden Rayleigh collision-induced light scattering was detected [25,26]. It was shown that an interacting pair of spherical molecules (atoms) possesses an excess anisotropic collision-induced polarizability and this excess polarizability leads to monomer forbidden depolarized light scattering. Kielich was strongly convinced that similar process exists also in the case of the hyper-Rayleigh (and hyper-Raman) light scattering. He shown that colliding pair of (even) centrosymmetric molecules has configurations with no center of inversion and the created fly-by supermolecule is a source of the second harmonic light scattering. This kind of scattering was detected by Kielich, Lalanne and Martin [27] during Kielich's sabbatical (1971–1972) year at the Bordeaux University.

3. Other subjects

Kielich has also been involved in many other scientific subjects. The number of subjects he studied is impressive. He started his scientific carrier studying statistical molecular theories of electric, magnetic, and optical saturation (with A. Piekara). Then he investigated intermolecular multipolar interactions in electro-optical and magneto-optical phenomena including optical activity. He considered linear and nonlinear spectroscopy of macromolecular and colloidal systems. He introduced to this field special functions now named Langevin-Kielich functions. Kielich contributed also to quantum optics. He studied photon anti-bunching and squeezed states of the electromagnetic field. All Kielich's papers are available in the pdf format on the web page http://zon8.physd.amu.edu.pl in the section: history.

Institutions and laboratories have a history which influence their future. Some scientists contribute strongly to this history. Stanisław Kielich was one of those.

References

[1] A. Piekara and S. Kielich, A non-linear theory of the electric permittivity and refractivity of dielectric liquids in electric and magnetic fields, *Acta Phys Polon* **17** (1958), 209–238.

[2] A.D. Buckingham, Permanent and induced molecular moments and long-range intermolecular forces, *Adv Chem Phys* **12** (1967), 107–142.

[3] *Optical, Electric and Magnetic Properties of Molecules: A review of the work of A. D. Buckingham*, (Elsevier, Amsterdam, 1997) edited by D.C. Clary and B.J. Orr.

[4] S. Kielich, Molecular interaction in the classical theory of light scattering Bull. de L'Academie Polonaise des Sciences Serie des sciences, *Math, Astr et Phys* **6** (1958), 215–221.

[5] S. Kielich, A molecular theory of light scattering in gases and liquids, *Acta Phys Polon* **19** (1960), 149–178.

[6] S. Kielich, Molecular theory of light scattering by multi-component systems, *Acta Phys Polon* **19** (1960), 573–597.

[7] S. Kielich, Rayleigh's ratio and turbidity of imperfect gases, *Acta Phys Polon* **19** (1960), 711–730.

[8] S. Kielich, Semi-macroscopic treatment of the theory of non-linear phenomena in dielectric liquids submitted to strong electric and magnetic fields, *Acta Phys Polon* **17** (1958), 239–255.

[9] S. Kielich, Theory of light scattering by nonlinear deformable spherical molecules of a gas, *Bull Soc Amis Sci Lettres* (*Poznan*) **16** (1961), 69–80.

[10] S. Kielich, On non-linear light scattering in gases, *Acta Phys Polon* **23** (1963), 321–332.

[11] S. Kielich, Classical theory of nonlinear molecular light scattering, *Bull Soc Amis Sci Lettres* (*Poznan*) **17** (1962–1963), 43–58.

[12] S. Kielich, Theory of molecular light scattering in the presence of an intense light beam, *Acta Phys Polon* **24** (1964), 135–154.

[13] S. Kielich, Influence of a strong optical electric field on the molecular scattering of light, *Bull Soc Amis Sci Lettres* (*Poznan*) **30** (1964), 1717–1724.
[14] S. Kielich, Sur la diffusion de la lumiere en presence d'un champ intense, electrique ou magnetique, *Acta Phys Polon* **23** (1965), 819–841.
[15] S. Kielich, Nonlinear light scattering by molecules without a centre of inversion Bull. de L'Academie Polonaise des Sciences Serie des sciences, *Math, Astr et Phys* **23** (1964), 53–60.
[16] S. Kielich, Non-linear processes to result from multipole interaction between molecules and electromagnetic fields, *Proc Phys Soc* **86** (1965), 709–725.
[17] S. Kielich, Role of molecular interaction in anisotropic light scattering by liquids, *J Chemical Physics* **46** (1967), 4090–4099.
[18] Y.Y. Li, *Acta Physica Sinica* **20** (1964), 164.
[19] S.J. Cyvin, J.E. Rauch and J.C. Decius, Theory of Hyper-Raman Effects (Nonlinear Inelastic Light Scattering): Selection Rules and Depolarization Ratios for the Second-Order Polarizability, *J Chem Phys* **43** (1965), 4083–4096.
[20] W. Terhune, P.D. Maker and C.M. Savage, Measurements of Nonlinear Light Scattering, *Phys Rev Lett* **14** (1965), 681–684.
[21] S.Kielich, The role of molecular multipole interactions in the electric polarization of multi-component systems: I. distortion polarization, *Acta Phys Polon* **27** (1965), 305–322.
[22] S. Kielich, The role of molecular multipole interactions in the electric polarization of multi-component systems. ii. orientation polarization, *Acta Phys Polon* **28** (1965), 95–121.
[23] S. Kielich, Second harmonic scattering by dense isotropic media, *Acta Phys Polon* **33** (1968), 89–104.
[24] S. Kielich, Frequency doubling of laser light in an isotropic medium with electrically destroyed centre of inversion, *Opto-Electronics* **2** (1970), 5–20.
[25] J.P. McTague and G. Birnbaum, Collision-Induced Light Scattering in Gaseous Ar and Kr, *Phys Rev Lett* **21** (1968), 661–664.
[26] W. Holzer and Y. Le Duff, Collision-Induced Light Scattering Observed at the Frequency Region of Vibrational Raman Bands, *Phys Rev Lett* **32** (1974), 205–208.
[27] S. Kielich, J.R. Lalanne and F.B. Martin, Double-photon elastic light scattering by liquids having centrosymnetric molecules, *Phys Rev Lett* **26** (1971), 1295–1298.

Journal of Computational Methods in Sciences and Engineering 10 (2010) 95
DOI 10.3233/JCM-2010-0354
IOS Press

In Memoriam

Stanisław Kielich – A personal memoir

A.D. Buckingham*
Department of Chemistry, Cambridge University, Cambridge, United Kingdom

In the 1950s I became interested in the interaction of electric fields with gases and liquids. Professor Arkadiusz Piekara was performing pioneering experiments in Poznań on dielectric saturation. He had discovered "the inverse saturation effect" in which the permittivity of dipolar liquids like nitrobenzene *increased* in strong applied electric fields; he correctly interpreted this effect in terms of the favouring of the more dipolar configurations of clusters of molecules by the applied field. I was invited to visit Poznań in April 1959 and there met Stanisław Kielich, Professor Piekara's outstanding young colleague. I particularly admired the close interaction of theory and experiment that was a feature of the Instytut Fiziki in Poznań. Kielich was four years my senior and his interests closely overlapped my own in optical, electric and magnetic properties of matter and in intermolecular forces We had many conversations and I remember his excitement on hearing about a new method of measuring molecular quadrupole moments. Poland was a poor country at that time but I was very generously and graciously entertained and had the pleasure of dancing with Stanisław's delightful wife Clare. When I departed from Poznań on the train for Warsaw he presented me with a paper knife bearing the arms of the city. It has been on my desk ever since.

Kielich went on to become a leader in various fields of molecular physics, and particularly in non-linear phenomena. He enjoyed the respect and affection of colleagues around the world and brought great credit to the Adam Mickiewicz University and to Poland. I am grateful for this opportunity to pay tribute to a friend and distinguished colleague.

*Corresponding author. E-mail: adb1000@cam.ac.uk.

Journal of Computational Methods in Sciences and Engineering 10 (2010) 97–98
DOI 10.3233/JCM-2010-0352
IOS Press

In Memoriam

My memories to Stanisław Kielich

Andrzej Graja*
Professor of Physics, Institute of Molecular Physics of the Polish Academy of Sciences, Poznań, Poland

Late in the fifties of the last century, as a young student of the Physics Department of Poznań University, I became fascinated with Professor Stanisław Kielich's lectures on the nonlinear optical phenomena. At that time, his first theoretical papers on the optical nonlinearity of matter were published. These publications were a consequence of his earliest works on the dielectric saturation of liquids. Just after my graduation from Poznań University, I applied for a post at the Institute of Physics of the Polish Academy of Sciences in Poznań, closely co-operating with the Division of the Experimental Physics at Poznań University. This was why our laboratory took up studies in the field of nonlinear optics. In those days (the beginning of the sixties), the first lasers were constructed at the best world-wide laboratories. Our knowledge on the lasers was residual but our enthusiasm was enormous. This enthusiasm let us construct, at the end of 1963, the first Polish ruby laser which emitted the coherent beam of the red light and so our laboratory was ready to undertake studies on nonlinear optical effects in matter. One of our aims was experimental confirmation of the Kielich's theory. My PhD thesis, defended in 1969, was devoted to the simplest nonlinear optical effect – second harmonic generation (SHG). I had proposed the generation of the light's harmonics not in single crystals but in powdered samples. My method of the investigations of SHG was fully original and relatively simple. It was published in *Acta Physica Polonica* – scientific journal of limited reach. Stanislaw Kielich was one of the scientists who appreciated this method and cited my paper on frequent occasions.

I made friends with my former professor and the oldest colleague in 1971, in Bordeaux (France) where I continued with my postdoctoral studies. At that time, Stanisław Kielich – Staszek for his friends – was Associate Professor at the University of Bordeaux in Talance. Though we were working in different laboratories, our relations were very close and friendly. Naturally I took part in his lectures devoted to recent developments in the theory of nonlinear optical effects; his lectures took place at the biggest conference room of the Centre de Recherches Paul Pascal, which was always filled to capacity. It is necessary to say that the participants of Staszek's lectures were bombarded with enormous, very long and complicated formulas written on a blackboard just from memory. What an extreme memory it was! In the midst of the audience many professors, younger scientists and PhD students. Novel, yet unpublished concepts, and the original form of Stanisław's lectures appealed hugely to the audience. Phenomena and new effects anticipated by theoretical investigations of Staszek were tested by experimenters of the

*Corresponding author. E-mail: Andrzej.Graja@ifmpan.poznan.pl.

Paul Pascal Centre without delay. This co-operation yielded a crop of series of publications of Stanisław Kielich and his French co-workers, J.R. Lalanne and P.B. Martin.

We spent our evenings discussing various problems, not only scientific, but also historical or moral ones, and very often our personal experiences. When talking till late at night, I saw Staszek as a clever, competent and brave man. I had occasions to learn about his tragic youth during the Second World War as well as times of poverty and hard labour just after the war. After long homelessness, he took up his studies of physics at Poznań University (now Adam Mickiewicz University). His studies were not only tenacity of purpose but a struggle for survival. Only a man as strong as Staszek would have been able to get University graduation (in 1955) and become one of the Eminent Professors (1971) of his maternal University, Full Member of the Polish Academy of Sciences (1983), director of the Institute of Physics (1969–1975) of Adam Mickiewicz University and one of the greatest Polish physicists, widely reputable in Poland and all over the world. Kielich, as a founding father of nonlinear optics, was awarded in 1993 the Medal of Marian Smoluchowski – the greatest Polish scientific award conferred by the Polish Physical Society. Professor Stanisław Kielich was one of the most respectable and honored scientists of our time.

Journal of Computational Methods in Sciences and Engineering 10 (2010) 99–101
DOI 10.3233/JCM-2010-0353
IOS Press

In Memoriam

To the memory of Stanislas Kielich

Geneviève Rivoire*
Molecular Nonlinear Optics, Faculty of Physics, University of Angers, Bd. Lavoisier 2, Angers, France

The publications of Stanislas Kielich, when I discovered them in the sixties, allowed me to make a clear link between two domains of knowledge. The first, which had a rather long history, concerned molecular physics, and especially molecular correlations. The second, which burst out following the discovery of the ruby laser in 1960, was related to laser physics. Non linear molecular optics was soaring.

In order to bring memory of these times alive, I would like to briefly tell here what was my first scientific exchange with Stanislas Kielich... Stimulated Raman scattering was the topic of the first letter I wrote him in 1965. Our laboratory had a long tradition of research in the field of Raman scattering, which – let us recall- was known experimentally only in its spontaneous form before 1962. My PhD director, René Dupeyrat, belonged to *the Laboratoire de Recherche Physique de la Sorbonne*, this very laboratory where Jean Cabanne had led his renowned pioneering studies which have contributed to the discovery of the Raman scattering, to its understanding and to the birth of its applications. This was the time where the production of the Raman spectrum of a material required an illumination of several hours with a very powerful light source (like a mercury vapor lamp). In 1962, the excitation of nitrobenzol with a ruby laser allowed the fortuitous discovery of stimulated Raman scattering. The spectrum was obtained with a single nanosecond pulse excitation. In fact, it was known, according to the theoretical studies of Placzek in 1937, that a stimulated scattering exists as well as the spontaneous scattering, similar to the existence of a stimulated emission together with a spontaneous emission. But its amplification needs exciting powers far larger than those delivered by classical sources. When we got our first ruby laser in Reims, we began the study of stimulated Raman scattering in various molecular materials.

As it is now well known, a lot of nonlinear effects appear simultaneously in the interaction laser/matter, leading to difficulties in the interpretation of the experimental results. Stimulated Raman Scattering properties revealed at first to be unrelated with the expected properties deduced from the spontaneous spectra. To say it briefly, the exciting beam propagation in the Raman medium was strongly perturbated by the nonlinear refraction index changes, and phenomena such as self focusing played an important role. In order to clarify the understanding of the experiments, we studied the influence of parameters changes- especially temperature- in a lot of molecular materials... and we were thus concerned with the role of molecular interactions. A bibliographic research on this subject pointed me to the publications of Stanilslas Kielich, and I got in touch with him.

I have kept the letters he wrote me in 1968... I read for example: "concerning the molecular correlations, I am sure that their influence in stimulated Raman scattering and in the coherence of the

*Corresponding author. E-mail: genevieve.rivoire@univ-angers.fr.

radiation is important... I hope that the relations between our two laboratories will increase..." And Stanislas Kielich enclosed in his letter a reprint of his publication "molecular interactions in optically induced nonlinearities" (IEEE-Journal of Quantum Electronics-QE-4 1968, p. 744). It was a very comprehensive and rich paper, dealing with non linearities of both refraction index and scatterings, taking into account the roles of molecular redistribution and of molecular fields. He listed the values of the Kerr constants of various liquids calculated with different models, which was a very interesting data source for the experimentator.

As concerns the continuation of our exchanges, without giving all the details, I would like to point out some prominent events... At first, the presence of Stanislas Kielich as Associate Professor in the University of Bordeaux, in 1971/1972... The lectures he gave there were first gathered in a handout "*polycopié*" which was- and is still- used in our laboratory as "the reference" for the calculation of the non linear susceptibility tensors... It was said in Bordeaux that "the Professor" was spending long hours of his nights to calculate tensors... These tensors, we can find them also in his books published at the University of Poznań in 1972, and in the book "interaction laser/molecule, laser physics and molecular non linear Optics" written with J.R.Lalanne and A.Ducasse and published in France in 1994(Ed Polytechnica).

Another event is the presence of Stanislas Kielich at the 31th meeting of the French *Société de Chimie Physique* organized in Fontevrault in 1978(photo). Stanislas Kielich gave there a lecture entitled "second harmonic generation of laser beam in electrically polarized atomic and molecular mixtures"... proving- if necessary- the success of the coupling realized by Stalislas Kielich between his exceptional knowledge of the molecules with all the new non linear phenomena induced by the use of powerful lasers.

As an echo to my first exchange with him reported above, which was devoted to Raman Scattering, I have kept the poster realized for the Non linear Optics Conference organized under his responsibility in Poznań in 1978: a beautiful colored poster displaying the famous rings of the anti Stokes Raman

scattering, orange, yellow, green rings, created by the interaction of a red ruby laser with a molecular liquid... an image symbolizing all these various changes- color, direction, polarization, coherence- induced by the interaction of laser with molecules. This Poznań Conference, wanted by Stanislas Kielich, completely placed under his scientific and human direction- and presenting some difficulties in an historical period where the opening to foreign researchers could yield to some suspicions- was possible because of the international notoriety he had acquired.

This notoriety has given a great recognition to the Poznań Institute of Physics, created to unify the previous chairs of Physics of the University, and placed under the Direction of Stanislas Kielich since its creation in September 1969. This Institute was very important for him, and I have a letter in which he explains me that he has to delay his stay in Bordeaux in order to assume his new management responsibilities.

When I read once again today all the publications of Stanislas Kielich, I am impressed by the wideness of his competences, the rigor of his calculations, his ability to make immediately the links between his previous knowledge and the new fields opened by the laser optics. It was difficult, in the beginning of the sixties, for laboratories having modest equipments – and I have also this experience- to step in the non linear Optics international scene... and we have to pay a tribute to the success of Stanislas Kielich and his group.

Stanislas Kielich loved physics, he loved his country, he had a deep scientific and human honesty and the vainglory was at the opposite of his choices. He remains for me one of a main guide mark I had the fortune to encounter in my researcher profession.

Journal of Computational Methods in Sciences and Engineering 10 (2010) 103–104
DOI 10.3233/JCM-2010-0350
IOS Press

In Memoriam

Working with Professor Stanisław Kielich

Ryszard Tanaś*
Nonlinear Optics Division, Department of Physics, Adam Mickiewicz University, 61-614 Poznań, Poland

Professor Stanisław Kielich was already a well known scientist when I met him for the first time during my studies at the Adam Mickiewicz University. He was giving lectures on molecular nonlinear optics that were designed, at that time of mid sixties of the twentieths century, to cover quite new material of rapidly developing nonlinear optics. The new field, and the way Kielich presented it in his lectures, attracted my attention so much that I decided to join Kielich's group. I completed my MSc thesis under Kielich's supervision and started my research in theoretical nonlinear optics. It was in 1969, and since then I had the opportunity to contact Kielich on the daily basis.

Professor Kielich's research at that time was aimed at revealing nonlinear properties of molecules, and nonlinear optics became a rich source of information on individual molecules and their interactions. The strategy was to exploit various nonlinear optical processes to collect as much information as possible about an individual molecule or a group of molecules. I started my work studying nonlinear optical activity and optical Kerr effect, but Kielich's favourite topic then was nonlinear light scattering. At that time, in our group, the electromagnetic field was treated classically and it was expected to be an agent that brings us information about the matter. A plethora of nonlinear optical processes discovered when the laser light was shined on the medium made it possible to study better and better optical properties of molecules, and it was the main goal of research in Kielich's group. The research was very successful with many interesting results. There was no need for field quantisation!

After few years of studying the nonlinear properties of molecules, I bought the Russian translation of the book *Quantum Optics and Electronics* with Glauber's lectures on photon statistics given in Les Houches. After reading the lectures I realized that nonlinear optical phenomena are important not only as a source of information about matter, but they radically change the properties of light itself. One day I came to Professor Kielich and presented him my new idea to study photon statistics of light produced in nonlinear phenomena. At first, he was not very enthusiastic about my idea. He told me that there is still a lot to be done in the "traditional" nonlinear optics, and this is the top priority in his group. He even suggested me to join another group, but, after some discussion, he accepted my idea, and he asked me to collect the results I already had and to send them for publication. Since he had just received a sample copy of the journal *Optik*, he said "you can send the paper to this journal". That was my first publication, it appeared in 1974, and I was really grateful to Professor Kielich for that advise. A year

*Corresponding author. E-mail: tanas@kielich.amu.edu.pl.

later I completed my PhD dissertation *On photon statistics in nonlinear optical phenomena* under the supervision of Professor Kielich.

Later on, we spent many hours discussing problems related with quantum properties of light generated by nonlinear optical phenomena, we had published many papers on the subject, and Professor Kielich had become more and more enthusiastic about the subject. He had included into the Russian translation of his book *Molecular Nonlinear Optics* an additional chapter devoted to the quantum properties of the optical fields.

As years went by, our personal relations had become very friendly, and it was a great honour to me when Professor Stanisław Kielich asked me to be on first name terms with him, since then he was Staszek for me. We were working together for a quarter of a century. When Staszek became seriously ill I gradually was taking over some administrative duties in Nonlinear Optics Division, but all the time being in good contact with Staszek and trying to realize his ideas. He passed away peacefully on October 15, 1993, after few years of struggle with his illness.

In my memory Staszek remains as a brilliant scientist, who belonged to the founding fathers of molecular nonlinear optics, the scientist who was open for new ideas and accepted convincing argumentation, the man who loved life, the man who was friendly to people, the great human being.

Journal of Computational Methods in Sciences and Engineering 10 (2010) 105–127
DOI 10.3233/JCM-2010-0313
IOS Press

On the quantization of the potential amplitude in the Schrödinger equation

B.Ya. Balagurov*
Emanuel Institute of Biochemical Physics, Russian Academy of Sciences, ul.Kosygina 4, Moscow, 119334, Russia

Abstract. A consistent scheme is proposed for quantizing the potential amplitude in the Schrödinger equation in the case of negative energies (lying in the discrete-spectrum domain). The properties of the eigenfunctions $\varphi_\nu(\mathbf{r})$ and eigenvalues α_ν corresponding to zero, small, and large absolute values of energy $E < 0$ are analyzed. Expansion in the set $\{\varphi_\nu(\mathbf{r})\}$ is used to develop a regular perturbation theory (for $E < 0$), and a general expression is found for the Green function associated with the time-independent Schrödinger equation. A similar method is used to solve several physical problems: the polarizability of a bound quantum-mechanical system, the two-center problem, and the elastic scattering of slow particles. The proposed approach is advantageous in that it does not require the use of continuum states (for $E > 0$).

Keywords: Potential amplitude, eigenfunction, eigenvalue

PACS numbers: 03.65.Ca, 03.65.Ge, 03.65.Nk

1. Introduction

One of the basic problems in non-relativistic quantum mechanics is the determination of the states of a particle (for any energies) in a prescribed potential (see [1,2]). Various characteristics of this quantum-mechanical system can be analyzed by solving this problem, including its responses to external perturbations (e.g., polarizability). Accordingly, a considerable part of the formal apparatus of quantum mechanics relies on perturbation theory (see [1,2]), i.e., on expansion of the required wave function in a complete set of "zeroth-order" (unperturbed) wave functions. Perturbation methods offer regular schemes for solving various problems. These schemes are especially simple and effective when the prescribed potential function has only bound-state solutions (as in the harmonic oscillator problem).

However, a totally different situation arises in the case of a realistic potential vanishing at infinity, when the problem involves a continuous spectrum of energy: the bound-state wave functions (corresponding to $E < 0$) must be combined with the continuum wave functions (corresponding to $E > 0$) to obtain a complete basis (see [1,2]). Therefore, states of both types must be taken into account in perturbation theory, which substantially complicates the problem. It would obviously be advantageous to find an approach that can be used to solve problems concerning negative-energy states without invoking continuum states.

In the present communication the procedure of quantization is applied to the amplitude of the potential (i.e., to the well depth). The idea behind the scheme can be explained as follows. The bound state corresponding to a certain energy $E < 0$ of a particle in a potential $U(\mathbf{r}) = U^0\, v(\mathbf{r})$ of prescribed

*Corresponding author. E-mail: balagurov@deom.chph.ras.ru.

form can be associated with an infinite discrete set of amplitudes U_ν^0. The values of $U_\nu^0 = U_\nu^0(E)$ and corresponding wave functions $\varphi_\nu(\mathbf{r})$ are treated as eigenvalues and eigenfunctions, respectively. Accordingly, an arbitrary wave function $\psi(\mathbf{r})$ corresponding to a state with $E < 0$ can be represented as an expansion in the set $\{\varphi_\nu(\mathbf{r})\}$, which is expected to be complete.

In this paper, the basic properties of the eigenfunctions $\varphi_\nu(\mathbf{r})$ and the corresponding eigenvalues α_ν are analyzed for the three-dimensional Schrödinger equation. The orthonormality and completeness of $\{\varphi_\nu(\mathbf{r})\}$ are established. The asymptotic behavior of $\varphi_\nu(\mathbf{r})$ (at $r \to \infty$) is determined, including the case of $E = 0$. The properties of α_ν and $\varphi_\nu(\mathbf{r})$ are analyzed in details for zero, small, and large absolute values of energy ($E \leqslant 0$). Expansion in the eigenfunction basis $\{\varphi_\nu(\mathbf{r})\}$ is used to develop a regular perturbation theory (for $E < 0$) without invoking continuum states. A general expression is found for the Green function associated with the time-independent Schrödinger equation (for $E < 0$).

To illustrate the resources of the proposed method, several physical problems are analyzed: the polarizability of a weakly bound quantum-mechanical system, the two-center problem, and the elastic scattering of slow particles. In each case, a consistent scheme is developed for calculating the required physical quantities by means of expansion in the eigenfunction basis $\{\varphi_\nu(\mathbf{r})\}$. In particular, the exact expression of scattering amplitude for $E = 0$ was derived. To illustrate the key points of the proposed method, Section 12 presents three exactly solvable examples in which eigenfunctions can be expressed in relatively simple analytical form. In these cases, the completeness of $\{\varphi_\nu(\mathbf{r})\}$ is proved directly.

Note that quantization has been applied previously to potentials in some special cases. For example, the Sturm functions corresponding to the three-dimensional Coulomb potential were analyzed and used to solve some quantum-mechanical problems (see [3–5]). However, the analysis given in [3–5] does not offer a general approach to the problem in the case of an arbitrary potential function. Recently such general approach was proposed in [6] for the one-dimensional case. Note that similar, but more formal, method of the quantization has been applied previously in Refs [7–9]. However, the method, used in present article, has a physical basis as distinguished from [7–9]. In addition to this, the problems, considered in our article, practically were not investigated in [7–9]. The difference is in investigation of basic properties of the eigenfunctions, the eigenvalues and decision of concrete physical tasks.

Note also that a somewhat analogous to [6] scheme for "quantization" the permittivities of macroscopic bodies relies on the eigenfunctions method proposed in [10,11] for various problems in the macroscopic electrostatics. Some techniques used in [10,11] may prove helpful in quantizing the amplitudes of finite–range potentials.

2. Eigenfunction basis

Consider a particle in a three-dimensional potential. If the potential function $U(\mathbf{r})$ is represented as $U(\mathbf{r}) = U^0\, v(\mathbf{r})$, where U^0 is the potential amplitude ($U^0 < 0$) and $v(\mathbf{r})$ $(\text{where } 0 \leqslant v(\mathbf{r}) \leqslant 1)$ defines its shape, then the time-independent Schrödinger equation can be written as

$$\nabla^2\psi(\mathbf{r}) + \varepsilon\,\psi(\mathbf{r}) = \alpha v(\mathbf{r})\psi(\mathbf{r})\,; \quad \varepsilon = \frac{2mE}{\hbar^2}\,,\ \alpha = \frac{2mU^0}{\hbar^2}. \tag{1}$$

Suppose that E is negative, i.e., $\varepsilon < 0$. Let us assume that $v(\mathbf{r})$ is rapidly (say, exponentially) decreasing at $r \to \infty$. The wave function $\psi(\mathbf{r})$ and its derivative are obey the standard conditions, i.e., bounded and continuous at any r and vanish at $r \to \infty$. In the common quantization scheme [1], these conditions are used to determine the bound-state energy levels E_ν and wave functions $\psi_\nu(\mathbf{r})$.

However, an alternative approach can be developed where the quantized value in Eq. (1) is α. Accordingly, the eigenvalues are discrete values α_ν of α (i.e., the potential amplitude). The corresponding eigenfunctions $\varphi_\nu(\mathbf{r})$ satisfy the equation

$$\nabla^2\varphi_\nu(\mathbf{r}) + \varepsilon\,\varphi_\nu(\mathbf{r}) = \alpha_\nu v(\mathbf{r})\,\varphi_\nu(\mathbf{r})\;;\;(\varepsilon = -\varkappa^2 < 0). \tag{2}$$

In this approach the energy ε is a parameter: $\alpha_\nu = \alpha_\nu(\varepsilon)$ and $\varphi_\nu = \varphi_\nu(\varepsilon;\mathbf{r})$. As noted in the Introduction, the set $\{\varphi_\nu(\mathbf{r})\}$ can be used to solve various quantum-mechanical problems (for $E < 0$). Therefore, the basic properties of $\varphi_\nu(\mathbf{r})$ and α_ν should be examined.

First of all, it follows from (2) that $\varphi_\nu(\mathbf{r}) \propto r^{-1}\exp(-\varkappa r)$ as $r \to \infty$ ($\varkappa = \sqrt{-\varepsilon}$). Furthermore, multiplying (2) by the complex conjugate $\varphi^*_\nu(\mathbf{r})$ and integrating the result over all space, we obtain

$$\alpha_\nu = -\left\{\int |\nabla\varphi_\nu(\mathbf{r})|^2\,d\mathbf{r} - \varepsilon\int |\varphi_\nu(\mathbf{r})|^2\,d\mathbf{r}\right\}\cdot\left[\int |\varphi_\nu(\mathbf{r})|^2 v(\mathbf{r})\,d\mathbf{r}\right]^{-1}. \tag{3}$$

It follows from (3) that α_ν are real numbers that are negative if $\varepsilon < 0$ and $v(\mathbf{r}) > 0$:

$$\alpha_\nu < 0.$$

Since α_ν are real, it can be assumed that $\varphi_\nu(\mathbf{r})$ are real too.

After the changes $\varepsilon \to \widetilde{\varepsilon}$ and $\nu \to \mu$ in (2), the equation for the corresponding eigenfunctions $\widetilde{\varphi}_\mu(\mathbf{r})$ has the form

$$\nabla^2\widetilde{\varphi}_\mu(\mathbf{r}) + \widetilde{\varepsilon}\,\widetilde{\varphi}_\mu(\mathbf{r}) = \widetilde{\alpha}_\mu v(\mathbf{r})\widetilde{\varphi}_\mu(\mathbf{r})\;;\;\widetilde{\alpha}_\mu = \alpha_\mu(\widetilde{\varepsilon}).$$

Multiplying this equation by $\varphi_\nu(\mathbf{r})$ and Eq. (2) by $\widetilde{\varphi}_\mu(\mathbf{r})$, subtracting one from the other, and integrating the result over all space, we obtain

$$(\alpha_\nu - \widetilde{\alpha}_\mu)\int \varphi_\nu(\mathbf{r})\widetilde{\varphi}_\mu(\mathbf{r})v(\mathbf{r})\,d\mathbf{r} = (\varepsilon - \widetilde{\varepsilon})\int \varphi_\nu(\mathbf{r})\widetilde{\varphi}_\mu(\mathbf{r})\,d\mathbf{r}. \tag{4}$$

Setting $\widetilde{\varepsilon} = \varepsilon$ in (4), we find that the functions $\varphi_\nu(\mathbf{r})$ and $\varphi_\mu(\mathbf{r})$ are orthogonal with the weight function $v(\mathbf{r})$ if $\alpha_\nu \neq \alpha_\mu$. Accordingly, the orthonormality condition for $\{\varphi_\nu(\mathbf{r})\}$ is

$$\int \varphi_\nu(\mathbf{r})\,\varphi_\mu(\mathbf{r})\,v(\mathbf{r})\,d\mathbf{r} = \delta_{\nu\mu}, \tag{5}$$

where $\varphi_\nu(\mathbf{r})$ and $\varphi_\mu(\mathbf{r})$ correspond to the same energy.

It can be argued that the eigenfunction set $\{\varphi_\nu(\mathbf{r})\}$ is complete for a broad class of potential functions (see below). Then, an arbitrary function $f(\mathbf{r})$ can be expanded in terms of eigenfunctions $\{\varphi_\nu(\mathbf{r})\}$, and the coefficients f_ν of the expansion can be determined by using orthonormality condition (5):

$$f(\mathbf{r}) = \sum_\nu f_\nu\,\varphi_\nu(\mathbf{r})\,,\quad f_\nu = \int f(\mathbf{r})\,\varphi_\nu(\mathbf{r})\,v(\mathbf{r})\,d\mathbf{r}. \tag{6}$$

This expansion converges to $f(\mathbf{r})$ only if the completeness condition

$$v(\mathbf{r})\sum_\nu \varphi_\nu(\mathbf{r})\,\varphi_\nu(\mathbf{r}') = \delta(\mathbf{r}-\mathbf{r}') \tag{7}$$

holds for $\{\varphi_\nu(\mathbf{r})\}$, where $\varphi_\nu(\mathbf{r})$ and $\varphi_\nu(\mathbf{r}')$ correspond to the same energy. Note that (7) is valid for finite-range potentials only for $\mathbf{r}$ and $\mathbf{r}'$ such that $v(\mathbf{r}) \neq 0$ and $v(\mathbf{r}') \neq 0$.

Setting $\mu = \nu$ in (4), taking the limit as $\widetilde{\varepsilon} \to \varepsilon$, and using (5), we obtain

$$\int [\varphi_\nu(\mathbf{r})]^2 \, d\mathbf{r} = \frac{d\alpha_\nu(\varepsilon)}{d\varepsilon}. \tag{8}$$

Hence,

$$\frac{d\alpha_\nu}{d\varepsilon} > 0. \tag{9}$$

By virtue of (5) and (8), it follows from (3) that

$$\int [\nabla\varphi_\nu(\mathbf{r})]^2 \, d\mathbf{r} = \varepsilon \, \frac{d\alpha_\nu(\varepsilon)}{d\varepsilon} - \alpha_\nu(\varepsilon),$$

which entails the inequality

$$\varepsilon \, \frac{d\alpha_\nu}{d\varepsilon} > \alpha_\nu. \tag{10}$$

Let us introduce the zeroth-order Green function:

$$\nabla^2_{\mathbf{r}} \, G^0(\mathbf{r} - \mathbf{r}') + \varepsilon \, G^0(\mathbf{r} - \mathbf{r}') = \delta(\mathbf{r} - \mathbf{r}'), \tag{11}$$

$$G^0(\mathbf{r} - \mathbf{r}') = - \, \frac{\exp(- \varkappa|\mathbf{r} - \mathbf{r}'|)}{4\pi|\mathbf{r} - \mathbf{r}'|} \; ; \; \varkappa = \sqrt{-\varepsilon} \, . \tag{12}$$

With the use of Eqs (11)–(12), Eq. (2) can be rewritten in integral form as

$$\varphi_\nu(\mathbf{r}) = - \, \frac{\alpha_\nu}{4\pi} \int \frac{\exp(-\varkappa|\mathbf{r} - \mathbf{r}'|)}{|\mathbf{r} - \mathbf{r}'|} \, \varphi_\nu(\mathbf{r}') v(\mathbf{r}') \, d\mathbf{r}', \tag{13}$$

which yields an asymptotic expression for eigenfunction $\varphi_\nu(\mathbf{r})$:

$$\begin{gathered} r \to \infty : \; \varphi_\nu(\mathbf{r}) \eqsim - \, \frac{\alpha_\nu u_\nu(\mathbf{n}, \varkappa)}{4\pi} \, \frac{e^{- \varkappa r}}{r} \; ; \; \mathbf{n} = \frac{\mathbf{r}}{r} \; ; \\ u_\nu(\mathbf{n}, \varkappa) = \int e^{\varkappa \mathbf{n} \mathbf{r}'} \, \varphi_\nu(\mathbf{r}') v(\mathbf{r}') \, d\mathbf{r}'. \end{gathered} \tag{14}$$

Note that (13) is a homogeneous Fredholm integral equation of the second kind with a polar kernel. It can be transformed into an equation with a symmetric kernel (for $v(\mathbf{r}) > 0$) by making transformation to the functions

$$\Omega_\nu(\mathbf{r}) = \sqrt{v(\mathbf{r})} \, \varphi_\nu(\mathbf{r}). \tag{15}$$

As a result, (13) becomes

$$\Omega_\nu(\mathbf{r}) = \mu_\nu \int K(\mathbf{r}, \mathbf{r}') \Omega_\nu(\mathbf{r}') \, d\mathbf{r}' \; ; \; \mu_\nu = - \, \alpha_\nu,$$

where

$$K(\mathbf{r},\mathbf{r}') = \frac{1}{4\pi}\sqrt{v(\mathbf{r})}\,\frac{\exp(-\varkappa|\mathbf{r}-\mathbf{r}'|)}{|\mathbf{r}-\mathbf{r}'|}\,\sqrt{v(\mathbf{r}')}$$

is a symmetric and positively definite kernel. Under certain conditions, the eigenvalues of the corresponding integral equation are positive: $\mu_\nu > 0$ (in which case $\alpha_\nu < 0$). Moreover, the corresponding eigenfunctions constitute an orthonormal and complete set $\{\Omega_\nu(\mathbf{r})\}$:

$$\int \Omega_\mu(\mathbf{r})\Omega_\nu(\mathbf{r})\,d\mathbf{r} = \delta_{\mu\nu}\,, \quad \sum_\nu \Omega_\nu(\mathbf{r})\Omega_\nu(\mathbf{r}') = \delta(\mathbf{r}-\mathbf{r}'). \tag{16}$$

It follows from (16) and (15) that the set $\{\varphi_\nu(\mathbf{r})\}$ satisfies the orthonormality and completeness conditions given by (5) and (7), respectively.

Comparing (14) with (6), we find that the values $u_\nu(\mathbf{n},\varkappa)$ are the coefficients in the expansion of the function $f(\mathbf{r}) = \exp(\varkappa\mathbf{n}\mathbf{r}')$ in terms of $\{\varphi_\nu(\mathbf{r})\}$:

$$e^{\varkappa\mathbf{n}\mathbf{r}'} = \sum_\nu u_\nu(\mathbf{n},\varkappa)\,\varphi_\nu(\mathbf{r}'),$$

where $\varphi_\nu(\mathbf{r}')$ correspond to $\varepsilon = -\varkappa^2$ and $\mathbf{n}$ – the arbitrary unit vector.

Replacing $\mathbf{r}'$ with $\mathbf{r}''$ in Eq. (13), multiplying the equation by $(\alpha_\nu)^{-1}\varphi_\nu(\mathbf{r}')$, summing the result over ν, and using (7), we obtain

$$G^0(\mathbf{r}-\mathbf{r}') = -\,\frac{\exp(-\varkappa|\mathbf{r}-\mathbf{r}'|)}{4\pi|\mathbf{r}-\mathbf{r}'|} = \sum_\nu \frac{\varphi_\nu(\mathbf{r})\varphi_\nu(\mathbf{r}')}{\alpha_\nu}\,. \tag{17}$$

Expansion (17) of $f(\mathbf{r}) = G^0(\mathbf{r}-\mathbf{r}')$ in terms of $\{\varphi_\nu(\mathbf{r})\}$ can also be obtained by using (6). The corresponding coefficients f_ν are calculated by using (2) and (11).

The "full" Green function $G(\mathbf{r},\mathbf{r}')$ satisfies the equation

$$\left\{\nabla^2_{\mathbf{r}} + \varepsilon - \alpha v(\mathbf{r})\right\} G(\mathbf{r},\mathbf{r}') = \delta(\mathbf{r}-\mathbf{r}').$$

Representing the solution to this equation as an expansion in the basis $\{\varphi_\nu(\mathbf{r})\}$, we obtain

$$G(\mathbf{r},\mathbf{r}') = \sum_\nu \frac{\varphi_\nu(\mathbf{r})\,\varphi_\nu(\mathbf{r}')}{\alpha_\nu - \alpha}\,. \tag{18}$$

If $\alpha = 0$, then this expression reduced to expansion (17) for the zeroth-order Green function $G^0(\mathbf{r}-\mathbf{r}')$. Using Eq. (17), we can rewrite expression (18) for $G(\mathbf{r},\mathbf{r}')$ as

$$G(\mathbf{r},\mathbf{r}') = G^0(\mathbf{r}-\mathbf{r}') + \alpha\sum_\nu \frac{\varphi_\nu(\mathbf{r})\,\varphi_\nu(\mathbf{r}')}{\alpha_\nu(\alpha_\nu - \alpha)}\,. \tag{18'}$$

For a finite-range potentials the expansions (17) and (18) are valid if the function $v(\mathbf{r})$ differs from zero at least for one of the coordinates ($\mathbf{r}$ or $\mathbf{r}'$). If both $v(\mathbf{r}) = 0$ and $v(\mathbf{r}') = 0$, then for the Green function $G(\mathbf{r},\mathbf{r}')$ one must use the expansion (18′) with $G^0(\mathbf{r}-\mathbf{r}')$ from Eq. (12).

3. Bound states

Let us apply the proposed approach to find the discrete energy spectrum for a particle in a potential $\alpha v(\mathbf{r})$, where α is a prescribed amplitude ($\alpha < 0$). Expand the bound-state wave function $\psi(\mathbf{r})$ in the eigenfunction basis $\{\varphi_\mu(\mathbf{r})\}$ corresponding to this potential function:

$$\psi(\mathbf{r}) = \sum_\mu C_\mu \, \varphi_\mu(\mathbf{r}).$$

Substitute this expression into (1) and use (2) we obtain

$$\sum_\mu C_\mu(\alpha_\mu - \alpha) v(\mathbf{r}) \varphi_\mu(\mathbf{r}) = 0.$$

Multiplied by $\varphi_\nu(\mathbf{r})$ and integrated over all space, this relation reduces to $C_\nu(\alpha_\nu - \alpha) = 0$. Therefore, $C_\nu \neq 0$ if

$$\alpha_\nu(\varepsilon) = \alpha \tag{19}$$

and the remaining coefficients C_μ (with $\mu \neq \nu$) vanish. Relations (19) provide equations for the bound-state energies $\varepsilon_\nu = \varepsilon_\nu(\alpha)$.

First of all, note that the inequality $\alpha_\nu < 0$ implies that Eq. (19) have solutions only if $\alpha < 0$ (i.e., if the potential is attractive), which is obvious from physical considerations. Furthermore, since (9) implies that $|\alpha_\nu|$ is a monotone increasing function of $|\varepsilon|$, Eq. (19) has a unique solution $\varepsilon_\nu = \varepsilon_\nu(\alpha)$ for each given ν. Therefore, the wave function $\psi_\nu(\mathbf{r})$ of a non-degenerate bound-state (with energy ε_ν) normalized to unity is

$$\psi_\nu(\mathbf{r}) = C_\nu \, \varphi_\nu(\varepsilon_\nu; \mathbf{r}) \,, \quad C_\nu = \left[\frac{d\alpha_\nu}{d\varepsilon} \right]^{-1/2}_{\varepsilon=\varepsilon_\nu} = \left[\frac{d\varepsilon_\nu(\alpha)}{d\alpha} \right]^{1/2} . \tag{20}$$

Expression (20) is derived by using (8) and the relation

$$\left[\frac{d\alpha_\nu}{d\varepsilon} \right]_{\varepsilon=\varepsilon_\nu} \cdot \left[\frac{d\varepsilon_\nu}{d\alpha} \right] = 1,$$

which follows from (19). At $r \to \infty$, we can combine (14) with (20) to find an asymptotic expression for $\psi_\nu(\mathbf{r})$:

$$r \to \infty \, : \; \psi_\nu(\mathbf{r}) \approx A_\nu(\mathbf{n}) \, \frac{e^{-\varkappa_\nu r}}{r} \,, \quad A_\nu(\mathbf{n}) = - \, C_\nu \left[\frac{\alpha_\nu u_\nu(\mathbf{n}, \varkappa)}{4\pi} \right]_{\varepsilon=\varepsilon_\nu} , \tag{21}$$

where $\varkappa_\nu = \sqrt{-\varepsilon_\nu}$, $\mathbf{n} = \mathbf{r}/r$.

If there exist several bound states in a potential well and $\varepsilon_\nu \neq \varepsilon_\mu$ (while $\alpha_\nu(\varepsilon_\nu) = \alpha_\mu(\varepsilon_\mu) = \alpha$), then it follows from (4) that the corresponding wave functions given by (20) are mutually orthogonal. Therefore, the set $\{\psi_\nu(\mathbf{r})\}$ satisfies the standard orthonormality condition [1]

$$\int \psi_\nu(\mathbf{r}) \, \psi_\mu(\mathbf{r}) \, d\mathbf{r} = \delta_{\nu\mu}.$$

However, the wave functions $\psi_\nu(\mathbf{r})$ do not constitute a complete set, in contrast to $\{\varphi_\nu(\mathbf{r})\}$.

4. Spherically symmetrical field

The function $v(\mathbf{r})$ depends only on modulus of $\mathbf{r}$ $\big(v(\mathbf{r}) = v(r)\big)$ for spherically symmetrical potentials. In this case the problem may be simplified by separating an angular part of eigenfunction $\varphi_\nu(\mathbf{r})$. In order the radial eigenfunctions to be real, we introduce two types of spherical harmonics $Y_{lm}^{(\lambda)}(\mathbf{n})$ ($\mathbf{n} = \{\sin\theta\cos\varphi, \sin\theta\sin\varphi, \cos\theta\}$; $\lambda = 1, 2$), which are the real and imaginary parts of usual spherical functions:

$$Y_{lm}^{(1)}(\mathbf{n}) = a_{lm}\, P_l^m(\cos\theta)\, \cos m\varphi\,,\ 0 \leqslant m \leqslant l\,,$$

$$Y_{lm}^{(2)}(\mathbf{n}) = a_{lm}\, P_l^m(\cos\theta)\, \sin m\varphi\,,\ 1 \leqslant m \leqslant l\,;$$

$$a_{lm} = \left[\frac{2l+1}{2\pi(1+\delta_{m0})} \cdot \frac{(l-m)!}{(l+m)!}\right]^{1/2}\ ;\ l = 0, 1, 2, \ldots\,.$$

Set of functions $\{Y_{lm}^{(\lambda)}(\mathbf{n})\}$ is orthonormal

$$\int Y_{lm}^{(\lambda)}(\mathbf{n})\, Y_{l'm'}^{(\lambda')}(\mathbf{n})\, do = \delta_{\lambda\lambda'}\, \delta_{ll'}\, \delta_{mm'}$$

(where $do = \sin\theta\, d\theta\, d\varphi$) and complete

$$\sum_{\lambda lm} Y_{lm}^{(\lambda)}(\mathbf{n})\, Y_{lm}^{(\lambda)}(\mathbf{n}') = \delta(\mathbf{n} - \mathbf{n}') = \frac{1}{\sin\theta}\, \delta(\theta - \theta')\, \delta(\varphi - \varphi').$$

Note also that

$$\sum_{\lambda m} Y_{lm}^{(\lambda)}(\mathbf{n})\, Y_{lm}^{(\lambda)}(\mathbf{n}') = \frac{2l+1}{4\pi}\, P_l(\mathbf{n}\mathbf{n}'),$$

where $P_l(x)$ – Legendre polynomials.

The eigenfunction function $\varphi_\nu(\mathbf{r}) \equiv \varphi_{\lambda lmn}(\mathbf{r})$ can be written as

$$\varphi_{\lambda lmn}(\mathbf{r}) = \varphi_{ln}(r)\, Y_{lm}^{(\lambda)}(\mathbf{n})\,;\ \mathbf{n} = \mathbf{r}/r. \tag{22}$$

Substitution of (22) in Eq. (2) yields the following equation for the radial eigenfunction $\varphi_{ln}(r)$

$$\frac{d^2\varphi_{ln}(r)}{dr^2} + \frac{2}{r}\, \frac{d\varphi_{ln}(r)}{dr} - \frac{l(l+1)}{r^2}\, \varphi_{ln}(r) + \varepsilon\, \varphi_{ln}(r) = \alpha_{ln} v(r)\, \varphi_{ln}(r). \tag{23}$$

Different solutions of Eq. (23) at fixed l are marked by subscript n. Energy levels ε_{ln} in potential $\alpha v(r)$ are found from the equation which is similar to (19):

$$\alpha_{ln}(\varepsilon) = \alpha.$$

Set of radial eigenfunctions $\{\varphi_{ln}(r)\}$ at fixed l is orthonormal

$$\int_0^\infty \varphi_{ln}(r)\, \varphi_{ln'}(r)\, v(r)\, r^2\, dr = \delta_{nn'} \tag{24}$$

and complete

$$v(r)\sum_n \varphi_{ln}(r)\,\varphi_{ln}(r') = \frac{1}{r^2}\,\delta(r-r'). \tag{25}$$

For the zeroth-order Green function $G^0(\mathbf{r}-\mathbf{r}')$ the following expansion is valid (see, e.g., Ref. [12, 13]):

$$\begin{aligned} G^0(\mathbf{r}-\mathbf{r}') &= -\frac{\exp(-\varkappa|\mathbf{r}-\mathbf{r}'|)}{4\pi|\mathbf{r}-\mathbf{r}'|} = \sum_{\lambda lm} G_l^0(r,r')Y_{lm}^{(\lambda)}(\mathbf{n})Y_{lm}^{(\lambda)}(\mathbf{n}')\,, \\ G_l^0(r,r') &= -\frac{2\varkappa}{\pi}\,\left\{k_l(\varkappa r)i_l(\varkappa r')\theta(r-r') + i_l(\varkappa r)k_l(\varkappa r')\theta(r'-r)\right\}. \end{aligned} \tag{26}$$

Here

$$k_l(x) = \sqrt{\frac{\pi}{2x}}\,K_{l+1/2}(x)\,, \quad i_l(x) = \sqrt{\frac{\pi}{2x}}\,I_{l+1/2}(x)\,,$$

where $K_\nu(x)$ – Macdonald function and $I_\nu(x)$ – Bessel function of the imaginary argument; $\theta(x)=1$ if $x>0$ and $\theta(x)=0$ if $x<0$.

Substitution of (22) and (26) in Eq. (13) gives

$$\varphi_{ln}(r) = \alpha_{ln}\int_0^\infty G_l^0(r,r')\,\varphi_{ln}(r')\,v(r')\,(r')^2\,dr'. \tag{27}$$

In the case when $x\to\infty$ we have $k_l(x) \approx \pi(2x)^{-1}\exp(-x)$ so that from (27) the following expression one can get

$$\begin{aligned} r\to\infty\,:\;\; \varphi_{ln}(r) &\approx -\frac{\alpha_{ln}u_{ln}(\varkappa)}{4\pi}\,\frac{e^{-\varkappa r}}{r}\,, \\ u_{ln}(\varkappa) &= 4\pi\int_0^\infty i_l(\varkappa r)\,\varphi_{ln}(r)\,v(r)\,r^2\,dr. \end{aligned} \tag{28}$$

Correspondingly if $r\to 0$ then $\varphi_{ln}(r)\propto i_l(\varkappa r)\propto r^l$. It is evident that values $u_{ln}/(4\pi)$ is the expansion coefficients of function $i_l(\varkappa r)$ according to system $\{\varphi_{ln}(r)\}$ and hence

$$i_l(\varkappa r) = \frac{1}{4\pi}\sum_n u_{ln}(\varkappa)\,\varphi_{ln}(r)$$

with $\varphi_{ln}(r)$ at $\varepsilon = -\varkappa^2$.

Taking into account (22), from Eq. (8) we have

$$\int_0^\infty [\varphi_{ln}(r)]^2\;r^2\,dr = \frac{d\alpha_{ln}}{d\varepsilon}.$$

For the radial wave function $R_{ln}(r)$ of bound-state with energy ε_{ln} from Eqs (20), (21) we found

$$\begin{aligned} & R_{ln}(r) = C_{ln}\,\varphi_{ln}(\varepsilon_{ln};r)\,, \quad C_{ln} = \left[\frac{d\varepsilon_{ln}(\alpha)}{d\alpha}\right]^{1/2}; \\ r\to\infty\,:\; & R_{ln}(r) \approx A_{ln}\,\frac{e^{-\varkappa_{ln}\,r}}{r}\,, \quad A_{ln} = -\,C_{ln}\,\left[\frac{\alpha_{ln}\,u_{ln}}{4\pi}\right]_{\varepsilon=\varepsilon_{ln}}. \end{aligned} \tag{29}$$

For the radial Green function the following expansion is valid

$$G_l(r,r') = \sum_n \frac{\varphi_{ln}(r)\,\varphi_{ln}(r')}{\alpha_{ln}-\alpha}\,.$$

The expansion for zeroth-order Green function $G_l^0(r,r')$ $\big($see Eq. (26)$\big)$ is obtained from this expression at $\alpha = 0$.

5. States with zero energy

Before analyzing the important case of small energies, the basic properties of states with $\varepsilon = 0$ should be established. The eigenfunctions $\zeta_\nu(\mathbf{r}) = \varphi_\nu(0;\mathbf{r})$ and eigenvalues $\lambda_\nu = \alpha_\nu(0)$ corresponding to zero-energy states satisfy the equation obtained from (2) at $\varepsilon \to 0$:

$$\nabla^2\zeta_\nu(\mathbf{r}) = \lambda_\nu v(\mathbf{r})\zeta_\nu(\mathbf{r}). \tag{30}$$

Assume that $\nabla\zeta_\nu(\mathbf{r}) \to 0$ at $r\to\infty$. Under this assumption, a standard analysis can be applied to (30) to demonstrate that $\zeta_\nu(\mathbf{r})$ and $\zeta_\mu(\mathbf{r})$ are orthogonal with the weight function $v(\mathbf{r})$ if $\lambda_\nu \neq \lambda_\mu$. Therefore, an orthonormality condition analogous to (5) is valid:

$$\int \zeta_\nu(\mathbf{r})\,\zeta_\mu(\mathbf{r})\,v(\mathbf{r})\,d\mathbf{r} = \delta_{\nu\mu}. \tag{31}$$

It is also natural to assume that the completeness condition (7) valid for $\varepsilon \neq 0$ holds at $\varepsilon \to 0$:

$$v(\mathbf{r})\sum_\nu \zeta_\nu(\mathbf{r})\,\zeta_\nu(\mathbf{r}') = \delta(\mathbf{r}-\mathbf{r}'). \tag{32}$$

Note that the potential amplitudes U_ν^0 corresponding to λ_ν are the critical values of well depth when zero-energy states appear (or disappear).

If $\varkappa \to 0$ then Eq.(13) reduces to

$$\zeta_\nu(\mathbf{r}) = -\,\frac{\lambda_\nu}{4\pi}\int \frac{1}{|\mathbf{r}-\mathbf{r}'|}\,\zeta_\nu(\mathbf{r}')\,v(\mathbf{r}')\,d\mathbf{r}'. \tag{33}$$

If $v(\mathbf{r})$ is sufficiently rapidly decreasing (e.g., exponentially) function at $r\to\infty$, then from (33) it follows that

$$r\to\infty\,:\; \zeta_\nu(\mathbf{r}) \approx \frac{Q_\nu}{r} + \frac{(\mathbf{r}\mathbf{d}_\nu)}{r^3} + \frac{(\mathbf{r}\hat{D}_\nu\mathbf{r})}{2r^5} + \cdots. \tag{34}$$

Here

$$Q_\nu = \int \rho_\nu(\mathbf{r})\, d\mathbf{r}\,, \quad \mathbf{d}_\nu = \int \mathbf{r}\, \rho_\nu(\mathbf{r})\, d\mathbf{r}\,, \quad D_\nu^{\alpha\beta} = \int (3x_\alpha x_\beta - r^2\delta_{\alpha\beta})\, \rho_\nu(\mathbf{r})\, d\mathbf{r}\,, \ldots$$

are analogues of electrostatic charge, dipole moment, tensor of quadrupolar moment, etc. and

$$\rho_\nu(\mathbf{r}) = -\frac{\lambda_\nu}{4\pi}\, \zeta_\nu(\mathbf{r})\, v(\mathbf{r})$$

– appropriate "density of charge". If $\varkappa \to 0$, then from Eq. (14) the expression for Q_ν follows:

$$Q_\nu = -\frac{1}{4\pi}\, \lambda_\nu\, u_\nu^{(0)}\,, \tag{35}$$

where $u_\nu^{(0)}$ – value $u_\nu(\mathbf{n}, \varkappa)$ from (14) at $\varkappa = 0$. For introduced quantities we have estimations: $|u_\nu^{(0)}| \sim a^{3/2}$, $|Q_\nu| \sim a^{-1/2}$, $|\mathbf{d}_\nu| \sim a^{1/2}$, $|\hat{D}_\nu| \sim a^{3/2}, \ldots$, where a is the "effective radius" of potential.

In the case of spherically symmetrical potentials and in the limits of $\varkappa \to 0$ from Eq. (23) and Eq. (27) we obtain

$$\zeta_{ln}''(r) + \frac{2}{r}\, \zeta_{ln}'(r) - \frac{l(l+1)}{r^2}\, \zeta_{ln}(r) = \lambda_{ln} v(r)\, \zeta_{ln}(r), \tag{36}$$

$$\zeta_{ln}(r) = \lambda_{ln} \int_0^\infty g_l^0(r, r')\, \zeta_{ln}(r')\, v(r')\, (r')^2\, dr', \tag{37}$$

where

$$g_l^0(r, r') = \lim_{\varkappa \to 0} G_l^0(r, r') = -\frac{1}{2l+1} \left\{ \frac{(r')^l}{r^{l+1}}\, \theta(r - r') + \frac{r^l}{(r')^{l+1}}\, \theta(r' - r) \right\}. \tag{38}$$

In (36), (37) $\zeta_{ln}(r)$ is the value of radial function $\varphi_{ln}(r)$ at $\varepsilon = 0$. From (37), (38) it follows that $\zeta_{ln}(r) \propto r^l$ at $r \to 0$ and

$$r \to \infty : \ \zeta_{ln}(r) \approx \frac{b_{ln}}{r^{l+1}}\,; \quad b_{ln} = -\frac{\lambda_{ln}}{2l+1} \int_0^\infty \zeta_{ln}(r)\, v(r)\, r^{l+2}\, dr. \tag{39}$$

The integral converges in (39) if the function $v(r)$ tends to zero faster then r^{-2} at $r \to \infty$.

For determining the states with zero energy for $n \gg 1$ in case of spherically symmetric potentials the semiclassical approximation can be used which is analogous to the standard approach [1]. At the same time at $\varepsilon = 0$ the WKB-method has the specific feature as there is no "outer region" in this case. Note that the semiclassical approximation becomes invalid at $r \to \infty$ and here it is necessary to use the exact solution of Eq. (36) with $v(r)$ given by an asymptotic expression.

Let us examine the model potential with $v(0) = 1$ characterized by the following asymptotic behavior

$$\gamma\, r \gg 1 : \quad v(r) \approx v_\infty\, e^{-2\gamma r}, \tag{40}$$

where $v_\infty \sim 1$ and $\gamma \sim 1/a$. Then for $l = 0$ and $n \gg 1$ the semiclassical expression for $\zeta_{0n}(r)$ (valid for $\exp(-\gamma r) \gg 1/n$) has the form

$$\zeta_{0n}(r) = \frac{1}{r}\sqrt{\frac{2}{b}}\,\frac{(-1)^n}{\sqrt[4]{v(r)}}\,\sin\left\{\sqrt{|\lambda_{0n}|}\int_0^r \sqrt{v(t)}\,dr\right\}. \tag{41}$$

The exact solution of Eq. (36) with potential (40) is

$$\zeta_{0n}(r) = \frac{Q_n}{r}\,J_0\left(\mu_n\,e^{-\gamma r}\right)\,,\ \mu_n = \frac{1}{\gamma}\sqrt{|\lambda_{0n}|\,v_\infty} \tag{42}$$

for $\exp(-\gamma r) \ll 1$. Here $Q_n = b_{0n}$ (see Eq. (39)), $J_0(z)$ – Bessel function and

$$b = \int_0^\infty \sqrt{v(r)}\,dr,$$

where $b \sim a$.

By matching the expressions (41) and (42) in region $1/n \ll \exp(-\gamma r) \ll 1$ we find the quantization rule

$$\int_0^\infty \sqrt{|\lambda_{0n}|\,v(r)} = \left(n + \frac{3}{4}\right)\pi\,,$$

which yields

$$\lambda_{0n} \simeq -\,n\left(n + \frac{3}{2}\right)\left(\frac{\pi}{b}\right)^2\,,\ (n \gg 1) \tag{43}$$

In (43) a term $\sim n^0$ is neglected since its exact calculation requires that a term $\sim 1/n$ be retained in the quantization rule. For values $Q_n = b_{0n}$ and $u_{0n}^{(0)}$ we find

$$Q_n = \frac{\pi}{b}\sqrt{\frac{1}{4\pi\gamma}\left(n + \frac{3}{4}\right)}\,,\ u_{0n}^{(0)} = \frac{2b}{\sqrt{\pi\gamma}}\,\frac{1}{(n+3/4)^{3/2}}\,. \tag{44}$$

From (43), (44) for $n \gg 1$ the next estimations are true: $|\lambda_{0n}| \sim (n/a)^2$, $Q_n \sim (n/a)^{1/2}$, $u_{0n}^{(0)} \sim (a/n)^{3/2}$.

6. States with small energies

Now, let us examine the properties of the eigenfunctions $\varphi_\nu(\mathbf{r})$ and eigenvalues α_ν corresponding to small absolute values of energies $\varepsilon\,(\varkappa a \ll 1)$. For states, having for $\varkappa = 0$ monopole asymptotic form ("s-states"), the solution to Eq. (2) at $r \gg a$ (when the r.h.s. of (2) can be neglected) is $\mathrm{const}\cdot r^{-1}\exp(-\varkappa r)$. By matching this expression and the asymptotic form $\zeta_\nu(\mathbf{r}) \eqsim Q_\nu/r$ in region $a \ll r \ll 1/\varkappa$ yields $\mathrm{const} = Q_\nu$ so that

$$r \gg a\,:\ \varphi_\nu^{(s)}(\mathbf{r}) \eqsim Q_\nu\,\frac{e^{-\varkappa r}}{r}\,. \tag{45}$$

To calculate the linear in $\varkappa$ term of $\alpha_\nu^{(s)}$ we use the formula (8). It is easy to see, that the distances $r \gg a$ are essential in the integral from (8) when the expression (45) is right. Substitution of (45) in (8) gives

$$\frac{d\alpha_\nu^{(s)}}{d\varepsilon} \simeq \frac{1}{\varkappa}\, 2\pi Q_\nu^2\,,$$

and it follows

$$\alpha_\nu^{(s)} = \lambda_\nu^{(s)} - 4\pi Q_\nu^2 \cdot \varkappa + \cdots\,. \tag{46}$$

Let us examine s-state in the case of spherically symmetric potential in more details. Substitution of

$$\varphi_{0n}(r) = \Phi_n(r)\,\frac{e^{-\varkappa r}}{r} \tag{47}$$

in Eq. (23) (with $l = 0$ and $\varepsilon = -\varkappa^2$) gives an equation for $\Phi_n(r)$:

$$\Phi_n''(r) - 2\varkappa\,\Phi_n'(r) = \alpha_{0n} v(r)\,\Phi_n(r). \tag{48}$$

The value $\Phi_n(r)$ at small $\varkappa$ ($\varkappa a \ll 1$) can be found as an expansion in the zero-energy eigenfunction basis $\{\eta_{0n}(r)\}$ which is introduced according to:

$$\zeta_{0n}(r) = \frac{1}{r}\,\eta_{0n}(r)$$

and satisfies the equation

$$\eta_{0n}''(r) = \lambda_{0n} v(r)\,\eta_{0n}(r), \tag{49}$$

where $\eta_{0n}(0) = 0$. The eigenfunctions $\eta_{0n}(r)$ constitute the orthonormal and complete set:

$$\int_0^\infty \eta_{0n}(r)\,\eta_{0m}(r)\,v(r)\,dr = \delta_{nm}\,, \quad v(r)\sum_n \eta_{0n}(r)\,\eta_{0n}(r') = \delta(r-r'). \tag{50}$$

Substituting an expansion

$$\Phi_n(r) = \sum_k \Phi_{nk}\,\eta_{0k}(r) \tag{51}$$

into Eq. (48), multiplying the obtained equation by $\eta_{0m}(r)$, integrating the result from 0 to ∞, and making use of (49) and (50), we finally obtain

$$(\alpha_{0n} - \lambda_{0m})\,\Phi_{nm} = -\,2\varkappa \sum_k \Phi_{nk}\,M_{mk}\,, \tag{52}$$

$$M_{mn} = \int_0^\infty \eta_{om}(r)\,\eta_{0n}'(r)\,dr = Q_m Q_n - \int_0^\infty \eta_{0m}'(r)\,\eta_{0n}(r)\,dr. \tag{53}$$

Considering a sum and a difference of the values M_{mn} and M_{nm}, we can be rewritten M_{mn} as

$$M_{mn} = \frac{1}{2}\, Q_m Q_n + \frac{1}{2}\,(\lambda_{0m} - \lambda_{0n}) \int_0^\infty r\, \zeta_{0m}(r)\, \zeta_{0n}(r)\, v(r)\, dr. \tag{54}$$

For derivation (54) we used the Eq. (49); here $Q_n = b_{0n}$ – see Eq. (39). Putting $m = n$ in (54), we obtain

$$M_{nn} = \frac{1}{2}\, Q_n^2. \tag{55}$$

When $\varkappa$ is small, system (52) can be solved by a perturbation method using the series expansions in power of $\varkappa$:

$$\alpha_{0n} = \lambda_{0n} + \alpha_{0n}^{(1)} + \alpha_{0n}^{(2)} + \cdots\ ;\ \Phi_{nm} = \delta_{nm} + \Phi_{nm}^{(1)} + \Phi_{nm}^{(2)} + \cdots\ .$$

In the linear in $\varkappa$ approximation, Eq. (52) yields

$$\alpha_{0n}^{(1)} = -\,2\varkappa\, M_{nn} = -\,\varkappa\, Q_n^2. \tag{56}$$

This expression is identical to the result (46), since in the spherically symmetric case we have $Q_\nu \Longrightarrow Q_n\, Y_{00}^{(1)} = Q_n/\sqrt{4\pi}$. In the same approximation we obtain

$$n \neq m\ :\ \Phi_{nm}^{(1)} = -\,2\varkappa\, \frac{M_{mn}}{\lambda_{0n} - \lambda_{0m}}\,. \tag{57}$$

In the linear approximation, orthonormality condition (7) yields

$$\Phi_{nm}^{(1)} + \Phi_{mn}^{(1)} = 2\varkappa \int_0^\infty r\, \eta_{0n}(r)\, \eta_{0m}(r)\, v(r)\, dr \tag{58}$$

and hence

$$\Phi_{nn}^{(1)} = \varkappa\, <r>_n\,, \quad <r>_n = \int_0^\infty r\ [\eta_{0n}(r)]^2\ v(r)\, dr. \tag{59}$$

It can be readily shown that relation (58) holds for $\Phi_{nm}^{(1)}$ given by Eq. (57) with M_{nm} defined by (54).

In the quadratic in $\varkappa$ approximation, we have

$$\alpha_{0n}^{(2)} = -\,\varkappa^2\, \beta_{0n}\,, \quad \beta_{0n} = -\,4 \sum_{m \neq n} \frac{M_{nm}\, M_{mn}}{\lambda_{0n} - \lambda_{0m}}\,, \tag{60}$$

where M_{nm} is defined in (53) and (54).

Substitution of the expression $\alpha_{0n} = \lambda_{0n} + \alpha_{0n}^{(1)}$ with $\alpha_{0n}^{(1)}$ from (56) in the equation $\alpha_{0n}(\varepsilon) = \alpha$ permits to find the energy of weakly bound s-state $(\varkappa_{0n} a \ll 1)$:

$$\varepsilon_{0n} = -\,\varkappa_{0n}^2\,, \quad \varkappa_{0n} = \frac{\lambda_{0n} - \alpha}{Q_n^2}\,. \tag{61}$$

The energy level (61) is real at $|\alpha| > |\lambda_{0n}|$. For the radial wave function of this bound s-state in the same approximation we have

$$R_{0n}(r) = \left[\frac{d\varepsilon_{0n}}{d\alpha}\right]^{1/2} \cdot \varphi_{0n}(\varepsilon_{0n}\,;\, r) = \frac{\sqrt{2\varkappa_{0n}}}{Q_n}\,\zeta_{0n}(r)\,e^{-\,\varkappa_{0n}r}\,.$$

From this at $r \gg a$ for the total wave function $\psi_{100n}(\mathbf{r}) = R_{0n}(r)\,Y_{00}^{(1)}(\mathbf{n})$ of a weakly bound s-state we obtain the expression

$$\psi_\nu^{(s)}(\mathbf{r}) \Longrightarrow \psi_{100n}(\mathbf{r}) \eqsim \sqrt{\frac{\varkappa_{0n}}{2\pi}}\;\frac{e^{-\,\varkappa_{0n}r}}{r}\,, \tag{62}$$

which agree with [1].

7. States with large $|E|$

As $|\varepsilon| \to \infty$, the values of $|\alpha_\nu|$ increase indefinitely. According to (10), the growth of $|\alpha_\nu|$ cannot be faster than linear in $|\varepsilon|$. However, if $v(\mathbf{r})$ is finite at any $\mathbf{r}$, then $|\alpha_\nu|$ cannot grow slower than $|\varepsilon|$, since a state with sufficiently large $|\varepsilon|$ cannot otherwise "be located" in the potential well. Thus, $|\alpha_\nu|$ scales linearly with $|\varepsilon|$ at $|\varepsilon| \to \infty$. If the potential function has a minimum at $r = 0$ and $v(0) = 1$, then the corresponding scaling factor is unity, and we have (for $\varepsilon = -\,\varkappa^2$)

$$\varepsilon \to -\infty\;:\;\alpha_\nu = -\,\varkappa^2\,(1 + \Delta_\nu + \cdots)\,, \tag{63}$$

where $|\Delta_\nu| \ll 1$. To calculate Δ_ν, we note that the value of α_ν is determined by the behavior of $v(\mathbf{r})$ in the vicinity of $\mathbf{r} = 0$ at $|\varepsilon| \to \infty$. Suppose that, at $r \to 0$,

$$v(r) \approx 1 - r^2\delta^2\,,\ (r \ll 1/\delta), \tag{64}$$

where $\delta \sim 1/a$. Thus, the eigenvalue problem is reduced to the spherical harmonic oscillator problem (see [1], §36, task 4). In this approximation we have

$$\alpha_{ln} \simeq -\,\varkappa^2(1 + \Delta_{ln})\,,\ \Delta_{ln} = (4n + 2l + 3)\,\frac{\delta}{\varkappa}\,;\ (n = 0, 1, 2, \ldots)\,; \tag{65}$$

$$\varphi_{ln}(r) = A_{ln}\,r^l\,\exp\left\{-\,(\varkappa\delta/2)r^2\right\}\,F\left(-\,n, l + {}^3\!/_2\,;\, r^2\varkappa\delta\right), \tag{66}$$

where $F(\alpha, \gamma; z)$ is a degenerate hypergeometric function (see, e.g., [1,12]). The oscillator approximation (65), (66) is valid if the correction term Δ_{ln} is much smaller than unity, i.e., if $\varkappa \gg (4n + 2l + 3)\delta$ or, since $\delta \sim 1/a\;:\;\varkappa a \gg 4n + 2l + 3$. The second condition of applicability is $r \ll 1/\delta \sim a$.

Below we restrict the discussion to the case of $l = 0$, when the radial eigenfunction $\varphi_{0n}(r)$ at $r \ll 1/\delta$ is given by

$$\varphi_{0n}(r) = \frac{1}{2^n}\,\left(\frac{\varkappa\delta}{\pi}\right)^{1/4}\,\frac{1}{\sqrt{(2n+1)!}}\cdot\frac{1}{r}\,\exp\left\{-\,(\varkappa\delta/2)r^2\right\}\,H_{2n+1}\left(\sqrt{\varkappa\delta}\,r\right)\,, \tag{67}$$

where $H_n(z)$ is a Hermitian polynomial. To find $\varphi_{0n}(r)$ at $r \gtrsim 1/\delta$ a semiclassical approximation is used:

$$
\begin{gathered}
r \gg r_0 \,:\; \varphi_{0n}(r) = \frac{1}{r}\,\frac{D_n}{\sqrt{k(r)}}\cdot\exp\left\{-\int\limits_{r_0}^{r} k(t)\,dt\right\}\,; \\
k(r) = \varkappa\,\left[1-(1+\Delta_{0n})\;v(r)\right]^{1/2}\,,\; r_0 = \frac{\sqrt{\Delta_{0n}}}{\delta}\,,
\end{gathered}
\tag{68}
$$

where $r_0 \ll 1/\delta$. By matching the expressions (67) and (68) in the region $r_0 \ll r \ll 1/\delta$ we find the coefficient D_n:

$$
D_n = \left(\frac{2}{\pi}\right)^{1/4}\sqrt{\frac{\varkappa\delta}{(2n+1)!}}\,\left(\frac{4n+3}{2e}\right)^{n+3/4}\,. \tag{69}
$$

It should be emphasized that semiclassical approximation (68), (69) is valid for any n such that $4n+3 \ll \varkappa/\delta$, including $n=0$.

At $r\to\infty$, the expression for $\varphi_{on}(r)$ from (68), (69) yields (28) (for $l=0$) where

$$
\begin{gathered}
u_{0n}(\varkappa) = \frac{4\pi}{\varkappa^2}\,\left(\frac{2}{\pi}\right)^{1/4}\sqrt{\frac{\delta}{(2n+1)!}}\,\left(\frac{2\varkappa}{\delta}\right)^{n+3/4}\cdot\exp\left\{\frac{\varkappa}{\delta}\left(I_1+\frac{\Delta_{0n}}{2}\,I_2\right)\right\}\,; \\
\frac{I_1}{\delta} = \int_0^\infty\left[1-\sqrt{1-v(r)}\right]\,dr\,,\quad \frac{I_2}{\delta} = \lim_{s\to 0}\left[\frac{1}{\delta}\,\ln(s\delta)+\int_s^\infty\frac{v(r)\,dr}{\sqrt{1-v(r)}}\right]\,,
\end{gathered}
\tag{70}
$$

and Δ_{0n} is given by (65) (with $l=0$).

8. Perturbation theory

Consider the bound state characterized by wave function $\psi_\nu^{(0)}(\mathbf{r})$ and energy $\varepsilon_\nu^{(0)}$ in potential well $\alpha v(\mathbf{r})$. There is a need to seek $\psi_\nu(\mathbf{r})$ and ε_ν in the case when the Hamiltonian contains a small perturbation $V'(\mathbf{r})$. The equation for $\psi_\nu(\mathbf{r})$ is written as

$$
\nabla^2\psi_\nu(\mathbf{r}) + \varepsilon\,\psi_\nu(\mathbf{r}) - \alpha\,v(\mathbf{r})\,\psi_\nu(\mathbf{r}) = V(\mathbf{r})\,\psi_\nu(\mathbf{r})\,;\; V(\mathbf{r}) = \frac{2m}{\hbar^2}\,V'(\mathbf{r})\,.
$$

To find a solution of this equation, the value $\psi_\nu(\mathbf{r})$ is decomposed in the complete set $\{\varphi_\mu(\mathbf{r})\}$ of eigenfunctions defined in Section 2:

$$
\psi_\nu(\mathbf{r}) = \sum_\mu A_{\nu\mu}\,\varphi_\mu(\mathbf{r}).
$$

Each $\varphi_\mu(\mathbf{r})$ satisfies Eq. (2) with ν replaced by μ and at $\varepsilon=\varepsilon_\nu^{(0)}$, where the energy $\varepsilon_\nu^{(0)}$ of the bound state is the solution of Eq. (19). Accordingly, the expression for the bound-state wave function $\psi_\nu^{(0)}(\mathbf{r})$ in terms of $\varphi_\nu(\mathbf{r})$ (corresponding to $\varepsilon=\varepsilon_\nu^{(0)}$) is given by (20).

A calculations, similar to that performed in Ref. [6], for linear and quadratic on $V(\mathbf{r})$ corrections to the energy of the bound state gives

$$\begin{aligned}
&\varepsilon_\nu^{(1)} = (C_\nu)^2 \ < \nu|V|\nu > = \int \psi_\nu(\mathbf{r}) V(\mathbf{r}) \psi_\nu(\mathbf{r})\, d\mathbf{r}\,, \\
&\varepsilon_\nu^{(2)} = -\,(C_\nu)^2 \sum_{\mu\neq\nu} \frac{\Big(< \nu|V|\mu > - \varepsilon_\nu^{(1)} < \nu|\mu > \Big)^2}{\alpha_\nu - \alpha_\mu}\,.
\end{aligned} \tag{71}$$

Here

$$< \nu|\mu > = \int \varphi_\nu(\mathbf{r})\varphi_\mu(\mathbf{r})\, d\boldsymbol{r}\,, \quad < \nu|V|\mu > = \int \varphi_\nu(\mathbf{r}) V(\mathbf{r}) \varphi_\mu(\mathbf{r})\, d\mathbf{r}\,.$$

In Eq. (71) functions $\varphi_\nu(\mathbf{r}), \varphi_\mu(\mathbf{r})$ and the values α_ν, α_μ correspond to the energy $\varepsilon = \varepsilon_\nu^{(0)}$. The expression for $\varepsilon_\nu^{(1)}$, as it must be, is identical to the well-known result (see Ref. [1]). In order to calculate the correction $\varepsilon_\nu^{(2)}$ according to (71), in contrast to the standard approach,it does not require the usage of continuum states (for $E > 0$).

A similar perturbation theory can also be developed for the eigenvalues α_ν and eigenfunctions $\varphi_\nu(\mathbf{r})$. The corresponding equation for $\varphi_\nu(\mathbf{r})$ is

$$\nabla^2 \varphi_\nu(\mathbf{r}) + \varepsilon\, \varphi_\nu(\mathbf{r}) - \alpha_\nu\, v(\mathbf{r}) \varphi_\nu(\mathbf{r}) = V(\mathbf{r}) \varphi_\nu(\mathbf{r})\,.$$

One can see that in this case the orthonormality condition for $\{\varphi_\nu(\mathbf{r})\}$ and the equation for the energy of the bound state hold its forms – see (5) and (19).The linear and quadratic in $V(\mathbf{r})$ corrections to the eigenvalue are given by the following expressions

$$\alpha_\nu^{(1)} = -\ < \nu|V|\nu >\,, \quad \alpha_\nu^{(2)} = -\sum_{\mu\neq\nu} \frac{< \nu|V|\mu >< \mu|V|\nu >}{\alpha_\mu^{(0)} - \alpha_\nu^{(0)}}\,,$$

where $< \nu|V|\mu >$ – the same, as in Eq. (71). Here both the eigenvalues $\alpha_\nu^{(0)}, \alpha_\mu^{(0)}$ and the eigenfunctions $\varphi_\nu(\mathbf{r}), \varphi_\mu(\mathbf{r})$ are determined for $V = 0$ and an arbitrary energy ε. In some cases, it may be easier to calculate corrections to bound-state energies by solving Eq. (19) for $\alpha_\nu = \alpha_\nu^{(0)} + \alpha_\nu^{(1)} + \alpha_\nu^{(2)} + \cdots$.

9. Polarizability

Consider the bound state ν of a point charge e in the uniform electric field of strength E. For this system $V'(\mathbf{r}) = -\,e\,\mathbf{r}E$ and $V(\mathbf{r}) = -\,(2me/\hbar^2)\mathbf{r}E$, and expression for $\varepsilon_\nu^{(2)}$ from (71) (in the case that $< \nu|\mathbf{r}|\nu > = 0$) can be used to find the tensor of polarizability $\hat{\Lambda}$ of this system:

$$\begin{aligned}
&\Lambda_{\alpha\beta}^{(\nu)} = \frac{4me^2}{\hbar^2}\ (C_\nu)^2 \sum_{\mu\neq\nu} \frac{< \nu|x_\alpha|\mu >< \mu|x_\beta|\nu >}{\alpha - \alpha_\mu}\,; \\
&\qquad < \nu|x_\alpha|\mu > = \int \varphi_\nu(\mathbf{r}) x_\alpha \varphi_\mu(\mathbf{r})\, d\mathbf{r}\,.
\end{aligned} \tag{72}$$

Here $(C_\nu)^2 = d\varepsilon_\nu(\alpha)/d\alpha$ $\big($see (20)$\big)$ and both α_ν and $\varphi_\nu(\mathbf{r}), \varphi_\mu(\mathbf{r})$ corresponding to $\varepsilon = \varepsilon_\nu$, where ε_ν is determined by solving the equation $\alpha_\nu(\varepsilon) = \alpha$.

Suppose that there exists only a weakly bound ($\varkappa_\nu a \ll 1$) s-state with energy $\varepsilon_\nu = -\varkappa_\nu^2$ and the corresponding wave function $\psi_\nu^{(s)}(\mathbf{r})$. In order to find the polarizability of such system rewrite (72) as

$$\Lambda = -\frac{4me^2}{\hbar^2}\int d\mathbf{r}\, z\, \psi_\nu^{(s)}(\mathbf{r}) \int d\mathbf{r}'\, z'\, \psi_\nu^{(s)}(\mathbf{r}') \sum_{\mu\neq\nu} \frac{\varphi_\mu(\mathbf{r})\varphi_\mu(\mathbf{r}')}{\alpha_\mu - \alpha}\,,$$

where E is aligned parallel to z–axis and it is taken into account that $C_\nu\varphi_\nu(\varepsilon_\nu;\mathbf{r}) = \psi_\nu^{(s)}(\mathbf{r})$. Using representation (17) for $G^0(\mathbf{r}-\mathbf{r}')$, we rearrange the sum contained in this expression as follows:

$$\sum_{\mu\neq\nu} \frac{\varphi_\mu(\mathbf{r})\varphi_\mu(\mathbf{r}')}{\alpha_\mu - \alpha} = G^0(\mathbf{r}-\mathbf{r}') - \frac{\varphi_\nu(\mathbf{r})\varphi_\nu(\mathbf{r}')}{\alpha_\nu} + \alpha \sum_{\mu\neq\nu} \frac{\varphi_\mu(\mathbf{r})\varphi_\mu(\mathbf{r}')}{\alpha_\mu(\alpha_\mu - \alpha)}\,,$$

where $G^0(\mathbf{r}-\mathbf{r}')$ – the zeroth-order Green function $\big($see Eq. (12)$\big)$. The second term in the r.h.s. of this equality does not contribute to Λ (since $< \nu|\mathbf{r}|\nu >= 0$), and the third term is smaller than the first one by the factor $(\varkappa_\nu a)^2 \ll 1$. Thus,

$$\Lambda \simeq -\frac{4me^2}{\hbar^2}\int d\mathbf{r}\, z\, \psi_\nu^{(s)}(\mathbf{r}) \int d\mathbf{r}'\, z'\, \psi_\nu^{(s)}(\mathbf{r}')\, G^0(\mathbf{r}-\mathbf{r}')\,. \tag{73}$$

At $\varkappa_\nu \to 0$ the intervals $r \gg a$ and $r' \gg a$ make the main contributions to these integrals. Therefore, the expression (62) (with replacement $\varkappa_{0n}$ by $\varkappa_\nu$) may be used as $\psi_\nu^{(s)}(\mathbf{r})$. In this case substitution of (26) in Eq. (73) is allowed (since $z = r\sqrt{4\pi/3}\, Y_{10}^{(1)}$) to carry out integration over angles

$$\Lambda \simeq -\frac{4me^2}{\hbar^2}\cdot\frac{4\pi}{3}\int_0^\infty r^3 dr \psi_\nu^{(s)}(r) \int_0^\infty (r')^3 dr' \psi_\nu^{(s)}(r') G_1^0(r,r')\,,$$

where $G_1^0(r,r')$ – the partial radial Green function from (26) at $l = 1$. And finally, substitution of (26) (at $l = 1$) and (62) (at $\varkappa_{0n} \Longrightarrow \varkappa_\nu$) into this expression gives

$$\Lambda \simeq \frac{me^2}{4\hbar^2\varkappa_\nu^4}\,,$$

that coincide with the result obtained in Ref. [1] (§76, task 5).

10. Two-center problem

A peculiar perturbation theory can be developed to find the bound states of a particle interacting with the field generated by two identical potential wells separated by a distance $R \gg a$. Denote their centers by $\mathbf{r}_1$ and $\mathbf{r}_2$ ($\mathbf{R} = \mathbf{r}_1 - \mathbf{r}_2$). The eigenfunctions $\varphi_\mu(\mathbf{r})$ and the eigenvalues α_μ in the two-center problem satisfy the equation

$$\nabla^2\varphi_\mu(\mathbf{r}) + \varepsilon\,\varphi_\mu(\mathbf{r}) = \alpha_\mu\,\left[v(\mathbf{r}-\mathbf{r}_1) + v(\mathbf{r}-\mathbf{r}_2)\right]\,\varphi_\mu(\mathbf{r}). \tag{74}$$

The eigenfunctions $\varphi_\nu^{(i)}(\mathbf{r}) \equiv \varphi_\nu(\mathbf{r}-\mathbf{r}_i)$ and the eigenvalues α_ν corresponding to the i-th isolated well obey Eq. (2) with replacement $\mathbf{r} \to \mathbf{r}-\mathbf{r}_i$.

It is reasonable to seek $\varphi_\mu(\mathbf{r})$ in the form

$$\varphi_\mu(\mathbf{r}) = \sum_\lambda \left\{ A_{\mu\lambda}\, \varphi_\lambda^{(1)}(\mathbf{r}) + B_{\mu\lambda}\, \varphi_\lambda^{(2)}(\mathbf{r}) \right\} . \tag{75}$$

Substituting (75) into (74), multiplying the obtained equation by $\varphi_\nu^{(1)}(\mathbf{r}) = \varphi_\nu(\mathbf{r}-\mathbf{r}_1)$, integrating the result over all space, and performing similar operations for $\varphi_\nu^{(2)}(\mathbf{r}) = \varphi_\nu(\mathbf{r}-\mathbf{r}_2)$, we obtain a set of equations for the coefficients $A_{\mu\nu}$ and $B_{\mu\nu}$:

$$\begin{aligned} (\alpha_\nu-\alpha_\mu)A_{\mu\nu} + \sum_\lambda (\alpha_\lambda-\alpha_\mu)B_{\mu\lambda}J_{\lambda\nu}^{(1)}(-\mathbf{R}) &= \alpha_\mu \sum_\lambda \left\{ A_{\mu\lambda}J_{\nu\lambda}^{(2)}(-\mathbf{R}) + B_{\mu\lambda}J_{\nu\lambda}^{(1)}(\mathbf{R}) \right\} , \\ \sum_\lambda (\alpha_\lambda-\alpha_\mu)A_{\mu\lambda}J_{\lambda\nu}^{(1)}(\mathbf{R}) + (\alpha_\nu-\alpha_\mu)B_{\mu\nu} &= \alpha_\mu \sum_\lambda \left\{ A_{\mu\lambda}J_{\nu\lambda}^{(1)}(-\mathbf{R}) + B_{\mu\lambda}J_{\nu\lambda}^{(2)}(\mathbf{R}) \right\} . \end{aligned} \tag{76}$$

Here

$$J_{\nu\lambda}^{(1)}(\pm\mathbf{R}) = \int \varphi_\nu(\mathbf{r})\varphi_\lambda(\mathbf{r}\pm\mathbf{R})v(\mathbf{r})\,d\mathbf{r},\ J_{\nu\lambda}^{(2)}(\pm\mathbf{R}) = \int \varphi_\nu(\mathbf{r}\pm\mathbf{R})\varphi_\lambda(\mathbf{r}\pm\mathbf{R})v(\mathbf{r})\,d\mathbf{r} . \tag{77}$$

Since $R \gg a$, asymptotic expression (14) for $\varphi_\nu(\mathbf{r})$ can be used to obtain

$$\begin{aligned} R\to\infty: \qquad J_{\nu\lambda}^{(1)}(\pm\mathbf{R}) &\approx -\frac{\alpha_\lambda\, u_\lambda(\pm\mathbf{N},\varkappa)\, u_\nu(\mp\mathbf{N},\varkappa)}{4\pi}\cdot\frac{e^{-\varkappa R}}{R}\,; \\ J_{\nu\lambda}^{(2)}(\pm\mathbf{R}) &\approx \frac{\alpha_\nu\, u_\nu(\pm\mathbf{N},\varkappa)}{4\pi}\,\frac{\alpha_\lambda\, u_\lambda(\pm\mathbf{N},\varkappa)}{4\pi}\cdot\frac{e^{-2\varkappa R}}{R^2}\int e^{\mp 2\varkappa\mathbf{N}\mathbf{r}}\, v(\mathbf{r})\,d\mathbf{r}, \end{aligned} \tag{78}$$

where $\mathbf{N} = \mathbf{R}/R$. In the case of short-range potentials $v(\mathbf{r})$ with asymptotic behavior described by (40), these potentials can be treated as non-overlapping if $\varkappa < \gamma \sim 1/a$. Note also that this condition ensures that the integral in (78) converges.

Consider a state μ "close" to the unperturbed state ν. Assuming that $R \gg a$, we can neglect the terms containing $(\alpha_\nu-\alpha_\mu)J_{\nu\nu}^{(1)}$ and $J_{\nu\nu}^{(2)}$ in (76), as well as the summands with $\lambda \neq \nu$, since they are proportional to $R^{-2}\exp(-2\varkappa R)$. As the result, Eq. (76) gives two solutions $\alpha_{\nu\sigma}$ $(\sigma = 1,2)$ for α_μ (where $\mu \Rightarrow \nu\sigma$), which correspond to $B_{\nu\sigma,\,\nu}/A_{\nu\sigma,\,\nu} = -(-1)^\sigma$:

$$\alpha_{\nu\sigma}(\mathbf{R}) = \alpha_\nu \left\{ 1 - \frac{(-1)^\sigma}{4\pi}\,\alpha_\nu\, u_\nu(\mathbf{N},\varkappa)\, u_\nu(-\mathbf{N},\varkappa)\,\frac{e^{-\varkappa R}}{R} \right\} . \tag{79}$$

The value $\sigma = 1$ corresponds to symmetrical, and $\sigma = 2$ – to antisymmetrical combination of the "atomic" eigenfunctions. Higher order corrections to (79) can be obtained in a consistent manner by taking into account the neglected terms in (76).

Substituting (79) into Eq. (19), we find the corresponding energy levels:

$$\varepsilon_{\nu\sigma}(\mathbf{R}) = \varepsilon_\nu + (-1)^\sigma\, 4\pi\, A_\nu(\mathbf{N})\, A_\nu(-\mathbf{N})\,\frac{e^{-\varkappa_\nu R}}{R} . \tag{80}$$

Here $A_\nu(\mathbf{n})$ are the coefficient in the asymptotic expression for the bound-state wave function $\psi_\nu(\mathbf{r})$ given by (21) in the case of an isolated potential well with $\varepsilon_\nu = -\varkappa_\nu^2$ determined by solving the equation $\alpha_\nu(\varepsilon) = \alpha$. Energy levels (80) are associated with the wave functions

$$\psi_{\nu\sigma}(\mathbf{r}) = \frac{1}{\sqrt{2}} \left\{\psi_\nu(\mathbf{r}-\mathbf{r}_1) - (-1)^\sigma \psi_\nu(\mathbf{r}-\mathbf{r}_2)\right\} ,$$

which are identical to those used in the standard analysis of the two-center problem [1].

It is possible that isolated potential well has no real level, but a virtual one, so that the bound state is absent. At the same time in a potential field of two such wells (even at $R \gg a$) the real level can appear. A solution of the corresponding problem having the certain difficulties at standard method [1] can be easily obtained from (79). Let us assume that $|\alpha| < |\lambda_\nu|$ therewith $|\alpha - \lambda_\nu| \ll |\lambda_\nu|$. At $\sigma = 1$ and $\varkappa \to 0$, it follows from (79) that

$$\lambda_{\nu 1} = \lambda_\nu + \frac{(\lambda_\nu u_\nu^{(0)})^2}{4\pi R} = \lambda_\nu + \frac{4\pi Q_\nu^2}{R} .$$

Therefore, at the condition

$$|\alpha| > |\lambda_\nu| - \frac{(\lambda_\nu u_\nu^{(0)})^2}{4\pi R} = |\lambda_\nu| - \frac{4\pi Q_\nu^2}{R}$$

bound state appear in such system.

For spherically symmetrical potentials this inequality takes the form

$$|\alpha| > |\lambda_{0n}| - \frac{Q_n^2}{R}$$

or, taking into account the definition of value $\varkappa_{0n}$ from (61),

$$R < -\frac{1}{\varkappa_{0n}} ,$$

what is consistent with the result obtained in Ref. [2]. The r.h.s. of this inequality is positive, since $\varkappa_{0n} < 0$ for the considered virtual case.

11. Elastic scattering of slow particles

Let us consider a plane wave $\exp(ikz)$ falling on the spherically symmetrical potential $\alpha v(r)$. Substituting the wave function $\psi(\mathbf{r})$ as

$$\psi(\mathbf{r}) = e^{ikz} + \varphi(\mathbf{r})$$

in the Schrödinger Eq. (1) (at $\varepsilon = k^2 > 0$), we obtain the nonuniform equation

$$\nabla^2\varphi(\mathbf{r}) + k^2\varphi(\mathbf{r}) - \alpha v(r)\varphi(\mathbf{r}) = \alpha v(r) e^{ikz} \tag{81}$$

for "response" function $\varphi(\mathbf{r})$. The expansion of the plane wave is [1]

$$e^{ikz} = \sum_{l=0}^{\infty} i^l (2l+1) P_l(\cos\theta) j_l(kr),$$

where $j_l(z)$ – spherical Bessel function. Therefore, we can find the value $\varphi(\mathbf{r})$ in the form

$$\varphi(\mathbf{r}) = \sum_{l=0}^{\infty} i^l (2l+1) P_l(\cos\theta) R_l(r),$$

so that for the radial function $R_l(r)$ we have

$$R_l''(r) + \frac{2}{r} R_l'(r) + \left[k^2 - \frac{l(l+1)}{r^2}\right] R_l(r) - \alpha v(r) R_l(r) = \alpha v(r) j_l(kr). \tag{82}$$

For the slow particles $(ka \ll 1)$ the main contribution to the scattering amplitude gives states with $l = 0$ [1]. Therefore, we shall restrict our consideration to the case $l = 0$ and find the function $R_0(r)$ as

$$R_0(r) = F(r)\,\frac{e^{ikr}}{r}\,.$$

Substitution of this expression in Eq. (82) (at $l = 0$) for the function $F(r)$ gives equation

$$F''(r) + 2ik\,F'(r) - \alpha\, v(r)\, F(r) = \alpha\, r\, v(r) j_0(kr)\, e^{-\,ikr}\,. \tag{83}$$

We solve this equation by the expansion in terms of the eigenfunctions $\{\eta_{0n}(r)\}$, determined in Section 6:

$$F(r) = \sum_m F_m\, \eta_{0m}(r). \tag{84}$$

In the considered approximation $(ka \ll 1)$, for the scattering amplitude f we have

$$f \simeq f_s = F(\infty) = \sum_m F_m\, Q_m, \tag{85}$$

where $Q_m = \eta_{0m}(\infty) = b_{0m}$ – see Eq. (39).

Substituting (84) in Eq. (83), multiplying the obtained equation by $\eta_{0n}(r)$, integrating the result from 0 to ∞ and making use of (49), we obtain

$$(\lambda_{0n} - \alpha) F_n + 2ik \sum_m M_{nm} F_m = -\,\alpha\,\frac{Q_n}{\lambda_{0n}} - ik\alpha \int_0^{\infty} r^2 \eta_{0n}(r) v(r)\, dr + \cdots\,, \tag{86}$$

where in the r.h.s. of this equation the expansion in power of k is fulfilled. In Eq. (86) the quantity M_{nm} is the same as in (53), (54). We shall find the value F_n in the form of the expansion in power of k: $F_n = F_n^{(0)} + F_n^{(1)} + \cdots$. From Eq. (86) in the zero-order approximation we obtain

$$F_n^{(0)} = -\,\frac{Q_n}{\lambda_{0n}(\lambda_{0n} - \alpha)}\,,$$

so that from Eq. (85) one has

$$f^{(0)} = -\,\alpha \sum_n \frac{Q_n^2}{\lambda_{0n}(\lambda_{0n} - \alpha)}\,. \tag{87}$$

The Eq. (87) is the exact formula for the scattering amplitude in the limit $k \to 0$.

For the repulsive potential $(\alpha > 0)$ the value $f^{(0)}$ is negative so that the scattering length is positive [1]. For the attractive potential $(\alpha < 0)$ the scattering amplitude can have any sign. Besides, under change of value α, the amplitude $f^{(0)}$ passes through the set of "resonances" at $\alpha = \lambda_{0n}\,(n = 0, 1, 2, \ldots)$. For determining the value F_n in the vicinity of the resonance $\alpha = \lambda_{0n}$ one must to take into account the summand with $m = n$ in sum from Eq. (86). As result, for$|\alpha - \lambda_{0n}| \ll |\lambda_{0n}|$ and $ka \ll 1$ we obtain

$$F_n \simeq - \frac{Q_n}{\lambda_{0n} - \alpha + ik\,Q_n^2}\,,$$

where we used the equality (55). Accordingly for the s-scattering amplitude we find

$$f_s \simeq - \frac{1}{\varkappa_{0n} + ik}\,, \quad \varkappa_{0n} = \frac{\lambda_{0n} - \alpha}{Q_n^2}\,. \tag{88}$$

This expression is formally identical to the result in Ref. [1] (see §133). At the same time for the value $\varkappa_{0n}$, introduced in Ref. [1] as phenomenological constant, we obtain the evident expression using the parameters, characterizing the given potential.

At $|\alpha| > |\lambda_{0n}|$ the value $\varkappa_{0n}$ is positive, so that according to Eq. (61) there is the real level with the energy $\varepsilon_{0n} = -\,\varkappa_{0n}^2$ in the potential $\alpha v(r)$. In this case, as one would expect (see Ref. [1]), the scattering amplitude (88) (more exactly – its analytic continuation in the plane of a complex energy) has the pole at $\varepsilon = -\,\varkappa_{0n}^2$ on the physical (or first Riemann) sheet Im $\sqrt{\varepsilon} > 0$. If $|\alpha| < |\lambda_{0n}|$, so that there is the virtual level, then the scattering amplitude has the pole on the nonphysical (second Riemann) sheet Im$\sqrt{\varepsilon} < 0$.

The s-scattering amplitude can be written, in view of the next term of expansion in power of k, as [1]:

$$f_s = - \frac{1}{\varkappa_{0n} + ik - \frac{1}{2}\,r_{0n}k^2}\,,$$

where r_{0n} – so-called effective radius of interaction. Since $r_{0n} \sim a$ and $ka \ll 1$, then at $\varkappa_{0n} = 0$ (i.e., at $\alpha = \lambda_{0n}$) we have

$$f_s = - \frac{1}{ik - \frac{1}{2}\,r_{0n}k^2} \simeq \frac{i}{k} + \frac{r_{0n}}{2}\,.$$

Therefore, to determine the value r_{0n} it is necessary to find the expansion of the s-scattering amplitude up to term $\sim k^0$. The corresponding cumbersome calculations leads us to the expression

$$r_{0n} = 2\int_0^\infty \left\{1 - \frac{[\eta_{0n}(r)]^2}{[\eta_{0n}(\infty)]^2}\right\} dr\,, \tag{89}$$

practically coinciding with the formula for r_0 from Ref. [1] (see §133, task 1).

12. Examples

As an illustration of the approach proposed in this paper, let us consider three exactly solvable examples.

1. For the potential function

$$v(r) = \frac{1}{\cosh^2 \gamma r} \tag{90}$$

both eigenvalues and eigenfunctions can be found in a relatively simple form at $l = 0$ (s-states). The Eq (23) (at $l = 0$) with $v(r)$ defined by (90) is solved by analogy with [1] (see §23, task 5). The eigenvalues are

$$\alpha_{0n} = -\gamma^2 \left(2n + 1 + \frac{\varkappa}{\gamma}\right) \left(2n + 2 + \frac{\varkappa}{\gamma}\right) \; ; \; n = 0, 1, 2, \ldots \; . \tag{91}$$

The corresponding radial eigenfunctions normalized according (24) are

$$\begin{aligned} \varphi_{0n}(r) &= \frac{B_n}{r} \left(1 - \xi^2\right)^{(2\rho-1)/4} \, C^{\rho}_{2n+1}(\xi) \; ; \; \xi = \tanh \gamma r \, , \; \rho = \frac{1}{2} + \frac{\varkappa}{\gamma} \, ; \\ B_n &= 2^{\rho} \, \Gamma(\rho) \left[\frac{\gamma}{\pi} \, \frac{(2n + 1 + \rho)(2n + 1)!}{\Gamma(2n + 1 + 2\rho)}\right]^{1/2} \, , \end{aligned} \tag{92}$$

where $C^{\rho}_m(\xi)$ are Gegenbauer polynomials [12–14]. The system of eigenfunctions defined by (92) is orthonormal and complete on the interval $0 < r < \infty$.

For function (90) the constants defined in the Sections 5 and 7 are

$$b = \frac{\pi}{2\gamma} \, , \; \delta = \gamma \, , \; I_1 = \ln 2 \, , \; I_2 = 0 \, .$$

It is easy to verify that the results, obtained in Sections 5–7 by the approximate methods, coincide with the results deduced from (92) in different limiting cases.

2. For the exponential well

$$v(r) = e^{-2\gamma r}$$

the eigenfunctions (at $l = 0$) are

$$\varphi_{0n}(r) = \frac{a_n}{r} \, J_{\nu}\left(\mu_n \, e^{-\gamma r}\right) \; , \; a_n = \frac{\sqrt{2\gamma}}{J_{\nu+1}\left(\mu_n\right)} \, ; \; \nu = \frac{\varkappa}{\gamma} \, , \; \mu_n = \frac{1}{\gamma} \sqrt{|\alpha_{0n}|} \, , \tag{93}$$

where $J_{\nu}(z)$ is the Bessel function. The corresponding eigenvalues α_{0n} are found by solving the equation

$$J_{\nu}(\mu) = 0 \, .$$

The orthonormality of the system defined by (93) can be verified directly. Its completeness follows from the convergence of the Fourier-Bessel expansions [13].

3. As an example of finite-range potential, consider the rectangular potential well

$$v(r) = \theta(a - r) \, .$$

The radial eigenfunctions are

$$r < a \; : \; \varphi^{(i)}_{ln}(r) = A_{ln} \, j_l(\mu_{ln} r) \, , \; \mu_{ln} = \sqrt{-\alpha_{ln} - \varkappa^2} \, ; \tag{94}$$

$$r > a \; : \; \varphi^{(e)}_{ln}(r) = B_{ln} \, k_l(\varkappa r) \, , \; B_{ln} = A_{ln} \, \frac{j_l(\mu_{ln} a)}{k_l(\varkappa a)} \, ; \tag{95}$$

$$A_{ln} = \frac{\sqrt{2}}{a^{3/2}} \left\{ [j_l(\mu_{ln}a)]^2 - j_{l+1}(\mu_{ln}a)\, j_{l-1}(\mu_{ln}a) \right\}^{-1/2} . \tag{96}$$

The corresponding eigenvalues α_{ln} are found by solving the equation:

$$\mu_{ln} \frac{j_l'(\mu_{ln}a)}{j_l(\mu_{ln}a)} = \varkappa \frac{k_l'(\varkappa a)}{k_l(\varkappa a)} \tag{97}$$

with μ_{ln} defined in (94). In the Eqs (94)–(96)

$$j_l(x) = \sqrt{\frac{\pi}{2x}}\, J_{l+1/2}(x)$$

are the spherical Bessel function, $k_l(x)$ are the spherical Macdonald function $\big($see Eq. (26)$\big)$.

Acknowledgment

I would like to thank Professor S.I. Manaenkov who drew my attention to the articles [7–9].

References

[1] L.D. Landau and E.M. Lifshitz, *Course of Theoretical Physics, Vol.3: Quantum Mechanics: Non-Relativistic Theory*, 4th ed. (Oxford Univ. Press, Oxford, 1980; Nauka, Moscow, 1989).
[2] A.I. Baz', Ya.B. Zel'dovich and A.M. Perelomov, *Scattering, Reactions, and Decays in Nonrelativistic Quantum Mechanics*, (2nd ed.), (Israel Program for Scientific Translations, Jerusalem, 1966; Nauka, Moscow, 1971).
[3] M. Rotenberg, *Ann Phys* (*N.Y.*) **19** (1962), 262.
[4] S.V. Khristenko and S.I. Vetchinkin, *Optika i Spectroskopiya* **37** (1974), 1017 (in Russian).
[5] S.M. Blinder, *Phys Rev A* **29** (1984), 1674 .
[6] B.Ya. Balagurov, *Zh Eksp Teor Fiz* **126** (2004), 986; [*JETP* **99** (2004), 856].
[7] S. Veinberg, *Phys Rev* **131** (1963), 440.
[8] I.M. Narodetskiĭ, *Yadernaya Fizika* **9** (1969), 1086 [*Physics of Atomic Nuclei* – in English].
[9] S.I. Manaenkov, *Teoreticheskaya i Matematicheskaya Fizika* **12** (1972), 397 (in Russian).
[10] B.Ya. Balagurov, *Zh Eksp Teor Fiz* **93** (1987), 316; [*Sov Phys – JETP* **66** (1987), 182].
[11] B.Ya. Balagurov, *Zh Eksp Teor Fiz* **94** (1988), 95; [*Sov Phys – JETP* **67** (1988), 1351].
[12] I.S. Gradshteĭn and I.M. Ryzhik, *Table of Integrals, Series, and Products*, (4th ed.), (Fizmatgiz, Moscow, 1962; Academic, New York, 1980).
[13] *Higher Transcendental Functions* (*Bateman Manuscript Project*), Ed. by A. Erdelyi (McGraw-Hill, New York, 1953; Nauka, Moscow, 1974), Vol.2.
[14] G. Szegó, *Orthogonal Polinomials* (Am. Math. Soc., New York, 1959; Fizmatgiz, Moscow, 1962).

Journal of Computational Methods in Sciences and Engineering 10 (2010) 129–138
DOI 10.3233/JCM-2010-0314
IOS Press

Irreducible spherical representation of some fourth-rank tensors

Tadeusz Bancewicz[a,*] and Zdzisław Ożgo[b]
[a]*Nonlinear Optics Division, Faculty of Physics, Adam Mickiewicz University, 61-614 Poznań, Poland*
[b]*Faculty of Physics, Adam Mickiewicz University, 61-614 Poznań, Poland*

Abstract. A process of decomposition of fourth-rank tensors into parts irreducible with reference to the continuous group of rotation is presented. The transformation matrices between the Cartesian and spherical reducible and irreducible fourth-rank tensors are given and discussed. We have focused our attention to the purely dipolar fourth-rank tensor $C_{i;jkl}$ symmetric to its last three indices and the dipole-octopole fourth-rank multipolar polarizability tensor $\mathbf{E}^{(1,3)}$. The fourth-rank tensors intervene in a number of very important nonlinear optics processes like Kerr effect, intensity-dependent refractive index phenomena, four wave mixing, third harmonic generation and several other effects. Tensors of this kind are also very important in piezo-electric phenomena and in elasticity studies. Cartesian tensor index permutation is discussed as well as its influence on the tensor irreducible spectrum is studied. Several examples concerning fourth-rank tensors are given.

1. Introduction

Tensors are widely used to describe physical properties of matter [1]. They are important mainly when considered system is anisotropic. Nonlinear optics and intermolecular interactions studies revealed us abundance of new tensorial properties of matter [2–10]. Many of them concern higher order polarizabilities and hyperpolarizabilities and have been developed using Cartesian notation [2,11,12]. However several calculations, especially in spectroscopic studies are more convenient in terms of spherical tensors [4,13,14]. Both Cartesian and spherical tensors can be expressed in the reducible and irreducible form [15–24]. The concept of irreducible tensors is based on the idea of rotational invariance with respect to the continuous group of rotations. Nonlinear optics [17,25,26], light scattering [27–32] and intermolecular interactions [27,33–35] were the favorable subjects of Kielich's scientific work. Kielich mastered tensor calculus, so nonlinear optics was the area he admired. He learned tensors while working with Piekara [25] and then he extended this formalism. From the early years of his scientific carrier he strongly admired works of Buckingham [2,36].

We devote this paper to discussion of some fourth rank tensors. We consider spherical form of these tensors and the way of transformation between Cartesian and spherical tensors. First we concentrate on the purely dipolar fourth rank tensor, symmetric with respect to permutation of its last three indices – for example the tensor appearing in the case of third harmonic generation. We discuss as well another fourth rank tensor, $\mathbf{E}^{(1,3)}$, this time composed of the coupled dipole and octopole moments; the tensor is known as the dipole-octopole multipolar polarizability tensor [37,38]. That tensor is studied in the far wings of

*Corresponding author. E-mail: tbancewi@zon12.physd.amu.edu.pl, http://zon8.physd.amu.edu.pl/~tbancewi.

the collision-induced light scattering (CILS) spectra, mainly in the case of molecules of the tetrahedral and octahedral symmetry. In recent years we have reported several CILS experimental and theoretical studies of the $\mathbf{E}^{(1,3)}$ tensor, for a number of cases as the isotropic and anisotropic CILS by gaseous carbon tetrafluoride [39,40], the anisotropic and isotropic CILS by carbon tetrafluoride in a Raman vibrational band [41], the isotropic CILS spectra from gaseous sulfur hexafluoride [42], the polarization components of rototranslational light scattering spectra from gaseous sulfur hexafluoride [43] and the multipolar polarizations of methane from isotropic and anisotropic CILS [44].

2. Pure dipole-type fourth-rank tensor

The permutation symmetry of tensor indices is determined by the physical phenomenon described by this tensor. From the mathematical point of view the symmetry of the n-rank tensor is described by the permutation groups. If the tensor $\mathbf{C}^n$ is symmetric with respect to all its indices, its permutational symmetry group is the so-called symmetry group S_n of the order n!, while otherwise its permutational symmetry group is a subgroup P_n of the group S_n [16,32]. The group of the permutational symmetry of the tensor is determined by the division of its indices into sets in such a way that all permutations within a given set are allowed but they cannot be made with the indices from any other set. Then sets of indices are separated with a semicolon, e.g. $C_{ij;kl}$. It is also possible that there is a symmetry that admits transposition of the whole sets, then the sets are separated by a colon, e.g. $C_{ij:kl}$. The permutation group P_n can be expressed by simple $\times$ and semisimple $\wedge$ products of symmetric groups. For instance, the permutational symmetry of the tensor $C_{ij;kl}$ is $P_4 = S_2 \times S_2$; that of the tensor $C_{ij:kl}$ is $P_4 = (S_2 \times S_2) \wedge S_2$. Therefore, the symmetry group of the tensor $\mathbf{C}^n$ is a simple product of P_n and G. We assume that G it is the point symmetry group of our system. All groups G are subgroups of the group O_3 being a simple product of the three-dimensional group of rotations and the group of inversion C_i.

The spherical components of some vector $\mathbf{A}$ make a base of the irreducible representation D_u^1 of group O_3, which is therefore called the vector representation. In general some tensor $\mathbf{A}^n$ belongs to the tensor representation $D(n)$ being the n-fold product of the vector repreentation. For the tensor of a well defined permutational symmetry its irreducible spherical representation is composed by the adequately symmetrized powers of the vector representation. The representation $D(n)$ is in general reducible and its reduction to the simple sum of representation $D^l_{g(u)}$ leads to a decomposition of the tensor into spherical tensors. The components of the irreducible spherical tensors of the order l are the linear combinations of the components of the tensor $\mathbf{A}^n$, which upon rotation of the reference system transform into each other and make a base of the irreducible representations $D^l_{g(u)}$. An important problem is to perform the reduction in such a way that the tensors would have specific permutation symmetry. It can be achieved using the full symmetry group of the tensor $G \times P_n$. Taking into regard that G is a subgroup of O_3 group and P_n is a subgroup of S_n group, it is sufficient to consider only the group $O_3 \times S_n$. The irreducible representations of the $O_3 \times S_n$ group are simple products $D^l_{g(u)} \times [\lambda]$, where $[\lambda]$ is the Young table uniquely characterizing the irreducible representation of the S_n group. For a fourth rank tensor we get

$$C^{(4)} = D^0_g \times [4] + D^0_g \times [2^2] + D^1_g \times [2\,1^2] + D^1_g \times [31] + D^2_g \times [4] + D^2_g \times [2^2] + D^2_g \times [31] + D^3_g \times [31] + D^4_g \times [4] \tag{1}$$

The problem of symmetrization can be approached in two ways. The first is based on the application of the Young operators. The second is analogous to the calculation of the atomic wave-function proposed

by Racah. He introduced into the atom theory very useful genealogical coefficients that can be used for finding the symmetrized irreducible bases of tensors. Let's denote by $d_m^{(k)}(n[\lambda]r)$ a unit base tensor attributed to the irreducible representation $D^l_{g(u))}$ of the tensor group $O_3 \times S_n$. m and r number the rows of the $D^{(k)}_{g(u)}$ and $[\lambda]$ representation. Let's assume that we know the symmetrized irreducible bases of a tensor of rank $n-1$ and using them we want to find the bases of a tensor of rank n. We will do it with the help of the genealogical coefficients $\langle n-1[\lambda^{'}]\, k^{'},\, 1; k|n[\lambda]\, k\rangle$ being elements of the matrix of the transformation

$$d_m^{(k)}(n[\lambda]\, r) \,=\, \sum_{k^{'}} d_m^{(k^{'},k)}\,(n-1\,[\lambda^{'}]\, r^{'}, 1)\;\langle n-1[\lambda^{'}]\, k^{'},\, 1; k|n[\lambda]\, k\rangle \tag{2}$$

The genealogical coefficients $\langle n-1[\lambda^{'}]\, k^{'},\, 1; k|n[\lambda]\, k\rangle$ do not depend on the values of m and r. Similar considerations lead us to higher rank basis.

The first tensor $C_{i;jkl}$ of relevance to us is the one that is symmetric in its last three indices. The tensor with the above index permutation symmetry apply e.g. to the Kerr effect, intensity-dependent refractive index phenomena, four wave mixing, third harmonic generation, third harmonic Raman and Rayleigh scattering [16]. In general this tensor has 81 nonzero components. Since this tensor is symmetric to the last three indices it is easy to write its reduction spectrum

$$1 \otimes (1 \,\oplus\, 3) \,=\, (0 \,\oplus\, 1 \oplus\, 2) \,+\, (2 \,\oplus\, 3 \,\oplus 4) \tag{3}$$

We note that we have one scalar, one vector, double-degenerate deviator, one septor and one nonor. Far from the absorption region the dispersion is negligible and the **C** tensor becomes invariant under its all four indices. It is interesting to note that the spectrum of the totally index symmetric fourth rank tensor reads

$$(0 \,\oplus\, 2 \oplus\, 4) \tag{4}$$

In our Tables we denote the irreducible tensors specific only to $C_{i;jkl}$ ($\tilde{C}^1$, $\tilde{C}^2$ and $\tilde{C}^3$) by tilde (see and compare Eqs (1) and (2)). The tensor considered has been symmetrized in such a way that the $\tilde{C}^1$, $\tilde{C}^2$ and $\tilde{C}^3$ components specific of tensor $C_{i;jkl}$ are reduced to zero if tensor **C** becomes fully symmetric. We write the following transformation from Cartesian tensor to the spherical one:

$$C_{i;jkl} \,=\, \sum_{J\,M} a^{(J\,M)}_{i;jkl}\, C^J_M \tag{5}$$

In this paper the transformation coefficients $a^{(J\,M)}_{i;jkl}$ are calculated and completed in the Table 1. As relation (5) is a unitary transformation the reverse transformation is thus uniquely defined.

As a first example let us calculate the laboratory frame C_{xxxx} component of the second hyperpolarizability tensor responsible for the polarized component of the third-harmonic scattered radiation. Using the results of Table 1 we obtain

$$\begin{aligned} C_{\mathrm{x;xxx}} = {} & \frac{1}{4}\,\left(C^4_4 \,+\, C^4_{-4}\right) \,-\, \frac{1}{2\,\sqrt{7}}\,\left(C^4_2 \,+\, C^4_{-2}\right) \,+\, \frac{3}{2\,\sqrt{70}}\,C^4_0 \\ & - \sqrt{\frac{3}{14}}\,\left(C^2_2 \,+\, C^2_{-2}\right)) \,+\, \frac{1}{\sqrt{7}}\,C^2_0 \,+\, \frac{1}{\sqrt{5}}\,C^0_0 \end{aligned} \tag{6}$$

Table 1
The spherical components of the fourth order tensor $C_{i;jkl}$, fully-symmetric to its three last indices jkl

Type	l	m	coeff.	xxxx(1)	xyyy(1)	xzzz(1)	xxyy(3)	xxzz(3)	xyzz(3)	xyxx(3)	xzxx(3)	xzyy(3)	xxyz(6)
C^4_m	4	4	$\frac{1}{4}$	1	-i	.	-1	.	.	i		.	.
	4	-4	$\frac{1}{4}$	1	i	.	1	.	.	-i	.	.	.
	4	3	$\frac{1}{4\sqrt{2}}$	.	.	.	.	.	.	.	-1	1	-i
	4	-3	$\frac{1}{4\sqrt{2}}$	.	.	.	.	.	.	.	1	-1	-i
	4	2	$\frac{1}{4\sqrt{7}}$	-2	-i	.	.	2	-2 i	-i	.	.	.
	4	-2	$\frac{1}{4\sqrt{7}}$	-2	i	.	.	2	-2 i	i	.	.	.
	4	1	$\frac{1}{4\sqrt{14}}$	.	.	-4	.	.	.	.	3	1	i
	4	-1	$\frac{1}{4\sqrt{14}}$	.	.	4	.	.	.	.	-3	-1	i
	4	0	$\frac{1}{2\sqrt{70}}$	.	.	-4	.	.	.	.	3	1	i
$\tilde{C}^3_m$	3	3	$\frac{1}{4\sqrt{6}}$	.	.	.	.	.	.	.	1	-1	i
	3	-3	$\frac{1}{4\sqrt{6}}$	.	.	.	.	.	.	.	1	-1	-i
	3	2	$\frac{1}{12}$	.	3 i	.	2	-2	-2 i	-i	.	.	3i
	3	-2	$\frac{1}{12}$	.	3 i	.	-2	2	-2 i	-i	.	.	3i
	3	1	$\frac{1}{12\sqrt{10}}$	.	.	12	.	.	.	.	-1	-11	5i
	3	-1	$\frac{1}{12\sqrt{10}}$	.	.	12	.	.	.	.	-1	-11	-5i
	3	0	$\frac{1}{2\sqrt{30}}$	.	3 i	.	.	.	-4 i	i	.	.	.
C^2_m	2	2	$\frac{1}{6\sqrt{35}}$	-9	6 i	.	7	2	2 i	-8 i	.	.	.
	2	-2	$\frac{1}{6\sqrt{35}}$	-9	6 i	.	7	2	-2 i	8 i	.	.	.
	2	1	$\frac{1}{6\sqrt{35}}$	.	.	-6	.	.	.	.	8	-2	5 i
	2	-1	$\frac{1}{6\sqrt{35}}$	.	.	6	.	.	.	.	-8	2	5 i
	2	0	$\frac{1}{\sqrt{210}}$	3	.	.	1	-4	.	.	.	.	.
$\tilde{C}^2_m$	2	2	$\frac{1}{6\sqrt{2}}$	.	3 i	.	2	1	i	-i	.	.	.
	2	-2	$\frac{1}{6\sqrt{2}}$	.	-3 i	.	2	1	-i	8 i	.	.	.
	2	1	$\frac{1}{6\sqrt{2}}$	.	.	-3	.	.	.	.	1	-1	i
	2	-1	$\frac{1}{6\sqrt{35}}$	.	.	3	.	.	.	.	1	1	i
	2	0	$\frac{1}{\sqrt{210}}$	.	.	.	.	-1	.	.	.	.	.
$\tilde{C}^1_m$	1	1	$\frac{1}{2\sqrt{15}}$	.	.	-3	.	.	.	.	-1	-1	.
	1	-1	$\frac{1}{2\sqrt{15}}$	.	.	-3	.	.	.	.	-1	-1	.
	1	0	$\frac{1}{\sqrt{30}}$	.	3 i	.	.	.	i	i	.	.	.
0	0	$\frac{1}{3\sqrt{5}}$	3	.	.	1	1	.	.	.	.	.	

Type	l	m	coeff.	yxxx(1)	yyyy(1)	yzzz(1)	yxyy(3)	yxzz(3)	yyzz(3)	yyxx(3)	yzxx(3)	yzyy(3)	yxyz(6)
C^4_m	4	4	$\frac{1}{4}$	i	1	.	-i	.	.	-1	.	.	.
	4	-4	$\frac{1}{4}$	-i	1	.	i	.	.	-1	.	.	.
	4	3	$\frac{1}{4\sqrt{2}}$	.	.	.	.	.	.	.	-i	i	1
	4	-3	$\frac{1}{4\sqrt{2}}$	.	.	.	.	.	.	.	-i	i	-1
	4	2	$\frac{1}{4\sqrt{7}}$	-i	2	.	-i	2 i	-2	.	.	.	.
	4	-2	$\frac{1}{4\sqrt{7}}$	i	2	.	i	-2 i	-2	.	.	.	.
	4	1	$\frac{1}{4\sqrt{14}}$	.	.	-4 i	.	.	.	.	i	3 i	1
	4	-1	$\frac{1}{4\sqrt{14}}$	.	.	4 i	.	.	.	.	i	3 i	-1
	4	0	$\frac{1}{2\sqrt{70}}$	.	3	.	.	.	-4	1	.	.	.
$\tilde{C}^3_m$	3	3	$\frac{1}{4\sqrt{6}}$	.	.	.	.	.	.	.	i	-i	-1
	3	-3	$\frac{1}{4\sqrt{6}}$	.	.	.	.	.	.	.	-i	i	-1
	3	2	$\frac{1}{12}$	3 i	.	.	-i	-2 i	2	-2	.	.	.
	3	-2	$\frac{1}{12}$	3 i	.	.	-i	2 i	-2	2	.	.	.
	3	1	$\frac{1}{12\sqrt{10}}$	.	.	12 i	.	.	.	.	-11 i	-i	5

Table 1, continued

	3	-1	$\frac{1}{12\sqrt{10}}$	.	.	12 i	.	.	.	.	11 i	i	5
	3	0	$\frac{1}{2\sqrt{30}}$	-3 i	.	.	-i	.	.	.	.	.	.
C^2_m	2	2	$\frac{1}{6\sqrt{35}}$	6 i	9	.	-8 i	2 i	-2	-7	.	.	.
	2	-2	$\frac{1}{6\sqrt{35}}$	-6 i	9	.	8 i	2 i	-2	-7	.	.	.
	2	1	$\frac{1}{6\sqrt{35}}$	.	.	-6ı	.	.	.	.	-2 i	8 i	5
	2	-1	$\frac{1}{6\sqrt{35}}$	.	.	-6 i	.	.	.	.	-2 i	8 i	-5
	2	0	$\frac{1}{\sqrt{210}}$	.	3	.	.	.	-4	1	.	.	.
$\tilde{C}^2_m$	2	2	$\frac{1}{6\sqrt{2}}$	3 i	.	.	-i	i	-1	-2	.	.	.
	2	-2	$\frac{1}{6\sqrt{2}}$	-3 i	.	.	i	-i	-1	-2	.	.	.
	2	1	$\frac{1}{6\sqrt{2}}$	.	.	-3ı	.	.	.	.	-i	i	1
	2	-1	$\frac{1}{6\sqrt{2}}$	.	.	-3 i	.	.	.	.	-i	i	-1
	2	0	$\frac{1}{\sqrt{2}}$	.	3	.	.	.	-1	.	.	.	.
$\tilde{C}^1_m$	1	1	$\frac{1}{2\sqrt{15}}$	.	.	-3 i	.	.	.	.	-i	-i	.
	1	-1	$\frac{1}{2\sqrt{15}}$	.	.	3 i	.	.	.	.	i	i	.
	1	0	$\frac{1}{\sqrt{30}}$	-3 i	.	.	-i	-i	.	.	.	.	.
C^0	0	0	$\frac{1}{3\sqrt{5}}$	.	3	.	.	.	1	1	.	.	.

Type	l	m	Coefficient	zxxx(1)	zyyy(1)	zzzz(1)	zxyy(3)	zxzz(3)	zyzz(3)	zyxx(3)	zzxx(3)	zzyy(3)	zxyz(6)
C^4_m	4	4	$\frac{1}{4}$	.	.	.	.	.	.	.	.	.	.
	4	-4	$\frac{1}{4}$	.	.	.	.	.	.	.	.	.	.
	4	3	$\frac{1}{4\sqrt{2}}$	-1	i	.	1	.	.	-i	.	.	.
	4	-3	$\frac{1}{4\sqrt{2}}$	1	i	.	-1	.	.	-i	.	.	.
	4	2	$\frac{1}{4\sqrt{7}}$	.	.	.	.	.	.	.	2	-2	2 i
	4	-2	$\frac{1}{4\sqrt{7}}$	.	.	.	.	.	.	.	2	-2	-2 i
	4	1	$\frac{1}{4\sqrt{14}}$	3	3 i	.	1	-4	-4 i	i	.	.	.
	4	-1	$\frac{1}{4\sqrt{14}}$	-3	3 i	.	-1	4	-4 i	i	.	.	.
	4	0	$\frac{1}{2\sqrt{70}}$	.	.	8	.	.	.	.	-4	-4	.
$\tilde{C}^3_m$	3	3	$\frac{1}{4\sqrt{6}}$	-3	3 i	.	3	.	.	3 i	.	.	.
	3	-3	$\frac{1}{4\sqrt{6}}$	-3	-3 i	.	3	.	.	3 i	.	.	.
	3	2	$\frac{1}{12}$	.	.	.	.	.	.	.	2	-2	2 i
	3	-2	$\frac{1}{12}$	.	.	.	.	.	.	.	-2	2	2 i
	3	1	$\frac{1}{12\sqrt{10}}$	3	3 i	.	1	-4	-4i	i	.	.	.
	3	-1	$\frac{1}{12\sqrt{10}}$	3	-3 i	.	1	-4	4 i	-i	.	.	.
	3	0	$\frac{1}{2\sqrt{30}}$	.	.	.	-i	.	.	.	.	.	.
C^2_m	2	2	$\frac{1}{6\sqrt{35}}$	.	.	.	.	.	.	.	-5	5	-5 i
	2	-2	$\frac{1}{6\sqrt{35}}$	.	.	.	.	.	.	.	-5	5	5 i
	2	1	$\frac{1}{6\sqrt{35}}$	6	-6 i	.	-2	8	8 i	-2 i	.	.	.
	2	-1	$\frac{1}{6\sqrt{35}}$	6	6 i	.	2	-8	8 i	-2 i	.	.	.
	2	0	$\frac{1}{\sqrt{210}}$	.	.	-6	.	.	.	.	3	3	.
$\tilde{C}^2_m$	2	2	$\frac{1}{6\sqrt{2}}$	.	.	.	.	.	.	.	-1	1	-i
	2	-2	$\frac{1}{6\sqrt{2}}$	.	.	.	.	.	.	.	1	1	i
	2	1	$\frac{1}{6\sqrt{2}}$	-3	-3 i	.	-1	1	i	-i	.	.	.
	2	-1	$\frac{1}{6\sqrt{2}}$	3	-3 i	.	1	-1	i	-i	.	.	.
	2	0	$\frac{1}{\sqrt{2}}$	.	.	.	.	.	.	.	1	.	.
$\tilde{C}^1_m$	1	1	$\frac{1}{2\sqrt{15}}$	3	3 i	.	1	1	i	i	.	.	.
	1	-1	$\frac{1}{2\sqrt{15}}$	3	-3 i	.	1	1	-i	-i	.	.	.
	1	0	$\frac{1}{\sqrt{30}}$	.	.	.	.	.	.	.	.	.	.
C^0	0	0	$\frac{1}{3\sqrt{5}}$	.	.	3	.	.	.	.	1	1	.

We note that for this configuration asymmetric components of the **C** does not intervene. However for the depolarized component we have

$$\begin{aligned} C_{\mathrm{z;xxx}} = & \frac{1}{4\sqrt{2}}\left(C_4^3 - C_{-3}^4\right) - \frac{3}{4\sqrt{14}}\left(C_1^4 - C_{-1}^4\right) + \sqrt{\frac{3}{56}}\left(C_1^2 - C_{-1}^2\right)) \\ & - \frac{3}{4\sqrt{6}}\left(\tilde{C}_3^3 + \tilde{C}_{-3}^3\right) + \frac{1}{4\sqrt{10}}\left(\tilde{C}_1^3 + \tilde{C}_{-1}^3\right) - \frac{1}{2\sqrt{2}}\left(\tilde{C}_1^2 - \tilde{C}_{-1}^2\right) \\ & + \frac{3}{2\sqrt{15}}\left(\tilde{C}_1^1 + \tilde{C}_{-1}^1\right) \end{aligned} \tag{7}$$

We note here the visible influence of the antisymmetric components of the second hyperpolarizability tensor.

Moreover Table 1 allows us to calculate the following very useful molecular parameters defined as

$$|C^J|^2 = \sum_M |C_M^J|^2 \tag{8}$$

It is convenient to express them also in Cartesian components:

$$\begin{aligned} |C^0|^2 &= \frac{1}{5}\left(C_{iikk}\, C_{jjll}\right) \\ |C^2|^2 &= \frac{2}{7}\left(3\, C_{ijkk}\, C_{ijll} - C_{iikk}\, C_{jjll}\right) \\ |C^4| &= \frac{1}{35}\left(35\, C_{ijkl}\, C_{ijkl}\right. \\ &\quad \left. - 30\, C_{ijkk}\, C_{ijll} + 3\, C_{iikk}\, C_{jjll}\right) \end{aligned} \tag{9}$$

3. The Dipole-octopole multipolar polarizability fourth rank tensor

Another fourth rank tensor appears in molecular spectroscopy and plays an important role especially when multipolar interactions are considered. The tensor in question results when the dipole moment μ is coupled with the octopole moment Ω. Then matrix elements of the type $< i|\mu|k >< k|\Omega|i >$ are present [2,4,45]. The tensor is usually denoted as the dipole-octopole **E** multipolar polarizability fourth rank tensor. Since octopole moment is symmetric to its indices and traceless the same applies to the **E** tensor. Sometimes this tensor is denoted more explicitly as $\mathbf{E}^{(1,3)}$. It is easy to show that this tensor in general has $3 \times 7 = 21$ independent components. Further reduction depends on the molecular symmetry of the system. Let us first to consider the dipole and octopole moments in a spherical basis. Then we obtain [4,46]:

for the dipole moment

$$\begin{aligned} Q_1^0 &= \mu_z \\ Q_1^{\pm 1} &= \mp \frac{(\mu_x \pm i\,\mu_y)}{\sqrt{2}} \end{aligned} \tag{10}$$

and, for the octopole moment

$$
\begin{aligned}
Q_3^0 &= \Omega_{zzz} \\
Q_3^{\pm 1} &= \mp \sqrt{\frac{3}{4}}\,(\Omega_{zzx} \pm i\,\Omega_{zzy}) \\
Q_3^{\pm 2} &= \sqrt{\frac{3}{10}}\,(\Omega_{zxx} - \Omega_{zyy} \pm 2\,i\,\Omega_{xyz}) \\
Q_3^{\pm 3} &= \mp \frac{1}{\sqrt{20}}\,(\Omega_{xxx} \pm 3\,i\,\Omega_{xxy} - 3\,\Omega_{xyy} \mp i\,\Omega_{yyy})
\end{aligned} \tag{11}
$$

Then we calculate all 21 spherical reducible $E_{l_1\,l_2}^{m_1\,m_2}$ components of the **E** tensor as the following combinations of its Cartesian components (l_1 and l_2 are equal to 1 or 3):

$$
\begin{aligned}
E_{1\,3}^{0\,0} &= E_{3\,1}^{0\,0} = E_{z,zzz} \\
E_{1\,3}^{1\,0} &= E_{3\,1}^{0\,1} = -\frac{1}{\sqrt{2}}(E_{x,zzz} + i\,E_{y,zzz}) \\
E_{1\,3}^{-1\,0} &= E_{3\,1}^{0\,-1} = \frac{1}{\sqrt{2}}\,(E_{x,zzz} - i\,E_{y,zzz}) \\
E_{1\,3}^{0\,2} &= E_{3\,1}^{2\,0} = \sqrt{\frac{3}{10}}\,(2\,i\,E_{z,xyz} + E_{z,zxx} - E_{z,zyy}) \\
E_{1\,3}^{0\,-2} &= E_{3\,1}^{-2\,0} = \sqrt{\frac{3}{10}}\,(-2\,i\,E_{z,xyz} + E_{z,zxx} - E_{z,zyy}) \\
E_{1\,3}^{0\,3} &= E_{3\,1}^{3\,0} = -\frac{1}{2\sqrt{5}}\,(E_{z,xxx} + 3\,i\,E_{z,xxy} - 3\,E_{z,xyy} - i\,E_{z,yyy}) \\
E_{1\,3}^{0\,-3} &= E_{3\,1}^{-3\,0} = \frac{1}{2\sqrt{5}}\,(E_{z,xxx} - 3\,i\,E_{z,xxy} - 3\,E_{z,xyy} + i\,E_{z,yyy}) \\
E_{1\,3}^{0\,1} &= E_{3\,1}^{1\,0} = -\frac{1}{2}\sqrt{3}\,(E_{z,zzx} + i\,E_{z,zzy}) \\
E_{1\,3}^{0\,1} &= E_{3\,1}^{1\,0} = \frac{1}{2}\sqrt{3}\,(E_{z,zzx} - i\,E_{z,zzy})
\end{aligned} \tag{12}
$$

$$
\begin{aligned}
E_{3\,1}^{1\,1} &= E_{1\,3}^{1\,1} = \frac{1}{2}\sqrt{\frac{3}{2}}\,(E_{x,zzx} + i\,E_{x,zzy} + i\,E_{y,zzx} - E_{y,zzy}) \\
E_{3\,1}^{-1\,-1} &= E_{1\,3}^{-1\,-1} = \frac{1}{2}\sqrt{\frac{3}{2}}\,(E_{x,zzx} - i\,E_{x,zzy} - i\,E_{y,zzx} - E_{y,zzy}) \\
E_{3\,1}^{-1\,1} &= E_{1\,3}^{1\,-1} = -\frac{1}{2}\sqrt{\frac{3}{2}}\,(E_{x,zzx} - i\,E_{x,zzy} + i\,E_{y,zzx} + E_{y,zzy}) \\
E_{3\,1}^{1\,-1} &= E_{1\,3}^{-1\,1} = -\frac{1}{2}\sqrt{\frac{3}{2}}\,(E_{x,zzx} + i\,E_{x,zzy} - i\,E_{y,zzx} + E_{y,zzy})
\end{aligned} \tag{13}
$$

$$E^{2\,1}_{3\,1} = E^{1\,2}_{1\,3} = \frac{1}{2}\sqrt{\frac{3}{5}}\,(-2\,i\,E_{x,xyz} - E_{x,zxx} + E_{x,zyy} + 2\,E_{y,xyz} - i\,E_{y,zxx} + i\,E_{y,zyy})$$

$$E^{-2\,-1}_{3\,1} = E^{-1\,-2}_{1\,3} = \frac{1}{2}\sqrt{\frac{3}{5}}\,(-2\,i\,E_{x,xyz} + E_{x,zxx} - E_{x,zyy} - 2\,E_{y,xyz} - i\,E_{y,zxx} + i\,E_{y,zyy})$$

$$E^{-2\,1}_{3\,1} = E^{1\,-2}_{1\,3} = \frac{1}{2}\sqrt{\frac{3}{5}}\,(2\,i\,E_{x,xyz} - E_{x,zxx} + E_{x,zyy} - 2\,E_{y,xyz} - i\,E_{y,zxx} + i\,E_{y,zyy})$$

$$E^{2\,-1}_{3\,1} = E^{-1\,2}_{1\,3} = \frac{1}{2}\sqrt{\frac{3}{5}}(2\,i\,E_{x,xyz} + E_{x,zxx} - E_{x,zyy} + 2\,E_{y,xyz} - i\,E_{y,zxx} + iE_{y,zyy}) \tag{14}$$

$$\begin{aligned}
E^{1\,3}_{1\,3} = E^{3\,1}_{3\,1} = &\frac{1}{2\sqrt{10}}\,(E_{x,xxx} + 3\,i\,E_{x,xxy} - 3\,E_{x,xyy} - i\,E_{x,yyy} \\
&+ i\,E_{y,xxx} - 3\,E_{y,xxy} - 3\,i\,E_{y,xyy} + E_{y,yyy}) \\
E^{-1\,3}_{1\,3} = E^{3\,-1}_{3\,1} = &-\frac{1}{2\sqrt{10}}\,(E_{x,xxx} + 3\,i\,E_{x,xxy} - 3\,E_{x,xyy} - i\,E_{x,yyy} \\
&- i\,E_{y,xxx} + 3\,E_{y,xxy} + 3\,i\,E_{y,xyy} - E_{y,yyy}) \\
E^{-1\,-3}_{1\,3} = E^{-3\,-1}_{3\,1} = &-\frac{1}{2\sqrt{10}}\,(E_{x,xxx} - 3\,i\,E_{x,xxy} - 3\,E_{x,xyy} + i\,E_{x,yyy} \\
&- i\,E_{y,xxx} - 3\,E_{y,xxy} + 3\,i\,E_{y,xyy} + E_{y,yyy}) \\
E^{1\,-3}_{1\,3} = E^{-3\,1}_{3\,1} = &-\frac{1}{2\sqrt{10}}\,(E_{x,xxx} - 3\,i\,E_{x,xxy} - 3\,E_{x,xyy} - i\,E_{x,yyy} \\
&+ i\,E_{y,xxx} + 3\,E_{y,xxy} - 3\,i\,E_{y,xyy} - E_{y,yyy})
\end{aligned} \tag{15}$$

The irreducible multipolar polarizability tensors are constructed from the above relations by standard coupling methods:

$$E^{(1,3)}_{j\,m} = \sum_{m_1,m_2,l_1,l_2} C^{j\,m}_{l_1\,m_1\;l_2\,m_2}\,E^{m_1\,m_2}_{l_1\,l_2} \tag{16}$$

where $C^{j\,m}_{j_1\,m_1\;j_2\,m_2}$ stands for the Clebsch-Gordan coefficient and $m = m_1 + m_2$.

We illustrate this method considering tetrahedral molecule. For the T_d symmetry molecule there are 21 nonzero elements for this tensor $\mathrm{E}_{x,xyy} = \mathrm{E}_{x,yxy} = \mathrm{E}_{x,yyx} = \mathrm{E}_{x,xzz} = \mathrm{E}_{x,zxz} = \mathrm{E}_{x,zzx} = \mathrm{E}_{y,yyx} = \mathrm{E}_{y,yxy} = \mathrm{E}_{y,xyy} = \mathrm{E}_{y,yzz} = \mathrm{E}_{y,zyz} = \mathrm{E}_{x,zzy} = \mathrm{E}_{z,zxx} = \mathrm{E}_{z,xzx} = \mathrm{E}_{z,xxz} = \mathrm{E}_{z,zyy} = \mathrm{E}_{z,yzy} = \mathrm{E}_{z,yyz} = -\frac{1}{2}\,\mathrm{E}_{x,xxx} = -\frac{1}{2}\mathrm{E}_{y,yyy} = -\frac{1}{2}\mathrm{E}_{z,zzz} \equiv E$ [47], but there is only one independent component. Using the projection operator [44,48] we find the following linear combination of spherical reducible dipole-octopole $E^{m_1\,m_2}_{1\quad 3}$ polarizability tensor components transforming as the totally symmetric representation of the molecular point group T_d

$$\sqrt{10}\,E^{-1\,-3}_{1\quad 3} + \sqrt{6}\,E^{-11}_{13} + 4\,E^{00}_{13} + \sqrt{6}\,E^{1-1}_{13} + \sqrt{10}\,E^{13}_{1\,3}. \tag{17}$$

The above formula allows us to find the following relative values of $E^{m_1\,m_2}_{1\quad 3}$ [13,44]:

$$E^{0\,0}_{1\;3} : E^{1\,3}_{1\,3} : E^{-1\,-3}_{1\quad 3} : E^{-1\,1}_{1\quad 3} : E^{1\,-1}_{1\quad 3} = 1 : \sqrt{\frac{3}{8}} : \sqrt{\frac{3}{8}} : \frac{\sqrt{10}}{4} : \frac{\sqrt{10}}{4}. \tag{18}$$

Then, using Eqs (12)–(15) and Eq. (16) for spherical irreducible components of the dipole-octopole polarizability tensor we obtain

$$E^{(1,3)}_{4\,0} \;=\; \frac{\sqrt{7}}{2}\,E \tag{19}$$

$$E^{(1,3)}_{4\,\pm 4} \;=\; \frac{1}{2}\sqrt{\frac{5}{2}}\,E. \tag{20}$$

The second example concerns the dipole–octopole tensor $\mathbf{E}^{(1,3)}$ for a $D_{\infty h}$ symmetry molecule like N_2, CO_2 etc. We note that for this type of microsystem only components of $E^{(1,3)}_{j\,m}$ with $m = 0$ survive ($m = m_1 + m_2$). The isotropic and vector-like components of such tensor with $j = 0$ and $j = 1$ are also excluded since form Eq. (16) it results that $2 \leqslant j \leqslant 4$. Assuming the Cartesian components $E_{z,zzz}$ and $E_{x,xxx}$ as mutually independent [47] from Eqs (12)–(15) we obtain [46]:

$$E^{0\,0}_{1\,3} \;=\; E_{z,zzz} \tag{21}$$

$$E^{1\,-1}_{1\;\;3} \;=\; E^{-1\,1}_{1\;\;3} \;=\; \sqrt{\frac{8}{3}}\,E_{x,xxx} \tag{22}$$

Then using Eq. (16)

$$E^{(13)}_{j\,0} \;=\; \sum_{m} C^{j\,0}_{1\,m\;3\,-m}\,E^{m\,-m}_{1\,3} \tag{23}$$

we obtain that for the $D_{\infty h}$ symmetry molecule in the frame of its principal axes the $\mathbf{E}^{(1,3)}$ tensor has two independent irreducible spherical components connected with the Cartesian ones as follows:

$$E^{(1,3)}_{20} = \frac{1}{\sqrt{21}}(8\,E_{x,xxx} - 3\,E_{z,zzz}) \tag{24}$$

$$E^{(1,3)}_{40} = \frac{2}{\sqrt{7}}(E_{z,zzz} + 2\,E_{x,xxx}) \tag{25}$$

4. Conclusion

A vast number of physical processes are described by fourth-rank tensors. They are important for describing the susceptibility of various materials especially because third-rank susceptibility tensors vanish for isotropic systems. The fourth-rank tensors intervene in a number of very important nonlinear optics processes like Kerr effect, intensity-dependent refractive index phenomena, four wave mixing, third harmonic generation [5,18] and several other effects. Tensors of this kind are also very important in piezo-electric phenomena and in elasticity studies [1]. We have presented in this paper a process of decomposition of the fourth-rank tensors into parts irreducible with reference to the continuous group of rotation. Various fourth-rank tensors with regard to their Cartesian index symmetry exist. We focused our attention to the purely dipolar 4-rank tensor $\mathbf{C}$ symmetric to its last three indices and the dipole-octopole 4-rank multipolar polarizability tensor $\mathbf{E}$. Tables of transformation matrices between Cartesian and irreducible spherical form of these tensors are given. Several examples utilizing these results have been proposed.

Acknowledgments

This paper has been supported by the research project Nb. N N202 069939 sponsored by the Government of Poland.

References

[1] J.F. Nye, *Physical Properties of Crystals*, (Clarendon Press, Oxford, 1957).
[2] A.D. Buckingham, *Adv Chem Phys* **12** (1967), 107.
[3] P.D. Maker, *Phys Rev A* **1** (1970), 923.
[4] C.G. Gray and B.W.N. Lo, *Chem Phys* **14** (1976), 73.
[5] S. Kielich, *Nonlinear Molecular Optics* (Nauka, Moscow, 1981).
[6] P.N. Butcher and D. Cotter, *The Elements of Nonlinear Optics* (Cambridge University Press, New York, 1990).
[7] G. Maroulis and D.M. Bishop, *J Phys B* **18** (1985), 4675.
[8] G. Maroulis, *J Phys Chem A* **104** (2000), 4772.
[9] G. Maroulis, *Chem Phys Lett* **334** (2001), 207.
[10] J. Zyss and I. Ledoux, *Chem Rev* **94** (1994), 77.
[11] A.D. McLean and M. Yoshimine, *J Chem Phys* **47** (1967).
[12] D.L. Andrews and W.A. Ghoul, *Phys Rev A* **25** (1982), 2647.
[13] C.G. Gray and K.E. Gubbins, *Theory of molecular fluids. Vol. 1: Fundamentals* (*Clarendon Press*, Oxford, 1984).
[14] A.J. Stone, *Mol Phys* **29** (1975), 1461.
[15] J.A.R. Coope, R.F. Snider and F.R. McCourt, *J Chem Phys* **43** (1965).
[16] J. Jerphagnon, D. Chemla and R. Bonneville, *Adv Phys* **27** (1978), 609.
[17] S. Kielich, *Prog Opt* **20** (1982), 155.
[18] S. Kielich, *J Phys Paris* **43** (1982), 1749.
[19] A.R. Edmonds, *Angular Momentum in Quantum Mechanics*, (Princeton University Press, 1957).
[20] U. Fano and G. Racah, *Irreducible Tensorial Sets Academic*, (New York, 1959).
[21] D.A. Varshalovich, A.N. Moskaliev, and V.K. Khersonskii, *Quantum Theory of Angular Momentum* (World Scientific, Singapure, 1988).
[22] Z. Ożgo , *Doctor Habituates Thesis* (1975), Poznań University.
[23] J. Zyss, *J Chem Phys* **98** (1993), 6583.
[24] T. Bancewicz, *PhD Thesis* (1976), Poznań University.
[25] A. Piekara and S. Kielich, *Acta Phys Polon* (1958), 209–238.
[26] S. Kielich, *Acta Phys Polon* **17** (1958), 239.
[27] S. Kielich, *Bull. de L'Academie Polonaise des Sciences Serie des sciences math., astr. et phys* **6** (1958), 215.
[28] S. Kielich, *Acta Phys Polon* **19** (1960), 149.
[29] S. Kielich, *Acta Phys Polon* **19** (1960), 573.
[30] S. Kielich, *Acta Phys Polon* **19** (1960), 711.
[31] S. Kielich, *Proc Phys Soc* **86** (1965), 709.
[32] Z. Ozgo and S. Kielich, *Physica B+C* **81** (1976), 151 .
[33] S. Kielich, *Acta Phys Polon* **27** (1965), 305.
[34] S. Kielich, *Acta Phys Polon* **28** (1965), 95.
[35] S. Kielich, *J Chemical Physics* **46** (1967), 4090.
[36] *Optical, Electric and Magnetic Properties of Molecules: A review of the work of A. D. Buckingham Elsevier*, (Amsterdam, 1997), edited by D. C. Clary and B. J. Orr.
[37] A.D. Buckingham and G.C. Tabisz, *Mol Phys* **36** (1978), 583 .
[38] H. Posch, *Mol Phys* **46** (1982), 1213.
[39] A. Elliasmine, J.-L. Godet, Y. Le Duff and T. Bancewicz, *Mol Phys* **90** (1997), 147.
[40] A. Elliasmine, J.-L. Godet, Y. Le Duff and T. Bancewicz, *Phys Rev A* **55** (1997, 4230.
[41] T. Bancewicz, A. Elliasmine, J.-L. Godet and Y. Le Duff, *J Chem Phys* **108** (1998), 8084.
[42] J.-L. Godet, F. Rachet, Y. Le Duff, K. Nowicka and T. Bancewicz, *J Chem Phys* **116** (2002).
[43] K. Nowicka, T. Bancewicz, J.-L. Godet, F. Rachet and Y. Le Duff, *Mol Phys* (2003), 389.
[44] T. Bancewicz, K. Nowicka, J.-L. Godet and Y. Le Duff, *Phys Rev A* **69** (2004), 062704.
[45] S. Kielich, *Proc Indian Acad Sci* (*Chem Sci*) **94** (1985), 403.
[46] T. Bancewicz, V. Teboul and Y. Le Duff, *Mol Phys* **81** (1994), 1353 .
[47] P. Isnard, D. Robert and L. Galatry, *Mol Phys* **31** (1976), 1798.
[48] W.A. Steele, *Mol Phys* **39** (1980), 1411.

Journal of Computational Methods in Sciences and Engineering 10 (2010) 139–147
DOI 10.3233/JCM-2010-0315
IOS Press

Theoretical study of the electronic structure of the alkaline earth $BeLi^{2+}$ ion

M. Farjallah[a], C. Ghanmi[a] and H. Berriche[a,b,*]
[a]*Laboratoire de Physique et Chimie d'Interfaces, Département de Physique, Faculté des Sciences de Monastir, Avenue de l'Environnement, 5019 Monastir, Tunisia*
[b]*Physics Department, College of Science, King Khalid University, P. O. Box 9004, Abha, Saudi Arabia*

Abstract. In this work, we present the structural and the spectroscopic properties of the alkaline earth $BeLi^{2+}$ ion for all the electronic states dissociating into $Be^{+}(2s, 2p, 3s, 3p, 3d, 4s, 4p,$ and $4d) + Li^{+}$ and Be^{2+} + Li ($2s$ and $2p$). We have used an *ab initio* approach involving a non-empirical pseudopoential for the Li^{+} and Be^{2+} cores and core-core and core-valence correlation corrections. For our best knoweledge, the adiabatic potential energy curves and the spectroscopic constants for nearly 18 electronic states of $^2\Sigma^+$, $^2\Pi$ and $^2\Delta$ symmetries are determined here for the first time. As neither experimental nor theoretical data are available for $BeLi^{2+}$, our results are discussed and compared with similar systems such as BeH^{2+}. Numerous avoided crossings between the electronic states of $^2\Sigma^+$ and $^2\Pi$ symmetries have been localised and analysed. Their existences are related to the interaction between the potential energy curves and the charge transfer process between the two ionic systems $Be^{(2+)}Li$ and $Be^{+}Li^{+}$. Furthermore, we have calculated the adiabatic transition dipole moments from $X^2\Sigma^+$, $2^2\Sigma^+$ and $3^2\Sigma^+$ states to the higher electronic states of the same symmetry. This study represents the necessary initial step towards the investigation of the charge transfer processes in collision between Be^{+}-Li^{+} and Be^{2+}-Li.

Keywords: *Ab initio*, pseudopotentials, potential energy curves, spectroscopic constants, avoided crossing, transition dipole moments

1. Introduction

The study of the charge transfer processes in collisions between atoms and ions play an important role in the different areas of astrophysical, physics, and chemistry of low density plasma and ionized gases. These collisions provide detailed informations about long-range interatomic potentials, scattering length [1], and excited-state radioactive life times. The collision between the Be^{2+} ion and the hydrogen or lithium atoms could be of great importance. The Be^{2+}-H collision has been studied by Shingal [2] (in 1986) and Allan et al. [3] (in 1987). Nicolaides et al. [4] have performed a theoretical study on the stability and physicochemical properties of light dications (BeH^{2+}, BH^{2+}, $BeHe^{2+}$ and Be_2^{2+}) in order to investigate thermodynamically stability of the system. Despite the great interest of the collisional processes, the comprehensive of the theoretical structure and spectroscopic properties for the alkaline earth $BeLi^{2+}$ ion is still missing. We extend in this work our *ab initio* study of the alkaline earth ion BeH^{2+} [5] to the $BeLi^{2+}$ ionic system. Accurate potential energy curves and their molecular spectroscopic constants for numerous electronic states of $^2\Sigma^+$, $^2\Pi$ and $^2\Delta$ symmetries dissociating up to $Be^{+}(4d) + Li^{+}$ and $Be^{2+} + Li\ (2p)$ have been performed. In addition, the transition dipole moments

*Corresponding author. E-mails: hamid.berriche@fsm.rnu.tn, hamidberriche@yahoo.fr.

from the ground state ($X^2\Sigma^+$) and the first excited states ($2^2\Sigma^+$ and $3^2\Sigma^+$) to the higher excited states of $^2\Sigma^+$ and $^2\Pi$ symmetries have been calculated. To our best knowledge, the results of the alkaline earth $BeLi^{2+}$ ion are presented here for the first time. In the following section, we briefly recall the *ab initio* approach and give numerical details. Section 3 is devoted to the presentation and discussion of our results: the potential energy curves and their spectroscopic constants, the vibrational energy levels for the metastable state $3^2\Sigma^+$ and the transition dipole moments between the neighbour states of $^2\Sigma^+$ symmetry. Finally, we summarize our conclusion in Section 4.

2. Method of calculations

As in our previous works on XY^+ (X and Y = H, Li, Na, K, Rb and Cs) [6–14], the alkaline earth $BeLi^{2+}$ ion is treated as a one-electron system using the non-empirical pseudopotential of Barthelat and Durand [15], in its semilocal form and used in many previous works [6–14,16–20]. For the simulation of the interaction between the polarizable Be^{2+} and Li^+ cores with the valence electrons, a core polarization potential V_{CPP} is used, according to the operator formulation of Müller, Flesh and Meyer [21]:

$$V_{CPP} = -\frac{1}{2}\sum_{\lambda}\alpha_\lambda \vec{f}_\lambda.\vec{f}_\lambda$$

where α_λ is the dipole polarizability of the core λ and $\vec{f}_\lambda$ is the electric field produced by valence electrons and all other cores on the core λ.

$$\vec{f}_\lambda = \sum_i \frac{\vec{r}_{i\lambda}}{r_{i\lambda}^3} F(r_{i\lambda},\rho_\lambda) - \sum_{\lambda'\neq\lambda}\frac{\vec{R}_{\lambda'\lambda}}{R_{\lambda'\lambda}^3}Z_\lambda$$

where $r_{i\lambda}$ is a core-electron vector and $\vec{R}_{\lambda'\lambda}$ is a core-core vector.

According to the formulation of Foucrault et al. [22] the cutoff function $F(r_{i\lambda},\rho_\lambda)$ is taken to be a function of l to consider in a different way the interaction of valence electrons of different spatial symmetry with core electrons. For the lithuim, we use the Gaussian basis set ($9s8p5d1f/8s6p3d1f$) of Ref. 7, while for the beryllium we use the Gaussian basis set ($7s9p10d/7s9p9$d) of ref. 17. The cuttoff radii for the lowest s, p, d and f, one electron states are reported in Table 1. The core dipole polarizability of the ionic atoms Li^+ and Be^{2+}, have been taken equal to the experimental ones, respectively, 0.1915 [21] and 0.052 a_0^3 [21]. We present in table 2 the calculated dissociation energies for all the electronic states dissociating into Be^+($2s$, $2p$, $3s$, $3p$, $3d$, $4s$, $4p$ and $4d$) + Li^+ and Be^{2+} + Li ($2s$ and $2p$). These values are compared with the available theoretical [23] and experimental [24] data. As can be seen, our dissociation energies are in good agreement with the experimental values. The difference between our values and the experimental ones does not exceed 46.30 cm^{-1} found for Be^+($2p$) atomic limit. This represents the accuracy of the present calculation at the atomic levels, which will be transmitted to the molecular energy.

3. Results and discussion

3.1. Potential energy curves and spectroscopic constants

The potential energy curves for the electronic states dissociating up to Be^+($4d$)+ Li^+ and Be^{2+}+ Li ($2p$) have been calculated for a large and dense grid of internuclear distances ranging from 2.1 to 200 a.

Table 1
l-dependant cut-off radii (in bohr) for Li and Be atoms

l	Li	Be
s	1.434	0.889
p	0.982	0.882
d	0.600	1.14
f	0.400	1.14

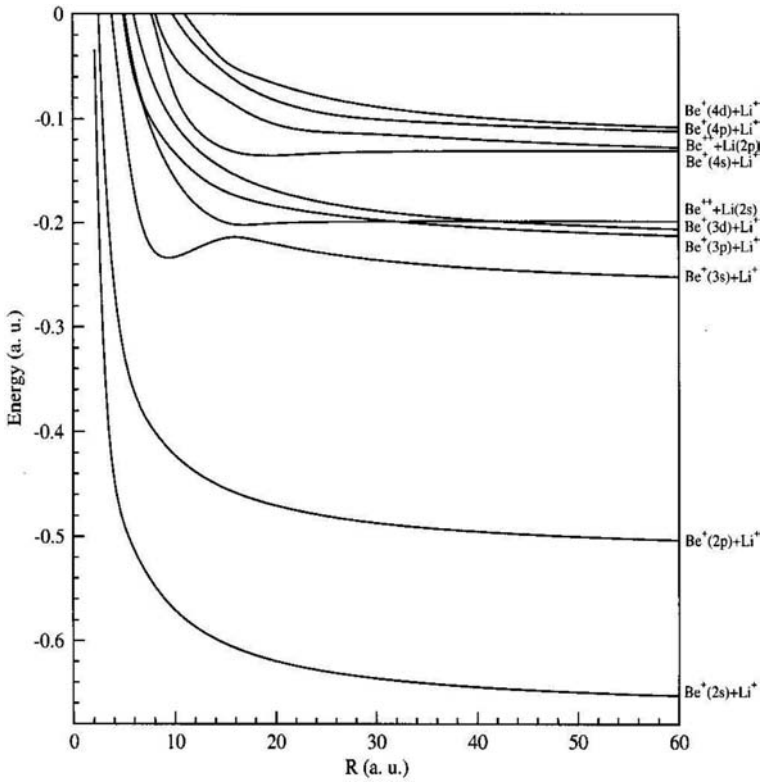

Fig. 1. Potential energy curves for the lowest 1–10 $^2\Sigma^+$ electronic states of the alkaline earth $BeLi^{2+}$ ion dissociating into $Be^+(2s, 2p, 3s, 3p, 3d, 4s, 4p$ and $4d) + Li^+$ and $Be^{++} + Li$ ($2s$ and $2p$).

u. The potential curves are displayed in Fig. 1 for the $^2\Sigma^+$ electronic states and Fig. 2 for the $^2\Pi$ and $^2\Delta$ electronic states. As neither experimental nor theoretical data are available, the similarity with other ionic systems such as BeH^{2+} will be discussed. Figure 1 shows that the ground ($X^2\Sigma^+$) and the first ($2^2\Sigma^+$) excited states dissociating respectively into $Be^+(2s) + Li^+$ and $Be^+(2p) + Li^+$ are repulsive. In contrast, the second excited state ($3^2\Sigma^+$) dissociating into Be^+ ($3s$) + Li^+ is thermodynamically unstable and presents a similar behaviour than that of the ground states of BeH^{2+} [4,5], Be_2^{2+} [4] and BH^{2+} [4]. This state presents a minimum located at 9.43 a. u. and a high potentail barrier of 11813 cm^{-1} located at 16.5 a. u. due to the interaction with the upper excited state. This state traps thirty one vibrationnal levels. Their energy spacings are reported in Table 3. In addition, an important general behaviour can be observed in the potential energy curves for the higher excited states. It corresponds to spectacular undulations due to the presence of the avoided crossings between neighbor states for a given

Table 2
Asymptotic energy of alkaline earth $BeLi^{2+}$ ion (in cm^{-1}): comparison between our energies, Errea et al. [23] theoretical energies and the experimental dissociation ones [24]. ΔE is the difference between the experimental and the theoretical dissociations energies

Asymptotic limit	Our work	Errea et al. [23]	Exp. [24]	ΔE	ΔE [23]
$Be^+(2s)+Li^+$	−146887.6	−147169.1	−146881.5	6.145	287.6
$Be^+(2p)+Li^+$	−114905.9	−114906.1	−114952.2	46.30	46.1
$Be^+(3s)+Li^+$	−58633	−58633.1	−58648.1	15.143	15
$Be^+(3p)+Li^+$	−50352.8	−50353	−50384.9	32.04	31.9
$Be^+(3d)+Li^+$	−48802	−48802.2	−48828.8	26.77	26.6
$Be^{2+}+Li(2s)$	−43487		−43487	0	
$Be^+(4s)+Li^+$	−31381.2		−31413.4	32.26	
$Be^{2+}+Li(2p)$	−28581.4		−28583.3	1.9	
$Be^+(4p)+Li^+$	−28094.5		−28119.1	24.58	
$Be^+(4d)+Li^+$	−27441.6		−27460.7	19.094	

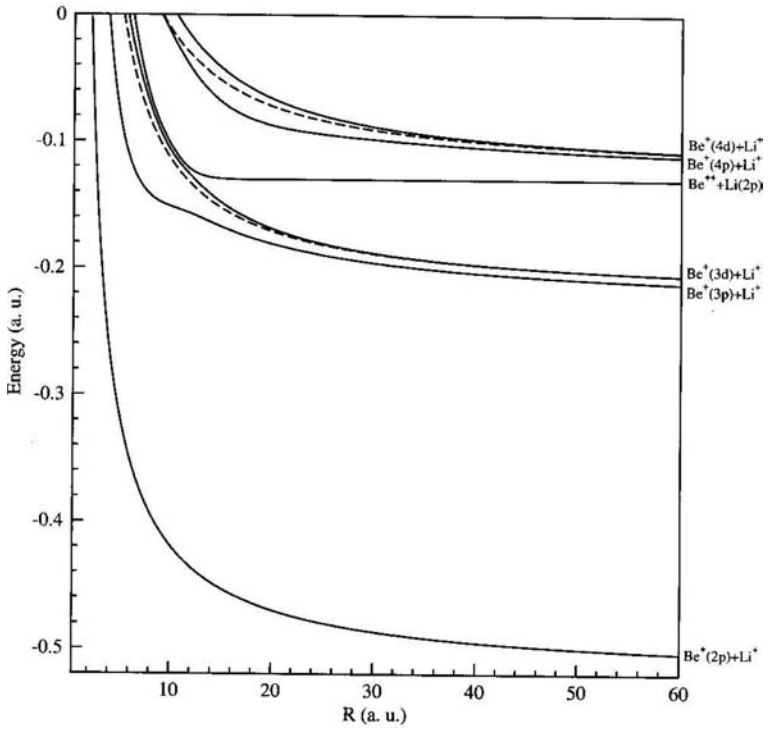

Fig. 2. Potential energy curves for the 1–$6^2\Pi$ (solid line) and 1-$2^2\Delta$ (dashed line) electronic states of the alkaline earth $BeLi^{2+}$ ion dissociating into $Be^+(2p, 3p, 3d, 4p$ and $4d) + Li^+$ and $Be^{2+}+$ Li $(2p)$.

symmetry. In particular, we mention the avoided crossings among $^2\Sigma^+$ electronic states, namely those between $3^2\Sigma^+$ and $4^2\Sigma^+$ located at 16.72 a. u., between $4^2\Sigma^+$ and $5^2\Sigma^+$ around 6.45 and 31.65 a. u., between $5^2\Sigma^+$ and $6^2\Sigma^+$ states at 41.87 a. u., and $7^2\Sigma^+$ and $8^2\Sigma^+$ states at 74.87 a. u. The avoided crossings between the $3^2\Sigma^+-4^2\Sigma^+$, $4^2\Sigma^+-5^2\Sigma^+$ and $5^2\Sigma^+-6^2\Sigma^+$ states are due to the charge transfer processes between the two ionic structures Be^+Li^+ and $Be^{(2+)}Li$.

The spectroscopic information of the $3^2\Sigma^+$, $4^2\Sigma^+$, $5^2\Sigma^+$ and $7^2\Sigma^+$ states, which are thermodynamically unstable, are collected in Table 4. The minimum for the $3^2\Sigma^+$, $4^2\Sigma^+$, $5^2\Sigma^+$ and $7^2\Sigma^+$ are located

Table 3
Vibrational energy level spacing (E(υ)-E(υ-1)) (in cm^{-1}) for the $3^2\Sigma^+$ electronic state of the alkaline earth $BeLi^{2+}$ ion

υ	$3^2\Sigma^+$
0	
1	172.903
2	170.980
3	169.043
4	167.128
5	165.243
6	163.276
7	161.380
8	159.430
9	157.443
10	155.453
11	153.461
12	151.421
13	149.349
14	147.273
15	145.111
16	142.927
17	140.701
18	138.400
19	136.028
20	133.560
21	131.024
22	128.334
23	125.499
24	122.447
25	119.159
26	115.535
27	111.399
28	106.485
29	100.261
30	90.832

Table 4
Spectroscopic informations for the $3^2\Sigma^+$, $4^2\Sigma^+$, $5^2\Sigma^+$ and $7^2\Sigma^+$ electronic states of the alkaline earth $BeLi^{2+}$ ion

State	R_{min} (a. u.)	R_{max} (a. u.)	ΔE_1 (cm^{-1})	ΔE_2 (cm^{-1})
$3^2\Sigma^+$	9.46	15.94	4369	−7351.7
$4^2\Sigma^+$	16.72	31.65	809	−5985.2
$5^2\Sigma^+$	32.04	41.47	46	−5244
$7^2\Sigma^+$	19.38	72.70	1103	−1681.1

$\Delta E_1 = E_{max}–E_{min}$.
$\Delta E_2 = E_{AL}–E_{min}$ where E_{AL} is the energy at asymptotic limit.

respectively, at $R_{min} = 9.46$, 16.72, 32.04 and 19.28 a. u. The maximum for the same electronic states are located respectively at $R_{max} = 15.94$, 31.65, 41.47 and 72.70 a. u. The difference of energy between the maxim and minimum $\Delta E_{1(}\Delta E_1 = E_{max}–E_{min})$ are respectively, 4369, 809, 46 and 1103 cm^{-1} for the $3^2\Sigma^+$, $4^2\Sigma^+$, $5^2\Sigma^+$ and $7^2\Sigma^+$ states. The well depths of the weakly bound excited states $6^2\Sigma^+$, $8^2\Sigma^+$ and $4^2\Pi$ are, respectively, 25, 13 and 6 cm^{-1} located at very large internuclear distances of 43.00, 75.00 and 17.31 a. u.

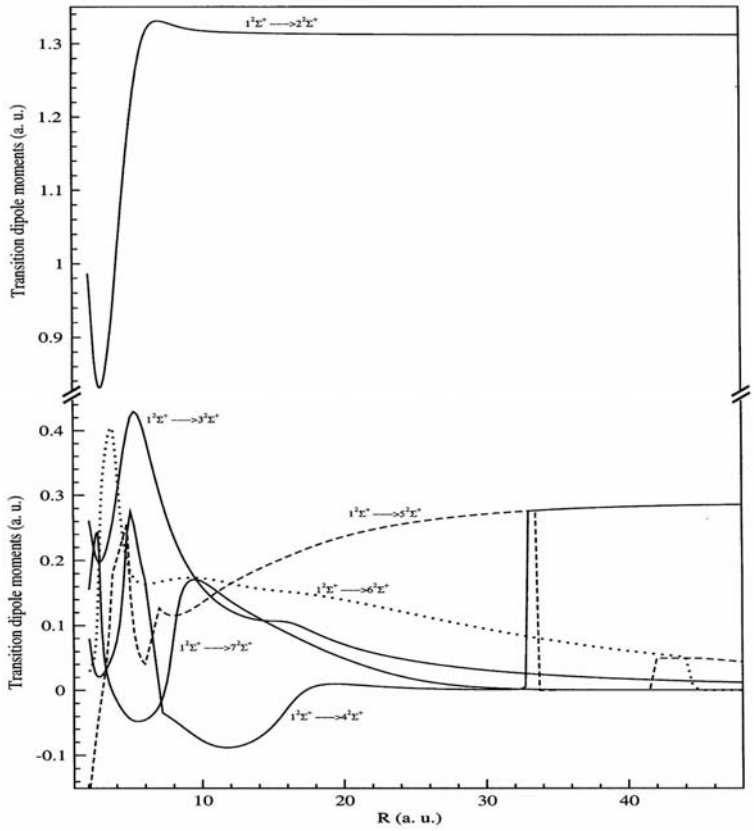

Fig. 3. Transition dipole moments from the ground state $X^2\Sigma^+$ to the 2–$7^2\Sigma^+$ higher excited states of the alkaline earth $BeLi^{2+}$ ion.

3.2. Transition dipole moments

To supplement this work on the alkaline earth $BeLi^{2+}$ ion we have determined the transition dipole moment, which is necessary for the formation prediction of ultracold dipolar heteronuclear alkali and alkaline earth ionic and neutral molecules. Furthermore, dipole function is considered as the sensitive test for the accuracy of the calculated electronic wavefunctions and energies. The transition dipole moments have been determined between the $X^2\Sigma^+$, $2^2\Sigma^+$ and $3^2\Sigma^+$ states and several higher electronic states for the same large and dense grid of internuclear distances, varying from 2.1 to 200 a. u. To our best knowledge, neither experimental nor theoretical studies have been determined for the transition dipole moments. The transition dipole moments from $X^2\Sigma^+$, $2^2\Sigma^+$ and $3^2\Sigma^+$ states to higher electronic states are presented, respectively, in Figs 3, 4 and 5. Figure 3 presents the transition dipole moments from the ground state $X^2\Sigma^+$dissociating into $Be^+(2s)+ Li^+$ to the 2–$7^2\Sigma^+$ states of the alkaline earth $BeLi^{2+}$ ion. We remark that the most significant transition dipole moments is related to the transition between $X^2\Sigma^+$ and $2^2\Sigma^+$ states; it increases between 3.00 and 6.30 a.u. and finally becomes a constant equal to 1.32 a. u., corresponding exactly to the atomic transition dipole moments between $Be^+(2s)$ and $Be^+(2p)$. For the transition from $X^2\Sigma^+$ to the higher excited states, we remark the presence of two brisk changes between the $X^2\Sigma^+$-$4^2\Sigma^+$ and $X^2\Sigma^+$-$5^2\Sigma^+$ transition dipole moments located at particular internuclear distances very close to the avoided crossing positions between $4^2\Sigma^+$ and $5^2\Sigma^+$ states mentioned earlier

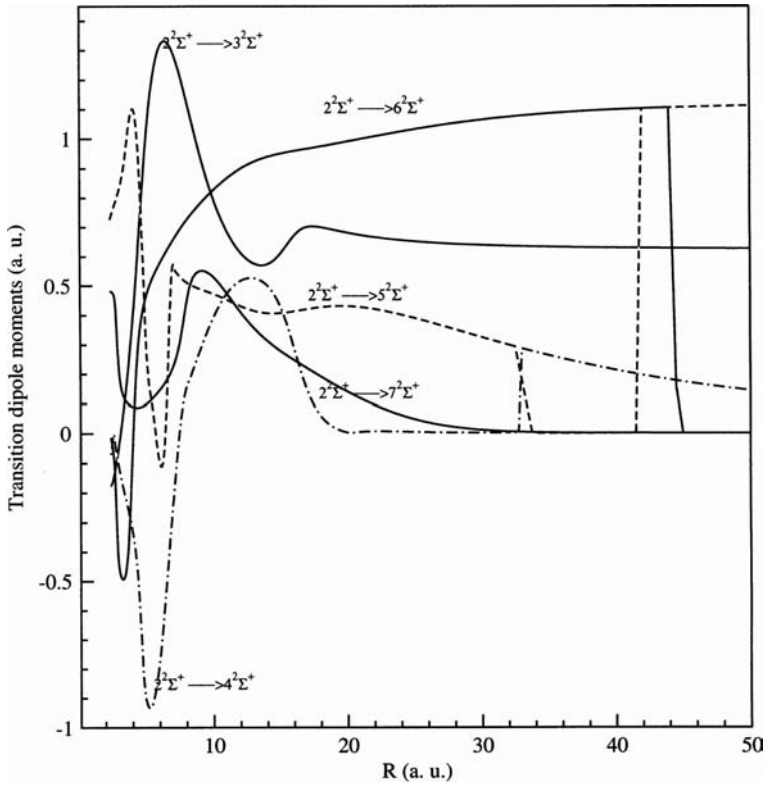

Fig. 4. Transition dipole moments from the $2^2\Sigma^+$ to the 3–$7^2\Sigma^+$ higher excited states of the alkaline earth $BeLi^{2+}$ ion.

(6.50 and 31.78 a. u.). In addition, we note the local change between the $X^2\Sigma^+$-$5^2\Sigma^+$ and $X^2\Sigma^+$-$6^2\Sigma^+$ transition dipole moments around 41.87 a. u., which is related to the avoided crossing between $5^2\Sigma^+$ and $6^2\Sigma^+$ electronic states.

Figures 3 and 4 show, respectively, the transition dipole moments from the first excited state ($2^2\Sigma^+$) dissociating into $Be^+(2p)+ Li^+$ and the second excited state ($3^2\Sigma^+$) dissociating into $Be^+(3s)+ Li^+$ to the higher excited states of the same symmetry of the alkaline earth ion $BeLi^{2+}$. The same behaviour, seen below for the transition between the ground state ($X^2\Sigma^+$) and the higher excited states $^2\Sigma^+$ is observed also here. Brisk changes between the transition dipole moments are localized at particular distances corresponding to the avoided crossings between neighbour electronic states.

4. Conclusion

We have performed an accurate *ab initio* investigation for the ground and many excited states of the alkaline earth $BeLi^{2+}$ ion using the pseudopotentials approach. The electronic structure of the alkaline earth $BeLi^{2+}$ ion, including the potential energy curves for $^2\Sigma^+$, $^2\Pi$ and $^2\Delta$ states, their spectroscopic constants, and the transition dipole moments from the ground ($X^2\Sigma^+$), the first ($2^2\Sigma^+$) and second ($3^2\Sigma^+$) states to the higher excited states of the same symmetry have been determined. Only our spectroscopic data are presented here as neither experimental nor theoretical results exist for this ionic system. A similar behaviour between the $3^2\Sigma^+$ state of the $BeLi^{2+}$ ionic system and the ground state of the BeH^{2+} [5] is observed. This state is thermodynamically unstable; however it presents a minimum

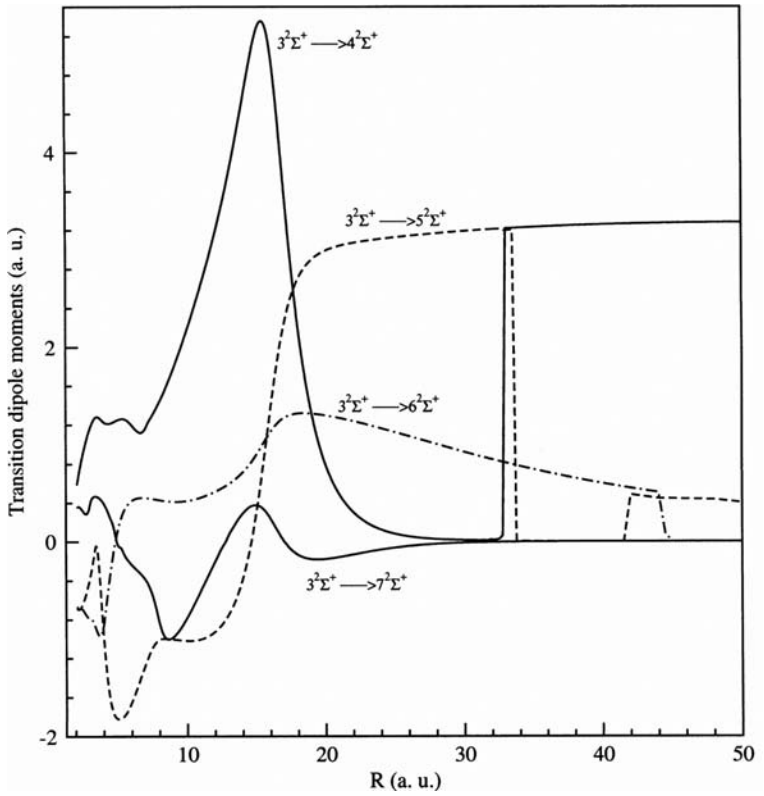

Fig. 5. Transition dipole moments from $3^2\Sigma^+$ to the 4–$7^2\Sigma^+$ higher excited states of the alkaline earth $BeLi^{++}$ ion.

and a high barrier due to the interaction with the upper state related to charge transfer process. Numerous avoided crossings between the higher electronic states and undulations have been observed for the $^2\Sigma^+$ and $^2\Pi$ symmetries. Their existences are related to the interaction between the electronic states and to the charge transfer process between the two ionic systems $Be^{(2+)}Li$ and Be^+Li^+. The calculated transition dipole moments are significant at particular distances corresponding to the avoided crossings between the electronic states. This work extends our recent study on the alkaline earth BeH^{2+} ion [5] and represents the necessary initial step towards the charge transfer processes in collisions of ions with atoms.

Acknowledgment

This work has been supported by the Advanced Materials Center and KACST through the Long-Term Comprehensive National Plan for Science, Technology and Innovation program (Project no. 08-NAN148-7).

References

[1] M. Movre and G. Pichler, *J Phys B* **10** (1977), 2631.
[2] R. Shingal, *Durham University Preprint*, (1986).

[3] R. Allan, R. Shingal and J. Hanssen, *Proc 15th Int Conf on Physics of Electronic and Atomic collisions*, (1987).
[4] C.A. Nicolaides, M. Chrysos and P. Valtazanos, *J Phys B: At Mol Opt Phys* **23** (1990), 791.
[5] M. Farjallah, C. Ghanmi and H. Berriche, *Can J Phys*, (submitted).
[6] H. Berriche and F.X. Gadea, *Chem Phys* **191** (1995), 119.
[7] H. Berriche, *J Mol Struct* (*THEOCHEM*) **663** (2003), 101.
[8] H. Berriche, C. Ghanmi and H. Ben Ouada, *J Mol Spect* **230** (2005), 161.
[9] C. Ghanmi, H. Berriche and H. Ben Ouada, *J Mol Spect* **235** (2006), 158.
[10] C. Ghanmi, H. Berriche and H. Ben Ouada, *Proceeding of the International Conference on Computational and Mathematical Methods in Science and Engineering*, CMMSE-2005 166–174, Alicante, (June 2005) 166.
[11] C. Ghanmi, H. Berriche and H. Ben Ouada, *Lect Ser Comp Comput Scien* **4** (2005), 703.
[12] H. Bouzouita, C. Ghanmi and H. Berriche, *J Mol Struct* (*THEOCHEM*) **777** (2006), 75.
[13] H. Berriche, C. Ghanmi, M. Farjallah and H. Bouzouita, *J Comp Meth Scien Eng* **8** (2008), 297.
[14] C. Ghanmi, H. Bouzouita, H. Berriche and H. Ben Ouada, *J Mol Struct* (*THEOCHEM*) **777** (2006), 81.
[15] J.C. Barthelat and Ph. Durand, *Theor Chem Acta* **38** (1975), 283; J.C. Barthelat and Ph. Durand, *Gazz Chim Ital* **108** (1978), 225.
[16] M. Farjallah, C. Ghanmi and H. Berriche, AIP Conf. Proc. (in press)
[17] M. Farjallah, C. Ghanmi and H. Berriche, *J Mol Struct* (*THEOCHEM*), in press.
[18] H. Berriche 1995, PhD Thesis, Paul Sabatier University (unpublished).
[19] N. Mabrouk and H. Berriche, *J Phys B: At Mol Opt Phys* **41** (2008), 155101.
[20] N. Mabrouk, H. Berriche, H. Ben Ouada and F.X. Gadea, *J Phys Chem A* **114** (2010), 6657.
[21] W. Müller, J. Flesh and W. Meyer, *J Chem Phys* **80** (1984), 3297.
[22] M. Foucrault, Ph. Millie and J.P. Daudey, *J Chem Phys* **96** (1992), 1257.
[23] L.F. Errea, B. Herrero, L. Méndez, I. Rabadán and P. Sánchez, *J Phys B: At Mol Opt Phys* **27** (1994), 753.
[24] C.E. Moore, Atomic Energy Levels, NSRDS-NBS No. 467 Washington, DC: US Governoment Printing Office (1989).

Journal of Computational Methods in Sciences and Engineering 10 (2010) 149–164
DOI 10.3233/JCM-2010-0316
IOS Press

Exploring NLO response of 9,10-donor-acceptor substituted Bichromophoric Anthracene Derivatives

Ramprasad Misra, Rahul Sharma and S.P. Bhattacharyya*
Department of Physical Chemistry, Indian Association for the Cultivation of Science, Jadavpur, Kolkata 700 032, India

Abstract. Ab-initio finite field SCF calculations with split valence double zeta basis set indicate that 9, 10- donor-acceptor substituted anthracene derivatives have large quadratic hyperpolarizabilities for suitable combinations of donor and acceptor moieties. A difference in the first hyperpolarizabilities (β_{total}) of isomeric organic chromophores containing the same donor and acceptor groups indicate the possible role of intramolecular charge transfer (ICT) in shaping the NLO response in these π-conjugated molecular chromophores. A correlation is sought to be established among calculated β_{total} on one hand and the donor strength, the strength of the acceptor, donor-acceptor interaction and the donor-acceptor separation, on the other by using Genetic Algorithm (GA) to search through the relevant parameter space. It appears that β_{total} of a molecule is dominantly determined by additive contributions from the donors and the acceptors. The results might be helpful in designing new NLO materials using the bichromophoric anthracene derivatives.

1. Introduction

There exist a class of materials, the so called NLO materials, that interact with applied electromagnetic fields generating new ones having altered frequency or phase or some other physical properties. The demand for such materials has been growing steadily due to the phenomenal progress in the fields of optical computing and communications, dynamic image processing, all optical switching devices, second or higher harmonic generations, etc [1–12]. Traditionally, inorganic solids like $FeNbO_3$ and KH_2PO_4 have been the most used NLO materials. Later on, multilayered semiconductor structures and macromolecular π – electron assemblies became hotly pursued alternatives [13,14]. Of the three classes of generic alternatives of NLO materials,viz., multilayered semi-conductor structures, molecular based macroscopic assemblies and traditional inorganic solids, the molecule-based macroscopic π – electron assemblies are endowed with several attractive features. We note here that the NLO response of molecule based materials is ultimately shaped by the NLO properties of the building blocks – the molecular chromophores [15,16]. The task of designing of the molecule based macromolecular π – assemblies therefore boils down to the designing of molecules or molecular assemblies with desirable NLO characteristics. Over the years, the rudimentary design clues or thumb rules have been upgraded – thanks to the availability of reliable computational techniques and the availability of the user friendly quantum chemistry softwares for computing NLO responses [17–19]. It has now reached a stage where

*Corresponding author. Fax: +9133 24732805; E-mail: pcspb@iacs.res.in.

experimentalists can sharpen their chemical intuition with the insight and the understanding provided by the computational analysis leading to efficient targeting of optimal chromophore structures capable of generating the desired level of NLO response. The origin of NLO response from a donor-acceptor based charge transfer molecules has been an intense area of research in molecular sciences [5,20–22]. The strength of conjugation, or more precisely the extent of charge transfer plays a crucial role in determining the efficiency of charge transfer, hence, the NLO response. Recently, Nandi et al. [23] have shown that two isomeric molecular chromophores with equal length of conjugation differs in their NLO response due to the difference in the extent of longitudinal charge transfer interaction. A difference in first hyperpolarizability in three isomeric buckministerfullarenes have been studied by Fanti et al. [24]. They have concluded that the conjugation and inductive effect together contribute at the same time to determine the value of β_{total} in the molecules referred to. Substituted anthracene derivatives have attracted attention of the scientific community due to their potential use as fluoroscent probes and application in methane uptake [25,26]. These molecules are well establised as intramolecular charge transfer (ICT) chromophores but little seems to be known about their NLO response. Substitution at 9th and 10th positions of an anthracene ring are easier to achieve as the resulting loss of resonance energy is minimum, these molecules are easy to synthesize. These molecules have relatively low dipole moments which make them good potential candidates for designing non-centrosymmertic NLO crystals. Muralidharan et al. [27] measured the ground and excited state dipole moments of 9,10 disubstituted anthracene derivatives and concluded that $\Delta\ \mu_{ge}$ values are generally much smaller compared to their benzene counterpart. Nevertheless, the $\Delta\ \mu_{ge}$ values does not appear to be too small to make the anthracene derivatives silent to nonlinear optical polarization.

In this contribution we explore theoretically the possibility of using 9,10 substituted anthracene derivatives (Fig. 1A–AD) as potential molecular chromophores for fabricating new NLO materials. The idea behind exploring these molecular chromophores lies in the fact that these molecules allow charge to be transferred from the donor to the acceptor moiety in the excited state resulting in generation of higher excited state dipole moment compared to the ground state [17]. A Zwitterionic species is expected to be formed as shown in Fig. 2. So, from a two state point of view [28] we can anticipate fairly high β_{total} values for the aforesaid molecules. Unsubstituted anthracene ring has $\beta_{total} = 0$, as expected on grounds of symmetry. A donor at C9 and an acceptor at C10 destroy the symmetry and create a 'push-pull' kind of polarized π – electronic structure that can, in principle, have large quadratic hyperpolarizability (β). To the best of our knowledge, such molecules have not so far been either experimentally or theoretically investigated for their NLO response. Our primary aim has been to investigate theoretically if such structures can lead to the emergence of large first hyperpolarizability and if so, what kind of donor-acceptor combinations could maximize it. The charge transfer-governed parameters for controlling the NLO response at our disposal are – (i) the strength of the donor, (ε_d), (ii) the acceptor strength, (ε_a), (iii) the distance (l) over which the donor to acceptor transfer of charge takes place (l), and the type of l-dependance (power law)that β_{total} could have. We plan to correlate the theoretically computed β_{total} with ε_d, ε_a and l^n using a simple Genetic Algorithm (GA). A cross-term involving ε_d and ε_a will also be introduced to model any non-linearity in the donor-acceptor interaction. The 9, 10 di-substituted anthracene derivatives chosen for the study are depicted in Fig. 1. There are essentially four types of molecules, viz., Fig. 1A, 1B, 1C and 1D of which molecules 1B and 1C are structural isomers. They have been chosen to provide a wide range of variation in donor-acceptor strengths and disposition, and a limited amount of variability in the conjugative π – electron network across which charge transfer takes place. The NLO response of a few isomeric systems have also been analyzed with a view to understanding the role of intramolecular charge transfer in the emergence of large β_{total}.

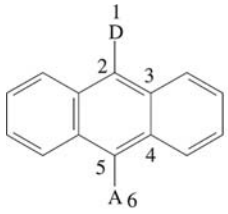

A

D = -NH_2 A = -NO_2 Molecule A1 D = -NMe_2 A = -NO_2 Molecule A9
D = -NH_2 A = -NO Molecule A2 D = -NMe_2 A = -NO Molecule A10
D = -NH_2 A = -CN Molecule A3 D = -NMe_2 A = -CN Molecule A11
D = -NH_2 A = -CHO Molecule A4 D = -NMe_2 A = -CHO Molecule A12

D = -OMe A = -NO_2 Molecule A5 D= -H A = -CHO Molecule A13
D = -OMe A = -NO Molecule A6
D = -OMe A = -CN Molecule A7
D = -OMe A = -CHO Molecule A8

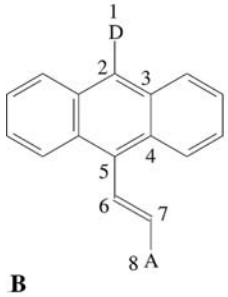

B

D = -NH_2 A = -NO_2 Molecule B1 D = -NMe_2 A = -NO_2 Molecule B9
D = -NH_2 A = -NO Molecule B2 D = -NMe_2 A = -NO Molecule B10
D = -NH_2 A = -CN Molecule B3 D = -NMe_2 A = -CN Molecule B11
D = -NH_2 A = -CHO Molecule B4 D = -NMe_2 A = -CHO Molecule B12

D = -OMe A = -NO_2 Molecule B5
D = -OMe A = -NO Molecule B6
D = -OMe A = -CN Molecule B7
D = -OMe A = -CHO Molecule B8

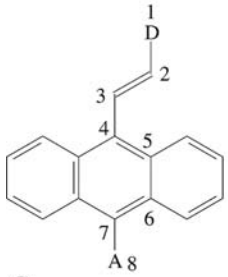

C

D = -NH_2 A = -NO_2 Molecule C1
D = -NH_2 A = -NO Molecule C2
D = -NH_2 A = -CN Molecule C3
D = -NH_2 A = -CHO Molecule C4

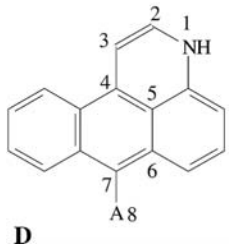

D

A = -NO_2 Molecule D1
A = -NO Molecule D2
A = -CN Molecule D3
A = -CHO Molecule D4

Fig. 1. The chemical structures of the molecules studied. The numberings of selected atoms are done for ready reference.

2. Computational method

2.1. Calculation of dipole moment, polarizability and first hyperpolarizability

We have computed linear and nonlinear polarizabilities of all the thirty two anthracene derivatives at their theoretically computed equilibrium geometries using Gaussian 03 [29] quantum mechanical software package on a LINUX computational platform. The geometry optimization was carried out in two steps: (i) closed shell restricted Hartree-Fock (RHF) method at Austin Model 1 (AM1) level of approximation was first employed to compute the equilibrium structural parameters of each; (ii) those optimized structural parameters obtained from AM1 level of calculations were used as input to the

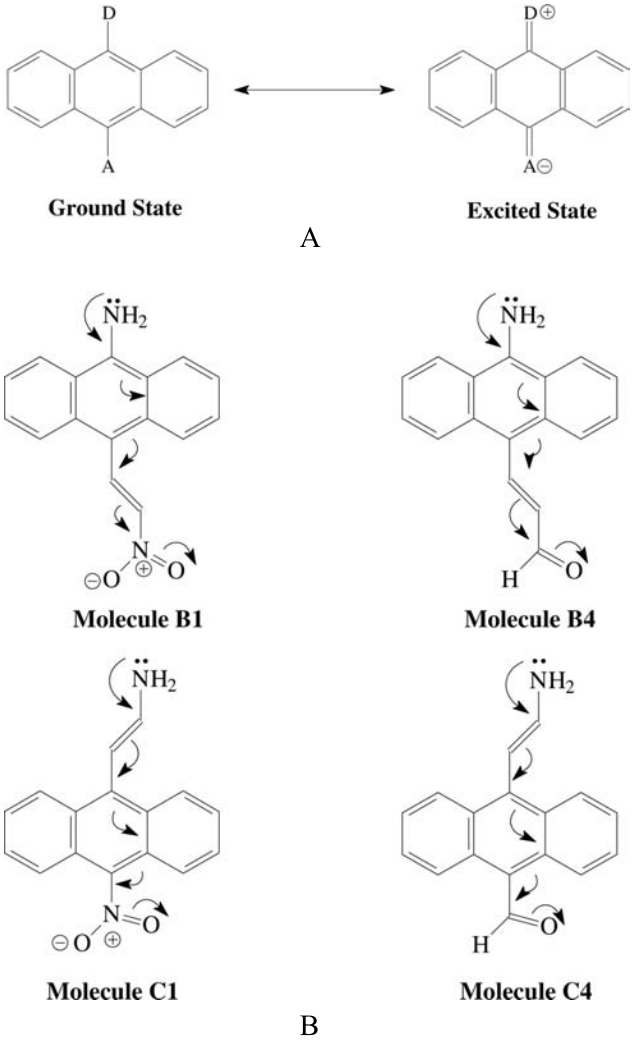

Fig. 2. (a)The mechanism of intramolecular charge transfer in the molecules studied (b) charge transfer mechanism in two pairs of isomeric NLO molecules.

Gaussian 03 and the geometry was re-optimized accurately at the Hatree-Fock level with 6-31G** basis set for all atoms. This split valence double zeta basis set uses linear combination of 6 primitive gaussians to describe the core electrons and linear combinations of 3 and 1 primitive gaussians to represent two basis functions of the valence electrons. Two asterisk denote polarization function added to both the heavy and light atoms in the molecule [30]. The level of theory used here has been reported to be adequate in describing the trends of the NLO response in organic chromophores [31–33]. Geometry optimization was carried out fully and linear and the first nonlinear optical response properties of the molecules were calculated using those optimized geometries. We have used the MOLDEN [34] software for the visualization of the optimized structures. CI singles (CIS) calculations were performed using the ground state optimized geometries of the molecules, whenever needed. The dipole moment of the molecules under investigation has been calculated using the following equation-

$$\mu = ({\mu_x}^2 + {\mu_y}^2 + {\mu_z}^2)^{1/2} \quad (1)$$

The components of linear polarizability appear in the Gaussiaon03 output in lower triangular order as follows: α_{xx}, α_{xy}, α_{yy}, α_{xz}, α_{yz} and α_{zz}. The average polarizability ($\overline{\alpha}$) of the molecules has been computed using the relation –

$$\overline{\alpha} = (\alpha_{xx} + \alpha_{yy} + \alpha_{zz})/3 \tag{2}$$

The first hyperpolarizability, β is a tensor of rank 3 with 27 components which can be reduced to 10 by virtue of Kleinman symmetry of the ($3 \times 3 \times 3$) matrix representing the β tensor. The Gaussian 03 output provide these 10 components of the ($3 \times 3 \times 3$) matrix as lower tetrahedral order, i.e., β_{xxx}, β_{xxy}, β_{xyy}, β_{yyy}, β_{xxz}, β_{xyz}, β_{yyz}, β_{xzz},β_{yzz} and β_{zzz}, respectively. These components have been used to define different types of hyperpolarizabilities in literature, such as β_{vector}, i.e., the β projected in the direction of the dipole moment of the molecule; $\beta_{parallel}$, that means, the components of the $\beta_{parallel}$ to the direction of the charge transfer in the ground state and β_{total} which is computed [31] by using –

$$\begin{aligned}\beta_{total} = \big[&(\beta_x)^2 \\ &+ (\beta y)^2 \\ &+ (\beta_z)^2\big]^{1/2}\end{aligned} \tag{3}$$

In general components of β appearing in Eq. (3) can be computed by using

$$\begin{aligned}\beta_i = &\beta_{iii} \\ &+ (1/3)\left[\sum\nolimits_{i\neq j} \beta_{ijj}^2 + \beta_{jij}^2\right. \\ &+ \left.\beta_{jji}^2\right]^{\frac{1}{2}}\end{aligned} \tag{4}$$

Expressed in terms of Cartesian components it leads to

$$\begin{aligned}\beta_{total} = \big[&(\beta_{xxx} + \beta_{xyy} + \beta_{xzz})^2 \\ &+ (\beta_{yyy} + \beta_{yzz} + \beta_{yxx})^2 \\ &+ (\beta_{zzz} + \beta_{zxx} + \beta_{zyy})^2\big]^{1/2}\end{aligned} \tag{5}$$

All the components of α and β reported here are in the atomic system of units.

2.2. Modeling the first hyperpolarizabilities of the molecules by using Genetic Algorithms (*GA*)

The β_{total} obtained in the manner described in the preceding paragraph has been sought to be represented as

$$\beta_{total} = \beta_0 + a\varepsilon_d + b\varepsilon_a + c\varepsilon_d\varepsilon_a + dl^n \tag{6}$$

where, β_0 is supposed to represent the additive part of β coming from the anthracene ring structure itself in the presence of symmetry breaking substituents; the second, third and the fourth terms represent the donor contribution, the acceptor contribution and contribution coming from the nonlinear donor-acceptor interaction, respectively. The last term represents contribution from the π – electron network across which the intramolecular charge transfer takes place. ε_d and ε_a are parameters representing donor

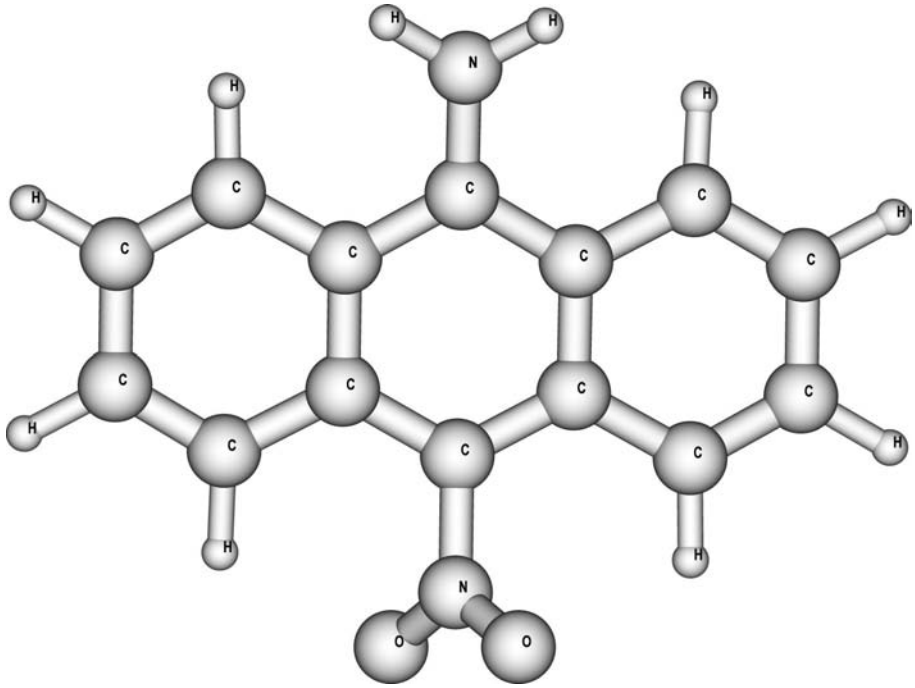

Fig. 3. The optimized geometry of 9-amino-10-nitroanthracene as calculated by using Restricted Hartree-Fock (RHF) method employing 6-31G** basis set in Gaussian03.

and acceptor strengths, respectively while l is the length of the conjugative electron transfer path. The ε_d and the ε_a are taken from references [35,36] and the 'l' has been calculated by adding the equilibrium lengths of bonds making up the π – electron transfer network. It is possible that strong electron demand created by the acceptor at C10 position would modify the electron releasing ability of the donor. This interaction between the donor and the acceptor can be incorporated in the modeling by introducing an electron demand parameter 'g' in the non-linear donor-acceptor interaction term. With this additional parameter, we have –

$$\beta_{total} = \beta_0 + a\varepsilon_d + b\varepsilon_a + c\varepsilon_d/(1 - g\varepsilon_a) + dl^n \tag{7}$$

After introducing the idea that the donor strength can be modified by the strength of the acceptor [37], we have fitted the calculated β_{total} values to the following equation –

$$\beta_{total} = \beta_0 + a\varepsilon_d + c\varepsilon_d/(1 - g\varepsilon_a) + dl^n \tag{8}$$

β_0, a, b, c, d, g and n are the free parameters that are optimized by a floating point GA developed locally [38,39]. The GA uses a population of n_p strings, each of which encodes 'm' floating point numbers representing the parameters β_0, a, b, c, d, g and n, which are randomly chosen from a wide range of possible values of each parameter. The range is user specified. The 'fitness', f_i of the i-th string S_i (${\beta_0}^i, a^i, b^i, c^i, g^i, l^i, d^i, n^i$) is defined as follows :

$f_i = e^{-O_i}$ where,

$$O_i = \sum\nolimits_j [\{\beta_{total}(j) - ({\beta_0}_j{}^i + a^i\varepsilon_{d,j} + b^i\varepsilon_{a,j} + c^i\varepsilon_{d,j}\varepsilon_{a,j}/(1 - g^i\varepsilon_{a,j}) + d^i l_j n_i)\}^2]^{\frac{1}{2}} \tag{9}$$

Table 1
The ground state interatomic distances (in Angstrom) between pairs of atoms in Molecules A1 – A13 as calculated by Restricted Hartree-Fock (RHF) theory employing 6-31G** basis set in Gaussian 03. The numberings of atoms are similar to those shown in Fig. 1. The 6–7 refers to the length of the relevant bond in the acceptor (N = O for nitro and nitroso, for example)

Compound	1–2	2–3	3–4	4–5	5–6	6–7
Molecule A1	1.382	1.408	1.422	1.396	1.459	1.196
Molecule A2	1.371	1.418	1.422	1.419	1.400	1.192
Molecule A3	1.379	1.410	1.420	1.401	1.437	1.138
Molecule A4	1.379	1.407	1.423	1.412	1.478	1.197
Molecule A5	1.357	1.394	1.424	1.394	1.462	1.194
Molecule A6	1.355	1.400	1.425	1.416	1.414	1.186
Molecule A7	1.356	1.395	1.422	1.401	1.441	1.138
Molecule A8	1.360	1.390	1.420	1.410	1.490	1.190
Molecule A9	1.422	1.401	1.426	1.389	1.465	1.194
Molecule A10	1.422	1.407	1.427	1.414	1.419	1.185
Molecule A11	1.422	1.402	1.424	1.398	1.443	1.137
Molecule A12	1.423	1.400	1.426	1.406	1.490	1.193
Molecule A13	1.077	1.386	1.426	1.411	1.489	1.193

Table 2
The ground state interatomic distances (in Angstrom) between pairs of atoms of Molecules B1–B12 as calculated by Restricted Hartree-Fock (RHF) theory employing 6-31G** basis set in Gaussian 03. The numberings of atoms are similar to those shown in Fig. 1. The 8–9 refers to the length of the corresponding bond in the acceptor (N = O for nitro and nitroso, for example)

Compound	1–2	2–3	3–4	4–5	5–6	6–7	7–8	8–9
Molecule B1	1.386	1.405	1.427	1.404	1.479	1.320	1.446	1.197
Molecule B2	1.389	1.404	1.426	1.403	1.480	1.326	1.416	1.185
Molecule B3	1.383	1.405	1.426	1.401	1.486	1.327	1.441	1.137
Molecule B4	1.390	1.403	1.427	1.403	1.484	1.327	1.473	1.191
Molecule B5	1.359	1.391	1.427	1.403	1.484	1.318	1.448	1.196
Molecule B6	1.360	1.391	1.427	1.403	1.483	1.325	1.418	1.184
Molecule B7	1.360	1.391	1.428	1.402	1.487	1.325	1.441	1.137
Molecule B8	1.359	1.391	1.427	1.403	1.484	1.328	1.448	1.192
Molecule B9	1.423	1.401	1.423	1.401	1.486	1.317	1.449	1.196
Molecule B10	1.424	1.399	1.429	1.400	1.486	1.324	1.419	1.184
Molecule B11	1.424	1.399	1.429	1.400	1.489	1.324	1.44 1	1.137
Molecule B12	1.424	1.401	1.424	1.402	1.488	1.325	1.475	1.191

assuming that the form of the fitting function described in the Eq. (7) is used. The summation runs over all the molecules studied in the set. The strings were allowed to evolve under the action of the genetic operators, viz., selection, crossover, mutation and diversification. Tournament selection was used with arithmetic crossover, mutation and diversification in every generation. For the crossover operation, the crossover probability p_c was kept fixed at 0.8, the mixing parameter f_c at 0.75 $\pm$ 0.25r (r is a random number with $0 \leqslant r \leqslant 1$). The mutation probability p_m also was kept fixed at 0.3, and the mutation amplitude was gradually and uniformly damped from an initial value of $f_m = 10$ to $f_m = 10^{-12}$. The diversification probability p_d was held fixed at $p_d = 0.01$ and the diversification amplitude f_d was damped gradually from $f_d = 10$ to $f_d = 10^{-12}$. From the pool of parents and offsprings, the two best strings were chosen after every generation while the remaining eight strings were randomly chosen from the offsprings. In all the calculations reported, population size $n_p = 10$ has been used.

Table 3
The ground state interatomic distances (in Angstrom) between pairs of atoms of Molecules C1–C4 and D1–D4 as calculated by Restricted Hartree-Fock (RHF) theory employing 6-31G** basis set in Gaussian 03. The numberings of atoms are similar to those shown in Fig. 1. The 8–9 refers to the length of the relevent bond in the acceptor (N = O for nitro and nitroso, for example)

Compound	1–2	2–3	3–4	4–5	5–6	6–7	7–8	8–9
Molecule C1	1.384	1.326	1.491	1.406	1.424	1.391	1.465	1.194
Molecule C2	1.382	1.326	1.488	1.413	1.425	1.416	1.416	1.187
Molecule C3	1.383	1.326	1.489	1.408	1.421	1.400	1.442	1.138
Molecule C4	1.385	1.325	1.492	1.404	1.424	1.408	1.489	1.194
Molecule D1	1.357	1.334	1.453	1.406	1.428	1.394	1.459	1.196
Molecule D2	1.351	1.340	1.446	1.413	1.432	1.420	1.390	1.194
Compound D3	1.356	1.333	1.450	1.407	1.425	1.401	1.437	1.138
Compound D4	1.353	1.336	1.450	1.407	1.430	1.416	1.475	1.198

Table 4
The values of dipole moments (Debye), $\alpha_{average}$ (in a.u.) and β_{total} (in a.u.) of Molecules A1–A13 as calculated by Restricted Hatree Fock (RHF) theory employing 6-31G** basis set in Gaussian 03

Molecule	Dipole Moment (debye)	$\alpha_{average}(a.u.)$	$\beta_{total}(a.u.)$
molecule A1	2.44	163.93	21.21
molecule A2	2.37	164.66	342.00
molecule A3	2.56	165.66	65.60
molecule A4	1.97	164.00	219.79
molecule A5	2.02	169.94	148.89
molecule A6	1.70	170.89	181.39
molecule A7	2.00	172.08	142.00
molecule A8	1.69	170.97	182.26
molecule A9	2.04	184.43	192.38
molecule A10	1.82	185.95	286.13
molecule A11	2.20	187.09	143.90
molecule A12	1.54	185.00	186.45
molecule A13	0.00	156.00	163.30

3. Results and Discussion

3.1. The structure and properties of the molecules studied

The computed structure of 9-amino-10-nitroanthracene has been displayed in Fig. 3. The predicted equilibrium bond lengths and bond angles are reported in Tables 1–3. It has been found that all the molecules are practically planar. There are notable changes in the ground state bond lengths of the anthracene moiety following substitution. The C2-C3 bond (Fig. 1) length, for example, varies from 1.386 angstroms to 1.418 angstroms for the molecules A1-A12, depending on the donor-acceptor combinations. The calculated dipole moments (in Debye) of the molecules studied has been reported in Tables 4–6. It has been observed that the dipole moments of these molecules are rather low, the lowest being 1.54 Debye (Molecule A12) and the highest one is 3.35 Debye (Molecule D3). The low dipole moment values decrease the tendency of these molecules to crystallize in centrosymmetric morphology, thereby increasing the possibility of using these chromophores for fabricating NLO materials. The ($\overline{\alpha}$) values computed by us for all the 33 molecules are reported in Tables 4–6. There is only a small dispersion in the computed ($\overline{\alpha}$) values, as expected. The ($\overline{\alpha}$) varies from 163.93 a.u. to 187.09 a.u. for

Table 5
The values of dipole moments (Debye), $\alpha_{average}$ (in a.u.) and β_{total} (in a.u.) of Molecules B1–B12 as calculated by Restricted Hatree Fock (RHF) theory employing 6-31G** basis set in Gaussian 03

Molecule	Dipole Moment (debye)	$\alpha_{average}(a.u.)$	$\beta_{total}(a.u.)$
molecule B1	2.87	193.33	841.29
molecule B2	2.34	192.00	889.77
molecule B3	2.62	192.30	327.00
molecule B4	1.98	192.85	628.36
molecule B5	2.34	197.56	432.05
molecule B6	1.66	197.00	561.60
molecule B7	2.12	197.56	136.75
molecule B8	2.45	196.82	142.00
molecule B9	2.50	211.89	319.99
molecule B10	1.86	211.50	457.00
molecule B11	2.25	212.00	89.85
molecule B12	1.75	212.25	289.53

Table 6
The values of dipole moments (Debye), $\alpha_{average}$ (in a.u.) and β_{total} (in a.u.) of Molecules C1–C4 and D1–D4 as calculated by Restricted Hatree Fock (RHF) theory employing 6-31G** basis set in Gaussian 03

Molecule	Dipole Moment (debye)	$\alpha_{average}(a.u.)$	$\beta_{total}(a.u.)$
molecule C1	2.67	188.07	143.37
molecule C2	2.42	190.98	689.87
molecule C3	2.77	191.59	283.44
molecule C4	2.16	189.66	398.00
molecule D1	3.24	187.05	245.12
molecule D2	3.22	190.21	326.03
molecule D3	3.35	190.00	402.00
molecule D4	2.70	189.55	412.26

the molecules of series A. It varies from 192 a.u. to 212 a.u, 188.07 a.u. to 191.59 a.u. and 187.05 a.u. to 190.21 a.u. for molecules of series B, C and D, respectively.

The computed values of β_{total} are also reported in Tables 4–6. The predicted β_{total} values show a large dispersion, the lowest value being 21.21 a.u. (molecule A1) and the highest being 889.77 a.u. (molecule B2). The highest β_{total} is exhibited by molecule- B2 which has $-NH_2$ as donor and -NO as acceptor and the length of the conjugative Π – electron transfer is maximum (l = 20.85 a.u.). If we compare the β_{total} values for molecule – B2 and molecule – B3, molecule – B4, molecule – C4, we can clearly detect a maximization of β_{total} as a function of the acceptor strength as both the donor strength (ε_{NH_2}) and the length of the electron transfer path (l) remains the same for these four molecules. It appears therefore, that every donor may have an optimum acceptor for maximizing the first hyperpolarizability in a structurally similar set of molecules. Similarly, comparison of β_{total} of molecules – B2 and B10 would tend to suggest that for the -NO moiety as acceptor, a better donor is provided by $-NH_2$ and not $-N(CH_3)_2$ for maximizing the β_{total}. The effect of the length of the Π- electron transfer path can be easily noticed by comparing β_{total} of molecules A2 and B2, molecules A3 and B3 and molecules A4 and B4. That the -NO group could be a good acceptor group that tends to maximize the quadratic NLO response can be once again noticed while comparing the β_{total} of molecule C2 and C3 which have the the same donor group $[-N(CH_3)_2]$ and identical 'l' value, but different acceptor groups (-CN and -NO). This feature was also noticed previously [35]. However, when all the factors are allowed to vary, the simple picture no longer works. The intramolecular charge transfer process in anthracene derivatives

Table 7
The excited state (S_1) dipole moments (μ_E) (in Debye) of two pairs of isomeric molecules and the first three vertical transitions energies ($\Delta\ E_1$, $\Delta\ E_2$ and $\Delta\ E_3$) (in eV) and oscillator strengths (f_{S0-S1}, f_{S0-S2} and f_{S0-S3}) calculated by CIS theory and employing 6-31G** basis set in Gaussian03. The ground state dipole moment (μ_G) (in Debye) has been reported for comparison

Molecule	β_{total} (a.u.)	μ_E (Debye)	μ_G (Debye)	Δ (eV)E_1	$\Delta\ E_2$ (eV)	$\Delta\ E_3$ (eV)	f_{S0-S1}	f_{S0-S2}	f_{S0-S3}
Molecule B1	841.29	9.05	2.87	3.84	4.62	4.67	0.4322	0.0547	0.0617
Molecule C1	143.37	8.40	2.67	3.98	4.70	4.98	0.3583	0.0077	0.0003
Molecule B4	628.36	5.76	1.98	3.76	4.56	4.63	0.4019	0.0107	0.0064
Molecule C4	398.00	4.87	2.16	3.87	4.60	4.63	0.3939	0.0162	0.0459

has been studied experimentally by Muralidharan [40,41]and Zachariasse [42]. Muralidharan [40] and coworkers have studied the photophysical properties of a series of 9,10-donor-acceptor substituted anthracene molecules. Dual fluoroscence has been detected for 9-amino-10-cyanoanthracene and its N-methyl and N,N-dimethyl analogues in polar solvents. The authors have argued that the dual emission originates from a locally excited (LE) and intramolecular charge transfer (ICT) states, which form in the excited state. To understand the role played by the ICT state, we have performed CIS calculations on two pairs of isomeric anthracene derivatives. The dipole moment (Debye)of the first excited state has been reported in Table 7. The ground state dipole moment has also been reported for comparison. It appears that a large change in dipole moment in the excited may be responsible for higher β_{total} in the molecules B1 and B4 compared to their corresponding isomers. The computed transition energies (in eV) alongwith the oscillator strengths of first three transitions ($S_0 - S_1, S_0 - S_2$ and $S_0 - S_3$) have been reported in Table 7. The oscillator strengths suggest that the absorption mainly populates the S_1 state, indicating that a two state model will suffice to explain the role of charge transfer, if any, in determining the value of β_{total}.

3.2. The NLO response of isomeric molecules

We have observed that the first hyperpolarizability of a molecule may be notably different from its structural isomer (Fig. 1). The molecules in the B and C series of Fig. 1 are corresponding structural isomers of each other, but their NLO responses are remarkably different. For example, the β_{total} value of Molecule B1 is 841.29 a.u. vis-a-vis 143.37 a.u. for Molecule C3, a structural isomer of the former. A difference in the first hyperpolarizability values shown by two isomeric molecular chromophores underscores the importance of the extent of charge transfer in these systems in determining the possible NLO response. A schematic diagram of charge transfer in two pairs of structural isomers, viz., B1 and C1 and B4 and C4 has been shown in Fig. 2b. The CIS calculations have been performed and the S_1 state dipole moment alongwith the transition energies and oscillator strengths of the first three vertical transitions have been reported in Table 7. It can be observed that higher β_{total} values have been associated with higher increase in dipole moment in the excited state S_1 compared to ground state S_0. It is also clearly seen that the isomer with the lower energy of the first excited singlet and higher oscillator strength of the $S_0 - S_1$ transition has much higher β_{total}. It would be interesting to check this feature for a much larger number of structurally isomeric pairs. We hope to return to the topic in the near future.

3.3. Modeling the NLO response in the anthracene derivatives

From the preceding discussion, it seems worthwhile to try to fit the predicted β_{total} values either as functions of the seven parameters of Eq. (7) or the six parameters of Eq. (8) and then examine how

Table 8
All the free parameters obtained from GA couple fitting for $\beta_{\cdot total}$ using Eqs (7) and (8)

Parameters	Eq. (7)	Eq. (8)
β_0	0.00	0.00
a	22.01	98.38
b	272.94	–
c	−20.41	−57.10
d	8.44	0.82
n	1.33	1.95
g	−1.25	−1.18

Table 9
The computed β_{total} (in atomic unit) of Molecules A1–A13 and the β_{total} obtained from fitting functions with parameters optimized by GA

Molecule	$\beta_{total}(a.u.)$	$\beta_{total}(GA)eqn.7$ (a.u.)	$\beta_{total}(GA)eqn.8$ (a.u.)
molecule A1	21.21	21.21	21.21
molecule A2	342.00	284.44	195.23
molecule A3	65.60	124.74	122.69
molecule A4	219.79	128.35	125.62
molecule A5	148.89	407.91	51.01
molecule A6	181.39	282.52	190.14
molecule A7	142.00	141.99	141.99
molecule A8	182.26	135.03	136.30
molecule A9	192.38	82.52	110.18
molecule A10	286.13	286.12	186.61
molecule A11	143.90	176.91	153.25
molecule A12	186.45	151.08	158.91
molecule A13	163.30	145.18	163.28

the two equations perform in correlating β_{total} of molecules outside the training set. The GA based search predicts the optimal values of the six parameters of Eq. (6) or the seven parameters of the Eq. (7), depending upon the model used. However, we have set $\beta_0 = 0$ in each case as actual calculation with symmetry broken bare anthracene ring (donor and acceptor replaced by H-atom after full geometry optimization) indicate that β_0 is very small are varies from 0 a.u. to 5 a.u., when calculated at the present level. The optimized parameters are shown in Table 8. The β_{total} values predicted by the respective optimal fitting functions along with the computed β_{total} are displayed in Tables 9–11 for the A, B, C and D series of molecules. Figure 4a shows the evolution of the fitness of the best fit individual during the GA-driven optimization of the parameters of the model represented by Eq. (7) while the Fig. 4b shows the evolution of various parameters during the search. The values of β_{total} predicted by the 7 parameter model have been compared with the quantum chemically predicted values of β_{total} in Fig. 4c. It is clear that the model works fairly well, but fails to reproduce the exalted β_{total} values of some of the molecules. Figures 5 (a–c) display similar profiles for the 6 parameter model. There are no major differences in the performances of the seven parameter model vis-a-vis its six parameter counterpart. It appears that the dominant contributions are the additive ones. The contribution from the chain-length dependent part of the response and that arising from the nonlinear donor-acceptor interaction are rather small. The predicted optimal value of the index (n) of the power law dependence of β_{total} on 'l' turns out to be rather low in the 7 parameter model compared to what is predicted by a uniform gas model [43]. The value of 'n' predicted by the 6 parameter model appears to be more realistic. The general quality of the fit is good, but too high values (B1 and B2, for example) are not reproduced. However, the fitting

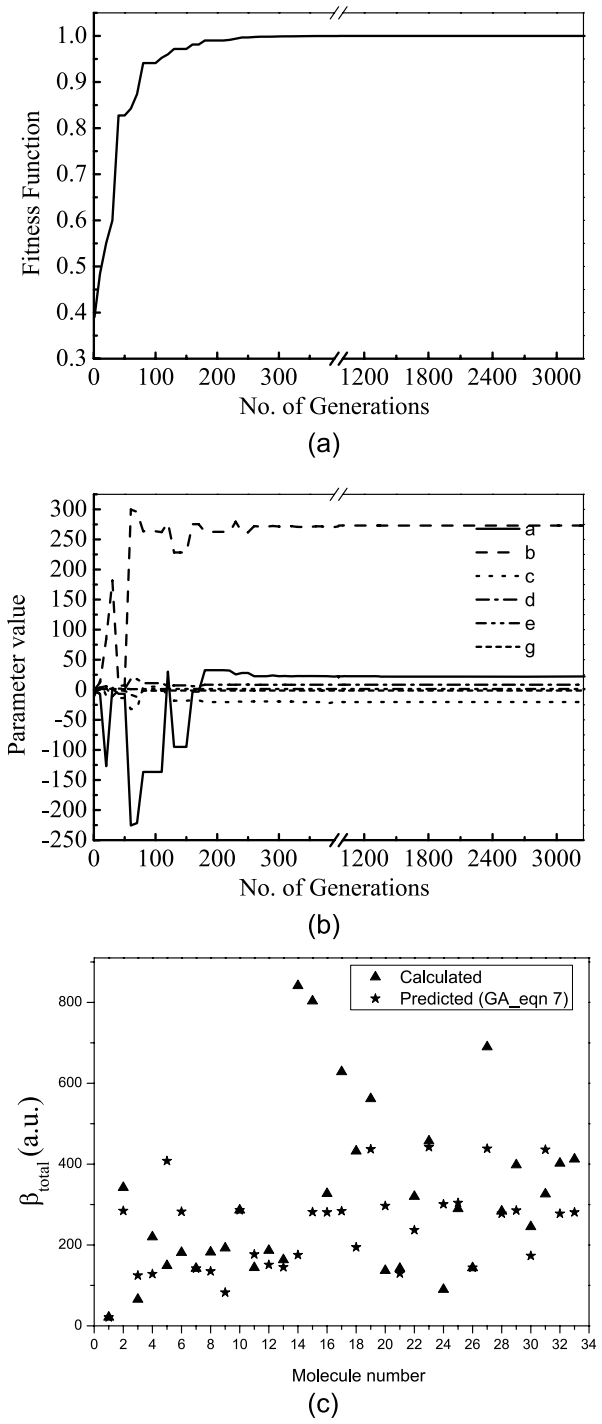

Fig. 4. GA evolution profiles with $\beta_{total} = 0$ in Eq. (7). (a) fitness evolution during the search (b) variations in the parameters of the model during the GA search (c) β_{total} predicted by the 7 parameter model compared with quantum chemically computed β_{total} values. In the figure the molecules numbered 1–13, 14–25, 26–19 and 30–33 refer to molecules A1-A13, molecules B1-B12, molecules C1-C4 and molecule D1-D4 of Fig. 1, respectively.

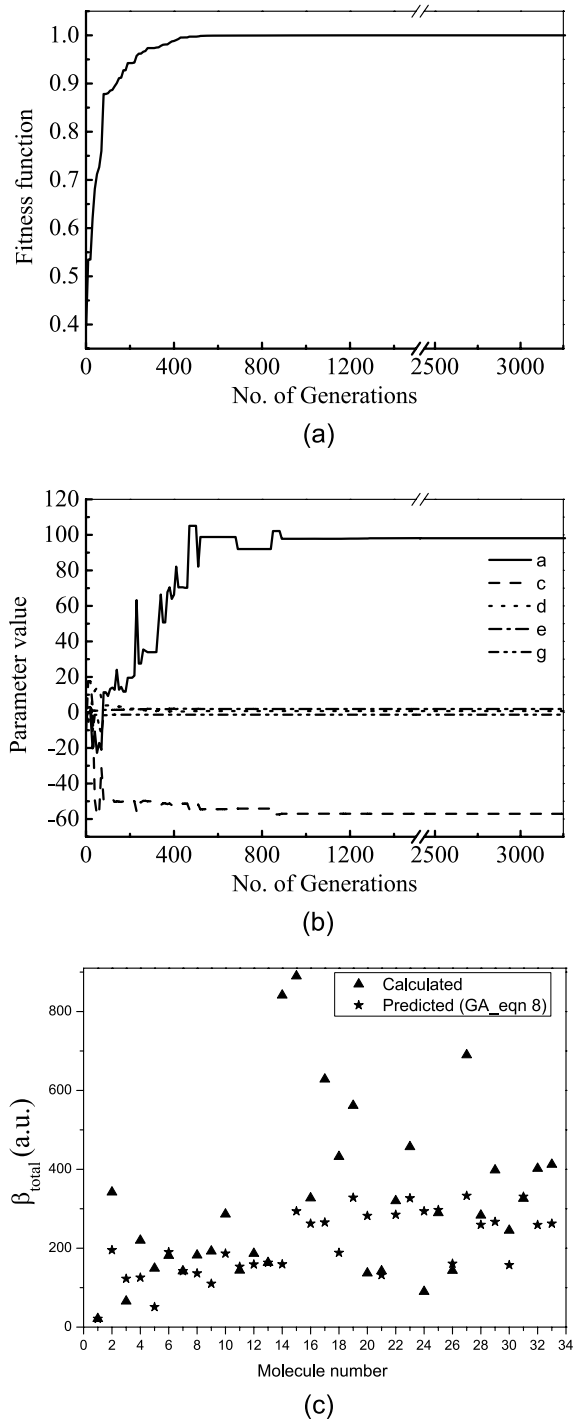

Fig. 5. GA evolution profiles with $\beta_{total} = 0$ in Eq. (8). (a) fitness evolution during the search (b) variations in the parameters of the model during the GA search (c) β_{total} predicted by the 6 parameter model compared with quantum chemically computed β_{total} values. In the figure the molecules numbered 1–13, 14–25, 26–19 and 30–33 refer to molecules A1–A13, molecules B1–B12, molecules C1–C4 and molecule D1–D4 of Fig. 1, respectively.

Table 10
The computed β_{total} (in atomic unit) of Molecules B1–B12 and the β_{total} obtained from different fitting functions with parameters optimized by GA

Molecule	$\beta_{total}(a.u.)$	$\beta_{total}(GA)eqn.7$ (a.u.)	$\beta_{total}(GA)eqn.8$ (a.u.)
molecule B1	841.29	175.39	159.38
molecule B2	889.77	281.49	293.78
molecule B3	327.00	280.86	262.44
molecule B4	628.36	283.92	265.45
molecule B5	432.05	194.52	188.53
molecule B6	561.60	437.06	328.25
molecule B7	136.75	296.74	282.13
molecule B8	142.00	129.76	132.03
molecule B9	319.99	236.92	248.94
molecule B10	457.00	442.20	326.73
molecule B11	89.85	300.92	293.75
molecule B12	289.53	304.29	297.04

Table 11
The computed β_{total} (in atomic unit) of Molecules C1–C4 and D1–D4 and the β_{total} obtained from different fitting functions with parameters optimized by GA

Molecule	$\beta_{total}(a.u.)$	$\beta_{total}(GA)eqn.7$(a.u.)	$\beta_{total}(GA)eqn.8$ (a.u.)
molecule C1	143.37	144.13	160.87
molecule C2	689.87	438.28	333.04
molecule C3	283.44	277.81	259.46
molecule C4	398.00	285.45	266.92
molecule D1	245.12	173.25	157.30
molecule D2	326.03	435.84	330.66
molecule D3	402.00	277.50	259.17
molecule D4	412.26	280.86	262.44

function can still be used for quick screening of molecules for their suitability for fabricating new NLO materials.

4. Conclusion

We have taken a step-wise approach to model the non-linear optical (NLO) response properties of a series of new charge transfer based organic chromophores that can be potential candidates for experimental screening. Our investigation shows that 9,10-substituted anthracene derivatives display large first hyperpolarizability (β_{total}) which can be maximized by the judicious selection of donor-acceptor pairs. The β_{total} has been modeled by a six or seven parameter function by GA. The dominant contributions to β_{total} are additive and are primarily from the donor and the acceptor moeities. The emergence of large β_{total} for some of the molecules indicate the creation of resonance condition not reproduced by the fitting equations.

Acknowledgement

We thank the Aneesur Rahman Center for high performance computing of this institute for providing us with computing facilities. RM thanks the Integrated PhD division, IACS for financial support.

References

[1] J. Zyss, ed., Molecular Non-linear Optics Materials, Physics and Devices, Academic Press, Boston, 1994.
[2] P.N. Prasad and D.J. Williams, Introduction to non-linear optical Effects in Molecules and Polymers. Wiley, New York. (1991).
[3] D.S. Chemla and J. Zyss, Non-Linear Optical Properties of Organic Molecules and Crystals, (vol. 1). Academic Press, New York, 1983.
[4] G. Maroulis, Atoms, Molecules and Clusters in Electric Field, Imperial College Press. (2006).
[5] D.R. Kanis, M.A. Ratner and T.J. Marks, *Chem Rev* **94** (1994), 195.
[6] R. Misra, S.P. Bhattacharyya and D.K. Maity, *Chem Phys Lett* **458** (2008), 54.
[7] B.R. Levine and C.G. Bethea, *J Chem Phys* **63** (1975), 2666.
[8] D. Jacquemin, E.A. Pertete, M. Medved, G. Scalmani, M.J. Frisch, R. Kobayashi and C. Adamo, *J Phys Chem* **126** (2007), 191108.
[9] M. Kozierowskii and S. Kielich, *J Phys A* **94** (1983), 213.
[10] S. Kielich, J.R. Lalnne and F.B. Martin, *Phys Rev Lett* **26** (1971), 1295.
[11] T. Kodaira, A. Watanabe, O. Ito, M. Matsuda, K. Clays and A. Persoons, *Japan J Appl Phys* **35** (1996), 6074.
[12] D. Jacquemin, E.A. Perpete and J.-M. Andre, *J Phys Chem* **252** (1991), 103.
[13] S.R. Marder, D.N. Meratan and L.-T. Cheng, *Science* **252** (1991), 103.
[14] K. Schmidt, S. Barlow, A. Leclercq, E. Zojer, S. Jang, S.R. Marder, A. Jen and J.L. Brédas, *J Mater Chem* **17** (2007), 2944.
[15] Y. Yokoyama, S. Yokoyama, T. Kamikado, Y. Okuno and S. Mashiko, *Nature* **413** (2001), 619.
[16] Y. Okuno, T. Yokoyama, S. Yokoyama, T. Kamikado and S. Mashito, *J Am Chem Soc* **124** (2002), 7218.
[17] S.R. Marder and J.W. Perry, *Adv Mater* **5** (1993), 804.
[18] K. Schmidt, S. Barlow, A. Leclercq, E. Zojer, S.H. Jang, S.R. Marder, A.K.Y. Jen and J.L. Brédas, *J Mater Chem* **17** (2007), 2944.
[19] J.Zyss, I. Ledoux, S. Volkov, V. Charnyak, S. Mukamel G.P. Bastholoman and G.C. Bazer, *J Am Chem Soc* **122** (2000), 61195.
[20] H. Kang, A. Facchetti, H. Jiang, E. Cariati, S. Righetto, R. Ugo, C. Zuccaccia, A. Macchioni, C.L. Stern, Z. Liu, S.T. Ho, E.C. Brown, M.A. Ratner and T.J. Marks, *J Am Chem Soc* **129** (2007), 3267.
[21] S.D. Bella, I.L. Fragala, M.A. Ratner and T.J. Marks, *J Am Chem Soc* **115** (1993), 682.
[22] C.R. Moylan, B.J. McNelis, L.C. Nathan, M.A. Marques, E.L. Hermstad and B.A. Brichler, *J Org Chem* **69** (2004), 8239.
[23] P.K. Nandi, N. Panja and P.K. Ghanty, *J Phys Chem A* **112** (2008), 4844.
[24] M. Fanti, G. Orlandi and F. Zerbetto, *J Phys Chem A* **101** (1997), 3015.
[25] Y. Zou, D.D. Young, A. Cruz-Montanez and A. Deiters, *Org Lett* **10** (2008), 4661.
[26] S. Ma, D. Sun, J.M. Simons, C.D. Collier, D. Yuan and H.C. Zhou, *J Am Chem Soc* **130** (2008), 1012.
[27] S. Muralidharan, H.K. Sinha and K. Yates, *J Phys Chem* **95** (1991), 8517.
[28] L.J. Ouder, *J Chem Phys* **67** (1977), 446.
[29] Gaussian 03, E. Revision 01, M.J. Frisch, G.W. Trucks, H.B. Schlegel, G.E. Scuseria, M.A. Robb, J.R. Cheeseman, J.A. Montgomery, Jr., T. Vreven, K.N. Kudin, J.C. Burant, J.M. Millam, S.S. Iyengar, J. Tomasi, V. Barone, B. Mennucci, M. Cossi, G. Scalmani, N. Rega, G.A. Petersson, H. Nakatsuji, M. Hada, M. Ehara, K. Toyota, R. Fukuda, J. Hasegawa, M. Ishida, T. Nakajima, Y. Honda, O. Kitao, H. Nakai, M. Klene, X. Li, J.E. Knox, H.P. Hratchian, J.B. Cross, V. Bakken, C. Adamo, J. Jaramillo, R. Gomperts, R.E. Stratmann, O. Yazyev, A.J. Austin, R. Cammi, C. Pomelli, J.W. Ochterski, P.Y. Ayala, K. Morokuma, G.A. Voth, P. Salvador, J.J. Dannenberg, V.G. Zakrzewski, S. Dapprich, A.D. Daniels, M.C. Strain, O. Farkas, D.K. Malick, A.D. Rabuck, K. Raghavachari, J.B. Foresman, J.V. Ortiz, Q. Cui, A.G. Baboul, S. Clifford, J. Cioslowski, B.B. Stefanov, G. Liu, A. Liashenko, P. Piskorz, I. Komaromi, R.L. Martin, D.J. Fox, T. Keith, M.A. Al-Laham, C.Y. Peng, A. Nanayakkara, M. Challacombe, P.M.W. Gill, B. Johnson, W. Chen, M.W. Wong, C. Gonzalez and J.A. Pople, Gaussian, Inc., Wallingford CT, 2004.
[30] C.J. Cramer, *Essential of Computational Chemistry*, Second Ed. Wiley, Boston. (2004).
[31] A.K. Jeewandara and K.M. Nalin de Silva, *J Mol Struct* (*THEOCHEM*) **686** (2004), 131.
[32] C. Dehu, F. Meyers, E. Hendrickx, K. Clays, A. Parsons, S.R. Marder and J.L. Brédes, *J Am Chem Soc* **117** (1995), 10127.
[33] F. Meyers and J.L. Bredas, *Zyss J J Am Chem Soc* **114** (1992), 2914.
[34] G. Schaftenaar and J.H. Noordik, *J Comput-Aided Mol Des* **14** (2000), 123.
[35] R. Sen, D. Majumdar, S.P. Bhattacharyya and S.N. Bhattacharyya, *J Phys Chem* **97** (1993), 7491.
[36] J. Bromilow, R.T.C. Brownlee, D.J. Craik, M. Sadek and R. Taft, *J Org Chem* **45** (1980), 2429.
[37] I.D.L. Albert, T.J. Marks and M.A. Ratner, *J Am Chem Soc* **119** (1997), 6575.
[38] R. Sharma, S. Nandi and S.P. Bhattacharyya, *Pramana* **66** (2006), 1125.
[39] M. Ghosh, R. Sharma and S.P. Bhattacharyya, *Chem Phys Lett* **499** (2007), 165.

[40] S. Muralidharan, A.J. Lough and K. Yates, *J Photochem Photobiol A: Chem* **71** (1993), 245.
[41] S. Muralidharan, H. Sinha and K. Yates, *J Phys Chem* **95** (1991), 8517.
[42] S. Dhruzinin, A. Demeter, M. Niebuer, E. Tauer and K.A. Zachariasse, *Research Chem Interm* **25** (1999), 531.
[43] A. Dulcic, C. Flytzanis, C.L. Tang, D. Pépin, M. Fétizon and Y. Hoppilliard, *J Chem Phys* **74** (1981), 1559.

Journal of Computational Methods in Sciences and Engineering 10 (2010) 165–181
DOI 10.3233/JCM-2010-0318
IOS Press

Asymptotic model of exchange interactions for polarizability calculation of van der Waals complexes

M.A. Buldakov[a] and V.N. Cherepanov[b,*]
[a]*Laboratory of Ecological Instrument Making, Institute of Monitoring of Climatic and Ecological Systems SB RAS, Tomsk 634055, Russia*
[b]*Department of Physics, Tomsk State University, Tomsk 634050, Russia*

Abstract. The asymptotic model of exchange interactions for calculation of the polarizability of van der Waals complexes is discussed. The model is employed for description of the polarizability of interacting systems when their valence electron shells are weakly overlapped. The analytical expressions for the interaction polarizabilities that include induction, dispersion and exchange contributions have been obtained for X-Y and X-Y_2 complexes. The calculation of the interaction polarizabilities of the complexes He-He, Ar-Ar, Kr-Xe, Xe-Xe, and Ar-H_2 have been carried out.

Keywords: Polarizability, exchange interactions, van der Waals complexes

1. Introduction

An interest to the polarizability tensor of interacting atoms and molecules arose many years ago and it continues to be actual one up today. The polarizability tensor of interacting atoms is of importance because of its fundamental significance for a wide range of optical and dielectric properties of real gases and their complexes [1–3]. Interactions between the components of such complexes lead to distortion of their charge distributions and, as a result, the polarizability of a complex is not a simple sum of polarizabilities of its components.

At long separations between atoms and molecules in the complex, the methods of classical electrodynamics considering the multipole induction and dispersion effects are effectively applied to describe the polarizability surface of interacting atom-molecular systems [4–21]. However, when the interacting atoms (or molecules) approach each other up to a distance where overlap and exchange effects are significant, the classical methods are not effective and, at present, correct values of the polarizability are obtained only from *ab initio* calculations. Usually *ab initio* calculations of the polarizability of interacting systems are carried out for the equilibrium configurations of complexes (see [22,23] and quoted there references). However, there are *ab initio* calculations of polarizability functions for a wide range of intermolecular separations an the most of them have been carried out for pairs of rare-gas atoms in the ground states (see, for example [21,24–38]). In spite of significant progress in *ab initio* calculations,

*Corresponding author. E-mail: vnch@phys.tsu.ru.

the last have the disadvantage caused by the fact that the polarizability functions (or surfaces) can be calculated only at single points. As a result, the analytical methods for calculations of polarizability functions of complexes are of interest until now. Presently, a lot of efforts is being made to improve the analytical calculation schemes for the polarizability functions both for long and for shorter range of R [39–46]. Nevertheless, the analytical expressions obtained in these works are difficult to be applied to practical calculations especially for molecular complexes.

In this work, the asymptotic method proposed in [47,48] has been used to include in the simple analytical form the exchange effect between interacting atoms (or molecules) for the polarizability calculations of binary complexes. Such description of the exchange effect is possible when a small overlap of electron shells occurs in interacting systems of a complex [49,50]. The asymptotic method is applied to calculate the polarizabilities of the van der Waals complexes where the small electron overlapping is common.

2. Theoretical treatment

Within the framework of the long-range approximation [1,51], when the molecules are presented as the point objects keeping their anisotropic electrical properties, the electronic polarizability $\alpha_{\alpha\beta}^{AB}$ of two interacting systems may be written in the form

$$\alpha_{\alpha\beta}^{AB} = \alpha_{\alpha\beta}^{A} + \alpha_{\alpha\beta}^{B} + \Delta\alpha_{\alpha\beta}^{AB}, \tag{1}$$

where $\alpha_{\alpha\beta}^{A}$ and $\alpha_{\alpha\beta}^{B}$ are the dipole polarizabilities of the atom-molecular systems A and B, and $\Delta\alpha_{\alpha\beta}^{AB}$ is the interaction polarizability. The interaction polarizability $\Delta\alpha_{\alpha\beta}^{AB}$ appears here due to different effects and may be written as

$$\Delta\alpha_{\alpha\beta}^{AB} = \alpha_{\alpha\beta}^{ind} + \alpha_{\alpha\beta}^{disp} + \alpha_{\alpha\beta}^{exch}, \tag{2}$$

where $\alpha_{\alpha\beta}^{ind}$, $\alpha_{\alpha\beta}^{disp}$ and $\alpha_{\alpha\beta}^{exch}$ are the induction, dispersive and exchange contributions to the polarizability of interacting systems. When the interacting systems are well separated, the interaction polarizability $\Delta\alpha_{\alpha\beta}^{AB}$ is determined entirely by well known induction and dispersive contributions $\alpha_{\alpha\beta}^{ind}$ and $\alpha_{\alpha\beta}^{disp}$ [8–10,12–14,46]. At shorter range, when the charge distributions of interacting systems overlap, the contribution of $\alpha_{\alpha\beta}^{exch}$, caused by the exchange effects, appears.

In this work, to take into account the exchange effects, the asymptotic methods [49,50] are used. These methods may be applied in a range of R where a weak overlapping of the valence electron shells of interacting systems takes places. Let us consider a case of two interacting atoms with the valence s-electrons. In this case, the exchange interaction of atoms can be approximately considered as an exchange interaction of two valence electrons (by one from each atom). Then the two-electron (one electron from atom A and one from atom B) molecular wave function of the state n can be written in the form:

$$\Psi_n(r_1, r_2, R) = c_n^{(1)}\psi_n^{(1)}(r_1, r_2, R) + c_n^{(2)}\psi_n^{(2)}(r_1, r_2, R), \tag{3}$$

where

$$\begin{aligned}
\psi_n^{(1)}(r_1, r_2, R) &= \left[\varphi^{(A)}(r_1, R)\varphi^{(B)}(r_2, R)\chi_I(r_1, r_2, R)\right]_n, \\
\psi_n^{(2)}(r_1, r_2, R) &= \left[\varphi^{(A)}(r_2, R)\varphi^{(B)}(r_1, R)\chi_{II}(r_1, r_2, R)\right]_n.
\end{aligned} \tag{4}$$

Here $\varphi^{(A)}(r_1, R)$, $\varphi^{(B)}(r_1, R)$ and $\varphi^{(A)}(r_2, R)$, $\varphi^{(B)}(r_2, R)$ are asymptotic wave functions of the first and of the second electrons located near corresponding atom cores. Equations (3) and (4) are written in the molecular coordinate system in which the interacting atoms are located on the axis z, and the center of the interatomic separation is taken as the origin of coordinates. In this coordinate system r_1 and r_2 are coordinates of the first and of the second electrons. The functions $\chi_I(r_1, r_2, R)$ and $\chi_{II}(r_1, r_2, R)$ accounting for the interaction of electrons with each other and with extraneous nuclei have complicated forms and are given in [50].

The asymptotic radial wave function of a valence electron of a neutral atom used in Eqs (3) and (4) in the coordinate system with the origin in the atom nuclear has the form [49]:

$$\varphi(r) = A_0 r^{1/\beta - 1} \exp(-r\beta), \tag{5}$$

where $\beta^2/2$ is the atom ionization potential and the value of the asymptotic coefficient A_0 depends on the electron distribution in the internal zone of the atom.

To calculate the exchange contributions to the static polarizability of a pair of interacting atoms we employ the well known form for tensor components of the electron polarizability

$$\alpha^{AB}_{\alpha\beta}(R) = 2 \sum_{m \neq n} \frac{\langle n | \, d_\alpha \, | m \rangle \, \langle m | \, d_\beta \, | n \rangle}{E_m - E_n}, \tag{6}$$

where the dipole matrix elements of dipole moments $\langle n | \, d_\gamma \, | m \rangle$ and the electronic energy levels E_k are the functions of R. The exchange contributions to the polarizability show itself mainly through its contribution into the matrix element of the dipole moment in Eq. (6). In the approximation applied the exchange interaction is the most substantial in the matrix element of the component$z$of the electron transition dipole moment and, as a result, in the polarizability tensor component $\alpha^{AB}_{zz}(R)$. The exchange interaction contribution into z-component of the dipole moment calculated by means of Eqs (4) and (5) for two interacting atoms may be represented as

$$\left\langle \psi^{(1)}_n(r_1, r_2, R) \right| d_z \left| \psi^{(2)}_m(r_1, r_2, R) \right\rangle^{exch} = B_{nm} R^\delta \exp(-\eta R), \tag{7}$$

where

$$\delta = \frac{1}{\beta_A} + \frac{1}{\beta_B} + \frac{1}{\beta_m} + \frac{3}{2\,(\beta_A + \beta_B)} - \frac{1}{\beta_A + \beta_B + 2\beta_m} + 1, \tag{8}$$

$$\eta = \frac{3}{4}\beta_A + \frac{3}{4}\beta_B + \frac{1}{2}\beta_m. \tag{9}$$

Here $\beta_A^2/2$ and $\beta_B^2/2$ are the ionization potentials of the atoms A and B at the ground electron state ($n = 0$) and the parameter $B_{nm} \equiv B_{nm}(\beta_A, \beta_B, \beta_m, R)$ is the function weakly dependent on R in the region of small electron shells overlapping. The use of the effective excited electron state $\bar{m}$ allows us to apply a two-level model to calculate the polarizability functions of a complex and so the procedure of summation over the excited electron states m of atoms in the expression for polarizability may be excluded. Then, substituting Eq. (7) into Eq. (6) and replacing β_m by some effective value $\bar{\beta}$ for the effective electron state $\bar{m}$, the expression for the exchange contributions into polarizability of interacting atoms takes the form

$$\alpha^{exch}_{zz}(R) = B_1(\beta_A, \beta_B, \bar{\beta}, R) R^\delta \exp(-\eta R) + B_2(\beta_A, \beta_B, \bar{\beta}, R) R^{2\delta} \exp(-2\eta R), \tag{10}$$

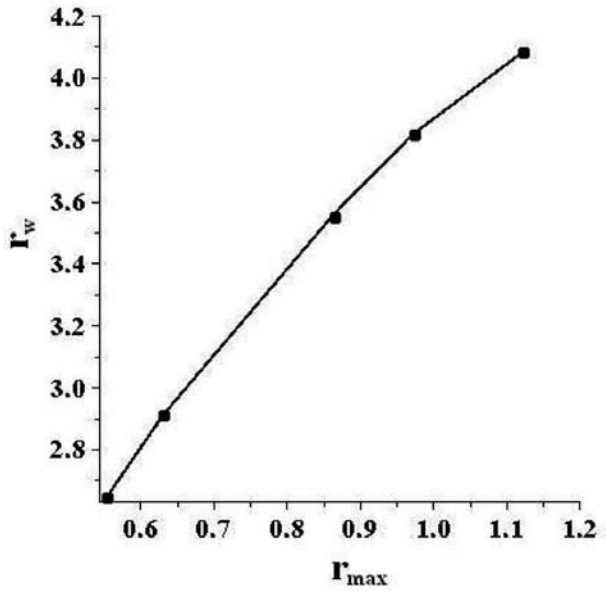

Fig. 1. Dependence of the van der Waals radii r_w of the noble gas atoms on the position of the maximum of the atomic electron density $r_{\max} = 1/\beta^2$. All values are in a.u.

where the parameters B_1 and B_2 are also the functions weakly dependent on R. The values of the parameter $\bar{\beta}$ may be estimated taking into account probabilities of radiation transitions of the atoms A and B, and the energy levels structure of these atoms. The first term in Eq. (10) gives the asymptotic behavior of the exchange polarizability $\alpha_{zz}^{exch}(R)$ at $R \to \infty$ and has the form similar the expression for exchange polarizability of the pair of hydrogen atoms [42].

In the approximation used the matrix elements $\left\langle \psi_n^{(1)}(r_1, r_2, R) \right| d_{x,y} \left| \psi_m^{(2)}(r_1, r_2, R) \right\rangle$ equal zero and the exchange contributions α_{xx}^{exch} and α_{yy}^{exch} as well equal zero. However, in a more strict approximation these contributions are to be appeared.

The results obtained for atoms with the valence s-electrons can also be applied after minimal changes to interacting atoms having the valence electrons of nonzero orbital moment l. Indeed, the exchange interaction occurs in the range of electron coordinates near the axis z where the angular wave functions of the electrons vary slightly and so may be substituted by their values on the axis z. Therefore, for this case taking into account the exchange interaction reduces to the problem considered above with the only difference that the coefficient A_0 in Eq. (5) should be multiplied by $\sqrt{2l+1}$ [50].

The exchange interactions in a range of weak overlapping of the valence electron shells due to their physical nature should depend on the sizes of interacting atoms. Within the framework of the asymptotic model of exchange polarizability $\alpha_{zz}^{exch}(R)$ the sizes of interacting atoms are taken into account by means of the parameters β_A and β_B. In fact, the position of the maximum of the atomic electron density $r_{\max} = 1/\beta^2$ calculated using the asymptotic radial wave function of a valence electron Eq. (5) reflects the size of an atom as illustrated in Fig. 1.

The results obtained for interacting atoms may be generalized for the case of interacting molecules. For this case the functional dependence of $\alpha_{zz}^{exch}(R)$ has the form Eq. (10) where β_A, β_B and $\bar{\beta}$ are the molecular parameters having the same physical meaning. Moreover, there is a need to take into account the configurations of interacting molecules.

Table 1
Atomic properties (in a.u.) used in calculating complex polarizabilities

Property	He	Ar	Kr	Xe
α	1.383[a]	11.080[a]	16.476[b]	27.71[c]
γ	41.9[a]	1329[a]	2260[b]	6913[c]
β	1.344[d]	1.076[d]	1.014[d]	0.944[d]

[a]The values are given in Ref. 10.
[b]Reference 52.
[c]Reference 32.
[d]The values are calculated using the ionization potentials from [53].

3. Results and discussion

In this work the exchange contributions to the interaction polarizability $\Delta\alpha_{\alpha\beta}^{AB}$ were considered for some atom-molecular binary complexes. At that, the values of the exchange contributions were calculated as

$$\alpha_{\alpha\beta}^{exch}(R) = \Delta\alpha_{\alpha\beta}^{AB}(R) - \alpha_{\alpha\beta}^{ind}(R) - \alpha_{\alpha\beta}^{disp}(R), \tag{11}$$

where the values of $\Delta\alpha_{\alpha\beta}^{AB}(R)$ are *ab intio* calculations of the interaction polarizability of complexes, $\alpha_{\alpha\beta}^{ind}(R)$ and $\alpha_{\alpha\beta}^{disp}(R)$ were calculated using analytical methods.

3.1. Atomic complexes

In this work the pairs of the noble gas atoms being at the ground states have been considered (the atoms are on the z-axis of the Cartesian coordinate system). In this case, the induction contributions into $\Delta\alpha_{\alpha\beta}^{AB}(R)$ up to terms $\sim R^{-6}$ inclusive have the well known forms

$$\alpha_{zz}^{ind}(R) = \frac{4\alpha^A\alpha^B}{R^3} + \frac{4\alpha^A\alpha^B(\alpha^A+\alpha^B)}{R^6}, \tag{12}$$

$$\alpha_{xx}^{ind}(R) = \alpha_{yy}^{ind}(R) = -\frac{2\alpha^A\alpha^B}{R^3} + \frac{\alpha^A\alpha^B(\alpha^A+\alpha^B)}{R^6}, \tag{13}$$

where α^A and α^B are the polarizabilities of the interacting atoms A and B. The dispersion contributions to $\Delta\alpha_{\alpha\beta}^{AB}(R)$ up to terms $\sim R^{-6}$ inclusive as well may be written, following to [9], as

$$\alpha_{zz}^{disp}(R) = \frac{7}{18}\left(\frac{\gamma^A}{\alpha^A} + \frac{\gamma^B}{\alpha^B}\right)\frac{C_6^0}{R^6}, \tag{14}$$

$$\alpha_{xx}^{disp}(R) = \alpha_{yy}^{disp}(R) = \frac{2}{9}\left(\frac{\gamma^A}{\alpha^A} + \frac{\gamma^B}{\alpha^B}\right)\frac{C_6^0}{R^6}, \tag{15}$$

where γ^A and γ^B are the second polarizabilities of the interacting atoms ($\gamma = \gamma_{zzzz}$), and C_6^0 is their isotropic dispersion coefficient.

Equatioins (11)–(15) were used to calculate the exchange contributions to the interaction polarizabilities of the atomic complexes He-He, Ar-Ar, Kr-Xe, and Xe-Xe. The required values of the atomic

Table 2
Equilibrium distances R_e, isotropic dispersion coefficients C_6^0, and the parameters used to calculate the exchange polarizability of the complexes (in a.u.)

Parameter	He-He	Ar-Ar	Kr-Xe	Xe-Xe
R_e	5.612[a]	7.102[a]	7.899[a]	8.241[a]
C_6	1.458[b]	64.543[c]	201.27[c]	302.29[c]
$\bar{\beta}$	0.35	0.31	0.29	0.27
δ	5.6081	6.4208	6.8659	7.2050
η	2.1910	1.7690	1.6135	1.5510
B_1	-0.0469	-0.0739	-0.00752	-0.00118
B_2	-0.5506	-0.1237	-0.02383	-0.00588

[a]Reference 54.
[b]Reference 55.
[c]Reference 56.

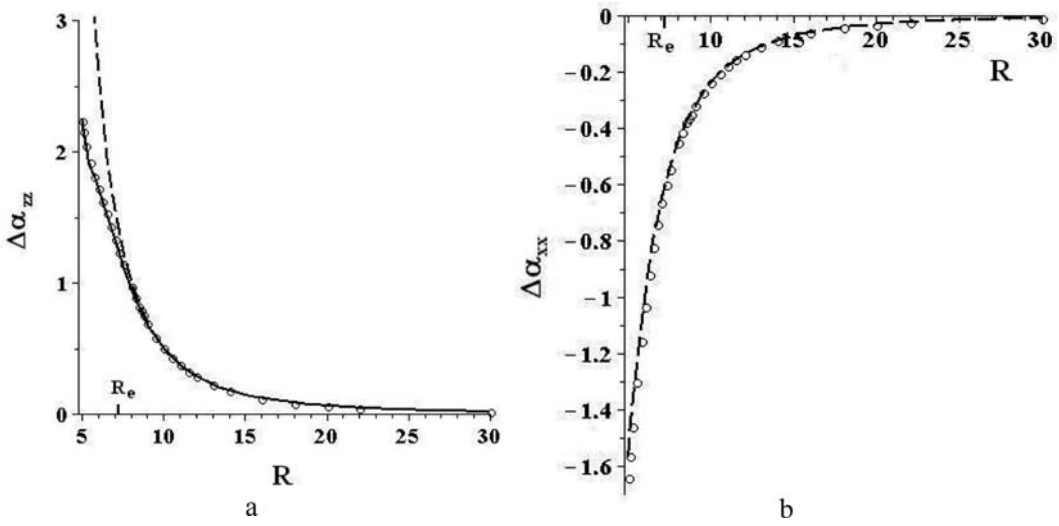

Fig. 2. The interaction polarizabilities $\Delta\alpha_{zz}^{AB}(R)$ (a) and $\Delta\alpha_{xx}^{AB}(R)$ (b) of the complex Ar-Ar. Solid line – analytical calculation taking into account the exchange polarizability; dashed lines – analytical calculations without considering the exchange polarizability; circles – *ab initio* calculation [27]. All values are in a.u.

polarizabilities α, γ and the isotropic dispersion coefficients C_6^0 are given in Tables 1 and 2. The parameters B_1 and B_2 (see, Eq. (10)) were determined by fitting to the exchange polarizabilities $\alpha_{zz}^{exch}(R)$. The fitting parameters B_1 and B_2 together with the parameters β, $\bar{\beta}$, δ, and η, required to describe the exchange polarizability $\alpha_{zz}^{exch}(R)$ of the complexes, are given also in Tables 1 and 2.

The calculation results of the interaction polarizability $\Delta\alpha_{zz}^{AB}(R)$ and $\Delta\alpha_{xx}^{AB}(R)$ of the complexes Ar-Ar and He-He are given in Figs 2 and 3. It's seen that the interaction polarizability $\Delta\alpha_{xx}^{AB}(R)$ is described with a good accuracy in the framework of the classical theory when using only induction and dispersive contributions $\alpha_{xx}^{ind}(R)$ and $\alpha_{xx}^{disp}(R)$. In contrast to $\Delta\alpha_{xx}^{AB}(R)$, for the interaction polarizabilities $\Delta\alpha_{zz}^{AB}(R)$ there are significant differences between the polarizabilities calculated by *ab initio* and classical methods in a vicinity of the equilibrium distances of the complexes. These discrepancies are caused by the exchange interactions being neglected in a classical approach. Taking into account the exchange polarizability $\alpha_{zz}^{exch}(R)$ allows us to reach very good agreement with *ab initio* results [27,28] for a wide range of R.

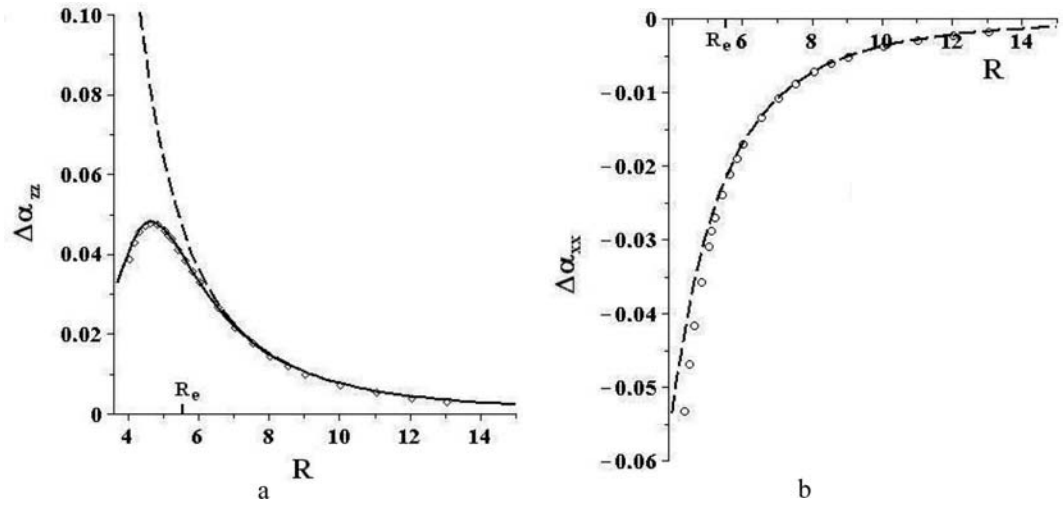

Fig. 3. The interaction polarizabilities $\Delta\alpha_{zz}^{AB}(R)$ (a) and $\Delta\alpha_{xx}^{AB}(R)$ (b) of the complex He-He. Solid line – analytical calculation taking into account the exchange polarizability; dashed lines – analytical calculations without considering the exchange polarizability; circles – *ab initio* calculation [28]. All values are in a.u.

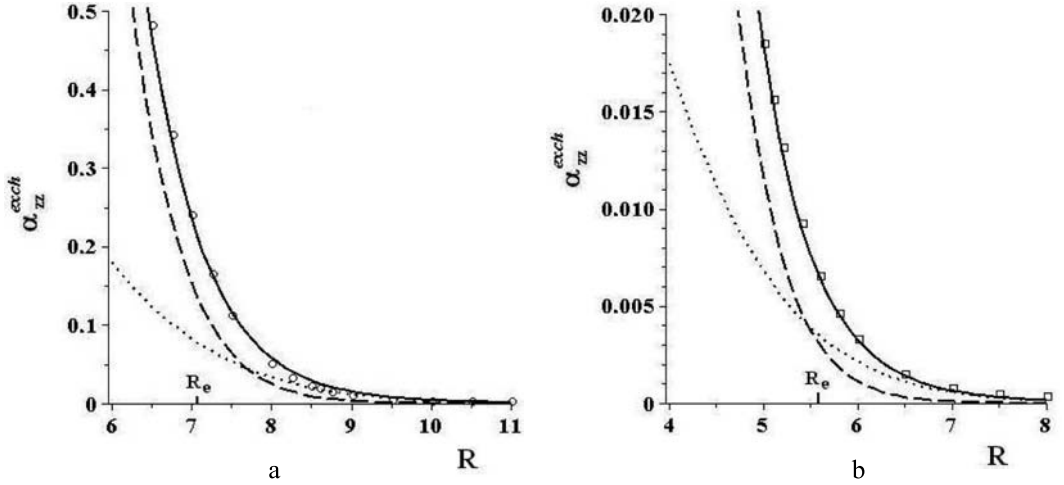

Fig. 4. The exchange polarizability $\alpha_{zz}^{exch}(R)$ of the complexes Ar-Ar (a) and He-He (b). Solid lines – analytical calculations taking into account the both terms of Eq. (10); dotted lines – analytical calculations taking into account the first term of Eq. (10); dashed lines – analytical calculations taking into account the second term of Eq. (10); circles – *ab initio* calculation [27]; squares – *ab initio* calculation [28]. All values are in a.u.

It is of interest to estimate the role of the first and the second terms of $\alpha_{zz}^{exch}(R)$ in Eq. (10) for different range of R. The calculation results of these contributions are given in Fig. 4 for the complexes Ar-Ar and He-He. As follows from the figure the behavior of the exchange polarizability $\alpha_{zz}^{exch}(R)$ are determined in the range of $R > R_e$ mainly by the first term in Eq. (10). In the range of $R < R_e$ the second term in Eq. (10) has more significance in describing the exchange polarizability $\alpha_{zz}^{exch}(R)$.

The interaction polarizability $\Delta\alpha_{zz}^{AB}(R)$ and $\Delta\alpha_{xx}^{AB}(R)$ calculated for the heavier complexes Kr-Xe and Xe-Xe are given in Figs 5 and 6. The regularities of behavior of the exchange polarizabilities $\alpha_{\beta\beta}^{exch}(R)$ found for the complexes He-He and Ar-Ar are also fulfilled both for the complex Xe-Xe and

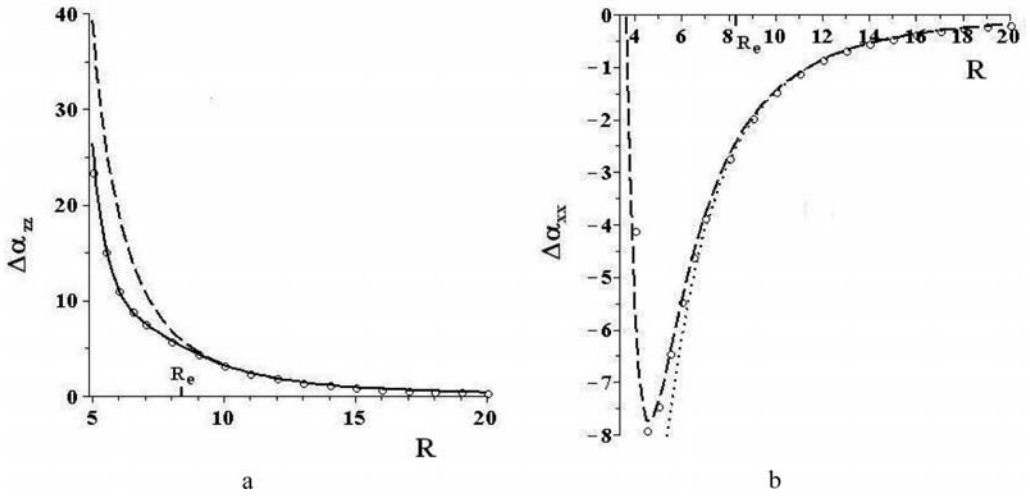

Fig. 5. The interaction polarizabilities $\Delta\alpha_{zz}^{AB}(R)$ (a) and $\Delta\alpha_{xx}^{AB}(R)$ (b) of the complex Xe-Xe. Solid line – analytical calculation taking into account the exchange polarizability; dashed lines – analytical calculations without considering the exchange polarizability; dotted line – analytical calculation taking into account only the induction polarizability; circles – *ab initio* calculation [32]. All values are in a.u.

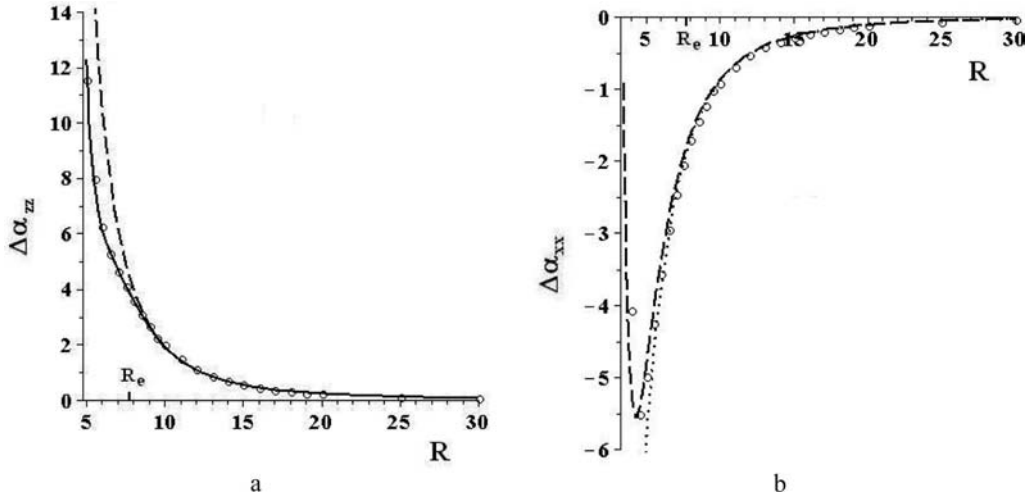

Fig. 6. The interaction polarizabilities $\Delta\alpha_{zz}^{AB}(R)$ (a) and $\Delta\alpha_{xx}^{AB}(R)$ (b) of the complex Kr-Xe. Solid line – analytical calculation taking into account the exchange polarizability; dashed lines – analytical calculations without considering the exchange polarizability; dotted line – analytical calculation taking into account only the induction polarizability; circles – *ab initio* calculation [34]. All values are in a.u.

for the heteroatomic complex Kr-Xe. It should be noted that the dispersion polarizability $\alpha_{xx}^{disp}(R)$ is important, as seen from Figs 5 and 6, for describing the interaction polarizability $\Delta\alpha_{xx}^{AB}(R)$ in the range of $R < R_e$.

To describe spectra of collision-induced light scattering the interaction mean polarizability $\Delta\alpha(R)$ and the interaction polarizability anisotropy $\Delta\gamma(R)$ are important and have the forms

$$\Delta\alpha(R)=\frac{1}{3}\left(\Delta\alpha_{zz}(R)+2\Delta\alpha_{xx}(R)\right)=\frac{2\alpha^A\alpha^B(\alpha^A+\alpha^B)}{R^6}+\frac{5}{18}\left(\frac{\gamma^A}{\alpha^A}+\frac{\gamma^B}{\alpha^B}\right)\frac{C_6}{R^6}+\frac{1}{3}\alpha_{zz}^{exch}(R), \quad (16)$$

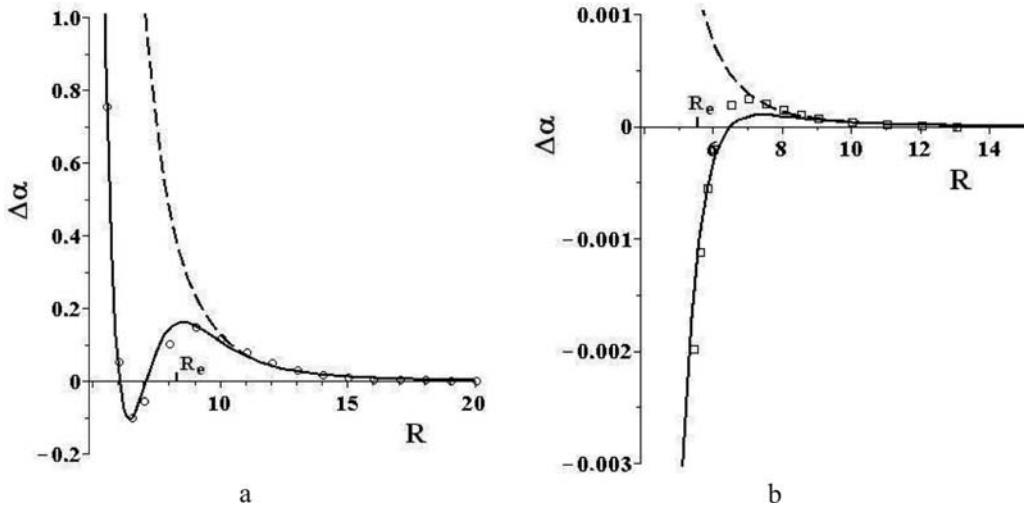

Fig. 7. The interaction polarizability invariants $\Delta\alpha(R)$ of the complexes Xe-Xe (a) and He-He (b). Solid lines – analytical calculations taking into account the exchange polarizability; dashed lines – analytical calculations without considering the exchange polarizability; circles – *ab initio* calculation [32]; squares – *ab initio* calculation [28]. All values are in a.u.

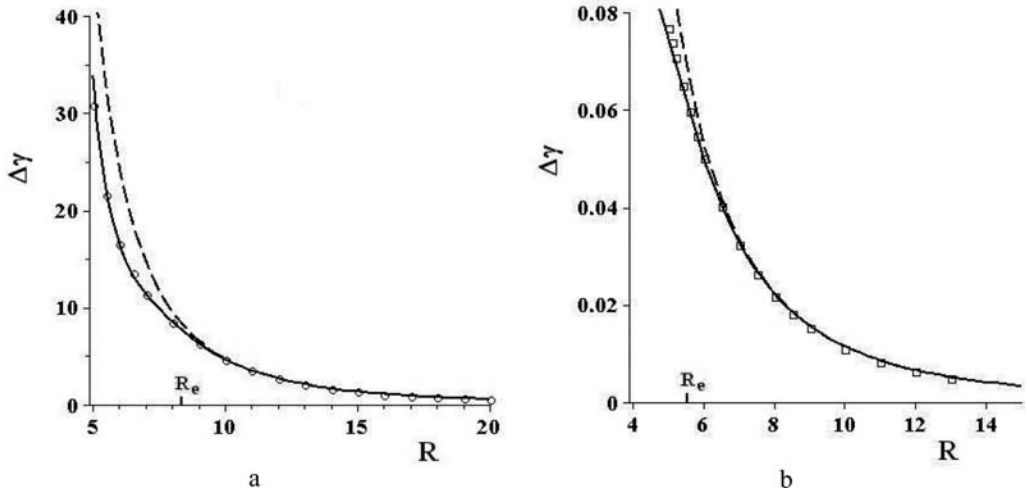

Fig. 8. The interaction polarizability invariants $\Delta\gamma(R)$ of the complexes Xe-Xe (a) and He-He (b). Solid lines – analytical calculations taking into account the exchange polarizability; dashed lines – analytical calculations without considering the exchange polarizability; circles – *ab initio* calculation [32]; squares – *ab initio* calculation [28]. All values are in a.u.

$$\Delta\gamma(R)=\Delta\alpha_{zz}(R)-\Delta\alpha_{xx}(R)=\frac{6\alpha^A\alpha^B}{R^3}+\frac{3\alpha^A\alpha^B(\alpha^A+\alpha^B)}{R^6}+\frac{1}{6}\left(\frac{\gamma^A}{\alpha^A}+\frac{\gamma^B}{\alpha^B}\right)\frac{C_6}{R^6}+\alpha_{zz}^{exch}(R). \quad (17)$$

The calculated polarizability invariants $\Delta\alpha(R)$ and $\Delta\gamma(R)$ for the heavy complex Xe-Xe and for the light complex He-He are given in Figs 7 and 8. As can be seen from Fig. 7 the exchange polarizability $\alpha_{zz}^{exch}(R)$ gives very significant contribution to the interaction mean polarizability $\Delta\alpha(R)$ because of the term $\sim R^{-3}$ is absent in Eq. (16). It should be noted that taking into account the terms $\sim R^{-8}$ in $\alpha_{\alpha\beta}^{ind}(R)$ and $\alpha_{\alpha\beta}^{disp}(R)$ [12] for the complex He-He doesn't improve the agreement between the interaction

polarizabilities calculated by *ab initio* and classical methods for the range of $R < 7$ a.u. The exchange contribution to $\Delta\gamma(R)$ is of less importance than to $\Delta\alpha(R)$. Nevertheless, taking into consideration the exchange contribution $\alpha_{zz}^{exch}(R)$ allows us to improve the accuracy of analytical calculations of $\Delta\gamma(R)$. As a whole, we can conclude that analytical calculations of $\Delta\alpha(R)$ and $\Delta\gamma(R)$ using the simple Eqs (16) and (17) are in a good agreement with *ab initio* calculations for long range of R including a vicinity of equilibrium distances of the considered complexes.

3.2. Ar-H_2 complex

To calculate the polarizability of the complex Ar-H_2 the Cartesian coordinate system was used where the z-axis is directed from the atom Ar to the mass center of H_2 molecule. The molecule H_2 is fixed in the xz plane and its orientation is given by the angle θ between z-axis and H-H bond axis. The distance from the atom Ar to the mass center of H_2 molecule is denoted as R.

For considered complex the induction contributions to $\Delta\alpha_{\alpha\beta}^{AB}(R)$ up to terms $\sim R^{-6}$ inclusive have the form [10]

$$\alpha_{\alpha\beta}^{ind} = \alpha_{\alpha\gamma}^{A} T_{\gamma\delta} \alpha_{\delta\beta}^{B} + \alpha_{\alpha\gamma}^{B} T_{\gamma\delta} \alpha_{\delta\beta}^{A} + \frac{1}{15} \alpha_{\alpha\gamma}^{A} T_{\gamma\delta\varepsilon\varphi} E_{\beta,\delta\varepsilon\varphi}^{B} + \frac{1}{15} E_{\alpha,\gamma\delta\varepsilon}^{B} T_{\gamma\delta\varepsilon\varphi} \alpha_{\varphi\beta}^{A} -$$

$$- \frac{1}{9} B_{\alpha\beta,\gamma\delta}^{A} T_{\gamma\delta\varepsilon\varphi} \Theta_{\varepsilon\varphi}^{B} + \alpha_{\alpha\gamma}^{A} T_{\gamma\delta} \alpha_{\delta\varepsilon}^{B} T_{\varepsilon\varphi} \alpha_{\varphi\beta}^{A} + \alpha_{\alpha\gamma}^{B} T_{\gamma\delta} \alpha_{\delta\varepsilon}^{A} T_{\varepsilon\varphi} \alpha_{\varphi\beta}^{B}, \tag{18}$$

where $\alpha_{\alpha\gamma}^{A}$ and $B_{\alpha\beta,\gamma\delta}^{A}$ are the dipole and dipole-dipole-quadrupole polarizabilities of the atom Ar, $\alpha_{\alpha\gamma}^{B}$, $E_{\beta,\delta\varepsilon\varphi}^{B}$, and $\Theta_{\delta\varepsilon}^{B}$ are the dipole and dipole-octupole polarizabilities and the quadrupole moment of the molecule H_2, and $T_{\gamma\delta\ldots\varphi} = \nabla_\gamma \nabla_\delta \ldots \nabla_\varphi (R^{-1})$ is the tensor, symmetric about the permutation of any pair of symbols. Here and after the Greek subscripts denote Cartesian components x, y, z, and a summation over the repeated subscripts is effected.

Dispersion contribution into $\Delta\alpha_{\alpha\beta}^{AB}(R)$ is calculated in the framework of the method [46]. In that case, the expression for the dispersion contribution with accuracy up to the leading term $\sim R^{-6}$ comes on the form

$$\alpha_{\alpha\beta}^{disp} = \frac{1}{2\pi} \int_0^\infty d\omega \left[T_{\gamma\delta} \gamma_{\delta\varepsilon\alpha\beta}^{B}(i\omega,0,0) T_{\varepsilon\eta} \alpha_{\eta\gamma}^{A}(i\omega) + T_{\gamma\delta} \gamma_{\delta\varepsilon\alpha\beta}^{A}(i\omega,0,0) T_{\varepsilon\eta} \alpha_{\eta\gamma}^{B}(i\omega) \right], \tag{19}$$

where $\alpha_{\eta\gamma}(i\omega)$ and $\gamma_{\delta\varepsilon\alpha\beta}(i\omega,0,0)$ are the polarizability and the second hyperpolarizability at the imaginary frequency $i\omega$. The dispersion contribution $\alpha_{\alpha\beta}^{disp}$ has been calculated using a "constant ratio" approximation (see, for example, [9]) where

$$I_{\delta\varepsilon\alpha\beta}^{A,B} = \frac{\gamma_{\delta\varepsilon\alpha\beta}^{A,B}(i\omega,0,0)}{\bar{\alpha}^{A,B}(i\omega)} \tag{20}$$

is a frequency-independent ratio, $\bar{\alpha}^{A,B}(i\omega)$ is a mean polarizability of A atom (or B molecule) at the imaginary frequency $i\omega$. Assuming, as in [13], that the relationship between $I_{\delta\varepsilon\alpha\beta}^{A,B}$ and static values of $\gamma_{\delta\varepsilon\alpha\beta}^{A,B}(0,0,0)$ and $\alpha^{A,B}(0)$ is the same as in the Unsöld approximation, we can write

$$I_{\delta\varepsilon\alpha\beta}^{A,B} = \frac{\gamma_{\delta\varepsilon\alpha\beta}^{A,B}(0,0,0)}{2\bar{\alpha}^{A,B}(0)}. \tag{21}$$

Table 3
Parameters used to calculate the interaction polarizability of the complex Ar-H_2 (in a.u.)

Parameter	Ar	H_2
α_{xx}	11.19[a]	4.79[a]
α_{zz}	11.19[a]	6.81[a]
Θ_{zz}	0	0.49[a]
$E_{x,xxx}$	0	-1.71[a]
$E_{z,zzz}$	0	4.41[a]
$B_{x,x,xx}$	-166[b]	-74[a]
$B_{x,z,xz}$	-125[c]	-67[a]
$B_{x,x,zz}$	83[c]	42[a]
$B_{z,z,zz}$	-166[b]	-101[a]
γ_{xxxx}	1211[b]	638[a]
γ_{zxzx}	404[d]	233[a]
γ_{zzzz}	1211[b]	753[a]
β	1.076[e]	1.065[f]

[a]Reference 37.
[b]Reference 58.
[c]$B_{x,z,xz} = 3\ B_{z,z,zz}/4$, $B_{x,x,zz} = -B_{z,z,zz}/2$.
[d]$\gamma_{zxzx} = \gamma_{zzzz}/3$.
[e]The value is calculated using the ionization potential from [53].
[f]The value is calculated using the ionization potential from [54].

Thus, in view of the Eqs (20) and (21) the expression (19) can be rewritten as follows

$$\alpha_{\alpha\beta}^{disp} = \frac{T_{\gamma\delta}\gamma^B_{\delta\varepsilon\alpha\beta}(0,0,0)T_{\varepsilon\eta}C_{\eta\gamma}}{2\bar{\alpha}^B(0)} + \frac{T_{\gamma\delta}\gamma^A_{\delta\varepsilon\alpha\beta}(0,0,0)T_{\varepsilon\eta}D_{\eta\gamma}}{2\bar{\alpha}^A(0)}, \tag{22}$$

where

$$\begin{aligned} C_{\eta\gamma} &= \tfrac{1}{2\pi}\int\limits_0^\infty \bar{\alpha}^B(i\omega)\alpha^A_{\eta\gamma}(i\omega)d\omega, \\ D_{\eta\gamma} &= \tfrac{1}{2\pi}\int\limits_0^\infty \bar{\alpha}^A(i\omega)\alpha^B_{\eta\gamma}(i\omega)d\omega. \end{aligned} \tag{23}$$

The tensor $C_{\eta\gamma}$ is not depended on the orientation of the molecule H_2 and is related to the isotropic dispersion coefficient C_6^0 by the simple relation $C_{\eta\gamma} = \frac{1}{6}C_6^0\delta_{\eta\gamma}$. The tensor $D_{\eta\gamma}$ is depended on the orientation of the molecule H_2 and can be expressed through the isotropic and anisotropic dispersion coefficients C_6^0 and C_6^2. In a case when the molecule H_2 is fixed on z-axis the tensor $D_{\eta\gamma}$ has only three nonzero elements: $D_{xx} = D_{yy} = \frac{1}{6}\left(C_6^0 - C_6^2\right)$ and $D_{zz} = \frac{1}{6}\left(C_6^0 + 2C_6^2\right)$. The explicit analytical expressions for the interaction polarizability of the complex X-Y_2 taking into account exchange polarizability are given in Appendix.

The exchange contributions into the interaction polarizabilities for three configurations ($\theta = 0$, $\pi/4$, $\pi/2$) of the complex Ar-H_2 were calculated using Eq. (11), Eq. (A3) from Appendix and *ab initio* calculations of polarizabilities [37,38]. The parameters of the atom Ar and the molecule H_2 required to calculate the induction and dispersive contributions into the interaction polarizability of the complex are given in Table 3 and the dispersion coefficients $C_6^0 = 27.63$ a.u. and $C_6^2 = 2.62$ a.u. were taken from [57].

Table 4
Parameters used to calculate the exchange polarizability of the complex Ar-H_2 (in a.u.)

Parameter	Value	Parameter	Value	Parameter	Value
$\bar{\beta}$	0.41	$B_1^{(0)}$	-0.3355	$B_1^{(0)}$	-0.6439
δ	5.6702	$B_1^{(2)}$	0.0418	$B_1^{(2)}$	-0.1158
η	1.8108	$B_1^{(4)}$	0.0150	$B_1^{(4)}$	-0.0162

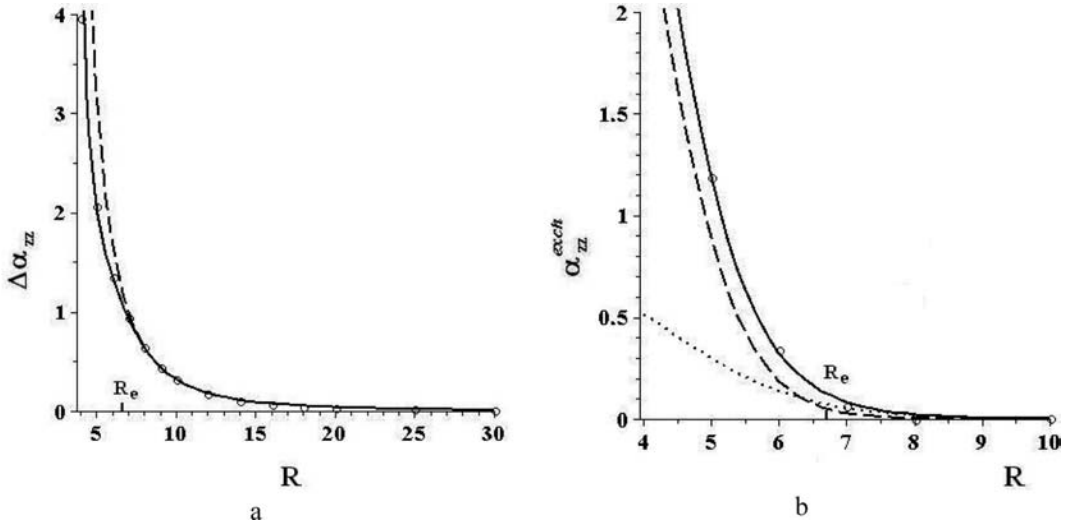

Fig. 9. The interaction polarizability $\Delta\alpha_{zz}^{AB}(R)$ (a) and the exchange polarizability $\alpha_{zz}^{exch}(R)$ (b) for L configuration ($\theta = 0$) of the complex Ar-H_2. Solid line in (a) – analytical calculation taking into account the exchange polarizability; dashed line in (a) – analytical calculation without considering the exchange polarizability; solid line in (b) – analytical calculation taking into account the both terms of Eq. (10); dotted line in (b) – analytical calculation taking into account the first term of Eq. (10); dashed line in (b) – analytical calculation taking into account the second term of Eq. (10); circles – *ab initio* calculation [37, 38]. All values are in a.u.

For considered complex the parameters B_1 and B_2 in the exchange polarizability (see, Eq. (10)) are the functions of the angle θ and can be written as

$$B_i = B_i^{(0)} + B_i^{(2)} P_2(\cos\theta) + B_i^{(4)} P_4(\cos\theta), \tag{24}$$

where $P_\lambda(\cos\theta)$ is the Legendre polynomial. The fitting parameters $B_i^{(\lambda)}$ and the parameters $\bar{\beta}$, δ, and η, required to describe the exchange polarizability $\alpha_{zz}^{exch}(R,\theta)$ of the complex Ar-H_2, are given in Table 4. It should be noted that the parameters $B_i^{(\lambda)}$ reflect the H-H bond length.

The calculation results of the interaction polarizability $\Delta\alpha_{zz}^{AB}(R,\theta)$ and of the exchange polarizability $\alpha_{zz}^{exch}(R,\theta)$ for L configuration ($\theta = 0$) of the complex Ar-H2 are given in Fig. 9. The interaction polarizabilities $\Delta\alpha_{zz}^{AB}(R,\theta)$ for T configuration ($\theta = \pi/2$) and for S configuration ($\theta = \pi/4$) of the same complex are given in Fig. 10. It can be seen that, as for atomic complexes considered above, the exchange contributions are appreciable for the interaction polarizability $\Delta\alpha_{zz}^{AB}(R,\theta)$. The exchange polarizability $\alpha_{zz}^{exch}(R,\theta)$ for L configuration of the complex has the same behavior as for atomic complexes. The exchange polarizabilities for the configurations T and S have the analogical form and are not given. The exchange contribution into the components of the interaction polarizabilities

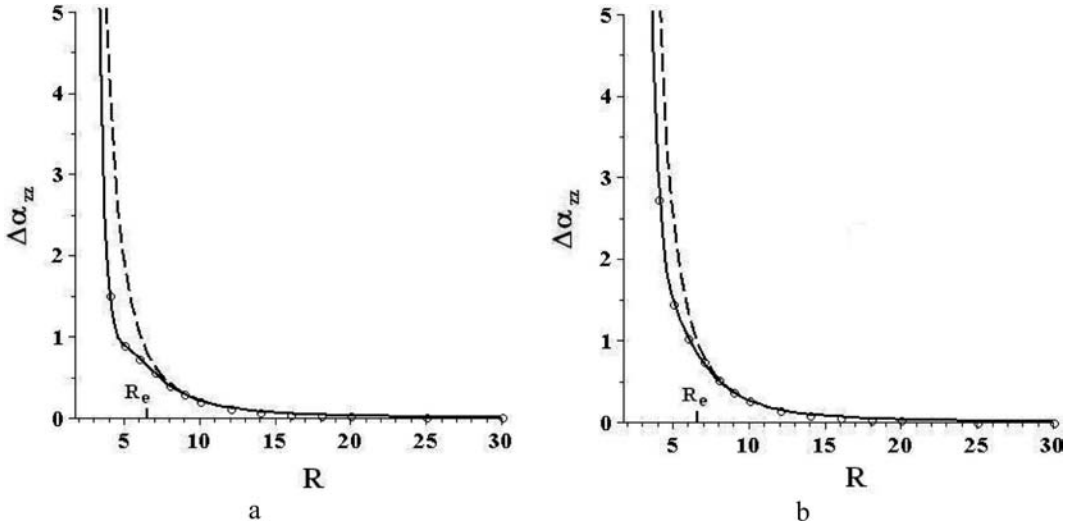

Fig. 10. The interaction polarizabilities $\Delta\alpha_{zz}^{AB}(R)$ for T configuration ($\theta = \pi/2$) (a) and S configuration ($\theta = \pi/4$) of the complex Ar-H_2. Solid lines – analytical calculations taking into account the exchange polarizability; dashed lines – analytical calculations without considering the exchange polarizability; circles – *ab initio* calculation [37,38]. All values are in a.u.

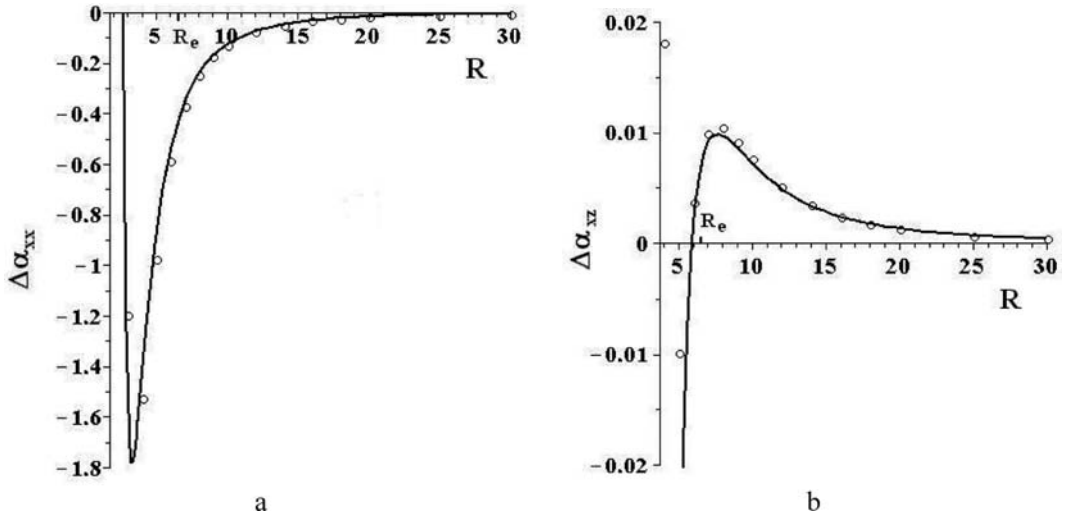

Fig. 11. The interaction polarizabilities $\Delta\alpha_{xx}^{AB}(R)$ (a) and $\Delta\alpha_{xz}^{AB}(R)$ for S configuration ($\theta = \pi/4$) (b) of the complex Ar-H_2. Solid lines – analytical calculations without considering the exchange polarizability; circles – *ab initio* calculation [37,38]. All values are in a.u.

$\Delta\alpha_{xx}^{AB}(R,\theta)$, $\Delta\alpha_{yy}^{AB}(R,\theta)$ and $\Delta\alpha_{zx}^{AB}(R,\theta)$ is of negligible quantity that's illustrated in Fig. 11.

The proposed approach allows us to describe analytically the surface of the interaction polarizability $\Delta\alpha_{\alpha\beta}^{AB}(R,\theta)$ of the complex Ar-H_2 for the considered range of R. For an example, the surfaces of the interaction polarizabilities $\alpha_{zz}^{AB}(R,\theta)$ with and without considering the exchange polarizabilities are given in Fig. 12. This figure gives the general representation of the exchange polarizability role for different orientations of the molecule H_2 in the complex Ar-H_2.

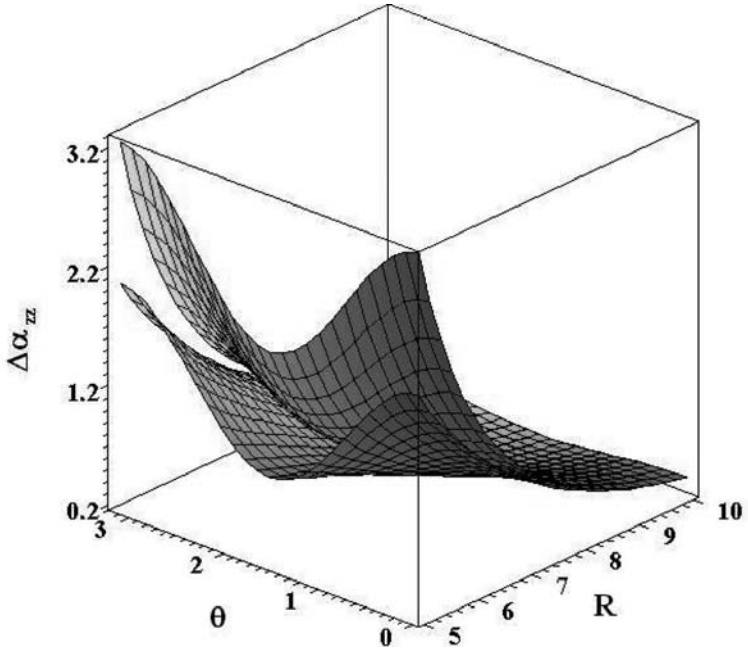

Fig. 12. The surface of the interaction polarizabilities $\Delta\alpha_{zz}^{AB}(R,\theta)$ of the complex Ar-H_2 with (lower surface) and without (upper surface) taking into account the exchange polarizability. The values of $\Delta\alpha_{zz}^{AB}$ and R are in a.u., the angle θ is in rad.

4. Conclusion

In this work, to describe the polarizability of interacting atom-molecular systems the model considering both long-range and exchange contributions as an arithmetic sum has been used. In fact, the correlation between long-range and exchange contributions even in a range of weak overlap of the valence electron shells of interacting systems has a more complicated form. In addition to the exchange contribution, other effects that take place due to overlapping of the electron shells of interacting systems are to contribute into the polarizability. Nevertheless, the proposed model allows us to describe with a good accuracy the polarizability of interacting systems for a long-range of R including the vicinity of R_e for the simple van der Waals complexes using the simple analytical expressions. So, this model can be used for describing of different collision-induced effects.

Appendix

Analytical expressions for the interaction polarizability of X-Y_2 complex

$$\Delta\alpha_{xx}^{AB}(R,\theta) = -\frac{2\alpha^A\left(\alpha_{xx}^B\cos^2\theta+\alpha_{zz}^B\sin^2\theta\right)}{R^3}+\frac{3B_{z,z,zz}^A\Theta_{zz}^B\left(7\cos^2\theta-3\right)}{4R^5}$$
$$+\frac{2\alpha^A E_{x,xxx}^B\cos^2\theta\left(15\cos^2\theta-11\right)}{R^5}-\frac{3\alpha^A E_{z,zzz}^B\sin^2\theta\left(5\cos^2\theta-1\right)}{R^5}$$

$$+\frac{\alpha^A\left(\alpha^B_{zz}\right)^2\sin^2\theta\left(3\cos^2\theta+1\right)}{R^6}-\frac{\alpha^A\left(\alpha^B_{xx}\right)^2\cos^2\theta\left(3\cos^2\theta-4\right)}{R^6}$$
$$-\frac{6\alpha^A\alpha^B_{xx}\alpha^B_{zz}\sin^2\theta\cos^2\theta}{R^6}+\frac{\left(\alpha^A\right)^2\left(\alpha^B_{xx}\cos^2\theta+\alpha^B_{zz}\sin^2\theta\right)}{R^6}+\frac{\gamma^A\left[8C^0_6+C^2_6\left(3\cos^2\theta+1\right)\right]}{36\alpha^AR^6}$$
$$+\frac{C^0_6\left[3\gamma^B_{zzzz}\sin^2\theta\left(3\cos^2\theta+1\right)+3\gamma^B_{zxzx}\left(18\cos^4\theta-19\cos^2\theta+5\right)-\gamma^B_{xxxx}\cos^2\theta\left(9\cos^2\theta-13\right)\right]}{12\left(\alpha^B_{zz}+2\alpha^B_{xx}\right)R^6}, \tag{A1}$$

$$\Delta\alpha^{AB}_{yy}(R,\theta)=-\frac{2\alpha^A\alpha^B_{xx}}{R^3}+\frac{3B^A_{z,z,zz}\Theta^B_{zz}\left(5\cos^2\theta-1\right)}{4R^5}+\frac{2\alpha^AE^B_{x,xxx}\left(5\cos^2\theta-1\right)}{R^5}$$
$$+\frac{2\alpha^A\alpha^B_{xx}\left(\alpha^A+\alpha^B_{xx}\right)}{R^6}+\frac{\gamma^A\left[8C^0_6+C^2_6\left(9\cos^2\theta-5\right)\right]}{36\alpha^AR^6}$$
$$+\frac{C^0_6\left[3\gamma^B_{zxzx}\left(3\cos^2\theta+1\right)-\gamma^B_{xxxx}\left(3\cos^2\theta-7\right)\right]}{12\left(\alpha^B_{zz}+2\alpha^B_{xx}\right)R^6}, \tag{A2}$$

$$\Delta\alpha^{AB}_{zz}(R,\theta)=\frac{4\alpha^A\left(\alpha^B_{xx}\sin^2\theta+\alpha^B_{zz}\cos^2\theta\right)}{R^3}-\frac{3B^A_{z,z,zz}\Theta^B_{zz}\left(3\cos^2\theta-1\right)}{R^5}$$
$$-\frac{8\alpha^AE^B_{x,xxx}\sin^2\theta\left(5\cos^2\theta-1\right)}{R^5}+\frac{4\alpha^AE^B_{z,zzz}\cos^2\theta\left(5\cos^2\theta-3\right)}{R^5}$$
$$+\frac{\alpha^A\left(\alpha^B_{zz}\right)^2\cos^2\theta\left(3\cos^2\theta+1\right)}{R^6}-\frac{\alpha^A\left(\alpha^B_{xx}\right)^2\sin^2\theta\left(3\cos^2\theta-4\right)}{R^6}$$
$$+\frac{6\alpha^A\alpha^B_{xx}\alpha^B_{zz}\sin^2\theta\cos^2\theta}{R^6}+\frac{4\left(\alpha^A\right)^2\left(\alpha^B_{xx}\sin^2\theta+\alpha^B_{zz}\cos^2\theta\right)}{R^6}+\frac{\gamma^A\left[14C^0_6+11C^2_6\left(3\cos^2\theta-1\right)\right]}{36\alpha^AR^6}$$
$$+\frac{C^0_6\left[3\gamma^B_{zzzz}\cos^2\theta\left(3\cos^2\theta+1\right)-3\gamma^B_{zxzx}\left(18\cos^4\theta-19\cos^2\theta-1\right)-\gamma^B_{xxxx}\sin^2\theta\left(9\cos^2\theta-13\right)\right]}{12\left(\alpha^B_{zz}+2\alpha^B_{xx}\right)R^6}$$
$$+\left\{\sum_{\lambda=0,2,4}B^{(\lambda)}_1P_\lambda(\cos\theta)\right\}R^\delta\exp(-\eta R)+\left\{\sum_{\lambda=0,2,4}B^{(\lambda)}_2P_\lambda(\cos\theta)\right\}R^{2\delta}\exp(-2\eta R), \tag{A3}$$

$$\Delta\alpha^{AB}_{zx}(R,\theta)=\Delta\alpha^{AB}_{xz}(R,\theta)=\sin^2\theta\cos^2\theta\left\{\frac{\alpha^A\left(\alpha^B_{zz}-\alpha^B_{xx}\right)}{R^3}+\frac{6B^A_{z,z,zz}\Theta^B_{zz}}{R^5}\right.$$
$$+\frac{\alpha^AE^B_{x,xxx}\left(5\cos^2\theta+7\right)}{R^5}+\frac{\alpha^AE^B_{z,zzz}\left(5\cos^2\theta-9\right)}{2R^5}$$
$$+\frac{\alpha^A\left(\alpha^B_{zz}-\alpha^B_{xx}\right)\left[\alpha^B_{zz}\left(3\cos^2\theta+1\right)-\alpha^B_{xx}\left(3\cos^2\theta-4\right)-2\alpha^A\right]}{R^6}-\frac{\gamma^AC^2_6}{3\alpha^AR^6}+$$
$$\left.+\frac{C^0_6\left[3\gamma^B_{zzzz}\left(3\cos^2\theta+1\right)-6\gamma^B_{zxzx}\left(9\cos^2\theta-5\right)+\gamma^B_{xxxx}\left(9\cos^2\theta-13\right)\right]}{12\left(\alpha^B_{zz}+2\alpha^B_{xx}\right)R^6}\right\}, \tag{A4}$$

$$\Delta\alpha_{xy}^{AB}(R,\theta) = \Delta\alpha_{yx}^{AB}(R,\theta) = \Delta\alpha_{zy}^{AB}(R,\theta) = \Delta\alpha_{yz}^{AB}(R,\theta) = 0. \quad \text{(A5)}$$

References

[1] S. Kielich, *Molekularna Optyka Nieliniowa* (*Nonlinear Molecular Optics*), Naukowe, Warszawa-Poznan, 1977.
[2] G. Birnbaum, ed., *Phenomena Induced by Intermolecular Interactions*, Plenum, New York, 1985.
[3] G.C. Tabitz and M.N. Neuman, eds, *Collision- and Interaction-Induced Spectroscopy*, Kluwer, Dordrecht, 1995.
[4] L. Silberstein, Molecular refractivity and atomic interaction. 1, *Phil Mag* **33** (1917), 92–128.
[5] L. Silberstein, Molecular refractivity and atomic interaction. 2, *Phil Mag* **33** (1917), 521–533.
[6] A.D. Buckingham, The polarizability of a pair of interacting atoms, *Trans Faraday Soc* **52** (1956), 1035–1041.
[7] K.R. Sundberg, A group-dipole interaction model of the molecular polarizability and the molecular first and second hyperpolarizabilities, *J Chem Phys* **66** (1977), 114–118.
[8] A.D. Buckingham and K.L. Clarke, Long-range effects of molecular interactions on the polarizability of atoms, *Chem Phys Lett* **57** (1978), 321–325.
[9] K.L.C. Hunt, B.A. Zilles and J.E. Bohr, Effects of van der Waals interactions on the polarizability of atoms, oscillators, and dipolar rotors at long range, *J Chem Phys* **75** (1981), 3079–3086.
[10] K.L.C. Hunt, Y.Q. Liang and S. Sethuraman, Transient, collision-induced changes in polarizability for atoms interacting with linear, centrosymmetric molecules at long range, *J Chem Phys* **89** (1988), 7126–7138.
[11] D.M. Bishop and J. Pipin, Calculation of the polarizability and hyperpolarizability tensors, at imaginary frequency, for H, He, and H_2 and the dispersion polarizability coefficients for interactions between them, *J Chem Phys* **97** (1992), 3375–3381.
[12] P.W. Fowler, K.L.C. Hunt, H.M. Kelly and A.J. Sadley, Multipole polarizabilities of the helium atom and collision-induced polarizabilities of pairs containing He and H atoms, *J Chem Phys* **100** (1994), 2932–2935.
[13] X. Li and K.L.C. Hunt, Transient changes in polarizability for centrosymmetric linear molecules interacting at long range: Theory and numerical results for $H_2 \cdot\cdot H_2$, $H_2 \cdot\cdot N_2$, and $N_2 \cdot\cdot N_2$, *J Chem Phys* **100** (1994), 7875–7889.
[14] S.M. El-Sheikh, G.C. Tabisz and A.D. Buckingham, Collision-induced light scattering by isotropic molecules: The role of the quadrupole polarizability, *Chem Phys* **247** (1999), 407–412.
[15] C. Domene, P.W. Fowler, P. Jemmer and P.A. Madden, Dipole-induced-dipole polarizabilities of symmetric clusters, *Mol Phys* **98** (2000), 1391–1407.
[16] L. Jensen, P.-O. Åstrand, A. Osted, J. Kongsted and K.V. Mikkelsen, Polarizability of molecular clusters as calculated by a dipole interaction model, *J Chem Phys* **116** (2002), 4001–4010.
[17] M.A. Buldakov, B.V. Korolev, I.I. Matrosov and V.N. Cherepanov, Polarizability of two interacting molecules N_2 and O_2, *Optics and Spectroscopy* **94** (2003), 185–190.
[18] M.A. Buldakov, V.N. Cherepanov and N.S. Nagornova, Polarizability of the van der Waals complexes $N_2 \cdot\cdot Y$ and $O_2 \cdot\cdot Y$ (Y = He, Ne, Ar, Kr, Xe). Part 1. Stable configurations, *Atmos Oceanic Opt* **18** (2005), 12–17.
[19] M.A. Buldakov, V.N. Cherepanov and N.S. Nagornova, Polarizability of the van der Waals complexes $N_2 \cdot\cdot Y$ and $O_2 \cdot\cdot Y$ (Y = He, Ne, Ar, Kr, Xe). Part 2. Unstable configurations, *Atmos Oceanic Opt* **18** (2005), 18–22.
[20] M.A. Buldakov, V.N. Cherepanov and N.S. Nagornova, Polarizability of the van der Waals complexes $N_2 \cdot\cdot Y$ and $O_2 \cdot\cdot Y$ (Y = He, Ne, Ar, Kr, Xe). Part 3. Frequency dependence, *Atmos Oceanic Opt* **19** (2006), 33–37.
[21] X. Li, C. Ahuja, J.F. Harrison and K.L.C. Hunt, The collision-induced polarizability of a pair of hydrogen molecules, *J Chem Phys* **126** (2007), 214302.
[22] G. Maroulis, ed., Atoms, Molecules and Clusters in Electric Fields. Theoretical Approaches to the Calculation of Electric Polarizability, Singapore, Imperial College Press, 2006.
[23] G. Maroulis, ed., *Computational Aspects of Electric Polarizability Calculations: Atoms, Molecules and Clusters*, Amsterdam, IOS Press, 2006.
[24] D.G. Bounds, The interaction polarizability of two hydrogen molecules, *Mol Phys* **38** (1979), 2099–2106.
[25] D.G. Bounds, A. Hinchliffe and C.J. Spicer, The interaction polarizability of two nitrogen molecules, *Mol Phys* **42** (1981), 73–82.
[26] C.E. Dykstra and S.-Y. Liu, The hydrogen bonding influence on polarizability and hyperpolarizability. A derivative hartree-fock study of the electric properties of hydrogen fluoride and the hydrogen fluoride dimer, *J Mol Structure: THEOCHEM* **135** (1986), 357–368.
[27] B. Fernandez, C. Hättig,, H. Koch and A. Rizzo, Ab initio calculation of the frequency-dependent interaction induced hyperpolarizability of Ar_2, *J Chem Phys* **110** (1999), 2872–2882.
[28] C. Hättig, H. Larsen, J. Olsen, P. Jørgensen, H. Koch, B. Fernandez and A. Rizzo, The effect of intermolecular interactions of the electric properties of helium and argon. I. *Ab initio* calculation of the interaction induced polarizability in He_2 and Ar_2, *J Chem Phys* **111** (1999), 10099–10107.

[29] G. Maroulis, Computational aspects of interaction hyperpolarizability calculations. A study on $H_2 \cdots H_2$, $Ne \cdots HF$, $Ne \cdots FH$, $He \cdots He$, $Ne \cdots Ne$, $Ar \cdots Ar$, and $Kr \cdots Kr$, *J Phys Chem A* **104** (2000), 4772–4779.
[30] L. Jensen, P.-O. Åstrand, A. Osted, J. Kongsted and K.V. Mikkelsen, Polarizability of molecular clusters as calculated by a dipole interaction model, *J Chem Phys* **116** (2002), 4001–4010.
[31] G. Maroulis and A. Haskopoulos, Interaction induced (hyper) polarizability in $Ne \cdots Ar$, *Chem Phys Lett* **358** (2002), 64–70.
[32] G. Maroulis, A. Haskopoulos and D. Xenides, New basis sets for xenon and interaction polarizability of two xenon atoms, *Chem Phys Lett* **396** (2004), 59–65.
[33] J.L. Cacheiro, B. Fernandez, D. Marchesan, S. Coriani, C. Hättig and A. Rizzo, Coupled cluster calculations of the ground state potential and interaction induced electric properties of the mixed dimers of helium, neon and argon, *Mol Phys* **102** (2004), 101–110.
[34] A. Haskopoulos, D. Xenides and G. Maroulis, Interaction dipole moment, polarizability and hyperpolarizability in the KrXe heterodiatom, *Chem Phys* **309** (2005), 271–275.
[35] P. Karamanis and G. Maroulis, How impotent are high-level *ab initio* treatments for the interaction dipole moment and polarizability of HeNe, *Comput Letters* **1** (2005), 117–122.
[36] W. Glaz, T. Bancewicz, J.-L. Godet, G. Maroulis and A. Haskopoulos, Hyper-Rayleigh light-scattering spectra determined by *ab initio* collisional hyperpolarizabilities of He-Ne atomic pairs, *Phys Rev A* **73** (2006), 042708.
[37] T. Bancewicz and G. Maroulis, Rotationally adapted studies of *ab initio* computed collision-induced hyperpolarizabilities: The H_2-Ar pair, *Phys Rev A* **79** (2009), 042704.
[38] T. Bancewicz and G. Maroulis, Modelling the polarizability of the dihidrogen-argon pair, *Chem Phys Lett* **471** (2009), 148–152.
[39] D.W. Oxtoby and W.M. Gelbart, Collisional polarizability anisotropies of the noble gases, *Mol Phys* **29** (1975), 1569–1576.
[40] D.W. Oxtoby and W.M. Gelbart, Collisional polarizability of the inert gases. Second-order overlap, exchange, and correlation effects, *Mol Phys* **30** (1975), 535–547.
[41] D.W. Oxtoby, The calculation of pair polarizabilities through continuum electrostatic theory, *J Chem Phys* **69** (1978), 1184–1189.
[42] K.L.C. Hunt and A.D. Buckingham, The polarizability of H_2 in the triplet state, *J Chem Phys* **72** (1980), 2832–2840.
[43] M.H. Proffitt, J.W. Keto and L. Frommhold, Collision-induced Raman spectra and diatom polarizabilities of the rare gases – an update, *Can J Phys* **59** (1981), 1459–1474.
[44] P.D. Dacre and M. Frommhold, Rare gas diatom polarizabilities, *J Chem Phys* **76** (1982), 3447–3460.
[45] K.L.C. Hunt, Nonlocal polarizability densities and the effects of short-range interactions on molecular dipoles, quadrupoles, and polarizabilities, *J Chem Phys* **80** (1984), 393–497.
[46] K.L.C. Hunt and J.E. Bohr, Field-induced fluctuation correlations and the effects of van der Waals interactions on molecular polarizabilities, *J Chem Phys* **84** (1986), 6141–6150.
[47] M.A. Buldakov and V.N. Cherepanov, Polarizability functions of diatomic homonuclear molecules: Semiempirical approach, *J Comput Meth Sci Eng* **4** (2004), 237–250.
[48] M.A. Buldakov, V.N. Cherepanov and N.S. Nagornova, Polarizability functions of diatomic heteronuclear molecules: Semiempirical approach, *J Comput Meth Sci Eng* **6** (2006), 153–163.
[49] B.M. Smirnov, *Asymptotic Methods in the Atomic Collision*, Atompress, Moscow, 1973, in Russian.
[50] B.M. Smirnov and E.E. Nikitin, *Atomic and Molecular Processes*, Nauka, Moscow, 1988, in Russian.
[51] A.D. Buckingham in: *Intermolecular Interaction: from Diatomic to Biopolymers*, B. Pullman, ed., Wiley, New York, 1978.
[52] J. Stiehler and J. Hinze, Calculation of static polarizabilities and hyperpolarizabilities for the atoms He through Kr with a numerical RHF method, *J Phys B* **28** (1995), 4055–4071.
[53] A.A. Radtsig and B.M. Smirnov, *Parameters of Atoms and Atomic Ions: Reference Book*, Atomizdat, Moscow, 1986, in Russian.
[54] K.P. Huber and G. Herzberg, *Molecular Spectra and Molecular Structure. IV. Constants of Diatomic Molecules*, New York, 1979.
[55] A. Kumar and W.J. Meath, Pseudo-spectral dipole oscillator strengths and dipole-dipole and triple-dipole dispersion energy coefficients for HF, HCl, HBr, He, Ne, Ar, Kr and Xe, *Mol Phys* **54** (1985), 823–833.
[56] A.J. Thakkar, H. Hettema and P.E.S. Wormer, *Ab initio* dispersion coefficients for interactions involving rare-gas atoms, *J Chem Phys* **97** (1992), 3252–3257.
[57] C. Bissonnette, C.E. Chuaqui, K.G. Crowell, R.J. Le Roy, R.J. Wheatley and W.J. Meath, A reliable new potential energy surface for H_2–Ar, *J Chem Phys* **105** (1996), 2639–2653.
[58] G. Maroulis and D.M. Bishop, On the electric polarizabilities of argon, *J Phys B: At Mol Phys* **18** (1985), 4675–4682.

Journal of Computational Methods in Sciences and Engineering 10 (2010) 183–188
DOI 10.3233/JCM-2010-0321
IOS Press

Anomalous diffusion in dielectric relaxation of polyelectrolytes

Jean-Louis Déjardin*
Laboratoire de Mathématiques et Physique des Systèmes, Université de Perpignan Via Domitia, 52 Avenue Paul Alduy, 66860 Perpignan Cedex, France

Abstract. Anomalous diffusion is considered in the context of fractional dynamics applied to dielectric relaxation of polyelectrolyte solutions. The approach starts from a fractional Smoluchowski equation in configuration space of molecular orientations of macroions and displacements of couterions. By using a perturbation procedure, we derive analytic expressions for the buildup and reversing field processes of the electric polarization given by the expectation value of the product of the first Legendre polynomial by the first Hermite polynomial. The first harmonic component of the ac dielectric response is also calculated. All these results are illustrated by plots demonstrating the effect of both the coupling (rotation-translation) parameter a and the critical exponent α (subdiffusion).

1. Introduction

Among many techniques for investigating macromolecular systems such as colloïdal suspensions, biopolymers and polyelectrolytic solutions, dielectric measurements remain still a matter of topical interest [1]. In particular, the relaxation processes can be studied over a very broad range either in time or frequency [2]. The problem of getting a better understanding of the complex behavior of polyelectrolytes [3–10] takes on special importance because of many applications in molecular biology (nucleic acids, peptides, proteins) or in industry (paper production, water filtration, absorbers). For such systems, all the question consists of describing the dynamic evolution of charged groups, namely macroions (with negative charges) surrounded by a ionic cloud of counterions (with positive charges). To follow the orientational motion of the molecules acted on by an electric field, one needs to consider the coupling between the vibration of the small cations and the rotation of the macroion. A theoretical approach taking into account this coupling effect was proposed by Szabo et al. [11] who derived a Smoluchowski equation for the probability distribution function $W(\vartheta, x, t)$ of orientations (ϑ) and displacements (x) of Brownian particles in configuration space. The solution of this partial differential equation led them to obtain analytic expressions for the linear Kerr effect response (low field limit). On using this method, we have also established in a previous paper [12] literal relations for the nonlinear dielectric increment of an assembly of nonpolar rodlike macroions.

The purpose of this paper is to deal with the problem of anomalous diffusion occurring in the dielectric response of polyelectrolytes composed of an ensemble of noninteracting polyion molecules with no permanent dipole moments. To our knowledge, this aspect has not been tackled yet. It is indeed

*Corresponding author. E-mail: dejardin@univ-perp.fr.

observed that the relaxation phenomena in complex fluids do not obey an exponential law in the time domain but rather a Mittag-Leffler function $E_\alpha\left[-\left(t/\tau\right)^\alpha\right]$, where τ^α plays the role of a specific waiting time scale and α is a fractional parameter different from unity ($\alpha = 1$ corresponds to the Brownian diffusion limit) [13–16]. In what follows, we shall consider the subdiffusion processes where $0 \leqslant \alpha \leqslant 1$.

2. Theory

We briefly recall [11,12] the one-dimensional Smoluchowski equation for a memoryless process of a symmetric-top charged particle under the action of an electric field $E\left(t\right)$. We have

$$\begin{aligned}\frac{\partial}{\partial t}W\left(\vartheta,x,t\right) = \frac{D_r}{\sin\vartheta}\frac{\partial}{\partial\vartheta}\left[\sin\vartheta\left(\frac{\partial}{\partial\vartheta}W\left(\vartheta,x,t\right)+\frac{W\left(\vartheta,x,t\right)}{kT}\frac{\partial}{\partial\vartheta}V\left(\vartheta,x,t\right)\right)\right]\\ +D_t\frac{\partial}{\partial x}\left[\frac{\partial}{\partial x}W\left(\vartheta,x,t\right)+\frac{W\left(\vartheta,x,t\right)}{kT}\frac{\partial}{\partial x}V\left(\vartheta,x,t\right)\right],\end{aligned} \tag{1}$$

where $D_r = \left(2\tau\right)^{-1}$ is the rotational diffusion coefficient with respect to the axis perpendicular to the symmetry axis of the macroion, D_t is the translational diffusion coefficient of the counterions, k is the Boltzmann constant, and T is the absolute temperature. The total potential energy of the macroion carrying an instantaneous dipole moment m induced by the application of the electric field $E\left(t\right)$ is

$$V\left(\vartheta,x,t\right) = \frac{n^2e^2}{2\sigma}x^2 - nexE\left(t\right)\cos\vartheta, \tag{2}$$

where n is the number of charged groups on the macroion, e is the electron charge, σ is the polarizability of the macroion, and $m = nex$. Oosawa [17] showed that the mean square dipole moment $\left\langle m^2\right\rangle$ equals $kT\sigma$, and defined a single relaxation time τ_t for the dynamics of the ion atmosphere related to D_t by

$$\tau_t = \left(bD_t\right)^{-1}, \tag{3}$$

where $b = n^2e^2/\left\langle m^2\right\rangle$.

From the Debye's theory, the electric polarization of the polyelectrolyte solution can be defined by $P\left(t\right) = N\left\langle m\cos\vartheta\right\rangle\left(t\right)$, where the value of the moment m, unlike usual polar liquids, is no longer constant but depends on the displacement coordinate x and N is the number of macromolecules per unit volume. Hence, the physical quantity appropriate to dielectric relaxation of a polyion in dilute solution, having only an instantaneous dipole moment m, will be given by the expectation value of the product of the first Legendre polynomial by the first Hermite polynomial [12], namely $\left\langle P_1\left(u\right)H_1\left(y\right)\right\rangle\left(t\right)$. The angular brackets stand for ensemble averages such that

$$q_{l,n}\left(t\right) = \left\langle P_l\left(u\right)H_n\left(y\right)\right\rangle\left(t\right) = \int_{-1}^{+1}\int_{-\infty}^{+\infty}W\left(u,y,t\right)P_l\left(u\right)H_n\left(y\right)dudy, \tag{4}$$

where $u = \cos\vartheta = P_1\left(u\right)$ and $y = \left(b/2\right)^{1/2}x = H_1\left(y\right)/2$. Multiplying both sides of Eq. (1) by $P_l\left(u\right)H_n\left(y\right)$ and integrating from -1 to $+1$ over the variable u and from $-\infty$ to $+\infty$ over the variable

y, we obtain the following infinite hierarchy of differential-recurrence relations for the $q_{l,n}(t)$

$$\begin{aligned}\dot{q}_{l,n}(t) = &-\left[l(l+1)D_r + n/\tau_t\right] q_{l,n}(t) \\ &+ \left(\frac{2\sigma}{kT}\right)^{1/2} E(t) D_r \frac{l(l+1)}{2(2l+1)} \left[q_{l-1,n+1}(t) - q_{l+1,n+1}(t)\right] \\ &+ \left(\frac{2\sigma}{kT}\right)^{1/2} E(t) \frac{l+1}{2l+1} \left(1/\tau_t - lD_r\right) n q_{l+1,n-1}(t) \\ &+ \left(\frac{2\sigma}{kT}\right)^{1/2} E(t) \frac{l}{2l+1} \left[(l+1)D_r + 1/\tau_t\right] n q_{l-1,n-1}(t).\end{aligned} \tag{5}$$

Now, in order to take account of anomalous diffusion, we apply the Riemann-Liouville operator [14,18] to the right-hand side of Eq. (5) given by

$${}_0D_t^{1-\alpha} f(t) = \frac{d}{dt} {}_0D_t^{-\alpha} f(t) = \frac{d}{dt}\left[\frac{1}{\Gamma(\alpha)} \int_0^t \frac{f(t')}{(t-t')^{1-\alpha}} dt'\right]. \tag{6}$$

Since we have to determine the dielectric response, we need to calculate $q_{1,1}(t)$, ($l = 1$, $n = 1$), the time evolution of which is

$$\tau {}_0D_t^{\alpha} q_{1,1}(t) + (1 + 1/a) q_{1,1}(t) = \frac{\tilde{E}}{3}(1 + 1/a), \tag{7}$$

if we restrict ourselves to the first order in the electric field strength, and where $a = \tau_t/\tau$, and

$$\tilde{E}(t) = \left(\frac{2\sigma}{kT}\right)^{1/2} E(t).$$

3. Results and discussion

3.1. Transients for the rise process and the reversing field

For such processes, the electric field $E(t)$ is constant, $E(t) = E$. By taking the Laplace transform (denoted by the symbol "L") of Eq. (7), we obtain

$$Q_{1,1}(s) = \frac{\tilde{E}}{3}(1 + 1/a) \frac{1}{s\left[(s\tau)^{\alpha} + (1 + 1/a)\right]}, \tag{8}$$

where

$$Q_{1,1}(s) = L\left[q_{1,1}(t)\right] = \int_0^{\infty} \exp(-st) q_{1,1}(t)\, dt. \tag{9}$$

By noting that the Laplace transform of the Mittag-Leffler function is

$$L\left\{E_{\alpha}\left[-(t/\tau)^{\alpha}\right]\right\} = \frac{1}{s\left[1 + (s\tau)^{-\alpha}\right]}, \tag{10}$$

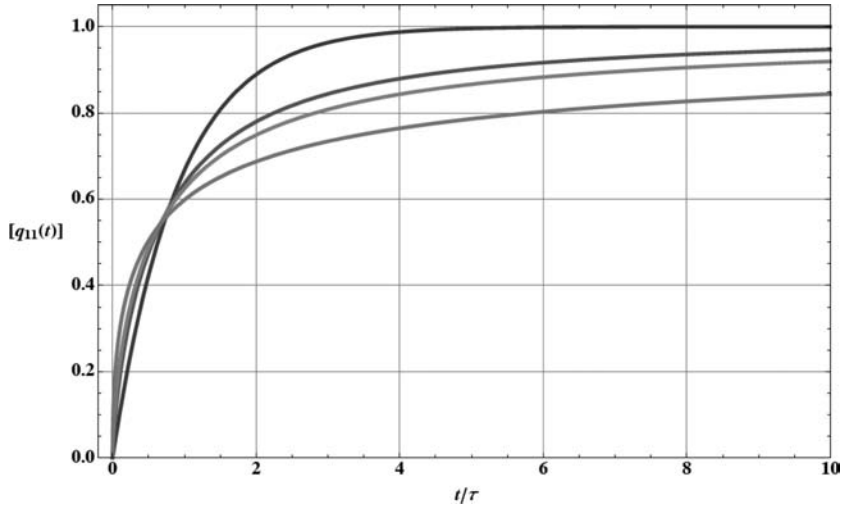

Fig. 1. Comparison of the rise processes of the electric polarization for different values of the fractional parameter α. From the bottom to the top : $\alpha = 0.5, 0.67, 0.75, 1$. The coupling parameter a is fixed to 10.

where $E_\alpha\left[-\left(t\right)^\alpha\right] = \sum_{j=0}^{\infty} \frac{(-1)^j (t)^j}{\Gamma(\alpha j+1)}$, and using the following property of the Riemann-Liouville operator

$$L\left[{}_0D_t^\alpha f\left(t\right)\right] = s^\alpha F\left(s\right) - s^{\alpha-1} f\left(0\right), \tag{11}$$

where $F\left(s\right) = L\left[f\left(t\right)\right]$, we obtain

$$q_{1,1}\left(t\right) = \frac{\tilde{E}}{3}\left\{1 - E_\alpha\left[-\left(1+1/a\right)\left(t/\tau\right)^\alpha\right]\right\} \tag{12}$$

for the buildup process where at $t = 0$, $q_{1,1}\left(0\right) = 0$, and

$$\left[q_{1,1}\left(t\right)\right]_r = \frac{\tilde{E}}{3}\left\{-1 + 2E_\alpha\left[-\left(1+1/a\right)\left(t/\tau\right)^\alpha\right]\right\} \tag{13}$$

for the reversing field with initial condition $\left[q_{1,1}\left(0\right)\right]_r = \tilde{E}/3$.

When $a \to \infty\,(\tau \gg \tau_t)$ and $\alpha = 1$, the well-known Debye's result of purely polar (permanent moment) is recovered [19], the Mittag-Leffler function reducing itself to the exponential function $\exp\left(-t/\tau\right)$. In Fig. 1, given $a = 10$, we have plotted the rise regime of $q_{1,1}\left(t\right)$ as a function of t/τ for different values of the fractional parameter α $(0.5 \leqslant \alpha \leqslant 1)$. We remark that the smaller α is, the steeper is the initial slope of the curves. The same considerations can be done in Fig. 2 about the variations of $\left[q_{1,1}\left(t\right)\right]_r$.

3.2. Dielectric response to an alternating field

We are here concerned with the derivation of an analytic expression for the dielectric relaxation of an assembly of noninteracting rodlike macroions acted on by an ac external electric field $E\left(t\right) = E_0\cos\left(\omega t\right)$. In the stationary regime, the system has removed all the transient effects and the stationary ac dielectric response which is independent of the initial conditions can be obtained by seeking all the $q_{l,n}\left(t\right)$ as a Fourier series

$$q_{l,n}\left(t\right) = \sum_{k=-\infty}^{+\infty} Q_{l,n}^k\left(\omega\right)\exp\left(ik\omega t\right), \tag{14}$$

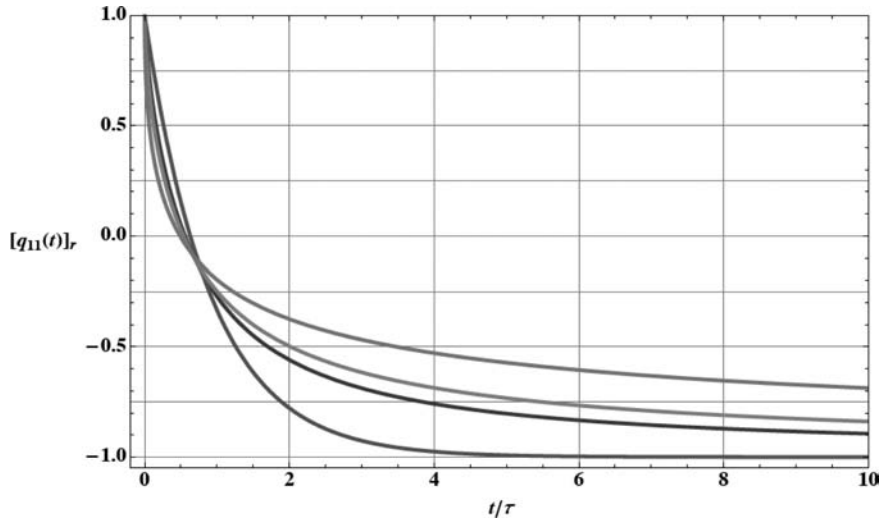

Fig. 2. Comparison of the decay processes (reversing field) of the electric polarization for different values of the fractional parameter α. From the top to the bottom : $\alpha = 0.5, 0.67, 0.75, 1$. The coupling parameter a is fixed to 10.

where the Fourier amplitudes satisfy the condition $Q_{l,n}^{-k}(\omega) = \left[Q_{l,n}^{k}(\omega)\right]^{*}$ (the asterisk denotes the complex conjugate). In particular, the solution for $q_{1,1}(t)$ can be presented in the form ("Re" stands for "the real part of")

$$q_{1,1}(t) = 2\sum_{k=1}^{\infty} Re\left[Q_{1,1}^{k}(\omega)\exp(ik\omega t)\right]. \tag{15}$$

For the linear response, we have $k = 1$ which yields

$$Q_{1,1}(\omega) = \frac{\tilde{E}_1}{6}\frac{1+1/a}{(1+1/a)+(i\omega\tau)^{\alpha}}, \tilde{E}_1 = \left(\frac{2\sigma}{kT}\right)^{1/2} E_0. \tag{16}$$

In the limit case of $a \to \infty$ (permanent dipole moment) and $\alpha = 1$ (normal diffusion), the well-known Debye's result [19] is recovered $[1/(1+i\omega\tau)]$. Figure 3 presents a series of Cole-Cole-like diagrams illustrating Eq. (16). We have introduced a reduced angular frequency variable $\Omega = \omega\tau = \omega/(2D_r)$, so that

$$Q_{1,1}(a,\Omega) = Re\left[Q_{1,1}(a,\Omega)\right] - iIm\left[Q_{1,1}(a,\Omega)\right], \tag{17}$$

where Re and Im stand for the real and imaginary parts of $Q_{1,1}(a,\Omega)$, respectively. In this figure, we have fixed to 1 the coupling parameter a $(= \tau_t/\tau)$ and chosen four different values of the fractional parameter α. Given a, the amplitudes of the arcs increase in proportion to α. Similarly, we could observe that given α, the amplitudes of the arcs would increase with increasing values of a.

To conclude, this paper contains some new features about dielectric relaxation in polyelectrolytes by considering the subdiffusion regime able to occur in such complex liquids. The analytic expressions are derived both for the transient and the stationary processes of a nonpolar macromolecular system in dilute solution. The results we have obtained demonstrate the influence of the coupling parameter a together with the fractional exponent α on the dielectric response.

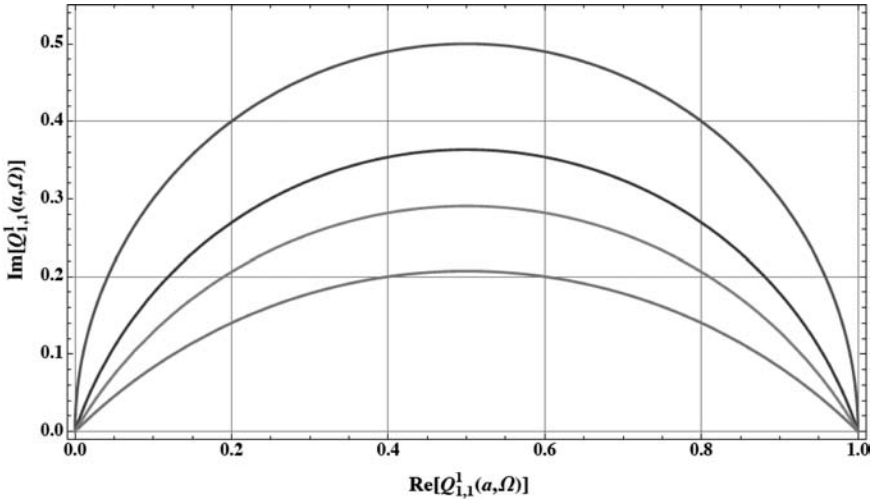

Fig. 3. Cole-Cole plots of the linear complex electric polarization $Q_{1,1}\,(a,\Omega)$ for different values of the fractional parameter α. From the bottom to the top : $\alpha = 0.5, 0.67, 0.8, 1$. The coupling parameter a is fixed to 1.

Acknowledgments

I am very indebted to Professor G. Maroulis for his invitation to publish an article in the special issue of the Journal of Computational Methods in Science and Engineering in honour of Professor S. Kielich.

References

[1] S. Takashima, *Electrical Properties of Biopolymers and Membranes* (Philadelphia: Institute of Physics Publishing, 1989).
[2] Y. Feldman, Y. Zuev, E. Polygalov and V. Fedotov, *Colloid Polym Sci* **270** (1992), 768.
[3] F. Oosawa, *Biopolymers* **9** (1970), 677 .
[4] A. Minakata, N. Imai and F. Oosawa, *Biopolymers* **11** (1972), 347.
[5] A. Warashina and A. Minakata, *J Chem Phys* **58** (1973), 4743.
[6] J.G. Elias and D. Eden, *Macromolecules* **14** (1981), 410.
[7] M. Mandel and T. Odijk, *Annu Rev Phys Chem* **35** (1984), 75.
[8] N. Ookubo, Y. Hirai, K. Ito and R. Hayakawa, *Macromolecules* **22** (1989), 1359 .
[9] J.F. Curry and S. Krause, *J Phys Chem* **96** (1992), 4643.
[10] D. Pörschke, *Biophys Chem* **49** (1994), 127.
[11] A. Szabo, M. Haleem and D. Eden, *J Chem Phys* **85** (1986), 7472.
[12] J.L. Déjardin and J. Jadzyn, *J Chem Phys* **129** (2008), 144903.
[13] G.M. Mittag-Leffler, *Acad Sci Paris C R* **137** (1903), 554.
[14] R. Metzler and J. Klafter, *Phys Rep* **339** (2000), 1.
[15] R. Metzler and J. Klafter, *Adv Chem Phys* **116** (2001), 223.
[16] K.B. Oldham and J. Spanier, *The Fractional Calculus*, (Academic Press, New York, 1974).
[17] F. Oosawa, *Polyelectrolytes*, (Marcel Dekker, New York, 1971), Chap. 5.
[18] I.M. Sokolov, J. Klafter and A. Blumen, *Physics Today* **48** (November 2002).
[19] P. Debye, *Polar Molecules*, (Chemical Catalog, New York, 1929).

Journal of Computational Methods in Sciences and Engineering 10 (2010) 189–204
DOI 10.3233/JCM-2010-0319
IOS Press

Isophlorin derivatives: Structures and materials for n-Channel Organic Semiconductors

A.K. Jissy and Ayan Datta*
School of Chemistry, Indian Institute of Science Education and Research Thiruvananthapuram, CET Campus, Thiruvananthapuram – 695016, Kerala, India

Abstract. DFT and NMR calculations performed on isophlorin (**1**) and their derivatives (**2–10**) show that the 4O and the *trans* 2O, 2S derivatives (**2** and **5**) are anti-aromatic. The presence of strong S. . . S p_π-p_π bonding interactions stabilizes the planar structure (**5**) compared to the non-planar cis-isomer (**8**). Isophlorins are predicted to have very low electron reorganization energies ($\lambda_{electron} \sim 0.10$ eV) which remain unaffected by puckering through steric interactions or solvation in aqueous media. We predict isophlorins to be the ideal candidates for n-Channel organic conductors.

Porphyrins and their structurally similar analogues are probably the most well-studied molecules in bio-inorganic chemistry [1,2]. Apart from their interest in bio-mimetic studies and redox processes in biological systems, porphyrin derivatives have many interesting applications in solar-energy harvesting devices, material chemistry and solid – state organic electronics [3–5]. Isophlorins are the latest addition to the increasing list of porphyrin derivatives [6]. Isophlorins have been predicted by Woodward to be the key intermediate in the bio-synthesis of chlorophylls [7]. The difficulty in synthesis of isophlorins can be understood on the basis of favorable structural rearrangement of the antiaromatic 20π electron system (amine), into an aromatic 18π electron system (imine). However, the propensity for such an isomerism is overcomed in synthesis by substituting the X = –NH groups by –O or –S.[6] Thus, the only existing synthesized planar isophlorins are the core modified ones with X = –O and –S. A mechanistic understanding of the trade-off between planarity/stability/substitution is yet to arrive in these interesting set of molecules. In this communication, we have studied the role of substitutions in X = NH, O, S and Se towards the planarity, conformation and anti-aromatic behavior. Based on the calculations for reorganization energies for hole and electron transport (λ_{hole} and $\lambda_{electron}$), isophlorins are predicted to be excellent candidates for n-channel organic conductors quite independent of their planarity although in aqueous medium, even the planar molecules are predicted to pucker.

Our calculations were performed using the B3LYP exchange-correlation functional of DFT, which is comprised of Becke's hybrid, three-parameter, functional and the correlation functional of Lee, Yang, and Parr [8].

The 6-31G(d) basis set was employed [9,10]. All the geometries were subjected to frequency calculations for removal of vibrational instabilities. The ring-currents are calculated using the Gauge –

*Corresponding author. E-mail: ayan@iisertvm.ac.in.

Independent Atomic Orbitals (GIAO), nucleus independent chemical shift (NICS) method [11]. The reorganization energies, λ are calculated as λ_{hole} [$\lambda_{electron}$] = Ionization Energy (vertical) – Ionization Energy (adiabatic) [|Electron Affinity (vertical) – Electron Affinity (adiabatic)|]. Effects of hydration on the planar isophlorins is studied by enclosing the molecules in periodic cubic box filled with TIP3P water molecules [12] with a minimum distance of 2.3 Å between the solute and the solvent. After removal of the 'bad' van – der – Waals contact pairs between the water molecules at the edges of the periodic cubes, dimensions of the boxes were fixed at $20.68 \times 20.68 \times 20.68$ Å^3 (with 293 H_2O) and $21.65 \times 21.65 \times 21.65$ Å^3 (with 336 H_2O) for 4O-isophlorin (**2**) and *trans*, 2O, 2S-isophlorin (**5**) respectively. The mixtures were subject to simulated annealing at 600 K for 10 ps using the CHARMM potentials [13] followed by an additional 30 ps simulation for equilibration at 300 K.

Scheme 1 shows the molecules for which geometry optimizations were performed. All but **2** and **5** were found to be non-planar. Crystal structures for F-phenyl-isophlorins of **2** and **5** are in harmony with the planarity of the four heterocyclic rings.[6] The origin for non-planarity of all other systems is traced to the small cavity size in isophlorins that leads to puckering due to small van der Waals contact distances between X, X or X, Y (see Supp. Info. File for structures). The sensitivity of planarity to the cavity size can be understood by the fact that while the *trans*-isomer of the 2O, 2S-compound, **5** is planar, the *cis*-isomer, **8** is not. Substituting O/S by Se/NH leads to puckering in the core. For all the X, Y systems, the *trans* isomers are more stable than the *cis*-isomers to minimize the dipolar repulsions with the exception of X = S and Y = Se (**7** and **10**). Se being less electronegative allows stabilization of **10** in comparison to **7** (by 1.0 kcal/mol) through Se . . . Se weak van der Waals attraction that overwhelms the weaker dipolar repulsion.

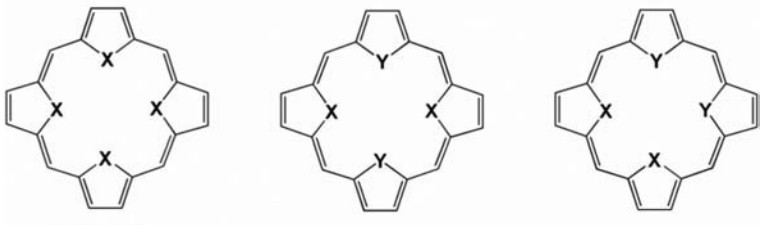

Scheme 1.

Based on structural planarity and formal 20π electrons count, **2** and **5** are expected to be anti-aromatic. Assignment of anti-aromaticity for these molecules is also justified from the strong bond-length alteration (BLA, Δr) in the C-C bonds along the perimeter of the macrocycles [$\Delta r = 0.07$ Å (expt. $\Delta r = 0.10$)[6] and 0.08 Å (expt. $\Delta r = 0.08$)[6]] for **2** and **5** respectively). For a quantitative estimation of aromaticity, NICS have been calculated for these two molecules along the perpendicular path of the center-of-mass of the rings Fig. 1(A). The high and positive value of NICS confirms anti-aromaticity for these rings. Interestingly, for all $\perp^r$ distances from the center-of-mass, **2** is more anti-aromatic than **5**. This is understood on the basis of the small *trans* S. . . S contact distance = 3.13 Å (expt. S. . . S = 3.10 Å) that facilitates cross-conjugation along the ring. Figure 1 (B) (HOMO-3) clearly shows the extended p_π-p_π interactions between the trans S atoms in **5** that is absent in **2**. Such π-conjugation explains the unusually large stabilization in **5** over **8** (19.1 kcal/mol) [14].

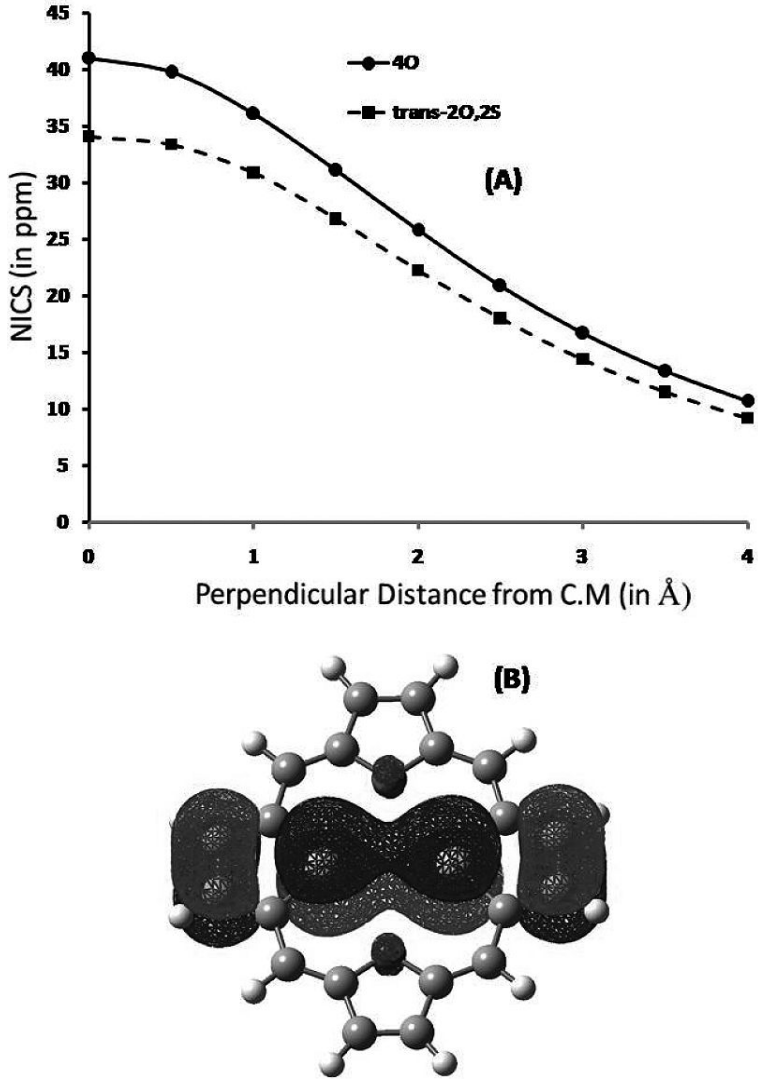

Fig. 1. (A) Profile for variation in NICS (in ppm) with increasing perpendicular distance (in Å) from the center-of-mass (C. M) for **2** and **5**. (B) Orbital showing $p\pi_\pi$-$p\pi_\pi$ interactions between the trans S-atoms in **5**.

Motivated by the fact that porphyrin derivates are nature's own optoelectronic materials, we calculated the electron and hole reorganization energies for these molecules. In Table 1, we report the computed magnitudes for $\lambda_{electron}$ and λ_{hole}. $\lambda_{electron}$ are smaller than λ_{hole} for all the systems due the presence of four highly electronegative atoms that stabilize the electron-rich molecules. $\lambda_{electron}$ for most of these molecules are even lower than the smallest reorganization values reported till now in organic electronics for CN-substituted penta-azapentacenes ($\sim$0.13 eV) [15].

An interesting observation from the computed $\lambda_{electron}$ and λ_{hole} is that the reorganization energies are not dependent on the planarity and thus anti-aromaticity of the isophlorins. This is important because in aqueous media, even **2** and **5** undergo puckering to accommodate the water molecules near the surface (Fig. 2).

Table 1
Hole (λ_{hole}) and electron ($\lambda_{electron}$) reorganization energies (in eV)

Molecule	λ_{hole}	$\lambda_{electron}$
1	0.12	0.10
2	0.11	0.09
3	0.20	0.10
4	0.24	0.03
5	0.11	0.08
6	0.13	0.09
7	0.24	0.23
8	0.16	0.09
9	0.14	0.10
10	0.22	0.21

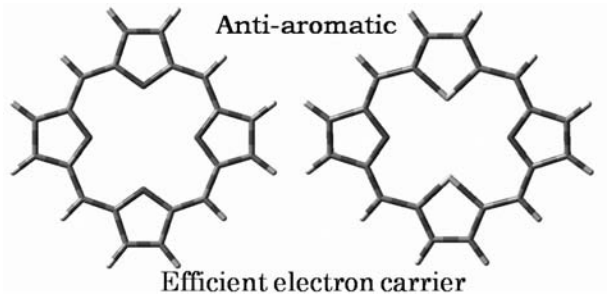

Scheme 2.

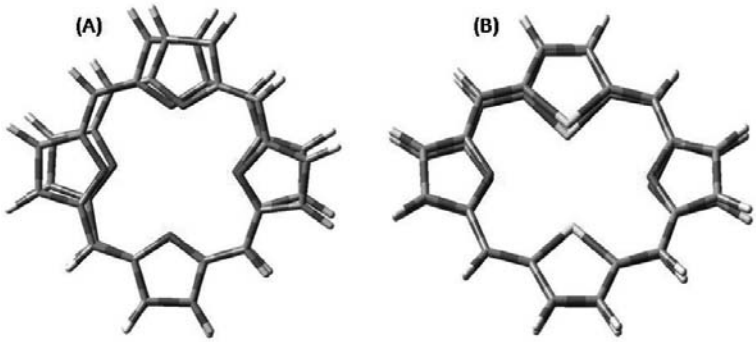

Fig. 2. Comparison of the gas-phase optimized planar structures (back) and their non-planar structures in aqueous medium (front) for (A) = **2** and (B) = **5**.

The average distortions in the four O plane and 2S+2O plane are 5.5 and 5.3 degrees for **2** and **5** respectively. However, such distortions are much smaller than that for any of the other distorted gas-phase structures, thereby suggesting solvation is not predicted to adversely affect the low reorganization energies.

Small $\lambda_{electron}$ is only one molecular property that increases the electron mobility ($\mu_{electron}$). In a molecular solid, $\mu_{electron}$ is also dependent on the transfer integral ($H_{m,n}$) between two pairs (m and n) [16] which within a good-approximation (coherent hopping model) is restricted between nearest neighbor-pairs [17]. Thus, small intermolecular distances (< 4 Å) created as a result of supramolecular

forces like C-H ... π and C-H ... X (X = F) favor large $\mu_{electron}$. Indeed, the crystal structure for the experimental analogues for isophorin derivatives show distinct patterns of such forces in their various modes of aggregations [6].

In summary, we have shown that isophlorin derivatives show an interesting diversity in their structures and anti-aromaticity is established unequivocally for **2** and **5**. We are encouraged by the very low reorganization energies for electron transport in these molecules (with very little effects of the aqueous medium) along-with the short inter-molecular contact distances in their molecular solids. Therefore, our calculations predict very large electron mobilities in crystals of isophlorins. We look forward to an experimental test to our computational predictions.

Acknowledgement

AD thanks DST-Fast Track scheme for young scientist for financial support. JAK thanks UGC – JRF for fellowship.

Supporting Information Available

Optimized B3LYP/6-31G(d) geometries, energies, harmonic frequencies for **1-10** and complete list of authors for ref 10.

References

[1] (a) K.M. Kadish, *The Porphyrin Handbook*, Academic Press (1999). (b) *The Colours of Life: An Introduction to the Chemistry of Porphyrins and Related Compounds*, L.R. Milgrom, Oxford univ. press (1997).
[2] J.L. Sessler and S.J. Weghorn, Pergamon *Expanded, Contracted and Isomeric Porphyrins*, (1997).
[3] D. Kim and A. Osuka, *Acc Chem Res* **37** (2004), 735.
[4] T.K. Chandrashekar and S. Venkatraman, *Acc Chem Res* **36** (2003), 676.
[5] J.M. Lim, Z.S. Yoon, J.-Y. Shin, K.S. Kim, M.-C. Yoon and D. Kim, *ChemComm* (2009), 261 and references therein.
[6] J.S. Reddy and V.G. Anand, *J Am Chem Soc* **130 2008**, 3718.
[7] R.B. Woodward, *Angew Chem* **72** (1960), 651.
[8] (a) A.D. Becke, *J Chem Phys* **98** (1993), 5648. (b) C. Lee, W. Yang and R.G. Parr, *Phys Rev B* **37** (1988), 78.
[9] P.C. Hariharan and J.A. Pople, *Theor Chim Acta* **28 1973**, 213.
[10] M.J. Frisch, G.W. Trucks, H.B. Schlegel, G.E. Scuseria, M.A. Robb, J.R. Cheeseman, J.A. Montgomery, Jr., T. Vreven, K.N. Kudin, J.C. Burant, J.M. Millam, S.S. Iyengar, J. Tomasi, V. Barone, B. Mennucci, M. Cossi, G. Scalmani, N. Rega, G.A. Petersson, H. Nakatsuji, M. Hada, M. Ehara, K. Toyota, R. Fukuda, J. Hasegawa, M. Ishida, T. Nakajima, Y. Honda, O. Kitao, H. Nakai, M. Klene, X. Li, J. E. Knox, H. P. Hratchian, J.B. Cross, C. Adamo, J. Jaramillo, R. Gomperts, R.E. Stratmann, O. Yazyev, A. J. Austin, R. Cammi, C. Pomelli, J.W. Ochterski, P.Y. Ayala, K. Morokuma, G.A. Voth, P. Salvador, J.J. Dannenberg, V.G. Zakrzewski, S. Dapprich, A.D. Daniels, M.C. Strain, O. Farkas, D.K. Malick, A.D. Rabuck, K. Raghavachari, J.B. Foresman, J.V. Ortiz, Q. Cui, A.G. Baboul, S. Clifford, J. Cioslowski, B.B. Stefanov, G. Liu, A. Liashenko, P. Piskorz, I. Komaromi, R.L. Martin, D.J. Fox, T. Keith, M.A. Al-Laham, C.Y. Peng, A. Nanayakkara, M. Challacombe, P.M.W. Gill, B. Johnson, W. Chen, M.W. Wong, C. Gonzalez and J.A. Pople, Gaussian, Inc., Wallingford CT, 2004., *Gaussian 03*, revision D.02; Gaussian, Inc.: Wallingford, CT, 2004.
[11] P.v.R. Schleyer, C. Maerker, A. Dransfeld, H. Jiao and N.J.R.v. Eikema-Hommas, *J Am Chem Soc* **118** (1996), 6317.
[12] W.L. Jorgensen, J. Chandrasekhar, J.D. Madura, R.W. Impey and M.L. Klein, *J Chem Phys* **79 1983**, 926.
[13] B.R. Brooks, R.E. Bruccoleri, B.D. Olafson, D.J. States, S. Swaminathan and M. Karplus, *J Comput Chem* **4** (1983), 187.
[14] While steric interactions also stabilize the *trans* over the *cis* form, such a large stabilization is prime-facie evidence for S ... S bonding interactions.
[15] M. Winkler and K.N. Houk, *J Am Chem Soc* **129** (2007), 1805.
[16] (a) J.L. Bredas, J.P. Calbert, D.A. da Silva Filho and J. Cornil, *PNAS* **99** (2002), 5804. (b) R.A. Marcus, *Rev Mod Phys* **65** (1993), 599.

[17] (a) W.-Q. Deng and W.A. Goddard III, *J Phys Chem B* **108** (2004), 8614. (b) A. Datta, S. Mohakud and S.K. Pati, *J Chem Phys* **126** (2007), 144710.

Supplementary Data

Isophlorin Derivatives: Structures and materials for n-Channel Organic Semiconductors

Available Information:

1. Molecular Structures with van-der-Waals contact distances (in Å) between X. . . X and X. . . Y (X, Y = NH, O, S, Se).
2. Ground State Optimized Geometries.
3. Harmonic Frequencies.
4. Solvated structures for **2** and **5**.
5. Complete list of authors for reference for 10.

1. X = NH

Atomic Number	Coordinates (Angstroms) X	Y	Z
6	−2.892377	1.156495	−0.177880
6	−4.230148	0.678648	−0.465527
6	−4.230148	−0.678496	−0.465723
6	−2.892398	−1.156396	−0.178052
1	−5.069658	1.333112	−0.664237
1	−5.069646	−1.332919	−0.664621
6	−2.480140	2.446832	−0.036244
6	−0.706514	4.197501	0.548107
6	1.140204	2.929231	0.169487
6	0.706735	4.197449	0.548129
1	−1.356066	5.021472	0.812507
1	1.356339	5.021382	0.812531
1	−3.250349	3.210957	−0.078230
6	2.480265	2.446767	−0.036510
1	3.250496	3.210861	−0.078654
6	4.230148	0.678496	−0.465723
6	4.230148	−0.678648	−0.465527
1	5.069646	1.332919	−0.664621
6	2.892377	−1.156495	−0.177880
1	5.069658	−1.333112	−0.664237
6	2.480140	−2.446832	−0.036244
1	3.250349	−3.210957	−0.078230
6	0.706514	−4.197501	0.548107
6	−0.706735	−4.197449	0.548129
1	1.356066	−5.021472	0.812507
6	−1.140204	−2.929231	0.169487
1	−1.356339	−5.021382	0.812531
6	1.140037	−2.929248	0.169608
6	2.892398	1.156396	−0.178052
6	−1.140037	2.929248	0.169608
6	−2.480265	−2.446767	−0.036510
1	−3.250496	−3.210861	−0.078654
7	0.000062	2.152864	−0.014774
7	2.069376	−0.000016	−0.080438
7	−0.000062	−2.152864	−0.014774
7	−2.069376	0.000016	−0.080438
1	−1.384279	−0.000050	0.668779
1	−0.000028	1.323326	−0.593963
1	1.384279	0.000050	0.668779
1	0.000028	−1.323326	−0.593963

E[RB3LYP/6-31G(d)] = −1070.14631560 Hartree;
Low frequencies (cm^{-1}): 38.8236 62.0772 93.7052 98.3879 101.8871 122.5752 138.3143 163.8924 173.6048 205.7350 277.1711 284.4113.

2. X = O

Atomic Number	Coordinates (Angstroms) X	Y	Z
6	0.000000	1.104575	2.934760
6	0.000000	0.707653	4.257132
6	0.000000	−0.707653	4.257132
6	0.000000	−1.104575	2.934760
1	0.000000	1.367658	5.113716
1	0.000000	−1.367658	5.113716
6	0.000000	2.430332	2.397205
6	0.000000	4.259801	0.676690
6	0.000000	2.883628	−1.117802
6	0.000000	4.259801	−0.676690
1	0.000000	5.110794	1.345103
1	0.000000	5.110794	−1.345103
1	0.000000	3.207916	3.155434
6	0.000000	2.430332	−2.397205
1	0.000000	3.207916	−3.155434
6	0.000000	0.707653	−4.257132
6	0.000000	−0.707653	−4.257132
1	0.000000	1.367658	−5.113716
6	0.000000	−1.104575	−2.934760
1	0.000000	−1.367658	−5.113716
6	0.000000	−2.430332	−2.397205
1	0.000000	−3.207916	−3.155434
6	0.000000	−4.259801	−0.676690
6	0.000000	−4.259801	0.676690
1	0.000000	−5.110794	−1.345103
6	0.000000	−2.883628	1.117802
1	0.000000	−5.110794	1.345103
6	0.000000	−2.883628	−1.117802
6	0.000000	1.104575	−2.934760
6	0.000000	2.883628	1.117802
6	0.000000	−2.430332	2.397205
1	0.000000	−3.207916	3.155434
8	0.000000	0.000000	2.123663
8	0.000000	−2.070228	0.000000
8	0.000000	0.000000	−2.123663
8	0.000000	2.070228	0.000000

E[RB3LYP/6-31G(d)] = −990.717530355 Hartree
Low frequencies (cm^{-1}): 51.2833 63.7874 92.2803 102.8785 122.0459 135.4876 146.4029 188.7732 193.1475 210.9916 285.1215 287.2806.

3. X = S

Atomic Number	Coordinates (Angstroms) X	Y	Z
6	−2.193862	−1.909171	1.719981
6	−2.192791	−1.910514	3.104755
6	−0.894272	−1.910205	3.682567
6	0.135020	−1.902664	2.750273
1	−3.101997	−1.818528	3.690452
1	−0.718895	−1.807635	4.748780
6	−3.270816	−1.678546	0.753861
6	−4.093156	−0.556919	−1.382734
6	−2.317450	0.857410	−2.082224
6	−3.649072	0.324302	−2.318371
1	−5.039861	−1.084329	−1.449453
1	−4.207933	0.589632	−3.210900
1	−4.213253	−2.206487	0.893042
6	−1.538162	1.579802	−2.945837
1	−1.961357	1.817255	−3.920754
6	0.894272	1.910205	−3.682567
6	2.192791	1.910514	−3.104755
1	0.718895	1.807635	−4.748780
6	2.193862	1.909171	−1.719981
1	3.101997	1.818528	−3.690452
6	3.270816	1.678546	−0.753861
1	4.213253	2.206487	−0.893042
6	4.093156	0.556919	1.382734
6	3.649072	−0.324302	2.318371
1	5.039861	1.084329	1.449453
6	2.317450	−0.857410	2.082224
1	4.207933	−0.589632	3.210900
6	3.164862	0.809925	0.294522
6	−0.135020	1.902664	−2.750273
6	−3.164862	−0.809925	−0.294522
6	1.538162	−1.579802	2.945837
1	1.961357	−1.817255	3.920754
16	−1.747997	0.255559	−0.509343
16	−0.545507	−2.065386	1.148466
16	1.747997	−0.255559	0.509343
16	0.545507	2.065386	−1.148466

E[RB3LYP/6-31G(d)] = −2361.99976696 Hartree
Low frequencies (cm^{-1}): 33.0320 40.9690 45.4770 71.2046 86.9553 101.1001 115.0773 141.0576 170.2404 210.6821 236.1583 242.1607.

4. X = Se

Atomic Number	Coordinates (Angstroms) X	Y	Z
6	0.225281	−3.126511	1.324961
6	1.247195	−3.813891	0.714842
6	1.247195	−3.813891	−0.714842
6	0.225281	−3.126511	−1.324961
1	2.076800	−4.224529	1.283830
1	2.076800	−4.224529	−1.283830
6	0.115263	−2.660670	2.712498
6	0.000000	−0.680415	4.307287
6	−0.016221	1.336838	3.011592
6	0.000000	0.680415	4.307287
1	0.001028	−1.267810	5.221994
1	−0.001028	1.267810	5.221994
1	0.217037	−3.381063	3.524133
6	−0.115263	2.660670	2.712498
1	−0.217037	3.381063	3.524133
6	−1.247195	3.813891	0.714842
6	−1.247195	3.813891	−0.714842
1	−2.076800	4.224529	1.283830
6	−0.225281	3.126511	−1.324961
1	−2.076800	4.224529	−1.283830
6	−0.115263	2.660670	−2.712498
1	−0.217037	3.381063	−3.524133
6	0.000000	0.680415	−4.307287
6	0.000000	−0.680415	−4.307287
1	−0.001028	1.267810	−5.221994
6	0.016221	−1.336838	−3.011592
1	0.001028	−1.267810	−5.221994
6	−0.016221	1.336838	−3.011592
6	−0.225281	3.126511	1.324961
6	0.016221	−1.336838	3.011592
6	0.115263	−2.660670	−2.712498
1	0.217037	−3.381063	−3.524133
34	0.000000	0.000000	1.643723
34	1.003460	2.546504	0.000000
34	0.000000	0.000000	−1.643723
34	−1.003460	−2.546504	0.000000

E[RB3LYP/6-31G(d)] = −10366.7820549 Hartree
Low frequencies (cm^{-1}): 9.2821 27.4630 43.4013 65.6960 77.6021 90.6019 98.0452 103.8485 140.4183 165.7495 167.5601 176.2506

5. X = O; Y = S

Atomic Number	Coordinates (Angstroms) X	Y	Z
6	0.000000	2.765728	1.264969
6	0.000000	4.039234	0.708265
6	0.000000	4.039234	−0.708265
6	0.000000	2.765728	−1.264969
1	0.000000	4.942916	1.309981
1	0.000000	4.942916	−1.309981
6	0.000000	2.389365	2.658085
6	0.000000	0.679307	4.554541
6	0.000000	−1.132180	3.184164
6	0.000000	−0.679307	4.554541
1	0.000000	1.338951	5.412375
1	0.000000	−1.338951	5.412375
1	0.000000	3.204225	3.377374
6	0.000000	−2.389365	2.658085
1	0.000000	−3.204225	3.377374
6	0.000000	−4.039234	0.708265
6	0.000000	−4.039234	−0.708265
1	0.000000	−4.942916	1.309981
6	0.000000	−2.765728	−1.264969
1	0.000000	−4.942916	−1.309981
6	0.000000	−2.389365	−2.658085
1	0.000000	−3.204225	−3.377374
6	0.000000	−0.679307	−4.554541
6	0.000000	0.679307	−4.554541
1	0.000000	−1.338951	−5.412375
6	0.000000	1.132180	−3.184164
1	0.000000	1.338951	−5.412375
6	0.000000	−1.132180	−3.184164
6	0.000000	−2.765728	1.264969
6	0.000000	1.132180	3.184164
6	0.000000	2.389365	−2.658085
1	0.000000	3.204225	−3.377374
8	0.000000	0.000000	−2.379590
8	0.000000	0.000000	2.379590
16	0.000000	1.566376	0.000000
16	0.000000	−1.566376	0.000000

E[RB3LYP/6-31G(d)] = −1716.09677468 Hartree
Low frequencies (cm^{-1}): 36.6753 52.0769 61.4629 81.2450 115.3463 120.5890 141.5636 163.8766 179.8199 189.2034 260.4585 274.5759

6. X = O; Y = Se

Atomic Number	Coordinates (Angstroms) X	Y	Z
6	−1.075511	−0.080508	3.256858
6	−0.675727	−0.059319	4.577908
6	0.742702	0.000000	4.589334
6	1.160316	0.000000	3.272751
1	−1.334034	−0.085411	5.435617
1	1.388269	0.034359	5.456304
6	−2.366513	−0.233863	2.634388
6	−3.910224	−0.547235	0.678600
6	−2.704964	−0.052414	−1.326169
6	−3.910224	−0.547235	−0.678600
1	−4.710318	−0.982085	1.271530
1	−4.710318	−0.982085	−1.271530
1	−3.142015	−0.612632	3.298730
6	−2.366513	−0.233863	−2.634388
1	−3.142015	−0.612632	−3.298730
6	−0.675727	−0.059319	−4.577908
6	0.742702	0.000000	−4.589334
1	−1.334034	−0.085411	−5.435617
6	1.160316	0.000000	−3.272751
1	1.388269	0.034359	−5.456304
6	2.459927	0.055364	−2.659290
1	3.287327	0.224475	−3.345566
6	4.020894	0.147246	−0.679868
6	4.020894	0.147246	0.679868
1	4.911693	0.340272	−1.271731
6	2.738390	−0.058982	1.327983
1	4.911693	0.340272	1.271731
6	2.738390	−0.058982	−1.327983
6	−1.075511	−0.080508	−3.256858
6	−2.704964	−0.052414	1.326169
6	2.459927	0.055364	2.659290
1	3.287327	0.224475	3.345566
34	−1.603301	0.763922	0.000000
34	1.419469	−0.395207	0.000000
8	0.048560	−0.035838	−2.464105
8	0.048560	−0.035838	2.464105

E[RB3LYP/6-31G(d)] = −5718.47740059 Hartree
Low frequencies (cm^{-1}): 25.3849 46.3145 80.2679 81.9983 82.1725 97.8985 117.9848 136.1300 169.9151 210.4992 213.1755 226.4770

7. X = S; Y = Se

Atomic Number	Coordinates (Angstroms) X	Y	Z
6	1.439656	3.083439	−0.078136
6	2.533109	3.326944	0.739369
6	3.514796	2.297298	0.711350
6	3.206955	1.246170	−0.130348
1	2.571077	4.163009	1.430538
1	4.378069	2.284395	1.369129
6	0.120750	3.693512	−0.016959
6	−2.387851	3.525456	0.210128
6	−3.035221	1.222740	0.100987
6	−3.389065	2.612491	0.331451
1	−2.533146	4.583543	0.413002
1	−4.394200	2.880711	0.645825
1	0.082107	4.736988	0.295413
6	−3.788096	0.098635	0.258044
1	−4.851306	0.201907	0.474474
6	−3.532397	−2.312386	−0.691625
6	−2.549904	−3.340566	−0.718858
1	−4.404406	−2.309897	−1.337918
6	−1.444308	−3.083210	0.079063
1	−2.596209	−4.186188	−1.397806
6	−0.124586	−3.686355	0.004231
1	−0.085696	−4.725051	−0.323817
6	2.380125	−3.521212	−0.241508
6	3.383642	−2.611154	−0.362742
1	2.517859	−4.576761	−0.462123
6	3.037078	−1.223145	−0.110541
1	4.383119	−2.878451	−0.695252
6	1.062245	−3.016811	0.108050
6	−3.212441	−1.246673	0.128174
6	−1.064348	3.021551	−0.117668
6	3.785388	−0.098001	−0.275709
1	4.842390	−0.198347	−0.522012
34	−1.203115	1.147891	−0.469948
34	1.215002	−1.150398	0.492731
16	−1.736963	−1.626668	1.005215
16	1.741526	1.637733	−1.019252

E[RB3LYP/6-31G(d)] = −6364.389317 Hartree
Low frequencies (cm^{-1}): 23.1652 38.7046 45.5006 74.9887 82.3959 104.5919 111.1692 119.2187 163.6189 200.7413 201.1848 205.5668

8. X = O; Y = S

Atomic Number	Coordinates (Angstroms) X	Y	Z
6	−3.195997	−0.345156	−0.019551
6	−3.803512	−1.351847	−0.749747
6	−3.107903	−2.592114	−0.689647
6	−1.965843	−2.552955	0.088310
1	−4.665292	−1.179977	−1.386598
1	−3.385356	−3.459526	−1.280273
6	−3.456268	1.081642	−0.002981
6	−2.736620	3.503573	0.017406
6	−0.506811	3.078241	0.022917
6	−1.523597	4.105260	0.018844
1	−3.712325	3.971102	0.007656
1	−1.309718	5.166163	0.003862
1	−4.488317	1.410636	−0.095590
6	0.840034	3.297891	−0.013140
1	1.084695	4.357306	−0.016881
6	3.342938	2.916051	−0.060360
6	4.155603	1.760946	−0.099820
1	3.670892	3.946484	−0.036036
6	3.305573	0.669914	−0.113873
1	5.236019	1.718157	−0.109327
6	3.564652	−0.740452	−0.109824
1	4.615517	−1.017848	−0.089538
6	2.818546	−3.166627	0.013988
6	1.669268	−3.886333	0.111856
1	3.812755	−3.603381	0.026290
6	0.454061	−3.091708	0.078914
1	1.635198	−4.966297	0.217279
6	2.624956	−1.732001	−0.091636
6	2.023430	2.492649	−0.052261
6	−2.525130	2.074830	0.028145
6	−0.845837	−3.493598	0.155629
1	−1.064009	−4.559412	0.195629
8	−1.148972	1.852402	0.044683
16	−1.840696	−0.985037	0.860837
8	2.003646	1.123597	−0.090570
16	0.899651	−1.375002	−0.127610

E[RB3LYP/6-31G(d)] = −1716.07355928 Hartree
Low frequencies (cm^{-1}): 33.9485 44.6348 67.1405 77.2005 102.4403 121.5092 133.0060 142.9845 176.8948 211.4966 257.4308 260.9271

9. X = O; Y = Se

Atomic Number	Coordinates (Angstroms) X	Y	Z
6	−0.772401	−2.803813	−0.099025
6	−0.046200	−3.969381	−0.275777
6	1.366948	−3.823673	−0.319870
6	1.829289	−2.521043	−0.211157
1	−0.529855	−4.936069	−0.393373
1	2.036949	−4.672576	−0.429821
6	−2.198088	−2.589905	−0.241468
6	−4.013806	−0.891186	−0.687654
6	−2.889341	1.177853	−0.280689
6	−4.023050	0.456496	−0.855213
1	−4.721788	−1.553843	−1.178371
1	−4.746411	0.972842	−1.480485
1	−2.757128	−3.376971	−0.751230
6	−2.420407	2.401623	−0.624793
1	−3.059197	3.018930	−1.256550
6	−0.780578	4.335668	−0.342883
6	0.615645	4.396081	−0.132134
1	−1.460657	5.164275	−0.486039
6	1.068301	3.094124	−0.020660
1	1.236090	5.280854	−0.088807
6	2.440704	2.687870	0.102018
1	3.098653	3.549039	0.187124
6	4.547504	1.297973	0.089385
6	4.785906	−0.036096	−0.023850
1	5.276133	2.094095	0.169438
6	3.517775	−0.710082	−0.101350
1	5.744708	−0.536675	−0.050114
6	3.118484	1.506120	0.066084
6	−1.135535	3.005253	−0.332635
6	−2.850991	−1.423289	0.012712
6	3.176001	−2.028209	−0.200692
1	3.988886	−2.746840	−0.269181
34	−2.054829	0.037327	0.993189
8	−0.002963	2.235660	−0.125145
8	2.529788	0.264523	−0.040969
34	0.397831	−1.320645	0.013700

E[RB3LYP/6-31G(d)] = −5718.45268244 Hartree
Low frequencies (cm^{-1}): 41.8541 48.2129 68.9185 75.6031 97.1331 115.8761 122.8442 135.3420 170.9553 193.6990 205.5085 227.4534

10. X = O; Y = Se

Atomic Number	Coordinates (Angstroms) X	Y	Z
6	3.135167	−0.507198	−0.098214
6	3.595364	0.211828	−1.172570
6	3.235900	1.594938	−1.214124
6	2.443130	2.048197	−0.185618
1	4.127441	−0.265159	−1.990936
1	3.478600	2.223902	−2.066037
6	3.046181	−1.966768	0.108919
6	1.428522	−3.947115	0.272071
6	−0.783820	−3.080314	−0.102345
6	0.093384	−4.198473	0.201277
1	2.156862	−4.700750	0.558613
1	−0.329729	−5.175421	0.422257
1	3.935559	−2.545765	0.356326
6	−2.146962	−3.061326	0.027371
1	−2.630774	−3.984888	0.345223
6	−4.122524	−1.575359	0.709897
6	−4.451308	−0.196216	0.711443
1	−4.636721	−2.308385	1.323419
6	−3.576720	0.595121	−0.022782
1	−5.245938	0.223194	1.320471
6	−3.395973	2.035595	−0.047563
1	−4.286412	2.657910	0.030786
6	−1.914815	4.092609	−0.073839
6	−0.599919	4.437578	−0.039579
1	−2.727027	4.812253	−0.117997
6	0.321631	3.315654	−0.015975
1	−0.241035	5.462215	−0.047470
6	−2.179720	2.665714	−0.064266
6	−2.983569	−1.882688	−0.027675
6	1.838568	−2.579147	0.011059
6	1.681226	3.300327	−0.105349
1	2.208476	4.246505	−0.219351
34	0.299685	−1.549344	−0.480235
16	−2.449819	−0.445280	−0.867753
34	2.210278	0.660722	1.077323
16	−0.620839	1.804644	0.027183

E[RB3LYP/6-31G(d)] = −6364.39099041 Hartree
Low frequencies (cm^{-1}): 30.6762 40.9430 44.0453 68.0845 78.5991 96.3687 107.8472 116.7636 150.6931 180.9952 208.6299 211.8604

Journal of Computational Methods in Sciences and Engineering 10 (2010) 205–212
DOI 10.3233/JCM-2010-0335
IOS Press

Enhanced first hyperpolarizability of donor-acceptor diethynylsilane oligomers

R.A. Brennand and A.E. de A. Machado*
Universidade Federal de Pernambuco, Departamento de Química Fundamental, 50670-901, Recife, Pernambuco, Brazil

Abstract. The modelling of the diethynylsilane derivatives reveals large magnitudes of the first hyperpolarizability (β). The electron donor (D) and acceptor (A) groups are attached at both ends of the oligomers that containing up to ten heterocyclic rings. Several D/A pairs with different strengths were tested in this investigation. The magnitude of static and dynamic β was computed using the AM1/TDHF methodology. The presence of the alkyl donor groups containing heteroatom in the oligomers investigated contributes most for the largest values of the β hyperpolarizability observed. The effect of the oligomer chain length on the β magnitude is also investigated. The results demonstrate that the diethynylsilane derivatives are promising as second-order nonlinear optical materials.

Keywords: β Hyperpolarizabilty, AM1/TDHF methodology, diethynylsilane oligomers

1. Introduction

Organic polymers and oligomers have been investigated for the improvement of the nonlinear coefficients in order to allow for applications in optoelectronic and photonic [1–4]. Oligomers present solubility and easier processability, not exhibited by the polymer itself, which make these compounds interesting for the devices manufacture. Polydiethynylsilane (PDES) is a conjugated polymer that displays large third-order optical susceptibility with exceptionally fast optical response. Wong et al. [5] showed that this material is a promising candidate for nonlinear optical devices in the sub-THz frequency range.

Experimental and theoretical studies demonstrated that PDES polymer has a four-membered backbone Si-ring structure, which presents two isomeric forms (PDES(I) and PDES(II)) that are almost degenerate in energy (Fig. 1) [6,7]. An earlier study indicated that the electrical and optical properties of PDES must be due to π-electrons in their structure of carbon since that the silicon atoms are in sp^3-hybridized state [8]. Another study performed calculations with the finite-field (FF) method, at level of the Møller-Plesset second-order perturbation theory (MP2), and demonstrated that polydiethynylsilane with the substituents at the silicon atom of the heterocyclic ring has the largest values of the longitudinal second hyperpolarizability (γ) among other polymers [9].

The second-order nonlinearities require a non-centrosymmetric molecular material [1,2]. In addition, large magnitude values of the first hyperpolarizability (β) are needed for applications as the eletrooptic modulation and frequency doubling. The strategy of introducing donor (D) and/or acceptor (A) groups of electron as well as the increasing of oligomer chain size successfuly worked to improve the nonlinear

*Corresponding author. E-mail: aeam@netuno.qui.ufmg.br.

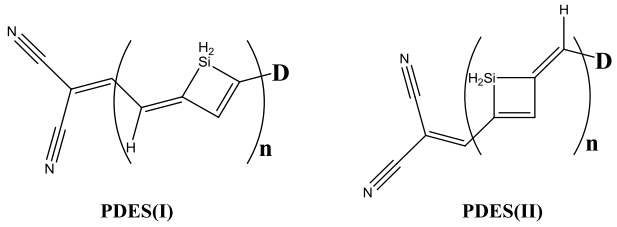

Fig. 1. Diethynylsilane oligomers structures investigated, where n show the values range from 1 to 10.

response β for thiophene [4] and aniline [10–12]. For the polyenic derivatives was found that large β values can also be obtained by using this approach [13]. Furthermore, the modelling of polyenic derivatives with efficient D/A pairs, having bridges with mesoionic rings and polyenic moieties, showed very large β values [14,15]. Also, earlier theoretical and experimental results for novel functionalized oligo-vinylthiophene molecules containing the silicon atom in the spacer display large β magnitudes in contrast with the observed to other spacers [16]. The silicon atom itself presents a large nonlinear coefficient [17,18]. These results demonstrated that the electronic asymmetry and length of conjugation, as well as the nature of the conjugation, is fundamental to optimize β for these classes of nonlinear materials. Hence, several donor-acceptor diethynylsilane oligomers containing up to ten Si-rings were modeled in the present work to test their use as second-order nonlinear optical material.

The methyl, ethyl, propyl, butyl donor groups and their equivalent alkoxides were selected to further increasing of the polarization in diethynylsilane oligomers. These groups contributed to large β and γ hyperpolarizabilities of the aniline disubstituted octamers [11,12]. The dicyanoethenyl group is the acceptor of the systems investigated. Hence, different D/A pairs were incorporated in the designed diethynylsilane oligomers. The nonlinear chromophores containing the dicyano group present large first and second hyperpolarizabilities according to theoretical and experimental studies [10–12,14,15,19–22]. The effect of chain length on the magnitude of the β hyperpolarizability was also investigated by studying donor-acceptor PDES oligomers containing up to ten Si-rings in the chain.

The magnitudes of the static and dynamic β hyperpolarizability were calculated with the variational time dependent Hartree-Fock (TDHF) approach [23]. The presence of the oxygen heteroatom in the alkoxides groups contributes significantly for the higher values obtained of β for both PDES(I) and PDES(II) structures. The best performance relative for the first hyperpolarizability was obtained for the donor-acceptor decamers of PDES(II), and the nonsaturation of the response was observed according with the AM1/TDHF calculations. The butoxi (D_8) and dicyanoethenyl (A) substituents groups contribute for the largest value of β (51,864.10^{-30} esu) obtained for the second harmonic generation (SHG) at 1060 nm. The large values of the β hyperpolarizability obtained in this work demonstrate that the donor-acceptor diethynylsilane oligomers can be used as active materials in second-order nonlinear optical media.

2. Methodology

The magnitudes of static and dynamic β hyperpolarizability for the second harmonic generation (SHG) were calculated using the time dependent Hartree-Fock (TDHF) approach [23] with the AM1 hamiltonian [24]. The calculations were performed using the MOPAC2000 computational code [25].

The donor-acceptor oligomeric systems investigated containing the methyl (D_1), methoxi (D_2), ethyl (D_3), ethoxi (D_4), propyl (D_5), propoxi (D_6), butyl (D_7) and butoxi (D_8) donor groups matched with the

Table 1
Calculated properties for the trimers and decamers of PDES(I)

system	$\beta_0(10^{-30}$esu)	$\beta_{1060}(10^{-30}$esu)	μ (D)	Δ_{H-L}(eV)	IP (eV)
trimer	6	13	1.79	7.37	8.17
D_1-Tri-A	47	193	4.58	6.83	8.41
D_2-Tri-A	60	262	4.58	6.63	8.20
D_3-Tri-A	62	340	4.78	6.69	8.33
D_{4-}Tri-A	95	701	5.20	6.42	8.04
D_5-Tri-A	61	314	4.74	6.71	8.34
D_6-Tri-A	98	751	5.32	6.40	8.04
D_7-Tri-A	70	432	4.89	6.61	8.25
D_8-Tri-A	96	698	5.26	6.42	8.04
decamer	13	268	8.75	6.94	7.81
D_1-Dec-A	50	168	4.04	6.12	7.78
D_2-Dec-A	65	286	3.58	6.06	7.72
D_3-Dec-A	51	178	4.05	6.12	7.78
D_4-Dec-A	69	312	3.29	6.05	7.70
D_{5-}Dec-A	51	180	4.06	6.13	7.79
D_6-Dec-A	70	326	3.28	6.03	7.70
D_7-Dec-A	52	190	4.06	6.14	7.80
D_8-Dec-A	71	327	3.25	6.02	7.70

β_0 is the static value, β_{1060} is the dynamic(SHG) value at 1060 nm, μ is the ground state dipole moment in Debye (D), Δ_{H-L} is the HOMO-LUMO energy gap in electronVolt (eV), Tri (Dec) is relative to the substituted trimer (decamer), where the donor groups are the methyl (D_1), ethyl (D_3), propyl (D_5), butyl (D_7) and their alkoxides equivalents (D_2, D_4, D_6, and D_8), respectively; A is the dicyanoethenyl group.

dicyanoethenyl as the electron acceptor (A) group. Several donor-acceptor derivatives were studied of both PDES(I) and PDES(II) isomeric forms containing up to ten Si-rings in the chain.

The correspondent experimental values must be superior for the theoretical ones computed with the AM1/TDHF methodology as reported in the literature, since that utilize a minimal basis, and the correlation effect as well as the role of solvent is not included in this semiempirical approach [1–3]. Vibrational effects can also be important for the nonlinear molecules investigated [2]. The semiempirical methodology has the advantage of requiring less computational time in contrast with more rigorous techniques as observed in the calculations of the nonlinear coefficients for large molecules carry out with the *ab initio* and DFT methods. Therefore, it may be assumed that the AM1/TDHF methodology is an useful instrument to indicate large systems belonging to a series of chemically related compounds having potential applications in nonlinear optics. The results of the second hyperpolarizability for the model trimers of neutral forms of polyaniline obtained using the AM1/TDHF methodology are in agreement with the experimental trends observed for the polymer [3]. For the β hyperpolarizability, the smallest value is estimated to the leucoemeraldine form, while the largest values are due to the pernigraniline and emeraldine, with fully oxidized and semioxidized structures, respectively.

3. Results and discussion

The selected AM1/TDHF results for the PDES trimers and decamers of the static and dynamic (SHG) β are shown in Tables 1–2. The ground state dipole moment (μ), the HOMO-LUMO energy gap (Δ_{H-L}) and the ionization potential (IP) also are reported.

The donor (D) and acceptor (A) groups of electron investigated are efficient to promoting the enhancement of the β magnitudes for PDES oligomers. In particular, the donor groups with the oxygen

Table 2
Calculated properties for the trimers and decamers of PDES(II)

system	$\beta_0(10^{-30}$esu)	$\beta_{1060}(10^{-30}$esu)	μ (D)	Δ_{H-L}(eV)	IP (eV)
trimer	2	2.2	1.10	7.36	8.06
D_1-Tri-A	57	470	8.67	6.79	8.30
D_2-Tri-A	69	614	8.40	6.73	8.22
D_3-Tri-A	58	475	8.66	6.80	8.30
D_4-Tri-A	78	731	10.86	6.70	8.13
D_5-Tri-A	58	484	8.70	6.80	8.30
D_6-Tri-A	80	742	10.90	6.70	8.13
D_7-Tri-A	59	488	8.71	6.80	8.30
D_8-Tri-A	81	749	10.93	6.70	8.13
decamer	51	3579	5.97	6.52	7.65
D_1-Dec-A	208	36030	14.47	6.26	7.75
D_2-Dec-A	237	48289	16.37	6.22	7.70
D_3-Dec-A	208	36268	14.46	6.26	7.75
D_4-Dec-A	243	51055	16.67	6.21	7.70
D_5-Dec-A	209	36663	14.49	6.26	7.75
D_6-Dec-A	244	51545	16.71	6.21	7.70
D_7-Dec-A	209	36836	14.50	6.26	7.75
D_8-Dec-A	245	51864	16.73	6.21	7.70

β_0 is the static value, β_{1060} is the dynamic (SHG) value at 1060 nm, μ is the ground state dipole moment in Debye (D), Δ_{H-L} is the HOMO-LUMO energy gap in electronVolt (eV), Tri (Dec) is relative to the substituted trimer (decamer), where the donor groups are the methyl (D_1), ethyl (D_3), propyl (D_5), butyl (D_7) and their alkoxides equivalents (D_2, D_4, D_6 and D_8), respectively; A is the dicyanoethenyl group.

heteroatom contribute for the higher values of β in contrast with the observed to the equivalent alkyls groups considering all oligomers studied (Figs 2–3). This effect is more significant for the extended derivatives of PDES(II). The butoxi (D_8), propoxi (D_6), ethoxi (D_4), methoxi (D_2) donor groups contribute for the highest values of β obtained in this investigation (Fig. 3). The best performance is obtained for the decamer of PDES(II) structure, which presents the butoxi and dicyanoethenyl groups as the donor and acceptor, respectively, with the value of β (SHG) to be 51,864.10^{-30} esu at 1060 nm (Table 2). All oligomers chains of PDES(II) have planar structures. Therefore, the resonance contributes for the enhanced values of β observed as is also verified for the alyciclic conjugated systems [1,2].

Must be emphasized that the saturation of the response is not observed until the size of the oligomer investigated for the derivatives of PDES(II) structure in contrast with the observed for PDES(I). In this case, the largest results of the β nonlinear coefficient are exhibited by the donor-acceptor trimers (Table 1). The butoxi (D_8) and propoxi (D_6) donor groups associated with the dicyanoethenyl acceptor contribute for the higher values of β obtained for the trimers of PDES(I) (Fig. 2). It is verified that the shorter oligomers chains of PDES(I) have planar geometries, while that the increasing the chain makes to appear the torsions between the rings, resulting in a nonplanar geometry and therefore reducing the π-conjugation length. Therefore, the mobility of electrons is decreased and consequently the polarization of these systems. The saturation at short chain length is also observed for oligomeric polyphenyl series according with experimental and theoretical results [26–28]. The absence of saturation of the β nonlinear response is observed for the donor-acceptor substituted thiophene oligomers with eight double bonds that were reported in the literature [4].

Furthermore, it is observed that the HOMO-LUMO energy gap decreases with the increasing of the oligomer chain for both structures of PDES. The PDES(II) decamer with the highest value of β has the least value of the Homo-Lumo energy gap among all oligomers investigated. Therefore in

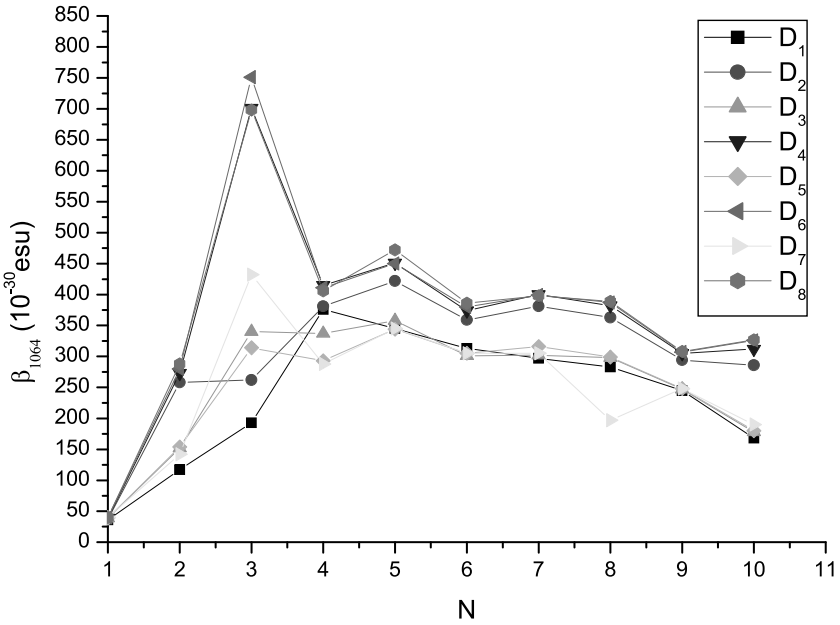

Fig. 2. Evolution of the β(SHG) hyperpolarizability at 1060 nm with the increasing of the number of Si-rings (N) for the donor-acceptor PDES(I) oligomers, where the donor groups are the methyl (D_1), methoxi (D_2), ethyl (D_3), ethoxi (D_4), propyl (D_5), propoxi (D_6), butyl (D_7), butoxi (D_8), and the dicyanoethenyl group is the electron acceptor of the systems investigated.

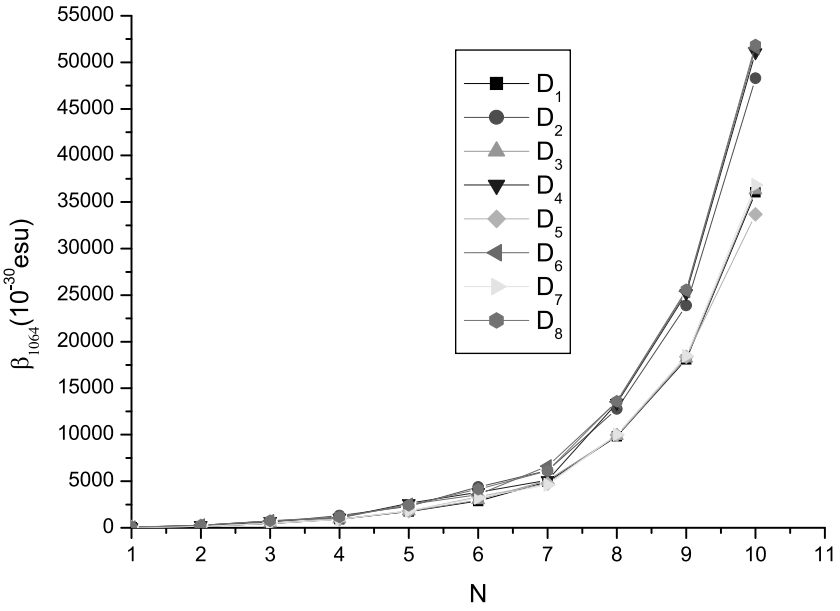

Fig. 3. Evolution of the β (SHG) hyperpolarizability at 1060 nm with the increasing of the number of Si-rings (N) for the donor-acceptor PDES(II) oligomers, where the donor groups are the methyl (D_1), methoxi (D_2), ethyl (D_3), ethoxi (D_4), propyl (D_5), propoxi (D_6), butyl (D_7), butoxi (D_8) and the dicyanoethenyl group is the electron acceptor of the systems investigated.

agreement with the simple two-level model based on perturbation theory, that relates the magnitude of β hyperpolarizability with the inverse of the energy gap [1,2]. Also, all systems derivatives investigated of PDES with alkoxides groups have a least HOMO-LUMO energy gap in contrast with ones where is missing the heteroatom.

The values of ground state dipole moment are strongly magnified with the increase in chain length for the PDES(II) oligomers according with the AM1/TDHF calculations (Table 2). Another observed feature for the PDES(I) systems, since that the magnitude of ground state dipole moment is significantly reduced with the increase of the size of these oligomers (Table 1). The dipolar terms can be responsible for this typical behaviour showed for the PDES oligomers by using approximate models for the β hyperpolarizability [1,2]. Furthermore, experimental and theoretical studies showed that the magnitude of β as well as the difference between the ground and excited state dipole moment is enhanced with the increase of the oligomer size for some polyenic compounds having D/A pairs [26,29]. In contrast, the lengthening of the push-pull diphenylpolyynes chain contributes for the decrease of the difference between the ground and excited state dipole moments [30,31].

As demonstrated by a survey of experimental and theoretical reports, the introduction of the D/A groups and the length of the effective conjugation changes substantially the spectroscopy properties, such the absorption threshold, the transition dipole and the difference between the ground and excited state dipole moments. Besides, it strongly influence the nonlinear coefficients values [15,26,27,29–31].

In addition, all designed donor-acceptor oligomers of PDES with the alkoxides groups have the smallest value of the ionization potential in contrast with ones where is missing the heteroatom. The ionization potential is make equal the HOMO energy by applied the Koopmans theory. The extended donor-acceptor oligomers of PDSE(II) structure show higher values of the ionization potential compared to the unsubstituted oligomers, which favors the stability chemical. The mislinked heterocyclic polymers have higher ionization potentials in comparison with the corresponding normally linked polymers, which values are sensitive to both the nature of the heteroatom and substitution at the backbone as demonstrated by *ab initio* band structure calculations [32]. Chemometric analysis demonstrated that the large values of the ionization potential are associated with higher magnitude values of the β and γ hyperpolarizabilities for donor-acceptor polyenic derivatives and aniline oligomers [11,14]. Also, some substituted oligoanilines and monomers with electron-withdrawing groups display the largest values of the ionization potential in comparison with the nonsubstituted systems [10,33]. In addition, the values of ionization potentials computed using AM1 and PM3 methods for the short oligoanilines are in agreement with the oxidation potentials obtained via electrochemical measurements, which demonstrate that these quantum chemical models predict the correct structure of oligomers [33].

Earlier AM1/TDHF results for the nonplanar aniline oligomers show that the largest values of the ionization potential are associated the smallest magnitude of the β hyperpolarizability, while for the corresponding simulated planar oligomers is observed an opposite behavior [3]. For linear polyacenes of increased length was observed that the smallest values of the potential of ionization are associated with to largest magnitudes of γ according with the finite-field calculations [34].

For the more extended systems with different D/A pairs, the values of the HOMO-LUMO energy gap, ground state dipole moment and ionization potential leveling-off according to the results obtained with the AM1 Hamiltonian, as can be seen in Table 2. Similar behaviour was found for the ground state dipole moment and transition energy, the later is correlated with the HOMO-LUMO energy gap, of planar polyphenyls and polyenic derivatives with increasing in chain length using the *ab initio* and CNDOVSB methods [26]. Also, the ground state dipole moment of the polyenic derivatives with enhanced chain levels out according with the experimental investigations [35].

4. Conclusions

This work points out that a strategy to increase the first hyperpolarizability in PDES(II) oligomers is to increase the chain length, since no saturation of this nonlinear response was observed for the chain size investigated here. In addition, other groups with different capacities as electron donor and acceptor can be used to increase the polarization in these systems. Particularly, the introduction of the substituents at silicon atoms in designed oligomers of PDES can to lead for the enhancement of the electronic asymmetry and hence to contribute for the increase of the β hyperpolarizability. In addition, more rigorous methods should be used to obtaining insight into the bond alternation (BLA) effect on the values of the β magnitudes for both PDES(I) and PDES(II) structures, in special due to the presence of the heteroatom in the substituent groups. The synthesis and characterization of the nonlinear coefficients of the PDES oligomers investigated is fundamental to understand the nonlinear process observed in these derivatives. Although polydiethynylsilane is a conjugated heterocyclic polymer that have been theoretically and experimentally investigated as third-order nonlinear optical material [5,8,9], the very large β values founded for the donor-acceptor PDSE oligomers demonstrate a promising perspective of applications also as second-order nonlinear media.

Acknowledgement

We gratefully acknowledge the financial support of the Conselho Nacional de Desenvolvimento Científico e Tecnológico (MCT/CNPQ) and Fundação de Amparo à Ciência e Tecnologia do Estado de Pernambuco (FACEPE).

References

[1] D.R. Kanis, M.A. Ratner and T.J. Marks, *Chem Rev* **94** (1994), 195.
[2] B. Champagne and B. Kirtman, in: *Handbook of Advanced Electronic and Photonic Materials and Devices*, (Vol. 9), H.S. Nalwa, ed., Academic: San Diego, 2001, Chapter 2.
[3] A.E. de A. Machado, D.V. Petrov, E.H.L. Falcão, A.A.S. da Gama and W.M. Azevedo, *Chem Phys Lett* **356** (2002), 451.
[4] F. Würthner, F. Effenberger, R. Wortmann and P. Krämer, *Chem Phys* **173** (1993), 305.
[5] K.S. Wong, S.G. Han, Z.V. Vardeny, J. Shinar, Y. Pang, S. Ijadi-Maghsoodi, T.J. Barton, S. Grigoras and B. Parbhoo, *Appl Phys Lett* **58** (1991), 1695.
[6] S. Grigoras, G.C. Lie, T.J. Barton, S. Ijadi-Maghsoodi, Y. Pang, J. Shinar, Z.V. Vardeny, K.S. Wong and S.G. Han, *Synth Met* **293** (1992), 49–50.
[7] Q.-X. Ni, J. Shinar, Z.V. Vardeny, S. Grigoras, Y. Pang, S. Ijadi-Maghsoodi and T.J. Barton, *Phys Rev B* **44** (1991), 5939.
[8] Y. Matsuzaki, M. Nakano, K. Yamaguchi, K. Tanaka and T. Yamabe, *Synth Met* **71** (1995), 1737.
[9] Y. Matsuzaki, M. Nakano, K. Yamaguchi, K. Tanaka and T. Yamabe, *Chem Phys Lett* **263** (1996), 119.
[10] A.E. de A. Machado, A.A.S. da Gama *Int J Quantum Chem* **103** (2005), 625.
[11] M.B.S. da Costa, A.E. de A. Machado and B.B. Neto, *Comp Lett* **3** (2007), 267.
[12] M.B.S. da Costa and A.E. de A. Machado, unpublished results.
[13] M. Blanchard-Desce, V. Alain, P.V. Bedworth, S.R. Marder, A. Fort, C. Runser, M. Barzoukas, S. Lebus and R. Wortmann, *Chem Eur J* **3** (1997)(7), 1091.
[14] A.E. de A. Machado, B.B. Neto and A.A.S. da Gama *J Comp Meth Sci Eng* **4** (2004), 267.
[15] A.E. de A. Machado and A.A.S. da Gama, *J Braz Chem Soc* **19** (2008), 1381.
[16] D.A. dos Santos, T. Kogej, J.L. Brédas, C. Boutton, E. Hendrickx, S. Houbrechts, K. Clays, A. Persoons, J.X. Xhang, P. Dubois and R. Jérôme, *J Mol Struct* (*Theochem*) **521** (2000), 221.
[17] A.D. Buckinham, *Adv Chem Phys* **12** (1967), 107.
[18] G. Maroulis and C.J. Pouchan, *J Phys B: At Mol Opt Phys* **36** (2003), 2011.
[19] A.E. de A. Machado and A.A.S. da Gama, *J Mol Struct* (*Theochem*) **620** (2003), 21.

[20] M. Blanchard-Desce, J.-M. Lehn, M. Barzoukas, C. Runser, A. Fort, G. Puccetti, I. Ledoux and J. Zyss, *Nonlinear Opt* **10** (1995), 23.
[21] M. Blanchard-Desce, R. Wortmann, S. Lebus, J.-M. Lehn and P. Krämer, *Chem Phys Lett* **243** (1995), 526.
[22] M. Blanchard-Desce, J.-M. Lehn, M. Barzoukas, I. Ledoux and J. Zyss, *Chem Phys* **181** (1994), 281.
[23] S.P. Karna and M.J. Dupuis, *Comp Chem* **12** (1991), 487.
[24] M.J.S. Dewar, E.G. Zoebisch, E.F. Healy and J.J.P. Stewart, *J Am Chem Soc* **107** (1985), 3902.
[25] J.J.P. Stewart, MOPAC2000 Manual, Fujitsu, Tokyo, Japan, 1999.
[26] J.O. Morley, V.J. Docherty and D. Pugh, *J Chem Soc Perkin Trans II* **2** (1987), 1351.
[27] L.-T. Cheng, W. Tam, S.H. Stevenson, G.R. Meredith, G. Rikken and S.R. Marder, *J Phys Chem* **95** (1991), 10643.
[28] I. Ledoux, J. Zyss, A. Jutand and C. Amatore, *Chem Phys* **150** (1991), 117.
[29] M. Blanchard-Desce, V. Alain, L. Midrier, R. Wortmann, S. Lebus, C. Glania, P. Krämer, A. Fort, J. Muller and M. Barzoukas, *J Photochem Photobiol A: Chem* **105** (1997), 115.
[30] E. Stiegman, E.M. Graham, K.L. Perry, L.R. Khundkar, L.-T. Cheng and J.W. Perry, *J Am Chem Soc* **113** (1991), 7658.
[31] C. Dehu, F. Meyers and J.L. Brédas, *J Am Chem Soc* **115** (1993), 6198.
[32] A.K. Bakhshi and N.K. Ray, *J Chem Phys* **88** (1988), 386.
[33] M.E. Vascheto and B.A. Retamal, *J Phys Chem* **101** (1997), 6945.
[34] S.-L. Lee, K.-W. Yang, J.-H. Sheu and Y.-J. Lu, *Int J Quantum Chem: Quantum Chemistry Symposium* **29** (1995), 509.
[35] H.H. Hutchinson and L.E. Sutton, *J Chem Soc* (1958), 4382.

Journal of Computational Methods in Sciences and Engineering 10 (2010) 213–223
DOI 10.3233/JCM-2010-0320
IOS Press

Sum frequency generation in chiral carbon nanotubes

L. De Dominicis*
ENEA – Italian National Agency for New Technologies, Energy and Sustainable Economic Development, Via. E. Fermi 45, C.P.65, I-00044 Frascati, Italy

Abstract. The process of Sum Frequency Generation (SFG) in chiral Carbon Nanotubes (CNTs), with the exciting laser beams propagating along the CNT symmetry axis, is here investigated. First the general form of the first hyperpolarizability third rank tensor β for chiral CNTs is determined with group projector technique method applied to the $\mathbf{L}\mathrm{n}_p22$ line group describing their symmetry. For this purpose, the group natural factorization has been adopted and the associated irreducible representations, parameterized in terms of helical quantum numbers, then used to construct the group projector operator in the relevant vector space. The method demonstrates that second harmonic generation is symmetry forbidden in the collinear geometry while, conversely, SFG is symmetry allowed. Subsequently, the SFG far-field radiation pattern has been modelled with a calculation scheme derived from antenna's theory and already used for simulation of Rayleigh scattering from a CNT. The method has been overhauled for describing the here considered nonlinear optical interaction. The study of the role played by two induced counter-propagating current density retarded waves in shaping the radiation pattern is addressed and simulations are reported in the limit regimes of strong and weak attenuation.

Keywords: Carbon nanotubes, line groups, first hyperpolarizability, sum frequency generation

1. Introduction

Carbon Nanotubes (CNTs) are synthetic nanostructures which are attracting, from the early days of their discovery in 1991, the interest of researchers due to their remarkable optical, electronic and mechanical properties [1]. Nevertheless, for more than a decade their second order nonlinear optical properties have been disregarded up to the breakthrough following the first experimental demonstration in 2003 of Second Harmonic Generation (SHG) in bulk samples [2,3]. Since then, experimental and theoretic investigations based on accurate measurements and calculation exploiting the mathematical apparatus of the irreducible representations of their symmetry group [4–10], have progressed at a steady pace adding relevant advances in the comprehension of the process.

From a topological point of view, a single wall CNT (SWCNT) is a graphite sheet rolled up into a cylinder with nanometer size diameter. SWCNTs are periodic structures, being the whole element obtained by repeated translations along the cylinder axis of a unit cell of length a. Moreover, according to the direction of the wrapping axis with respect the basic vectors of the graphite unit cell, they may also display a chiral structure characterized by the lack of invariance under reflection through a plane perpendicular to the cylinder axis. In any case, the wrapping procedure maps the symmetry group of graphite into a new class of symmetry operations leaving the SWCNT structure invariant, which for chiral structures, are described by the $\mathbf{L}n_p22$ line group. Theoretic considerations [5] demonstrate that

*Corresponding author. Tel.: +39 06 94005857; E-mail: luigi.dedominicis@enea.it.

SHG is symmetry forbidden for an experimental set-up where the exciting laser is linearly polarized and propagates along the CNT symmetry axis, here assumed as z. This because the $\beta_{zxy}\left(2\omega;\omega,\omega\right)$ component of CNT first hyperpolarizability vanishes as a consequence of the general transformation properties of a third rank tensor under the $\mathbf{L}n_p22$ symmetry group, in conjunction with the intrinsic permutation symmetry property. Conversely, for a non-degenerate laser excitation scheme, where two cross polarized collinear laser fields at frequencies ω_1 and ω_2 propagate along z, the $\beta_{zxy}\left(\omega_1+\omega_2;\omega_1,\omega_2\right)$ component is expected to be non-vanishing, thus giving rise to a second order induced current $\vec{J}^{SFG}\left(\omega_1+\omega_2\right)$ on the CNT surface at the sum frequency $\omega_{SFG}=\omega_1+\omega_2$ and responsible for a Sum Frequency Generation (SFG) scattered electromagnetic field. Sum Frequency Generation (SFG) is thus an alternative scheme for probing CNTs in a collinear excitation, but which to date has never been studied neither theoretically or experimentally. As a first step to fill this gap, in the present paper a rigorous determination of the non-vanishing components of the SFG first hyperpolarizability third rank tensor $\beta\left(\omega_1+\omega_2;\omega_1,\omega_2\right)$ is reported. For this task the formalism of group projector method [11], already adopted to find the general invariant form of tensors with rank up to two for the chiral CNTs line symmetry group $\mathbf{L}n_p22$, is extended to third rank tensors. However, for our specific task, it is necessary to adopt an alternative set of irreducible representation (irreps) for $\mathbf{L}n_p22$ with respect to irreps constructed by decomposing $\mathbf{L}n_p22$ onto the invariant cyclic subgroup $\mathbf{T}(a)$ of pure translations of a (unit cell length) along CNT axis and the isogonal rotational group $\mathbf{L}/\mathbf{T}(a)$. In this different approach, the line group is factorized onto the semi-direct product of two cyclic subgroups and the irreps computed through the induction procedure. These irreps are used to reduce the group representation in the three dimensional space D^{pv} of the polar vector and the invariant form in the vector space $\Re=D^{pv}\otimes D^{pv}\otimes D^{pv}$, transforming like $\beta\left(\omega_1+\omega_2;\omega_1,\omega_2\right)$, is obtained with the group projector operator P,projecting out the generic vector of $\Re$ on the symmetry adapted sub-basis for the identical representation.

The second part of the paper is devoted to simulation of SFG process by adopting a calculation method already used by Slepyan et al. [12] for modelling linear Rayleigh scattering in a CNT. The method is based on a formalism largely adopted in antenna's theory and opportunely revised to take into account the CNT's geometry. Alike for linear Rayleigh scattering, also for SFG the exciting fields induce on the CNT surface a current density which consists of two counter-propagating retarded waves in addition to a wave propagating with the same wavevector of the SFG scattered field.

The shape of the radiation pattern radiated by this induced density current is governed by several parameters whose relative weight determines different scattering regimes, thus making the experimental technique a potential probe for physical quantities whose estimation for CNTs is still an open issue, like for instance the longitudinal optical conductivity.

2. The first hyperpolarizability tensor for chiral CNTs

In this section the nonvanishing components of the first hyperpolarizability tensor for the SFG process in a chiral CNT are determined. The properties of the $\mathbf{L}n_p22$ relevant irreps are determined and the projector operator method applied in the $\Re=D^{pv}\otimes D^{pv}\otimes D^{pv}$ space.

2.1. The Ln$_p$ 22 Line Group of Chiral CNT and its D^{pv} Representation

A typical chiral SWCNT is shown in Fig. 1. $\mathbf{L}n_p22$ is the line group which describes the symmetry of this structure. The group parameter n is strictly related to the CNT topology, being the quasi 1D-crystalline structure the repetition along the cylinder axis of a unit cell containing $2n$ carbon atoms, while

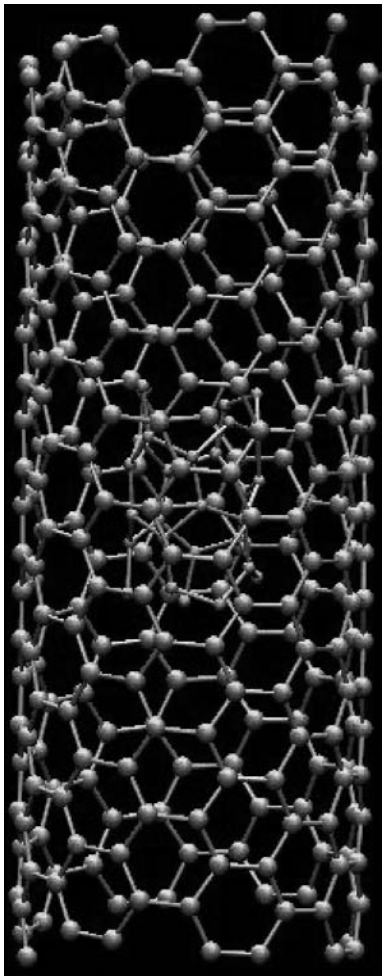

Fig. 1. Chiral CNT structure. The tube diameter is of the order of few nanometers while length stretches up to some microns.

the p parameter is an integer ranging from 1 to $n-1$. If attention is restricted to CNTs topologies with n and p coprime, the unit cell length is $a = \sqrt{\frac{3n}{2}}a_0$ and the tube diameter $D = \frac{1}{\pi}\sqrt{\frac{n}{2}}a_0$, where $a_0 =$ 2.461Å.

The element of $\mathbf{L}n_p22$ (n >2), in the so called central extension decomposition into the invariant cyclic subgroup $\mathbf{T}(a)$ of pure translations of a along the tube axis and into the isogonal rotational group $\mathbf{L}n_p22/\mathbf{T}(a)$, can be written (Koster-Seitz notation [13]) as $\left(U^l C_n^s \,|[Fr\,(sp/n) + t']\; a\right)$, where n even, $s =$ 0,1,..., $n-1$, $l =$ 0,1 and t' integer. It follows that, the p parameter is related to the fractional translations proper of the chiral topology. Here U represents a rotation of π around an axis perpendicular to the CNT axis and passing through the centre of the deformed graphite hexagon, while C_n^s a rotation of $2\pi s/n$ around the CNT axis. The associated irreps are classified in terms of the linear quantum numbers (k, m), where only the quasi momentum k is conserved due the non-symmorphic nature of the group ($\mathbf{L}n_p22/\mathbf{T}(a)$ not a subgroup of $\mathbf{L}n_p22$). Nevertheless, an alternative set of irreps is much more convenient for the scope of the present work. In this case the irreps are calculated with the induction procedure based on the natural factorization $\mathbf{L}n_p22=\mathrm{q}_r \wedge D_q$, where $\wedge$ indicates the group semi-direct product.

Table 1
Reduction of the polar vector representation of $\mathbf{L}n_p22$ into irreps from Eq. (1). Here $\tilde{k}^* = \frac{2\pi r}{an}\ (2r \leqslant n)$, $\tilde{k}^* = 2\pi\left(\frac{r}{q}-1\right)\ (2r \geqslant n)$

Factorization	$n=1$	$n=2$	$n>2$
Natural	${}_0A_0^- + {}_{\tilde{k}^*}^{-\tilde{k}^*}E_0^0$	${}_0A_0^- + {}_{\tilde{k}^*}^{-\tilde{k}^*}E_1^1$	${}_0A_0^- + {}_{\tilde{k}^*}^{-\tilde{k}^*}E_1^{-1}$
Central Extension	$2{}_0A_0^- + {}_0A_0^+$	${}_0A_0^- + {}_0A_1^+ + {}_0A_1^-$	${}_0A_0^- + {}_0E_1^{-1}$

Here q_r is the cyclic invariant subgroup with generator $(C_n^r\,|(q/n)a)$, D_q the dihedral point group with $q = GCD(n,p)$ greatest common divisor of n and p, and the helical parameter $r$solution of the equation $\frac{p}{q} = r^{\varphi\left(\frac{n}{q}\right)-1}\ \left(\mathrm{mod}\,\frac{n}{q}\right)$, where $\phi(m)$ is the Euler function giving the number of coprime lower than m . In this factorization scheme the generic symmetry operation of $\mathbf{L}n_p22$ is given by $\left(C_n^{rt}U^lC_q^s\,|(tq/n)\,a\right)$. The associated irreps, calculated [14] with the induction procedure, are labelled with the helical quantum numbers $\left(\tilde{k},\tilde{m}\right)$, both conserved in electromagnetic interactions and are reported below

$$
\begin{aligned}
&{}_0A_0^{\pm}\left(C_n^{rt}U^lC_q^s\,|(tq/n)a\right) = (\pm1)^l\\
&{}_0E_{\tilde{m}}^{-\tilde{m}}\left(C_n^{rt}U^lC_q^s\,|(tq/n)a\right) = \begin{bmatrix}0&1\\1&0\end{bmatrix}^l\begin{bmatrix}e^{2\pi i\tilde{m}s/q}&0\\0&e^{-2\pi i\tilde{m}s/q}\end{bmatrix},\ \tilde{m}\in[0,q/2]\\
&{}_{\tilde{k}}^{-\tilde{k}}E_{\tilde{m}}^{-\tilde{m}}\left(C_n^{rt}U^lC_q^s\,|(tq/n)a\right) = \begin{bmatrix}0&1\\1&0\end{bmatrix}^l\begin{bmatrix}e^{i(\tilde{k}tqa/n+2\pi\tilde{m}s/q)}&0\\0&e^{-i(\tilde{k}tqa/n+2\pi\tilde{m}s/q)}\end{bmatrix},\\
&\qquad\qquad \tilde{m}\in[-q/2,q/2]\ ,\ \tilde{k}\in\left(0,\tfrac{\pi n}{qa}\right]\\
&{}_\pi A_0^{\pm}\left(C_n^{rt}U^lC_q^s\,|(tq/n)a\right) = (\pm1)^l(-1)^t\\
&{}_\pi E_{\tilde{m}}^{-\tilde{m}}\left(C_n^{rt}U^lC_q^s\,|(tq/n)a\right) = (-1)^t\begin{bmatrix}0&1\\1&0\end{bmatrix}^l\begin{bmatrix}e^{2\pi i\tilde{m}s/q}&0\\0&e^{-2\pi i\tilde{m}s/q}\end{bmatrix},\ \tilde{m}\in[0,q/2]
\end{aligned}
\tag{1}
$$

Despite this set of irreps is the same up to equivalence with those reported in Ref [15,16], a difference arises when the three dimensional D^{pv} representation of $\mathbf{L}n_p22$ is reduced into irreducible components. As Table 1 shows, the reduction in the natural factorization scheme contains contributions from two-dimensional irreps E with a non-vanishing helical momentum parameter $\tilde{k}^* = \frac{2\pi r}{an}$, while, conversely, in central extension decomposition only irreps with vanishing values of the linear momentum are involved. The advantage of maintaining the dependence on t in the D^{pv} decomposition, as a consequence of contributions from non-vanishing helical momentum, consists in the possibility to use the formalism of finite groups for calculations and then to check the convergence of the tensor to the invariant form as partial sums tends to series.

2.2. The projector operator in the $D^{pv}\otimes D^{pv}\otimes D^{pv}$ space

Basing on the formalism introduced in Section 2.1, it's possible to derive explicitly the projector operator $P(I)$ in the vector space of the third rank tensor $\Re = D^{pv}\otimes D^{pv}\otimes D^{pv}$. The so obtained operator projects out, from a generic element of $\Re$, the part transforming like the identity representation. Indicating with $D(g)$ a representation (also reducible) of the group $\mathbf{L}$ on a vector space V, the projector operator $P(I)$ on V is a homomorphism of V into V, given by [17]

$$P(I) = \frac{1}{\|G\|}\sum_{g\in L}D(g) \tag{2}$$

where $\|G\|$ is the order of G.

A set of reducible representation $D(G)$ of $\mathbf{L}n_p22$ on the carrier space $\Re$ can be constructed by using the tensor product of irreps calculated in the natural factorization scheme. A basis in $\Re$ is obtained with the tensor product $e_{ijk} = e_i \otimes e_j \otimes e_k$, where $\{e_i\}_{i=1}^{3}$ is a basis in D^{pv}. In the following the indexes $i, j, k = 1, 2, 3$ are used to enumerate the basis vector and $I, J, K =$ 1,2,3 the components of the third rank tensor. The generic vector β in $\Re$ can be decomposed as

$$\beta_{IJK} = \left(\sum_{ijk} a_{ijk} e_{ijk} \right)_{IJK} = \begin{pmatrix} a_{111} & a_{112} & a_{113} \\ a_{121} & a_{122} & a_{123} \\ a_{131} & a_{132} & a_{133} \\ a_{211} & a_{212} & a_{213} \\ a_{221} & a_{222} & a_{223} \\ a_{231} & a_{232} & a_{233} \\ a_{311} & a_{312} & a_{313} \\ a_{321} & a_{322} & a_{323} \\ a_{331} & a_{332} & a_{333} \end{pmatrix} \tag{3}$$

where a_{ijk} are the coordinates of β in the e_{ijk} base. An orthogonal crystallographic reference frame with direction 1 along the tube axis and direction 2 along the symmetry axis U of the CNT has been introduced. For the SHG process the intrinsic permutation condition $a_{ijk} = a_{ikj}$ is valid, while for SFG the condition does not hold. The part $\tilde{\beta}$ of β transforming as the identical representation, giving the invariant form of a vector in $\Re$ under the symmetry operations of $\mathbf{L}n_p22$, is obtained with

$$\tilde{\beta} = P(I)\beta = \frac{1}{\|G\|} \sum_{G \in L} \sum_{ijk} a_{ijk} \sum_{\mu\nu\alpha} D^{pv}_{\mu i}(g) D^{pv}_{\nu j}(g) D^{pv}_{\alpha k}(g) e_{\mu\nu\alpha} \tag{4}$$

where $D^{pv}(g)$ is the polar vector representation of the elements of $\mathbf{L}n_p22$ constructed with expressions in Eq. (1) and the decomposition in Table 1. Notation and calculations are greatly simplified for the assumed CNTs topologies with $q = 1$ (n and p coprime) and in this case the application of the projector operator to the generic vector of $\Re$ gives

$$\tilde{\beta} = P(I)\beta = \lim_{N \to \infty} \frac{1}{4N} \sum_{l=0}^{1} \sum_{t=-N}^{N} \sum_{ijk} \sum_{\mu\nu\alpha} a_{ijk} D^{pv}_{\mu i}(l,t) D^{pv}_{\nu j}(l,t) D^{pv}_{\alpha k}(l,t) e_{\mu\nu\alpha} \tag{5}$$

with

$$\begin{aligned} D^{pv}(0,t) &= \left(C_n^{rt} \,|(t/n)a \right) = \begin{bmatrix} 1 & 0 & 0 \\ 0 & e^{i\tilde{k}ta/n} & 0 \\ 0 & 0 & e^{-i\tilde{k}ta/n} \end{bmatrix} \\ D^{pv}(1,t) &= \left(C_n^{rt} U \,|(t/n)a \right) = \begin{bmatrix} 1 & 0 & 0 \\ 0 & 0 & e^{i\tilde{k}ta/n} \\ 0 & e^{-i\tilde{k}ta/n} & 0 \end{bmatrix} \end{aligned} \tag{6}$$

and where the SWCNT structure is obtained by letting the number $2N$ of carbon atoms to extend up to infinity. Calculation in Eq. (5) finally gives the following result

$$\tilde{\beta}_{IJK} = \lim_{N\to\infty} \frac{1}{4N} \sum_{t=-N}^{N} \begin{bmatrix} 0 & e^{i\alpha t}a_{121} + e^{-i\alpha t}a_{131} & e^{i\alpha t}a_{121} + e^{-i\alpha t}a_{131} \\ e^{i\alpha t}a_{112} + e^{-i\alpha t}a_{113} & e^{2i\alpha t}a_{122} - e^{-2i\alpha t}a_{133} & a_{132} - a_{123} \\ e^{i\alpha t}a_{112} + e^{-i\alpha t}a_{113} & a_{123} - a_{132} & -e^{2i\alpha t}a_{122} + e^{-2i\alpha t}a_{133} \\ e^{i\alpha t}a_{211} + e^{-i\alpha t}a_{311} & e^{2i\alpha t}a_{221} - e^{-2i\alpha t}a_{331} & a_{231} - a_{321} \\ e^{2i\alpha t}a_{212} - e^{-2i\alpha t}a_{313} & e^{3i\alpha t}a_{222} + e^{-3i\alpha t}a_{333} & e^{i\alpha t}a_{232} + e^{-i\alpha t}a_{322} \\ a_{213} - a_{312} & e^{i\alpha t}a_{223} + e^{-i\alpha t}a_{332} & e^{i\alpha t}a_{222} + e^{-i\alpha t}a_{322} \\ e^{i\alpha t}a_{211} + e^{-i\alpha t}a_{311} & a_{321} - a_{231} & -e^{2i\alpha t}a_{221} + e^{-2i\alpha t}a_{331} \\ a_{312} - a_{213} & e^{i\alpha t}a_{322} + e^{-i\alpha t}a_{233} & e^{i\alpha t}a_{223} + e^{-i\alpha t}a_{332} \\ -e^{2i\alpha t}a_{212} + e^{-2i\alpha t}a_{313} & e^{i\alpha t}a_{232} + e^{-i\alpha t}a_{323} & e^{3i\alpha t}a_{222} + e^{-3i\alpha t}a_{333} \end{bmatrix} \quad (7)$$

where $\alpha(n,p) = \frac{2\pi r}{n^2}$ is the product of the isogonal rotation generator C_n^rangle and the basic unit $\tilde{\mathrm{T}} = a/n$ of the fractional translations. Each atom, labelled by the fractional translation parameter t, contributes to tensor component with the same amplitude but with a different phase αt. Only the so-called chiral components with I≠J≠K in the third rank tensor of Eq. (7) do not depend on N and α, while all others matrix elements are combination of a basic function $\Gamma(N,n,p)$, given by

$$\Gamma(N,n,p) = \frac{1}{N}\sum_{t=-N}^{N} e^{i\alpha(n,p)t} = \frac{1}{N}\frac{\sin\left[\left(N+\frac{1}{2}\right)\alpha(n,p)\right]}{2\sin\left(\frac{\alpha(n,p)}{2}\right)} \quad (8)$$

The function $\Gamma(N,n,p)$, for any values of the parameters n and p, vanishes as N→ ∞. For SHG the intrinsic permutation condition imposes $a_{ijk} = a_{ikj}$ and hence the invariant form of the third rank tensor $\tilde{\beta}_{IJK}$ has four non-vanishing components $\tilde{\beta}_{213} = \tilde{\beta}_{231} = -\tilde{\beta}_{312} = -\tilde{\beta}_{321}$. For SFG instead, the intrinsic permutation symmetry does not hold adding the non-vanishing components $\tilde{\beta}_{123} = -\tilde{\beta}_{132}$. The second order nonlinear dipole moment $\vec{P}$ induced by two exciting laser beams $\vec{E}_1$ and $\vec{E}_2$, is obtained by the contraction $\vec{P} = \tilde{\beta} : \vec{E}_1\vec{E}_2$ with the first hyperpolarizability tensor. It is clear that the induced dipole moment for two exciting laser beams propagating along the direction 1 of the CNT symmetry axis is non-vanishing only if the two laser beams have different frequency (SFG) as a consequences of the proven property $\tilde{\beta}_{123} = -\tilde{\beta}_{132} \neq 0$.

3. SFG radiation pattern simulation

In the simulated geometry (Fig. 2) two electromagnetic plane waves $\vec{E}_1 = \hat{x}E_0 e^{-i\omega_1\left(\frac{\hat{z}}{c}\cdot\vec{r}-t\right)}$ and $\vec{E}_2 = \hat{y}E_0 e^{-i\omega_2\left(\frac{\hat{z}}{c}\cdot\vec{r}-t\right)}$ at frequency ω_1 and ω_2, linearly polarized along perpendicular directions assumed as $\hat{x}$ and $\hat{y}$, propagate along the symmetry axis $\hat{z}$ of a chiral SWCNT. The field $\vec{E} = \vec{E}_1 + \vec{E}_2$ couples with the CNT first hyperpolarizability tensor and induces a nonlinear surface current density $\vec{J}(\vec{r},t)$ which re-radiates a scattered field. If attention is restricted to the scattered field at frequency $\omega_{SFG} = \omega_1 + \omega_2$ and taking into account only the axial component $J_z^{SFG}(\omega_1+\omega_2)$ of the current density, the SFG field can be obtained by the Hertz potential $\vec{\Pi}_e = \Pi_e(z,\phi,\rho)\,\hat{z}$ satisfying in the free space the Helmoltz equation

$$\left(\nabla^2 + k^2\right)\Pi_e = 0 \quad (9)$$

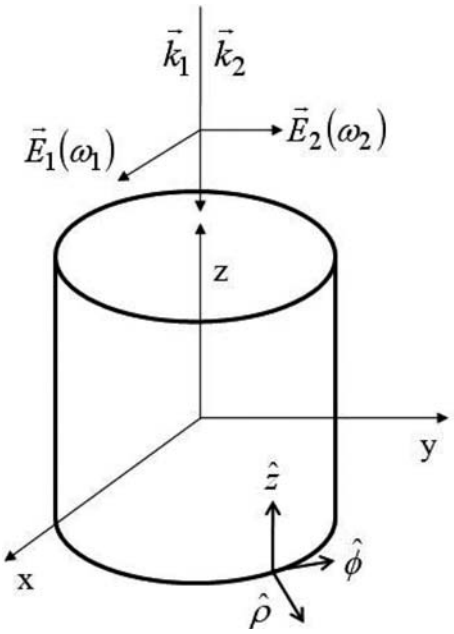

Fig. 2. SFG from a CNT in a collinear geometry. The two laser beams propagate along the CNT axis of symmetry. The local cylindrical coordinate system used for calculation is also displayed.

with $k = \frac{\omega_1+\omega_2}{c}$ and where a cylindrical coordinate system z, ρ, ϕ with z along the SWCNT symmetry axis has been introduced to better exploit its symmetry.

The tangential component of the magnetic field of the SFG scattered electromagnetic wave is given by $H_\phi^{\omega_{SFG}} = \frac{1}{c} i\omega_{SFG} \frac{\partial \Pi_e}{\partial \rho}$ and is also subject to the boundary condition $H_\phi|_{\rho=R^+} - H_\phi|_{\rho=R^-} = J_z^{SFG}(R, \phi, z)$ on the CNT surface, where R is the CNT diameter. This, together with the constituent relation $\vec{J} = \frac{\partial \vec{P}}{\partial t}$ between the surface current density and the induced surface polarization $\vec{P}$, leads to the fundamental equation

$$J_z^{SFG}(R,z,\phi) = -i\omega_{SFG}\left\{\beta_{z\rho\phi}\left[E_\rho^{\omega_1}(R,z,\phi)\,E_\phi^{\omega_2}(R,z,\phi) + E_\rho^{\omega_2}(R,z,\phi)\,E_\phi^{\omega_1}(R,z,\phi)\right] + \alpha_{zz}\left[\frac{\partial^2 \Pi_e}{\partial z^2} + k^2 \Pi_e\right]\right\} \tag{10}$$

where α_{zz} is the axial component of the linear polarizability per unit area at frequency ω_{SFG}.

From antenna's theory [18] a cylindrical antenna of radius R and length L carrying a current density J_z^{SFG} radiates an electromagnetic field whose Hertz potential is given by

$$\Pi_e(\rho,z,\phi) = -\frac{iR}{\omega_{SFG}} \int_0^{2\pi} \int_{-L/2}^{L/2} J_z^{SFG}\left(R,z',\phi'\right) \frac{e^{-ikR'}}{R'} dz' d\phi' \tag{11}$$

where $R' = \sqrt{\rho^2 + R^2 - 2R\rho\cos(\phi-\phi') + (z-z')^2}$. The substitution of J_z^{SFG} from Eq. (10) into Eq. (11) provides an Hallen integro-differential equation for Π_e with a source term depending both on the CNT first hyperpolarizability and on the exciting lasers fields. Instead of trying to solve this equation, it

is possible [12] to manage Eqs (10,11) for obtaining a solvable equation for $\tilde{J}_z^{SFG} = \frac{i}{\omega_{SFG}} J_z^{SFG}$. This leads to the following Leontovich–Levin equation

$$\left[\frac{\partial^2}{\partial z^2} + k^2 - \frac{1}{\alpha_{zz} RX}\right] \tilde{J}_z^{SFG}(z) = -\frac{2\beta_{z\rho\phi} E_0^2}{\pi \alpha_{zz} RX} e^{ikz} + \frac{1}{X}\left(\frac{\partial^2}{\partial z^2} + k^2\right) V\left(z, \tilde{J}_z^{SFG}(z)\right) \tag{12}$$

where $X = 2\pi \ln(qR)$, with q arbitrary constant with the dimension of the inverse of a length and

$$V\left(z, \tilde{J}_z^{SFG}\right) = \int_{-\frac{L}{2}}^{\frac{L}{2}} \ln\left(2q\left|z - z'\right|\right) e^{ik|z-z'|} \left[\frac{z - z'}{|z - z'|} \frac{\partial \tilde{J}_z^{SFG}(z')}{\partial z'} - ik \tilde{J}_z^{SFG}(z')\right] dz' \tag{13}$$

Equation (12) is the same equation describing the linear Rayleigh scattering from a chiral CNT but with a different value for the first term in the right side. Within the approximation $\frac{1}{X} << 1$, which holds for $q \approx k$ at optical frequencies, it is possible to adopt the series expansion $\tilde{J}_z^{SFG} \approx \tilde{J}_z^{(0)SFG} + \frac{1}{X}\tilde{J}_z^{(1)SFG} + \frac{1}{X^2}\tilde{J}_z^{(2)SFG} + \ldots$, with $\tilde{J}_z^{(0)SFG}$ satisfying the equation

$$\left(\frac{\partial^2}{\partial z^2} + k^2 - \frac{1}{\alpha_{zz} RX}\right) \tilde{J}_z^{(0)SFG} = -\frac{2\beta_{z\rho\phi} E_0^2}{\pi \alpha_{zz} RX} e^{ikz} \tag{14}$$

The general solution of this differential equation can be find easily and, after imposing the boundary conditions $\tilde{J}_z^{(0)SFG}\left(\pm\frac{L}{2}\right) = 0$ giving a vanishing induced current at the CNT edges, the following particular solution is obtained

$$\begin{aligned} J_z^{(0)SFG}(z,t) = \beta_{z\rho\phi} \frac{\omega_{SFG} E_0^2}{\pi} \Bigg\{ & \frac{\cos\left(\frac{kL}{2}\right)\left[1 - tg\left(\tilde{k}\frac{L}{2}\right)\right] - 2\sin\left(\frac{kL}{2}\right)}{\sin\left(\frac{\tilde{k}L}{2}\right)} e^{i\tilde{k}z} + \\ & \frac{\cos\left(\frac{kL}{2}\right)\left[1 - tg\left(\tilde{k}\frac{L}{2}\right)\right]}{\sin\left(\frac{\tilde{k}L}{2}\right)} e^{-i\tilde{k}z} + 2e^{ikz} \Bigg\} e^{i\omega_{SFG} t} \end{aligned} \tag{15}$$

with $\tilde{k} = \sqrt{k^2 - \frac{1}{RX\alpha_{zz}}}$.

The zero order induced current density has three contributions oscillating at ω_{SFG}, one propagating along the CNT with the same wave-vector k of the SFG field and two counter-propagating retarded waves propagating with wave-vector $\tilde{k}' = Re(\tilde{k})$ and with an attenuation $\tilde{k}'' = Im(\tilde{k})$. The knowledge of the induced surface current density allows to calculate the far field radiation pattern in polar coordinates by means of the relation $E_\theta^{sc}(r,\theta) = \frac{-2i\pi RL\omega_{SFG}}{c^2}\frac{e^{ikr}}{r} F(\theta)$, where $F(\theta) = \sin\theta \int_{-L/2}^{L/2} J_z^{(0)SFG}(z)\, e^{-ikz\cos\theta} dz$ is the scattering pattern.

The SFG far field radiation pattern depends strongly on the complex wave-vector $\tilde{k}$ of the two retarded waves and in particular on the relative weight of its real and imaginary part $\tilde{k}'$ and $\tilde{k}''$. A long but simple

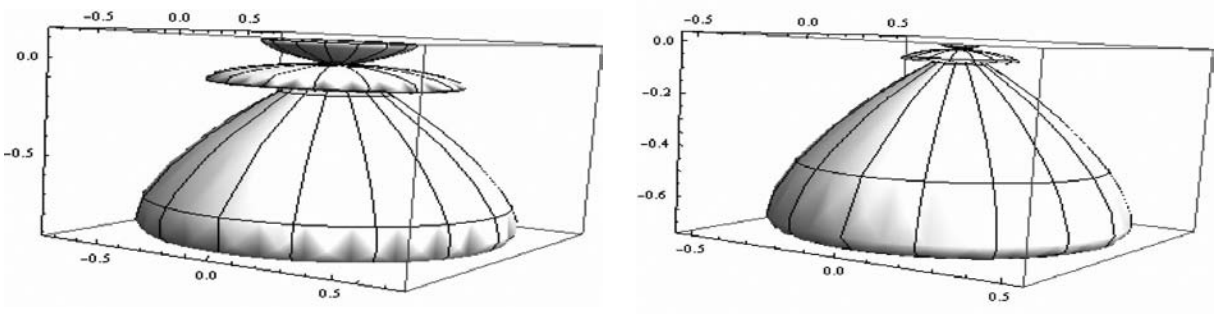

Fig. 3. SFG radiation pattern for L = 1 μm, $\lambda_{SFG} = 0.532$ μm, $\frac{Re\beta_{z\rho\phi}}{Im\beta_{z\rho\phi}} = 10^{-2}$. Left: weak attenuation $\tilde{k}' = 2k$. Right: strong attenuation $\tilde{k}' = \tilde{k}'' = 10^4 k$.

algebras gives for them the following expression

$$\begin{aligned} \tilde{k}' &= \frac{1}{\sqrt{2}} \left\{ k^2 - \frac{\omega_{SFG} Im\sigma}{2\pi RX \left|\sigma\right|^2} \pm \sqrt{\left(k^2 - \frac{\omega_{SFG} Im\sigma}{2\pi RX \left|\sigma\right|^2} \right)^2 + \frac{4\omega_{SFG}^2 \left(Re\sigma\right)^2}{4\pi^2 R^2 X^2 \left|\sigma\right|^2}} \right\}^{1/2} \\ \tilde{k}'' &= -\frac{\omega_{SFG} Re\sigma}{2\pi RX \left|\sigma\right|^2} \frac{1}{2\tilde{k}'} \end{aligned} \tag{16}$$

where $\sigma = \omega\alpha_{zz}$ is the longitudinal optical conductivity per unit area, which has the dimension of a velocity. It is straightforward to note that for $Re\sigma = 0$, as true far from any absorption resonances, the retarded waves are not attenuated ($\tilde{k}'' = 0$) and propagate with a retardation due to the electrons polarization to shield the external field. In the other limit, $Im\sigma = 0$, we have $\tilde{k}' = \frac{1}{\sqrt{2}} \left[k^2 \pm \sqrt{k^4 + \left(\frac{\omega_{SFG}}{\pi RX Re\sigma}\right)^2} \right]^{1/2}$.

The condition $k^2 << \frac{\omega_{SFG}}{\pi RX Re\sigma}$ characterizes a strong attenuation regime with $\tilde{k}' \approx k'' \approx \frac{1}{\sqrt{2}} \sqrt{\frac{\omega_{SFG}}{\pi RX Re\sigma}}$ and $\tilde{k}'' >> k$. While for $k^2 >> \frac{\omega_{SFG}}{\pi RX Re\sigma}$ we fall into the weak attenuation regime, with $\tilde{k}' \approx k$ and $\tilde{k}'' \approx 0$. However a quantitative determination of $\tilde{k}'$ and $\tilde{k}''$, which is essential for radiation pattern simulation, relies on the knowledge of σ whose estimation is far the scope of the present work. Nevertheless, as an explicative example on how much the two investigated regime differ, in Fig. 3 is reported the radiation pattern for $L = 1$ μm, $\lambda_{SFG} = 0.532$ μm, $\frac{Re\beta_{z\rho\phi}}{Im\beta_{z\rho\phi}} = 10^{-2}$ and for weak ($\tilde{k}' = 2k$) and strong attenuation ($\tilde{k}' = \tilde{k}'' = 10^4 k$). The SWCNT is aligned along the symmetry axis of the radiation pattern and the exciting laser beams propagate along the negative values of this axis. For both the regimes the radiation pattern is characterized by a strong SFG forward lobe and only for the weak attenuation regime by a backscattered lobe. This feature is even more pronounced for $\frac{Re\beta_{z\rho\phi}}{Im\beta_{z\rho\phi}} = 1$, as shown in Fig. 4.

It is worthwhile to note that for $L >> \lambda_{SFG}$ the radiation pattern resembles the shape of a point-like oscillating dipole along z, regardless the values of the other involved parameters, as Fig. 5 demonstrates. The occurrence of a backscattered lobe is thus a signature of a weak attenuation regime as a far only the zero order $\tilde{J}_z^{(0)SFG}$ of the series expansion for the current density is retained. However, due to the $1/R$ dependence in the dispersion relations for $\tilde{k}'$ and $\tilde{k}''$, a backscattered lobe is more likely to be detected in larger CNTs. Being the CNT radius R measurable by means of Raman scattering, the intensity of

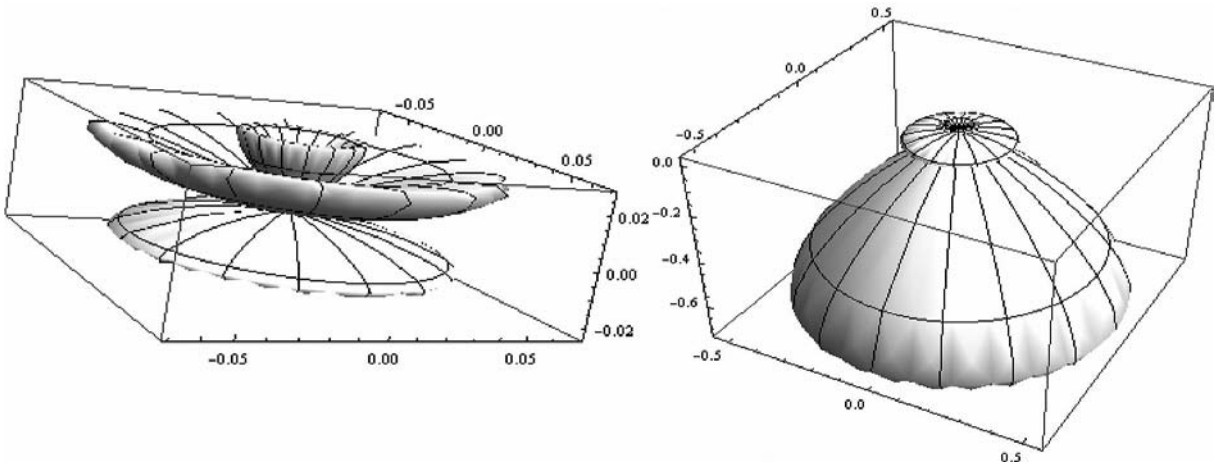

Fig. 4. SFG radiation pattern for L $= 1\mu$m, $\lambda_{SFG} = 0.532$ μm, $\frac{Re\beta_{z\rho\phi}}{Im\beta_{z\rho\phi}} = 1$. Left: weak attenuation$\tilde{k}' = 2k$. Right: strong attenuation $\tilde{k}' = \tilde{k}'' = 10^4 k$.

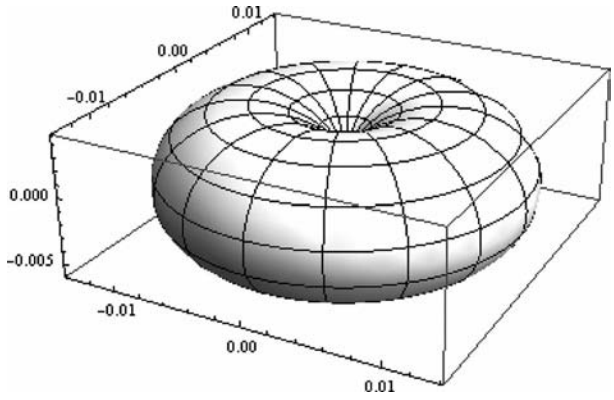

Fig. 5. SFG radiation pattern for L $= 10$ μm and $\lambda_{SFG} = 0.532$ μm.

the SFG backscattered lobe can be used, in principle, to estimate the magnitude, or at least to set an upper limit, of the CNT the longitudinal optical conductivity. On the basis of the qualitative assumption of Burke et al. [18], that retarded waves in CNTs are mostly due to electrons at the Fermi level it is possible to assume that $\sigma \approx \mathrm{v}_F$, where v_F is the Fermi velocity. This makes possible an estimation of $\frac{\omega_{SFG}}{\pi R X Re\sigma}$, which for $q \approx k$, $\mathrm{v}_F \approx 10^{-2}c$, $R = 1$ nm and at optical frequencies turns to be nearly one order of magnitude greater than k^2, thus theorizing a strong attenuation regime in CNTs. Nevertheless, the assumption $q \approx k$ while holds for a conducting wire antenna, it is not justified in CNTs [12]. At the same time, models [19] based on band energy structures for electrons in a SWCNTs, demonstrate that also other energy levels contribute significantly to σ thus questioning the $\sigma \approx \mathrm{v}_F$ assumption. In addition, it should be pointed out that the present treatment takes into account only the axial component of the induced current density. Neglecting the circumferential component is less justified in CNTs of larger diameter, where weak retardation regime is more likely to occur. Moreover, while the truncation at the zero order term for the series expansion of $\tilde{J}_z^{SFG}$ has been demonstrated to be a good approximation for linear scattering [12] by comparing the approximated solution with those obtained with direct numerical methods, for the SFG process this verification still lacks and deserves further studies.

All these considerations add up and make the here presented model just a starting point for accurate simulations of SFG radiation pattern in chiral SWCNTs.

4. Conclusions

In the present paper the study of the process of Sum Frequency Generation from a chiral Single Wall Carbon Nanotube has been addressed. First, a calculation method based on line group theory has been used to validate the assumption that the process is symmetry allowed for a collinear geometry where the two non-degenerate exciting laser beams propagate along the CNT symmetry axis. Subsequently, the radiation pattern for this experimental geometry has been simulated by adapting to nonlinear interaction the formalism developed by Slepyan et al. to calculate the linear Rayleigh scattering pattern from a CNT. It has been found that the SFG radiation pattern is rather sensitive to the magnitude of CNT physical quantities like the longitudinal optical conductivity and the real and imaginary parts of the first hyperpolarizability, as also demonstrated by numerical simulations for particular scattering regimes. Nevertheless, to ascertain the feasibility of such a kind of measurements in order to compare theoretic predictions with experimental outcomes, calculations of the magnitude of $\beta_{zxy}\left(\omega_1+\omega_2;\omega_1,\omega_2\right)$ are also underway to estimate the SFG efficiency and the occurrence of resonances enhancing the process quantum yield.

References

[1] P.J.F. Harris, *Carbon Nanotubes Science* Cambridge University Press, 2009.
[2] S.O. Konorov, D.A. Akimonv, A.A. Ivanov, M.V. Alfimov, R. Ciardi, L. De Dominicis, L. Asilyan, A.A. Podshivalov, D.A. Sidorov-Byriukov, R. Fantoni and A.M. Zheltikov, *Las Phys* **13** (2003), 1279.
[3] S.O. Konorov, D.A. Akimonv, A.A. Ivanov, M.V. Alfimov, R. Ciardi, L. De Dominicis, L. Asilyan, A.A. Podshivalov, D.A. Sidorov-Byriukov, R. Fantoni and A.M. Zheltikov, *J Raman Spectrosc* **34** (2003), 1018.
[4] G.Y. Guo, K.C. Chu, D.S. Wang and G. Duan, *Phys Rev B* **69** (2004), 205416.
[5] L. De Dominicis, R. Fantoni, S. Botti and L. Asylian, *Las Phys Lett* **1** (2004), 598.
[6] L. De Dominicis, R. Fantoni, S. Botti, R. Ciardi, A Fiori, S. Orlanducci, L. Asylian, L. Terranova and R. Appolloni, *Appl Phys Lett* **85** (2004), 1418.
[7] L. De Dominicis, R. Fantoni, S. Botti, R. Ciardi, A Fiori, S. Orlanducci and L. Asylian, *J Raman Spectrosc* **36** (2005), 165.
[8] H.M. Su, J.T. Ye, Z.K. Tang and K.S. Wong, *Phys Rev B* **77** (2008), 125428.
[9] L. De Dominicis and R. Fantoni, *J Raman Spectrosc* **40** (2009), 840.
[10] M. Damnjanović, I. Milošević, T. Vuković and R. Sredanović, *Phys Rev B* **60** (1999), 2728.
[11] I. Milošević, *Phys Lett A* **204** (1995), 63.
[12] G.Y. Slepyan, M.V. Shuba, S.A. Maksimenko and A. Lakhtakia, *Phys Rev B* **73** (2006), 195416.
[13] The generic element of the group G, in the Koster-Seitz notation, is of the form $(R\,|(v+t)a)$ where R is a proper or improper rotation around a fixed point chosen to lie on cylinder axis, whereas $v \in$[0,1) and $t = 0, \pm 1, \pm 2 \ldots$, determine a fractional and pure translation, respectively, along the same line.
[14] M. Damnjanović and I. Milošević, *Phys Rev B* **47** (1993), 7805.
[15] I.B. Božović, M. Vujičić and F. Herbut, *J Phys A* **11** (1978), 2133.
[16] I.B. Božović and M. Vujičic, *J Phys A* **14** (1981), 777.
[17] J.F. Cornwell, *Selected Topics in Solid State Physics*, North Holland, Amsterdam, 1969.
[18] P.J. Burke, S. Li and Z. Yu, cond-mat/0408418 (unpublished).
[19] G.Y. Slepyan, O. Yevtushenko, S.A. Maksimenko, A. Lakhtakia and A.V. Gusakov, *Phys Rev B* **60** (1999), 17136.

Journal of Computational Methods in Sciences and Engineering 10 (2010) 225–242
DOI 10.3233/JCM-2010-0343
IOS Press

Gaussian basis sets for *ab initio* calculation of NLO properties of polyatomic molecules

Diego Paschoal[a], Marcello F. Costa[b], Georgia M.A. Junqueira[a] and Hélio F. Dos Santos[a,*]
[a]*NEQC: Núcleo de Estudos em Química Computacional, Departamento de Química – ICE, Universidade Federal de Juiz de Fora. Campus Universitário, 36.036-330, Juiz de Fora – MG, Brasil*
[b]*LMMB: Laboratório de Modelagem de Moléculas Bioativas, Departamento de Física – CCE, Universidade Estadual de Londrina. Campus Universitário, 86051-990, Londrina – PR, Brasil*

Abstract. In this paper, basis sets for H, C, N and O atoms were adjusted to obtain electric properties of diatomic molecules. The dipole moment, polarizability and first-order hyperpolarizability were calculated for H_2, CH^+, CN^- and CO molecules and the basis sets modified to reproduce the reference data available. A sequential methodology was used, where the basis set for H is firstly adjusted and then used to fit the basis set for C in the CH^+ molecule and so on. The final basis sets were (7s2p1d)→[3s2p1d] for H and (9s5p2d)→[5s3p2d] for C and O. In the case of N atom, the best basis set was found to be (9s5p1d)→[5s3p1d], where only one set of d polarization functions was needed. The atomic basis sets fitted were further utilized for calculation of geometry and electric properties of 36 benzene derivatives mono- and di-substituted by electron donor and acceptor groups attached at *ortho*, *meta* and *para* positions. The results were satisfactory for most of molecules. For instance, in the case of *p*-nitroaniline, an important *push-pull* benzene derivative, the first hyperpolarizability was predicted to be 9.4×10^{-30} e.s.u. in excellent agreement with experimental value, 9.2×10^{-30} e.s.u.. Besides electric properties, our basis sets also gave good geometries for polyatomic molecules at reasonable computational cost. Therefore, the results reported in the present paper suggest the use of our modified basis sets for calculation of geometry and electric properties (linear and non-linear) of *push-pull* benzene derivatives like molecules.

Keywords: *ab initio*, electrical properties, Gaussian basis set, hyperpolarizability, NLO

1. Introduction

Investigation of molecular materials that have nonlinear optics (NLO) properties has been subject of intensive studies because their potential technological applications, such as the telecommunications industry, laser technology and the development of optical fibers. These materials interact with electromagnetic applied fields generating new fields, altered in frequency or phase [1–3]. The interaction of light or other electromagnetic fields with a molecule can polarize the charge distribution and alter the propagated field. The linear response of the field is described by molecular polarizability and the nonlinear responses are represented by molecular hyperpolarizabilities [4]. Development of optical switches, frequency converters and electro optics modulators are examples of potential uses of these materials [5]. Besides the technological applications, molecular electric properties are also important in the interpretation of a wide range of phenomena, from intermolecular interactions to NLO processes [6–9]. These

*Corresponding author. H.F. Dos Santos, E-mail: helio.santos@ufjf.edu.br.

properties are also related with intrinsic features of electronic structure such as softness/hardness [10], acidity/basicity. [11,12] and ionization potential [11,12].

In general, the experimental determination of electric properties is a difficult task [13,14] and therefore, theoretical methods based on quantum mechanics theory have become an useful alternative to overcome this drawback and assist the experimentalists [15–17]. Several authors have achieved success with the calculation of reliable values for these properties. Sadlej et al. [18–22] reported in a series of works new basis sets obtained from the basis set polarization method, suitable for highly accurate correlated calculations of electric properties of small molecules. Neogrady et al. [23] present a study of dipole moment and polarizability of CN^- and Maroulis et al. [7,24,25] also reported accurate calculated values of polarizability and hyperpolarizabilities of the H_2, N_2 and CO molecules. More recently, Paschoal et al. [26] reported a study about *ab initio* calculation of electric properties for BH, CO, CS and N_2 molecules, defining new atomic basis sets.

Regarding molecular NLO properties, it is longer recognized that organic compounds with delocalized π-electrons are likely to have intensified NLO responses, with the interest in such systems increasing considerably in recent years [27–31]. The development of organic materials with potential application in NLO involves different branches of science such as physics, chemistry and engineering. Quantum chemistry calculations have also been of great importance in the study of these systems, especially with regard to electronic structure and polarization effects of these compounds [30]. Systems with donor and acceptor groups represent an important class of NLO chromophores [32,33], being the p-nitroaniline the most famous representative.

In general, electric properties are strongly dependent on the theoretical method; therefore, highly correlated methods with extended basis set usually give satisfactory results. However, such levels of theory are restricted to relatively small molecules. An alternative is to develop a suitable basis set in order to reach the desired precision at a feasible computational cost [34,35]. Thus, the construction of a relatively small basis set, flexible and properly polarized is very relevant to the calculation of electrical properties for large polyatomic molecules. In the present paper, we report new atomic Gaussian basis set for *ab initio* calculations of dipole moment, polarizability and hyperpolarizabilities for organic molecules derived from *push-pull* substituted benzene. The diatomic molecules H_2, CH^+, CN^- and CO were used to firstly fit the basis set, once these molecules have been mostly studied as model compounds to evaluate the performance of different levels of theory [7–9,24,25,36–39,41]. The available experimental and theoretical values for electrical properties for these diatomic molecules constitute a broad databank to be used in the adjustment and construction of new basis sets.

2. Theoretical methodology

The interaction energy of a molecule with an external electric field can be written as a series involving coefficients identified as permanent multipole moments and polarizabilities. Following McLean and Yoshimine [42], when a linear molecule is placed in the presence of an external electric field its energy is modified according to Eq. (1) [8].

$$\begin{aligned} E^p = {} & E^0 - \mu_\alpha F_\alpha - (1/3)\,\Theta_{\alpha\beta}F_{\alpha\beta} - (1/15)\,\Omega_{\alpha\beta\gamma}F_{\alpha\beta\gamma} - (1/105)\,\Phi_{\alpha\beta\gamma\delta} + \ldots - \\ & - (1/2)\,\alpha_{\alpha\beta}F_\alpha F_\beta - (1/3)\,A_{\alpha,\beta\gamma}F_\alpha F_{\beta\gamma} - (1/6)\,C_{\alpha\beta,\gamma\delta}F_{\alpha\beta}F_{\gamma\delta} - (1/15)\,E_{\alpha,\beta\gamma\delta}F_\alpha F_{\beta\gamma\delta} + \\ & + \ldots - (1/6)\,\beta_{\alpha\beta\gamma}F_\alpha F_\beta F_\gamma - (1/6)\,B_{\alpha\beta,\gamma\delta}F_\alpha F_\beta F_{\gamma\delta} + \ldots - (1/24)\,\gamma_{\alpha\beta\gamma\delta}F_\alpha F_\beta F_\gamma F_\gamma + \ldots \end{aligned} \quad (1)$$

Where F_α, $F_{\alpha\beta}$, etc., are the field, field gradient, etc. at the origin. E^0 and μ_α are the energy and the permanent dipole moment. The quantities $\alpha_{\alpha\beta}$, $\beta_{\alpha\beta\gamma}$, $\gamma_{\alpha\beta\gamma\delta}$ are the dipole polarizability, the first and the second dipole hyperpolarizabilities. The subscripts represent the Cartesian coordinates.

In the presence of a homogeneous electric field the Eq. (1) is reduced to Eq. (2) [8,43].

$$E^p = E^0 - \mu_\alpha F_\alpha - (1/2)\,\alpha_{\alpha\beta}F_\alpha F_\beta - (1/6)\,\beta_{\alpha\beta\gamma}F_\alpha F_\beta F_\gamma - (1/24)\,\gamma_{\alpha\beta\gamma\delta}F_\alpha F_\beta F_\gamma F_\gamma + . \quad (2)$$

Where $E^p = E(F_x, F_y, F_z)$, denotes the energy of the molecule in the presence of a homogeneous field with components F_x, F_y, F_z.

Following the Finite Field (FF) method [44], the multipole moments and polarizabilities of diatomic molecules can be obtained by numerical differentiation of energy calculated in the presence of different intensities of applied electric fields, as given by Eq. (3) [8].

$$\mu_z = \left(256D_z\left(F\right) - 40D_z\left(2F\right) + D_z\left(4F\right)\right)/\left(180F\right) \quad (3a)$$

$$\alpha_{zz} = \left(1024S_z\left(F\right) - 80S_z\left(2F\right) + S_z\left(4F\right)\right)/\left(360F^2\right) \quad (3b)$$

$$\alpha_{xx} = \left(1024S_x\left(F\right) - 80S_x\left(2F\right) + S_x\left(4F\right)\right)/\left(360F^2\right) \quad (3c)$$

$$\beta_{zzz} = \left(-64D_z\left(F\right) + 34D_z\left(2F\right) - D_z\left(4F\right)\right)/\left(24F^3\right) \quad (3d)$$

$$\beta_{zxx} = \left(32D_{xz}\left(F\right) - D_{xz}\left(2F\right)\right)\left(12F^3\right) \quad (3e)$$

$$\gamma_{zzzz} = \left(-256S_z\left(F\right) + 68S_z\left(2F\right) - S_z\left(4F\right)\right)/\left(24F^4\right) \quad (3f)$$

$$\gamma_{xxxx} = \left(-256S_x\left(F\right) + 68S_x\left(2F\right) - S_x\left(4F\right)\right)/\left(24F^4\right) \quad (3g)$$

$$\gamma_{xxzz} = \left(64S_{xz}\left(F\right) - S_{xz}\left(2F\right)\right)/\left(12F^4\right) \quad (3h)$$

Where,

$$S_z\left(F\right) = \left(2E^0 - E\left(0,0,F\right) - E\left(0,0,-F\right) + E\left(0,0,F\right)\right)/2 \quad (4a)$$

$$D_z\left(F\right) = \left(E\left(0,0,-F\right) - E\left(0,0,F\right)\right)/2 \quad (4b)$$

$$S_x\left(F\right) = \left(E^0 - E\left(F,0,0\right)\right) \quad (4c)$$

$$S_{xz}\left(F\right) = \left(-2E^0 - E\left(F,0,F\right) - E\left(F,0,-F\right) + E\left(0,0,F\right) + E\left(0,0,-F\right) + 2E\left(F,0,0\right)\right)/2 \quad (4d)$$

$$D_{xz}\left(F\right) = \left(-E\left(F,0,F\right) + E\left(F,0,-F\right) + E\left(0,0,F\right) - E\left(0,0,-F\right)\right)/2 \quad (4e)$$

We also calculate the average values and anisotropies for some properties of diatomic molecules, as defined by Eq. (5) [8,43].

$$\langle\alpha\rangle = \left(\alpha_{zz} + 2\alpha_{xx}\right)/3 \quad (5a)$$

$$\Delta\alpha = \alpha_{zz} - \alpha_{xx} \quad (5b)$$

$$\langle\beta\rangle = (3/5)\left(\beta_{zzz} + 2\beta_{zxx}\right) \quad (5c)$$

$$\Delta\beta = \beta_{zzz} - 3\beta_{zxx} \tag{5d}$$

$$\langle\gamma\rangle = \left(3\gamma_{zzzz} + 8\gamma_{xxxx} + 12\gamma_{xxzz}\right)/15 \tag{5e}$$

$$\Delta_1\gamma = 3\gamma_{zzzz} - 4\gamma_{xxxx} + 3\gamma_{xxzz} \tag{5f}$$

$$\Delta_2\gamma = \gamma_{zzzz} + \gamma_{xxxx} - 6\gamma_{xxzz} \tag{5g}$$

In the present work all properties for the diatomic molecules were calculated applying weak homogeneous electric fields of 0.005 (F), 0.01 (2F) and 0.02 $e^{-1}a_0^{-1}E_h$ (4F) (the conversion factors to SI units are given in the Appendix). Calculations at various levels of theory were carried out, including Hartree-Fock (HF), Möller-Plesset perturbation theory (MP2, MP3, MP4(SDQ) and MP4(SDTQ)) and coupled-cluster (CCSD and CCSD(T)) using the GAUSSIAN 03 program [45].

Standard contracted Gaussian basis set (CGTO) was used in the calculations, modified by adding some extra basis. The general procedure followed to fit the exponents (ξ) of radial Gaussian functions is described below:

1. Select a reference basis set. In the present work, the Dunning double-zeta (DZ) basis set [46] was chosen, which is represented by the scheme (9s5p/4s)→[4s2p/2s] for C, N, O/H atoms;
2. The selected basis set is uncontracted and then, new sets of functions with the same angular momentum of the existing one are added;
3. Fit the exponents of new functions by minimizing the molecular energy at HF level;
4. The basis set is contracted again following the protocol described elsewhere [47] and then, new sets of polarization and diffuse functions are added;
5. Fit the exponents of polarization and diffuse functions by minimizing the molecular energy at HF level;
6. Optimize the geometry and calculate properties at CCSD(T) level;
7. Compare the values with reference data, by calculating the RMS as in Eq. (6).

$$RMS = \sqrt{\frac{1}{N}\sum_{i=1}^{N}\left(\frac{P_i - P_i^R}{P_i^R}\right)^2} \tag{6}$$

Where P_i is the electric property and P_i^R its reference value. The properties used were, when available, the dipole moment, average polarizability, first and second hyperpolarizabilities. The steps 4 to 7 are repeated until the RMS reaches the threshold established, usually below 1.0.

The final basis sets obtained for atoms in diatomic molecules were further used to calculate geometries and electric properties for *push-pull* benzene derivatives. HF, DFT (B3LYP) and MP2 levels of theory were applied to calculate the electric dipole moment, the mean polarizability Eq. (7) [48] and the intrinsic quadratic hyperpolarizability, also named total hyperpolarizability Eq. (8) [48].

$$<\alpha> = \frac{1}{3}(\alpha_{xx} + \alpha_{xy} + \alpha_{zz}) \tag{7}$$

$$<\beta> = \sqrt{\beta_x^2 + \beta_y^2 + \beta_z^2} \tag{8}$$

With [48]

$$\beta_i = \beta_{iii} + \sum_{i \neq k} (\beta_{ikk} + \beta_{kik} + \beta_{kki}) \tag{9}$$

Where i and j run over the molecular Cartesian directions x, y, and z. All the calculations for polyatomic molecules were carried out using GAUSSIAN 03 program [45].

3. Results and discussion

3.1. Basis set development:

The diatomic molecules used to the basis set development were H_2, CH^+, CN^- and CO. We applied the protocol described in the last section in a sequential way, where the basis set fitted for H atom, using the H_2 molecule, is used in CH^+ molecule to obtain the basis set for C. The latter is used in CN^- and CO calculations to adjust the basis set for N and O atoms, respectively.

We begin the discussion with the H_2 molecule in order to firstly adjust the basis set for H atom. As stated before the Dunning double zeta (DZ) basis set were chosen as initial guess for all atoms, being defined as (4s) $\rightarrow$ [2s] for H atom. The procedure of fitting basis set, described in the last section, was applied for H_2 molecule, with final basis set, giving the lowest RMS value, including three new s functions ($\xi_s = 8.109$; $\xi_s = 1.7669$; $\xi_s = 0.051652$), two p ($\xi_p = 0.66536$; $\xi_p = 0.077379$) and one set of d polarization functions ($\xi_d = 0.086804$). The new contracted basis set was (7s2p1d) $\rightarrow$ [3s2p1d].

The electric properties calculated for H_2 molecule are gathered in Table S1. For this molecule only the mean polarizability is known experimentally ($< \alpha >= 5.31$. [49]). The calculated values, using the experimental geometry, R = 0.7361 Å [50], ranged from 4.94 (HF) to 4.88 (CCSD(T)), which are within 8% from actual value. When optimized geometry is used, the agreement is better with $< \alpha >$ found 4.98 and 5.00 at MP2 and CCSD(T) levels, respectively. All the theoretical data available in the literature were obtained using the experimental geometry. Maroulis and Bishop [25] reported the values of $< \alpha >=$ 5.08, $\alpha_{zz} = 6.38$ and $< \gamma >= 670$ at HF level with the larger basis set (11s5p2d) $\rightarrow$ [8s5p2d]. Our results were $< \alpha >= 4.94$, $\alpha_{zz} = 6.36$ and $< \gamma >= 732$ at HF level, in satisfactory agreement with Maroulis and Bishop's values (deviation lower than 10%). In addition to electric properties we also calculated vibrational frequency. For H_2 molecule the values were found between 4563 (HF) and 4355 cm^{-1} (CCSD(T)) in good accordance to the experimental frequency of 4401 cm^{-1} [25].

The next step was to modify the DZ basis set for C atom, using the CH^+ molecule as reference system. For C, N and O atoms the DZ basis set is represented as (9s5p) $\rightarrow$ [4s2p]. The lowest RMS value was found when only two sets of d polarization functions were added ($\xi_d = 0.63212$; $\xi_d = 0.130721$) and the basis set re-contracted according to (9s5p2d) $\rightarrow$ [5s3p2d]. Thus, the full basis set used in the calculations for the CH^+ cation is represented by: (9s5p2d/7s2p1d) $\rightarrow$ [5s3p2d/3s2p1d] for C/H. For CH^+ molecule, only few data are available in the literature. Maroulis and Bishop [39] obtained $< \alpha >=$ 7.73 at HF/[8s6p4d/6s4p] level that is close to ours $< \alpha >= 7.68$ calculated at lower computational cost HF/[5s3p2d/3s2p1d]. The difference between our values and those obtained by Maroulis and Bishop [39] was 18% for the dipole moment and average first dipole hyperpolarizability and, 28% for the average second dipole hyperpolarizability, with our values found lower. The optimized geometry with the new basis set was also in satisfactory agreement with experimental value of 1.1309 Å [50], with deviation within 1% regardless the level of theory. The vibrational frequency was also predicted in excellent

Table S1
Dipole moment, polarizability, first and second hyperpolarizabilities tensor components (α_{ij}, β_{ijk} and γ_{ijkw}), average polarizability, first and second hyperpolarizabilities ($\langle\alpha\rangle$, $\langle\beta\rangle$, $\langle\gamma\rangle$) and anisotropies ($\Delta\alpha$, $\Delta\beta$, $\Delta\gamma$) for H_2 molecule (values in a.u.)

	HF	MP2	MP3	MP4(SDQ)	MP4(SDQT)	CCSD	CCSD(T)
α_{xx}	4.25	4.24	4.24	4.24	4.24	4.24	4.24
	[4.24]	[4.19]	[4.17]	[4.17]	[4.17]	[4.16]	[4.16]
α_{zz}	6.38	6.44	6.48	6.50	6.50	6.51	6.51
	[6.36]	[6.35]	[6.35]	[6.34]	[6.34]	[6.34]	[6.34]
$\Delta\alpha$	2.13	2.20	2.24	2.26	2.26	2.27	2.27
	[2.12]	[2.15]	[2.17]	[2.18]	[2.18]	[2.18]	[2.18]
$\langle\alpha\rangle$	4.96	4.98	4.99	5.00	5.00	5.00	5.00
	[4.94]	[4.91]	[4.90]	[4.89]	[4.89]	[4.88]	[4.88]
γ_{zzzz}	625	687	701	710	710	715	715
	[621]	[671]	[677]	[683]	[683]	[685]	[685]
γ_{xxxx}	845	911	925	929	929	928	928
	[840]	[892]	[899]	[897]	[897]	[893]	[893]
γ_{xxzz}	202	219	221	224	224	225	225
	[200]	[213]	[213]	[214]	[214]	[214]	[214]
$\Delta_1\gamma$	-898	-925	-932	-912	-912	-892	-892
	$[-895]$	$[-917]$	$[-925]$	$[-898]$	$[-898]$	$[-876]$	$[-876]$
$\Delta_2\gamma$	261	285	300	296	296	295	295
	[260]	[283]	[296]	[296]	[296]	[214]	[214]
$\langle\gamma\rangle$	737	798	810	816	816	817	817
	[732]	[781]	[786]	[787]	[787]	[785]	[785]
R	0.7382	0.7436	0.7467	0.7485	0.7485	0.7500	0.7500
ν	4563	4471	4419	4386	4387	4354	4355

The first entries refer to the calculations performed at the optimized geometry and the entries in brackets refer to the calculations performed at the experimental geometry. Experimental values: $<\alpha>= 5.31$ [49], $R = 0.7361$ Å [50], $\nu = 4401$ cm^{-1} [50].

agreement with the experiment, with larger error found at HF level where the calculated value was 7% higher. All properties calculated for CH^+ are given in Table S2.

The basis set for N atom was fitted taking the CN^- molecule as template, which basis set for C was taken from CH^+ molecule. The final basis set was (9s5p1d) → [5s3p1d] ($\xi_d = 1.20135$), which differs from C by only one set of d polarization functions. The basis set for CN^- molecule is then represented as (9s5p2d/9s5p1d) → [5s3p2d/5s3p1d] for C/N. The calculated properties are included in Table S3. Besides bond length and vibrational frequency, only the dipole moment is known experimentally ($\mu =$ 0.57 D [51]). For the latter our results are poor, being 60% lower at HF level and around 40% at all correlated levels of theory. At the limit of complete basis set (CBS), the results from Neogrady et al. [23] for dipole moment was only 11% lower at CCSD(T) level. Nonetheless, our predicted values for the other electric properties are in fairly good agreement with those described in the literature calculated at larger basis set. Neogrady et al. [23] report $\alpha_{zz} = 20.06$ at HF/aug-cc-pV6Z level, being our value equal to 25.23 at HF level. At CCSD(T)/CBS the value of α_{zz} given by Neogrady et al. [23] was 25.23 in excellent accordance with the value from present work, 25.96. The previous results suggest that our basis set might be a better choice even for HF calculation. Bond length and calculated vibrational frequency were also predicted close to the actual value for CN^- molecule as shown in Table S3.

The last step before calculating properties of benzene derivatives was to fit the basis set for O atom using CO molecule as standard system. For this molecule many experimental data are available for μ (0.0484 ± 0.0008 [52], 0.0481 [53]), $<\alpha>$ (13.0891 [54]), $\Delta\alpha$ (3.59 ± 0.07 [55], 3.58 ± 0.13 [56], 3.54. [57], 3.66 ± 0.13 [58]), $<\beta>$ (30.2 ± 3.2 [33]) and $<\gamma>$ (1730 ± 50 [33]). The DZ basis set was re-contracted and two sets of d polarization functions added ($\xi_d = 1.09213$, $\xi_d = 0.6437$)

Table S2
Polarizability, first and second hyperpolarizabilities tensor components (α_{ij}, β_{ijk} and γ_{ijkw}), average polarizability, first and second hyperpolarizabilities ($\langle\alpha\rangle$, $\langle\beta\rangle$, $\langle\gamma\rangle$), anisotropies ($\Delta\alpha$, $\Delta\beta$, $\Delta\gamma$) for CH^+ molecule (values in a.u.)

	HF	MP2	MP3	MP4(SDQ)	MP4(SDQT)	CCSD	CCSD(T)
μ	0.6161	0.5752	0.5501	0.5328	0.5330	0.5097	0.5046
	[0.6164]	[0.5752]	[0.5505]	[0.5337]	[0.5338]	[0.5104]	[0.5054]
α_{xx}	7.54	7.29	7.10	6.97	6.98	6.83	6.81
	[7.54]	[7.29]	[7.09]	[6.97]	[6.97]	[6.83]	[6.91]
α_{zz}	7.78	8.15	8.32	8.41	8.42	8.47	8.52
	[7.96]	[8.14]	[8.23]	[8.29]	[8.29]	[8.35]	[8.39]
$\Delta\alpha$	0.24	0.87	1.22	1.44	1.45	1.64	1.71
	[0.42]	[0.86]	[1.13]	[1.32]	[1.32]	[1.53]	[1.58]
$\langle\alpha\rangle$	7.62	7.58	7.50	7.45	7.46	7.38	7.38
	[7.68]	[7.57]	[7.47]	[7.41]	[7.41]	[7.33]	[7.33]
β_{zzz}	−13.4	−15.4	−15.7	−15.6	−15.7	−14.6	−14.7
	[−14.4]	[−15.3]	[−15.2]	[−15.1]	[−15.1]	[−14.1]	[−14.2]
β_{zxx}	−1.4	0.4	1.5	2.2	2.2	2.9	3.1
	[−1.2]	[0.3]	[1.4]	[2.1]	[2.1]	[2.9]	[3.0]
$\Delta\beta$	−9.2	−16.5	−20.1	−22.3	−22.4	−23.4	−24.1
	[−10.8]	[−16.4]	[−19.4]	[−21.5]	[−21.5]	[−22.7]	[−23.3]
$\langle\beta\rangle$	−9.7	−8.8	−7.6	−6.7	−6.8	−5.3	−5.1
	[−10.1]	[−8.8]	[−7.5]	[−6.5]	[−6.5]	[−5.0]	[−4.9]
γ_{zzzz}	598	676	689	686	682	863	899
	[619]	[675]	[684]	[677]	[676]	[850]	[869]
γ_{xxxx}	131	171	188	194	198	1203	1269
	[131]	[171]	[197]	[211]	[198]	[1178]	[1244]
γ_{xxzz}	67	67	68	56	56	221	242
	[68]	[67]	[68]	[65]	[57]	[217]	[230]
$\Delta_1\gamma$	1474	1546	1519	1451	1424	−1561	−1652
	[1537]	[1542]	[1469]	[1385]	[1408]	[−1511]	[−1678]
$\Delta_2\gamma$	324	448	469	541	542	740	717
	[340]	[447]	[470]	[495]	[533]	[724]	[734]
$\langle\gamma\rangle$	243	280	293	286	287	991	1050
	[249]	[279]	[296]	[300]	[286]	[972]	[1021]
R	1.1182	1.1316	1.1370	1.1394	1.1398	1.1390	1.1400
ν	3054	2921	2869	2845	2839	2836	2826

The first entries refer to the calculations performed at the optimized geometry and the entries in brackets refer to the calculations performed at the experimental geometry. Experimental values: R = 1.1309 Å [50], $\nu = 2859$ cm^{-1} [50].

yielding the final basis set (9s5p2d) → [6s3p2d] for O atom and the full basis set (9s5p2d/9s5p2d) → [5s3p2d/6s3p2d] for C/O. The calculated properties are included in Table S4 at several levels of theory. Firstly analyzing the HF values calculated using the experimental geometry (R = 1.1283 Å [50]), we found $\mu = 0.1011$ (110%), $< \alpha >= 11.55$ (12%), $\Delta\alpha = 3.25$ (9%), $< \beta >= 34.1$ (13%) and $< \gamma >=$ 398 (77%), where absolute deviations are given in parenthesis. When the level of theory is improved to MP4(SDQ) the errors decrease significantly for μ (22%), $< \alpha >$ (8%) and $\Delta\alpha$ (2%). For $< \beta >$ and $< \gamma >$ the deviations were of the same order, with a slightly improvement in $< \gamma >$ value, leading to a deviation of 68% from experimental value. At our highest level of theory, CCSD(T), the values were close to MP4(SDQ) ones as noted in Table S4. The other properties are not much affected by electronic correlation. It is interesting to compare our results with those calculated with larger basis set. The data from Maroulis [7] at HF/[6s4p4d2f] were $\mu = 0.1052$, $< \alpha >= 12.307$, $< \beta >= 24.75$ and $< \gamma >=$ 1008, showing a better agreement to the experiment for $< \beta >$ and $< \gamma >$ values. The results from our previous paper [26] using a slightly larger basis set [6s3p5d/6s3p4d] also give $< \beta >$ (= 25.2) and

Table S3
Polarizability, first and second hyperpolarizabilities tensor components (α_{ij}, β_{ijk} and γ_{ijkw}), average polarizability, first and second hyperpolarizabilities ($\langle\alpha\rangle$, $\langle\beta\rangle$, $\langle\gamma\rangle$), anisotropies ($\Delta\alpha$, $\Delta\beta$, $\Delta\gamma$) for CN^- molecule (values in a.u.)

	HF	MP2	MP3	MP4(SDQ)	MP4	CCSD	CCSD(T)
μ	−0.2218	−0.3949	−0.3392	−0.3373	−0.3646	−0.3362	−0.3537
	[−0.2051]	[−0.3966]	[−0.3388]	[−0.3415]	[−0.3708]	[−0.3388]	[−0.3584]
α_{xx}	17.35	18.52	18.21	18.35	18.70	18.41	18.72
	[17.50]	[18.41]	[18.21]	[18.28]	[18.56]	[18.37]	[18.63]
α_{zz}	4.69	25.72	25.53	25.88	26.36	25.89	26.31
	[25.23]	[25.26]	[25.55]	[25.60]	[25.77]	[25.72]	[25.96]
$\Delta\alpha$	0.34	7.20	7.32	7.53	7.66	7.48	7.59
	[7.73]	[6.85]	[7.34]	[7.32]	[7.21]	[7.36]	[7.32]
$\langle\alpha\rangle$	19.80	20.92	20.65	20.86	21.25	20.90	21.25
	[20.08]	[20.70]	[20.66]	[20.72]	[20.96]	[20.82]	[21.07]
β_{zzz}	−65.2	−59.1	−63.7	−67.3	−74.1	−65.4	−69.6
	[−66.6]	[−58.9]	[−63.7]	[−66.7]	[−71.9]	[−65.1]	[−68.9]
β_{zxx}	−34.1	−36.6	−37.1	−37.3	−39.4	−37.7	−39.3
	[−35.1]	[−35.8]	[−37.2]	[−36.8]	[−38.2]	[−37.4]	[−38.7]
$\Delta\beta$	37.1	50.7	47.7	44.7	44.2	47.9	48.2
	[38.6]	[48.5]	[47.8]	[43.8]	[42.8]	[47.2]	[47.3]
$\langle\beta\rangle$	−80.1	−79.4	−82.8	−85.2	−91.8	−84.5	−88.9
	[−82.1]	[−78.3]	[−82.8]	[−84.2]	[−89.1]	[−84.0]	[−87.8]
γ_{zzzz}	582	671	649	756	839	827	792
	[590]	[653]	[649]	[737]	[802]	[657]	[698]
γ_{xxxx}	514	514	569	579	565	576	590
	[511]	[524]	[552]	[573]	[575]	[419]	[412]
γ_{xxzz}	157	112	135	143	139	195	140
	[160]	[111]	[127]	[135]	[137]	[81]	[81]
$\Delta_1\gamma$	160	292	74	381	674	762	436
	[207]	[197]	[117]	[324]	[517]	[538]	[691]
$\Delta_2\gamma$	153	515	407	479	570	235	543
	[141]	[511]	[442]	[502]	[557]	[590]	[621]
$\langle\gamma\rangle$	516	497	542	574	581	628	585
	[518]	[499]	[526]	[561]	[576]	[420]	[424]
R	1.1527	1.1899	1.1709	1.1825	1.1942	1.1781	1.1851
ν	2326	1987	2195	2062	1939	2114	2053

The first entries refer to the calculations performed at the optimized geometry and the entries in brackets refer to the calculations performed at the experimental geometry. Experimental values: $\mu = 0.57$ [51], R $= 1.1718$ Å [50], $\nu = 2069$ cm^{-1} [50].

$< \gamma >$ (= 968) values in better agreement to the experimental data. Comparing our basis set with the previous ones described in the literature, it can be said that polarization functions may have an important role in describing higher order polarizabilities for CO molecule. It is also worth mention that when geometry is optimized with our basis set, we found an important improvement of results, with absolute error decreasing to 63% for $< \gamma >$ at MP4(SDQ) level of theory (see values in Table S4).

Lately, in Table 1 we summarize the main information about the atomic basis set adjusted in the present work, which were applied for polyatomic benzene derivatives as discussed in the next section.

3.2. Structure and properties of benzene derivatives:

It is longer recognized that *push-pull* benzene derivatives are potential molecules to develop new molecular based NLO devices. In the present section we discuss the results of electric properties for benzene derivatives, including mono- and di-substituted molecules. Our basis sets, discussed in the last

Table S4
Polarizability, first and second hyperpolarizabilities tensor components (α_{ij}, β_{ijk} and γ_{ijkw}), average polarizability, first and second hyperpolarizabilities ($\langle\alpha\rangle$, $\langle\beta\rangle$, $\langle\gamma\rangle$), anisotropies ($\Delta\alpha$, $\Delta\beta$, $\Delta\gamma$) for CO molecule (values in a.u.)

	HF	MP2	MP3	MP4(SDQ)	MP4(SDQT)	CCSD	CCSD(T)
μ	0.0624	−0.1119	−0.0317	−0.0451	−0.0791	−0.0331	−0.0471
	[0.1011]	[−0.1260]	[−0.0293]	[−0.0591]	[−0.1008]	[−0.0410]	[−0.0630]
α_{xx}	10.39	11.08	10.74	10.89	11.08	10.85	10.99
	[10.47]	[11.02]	[10.74]	[10.84]	[10.98]	[10.82]	[10.94]
α_{zz}	3.39	15.05	14.36	14.74	15.03	14.70	14.88
	[13.72]	[14.71]	[14.39]	[14.51]	[14.56]	[14.58]	[14.63]
$\Delta\alpha$	3.00	3.97	3.62	3.85	3.95	3.85	3.89
	[3.25]	[3.70]	[3.64]	[3.67]	[3.58]	[3.76]	[3.69]
$\langle\alpha\rangle$	11.39	12.40	11.95	12.17	12.40	12.13	12.28
	[11.55]	[12.25]	[11.96]	[12.07]	[12.18]	[12.08]	[12.17]
β_{zzz}	−36.7	−36.8	−36.6	−36.4	−35.2	−37.2	−37.3
	[−37.8]	[−36.2]	[−36.7]	[−36.0]	[−35.1]	[−36.9]	[−36.9]
β_{zxx}	−9.3	−12.3	−11.5	−12.4	−13.1	−12.2	−12.9
	[−9.5]	[−11.9]	[−11.4]	[−12.0]	[−12.4]	[−12.2]	[−12.7]
$\Delta\beta$	−8.9	−0.1	−2.0	0.6	4.0	−0.5	1.3
	[−9.2]	[−0.5]	[−2.4]	[0.0]	[2.1]	[−0.5]	[1.1]
$\langle\beta\rangle$	−33.2	−36.8	−35.8	−36.7	−36.8	−37.0	−37.8
	[−34.1]	[−36.0]	[−35.7]	[−36.0]	[−35.9]	[−36.7]	[−37.3]
γ_{zzzz}	448	499	517	569	581	567	639
	[462]	[496]	[538]	[612]	[542]	[462]	[536]
γ_{xxxx}	360	466	446	567	476	479	515
	[361]	[470]	[446]	[482]	[473]	[395]	[470]
γ_{xxzz}	137	158	119	203	160	160	159
	[141]	[157]	[163]	[203]	[160]	[118]	[116]
$\Delta_1\gamma$	316	104	124	45	319	263	331
	[364]	[79]	[318]	[517]	[212]	[162]	[76]
$\Delta_2\gamma$	−16	19	247	−80	97	86	202
	[−22]	[26]	[8]	[-122]	[55]	[149]	[310]
$\langle\gamma\rangle$	391	474	437	578	498	497	530
	[398]	[475]	[476]	[542]	[489]	[397]	[451]
R	1.1080	1.1439	1.1267	1.1402	1.1526	1.1342	1.1413
ν	2412	2093	2284	2118	1969	2195	2125

The first entries refer to the calculations performed at the optimized geometry and the entries in brackets refer to the calculations performed at the experimental geometry. Experimental values: $\mu = 0.0484 \pm 0.0008$ [52]/0.0481, $\langle\alpha\rangle = 13.0891$ [53], $\Delta\alpha = 3.59 \pm 0.07$ [54]/3.58 ± 0.13 [55]/3.54 [56]/3.66 ± 0.13 [57], $\langle\beta\rangle = 30.2 \pm 3.2$ [33], $\langle\gamma\rangle = 1730 \pm 50$ [33], $R = 1.1283$ Å [49], $\nu = 2170$ cm^{-1} [49].

Table 1
Atomic basis sets obtained in present work

		Contraction scheme	#GTO	#CGTO
H	(7s2p1d)→[3s2p1d]	4,2,1(s); 1,1(p); 1(d)	19	15
C	(9s5p2d)→[5s3p2d]	4,2,1,1,1(s); 3,1,1(p); 1,1(d)	36	26
N	(9s5p1d)→[5s3p1d]	4,2,1,1,1(s); 3,1,1(p); 1(d)	30	20
O	(9s5p2d)→[6s3p2d]	3,2,1,1,1,1(s); 3,1,1(p); 1,1(d)	36	27

section and summarized in Table 1, were used for geometry optimization and calculation of properties with all results being compared to the experimental data available and discussed regarding electronic substituent effects.

The Table 2 gathered the results for dipole moment, dipole polarizability and first dipole hyperpolarizability obtained for mono-substituted benzenes at HF, MP2 and B3LYP levels of theory. The electronic

Table 2
Dipole moment (μ), average polarizability ($\langle\alpha\rangle$) and first hyperpolarizability ($\langle\beta\rangle$) for mono-substituted benzene derivatives (units in esu)

X	$\mu/10^{-18}$				$<\alpha>/10^{-23}$				$<\beta>/10^{-30}$				σ_p^a
	HF	MP2	B3LYP	Expt[b]	HF	MP2	B3LYP	Expt[b]	HF	MP2	B3LYP	Expt[b]	
$N(CH_3)_2$	1.9	2.2	2.2	1.6	1.5	1.6	1.6	1.7	3.0	4.3	2.9	1.1	−0.83
NH_2	1.5	1.6	1.7	1.5	1.1	1.2	1.2	1.3	1.9	2.5	2.2	0.55	−0.66
OH	1.5	1.5	1.5	1.5	1.0	1.1	1.1	1.2	1.7	2.2	2.1	0.2	−0.37
OMe	1.5	1.5	1.5	1.4	1.2	1.3	1.3	1.4	1.8	2.5	2.3	0.2	−0.27
CH_3	0.5	0.4	0.5	0.38	1.2	1.2	1.2	1.3	0.5	0.5	0.4	0.2	−0.17
CHO	3.6	3.3	3.6	2.8	1.2	1.3	1.3	1.3	1.0	1.9	1.8	0.80	0.42
CN	4.9	4.3	4.6	3.9	1.2	1.3	1.3	1.3	1.2	1.0	1.7	0.36	0.66
NO_2	4.9	4.1	4.6	4.0	1.2	1.3	1.3	1.4	0.8	0.6	0.7	1.9	0.78
NO	3.4	3.3	3.8	3.1	1.1	1.2	1.2	1.4	0.6	3.1	1.3	1.7	0.91

[a]This parameter stands by the Hammett electronic constant [59], which negative value indicates donor groups and positive value electron-withdrawing substituent.
[b]Experimental values [28].

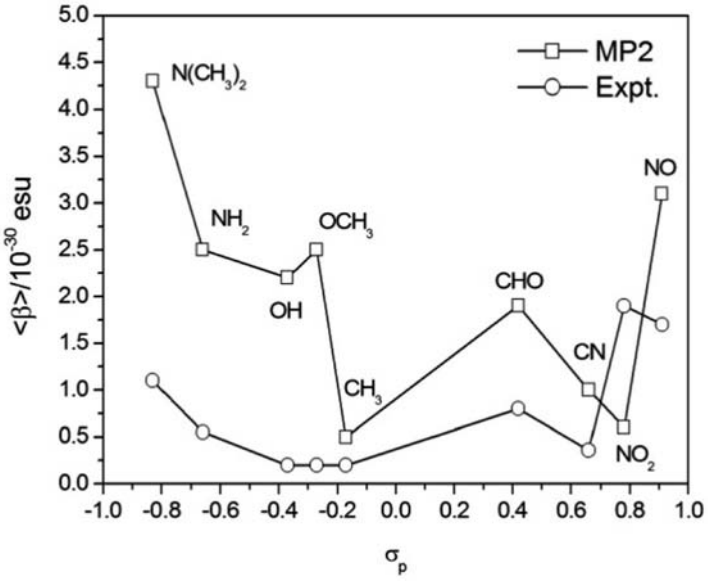

Fig. 1. Calculated (MP2 only) and experimental values of $<\beta>$ for mono-substituted benzene derivatives.

Hammett constants for substituent (σ_p) are also included in the last column of Table 2. Electron-donating substituents (donor groups) present $\sigma_p < 0$ and for electron-withdrawing substituents (acceptor groups) $\sigma_p > 0$. The extent of the electronic effect is given by the magnitude of the substituent constant. Our results for dipole moment and dipole polarizability of all molecules are in good accordance with experimental data obtained by Cheng et al. [28], regardless the level of theory. The highest deviation were 25% for μ (X = CN) and 20% for $<\alpha>$ (X = NO) at HF level. When first hyperpolarizability is considered, no systematic trends are observed throughout the whole series. Using the Hammett electronic index (σ_p) as reference, we can see a decrease in $<\beta>$ value as the donor power decreases from X = $N(CH_3)_2$ ($\sigma_p = -0.83$) to X = CH_3 ($\sigma_p = -0.17$). This is the same trend observed experimentally, even though the absolute calculated values are overestimated. A qualitative agreement with experiment is also observed for the weak to medium acceptor groups CHO ($\sigma_p = 0.42$) and CN ($\sigma_p = 0.66$) as shown

Table 3
Structural parameters, dipole moment, dipole polarizability and first dipole hyperpolarizability calculated for p-nitroaniline (pNA)

	HF[a]	MP2[a]	B3LYP[a]	Expt.
C5-C6	1.376 (0.07%)	1.393 (1.2%)	1.383 (0.4%)	1.377
C6-C1	1.383 (1.0%)	1.394 (0.2%)	1.394 (0.2%)	1.397
C4-C5	1.397 (1.3%)	1.406 (0.6%)	1.408 (0.5%)	1.415
C4-N7	1.380 (1.8%)	1.395 (3.0%)	1.380 (1.8%)	1.355
C1-N8	1.455 (1.5%)	1.467 (2.3%)	1.462 (2.0%)	1.433
N8-O9	1.191 (3.5%)	1.235 (0.08%)	1.230 (0.3%)	1.234
g	121.1 (0.08%)	121.7 (0.4%)	121.0 (0.2%)	121.2
h	119.1 (0.3%)	118.7 (0.08%)	118.9 (0.08%)	118.8
a	113.2 (5.1%)	111.6 (6.5%)	114.4 (4.1%)	119.3
b	124.3 (1.9%)	124.6 (2.1%)	124.1 (1.7%)	122.0
$\mu/10^{-18}$ esu	6.7 (8%)	5.9 (5%)	7.1 (15%)	6.2
$<\alpha>/10^{-23}$ esu	1.4 (18%)	1.5 (12%)	1.5 (12%)	1.7
$<\beta>/10^{-30}$ esu	3.8 (59%)	9.4 (2%)	10.0 (9%)	9.2

The bond length and bond angles are in Å and degree, respectively. The numbering scheme is defined in Scheme 1.
[a]The values in parentheses refer to the absolute deviations from the experimental data [60].

in Fig. 1 for values obtained at MP2 level. However, for strong withdrawing substituent the predicted behavior is in poor agreement with experiment, although the MP2 level was able to reproduce most of the qualitative trend with exception found for X = NO_2 derivative (see Fig. 1). In general, the B3LYP trends for electric properties of mono-substituted benzene derivatives are similar to those found at MP2 level (see values in Table 2).

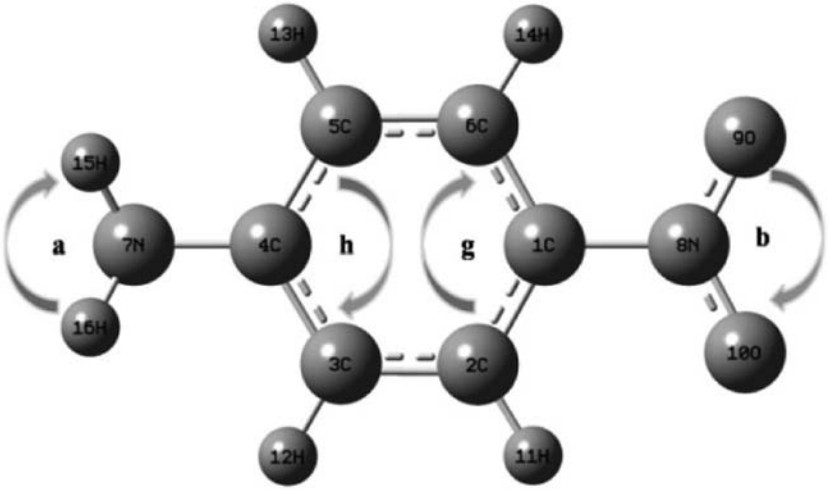

Scheme 1.

The p-di-substituted benzene derivatives are the most important representatives of this broad class of molecules that constitute the basic units for NLO molecular devices. In general, those compounds with donor and acceptor substituents are more promising for NLO application. Belonging to this particular class, the p-nitroaniline (pNA) has been mostly studied as a prototype for molecules with NLO properties. In this molecule, the NO_2 substituent is considered a strong acceptor group ($\sigma_p = 0.78$) and the NH_2 a

Table 4
Dipole moment (μ), average polarizability ($\langle\alpha\rangle$) and first hyperpolarizability ($\langle\beta\rangle$) for *para*-disubstituted benzenes (units in esu)

X	Y		$\mu/10^{-18}$				$<\alpha>/10^{-23}$				$<\beta>/10^{-30}$			
		σ_t^{a}	HF	MP2	B3LYP	Expt.[b]	HF	MP2	B3LYP	Expt.[b]	HF	MP2	B3LYP	Expt.[b]
NO_2	CN	0.12	0.3	0.4	0.3	0.9	1.4	1.5	1.5	1.7	0.8	2.8	5.0	0.6
NO_2	CHO	0.36	3.2	2.5	2.7	2.5	1.4	1.5	1.5	1.7	1.2	1.0	1.3	0.2
CHO	Me	0.59	4.1	3.7	4.1	3.0	1.4	1.5	1.5	1.6	1.8	3.6	3.4	1.7
CHO	OMe	0.69	5.2	4.6	5.3	3.5	1.5	1.6	1.6	1.7	3.9	7.8	7.4	2.2
CN	Me	0.83	5.5	4.9	5.3	4.4	0.8	1.5	1.5	1.5	0.3	0.1	0.5	0.7
CN	OMe	0.93	5.6	5.4	5.8	4.8	1.2	1.6	1.6	1.7	2.2	3.3	2.4	1.9
NO_2	Me	0.95	5.6	4.7	5.3	4.2	1.4	1.5	1.5	1.6	0.4	2.6	3.3	2.1
NO_2	OMe	1.05	6.0	5.2	6.0	4.6	1.4	1.6	1.6	1.5	2.6	7.3	8.4	5.1
NO_2	OH	1.15	5.2	4.6	5.1	5.0	1.3	1.4	1.4	1.5	2.1	5.7	6.3	3.0
CHO	$N(CH_3)_2$	1.25	6.2	5.7	6.8	5.1	1.8	1.9	2.0	2.0	7.9	14.3	12.4	6.3
CN	NH_2	1.32	6.5	6.0	6.8	5.0	1.4	1.5	1.5	1.6	2.1	4.1	2.8	3.1
NO_2	NH_2	1.44	6.7	5.9	7.1	6.2	1.4	1.5	1.5	1.7	3.8	9.4	10.0	9.2
CN	$N(CH_3)_2$	1.49	7.4	7.8	7.8	5.6	1.7	1.9	1.9	2.1	4.0	7.3	5.2	5.0
NO_2	$N(CH_3)_2$	1.61	7.9	6.8	8.2	6.4	1.7	1.9	2.0	2.2	7.3	16.0	17.0	12
NO	$N(CH_3)_2$	1.73	6.4	6.3	7.8	6.2	1.7	1.9	2.0	2.1	9.5	21.7	13.3	12

[a]The σ_t is defined as $\sigma_p^+ - \sigma_p^-$, where σ_p^+ is the largest positive parameter (stronger acceptor group) and σ_p^- the lowest positive value (weaker acceptor group) or the negative value (donor substituent).
[b]Experimental data [28].

strong donor group ($\sigma_p = -0.66$). In the present work, geometry and electric properties were calculated for pNA molecule and compared to the experimental data as given in Table 3. The geometry was well reproduced at all levels of theory, proving the flexibility and utility of our basis set. For bond lengths, the largest error found was about 3.5% for N8-O9 bond at HF level. As for the bond angles, the largest error was about 6.5% for the H-N-H angle (indicated by "a" in Table 3) at MP2 level. Regarding the electric properties, our HF result of $\mu = 6.7 \times 10^{-18}$ e.s.u. are in excellent agreement with the experimental value of $\mu = 6.2 \times 10^{-18}$ e.s.u. obtained by Cheng et al. [28], deviation of only 8%. At MP2 and B3LYP levels, our results show errors of 5% and 18%, respectively. Our calculated values of $<\alpha>= 1.4 \times 10^{-23}$ esu are also in good agreement with experimental data of $<\alpha>= 1.7 \times 10^{-23}$ esu [28]. At MP2 and B3LYP levels the mean polarizability was $<\alpha>= 1.5 \times 10^{-23}$ esu, being 12% lower than the actual value. Interesting, for the first dipole hyperpolarizability, the electron correlation effect plays a very important role in the predicted value. Our HF result of $<\beta>= 3.8 \times 10^{-30}$ esu showed deviation of 59% compared to the experimental value of $<\beta>= 9.2 \times 10^{-30}$ esu obtained by Cheng et al. [28]. When we included the electron correlation effect, the error decreases to 2% at MP2 level and to 9% at B3LYP level (see values in Table 3). We also compare our calculated values of dipole polarizability for pNA with the values obtained by Junqueira et al. [36] with the CBS-extrapolated (aug-cc-pVDZ, aug-cc-pVTZ//B3LYP/6-31+G). Our values of $<\alpha>= 1.5 \times 10^{-23}$ esu are in excellent agreement with the values of $<\alpha>= 1.6 \times 10^{-23}$ esu found by Junqueira and co-workers [36]. The deviation was only 6%, however, with a significant lower computational cost.

Table 4, includes the calculated and experimental electronics properties for p-di-substituted benzene derivatives. The molecules are organized in table according the increase of net Hammett parameter defined as $\sigma_t = \sigma_p^+ - \sigma_p^-$, where σ_p^+ is the largest positive parameter (stronger acceptor group) and σ_p^- the lowest positive value (weaker acceptor group) or the negative value (donor substituent). In this way the electronic effect on the properties can be quantified. In general, the largest the value of $\sigma_p^+ - \sigma_p^-$ more polar is the molecule as clearly seen in Table 4. Comparing the calculated values of dipole moment with experimental data, we found an average absolute deviation of 27% at HF level. The electron correlation

Table 5
Dipole moment (μ), average polarizability ($\langle\alpha\rangle$) and first hyperpolarizability ($\langle\beta\rangle$) for *ortho*-disubstituted benzenes (units in esu)

X	$\mu/10^{-18}$				$<\alpha>/10^{-23}$				$<\beta>/10^{-30}$			
	HF	MP2	B3LYP	Expt.[a]	HF	MP2	B3LYP	Expt.[a]	HF	MP2	B3LYP	Expt.[a]
Me	4.7	3.9	4.4	3.9	1.4	1.5	1.5	1.6	0.9	0.2	0.5	1.0
OH	3.8	3.1	3.7	3.4	1.3	1.4	1.4	1.5	1.3	3.2	2.1	1.2
OMe	6.0	4.9	5.6	3.8	1.4	1.5	1.6	1.7	2.3	2.7	1.9	1.4
NH_2	5.0	4.2	4.9	4.1	1.3	1.5	1.5	1.6	1.7	3.2	2.0	2.5
CN	7.3	6.3	6.7	5.5	1.4	1.5	1.5	1.7	1.6	1.4	1.9	1.2
CHO	4.7	4.0	4.4	4.0	1.4	1.5	1.5	1.6	0.6	1.0	1.2	0.8

[a]Experimental data [28].

Table 6
Dipole moment (μ), average polarizability ($\langle\alpha\rangle$) and first hyperpolarizability ($\langle\beta\rangle$) for *meta*-disubstituted benzenes (units in esu)

X	$\mu/10^{-18}$				$<\alpha>/10^{-23}$				$<\beta>/10^{-30}$			
	HF	MP2	B3LYP	Expt.[a]	HF	MP2	B3LYP	Expt.[a]	HF	MP2	B3LYP	Expt.[a]
Me	5.2	4.4	4.9	3.9	1.4	1.5	1.5	1.6	0.7	1.0	1.2	1.5
OH	3.8	3.1	3.6	3.6	1.2	1.4	1.4	1.3	1.2	2.6	2.8	0.8
OMe	6.4	5.7	6.2	3.9	1.4	1.6	1.6	1.7	1.4	2.6	2.5	1.6
NH_2	5.7	5.1	5.6	4.7	1.3	1.4	1.5	1.5	1.5	2.9	2.9	1.9
CN	4.9	4.2	4.6	3.7	1.4	1.5	1.5	1.7	1.0	1.2	2.0	0.8
CHO	2.4	2.1	2.4	2.8	1.4	1.5	1.5	1.6	0.6	1.6	1.7	1.7

[a]Experimental data [28].

effect influences positively in the calculated values. At MP2 level the mean error drops to 15% (B3LYP gave the highest deviation for dipole moment, 29%). For the dipole polarizability, $<\alpha>$, all methods give good results when compared to the experimental data. The average errors were 18% at HF level and around 7% at MP2 and B3LYP levels of theory. This property is not much sensitive to the electronic substituent effect, being on average 1.7 ± 0.2 for the set of *push-pull* derivatives shown in Table 4.

The most relevant property for such molecules, which is directly related to the NLO property, is the first dipole hyperpolarizability, $<\beta>$. In general, from values in Table 4, the results can be considered satisfactory when compared to the experimental data, except for molecules with very low value of $<\beta>$, usually lower than 1, where error is quite large. For molecules with $<\beta> \ > 1$, the best average results were obtained at HF level, which deviation was 38%. However, it is important to mention that for some molecules the electronic correlation play a primary role on the absolute value of property. For instance, for the derivative with X/Y = NO_2/CH_3 the error was found equal to 81% at HF and only 24% at MP2 level of theory. The same effect was discussed for pNA, where absolute errors in $<\beta>$ were 59% and 2% at HF and MP2 levels, respectively (see data in Tables 3 and 4). It is worth noting that the qualitative trend is correctly predicted at MP2 level, with the increase of $<\beta>$ value with the net Hammett parameter (see Fig. 2). Therefore, calculation at this level of theory with the basis set fitted here can be used as a predictive tool of NLO properties for *push-pull* benzene derivatives.

In the last part of the present paper we calculated the electric properties for *ortho* and *meta*-substituted nitro-benzene. The values for μ, $<\alpha>$ and $<\beta>$ at distinct levels of theory are given in Tables 5 and 6 for *ortho* and *meta* derivatives, respectively. The behavior compared to the experimental data is similar to those discussed for p-derivatives, with MP2 working better for μ and $<\alpha>$. In the case of dipole moment and polarizability, the MP2 average errors for o- and m-derivatives were 23% and 9%, respectively, compared to 31% and 16% at HF level. As expected, the values of $<\beta>$ are

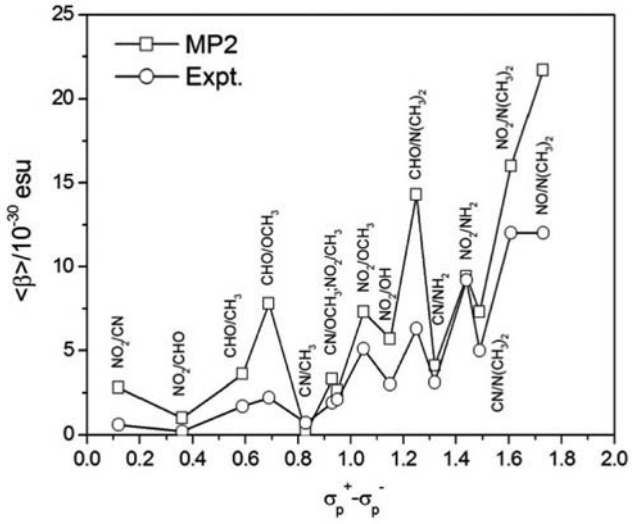

Fig. 2. Calculated (MP2 only) and experimental values of $< \beta >$ for p-di-substituted benzene derivatives.

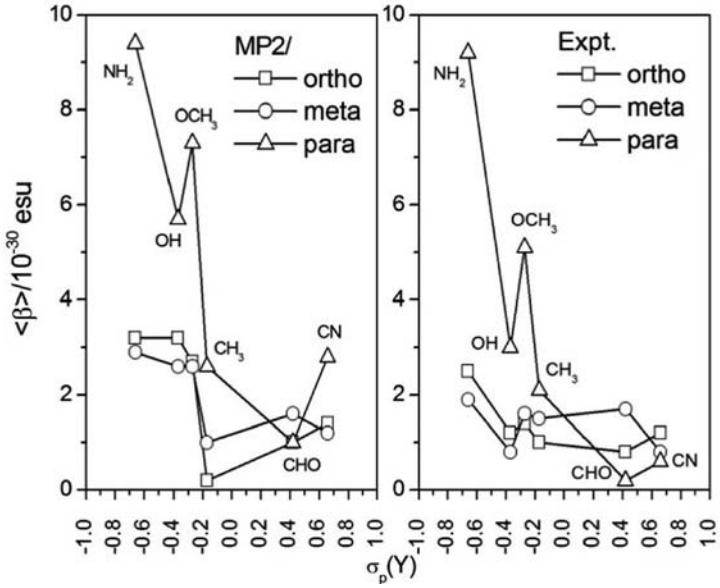

Fig. 3. First hyperpolarizability for a series of o-, m- and p-substituted nitro-benzene derivatives.

smaller compared to p-derivatives. For instances, for pNA $< \beta >= 9.2$ and for oNA and mNA the corresponding values were 2.5 and 1.9, respectively (experimental data). The HF results are, on average, in better agreement to the experiment, with absolute mean error of 32% compared to 65% found at MP2 and B3LYP levels.

In Fig. 3 the $< \beta >$ values are plotted against Hammett constant for substituent (Y) in a series of o-, m- and p-substituted nitro-benzene derivatives. Calculated (MP2 only) and experimental data are shown. From Fig. 3 we see that the qualitative agreement between predicted and actual values is fairly good, mainly for p-derivatives, whose trend throughout the whole series is mostly reproduced at MP2 level

using the basis set proposed here. The overall substituent effect is also correctly predicted, including the strength of electronic effect of individual group and those from relative position of both substituents. Moreover, we believe the basis set adjusted in the present work might be a suitable alternative for calculation of electric properties up to first hyperpolarizability for benzene derivatives.

4. Conclusions

The present paper presented modified basis sets for first row elements including H, C, N and O atoms, adjusted to reproduce electric properties of diatomic molecules. A sequential procedure was applied to fit Gaussian exponents, where the basis set for H was firstly obtained using H_2 as standard system and then, further used for fitting C basis set with the CH^+ molecule taken as template. The basis sets for N and O were obtained to reproduce electric properties of CN^- and CO molecules, keeping the carbon basis set unchanged. The final basis sets were of double zeta (DZ) quality augmented by diffuse and one or two sets of first polarization functions (DZ+P): (9s5p2d(1d only for N)/7s2p1d) → [5s(6s only for O)3p2d(1d only for N)/3s2p1d] for C,O,N/H. For diatomic molecules, several *ab initio* methods were used, from HF to highly correlated CCSD(T). In the case of CO molecule, for which a large amount of experimental data are available, the agreement between predicted and actual values were satisfactory for most of properties, when correlated methods are applied, (error $< 20\%$), except for second hyperpolarizability, $< \gamma >$, that presented a deviation around 60% at MP4(SDQ) level. Comparing these data with those reported in the literature with more complete basis set, we conclude that higher order polarization functions are needed in order to improve the $< \gamma >$ prediction. This is out of the scope of the present paper, nonetheless, deserves attention when second hyperpolarizability was the property of primary interest.

The basis sets adjusted were used for calculation of dipole moment, polarizability and first hyperpolarizability of a series of 36 $o-$, $m-$ and p-substituted benzene derivatives. The results were quite satisfactory for geometry and electric properties. For the important representative p-nitroaniline (pNA) the predicted $< \beta >$ value was only 2% higher than the experimental one at MP2 level. For the other analogues the results were also good enough, with qualitative trends always correctly predicted at MP2 level. In the case of o-, m- and p-substituted nitro-benzene series, the observed electronic effect of individual group and those arising from relative position of both substituents were well reproduced at MP2 level using our basis set. Thus, we are confident that the basis set adjusted in the present work might be a suitable alternative for calculation of electric properties up to first hyperpolarizability for benzene derivatives. Further work is still necessary in order to expand the basis set for higher order hyperpolarizability and larger conjugated molecular systems. Our group in engaged in this challenging task.

Appendix

R : $1a_0 = 0.529177249 \times 10^{-10}$ m
μ : $1e.a_0 = 8.478358 \times 10^{-30}$ C.m $= 2.541746$ Debye $= 2.541746 \times 10^{-18}$ cm.esu
α : $1e^2a_0^2E_h^{-1} = 1.659889 \times 10^{-41}$ $C^2.m^2.J^{-1} = 1.481847 \times 10^{-25}$ cm^3
β : $1e^3a_0^3E_h^{-2} = 3.206361 \times 10^{-53}$ $C^3.m^3.J^{-2} = 0.008641 \times 10^{-30}$ $cm^5.esu^{-1}$
γ : $1e^4a_0^4E_h^{-3} = 6.235378 \times 10^{-65}$ $C^4.m^4.J^{-3}$

Acknowledgements

The authors thank the Brazilian agencies CNPq (Proc. 479682/2008-9) and FAPEMIG (Proc. CEX-APQ-00498-08) for financial support. D. Paschoal also thanks to the FAPEMIG for graduate scholarship.

References

[1] J.A. Delaire and K. Nakatani, Linear and nonlinear optical properties of photochromic molecules and materials, *Chemical Reviews* **100** (2000), 1817–1845.
[2] M. Gonzalez, N. Martin, J.L. Segura, C. Seoane, J. Garin, J. Orduna, R. Alcala, C. Sanchez and B. Villacampa, Second-order nonlinear optical properties of tetrathiafulvalene-pi-3-(dicyanomethylidene)-indan-1-one chromophores, *Tetrahedron Letters* **40** (1999), 8599–8602.
[3] I. Ledoux, J. Zyss, E. Barni, C. Barolo, N. Diulgheroff, P. Quagliotto and G. Viscardi, Properties of novel azodyes containing powerful acceptor groups and thiophene moiety, *Synthetic Metals* **115** (2000), 213–217.
[4] G.J.B. Hurst, M. Dupuis and E. Clementi, Ab initio Analytic Polarizability, 1st-Hyperpolarizability and 2nd-Hyperpolarizability of Large Conjugated Organic-Molecules – Applications to Polyenes C_4H_6 to $C_{22}H_{24}$, *Journal of Chemical Physics* **89** (1988), 385–395.
[5] J.L. Bredas, C. Adant, P. Tackx, A. Persoons and B.M. Pierce, 3rd-Order Nonlinear-Optical Response in Organic Materials – Theoretical and Experimental Aspects, *Chemical Reviews* **94** (1994), 243–278.
[6] M.F. Costa, T.L. Fonseca, O.A.V. Amaral and M.A. Castro, Calculations of the polarizability and hyperpolarizability of the NaH molecule including vibrational corrections, *Physics Letters A* **263** (1999), 186–192.
[7] G. Maroulis, Electric polarizability and hyperpolarizability of carbon monoxide, *Journal of Physical Chemistry* **100** (1996), 13466–13473.
[8] G. Maroulis, A systematic study of basis set, electron correlation, and geometry effects on the electric multipole moments, polarizability, and hyperpolarizability of HCl, *Journal of Chemical Physics* **108** (1998), 5432–5448.
[9] G. Maroulis, Electric multipole moment, dipole and quadrupole (hyper)polarizability derivatives for HF (X-1 Sigma(+)), *Journal of Molecular Structure-Theochem* **633** (2003), 177–197.
[10] A. Vela and J.L. Gazquez, A Relationship between the Static Dipole Polarizability, the Global Softness, and the Fukui Function, *Journal of the American Chemical Society* **112** (1990), 1490–1492.
[11] A.D. Headley, Substituent Effects on the Basicity of Dimethylamines, *Journal of the American Chemical Society* **109** (1987), 2347–2348.
[12] W.J. Hehre, Ching-Fong Pau, A.D. Headley and R.W. Taft, A Scale of Directional Substituent Polarizability Parameters from Abinitio Calculations of Polarizability Potentials, *Journal of the American Chemical Society* **108** (1986), 1711–1712.
[13] T.M. Miller and B. Bederson, Electric-Dipole Polarizability Measurements, *Advances in Atomic and Molecular Physics* **25** (1988), 37–60.
[14] J.F. Ward and C.K. Miller, Measurements of Non-Linear Optical Polarizabilities for 12 Small Molecules, *Physical Review A* **19** (1979), 826–833.
[15] S.Y. Liu and C.E. Dykstra, Multipole Polarizabilities and Hyperpolarizabilities of Ahn and A2hn Molecules from Derivative Hartree-Fock Theory, *Journal of Physical Chemistry* **91** (1987), 1749–1754.
[16] H. Sekino and R.J. Bartlett, Molecular Hyperpolarizabilities, *Journal of Chemical Physics* **98** (1993), 3022–3037.
[17] M.A. Spackman, Accurate Prediction of Static Dipole Polarizabilities with Moderately Sized Basis-Sets, *Journal of Physical Chemistry* **93** (1989), 7594–7603.
[18] A.J. Sadlej, Medium-Size Polarized Basis-Sets for High-Level Correlated Calculations of Molecular Electric Properties, *Collection of Czechoslovak Chemical Communications* **53** (1988), 1995–2016.
[19] A.J. Sadlej, Medium-Size Polarized Basis-Sets for High-Level-Correlated Calculations of Molecular Electric Properties .4. 3rd-Row Atoms – Ge through Br, *Theoretica Chimica Acta* **81** (1991), 45–63.
[20] A.J. Sadlej, Medium-Size Polarized Basis-Sets for High-Level-Correlated Calculations of Molecular Electric Properties .2. 2nd-Row Atoms – Si through Cl, *Theoretica Chimica Acta* **79** (1991), 123–140.
[21] A.J. Sadlej, Medium-Size Polarized Basis-Sets for High-Level-Correlated Calculations of Molecular Electric Properties .5. 4th-Row Atoms – Sn through I, *Theoretica Chimica Acta* **81** (1992), 339–354.
[22] A.J. Sadlej and M. Urban, Medium-Size Polarized Basis-Sets for High-Level-Correlated Calculations of Molecular Electric Properties .3. Alkali (Li, Na, K, Rb) and Alkaline-Earth (Be, Mg, Ca, Sr) Atoms, *Theochem-Journal of Molecular Structure* **80** (1991), 147–171.
[23] P. Neogrady, M. Medved, I. Cernusak and M. Urban, Benchmark calculations of some molecular properties of O-2, CN and other selected small radicals using the ROHF-CCSD(T) method, *Molecular Physics* **100** (2002), 541–560.

[24] G. Maroulis, Accurate electric multipole moment, static polarizability and hyperpolarizability derivatives for N-2, *Journal of Chemical Physics* **118** (2003), 2673–2687.
[25] G. Maroulis and D.M. Bishop, Hf Scf Electric Polarizabilities and Hyperpolarizabilities for the Ground-State of the Hydrogen Molecule, *Chemical Physics Letters* **128** (1986), 462–465.
[26] D. Paschoal, M.F. Costa, G.M.A. Junqueira and H.F. Dos Santos, Ab initio calculation of electric properties for the BH, CO, CS and N-2 molecules, *Journal of Molecular Structure-Theochem* **913** (2009), 200–206.
[27] L.T. Cheng, W. Tam, S.R. Marder, A.E. Stiegman, G. Rikken and C.W. Spangler, Experimental Investigations of Organic Molecular Nonlinear Optical Polarizabilities .2. a Study of Conjugation Dependences, *Journal of Physical Chemistry* **95** (1991), 10643–10652.
[28] L.T. Cheng, W. Tam, S.H. Stevenson, G.R. Meredith, G. Rikken and S.R. Marder, Experimental Investigations of Organic Molecular Nonlinear Optical Polarizabilities .1. Methods and Results on Benzene and Stilbene Derivatives, *Journal of Physical Chemistry* **95** (1991), 10631–10643.
[29] S.P. Karna, P.N. Prasad and M. Dupuis, Nonlinear Optical-Properties of Para-Nitroaniline – an Abinitio Time-Dependent Coupled Perturbed Hartree-Fock Study, *Journal of Chemical Physics* **94** (1991), 1171–1181.
[30] F. Meyers, S.R. Marder, B.M. Pierce and J.L. Bredas, Electric-Field Modulated Nonlinear-Optical Properties of Donor-Acceptor Polyenes – Sum-over-States Investigation of the Relationship between Molecular Polarizabilities (Alpha, Beta, and Gamma) and Bond-Length Alternation, *Journal of the American Chemical Society* **116** (1994), 10703–10714.
[31] F. Sim, S. Chin, M. Dupuis and J.E. Rice, Electron Correlation-Effects in Hyperpolarizabilities of P-Nitroaniline, *Journal of Physical Chemistry* **97** (1993), 1158–1163.
[32] D.R. Kanis, M.A. Ratner and T.J. Marks, Design and Construction of Molecular Assemblies with Large 2nd-Order Optical Nonlinearities – Quantum-Chemical Aspects, *Chemical Reviews* **94** (1994), 195–242.
[33] D.P. Shelton and J.E. Rice, Measurements and Calculations of the Hyperpolarizabilities of Atoms and Small Molecules in the Gas-Phase, *Chemical Reviews* **94** (1994), 3–29.
[34] E.R. Davidson and D. Feller, Basis Set Selection for Molecular Calculations, *Chemical Reviews* **86** (1986), 681–696.
[35] G. Maroulis, On the accurate theoretical determination of the static hyperpolarizability of trans-butadiene, *Journal of Chemical Physics* **111** (1999), 583–591.
[36] G.M.A. Junqueira and A.J.C. Varandas, Extrapolating to the One-Electron Basis Set Limit in Polarizability Calculations, *Journal of Physical Chemistry A* **112** (2008), 10413–10419.
[37] G. Maroulis, Accurate Dipole Polarizability for Cl_2(Chi-1-Sigma-G+), *Molecular Physics* **77** (1992), 1085–1094.
[38] G. Maroulis, Is the dipole polarizability of hydrogen iodide accurately known, *Chemical Physics Letters* **318** (2000), 181–189.
[39] G. Maroulis and D.M. Bishop, Electric Moments, Polarizabilities and Hyperpolarizabilities for BH(X1sigma+) and CH^+(X1sigma+), *Chemical Physics* **96** (1985), 409–418.
[40] G. Maroulis, C. Makris, D. Xenides and P. Karamanis, Electric dipole and quadrupole moment and dipole polarizability of CS, SiO and SiS, *Molecular Physics* **98** (2000), 481–491.
[41] G. Maroulis and A.J. Thakkar, Ab initio Static Polarizabilities and Multipole Moments of I_2, *Molecular Physics* **73** (1991), 1235–1240.
[42] A.D. McLean and M. Yoshimine, Theory of Molecular Polarizabilities, *Journal of Chemical Physics* **47** (1967), 1927–&.
[43] A.D. Buckingham and B.J. Orr, Molecular Hyperpolarizabilities, *Quarterly Reviews* **21** (1967), 195–&.
[44] H.A. Kurtz, J.J.P. Stewart and K.M. Dieter, Calculation of the Nonlinear Optical-Properties of Molecules, *Journal of Computational Chemistry* **11** (1990), 82–87.
[45] M.J. Frisch, Gaussian 2003 Revision B.04 (2003), Gaussian Inc.: Pittsburgh PA.
[46] T.H. Dunning, Gaussian Basis Functions for Use in Molecular Calculations .1. Contraction of (9s5p) Atomic Basis Sets for First-Row Atoms, *Journal of Chemical Physics* **53** (1970), 2823–&.
[47] D. Young, Computational Chemistry – A Practical Guide for Applying Techniques to Real-World Problems (2001), John Wiley &Sons.
[48] Y. Atalay, D. Avci and A. Basoglu, Linear and non-linear optical properties of some donor-acceptor oxadiazoles by ab initio Hartree-Fock calculations, *Structural Chemistry* **19**(2) (2008), 239–246.
[49] NIST Standard Reference 101. http://srdata.nist.gov/cccbdb/.
[50] K.P. Huber and G. Herzberg, Molecular Spectra and Molecular Structure: IV. Constants of Diatomic Molecules (1979) Van Nostrand, New York.
[51] R. Thomson and F.W. Dalby, Experimental Determination of Dipole Moments of X(2sigma+) and B(2sigma+) States of Cn Molecule, *Canadian Journal of Physics* **46** (1968), 2815–&.
[52] W.L. Meerts, F.H. Deleeuw and A. Dymanus, Electric and Magnetic-Properties of Carbon-Monoxide by Molecular-Beam Electric-Resonance Spectroscopy, *Chemical Physics* **22** (1977), 319–324.
[53] J.S. Muenter, Electric Dipole-Moment of Carbon-Monoxide, *Journal of Molecular Spectroscopy* **55** (1975), 490–491.
[54] G.A. Parker and R. Pack, Van der waals Interactions of Carbon-Monoxide, *Journal of Chemical Physics* **64** (1976), 2010–2012.

[55] N.J. Bridge and A.D. Buckingham, Polarization of Laser Light Scattered by Gases, *Proceedings of the Royal Society of London Series a-Mathematical and Physical Sciences* **295** (1966), 334–&.
[56] F. Baas and K.D. Vandenhout, Measurements of Depolarization Ratios and Polarizability Anisotropies of Gaseous Molecules, *Physica A* **95** (1979), 597–601.
[57] C. Asawaroengchai and G.M. Rosenblatt, Rotational Raman Intensities and the Measured Change with Inter-Nuclear Distance of the Polarizability Anisotropy of H-2, D-2, N-2, O-2, and Co, *Journal of Chemical Physics* **72** (1980), 2664–2669.
[58] H. Kling and W. Huttner, The Temperature-Dependence of the Cotton Mouton Effect of N2, Co, N2o, Co2, Ocs, and Cs2 in the Gaseous State, *Chemical Physics* **90** (1984), 207–214.
[59] C. Hansch, A. Leo and R.W. Taft, A Survey of Hammett Substituent Constants and Resonance and Field Parameters, *Chemical Reviews* **91** (1991), 165–195.
[60] M. Tonogaki, T. Kawata, S. Ohba, Y. Iwata and I. Shibuya, Electron-Density Distribution in Crystals of P-Nitrobenzene Derivatives, *Acta Crystallographica Section B-Structural Science* **49** (1993), 1031–1039.

Journal of Computational Methods in Sciences and Engineering 10 (2010) 243–249
DOI 10.3233/JCM-2010-0322
IOS Press

Quadrupole polarizabilities of the rare-gas homonuclear diatoms and methane molecules

M.S.A. El-Kader*
Department of Engineering Mathematics and Physics, Faculty of Engineering, Giza, 12211, Egypt

Abstract. The contribution of the quadrupole polarizability C to the long-range polarizability of two interacting rare-gas atoms and methane molecules is specified by fitting the trace and anisotropy models to the intensity of the isotropic and anisotropic interaction-induced light scattering spectra. Good agreement with *ab initio* results in the literature is obtained and the first few even moments of these profiles are in excellent agreement with experiments.

Keywords: Quadrupole polarizabilities/rare-gas/CH_4

1. Introduction

Collision-induced light scattering (CILS) has been widely used in the past to study intermolecular properties, especially the invariant of the interaction-induced polarizability tensor of collisional pairs of atoms or molecules [1–4]. Accurate Raman spectra of the rare-gases and spherical top molecules like methane could be recorded at low enough densities so that the spectra are due to binary interactions, virtually unaffected by many body-interactions. Empirical models of the rare-gas diatom and methane polarizabilities were obtained by comparing observed spectroscopic features with calculations based on advanced interatomic potentials and suitable models of the diatom polarizability invariants.

Empirical diatom polarizability models are typically based on the classical long-range dipole-induced dipole (DID) mechanism [5,6] to which a short-range term is added to simulate the quantal exchange and overlap contributions [3,7]. For example, very successful models of the trace and anisotropy of the diatom polarizability tensor are given by the sum of the DID contributions (often up to second order) and added short-range term, which falls off exponentially with increasing interatomic separation r [3, 8,9]. Such models typically contain two adjustable parameters that are chosen to obtain a close fit of the measured moments of the isotropic and anisotropic Raman spectra and, some times, of other experimental data [3,8]. These parameters are the amplitude and range parameters of the exponential short-range term in both models of the polarizabilities.

However, we note that these previous models all suffer from the fact that the different experimental data like as line shapes, integrated intensities and second dielectric constant are not fitted well. Some modifications have been made on the trace and anisotropy models such as the computation of the coefficient A_8 of $(1/r^8)$ [10] to reproduce both measurements, light scattering spectra, and virial coefficient. A precise determination of a model of the induced trace and anisotropy is thought to be important not only for its own sake, for comparison with *ab initio* calculations of the same quantities, but also for the

*Corresponding author. E-mail: mohamedsayedabdelkader@yahoo.com.

investigation of collision-induced light scattering (CILS) phenomena at high density which are believed to be critically shaped by the pair polarizability.

In this paper we present the analysis of the isotropic and anisotropic light scattering spectra of helium gas at T = 294.5 and 99.6 K, neon, argon, krypton, xenon and CH_4 gases at room temperature, based on fitting the spectral profiles rather than just the spectral moments of the measurements. Spectral profiles have a number of characteristic features, such as the bound dimer contributions, logarithmic slopes and curvatures of the line core and the wings, etc.... which may all be utilized in line-shape analyses. Spectral profiles are calculated numerically with the help of a quantal computer program, and compared with the measured spectra. The comparison of calculated and measured spectra provides valuable clues concerning the quality of existing models of both the interaction-induced pair polarizabilities and the interatomic potential.

2. Analysis of spectral profiles to determine the quadrupole polarizability C

In the molecular frame, for a pair of identical isotropic molecules the total pair-polarizability trace and anisotropy contributing to the purely translational scattering can be modeled as [10–13]

$$\alpha(r) = \frac{(4\alpha_o^3 + \frac{5}{9\alpha_o}\gamma C_6)}{r^6} + \frac{20\alpha_o^2 C}{r^8} - t_o \exp\left(-\frac{r-\sigma}{r_t}\right) \tag{1}$$

$$\beta(r) = \frac{6\alpha_o^2}{r^3} + \frac{(6\alpha_o^3 + \frac{\gamma C_6}{3\alpha_o})}{r^6} + \frac{24\alpha_o^2 C}{r^8} - g_o \exp\left(-\frac{r-\sigma}{r_o}\right) \tag{2}$$

where the first term in Eq. (1) and the first two terms in Eq. (2) are the corrected DID trace and anisotropy, attempting to analytically models the London dispersion effects in terms of the hyperpolarizability γ and the van der Waals coefficient C_6 [14]. The exponentials represent the "electron exchange" contributions at short range. The other terms, referred to as asymptotic, long-range, or dispersion term, describes the correct asymptotic behavior [4]. Here, α_o and C designate atomic polarizability and quadrupole polarizability. The values of the parameters are given in Refs [15–22].

The term in r^{-6} and the exponential term in both models of the trace and anisotropy polarizabilities with C = 0 are the empirical Proffitt-Keto-Frommhold (PKF) models, fitting their experimental polarized and depolarized spectra [23].

The quantum theory is applied for the accurate computation of the CILS absolute intensities of the atomic pairs. Numerically, this is done by means of the propagative two-point Fox-Goodwin integrator [24,25], where the ratio of the wavefunction, defined at adjacent points on a spatial grid, is built step-by-step.

As regards our problem, binary isotropic and anisotropic spectra are computed quantum-mechanically, as a function of ν, at temperature T by using the expressions [26,27]:

$$I_{\rm iso}(\nu) = hc\lambda^3 k_s^4 \sum_{J=o,J{\rm even}}^{J_{\max}} (2J+1) \int_0^{E_{\max}} \left|\left\langle \psi_{E',J'} \left| \alpha \right| \psi_{E,J} \right\rangle\right|^2 \exp\left(-\frac{E}{k_B T}\right) {\rm dE} \tag{3}$$

$$I_{\rm aniso}(\nu) = \frac{2}{15} hc\lambda^3 k_s^4 \sum_{J=o,J{\rm even}}^{J_{\max}} g_J b_J^{J'} (2J+1) \int_0^{E_{\max}} \left|\left\langle \psi_{E',J'} \left| \beta \right| \psi_{E,J} \right\rangle\right|^2 \exp\left(\frac{-E}{k_B T}\right) {\rm dE} \tag{4}$$

The symbol k_s stands for the Stokes wave number of the scattered light, h is Planck's constant and c is the speed of the light. Constant λ account for the thermal de Broglie wavelength, $\lambda = h/\sqrt{2\pi\mu k_B T}$, with μ the reduced mass of atomic pairs and k_BBoltzmann's constant. Symbol $\psi_{E,J}$ designates the scattering wave function and $E_{\max}$ the maximum value of the energy that is required to obtain convergence of the integrals.

In these expressions, $\alpha = \alpha(r)$ and $\beta = \beta(r)$ denote the trace and anisotropy of the quasimolecule, $g_{_J}$ the nuclear statistical weight; for a rare gas, one has $g_{_J} = 0$ for J odd and $g_{_J} = 2$ for J even. Finally, $b_J^{J'}$ are intensity factors involving the rotational quantum numbers J and $J^{'}$ of the initial and final states, respectively.

With the spectral intensities $I_{iso}(\nu)$ and $I_{aniso}(\nu)$ in cm^6 as input and through the following analytical expressions we are able to deduce the experimental isotropic moments [28,29]

$$M_{2n} = \left(\frac{\lambda_o}{2\pi}\right)^4 \int_{-\infty}^{\infty} (2\pi\nu c)^{2n} I_{\rm iso}(\nu) d\nu \tag{5}$$

and anisotropic moments

$$M_{2n} = \frac{15}{2}\left(\frac{\lambda_o}{2\pi}\right)^4 \int_{-\infty}^{\infty} (2\pi\nu c)^{2n} I_{\rm aniso}(\nu) d\nu \tag{6}$$

where λ_o denotes the laser wavelength and n is a non-negative integer.

Theoretical calculations of the first two even moments of the isotropic and anisotropic spectra can be easily performed within the framework of classical mechanics by means of the standard expressions [28, 29]

$$M_0 = 4\pi \int_0^{\infty} \alpha^2(r) \exp(-V(r)/k_{_B}T) r^2 dr \tag{7}$$

$$M_2 = \frac{4\pi k_B T}{\mu} \int_0^{\infty} \left(\frac{d\alpha}{dr}\right)^2 \exp(-V(r)/k_{_B}T) r^2 dr \tag{8}$$

for the isotropic spectrum

$$M_0 = 4\pi \int_0^{\infty} \beta^2(r) \exp(-V(r)/k_{_B}T) r^2 dr \tag{9}$$

$$M_2 = \frac{4\pi k_B T}{\mu} \int_0^{\infty} \left(\left(\frac{d\beta}{dr}\right)^2 + 6\left(\frac{\beta}{r}\right)^2\right) \exp(-V(r)/k_{_B}T) r^2 dr \tag{10}$$

for the anisotropic spectrum.

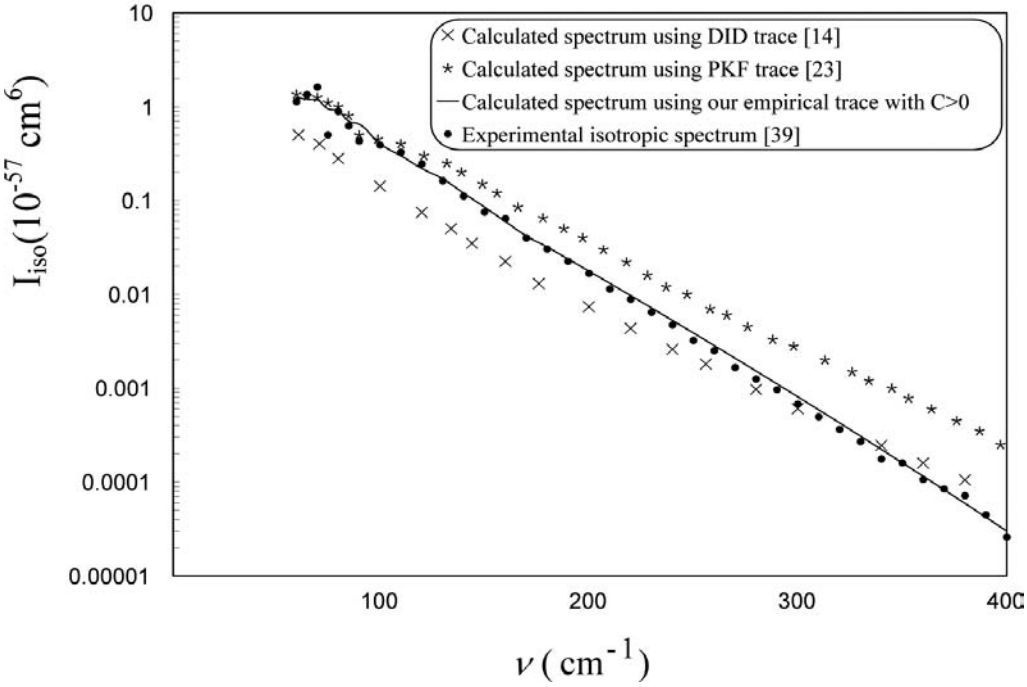

Fig. 1. Comparison between the calculated isotropic spectrum of argon gas at T = 295 K using the *ab initio* potential [19] and different models of the trace with the experimental one.

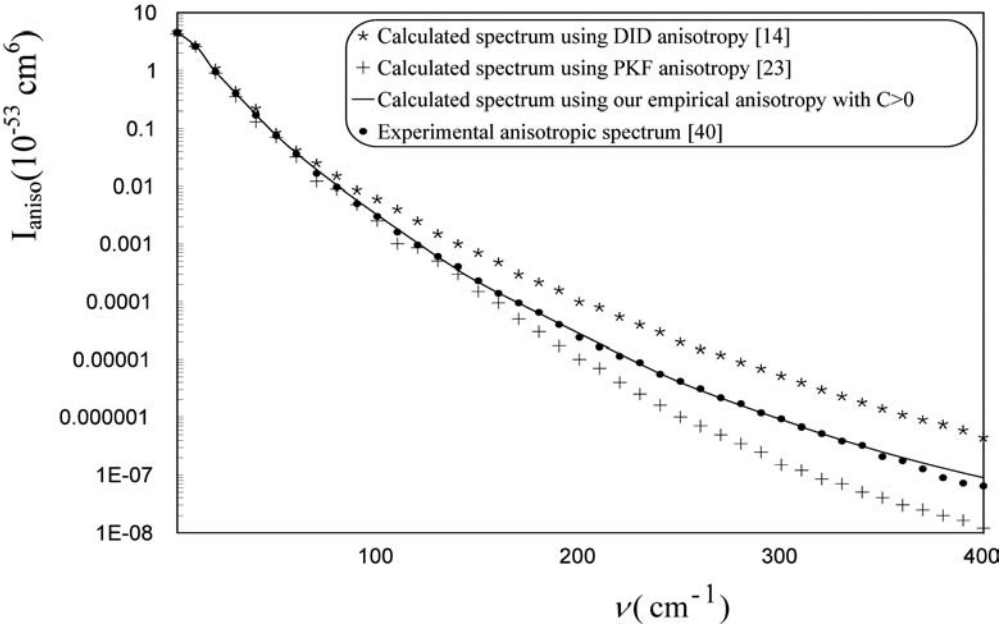

Fig. 2. Comparison between the calculated anisotropic spectrum of argon gas at T = 295 K using the *ab initio* potential [19] and different models of the pair polarizability anisotropy with the experimental one.

An effective means for checking the values of the quadrupole polarizability C is to compare the computed second dielectric constant B_ε with the experimental one. This is done by using the following formula [12,30]:

$$B_\varepsilon = \frac{8\pi^2}{3} N_A^2 \int_0^\infty \alpha(r) e^{(-V(r)/k_B T)} r^2 dr \tag{11}$$

As a first step in our analysis we calculate the pair spectra of all inert gases and methane, using the recent potentials [17–22] and polarizability models used previously in the moment analysis [4]. While the experimental spectrum is roughly reproduced with that calculation, differences between the computed and measured spectral profiles remain, which are clearly greater than the combined uncertainties of the numerical calculation and the experiment. In other words, the combination of the previously used potentials and polarizability model does not reproduce the measurement within the given uncertainties, despite the fact that consistency of measured and computed zeroth and second spectral moments was observed. The measured integrated intensity (the zeroth moment) cannot be known very accurately, because the low frequency part of the spectrum, which contributes significantly to the zeroth moment, is inaccessible to measurement; extrapolations to zeroth frequency are necessary which limit the accuracy attainable. We therefore decided to use the analytical polarizability trace and anisotropy models Eqs (1,2) and estimate the quadrupole polarizability C at room temperature of different inert gases and CH_4 from the second moment for different values of the parameters r_t and r_o, and to study the variations of the spectral profiles in response to the variations of r_t and r_o.

Again, suitable C values are determined by variations of the parameters r_t and r_o forcing the theoretical second spectral moment to reproduce the experimental value. The line-shapes calculations are continued for different values of r_t and r_o until a good fit of the profiles are obtained, with the values in Table 1. As can be seen for example in Figs (1) and (2) we now observe agreement of the computed and measured profiles of isotropic and anisotropic light scattering of argon gas over the complete frequency range. The agreement is much closer than anything that was seen before with gas spectra, particularly when we compare the far wings of the spectra. Agreement at that level apparently requires adding the long-range part in the trace and anisotropy models at small separations, presumably in the polarizability models.

Comparison between calculations and experiments for the zeroth and second moments of the isotropic and anisotropic light scattering profiles and second dielectric constant using these models of the polarizability trace and anisotropy are shown in Tables 2 and 3.

Also, it is interesting to note that the quadrupole polarizability C of these models of the polarizabilities agree reasonably well with *ab initio* calculations [15,16,31–34] for the systems of the noble and methane gases and produce moments in good agreement with experiments.

3. Conclusion

We have adopted a models for the pair polarizability trace $\alpha(r)$ and anisotropy $\beta(r)$ of the rare gas diatoms and methane molecule as a functions of the interatomic separation, which we determine by fitting to the spectral profiles of isotropic and anisotropic light scattering at room temperature rather than just the spectral moments of the measurements using a computer optimization process. The results of our analysis is therefore that rare and methane gases during collisions develop an incremental polarizability trace and anisotropy, beside the first and second order dipole induced dipole ones, which contribute

Table 1
Parameters of the extra-DID part of the diatom trace and anisotropy obtained by fitting the isotropic and anisotropic light scattering spectra of different inert gases and methane molecules

Gas	Trace parameters		Anisotropy parameters		Quadrupole polarizability	
	$r_t(\mathring{A})$	$t_o(\mathring{A}^3)$	$r_o(\mathring{A})$	$g_o(\mathring{A}^3)$	$C(\mathring{A}^5)$	
					Calculated	Ab initio
He	0.33	0.001393	0.348	0.0021	0.0953	0.0961 [31]
Ne	0.394	0.0055	0.43	0.0074	0.275	0.3 [32]
Ar	0.395	0.0309	0.40	0.08	2.065	2.08 [15,16]
Kr	0.4217	0.0414	0.45	0.2142	3.925	3.938 [33]
Xe	0.382	0.201	0.41	0.265	8.7	8.76 [33]
CH_4	0.355	0.052	0.389	0.17	2.487	2.50854 [34]

Table 2
Isotropic and anisotropic zeroth-order M_0, second-orderM_2 moments deduced from experiment and theory using our empirical models of the pair polarizability trace and anisotropy and the different interatomic potentials [17–22]

	Isotropic light scattering				Anisotropic light scattering			
	$M_0(10^{-2}\,\mathring{A}^9)$		$M_2(10^{24}\,\mathring{A}^9/S^2)$		$M_0(\mathring{A}^9)$		$M_2(10^{25}\,\mathring{A}^9/S^2)$	
	Cal.	Exp.	Cal.	Exp.	Cal.	Exp.	Cal.	Exp.
He								
T = 294.5 K	0.026	0.026 [35]	0.3234	0.32 [35]	0.0174	0.017 [36]	0.318	0.318 [36]
T = 99.6 K	0.00923	0.00906 [37]	0.0397	0.0415 [37]	0.0156	0.0146 [37]	0.0921	0.0935 [37]
Ne								
T = 294.5 K	0.0523	0.0521 [38]	0.6406	0.6407 [38]	0.257	0.257 [38]	0.555	0.5548 [38]
Ar								
T = 295 K	3.77	3.825 [39]	3.293	3.29 [39]	43.03	42.8 [40]	38.7	39.0 [40]
Kr								
T = 294.5 K	7.45	7.6 [41]	6.055	6.05 [41]	193.6	194 [41]	82.45	82.6 [41]
Xe								
T = 294.5 K	80.0	86.5 [41]	10.5	10.75 [41]	1339.4	1330.0 [41]	373.6	373.76 [41]
CH_4								
T = 294.5 K	1.34	–	15.17	–	209.2	192.24 [42]	681.32	684.45 [42]

Table 3
Second dielectric constant B deduced from experiment and theory using our empirical models of the pair polarizability trace and the different interatomic potentials [17–22]

	He	Ne	Ar	Kr	Xe	CH_4
	T = 323.15 K	T = 323.15 K	T = 242.95 K	T = 323.15 K	T = 242.95 K	T = 373.4 K
$B(cm^6/mol^2)$						
Cal.	−0.027	−0.094	1.823	4.318	33.33	6.77
Exp. [43]	-0.02 ± 0.02	-0.12 ± 0.06	1.84 ± 0.07	4.3 ± 0.7	35 ± 2	6.75 ± 0.29

substantially at intermediate range distances and can be ascribed to other mechanisms of electron cloud distortion, like overlap and correlation effects.

Also, it is interesting to note that the quadrupole polarizability C of these models of the polarizabilities agree reasonably well with *ab initio* calculations [15,16,31–34] for the systems of the noble gases and produce moments in good agreement with experiments.

References

[1] G.C. Tabisz, Mol. Spectrosc. (Specialist Periodical Reports, The Chemical Societies, London), 6, 136, 1979.
[2] L. Frommhold, *Adv Chem Phys* **46** (1981), 1.
[3] F. Barocchi and M. Zoppi, in: *Intermolecular Spectroscopy and Dynamical Properties of Dense Systemm Proceedings of the Int School of Physics*, Ennco Fermi, Course LXXV, J. van Kranendonk, ed., (North Holland, Amsterdam), 1980, P. 263.
[4] N. Meinander, G.C. Tabisz and M. Zoppi, *J Chem Phys* **84**(6) (1986), 3005.
[5] L. Silberstein, *Philos Mag* **33** (1917), 92.
[6] L. Silberstein, *Philos Mag* **33** (1917), 521.
[7] K.L.C. Hunt, in: *Phenomena Induced by Intermolecular Interactions*, G. Birnbaum, ed., (Plenum, New York), 1985, P. 1.
[8] A. Borysow and L. Frommhold, *Adv Chem Phys* **75** (1989), 439.
[9] L. Ulivi and L. Frommhold, *A Second Bibliography on Collision-Induced Light Scattering*, 1993.
[10] S.M. El-Sheikh, G.C. Tabisz and A.D. Buckingham, *Chem Phys* **247** (1999), 407.
[11] U. Bafile, R. Magli, F. Barocchi, M. Zoppi and L. Frommhold, *Molec Phys* **49** (1983), 1149.
[12] A.D. Buckingham, *Trans Faraday Soc* **52** (1956), 1035.
[13] L. Jansen and P. Mazur, *Physica* **21** (1955), 193.
[14] A.D. Buckingham and K.L. Clarke, *Chem Phys Lett* **57** (1978), 321.
[15] G. Maroulis, *J Phys Chem A* **104** (2000), 4772.
[16] G. Maroulis, A. Haskopoulos and D. Xenides, *Chem Phys Lett* **396** (2004), 59.
[17] R. Hellmann, E. Bich and E. Vogel, *Mol Phys* **105** (2007), 3013.
[18] R. Hellmann, E. Bich and E. Vogel, *Mol Phys* **106** (2008), 133.
[19] B. Jäger, R. Hellmann, E. Bich and E. Vogel, *Mol Phys* **107** (2009), 2181.
[20] K.T. Tang and J.P. Toennies, *J Chem Phys* **118** (2003), 4976.
[21] M.S.A. El-Kader, *Chem Phys* **352** (2008), 311.
[22] R. Hellmann, E. Bich and E. Vogel, *J Chem Phys* **128** (2008), 214303.
[23] M.H. Proffitt, J.W. Keto and L. Frommhold, *Can J Phys* **59** (1981), 1459.
[24] D.W. Norcross and M.J. Seaton, *J Phys* **B6** (1973), 614.
[25] M. Chrysos and R. Lefebvre, *J Phys* **B26** (1993), 2627.
[26] M. Chrysos, O. Gaye and Y. Le Duff, *J Phys B29* (1996), 583.
[27] M. Chrysos, O. Gaye and Y. Le Duff, *J Chem Phys* **105** (1996), 31.
[28] H.B. Levine and G. Birnbaum, *J Chem Phys* **55** (1971), 2914.
[29] F. Barocchi and M. Zoppi, in: *Phenomena Induced by Intermolecular Interactions*, G. Birnbaum, ed., Plenum, New York, 1985, p. 311.
[30] A.D. Buckingham and D.A. Dunmur, *Trans Faraday Soc* **64** (1968), 1776.
[31] A. Dalgarno and A.E. Kingston, *Proc R Soc A* **259** (1960), 424.
[32] G.H.F. Diercksen and A.J. Sadlej, *Phys Rev A* **27**(6) (1983), 2795.
[33] G. Maroulis and A.J. Thakkar, *J Chem Phys* **89**(12) (1988), 7320.
[34] G. Maroulis, *Chem Phys Lett* **226** (1994), 420.
[35] F. Rachet, Y. Le Duff, C. Guillot-Noël and M. Chrysos, *Phys Rev A* **61** (2000), 62501.
[36] C. Guillot-Noël, M. Chrysos, Y. Le Duff and F. Rachet, *J Phys B* **33** (2000), 569.
[37] C. Guillot-Noël, Y. Le Duff, F. Rachet and M. Chrysos, *Phys Rev A* **66** (2002), 012505.
[38] F. Rachet, M. Chrysos, G. Lothon, R. Moszynski and A. Milet, 16th ICSLS edited by C.A. Back, Vol. 12, 2002.
[39] O. Gaye, M. Chrysos, V. Teboul and Y. Le Duff, *Phys Rev* **A55** (1997), 3484.
[40] F. Chapeau-Blondeau, V. Teboul, J. Berrue and Y. Le Duff, *Phys Lett* **173A** (1993), 153.
[41] P.D. Dacre and L. Frommhold, *J Chem Phys* **76** (1982), 3447.
[42] T. Bancewicz, K. Nowicka, J.-L. Godet and Y. Le Duff, *Phys Rev* **A 69** (2004), 062704.
[43] G.C. Tabsiz and M.N. Neuman, in: *Collision- and Interaction-Induced Spectroscopy*, (Vol. C452 of NATO Advanced Study Institute), Series C: Mathematical and Physical Sciences, edited by G.C. Tabisz and M.N. Neuman, eds, Kluwer, Dordrescht, 1995, p. 77.

Journal of Computational Methods in Sciences and Engineering 10 (2010) 251–275
DOI 10.3233/JCM-2010-0323
IOS Press

Sudden birth and sudden death of entanglement

Zbigniew Ficek[a,*] and Ryszard Tanaś[b]
[a]*The National Centre for Mathematics and Physics, KACST, P.O. Box 6086, Riyadh 11442, Saudi Arabia*
[b]*Nonlinear Optics Division, Department of Physics, Adam Mickiewicz University, 61-614 Poznań, Poland*

Abstract. We discuss a simple model for creation of entanglement in a system composed of two two-level atoms interacting with a common environment. The role of the environment in entangling and disentangling of the atoms is explored. We demonstrate how the spontaneous decay of an initial excitation of the system can create a transient entanglement between the atoms. The opposite situation is also discussed where a spontaneous disentanglement of initially entangled atoms may exhibit some unusual features such as entanglement sudden birth, the phenomenon of entanglement sudden death and revival of entanglement. We provide a discussion of these unusual phenomena in terms of the density matrix elements of the system and show the connection of the phenomena with the threshold behaviour of the concurrence.

1. Introduction

Entanglement is a unique feature of quantum mechanics that can be created between different objects such as individual photons, atoms, nuclear spins and even between biological living cells [1]. Theoretical studies have demonstrated that entanglement can be used as a resource for transmission of quantum information over long distances. However, a transfer of the information requires ingredients for the control and transmission in the form of long-lived entangled states that are immune to environmental noise and decoherence. The transfer of information has been accomplished between light, which appears as a carrier of the information, and atoms whose stable ground states serve as a storage system [2–4]. The ability to store quantum information in long-lived atomic ground states opens possibilities for a long time controlled processing of information and communication of the information on demand.

An important issue in the creation of entanglement between the qubits is the presence of unavoidable decoherence which is a source of an irreversible loss of the coherence. It is often regarded as the main obstacle in practical implementation of coherent effects and entanglement. A typical source of decoherence is spontaneous emission resulting from the interaction of a system with an external environment. For a composed system, each part of the system can interact with own independent environments or all the parts can be coupled to a common environment. In both cases, an initial entanglement encoded into the system degrades during the evolution. Nevertheless, the degradation process can be much slower when the parts of the system are coupled to a common rather than separate environments and, contrary to our intuition, might even entangle initially unentangled qubits. This effect,

*Corresponding author. E-mail: zficek@kacst.edu.sa.

called the environment induced entanglement has been studied for discrete (atomic) [5–11], as well as for continuous variable systems [12,13]. A crucial parameter in the case of the atoms coupled to the same external environment is the collective damping [14–19], which results from an incoherent spontaneous exchange of photons between the qubits.

The destructive effect of spontaneous emission on entanglement can take different time scales. The decoherence time depends on the damping rate of the state in which the entanglement was initially encoded and usually the decay process induced by spontaneous emission occurs exponentially in time. However, some entangled states can have interesting unusual decoherence properties that an initial entanglement can vanish abruptly in a finite time [20–23]. This drastic non-asymptotic feature of entanglement has been termed as the "entanglement sudden death", and is characteristic of the dynamics of a special class of initial entangled states. The qubits may remain separable for the rest of the evolution or entanglement may revive after a finite time [24–28].

Although the sudden death feature is concerned with the disentangled properties of spontaneous emission there is an interesting "sudden" feature in the temporal creation of entanglement from initially independent qubits [29,30]. The phenomenon termed as sudden birth of entanglement, as it is opposite to the sudden death of entanglement arises dynamically during the spontaneous evolution of an initially separate qubits. The sudden birth of entanglement is now intensively studied as it would provide a resource for a controlled creation of entanglement on demand in the presence of a dissipative environment [23].

In this paper we illustrate the effect of spontaneous emission and the interactions between atoms on entanglement creation and its transient evolution. We introduce the concurrence, the necessary and sufficient conditions for entanglement in a two-atom system. Then we turn into the dynamics of atoms interacting with a common environment and examine a possibility for entanglement creation between two atoms. We employ the dynamics of the atoms to illustrate some unusual temporary behaviours of the disentanglement process, the sudden birth and sudden death of entanglement. Next, we demonstrate under what kind of conditions the already destroyed entanglement could revive during the evolution. Finally, we discuss the role of thermal reservoir on the evolution of an initial entanglement.

The collective properties of interacting atoms, which we consider here, is a fascinating research topic in which Professor Stanisław Kielich was interested for many years. In a series of publications, he has explored the role of the interactions in light scattering [31], especially intermolecular interactions play crucial role in the cooperative light scattering discovered by Kielich and his French colleagues [32]. Another important topic investigated by Kielich since the beginning of his scientific career was the problem of optical reorientation of molecules, which started before the first laser became operational [33]. More on the research done in Kielich's group can be found in articles published in [34].

2. Two-atom system

We consider a system composed of two identical atoms located at fixed positions $\vec{r}_i$, and separated by a distance $r_{ij} = |\vec{r}_j - \vec{r}_i|$ large compared to the atomic diameter, so that overlap between the atoms can be ignored. The atoms are modeled as two-level systems with ground states $|g_i\rangle$ and excited states $|e_i\rangle$, separated by transition frequencies ω_0 and connected by a transition dipole moment $\vec{\mu}$. Both atoms are assumed to be damped with the same rates $\gamma-$the spontaneous emission rates arising from the coupling of the atoms to a common reservoir.

The dynamics of the atoms interacting with a reservoir of electromagnetic field modes at some temperature T are determined by the master equation of the density operator of the system, which in the

limit of $\omega_0 t \gg 1$ has the form [17,18]

$$\frac{\partial \rho}{\partial t} = -i\omega_0 \sum_{i=1}^{2} [S_i^z, \rho] - i \sum_{i \neq j=1}^{2} \Omega_{ij} \Big[S_i^+ S_j^-, \rho \Big]$$
$$- \frac{1}{2} \sum_{i,j=1}^{2} \gamma_{ij}(1+N) \Big\{ \Big[\rho S_i^+, S_j^- \Big] + \Big[S_i^+, S_j^- \rho \Big] \Big\},$$
$$- \frac{1}{2} \sum_{i,j=1}^{2} \gamma_{ij} N \Big\{ \Big[\rho S_i^-, S_j^+ \Big] + \Big[S_i^-, S_j^+ \rho \Big] \Big\}, \tag{1}$$

where S_i^+, S_i^-, and S_i^z are the dipole raising, lowering, and population difference operators, respectively, of the ith atom, $\gamma_{ii} \equiv \gamma$ are the spontaneous decay rates of the atoms, equal to the Einstein A coefficient for spontaneous emission, and N is the mean number of photons of the reservoir at temperature T. The photon number $N \equiv N(\omega_0)$ is given by the Planck distribution

$$N(\omega) = \frac{1}{\mathrm{e}^{\frac{\hbar\omega}{k_B T}} - 1}, \tag{2}$$

where k_B is the Boltzmann constant.

The terms in the master equation that depend on γ_{ij} and Ω_{ij} $(i \neq j)$ are the so-called *collective* terms and determine collective properties of the system. The parameter γ_{ij} represents the collective damping, while the parameter Ω_{ij} represents the dipole-dipole interaction between the atoms. The effect of Ω_{12} on the atomic system is the shift of the energy of the single excitation collective states from the single-atom energy. The collective parameters can be evaluated explicitly and are given by the expressions [15–18, 35,36]

$$\gamma_{ij} = \frac{3}{2}\gamma \left\{ \Big[1 - (\hat{\mu} \cdot \hat{r}_{ij})^2 \Big] \frac{\sin(kr_{ij})}{kr_{ij}} + \Big[1 - 3(\hat{\mu} \cdot \hat{r}_{ij})^2 \Big] \left[\frac{\cos(kr_{ij})}{(kr_{ij})^2} - \frac{\sin(kr_{ij})}{(kr_{ij})^3} \right] \right\}, \tag{3}$$

and

$$\Omega_{ij} = \frac{3}{4}\gamma \left\{ - \Big[1 - (\hat{\mu} \cdot \hat{r}_{ij})^2 \Big] \frac{\cos(kr_{ij})}{kr_{ij}} + \Big[1 - 3(\hat{\mu} \cdot \hat{r}_{ij})^2 \Big] \left[\frac{\sin(kr_{ij})}{(kr_{ij})^2} + \frac{\cos(kr_{ij})}{(kr_{ij})^3} \right] \right\}, \tag{4}$$

where $\hat{\mu}$ is the unit vector along the dipole moments of the atoms, which we have assumed to be parallel $(\hat{\mu} = \hat{\mu}_i = \hat{\mu}_j)$, $\hat{r}_{ij}$ is the unit vector in the direction of $\vec{r}_{ij}$, $k = \omega_0/c$, and r_{ij} is the distance between the atoms. For small distances between the atoms, $\gamma_{12} \approx \gamma$, whereas for large distances the collective damping vanishes as $(kr_{12})^{-1}$ and becomes negligible for $kr_{12} \gg 1$. In this limit, the atoms decay independently with a rate identical to that of a single atom.

The density operator of the system can be represented in a complete set of basis states spanned by four product (separable) states

$$|1\rangle = |g_1\rangle \otimes |g_2\rangle, |2\rangle = |g_1\rangle \otimes |e_2\rangle,$$
$$|3\rangle = |e_1\rangle \otimes |g_2\rangle, |4\rangle = |e_1\rangle \otimes |e_2\rangle. \tag{5}$$

Written in the basis (5), the density operator can have a diagonal or non-diagonal form and the presence of any non- diagonal terms simply indicates the existence of coherence effects in the system. For the examples considered in the following sections, the density matrix of a two-atom system will occur in the so-called X-state form [37,38]

$$\rho = \begin{pmatrix} \rho_{11} & 0 & 0 & \rho_{14} \\ 0 & \rho_{22} & \rho_{23} & 0 \\ 0 & \rho_{32} & \rho_{33} & 0 \\ \rho_{41} & 0 & 0 & \rho_{44} \end{pmatrix}, \tag{6}$$

where non-zero matrix elements occur only along the main diagonal and anti-diagonal. Physically, the X-state form corresponds to a situation where all coherences between the ground state $|1\rangle$ and the single excitation states $|2\rangle$ and $|3\rangle$, and between $|2\rangle$, $|3\rangle$ and the double excitation state $|4\rangle$ are zero. The X-state density matrix can be easily created by an appropriate initial preparation of a two-atom system. Also, one can find processes that not only retain the initial X-state form of the density matrix, but even could lead to the X-state form under the evolution.

One can see from Eq. (6) that in the presence of coherence, the density matrix is not diagonal. This means that the product states (5) do not correspond in general to the eigenstates of the system. In this case, a different choice of basis states is found particularly useful to work with, the basis of collective states of the system, or the Dicke states, defined as [14,15,17]

$$\begin{aligned} |g\rangle &= |g_1\rangle \otimes |g_2\rangle, \\ |s\rangle &= \frac{1}{\sqrt{2}} \left(|e_1\rangle \otimes |g_2\rangle + |g_1\rangle \otimes |e_2\rangle \right), \\ |a\rangle &= \frac{1}{\sqrt{2}} \left(|e_1\rangle \otimes |g_2\rangle - |g_1\rangle \otimes |e_2\rangle \right), \\ |e\rangle &= |e_1\rangle \otimes |e_2\rangle. \end{aligned} \tag{7}$$

It is interesting to note that the collective basis contains two states, $|s\rangle$ and $|a\rangle$ that are linear symmetric and antisymmetric superpositions of the product states, respectively. The most important is that the states are in the form of maximally entangled states. The remaining two states $|e\rangle$ and $|g\rangle$ are separable states.

3. Entanglement measure

The usual way to identify entanglement in a system being in a mixed state and composed of two sub-systems (qubits) is to examine the concurrence [39,40]. For a system described by the density matrix ρ, the concurrence $\mathcal{C}$ is defined as

$$\mathcal{C}(t) = \max\left(0, \lambda_1(t) - \lambda_2(t) - \lambda_3(t) - \lambda_4(t)\right), \tag{8}$$

where $\{\lambda_i(t)\}$ are the square roots of the eigenvalues of the non-Hermitian matrix $R = \rho(t)\tilde{\rho}(t)$ with

$$\tilde{\rho}(t) = \sigma_y \otimes \sigma_y \, \rho^*(t) \, \sigma_y \otimes \sigma_y, \tag{9}$$

and σ_y is the Pauli matrix. The range of concurrence is from 0 to 1. For unentangled (separated) atoms $\mathcal{C}(t) = 0$, whereas $\mathcal{C}(t) = 1$ for the maximally entangled atoms.

A particularly interesting behaviour of concurrence is found for a system of qubits determined by the density matrix of the X-state form, Eq. (6). To determine the concurrence, we first find the square roots of the eigenvalues of the matrix R:

$$\sqrt{\lambda_{1,2}} = \sqrt{\rho_{22}(t)\rho_{33}(t)} \pm |\rho_{14}(t)|,$$

$$\sqrt{\lambda_{3,4}} = \sqrt{\rho_{11}(t)\rho_{44}(t)} \pm |\rho_{23}(t)|, \tag{10}$$

from which it is easily verified that for a particular value of the matrix elements there are two possibilities for the largest eigenvalue, either $\sqrt{\lambda_1}$ or $\sqrt{\lambda_3}$. The two possibilities result in the concurrence of the form

$$\mathcal{C}(t) = \max\left\{0, \mathcal{C}_1(t), \mathcal{C}_2(t)\right\}, \tag{11}$$

where

$$\begin{aligned}\mathcal{C}_1(t) &= 2\left\{|\rho_{14}(t)| - \sqrt{\rho_{22}(t)\rho_{33}(t)}\right\} \\ &= 2\left\{|\rho_{ge}(t)| - \sqrt{\left[\frac{\rho_{ss}(t)+\rho_{aa}(t)}{2}\right]^2 - [\mathrm{Re}\,\rho_{sa}(t)]^2}\right\},\end{aligned} \tag{12}$$

and

$$\begin{aligned}\mathcal{C}_2(t) &= 2\left\{|\rho_{23}(t)| - \sqrt{\rho_{11}(t)\rho_{44}(t)}\right\} \\ &= 2\left\{\sqrt{\left[\frac{\rho_{ss}(t)-\rho_{aa}(t)}{2}\right]^2 + [\mathrm{Im}\,\rho_{sa}(t)]^2} - \sqrt{\rho_{ee}(t)\rho_{gg}(t)}\right\}.\end{aligned} \tag{13}$$

From this it is clear that the concurrence $\mathcal{C}(t)$ can always be regarded as being made up of either $\mathcal{C}_1(t)$ or $\mathcal{C}_2(t)$ that are associated with two different coherences which can be generated in a two qubit system. From the forms of $\mathcal{C}_1(t)$ and $\mathcal{C}_2(t)$, it is obvious that $\mathcal{C}_1(t)$ provides a measure of an entanglement produced by the two-photon coherence $\rho_{14}(t)$, whereas $\mathcal{C}_2(t)$ provides a measure of an entanglement produced by the one-photon coherence $\rho_{23}(t)$. The two alternative contributions $\mathcal{C}_1(t)$ and $\mathcal{C}_2(t)$ are traditionally understood as the *criteria* for one and two-photon entanglement, respectively.

Inspection of Eqs (12) and (13) shows that non-zero coherences $\rho_{14}(t)$ and $\rho_{23}(t)$ are the necessary condition for entanglement, but not in general sufficient one since there are also threshold terms in the concurrence measures involving the diagonal (population) terms. For example, there might be situations where the quantity $\sqrt{\rho_{11}(t)\rho_{44}(t)}$ is different from zero, and $|\rho_{23}(t)|$ may be positive but not large enough to enhance the concurrence $\mathcal{C}_2(t)$ above the threshold for entanglement. Thus, the necessary and sufficient condition for entanglement between two qubits whose the dynamics are determined by the density matrix (6) is

$$|\rho_{14}(t)| \neq 0 \quad \text{and} \quad |\rho_{14}(t)| > \sqrt{\rho_{22}(t)\rho_{33}(t)}, \tag{14}$$

or

$$|\rho_{23}(t)| \neq 0 \quad \text{and} \quad |\rho_{23}(t)| > \sqrt{\rho_{11}(t)\rho_{44}(t)}, \tag{15}$$

The thresholds for the coherences are sort of "boundaries" between classical and quantum behaviour of a two-qubit system. Above the threshold, the behaviour of the system is determined in terms of superposition states, the basic principle of quantum mechanics. Below the threshold, the qubits are separable and no superposition principle is required to determine their properties.

4. Evolution of the density matrix elements

We choose the collective states (7), as a basis for the representation of the density operator and the analysis of entanglement in the system. The equations of motion for the density matrix elements are found from the master equation (1), and are given by

$$\begin{aligned}
\dot{\rho}_{ee} &= -2\gamma(1+N)\rho_{ee} + N\left[(\gamma+\gamma_{12})\rho_{ss} + (\gamma-\gamma_{12})\rho_{aa}\right], \\
\dot{\rho}_{ss} &= (\gamma+\gamma_{12})\left[\rho_{ee} - (1+3N)\rho_{ss} - N\rho_{aa} + N\right], \\
\dot{\rho}_{aa} &= (\gamma-\gamma_{12})\left[\rho_{ee} - N\rho_{ss} - (1+3N)\rho_{aa} + N\right], \\
\dot{\rho}_{as} &= -\left[\gamma(1+2N) + 2i\Omega_{12}\right]\rho_{as}, \\
\dot{\rho}_{ge} &= -\gamma(1+2N)\rho_{ge}.
\end{aligned} \tag{16}$$

Equations (16) describe the evolution of the two-atom system in a quite general case of thermal reservoir with nonzero mean number of photons N. In case of the ordinary vacuum, the mean number of photons of the reservoir is equal to zero, $N = 0$, and Eqs (16) simplify considerably.

We begin with the simple case of reservoir being the vacuum of the electromagnetic modes, so that we put $N = 0$. One can see from Eqs (16) that the transitions rates to and from the symmetric and antisymmetric states are modified by the collective damping γ_{12}. Provided that $\gamma_{12} > 0$, the transitions to and from the symmetric state occur with an enhanced rate $\gamma + \gamma_{12}$, whereas the transitions to and from the antisymmetric state occur with a reduced rate $\gamma - \gamma_{12}$. For small separations between the atoms, $\gamma_{12} \approx \gamma$, and then the state $|s\rangle$ becomes *superradiant* with a decay rate double that of the single atom γ, whereas the state $|a\rangle$ becomes *subradiant*, with a decay rate of order $(kr_{12})\gamma$ which vanishes in the limit of small distances $kr_{12} \ll 1$.

The set of coupled equations for the populations of the collective states can be easily solved, and the solution, valid for arbitrary initial conditions and $N = 0$ is given by [15,17]

$$\begin{aligned}
\rho_{ee}(t) &= \rho_{ee}(0)\,\mathrm{e}^{-2\gamma t}, \\
\rho_{ss}(t) &= \rho_{ss}(0)\,\mathrm{e}^{-(\gamma+\gamma_{12})t} + \rho_{ee}(0)\frac{\gamma+\gamma_{12}}{\gamma-\gamma_{12}}\left[\mathrm{e}^{(\gamma-\gamma_{12})t} - 1\right]\mathrm{e}^{-2\gamma t}, \\
\rho_{aa}(t) &= \rho_{aa}(0)\,\mathrm{e}^{-(\gamma-\gamma_{12})t} + \rho_{ee}(0)\frac{\gamma-\gamma_{12}}{\gamma+\gamma_{12}}\left[\mathrm{e}^{(\gamma+\gamma_{12})t} - 1\right]\mathrm{e}^{-2\gamma t},
\end{aligned} \tag{17}$$

and $\rho_{gg}(t) = 1 - \rho_{ee}(t) - \rho_{ss}(t) - \rho_{aa}(t)$.

We see from Eq. (17) that the decay of the populations depends strongly on the initial state of the system. When the system is initially prepared in the state $|s\rangle$, the population of the initial state decays exponentially with an enhanced rate $\gamma + \gamma_{12}$, while the initial population of the antisymmetric state decays with a reduced rate $\gamma - \gamma_{12}$. This occurs because the photons emitted from the excited atom can be absorbed by the atom in the ground state, so that the photons do not escape immediately from the

system. For a general initial state that includes in the state $|e\rangle$, the populations of the symmetric and the antisymmetric states do not decay with a single exponential.

Similarly, equations of motion for the coherences, Eq. (16), are straightforward to solve, giving

$$\rho_{sa}(t) = \rho_{sa}(0)\,\mathrm{e}^{-(\gamma+2i\Omega_{12})t},$$
$$\rho_{ge}(t) = \rho_{ge}(0)\,\mathrm{e}^{-\gamma t}. \tag{18}$$

The time evolution of the density matrix elements depends on the initial state of the system. In the following sections, we will apply the solutions to analyse the time evolution of the concurrence for different initial states. We consider both separable and entangled initial states to see how spontaneous emission can affect separable and entangled properties of the system.

5. Spontaneous creation of entanglement

Let us consider first the problem of creation of entanglement in spontaneous emission from an initial separable state. We take for the initial state of our system the single-excitation state $|I\rangle = |3\rangle = |e_1\rangle \otimes |g_2\rangle$, which corresponds to atom 1 initially prepared in the excited state and atom 2 in the ground state. The initial state is, of course, a separable state. In other words, there is no entanglement in the system at $t = 0$. It is easily verified that in this case, the only non-vanishing matrix elements are

$$\rho_{ss}(0) = \rho_{aa}(0) = \rho_{sa}(0) = \rho_{as}(0) = \frac{1}{2}, \tag{19}$$

and then the initial density matrix has the following form

$$\rho(0) = \begin{pmatrix} 0 & 0 & 0 & 0 \\ 0 & \rho_{ss}(0) & \rho_{sa}(0) & 0 \\ 0 & \rho_{as}(0) & \rho_{aa}(0) & 0 \\ 0 & 0 & 0 & 0 \end{pmatrix}. \tag{20}$$

According to the solutions (17) and (18), the matrix elements which are zero at the initial time $t = 0$ will remain zero for all time, except the population of the ground state $|g\rangle$ which will buildup during the evolution. Hence, the diagonal form of the density matrix will be preserved during the evolution. Moreover, the dynamics of the systems can be confined to the subspace spanned by three state vectors only, $|g\rangle, |s\rangle$ and $|a\rangle$.

We now examine the concurrence, Eq. (11). Looking at the density matrix (20), two conclusions can be made. First of all, since the coherence $\rho_{ge}(t)$ is equal to zero for all times t, we see from Eq. (12) that the criterion $\mathcal{C}_1(t)$ is always negative. Consequently, $\mathcal{C}_1(t)$ will not contribute to the concurrence. Secondly, the upper state $|e\rangle$ is not involved in the dynamics of the system which, according to Eq. (13) rules out a possibility for the threshold behaviour of the criterion $\mathcal{C}_2(t)$. Under this situation, the time evolution of the concurrence is determined solely by the time evolution of the coherence $|\rho_{23}(t)|$, which in terms of the collective states can be written as [19]

$$\mathcal{C}(t) \equiv \mathcal{C}_2(t) = \sqrt{\left[\rho_{ss}(t) - \rho_{aa}(t)\right]^2 + 4\left[\mathrm{Im}\rho_{sa}\right]^2}$$
$$= \mathrm{e}^{-\gamma t}\sqrt{\sinh^2(\gamma_{12}t) + \sin^2(2\Omega_{12}t)}. \tag{21}$$

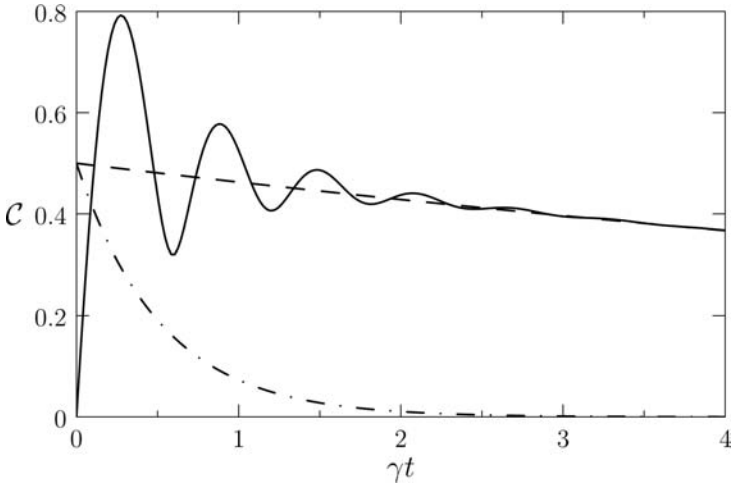

Fig. 1. Time evolution of the concurrence (solid line) and the populations of the antisymmetric (dashed line) and the symmetric (dashed-dotted line) states for the atoms prepared initially in the separable state $|3\rangle = |e_1\rangle \otimes |g_2\rangle$, with $\hat{\mu} \perp \hat{r}_{12}$, and $r_{12} = \lambda/10$.

There are two contributions to the time evolution of the concurrence. First, there is an imaginary part of the coherence between the states $|s\rangle$ and $|a\rangle$. Since this is off-resonance coupling, it leads to oscillation in the concurrence with frequency $2\,\Omega_{12}$, the frequency difference between the two states. The second contribution is the difference between the populations of the states $|s\rangle$ and $|a\rangle$. This contribution is non-oscillatory. We see that the effect of the non-oscillatory term is apparently to lengthen the lifetime of the concurrence.

Figure 1 shows the time evolution of the concurrence $\mathcal{C}(t)$, calculated from Eq. (21), together with the populations of the symmetric and the antisymmetric states. The time evolution of the concurrence reflects the time evolution of the entanglement between the atoms. It is seen that the concurrence builds up immediately after $t = 0$ and remains positive for all time, which indicates that spontaneous emission can indeed create entanglement between the initially unentangled atoms. The buildup of the concurrence in time generally consists of oscillatory and non-oscillatory components, so that two time scales of completely different behaviour of the concurrence can be distinguished. At early times, the concurrence builds up in an oscillatory manner, and the oscillatory structure is smoothed out on a time scale of $t = (\gamma + \gamma_{12})^{-1}$, the lifetime of the symmetric state. The oscillations vanish at time close to the point where the symmetric state becomes depopulated. At later times, the concurrence evolves in a non-oscillatory manner and overlaps with the population of the antisymmetric state. As a result, the concurrence decays slowly on the time scale of $t = (\gamma - \gamma_{12})^{-1}$. Although the concurrence (21) involves both symmetric and antisymmetric states, it is clear that crucial for the entanglement is the presence of the antisymmetric state.

The decay time of the population of the antisymmetric state, so that the transient entanglement seen in Fig. 1, varies with the distance between the atoms. The time goes to infinity when $kr_{12} \to 0$. In this limit the transition rates to and from the antisymmetric state vanish and the state decouples from the remaining states. Hence, any initial population encoded into the state will remain there for all times. For example, with the initial state $|3\rangle$ and $t \to \infty$, half of the population, that initially encoded into the antisymmetric state, still remains in the atomic system, and half of the population, that initially encoded into the symmetric state, is emitted into the field. As a result, the concurrence evolves to its stationary value of $\mathcal{C}(\infty) = 0.5$ indicating that in the limit of $t \to \infty$, the spontaneous emission could produce steady state entanglement to the degree of 50% with the corresponding pure state of the system.

The creation of the transient entanglement can be understood by considering the properties of the density matrix of the system. For the initial state of only one atom excited the density matrix is not diagonal due to the presence of coherences $\rho_{sa}(0)$ and $\rho_{as}(0)$. Since the form of the matrix is preserved during the evolution, it remains non-diagonal for all times. Consequently, the collective states are no longer the eigenstates of the system. The density matrix can be diagonalized to give new diagonal states. It is easy to verify that the states $|g\rangle$ and $|e\rangle$ remain unchanged, whereas the states $|s\rangle$ and $|a\rangle$ recombine into new diagonal symmetric

$$|+\rangle = \frac{[\rho_{++}(t)-\rho_{ss}(t)]|a\rangle+\rho_{as}(t)|s\rangle}{\left\{[\rho_{++}(t)-\rho_{ss}(t)]^2+|\rho_{as}(t)|^2\right\}^{\frac{1}{2}}}, \tag{22}$$

and antisymmetric

$$|-\rangle = \frac{\rho_{as}(t)|a\rangle+[\rho_{--}(t)-\rho_{aa}(t)]|s\rangle}{\left\{[\rho_{--}(t)-\rho_{aa}(t)]^2+|\rho_{as}(t)|^2\right\}^{\frac{1}{2}}}, \tag{23}$$

states, with the eigenvalues $\rho_{++}(t)$ and $\rho_{--}(t)$, the populations of the diagonal states, given by

$$\begin{aligned}\rho_{++}(t) &= \frac{1}{2}\left[\rho_{aa}(t)+\rho_{ss}(t)\right]+\frac{1}{2}\left\{[\rho_{aa}(t)-\rho_{ss}(t)]^2+4|\rho_{as}(t)|^2\right\}^{\frac{1}{2}},\\ \rho_{--}(t) &= \frac{1}{2}\left[\rho_{aa}(t)+\rho_{ss}(t)\right]-\frac{1}{2}\left\{[\rho_{aa}(t)-\rho_{ss}(t)]^2+4|\rho_{as}(t)|^2\right\}^{\frac{1}{2}}.\end{aligned} \tag{24}$$

It follows from Eq. (23) that the coherences $\rho_{sa}(t)$ and $\rho_{as}(t)$ cause the system to evolve between two "new" states $|+\rangle$ and $|-\rangle$, which are linear combinations of the collective states $|s\rangle$ and $|a\rangle$. It is easy verified that for the initial condition (19), the population $\rho_{--}(t)=0$ for all times, whereas the population $\rho_{++}(t)$ is different from zero and equals to the sum of the populations $\rho_{ss}(t)$ and $\rho_{aa}(t)$. The lack of population in the states $|-\rangle$ together with no population in the state $|e\rangle$ reduces the four-level system to an effective two-level system with the excited non-maximally entangled state $|+\rangle$ and the separable ground state $|g\rangle$. In this case, the density matrix of the system has a simple diagonal form

$$\rho(t) = \rho_{++}(t)|+\rangle\langle+| + \rho_{gg}(t)|g\rangle\langle g|. \tag{25}$$

Since $\rho_{--}(t)=0$ for all times t, we can easily find from Eq. (24) that in this case $|\rho_{as}(t)|^2=\rho_{aa}(t)\rho_{ss}(t)$, and then the state $|+\rangle$ can be written as

$$|+\rangle = \frac{\sqrt{\rho_{ss}(t)}|s\rangle+\sqrt{\rho_{aa}(t)}|a\rangle}{\sqrt{\rho_{aa}(t)+\rho_{ss}(t)}}. \tag{26}$$

When the collective states $|s\rangle$ and $|a\rangle$ are equally populated, the state $|+\rangle$ reduces to a separable state $|e_1\rangle\otimes|g_2\rangle$. On the other hand, the state $|+\rangle$ reduces to a maximally entangled state, $|s\rangle$ or $|a\rangle$, when either $\rho_{ss}(t)$ or $\rho_{aa}(t)$ is equal to zero. Since the population of the symmetric state decays faster than the antisymmetric state, see Eq. (16), at time when the state $|s\rangle$ becomes depopulated, the state $|+\rangle$ reduces to the maximally entangled antisymmetric state $|a\rangle$. This explains why at later times the evolution of the concurrence follows the evolution of the population of the state $|a\rangle$.

The above analysis gives clear evidence that the creation of transient entanglement from the separable state by spontaneous emission depends crucially on the presence of the antisymmetric state.

6. Sudden birth of entanglement

We have already seen that an entanglement can be created by spontaneous emission from an initially separable state. However, spontaneous emission offers more opportunities for unusual effects. We shall see that the creation of entanglement by spontaneous emission is not a common phenomenon for all separable states, and that for some initial states the spontaneous creation of entanglement is possible but can be delayed in time. To illustrate this phenomenon, which we shall term as *sudden birth of entanglement*, we consider two initial separable states that differ from that considered in the preceding section. In the first, we assume that initially both atoms were inverted, and in the second, we assume that the atoms were initially separable and each prepared in a linear superposition of its energy states.

We start by assuming that initially the system was prepared in the separable two-excitation state $|e\rangle$. In this case, $\rho_{ee}(0) = 1$ and all the remaining density matrix elements are zero. According to Eq. (18), the off-diagonal terms (coherences) will remain zero for all times, but the populations $\rho_{ss}(t)$, $\rho_{aa}(t)$ and $\rho_{gg}(t)$ will buildup during the evolution. This implies that for $t > 0$, the density matrix of the system spanned in the basis of the collective states (7), will have a diagonal form for all t:

$$\rho(t) = \begin{pmatrix} \rho_{gg}(t) & 0 & 0 & 0 \\ 0 & \rho_{ss}(t) & 0 & 0 \\ 0 & 0 & \rho_{aa}(t) & 0 \\ 0 & 0 & 0 & \rho_{ee}(t) \end{pmatrix}, \tag{27}$$

with the time dependent density matrix elements given by

$$\begin{aligned} \rho_{ee}(t) &= \mathrm{e}^{-2\gamma t}, \\ \rho_{ss}(t) &= \frac{\gamma + \gamma_{12}}{\gamma - \gamma_{12}} \left[\mathrm{e}^{(\gamma - \gamma_{12})t} - 1 \right] \mathrm{e}^{-2\gamma t}, \\ \rho_{aa}(t) &= \frac{\gamma - \gamma_{12}}{\gamma + \gamma_{12}} \left[\mathrm{e}^{(\gamma + \gamma_{12})t} - 1 \right] \mathrm{e}^{-2\gamma t}, \end{aligned} \tag{28}$$

and $\rho_{gg}(t) = 1 - \rho_{ee}(t) - \rho_{ss}(t) - \rho_{aa}(t)$.

Looking at the density matrix (27) and the criteria for entanglement, Eqs (12) and (13), one can easily find that in this case $\mathcal{C}_1(t)$ is always negative. Thus, positive values of the concurrence, so that the entanglement are determined only by the criterion $\mathcal{C}_2(t)$:

$$\mathcal{C} = \max\left\{0, \mathcal{C}_2(t)\right\}, \tag{29}$$

with

$$\mathcal{C}_2(t) = |\rho_{ss}(t) - \rho_{aa}(t)| - 2\sqrt{\rho_{gg}(t)\rho_{ee}(t)}. \tag{30}$$

It is clear from Eq. (30) that entanglement, if any, may only result from an unequal population of the symmetric and antisymmetric states. When the system is prepared in the state $|e\rangle$, the resulting spontaneous transitions are cascades: The system decays first to the intermediate states $|s\rangle$ and $|a\rangle$, from which then decays to the ground state $|g\rangle$. Since the transition rates to and from the states $|s\rangle$ and $|a\rangle$ are different when $\gamma_{12} \neq 0$, there appears unbalanced population distribution between these states. According to Eq. (30), this may result in a transient entanglement between the atoms.

To visualise the behaviour of the concurrence, we plot $\mathcal{C}(t)$ as a function of time and the distance between the atoms in Fig. 2. The system was initially in the separable two-excitation state $|e\rangle$. We

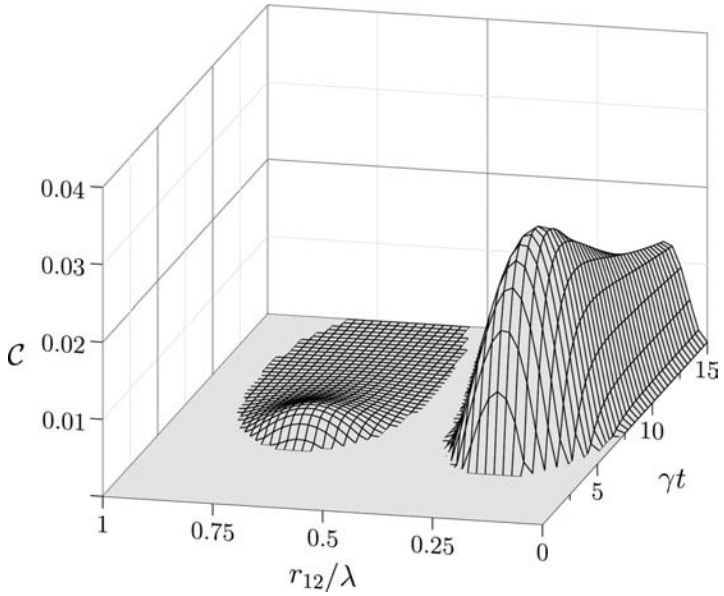

Fig. 2. A three-dimensional plot of the concurrence $\mathcal{C}(t)$ as a function of time γt and the distance r_{12}/λ between two, initially inverted atoms with the polarisation of the atomic dipole moments perpendicular to the inter-atomic axis, $\hat{\mu} \perp \hat{r}_{12}$.

see that there is no entanglement at earlier times, but suddenly at some finite time an entanglement emerges. However, it happens only for a limited range of the distances r_{12}. It is easily verified that the "islands" of entanglement seen in Fig. 2 appear at distances for which γ_{12} is different from zero. Again, it reflects the role of the collective damping which is responsible for creation of entanglement by spontaneous emission from an initial separable state. This result also demonstrates how the collective damping leading to entanglement between the atoms becomes less important as the interatomic distance is increased. Atoms separated by more than just a few wave-lengths become separable.

We have seen that γ_{12} modifies the damping rates of the transitions between the collective states and, on the other hand, introduces two time scales for the decay of the population of the system. One can easily find that the entanglement seen in Fig. 2 decays out on a time scale $(\gamma-\gamma_{12})^{-1}$ that is the time scale of the population decay from the antisymmetric state. Again, this shows that crucial for entanglement creation by spontaneous emission is the presence of the antisymmetric state. This is perhaps not surprising, as the population of the antisymmetric state builds up on a much longer time scale than the population of the symmetric state. At long times, the antisymmetric state will posses a large population with no population left in the symmetric state. What is surprising and, in fact, is very similar to the situation found in the Dicke model that at early times $\gamma t \ll 1$ and $\gamma_{12} \neq 0$, the symmetric state is significantly populated with almost no population in the antisymmetric state, and no entanglement is created.

The above considerations are supported by the analysis of the time evolution of the population of the excited states of the system that is illustrated in Fig. 3. It is quite evident from the figure that at the time $t \approx 4/\gamma$ when the entanglement starts to build up, the antisymmetric state is the only excited state of the system being populated. Clearly, the effect of the delayed creation of entanglement is attributed to the slow decay rate of the antisymmetric state. The state decays on the time scale of $(\gamma - \gamma_{12})^{-1}$ that is much longer than the decay time of the symmetric and the upper states.

Let us consider an another example of a delayed creation of entanglement from an initial separable state. This time, we consider an initial separable state which leads to a very general form of the initial

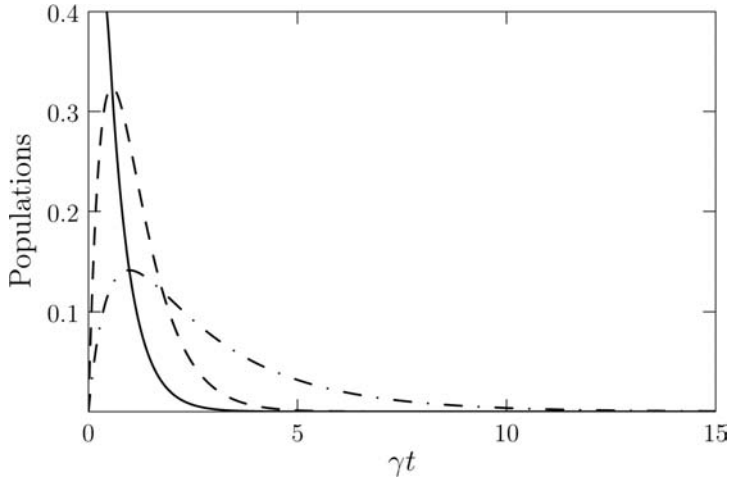

Fig. 3. The time evolution of the populations $\rho_{ee}(t)$ (solid line), $\rho_{ss}(t)$ (dashed line) and $\rho_{aa}(t)$ (dash-dotted line) for $r_{12}/\lambda = 0.25$ and $\vec{\mu} \perp \vec{r}_{12}$.

density matrix, in which all the initial density matrix elements are different from zero. An example of such a state is a product state in which the atoms are prepared in the superposition of their energy states by a short $\pi/2$ pulse

$$|\Phi_0\rangle = \frac{1}{2}\Big(|g_1\rangle + i\mathrm{e}^{i\vec{k}_L\cdot\vec{r}_1}|e_1\rangle\Big)\otimes\Big(|g_2\rangle + i\mathrm{e}^{i\vec{k}_L\cdot\vec{r}_2}|e_2\rangle\Big)\,, \tag{31}$$

where $\vec{k}_L$ is the wave vector of the excitation field.

With the state $|\Phi_0\rangle$, the initial values of the density matrix elements are

$$\begin{aligned}
&\rho_{ea}(0) = \rho_{ag}(0) = -\frac{1}{2\sqrt{2}}\sin\left(\frac{1}{2}\vec{k}_L\cdot\vec{r}_{12}\right),\\
&\rho_{es}(0) = \rho_{sg}(0) = \frac{i}{2\sqrt{2}}\cos\left(\frac{1}{2}\vec{k}_L\cdot\vec{r}_{12}\right),\\
&\rho_{gg}(0) = \frac{1}{4}, \quad \rho_{eg}(0) = -\frac{1}{4},\\
&\rho_{sa}(0) = \frac{1}{4}i\sin\vec{k}_L\cdot\vec{r}_{12}, \quad \rho_{ss}(0) = \frac{1}{4}\left(1+\cos\vec{k}_L\cdot\vec{r}_{12}\right),\\
&\rho_{aa}(0) = \frac{1}{4}\left(1-\cos\vec{k}_L\cdot\vec{r}_{12}\right), \quad \rho_{ee}(0) = \frac{1}{4},
\end{aligned} \tag{32}$$

where $\vec{k}_L\cdot\vec{r}_{12} = k_L r_{12}\cos\theta$, with $\theta-$the angle between the excitation direction $\vec{k}_L$ and the vector $\vec{r}_{12}$ connecting the atoms. In the derivation of the initial values (32) we have assumed, without loss of generality, that the atoms are located at points $\vec{r}_1 = (-\frac{1}{2}r_{12},0,0)$ and $\vec{r}_2 = (\frac{1}{2}r_{12},0,0)$, such that $\vec{r}_1 + \vec{r}_2 = 0$. We see that the initial values of the density matrix elements involving the single-excitation states depend on the distance between the atoms and the direction of excitation relative to the interatomic axis.

It is important to note here that the density matrix of the system prepared initially in the state (32) has no longer the X-state form. In this case, all of the density matrix elements are initially different from

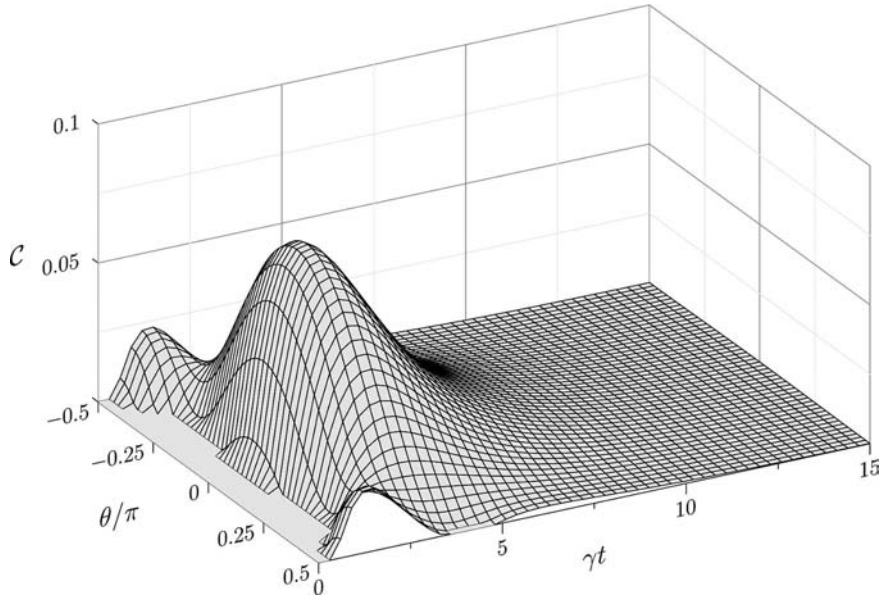

Fig. 4. The time evolution of the concurrence and its dependence on the direction of excitation relative to the inter-atomic axis for $r_{12}/\lambda = 0.25$ and the polarization of the atomic dipole moments $\vec{\mu} \perp \vec{r}_{12}$.

zero. Consequently, the concurrence must be calculated according to the general formula (8) rather than the criteria (12) and (13).

Figure 4 shows the concurrence as a function of time and the angle θ. It is seen that there is no entanglement at earlier times independent of the direction of excitation, and *suddenly* at some finite time an entanglement emerges. The magnitude of the entanglement created depends on the direction of excitation. A large entanglement is created when the system is excited in the direction of the interatomic axis, $\theta = 0$. This means that crucial for entanglement creation by spontaneous emission is to excite the system through the antisymmetric state. This is seen from analysis of the time evolution of the population of the excited states. Figure 5 shows the time evolution of the populations of the excited states of the system. It is clear from the figure that at the time $t \approx 4/\gamma$ when the entanglement starts to build up, the antisymmetric state is the only excited state of the system being populated. This effect is attributed to the slow decay rate of the antisymmetric state. As we have already noticed, the state decays on the time scale of $(\gamma - \gamma_{12})^{-1}$ that is much longer than the decay time of the symmetric and the upper states.

We may summarize that the phenomenon of sudden birth of entanglement is characteristic of initial states which include a population of the two-excitation state. The delayed sudden birth of entanglement is not found in a system with initially only one qubit excited. In experimental practice, the initial conditions of both atoms inverted can be done by using a standard technique of a short π pulse excitation. One could also use a short $\pi/2$ pulse excitation which leaves atoms separable and simultaneously prepared in the superposition of their energy states that populates the state with both atoms inverted.

7. Sudden death of entanglement

We now turn to an another "sudden" feature of entanglement, the phenomenon of entanglement *sudden death*, i.e., abrupt disappearance of an inital entanglement at a finite time. The subject received its initial

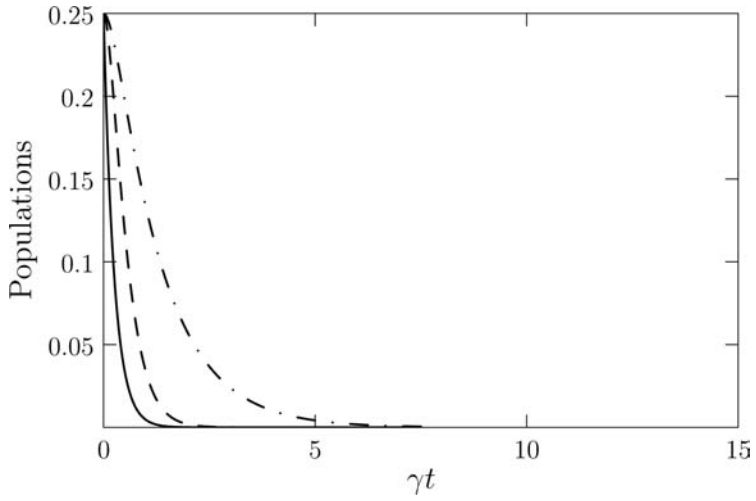

Fig. 5. The time evolution of the populations $\rho_{ee}(t)$ (solid line), $\rho_{ss}(t)$ (dashed line) and $\rho_{aa}(t)$ (dash-dotted line) for $\theta = 0$, $r_{12}/\lambda = 0.25$ and $\vec{\mu} \perp \vec{r}_{12}$.

stimulus in an article by Yu and Eberly [20,21], in which they for the first time introduced the concept of sudden death of entanglement. Many authors since have dealt with the entanglement sudden death in systems composed of two atoms or two harmonic oscillators. The literature on this subject can be divided into two categories: (i) evolution of an initial entanglement of independent atoms interacting with local environments [44], and (ii) entangled evolution of interacting atoms coupled to a common environment [45–50]. We postpone the studies of the latter group to the following section, where we will mostly focus on the phenomenon of entanglement revival. Here, we focus on the original concept of Yu and Eberly, and discuss in details the phenomenon of sudden death of entanglement in a system of two independent atoms interacting with local environments. This model is also applicable to a situation of two distant atoms interacting with a common environment. At large distances, the collective parameters γ_{12} and Ω_{12} are very small, so that the interaction between the atoms can be ignored and the atoms can be treated as independent sub-systems.

Let us suppose that at $t = 0$, a system of two independent atoms is prepared in a non-maximally entangled state of the form

$$|\Psi_0\rangle = \sqrt{q}\,|e_1\rangle \otimes |e_2\rangle + \sqrt{1-q}\,|g_1\rangle \otimes |g_2\rangle, \tag{33}$$

where q is a positive real number such that $0 \leqslant q \leqslant 1$. The state corresponds to an excitation of the system into a coherent superposition of its product states in which both or neither of the atoms is excited. In the special case of $q = 1/2$, the state (33) reduces to the maximally entangled Bell state.

Consider now the time evolution of the concurrence when the system is initially prepared in the state (33). It is not difficult to verify that the initial values for the density matrix elements are

$$\rho_{ee}(0) = q,\ \rho_{ge}(0) = \sqrt{q(1-q)},\ \rho_{gg}(0) = 1-q, \tag{34}$$

and the other matrix elements, the populations of the symmetric and antisymmetric states, and all one-photon coherences are zero, i.e. $\rho_{ss}(0) = \rho_{aa}(0) = 0$ and $\rho_{es}(0) = \rho_{ea}(0) = \rho_{sg}(0) = \rho_{ag}(0) = \rho_{as}(0) = 0$. According to Eq. (18), the coherences will remain zero for all time, that they cannot be produced by spontaneous decay. However, the populations $\rho_{ss}(t)$ and $\rho_{aa}(t)$ can buildup during the

evolution. This implies that for all times, the density matrix of the system spanned in the basis of the collective states (7), is in the X-state form

$$\rho(t) = \begin{pmatrix} \rho_{gg}(t) & 0 & 0 & \rho_{ge}(t) \\ 0 & \rho_{ss}(t) & 0 & 0 \\ 0 & 0 & \rho_{aa}(t) & 0 \\ \rho_{eg}(t) & 0 & 0 & \rho_{ee}(t) \end{pmatrix}, \tag{35}$$

with the density matrix elements evolving as

$$\begin{aligned} \rho_{ee}(t) &= q\,\mathrm{e}^{-2\gamma t}, \\ \rho_{ge}(t) &= \sqrt{q(1-q)}\,\mathrm{e}^{-(\gamma-2i\omega_0)t}, \\ \rho_{ss}(t) &= \rho_{aa}(t) = q\left(1-\mathrm{e}^{-\gamma t}\right)\mathrm{e}^{-\gamma t}, \end{aligned} \tag{36}$$

subject to conservation of the trace of $\rho(t)$: $\rho_{gg}(t) = 1 - \rho_{ss}(t) - \rho_{aa}(t) - \rho_{ee}(t)$. It is to be noticed that the symmetric and antisymmetric states are equally populated for all time. This holds for any initial state and results from the fact that the atoms radiate independently from each other. In this case, the populations of the collective states decay with the same rate, equal to the single-atom damping rate. Therefore, the initial relation between the populations cannot be changed during the spontaneous emission.

The density matrix (35) leads to a particularly simple expression for the concurrence. In general, the concurrence is given in terms of two entanglement criteria $\mathcal{C}_1(t)$ and $\mathcal{C}_2(t)$, as seen from Eq. (11). However, with the initial state (33), the two-photon coherence $\rho_{ge}(t)$ is different from zero and the symmetric and antisymmetric states are equally populated for all time. As a consequence, the criterion $\mathcal{C}_2(t)$ is always negative, irrespective of q and times t. Therefore, entangled properties of the system are solely determined by the criterion $\mathcal{C}_1(t)$. On substituting from Eq. (36) into Eq. (12), we obtain the following expression for the concurrence

$$\mathcal{C}(t) = \max\left\{0,\, D(t)\,\mathrm{e}^{-\gamma t}\right\}, \tag{37}$$

where

$$D(t) = 2\sqrt{q(1-q)}\left[1 - \sqrt{\frac{q}{1-q}}\left(1-\mathrm{e}^{-\gamma t}\right)\right]. \tag{38}$$

This shows that transient features of the initial entanglement are determined by the properties of the function $D(t)$ which, on the other hand, is dependent on the parameter q. It is evident from Eq. (38) that there is a threshold for values of q; $q = 1/2$, below which $D(t)$ is always positive. However, above the threshold, $D(t)$ can take negative values indicating that the initial entanglement can vanish at a finite time. Consequently, the sudden death of the entanglement is possible for initial states with $q > 1/2$. Since $\rho_{ee}(0) = q$, we can conclude that the entanglement sudden death is ruled out for the initially not inverted system.

Figure 6 shows the concurrence $\mathcal{C}(t)$, calculated from Eq. (37), as a function of time for two different values of the parameter q. It is evident from the figure that for $q < 1/2$ the initial entanglement decays exponentially in time without any discontinuity. The entanglement sudden death appears for $q > 1/2$ that the concurrence decays in a non-exponential way and vanishes at a finite time. In addition, we plot the two-photon coherence $2|\rho_{eg}(t)|$ for $q = 2/3$. It is apparent that the coherence decays exponentially

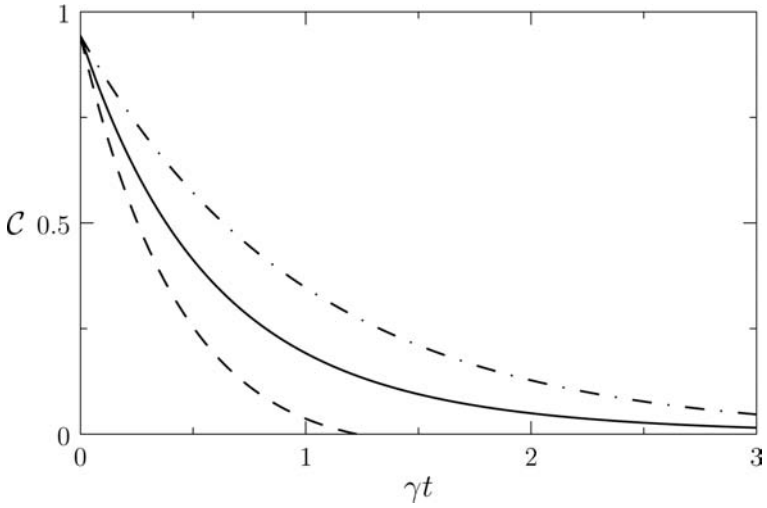

Fig. 6. Time evolution of the concurrence $\mathcal{C}(t)$ for two values of the parameter q: $q = 1/3$ (solid line) and $q = 2/3$ (dashed line). We also plot the time evolution of the two-photon correlation $2|\rho_{eg}(t)|$ (dashed-dotted line), with $q = 2/3$.

in time, which clearly illustrates that the entanglement disappears at finite time despite the fact that the two-photon coherence is different from zero for all time.

As we have already stated, time at which the entanglement disappears is a sensitive function of the initial conditions determined by the parameter q. It is easily verified from Eq. (38) that the time t_d at which the entanglement disappears is given by

$$t_d = \frac{1}{\gamma} \ln \left(\frac{q + \sqrt{q(1-q)}}{2q-1} \right). \tag{39}$$

The time t_d gives the collapse time of the entanglement beyond which the entanglement disappears. The dead zone of the entanglement continues till infinity that the entanglement never revives. It may continue for a finite rather than infinite time that under some circumstances the already dead entanglement may revive after some finite time. A revival of the entanglement may occur when the atoms directly interact with each other. We leave the discussion of this problem to the following section.

7.1. Experimental demonstration of entanglement sudden death

The phenomenon of entanglement sudden death has been experimentally demonstrated by Almeida et al. [51]. The apparatus used in the experiment involved a tomographic reconstruction of the density matrix and from it the concurrence by measuring polarisation entangled photon pairs produced in the process of spontaneous parametric down-conversion by a system composed of two adjacent nonlinear crystals. One of the crystals produced photon pairs with V-polarisation and the other produced pairs with H-polarisation. Parametric down conversion is a nonlinear process used to produce polarisation entangled photon pairs, which are manifested by the simultaneous or nearly simultaneous production of pairs of photons in momentum-conserving, phase matched modes. Since the pairs of polarised photons are spatially indistinguishable, they are described by a pure state

$$|\Phi\rangle = |\alpha||HH\rangle + |\beta|\mathrm{e}^{i\delta}|VV\rangle. \tag{40}$$

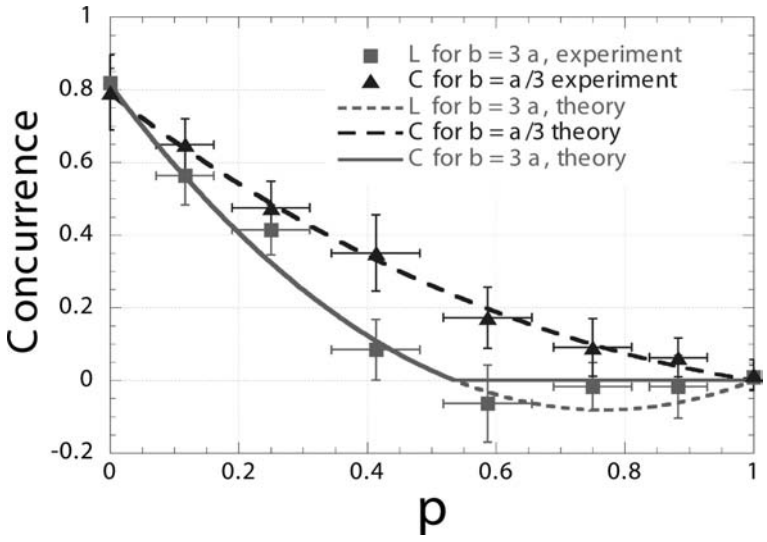

Fig. 7. Experimental results demonstrating the phenomenon of entanglement sudden death. The theoretical prediction for the concurrence is plotted as a function of $p = 1 - \exp(-\gamma t)$ for two values of the ratio $|\beta|/|\alpha|$: $|\beta|/|\alpha| = 3$ (solid line) and $|\beta|/|\alpha| = 0.333$ (dashed line). The squares and triangles are experimentally measured values for the concurrence.

where the coefficients $|\alpha|$ and $|\beta|$, and the phase δ were adjusted by applying half- and quarter-wave plates in the laser beam pumping the crystals to control the creation of pairs of a desired polarisation. In the experiment, they measured the decay of a single polarised beam, serving as a qubit, which was monitored by generating pairs of photons of the same polarisation and registering coincidence counts with one photon propagating through the interferometer and the other serving as a trigger.

Figure 7 shows the results of the measured concurrence for two different values of the ratio $|\beta|/|\alpha|$. The solid and dashed lines represent the theoretically predicted concurrence. The measured values for the concurrence are found to be in good agreement with the theoretical predictions. Thus, it was confirmed that entanglement may display the sudden death feature and that the spontaneous decay of the initial entanglement depends on the relation between the coefficients $|\alpha|$ and $|\beta|$. For $|\beta| < |\alpha|$ the entanglement decays exponentially in time, while for $|\beta| > |\alpha|$, the entanglement vanishes at finite time.

8. Revival of entanglement

We have already shown that under appropriate conditions, two initially entangled and afterwards not interacting qubits can become completely disentangled in a finite time. We have discussed this phenomenon for the case of independent atoms. In this section, we extend these analysis to include the direct interactions between the atoms and study in details the time evolution of an initial entanglement. As we shall see, the interactions impose strong qualitative changes to the time evolution of entanglement that the irreversible spontaneous decay can lead to a *revival* of the entanglement that has already been destroyed [24–26].

Consider again the initial state of the system given by Eq. (33), but now assume that the atoms can interact with each other. In this case, the initial values of the density matrix of the system are the same as for independent atoms, but the time evolution of the density matrix elements is different. It is now

given by

$$\begin{aligned}
\rho_{ee}(t) &= q\,\mathrm{e}^{-2\gamma t},\\
\rho_{eg}(t) &= \sqrt{q(1-q)}\,\mathrm{e}^{-(\gamma-2i\omega_0)t},\\
\rho_{ss}(t) &= q\,\frac{\gamma+\gamma_{12}}{\gamma-\gamma_{12}}\left[\mathrm{e}^{(\gamma-\gamma_{12})t}-1\right]\mathrm{e}^{-2\gamma t},\\
\rho_{aa}(t) &= q\,\frac{\gamma-\gamma_{12}}{\gamma+\gamma_{12}}\left[\mathrm{e}^{(\gamma+\gamma_{12})t}-1\right]\mathrm{e}^{-2\gamma t},
\end{aligned} \tag{41}$$

and $\rho_{gg}(t) = 1-\rho_{ee}(t)-\rho_{ss}(t)-\rho_{aa}(t)$. As before for independent atoms, the remaining density matrix elements are equal to zero. By comparing Eq. (41) with Eq. (36) for independent atoms, we see that a major difference between the time evolution of the density matrix elements for independent and interacting atoms is that in the later the symmetric and antisymmetric states are populated with different rates. As a result, the transient buildup of the populations from $\rho_{ss}(0) = \rho_{aa}(0) = 0$ at $t = 0$ will lead to unequal populations of the states for all later times $t > 0$.

A direct consequence of unequal populations of the symmetric and antisymmetric states is seen in the transient evolution of an initial entanglement which may now depend on both criteria $\mathcal{C}_1(t)$ and $\mathcal{C}_2(t)$, that are needed to construct the concurrence $\mathcal{C}(t)$, rather than on one of them. According to Eqs (12) and (34), a two-atom system initially prepared in the state (33) can be entangled according to the criterion $\mathcal{C}_1(t)$, and the degree to which the system is initially entangled is $\mathcal{C}_1(0) = 2\sqrt{q(1-q)}$. The other criterion, $\mathcal{C}_2(t)$, is negative at $t = 0$. Nevertheless, during the spontaneous evolution, a population builds up in the symmetric and antisymmetric states and according to Eq. (41), $\rho_{ss}(t) \neq \rho_{aa}(t)$ for all $t > 0$. As discussed in Sec. 3, an unequal population of the states gives rise to positive values of the criterion $\mathcal{C}_2(t)$ which then may result in an entanglement of the atoms. Of course, in order to create the entanglement, the population difference has to overweight the threshold term in the criterion $\mathcal{C}_2(t)$. If this is the case, we could see an entanglement having its origin in the correlation determined by the criterion $\mathcal{C}_2(t)$.

According to the above discussion, the concurrence, in general, is determined by both, $\mathcal{C}_1(t)$ and $\mathcal{C}_2(t)$ criteria

$$\mathcal{C}(t) = \max\left\{0,\, \mathcal{C}_1(t),\, \mathcal{C}_2(t)\right\}, \tag{42}$$

where $\mathcal{C}_1(t)$ and $\mathcal{C}_2(t)$, written in the basis of the collective states are of the form

$$\mathcal{C}_1(t) = 2|\rho_{eg}(t)| - \left[\rho_{ss}(t) + \rho_{aa}(t)\right], \tag{43}$$

and

$$\mathcal{C}_2(t) = |\rho_{ss}(t) - \rho_{aa}(t)| - 2\sqrt{\rho_{gg}(t)\rho_{ee}(t)}. \tag{44}$$

We point out again, that initially at $t = 0$, the criterion $\mathcal{C}_2(0)$ is negative, but it may rise to positive values during the evolution of the system. Thus, an entanglement can be generated during the spontaneous evolution of the system. This kind of entanglement is an example of spontaneously generated entanglement.

Figure 8 shows the deviation of the time evolution of the concurrence for two interacting atoms ($\gamma_{12} \neq 0$) from that of independent atoms ($\gamma_{12} = 0$). In both cases, the initial entanglement falls sharply in time. For independent atoms we observe the collapse of the entanglement without any revivals.

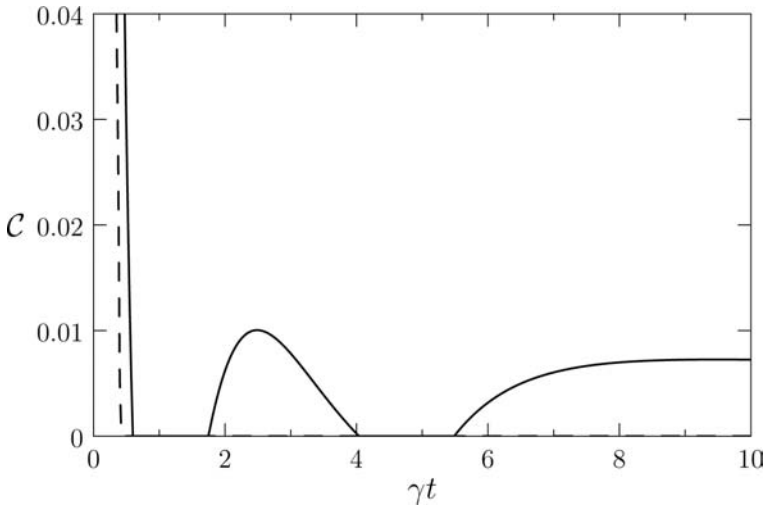

Fig. 8. Time evolution of the concurrence $\mathcal{C}(t)$ for the initial state (33) with $q = 0.9$. The solid line represents $\mathcal{C}(t)$ for the collective system with the interatomic separation $r_{12} = \lambda/20$. The dashed line shows $\mathcal{C}(t)$ for independent atoms, $\gamma_{12} = 0$.

However, for interacting atoms, the system collapses over a short time and remains disentangled until a time $t_r \approx 1.5/\gamma$ at which, somewhat counterintuitively, the entanglement revives. This revival then decays asymptotically to zero, but after some period of time it revives again. Thus, important features of the transient evolution of the entanglement is that there are two time intervals at which the entanglement vanishes and two time intervals at which the entanglement revives.

The origin of the sudden death and revivals of the entanglement can be explained in terms of the populations of the collective states and the rates with which the populations and the two-photon coherence decay. It is easily verified from Eq. (41) that at early times of $\gamma t \ll 1$, the population $\rho_{aa}(t) \approx 0$, but $\rho_{ss}(t)$ is large. Moreover, the two-photon coherence $|\rho_{eg}(t)|$ is also large at that short time. Thus, the entanglement behaviour can be understood entirely in terms of the population $\rho_{ss}(t)$ and the coherence $|\rho_{eg}(t)|$. In this connection, we compare in Fig. 9 the transient behaviour of the concurrence $\mathcal{C}(t)$, with the transient properties of the population $\rho_{ss}(t)$, and the coherence $\rho_{eg}(t)$ for the same choice of parameters as in Fig. 8. As can be seen from the graphs, the entanglement vanishes at the time where $\rho_{ss}(t)$ is maximal, and remains zero until the time t_r at which $\rho_{ss}(t)$ becomes smaller than $|\rho_{eg}(t)|$. Clearly, the first dead zone of the entanglement arises due to the significant accumulation of the population in the symmetric state.

The reason for the first revival of the entanglement is in the unequal decay rates of the population $\rho_{ss}(t)$ and the coherence $|\rho_{ge}(t)|$. According to the criterion $\mathcal{C}_1(t)$, entanglement would be generated if the sum of the populations of the single-photon collective states is small while at the same time the two-photon coherence is large. Since the coherence $\rho_{ge}(t)$ decays more slowly than the population of the symmetric state, and keeping in mind that the population of the antisymmetric state is negligibly small at that time, the two-photon coherence can become significant and entanglement generated over some period of time during the decay. Note, that this is the same coherence that produced the initial entanglement. Therefore, we may call the first revival as an "echo" of the initial entanglement that has been unmasked by destroying the population of the symmetric state.

The revival of the entanglement depends on the initial state of the system, which is determined by the parameter q. There is a range of values of q for which the concurrence is positive. This range defines the values of q for which the first revival occurs. The range depends on the values of γ_{12} and

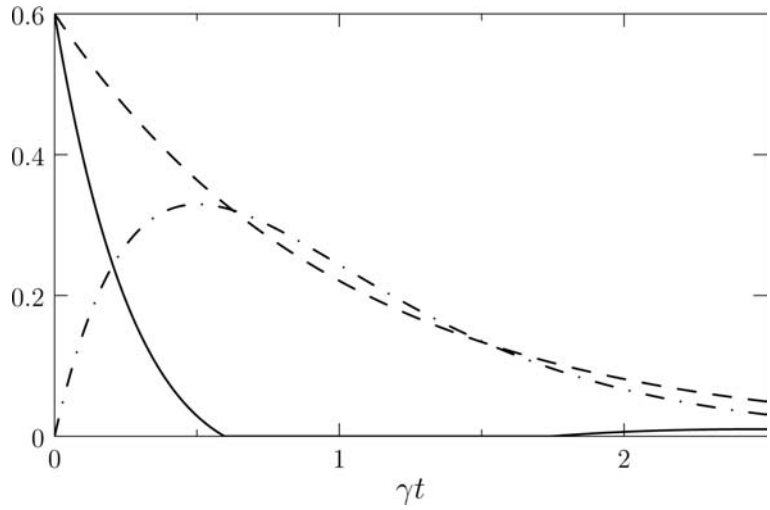

Fig. 9. Time evolution of the concurrence $\mathcal{C}(t)$ (solid line), the two-photon coherence $2|\rho_{eg}(t)|$ (dashed line) and the population $\rho_{ss}(t)$ (dashed-dotted line) plotted for the same parameters as in Fig. 8.

the revival is most pronounced for q over the range $0.85 \leqslant q \leqslant 0.95$. For values outside this range, no revival is observed. Note that the values of q at which a pronounced revival exists are close to one. This is not surprised because for $q > 1/2$ the system is initially inverted that increases the rate of spontaneous emission.

We may estimate approximate values for the first death and revival times of the entanglement. Using Eqs (12) and (41) we find that in the case of small inter-atomic separations, at which $\gamma_{12} \approx \gamma$, the entanglement criterion $\mathcal{C}_1(t)$ attains zeroth at times satisfying the relation

$$\gamma t \, \exp(-\gamma t) = \sqrt{\frac{1-q}{q}}, \tag{45}$$

which for $q > 0.85$ has two non-degenerate solutions, t_d and $t_r > t_d$. The solution t_d gives the death time of the entanglement beyond which it disappears. At this time, the atoms become disentangled and remain separable until the time t_r, at which the entanglement revives. The analytic expression (45) makes clear that for the parameters of Fig. 8, the system disentangles at $t_d = 0.6/\gamma$ and entangles again at the time $t_r = 1.7/\gamma$.

As we have seen in Fig. 8, the entanglement revives not once but twice, and the second revival occurs at long times. The long time entanglement has completely different origin than that at short times. At long times, all the density matrix elements are almost zero except $\rho_{aa}(t)$, which remains large even for long times due to the small decay rate of the antisymmetric state. These considerations imply that the long time entanglement comes from the population $\rho_{aa}(t)$ which determines positive values of the criterion $\mathcal{C}_2(t)$. The entanglement decays asymptotically with the reduced rate $\gamma - \gamma_{12}$, and vanishes at

$$t_{d2} \approx \frac{1}{\gamma} \mathrm{arcsinh}\left(\sqrt{\frac{1-q}{q}} \frac{2\gamma}{\gamma - \gamma_{12}}\right). \tag{46}$$

This explicitly shows that lifetime of the entanglement depends on the collective damping parameter γ_{12} and approaches infinity when $\gamma_{12} \to \gamma$. The rich structure of the death and revival of entanglement is illustrated in Fig. 10, where the dependence of both, death time t_d and revival time t_r is plotted versus

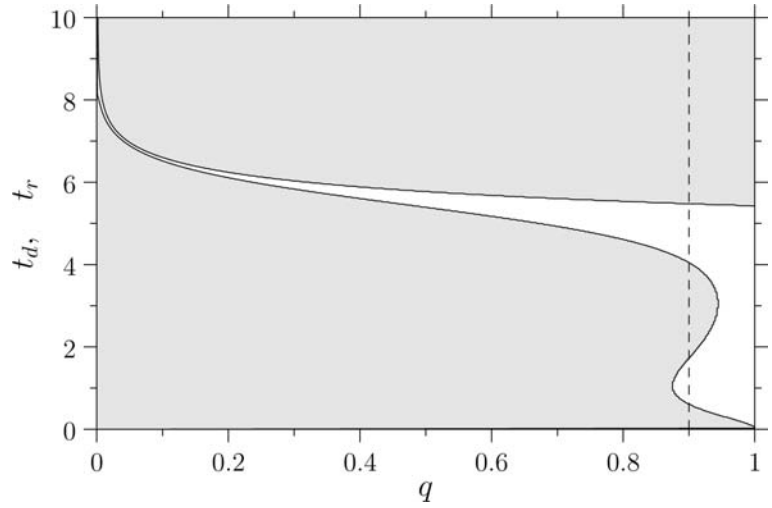

Fig. 10. Dependence of the entanglement death time t_d and revival time t_r on the parameter q, plotted in units of γ^{-1}, for the initial state given by (33) and $r_{12} = \lambda/20$. Shadowed area indicates presence of entanglement. The dashed line shows the trajectory for $q = 0.9$ illustrated in Fig. 8.

q for the whole range of values of the parameter q. The dashed line in Fig. 10 indicates the trajectory illustrated in Fig. 8. Gray area marks the area of nonzero concurrence, i.e., presence of entanglement.

We may conclude that the most interesting consequence of the collective damping is the possibility of entanglement revival. What is even more remarkable, the revival of entanglement occurs under the spontaneous evolution of the system without the presence of any external coherent fields. We may say that entanglement is reversible even if it evolves under the irreversible process.

Finally, we would like to point out that entanglement revival is associated not only with the collective damping, but may occur in a number of other situations. For example, it has been found that entanglement revival may occur under non-Markovian dynamics of two independent atoms coupled to local reservoirs [27]. Here, the memory effects of the non-Markovian dynamics may result in the "return" of the correlation from the reservoirs to the atoms. Entanglement revival has also been found in reversible systems whose dynamics are determined by the Jaynes-Cummings Hamiltonian [28,25,26]. In these models, an initial entanglement encoded into atoms undergoes a coherent transfer forth and back to the field modes, so it returns periodically to the atoms.

9. Thermal reservoir

So far, we have discussed entanglement evolution of the two-atom system interacting with the ordinary vacuum, that can be considered as the thermal reservoir at zero temperature. In this case the mean number of photons of the reservoir is zero, i.e., we have assumed $N = 0$. Now, we extend our discussion to the situation when the temperature of the reservoir is not zero. In this case we have to come back to equations (16). Before we calculate the time evolution, let us note that equations (16) for $N \neq 0$ have nonzero steady state solutions, which are given by [52]

$$\rho_{ee}(\infty) = \frac{N^2}{(2N+1)^2},$$

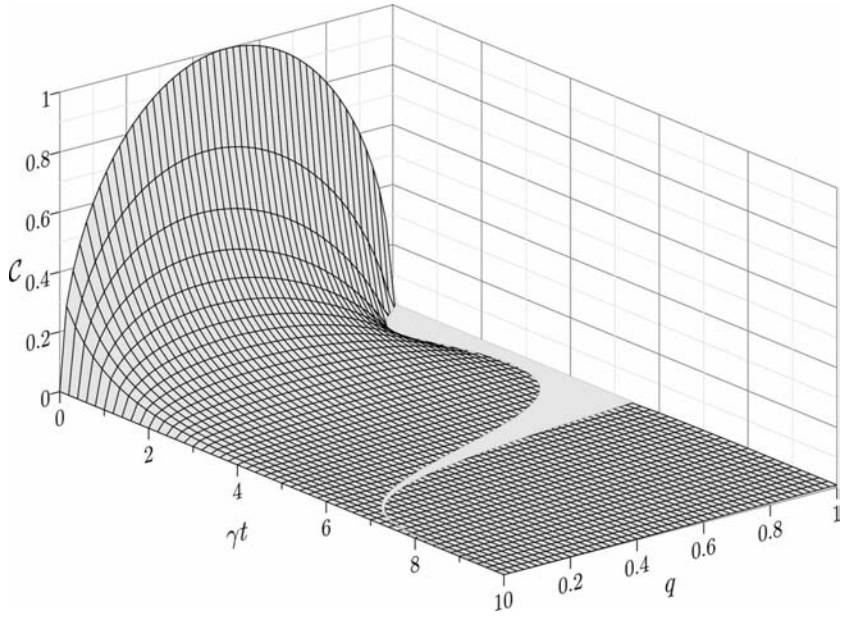

Fig. 11. Concurrence evolution for various values of the parameter q and the initial state (33) with $r_{12}/\lambda = 1/20$ and $N = 0$.

$$\rho_{ss}(\infty) = \rho_{aa}(\infty) = \frac{N(N+1)}{(2N+1)^2}, \tag{47}$$

$$\rho_{gg}(\infty) = \frac{(N+1)^2}{(2N+1)^2},$$

and the steady state values of the coherences $\rho_{as}(\infty)$ and $\rho_{eg}(\infty)$ are zeros. From the solutions (47) and the entanglement criteria (12) and (13), it is immediately seen that $\mathcal{C}_1(t)$ must become negative at some finite time t_d. Moreover, since $\sqrt{\rho_{ee}(\infty)\rho_{gg}(\infty)} = \rho_{ss}(\infty) = \rho_{aa}(\infty)$, it means that $\mathcal{C}_2(t)$ must also become negative at some finite time t_d. Note, that the steady-state solutions (47) do not depend on the collective parameters γ_{12} and Ω_{12}, which means that independently of the interatomic distance, there is always entanglement sudden death if the mean number of photons of the reservoir is different from zero. This confirms the results found earlier for atoms coupled to local, separate reservoirs [53,54]. Thus, one can conclude that for the long time behaviour of the system in a thermal reservoir, it is not important whether the atoms behave collectively or not. The evolution of the concurrence for the initial state given by (33), for the interatomic distance $r_{12} = \lambda/20$ and the reservoir at zero temperature (vacuum reservoir) is illustrated in Fig. 11. It shows the sudden death and revival of entanglement for the whole range of q values. This is in contrast to the situation for two independent atoms for which there is an asymptotic behaviour of entanglement for $q < 0.5$. The death and revival times depend on the values of q and the interatomic distance r_{12}, which has been discussed in details in the previous section and illustrated in Fig. 10.

When the temperature of the reservoir is not zero, however, the evolution of entanglement changes dramatically even if the mean number of photons of the reservoir is small [55]. In Fig. 12 we illustrate the evolution of entanglement for the same initial state and the same values of the other parameters but for the mean number of photons of the reservoir being $N = 0.01$. It is clearly seen that the reservoir with finite temperature degrades entaglement very fastly, and we observe sudden death of entanglement

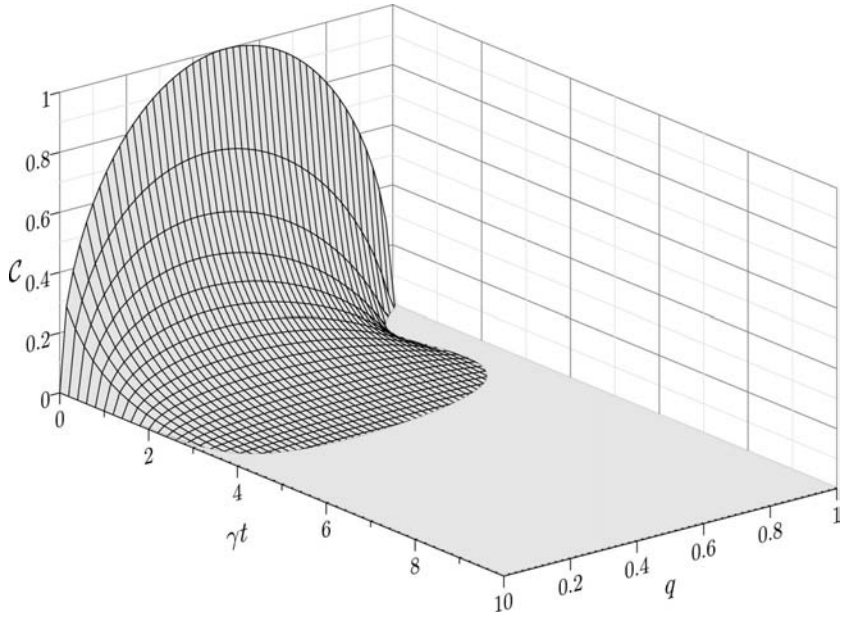

Fig. 12. Same as Fig. 10, but for $N = 0.01$.

for any value of q. Moreover, there is no revival of entanglement even for not very high mean number of photons of the reservoir.

We may conclude that the phenomenon of sudden death of entanglement appears to be a general feature of thermal reservoirs with nonzero temperature. It is rather the asymptotic decay of concurrence that is unusual and takes place only when the reservoir is the ordinary vacuum state.

10. Summary

We have reviewed the recent research on entanglement creation and disentanglement of two-atom systems coupled to a noisy environment. Particular attention has been paid to unexpected behaviours of entanglement, such as entanglement sudden death, spontaneous revival and sudden birth of entanglement. We have explored the role of the irreversible process of spontaneous emission in creation of entanglement and in disentanglement of two atoms. Simple analysis have shown that spontaneous emission does not necessary lead to disentanglement of an initial entangled atoms. Under some circumstances, this irreversible process can entangle already disentangled atoms. We have also discussed the effect of thermal fluctuations on the evolution of entanglement.

References

[1] M.A. Nielsen and I.L. Chuang, *Quantum Computation and Quantum Information*, Cambridge University Press, Cambridge, 2000.
[2] C. Schori, B. Julsgaard, J.L. Sorensen and E.S. Polzik, *Phys Rev Lett* **89** (2002), 057903.
[3] A. Dantan, G. Reinaudi, A. Sinatra, F. Laloe, E. Giacobino and M. Pinard, *Phys Rev Lett* **95** (2005), 123002.
[4] J.F. Sherson, H. Krauter, R.K. Olsson, B. Julsgaard, K. Hammerer, I. Cirac and E.S. Polzik, *Nature* **443** (2006), 557.
[5] D. Braun, *Phys Rev Lett* **89** (2002), 277901.

[6] M.S. Kim, J. Lee, D. Ahn and P.L. Knight, *Phys Rev A* **65** (2002), 040101(R).
[7] X.X. Yi, C.S. Yu, L. Zhou and H.S. Song, *Phys Rev A* **68** (2003), 052304.
[8] A.M. Basharov, *JETP Lett* **75** (2002), 123.
[9] L. Jakóbczyk, *J Phys A: Math Theor* **35** (2002), 6383.
[10] Z. Ficek and R. Tanaś, *J Mod Opt* **50** (2003), 2765.
[11] F. Verstraete, M.M. Wolf and J.I. Cirac, *Nature Physics* **10** (2009), 1.
[12] K.-L. Liu and H.-S. Goan, *Phys Rev A* **76** (2007), 022312.
[13] C. Hörhammer and H. Büttner, *Phys Rev A* **77** (2008), 042305.
[14] R.H. Dicke, *Phys Rev* **93** (1954), 99.
[15] Z. Ficek and R. Tanaś, *Phys Rep* **372** (2002), 369.
[16] Z. Ficek and S. Swain, *Quantum Interference and Coherence: Theory and Experiments*, Springer, New York, 2005.
[17] R.H. Lehmberg, *Phys Rev A* **2** (1970), 883, 889.
[18] G.S. Agarwal, Quantum Statistical Theories of Spontaneous Emission and their Relation to other Approaches, edited by G. Höhler, *Springer Tracts in Modern Physics* **70** Berlin, Springer–Verlag, 1974.
[19] R. Tanaś and Z. Ficek, *J Opt B* **6** (2004), S90.
[20] T. Yu and J.H. Eberly, *Phys Rev Lett* **93** (2004), 140404.
[21] J.H. Eberly and T. Yu, *Science* **316** (2007), 555; T. Yu and J.H. Eberly, *Science* **323** (2009), 598.
[22] K. Życzkowski, P. Horodecki, M. Horodecki and R. Horodecki, *Phys Rev A* **65** (2001), 012101.
[23] Z. Ficek, *App Math Inf Sci* **3** (2009), 375.
[24] Z. Ficek and R. Tanaś, *Phys Rev A* **74** (2006), 024304.
[25] M. Yonac, T. Yu, and J.H. Eberly, *J Phys B: At Mol Opt Phys* **39** (2006), S621.
[26] M. Yonac, T. Yu and J.H. Eberly, *J Phys B: At Mol Opt Phys* **40** (2007), S45.
[27] J.-H. An and W.-M. Zhang, *Phys Rev A* **76** (2007), 042127; X. Cao and H. Zheng, *Phys Rev A* **77** (2008), 022320; F.-Q. Wang, Z.-M. Zhang and R.-S. Liang, *Phys Rev A* **78** (2008), 062318; Z.Y. Xu and M. Feng, *Phys Lett A* **373** (2009), 1906; X.F. Cao and H. Zheng, *Eur Phys J B* **68** (2009), 209; X.L. Huang, L.C. Wang and X.X. Yi, *Int J Quant Inf* **7** (2009), 385; B. Bellomo, R. Lo Franco and G. Compagno, *Phys Rev A* **77** (2008), 032342; C.H. Chou, T. Yu and B.L. Hu, *Phys Rev E* **77** (2008), 011112; Y.J. Zhang, Z.X. Man and Y.J. Xia, *Eur Phys Jour D* **55** (2009), 173; Z.-Z. Li, X.-T. Liang and X.-Y. Pan, *Phys Lett A* **373** (2009), 4028; J. Zhou, C. Wu, M. Zhu and H. Guo, *J Phys B: At Mol Opt Phys* **42** (2009), 215505.
[28] S. Chan, M.D. Reid and Z. Ficek, *J Phys B: At Mol Opt Phys* **42** (2009), 065507.
[29] Z. Ficek and R. Tanaś, *Phys Rev A* **77** (2008), 054301.
[30] C.E. Lopez, G. Romero, F. Lastra, E. Solano and J.C. Retamal, *Phys Rev Lett* **101** (2008), 080503.
[31] S. Kielich, *Acta Phys Polonica* **19** (1960), 149; *ibidem* **23** (1963), 321; *ibidem* **25** (1964), 85.
[32] S. Kielich, *Acta Phys Polonica* **32** (1967), 297; S. Kielich, J.R. Lalanne and F.B. Martin, *Phys Rev Lett* **26** (1971), 1295.
[33] A. Piekara and S. Kielich, *J Chem Phys* **29** (1958), 1297; S. Kielich and A. Piekara, *Acta Phys Polonica* **18** (1959), 439; S. Kielich, *Acta Phys Polonica* **37** (1970), 719.
[34] *Modern Nonlinear Optics*, Vol. 85 of *Advances in Chemical Physics*, eds. M. Evans and S. Kielich, (Wiley, New York, 1993), Part 1; *Modern Nonlinear Optics*, Vol. 119 of *Advances in Chemical Physics*, ed. M. Evans, (Wiley, New York, 2001), Part 1.
[35] S.I. Schmid and J. Evers, *Rev A* **77** (2008), 013822.
[36] M.J. Stephen, *J Chem Phys* **40** (1964), 669.
[37] T. Yu and J.H. Eberly, *Quant Inf and Comp* **7** (2007), 459.
[38] B. Corn and T. Yu, *Quant Inf Process* **8** (2009), 565.
[39] S. Hill and W.K. Wootters, *Phys Rev Lett* **78** (1997), 5022.
[40] W.K. Wootters, *Phys Rev Lett* **80** (1998), 2245.
[41] Z. Ficek, R. Tanaś and S. Kielich, *Optics Commun* **36** (1981), 121.
[42] Z. Ficek, R. Tanaś and S. Kielich, *Optica Acta* **30** (1983), 713.
[43] H.S. Freedhoff, *Phys Rev A* **26** (1982), 684.
[44] L. Jakóbczyk and A. Jamróz, *Phys Lett A* **333** (2004), 35; F. Lastra, G. Romero, C.E. Lopez, M. Frana Santos and J.C. Retamal, *Phys Rev A* **75** (2007), 062324; K. Ann and G. Jaeger, *Phys Rev A* **76** (2007), 044101; I. Sainz and G. Björk, *Phys Rev A* **76** (2007), 042313; J.-H. Huang and S.-Y. Zhu, *Phys Rev A* **76** (2007), 062322; A. Vaglica and G. Vetri, *Phys Rev A* **75** (2007), 062120; M. Macovei and G.-X. Li, *Phys Rev A* **76** (2007), 023818; L. Aolita, R. Chaves, D. Cavalcanti, A. Acn and L. Davidovich, *Phys Rev Lett* **100** (2008), 080501; I. Sainz and G. Björk, *Phys Rev A* **77** (2008), 052307; A. Salles, F. de Melo, M.P. Almeida, M. Hor-Meyll, S.P. Walborn, P.H. Souto Ribeiro and L. Davidovich, *Phys Rev A* **78** (2008), 022322; N. Yamamoto, H.I. Nurdin, M.R. James and I.R. Petersen, *Phys Rev A* **78** (2008), 042339; B. Bellomo, R.L. Franco, S. Maniscalco and G. Compagno, *Phys Rev A* **78** (2008), 060302; S.-Y. Lin, C.-H. Chou and B.L. Hu, *Phys Rev D* **78** (2008), 125025; J. Leon and C. Sabin, *Phys Rev A* **79** (2009), 012301; L. Mazzola, S. Maniscalco, J. Piilo, K.-A. Suominen and B.M. Garraway, *Phys Rev A* **79** (2009), 042302; W. Song, L. Chen and S.-L. Zhu, *Phys Rev A* **80** (2009), 012331; M. Al-Amri, G.-X. Li, R. Tan and M.S. Zubairy, *Phys Rev A* **80** (2009), 022314; L. Derkacz and L.

Jakóbczyk, *Phys Rev A* **76** (2007), 042304; X.Q. Yan, *Mod Phys Lett B* **22** (2008), 2503; M. Scala, R. Migliore and A. Messina, *J Phys A: Math Theor* **41** (2008), 435304; M. Ban, *Opt Commun* **281** (2008), 3943; Z.X. Man, Y.J. Xia and N.B. An, *J Phys B: At Mol Opt Phys* **41** (2008), 085503; M. Abdel-Aty, *Eur Phys Jour D* **46** (2008), 537; H.T. Cui, K. Li and X.X. Yi, *Phys Lett A* **365** (2007), 44; Y.J. Zhang and Y.J. Xia, *Int J Quant Inf* **7** (2009), 949; J.S. Zhang and J.B. Xu, *Opt Commun* **282** (2009), 3652; A. Kowalewska-Kudlaszyk and W. Leoński, *J Opt Soc Am B* **26** (2009), 1289; K. Xia, M. Macovei, J. Evers and C.H. Keitel, *Phys Rev B* **79** (2009), 024519.

[45] C.-Y. Lai, J.-T. Hung, C.-Y. Mou and P. Chen, *Phys Rev B* **77** (2008), 205419.

[46] J. Dajka and J. Łuczka, *Phys Rev A* **77** (2008), 062303.

[47] J.P. Paz and A.J. Roncaglia, *Phys Rev Lett* **100** (2008), 220401.

[48] M. Hernandez and M. Orszag, *Phys Rev A* **78** (2008), 042114.

[49] J.P. Paz and A.J. Roncaglia, *Phys Rev A* **79** (2009), 032102.

[50] G.-X. Li, L.H. Sun and Z. Ficek, *J Phys B: At Mol Opt Phys* **43** (2010), 135501.

[51] M.P. Almeida, F. de Melo, M. Hor-Meyll, A. Salles, S.P. Walborn, P.H.S. Ribeiro and L. Davidovich, *Science* **316** (2007), 579.

[52] R. Tanaś and Z. Ficek, *J Opt B* **6** (2004), S610.

[53] M. Ikram, F.-L. Li and M.S. Zubairy, *Phys Rev A* **75** (2007), 062336; R. Tahira, M. Ikram, T. Azim and M.S. Zubairy, *J Phys B: At Mol Opt Phys* **41** (2008), 205501.

[54] A. Al-Qasimi and D.F.V. James, *Phys Rev A* **77** (2008), 012117.

[55] L. Jakóbczyk, *J Phys B: At Mol Opt Phys* **43** (2010), 015502.

Journal of Computational Methods in Sciences and Engineering 10 (2010) 277–305
DOI 10.3233/JCM-2010-0324
IOS Press

Two-photon-excitation fluorescence depolarization in solutions and nano-scale-organized (macro)molecular media: Application of the wide-angular detection-aperture technique

Jacek J. Fisz[a,*], Marcin Buczkowski[b], Anna Rożnowska[a] and Przemysław Miszta[a]
[a]*Institute of Physics, Nicholaus Copernicus University, ul. Grudziądzka 5/7, PL 87-100 Toruń, Poland*
[b]*Department pf Physics and Biophysics, Unversity of Warmia and Mazury, Olsztyn, Poland*

Abstract. We here discuss a problem of time-resolved fluorescence polarization spectroscopy at two-photon excitations of macroscopically isotropic molecular media, that can be organized locally on a nano-scale. The simplifying assumptions on the hydrodynamical shape of fluorophores and on the form of the two-photon absorption tensor, are considered and displayed on the corresponding examples of the emission anisotropy synthetic decays. These assumptions reduce the number of the model parameters making the theoretical description of the discussed spectroscopic technique applicable in the experimental practice. Because the two-photon excitations of fluorescence require the application of the exciting light of appropriately high intensity, and that may have a negative influence on the quality of the experimental data collected, we discuss the application of the wide-angular detection-aperture technique in such experiments. Furthermore, we consider the application of the symmetry adapted callibration (SAC) method enabling one to accurately analyze the experimental data even if the collecting optics employed is not ideal and is affected by several unexpected technical imperfections that are hard to be accounted for analytically.

Keywords: Two-photon excitation, fluorescence depolarization, intermolecular interactions, rotational dynamics, order parameters, membrane vesicles, labeled macromolecules, solutions

1. Introduction

In the nonlinear optical spectroscopy the intensive laser light probes the nonlinear molecular properties. Nonlinear molecular spectroscopy is covered by a wide class of different nonlinear phenomena, e.g., the two- or multi-photon absorption of the light and different kinds of nonlinear light scattering processes (e.g. the second and third harmonic generation process or hyper-Raman scattering) (see Refs. [1,11] and the research and review articles cited therein). The nonlinear optical spectroscopy has found many practical applications in chemistry, biology and medicine (see, e.g., Refs. [12,20] and the very many literature references cited therein). Undoubtedly, one of the eminent contributors to the filed of nonlinear

*Corresponding author. E-mail: jjfisz@phys.uni.torun.pl.

molecular spectroscopy, who has displayed many essentially important aspects of the nonlinear molecular properties probed by the light, was Stanisław Kielich (see, e.g., [1,4]).

The time-resolved two-photon induced fluorescence polarization spectroscopy is one of the examples of the nonlinear optical spectroscopy involving three photons, namely two photons exciting the fluorophores and one photon of the fluorescence light. The two-photon induced fluorescence polarization spectroscopy of isotropic molecular media, under the assumption that the fluorophores do not undergo rotational motion, was the subject of a systematic study in a series of articles by Monson and McClain [21] and McClain [22],[23]. They have discussed, in a very systematic way, the problem of two-photon excitations (resonant and non-resonant) with linearly, circularly and ellipticaly polarized light. In all of these cases different linear combinations of the two-photon absorption tensor elements are probed [21, 23]. Morover, McClain [23] has demonstrated that the two-photon excitation fluorescence enables an empirical symmetry assignment of the two-photon excited states.The experimental and theoretical aspects of two-photon excitation fluorescence spectroscopy, in macroscopically isotropic systems, were the subject of many discussions in the literature [24,30], and the central point of the discussion was to display the basic properties of the two-photon-excitation fluorescence polarization spectroscopy of solutions, in the Cartesian or mixed Cartesian and spherical representations.

In this article we discuss the case of one-color two-photon induced time-resolved fluorescence depolarization of the molecular media that are macroscopically isotropic and which can be entirely isotropic (a solution phase) or they can be organized locally on a nano-scale (e.g., labeled macromolecules, labeled biopolymers, small porous systems, membrane vesicles suspensions). The local organization of macroscopically isotropic media means that, although the macroscopic angular distribution of fluorophores introduced into such media is isotropic, their local angular orientations in such media are resticted by different kinds of local intermolecular interactions or hindered by the shape of the nano-cavities within small porous systems. Consequently, in the case of a solution phase, fluorescence polarization vanishes on the time-scale longer than the time-scale for rotational dynamic of fluorophores since the photoselected fluorophores relax to macroscopically isotropic angular distribution. In contrast, in the case of the media of local anisotropic distribution of fluorophores, the fluorescence polarization does not vanish because the photoselected fluorophores relax rotationally to locally anisotropic angular distributions, assuming that rotational motion of fluorophores is the only dynamical process on the time-scale of the fluorescence decay [31],[32]. Our discussion will be based on the formalism outlined by us in Ref. [36] where we have demonstrated the most compact, on one hand, and very transparent from the mathematical point of view, on the other hand, description of the one-color two-photon-excitation time-resolved fluorescence polarization spectroscopy for arbitrary molecular media. Our treatment is based entirely on the formalism of spherical irreducible tensorial sets and the derived relations concern arbitrarily organized (ordered) molecular media. With the application of appropriate methods of the group theory the obtained general description was reduced to the ones describing: (a) macroscopically ordered media of uniaxial macroscopic symmetry (e.g., planar membranes, LB films and stretched polymer films (as being assumed to be the rigid media), (b) macroscopically isotropic but locally ordered media (e.g. membrane vesicles, labeled macromolecules or biopolymers) and (c) solutions. The formalism described in Ref. [36] exhibits several advantages, all resulting from the fact that when deriving it, we have not assumed any particular model for the rotational motion of the photoselected fluorophores. The dynamical properties of the systems is represented by a Green function and which can be replaced by a particular mathematical solution to the equation of motion corresponding to the experimental case of interest (e.g., solution, locally organized media, macroscopically ordered molecular system with differently modelled ordering of molecules, symmetric rotors or asymmetric rotors). As was discussed in Ref. [36], the general solutions of the equation of motion describing the time evolution of the Green functions, known already

for isotropic and ordered (macroscopically or locally) molecular molecular media for the the case of one-photon-excitation fluorescence spectroscopy can be used to describe the dynamical evolution of the fluorophores excited by two photons.

The aim of this article is to discuss the one-color two-photon-excitation fluorescence depolarization experiments as the source of information on the rotational dynamics of fluorophores in solutions, reflecting the rotational fluidity of such media, and also on the hindered rotational dynamics and the anisotropy of local (nano-scale) angular distributions of fluorophores, embedded in the media of local structural organization. When discussing this problem we assume that rotatonal motion of fluorophores can be approximated within the diffusion model for symmetric rotors and that, in the case of locally organized media, the ground- and excited-state interactions of fluorophores with their nearest nano-scale-organized environments can be different ([37],[39,41]). This last seems to be a very obvious consequence of the nature of electronic excitations of fluorophores that modify, in general, the polarity and/or polarizability of the fluorophores [31,35]. We demonstrate that in both cases of the molecular media in question the two-photon-excitation fluorescence depolarization experiments may provide the information on the rotational dynamics of fluorophores and their local anisotropic angular distribution even if the two-photon absorption tensor is not diagonal in the principal axes of the diffusion tensor of a symmetric rotor. Hence, to analyze such experiments no information on the shape of the symmetric two-photon absorption tensor is required.

Because the two-photon excitations of fluorescence require the application of the exciting light of appropriately high intensity, and that may have a negative influence on the quality of the experimental data collected (a high-intensity light induced local field effects or modification of the photophysical properties of fluorophores), we discuss the application of the wide-angular detection-aperture technique in such experiments. Furthermore, we consider the application of the symmetry adapted callibration (SAC) method enabling one to accurately analyze the experimental data even if the collecting optics employed is not ideal and is affected by several unexpected technical imperfections that are hard to be accounted for analytically.

2. Two-photon-excitation polarized fluorescence decays

Indepedently of the molecular system under considerations (e.g., planar organized membranes, Langmuir-Blodgett (LB) films, stretched polymer films, membrane vesicles, labeled macromolecules and solutions), the intensity of two-photon excitation polarized fluorescence decay is defined by the following relation [36]

$$I_{\hat{e}_i,\hat{e}_f}(t) = C\ Ph(t)\ \int_{\Omega}\int_{\Omega_0} f_g(\Omega_0)\ P_{ex}^{(\hat{e}_i)}(\Omega_0)\ p(\Omega_0,0|\Omega,t)\ P_{em}^{(\hat{e}_f)}(\Omega)\ d\Omega_0 d\Omega\ . \tag{1}$$

In this formula C includes all experimental constant factors, $Ph(t)$ represents the photophysics (kinetic fluorescence decay) of the system and $f_g(\Omega_0)$ is an equilibrium orientational distribution of fluorophores in the ground state. The $p(\Omega_0,0|\Omega,t)$ is the Green function describing rotational dynamics of fluorophores and it describes a conditional probability for finding an excited molecule at time t and at angular orientation Ω, at the condition that it was excited at $t=0$ and its orientation was Ω_0. The Euler angles $\Omega_0=(\alpha_0,\beta_0,\gamma_0)$ and $\Omega=(\alpha,\beta,\gamma)$ describe angular orientation of a molecule-fixed frame $X_MY_MZ_M$ in the laboratory-fixed frame $X_LY_LZ_L$, at time moments $t=0$ and $t\geqslant 0$, correspondingly.

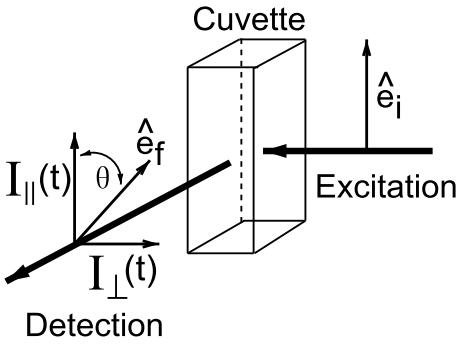

Scheme 1

$P_{ex}^{(\hat{e}_i)}(\Omega_0)$ and $P_{em}^{(\hat{e}_f)}(\Omega)$ describe angular dependence of polarized excitation and detection of polarized fluorescence, and [36]

$$P_{ex}^{(\hat{e}_i)}(\Omega_0) = |\hat{e}_i \, \mathbf{A} \, \hat{e}_i|^2 \;=\; |(\hat{e}_i \otimes \hat{e}_i) : \mathbf{A}|^2 \;=\; (\mathbf{E}_i : \mathbf{A})(\mathbf{E}_i : \mathbf{A})^* \,, \tag{2}$$

$$P_{em}^{(\hat{e}_f)}(\Omega) = |\hat{e}_f \; \hat{\mu}_{em}|^2 \;=\; (\hat{e}_f \otimes \hat{e}_f^*) : (\hat{\mu}_{em} \otimes \hat{\mu}_{em}^*) \;=\; \mathbf{E}_f : \mathbf{F} \,. \tag{3}$$

The unit vectors $\hat{e}_i$ and $\hat{e}_f$, occuring in Eqs (2) and (3), and indicated in Scheme 1, represent polarization directions of the exciting light and detected fluorescence. In the above equations $\mathbf{A}$ represents a two-photon absorption tensor, the unit vector $\hat{\mu}_{em}$ denotes direction of emission dipole moment, and $\hat{e}_i$, $\hat{e}_f$, $\mathbf{A}$ and $\hat{\mu}_{em}$ are defined in the $X_L Y_L Z_L$ frame. Angular orientations of $\hat{e}_i$, $\hat{e}_f$ and $\hat{\mu}_{em}$ are described, in the $X_L Y_L Z_L$ frame, by polar angles (θ_i, φ_i) and (θ_f, φ_f) and (θ_e', φ_e'), respectively. The $\mathbf{E}_i = (\hat{e}_i \otimes \hat{e}_i)$, $\mathbf{E}_f = (\hat{e}_f \otimes \hat{e}_f^*)$ and $\mathbf{F} = (\hat{\mu}_{em} \otimes \hat{\mu}_{em}^*)$ are the second-rank Cartesian tensors defined as the tensor products of the corresponding vectors, where a tensor product of two vectors $\vec{a}$ and $\vec{b}$ is defined by $\vec{a} \otimes \vec{b} = [a_i b_j]$. The colon at the right-hand sides of (2) and (3) means the scalar product of two Cartesian tensors. In other words, $P_{ex}^{(\hat{e}_i)}(\Omega_0)$ and $P_{em}^{(\hat{e}_f)}(\Omega)$ can be expressed in terms of scalar products of the second-rank Cartesian tensors namely, excitation tensor $\mathbf{E}_i$, two-photon absorption tensor $\mathbf{A}$, detection tensor $\mathbf{E}_f$ and emission tensor $\mathbf{F}$.

An experimental example to which the above expressions apply is shown in Scheme 1. This particular case relates to a typical two-photon-excitation time-resolved fluorescence depolarization measurements on macroscopically isotropic media in a cuvette. The medium can be entirely isotropic (a solutions phase) or it can be organized on a nano-scale (e.g., membrane vesicles, labeled macromolecules or biopolymers).

The relations (2) and (3) can be expressed in terms of irreducible spherical tensors [36], [37]. The scalar product of two second-rank Cartesian tensors is given by

$$\mathbf{A} : \mathbf{B} = \sum_{K=0}^{2} A^{(K)} \odot B^{(K)} = \sum_{K=0}^{2} \sum_{m=-K}^{K} (-1)^m A_m^{(K)} B_{-m}^{(K)} \,. \tag{4}$$

$A^{(K)}$ and $B^{(K)}$ $(K = 0, 1, 2)$ are two irreducible tensorial sets and $A_m^{(K)}$ and $B_m^{(K)}$ $(m = -K, ..., K)$ are their spherical components, which transform under proper rotations of the coordinate frames (e.g.

from $X_L Y_L Z_L$ to $X_M Y_M Z_M$) by the Euler angles $\Omega = (\alpha, \beta, \gamma)$, like the spherical harmonics $Y_{j,n}(\theta, \varphi)$, i.e. [42],[43]

$$T_m^{(K)}(L) = \sum_{m'=-K}^{K} D_{mm'}^{(K)*}(\Omega)\, T_{m'}^{(K)}(M)\,, \tag{5}$$

where $T = A, B$. $D_{mm'}^{(K)}(\Omega)$ are the elements of Wigner rotation matrices [42] and

$$\begin{aligned} T_0^{(0)} &= -\frac{1}{\sqrt{3}} Tr\,\mathbf{T}, \qquad T_0^{(2)} \;=\; \frac{1}{\sqrt{6}}\,(3\,T_{zz} - Tr\,\mathbf{T})\,, \\ T_{\pm 1}^{(2)} &= \mp (T_{xz} \pm i\,T_{zy}), \quad T_{\pm 2}^{(2)} \;=\; \frac{1}{2}(T_{xx} - T_{yy} \pm 2\,i\,T_{xy})\,. \end{aligned} \tag{6}$$

Irreducible tensorial sets $E_i^{(K)}$, $E_f^{(K)}$ and $F^{(K)}$, corresponding to Cartesian tensors $\mathbf{E}_i$, $\mathbf{E}_f$ and $\mathbf{F}$, can be calculated from the relation for a tensorial product of spherical tensor components, after replacing the unit vectors $\hat{e}_i$, $\hat{e}_f$ and $\hat{\mu}_{em}$ by the corresponding spherical components, and which are the modified spherical harmonics of the first rank [37]. If $\hat{e}$ is an unit vector, the tensorial product $(\hat{e} \otimes \hat{e})$ can be expressed in terms of the corresponding product of spherical vector $e^{(1)}$, i.e. in terms of irreducible tensorial sets $E^{(K)} = (e^{(1)} \otimes e^{(1)})^{(K)}$ ($K = 0, 1, 2$) (see Eq. (A5) in Ref. [37]). The spherical components $E_m^{(K)}$ can be calculated from the relation [42], [43]

$$E_m^{(K)} = (e^{(1)} \otimes e^{(1)})_m^{(K)} = \sum_{l,l'} C_{1,l}(\theta, \varphi)\, C_{1,l'}(\theta, \varphi)\, C(11K; ll')\,, \tag{7}$$

where spherical components $e_l^{(1)}$ have been replaced by modified spherical harmonics $C_{1,l}(\theta, \varphi) = \sqrt{4\pi/3}\, Y_{1,l}(\theta, \varphi)$, and where (θ, φ) are the polar angles describing orientation of $\hat{e}$. Finally, one gets

$$E_0^{(0)} = -\frac{1}{\sqrt{3}}, \quad E_0^{(1)} = E_{\pm 1}^{(1)} = 0, \quad E_m^{(2)} = \sqrt{\frac{2}{3}}\, C_{2,m}(\theta, \varphi) \;\; (m = 0, \pm 1, \pm 2)\,, \tag{8}$$

where the tensorial set $E^{(1)}$ disappears because $(\hat{e} \otimes \hat{e})$ is a symmetric Cartesian tensor. Finally, the relationships (2) and (3) take the following forms [36]

$$\begin{aligned} P_{ex}^{(\hat{e}_i)}(\Omega_0) \sim \frac{1}{3}\,(Tr\mathbf{A})^2 \;+\; 2\sqrt{\frac{2}{3}}\, Tr\mathbf{A} \sum_{m=-2}^{2} C_{2,m}^*(\theta_i, \varphi_i)\, A_m^{(2)}(0) \\ +\, 2 \sum_{m,m'=-2}^{2} C_{2,m}^*(\theta_i, \varphi_i)\, C_{2,m'}(\theta_i, \varphi_i)\; A_m^{(2)}(0)\, A_{m'}^{(2)*}(0)\,, \end{aligned} \tag{9}$$

$$P_{em}^{(\hat{e}_f)}(\Omega) \sim 1 \;+\; 2 \sum_{p=-2}^{2} C_{2,p}(\theta_f, \varphi_f)\, C_{2,p}^*(\theta_e'(t), \varphi_e'(t))\,. \tag{10}$$

By inserting the above expressions into (1), one finds that Eq. (1) can be transformed into the following form [36]

$$I_{\hat{e}_i,\hat{e}_f}(t) = C\ Ph(t)\ \Bigg[\frac{1}{3}\,(Tr\,\mathbf{A})^2\ +\ 2\sqrt{\frac{2}{3}}\,Tr\,\mathbf{A}\sum_{m=-2}^{2} C_{2,m}(\theta_i,\varphi_i)\ \langle A_m^{(2)*}(0)\rangle$$

$$+\,2\sum_{m,m'=-2}^{2} C^*_{2,m}(\theta_i,\varphi_i)\,C_{2,m'}(\theta_i,\varphi_i)\ \langle A_m^{(2)}(0)\,A_{m'}^{(2)*}(0)\rangle$$

$$+\,\frac{2}{3}\,(Tr\,\mathbf{A})^2\sum_{p=-2}^{2} C_{2,p}(\theta_f,\varphi_f)\ \langle C^*_{2,p}(\theta'_e(t),\varphi'_e(t))\rangle$$

$$+\,4\sqrt{\frac{2}{3}}\,Tr\,\mathbf{A}\sum_{m,p=-2}^{2} C^*_{2,m}(\theta_i,\varphi_i)\,C_{2,p}(\theta_f,\varphi_f)\ \langle A_m^{(2)}(0)\,C^*_{2,p}(\theta'_e(t),\varphi'_e(t))\rangle$$

$$+\,4\sum_{m,m',p=-2}^{2} C^*_{2,m}(\theta_i,\varphi_i)C^*_{2,m'}(\theta_i,\varphi_i)C_{2,p}(\theta_f,\varphi_f)\ \langle A_m^{(2)}(0)A_{m'}^{(2)*}(0)C^*_{2,p}(\theta'_e(t),\varphi'_e(t))\rangle\Bigg], \quad (11)$$

The orientational averages $\langle(...)\rangle$ denote the following double integration

$$\langle(...)\rangle = \int_{\Omega}\int_{\Omega_0} f_g(\Omega_0)\,p(\Omega_0,0|\Omega,t)\,(...)\,d\Omega_0 d\Omega\ . \quad (12)$$

and the angular averages in (11) of the components of tensorial set $A^{(2)}(0)$, modified spherical harmonics $C_{2,p}(\theta'_e(t),\varphi'_e(t))$ and their products are defined in the laboratory frame. They can be expressed in terms of the corresponding components defined in the molecule-fixed frame $X_M Y_M Z_M$ by employing relation (5), as was discussed in Ref [36].

3. Macroscopically isotropic systems

As was mentioned before, the formula (11) describes a more general case from the point of view of molecular media that can be of the experimental interest, and that can be macroscopically ordered (bi-axial or uniaxial) media or macroscopically isotropic ones (with a possible local molecular ordering). This formula can be adapted to the media of particular symmetry by employing the appropriate projection operators. This point was discussed in Ref [36] in the case planar organized membranes, LB films, stretched polymer films, membrane vesicles, labeled macromolecules and solutions.

In the case of a macroscopically isotropic systems (e.g. solutions, membrane vesicles or labeled macromolecules – see Scheme 2) Eq. (11) has to be invariant with respect to arbitrary rotation of the laboratory-fixed frame, and what means that this equation has to be invariant with respect to all symmetry operations in a proper rotation group of symmetry $O^{(+)}(3)$ (see Section 8.3 of Ref. [39] for a detailed discussion). By applying to Eq. (11) the projection operator representing the symmetry group $O^{(+)}(3)$, one obtains [36]

$$I(\theta,t) = C\,\Big(C_A\,Ph(t)\ +\ \frac{4}{5}\,P_2(\theta)\,W(t)\,Ph(t)\Big)\,, \quad (13)$$

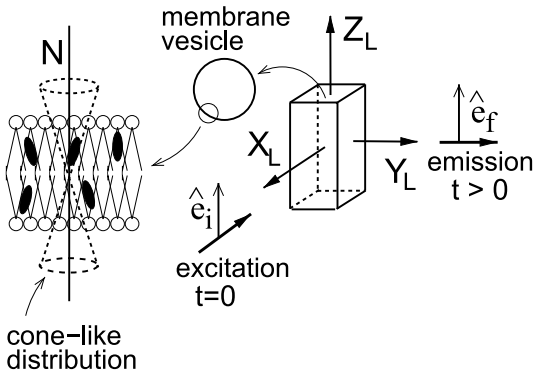

Scheme 2

where θ is an angle between the versors $\hat{e}_i$ and $\hat{e}_f$ (see Scheme 1), $W(t)$ is the correlation function describing rotational dynamics of photoselected fluorophores, and where

$$W(t) = \sqrt{\frac{2}{3}}\, Tr\, \mathbf{A} \sum_{s=-2}^{2} G_s^{(22)}(t) \; - \; \sqrt{\frac{2}{7}} \sum_{s=-2}^{2} G_s^{(222)}(t)\,. \tag{14}$$

The constituent correlation functions $G_s^{(22)}(t)$ and $G_s^{(222)}(t)$, in their more general forms from the point of view of the hydrodynamical shape and symmetry of the fluorophores, can be obtained from the general considerations presented in Ref. [36]. Their forms, simplified to the case of a symmetric-rotor diffusion model, can be written in the following way [36]

$$G_s^{(22)}(t) = \sum_{p=-2}^{2} {}^{22}V_{sp}^{sp}(t)\; A_p^{(2)}\, C_{2,p}^{*}(\theta_e, \varphi_e)\,, \tag{15}$$

$$G_s^{(222)}(t) = \sum_{n,p=-2}^{2} C(222; -n\; n-p)\; {}^{22}V_{sp}^{sp}(t)\; A_n^{(2)}\, A_{p-n}^{(2)}\, C_{2,p}^{*}(\theta_e, \varphi_e)\,. \tag{16}$$

and

$$C_A = \frac{1}{3}\,(Tr\,\mathbf{A})^2 \; + \; \frac{2}{5}\left[\frac{1}{6}(3A_{zz} \; - \; Tr\,\mathbf{A})^2 \; + \; \frac{1}{2}(A_{xx} - A_{yy})^2 \; + \; 2\,(A_{xy}^2 + A_{xz}^2 + A_{yz}^2)\right], \tag{17}$$

The $G_s^{(22)}(t)$ and $G_s^{(222)}(t)$ are the correlation functions between the molecules photoselected by the two identical photons at the time moment $t = 0$ and emitting the fluorescence light at any later time moment. They are described in terms of the symmetric two-photon absorption tensor components A_{ij} and the modified spherical harmonics $C_{2,n}(\theta_e, \varphi_e)$ defined in the molecule-fixed frame. The second-rank molecular correlation functions ${}^{22}V_{sp}^{sp}(t)$ in (15) and (16) describe the time-dependent correlation between the angular orientations of the molecule-fixed frames in the laboratory-fixed frame, from the time moment of the photoselection process and to the time moment of emission of the fluorescence light. According to Eq. (12), these correlation functions are given by

$${}^{22}V_{sp}^{sp}(t) = \int_{\Omega}\int_{\Omega_0} f_g(\Omega_0)\, p(\Omega_0, 0|\Omega, t)\; D_{sp}^{(2)\,*}(\Omega_0)\, D_{sp}^{(2)}(\Omega)\; d\Omega_0 d\Omega\;, \tag{18}$$

where $D^{(2)}_{mn}(\Omega)$ are the elements of the Wigner rotation matrices [42],[43]. It is important to emphasize here that the ground-state equilibrium angular distribution function $f_g(\Omega_0)$ reflects the anisotropic aligning interactions between the fluorophores in their electronic ground state and the locally organized (on a nano-scale) environment. Assuming that these interactions are described by the ground-state aligning potential $V_g(\Omega)$, $f_g(\Omega_0)$ can be represented by the Boltzmann distribution

$$f_g(\Omega) = N_g \exp(-V_g(\Omega)/k_B T)\,, \tag{19}$$

where N_g is the normalization constant, k_B is the Boltzmann constant and T means temperature.

In Scheme 2 we demonstrate an example of a molecular medium of macroscopic spherical symmetry which is the suspension of membrane vesicles doped with fluorophores. The macroscopic angular distribution of fluorophores in the laboratory frame $X_L Y_L Z_L$ is isotropic. However, each small fragment of the vesicle can be assumed to be a fragment of a planar membrane and the fluorophores in such a fragment exhibit local anisotropic angular distribution around the normal N perpendicular to this fragment of the membrane. In Scheme 2 this anisotropic distribution is indicated by a double cone (we assume that the distribution has apolar character). Assuming that on the time scale of the experiment (i.e. as compared to the fluorescence lifetime) the vesicles do not rotate, the only rotational motion that occurs is due to the rotational diffusion of fluorophores hindered by the anisotropic alignment of their environment. Thus, photoselected fluorophores will relax dynamically to a cone-like distribution whilst not to an isotropic one. The same concerns the fluorophores inside the proteins or the fluorophores attached to the biopolymers.

Our description of the two-photon-excitation fluorescence polarization, introduced in Ref. [36], and which is based solely on the spherical tensor algebra and the group theory, enables one to consider different models for rotational dynamics of the excited-state fluorophores. This is because when describing this problem we have not assumed any particular explicit form for the Green function $p(\Omega_0, 0|\Omega, t)$ in Eq. (18). In the case of the molecular media ordered locally on a nano-scale (e.g., a membrane vesicles suspension shown in Scheme 2) $p(\Omega_0, 0|\Omega, t)$ describes the excited-state aligning-potential-restricted rotational dynamics of fluorophores ([37], [40], [41]), and it obeys the Smoluchowski equation

$$\frac{\partial}{\partial t} p(\Omega_0, 0|\Omega, t) = -\hat{H}\, p(\Omega_0, 0|\Omega, t)\,, \tag{20}$$

with the time-development operator $\hat{H}$ of the form

$$\hat{H} = \sum_{i=x,y,z} \Big[D_i\, \hat{L}_i^2 \;+\; D_i\, \hat{L}_i \Big(\hat{L}_i\, V_{ex}(\Omega) \Big) / k_B T \Big]\,, \tag{21}$$

where D_i are the components of diffusion tensor and $\hat{L}_i$ are the components of the orbital momentum operator. The $V_{ex}(\Omega)$ in the above equation means the aligning interaction potential of the excited fluorophores with their organized nano-environments. This potential defines the equilibrium (local) orientational distribution function $f_{ex}(\Omega)$ of excited fluorophores that can be approached on the time-scale appropriately longer than the time-scale for rotational motion of these molecules, and which is given by the Boltzmann distribution

$$f_{ex}(\Omega) = N_{ex} \exp(-V_{ex}(\Omega)/k_B T)\,, \tag{22}$$

where N_{ex} is the normalization constant. By taking into account the boundary conditions for $p(\Omega_0, 0|\Omega, t)$

$$p(\Omega_0, 0|\Omega, t) = \begin{cases} \delta(\Omega_0 - \Omega) \text{ if } t = 0 \\ f_{ex}(\Omega) \qquad \text{if } t \to \infty \end{cases}\,, \tag{23}$$

where $\delta(\Omega_0 - \Omega)$ is the δ-Dirac function, one finds the following solution to the equation of motion (20)

$$p(\Omega_0, 0|\Omega, t) = \sum_{jmn} \frac{2j+1}{8\pi^2} \sum_{j'm'n'} R_{jmn,j'm'n'}(t)\, D^{(j)*}_{mn}(\Omega_0)\, D^{(j')}_{m'n'}(\Omega)\,, \tag{24}$$

in which $R_{jmn,j'm'n'}(t)$ are the elements of the relaxation matrix $\mathbf{R}(t)$ describing the rotational dynamics of photoselected fluorophores within the excited-state potential-restricted diffusion model (see Refs. [39], [40] for a detailed discussion). By substituting the above solution into Eq. (18) one finds

$${}^{22}V^{sp}_{sp}(t) = \sum_{j'=0}^{\infty} R_{2sp,j'sp}(t)\, {}^{2j'}V^{sp}_{sp}(t=0)\,, \tag{25}$$

where ${}^{2j'}V^{sp}_{sp}(t=0)$ is defined according to the relations (12) and (18), and these mixed-rank correlation functions at $t = 0$ represent the initial conditions for the time-dependent correlation functions ${}^{22}V^{sp}_{sp}(t)$. The time evolution of ${}^{22}V^{sp}_{sp}(t)$ involves two kinds of the aligning interactions potentials, the ground-state one $V_g(\Omega)$ and the excited-state one $V_{ex}(\Omega)$. They differ in a general case, and hence, also the corresponding equilibrium angular distributions $f_g(\Omega_0)$ and $f_{ex}(\Omega_0)$, given by Eqs (19) and (22), differ either. The assumed difference reflects a very natural property of the electronic excitation of fluorophores. In most of the cases (in principle, one should rather try to indicate the particular molecular cases in which this assumption can be ignored) the polarity and/or polarizability of the fluorophores are different in the ground and excited electronic states [31,35], and what may lead to even very strong changes in the aligning interaction of the fluorophores with their nano-scale environments. Thus, when employing the fluorescence spectroscopy for probing the local (nano-scale) ordering of the molecular media, such effects cannot be entirely excluded from the considerations. This problem becomes essentially important in the case of macroscopically organized media. If the aligning interactions do not change upon the electronic excitation of fluorophores (or if their possible changes can be assumed to be very slight) $V_g(\Omega) \equiv V_{ex}(\Omega)$, and hence, $f_g(\Omega_0) \equiv f_{ex}(\Omega_0)$.

In the case of solutions both aligning potentials are the scalars (they take the same values independently of the angular orientation of the fluorophores). Hence, $f_g(\Omega_0) = f_{ex}(\Omega_0) = 1/8\pi^2$. Furthermore, the term $D_i\, \hat{L}_i(\hat{L}_i\, V_{ex}(\Omega))$ in Eq. (21) dissappears. Consequently, Eqs (20) and (21) describe asymmetric-rotor free diffusion model. In this model the time evolution of $p(\Omega_0, 0|\Omega, t)$ involves five time-dependent terms of the second rank with five different relaxation times, expressed in terms of three components of the diffusion tensor [44]. In the case of rotational diffusion model for a symmetric rotor, the time evolution of $p(\Omega_0, 0|\Omega, t)$ is described solely by three terms of the second rank with three independent relaxation times, expressed through two components of the diffusion tensor [44]. Thus the relaxation matrix elements $R_{jmn,j'm'n'}(t)$ in Eq. (24) take in this model the well-know form, namely

$$R_{jmn,j'm'n'}(t) = \exp\Big\{ -[j(j+1)D_\perp + n^2\,(D_\parallel - D_\perp]\, t \Big\}\, \delta_{jmn,j'm'n'}\,, \tag{26}$$

where $D_\perp$ and $D_\parallel$ are two independent components of the diffusion tensor in the case of a symmetric rotor.

In a general case of the two-photon excitation fluorescence depolarization in a solution phase, polarized fluorescence decays depend on six components of the two-photon absorption tensor, three components of the diffusion tensor (for the asymmetric-rotor diffusion model), two polar angles describing the angular orientation of the emission dipole moment in the molecule-fixed frame and on at least one kinetic

fluorescence decay occuring in $Ph(t)$. Taken together, at least twelve model parameters are required to describe such experiments. However, from the experimental point of view, in the cease of the two-photon excitation experiments, only three independent polarized fluorescence decays can be detected, according to Eq. (13), namely parallel component $I_{\parallel}(t)$ (detected at $\theta_{if} = 0^0$), perpendicular component $I_{\perp}(t)$ (detected at $\theta_{if} = 90^0$) and the magic-angle-detected ($\theta_{if} = \theta_{mag} = 54,7^0$) fluorescence decay $I_{mag}(t) = C\,C_A\,Ph(t)$.

The situation becomes more complicated in the case of locally organized molecular media (Secheme 2) because, as mentioned before, in addition to the model parameters occuring in the case of free rotational diffusion model, further model parameters have to be included, and which describe the local alignment of the fluorophores. Even in the simplest description of the fluorophore-medium aligning interactions for cylindrical (axially symmetric) fluorophores, if the ground- and excite-state aligning interactions differ, one has to take into account additionally two pairs of the expansion coefficients (four additional model parameters), i.e. $u_g^{(2)}$, $u_g^{(4)}$, and $u_{ex}^{(2)}$, $u_{ex}^{(4)}$, occuring in $V_g(\Omega)$ and $V_g(\Omega)$ expanded into the forms [40]

$$V_g(\Omega) = k_B T\,(u_g^{(2)}\,D_{00}^{(2)}(\Omega) + u_g^{(4)}\,D_{00}^{(4)}(\Omega))\,, \tag{27}$$

$$V_{ex}(\Omega) = k_B T\,(u_{ex}^{(2)}\,D_{00}^{(2)}(\Omega) + u_{ex}^{(4)}\,D_{00}^{(4)}(\Omega))\,. \tag{28}$$

If the number of parameters occuring in the above expansions is to high (in particular for the media of isotropic macroscopically), the above expansions can be further reduced to solely the first terms. Undoubtedly, systematic numerical studies on the synthetic data are required to verify how many terms in the above expansions have to taken into account to ensure their numerical identification. This point is essentially important from the point of view of the experimental practice. If both potentials are indistinguishable, i.e. $V_g(\Omega) \equiv V_{ex}(\Omega)$, the minimum number of additional model parameters becomes reduced to two ones, namely to $u^{(2)}$ and $u^{(4)}$, occuring in the expanded form of the aligning potential $V(\Omega)$ being the same one for the ground- and excited-state fluorophores.

In many experimental cases (for appropriately selected fluorophores; e.g. of appropriately high symmetry) the reasonable simplifying assumptions on the hydrodynamical shapes of fluorophores and on the shape of the two-photon absorption tensor can be introduced and which may reduce the number of the model parameters to the extend that probably will make (to a good approximation) the description of two-photon-excitation fluorescence polarization spectroscopy applicable in the experimental practice. Such reduction of the number of model parameters is necessary if one wants to recover from the data analysis the information on the medium properties being probed by the fluorophores (fluidity of the medium and its local anisotropic organization), and futhermore, also the information on the components of the two-photon absorption tensor and on the orientation of the emission dipole moment. In the next two Section we, first, discuss the properties of the two-photon-excitation polarized fluorescence experiments on a solution phase with the fluorophores for which one may assume that they are symmetric rotors and that the two-photon absorption tensor is diagonal, and afterwards, we discuss the case of similar fluorophores embedded in the locally organized molecular media. In both case, however, we provide clear arguments that if the aim of two-photon-excitation time-resolved fluorescence polarization studies is to obtain the information on rotational dynamics of fluorophores and on their local anisotropic angular distributions (in case of locally organized media), the two-photon symmetric absorption tensor does not have to be diagonal in the principal axes of the diffusion tensor.

4. Symmetric rotors: Spatial, planar and linear two-photon absorbers

In the case of a symmetric-rotor diffusion model in a solution phase, with diagonal (spatial) two-photon absorption tensor, the symmetry adapted form of correlation function $W(t)$, given by Eq. (14), reduces to

$$W(t) = \alpha_0\, U_0(t) \;+\; \alpha_0\, U_2(t)\,. \tag{29}$$

The factors α_0 and α_2 read

$$\alpha_0 = \tilde{A}_0\, P_2(\theta_e)\,, \qquad \alpha_2 = \tilde{A}_2\, \sin^2\theta_e\, \cos 2\varphi_e\,, \tag{30}$$

where $\tilde{A}_0$ and $\tilde{A}_2$ are expressed through the spherical components of the two-photon absorption tensor, namely

$$\tilde{A}_0 = \sqrt{\frac{2}{3}}\, Tr\mathbf{A}\, A_0^{(2)} - \frac{2}{3}\Big(2(A_2^{(2)})^2 - (A_0^{(2)})^2\Big)\,, \tag{31}$$

$$\tilde{A}_2 = \Big(Tr\mathbf{A} - 2\frac{\sqrt{6}}{7}A_0^{(2)}\Big) \tag{32}$$

where

$$A_0^{(2)} = \frac{1}{\sqrt{6}}\,(3\,A_{zz} - Tr\,\mathbf{A})\,, \qquad A_{\pm1}^{(2)} \;=\; 0\,, \quad A_{\pm2}^{(2)} \;=\; \frac{1}{2}(A_{xx} - A_{yy})\,. \tag{33}$$

The $A_{\pm1}^{(2)}$ dissapears because tensor $\mathbf{A}$ is diagonal and only the components A_{xx}, A_{yy} and A_{zz} are the non-zero ones. This is the reason why the correlation function $U_1(t)$ do not occur in Eq. (29). Furthermore, the factor C_A, given by Eq. (17), reduces now to

$$C_A = \frac{1}{3}(Tr\mathbf{A})^2 + \frac{2}{5}\left[\frac{1}{6}(3A_{zz} - Tr\mathbf{A})^2 + \frac{1}{2}(A_{xx} - A_{yy})^2\right] \equiv \Big(A_0^{(0)}\Big)^2 + \frac{2}{5}\left[\Big(A_0^{(2)}\Big)^2 + 2\Big(A_2^{(2)}\Big)^2\right], \tag{34}$$

In the case of a solution phase the molecular correlation functions $U_0(t)$ and $U_2(t)$, occuring in Eq. (29), are obtained from Eq. (18) with the applications of Eqs (24) and (26), and

$$U_0(t) = \exp(-t/\tau_0) = \exp(-6D_\perp\, t), \tag{35}$$

$$U_2(t) = \exp(-t/\tau_2) = \exp[-(2D_\perp + 4D_\parallel)\, t]\,. \tag{36}$$

From the relationship (13) one finds both polarized fluorescence decays, i.e., $I_\parallel(t)$ calculated for $\theta = 0^0$, $I_\perp(t)$ obtained for $\theta = 90^0$, and also the so-called magic-angle detected fluorescence decay $I_{mag}(t)$ detected at $\theta = 54.7^0$; hence $P_2(\theta_{mag}) = 0$, that is

$$I_\parallel(t) = C\,\Big(C_A\, Ph(t) + \frac{4}{5}W(t)\, Ph(t)\Big), \tag{37}$$

$$I_\perp(t) = C\,\Big(C_A\, Ph(t) - \frac{2}{5}W(t)\, Ph(t)\Big), \tag{38}$$

$$I_{mag}(t) = C\, C_A\, Ph(t)\,, \tag{39}$$

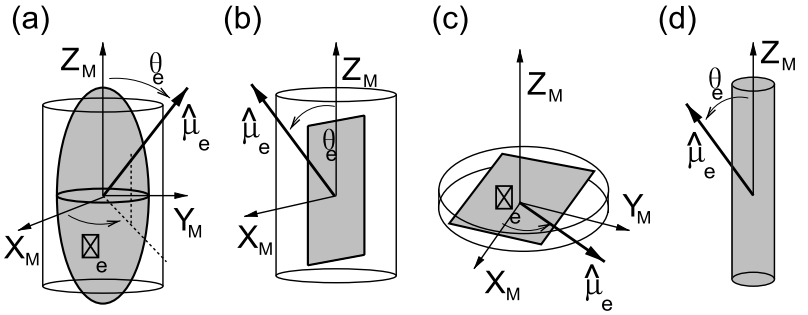

Scheme 3

Thus the expression for the emission anisotropy, in the case of the two-photon excitation case (2PE), is given by

$$r_{2PE}(t) = \frac{I_{\parallel}(t) - I_{\perp}(t)}{I_{\parallel}(t) + 2I_{\perp}(t)} = \frac{0.4}{C_A}\, W(t)\,. \tag{40}$$

The case (a) of Scheme 3 represents schematically a symmetric diffusor whose rotational dynamics is described by two diffusion tensor elements ($D_{\parallel} = D_z$ and $D_{\perp} = D_y = D_z$) and that exhibits three non-zero two-photon absorption tensor elements (A_{xx}, A_y and A_z)) in the molecule-fixed frame $X_M Y_M Z_M$. The orientation of emission dipole moment takes an arbitrary orientation described by two spherical angles θ_e and φ_e.

In Fig. 1 we show the synthetic time-evolutions of the emission anisotropy decays $r_{2PE}(t)$ calculated from Eq. (40). Both synthetic polarized decays, $I_{\parallel}(t)$ and $I_{\perp}(t)$, have been obtained by convoluting the corresponding δ-pulse-excitation model fluorescence decays (37) and (38) with the experimentally recovered histogram of the scattered laser pulse collected in 600 channels (channel width 5 ps). The synthetic decays were obtained according to the following relationship

$$I^{(conv)}(t) = R(t) \otimes I(t) = \int_0^t R(t')\; I(t - t')\, dt'\,, \tag{41}$$

where $I^{(conv)}(t)$ is the convoluted decay, $R(t)$ is the instrument response function to the exciting laser pulse and $I(t)$ is the δ-pulse-excitation model fluorescence decay. In the simulations the kinetic fluorescence decay was assumed monoexponential, i.e.

$$Ph(t) = \exp(-t/\tau_F) \tag{42}$$

with the fluorescence decay time $\tau_F = 3$ ns. The rotational correlation times $\tau_0 = 1$ ns and $\tau_2 = 0.5$ ns were used in Eqs (35) and (36) (after assuming that$1/D_{\perp} = 6$ ns and $1/D_{\parallel} = 2.4$ ns). The curves 1, 2, 3 and 4 shown in Figs 1(a–c) refer to the same orientations of the emission dipole moment, namely curve 1 ($\theta_e = 0^0$, $\varphi_e = 0^0$), curve 2 ($\theta_e = 15^0$, $\varphi_e = 0^0$), curve 3 ($\theta_e = 45^0$, $\varphi_e = 0^0$) and curve 4 ($\theta_e = 90^0$, $\varphi_e = 0^0$. Figures 1(a–c) differ in the magnitudes of the three diagonal elements of the normalized two-photon absorption tensor, namely Fig. 1(a) ($A_{xx} = 0.2$, $A_{yy} = 0.1$ and $A_{zz} = 0.7$), Fig. 1(b) ($A_{xx} = 0.3$, $A_{yy} = 0.2$ and $A_{zz} = 0.5$) and Fig. 1(c) ($A_{xx} = 0.1$, $A_{yy} = 0.6$ and $A_{zz} = 0.3$).

The plots of the two-photon-excitation emission anisotropy decays shown in Fig. 1 demonstrate evident dependence of the time evolution of $r_{2PE}(t)$ on the magnitudes of the two-photon absorption tensor components A_{xx}, A_{yy} and A_{zz}, and also on the orientation of the emission dipole moment. This

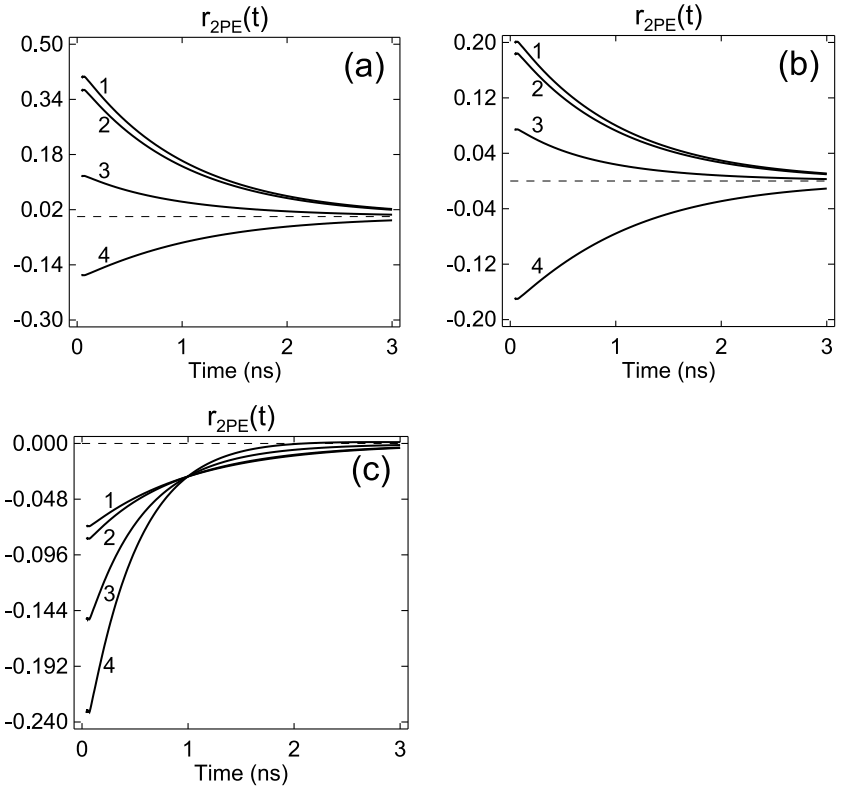

Fig. 1. Emission anisotropy decays for an asymmetric fluorophore considered as a symmetric rotor and exhibiting diagonal two-photon absorption tensor (see the text). The obtained initial values of the emission anisotropy r_{2PE} in Fig. 1(a) are: 0.407 (curve 1), 0.368 (curve 2), 0.118 (curve 3) and -0.170 (curve 4). In Fig. 1(b) they are: 0.201 (curve 1), 0.184 (curve 2), 0.126 (curve 3) and -0.170 (curve 4). In Fig. 1(c) they are: -0.071 (curve 1), -0.082 (curve 2), -0.152 (curve 3) and -0.234 (curve 4).

dependence is reflected in the shape of the time course of $r_{2PE}(t)$, and in particular, in the initial values of the emission anisotropy $r_{2PE}(t=0)$. The only simplifying assumption made in the simulations of the data was that we set $\varphi_e = 0^0$. Otherwise many more synthetic data had to be demonstrated in this work.

From the experimental point of view, the parameters describing kinetic fluorescence decay $Ph(t)$ can be recovered from the analysis of the "magic"-angle detected fluorescence decay (39). The dynamic evolution $W(t)$ of the system can be obtained from the analysis of the both polarized fluorescence signals (and which is a biexponential decay), namely

$$I_{\|}(t) = C\Big[C_A + \frac{4}{5}\Big(\alpha_0 \exp(-6D_\perp\, t) + \alpha_2 \exp[-(2D_\perp + 4D_{\|})\, t]\Big)\Big]\, Ph(t), \tag{43}$$

$$I_{\perp}(t) = C\Big[C_A - \frac{2}{5}\Big(\alpha_0 \exp(-6D_\perp\, t) + \alpha_2 \exp[-(2D_\perp + 4D_{\|})\, t]\Big)\Big]\, Ph(t), \tag{44}$$

where α_0 and α_2 are given by Eqs (30), and where the evolution of $Ph(t)$ is assumed to be known from the before mentioned analysis. In principle, the decays $I_{mag}(t)$, $I_{\|}(t)$ and $I_{\perp}(t)$ should be subjected to a simultaneous (global) analysis with the fluorescence decay parameters occuring in $Ph(t)$ being

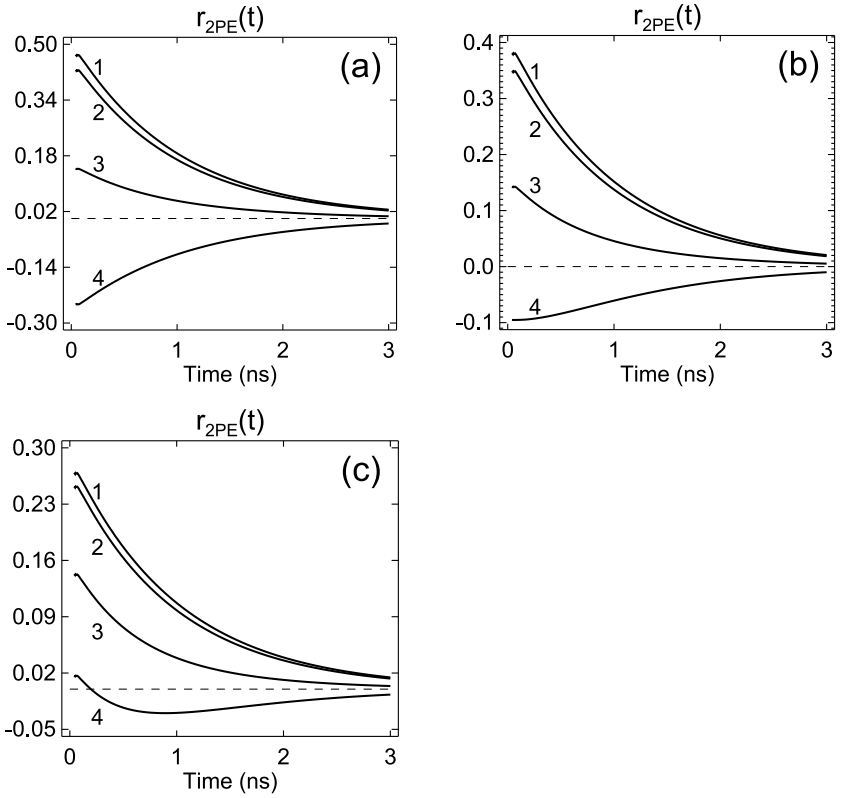

Fig. 2. Emission anisotropy decays for a planar fluorophore considered as a symmetric rotor and characterizing by diagonal two-photon absorption tensor with two non-zero elements (A_{zz} and A_{xx}) (see the text). The obtained initial values of the emissionanisotropy r_{2PE} in panel (a) are: 0.47 (curve 1), 0.426 (curve 2), 0.148 (curve 3) and -0.587 (curve 4). In panel (b) they are: 0.381 (curve 1), 0.349 (curve 2), 0.143 (curve 3) and -0.476 (curve 4). In panel (c) they are: 0.672 (curve 1), 0.252 (curve 2), 0.143 (curve 3) and 0.017 (curve 4).

andjustable in $I_{mag}(t)$ and being kept constant ones in $I_{\parallel}(t)$ and $I_{\perp}(t)$. The parameters α_0/C_A, α_2/C_A, $D_{\perp}$ and $D_{\parallel}$, are the freely adjustable model parameters in $I_{\parallel}(t)$ and $I_{\perp}(t)$. The analysis of such data will provide the information on the fluidity of the medium probed by rotational diffusion of fluorophores and which is reflected by the values of both components of the diffusion tensor. However, from both amplitudes α_0/C_A and α_2/C_A no additional information can be deduced because these two parameters depend on four molecular parameters, namely on $A_{zz}/Tr\mathbf{A}$, $(A_{xx}-A_{yy})/Tr\mathbf{A}$, θ_e and φ_e.

In Fig. 2 are displayed similar results for a prolonged planar fluorophore (see Scheme 3(b)), with the assumptions that (a) the particular shape of this molecule enables one to assume a symmetric-rotor diffusion model, (b) the emission dipole moment is in-plane polarized (hence, θ_e can take an arbitrary value, whilst $\varphi_e = 0$) and (c) that the two-photon absorption tensor is diagonal with two non-zero elements, namely A_{xx} and A_{zz} (while $A_{yy} = 0$). In the simulations we employed the same rotational correlation times and the same fluorescence decay time like in the case of Fig. 1. The curves 1, 2, 3 and 4 shown in Figs 2(a–c) refer to the same orientations of the emission dipole moment (in-plane oriented), namely curve 1 for $\theta_e = 0^0$, curve 2 for $\theta_e = 15^0$, curve 3 for $\theta_e = 45^0$ and curve 4 for $\theta_e = 90^0$. Figures 2(a–c) differ in the magnitudes of the two non-zero diagonal elements of the normalized two-photon absorption tensor, namely Fig. 2(a) ($A_{xx} = 0.2$, $A_{zz} = 0.8$), Fig. 2(b) ($A_{xx} = 0.3$, $A_{zz} = 0.7$) and Fig. 2(c) ($A_{xx} = 0.4$, $A_{zz} = 0.6$). In this case the amplitudes α_1 and α_2, defined by Eqs (30),

simplify to

$$\alpha_0 = \tilde{A}_0\, P_2(\theta_e)\,, \quad \alpha_2 = \tilde{A}_2\, \sin^2\theta_e\,. \tag{45}$$

Likewise in the case of Fig. 1, the also in this case Fig. 2 displays evident dependence of the time evolution of $r_{2PE}(t)$ on the magnitudes of the two-photon absorption tensor components A_{xx}, A_{yy} and A_{zz}, and also on the orientation of the emission dipole moment. These features are clearly seen in the time evolution of $r_{2PE}(t)$ and its initial ($t = 0$) values.

A global numerical analysis of $I_{mag}(t)$ (with freely adjustable decays parameters of $Ph(t)$) and both polarized decays $I_{\|}(t)$ and $I_{\perp}(t)$ (with the decay parameters of $Ph(t)$ kept fixed, whilst with α_0/C_A and α_2/C_A as being freely adjustable) should enable one to precisely determine the kinetic fluorescence decay parameters and also the information on the values of α_0/C_A and α_2/C_A, $D_{\perp}$ and $D_{\|}$. However, likewise in the former case, also in this case α_0/C_A and α_2/C_A are expressed through too many molecular parameters, namely in terms of $A_{zz}/Tr\mathbf{A}$, $(A_{xx} - A_{yy})/Tr\mathbf{A}$ and θ_e, and for these reason the values of these three parameters cannot be determined in a direct way. Nevertheless, the main information on dynamic properties of the systems, described by both components of the diffusion tensor, is avaliable from the two-photon excited time-resolved fluorescence polarization experiments on this kind of the fluorophores.

In Fig. 3 we show again the plots of the emission anisotropies for a planar fluorophore but being treated as the disk-like (symmetric) rotor (see Scheme 3(c)). This time, however, $\theta_e = 90^0$ and φ_e may take an arbitrary value. Furthermore, the non-zero elements of the diagonal two-photon absorption tensor are A_{xx} and A_{yy}, while $A_{zz} = 0$. The curves 1, 2, 3 and 4 shown in Figs 3(a–c) refer to the same orientations of the in-plane polarized emission dipole moment , namely curve 1 for $\theta_e = 0^0$, curve 2 for $\theta_e = 15^0$, curve 3 for $\theta_e = 45^0$ and curve 4 for $\theta_e = 90^0$. Figures 3(a–c) differ in the magnitudes of the two non-zero diagonal elements of the normalized two-photon absorption tensor, namely Fig. 3(a) ($A_{xx} = 0.8$, $A_{yy} = 0.2$), Fig. 3(b) ($A_{xx} = 0.4$, $A_{yy} = 0.6$) and Fig. 3(c) ($A_{xx} = 0.2$, $A_{zz} = 0.8$). This time the constant factors α_0 and α_2 take the forms

$$\alpha_0 = -\frac{1}{2}\tilde{A}_0\,, \quad \alpha_2 = \tilde{A}_2\, \cos 2\varphi_e\,. \tag{46}$$

Likewise in the former case of prolonged planar fluorophores, also in the case of a disk-like planar fluorophore, the global analysis of the the decays $I_{mag}(t)$, $I_{\|}(t)$ and $I_{\perp}(t)$ will provide the information on the photophysical properties of fluorophores (decay parameters of $Ph(t)$) and their dynamical properties ($D_{\perp}$ and $D_{\|}$) but still the values of α_0/C_A and α_2/C_A depend on three unknown molecular parameters, namely $A_{zz}/Tr\mathbf{A}$, $(A_{xx} - A_{yy})/Tr\mathbf{A}$ and φ_e.

What has been demonstrated above for the fluorophores whose rotational diffusion can considered within the symmetric rotor model and with a simplifying assumption that the two-photon absorption tensor is anisotropic with solely diagonal non-zero elements (cases (a), (b) and (c) of Scheme 3) , means that the both components of the diffusion tensor $D_{\perp}$ and $D_{\|}$ can be directly recovered from the global analysis of the time-resolved two-photon-excitation fluorescence polarizations studies. However, no additional information on the properties of the two-photon absorption tensor and on the angular orientation of the emission dipole moment is avaliable from such experiments. This is because the evolution of correlation function $W(t)$ is solely biexponential, and thus, only two amplitudes α_0/C_A and α_2/C_A can be adjusted from the data analysis and that depend on four parameters $A_{zz}/Tr\mathbf{A}$, $(A_{xx} - A_{yy})/Tr\mathbf{A}$, θ_e and φ_e, in general. Nevertheless, the basic information on the fluidity (viscosity) properties of a solution phase being probed by the two-photon absorbers can be successfully attained.

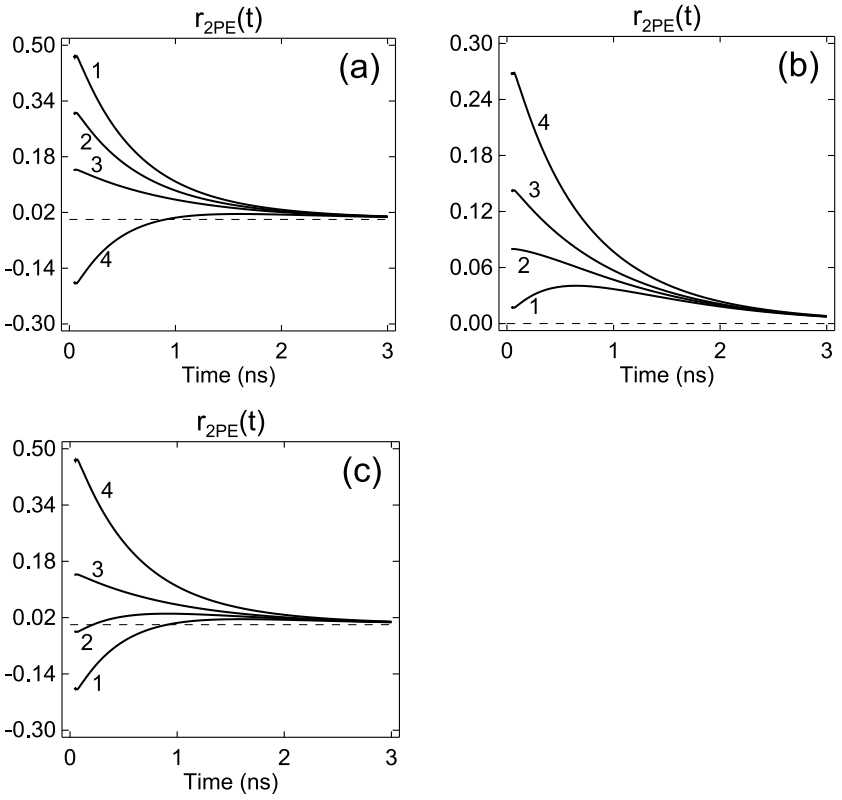

Fig. 3. Emission anisotropy decays for a planar fluorophore considered as a disk-like (symmetric) rotor and characterizing by diagonal two-photon absorption tensor with two non-zero elements A_{xx} and A_{yy} (see the text). The obtained initial values of the emission anisotropy r_{2PE} in panel (a) are: 0.47 (curve 1), 0.306 (curve 2), 0.143 (curve 3) and -0.184 (curve 4). In panel (b) they are: 0.017 (curve 1), 0.08 (curve 2), 0.143 (curve 3) and 0.269 (curve 4). In panel (c) they are: -0.184 (curve 1), -0.021 (curve 2), 0.143 (curve 3) and 0.47 (curve 4).

The values of $A_{zz}/Tr\mathbf{A}$ and $(A_{xx} - A_{yy})/Tr\mathbf{A}$ can be determine provided that the spherical angles θ_e and φ_e, describing the orientation of the emission dipole moment, are known from independent experiments. One of such independent methods is the traditional time-resolved fluorescence polarization spectroscopy with one-photon excitation. In this case the term $|\hat{e}_i\ \mathbf{A}\ \hat{e}_i|^2$ in Eq. (2) has to be replaced by $|\hat{e}_i\ \hat{\mu}_{ab}|^2$, where $\hat{\mu}_{ab}$ denotes the unit vector of the absorption transition dipole moment [37],[36]. In the case of the symmetric diffusor model with the absorption and emission dipole moments of arbitrary angular orientations in the molecule-fixed frame, the correlation function $W(t)$ exhibits three terms [31],[32], i.e.

$$W(t) = U_0(t)\,\beta_0\ +\ U_1(t)\,\beta_1\ +\ U_2(t)\,\beta_2, \tag{47}$$

where the additional molecular correlation function $U_1(t)$ has the form [44]

$$U_1(t) = \exp(-t/\tau_1) = \exp[-(5D_\perp + D_\parallel)\,t]\,. \tag{48}$$

The explicit expressions for both one-photon-excitation polarized fluorescence decays, $I_\parallel(t)$ and $I_\perp(t)$, and the decay $I_{mag}(t)$, can be obtained from the Eqs (37)–(39) after replacying C_A by unity and the

correlation function $W(t)$ by the one given by Eq. (47). Finally one gets [31],[32]

$$I_{\parallel}(t) = C\left[1+\frac{4}{5}\left(\beta_0 \exp(-6D_{\perp}t)+\beta_1 \exp[-(5D_{\perp}+D_{\parallel})t]+\beta_2 \exp[-(2D_{\perp}+4D_{\parallel})t]\right)\right] Ph(t), \quad (49)$$

$$I_{\perp}(t) = C\left[1-\frac{2}{5}\left(\beta_0 \exp(-6D_{\perp}t)+\beta_1 \exp[-(5D_{\perp}+D_{\parallel})t]+\beta_2 \exp[-(2D_{\perp}+4D_{\parallel})t]\right)\right] Ph(t), \quad (50)$$

$$I_{mag}(t) = C\, Ph(t), \quad (51)$$

where the amplitudes β_0, β_1 and β_2 are expressed by the spherical angles describing the angular orientations of the absorption and emission dipoles, namely

$$\beta_0 = P_2(\theta_a)\, P_2(\theta_e)\,, \quad (52)$$

$$\beta_1 = \frac{3}{4} \sin 2\theta_a \, \sin 2\theta_e \, \cos(\varphi_a - \varphi_e)\,, \quad (53)$$

$$\beta_2 = \frac{3}{4} \sin^2 \theta_a \, \sin^2 \theta_e \, \cos 2(\varphi_a - \varphi_e) \quad (54)$$

A global analysis of the experimentally collected decays $I_{\parallel}(t)$, $I_{\perp}(t)$ and $I_{mag}(t)$ (with the kinetic decay parameters freely adjustable in $I_{mag}(t)$ but being kept constant in $I_{\parallel}(t)$ and $I_{\perp}(t)$) enables one to optimize the values of the remaining five model parameters, namely $D_{\parallel}$, $D_{\perp}$, θ_a, θ_e and $\varphi_a - \varphi_e$.

Assuming that the angular orientation of the emission dipole moment within fluorophores is the same at the one- and two-photon excitations, the value of angle θ_e recovered from one-photon-excitation fluorescence polarization experiments can be assumed as being the known parameter in the analysis of similar data obtained at two-photon excitations for prolonged planar fluorophores indicated in Scheme 3(b) and whose synthetic emission anaisotropy histograms are shown in Fig. 2. In this particular case, the values of $A_{zz}/Tr\mathbf{A}$ and $(A_{xx} - A_{yy})/Tr\mathbf{A}$ can be recovered and which provides the information on the Z-axis component of two-photon absorption tensor and on the anisotropy of this tensor in the molecular XY-plane, both normalized by $Tr\mathbf{A}$. Regarding the two other cases of fluorophores pictured in Scheme 3(a) and Scheme 3(c) (with the histograms of $r_{2PE}(t)$ displayed in Figs 1 and 3, correspondingly) such information is unavailable because no direct information on the value of angle φ_e can be obtained from the above-mentioned fluorescence polarization studies at the one-photon excitation.

Fluorescence polarization studies on amorphous ordered (stretched) polymers seem to be the most proper method for obtaining the information on angular orientation of absorption and emission transition dipole moments, i.e., on the values of the angles θ_a, θ_e, φ_a and φ_e (Ref. [45] and the references cited therein). Because the amorphous polymers (even if they are stretched to a high extend) are porous media (they exhibit cavities of single nanometer-sized widths), appropriate mathematical model describing the uniaxial alignment of the prolonged nanocavities and a narrow-cone-like distribution of fluorophores inside the pores has to be adapted to precisely describe the variable-angle fluorescence polarization experiments on such systems [45]. With this model, after collecting appropriately large set of the dichroic ratios of polarized fluorescence signals, measured at diffrent combinations of the angles of excitation and detection directions with respect to the direction of the macroscopic ordering of the polymer, a global analysis of the data enables one to estimate the values of the angles θ_a, θ_e, φ_a and φ_e, the with of the angular distribution of fluorophores within the nanocavities and also two order parameters of the long axes of the nanocavities with respect to the axis of stretching of the polymer film [45]. The

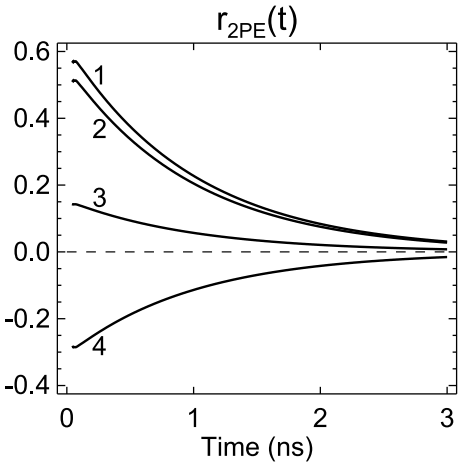

Fig. 4. Emission anisotropy decays for a rod-like rotor (with $1/D_{\perp} = 6$ ns; $\tau_0 = 1$ ns) and diagonal two-photon absorption tensor (with $A_{xx} = A_{yy} = 0$ and $A_{zz} = 1$), for $\theta_e = 0^0$ (curve 1), $\theta_e = 15^0$ (curve 2), $\theta_e = 45^0$ (curve 3) and $\theta_e = 90^0$ (curve 4).

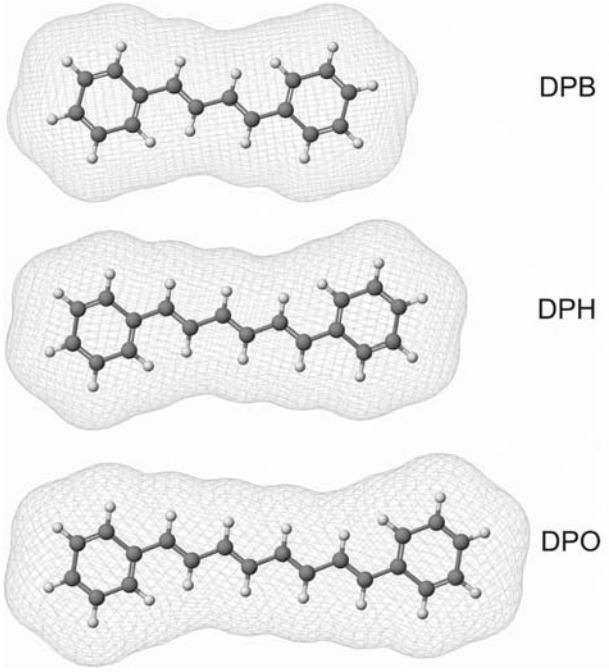

Scheme 4

recovered information on the direction of the emission dipole moment can be employed in the analysis of the time-resolved two-photon-excitation fluorescence depolarization data obtained in the case of the fluorophores depicted schematically in Scheme 3(a) and 3(c). Hence, the values of the parameters $A_{zz}/Tr\mathbf{A}$ and $(A_{xx} - A_{yy})/Tr\mathbf{A}$ can be obtained in the case of such fluorophores.

As the last case, in Fig. 4 are demonstrated the histograms of emission anisotropy r_{2PE} for a particular class of fluorophores which can be treated as the two-photon linear absorbers (i.e., the absorption tensor

is diagonal with solely one (essentially dominating) element A_{zz}, i.e., $A_{zz} \gg A_{xx} \simeq A_{yy}$. The family of trans-diphenyl-polyenes shown in Scheme 4, namely 1,4-diphenylbutadiene (DPB), 1,6-diphenyl-hexatriene (DPH) and 1,8-diphenyloctatetraene (DPO), is an example of the fluorophores to which this simplifying assumption very likely (to the first approximation) can be applied [25,26]. From the experimental point of view, they are symmetric rotors, on one hand, and linear two-photon absorbers, on the other hand. Hence, they can be trated as the rod-like fluorescence probes from the both points of view (see Scheme 3(d)). The structures of DPB, DPH and DPO, together with the van der Waals accessible surface, are shown in Scheme 4 were obtained with the use of CAChe WorkSystem Pro 7.5.0.85. The geometries of these molecules were obtained from Beautify Comprehensive module, which corrects the valence, hybridization, ring structure and geometry, implemented in the CAChe WorkSystem Pro 7.5.0.85. The obtained sizes of these molecules, i.e. [length, width], including the accessible surface of 1.9 Ï (and which is assumed as the thickness of the trans-diphenyl-polyenes), are: for DPB [13.68 Ï, 6.29 Ï], for DPH [18.43 Ï, 7.02Ï] and for DPO [20.85 Ï, 7.02 Ï]. The volumes of these three molecules are: 294,32 Ï^3 for DPB, 337,54 Ï^3 for DPH and 389.9 Ï^3 for DPO. The 1,6-diphenyl- hexatriene (DPH) is a widely used fluorescence sensor of the ordering and fluidity of biological membranes and their models [31] because of their very simple dynamic properties and a very particular geometrical shape, which make them favorable probes in such studies. As will be argued below, the above-mentioned simplifying assumption regarding the shape of the two-photon absorption tensor has been verified experimentally [26]. It is very likely that the same assumption will apply to DPO. In the case of DPB the time-resolved experimental studies are required to check up the validity of this assumption.

For this kind of fluorophores the equalities (33) return

$$A_0^{(2)} = \frac{2}{\sqrt{6}}\, A_{zz}\,, \quad A_{\pm 1}^{(2)} \;=\; 0\,, \quad A_{\pm 2}^{(2)} \;=\; 0\,, \tag{55}$$

and hence

$$C_A = \frac{3}{5}\,(A_{zz})^2\,. \tag{56}$$

Consequently, the correlation function $W(t)$ (see Eq. (29)) becomes monoexponential because the second term with $U_2(t)$ does not contribute ($\tilde{A}_2 = 0$). With these results, the intensity of two-photon-excitation polarized fluorescence decay (13) has the form

$$I(\theta, t) = C\left(Ph(t) + \frac{8}{7}\, P_2(\theta)\, W^{(N)}(t)\, Ph(t)\right), \tag{57}$$

where the constant factor C_A has been included into C, $W^{(N)}(t) = (7/6)\, W(t)$ and where

$$W^{(N)}(t) = U_0(t)\, P_2(\theta_e) = \exp(-6D_\perp\, t)\, P_2(\theta_e)\,. \tag{58}$$

Both polarized decays of fluorescence (for $\theta = 0^0$ and $\theta = 90^0$) read

$$I_\parallel(t) = C\left(Ph(t) + \frac{8}{7}\, W^{(N)}(t)\, Ph(t)\right), \tag{59}$$

$$I_\perp(t) = C\left(Ph(t) - \frac{4}{7}\, W^{(N)}(t)\, Ph(t)\right), \tag{60}$$

according to (57) and the emission anisotropy $r_{2PE}(t)$ takes the form of

$$r_{2PE}(t) = \frac{4}{7}\, W^{(N)}(t) \simeq 0.571\, W^{(N)}(t)\,. \tag{61}$$

At $t = 0$ Eq. (61) returns

$$r_{2PE}(t=0) = \frac{4}{7}\, P_2(\theta_e) \simeq 0.571\, P_2(\theta_e)\,. \tag{62}$$

This last result was obtained in Ref. [26] from very simple considerations focused on initial distribution of fluorophores, induced by a two-photon excitation, and was confirmed experimentally for DPH (see Scheme 3), for which an experimental value $r_{2PE}(0) = 0.518$ was found [26]. This may mean that the emission dipole moment makes an angle $\theta_e \simeq 14^0$ with the long axis of DPH.

In Fig. 4 we show the synthetic decays of the emission anisotropy r_{2PH} for the diphenyl-polyenes-like fluorophores (see Scheme 3(d)), obtained as was described before, with the assumption that $A_{zz} = 1$ and $A_{xx} = A_{yy} = 0$, for different orientations of the emission dipole moment, namely for $\theta_e = 0^0$, $\theta_e = 15^0$, $\theta_e = 45^0$ and $\theta_e = 90^0$. The initial values of the emission anisotropy for these four cases are: $r_{2PE}(t=0) = 0.571$ (curve 1), $r_{2PE}(t=0) = 0.306$ (curve 2), $r_{2PE}(t=0) = 0.143$ (curve 3), $r_{2PE}(t=0) = -0.286$ (curve 4). The initial values of $r_{2PE}(t=0)$ are in between the following upper and lower limits $4/7 \leqslant r_{2PE}(t=0) \leqslant -2/7$, according to Eq. (62). For the comparison, in the case of one-photon excitation (1PE) case [31], [32]

$$r_{1PE}(t=0) = 0.4\, P_2(\theta_e)\,, \tag{63}$$

and these limits are $0.4 \leqslant r_{1PE}(t=0) \leqslant -0.2$.

If the two-photon absorption tensor is not diagonal in the fluorophore-fixed frame (the principal axes of the diffusion tensor), the correlation functions (29) will contain three time-dependent terms, i.e.

$$W(t) = \alpha_0\, U_0(t) \;+\; \alpha_1\, U_1(t) \;+\; \alpha_0\, U_2(t)\,, \tag{64}$$

where the additional correlation function $U_1(t)$ is given by Eq. (48). This time, however, the amplitides α_0, α_1 and α_2 will involve all six components of the symmetric two-photon absorption tensor. Nevertheless, in this a more general case, the two-photon-excitation time-resolved fluorescence polarization experiments can be analyzed in terms of the five model parameters, namely with three amplitudes α_0/C_A, α_1/C_A and α_2/C_A, and two components of the symmetric-rotor diffusion tensor $D_{\|}$ and $D_{\perp}$. Hence, the information on rotational mobility of fluorophores in a solution phase can be successfully recovered, and no additional information on the magnitudes of the non-diagonal two-photon absorption tensor elements is needed.

5. Macroscopically isotropic molecular media organized on a nano-scale

In the case of macroscopically isotropic molecular media and axially symmetric fluorophores of local angular ordering (as shown in Scheme 2 for membrane vesicles suspension) both polarizes component of polarized fluorescence decay and magic-angle-detected fluorescence decay are given by Eqs (37), (38) and (39), this time however with the general form of the correlation function $W(t)$ given Eq. (14).

Following the discussion in Ref. [40], each correlation function ${}^{22}V^{sp}_{sp}(t)$ (where $s,p=0,\pm1,\pm2$) in (14) can be replaced by the symmetry adapted form

$$W_{sp}(t)=\frac{1}{4}\Big({}^{22}V^{sp}_{sp}(t)+{}^{22}V^{-sp}_{-sp}(t)+{}^{22}V^{s-p}_{s-p}(t)+{}^{22}V^{-s-p}_{-s-p}(t)\Big)\,. \tag{65}$$

The form of the symmetry adapted correlation function $W_{sp}(t)$ means that, in the fluorescence polarization experiments, all the constituent correlation functions ${}^{22}V^{sp}_{sp}(t)$ are equivalent independently of whether the uniaxial distribution of the fluorophores has polar or apolar character, namely ${}^{22}V^{sp}_{sp}(t)={}^{22}V^{-sp}_{-sp}(t)={}^{22}V^{s-p}_{s-p}(t)={}^{22}V^{-s-p}_{-s-p}(t)$, because each $W_{sp}(t)$, when expanded in the Clebsch-Gordan series at $t=0$, does not contain the odd-rank correlation functions. From mathematical point of view, this condition means that the od-rank order parameters $\langle D^{(j)}_{00}\rangle_g$ ($j=1,3,...$) has to be eliminated in the constituent correlation functions ${}^{22}V^{sp}_{sp}(t)$ occuring in the linear combination (65) (see Ref. [40] for a more detailed discusson on this point). As was mentioned already in this article, in the case of locally organized media, when considering the potential-restricted diffusion model, additional four model parameters , i.e. $u^{(2)}_g$, $u^{(4)}_g$, and $u^{(2)}_{ex}$, $u^{(4)}_{ex}$ (occuring in $V_g(\Omega)$ and $V_g(\Omega)$) have to be adjusted in the experimental data analysis. Knowing these parameters, the second- and four-rank ground- and excited-state order parameters, i.e. $\langle D^{(2)}_{00}\rangle_g$, $\langle D^{(4)}_{00}\rangle_g$, $\langle D^{(2)}_{00}\rangle_{ex}$ and $\langle D^{(4)}_{00}\rangle_{ex}$, can be calculated from the following integrals

$$\langle D^{(j)}_{00}\rangle_x=\int_\Omega f_x(\Omega)\,D^{(j)}_{00}(\Omega)\,d\Omega\,, \tag{66}$$

where $j=2,4$ and $x=g,ex$. The initial ($t=0$) and the long-time-limit ($t\to\infty$) values of the symmetry adapted correlation functions $W_{sp}(t)$ for $s,p=0,\pm1,\pm2$), expressed in terms of the appropriate combinations of the order parameters, are listed in Table 1 of Ref. [40]. The values of $W_{sp}(t=0)$ are given by linear combinations of $\langle D^{(2)}_{00}\rangle_g$ and $\langle D^{(4)}_{00}\rangle_g$. The value of $W_{sp}(t\to\infty)$ for $s,p=0$ is given by the product $\langle D^{(2)}_{00}\rangle_g\,\langle D^{(2)}_{00}\rangle_{ex}$, while $W_{sp}(t\to\infty)=0$ for $s,p\neq0$. In the case when the ground- and excited-state aligning interaction do not differ only two additional model parameters, i.e. $u^{(2)}$ and $u^{(4)}$, have to be taken into account, and hence, $W_{00}(t\to\infty)=(\langle D^{(2)}_{00}\rangle)^2$ where $\langle D^{(2)}_{00}\rangle$ is the second-rank order parameter being the same for the fluorophores in their ground and excited electronic states. Furthermore, the initial values of $W_{sp}(t=0)$ are given by appropriate linear combinations of the order parameters $\langle D^{(2)}_{00}\rangle$ and $\langle D^{(4)}_{00}\rangle$.

In the case of macroscopically isotropic media in which the fluorophores exhibit local anisotropic angular distribution, and hence, they undergo an orientation-restricted rotational dynamics, the correlation functions $U_0(t)$ and $U_2(t)$ are given by the following expressions

$$U_0(t)=W_{00}(t)+2W_{10}(t)+2W_{20}(t)\,, \tag{67}$$

$$U_2(t)=W_{02}(t)+2W_{12}(t)+2W_{22}(t)\,. \tag{68}$$

where, according to what has been said before, $W_{sp}(t)\equiv{}^{22}V^{sp}_{sp}(t)$, and the time-evolution of ${}^{22}V^{sp}_{sp}(t)$ is given by Eq. (25).

After substituting the above forms of $U_0(t)$ and $U_2(t)$ into Eqs (37) and (38) one immediately obtains the expressions for both polarized fluorescence decays, $I_\parallel(t)$ and $I_\perp(t)$, corresponding to the class of molecular media here discussed. From the experimentally recovered both polarized decays a histogram

of the emission anisotropy decay $r_{2PE}(t)$ can be reconstructed (see Eq. (40)). The initial ($t = 0$) value and the long-time ($t \to \infty$) limit of $r_{2PE}(t)$ take the forms

$$r_{2PE}(t=0) = \frac{0.4}{C_A}\, W(t=0) \;=\; 0.4\,\frac{\alpha_0 + \alpha_2}{C_A}, \tag{69}$$

$$r_{2PE}(t\to\infty) = \frac{0.4}{C_A}\, W(t\to\infty) \;=\; 0.4\,\frac{\alpha_0}{C_A}\, W_{00}(t\to\infty)\,, \tag{70}$$

where the before mentioned properties of the correlation functions $W_{sp}(t)$ have been employed. The value $r_{2PE}(t = 0)$ is the same as in the case of solutions. This is nothing surprising because from the point of view of the photoselection process of the fluorophores their macroscopic angular distribution is isotropic in both cases. However, the long-time limits $r_{2PE}(t \to \infty)$ differ in both cases. For a solution phase $r_{2PE}(t \to \infty) = 0$. For the media of local angular restrictions for the possible orientations of fluorophores $r_{2PE}(t \to \infty)$ approaches a non-zero constant (plateau) value (70) because the photoselected fluorophores cannot relax to a macroscopically isotropic angular distribution.

The experimentally collected two-photon-excitation polarized fluorescence decays $I_{\parallel}(t)$ and $I_{\perp}(t)$ with the correlation functions (67) and (68), and the 'magic'-angle detected decay $I_{mag}(t)$ can be analyzed globally, with the assumption that the model parameters describing the time-evolution of the photophysical decay $Ph(t)$ are adjustable parameters in $I_{mag}(t)$, while they are kept fixed in the polarized decays $I_{\parallel}(t)$ and $I_{\perp}(t)$. The dynamic evolution of $I_{\parallel}(t)$ and $I_{\perp}(t)$, when being considered within a simpler model that does not distinguishes between the ground- and excited-state aligning interactions, can be analyzed in terms of two amplitudes, α_0/C_A and α_2/C_A, two components of the diffusion tensor, $D_{\parallel}$ and $D_{\perp}$, and two parameters describing the aligning interactions, u_2 and u_4. When considering the aligning interactions as being different for both electronic states, the last two before mentioned parameters must be replaced by the corresponding four ones $u_g^{(2)}$, $u_g^{(4)}$, and $u_{ex}^{(2)}$, $u_{ex}^{(4)}$ or, in the simplified version of this model, by the two ones $u_g^{(2)}$ and $u_{ex}^{(2)}$. Both models, when applied to the experimental data, will provide the information on rotational dynamics (mobility) of fluorophores and on their local angular alignment. We here do not discuss the particular shapes of the two-photon absorption tensor for the symmetric rotors shown in Schemes 3(a–d) because all what has been said on this point in the previous section applies also to the class of the molecular media discussed in this section.

Likewise in the case of solutions, also in the case here discussed, if the two-photon absorption tensor is not diagonal in the principal axes of the diffusion tensor, the correlation function $W(t)$ will contain three time dependent constituent terms $U_0(t)$, $U_1(t)$ and $U_2(t)$, with the amplitudes α_0, α_1 and α_2. Hence, the information on the orientationally hindered mobility and anisotropy of local angular distribution of fluorophores can be obtained. In this case Eq. (69) has to be replaced by

$$r_{2PE}(t=0) = \frac{0.4}{C_A}\, W(t=0) \;=\; 0.4\,\frac{\alpha_0 + \alpha_1 + \alpha_2}{C_A}\,, \tag{71}$$

while Eq. (70) remains unchanged.

6. High-aperture detection of two-photon excited fluorescence. Application of the symmetry adapted calibration (SAC) method

The two-photon excitation fluorescence polarization experiments require the application of the pulsed exciting light of appropriately high intensity. This is because every one photon of the emitted fluorescence

is a result of the simultaneous absorption of two photons of the exciting light. Genrally speaking, (a) the two-photon absorption process for different fluorophores is characterized by different (higher or lower) absorption cross-sections, (b) the fluorescence quantum yields differ (sometimes even much) for different fluorophores, (c) the concentration of fluorophores must be kept at appropriately low level to avoid the formation of the ground-state, excited-state and mixed-character complexes of the fluorophores, and finally, (d) the application of an analyzer in the detection channel of the polarized fluorescence collected seriously reduce the intensity of the fluorescence signal. A very important case are the fluorescence sensors for probing the structural and dynamic properties of different kinds of molecular media, where the concentration of the sensors must be kept at particularly low level to eliminate their influence on the medium properties being probed (e.g., membranes probed by fluorescence sensors). For the reasons here mentioned, in very many practical cases the intensity of the exciting light must be high enough to ensure appropriate number of two-photon absorption events leading. finally, to the fluorescence signals of sufficiently high photon counts number at the maximum of the fluorescence decay collected. On the other hand, however, a very high intensity of the exciting light may have (sometimes even essential) negative consequences on the medium properties. In particular, a high intensity of the light means automatically a high intensity of the electric field near the fluorophore being excited and which may modify its photophysical properties (e.g., by increasing the local field effect or by leading to the photobleaching of fluorophores). Therefore, from this point of view, the intensity of the exciting light should not be rather too high.

In order to keep the experimental conditions for the two-photon-excitation polarized fluorescence measurements in agreement with all of the above-mentioned physical requirements, the application of the collecting optics of possibly high angular aperture seems to be a very good compromise, making the experiment not too invasive when studying the molecular media properties with the two-photon excitation technique. As shown in Scheme 4(a) the linear polarization of the fluorescence light selected by an analyzer ($\hat{e}$) (laboratory space) corresponds to the three components of polarized fluorescence emitted at the focus [49]. When considering the meridional planes properties of the objective lenses ([50],[51]), polarization direction $\hat{e}$ selected in the laboratory space corresponds to a cone-like distribution of the coresponding linear polarization directions in the focal space. Scheme 4(b) shows schematically the physical conditions of the fluorescence polarization experiments with parallel beam of linearly polarized ($\hat{e}_i$) exciting light. The fluorescence emitted at the focus is collected by an objective lens of a cone half-angle α and the polarization direction $\hat{e}_f$ of the emitted fluorescence is selected by the analyzer, and afterwards, the fluorescence light is detected by a detector. In the laboratory space both directions make an angle θ and which, in the focal space, corresponds to the angle between the direction $\hat{e}_i$ and the long axis of the cone-like distribution of versors $\hat{e}_f$ [46,48].

In Scheme 5(a) we show schematically an experimental arrangenet for the possibly accurate (from the physical point of view) one- or multiphoton-excitation fluorescence polaryzation studies with the application of a wide-angular-aperture collecting optics. The fluorescence is exited by a parallel beam of exciting light of linear polarization $\hat{e}_i$. The emitted fluorescence signal is collected by the objective lens of the cone half-angle α. To eliminate or reduce the refraction effect, the emitted fluorescence before entering the objective lens, it passes through a semi-sphere of appropriate refractive index being close to the refractive index of the medium in the cuvette. Hence, to the first approximation, one may assume that the collecting angle α inside and outside the cuvette can be assumed to be the same ones.

The desired polarized fluorescence components of polarization $\hat{e}_f$ are selected by the analyzer, and afterwards, the polarized fluorescence signal is being focused onto a detector. The aperture shown in Scheme 5(a) enables one to continuously modify the value of the collecting angle α.

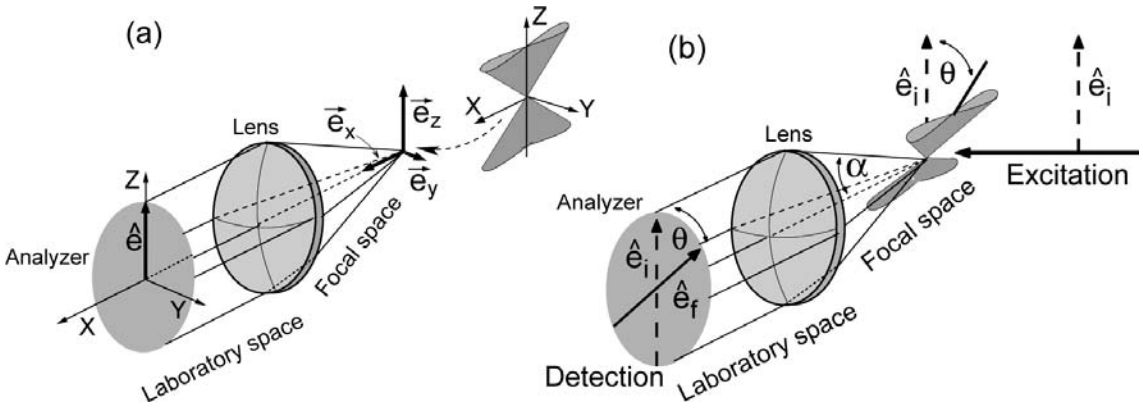

Scheme 5

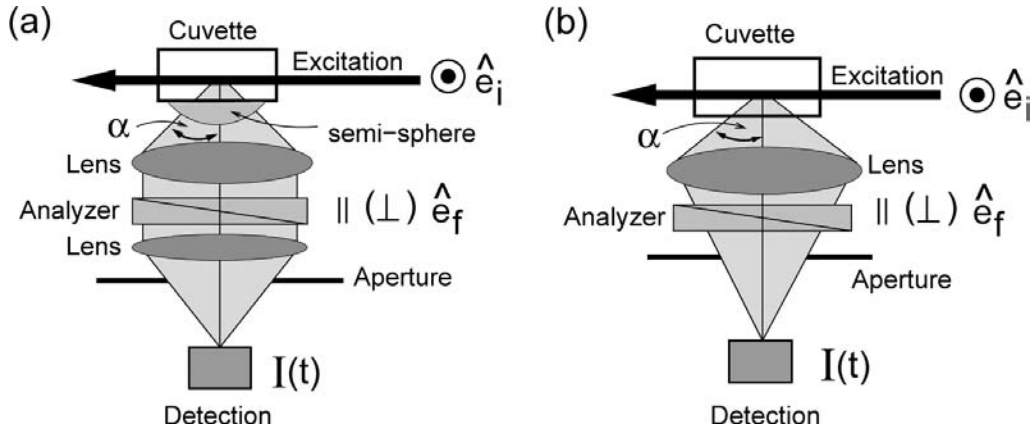

Scheme 6

The experimental configuration shown in Scheme 5(a), in the sence of the polarization directions of the exciting light and fluorescence light detected, corresponds to the parallel-beam-excitation fluorescence polarization microspectroscopy [46,48]. Therefore, polarized fluorescence decay (13) in the case of the application of the collecting optics must be replaced by

$$I(\alpha,\theta,t) = C\,\Big(C_A\,Ph(t)\;+\;\frac{4}{5}\,K(\alpha,\theta)\,W(t)\,Ph(t)\Big)\,, \tag{72}$$

where $P_2(\theta)$ has been replaced by the aperture-dependent function $K(\alpha,\theta)$, and where

$$K(\alpha,\theta) = \frac{1}{4}\Big(3\,Q_2(\alpha)\cos 2\theta + Q_0(\alpha)\Big)\,. \tag{73}$$

The above form of $K(\alpha,\theta)$ differs from the one given by Eq. (9) of Ref. [47] by the factor $4/5$ which is now standing explicitly in Eq. (72). The coefficients $Q_0(\alpha)$ and $Q_2(\alpha)$ are given by

$$Q_0(\alpha) = (\cos^2\alpha + \cos\alpha)/2\,, \tag{74}$$

$$Q_2(\alpha) = (\cos^2\alpha + 4\cos\alpha + 7)/12\,, \tag{75}$$

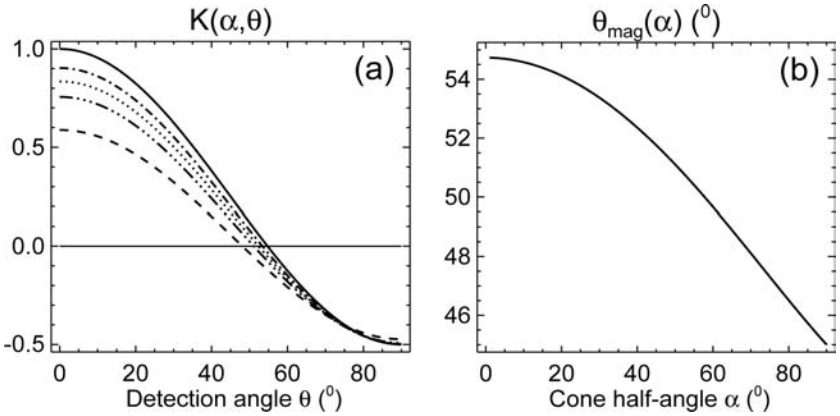

Fig. 5. (a) The plots of $K(\alpha,\theta)$ versus the detection angle θ, for the following detection cone half-angles: $\alpha = 0^0$ (solid line), $\alpha = 70^0$ (dashed line), and for the intermediate cases $\alpha = 30^0$, $\alpha = 40^0$ and $\alpha = 50^0$ (the corresponding lines between the two former cases). (b) The dependence of $\theta_{mag}(\alpha)$ on the detection cone half-angle α.

and they are the simplified version of the ones given by Eqs (6) and (7) of Ref. [48]. For the parallel-beam-detection conditions $K(\alpha,\theta)$ and $P_2(\theta)$ become equivalent functions, namely

$$K(\alpha = 0^0, \theta) \equiv P_2(\theta)\,. \tag{76}$$

In Fig. 5(a) we show the plots of $K(\alpha,\theta)$ for the cone half-angles of the collecting lens $\alpha = 0^0, 30^0, 40^0, 50^0, 70^0$, and which demonstrate a strong dependence of $K(\alpha,\theta)$ for the parallel component of polarized fluorescence with the coefficient $K_{\parallel}(\alpha) = K(\alpha, \theta = 0^0)$, e.g., $K_{\parallel}(20^0) = 0.956$, $K_{\parallel}(25^0) = 0.931$, $K_{\parallel}(30^0) = 0.903$, $K_{\parallel}(35^0) = 0.871$ and $K_{\parallel}(40^0) = 0.835$. For the perpendicular component of polarized fluorescence with $K_{\perp}(\alpha) = K(\alpha, \theta = 90^0)$ this effect is negligible because the values of $K_{\perp}(\alpha)$ for the cone half-angles $0^0 \div 40^0$ are all equal to the same value of $-1/2$, as can be seen in Fig. 5(a).

Figure 5(a) shows also that each curve $K(\alpha,\theta)$ takes the zero-value $K(\alpha,\theta) = 0$ at different values of the detection angle θ within the range from 45^0 to 54.7^0. We have discussed this point in very detail in Refs. [47,48] in the case of the fluorescence polarization microspectroscopy. The condition

$$K(\alpha, \theta_{mag}) = 0\,, \tag{77}$$

defines the "magic" value of the detection angle θ at which the detected fluorescence decay solely represents the kinetic evolution of the photoselected fluorophores $I_{mag}(t)$ because the kinetic-dynamic term (i.e. $W(t)\,Ph(t)$) does not contribute at such condition, according to Eq. (72).

By applying condition (77) to Eq. (73) we obtain the dependence of the magic angle value θ_{mag} on cone half-angle α, namely

$$\theta_{mag}(\alpha) = \frac{1}{2}\arccos\Big(-\frac{Q_0(\alpha)}{3\,Q_2(\alpha)}\Big)\,. \tag{78}$$

The plot of $\theta_{mag}(\alpha)$ is displayed in Fig. 5(b) and it shows that for the angles α ranging between 20^0 and 40^0 the changes of the values $\theta_{mag}(\alpha)$ are not negligible, e.g., $\theta_{mag}(20^0) = 54.1^0$, $\theta_{mag}(25^0) = 53.8^0$, $\theta_{mag}(30^0) = 53.4^0$, $\theta_{mag}(35^0) = 52.9^0$ and $\theta_{mag}(40^0) = 52.4^0$.

What has been demonstrated above means that when performing the time-resolved fluorescence polarization measurements according to the experimental arrangement depicted in Scheme 5(a), the

effects resulting from the application of the collecting optics must be taken into account if the cone half-angles of the objective lenses are above the values of $10^0 \div 15^0$. In such cases the three independent fluorescence decays, given for traditional parallel beam detection case by Eqs (37–(39), must be replaced by the following ones

$$I_{\parallel}(\alpha, t) = C\left(C_A\, Ph(t) + \frac{4}{5} K_{\parallel}(\alpha)\, W(t)\, Ph(t)\right), \tag{79}$$

$$I_{\perp}(\alpha, t) = G\, C\left(C_A\, Ph(t) - \frac{2}{5} K_{\perp}(\alpha)\, W(t)\, Ph(t)\right), \tag{80}$$

$$I_{mag}(t) = C' C_A Ph(t), \tag{81}$$

where this last decay must be collected at the right value of $\theta_{mag}(\alpha)$. The constant factor G (the so-called G-factor) and a new constant C' (in the last equation) reflect diffrerent sensitivity of the detector on the polarization direction of the collected fluorescence. The G-factor can be determined experimentally [31,32]. In order to recover the model parameters occuring in $Ph(t)$ and $W(t)$, the above three polarized fluorescence decays must be subjected to a global (simultaneous) numerical analysis with the appropriately linked model parameters. For example, the model parameters occuring in the photophysical evolution of the excited fluorophores $Ph(t)$ can be the fitted ones in Eq. (81), while they are kept constant values in (79) and (80). The all other model parameters occuring in $W(t)$ are thus the solely adjustable ones in both polarized fluorescence decays (79) and (80).

What has been said above apply also to the case of similar experiments pictured schematically in Fig. 5(a) but on the samples closed between two glass plates and with the application of the microscope objective of hight numerical aperture. In such experiments the angle between the excitation direction and the propagation direction of the exciting is must be larger than 90^0. In such experiments the cone half-angle of the detection optics can range from 50^0 and even up to almost 70^0. Therefore, according to Figs 5(a) and 5(b), in such cases the effects caused by the application of the high-aperture collecting optics become substantially enhanced.

The experimental protocol for an accurate determination of the model parameters occuring in the kinetic $Ph(t)$ and dynamic $W(t)$ evolutions of the excited-state fluorophores, and performed according to the experimental arrangement shown in Scheme 5(a), can be employed in the experimental practice if the there are no optical effects (artifacts) that can modify the quality of the collected fluorescence decays and which can be described theoretically by Eqs (79), (80) and (81). A fundamental assumption underlying this protocol is that the cone half-angle α assumed in these equations really coresponds to the experimental one. This means the the collecting optics is free of the spherical and chromatic aberration effects. Furthermore, the refractive index of the sample is the same as the refractive index of the semi-sphere indicated in Scheme 5(a). This assumption must also hold to assume that no reflection of the fluorescence light occurs and which may modify the intensity of the fluorescence light rays passing through the cuvette and the semi-sphere at diffrent angles to optical axis of the collecting optic. Because not all of these effects can be accounted for in the theoretical expressions (79), (80) and (81), the problem can be solved by applying the symmetry adapted calibration (SAC) method introduced by us in Ref. [46] and further discussed in Ref. [48], for the case of the time-resolved fluorescence polarization microspectroscopy and which can be employed in the experiments being performed according to Scheme 5(a), and in particular to the experiments being performed according to Scheme 5(b) where no semi-sphere is employed and where the analyzer selecting the polarized fluorescence decay is placed incorrectly from the physical

point of view. In the SAC method the polarized fluorescence decay can be represented as the linear combination of two time-dependent basis functions, $Ph(t)$ and $W(t)\,Ph(t)$, namely

$$I(\alpha,\theta,t) = \gamma_1\,Ph(t) + \gamma_2\,W(t)\,Ph(t)\,, \tag{82}$$

where γ_1 and γ_2 are the scalling factors describing the degree of contribution of both time-dependent basis functions. By performing two independent measurements of two polarized fluorescence decays on a reference fluorophore in a solution phase, of known photophysical $Ph_r(t)$ and dynamical $W_r(t)$ properties, and dissolved in a solvent of similar refractive index as the one of the sample studied, one can determine the values of the scalling factors γ_1 and γ_2. Knowing γ_1 and γ_2 one can recover the values of the G-factor, $K_{\parallel}(\alpha)$ and $K_{\perp}(\alpha)$. The values of these three parameters can be used in Eqs (79) and (80) when analyzing similar experiments for the sample studied, provided that both polarized fluorescence decays are collected at the same experimental conditions, for the reference fluorophore solution and the sample studied. The value of the magic angle $\theta_{mag}(\alpha)$ can be determined empirically by performing a few time-resolved fluorescence decays for the reference fluorophore. The detection angle θ at which the fluorescence signal detected depends solely on the kinetic evolution $Ph_r(t)$ can be assumed as being the right value of $\theta_{mag}(\alpha)$ and can be used for the kinetic fluorescence studies of the sample studied.

The SAC method enables one to eliminate several unwanted and unexpected experimental complications and artifacts (aberration effects or partial damage of the lenses used in the experiments). Secondly, it enables to analyze the experimental data collected according to both experimental arrangenets shown in Scheme 5 without the necessity of derivation the theoretical expressions precisely describing such experiments. For these reasons, in our opinion, the SAC method can be very helpful in the time-resolved two- and multi-photon-excitation fluorescence polarization studies with the application of wide-angular-aperture collecting optics. The same method, after very simple adaptation, can be employed in all types of the nonlinear molecular spectroscopy, in particular in such cases when the detected signals are of very low light intensity.

7. Discussion

In this article we have considered the two-photo-excitation fluorescence depolarization technique in the case of solutions and the media organized locally on a nano-scale. We have demonstrated several aspect of this technique. First, we have demonstrated several synthetic decays of the emission anisotropy showing very strong dependence of their initial values on the shape of the two-photon absorption tensor and on the orientation of the emission dipole moment. An important result of this work is a clear demonstration that when employing the description of the two-photon induced time-resolved fluorescence polarization technique in entirely spherical representation, the expressions describing the polarized fluorescence decays are written in a very compact and simple way, making them easily applicable in the experimental practice. Secondly, we have shown that even if the two-photon absorption tensor is not diagonal in the principal axes of the symmetric-rotor diffusion tensor, the information on the rotational mobility of fluorophores in a solution phase, and on the aligning-potential hindered rotational mobility and local anisotropic angular distribution of fluorophores, in the case of locally organized media, can be successfully recovered. Finally, we have described the polarized fluorescence decays for the case when the fluorescence signal is collected through a collecting optics of arbitrary aperture. This point is essentially important from the point of view of the experimental practice because with this technique the intensity of the exciting light can be reduced even much, and hence, several unwanted high-intensity-light effects can be essentially reduced or even completely eliminated.

References

[1] S. Kielich, *Acta Physica Polonica* **XXXIII** (1968), 89.
[2] S. Kielich, J.R. Lalanne and F.B. Martin, *Phys Rev Letters* **26**(21) (1971), 1295.
[3] S. Kielich, J.R. Lalanne, F.B. Martin and J. Raman, Spectroscopy, 1 (1973) 119.
[4] S. Kielich, Multi-Photon Scattering Molecular Spectroscopy, in: *Progress in Optics XX*, E. Wolf, ed. North-Holland, 1983, p. 155.
[5] T. Bancewicz, *J Phys Chem* **111** (1999), 7440.
[6] T. Bancewicz, Y. Le Duff and J.-L. Godet, in: *Modern Nonlinear Optics*, M. Evans, ed., Advances in Chemical Physics Vol. 119, 2nd ed. (Wiley, New York, 2001), Pt. 1.
[7] T. Bancewicz, K. Nowicka, J.-L. Godet and Y. Le Duff, *Phys Rev A* **69** (2004), 062704–062711.
[8] T. Bancewicz and G. Maroulis, *Phys Rev A* **79** (2009), 042704–042711.
[9] S. Mukamel, *Principles of Nonlinear Optical Spectroscopy* (Oxford Univ. Press, New York, 1995).
[10] S. Brasselet and J. Zyss, *J Opt Soc Am B* **15**(1) (1998), 257.
[11] K. Horie, H. Ushiki and F.M. Winnik, *Molecular Photonics: Fundamentals and Practical Aspects* (Wiley-VCH GmbH, Weinheim, 2000).
[12] N.P. Prasad and D.J. Williams, *Introduction to Nonlinear Optical Effects in Molecules and Polymers* (Wley, New York, 1991).
[13] J.R. Lakowicz (ED.), *Topics in Fluorescence Spectroscopy, vol. 5: Nonlinear and Two-Photon Induced Fluorescence* (Springer-Verlag, Berlin, Heidelberg, 1997).
[14] H. Abramczyk, Introduction to Laser Spectroscopy (Elsevier, Amsterdam, San Diego, Oxford, London, 2005).
[15] H. Gerritsen and C.J. Grauw, *One- and two-Photon Confocal Fluorescence Lifetime Imaging and its Applications*, Oxford University Press, Oxford, 2001.
[16] A. Diaspro, *Confocal and Two-Photon Microscopy: Foundations, Applications and Advances* (Wiley-Liss Inc., New York, 2002).
[17] S. Brasselet, J. Zyss and C.R. Physique, **8** (2007), 165.
[18] H. Mojzisova, J. Olesiak, M. Zielinski, K. Matczyszyn, D. Chauvat and J. Zyss, *Biophys J* **97** (2009), 2348.
[19] B.R. Masters and P.T.C. So (EDS.), *Handbook of Biomedical Nonlinear Optical Microscopy* (Oxford University Press, Oxford, 2008).
[20] V.V. Yakovlev (ED.), *Biochemical Applications of Nonlinear Spectroscopy* (Taylor and Francis Group / CRC Press, Boca Raton, London, New York, 2009).
[21] P.R. Monson and W.M. McClain, *J Chem Phys* **53** (1970), 29.
[22] W.M. McClain, *J Chem Phys* **57** (1972), 2264.
[23] W.M. McClain, *J Chem Phys* **58** (1972). 324.
[24] J.R. Cable and A.C. Albrecht, *J Chem Phys* **85** (1986), 3155.
[25] J.R. Lakowicz, I. Gryczynski, E. Danielsen and M.J. Wirth, *J Phys Chem* **96** (1992), 3000.
[26] J.R. Lakowicz, I. Gryczynski and E. Danielsen, *Chem Phys Lett* **47** (1992), 191.
[27] P. R. Callis, *J Chem Phys* **99** (1993), 27.
[28] C. Wan and C.K. Johnson, *Chem Phys* **179** (1994), 513.
[29] C. Wan and C.K. Johnson, *J Chem Phys* **101** (1994), 10283.
[30] S.W. Pauls, J.F. Hedstrom and C.K. Johnson, *Chem Phys* **237** (1998), 205.
[31] J.R. Lakowicz, *Principles of Fluorescence Spectroscopy* (*Kluwer Academic / Plenum Publishers*, New York, Boston, Dordrecht, London, Moscow, 1999).
[32] B. Valeur, *Molecular Fluorescence* (Wiley-VCH, Weinheim, 2002).
[33] W. Liptay, *Ber Physik Chem* **80** (1975), 207.
[34] T. Werner, in: *Modern Fluorescence Spectroscopy*, E.L. Wehry (ED.), (vol. 2, Plenum Press, New York, 1972).
[35] B.S. Hudson, B.E. Kohler and K. Schulten, in: *Excited States*, E.C. Lim (ED.), (vol. 6, Academic Press, New York, 1982).
[36] J.J. Fisz, *Chem Phys Lett* **373** (2003) 299.
[37] J.J. Fisz, *Chem Phys* **99** (1985), 177.
[38] J.J. Fisz, *Chem Phys* **114** (1987), 165.
[39] J.J. Fisz, *Chem Phys* **181** (1994), 425.
[40] J.J. Fisz, *Chem Phys Lett* **286** (1998), 190.
[41] J.J. Fisz, *Chem Phys Lett* **355** (2002), 94.
[42] M.E. Rose, *Elementary Theory of Angular Momentum* (Wiley, New York, 1957).
[43] D.M. Brink and G.R. Satchler, *Angular Momentum* (Oxford Univ. Press., Oxford, 1968).
[44] B.J. Bern and R. Pecora, *Dynamic Light scattering with Applications to Chemistry*, Biology and Physics (Wiley, New York, 1976).

[45] A. Roznowska, *Linear Dichroism and Fluorescence Polarization in Ordered Polymers*, Ph.D. thesis, Nicolaus Copernicus University, Toruń, Poland, 2010.
[46] J.J. Fisz, *J Phys Chem A* **111** (2007), 8606.
[47] J.J. Fisz, *J Phys Chem A* **111** (2007), 12867.
[48] J.J. Fisz, *J Phys Chem A* **113** (2009), 3505.
[49] P.R. Dragsten, *Mechanism of Voltage-Induced Fluorescence Changes of the Membrane Probe Merocyanine 540*, A fluorescence polarization studies, Ph.D. thesis, Cornell University: United States of America, 1977.
[50] B. Richards and E. Wolf, *Proc R Soc London, Ser A: Math Phys Sci* **253** (1959), 358.
[51] D. Axelrod, *Biophys J* **26** (1979), 557.

Journal of Computational Methods in Sciences and Engineering 10 (2010) 327–342
DOI 10.3233/JCM-2010-0311
IOS Press

Linear dielectric relaxation of dipolar, rigid, non-interacting and asymmetric-top molecules in Smoluchowski-Debye approach

Wladyslaw Alexiewicz† and Krzysztof Grygiel*
Nonlinear Optics Division, Institute of Physics, Adam Mickiewicz University, ul. Umultowska 85, 61-614 Poznań, Poland

Received 21 December 2009

Abstract. Assuming the low molecular reorientation approximation, the formulae for linear electric polarization induced in liquids composed of rigid, noninteracting, dipolar and asymmetric-top molecules in spherical solvents were derived. The Kalmykov's equation [Phys.Rev., E 65 (021101) 2001] – equivalent to the classical, noninertial Smoluchowski-Debye model of rotational diffusion was applied. In order to highlight the influence of the anisotropy of rotational diffusion tensor components and the orientation of permanent dipole moment of the molecule on the complex linear electric susceptibility, we present three-dimensional plots of the dispersion and absorption spectra, Cole-Cole diagrams for different values of the anisotropies of rotational diffusion tensor components and different frequencies of an ac electric field.

1. Introduction

Since to the pioneering works of Peter Debye the dielectric relaxation studies have been intensively developed in the fields of rotational and translational molecular motions in liquids, correlations between molecules dipoles and dynamics of liquid structure [1]. The classical papers of Perrin [2], and other physicists [3–5], have shown that the asymmetry of the rotational difussion coefficients of the molecule appeares in the rotational diffusion equation leading to three different rotational relaxation times along the principal symmetry axes of the ellipsoidal molecule. An interesting modern approach to the noninertial dielectric relaxation of the asymmetric top molecules was proposed by Kalmykov [6], who used the elegant methods of algebra of the angular momentum [7,8]. An extensive and recent review of dielectric relaxations phenomena in liquids was given by Coffey [9]. The Smoluchowski-Debye equation (SDE) for rotational diffusion of noninteracting, spherical-top molecules in solutions has been succefully applied in description of the optical Kerr effect [10,11] and in the extensive theory of nonlinear ac dielectric response of symmetric-top molecules in liquids [12].

SDE of rotational diffusion motion in liquids was also used by Kasprowicz-Kielich, Kielich and coworkers [13–15], in the theory of nonlinear electro-optical processes of molecular relaxation in intense electric fields of high and low frequencies, and by the present authors [16,17], in the kinetic theory of the

*Corresponding author. E-mail: grygielk@amu.edu.pl.

Langevin saturation in dilute solutions of dipolar, symmetric-top molecules in spherical solvents. This effect, known also as nonlinear dielectric effect, is still the subject of many interesting works [18–20].

It is our aim to present graphical analysis of the linear dielectric relaxation of rigid, non interacting asymmetric-top dipolar molecules in spherical solvents, the phenomenon which strongly depends both on the anisotropy of rotational diffusion tensor and on the angle between the permanent dipole moment and the molecular symmetry axis.

In Sections 2,3 we present the equations, and their solutions for the linear dielectric relaxation of an asymmetric-top molecules in the presence of harmonic electric field, resulting from the Kalmykov's theory Eq. (15) in [6].

Section 4 is concerned with graphical analyses performed on the basis of our results. We present:

- the dependence of dispersional and absorptional Debye-Kielich functions for asymmetric-top molecules on the reduced frequency $\omega\tau_D$,
- the influence of the asymmetry of rotational diffusion tensor components on the relaxations times τ_x, τ_y, τ_D,
- the time evolution of the electric polarization in ac electric fields,
- 3D plots of the dispersional and absorptional Debye-Kielich functions versus frequency $\omega\tau_D$ and the parameters of the anisotropy of rotational diffusion tensor,
- 3D Cole-Cole plots for the electric linear susceptibilities and 3D plots for the loss tangent δ of our medium.

Our results indicate that the spherical-top approximation can be used only in special cases and the asymmetric shape of the molecule cannot be neglected.

2. Theory linear polarization and equations of rotational diffusion for asymmetric-top molecules

We consider a dielectric system of volume V composed of a great number N of dipolar molecules, with the permanent dipole moment of $\vec{\mu} = \mu\vec{u}$. On neglecting the induced molecular polarizabilities and molecular interactions, the Z component of the permanent dipole moment is equal

$$\mu_Z(\Omega) = \frac{\mu}{\sqrt{2}}[(u_x + iu_y)D^1_{0,-1}(\Omega) - (u_x - iu_y)D^1_{0,1}(\Omega) + \sqrt{2}u_z D^1_{0,0}(\Omega)] \tag{1}$$

where $D^j_{m,m'}(\Omega)$ are the Wigner's functions [7,8], depending on the Euler's angles $\Omega = (\alpha, \beta, \gamma)$ determining the orientation of the molecular coordinate (body-fixed) system (x, y, z) with respect to the laboratory system (X, Y, Z), defined as:

$$D^j_{m,m'}(\Omega) = e^{-im\alpha}\, d^j_{m,m'}(\beta)\, e^{-im'\gamma} \tag{2}$$

where

$$\begin{aligned} u_x &= \sin\Theta\cos\Phi \\ u_y &= \sin\Theta\sin\Phi \\ u_z &= \cos\Theta \end{aligned} \tag{3}$$

are the components of a unit vector $\vec{u}$ in the direction of $\vec{\mu}$; moreover Θ, Φ are the polar and azimuthal angles of $\vec{\mu}$ in the molecular coordinate system; $i^2 = -1$. Here $d^j_{m,m'}(\beta)$ are real functions with various

explicite forms given in [8], for example. It is convenient to express changes in the potential energy $V(\Omega,t)$ of the molecule in an external electric field $E_Z(t)$ applied to the dielectric along the Z-axis in the form:

$$V(\Omega,t) = kT \sum_{Q=-1,0,1} \nu_{10Q}(t) D^1_{0,Q}(\Omega) \tag{4}$$

where

$$\begin{aligned} \nu_{100}(t) &= -\xi u_z g(t) \\ \nu_{10\pm1}(t) &= \pm\frac{1}{\sqrt{2}}\xi(u_x \pm i u_y) g(t); \\ E_Z(t) &= E g(t), \\ \xi &= \frac{\mu E}{kT}, \end{aligned} \tag{5}$$

and k is the Boltzmann's constant and T – Kelvin temperature. It is our aim to find the electric polarisation

$$\langle P_Z[E_Z(t)]\rangle = \rho\langle \mu_Z(\Omega)\rangle \tag{6}$$

Here brackets denote the ensemble average for the rotational diffusion of the molecule, $\rho = N/V$ is the number density of our dielectric system. From Eqs (1,6) we have

$$\langle P_Z[E_Z(t)]\rangle = \frac{\rho}{\sqrt{2}}[-u_x\langle A_y(\Omega)\rangle + i u_y\langle A_x(\Omega)\rangle + \sqrt{2}u_z\langle D^1_{0,0}(\Omega)\rangle] \tag{7}$$

where we introduce, for further convenience, the averages:

$$\begin{aligned} \langle A_x(\Omega)\rangle &= \langle D^1_{0,1}(\Omega)\rangle + \langle D^1_{0,-1}(\Omega)\rangle, \\ \langle A_y(\Omega)\rangle &= \langle D^1_{0,1}(\Omega)\rangle - \langle D^1_{0,-1}(\Omega)\rangle \end{aligned} \tag{8}$$

We will not denote the obvious time dependence of the Euler's angles in the ensemble averages in Eq. (7), resulting from molecular dynamic. The general description of the rigid molecule rotational motion is governed by the well-known Euler-Langevin equation, describing the angular velocity $\vec{\omega}(t)$ of the molecule with the moment of inertia **I**:

$$\mathbf{I}\frac{d}{dt}\vec{\omega}(t) + \vec{\omega}(t)\times\mathbf{I}\times\vec{\omega}(t) + \varsigma\vec{\omega}(t) + \bigtriangledown V(\Omega,t) + \vec{\lambda}(t) = 0 \tag{9}$$

where ς is the rotational friction tensor. The term $\bigtriangledown V(\Omega,t)$ describes the torque acting on the molecule in the electric field and $\vec{\lambda}(t)$ denotes the white noise driving torque due to the rotational Brownian motion. The Smoluchowski-Debye model of dielectric relaxation may be obtained by neglecting all terms in Eq. (9) with the tensor of inertia **I** of the molecule, so it is valid only for "noninertial limit" of molecular dynamic. This approximation is a very good model. Kalmykov [6] succesfully proved the validity of this approach, analyzing the experimental results of Jad/xyn and coworkers [18] obtained for the dielectric increments $\delta\epsilon$ of dilute solutions of mesogenic 10-TPEB molecules in benzene.

In [6] the elegant method of obtaining the following noninertial equation for the ensemble averages $\langle D^j_{m,m'}(\Omega)\rangle$ from Euler-Langevin equation was developed:

$$\begin{aligned}
&\frac{d}{dt}\langle D^j_{m,m'}(\Omega)\rangle \;=\; \langle \Delta_\Omega D^j_{m,m'}(\Omega)\rangle \\
&-\frac{1}{2kT}\{\langle \Delta_\Omega[V(\Omega,t)D^j_{m,m'}(\Omega)]\rangle - \langle V(\Omega,t)\Delta_\Omega D^j_{m,m'}(\Omega)\rangle \\
&-\langle D^j_{m,m'}(\Omega)\Delta_\Omega V(\Omega,t)\rangle\}
\end{aligned} \tag{10}$$

and the result, Eq. (15) in Ref. [1], is equivalent to the Smoluchowski-Debye model of rotational diffusion of asymmetric-top molecules. In Eq. (10) Δ_Ω denotes the angular part of Laplace's operator and $V(\Omega,t)$ is simply the change in potential energy of molecule in an applied external electric field $E_Z(t)$. The fundamental differential equation for ensemble averages $\langle D^j_{m,m'}(\Omega)\rangle$ for arbitrary j and for the potential energy $V(\Omega,t)$ given by Eq. (4) was derived by Kalmykov [6] using the algebra of angular momentum and properties of the Wigner's functions.

In our paper we assume $\xi << 1$, which is correct for the electric fields with the strenghts of order $10^7 V/m$. This widely used approximation corresponds to the case when we neglect in the fundamental Kalmykov's Eq. (15) in Ref. [1] all terms with averages $\langle D^{j'}_{m,m'}(\Omega)\rangle$ having $j' > j$. So in order to obtain the polarization (7) we will use this approximated form, valid only in the case of "low molecular reorientation limit", of the exact Kalmykov equation:

$$\begin{aligned}
&\tau_D\frac{d}{dt}\langle D^1_{0,m}(\Omega)\rangle + \;(1+m^2\Delta)\langle D^1_{0,m}(\Omega)\rangle \\
&= -\sigma[C^{1,m+1}_{1,m,1,1}C^{1,m+2}_{1,m+1,1,1}\langle D^1_{0,m+2}(\Omega)\rangle + C^{1,m-1}_{1,m,1,-1}C^{1,m-2}_{1,m-1,1,-1}\langle D^1_{0,m-2}(\Omega)\rangle] \\
&+\frac{1}{4}\sum_{Q=-1,0,1}\nu_{10Q}\sum_{J=0,1}C^{J,0}_{1,0,1,0}\{[J(J+1)+4mQ\Delta-4]C^{J,Q}_{1,0,1,Q}\langle D^J_{0,m+Q}(\Omega)\rangle \\
&+\sigma[J(J+1)C^{J,m+Q+1}_{J,m+Q+1,1,1}C^{J,m+Q+2}_{J,m+Q+1,1,1}C^{J,m+Q}_{J,m,1,Q} - 2C^{1,m+1}_{1,m,1,1}C^{1,m+2}_{1,m+1,1,1}C^{J,m+2+Q}_{1,m+2,1,Q} \\
&-2C^{1,Q+1}_{1,Q,1,1}C^{1,Q+2}_{1,Q+1,1,1}C^{J,m+Q+2}_{1,m,1,Q+2}]\langle D^J_{0,m+Q+2}\rangle \\
&+\sigma[J(J+1)C^{J,m+Q-1}_{J,m+Q,1,-1}C^{J,m+Q+2}_{J,m+Q-1,1,-1}C^{J,m+Q}_{J,m,1,Q} - 2C^{1,m-1}_{1,m,1,-1}C^{1,m-2}_{1,m-1,1,-1}C^{J,m-2+Q}_{1,m-2,1,Q} \\
&-2C^{1,Q-1}_{1,Q,1,-1}C^{1,Q-2}_{1,Q-1,1,-1}C^{J,m+Q-2}_{1,m,1,Q-2}]\langle D^J_{0,m+Q-2}(\Omega)\rangle\}.
\end{aligned} \tag{11}$$

Here $C^{j,l_1+l_2}_{j_1,l_1,j_2,l_2}$ are the well known Clebsch-Gordan coefficients [8,7], and the dimensionless coeficients Δ and σ define the anisotropy of the rotational diffusion tensor components – ($D_{\alpha\alpha}$; where $\alpha = x,y,z$) – [6]:

$$\begin{aligned}
\Delta &= \frac{D_{zz}}{D_{xx}+D_{yy}} - \frac{1}{2}, \\
\sigma &= \frac{D_{xx}-D_{yy}}{D_{xx}+D_{yy}}.
\end{aligned} \tag{12}$$

We assume that only diagonal components of the rotational diffusion tensor are nonzero. Starting from Eq. (11) we obtain:

$$\begin{aligned}
\tau_x \frac{d}{dt}\langle A_x(\Omega)\rangle + \langle A_x(\Omega)\rangle &= -\frac{\sqrt{2}}{3} u_x \xi(t), \\
\tau_y \frac{d}{dt}\langle A_y(\Omega)\rangle + \langle A_y(\Omega)\rangle &= i\frac{\sqrt{2}}{3} u_y \xi(t), \\
\tau_z \frac{d}{dt}\langle D^1_{0,0}(\Omega)\rangle + \langle D^1_{0,0}(\Omega)\rangle &= u_z \xi(t),
\end{aligned} \tag{13}$$

where the asymmetric-top molecule's linear relaxation times τ_x, τ_y, τ_z are equal:

$$\begin{aligned}
\tau_x &= (D_{xx} + D_{zz})^{-1}, \\
\tau_y &= (D_{yy} + D_{zz})^{-1}, \\
\tau_z = \tau_D &= (D_{xx} + D_{yy})^{-1},
\end{aligned} \tag{14}$$

and

$$\tau_z = \tau_x(1 + \Delta - \frac{\sigma}{2}) = \tau_y(1 + \Delta + \frac{\sigma}{2}) \tag{15}$$

The linear ordinary differential Eq. (13) are the main result of this section and their stationary solutions will be used in graphical analyses of linear dielectric relaxation of dipolar, rigid and non-interacting, asy mmetric-top molecules.

3. Linear dielectric relaxation of asymmetric-top molecules in harmonic electric field

We assume that our system is acted on by

- constant electric field with intensity equal to E_0 switched on at the time $t = -\infty$ and switched off at $t = 0$ and
- harmonic electric field $E_\omega \cos(\omega t)$ switched on at $t = 0$. So we have

$$\xi(t) = \xi_0 + \xi_\omega \cos \omega t. \tag{16}$$

If the medium is at the termodynamic equilibrium at $t = 0$ we have, in our approximation [6]:

$$\begin{aligned}
\langle A_x(t=0)\rangle &= -i\frac{\sqrt{2}}{3}\xi_0 u_y, \\
\langle A_y(t=0)\rangle &= -\frac{\sqrt{2}}{3}\xi_0 u_x, \\
\langle D^1_{0,0}(t=0)\rangle &= \frac{1}{3}\xi_0 u_z
\end{aligned} \tag{17}$$

It is easy to find solutions of Eq. (13) in the form:

$$\begin{aligned}\langle D^1_{0,0}(\Omega)\rangle &= \frac{1}{3}\xi_0 u_z exp(-\frac{t}{\tau_z}) \\ &+\xi_\omega u_z r_z(\omega\tau_z)[\cos(\omega t-\varphi_z)+\omega\tau_z r_z(\omega\tau_z)exp(-\frac{t}{\tau_z})]\end{aligned} \tag{18}$$

Here, the relaxational Debye-Kielich functions $r_i(\omega)$ are defined as

$$r_i(\omega\tau_i)=(1+\omega^2\tau_i^2)^{-\frac{1}{2}},\ i=x,y,z, \tag{19}$$

and the phase shifts φ_i are given by

$$\begin{aligned}&\sin\varphi_i=\omega\tau_i r_i(\omega\tau_i);\\ &\cos\varphi_i=r_i(\omega\tau_i).\end{aligned} \tag{20}$$

The functions $r_i(\omega)$ decrease from the maximal value $r_i=1$ for $\omega=0$ to $r_i=0$ when $\omega\tau_i\to\infty$. The others two Eq. (13) have analogous solutions.

For the stationary state, denoted by (s.s.), when $t\gg\tau_z>0$, Eq. (18) is reduced to

$$\langle D^1_{0,0}(s.s.)\rangle=\xi_\omega u_z r_z(\omega\tau_z)\cos(\omega t-\varphi_z). \tag{21}$$

By using the well known properties of the Wigners functions in Eqs (7–8) we obtain the main result of this section

$$\begin{aligned}\langle P_Z(t)\rangle &= \frac{1}{3}\mu\rho\xi_0\sum_{i=x,y,z}u_i^2 exp(-\frac{t}{\tau_i}) \\ &+\frac{1}{3}\mu\rho\xi_\omega\sum_{i=x,y,z}[u_i^2 r_i(\omega\tau_i)\cos(\omega t-\varphi_i)+\omega\tau_i r_i(\omega\tau_i)exp(-\frac{t}{\tau_i})].\end{aligned} \tag{22}$$

The first term in Eq. (22) describes the decay, which is a sum of three exponential functions of linear electric polarization after switching off the constant field ξ_0. Equation (22) in the experimentaly important case of the stationary state is reduced to the formula

$$\begin{aligned}\langle P_Z(s.s.)\rangle &= \frac{1}{3}\mu\rho\xi_\omega\sum_{i=x,y,z}u_i^2 r_i(\omega\tau_i)\cos(\omega t-\varphi_i) \\ &= \frac{1}{3}\mu\rho\xi_\omega\sum_{i=x,y,z}[C^{/}(-\omega;\omega)\cos\omega t+C^{//}(-\omega;\omega)\sin\omega t]\end{aligned} \tag{23}$$

in which the normalized linear electric susceptibilities are given by

$$\begin{aligned}C^{/}(-\omega;\omega)&=\sum_{i=x,y,z}u_i^2[r_i(\omega\tau_i)]^2,\\ C^{//}(-\omega;\omega)&=\sum_{i=x,y,z}u_i^2\omega\tau_i[r_i(\omega\tau_i)]^2\end{aligned} \tag{24}$$

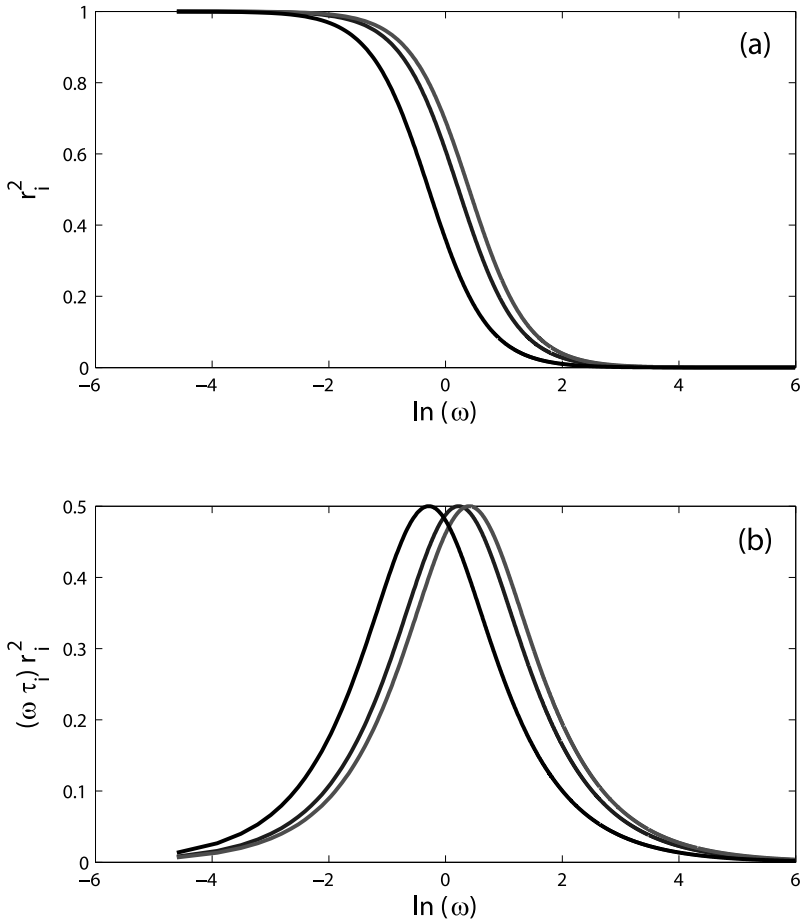

Fig. 1. The quadratic Debye-Kielich relaxation functions of the asymmetric-top molecule $[r_x(\omega\tau_x)]^2$ in red; $[r_y(\omega\tau_y)]^2$ in blue and $[r_D(\omega\tau_D)]^2$ in black, for $a_x = 0.25$; $a_y = 0.5$. Figure 1 a – the dispersion, Fig. 1 b – absorption curves.

We see that Eqs (23–24) for symmetric-top molecules,when $\tau_x = \tau_y = \tau_\perp$, $\tau_z = \tau_\parallel$, are reduced to

$$\begin{aligned}\langle P_Z(s.s.)\rangle = \frac{1}{3}\mu\rho\xi_\omega[r_\perp(\omega\tau_\perp)\cos(\omega t - \varphi_x)\cos^2\Theta \\ + r_\parallel(\omega\tau_\parallel)\cos(\omega t - \varphi_z)\sin^2\Theta]\end{aligned} \tag{25}$$

and for spherical-top, when $\tau_x = \tau_y = \tau_z = \tau_D$, to

$$\langle P_Z(s.s.)\rangle \;=\; \frac{1}{3}\mu\rho\xi_\omega r_D(\omega\tau_D)\cos(\omega t - \varphi_z) \tag{26}$$

A detailed discussion, based on Eq. (25), of the influence of the anisotropy of the rotational diffusion tensor of symmetric-top molecules, in the dielectric linear and nonlinear relaxation, was recently given by us in [16,17]. In these papers the coefficient of anisotropy $\xi = D_{xx}/D_{zz}$ corresponds to $2\Delta = 1/\xi - 1$.

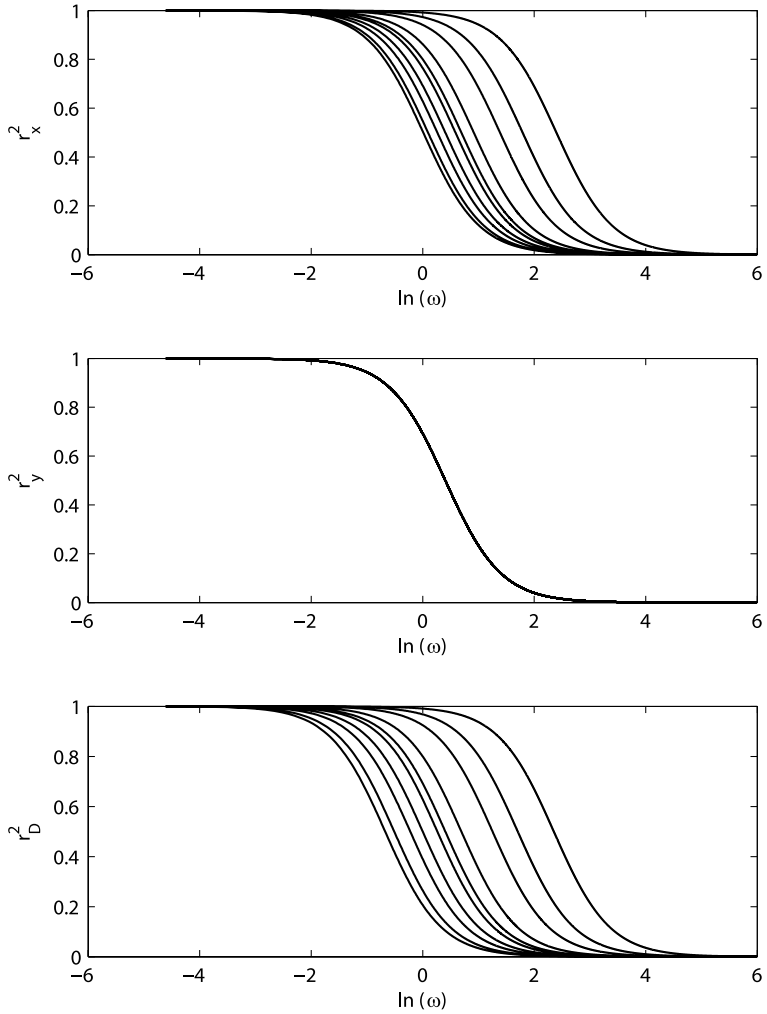

Fig. 2. The Debye-Kielich quadratic dispersion functions $[r_x(\omega\tau_i)]^2$, $[r_y(\omega\tau_i)]^2$ and $[r_D(\omega\tau_D)]^2$ for the asymmetric-top and disk molecules, for $a_x = 0.01; 0.1; 0.3; 0.5$ (symmetric top), 0.8; 1(disk); 1.5; 5; 10 and for $a_y = 0.5$.

For loss tangent of the asymmetric-top molecules we simply have from Eq. (24)

$$\tan\delta = \frac{C^{//}(-\omega;\omega)}{C^{/}(-\omega;\omega)} = \frac{\sum\limits_{i=x,y,z} u_i^2 \omega\tau_i [r_i(\omega\tau_i)]^2}{\sum\limits_{i=x,y,z} u_i^2 [r_i(\omega\tau_i)]^2}. \tag{27}$$

So for symmetric-top molecules

$$\tan\delta = \frac{\omega\tau_\perp [r_\perp(\omega\tau_\perp)]^2 \sin^2\Theta + \omega\tau_\parallel [r_\parallel(\omega\tau_\parallel)]^2 \cos^2\Theta}{[r_\perp(\omega\tau_\perp)]^2 \sin^2\Theta + [r_\parallel(\omega\tau_\parallel)]^2 \cos^2\Theta} \tag{28}$$

and finally, for spherical-top molecules

$$\tan\delta = \omega\tau_D. \tag{29}$$

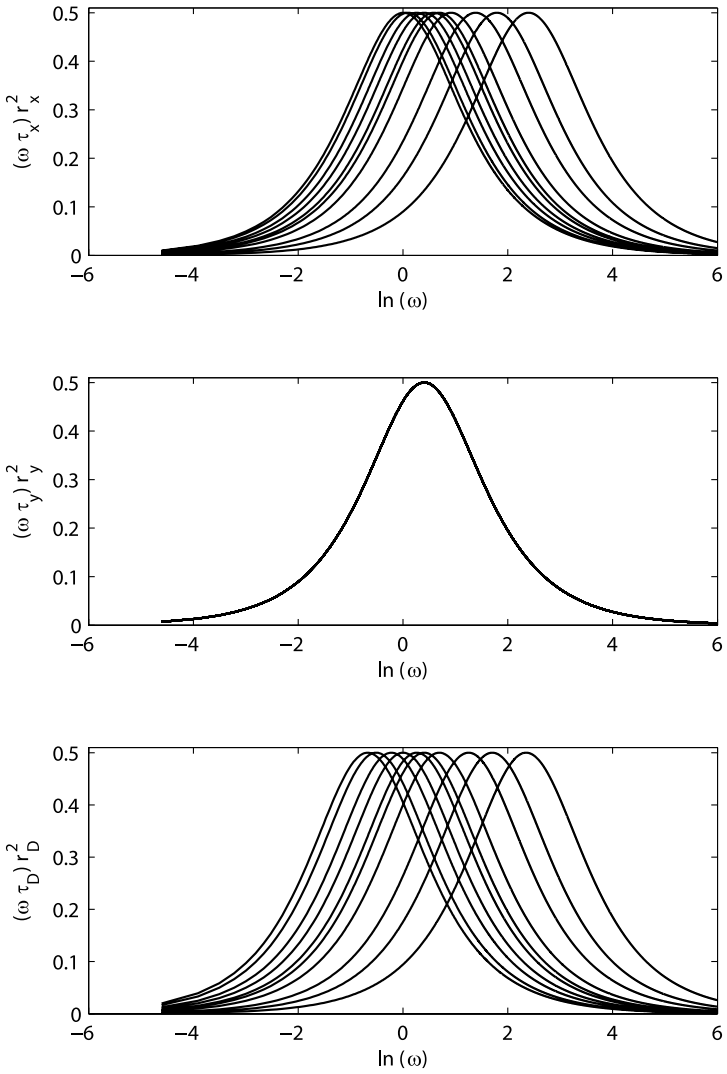

Fig. 3. The absorptional Debye-Kielich functions $\omega\tau_i[r_i(\omega\tau_i)]^2$ for the asymmetric-top and disk molecules for $a_x = 0.01$; 0.1; 0.3; 0.5 (symmetric top), 0.8; 1 (disk); 1.5; 5; 10 and for $a_y = 0.5$.

4. Graphical analysis of the linear dielectric relaxation processes of asymmetric-top molecules

Our aim is to analyze changes in the dielectric relaxation related to the asymmetric shape of molecules, in comparison with those caused by the relaxation of spherical molecules. As first we present spectral properties of the quadratic Debye-Kielich relaxation functions $[r_i(\omega\tau_i)]^2$, given by Eq. (19). In Fig. 1 A all three functions $[r_i(\omega\tau_i)]^2;\ i = x, y, z$ are plotted versus the frequency ω of the ac electric field, in logarithmic scale, while Fig. 1 b present the absorption functions $\omega\tau_i[r_i(\omega\tau_i)]^2;\ i = x, y, z$.

In order to describe the asymmetry of the components of the rotational diffusion tensor of the molecule $D_{ii};\ i = x, y, z$; we introduce the coefficients a_x and a_y defined as follows:

$$a_x = D_{xx}/D_{zz};\ a_y = D_{yy}/D_{zz}. \tag{30}$$

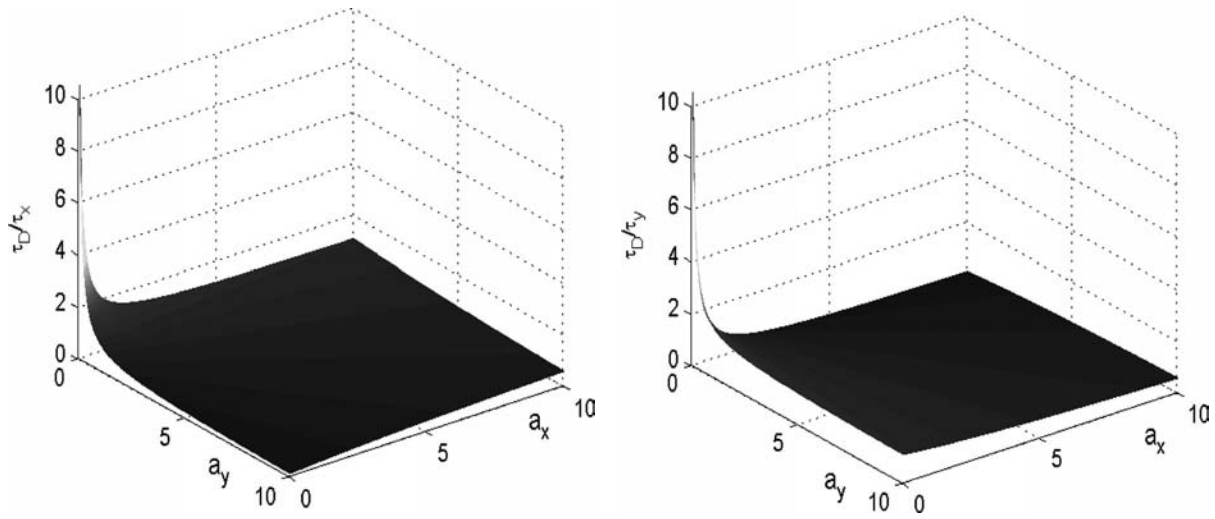

Fig. 4. Ratios (a) τ_D/τ_x and (b) τ_D/τ_y as functions of anisotropy of the components of the rotational diffusion tensor.

In graphical analyses we take $D_{zz} = 1$, for simplicity. So from Eq. (14) we have

$$\tau_x = 1/(1 + a_x);\ \tau_y = 1/(1 + a_y);\ \tau_D = 1/(a_x + a_y) \tag{31}$$

Figure 2 illustrates the influence of anisotropy of the components of molecular rotational diffusion tensor on Debye-Kielich dispersion functions $[r_i(\omega\tau_i)]^2$.

We observe the shift of the dispersion curves towards smaller frequencies, with increasing the asymmetry parameter a_x, from the large asymmetry top ($a_x = 0.01, a_y = 0.5$), through the symmetrical top ($a_x = a_y = 0.5$), and the symmetrical disk ($a_x = 1$, $a_y = 0.5$) to the large asymmetrical disk ($a_x = 10$, $a_y = 0.5$).

The absorptional Debye-Kielich functions $\omega\tau_i[r_i(\omega\tau_i)]^2$ are given in Fig. 3. With increasing asymmetry of the molecule, the maximum of the absorption function $\omega\tau_i[r_i(\omega\tau_i)]^2$ is shifted towards smaller frequencies ω. For dispersion and absorption we notice that the functions with indexes x and D are sensitive to the changes in the parameter of asymmetry a_x but those with the index y are constant (as a_y is fixed). In contrast, when we change a_y at a fixed a_x, the functions with indexes y and D are more sensitive to the changes in a_y and those with indexes x will be constant.

In Fig. 4 the ratios of relaxation times τ_D/τ_x and τ_D/τ_y to the parameters of asymmetry of the components of rotational diffusion tensor are plotted. Both these values increase rapidly for small a_x and a_y, also for extremely thin top molecules. The changes for the other shapes of the molecules are rather small. The linear electric polarisation $\langle P_Z(t)\rangle$, given by Eq. (22) is an important parameter describing dielectric properties of the molecules.

The beginning of the time evolution after the dc electric field is turned off is presented in Fig. 5A and 5C. The transient effects due to the exponential terms dominate. The time evolution in the stationary state, given by Eq. (23) is illustrated in Fig. 5B and 5D. We start with time sufficiently late to fulfil the condition of the stationary state (when the third term in Eq. (22) vanishes). We see that the increasing asymmetry in diffusion leads to increasing amplitude of oscillations and induces a small phase shift. The decrease in the amplitude of oscillation in the stationary state was much greater when the frequency ω was increasing.

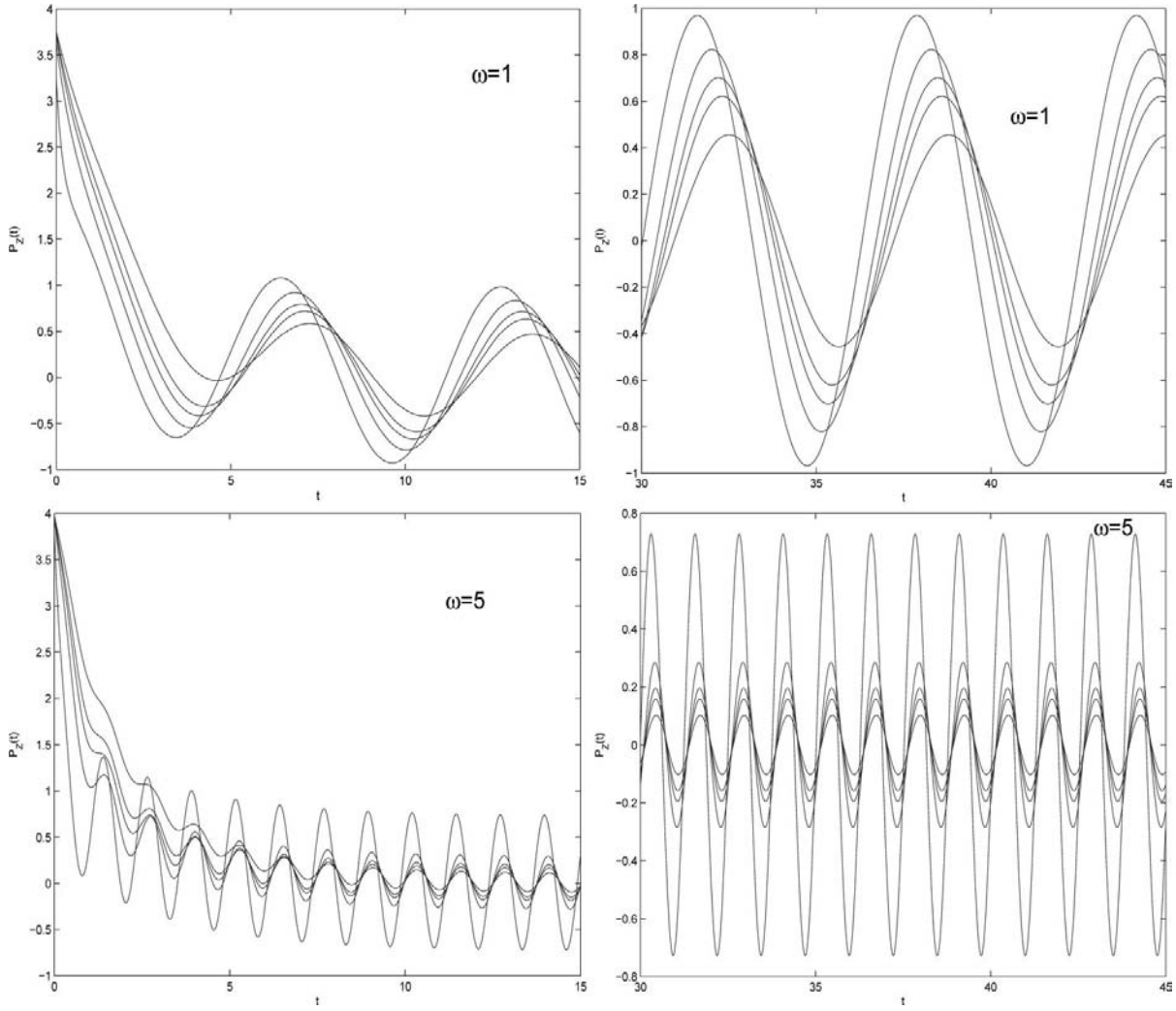

Fig. 5. Time evolution of the linear electric polarization for selected cases of asymmetric-top molecules ($a_y = 0.5$ and $a_x =$ 0.01, 0.3, 0.5, 1, 5) (A,C) and after the initial transient evolution the electric polarization reach the stationary state (B,D). Increasing asymmetry of the molecule leads to increase in the amplitude and a small phase shift of the oscillations. The evolution is presented for two different frequencies ω.

It is very important to know the effect of asymmetry in molecular rotational diffusion on the linear electric susceptibilities $C^{/}(-\omega;\omega)$ and $C^{//}(-\omega;\omega)$. We have made numerical analysis of the dispersional part $C^{/}(-\omega;\omega)$ given by Eq. (24) and the results are presented in Fig. 6.

It is easy to see that dispersion curves are shifted towards higher frequencies of ac field when the asymmetry of molecule is increased. Moreover, the dispersion curves become more linear and perturbed for the higher values of the polar angle θ between the dipole moment and the z molecular coordinate axis. Similar behaviour of the dispersion phenomenon is observed for different azimuthal angles ϕ.

Figure 7 presents the plot of the susceptibility $C^{//}(-\omega;\omega)$ versus $C^{//}(-\omega;\omega)$ and the ratio a_x/a_y for selected values of the polar angle θ of the permanent dipole moment in the molecular coordinate system. A similar phenomenon of the maximum absorption shift towards higher frequencies ω with increasing asymmetry of the molecule is observed. For the large asymmetry we notice an interesting effect of

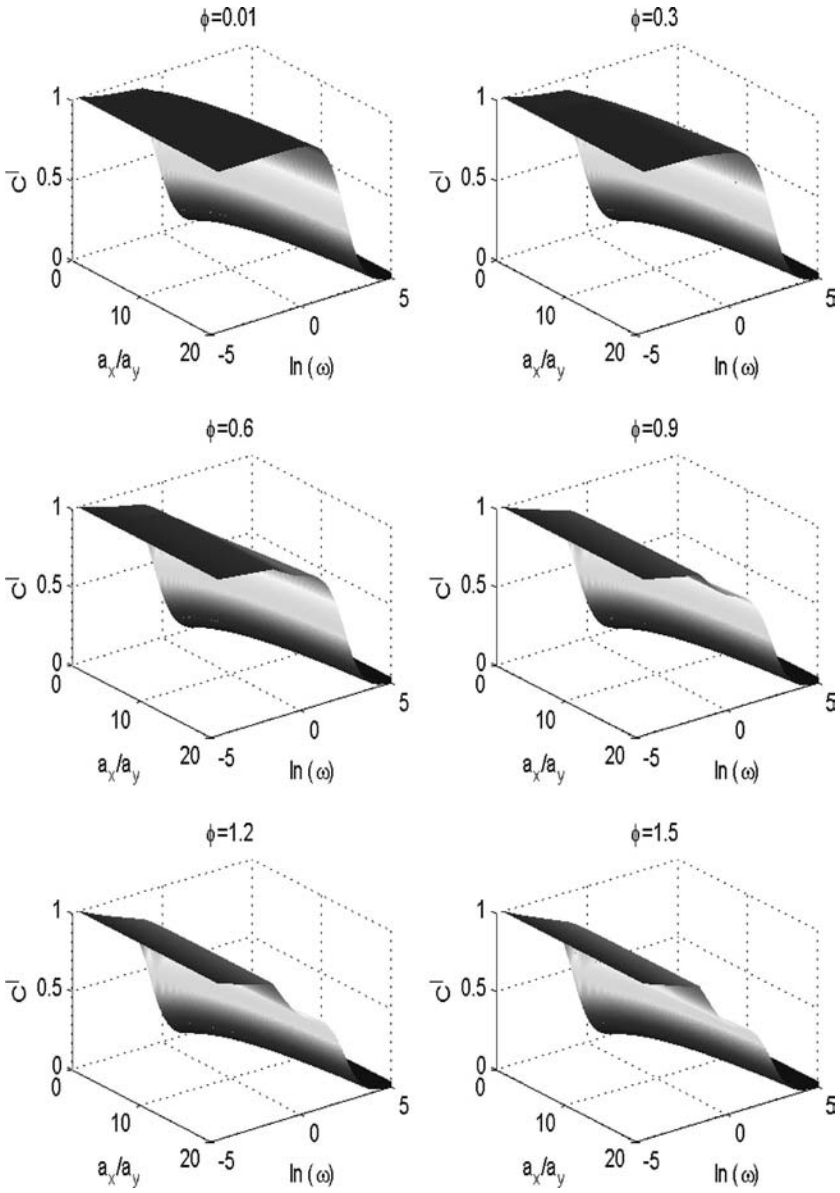

Fig. 6. Plots of the linear electric susceptibility $C^{/}(-\omega;\omega)$ versus frequency ω of harmonic electric field and versus the parameter of asymmetry of components of the rotational diffusion tensor a_x/a_y for selected values of the polar angle θ of the permanent dipole moment in the molecular coordinate system.

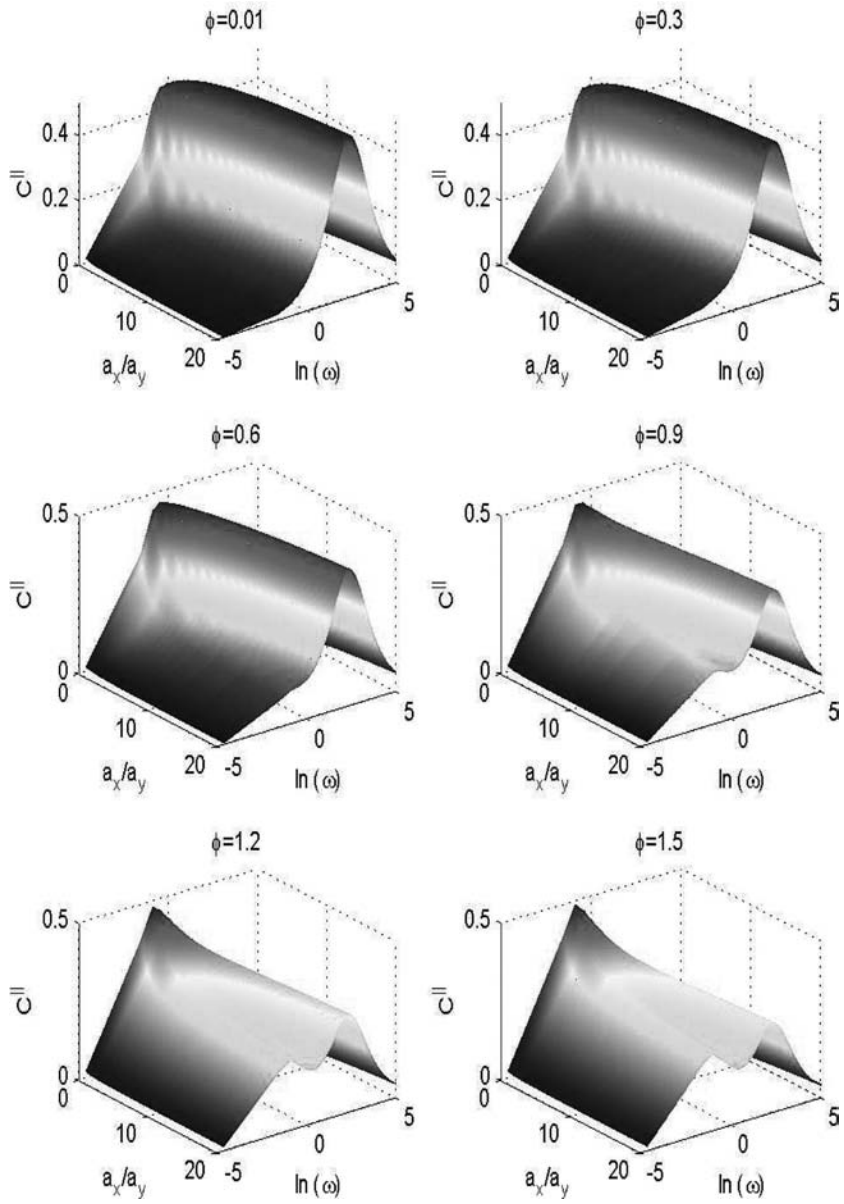

Fig. 7. Plots of the linear electric susceptibility $C^{//}(-\omega;\omega)$ versus frequency ω of harmonic electric field and versus the parameter of asymmetry of components of the rotational diffusion tensor a_x/a_y for selected values of the polar angle θ of the permanent dipole moment in the molecular coordinate system.

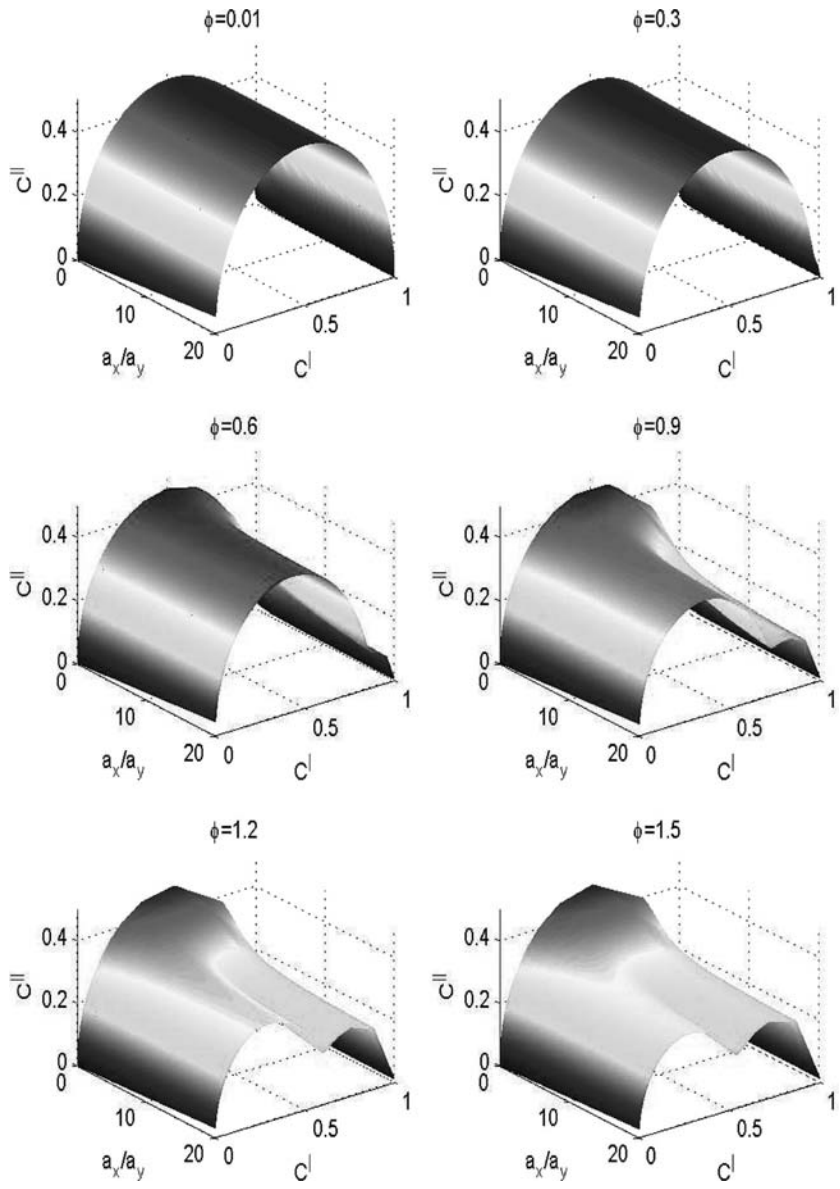

Fig. 8. Cole-cole plots of the linear electric susceptibilities $C^{//}(-\omega;\omega)[C^{/}(-\omega;\omega)]$ versus the parameter of asymmetry of components of the rotational diffusion tensor a_x/a_y, for selected values of the polar angle θ of the permanent dipole moment in the molecular coordinate system.

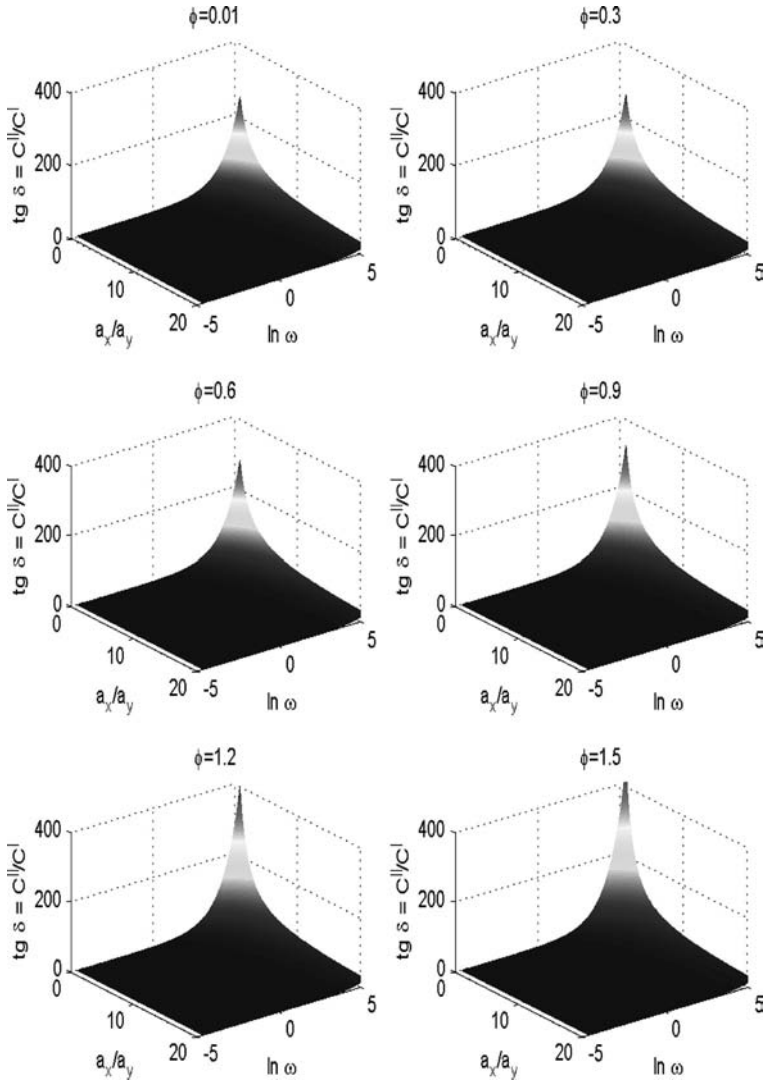

Fig. 9. Loss tangent $\tan\delta$, given by Eq. (27) versus the ratio a_x/a_y and the frequency ω of harmonic electric field for selected values of the polar angle θ of the permanent dipole moment in the molecular coordinate system.

the appearance of a second maximum in the absorption curve. Similar behaviour of the absorption for different azimuthal angles ϕ is also observed.

It is very useful to analyse the frequency dependence of the rotational diffusion in molecular systems with the familar Cole-Cole diagrams. We present the Cole-Cole diagram of $C^{//}(-\omega;\omega)$ versus $C^{/}(-\omega;\omega)$ as a function of the ratio of the asymmetry parameters a_x/a_y, for selected values of the polar angle θ between the permanent dipole moment and z-axis in the molecular coordinate system. We observe, again, the perturbations for the large asymmetry of molecules. One can find the irregularity in the circle-like Cole-Cole plots as well as decreasing the size of the plots for the case $\theta > 0.5$.

Finally we investigated the so-called loss tangent for the asymmetric-top molecules $\tan\delta = C^{//}(-\omega;\omega)/C^{/}(-\omega;\omega)$, given by Eq. (27). Figure 9 shows the dependence of loss tangent of the ratio a_x/a_y and the frequency ω for selected values of the polar angle θ. Large increase in the value of

loss tangent is observed for large values of the frequency ω and for low ratio a_x/a_y, but this increase is weakly reduced, when the angle θ is growing up.

We dedicate this article to our master, Professor Stanislaw Kielich, whose vast knowledge and scientific insight were often of great help and inspiration in our scientific work. It was a great honor for us to have had the oportunity of working with him for many years and be disciples one of the founders of nonlinear optics.

References

[1] P. Debye, *Ver Deut Phys Gesell* **15** (1913), 777, reprinted in collected papers of Peter J. W. Debye, Interscience, New York (1954); Polare Molekeln, Hirzel, Leipzig, 1929; Polar Molecules, reprinted by Dover, New York (1954).
[2] F. Perrin, *J Phys Radium* **5** (1934), 497; **7** (1936), 1.
[3] A. Budo, E. Fisher and S. Miyamoto, *Phys Z* **40** (1939), 337.
[4] E. Fisher and F.C. Frank, *Phys Z* **40** (1939), 345.
[5] A. Morita and H. Watanabe, *J Chem Phys* **77** (1982), 1193.
[6] Y.P. Kalmykov, *Phys Rev E* **65** (2001), 021101.
[7] A.R. Edmonds, Angular Momentum in Quantum Mechanics. (Princeton University Press, Princeton, 1957).
[8] D.A. Varshalovich, A.N. Moskalev and V.K. Khersonskii, Kwantovaya Teoria Uglovogo Momenta, (The Quantum Theory of Angular Momentum), Nauka, Leningrad, 1975 (in Russian); Quantum Theory of Angular Momentum (World Scientific, Singapore, 1998).
[9] W.T. Coffey, *J Mol Liq* **114** (2004), 5.
[10] J.-L. Dejardin, Dynamic Kerr Effect, The Use and Limits of the Smoluchowski Equation and Nonlinear Inertial Responses, World Scientific, Singapore, (1995).
[11] J.L. Dejardin, P.M. Dejardin and Y.P. Kalmykov, *J Chem Phys* **107** (1997), 508; **108** (1998), 3081.
[12] J.L. Dejardin, *J Mol Liq* **114** (2004), 51.
[13] B. Kasprowicz-Kielich and S. Kielich, *Adv Mol Relax Proc* **7** (1975), 275.
[14] B. Kasprowicz-Kielich, S. Kielich and J.R. Lalanne, in: *Molecular Motions in Liquids*, J. Lascombe, ed., D. Reidel, Dordrecht, Holland, 1974, pp. 563–573.
[15] W. Alexiewicz and B. Kasprowicz-Kielich, in: *Modern Non-linear Optics*, M. Evans and S. Kielich, eds, Part.1, 1, Wiley, New York, 1993.
[16] W. Alexiewicz and K. Grygiel, *Acta Phys Pol A* **114** (2008), 667.
[17] W. Alexiewicz and K. Grygiel, *Acta Phys Pol A* **114** (2008), 687.
[18] J. Jadzyn, G. Czechowski, J.-L. Dejardin, M. Ginovska, *J Phys Chem A* **111** (2007), 8325.
[19] J.L. Dejardin and J. Jadzyn, *J Chem Phys* **122** (2005), 074502.
[20] J.L. Dejardin and J. Jadzyn, *J Chem Phys* **125** (2006), 114503.

Journal of Computational Methods in Sciences and Engineering 10 (2010) 343–352
DOI 10.3233/JCM-2010-0334
IOS Press

Intermolecular covalent interaction: 20-center-2-electron covalent π/π bonding in tetrathiafulvalene radical-cation dimer $TTF^{\cdot+}$–$TTF^{\cdot+}$

Bing-Qiang Wang[a], Fang-Fang Wang[a], Fang Ma[a], Zhi-Ru Li[a,*], Di Wu[a], Hong-Liang Xu[a] and Feng Long Gu[b]

[a]*State Key Laboratory of Theoretical and Computational Chemistry, Institute of Theoretical Chemistry Jilin University, Changchun, 130023, China*

[b]*Center for Computational Quantum Chemistry, South China Normal University, Guangzhou, 510631, China*

Abstract. Recently, a novel type of intermolecular covalent interaction has been found in dimers with π-radical(s). In this paper, the optimized structure of the tetrathiafulvalence radical-cation dimer ($TTF^{\cdot+}$–$TTF^{\cdot+}$) is obtained with all-real frequencies, in which a 20-center-2-electron intermolecular covalent π/π bonding with a double-tube shape is theoretically predicted. The covalent π/π bonding energy is estimated to be about -21 kcal·mol^{-1} which counteracts partly the Coulombic repulsion between two $TTF^{\cdot+}$ cations. This intermolecular covalent bonding can also influence the structure of the $TTF^{\cdot+}$ subunit, i.e., its molecular plane is bent by an angle $\theta = 5.6^{\circ}$. In addition, adding the background charges based on the TTF-TCNQ crystal structure, the interaction energy of $TTF^{\cdot+}$–$TTF^{\cdot+}$ changes from a positive value to a large negative value.

This work indicates that the TTF-TCNQ crystal structure built up from parallel, segregated stacks of cation radicals $TTF^{\cdot+}$ and anions $TCNQ^{\cdot-}$ is stabilized by two main factors: the intermolecular covalent π/π bonding interaction between like-charged radicals and the effect of counterions.

1. Introduction

Tetrathiafulvalene (TTF) and its derivatives have been extensively employed in the development of electrical, magnetic, and optical material, and more recently utilized as building blocks for the construction of supramolecular structures including molecular machines [1–10]. The famous one-dimensional organic conductor tetrathiafulvalene-tetracyanoquinodimethane (TTF-TCNQ) is a charge transfer salt exhibiting monoclinic crystal structures built up from parallel, segregated stacks of cations TTF^{+} and anions $TCNQ^{-}$ [11–17]. Noticeably, these two ions TTF^{+} and $TCNQ^{-}$ are two radicals. In this organic conductor, the unusual associations of like-charged radicals $TTF^{\cdot+}$–$TTF^{\cdot+}$ and $TCNQ^{\cdot-}$–$TCNQ^{\cdot-}$ cause the one-dimensional metallic behavior [16,17]. The similar cases also exhibit in other one-dimensional organic conductors [18–21] Because of the strong Coulombic repulsion, the isolated

*Corresponding author. E-mail: lzr@mail.jlu.edu.cn.

$TTF^{\cdot+}$–$TTF^{\cdot+}$ should be unstable. Thus the stability of $TTF^{\cdot+}$–$TTF^{\cdot+}$ in the charge transfer salt TTF-TCNQ should mainly ascribe to the counterion $TCNQ^{-}$. The cation radical dimer $TTF^{\cdot+}$–$TTF^{\cdot+}$ encapsulated in the cavity of cucurbit[8]uril is also stable and has been isolated at room temperature by Ziganshina and coworkers [10]. In addition, the identification of the infrared spectra demonstrates the stability of the $TTF^{\cdot+}$–$TTF^{\cdot+}$ dimer in the dimethylsulphoxide solution [22]. However, is there an intermolecular attraction in the like-charged radical pair $TTF^{\cdot+}$–$TTF^{\cdot+}$? If there is, what is the nature of the possible intermolecular attraction? These challenging questions have not yet been solved.

Traditional π/π stacking systems normally consist of the closed-shell π-systems [23–30]. For example, the parallel benzene dimer with its inter-plane distance of 3.616 Å is a closed-shell π-system [30]. The interactions of these π/π stacking systems are noncovalent π/π stacking interactions.

Contrast to the traditional noncovalent π/π stacking systems between two closed-shell molecules, the $TTF^{\cdot+}$–$TTF^{\cdot+}$ dimer is a π/π stacking system between two open-shell cation radicals with unpaired electron. For the dimer consisting of two radicals, it is possible that these two unpaired electrons interact each other to form an intermolecular covalent bond. Recently, the unusual intermolecular π/π covalent bonding interaction [31–42] has been discovered in some dimers of π-radicals such as phenalenyl radical and its derivatives [31–34], biphenylene cation radical [34], bithiophene cation radical ($BT^{\cdot+}$) [36], $TCNQ^{\cdot-}$ [35], and tetracyanoethylene cation radical ($TCNE^{\cdot-}$) [35,37]. The interplanar distances of interacting π-radicals (about $3.0 \sim 3.5$ Å) [31–42] are about twice that of a typical C–C bond but are less than those of interacting closed-shell π-systems (e.g. 3.616 Å [30] interplanar distance of the parallel benzene dimer) which indicates further attractive intermolecular interactions (intermolecular covalent π/π bonding) in addition to van der Waals forces.

The intermolecular covalent π/π boding is an interesting research topic. Intermolecular interaction effects on the second hyperpolarizabilityof open-shell singlet diphenalenyl radical dimmer is also reported [43].

The aim of this paper is to explore the covalent bonding in the radical-cation dimer $TTF^{\cdot+}$–$TTF^{\cdot+}$, which is concealed by the strong Coulombic repulsion. Its nature, bonding form in $TTF^{\cdot+}$–$TTF^{\cdot+}$ in gas phase and in TTF-TCNQ crystal are investigated to assess the existence of dimerized bound states and the role played by the environment.

2. Computational details

Geometry optimizations of the $TTF^{\cdot+}$–$TTF^{\cdot+}$ dimer were performed at the DFT (B3LYP) and MP2 levels. Both the spin-restricted methods (RB3LYP and RMP2) and spin-unrestricted methods with the broken-symmetry (UB3LYP and UMP2 with the "guess=mix" command in a Gaussian03 input file) were employed in geometry optimizations, and they all gave stable $TTF^{\cdot+}$–$TTF^{\cdot+}$ close-shell singlet dimer structures ($<S^2>= 0.0$) with all-real frequencies. We found that, at either the B3LYP or the MP2 level, both spin-restricted and spin-unrestricted geometry optimizations converge to the same singlet geometry. The local minimum of triplet state structure was not found. This indicates that $TTF^{\cdot+}$–$TTF^{\cdot+}$ dimer have a close-shell singlet ground state and that an intermolecular covalent interaction should occur in it.

In this work, the effect of basis set on the geometrical optimization of the $TTF^{\cdot+}$–$TTF^{\cdot+}$ was tested by the UB3LYP method with six basis sets. As the geometry obtained by the 6-311G basis set is closest to that obtained by the larger basis set 6-311+G(2df) at the UB3LYP level, the 6-311G basis set was chosen for the geometrical optimization of the $TTF^{\cdot+}$–$TTF^{\cdot+}$ dimer at the higher UMP2 level. The NBO analysis [44] is carried out at the MP2/6-311+G* level. The interaction energy is calculated at

Table 1
The interplanar distances and the $<S^2>$ values of $TTF^{\cdot+}$–$TTF^{\cdot+}$ at the UB3LYP and UMP2 levels[a]

	Basis set	$<S^2>$	R	R1	R2
UB3LYP	6-31G	0.0	3.713	3.799	4.136
	6-31+G	0.0	3.714	3.812	4.173
	6-311G	0.0	3.689	3.795	4.166
	6-311+G	0.0	3.626	3.743	4.119
	6-311+G(d)	0.0	3.641	3.738	4.071
	6-311+G(2df)	0.0	3.679	3.748	4.059
UMP2	6-311G	0.0	3.394	3.544	3.901
	6-311G(d)	0.0	3.231	3.386	3.636
	6-311+G(2d)	0.0	3.150	3.373	3.695
EXP[b]			3.470		

[a]The UB3LYP and UMP2 methods give the same optimized structures as the RB3LYP and RMP2, respectively. [b] The interplanar distance of TTF cation in the TTF-TCNQ crystal from Ref 51.

the performable UMP2/6-311+G* level and the counterpoise method [45] is used to correct the basis set superposition error (BSSE) in the calculation of the interaction energy.

The calculations in this paper are carried out with Gaussian03 [46] program package. The molecular structure and molecular orbitals are plotted with GaussView program.

3. Results and discussions

3.1. Bond length of the intermolecular bonding in $TTF^{\cdot+}$–$TTF^{\cdot+}$

The effect of basis set on the geometrical optimization of the $TTF^{\cdot+}$–$TTF^{\cdot+}$ was tested by the UB3LYP method with six basis sets (see Table 1). As can be seen from Table 1, with increasing of basis sets from 6-311G to 6-311+G(2df), the change of the interplanar distance of the $TTF^{\cdot+}$–$TTF^{\cdot+}$ dimer is very small and the 6-311G basis set is enough to optimize the structure of this dimer. Thus the 6-311G basis set was chosen for the geometrical optimization of the $TTF^{\cdot+}$–$TTF^{\cdot+}$ dimer at the MP2 level.

Density functional theory (DFT) calculations [47], such as B3LYP, are the most common choice for organic molecules. DFT calculations, however, are not necessarily appropriate for the $TTF^{\cdot+}$–$TTF^{\cdot+}$ π-radical dimer, because they do not properly describe the long-range dispersion interactions [48] or the separation of charged π-dimers into fragments [31,49]. Alternatively, the MP2 method, in which the dispersion can be reincorporated, has been shown to be reasonably accurate for calculations of stacking interactions [50]. While, special care should be taken onto the unrestricted UMP2 as it is very sensitive to spin contamination [51].

For the $TTF^{\cdot+}$–$TTF^{\cdot+}$ dimer, the unrestricted UMP2 singlet geometry optimization gives the close-shell singlet stable structure ($<S^2>= 0.0$) same as that obtained by RMP2 method. As can be seen from Table 1, the interplanar C-C distance (3.394 Å) at the UMP2/6-311G level is obviously shorter than that (3.626 Å) at the UB3LYP/6-311G level, and the former is much closer to the interplanar distance (3.47 Å) of TTF cations in the TTF-TCNQ crystal [52]. The geometry at the UMP2/6-311G level is used in the following discussions.

In the $TTF^{\cdot+}$–$TTF^{\cdot+}$ dimer, the calculated R(C-C) value of 3.394 Å is the shortest interplanar atomic distance between two $TTF^{\cdot+}$ which is close to the interplanar stack distance of $TTF^{\cdot+}$ 3.47 Å in the

Table 2
The NBO charges and intermolecular Wiberg bond index of $TTF^{\cdot+}$–$TTF^{\cdot+}$ and $TTF^{\cdot+}$ calculated at the MP2/6-311+G* level. n is the number of pair of atoms between two monomers

NBO charge	C	S	C'	H	
$TTF^{\cdot+}$–$TTF^{\cdot+}$	−0.439	0.528	−0.333	0.275	
Wiberg bond index	n C···C	n S···S	n C'···C'		total
$TTF^{\cdot+}$–$TTF^{\cdot+}$	2 0.011	4 0.027	4 0.001		0.134
TTF–TTF	2 0.001	4 0.001	4 0.000		0.006
$(Phenalenyl)_2^a$	6 0.029		1 0.003		0.177
H_3C-CH_3	1 0.986				0.986

[a]The results of phenalenyl radical/radical π-dimer with the interplanar distance of 3.3 Å at the MP2/6-31G* level.

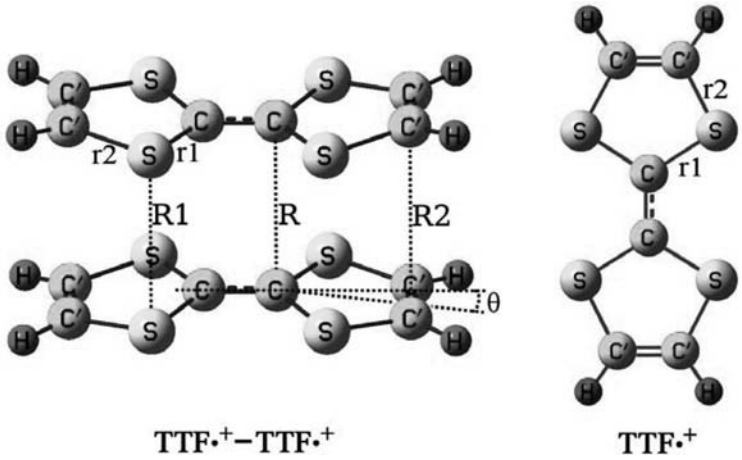

Fig. 1. The optimized geometrical structures of the $TTF^{\cdot+}$–$TTF^{\cdot+}$ dimer and $TTF^{\cdot+}$.

TCNQ-TTF crystal [52] and lies in the reported range of 3.0–3.5 Å [31–42] for intermolecular covalent π/π bonding. This indicates that there is a further attractive intermolecular interaction in addition to van der Waals forces, which may be intermolecular covalent π/π bonding. The R(C-C 3.394 Å) distance is shorter than the R1(S-S 3.544 Å)) and R2(C'-C' 3.901 Å) values, so that the $TTF^{\cdot+}$ plane is bent with the angle $\theta = 5.6^\circ$ in the $TTF^{\cdot+}$–$TTF^{\cdot+}$ dimer (see Figure 1). While geometry optimization at the UMP2/6-311+G(2d) level shows that the isolated $TTF^{\cdot+}$ cation radical has a planar structure with the r1(S-C 1.731 Å) and r2(S-C' 1.725 Å) values which are close to the r1(S-C 1.732 Å) and r2(S-C' 1. 723 Å) values at UMP2/6-311+G(2d) level for $TTF^{\cdot+}$–$TTF^{\cdot+}$ dimer.

The intermolecular potential energy surfaces of the dimmers $TTF^{\cdot+}$–$TTF^{\cdot+}$ and TTF–TTF at the UMP2/6-311+G* level show that the minimum interplanar distance of $TTF^{\cdot+}$–$TTF^{\cdot+}$ with the cation-cation repulsion is not larger than that of TTF–TTF without the cation-cation repulsion, but smaller by about 0.3 Å (Fig. 2). This indicates that the attraction interaction in $TTF^{\cdot+}$–$TTF^{\cdot+}$ is stronger than that in TTF–TTF.

3.2. Natural Bond Orbital (NBO) analysis

The NBO charges of $TTF^{\cdot+}$–$TTF^{\cdot+}$ and Wiberg bond indexes [53] of the intermolecular bond at the MP2/6-311+G* level are listed in Table 2.

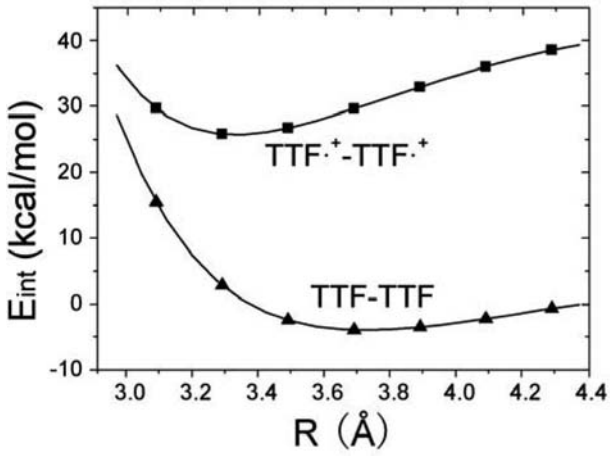

Fig. 2. The interaction potential energy surfaces (PES) at the UMP2/6-311+G* level, as functions of the interplanar distance R, for the TTF$^{\cdot+}$–TTF$^{\cdot+}$ and TTF–TTF dimers. For the R values corresponding to the minimum of E_{int}, R(TTF$^{\cdot+}$–TTF$^{\cdot+}$) is smaller than R(TTF–TTF).

From Table 2, the NBO charges of TTF$^{\cdot+}$–TTF$^{\cdot+}$ show that the C atoms carry negative charges but the S and H atoms carry positive charges. The values of NBO charges are respectively $Q_C = -0.439$, $Q_{C'} = -0.333$, $Q_S = 0.528$, and $Q_H = 0.275$. These atomic charges will be used to estimate the Coulombic repulsion between two cations in the dimer TTF$^{\cdot+}$–TTF$^{\cdot+}$.

The study on the bond index of the intermolecular interaction should be an interesting try. The Wiberg bond indexes of the intermolecular C-C, S-S, and C'-C' are respectively 0.011, 0.027, 0.001. The total bond index of this intermolecular interaction is 0.134 which is the sum of the bond indexes of two C-C, four S-S, and four C'-C'. In order to compare with the corresponding noncovalent interaction, we calculated the bond index of the neutral dimer TTF–TTF (R = 3.7 Å) to be 0.006 (see Table 2). The bond index 0.134 of the cation radical dimer TTF$^{\cdot+}$–TTF$^{\cdot+}$ is much larger than the bond index 0.006 of this noncovalent π/π stacking interaction and is about 26 times of the bond index of TTF–TTF. This supports that the long-range interaction between two cation TTF$^{\cdot+}$ is a covalent intermolecular interaction.

For intermolecular multicenter covalent π/π bonding, we also calculated the intermolecular Wiberg bond index for the phenalenyl radical dimer. We found that the intermolecular Wiberg bond index (0.134) of TTF$^{\cdot+}$–TTF$^{\cdot+}$ approximates to the 0.177 of the phenalenyl radical dimer, which also supports that the interaction between two cation TTF$^{\cdot+}$ is an intermolecular covalent bonding.

Compared with the intramolecular covalent C-C single bond, the bond index between two cation TTF$^{\cdot+}$ is 1/7 of the bond index (0.986) of the C-C single bond of ethane (H_3C-CH_3) at the same level. It indicates that the long-range intermolecular interaction between two cation TTF$^{\cdot+}$ is a weak covalent interaction.

3.3. Energy of the intermolecular covalent bonding in TTF$^{\cdot+}$–TTF$^{\cdot+}$

The interaction energy (E_{int}) of the dimer TTF$^{\cdot+}$–TTF$^{\cdot+}$ are calculated at the UMP2 level with the 6-311+G* basis set, and the counterpoise method [45] is used to correct the basis set superposition error (BSSE). Energy data are listed in Table 3.

The interaction energy of TTF$^{\cdot+}$–TTF$^{\cdot+}$ is a positive value of 26 kcal·mol^{-1} which indicates that the isolated dimer TTF$^{\cdot+}$–TTF$^{\cdot+}$ in vacuum is unstable because of the strong Coulombic repulsion.

Table 3
The intermolecular interaction energy ($E_{\rm int}$), the Coulomb repulsion energy ($E_{\rm coul}$), the van der Waals energy ($E_{\rm vdw}$), and the intermolecular covalent bonding energy ($E_{\rm cov}$) of TTF$^{\cdot+}$–TTF$^{\cdot+}$ (in kcal·mol^{-1}) at the MP2/6-311+G* level

	$E_{\rm int}$	$E_{\rm elst}$(TTF$^{\cdot+}$–TTF$^{\cdot+}$)	$E_{\rm elst}$(TTF–TTF)	$E_{\rm coul}$	$E_{\rm cov}$	$E_{\rm vdw}$
TTF$^{\cdot+}$–TTF$^{\cdot+}$	26	58	8	50	−21	−3
TTF–TTF	−3					−3
(Phenalenyl)$_2$[a]	−11					

[a] Ref 31.

While the interaction potential energy surfaces (PES) (Fig. 2) shows that there is a local minimum for TTF$^{\cdot+}$–TTF$^{\cdot+}$ at R = 3.47 Å, that is to say TTF$^{\cdot+}$–TTF$^{\cdot+}$ is metastable in gas phase. Obviously, some attractive interactions exist in the dimer TTF$^{\cdot+}$–TTF$^{\cdot+}$. On the other hand, the minimum interplanar distance of TTF$^{\cdot+}$–TTF$^{\cdot+}$ with the cation-cation repulsion actually is smaller by about 0.3 Å than that of TTF–TTF without the cation-cation repulsion, and thus a covalent π/π bonding interaction obviously emerge. It is a challenging question how to calculate the covalent bonding energy concealed by the strong Coulombic repulsion.

The interaction energy ($E_{int} = 26$ kcal·mol^{-1}) between two TTF$^{\cdot+}$ can be described by an approximate fomula:

$$E_{\rm int} = E_{\rm cov} + E_{\rm coul} + E_{\rm vdw},$$

where E_{cov} is the covalent bonding energy, $E_{\rm coul}$ is the Coulombic repulsion energy, and $E_{\rm vdw}$ is the van der Waals energy of the neutral dimer TTF–TTF (-3 kcal·mol^{-1}).

The Coulombic repulsion energy $E_{\rm coul}$ can be estimated by the following equation:

$$E_{\rm coul} = E_{\rm elst}(\mathrm{TTF}^{\cdot+} - \mathrm{TTF}^{\cdot+}) - E_{\rm elst}(\mathrm{TTF} - \mathrm{TTF}),$$

where $E_{\rm elst}$(TTF$^{\cdot+}$–TTF$^{\cdot+}$) (58 kcal·mol^{-1}) is calculated by an atomic point charge model using the NBO atomic charges of TTF$^{\cdot+}$–TTF$^{\cdot+}$, and $E_{\rm elst}$(TTF–TTF) (8 kcal·mol^{-1}) is calculated by the same model using the NBO atomic charges of TTF–TTF:

$$E_{\rm elst} = \sum_{i<j} \frac{Q_i Q_j}{R_{ij}}$$

Then, the intermolecular covalent bonding energy $E_{\rm cov}$ can be estimated by

$$E_{\rm cov} = E_{\rm int} - E_{\rm coul} - E_{\rm vdw}$$

For the UMP2/6-311+G* result, the $E_{\rm cov}$ value is about –21 kcal·mol^{-1} (see Table 3).

The covalent bonding interaction $E_{\rm cov}$ of the dimer TTF$^{\cdot+}$–TTF$^{\cdot+}$ is actually larger than that of the phenalenyl radical dimer (-11 kcal·mol^{-1})[31]. Its main reasons may be (1) the intermolecular covalent interaction of S$\cdots$S in the dimer TTF$^{\cdot+}$–TTF$^{\cdot+}$ is much stronger than that of C$\cdots$C in the dimer; (2) 10 intermolecular atomic pair interactions in the parallel dimer TTF$^{\cdot+}$–TTF$^{\cdot+}$ is more than 7 intermolecular atomic pair interaction in the antiparallel phenalenyl radical dimmer; (3) the covalent bonding energy $E_{\rm cov}$ may include the attractive interaction between the cation charge of one TTF$^{\cdot+}$ and the π electronic cloud of the other TTF$^{\cdot+}$.

Compared with a common covalent bond, the ratio of intermolecular covalent bonding interaction $E_{\rm cov}$ to the average bond energy of the C-C single bond (89.6 kcal·mol^{-1})[55] is about 1/4. This indicates that this intermolecular covalent bonding is a weak covalent interaction and a strong intermolecular interaction.

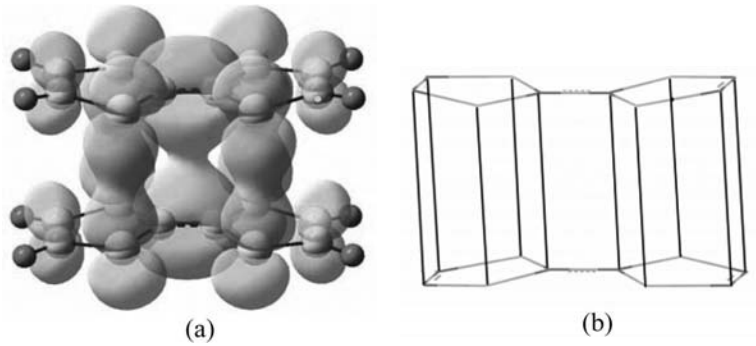

Fig. 3. (a) The intermolecular 20-center-2-electron π/π bonding orbital, and (b) double tube type 20-center-2-electron π/π bonding for the radical pair $TTF^{\cdot+}$–$TTF^{\cdot+}$.

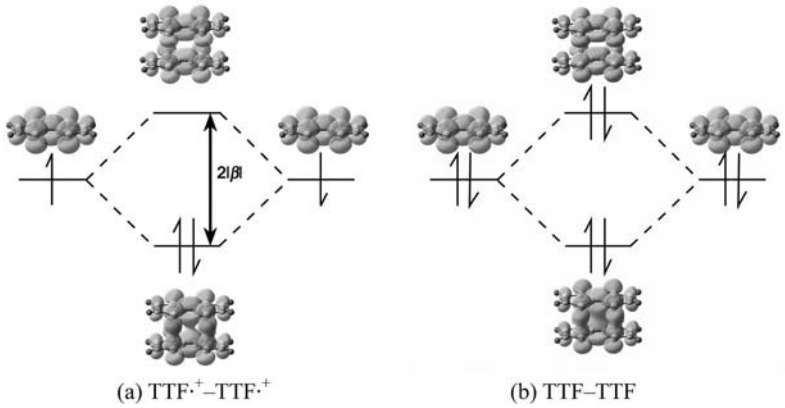

Fig. 4. (a) The intermolecular π/π bonding interaction of $TTF^{\cdot+}$–$TTF^{\cdot+}$ and (b) The intermolecular π/π nonbonding interaction of TTF–TTF.

3.4. Intermolecular covalent bonding from SOMO-SOMO π/π overlapping

Figure 3 shows the nature of the covalent bonding interaction between two $TTF^{\cdot+}$ cation radicals which comes from double occupied highest occupied bonding orbitals (HOMO) of dimer $TTF^{\cdot+}$–$TTF^{\cdot+}$. The intermolecular covalent bonding is concealed by the strong Coulombic repulsion.

In order to understand the nature of the intermolecular covalent bonding, the analysis of molecular orbitals is carried out. Figure 4 shows the difference between $TTF^{\cdot+}$–$TTF^{\cdot+}$ and TTF–TTF. As a cation radical, the HOMO of $TTF^{\cdot+}$ is a single occupied molecular orbital (SOMO). In $TTF^{\cdot+}$–$TTF^{\cdot+}$, the SOMO-SOMO π/π overlapping forms a new bonding molecular orbital and a new antibonding molecular orbital of the dimer. The two unpaired electrons of $TTF^{\cdot+}$ pair in the overlapping of two SOMOs in $TTF^{\cdot+}$–$TTF^{\cdot+}$ and occupy the bonding molecular orbital with lower energy. The antibonding molecular orbital is unoccupied. Thus, the total energy of this system decreases. Then this intermolecular covalent interaction is called as a double-tube shaped 20-center 2-electron intermolecular π/π bonding.

The intermolecular covalent bonding energy E_{cov} can also be approximated by the stablilization energy coming from the π/π through-space overlap between the SOMOs of TTF cation radical. The dimer level splitting of $2|\beta|$ reflects the overlap between the two SOMOs; the better the overlap, the larger the value of $2|\beta|$. Since the dimer bonding orbital is lower than the SOMO by approximately the same amount as

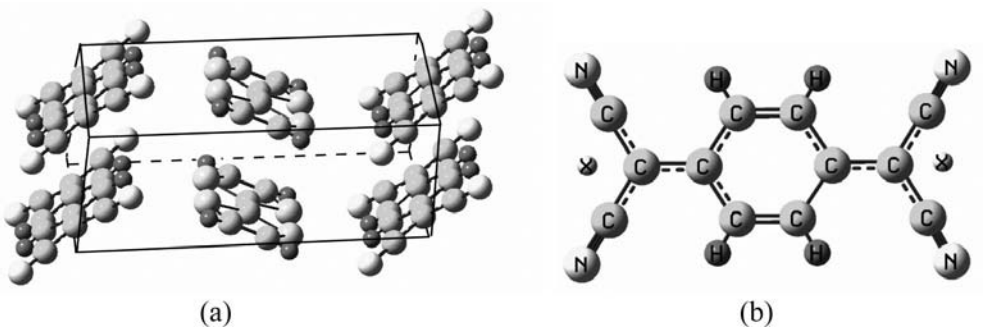

Fig. 5. (a) A model constructed for the TTF·$^+$–TTF·$^+$ dimer with a background charge distribution according to the part in the frame. The structural parameters of TTF and TCNQ are taken from those of TTF-TCNQ crystal. (b) The negative charges of every half TCNQ anion are replaced by two point charges of -0.25 which are located at the two ghost atoms X. The TTF·$^+$–TTF·$^+$ dimer is wrapped by 8 point charges of -0.25.

the dimer antibonding orbital is higher than the SOMO, $2|\beta|$ is the approximately the magnitude of the intermolecular covalent bonding energy E_{cov} [54]. At the LDA/6-31G* level, the $2|\beta|$ is calculated to be 18 kcal·mol^{-1}, thus the E_{cov} value is –18 kcal·mol^{-1}, which is close to –21 kcal·mol^{-1} estimated by the former method.

3.5. The intermolecular covalent interaction in TTF-TCNQ crystal

In this section, we roughly calculated the interaction energy of the dimer TTF·$^+$–TTF·$^+$ with the background charge distribution of TCNQ to partly mimick the case in TTF-TCNQ crystal. The system calculated is shown in Fig. 5. The structure of TTF and TCNQ is from the parameters of TTF-TCNQ crystal. The negative charges of every half TCNQ anion are replaced by two point charge of –0.25 which locate at the two ghost atoms X, because the negative charges of every TCNQ anion are shared by two TTF cations.

With the background charges, the rough interaction energy of TTF·$^+$–TTF·$^+$ is estimated to be –77.6 kcal·mol^{-1} at the MP2/6-311+G* level with the counterpoise [45] method. It indicates that the dimer TTF·$^+$–TTF·$^+$ with the strong Coulombic repulsion can be stable in an environment with TCNQ$^-$ counterions. In the stable crystal structure, the electron delocalization caused by the intermolecular covalent π/π bonding interaction is closely related to the one-dimensional organic metallic property.

4. Conclusion

This work demonstrates that there exists intermolecular covalent bonding interaction in the radical-cation dimer TTF·$^+$–TTF·$^+$, which is concealed by the strong Coulombic repulsion. The key points of this work are summarized as followings.

1. The two cation radical TTF·$^+$ can interact each other to form an intermolecular covalent dimer.
2. The interplanar distance of the radical-cation dimer TTF·$^+$–TTF·$^+$ with strong cation-cation repulsion is actually shorter than that of the neutral dimer TTF–TTF with noncovalent π/π attractive interaction. The interplanar distance of TTF·$^+$–TTF·$^+$ lies in the range of 3.0–3.5 Å [31–42] for intermolecular covalent π/π bonding. It shows that the attractive interaction in TTF·$^+$–TTF·$^+$ is covalent π/π bonding interaction.

3. The Wiberg bond index of the intermolecular interaction of the parallel dimer $TTF^{\cdot+}$–$TTF^{\cdot+}$ (0.134) is approximate to that of the multicenter covalent π/π bonding for the antiparallel phenalenyl radical dimer (0.177). It indicates that there is an intermolecular covalent bonding interaction between two radical-cation $TTF^{\cdot+}$ in $TTF^{\cdot+}$–$TTF^{\cdot+}$.
4. The intermolecular covalent bonding energy of the parallel dimer $TTF^{\cdot+}$–$TTF^{\cdot+}$ is estimated by reducing the Coulombic repulsion energy and the van der Waals energy from the total interaction energy. It is about -21 kcal·mol^{-1}.
5. The molecular orbital analysis shows the existence of the doubly-occupied covalent bonding orbital between two cation radicals in $TTF^{\cdot+}$–$TTF^{\cdot+}$.
6. This intermolecular covalent interaction is the nature of the interaction between the like-charged radicals in $TTF^{\cdot+}$–$TTF^{\cdot+}$. It results in the charge transfer crystal structures built up from parallel, segregated stacks of cations TTF^{+} and anions $TCNQ^{-}$.

These results support the conclusion that there exists an intermolecular 20-center 2-electron covalent π/π bonding interaction in the radical-cation dimer $TTF^{\cdot+}$–$TTF^{\cdot+}$. This intermolecular covalent interaction relates to the one-dimensional organic conductor of the TTF-TCNQ salt.

Acknowledgment

This work was supported by the National Natural Science Foundation of China (No. 20773046).

References

[1] M.R. Bryce, *Chem Soc Rev* **20** (1991), 355.
[2] M.R. Bryce, *J Mater Chem* **10** (2000), 589.
[3] P. Day and M. Kurmoo, *J Mater Chem* **8** (1997), 1291.
[4] J.L. Segura and N. Martin, *Angew Chem, Int Ed* **40** (2001), 1372.
[5] M.R. Bryce, W. Devonport, L.M. Goldenberg and C. Wang, *Chem Commun* (1998), 945.
[6] T. Jurgensen, T.K. Hansen and J. Becher, *Chem Soc Rev* **27** (1994), 41.
[7] M.R. Bryce, *Adv Mater* **11** (1999), 11.
[8] M.B. Nielsen, C. Lomholt and J. Becher, *Chem Soc Rev* **29** (2000), 153.
[9] K.B. Simonsen and J. Becher, *Synlett* **11** (1997), 1211.
[10] A.Y. Ziganshina, Y.H. Ko, W.S. Jeon and K. Kim, *Chem Commun* (2004), 806.
[11] F. Zwick, D. Jérome, G. Margaritondo, M. Onellion, J. Voit and M. Grioni, *Phys Rev Lett* **81** (1998), 2974.
[12] T. Sleator and R. Tycko, *Phys Rev Lett* **60** (1988), 1418.
[13] A. Andrieux, H.J. Schulz, D. Jerome and K. Bechgarrd, *Phys Rev Lett* **43** (1979), 227.
[14] Y. Tomkiewicz, A.R. Taranko and J.B. Torrance, *Phys Rev Lett* **36** (1976), 751.
[15] W.D. Grobman, R.A. Pollak, D.E. Eastman, Jr., E.T. Maas and B.A. Scott, *Phys Rev Lett* **32** (1974), 534.
[16] J.B. Torrance, Y. Tomkiewicz and B.D. Silverman, *Phys Rev B* **15** (1977), 4738.
[17] R. Claessen, M. Sing, U. Schwingenschlögl, P. Blaha, M. Dressel and C.S. Jacobsen, *Phys Rev Lett* **88** (2002), 096402.
[18] M. Meneghetti and C. Pecile, *J Chem Phys* **105** (1996), 397.
[19] A.N. Bloch, D.O. Cowan, K. Bechgaard, R.E. Pyle, R.H. Banks and T.O. Poehler, *Phys Rev Lett* **34** (1975), 1561.
[20] Y. Tomkiewicz, A.R. Taranko and R. Schumaker, *Phys Rev B* **16** (1997), 1380.
[21] M. Dressel, *Naturwissenschaften* **90** (2003), 337.
[22] R. Bozio, I. Zanon, A. Girlando and C. Pecile, *J Chem Phys* **71** (1979), 2282.
[23] S.K. Burley and G.A. Petsko, *Science* **229** (1985), 23.
[24] F. Diederich, *Angew Chem Int Ed* **27** (1988), 362.
[25] J.-Y. Ortholand, A.M.Z. Slawin, N. Spencer, J.F. Stoddart and D.J. Williams, *Angew Chem Int Ed* **28** (1989), 1394.
[26] C.A. Hunter and J.K.M. Sanders, *J Am Chem Soc* **112** (1990), 5525.
[27] Y. Zhao and D.G. Truhlar, *J Phys Chem A* **109** (2005), 4209.
[28] D. Philp and J.F. Stoddart, *Angew Chem Int Ed* **35** (1996), 1154.

[29] V.R. Talladi, S. Brasselet, H.-C. Weiss, D. Bläser, A.K. Katz, H.L. Carrell, R. Boese, J. Zyss, A. Nangia and G.R. Desiraju, *J Am Chem Soc* **120** (1998), 2563.
[30] X. Ye, Z.-H. Li, W. Wang, K. Fan, W. Xu and Z. Hua, *Chem Phys Lett* **397** (2004), 56.
[31] D. Small, V. Zaitsev, Y. Jung, S.V. Rosokha, M. Head-Gordon and J.K. Kochi, *J Am Chem Soc* **126** (2004), 13850.
[32] Y. Takano, T. Taniguchi, H. Isobe, T. Kubo, Y. Morita, K. Yamamoto, K. Nakasuji, T. Takui and K. Yamaguchi, *J Am Chem Soc* **124** (2002), 11122.
[33] J. Huang and M. Kertesz, *J Am Chem Soc* **128** (2006), 7277.
[34] J. Huang and M. Kertesz, *J Am Chem Soc* **129** (2007), 1634.
[35] J.-M. Lü, S.V. Rosokha and J.K. Kochi, *J Am Chem Soc* **125** (2003), 12161.
[36] D.A. Scherlis and N. Marzari, *J Phys Chem B* **108** (2004), 17791.
[37] J.J. Novoa, P. Lafuente, R.E. Del Sesto and J.S. Miller, *Angew Chem, Int Ed* **40** (2001), 2540.
[38] R.E. Del Sesto, J.S. Miller, P. Lafuente and J.J. Novoa, *Chem Eur J* **8** (2002), 4894.
[39] J. Jakowski and J. Simons, *J Am Chem Soc* **125** (2003), 16089.
[40] Y. Jung and M. Head-Gordon, *Phys Chem Chem Phys* **6** (2004), 2008.
[41] G. Brocks, *J Chem Phys* **112** (2000), 5353.
[42] T. Devic, M. Yuan, J. Adams, D.C. Fredrickson, S. Lee and D. Venkataraman, *J Am Chem Soc* **127** (2005), 14616.
[43] M. Nakano, A. Takebe, R. Kishi, H. Fukui, T. Minami, K. Kubota, H. Takahashi, T. Kubo, K. Kamada, K. Ohta, B. Champagne and E. Botek, *Chem Phys Lett* **454** (2008), 97.
[44] NBO 5.0. E.D. Glendening, J.K. Badenhoop, A.E. Reed, J.E. Carpenter, J.A. Bohmann, C.M. Morales and F. Weinhold, Theoretical Chemistry Institute, University of Wisconsin, MI, 2001
[45] S.F. Boys and F. Bernardi, *Mol Phys* **19** (1970), 553.
[46] M.J. Frisch, et al., GAUSSIAN 03, revision B03, Gaussian, Inc., Wallingford, CT, 2004.
[47] W. Kohn, A.D. Becke and R.G. Parr, *J Phys Chem* **100** (1996), 12974–12980.
[48] S. Kristyan and P. Pulay, *Chem Phys Lett* **229** (1994), 175–180.
[49] T. Bally and G.N. Sastry, *J Phys Chem A* **101** (1997), 7923–7925.
[50] (a) S. Tsuzuki, K. Honda, T. Uchimaru, M. Mikami and K. Tanabe, *J Am Chem Soc* **124** (2002), 104. (b) M.O. Sinnokrot, E.F. Valeev and C.D. Sherrill, *J Am Chem Soc* **124** (2002), 10887. (c) M.O. Sinnokrot and C.D. Sherrill, *J Phys Chem A* **107** (2003), 8377.
[51] T. Bally and W.T. Borden, in: *Reviews in Computational Chemistry*, K.B. Lipkowitz and D.B. Boyd, eds, Wiley-VCH: New York, 1999, Vol. 13, pp. 1–97, *Calculations on Open-Shell Molecules: A Beginner's Guide*.
[52] P.W.R. Corfield and S.J. La Placa, *Acta Cryst* **B52** (1996), 384.
[53] K. Wiberg, *Tetrahedron* **24** (1968), 1083–1096.
[54] J. Huang, M. Kertesz, *J Chem Phys* **122** (2005), Art. No. 234707.
[55] J.M. Martell and R.J. Boyd, *J Phys Chem* **96** (1992), 6287.

Journal of Computational Methods in Sciences and Engineering 10 (2010) 353–385
DOI 10.3233/JCM-2010-0328
IOS Press

The anisotropic polarizability of pairs of hydrogen molecules and the depolarized collision-induced roto-translational Raman light scattering spectra

Xiaoping Li[a], James F. Harrison[a], Magnus Gustafsson[b], Lothar Frommhold[c] and Katharine L. C. Hunt[a,*]
[a]*Department of Chemistry, Michigan State University, East Lansing, MI 48824-1322, USA*
[b]*Department of Chemistry, University of Gothenburg, SE 412 96, Gothenburg, Sweden*
[c]*Physics Department, University of Texas at Austin, Austin, TX 78712-1081, USA*

Abstract. In earlier work, Li, Ahuja, Harrison, and Hunt have calculated the collision-induced polarizability $\Delta\alpha$ of a pair of hydrogen molecules at CCSD(T) level with an aug-cc-pV5Z basis, for 178 relative orientations of the pair, with the bond length in each molecule fixed at $r = 1.449$ a.u. Here we present new results from an expansion of the second-rank tensor components of $\Delta\alpha$ as series in the spherical harmonics of the molecular orientation angles and the orientation angles of the intermolecular vector. The coefficients in this expansion depend on the separation R between the molecules. We compare the *ab initio* coefficients with predictions from long-range perturbation theory, including the dipole-induced-dipole interactions at first and second order, higher-multipole induction, effects of nonuniform local fields, hyperpolarization, and van der Waals dispersion. Li and Hunt have derived equations for the long-range coefficients complete to order R^{-6}, using spherical-tensor methods developed by Bancewicz, Głaz, and Kielich for collision-induced light scattering by centrosymmetric linear molecules. We also give new results here for the van der Waals dispersion terms in both isotropic and anisotropic polarizability coefficients. We have calculated these coefficients by 64-point Gauss-Legendre quadrature, using the H_2 polarizabilities and hyperpolarizabilities at imaginary frequencies computed by Bishop and Pipin, with explicitly correlated wave functions for isolated H_2 molecules. We show that the *ab initio* values for the larger anisotropic polarizability coefficients converge to the predictions of the long-range theory, as the separation R between the molecules increases. The coefficients computed *ab initio* have been used by Gustafsson, Frommhold, Li, and Hunt to calculate the depolarized collision-induced roto-translational Raman spectra of hydrogen gas at 36 K and 50 K out to 800 cm^{-1}, and at 296 K out to 300 cm^{-1}. The general features of the experimental spectra are well reproduced, although the calculated intensities are $\sim$30% too large over much of the frequency range.

Keywords: Collision-induced light scattering, depolarized Raman spectra, *ab initio* pair polarizabilities

Mathematics Subject Classification: 81-04, 81-08, 81U05, 81U15

1. Introduction

Interaction-induced changes $\Delta\alpha$ in the polarizabilities of a pair of colliding molecules give rise to Rayleigh and Raman scattering with an intensity that is quadratic in the density of the molecules in the

*Corresponding author. E-mail: klch@chemistry.msu.edu.

gas phase; interaction effects on molecular polarizabilities are also detected in the spectra of liquids and solids [1–4]. In this work, we focus on the collision-induced anisotropic polarizability of a pair of hydrogen molecules and the associated binary depolarized roto-translational Raman scattering spectra.

In earlier work, Li, Ahuja, Harrison and Hunt have obtained $\Delta\alpha$ for $H_2 \cdots H_2$ *ab initio* [5], from finite-field calculations at the CCSD(T) level [6–8], i.e., using coupled-cluster calculations [9–13] with single and double excitations in the exponential operator applied to the reference state wave function, and with triple excitations treated perturbatively. The Cartesian polarizability components have been determined from quartic fits to the energy E($\mathbf{F}^e$) in uniform applied fields $\mathbf{F}^e$ that have randomly selected components in the range from 0.001 to 0.01 a.u. [5]. We have employed Dunning's aug-cc-pV5Z basis [14–16] for this work, because this basis is sufficiently large to give an accurate representation of the collision-induced polarizability, yet sufficiently compact to permit the very large number of calculations needed to determine $\Delta\alpha$ for a range of intermolecular distances R and a set of 18 relative orientations. In this work, the bond lengths in the two interacting molecules have been fixed at $r = 1.449$ a.u., the averaged bond length in ground vibrational state of H_2.

We have used the *ab initio* results to derive coefficients for the expansion of both the rank-zero and the rank-two spherical tensor components of the collision-induced polarizability, $\Delta\alpha^{(0)}$ and $\Delta\alpha^{(2)}$, cast as series in the spherical harmonics of the orientation angles of the two H_2 molecules and the angles of the intermolecular vector. In earlier work, we have analyzed the expansion coefficients for the isotropic (rank-zero) component of $\Delta\alpha$ [17]. In the current work, we present and analyze the coefficients for the second-rank tensor component $\Delta\alpha^{(2)}$. We have fit the *ab initio* results for the five spherical tensor elements $\Delta\alpha_k^{(2)}$ with k = -2, -1, 0, 1, 2 to determine 23 distinct polarizability coefficients $A_{2\lambda\lambda'\Lambda L}$ in this expansion. These coefficients have molecular angular momentum indices λ and λ' up to 4 on one molecule and 2 on the other.

We briefly review polarization mechanisms that affect $\Delta\alpha$ at long range, as obtained from perturbation theory [18]. These mechanisms include dipole-induced-dipole interactions [19] of first and second order. For molecules of $D_{\infty h}$ symmetry, additional contributions derive from higher-multipole induction and the nonuniformity of the local field [20–22], both associated with the dipole-octopole polarizability E [23]. Hyperpolarization effects contribute to $\Delta\alpha$, since each molecule responds nonlinearly to the external field acting together with the field from the permanent quadrupole of a neighboring molecule [18,24]; the response is governed by the dipole-dipole-quadrupole hyperpolarizability B [23]. Van der Waals dispersion effects [24–28] influence the pair dipole at order R^{-6}, due to hyperpolarization of each molecule by the field from the fluctuating charge distribution of its neighbor [25–27], and also due to changes in the spontaneous fluctuation correlations, induced by the applied field [28].

We have used spherical-tensor analysis [29] in order to obtain the long-range forms of the polarizability coefficients $A_{2\lambda\lambda'\Lambda L}$. Spherical-tensor methods were developed in this context by Bancewicz [30,31]; Kaźmierczak and Bancewicz [32]; Bancewicz, Głaz, and Kielich [33,34]; Głaz [35,36]; and Kielich, Bancewicz, and Woźniak [37] (see also the work of Kielich [38,39], Frenkel and McTague [40] and Samson and Ben-Reuven [41]). To calculate the coefficients at long range, we require accurate values for the multipole moments, polarizabilities, and hyperpolarizabilities of the isolated molecules.

Accurate values of the single-molecule properties have been made available for a number of molecular species, from the *ab initio* work of Maroulis for the non-polar diatomics N_2 [42] and Cl_2 [43], the non-polar triatomics CO_2 [44,45] and CS_2 [46], the tetrahedral molecules CH_4 and CF_4 [47], and other polyatomics [48,49]; from the work of Maroulis and Thakkar on N_2 [50], F_2 [51], CO_2 [52], and linear polyynes [53]; from the work of Hohm and Maroulis on $Ge(CH_3)_4$ [54], $TiCl_4$, $ZrCl_4$, $HfCl_4$ [55], and OsO_4 [56]; from the work of Maroulis and Makris on Br_2 [57], and the work of Maroulis, Makris, Hohm,

and Goebel on I_2 [58], as well as the work of Haskopoulos and Maroulis on property derivatives with respect to the asymmetric stretch of CO_2 [59]; and from studies of molecules as large as adamantane, $C_{10}H_{16}$, by Maroulis, Xenides, Hohm, and Loose [60]. In our perturbation analysis for $H_2 \cdots H_2$, we have used the values of the quadrupole moment given by Poll and Wołniewicz [61], interpolated to $r = 1.449$ a.u., by Visser, Wormer, and Jacobs [62], the polarizability and the E-tensor values computed by Bishop and Pipin [63], and static B-tensor values provided by Bishop [64].

In this paper, we also give new numerical results for the dispersion contributions to the polarizability coefficients, using the equations derived by Li and Hunt [18]. These equations link the dispersion effects in $\Delta\alpha$ to integrals containing the polarizabilities and hyperpolarizabilities of H_2 at imaginary frequencies. The necessary properties $\alpha_{\alpha\beta}(\mathrm{i}\omega)$ and $\gamma_{\alpha\beta\gamma\delta}(-\mathrm{i}\omega;\ \mathrm{i}\omega,\ 0,\ 0)$ have been determined by Bishop and Pipin [65], using explicitly correlated wave functions, and the values have been tabulated for a number of imaginary frequencies. We have used the results of Bishop and Pipin [65] in 64-point Gauss-Legendre quadratures, to evaluate the dispersion contributions through order R^{-6} to both the isotropic polarizability coefficients $A_{0\lambda\lambda'\Lambda L}$ and the anisotropic coefficients $A_{2\lambda\lambda'\Lambda L}$. Previously, Bishop and Pipin have calculated the dispersion coefficients that have angular momentum indices for either of the H_2 molecules (λ and λ') equal to zero [65]. For those coefficients, our results agree with the results of Bishop and Pipin, to all figures given. Dispersion polarizability coefficients with non-zero values for both λ and λ' have not been reported prior to this work.

Below, we compare the direct *ab initio* results for $A_{2\lambda\lambda'\Lambda L}$ with the coefficients obtained from the long-range perturbation analysis [18]. We also compare the numerical values with coefficients derived from a few-parameter fit of our *ab initio* results by Gustafsson, Frommhold, Li, and Hunt [66], and with coefficients obtained by Ulivi and Zoppi [67], from a fit to earlier self-consistent field (SCF) results for $\Delta\alpha$ obtained by Bounds [68].

Gustafsson, Frommhold, Li, and Hunt have used the anisotropic polarizability coefficients to calculate the binary depolarized roto-translational Raman spectra of $H_2 \cdots H_2$ in close-coupled scattering calculations with "dressed" basis states, which include the states of the laser field [66]. These calculations account for the collision-induced light scattering as well as collisional broadening of the allowed rotational transitions of H_2. We have obtained good agreement with experiments [69–71], for the spectra at 36 K, 50 K, and 296 K. The calculated intensities are affected by the difference between the static polarizabilities $\Delta\alpha$ (from the *ab initio* calculations) and the frequency-dependent values of $\Delta\alpha(\omega)$ at $\lambda = 514.5$ nm, probed in the light scattering experiments. The scattered intensity due to dipole-induced-dipole effects scales as the single-molecule polarizability α to the fourth power, so that a 3% difference between $\alpha(\omega)$ and $\alpha(\omega = 0)$ would lead to a difference of slightly more than 12% in the intensities. However, we note that the calculated intensities are *higher* than the experimental intensities [66], while the static polarizability of an H_2 molecule is *smaller* than the frequency-dependent polarizability for light of wavelength $\lambda = 514.5$ nm. Discrepancies between our calculated spectra and the experimental spectra may derive in part from our use of fixed bond lengths ($r = 1.449$ a.u.) for both H_2 molecules, to approximate the effects of ground-state vibrational averaging. This approach contrasts with the studies by Li, Hunt, Wang, Abel, and Frommhold of collision-induced roto-translational absorption by $H_2 \cdots H_2$ [72]; in that case, we were able to determine the collision-induced dipoles *ab initio* for a range of bond lengths, and we carried out the vibrational averaging explicitly [72,73]. Values of $\Delta\alpha$ for $H_2 \cdots H_2$ with different bond lengths are not yet available.

2. Related work of Professor Stanisław Kielich and collaborators

This paper is dedicated in honor Professor Stanisław Kielich's ground-breaking contributions to the

fields of intermolecular interactions in light scattering and nonlinear optical processes. Kielich was among the first contributors to the theories of the Kerr effect [74,75], second harmonic scattering [76–78], and collision-induced light scattering [79–81]. With J. R. Lalanne and F. B. Martin, Kielich reported the first measurements of hyper-Rayleigh scattering by centrosymmetric molecules in liquids [82,83]; he subsequently developed the theory of hyper-Rayleigh and hyper-Raman scattering, in collaboration with Ożgo, Bancewicz, and Kozierowski [84–90]. With Lalanne, Sein, Buchert, Skupinski, Pouligny, Chmielowski, and Knast [91–94], he investigated thermal effects, such as light scattering by fluids in temperature gradients [91,92], thermal lensing [93], and laser-induced thermal blooming [94]. His major theoretical contributions covered an unusually wide range of dielectric and optical phenomena, including magneto-optical effects, with Zawodny, Manakov, and Ovsiannikov [95–100]; circular birefringence [101,102], reversal coefficients [90] and differential scattering of circularly polarized radiation [103], with Zawodny, Bancewicz, and Woźniak; reorientation of molecules that can form liquid crystals, with Lalanne, Martin, and Pouligny [104,105]; quantum statistical properties of photons in Raman and hyper-Raman scattering by phonons, with Peřinová, Peřina, and Szlachetka [106–109]; and second harmonic and sum-frequency generation, with Fizek and Chmela [110–112].

In the 1980's, Professor Kielich turned his attention to the phenomena of photon antibunching and squeezing, with studies of resonance fluorescence from two interacting atoms, in work with Ficek and Tanaś [113–117]. This was extended to considerations of N atoms [118] and to observables such as quantum beats and super-radiant effects in spontaneous emission [119]. Together with Tanaś, Zawodny, and later Miranowicz, Kielich made major contributions to the theory of self-squeezed light [120–126].

This brief overview can cover only a small fraction of the scientific contributions by Kielich, beginning from his first publications co-authored with Piekara, and then continuing with his co-workers Przeniczny, Wołejko, Alexiewicz, Kasprowicz-Kielich, Dębska-Kotłowska, Sczaniecki, Steele, Roman, Gadomski, Leonski, Grygiel, Kaczmarek, and Gantsog, in addition to the collaborators mentioned above. The new results derived by Kielich and co-workers have continued importance for research in light scattering, dielectric theory, and opto-electronics.

In the current work, we draw upon contributions of Kielich and his collaborators Bancewicz, Głaz, Woźniak, Knast, Chmielowski, and Steele [33,34,37,39,79,81,127–134] to the theory of collision-induced light scattering. In early publications, Kielich analyzed the role of molecular interactions in anisotropic light scattering by liquids [79,127,128]. Prior to the experimental measurements by McTague and Birnbaum [135] of the intensity of depolarized Rayleigh scattering (translational Raman) by argon, krypton, and xenon gases as a function of frequency shift, Kielich [79,127,128] – and independently Buckingham and Stephen [136] and Theimer and Paul [137] – noted that atomic fluids could scatter anisotropically, due to the radial correlations in the fluids. Kielich identified contributions to depolarized light scattering by centrosymmetric, quadrupolar molecules [79,128], due to nonlinear response to the field of the incident light wave and the gradient of the quadrupolar field from a neighboring molecule, via the B-tensor (labeled as $q_{\alpha\beta\gamma\delta}$). He also commented on the relationship between anisotropic light scattering and the optical Kerr effect [79].

Kielich analyzed the effects of three-body correlations on depolarized light scattering, and observed that ternary interactions generally reduce the effective optical anisotropy [81]. Later Bancewicz, Kielich, and Steele used projection operator techniques to analyze interaction-induced Rayleigh light scattering by fluids [134], separating the interaction-induced changes in polarizability into part that behaves like the single-molecule polarizability (isotropic or anisotropic) and an orthogonal part that is purely collision-induced. (See also the related work of Frenkel and McTague [40], Felderhof [138], Keyes [139], Ladanyi and Keyes [140,141], and Ladanyi [142].) In several analyses of Rayleigh scattering by linear

centrosymmetric molecules, the simplifying assumption has been made that the molecules are correlated radially, but not angularly. Bancewicz, Głaz and Kielich [33] traced the success of this assumption in fluid N_2 to a near cancellation of the binary and ternary angular-radial correlations, which operates at the dipole-induced-dipole level, but not when dipole-induced-octopole interactions are also taken into account. Bancewicz and Kielich first noted the possibility of isotropic Raman scattering for non-totally symmetric vibrations of correlated, anisotropic molecules [132].

In particular, in this work we employ the elegant spherical-tensor methods developed in the context of collision-induced light scattering by linear, centrosymmetric molecules, in the work of Bancewicz, Głaz, and Kielich [33,34] and Bancewicz [30,31,143]. We use results for the polarizability coefficients associated with first- and second-order DID and E-tensor mechanisms derived in that work ([30,31,33, 34,143]; also [32]) and results for the B-hyperpolarization and dispersion contributions derived by Li and Hunt [18]. The spherical-tensor results are important for two major reasons: First, they greatly facilitate the derivation of the expansion coefficients for the collision-induced polarizability components, as series in the spherical harmonics of the molecular orientations and the orientations of the intermolecular vector. Second, the spherical-tensor analysis separates different physical contributions to $\Delta\alpha$ into different coefficients: first-order dipole-induced-dipole (DID) interactions appear in five distinct coefficients, but not in others. Second-order DID and van der Waals dispersion effects appear in most coefficients, but the effects of hyperpolarization (represented by B) and higher-multipole susceptibilities such as the dipole-octopole polarizability E are clearly discernible in coefficients that lack a first-order DID term. In contrast, the effects are not separated in the Cartesian components of the polarizability $\Delta\alpha$.

3. *Ab initio* calculations of the collision-induced polarizability anisotropy of $H_2 \cdots H_2$

The results of Li, Ahuja, Harrison, and Hunt [5] for the interaction-induced polarizability $\Delta\alpha$ of $H_2 \cdots H_2$ are based on approximately 20,000 individual *ab initio* calculations, performed with MOLPRO [144]. The H_2 molecules are separated along the Z axis by distances R beginning with $R = 2.0$ a.u. and $R = 2.5$ a.u. and then increasing in steps of 1.0 a.u., from 3.0 a.u. to 10.0 a.u. (except for the linear configuration, where the smallest value of R is 3.0 a.u.). The analysis of the pair polarizability anisotropy given in the current work is based on results for 18 geometrical configurations of the H_2 pair at each R value [5]. The strengths of the finite fields in the calculations were selected randomly in the range from 0.001 to 0.01 a.u., with the field confined to the XY, XZ, or YZ plane in each case. A total of 80 calculations with different field strengths were performed at each R, for each of the pair configurations such that $\alpha_{XY} = 0$; and 120 calculations were performed for each of the pair configurations with $\alpha_{XY} \neq 0$. The bond lengths in both molecules have been held fixed at $r_o = 1.449$ a.u.

To obtain the collision-induced polarizability $\Delta\alpha_{\alpha\beta}$ from the total polarizability of the pair, we have subtracted the $\alpha\beta$ components of the polarizabilities of the isolated H_2 molecules from the $\alpha\beta$ component for the pair, in the pair-fixed XYZ frame. The symmetry axis of the H_2 molecule is chosen as the z axis of the molecular frame. In the aug-cc-pV5Z (spdf) basis [14–16], $\alpha_{xx} = \alpha_{yy} = 4.729$ a.u. and $\alpha_{zz} = 6.720$ a.u. [5]. For comparison, the accurate values obtained by Bishop and Pipin with an explicitly correlated wave function are $\alpha_{xx} = \alpha_{yy} = 4.7369$ a.u. and $\alpha_{zz} = 6.7161$ a.u. [63]. For an individual H_2 molecule, with orientation angles (θ, φ) for the molecular z axis relative to the XYZ frame,

$$\alpha_{\alpha\beta} = \alpha_{xx}[\delta_{\alpha\beta} - cos(z,\alpha)cos(z,\beta)] + \alpha_{zz}cos(z,\alpha)cos(z,\beta), \quad (1)$$

where cos(z, α) denotes the direction cosine between the molecular z axis and the α axis in the XYZ frame; thus cos(z, Z) = cos θ, cos(z, X) = sin θ cos φ and cos(z, Y) = sin θ sin φ.

We fit the computed energies E($\mathbf{F}^e$) to a quartic polynomial in the applied field and then selected the coefficients of the quadratic terms to obtain the total polarizability for the pair of molecules. As described in the work of Li, Ahuja, Harrison, and Hunt [5], the reliability of the computational procedure has been tested in multiple ways:

a) The 120-field fit of E($\mathbf{F}^e$) to a quartic polynomial was compared with 120-field fits to a quintic, and with 200-field fits to quartic, quintic, and sixth-order polynomials.
b) The results were compared to an analytic fit using a truncated polynomial for E($\mathbf{F}^e$), with field strengths in the following sets: $\{f, 2^{1/2}f, 3^{1/2}f, -f, -2^{1/2}f, -3^{1/2}f\}$, $\{f, 2^{1/2}\ f, 5^{1/2}f, -f, -2^{1/2}f, -5^{1/2}f\}$, and $\{f, 2^{1/2}f, 3^{1/2}f, 5^{1/2}f, -f, -2^{1/2}f, -3^{1/2}f, -5^{1/2}f\}$, where $f = 0.001$, 0.002, 0.003, and 0.004 a.u.
c) Values of $\Delta\alpha_{XX}$ obtained with fields in the XZ plane were compared with the values obtained with field in the XY plane, and $\Delta\alpha_{ZZ}$ values obtained with fields in the XZ and YZ planes were compared.
d) At the self-consistent field (SCF) level, the random-field results were compared with the results of analytic differentiation, using GAUSSIAN 98 [145].
e) Basis-set superposition errors have been estimated using function counterpoise techniques [146] for the linear and rectangular configurations, over the full range of R values.

The results of the numerical tests are detailed in Ref. [5].

We have also compared the CCSD(T) values of Li, Ahuja, Harrison, and Hunt [5] with those obtained by Maroulis at two relative orientations (linear and T-shaped) at $R = 6.5$ a.u., in a study with a [6s, 4p 1d] basis [147]. We have found quite close agreement between the results of Maroulis [147] and results from a new interpolating polynomial, generated to estimate the values at $R = 6.5$, based on Ref. 5: For the linear configuration at $R = 6.5$ a.u., the interpolation gives $\Delta\alpha_{XX} = -0.189$ a.u., while Maroulis obtained $\Delta\alpha_{XX} = -0.1931$ a.u. [147]; for the ZZ component, the interpolation gives $\Delta\alpha_{ZZ} = 0.773$ a.u., while Maroulis obtained $\Delta\alpha_{ZZ} = 0.7870$ a.u. [147]. Similarly, for the T-shape, the interpolation gives $\Delta\alpha_{XX} = -0.230$ a.u., $\Delta\alpha_{YY} = -0.168$ a.u., and $\Delta\alpha_{ZZ} = 0.468$ a.u., for comparison with $\Delta\alpha_{XX} = -0.2354$ a.u., $\Delta\alpha_{YY} = -0.1704$ a.u., and $\Delta\alpha_{ZZ} = 0.4636$ a.u., as obtained by Maroulis [147]. The differences between values in the two sets (based on interpolation from Ref. 5 vs. Ref. 147) range from 0.95% to 2.29%.

In 1979, Bounds [68] obtained values of $\Delta\alpha$ for 6 relative orientations of the H_2 molecules, at separations from 2.0 a.u. to 6.0 a.u. for four of the relative orientations, and at separations from 2.0 a.u. to 8.0 a.u. for the remaining two. Bounds carried out the calculations at self-consistent field (SCF) level, with a (3s 2p) Gaussian basis set on each H center – small by current standards, but not by those of 1979! Li, Ahuja, Harrison, and Hunt [5] carried out separate CCSD(T) calculations for the relative orientations studied by Bounds [68], with the H_2 bond lengths fixed at $r = 1.4008$ a.u., the location of the minimum in the ground-state potential. Given the differences in basis sets and computational methodology between the two calculations, the results of Li, Ahuja, Harrison, and Hunt agree remarkably well with the results obtained by Bounds. Comparisons are made in detail in Table 3 of Ref. 5 and illustrated in Figs 1 and 2. The discrepancies between the results are less than 10% for half of the Cartesian components, and less than 20% for more than four-fifths of the Cartesian components available for comparison (90 in all).

The results for $\Delta\alpha_{ZZ}$ in Ref. 5 are larger than those obtained by Bounds and positive, while the results for $\Delta\alpha_{XX}$ and $\Delta\alpha_{YY}$ are smaller in absolute value and negative. As a result, the differences largely cancel in the polarizability anisotropy, $2\,\Delta\alpha_{ZZ} - \Delta\alpha_{XX} - \Delta\alpha_{YY}$. On the other hand, the differences in $\Delta\alpha_{XX}$, $\Delta\alpha_{YY}$, and $\Delta\alpha_{ZZ}$ shift the trace of the polarizability in the same direction, making values from Ref. [5] larger (more positive in some cases, less negative in others) than those obtained by Bounds [68].

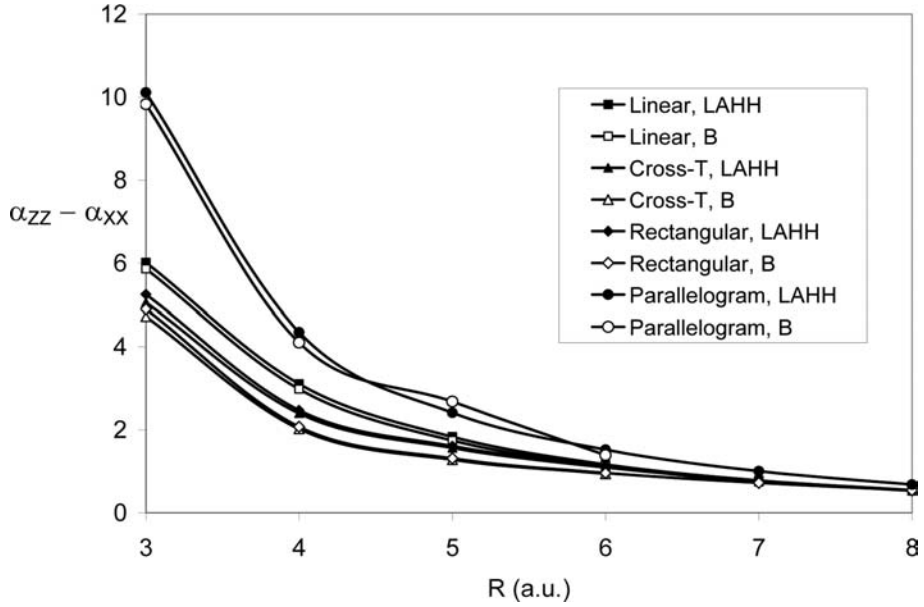

Fig. 1. Values of the polarizability anisotropy $\alpha_{ZZ} - \alpha_{XX}$ of $H_2 \cdots H_2$ vs. intermolecular separation R, for four relative orientations of the two molecules. CCSD(T) results, filled symbols, LAHH (Li, Ahuja, Harrison, and Hunt, Ref. 5). SCF results, open symbols, B (Bounds, Ref. 68). All results are given in atomic units (a.u.).

In Fig. 1, the results for $\alpha_{ZZ} - \alpha_{XX}$ from the *ab initio* CCSD(T) calculations of Li, Ahuja, Harrison, and Hunt [5] are plotted vs. the intermolecular separation R along the Z axis, for comparison with the earlier SCF results [68], for four of the six geometrical configurations studied by Bounds: linear, cross-T, rectangular, and parallelogram. We have omitted two configurations for clarity in the figure. Figure 1 shows excellent agreement between the two calculations of the polarizability anisotropy $\alpha_{ZZ} - \alpha_{XX}$ in the linear and parallelogram configurations. The results for $\alpha_{ZZ} - \alpha_{XX}$ for the cross-T configuration are very close to the results for the rectangular configuration, in both sets of calculations [5,68]; however the CCSD(T) anisotropy is slightly larger than the SCF value, for R $\leqslant$ 6.0 a.u. The anisotropy is positive for all of the configurations studied by Bounds. The CCSD(T) values for the anisotropy [5] differ from those of Bounds [68] by ∼7.6%, averaged over the geometrical configurations.

In Fig. 2, the CCSD(T) results for $\Delta\overline{\alpha} = (\Delta\alpha_{XX} + \Delta\alpha_{YY} + \Delta\alpha_{ZZ})/3$ in Ref. 5 are compared with the SCF results [68], for the linear, cross-T, rectangular, and T-shaped configurations. For the linear configuration, the results agree well for R $\geqslant$ 6.0 a.u.; but at shorter range, the effects of correlation and basis functions of higher angular momentum become more important, and the CCSD(T) trace differs significantly from the SCF values. Similarly, the CCSD(T) and SCF results for the T-shaped configuration diverge from each other as R decreases. As found for the pair polarizability anisotropy, the trace of the pair polarizability is quite similar in the rectangular and cross-T configurations, though the CCSD(T) results are shifted up (to smaller absolute values), relative to the SCF results. For three of the configurations, the sign of $\Delta\alpha$ is unchanged over the range from $R = 3.0$ a.u. to $R = 8.0$ a.u.; it is positive for collinear pairs and negative for the rectangular and cross-T pairs. For the T-shaped pairs, $\Delta\alpha$ is negative at short range and positive at long range. Results for the parallelogram (not shown in Fig. 2) have a more complicated R dependence: $\Delta\alpha$ is positive at short range, negative at intermediate range, and positive again at long range in both calculations, although the actual magnitudes of $\Delta\alpha$ are quite different in the two calculations (see Table 3 in Ref. 5). The differences in $\Delta\alpha$ values from the

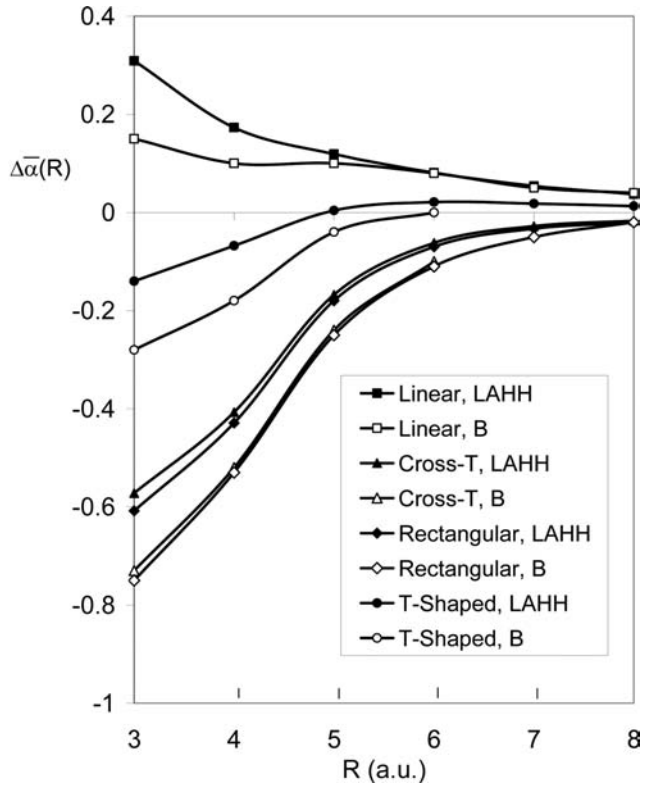

Fig. 2. Values of the isotropically averaged pair polarizability $\Delta\overline{\alpha}$(R) of $H_2 \cdots H_2$ vs. intermolecular separation R, for four relative orientations of the two molecules. CCSD(T) results, filled symbols, LAHH (Li, Ahuja, Harrison, and Hunt, Ref. 5). SCF results, open symbols, B (Bounds, Ref. 68). All results are given in atomic units (a.u.).

two calculations [5,68] average to 97%, for the six relative orientations and all R values studied. The difference is largest for the parallelogram at $R = 5.0$ a.u., near the R value where $\Delta\alpha$ changes sign; in this case the results differ by a factor of $\sim$6 [5,68].

4. Spherical-tensor form of collision-induced polarizabilities

The static polarizability has spherical-tensor components of ranks 0 and 2, the isotropic and anisotropic polarizabilities, respectively. Li, Harrison, Gustafsson, Wang, Abel, Frommhold, and Hunt have analyzed the isotropic pair polarizability in earlier work [17]. Here we focus on the second-rank tensor components $\Delta\alpha_k^{(2)}$, which give rise to depolarized, collision-induced scattering. The components have $k = 2$, 1, 0, -1, and -2, where [148,149]

$$\Delta\alpha_{20} = (1/\sqrt{6})(2\Delta\alpha_{ZZ} - \Delta\alpha_{XX} - \Delta\alpha_{YY}) \tag{2}$$

$$\Delta\alpha_{2\pm1} = \mp\,(1/2)[(\Delta\alpha_{XZ} + \Delta\alpha_{ZX}) \pm i(\Delta\alpha_{YZ} + \Delta\alpha_{ZY})] \tag{3}$$

$$\Delta\alpha_{2\pm2} = (1/2)[(\Delta\alpha_{XX} - \Delta\alpha_{YY}) \pm i(\Delta\alpha_{XY} + \Delta\alpha_{YX})]. \tag{4}$$

The collision-induced polarizability $\Delta\alpha_k^{(2)}$ of second rank has an expansion in the spherical harmonics of the orientation angles (θ_A, φ_A) of the bond axis of molecule A, the orientation angles (θ_B, φ_B) of the

bond axis of molecule B, and the orientation angles (θ, φ) of the intermolecular vector, given by [18, 30–37,39,150–152]

$$\Delta\alpha_k^{(2)} = \sum_{\substack{\lambda,\lambda',m,m' \\ \Lambda,\mu,L,M}} A_{2\lambda\lambda'\Lambda L}(r_A, r_B, R) Y_{\lambda m}(\theta_A, \varphi_A) Y_{\lambda' m'}(\theta_B, \varphi_B) Y_{LM}(\theta, \varphi) \times \langle \lambda\lambda' m m' | \Lambda\mu \rangle \langle \Lambda L \mu M | 2k \rangle. \quad (5)$$

In Eq. (5), $\langle \lambda\lambda' \, \mathrm{m} \, \mathrm{m}' | \, \Lambda\mu \rangle$ denotes a Clebsch-Gordan coefficient. We fit the *ab initio* results to expressions of this form, for the sets of 18 relative orientations of $H_2 \cdots H_2$ at each R value from 3.0 a.u. to 10.0 a.u. We have obtained 23 distinct coefficients $A_{2\lambda\lambda'\Lambda L}(r_A, r_B, R)$ as functions of R, with $r_A = r_B = 1.449$ a.u. Results for 13 coefficients with λ, $\lambda' = 0$ or 2 are listed in Table 1.

5. Long-range pair polarizability anisotropy from perturbation theory

The interaction-induced polarizability $\Delta\alpha_{\alpha\beta}$ of a pair of well-separated molecules is determined by classical polarization and van der Waals dispersion effects. The classical polarization terms in $\Delta\alpha$ are obtained by solving self-consistently for the multipole moments of the two molecules in a uniform applied field $\mathbf{F}^e$. Then $\Delta\alpha_{\alpha\beta}$ is computed by summing the net dipoles μ^A and μ^B of molecules A and B, taking the zero-field limit of the derivative with respect to the external field, and subtracting the sum of the individual molecule polarizabilities,

$$\Delta\alpha_{\alpha\beta} = \lim_{F^e \to 0} \partial(\mu_\alpha^A + \mu_\alpha^B)/\partial F_\beta^e - \alpha_{\alpha\beta}^A - \alpha_{\alpha\beta}^B \quad (6)$$

The moments of each molecule are expressed as Taylor series in the local field $\mathbf{F}$, the local field gradient $\mathbf{F}'$, and higher gradients; the local field is the sum of the applied field $\mathbf{F}^e$ and the field due to the moments of the neighboring molecule, both permanent and induced. For a non-dipolar molecule A, the induced dipole moment μ_α^A is [18,23,24]

$$\begin{aligned} \mu_\alpha^A = {} & \alpha_{\alpha\beta}^A F_\beta + (1/3) A_{\alpha,\beta\gamma}^A F'_{\beta\gamma} + (1/15) E_{\alpha,\beta\gamma\delta}^A F''_{\beta\gamma\delta} + (1/105) G_{\alpha,\beta\gamma\delta\varepsilon}^A F'''_{\beta\gamma\delta\varepsilon} \\ & + (1/2)\beta_{\alpha\beta\gamma}^A F_\beta F_\gamma + (1/3) B_{\alpha,\beta,\gamma\delta}^A F_\beta F'_{\gamma\delta} + (1/15) D_{\alpha,\beta,\gamma\delta\varepsilon}^A F_\beta F''_{\gamma\delta\varepsilon} + \ldots \\ & + (1/6)\gamma_{\alpha\beta\gamma\delta}^A F_\beta F_\gamma F_\delta + \ldots \end{aligned} \quad (7)$$

Similarly, the net quadrupole moment $\Theta_{\alpha\beta}^A$, octopole moment $\Omega_{\alpha\beta\gamma}^A$, and hexadecapole moment $\Phi_{\alpha\beta\gamma\delta}^A$ are given to leading order by

$$\Theta_{\alpha\beta}^A = \Theta_{\alpha\beta}^{A,0} + A_{\gamma,\alpha\beta}^A F_\gamma + C_{\alpha\beta,\gamma\delta}^A F'_{\gamma\delta} + (1/2) B_{\gamma,\delta,\alpha\beta}^A F_\gamma F_\delta + \ldots \quad (8)$$

$$\Omega_{\alpha\beta\gamma}^A = \Omega_{\alpha\beta\gamma}^{A,0} + E_{\delta,\alpha\beta\gamma}^A F_\delta + (1/2) D_{\delta,\varepsilon,\alpha\beta\gamma}^A F_\delta F_\varepsilon + \ldots \quad (9)$$

$$\Phi_{\alpha\beta\gamma\delta}^A = \Phi_{\alpha\beta\gamma\delta}^{A,0} + G_{\varepsilon,\alpha\beta\gamma\delta}^A F_\varepsilon + \ldots \quad (10)$$

where $\Theta_{\alpha\beta}^{A,0}$, $\Omega_{\alpha\beta\gamma}^{A,0}$, and $\Phi_{\alpha\beta\gamma\delta}^{A,0}$ denote the permanent moments. The linear response tensors in Eqs (7)–(10) are the dipole polarizability $\alpha_{\alpha\beta}^A$, the dipole-quadrupole polarizability $A_{\alpha,\beta\gamma}^A$, the dipole-octopole polarizability $E_{\alpha,\beta\gamma\delta}^A$, the dipole-hexadecapole polarizability $G_{\alpha,\beta\gamma\delta\varepsilon}^A$, and the quadrupole polarizability $C_{\alpha\beta,\gamma\delta}^A$. The nonlinear response to the local field depends on the dipole hyperpolarizability $\beta_{\alpha\beta\gamma}^A$,

Table 1
Spherical-tensor expansion coefficients for the anisotropic polarizability of $H_2 \cdots H_2$

R (a.u.)	3.0	4.0	5.0	6.0	7.0	8.0	9.0	10.0
A_{20002}								
LAHH	310300	134400	75400	48200	32000	21800	15400	11200
GFLH	310300	134200	76250	47580	31230	21350	15120	11060
BUZ	135200	64750	42790	31510	23690	17870	13530	10340
DID-1	409300	172700	88410	51160	32220	21580	15160	11050
LR	540000	195900	94510	53210	33030	21950	15340	11150
$A_{20220} = A_{22020}$								
LAHH	22100	5100	1170	340	130	52	12	3
GFLH	22100	5101	1162	353	139	65	33	18
LR	27940	4972	1303	436	173	78	38	20
$A_{20222} = A_{22022}$								
LAHH	−47900	−20200	−9680	−5430	−3390	−2260	−1580	−1150
GFLH	−47900	−20180	−9741	−5394	−3321	−2204	−1544	−1125
BUZ	−11220	−9527	−6664	−4507	−3065	−2131	−1523	−1119
DID-1	−41870	−17660	−9043	−5233	−3296	−2208	−1551	−1130
LR	−49210	−18970	−9386	−5348	−3341	−2228	−1561	−1136
$A_{20224} = A_{22024}$								
LAHH	47700	19900	7880	3360	1570	800	450	260
GFLH	47700	19870	7959	3350	1504	725	378	212
LR	112700	25850	8295	3287	1505	766	423	248
A_{22202}								
LAHH	−1080	240	160	73	43	31	16	8
BUZ	2247	370	141	75	46	30	21	15
DID-1	547	231	118	68	43	29	20	15
LR	876	289	134	74	45	30	21	15
A_{22222}								
LAHH	−1690	−290	−170	−130	−91	−59	−32	−21
BUZ	2448	1341	340	59	−12	−27	−27	−23
DID-1	−1223	−516	−264	−153	−96	−65	−45	−33
LR	163	−269	−200	−131	−88	−61	−43	−32
A_{22224}								
LAHH	−2240	−1310	−510	−190	−83	−25	7	12
LR	−6842	−1551	−494	−195	−89	−45	−25	−15
A_{22242}								
LAHH	17600	6280	2650	1340	810	530	360	260
GFLH	17600	6280	2649	1349	798	522	363	265
BUZ	−4295	−765	376	603	549	438	335	255
DID-1	9849	4155	2127	1231	775	519	365	266
LR	11350	4422	2197	1255	785	524	367	267
A_{22244}								
LAHH	−12700	−4190	−1400	−530	−240	−120	−66	−40
GFLH	−12700	−4184	−1419	−523	−215	−100	−52	−30
LR	−17940	−4065	−1294	−510	−233	−118	−65	−38
A_{22246}								
LAHH	10400	3650	1120	360	120	56	29	17
GFLH	10400	3646	1137	347	105	32	10	3

Coefficients $A_{2\lambda\lambda'\Lambda L}$ (in a.u., multiplied by 10^5) in Eq. (5). LAHH: Fit of the *ab initio* anisotropic polarizability from Ref. 5, for 18 relative orientations. GFLH: Few-parameter fit from Ref. 66 to the results of Ref. 5. BUZ: Fit by Ulivi and Zoppi [67] to the SCF results of Bounds [68]. DID-1: First-order DID approximation. LR: Long-range perturbation theory, complete to order R^{-6}.

the dipole-quadrupole hyperpolarizability $\mathrm{B}^A_{\alpha,\beta,\gamma\delta}$, the dipole-octopole hyperpolarizability $\mathrm{D}^A_{\alpha,\beta,\gamma\delta\varepsilon}$, the second dipole hyperpolarizability $\gamma^A_{\alpha\beta\gamma\delta}$, and higher-order tensors.

For molecule A in a uniform applied field $\mathbf{F}^e$ and the nonuniform field from molecule B, the total field acting on A and its gradients are given by

$$F_\alpha = F^e_\alpha + T_{\alpha\beta}\mu^B_\beta + (1/3)T_{\alpha\beta\gamma}\Theta^B_{\beta\gamma} + (1/15)T_{\alpha\beta\gamma\delta}\Omega^B_{\beta\gamma\delta} + (1/105)T_{\alpha\beta\gamma\delta\varepsilon}\Phi^A_{\beta\gamma\delta\varepsilon} + \ldots \tag{11}$$

$$F'_{\alpha\beta} = -T_{\alpha\beta\gamma}\mu^B_\gamma - (1/3)T_{\alpha\beta\gamma\delta}\Theta^B_{\gamma\delta} - (1/15)T_{\alpha\beta\gamma\delta\varepsilon}\Omega^B_{\gamma\delta\varepsilon} - \ldots \tag{12}$$

$$F''_{\alpha\beta\gamma} = T_{\alpha\beta\gamma\delta}\mu^B_\delta + (1/3)T_{\alpha\beta\gamma\delta\varepsilon}\Theta^B_{\delta\varepsilon} + \ldots \tag{13}$$

$$F'''_{\alpha\beta\gamma\delta} = -T_{\alpha\beta\gamma\delta\varepsilon}\mu^B_\varepsilon + \ldots \tag{14}$$

The dipole propagator $\mathrm{T}_{\alpha\beta}$ is defined by

$$T_{\alpha\beta}(\mathbf{R}) = (4\pi\varepsilon_o)^{-1}\partial/\partial R_\alpha \partial/\partial R_\beta (1/R) \tag{15}$$

and similarly

$$T_{\alpha\beta\gamma\,\cdot\,\zeta}(\mathbf{R}) = (4\pi\varepsilon_o)^{-1}\partial/\partial R_\alpha \partial/\partial R_\beta \partial/\partial R_\gamma \cdots \partial/\partial R_\zeta (1/R) \tag{16}$$

in terms of the vector $\mathbf{R}$ which runs from a center in molecule A to a center in B. The T-tensors of even order are even in $\mathbf{R}$, and those of odd order are odd. The Einstein convention of summation over repeated Greek indices is followed throughout this work.

For centrosymmetric molecules, the permanent octopole $\Omega^{A,0}_{\alpha\beta\gamma}$ and the response tensors $\mathrm{A}^A_{\alpha,\beta\gamma}$, $\mathrm{G}^A_{\alpha,\beta\gamma\delta\varepsilon}$, $\beta^A_{\alpha\beta\gamma}$, and $\mathrm{D}^A_{\alpha,\beta,\gamma\delta\varepsilon}$ vanish identically, although these properties are non-vanishing for nonpolar molecules of T_d symmetry, such as CH_4 and CCl_4. The remaining tensors appearing in Eqs (7)–(10) are nonzero for centrosymmetric species.

Solving Eqs (6)–(16) and the corresponding equations for molecule B self-consistently gives the classical polarization contributions to the collision-induced polarizability as [18]

$$\begin{aligned}\Delta\alpha_{\alpha\beta} = (1+P^{AB})[&\alpha^A_{\alpha\gamma}T_{\gamma\delta}(\mathbf{R})\alpha^B_{\delta\beta} + \alpha^A_{\alpha\gamma}T_{\gamma\delta}(\mathbf{R})\alpha^B_{\delta\varepsilon}T_{\varepsilon\zeta}(\mathbf{R})\alpha^A_{\zeta\beta}\\ &+(1/15)\alpha^A_{\alpha\gamma}T_{\gamma\delta\varepsilon\zeta}(\mathbf{R})E^B_{\beta,\delta\varepsilon\zeta} + (1/15)E^A_{\alpha,\gamma\delta\varepsilon}T_{\gamma\delta\varepsilon\zeta}(\mathbf{R})\alpha^B_{\zeta\beta}\\ &-(1/9)B^A_{\alpha,\beta,\gamma\delta}T_{\gamma\delta\varepsilon\zeta}(\mathbf{R})\Theta^{B,0}_{\varepsilon\zeta} + \ldots],\end{aligned} \tag{17}$$

where all classical terms that contribute to the pair polarizability through order R^{-6} have been included. The operator P^{AB} in Eq. (17) and below interchanges the labels of molecules A and B.

The first two terms in Eq. (17) represent dipole-induced-dipole (DID) contributions to $\Delta\alpha$, first treated by Silberstein [19]. The first order DID term varies as R^{-3} in the distance between A and B and gives the dominant contribution to the collision-induced polarizability, while the second-order DID term varies as R^{-6}. For atoms in S states, the first order DID term in the *trace* of the pair polarizability vanishes identically, but for linear centrosymmetric molecules, this effect is non-vanishing, as discussed below.

The E-tensor terms in Eq. (17) reflect higher-multipole induction and nonuniform field effects: The applied field $\mathbf{F}^e$ induces an octopole moment $\Omega_{\alpha\beta\gamma}$ in each molecule, as well as a dipole (both are linear in $\mathbf{F}^e$); and the field from the induced octopole polarizes the neighboring molecule. In addition, a dipole moment is induced in each molecule by the nonuniform local field gradient arising from the

dipole induced in the neighboring molecule by $\mathbf{F}^e$. Both of these effects vary as R^{-5}. E-tensor effects have been treated by Buckingham and Tabisz, in a study of the Rayleigh scattering by molecules of O_h symmetry, such as SF_6 [21], by Kielich [131], and by Bancewicz, Głaz and Kielich, with application to light scattering by linear centrosymmetric molecules [33,34]. The E-tensor terms contribute to scattering in the far wings of the Rayleigh spectra (roto-translational Raman), because they permit transitions with ΔJ up to ± 4, even when the intermolecular potential is isotropic. For T_d molecules, the analogous A-tensor terms also contribute to scattering in the far wings of the roto-translational Raman spectrum [21], by permitting transitions with ΔJ up to ± 3 (for an isotropic intermolecular potential).

The remaining classical polarization effect in Eq. (17) depends on the B-tensor [18,23,24]. This effect results from the simultaneous response of each molecule to the applied field and the field-gradient from the permanent quadrupole moment of the neighboring molecule, and it varies as R^{-5}.

Advances in the *ab initio* computation of higher multipole polarizabilities and hyperpolarizabilities, in the work of Maroulis and other researchers (see, e.g. Refs. 42–65), have made it possible to determine the classical polarization contributions to $\Delta\alpha$ to high accuracy. The magnitudes of these terms in the Cartesian components of $\Delta\alpha$ for $H_2 \cdots H_2$ have been analyzed in detail by Li and Hunt [18].

Van der Waals dispersion interactions result from correlations between the spontaneous quantum mechanical fluctuations in the charge density on each molecule. These fluctuations also affect the pair polarizability. Buckingham introduced the first model for the dispersion contributions to $\Delta\alpha$, by considering the hyperpolarization of each of the interacting molecules, in the fluctuating field from its neighbor [25]. Buckingham estimated the mean square dipoles of the interacting charge distributions, using the C_6 dispersion energy coefficient (with the convention $C_6 > 0$), as

$$\overline{\mu^2} = (4\pi\varepsilon_o)^2 C_6/(2\alpha). \tag{18}$$

For two atoms A and B in S states, this approach gives an estimate of the van der Waals contribution to the isotropically averaged pair polarizability [25], as

$$\Delta\overline{\alpha}_{vdW} = (5/18)(1 + P^{AB})C_6^{AA}\gamma^B R^{-6}/\alpha^A \tag{19}$$

in terms of the static atomic hyperpolarizability γ, where

$$\gamma_{\alpha\beta\gamma\delta} = (\gamma/3)(\delta_{\alpha\beta}\delta_{\gamma\delta} + \delta_{\alpha\gamma}\delta_{\beta\delta} + \delta_{\alpha\delta}\delta_{\beta\gamma}). \tag{20}$$

Buckingham and Clarke [26] subsequently extended the model to estimate the van der Waals contribution to the anisotropy of the pair polarizability for two atoms in S states as

$$(\Delta\alpha_{ZZ} - \Delta\alpha_{XX})_{vdW} = (1 + P^{AB})C_6^{AA}\gamma^B R^{-6}/(6\alpha^A) \tag{21}$$

with the atoms separated along the Z axis. Compared with the accurate results from fourth-order perturbation theory, obtained by Buckingham, Martin, and Watts for $H \cdots H$ [153] and by Certain and Fortune for $He \cdots He$ [154], the model in Eqs (19) and (21) has errors of $\sim$15% or less (as low as 2%, for the polarizability anisotropy of $He \cdots He$).

Hunt, Zilles, and Bohr [27] proved that the fourth-order perturbation expression for the van der Waals contribution to $\Delta\alpha$ for a pair of atoms in S states reduces to an integration over imaginary frequencies:

$$\Delta\alpha_{\alpha\beta} = \hbar/(4\pi)T_{\gamma\varepsilon}T_{\delta\varepsilon}(1 + \mathcal{P}^{AB}) \int_{-\infty}^{\infty} \gamma^A_{\alpha\beta\gamma\delta}(0;0,i\omega,-i\omega)\alpha^B(i\omega)d\omega. \tag{22}$$

They also showed that van der Waals interactions *decrease* the orientational polarizability of a pair of dipolar rotors, since γ is negative for rotors, due to saturation effects; and van der Waals interactions have no effect on the polarizability of a pair of harmonic oscillators, for which $\gamma = 0$. Based on Eq. (22), Hunt, Zilles, and Bohr developed a mean-frequency approximation [27],

$$\Delta\overline{\alpha}_{vdW} = (5/18)(1 + \mathcal{P}^{AB})C_6^{AB}\gamma^A R^{-6}/\alpha^A \tag{23}$$

$$(\Delta\alpha_{ZZ} - \Delta\alpha_{XX})_{vdW} = (1 + \mathcal{P}^{AB})C_6^{AB}\gamma^A R^{-6}/(6\alpha^A). \tag{24}$$

This approximation is equivalent to Eqs (19) and (21) for identical atoms, but different for heterodiatoms; Eqs (23) and (24) are expected to be more accurate than (19) and (21) when the dipole transition energies for the two atoms differ significantly.

For atoms and centrosymmetric molecules, the next terms in the series for the van der Waals contributions to the pair polarizability vary as R^{-8}. Buckingham and Clarke [26] approximated these, using an estimate of the mean-square fluctuating quadrupole moment based on C_6 and C_8 dispersion energy coefficients, α, and the quadrupole polarizability C. Fowler, Hunt, Kelly, and Sadlej [155] later extended the theory to obtain the R^{-8} effects accurately in terms of integrals over imaginary frequencies. In this case, the integrals contain the nonlinear higher-multipole susceptibilities P(0; 0, $-i\omega$, $i\omega$) and Q($-i\omega$; 0, 0, $i\omega$), as well as $\alpha(i\omega)$, the quadrupole polarizability C($i\omega$), $\gamma(-i\omega; i\omega, 0, 0)$, and the dipole-dipole-quadrupole hyperpolarizability B($-i\omega$; 0, $i\omega$). Thus, the R^{-8} terms have been evaluated numerically only for the pairs H $\cdots$ H, H $\cdots$ He, and He $\cdots$ He [155].

6. Spherical-tensor analysis of $\Delta\alpha$ at long-range

In the context of collision-induced light scattering by centrosymmetric molecules, spherical-tensor analysis and angular momentum recoupling were suggested and applied by Bancewicz, Głaz, Kielich, and Kaźmierczak (see Refs. 30–36), in order to separate terms in the collision-induced polarizabilities according to their transformations under rotations of the molecular axes and the intermolecular vector **R**. The analysis casts the results for $\Delta\alpha$ into the symmetry-adapted form needed for line shape calculations. In addition, we find that the dipole-induced-dipole interaction effects are separated – at least in part – from the effects of higher-multipole induction, hyperpolarization, and nonuniform fields, when $\Delta\alpha$ is cast as a series in spherical harmonics of the orientation angles Ω_A, Ω_B, and Ω_R. For example, through order R^{-6}, the only non-zero contributions to the coefficients A_{00444}, A_{02444}, $A_{04044,}A_{04244}$, A_{20444}, and A_{24044} come from the E-tensor polarization mechanisms, which vary as R^{-5}.

At first order in the molecular interaction, perturbation theory gives the net dipole induced by a uniform applied field in terms of two pair dipole operators ($\mu^A + \mu^B$), coupled with operators representing the intermolecular interactions. The long-range interaction operators consist of a multipole operator on molecule A, a multipole operator on B, and a T-tensor, coupled to give a quantity of spherical-tensor rank zero. At second order, the net dipole is given in terms of two pair dipole operators (as before) and two sets of operators for the molecular interactions, individually coupled to rank zero.

For the first-order DID terms, Bancewicz [30,31] has obtained

$$A^{\alpha\alpha}_{Jjk\Lambda 2} = 6\sqrt{2}(2\Lambda + 1)^{1/2}(-1)^{1+J/2} \times \begin{Bmatrix} j & 1 & 1 \\ k & 1 & 1 \\ \Lambda & 2 & J \end{Bmatrix} \alpha^A(j,0)\alpha^B(k,0)R^{-3}, \tag{25}$$

where the brackets denote a 9-j symbol,

$$\alpha(0,0) = -\sqrt{3}\overline{\alpha} \tag{26}$$

and

$$\alpha(2,0) = (2/\sqrt{6})(\alpha_{zz} - \alpha_{xx}), \tag{27}$$

for both molecules A and B.

The contribution of the α-E term to the Jth-rank part of $\Delta\alpha$ transforms as

$$T^{\alpha E} = [\mu^{A(1)} \otimes \{[\mu^{A(1)} \otimes (T^{(4)} \otimes \Omega^{B(3)})^{(1)}]^{(0)} \otimes \mu^{B(1)}\}^{(1)}]^{(J)}. \tag{28}$$

In this equation, $T^{(4)}$ denotes the spherical tensor of fourth rank that corresponds to the Cartesian propagator $T_{\alpha\beta\gamma\delta}$ given by Eq. (16).

Each of the operators in $T^{\alpha E}$ has non-vanishing components of a single spherical-tensor rank. Li and Hunt [18] have simplified $T^{\alpha E}$ using results given by Zare in Eqs (4.3), (4.9), (4.19), and (4.24) of Ref. 149. They have also used the fact that only the components of α(j, q) and E(k, q) with $q = 0$ are non-vanishing in the molecule-fixed frame, for molecules of $D_{\infty h}$ symmetry. Hence the spherical tensor components α(j, q′) and E(k, q′) in the space-fixed frame take the relatively simple form given in Eq. (24) of Ref. 18. Li and Hunt have obtained results for the expansion coefficients derived from the α-E terms that are consistent with those of Bancewicz, Głaz, and Kielich [33,34]:

$$A^{\alpha E}_{Jjk\Lambda 4} = 4\sqrt{21}(2\Lambda+1)^{1/2}(-1)^{1+J/2} \times \begin{Bmatrix} j & 1 & 1 \\ k & 3 & 1 \\ \Lambda & 4 & J \end{Bmatrix} \alpha^A(j,0)E^B(k,0)R^{-5}. \tag{29}$$

The relevant spherical-tensor components of E are given by

$$E(2,0) = 3\sqrt{21}E_3 = (1/\sqrt{21})(8E_{x,xxx} - 3E_{z,zzz}) \tag{30}$$

and

$$E(4,0) = 4\sqrt{7}E_7 = (2/\sqrt{7})(E_{z,zzz} + 2E_{x,xxx}) \tag{31}$$

The E tensor has no isotropic component: E(0, 0) = 0. The corresponding coefficients that depend on the E tensor for molecule A and the dipole polarizability of molecule B are given by

$$A^{E\alpha}_{Jkj\Lambda 4} = (-1)^{\Lambda} P^{AB} A^{\alpha E}_{Jjk\Lambda 4}. \tag{32}$$

The coefficients that depend on E(2, 0) agree with the results of Borysow and Moraldi [22] as well as the results of Bancewicz, Głaz, and Kielich [33,34].

The hyperpolarization and dispersion effects were first analyzed using spherical-tensor algebra by Li and Hunt [18]. The contribution to $\Delta\alpha$ that depends on polarization of molecule A bilinear in the external field and the field from the permanent quadrupole of molecule B yields the coefficients

$$A^{B\Theta}_{Jj2\Lambda 4} = -\sqrt{42}[(2\Lambda+1)/(2J+1)]^{1/2}(-1)^{1+J/2} \times \begin{Bmatrix} j & 2 & \Lambda \\ 4 & J & 2 \end{Bmatrix} B^A(J;j,0)\Theta^B(2,0)R^{-5}, \tag{33}$$

where the brackets denote a 6-j symbol, and

$$\Theta^{\mathrm{B}}(2,0) = \Theta^B = \Theta^B_{zz} = -2\Theta^B_{xx} = -2\Theta^B_{yy}, \tag{34}$$

Table 2
Molecular properties (in a.u.) of H_2 used to calculate collision-induced polarizabilities at long range

Property	Value	Reference
Θ^0	0.4828	[61,62]
α_{zz}	6.7161	[63]
α_{xx}	4.7369	[63]
$\mathrm{E}_{z,zzz}$	4.4424	[63]
$\mathrm{E}_{x,xxx}$	−1.7740	[63]
$\mathrm{B}_{z,z,zz}$	−97.671	[64]
$\mathrm{B}_{x,z,xz}$	−63.417	[64]
$\mathrm{B}_{x,x,zz}$	36.746	[64]
$\mathrm{B}_{x,x,xx}$	−71.250	[64]

in terms of the components of the quadrupole moment in the molecular frame. The tensor operators that appear in B^A(J; j, 0) have the structure $[(\mu^{A(1)} \otimes \mu^{A(1)})^{(J)} \otimes \Theta^{A(2)}]^{(j)}$, where $\otimes$ denotes the direct product. The quantities B^A(J; j, 0) in Eq. (33) are related to the B-tensor coefficients B_1-B_7 given in terms of the four independent static components of the B-tensor, $\mathrm{B}_{z,z,zz}$, $\mathrm{B}_{x,z,xz}$, $\mathrm{B}_{x,x,zz}$, and $\mathrm{B}_{x,x,xx}$, by Eq. (19) and Table 2 of Ref. 18, according to

$$B^A(0;2,0) = -2/\sqrt{3}\ (3B_4^A + 4B_5^A) \tag{35}$$

$$B^A(2;0,0) = 2\sqrt{10}/3\ B_2^A \tag{36}$$

$$B^A(2;2,0) = -4/3\sqrt{21}\ B_5^A \tag{37}$$

$$B^A(2;4,0) = 140/\sqrt{105}\ B_7^A. \tag{38}$$

The corresponding polarization effects that depend on Θ^A and B^B yield coefficients of the form

$$A^{\Theta B}_{J2j\Lambda 4} = (-1)^{\Lambda} P^{AB} A^{B\Theta}_{Jj2\Lambda 4}, \tag{39}$$

where P^{AB} interchanges the labels A and B on the molecular properties.

The second-order dipole-induced-dipole and dispersion terms both derive from perturbation expressions with an underlying tensor-operator structure of the form

$$\begin{aligned} T^{AAB} = \{\mu^{A(1)} \otimes [\{[\mu^{A(1)} \otimes (T^{(2)} \otimes \mu^{B(1)})^{(1)}]^{(0)} \\ \otimes [\mu^{A(1)} \otimes (T^{(2)} \otimes \mu^{B(1)})^{(1)}]^{(0)}\}^{(0)} \otimes \mu^{A(1)}]^{(1)}\}^{(J)}. \end{aligned} \tag{40}$$

The four operators $\mu^{A(1)}$ can either be recoupled to produce two factors of the polarizability of molecule A, or to give the γ hyperpolarizability of A [18]. Both re-coupling schemes contribute to $\Delta\alpha$, the first giving the second-order DID effects and the second giving the dispersion terms.

Bancewicz has obtained the second-order DID coefficients [30,31], which can be cast as

$$\begin{aligned} A^{ABA}_{Jjk\Lambda L} = (-1)^{1+J/2}\ 30\sqrt{3}\ \Sigma_a\ \Sigma_b\ \Sigma_n\ (2n+1) \\ \cdot \Pi_{ab\Lambda} \langle ab00|j0\rangle \langle 2200|L0\rangle \alpha^A(a,0)\alpha^A(b,0)\alpha^B(k,0) R^{-6} \\ \times \begin{Bmatrix} 1 & 1 & 2 \\ 1 & 1 & 2 \\ k & n & L \end{Bmatrix} \quad \begin{Bmatrix} 1 & 1 & a \\ 1 & 1 & b \\ n & J & j \end{Bmatrix} \quad \begin{Bmatrix} j & k & \Lambda \\ L & J & n \end{Bmatrix} \end{aligned} \tag{41}$$

where $\Pi_{ab\cdots z}$ = [(2a + 1) (2b + 1)· · ·(2z+1)]$^{1/2}$. The R^{-6} DID coefficients for the $\alpha^B\alpha^A\alpha^B$ term are

$$A^{BAB}_{JkjΛL} = (-1)^{\Lambda} P^{AB} A^{ABA}_{JjkΛL}. \tag{42}$$

The dispersion coefficients have been given by Li and Hunt [18] as

$$\begin{aligned} A^{\gamma\alpha}_{JjkΛL} = &(-1)^{1+J/2}\ 15\sqrt{3}\ \Sigma_a \Pi_{La}/\Pi_j \langle 2200|L0\rangle (\hbar/\pi) R^{-6} \\ &\times \begin{Bmatrix} 2 & 1 & 1 \\ 2 & 2 & 1 \\ L & k & a \end{Bmatrix} \begin{Bmatrix} j & k & \Lambda \\ L & J & a \end{Bmatrix} \\ &\times \int_0^\infty \gamma^A(a, J; j, 0|i\omega, 0, 0)\alpha^B(k, 0; i\omega) d\omega, \end{aligned} \tag{43}$$

with (a, J) = (0, 0) or (2, 0) combined with (j, 0) = (0, 0); (a, J) = (0, 2), (2, 0), or (2, 2) combined with (j, 0) = (2, 0); and (a, J) = (2, 2) combined with (j, 0) = (4, 0). Explicit equations for these components and their relations to the coefficients γ_1 through γ_7 in the general Cartesian form of the hyperpolarizability are given by Eqs (37a)–(37f), together with Eqs (17) and (18) and Table 1 by Li and Hunt [18]. The corresponding dispersion terms that depend on the γ-hyperpolarizability of molecule B and the dipole polarizability of molecule A are given by

$$A^{\alpha\gamma}_{JkjΛL} = (-1)^{\Lambda} P^{AB} A^{\gamma\alpha}_{JjkΛL}. \tag{44}$$

7. Anisotropic polarizability coefficients for like pairs at long range

In this section, we simplify the results from Sec. 6 to obtain $\Delta\alpha$ for two identical diatomic molecules that are interacting. Averaging isotropically over the orientations of the molecular axes $\hat{\mathbf{r}}_A$ and $\hat{\mathbf{r}}_B$ yields a non-zero anisotropic polarizability, analogous to $\Delta\alpha^{(2)}_k$ found for interacting atoms in S states at first order in the DID approximation, and higher orders. For diatomics, A_{20002} depends on $(\alpha_{zz} - \alpha_{xx})^2$ as well as the isotropically averaged polarizability $\overline{\alpha}$, and

$$\begin{aligned} A_{20002} = &6\sqrt{10}/5\ \overline{\alpha}^2 R^{-3} + 6\sqrt{10}/5\ \overline{\alpha}^3 R^{-6} + 2\sqrt{10}/75(\alpha_{zz} - \alpha_{xx})^2\ \overline{\alpha} R^{-6} \\ &+6\sqrt{10}/5\ (\hbar/\pi) \int_0^\infty d\omega\ \gamma_2(i\omega, 0, 0)\overline{\alpha}(i\omega) R^{-6}. \end{aligned} \tag{45}$$

The coefficients A_{2202L} give rise to transitions with $\Delta J = \pm 2$ on one molecule and no change in the J value for the other (with an isotropic potential). These coefficients have contributions from all of the polarization mechanisms through order R^{-6}: first- and second-order DID, higher-multipole induction, field nonuniformity, hyperpolarization, and dispersion.

$$\begin{aligned} A_{2202L} = &-2\sqrt{7}/5\ \delta_{L2}\overline{\alpha}(\alpha_{zz} - \alpha_{xx}) R^{-3} \\ &+4\sqrt{35}/35\ \delta_{L4}[\overline{\alpha}(3E_{z,zzz} - 8E_{x,xxx}) - 7B_2\Theta^0] R^{-5} \\ &+[(a_L + b_L)\overline{\alpha}^2(\alpha_{zz} - \alpha_{xx}) + c_L\overline{\alpha}(\alpha_{zz} - \alpha_{xx})^2 + d_L(\alpha_{zz} - \alpha_{xx})^3] R^{-6} \\ &+e_L(\hbar/\pi) \int_0^\infty d\omega\ \gamma_2(i\omega, 0, 0)[\alpha_{zz}(i\omega) - \alpha_{xx}(i\omega)] R^{-6} \\ &+(\hbar/\pi) \int_0^\infty d\omega [9\sqrt{10}/5\ \delta_{L0}\ \gamma_4(i\omega, 0, 0) + f_L\ \gamma_5(i\omega, 0, 0)]\overline{\alpha}(i\omega) R^{-6} \end{aligned} \tag{46}$$

Table 3
Coefficients of R^{-6} for van der Waals dispersion terms in the polarizability of $H_2 \cdots H_2$. Results in this work have been obtained by 64-point Gauss – Legendre quadrature, based on the values of the imaginary-frequency components of the polarizability and hyperpolarizability tensors for H_2, tabulated by Bishop and Pipin [65]. Results of Bishop and Pipin from Table 7 of [65] have been scaled by $\sqrt{3}/(4\pi)$ to allow for differences of prefactors in the definitions of the coefficients. All values are given in atomic units (a.u.)

	This work	Ref. 65
A_{00000}	2960.82	2960.8
$A_{00222} = A_{02022}$	90.63	90.6
A_{02200}	0.80	–
A_{02222}	0.96	–
A_{02244}	7.73	–
A_{20002}	354.79	354.8
$A_{20220} = A_{22020}$	41.56	41.6
$A_{20222} = A_{22022}$	−2.28	−2.3
$A_{20224} = A_{22024}$	38.76	38.7
$A_{20442} = A_{24042}$	−1.20	−1.2
A_{22202}	0.58	–
A_{22220}	−0.34	–
A_{22222}	1.79	–
A_{22224}	−0.93	–
A_{22242}	2.13	–
A_{22244}	−2.43	–
$A_{22420} = A_{24220}$	−0.03	–
$A_{22422} = A_{24222}$	−0.01	–
$A_{22424} = A_{24224}$	−0.002	–
$A_{22442} = A_{24242}$	−0.02	–
$A_{22444} = A_{24244}$	−0.04	–
$A_{22464} = A_{24264}$	−0.23	–

with coefficients $a_L - f_L$ listed in Table 3 of Ref. 18. Analogously, the coefficients A_{24042} and A_{24044} give rise to transitions with $\Delta J = \pm 4$ on one molecule and no change in the J value for the other. A_{24042} depends on second-order DID and dispersion interactions (through order R^{-6}), while A_{24044} depends exclusively on the E-tensor mechanisms (i.e., higher-multipole induction and field nonuniformity):

$$A_{24042} = 12\sqrt{35}/175\ \overline{\alpha}(\alpha_{zz} - \alpha_{xx})^2 R^{-6} + 6\sqrt{35}/5(\hbar/\pi) \int_0^\infty d\omega\ \gamma_7(i\omega, 0, 0)\overline{\alpha}(i\omega) R^{-6} \tag{47}$$

$$A_{24044} = -2\sqrt{154}/21\ \overline{\alpha}(E_{z,zzz} + 2E_{x,xxx}) R^{-5} \tag{48}$$

The coefficients $A_{222\Lambda L}$ and $A_{242\Lambda L}$ give rise to simultaneous rotational transitions on both molecules. $A_{222\Lambda L}$ varies as R^{-3} at long range and depends on all of the polarization mechanisms through order R^{-6}, while $A_{242\Lambda L}$ has no first-order DID contributions and varies as R^{-5} at lowest order.

$$\begin{aligned} A_{222\Lambda L} = {} & a_{\Lambda L}(\alpha_{zz} - \alpha_{xx})^2 R^{-3} \\ & + [(-1)^\Lambda + 1][b_{\Lambda L} B_5 \Theta^0 - c_{\Lambda L}(\alpha_{zz} - \alpha_{xx})(3E_{z,zzz} - 8E_{x,xxx})] R^{-5} \\ & + [(-1)^\Lambda + 1][d_{\Lambda L}\overline{\alpha}(\alpha_{zz} - \alpha_{xx})^2 + e_{\Lambda L}(\alpha_{zz} - \alpha_{xx})^3] R^{-6} \\ & + (\hbar/\pi) \int_0^\infty d\omega [f_{\Lambda L}\gamma_4(i\omega, 0, 0) + g_{\Lambda L}\gamma_5(i\omega, 0, 0)][\alpha_{zz}(i\omega) - \alpha_{xx}(i\omega)] R^{-6} \end{aligned} \tag{49}$$

Table 4
Long-range contributions to the polarizability coefficient A_{22024}. The table lists the αER^{-5} terms, the $B\Theta R^{-5}$ terms, the sum of those terms (labeled E+B), the full long-range expansion through order R^{-6} (LR), and the fit to the *ab initio* calculations (LAHH). All entries are scaled by 10^5 and given in a.u.

R	αER^{-5}	$B\Theta R^{-5}$	E+B	LR	LAHH
3.0	41320	56380	97700	112700	47700
4.0	9806	11380	23190	25850	19900
5.0	3213	4384	7597	8295	7880
6.0	1291	1762	3053	3287	3360
7.0	597	815	1413	1505	1570
8.0	306	418	725	766	800
9.0	170	232	402	423	450
10.0	100	137	237	248	260

with coefficients $a_{\Lambda L} - g_{\Lambda L}$ in Table 4 of the work by Li and Hunt [18], for L = 0, 2, or 4.

$$\begin{aligned} A_{242\Lambda L} = & [(-1)^{\Lambda+1} h_{\Lambda L} B_7 \Theta^0 + (-1)^{\Lambda} q_{\Lambda L} (\alpha_{zz} - \alpha_{xx})(E_{z,zzz} + 2E_{x,xxx})] R^{-5} \\ & + (-1)^{\Lambda} s_{\Lambda L} (\alpha_{zz} - \alpha_{xx})^3 R^{-6} \\ & + t_{\Lambda L} (\hbar/\pi) \int_0^{\infty} d\omega \, \gamma_7(i\omega, 0, 0)[\alpha_{zz}(i\omega) - \alpha_{xx}(i\omega)] R^{-6} \end{aligned} \tag{50}$$

with $h_{\Lambda L}$, $q_{\Lambda L}$, $s_{\Lambda L}$, and $t_{\Lambda L}$ listed in Table 5 of the work by Li and Hunt [18]. The remaining non-vanishing coefficients are given by

$$A_{2022L} = A_{2202L} \quad (for L = 0, 2, 4) \tag{51}$$

$$A_{2044L} = A_{2404L} \quad (for L = 2, 4) \tag{52}$$

and

$$A_{224\Lambda L} = (-1)^{\Lambda} A_{242\Lambda L} \tag{53}$$

for like pairs.

The equations of Li and Hunt [18] for the dispersion terms in $A_{2\lambda\lambda'\Lambda L}$ follow from the theory of Hunt and Bohr [28] for the van der Waals dispersion effects on $\Delta\alpha$. The results are equivalent to those obtained from two-center, fourth-order perturbation theory, as in Refs. 153 and 154, but they are expressed as quadratures – integrals over imaginary frequencies, with integrands that depend on the polarizability components for one of the molecules (at frequency iω) and the γ-hyperpolarizability of the other molecule as a function of frequency, γ(iω, 0, 0).

We have evaluated the long-range coefficients, complete to order R^{-6} in the separation R between the two H_2 molecules, using the values of the quadrupole moment and the static susceptibilities for H_2 listed in Table 2.

We have obtained the dispersion contributions in Table 3 by 64-point Gauss-Legendre quadrature, based on the imaginary-frequency polarizabilities and hyperpolarizabilities of H_2, tabulated by Bishop and Pipin [65]. For comparison, Table 3 also lists the values of the coefficients with λ_A or $\lambda_B = 0$, as calculated by Bishop and Pipin [65], by use of equations for the dispersion effects in atom-diatom

systems derived by Hunt, Liang, and Sethuraman [24]. Our results agree, in those cases. Results for coefficients with λ_A and λ_B both non-zero have not been obtained previously. These are relatively small, as the dispersion effects tend to be highly isotropic: The largest dispersion coefficient in $\Delta\alpha$, by an order of magnitude, is A_{00000}, and the next largest is A_{20002}, which is proportional to the pair polarizability anisotropy, isotropically averaged over the molecular orientations.

8. Comparison of *ab initio* and long-range results for the anisotropic polarizability coefficients

Results for the anisotropic polarizability coefficients $A_{2\lambda\lambda'\Lambda L}$ are listed in Table 1. The rows labeled LAHH give the coefficients obtained directly by least-squares fit of the angular dependence in the *ab initio* results of Li, Ahuja, Harrison, and Hunt [5] for each intermolecular separation R, based on 18 different geometrical configurations for the pair. The dominant coefficient is A_{20002}, which is directly related to the pair polarizability anisotropy averaged over all orientations of molecules A and B. In fact, at frequency shifts less than 240 cm^{-1} in the calculated Raman spectrum, the coefficient A_{20002} accounts for approximately 97% of the observed spectral intensity [66]. Other large coefficients include A_{20220}, A_{22020}, A_{20222}, A_{22022}, A_{20224}, A_{22024}, A_{22242}, A_{22244}, and A_{22246}. Coefficients with $\lambda_A = 4$ and $\lambda_B = 2$ (or vice versa) are smaller; these are not listed.

The rows of entries that are labeled GFLH give the results from a few-parameter fit by Gustafsson, Frommhold, Li, and Hunt [66] to the coefficients derived from the *ab initio* results in Ref. 5. Ten of the pair polarizability coefficients – the most important for the spectra – were fit with functions of the form

$$A_{2\lambda\lambda'\Lambda L} = D_m R^{-m} + D_n R^{-n} + D_e\, exp(-DR), \tag{54}$$

with n > m, for $H_2{-}H_2$ separations from 2.0 a.u. to 10.0 a.u. (For the linear configuration of the pairs, the smallest value of R in the calculations is R = 3.0 a.u.) The exponents were set by the leading long-range terms in the collision-induced polarizability. Thus, for example, A_{20002}, A_{22022}, A_{20222}, and A_{22242} have $m = 3$ and $n = 6$; A_{22024}, A_{20224}, and A_{22244} have $m = 5$ and $n = 6$; A_{22020} and A_{20220} have $m = 6$ and $n = 8$, and A_{22246} has $m = 8$ and $D_n = 0$ (i.e., no second term at long range). The exponential term reflects short-range exchange effects. In calculating the spectra, additional values of the A coefficients are needed at longer range, beyond the R values covered by the *ab initio* calculations. For R > 10.0 a.u., the A coefficients were assumed to have the form

$$A_{2\lambda\lambda'\Lambda L} = D_m R^{-m} + D_n^{\infty} R^{-n}. \tag{55}$$

The values of D_m are identical in both equations and the fitting parameters are selected to make $A_{2\lambda\lambda'\Lambda L}$ continuous at R = 10.0 a.u. The resulting values of the parameters D_m, D_n, D_e, D, and D_n^{∞} from the fit are listed in Table 1 of Ref. 66.

As shown by Table 1, the agreement between the *ab initio* values of the A coefficients and the fit to the comparatively simple functional forms of Eqs (54) and (55) is excellent, particularly in light of the small number of parameters used.

The rows labeled BUZ give the anisotropic polarizability coefficients from a fit by Ulivi and Zoppi [67] to the SCF pair polarizabilities of Bounds [68]. Ulivi and Zoppi fit the coefficients A_{20002}, A_{20222}, A_{22022}, A_{22202}, A_{22222}, and A_{22242}, using the form

$$A_k(R) = A_{3k} R^{-3} + B_{1k} R^{-6} + B_{2k}\, exp(-R/R_{0k}), \tag{56}$$

where k denotes the indices 2, λ_A, λ_B, Λ, and L. The coefficients A_{3k} were constrained to equal the DID-1 values, but no constraints were imposed on B_{1k}, B_{2k} or R_{0k}.

Table 1 shows that the BUZ results approximately equal the LAHH and GFLH results at larger R, where all are approximately equal to the DID-1 results. For purposes of comparison with our results, we have scaled the numerical values of Ulivi and Zoppi by $(3/5)^{1/2}$, to account for the differences in the definition of the A coefficients. We have also scaled their coefficients to reflect differences in the isotropic polarizability and the polarizability anisotropy of an isolated H_2 molecule, as obtained from the accurate, explicitly correlated method of Bishop and Pipin [63], vs. those obtained from the SCF calculations by Bounds [68]. The scaling was determined by the form of the first-order DID expressions for the coefficients: All are quadratic in the polarizability, but they depend differently on $\overline{\alpha}$ vs. $\alpha_{zz} - \alpha_{xx}$. Thus, we have scaled Ulivi and Zoppi's value of A_{20002} by $(5.3966/5.26)^2$, their values of A_{20222} and A_{22022} by (5.3966/5.26) (1.9792/1.800), and their values of A_{22202}, A_{22222}, and A_{22242} by $(1.9792/1.800)^2$.

At shorter range, the BUZ values are noticeably smaller those of LAHH and GFLH. These differences stem in part from the differences between the SCF results [68] and our CCSD(T) results, and in part from limitations in the size of data set available for fitting. Bounds computed the pair polarizabilities for 6 relative orientations of the pair [68]. This represented a major computational effort at the time! From this set of relative orientations, Ulivi and Zoppi [67] determined the 6 anisotropic polarizability coefficients (5 of them distinct) that have non-zero values at DID-1 level. At short range, other coefficients such as A_{20220}, A_{22020}, A_{20224}, A_{22024}, A_{22244}, and A_{22246} are sizeable, and this affects the 6-coefficient fits. We note that the BUZ coefficients yield values for the first three moments of the depolarized light scattering spectra that are too low by $\sim$45% at 50 K [67,71] and at 297 K [67,156]. Our coefficients would therefore be expected to yield improved agreement with experiment, for these moments.

The first-order DID results are listed in the rows labeled DID-1, for coefficients that are non-vanishing at that level of approximation. The coefficients with a first-order DID contribution tend to converge to the DID-1 values at large R. Exceptions are observed – in terms of the relative error – only for the coefficients A_{22202} and A_{22222}, which are quite small at long range.

Finally, in Table 1 the rows labeled LR give the results from the long-range model that includes all polarization mechanisms through order R^{-6}: first- and second-order DID effects, van der Waals dispersion, polarization in the local field from the octopole moment induced in a neighboring molecule by the external field, polarization by the gradient of the field gradient from the dipole induced in a neighboring molecule by the external field, and hyperpolarization by the external field and the field gradient of the permanent quadrupole of the neighboring molecule [18]. At short range, exchange and overlap damping of the long-range polarization mechanisms become significant, with the result that the LR values may be farther from the *ab initio* results than the DID-1 values are. However, at larger R, for coefficients with non-vanishing DID-1 contributions, the LR approximation generally models the coefficient more closely than DID-1.

Over a range of R values, the LR approximation accurately models several coefficients that lack a first-order DID contribution. The coefficients A_{22024} and A_{22244} illustrate this point. The leading polarization mechanisms in A_{22024} and A_{22244} vary as R^{-5} (E- and B-tensor terms). Except for the smallest R values, the long-range model based on perturbation theory agrees well with the *ab initio* results. The same is true for A_{22224}, at intermediate range. For this coefficient, the discrepancies found at longer range ($R >$ 8.0 a.u.) reflect in part the uncertainties in all of the smaller coefficients from the fit to the *ab initio* results for various geometrical configurations.

In Fig. 3, we have plotted the values of A_{20002}, the largest coefficient in the pair polarizability of second rank, vs. the intermolecular separation R. The diamonds (♦) mark the results from the direct fit

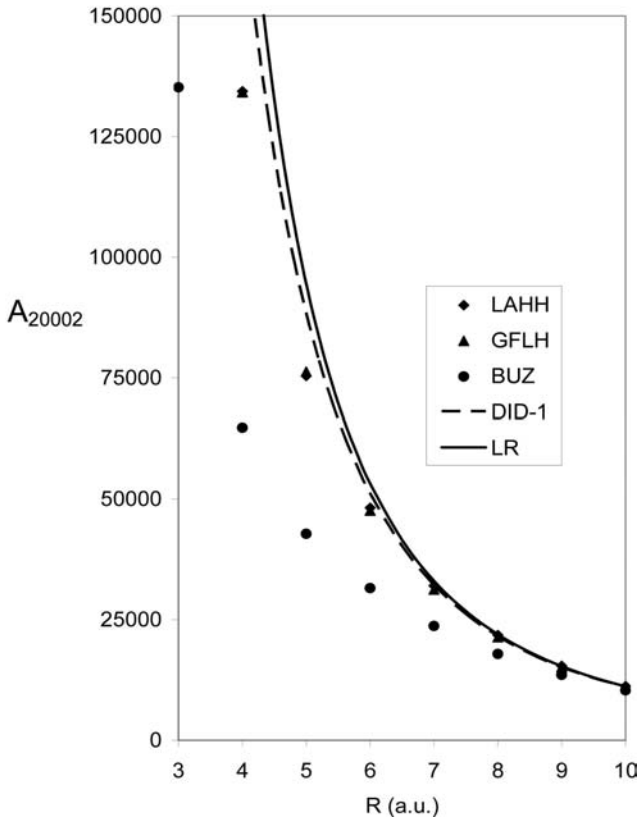

Fig. 3. Polarizability coefficient A_{20002} in Eq. (5). LAHH (⧫): Direct fit of *ab initio* results in Ref. 5. GFLH (▲): Few-parameter fit [66] to the *ab initio* results in Ref. 5. BUZ (●): Fit by Ulivi and Zoppi [67] to the SCF results of Bounds [68]. DID-1: First-order DID approximation. LR: Long-range perturbation result through order R^{-6}, from Eq. (45), with the dispersion coefficient from Table 3.

of the *ab initio* calculations by Li, Ahuja, Harrison, and Hunt [5], with 18 geometrical configurations at each R value. The triangles (▲) mark the results from the few-parameter fit to the results in Ref. 5, by Gustafsson, Frommhold, Li, and Hunt [66]. These two sets of points very nearly coincide. The circles (●) show the results from the fit by Ulivi and Zoppi [67] to the SCF values obtained by Bounds [68]. These results converge to the first-order DID form at long range ($R \sim 9$ a.u. or larger), but the BUZ values of A_{20002} are generally much smaller than the other values at smaller R, which would lead to lower predicted intensities for depolarized scattering. The discrepancy probably results primarily from the limited number of pair orientations (six) available for the earlier fit by Ulivi and Zoppi [67]. The dashed line shows the first-order dipole-induced-dipole values for this coefficient (DID-1), while the solid line (LR) shows the full long-range results [18], through order R^{-6}. The LR-results include second-order DID and van der Waals dispersion contributions, as well as the first-order DID terms. Table 1 shows that the LR results are closer to the *ab initio* results than the DID values are, for $R \geqslant 8.0$ a.u. At $R = 7.0$ a.u. and $R = 6.0$ a.u., the DID-1 approximation is closer to the *ab initio* results than the full LR approximation. This probably reflects an approximate cancellation of (negative) overlap effects with (positive) higher-order polarization effects that are present in the LR approximation, but not in DID-1. At short range, exchange and overlap damping reduce the *ab initio* values of A_{20002} significantly below the DID-1 and LR results.

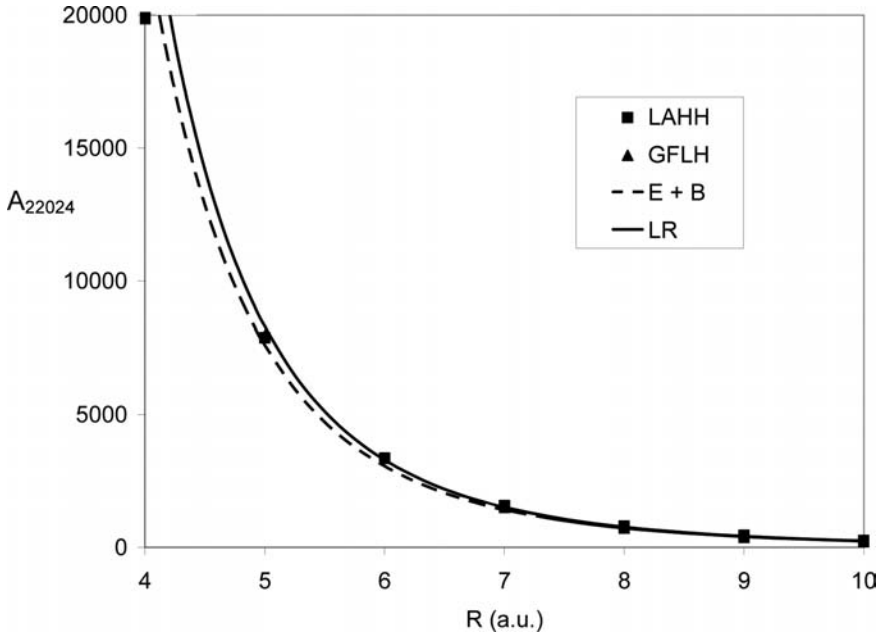

Fig. 4. Polarizability coefficient A_{22024} in Eq. (5). LAHH (⧫): Direct fit of *ab initio* results in Ref. 5. GFLH (▲): Few-parameter fit [66] to the *ab initio* results in Ref. 5. E + B: Sum of the terms in A_{22024} that vary as R^{-5} (higher-multipole induction, nonuniform field effects and hyperpolarization). LR: Long-range perturbation result through order R^{-6}, from Eq. (46), with the dispersion coefficient from Table 3.

Figure 4 shows the coefficient A_{22024}, which vanishes at first order in the DID approximation. This coefficient is smaller than A_{20002} by roughly a factor of 10 at R = 5.0 a.u. The LAHH and GFLH values are almost identical for this coefficient. For comparison, the solid line in Fig. 4 shows the long-range approximation (LR). The LR approximation includes E-tensor induction, the BΘ terms, second-order DID effects, and van der Waals dispersion. The LR approximation agrees very well with the *ab initio* results over the range from R = 5.0 a.u. to R = 10.0 a.u.; the terms through order R^{-6} seem to be sufficient to characterize this coefficient. At R = 4.0 a.u., the LR result is $\sim$ 30% too large; and at R = 3.0 a.u., it is too large by a factor of $\sim$ 2.4, due to short-range overlap and exchange effects. In the figure, the dotted line shows the contributions to this coefficient that vary as R^{-5}, i.e., terms in A_{22024} that vary as α (3 $E_{z,zzz}$ − 8 $E_{x,xxx}$) R^{-5} and $B_2\Theta_0R^{-5}$, where B_2 is a linear combination of the dipole-dipole-quadrupole hyperpolarizability components $B_{z,z,zz}$, $B_{x,z,xz}$, $B_{x,x,zz}$, and $B_{x,x,xx}$, as specified by Eq. (19) and Table 2 of Ref. 18. The major contribution to A_{22024} comes from these classical polarization and hyperpolarization effects. The remaining terms in the LR approximation come from second-order DID effects and van der Waals dispersion. The full long-range series (LR) provides a better fit to the *ab initio* results than is provided by the R^{-5} terms alone, for R $\geqslant$ 6.0 a.u. However, the LR curve rises too rapidly as R decreases.

Table 4 shows the breakdown of the LR approximation into the E-tensor, B-tensor, and total R^{-5} parts (E + B). The *ab initio* values are also shown in Table 4 for comparison. From the table, it is apparent that the B-hyperpolarization contributions to A_{22024} are actually larger than the E- tensor terms, with the contributions from $B_2\Theta_0R^{-5}$ accounting for $\sim$58% of the R^{-5} terms, more than 50% of the full LR sum for R $\geqslant$ 5.0 a.u., and more than 50% of the *ab initio* values [5] over the same range of R values. In contrast, the coefficient A_{24044} depends solely on the E-tensor mechanism, through order R^{-5}, as shown in Eq. (48).

9. Comparison of experimental results and calculations of the depolarized collision-induced roto-translational Raman spectra of $H_2 \cdots H_2$

The depolarized light scattering spectra for H_2 in the gas phase have been obtained by Bafile *et al.* [69,71,156–158], by Brown *et al.* [70,159,160], by Le Duff and Ouillon [161], and by Fleury and McTague [162,163]. The binary scattering profile (with intensity quadratic in the density) has been derived from the experimental gas-phase spectra for both H_2 [69–71,156,157] and D_2 [70]. Pure collision-induced scattering, pressure-broadened rotational transitions, and interference between these two mechanisms determine the binary light scattering spectra [1–4]. The current work focuses on gas-phase spectra; however, depolarized spectra for H_2 in the liquid phase have been determined by Fleury and McTague [162,163] and by Barocchi and co-workers [164,165]. Barocchi *et al.* have also studied depolarized light scattering by solid H_2 [164].

Roto-translational Raman scattering has been observed experimentally in the frequency range from 0 to ∼900 cm^{-1}. This range includes the single-molecule rotational Raman lines $S_0(0)$ at 354.4 cm^{-1} ($J = 0 \rightarrow 2$), $S_0(1)$ at 587.3 cm^{-1} ($J = 1 \rightarrow 3$) and $S_0(2)$ at 815.2 cm^{-1} ($J = 2 \rightarrow 4$) [156,166–169]. In addition, a double Raman transition $S_0(0) + S_0(0)$ has been observed at 705 cm^{-1} in the solid and liquid phases of para-hydrogen [164,165]. The double transitions have been studied in liquid para-hydrogen over a temperature range from 18.5 to 28 K and a pressure range from 17 to 600 bar [164,165]. In the solid phase, the $S_0(0) + S_0(0)$ band shows structure at various densities [40,164,170,171].

At very low frequency shifts, near room temperature, scattered light comes preponderantly from pressure broadening of the wings of the $Q_0(J)$ bands [22,71,150,172,173]. As the temperature is reduced, these bands disappear from the depolarized scattering spectrum of pure para-hydrogen, but the $Q_0(1)$ line remains in the ortho-hydrogen spectrum [150,172]. There is no $Q_0(0)$ line. Scattering from bound dimers is also expected to contribute at low frequency shifts, but this has not yet been observed experimentally [70,173,174].

Collision-induced light scattering predominates [22,70,156] between the Q bands and the pressure-broadened wing of the $S_0(0)$ line; that is, in the range from 40 to 240 cm^{-1} at 297 K and densities between 17.8 and 129 amagat [156]; and from 15 to 280 cm^{-1} at 50 K and densities from 20 to 530 amagat [157]. In this region, the logarithmic slopes of the polarized and depolarized light scattering intensities vs. frequency nearly match, suggesting that the spatial ranges of the trace and the anisotropy of $\Delta\alpha$ are comparable for $H_2 \cdots H_2$ [70,175]. The DID model [19] accounts qualitatively for the similarity in the logarithmic slopes, because both $\Delta\alpha_0^{(0)}$ and $\Delta\alpha_k^{(2)}$ vary as R^{-3} in the separation R between the two hydrogen molecules. However, the DID model does not provide the quantitative theory needed to extract accurate information on intermolecular interactions from the spectra: This model overestimates the binary depolarized scattering intensities between the Q and $S_0(0)$ bands, while underestimating the intensities at higher frequencies [69,70,150].

To calculate the roto-translational Raman spectra, we have relied (for the present) on calculations of the pair polarizabilities with the bond lengths in each H_2 molecule fixed at the ground-state vibrational average. This provides a lowest-order representation of the vibrational effects on the rotational transitions. Gustafsson, Frommhold, Li, and Hunt [66] have solved the Schrödinger equation in the presence of the radiation field, using a basis of dressed states, with specified numbers of photons n_0' and n_s' at the incident and scattered frequencies respectively:

$$\Psi^M_{\alpha n_0 n_s}(\hat{\mathbf{r}}_A, \hat{\mathbf{r}}_B, \mathbf{R}; E) = \sum_{\alpha' n_0' n_s'} (1/R) F^{\alpha n_0 n_s}_{\alpha' n_0' n_s'}(R; E) Y^{J'M}_{jA'jB'j'l'}(\hat{\mathbf{r}}_A, \hat{\mathbf{r}}_B, \widehat{\mathbf{R}}) \otimes |n_0' n_s'\rangle \tag{57}$$

where $\hat{\mathbf{r}}_A$ and $\hat{\mathbf{r}}_B$ denote unit vectors along the molecular axes of A and B. The angular functions $\mathrm{Y}^{J'M}_{jA'jB'j'l'}(\hat{\mathbf{r}}_A, \hat{\mathbf{r}}_B, \widehat{\mathbf{R}})$ are obtained from

$$Y^{JM}_{j_A j_B j l}(\hat{\mathbf{r}}_A, \hat{\mathbf{r}}_B, \widehat{\mathbf{R}}) = \sum_{m_A, m_B, m_j, m_l} Y_{j_A m_A}(\hat{\mathbf{r}}_A) Y_{j_B m_B}(\hat{\mathbf{r}}_B) Y_{l m_l}(\widehat{\mathbf{R}}) \times \langle j_A j_B m_A m_B | j m_j \rangle \langle j l m_j m_l | J M \rangle, \tag{58}$$

by coupling the spherical harmonics of the molecular orientations to give a resultant angular momentum j, and then coupling that resultant to a spherical harmonic of the orientation angles of the intermolecular vector, using the Clebsch-Gordan coefficients. In Eq. (57), the index $\alpha = (\mathrm{j}_A, \mathrm{j}_B, \mathrm{j}, \mathrm{l}, \mathrm{J})$ specifies the set of angular momentum quantum numbers [66].

After integrating over the angular coordinates, Gustafsson, Frommhold, Li, and Hunt obtained the radial Schrödinger equation for light scattering by an H_2 pair in the form [66]

$$\begin{aligned} &[E_{v_{A''} j_{A''}} + E_{v_{B''} j_{B''}} - (\hbar^2/2\mu) d^2/dR^2 + \hbar^2 l''(l''+1)/(2\mu R^2) \\ &+ n''_0 \hbar\omega_0 + n''_s \hbar\omega_s - E] F^{\alpha n_0 n_s}_{\alpha'' n''_0 n''_s}(R; E) \\ &+ \sum_{\alpha' n'_0 n'_s} [V_{\alpha''\alpha'}(R) \delta(n''_0, n'_0) \delta(n''_s, n'_s) + W_{\alpha''\alpha'}(R) \delta(n''_0 \pm 1, n'_0) \delta(n''_s \pm n'_s)] \\ &\times F^{\alpha n_0 n_s}_{\alpha' n'_0 n'_s}(R; E) = 0, \end{aligned} \tag{59}$$

where E_{vj} denotes the energy of an isolated H_2 molecule with vibrational quantum number v and rotational quantum number j, μ is the reduced mass of $H_2 \cdots H_2$, ω_0 is the angular frequency of the incident radiation, ω_s is the angular frequency of the scattered radiation, and we have used the notation δ(j, k) for the Kronecker delta δ_{jk}. The potential matrix elements $\mathrm{V}_{\alpha\alpha'}$ are defined in Ref. 176. Due to the anisotropy of the potential, $\mathrm{V}_{\alpha\alpha'}$ contains off-diagonal elements, which mix angular momentum states in the scattering eigenfunctions, even in the absence of the radiation field. In the isotropic potential approximation (IPA), $\mathrm{V}_{\alpha\alpha'}$ is diagonal in the angular momentum quantum number representation.

The radiative coupling $\mathrm{W}_{\alpha\alpha'}$(R) for depolarized light scattering by para-H_2 colliding with ortho-H_2 is specified in Eqs (14) and (15) of Ref. 66, in terms of the polarizability coefficients $\mathrm{A}_{2\lambda\lambda'\Lambda L}$(R) and the polarizability anisotropy of an isolated H_2 molecule, the radiation fluxes ϕ_0 and ϕ_s, and frequencies ω_0 and ω_s, as well as 3j- and 9j-symbols and other numerical factors. The collision-broadened wings of the allowed rotational Raman lines are obtained with this form of $\mathrm{W}_{\alpha\alpha'}$(R), since the single-molecule anisotropy is included in $\mathrm{W}_{\alpha\alpha'}$(R) [66]. For collisions of para-H_2 with para-H_2 or ortho-H_2 with ortho-H_2, the expressions for the radiative coupling matrix elements allow for the appropriate symmetrization. The symmetrized versions and the corresponding statistical weights are given in the Appendix of Ref. 176. The radiative coupling matrix elements for polarized scattering are given in Ref. 177.

The radial Schrödinger equation has been solved [66] using the COUPLE program of Mies, Julienne, and Sando [178], to obtain the scattering matrix elements $\mathrm{S}^f_i(\mathrm{E}_i)$, representing transitions accompanied by the loss of a photon at the incident frequency ω_0 and the gain of a photon at the scattered frequency ω_s. The initial and final state vectors are specified by the sets of quantum numbers $\mathrm{f} = (\mathrm{j}_{Af}, \mathrm{j}_{Bf}, \mathrm{j}_f, \mathrm{l}_f, \mathrm{J}_f, \mathrm{n}_0 - 1, \mathrm{n}_s + 1)$ and $\mathrm{i} = (\mathrm{j}_{Ai}, \mathrm{j}_{Bi}, \mathrm{j}_i, \mathrm{l}_i, \mathrm{J}_i, \mathrm{n}_0$ and $\mathrm{n}_s)$.

With a right-angle experimental scattering geometry and linearly polarized incident radiation, the cross section (per pair of molecules) for light scattered to a detector placed parallel to the direction of polarization of the incident radiation is $\sigma_{||}$ and with a detector placed perpendicular to that direction, the

cross section is $\sigma_\perp$. These cross sections are connected to the depolarized intensity D and the polarized intensity P, and to the VV and VH scattering intensities by [148,151,179]

$$V\partial^2\sigma_{||}/(\partial\Omega\partial\nu) = D = 2I_{VH} \tag{60}$$

and

$$V\partial^2\sigma_\perp/(\partial\Omega\partial\nu) = P + (7/6)D = I_{VV} + I_{VH} \tag{61}$$

where Ω denotes the solid angle and ν the frequency. The cross-section $\sigma_{||}$ is related to the S matrix computed with the radiative coupling matrix elements $W_{\alpha\alpha'}(R)$ from Eqs (14) and (15) of Ref. 66,

$$V\partial^2\sigma_{||}/(\partial\Omega\partial\nu) = 2c\lambda_0^3\nu_s^2/(\phi_0\phi_s h)\sum P_{0jA_i}P_{0jB_i}\int_0^\infty dE_i exp(-\beta E_i)|S_i^f(E_i)|^2 \tag{62}$$

and similarly for $\sigma_\perp$ [66]. In Eq. (62), λ_0 denotes the thermal de Broglie wavelength and P_{vj} gives the thermal roto-vibrational population of the H_2 state with vibrational quantum number v and rotational quantum number j. Here we consider only the ground vibrational state. The results in the weak field limit (as here) are equivalent to the results from the distorted-wave approximation [180].

Gustafsson, Frommhold, Li, and Hunt [66] have used the symmetry of the $H_2 \cdots H_2$ system, parity, and angular momentum conservation to simplify the computations. For example, the total angular momentum J of an $H_2 \cdots H_2$ pair changes by a maximum of ± 2 in the scattering process in the radiation field, the symmetry of the para-para and ortho-ortho pairs is maintained, and the orbital angular momentum l for such pairs does not change parity. As noted in Ref. 66, for collisions of ortho-H_2 with ortho-H_2, these considerations lead to 20 separate sets of equations to be solved (allowing for rotational states with j_A and j_B each equal to 1 or 3 in the initial and final states). Each set has from 25 to 43 coupled equations. Overall, the calculated intensities in the spectra are accurate to within a few percent, or better. For purposes of comparison, the spectra have also been calculated within the isotropic potential approximation, which reduces $V_{\alpha\alpha'}$ to a diagonal form [66].

The binary, collision-induced depolarized translational Raman spectrum of H_2 at 36 K has been computed from the *ab initio* values of $\Delta\alpha$ [5] in Ref. [66], for a sample consisting of 92.6% para-hydrogen and 7.4% ortho-hydrogen. For the Stokes side of the translational Raman spectrum, measurements of the spectrum at 36 K [69] extend out to 100 cm^{-1}. Pressure broadening of the allowed rotational transitions does not contribute significantly in this frequency range. Intensities predicted with the DID-1 approximation and the isotropic potential approximation (IPA) are appreciably larger than the *ab initio* intensities [66].

When the *ab initio* values of $\Delta\alpha$ are used in the calculations, the close-coupled intensities exceed the measured intensities at 36 K by ∼10–30%, depending on the frequency shift [66]. This direction of the discrepancy between theory and experiment is difficult to explain, because the static polarizability of an isolated H_2 molecule is *smaller* than the polarizability of H_2 in light of wavelength $\lambda = 514.5$ nm (the green line of an argon-ion laser); and the principal contributions to the spectrum at low frequency come from A_{20002}.

The IPA intensities computed with the *ab initio* values of $\Delta\alpha$ [5] are also higher than the measured intensities; and in fact, the IPA intensities almost superimpose on the close-coupled results (see Fig. 1 of Ref. 66). This means that the anisotropy of the interaction potential does not affect the translational part of the spectrum significantly, at low frequencies.

At 296 K, the Stokes side of the binary, depolarized translational Raman spectrum has been measured out to ~ 250 cm^{-1} [70], and the spectrum has been calculated in the IPA [66], with the *ab initio* values

of $\Delta\alpha$ [5] (Close-coupled calculations are impracticable at this temperature, due to the large number of rotational states involved.) In this case, the slope of the experimental intensity vs. frequency shift is very well reproduced by the calculations, as shown in Fig. 2 of Ref. 66. Again, the calculated intensities are $\sim$30% larger than the experimental intensities. The discrepancy between the experimental and calculated DID-1 intensities is appreciably larger, and the slope of the DID-1 results differs from experiment at the larger frequency shifts [66].

The binary roto-translational Raman spectrum of pure para-hydrogen at 36 K has been calculated over a broader frequency range, extending to 800 cm^{-1}. The calculated spectrum is shown in Fig. 3 of Ref. 66. At low frequencies ($<$ 200 cm^{-1}), the collision-induced polarizability $\Delta\alpha$ accounts for most of the intensity. The allowed $S_0(0)$ rotational transition of para-hydrogen occurs at 354.4 cm^{-1}. Near 300 cm^{-1}, interference between collision-induced scattering and the pressure-broadened wings of the single-molecule rotational transition reduces the calculated intensity below either of these intensities, computed individually. Constructive interference occurs near 600 cm^{-1} [66]. The interference effects are due to rotational couplings and thus they appear in the close-coupled calculations, but not in the IPA.

Near 700 cm^{-1} the feature $S_0(0) + S_0(0)$, due to simultaneous rotational transitions on both of the interacting para-hydrogen molecules, is apparent in the calculations [66]. The band is rather broad, since collision durations of 10^{-13} s correspond to a line width of $\pm$ 30 cm^{-1}. The feature is observed in the collision-induced intensities calculated with $\Delta\alpha$ in the IPA, and in the calculations based on the permanent polarizability anisotropy of an isolated H_2 molecule, but not $\Delta\alpha$ (as well as in the close-coupled calculations). This shows that the double rotational transitions result both from collision-induced changes in the polarizability and from mixing of the rotational channels due to the anisotropy of the pair potential. The double transitions are interesting because they provide a direct probe of the pair dynamics, if the collision-induced polarizability of a cluster can be approximated as pairwise additive. In that case, the line shapes for $S_0(0) + S_0(0)$ are unaffected by three-and four-body correlations, in contrast with the translational line shapes [40,165].

Additional narrow features are expected near the Rayleigh line center and the $S_0(j)$ lines, due to bound dimers [174]. These are not represented in the calculations of Gustafsson, Frommhold, Li, and Hunt [66], which primarily involve free-to-free transitions. The calculations in Ref. 66 do include pre-dissociating dimer states (having energies higher than the asymptotic potential energy), however. These decay and give rise to weak structures near the $S_0(0) + S_0(0)$ band close to 700 cm^{-1}, but the effects are not discernible in the calculated spectrum at 36 K [66].

At 50 K, the roto-translational Raman intensities have been determined experimentally [71], out to 800 cm^{-1} (and slightly beyond). The spectrum has been calculated for a gas composition of 65% para-hydrogen and 35% ortho-hydrogen; see Fig. 4 in Ref. 66. In addition to the prominent $S_0(0)$ line at 354.4 cm^{-1}, the ortho-hydrogen $S_0(1)$ line centered at 587.3 cm^{-1} is present in the spectrum, and the double transition near 700 cm^{-1} appears as a shoulder on the high-frequency side of the $S_0(1)$ line. Generally, the close-coupled calculation reproduces the experimental spectrum well [66], while the IPA approximation (above 150 cm^{-1}) does not. However, unexplained differences remain between the close-coupled theory and experimental intensities. Above 700 cm^{-1}, the difference amounts to more than a factor of two.

We note that the trace spectrum of H_2 and an appropriately scaled trace spectrum of D_2 at 296 K have been reproduced for the first time, within the experimental error bars [70], based on the *ab initio* values of $\Delta\alpha$ from Ref. 5 and the isotropic potential approximation for the scattering [66]. Calculations based on the second-order DID trace lead to intensities that are too small by a factor of $\sim$5.

10. Summary and relation to other work

In Table 1, we have listed the coefficients $A_{2\lambda\lambda'\Lambda L}$ for the spherical-harmonic expansion of the second-rank collision-induced polarizability, derived from a direct fit of the *ab initio* calculations of Li, Ahuja, Harrison, and Hunt [5], with CCSD(T) methods and an aug-cc-pV5Z basis. A comparison of these coefficients with the few-parameter fit by Gustafsson, Frommhold, Li, and Hunt [66] shows excellent agreement. At long range – when $R \gtrsim 5$ a.u or 6 a.u., depending on the coefficient – we find excellent agreement with the results from perturbation theory [18] for the larger coefficients. Agreement is found not only for the coefficients that are dominated by the first-order dipole-induced-dipole effects, but also for coefficients that vary as R^{-5} at leading order. At shorter range, exchange, overlap damping, and orbital distortion tend to reduce the coefficients below their long-range values.

Increases in computer speed and memory – as well as advances in *ab initio* computational methods – have made it possible to calculate collision-induced properties accurately. Examples involving H_2 interactions include the current work, the work of Haskopoulos and Maroulis [181] on the polarizability and β hyperpolarizability of $H_2 \cdots He$, and the work of Bancewicz and Maroulis on the polarizability [182] and hyperpolarizability [183] of $H_2 \cdots Ar$. Beginning with the calculations by Dacre of the pair polarizability of helium at the single- and double-excitation configuration interaction level [184,185], extensive studies based on fourth-order Møller-Plesset perturbation theory (MP4) [186], symmetry-adapted perturbation theory (SAPT) [187,188], CCSD methods [189], smaller-basis full configuration-interaction calculations [189], and explicitly correlated CCSD(T)-R12 calculations [190] have led to very accurate determinations of the trace and anisotropy of the polarizability of $He \cdots He$. Similarly, accurate results for the polarizabilities of heavier inert gas pairs have become available, with correlation effects treated by SAPT methods [191] for Ne_2, at the CCSD [192] and CCSD(T) [147] levels for Ne_2, at second-order Møller-Plesset (MP2) level with a frozen core for Ar_2 [193], at CCSD level for Ar_2 [189, 194], at MP2 level for Xe_2 [195], from density functional theory (DFT) with the B3LYP functional for Xe_2 [195], and from time-dependent DFT with the Amsterdam Density Functional package for Xe_2 [196]. Pair polarizabilities for heavy hetero-diatoms such as $Kr \cdots Xe$ have also been determined at the MP2 and B3LYP/DFT levels [197]. Dispersion polarizability coefficients have been calculated not only for pairs containing H, He, and H_2 [65], but also for pairs containing Ne, Ar, Kr and N_2 [198]. Relativistic DFT methods have been used to obtain the polarizability of Hg_2 [199]. Calculations at the MP2 level have provided results for the collision-induced polarizability of CO_2 interacting with He, Ne, Ar, Kr, or Xe [200]. Recently, *ab initio* work on collision-induced polarizabilities has been extended to include frame-distortion effects in a system with a relatively large number of degrees of freedom, $CH_4 \cdots N_2$ [201].

Beginning with the work of Proffitt, Keto, and Frommhold [202], quantum mechanical line shapes for collision-induced light scattering have been obtained with *ab initio* values of $\Delta\alpha$ that include correlation effects [184]. In addition to further analysis of the isotropic [203,204] and anisotropic [204,205] light scattering by $He \cdots He$, line shapes have been calculated recently for the collision-induced Rayleigh spectra extending into the far wings for neon gas [206] and for neon/argon [207], and krypton/xenon [208] mixtures. Related properties such as dielectric and refractivity virial coefficients [209] have also been determined from high quality *ab initio* results for $\Delta\alpha$ (see, e.g., Refs. 192 and 210). Papadopoulos and Waite carried out an early investigation of interaction-induced hyperpolarizabilities of He_2, Ne_2, and He_3 at self-consistent field level [211]. This work was followed by the experimental determination of hyperpolarizability virial coefficients [212] and by calculations at the CCSD(T) level [147]. Accurate calculations of collision-induced β hyperpolarizabilities have now made it possible to compute collision-induced hyper-Rayleigh spectra from first principles for systems including $He \cdots Ne$ [213], $He \cdots$

Ar [214], Ne $\cdots$ Ar [215,216], Kr $\cdots$ Xe [217], $H_2 \cdot \cdot$ He [218], and $H_2 \cdots$ Ar [219]. Studies of the optical Kerr effect on the femtosecond time scale [220–227] and transient grating experiments [228,229] offer further challenges for computational work on interaction-induced changes in the polarizabilities of molecules in condensed phases.

The far wings of the Rayleigh spectra (i.e., the collision-induced rotational Raman spectra) of polyatomic molecules in the gas phase provide information on higher-multipole polarizabilities. The light scattering intensities depend upon the dipole-quadrupole polarizability A and the dipole-octopole polarizability E for tetrahedral molecules such as CH_4 [21,230–232] and CF_4 [21,233,234], and upon the dipole-octopole polarizability E for octahedral molecules, such as SF_6 [21]. Although $\Delta\alpha$ for these species is expected to differ from the multipolar-induction form at short range, agreement is excellent between the values of A and E derived from the spectra [230–232] and the *ab initio* values: For CH_4, the value of A obtained by Amos [235] from a single- and double-excitation configuration-interaction calculation lies just outside the error bars of the most recent determination of A from the isotropic scattering spectrum [231], but within the error bars of the value derived from the anisotropic scattering spectrum [232]. The value of A for CH_4 obtained by Maroulis at CCSD(T) level [47] lies within the experimental error bars from both sources [231,232]; and the two *ab initio* values of E [47,235] lie within the somewhat larger error bars from both the isotropic [231] and the anisotropic [232] scattering spectra. The values of A and E obtained by Maroulis at MP4 level for CF_4 [47] agree with the best values determined experimentally [233,234]; however, these values yield intensities that are too low at the highest frequency shifts observed in experiments – a probable indicator of short-range effects in $\Delta\alpha$. For SF_6, the value of E derived from the roto-translational light scattering spectrum [236] depends on the pair potential used for the analysis [236], but the recommended value of E is consistent with the MP2 result obtained by Maroulis [237]. The derivative of the E-tensor with respect to the normal mode coordinate for the ν_1 vibration has been obtained from collision-induced vibrational Raman intensities [238], in this case agreeing in order of magnitude with the *ab initio* derivative [237]. The collision-induced hyper-Rayleigh spectrum has also been calculated for SF_6 [239].

Ab initio methods for calculating pair polarizabilities have now advanced sufficiently to predict experimental spectra for binary collision-induced Rayleigh and roto-vibrational Raman light scattering. It has also become possible to predict hyper-Rayleigh and roto-vibrational hyper-Raman scattering spectra, based on β-hyperpolarizability calculations for pairs of molecules. At the same time, single-molecule properties are needed to evaluate collision-induced polarizability coefficients (such as $A_{2\lambda\lambda'\Lambda L}$) derived from perturbation theory, in order to test *ab initio* results for convergence to the perturbation-theoretic forms at long range, as found here. Similarly, experimental line shape studies highlight the significance and utility of accurate calculations of the multipole moments, polarizabilities, and hyperpolarizabilities of individual molecules.

Acknowledgments

This work has been supported in part by the National Science Foundation, through Grants AST-0708496, CHE-9817297, CHE-9974834 (to KLCH), and AST-0709106 (to LF).

References

[1] *Phenomena Induced by Intermolecular Interactions*, edited by G. Birnbaum, Plenum, New York, 1985.
[2] *A Symposium on Interaction-Induced Spectra in Dense Fluids and Disordered Solids*, *J Chem Soc, Faraday Trans 2* **83** (1987).

[3] A. Borysow and L. Frommhold, *Adv Chem Phys* **75** (1989), 439.
[4] *Collision- and Interaction-Induced Spectroscopy*, edited by G.C. Tabisz and M.N. Neuman, Kluwer, Dordrecht, 1995.
[5] X. Li, C. Ahuja, J.F. Harrison and K.L.C. Hunt, *J Chem Phys* **126** (2007), 214302.
[6] K. Raghavachari, G.W. Trucks, J.A. Pople and M. Head-Gordon, *Chem Phys Lett* **157** (1989), 479.
[7] Z. He and D. Cremer, *Theor Chim Acta* **85** (1993), 305.
[8] M.J.O. Deegan and P.J. Knowles, *Chem Phys Lett* **227** (1994), 321.
[9] J. Čížek, *J Chem Phys* **45** (1966), 4256.
[10] J. Čížek, *Adv Chem Phys* **14** (1969), 35.
[11] J. Čížek and J. Paldus, *Int J Quantum Chem* **5** (1971), 359.
[12] G.D. Purvis and R.J. Bartlett, *J Chem Phys* **76** (1982), 1910.
[13] C. Hampel, K.A. Peterson and H.-J. Werner, *Chem Phys Lett* **190** (1992), 1.
[14] T.H. Dunning, Jr., *J Chem Phys* **90** (1989), 1007.
[15] R.A. Kendall, T.H. Dunning, Jr. and R.J. Harrison, *J Chem Phys* **96** (1992), 6796.
[16] K.A. Peterson, R.A. Kendall and T.H. Dunning, Jr., *J Chem Phys* **99** (1993), 9790.
[17] X. Li, J.F. Harrison, M. Gustafsson, F. Wang, M. Abel, L. Frommhold and K.L.C. Hunt, *ICCMSE 2009, AIP Conference Proceedings/Atomic, Molecular, Chemical Physics*, edited by G. Maroulis and T.E. Simos (to be published).
[18] X. Li and K.L.C. Hunt, *J Chem Phys* **100** (1994), 7875.
[19] L. Silberstein, *Philos Mag* **33** (1917), 92, 521.
[20] T. Bancewicz, V. Teboul and Y. Le Duff, *Phys Rev A* **46** (1992), 1349.
[21] A.D. Buckingham and G.C. Tabisz, *Mol Phys* **36** (1978), 583.
[22] A. Borysow and M. Moraldi, *Phys Rev A* **48** (1993), 3036.
[23] A.D. Buckingham, *Adv Chem Phys* **12** (1967), 107.
[24] K.L.C. Hunt, Y.Q. Liang and S. Sethuraman, *J Chem Phys* **89** (1988), 7126.
[25] A.D. Buckingham, *Trans Faraday Soc* **52** (1956), 1035.
[26] A.D. Buckingham and K.L. Clarke, *Chem Phys Lett* **57** (1978), 321.
[27] K.L.C. Hunt, B.A. Zilles and J.E. Bohr, *J Chem Phys* **75** (1981), 3079.
[28] K.L.C. Hunt and J.E. Bohr, *J Chem Phys* **84** (1986), 6141.
[29] A. J. Stone, *Mol Phys* **29** (1975), 1461.
[30] T. Bancewicz, *Mol Phys* **50** (1983), 173.
[31] T. Bancewicz, *Chem Phys* **111** (1987), 409.
[32] M. Kaźmierczak and T. Bancewicz, *J Chem Phys* **80** (1984), 3504.
[33] T. Bancewicz, W. Głaz and S. Kielich, *Chem Phys* **128** (1988), 321.
[34] T. Bancewicz, W. Głaz and S. Kielich, *Phys Lett A* **148** (1990), 78.
[35] W. Głaz, *Physica A* **148** (1988), 610.
[36] W. Głaz, *Mol Phys* **74** (1991), 1019.
[37] S. Kielich, T. Bancewicz and S. Woźniak, *Can J Phys* **59** (1981), 1620.
[38] S. Kielich, *J Phys* (*Paris*) **29** (1968), 619.
[39] S. Kielich, *J Phys* (*Paris*) **43** (1982), 1749.
[40] D. Frenkel and J.P. McTague, *J Chem Phys* **72** (1980), 2801.
[41] R. Samson and A. Ben-Reuven, *J Chem Phys* **65** (1976), 3586.
[42] G. Maroulis, *J Chem Phys* **118** (2003), 2673.
[43] G. Maroulis, *J Mol Struct THEOCHEM* **98** (1993), 79.
[44] G. Maroulis, *Chem Phys Lett* **396** (2004), 66.
[45] G. Maroulis, *Chem Phys* **291** (2003), 81.
[46] G. Maroulis, *Chem Phys Lett* **199** (1992), 250.
[47] G. Maroulis, *J Chem Phys* **105** (1996), 8467.
[48] G. Maroulis, *J Phys B* **26** (1993), 775.
[49] G. Maroulis, *Chem Phys Lett* **177** (1991), 352.
[50] G. Maroulis and A.J. Thakkar, *J Chem Phys* **88** (1988), 7623.
[51] G. Maroulis and A.J. Thakkar, *J Chem Phys* **90** (1989), 366.
[52] G. Maroulis and A.J. Thakkar, *J Chem Phys* **93** (1990), 4164.
[53] G. Maroulis and A.J. Thakkar, *J Chem Phys* **95** (1991), 9060.
[54] G. Maroulis and U. Hohm, *Phys Rev A* **76** (2007), 032504.
[55] U. Hohm and G. Maroulis, *J Chem Phys* **124** (2006), 124312.
[56] U. Hohm and G. Maroulis, *J Chem Phys* **121** (2004), 10411.
[57] G. Maroulis and C. Makris, *Mol Phys* **91** (1997), 333.
[58] G. Maroulis, C. Makris, U. Hohm and D. Goebel, *J Phys Chem A* **101** (1997), 953.
[59] A. Haskopoulos and G. Maroulis, *Chem Phys Lett* **417** (2006), 235.

[60] G. Maroulis, D. Xenides, U. Hohm and A. Loose, *J Chem Phys* **115** (2001), 7957.
[61] J.D. Poll and L. Wołniewicz, *J Chem Phys* **68** (1978), 3053.
[62] F. Visser, P.E.S. Wormer and W.P.J.H. Jacobs, *J Chem Phys* **82** (1985), 3753.
[63] D. M. Bishop and J. Pipin, *Int J Quantum Chem* **45** (1993), 349.
[64] Static B-values provided by D.M. Bishop, personal communication; values of the B-tensor at imaginary frequencies have been reported by D.M. Bishop and J. Pipin, *J Chem Phys* **98** (1993), 4003.
[65] D.M. Bishop and J. Pipin, *J Chem Phys* **97** (1992), 3375.
[66] M. Gustafsson, L. Frommhold, X. Li and K.L.C. Hunt, *J Chem Phys* **130** (2009), 164314.
[67] L. Ulivi and M. Zoppi, *Mol Phys* **90** (1997), 971.
[68] D.G. Bounds, *Mol Phys* **38** (1979), 2099.
[69] U. Bafile, M. Zoppi, F. Barocchi, M.S. Brown and L. Frommhold, *Phys Rev A* **40** (1989), 1654.
[70] M.S. Brown, S.K. Wang and L. Frommhold, *Phys Rev A* **40** (1989), 2276.
[71] U. Bafile, L. Ulivi, M. Zoppi, F. Barocchi, M. Moraldi and A. Borysow, *Phys Rev A* **42** (1990), 6916.
[72] X. Li, K.L.C. Hunt, F. Wang, M. Abel and L. Frommhold, *Int J Spectrosc* **2010** (2010), 371201.
[73] L. Frommhold, M. Abel, F. Wang, M. Gustafsson, X. Li and K.L.C. Hunt, *Mol Phys* **108** (2010), 2265.
[74] S. Kielich, *Mol. Phys.* **6** (1963), 49.
[75] S. Kielich, *Phys. Lett. A* **24** (1967), 383.
[76] S. Kielich, *Proc Phys Soc London* **86** (1965), 709.
[77] S. Kielich, *Chem Phys Lett* **2** (1968), 569.
[78] S. Kielich, *Phys Lett A* **27** (1968), 307.
[79] S. Kielich, *J Chem Phys* **46** (1967), 4090.
[80] S. Kielich, *Proc Indian Acad Sci Chem Sci* **94** (1985), 403.
[81] S. Kielich, *Chem Phys Lett* **10** (1971), 516.
[82] S. Kielich, J.R. Lalanne and F.B. Martin, *Phys Rev Lett* **26** (1971), 1295.
[83] J.R. Lalanne, F.B. Martin and S. Kielich, *Chem Phys Lett* **30** (1975), 73.
[84] Z. Ożgo and S. Kielich, *Physica* **72** (1974), 191.
[85] T. Bancewicz, Z. Ożgo and S. Kielich, *Acta Phys Polonica* **47** (1975), 645.
[86] T. Bancewicz and S. Kielich, *Mol Phys* **31** (1976), 615.
[87] M. Kozierowski and S. Kielich, *Acta Phys Polonica A* **66** (1984), 753.
[88] M. Kozierowski, Z. Ożgo and S. Kielich, *J Chem Phys* **84** (1986), 5271.
[89] T. Bancewicz and S. Kielich, *J. Raman Spectrosc* **21** (1990), 207.
[90] S. Kielich and T. Bancewicz, *J Raman Spectrosc* **21** (1990), 791.
[91] W. Chmielowski, K. Knast and S. Kielich, *Physica A* **154** (1988), 89.
[92] W. Chmielowski, K. Knast and S. Kielich, *Physica A* **170** (1991), 624.
[93] J. Skupinski, J. Buchert, S. Kielich, J. R. Lalanne and B. Pouligny, *Acta Phys Polonica A* **67** (1985), 719.
[94] J. R. Lalanne, E. Sein, J. Buchert and S. Kielich, *Appl Phys Lett* **36** (1980), 973.
[95] S. Kielich and R. Zawodny, *Optica Acta* **20** (1973), 867.
[96] S. Kielich and R. Zawodny, *Physica B & C* **89** (1977), 122.
[97] N.L. Manakov, V.D. Ovsiannikov and S. Kielich, *Acta Phys Polonica A* **53** (1978), 581.
[98] N.L. Manakov, V.D. Ovsiannikov and S. Kielich, *Acta Phys Polonica A* **53** (1978), 595.
[99] S. Kielich, N.L. Manakov and V.D. Ovsiannikov, *Acta Phys Polonica A* **53** (1978), 737.
[100] N.L. Manakov, V.D. Ovsiannikov and S. Kielich, *Phys Rev A* **21** (1980), 1589.
[101] S. Kielich, *Chem Phys Lett* **33** (1975), 79.
[102] S. Kielich and R. Zawodny, *Opt Comm* **15** (1975), 267.
[103] S. Woźniak and S. Kielich, *J Chem Phys* **94** (1991), 7588.
[104] J.R. Lalanne, B. Martin, B. Pouligny and S. Kielich, *Opt Comm* **18** (1976), 197.
[105] J.R. Lalanne, B. Martin, B. Pouligny and S. Kielich, *Opt Comm* **18** (1976), 440.
[106] V. Peřinová, J. Peřina, P. Szlachetka and S. Kielich, *Acta Phys Polonica* **56** (1979), 267.
[107] V. Peřinová, J. Peřina, P. Szlachetka and S. Kielich, *Acta Phys Polonica* **56** (1979), 275.
[108] P. Szlachetka, S. Kielich, J. Peřina and V. Peřinová, *J Phys A* **12** (1979), 1921.
[109] P. Szlachetka, S. Kielich, J. Peřina and V. Peřinová, *Optica Acta* **27** (1980), 1609.
[110] P. Chmela, Z. Ficek and S. Kielich, *Czech J Phys* **39** (1989), 509.
[111] P. Chmela, Z. Ficek and S. Kielich, *Czech J Phys* **39** (1989), 642.
[112] Z. Ficek, S. Kielich and P. Chmela, *Opt Quant Electron* **22** (1990), 123.
[113] Z. Ficek, R. Tanaś and S. Kielich, *Phys Rev A* **29** (1984), 2004.
[114] Z. Ficek, R. Tanaś and S. Kielich, *J Opt Soc Am B* **1** (1984), 882.
[115] Z. Ficek, R. Tanaś and S. Kielich, *Optica Acta* **33** (1986), 1149.
[116] Z. Ficek, R. Tanaś and S. Kielich, *Physica A* **146** (1987), 452.

[117] Z. Ficek, R. Tanaś and S. Kielich, *J Mod Opt* **35** (1988), 81.
[118] Z. Ficek, R. Tanaś and S. Kielich, *J Phys* (*Paris*) **48** (1987), 1697.
[119] Z. Ficek, R. Tanaś and S. Kielich, *Opt Comm* **69** (1988), 20.
[120] R. Tanaś and S. Kielich, *Opt Comm* **45** (1983), 351.
[121] R. Tanaś and S. Kielich, *Opt Acta* **31** (1984), 81.
[122] S. Kielich, R. Tanaś and R. Zawodny, *J Mod Opt* **34** (1987), 979.
[123] S. Kielich, R. Tanaś and R. Zawodny, *J Opt Soc Am B* **4** (1987), 1627.
[124] S. Kielich, R. Tanaś and R. Zawodny, *Phys Rev A* **36** (1987), 5670.
[125] S. Kielich, R. Tanaś and R. Zawodny, *App Phys B* **45** (1988), 249.
[126] R. Tanaś, A. Miranowicz and S. Kielich, *Phys Rev A* **43** (1991), 4014.
[127] S. Kielich, *Acta Phys Polonica* **19** (1960), 149, 711.
[128] S. Kielich, *Acta Phys Polonica* **22** (1962), 299.
[129] S. Woźniak and S. Kielich, *Acta Phys Polonica A* **52** (1977), 863.
[130] K. Knast, W. Chmielowski and S. Kielich, *J Mol Struct* **61** (1980), 137.
[131] S. Kielich, *Opt Comm* **34** (1980), 367.
[132] T. Bancewicz and S. Kielich, *J Chem Phys* **75** (1981), 107.
[133] S. Kielich, *J Phys Lett* (*Paris*) **43** (1982), L389.
[134] T. Bancewicz, S. Kielich and W.A. Steele, *Mol Phys* **54** (1985), 637.
[135] J.P. McTague and G. Birnbaum, *Phys Rev Lett* **21** (1968), 661.
[136] A.D. Buckingham and M.J. Stephen, *Trans Faraday Soc* **53** (1957), 884.
[137] O. Theimer and R. Paul, *J Chem Phys* **42** (1965), 2508.
[138] B.U. Felderhof, *Physica* **76** (1974), 486.
[139] T. Keyes, *J Chem Phys* **70** (1979), 5438.
[140] B.M. Ladanyi and T. Keyes, *Mol Phys* **33** (1977), 1063.
[141] B.M. Ladanyi and T. Keyes, *Mol Phys* **33** (1977), 1247.
[142] B.M. Ladanyi, *J Chem Phys* **78** (1983), 2189.
[143] T. Bancewicz, *Chem Phys Lett* **213** (1993), 363.
[144] H.-J. Werner, P.J. Knowles, J. Almlöf *et al*., MOLPRO, Version 2000.1, Universität Stuttgart and Cardiff University, 2000.
[145] M.J. Frisch, G.W. Trucks, H.B. Schlegel *et al*., GAUSSIAN 98, Revision A.11.1, Gaussian, Inc., Pittsburgh, PA, 2001.
[146] S.F. Boys and F. Bernardi, *Mol Phys* **19** (1970), 553.
[147] G. Maroulis, *J Phys Chem A* **104** (2000), 4772.
[148] B.J. Berne and R. Pecora, *Dynamic Light Scattering*, Wiley-Interscience, New York, 1976. The sign of $\Delta\alpha^{(2)}_{\pm 1}$ in Eq. (3) differs from this reference.
[149] R.N. Zare, *Angular Momentum*, Wiley-Interscience, New York, 1988.
[150] A. Borysow and M. Moraldi, *Phys Rev A* **40** (1989), 1251.
[151] M.H. Proffitt, J.W. Keto and L. Frommhold, *Can J Phys* **59** (1981), 1459.
[152] M. Moraldi, A. Borysow and L. Frommhold, *Chem Phys* **86** (1984), 339.
[153] A.D. Buckingham, P.H. Martin and R.S. Watts, *Chem Phys Lett* **21** (1973), 186.
[154] P.R. Certain and P.J. Fortune, *J Chem Phys* **55** (1971), 5818.
[155] P.W. Fowler, K.L.C. Hunt, H.M. Kelly and A.J. Sadlej, *J Chem Phys* **100** (1994), 2932.
[156] U. Bafile, L. Ulivi, M. Zoppi and F. Barocchi, *Phys Rev A* **37** (1988), 4133.
[157] U. Bafile, L. Ulivi, M. Zoppi, M. Moraldi and L. Fromhold, *Phys Rev A* **44** (1991), 4450.
[158] U. Bafile, L. Ulivi, M. Zoppi and F. Barocchi, *Chem Phys Lett* **117** (1985), 247.
[159] M.S. Brown and L. Frommhold, *Mol Phys* **66** (1989), 527.
[160] M.S. Brown, M.H. Proffitt and L. Frommhold, *Chem Phys Lett* **117** (1985), 243.
[161] Y. Le Duff and R. Ouillon, *J Chem Phys* **82** (1985), 1.
[162] P.A. Fleury and J.P. McTague, *Phys Rev Lett* **31** (1973), 914.
[163] J.P. McTague and P.A. Fleury, *Bull Am Phys Soc* **20** (1975), 44.
[164] F. Barocchi, M. Moraldi, M. Santoro, L. Ulivi and M. Zoppi, *Phys Rev B* **55** (1997), 12223.
[165] M. Zoppi, L. Ulivi, M. Santoro, M. Moraldi and F. Barocchi, *Phys Rev A* **53** (1996), R1935.
[166] K.D. Van Den Hout, P.W. Hermans, E. Mazur and H.F.P. Knaap, *Physica A* **104** (1980), 509.
[167] K.D. Van Den Hout, P.W. Hermans and H.F.P. Knaap, *Physica A* **104** (1980), 548.
[168] J. Fiutak and J. Van Kranendonk, *Can J Phys* **41** (1963), 21.
[169] D.A. Coombe and W.E. Köhler, *Physica A* **100** (1980), 2801.
[170] A. Crane and H.P. Gush, *Can J Phys* **44** (1966), 373.
[171] F. Barocchi, A. Guasti, M. Zoppi, J.D. Poll and R.H. Tipping, *Phys Rev B* **37** (1988), 8377.
[172] M. Moraldi, A. Borysow and L. Frommhold, *J Chem Phys* **88** (1988), 5344.

[173] Y. Le Duff, *J Phys B* **14** (1981), 55.
[174] M.S. Brown and L. Frommhold, *Chem Phys Lett* **127** (1986), 197.
[175] L. Frommhold, J.D. Poll and R.H. Tipping, *Phys Rev A* **46** (1992), 2955.
[176] M. Gustafsson, L. Frommhold, D. Bailly, J.-P. Bouanich and C. Brodbeck, *J Chem Phys* **119** (2003), 12264.
[177] M. Gustafsson, Ph.D. Thesis, University of Texas at Austin, 2002.
[178] F.H. Mies, P.S. Julienne and K.M. Sando, personal communication to L. Frommhold, 1993.
[179] L. Frommhold, *Adv Chem Phys* **46** (1981), 1.
[180] F.H. Mies, in: *Theoretical Chemistry: Advances and Perspectives*, D. Henderson, ed., Academic, New York, 1981, Vol. 6B, pp. 127–198.
[181] A. Haskopoulos and G. Maroulis, *Chem Phys* **367** (2010), 127.
[182] T. Bancewicz and G. Maroulis, *Chem Phys Lett* **471** (2009), 148.
[183] T. Bancewicz and G. Maroulis, *Phys Rev A* **79** (2009), 042704.
[184] P.D. Dacre, *Mol Phys* **36** (1978), 541.
[185] P.D. Dacre, *Mol Phys* **45** (1982), 17.
[186] D.M. Bishop and M. Dupuis, *Mol Phys* **88** (1996), 887.
[187] R. Moszyński, T.G.A. Heijmen, P.E.S. Wormer and A. van der Avoird, *J Chem Phys* **104** (1996), 6997.
[188] T.G.A. Heijmen, R. Moszyński, P.E.S. Wormer and A. van der Avoird, *Mol Phys* **89** (1996), 81.
[189] C. Hättig, H. Larsen, J. Olsen, P. Jørgensen, H. Koch, B. Fernández and A. Rizzo, *J Chem Phys* **111** (1999), 10099.
[190] M. Jaszuński, W. Klopper and J. Noga, *J Chem Phys* **113** (2000), 71.
[191] F. Rachet, M. Chrysos, G. Lothon, R. Moszyński and A. Milet, *J Raman Spectrosc* **34** (2003), 972.
[192] C. Hättig, J.L. Cacheiro, B. Fernández and A. Rizzo, *Mol Phys* **101** (2003), 1983.
[193] C.G. Joslin, J.D. Goddard and S. Goldman, *Mol Phys* **89** (1996), 791.
[194] B. Fernández, C. Hättig, H. Koch and A. Rizzo, *J Chem Phys* **110** (1999), 2872.
[195] G. Maroulis, A. Haskopoulos and D. Xenides, *Chem Phys Lett* **396** (2004), 59.
[196] N.H. Boeijenga, A. Pugzlys, T.L.C. Jansen, J.G. Snijders and K. Duppen, *J Chem Phys* **117** (2002), 1181.
[197] A. Haskopoulos, D. Xenides and G. Maroulis, *Chem Phys* **309** (2005), 271.
[198] M. Jaszuński, A. Rizzo and P. Jørgensen, *Theor Chem Acc* **106** (2001), 251.
[199] N. Gaston, P. Schwerdtfeger, T. Saue and J. Greif, *J Chem Phys* **124** (2006), 044304.
[200] G. Maroulis and A. Haskopoulos, *Chem Phys Lett* **349** (2001), 335.
[201] M.A. Buldakov, V.N. Cherepanov, Y.N. Kalugina, N. Zvereva-Loete and V. Boudon, *J Chem Phys* **132** (2010), 164304.
[202] M.H. Proffitt, J.W. Keto and L. Frommhold, *Phys Rev Lett* **45** (1980), 1843.
[203] F. Rachet, Y. Le Duff, C. Guillot-Noel and M. Chrysos, *Phys Rev A* **61** (2000), 062501.
[204] C. Guillot-Noel, Y. Le Duff, F. Rachet and M. Chrysos, *Phys Rev A* **66** (2002), 012505.
[205] C. Guillot-Noel, M. Chrysos, Y. Le Duff and F. Rachet, *J Phys B* **33** (2000), 569.
[206] M. Chrysos, S. Dixneuf and F. Rachet, *Phys Rev A* **80** (2009), 054701.
[207] S. Dixneuf, M. Chrysos and F. Rachet, *Phys Rev A* **80** (2009), 022703.
[208] S. Dixneuf, M. Chrysos and F. Rachet, *J Chem Phys* **131** (2009), 074304.
[209] H.J. Achtermann, G. Magnus and T.K. Bose, *J Chem Phys* **94** (1991), 5669.
[210] H. Koch, C. Hättig, H. Larsen, J. Olsen, P. Jørgensen, B. Fernández and A. Rizzo, *J Chem Phys* **111** (1999), 10108.
[211] M.G. Papadopoulos and J. Waite, *Chem Phys Lett* **135** (1987), 361.
[212] E.A. Donley and D.P. Shelton, *Chem Phys Lett* **215** (1993), 156.
[213] W. Głaz, T. Bancewicz, J.-L. Godet, G. Maroulis and A. Haskopoulos, *Phys Rev A* **73** (2006), 042708.
[214] G. Maroulis, A. Haskopoulos, W. Głaz, T. Bancewicz and J.-L. Godet, *Chem Phys Lett* **428** (2006), 28.
[215] G. Maroulis and A. Haskopoulos, *Chem Phys Lett* **358** (2002), 64.
[216] W. Głaz and T. Bancewicz, *J Chem Phys* **118** (2003), 6264.
[217] W. Głaz, T. Bancewicz and J.-L. Godet, *J Chem Phys* **122** (2005), 224323.
[218] J.-L. Godet, T. Bancewicz, W. Głaz, G. Maroulis and A. Haskopoulos, *J Chem Phys* **131** (2009), 204305.
[219] T. Bancewicz, W. Głaz, J.-L. Godet and G. Maroulis, *J Chem Phys* **129** (2008), 124306.
[220] D. McMorrow, W.T. Lotshaw and G.A. Kenney-Wallace, *IEEE J Quantum Electron* **24** (1988), 443.
[221] D. McMorrow, N. Thantu, J.S. Melinger, S.K. Kim and W.T. Lotshaw, *J Phys Chem* **100** (1996), 10389.
[222] R.A. Farrer, B.J. Loughnane, L.A. Deschenes and J.T. Fourkas, *J Chem Phys* **106** (1997), 6901.
[223] T. Steffen, N.A.C.M. Meinders and K. Duppen, *J Phys Chem A* **102** (1998), 4213.
[224] X.D. Ji, H. Ahlborn, B. Space, P.B. Moore, Y. Zhou, S. Constantine and L.D. Ziegler, *J Chem Phys* **112** (2000), 4186.
[225] X. D. Ji, H. Ahlborn, B. Space and P.B. Moore, *J Chem Phys* **113** (2000), 8693.
[226] K. Kiyohara, Y. Kimura, Y. Takebayashi, N. Hirota and K. Ohta, *J Chem Phys* **117** (2002), 9867.
[227] H. Shirota, T. Fujisawa, H. Fukazawa and K. Nishikawa, *Bull Chem Soc Japan* **82** (2009), 1347.
[228] S. Ruhman, L.R. Williams, A.G. Joly and K.A. Nelson, *J Phys Chem* **91** (1987), 2237.
[229] A. Waldman, U. Banin, E. Rabani and S. Ruhman, *J Phys Chem* **96** (1992), 10840.

[230] N. Meinander, G.C. Tabisz, F. Barocchi and M. Zoppi, *Mol Phys* **89** (1996), 521.
[231] T. Bancewicz, K. Nowicka, J.-L. Godet and Y. Le Duff, *Phys Rev A* **69** (2004), 062704.
[232] M.S.A. El-Kader, S.M. El-Sheikh, T. Bancewicz and R. Hellmann, *J Chem Phys* **131** (2009), 044314.
[233] A. Elliasmine, J.-L. Godet, Y. Le Duff and T. Bancewicz, *Phys Rev A* **55** (1997), 4230.
[234] A. Elliasmine, J.-L. Godet, Y. Le Duff and T. Bancewicz, *Mol Phys* **90** (1997), 147.
[235] R.D. Amos, *Mol Phys* **38** (1979), 33.
[236] K. Nowicka, T. Bancewicz, J.-L. Godet, Y. Le Duff and F. Rachet, *Mol Phys* **101** (2003), 389.
[237] G. Maroulis, *Chem Phys Lett* **312** (1999), 255.
[238] Y. Le Duff, J.-L. Godet, T. Bancewicz and K. Nowicka, *J Chem Phys* **118** (2003), 11009.
[239] T. Bancewicz, J.-L. Godet and G. Maroulis, *J Chem Phys* **115** (2001), 8547.

Journal of Computational Methods in Sciences and Engineering 10 (2010) 387–409
DOI 10.3233/JCM-2010-0329
IOS Press

Stimulated thermal scattering induced by two-photon absorption and experimental observation of genuine stimulated brillouin scattering in the near-ultraviolet region

V.B. Karpov and V.V. Korobkin
Coherent and Nonlinear Optics Department, A.M.Prokhorov General Physics Institute, Russian Academy of Sciences, Vavilov Street 38, 119991 Moscow, Russia
E-mail: karpov@kapella.gpi.ru; korobkin@kapella.gpi.ru

Abstract. Some of the experimental measurements of the frequency shift and phase-conjugation fidelity gained from previous studies of stimulated scattering (SS) of nanosecond (5 ÷ 10 ns) near-ultraviolet (uv) ($\lambda = 193 \div 351$ nm) laser pulses in liquids (hexane, heptane, and others) are found to disagree with the theory of SS, which takes into account only the linear (single-photon) light absorption. To resolve the inconsistency, SS of XeCl excimer laser radiation ($\lambda = 308$ nm) with the duration of 8 ns in liquid hexane is investigated experimentally. A theoretical analysis of the results obtained revealed three nonlinear optical phenomena induced by the heating due to two-photon absorption: stimulated thermal scattering (two-photon STS-2), phase mismatch for stimulated Brillouin scattering (SBS), and phase self-modulation. The experimental SS spectrum contains two additional lines – a two-photon STS-2 line and a genuine SBS line in the near-uv region.

1. Introduction

Stimulated scattering (SS) is widely used in scientific research and practical applications [1–5]. This motivates studies of the physical mechanisms responsible for SS in various spectral regions. An important application is phase conjugation (PC) via stimulated backscattering [6]. Various SS mechanisms have specific characteristics (frequency shift, decay time, etc.) that manifest themselves in the PC mirror properties [4].

Detailed experimental studies of SS have been conducted only in the near-infrared (near-ir) region. For such experiments the pump radiation must have both high power and narrow bandwidth. The first sources of this kind were Q-switched single-mode ruby ($\lambda = 0.69$ μm) and Nd:glass ($\lambda = 1.06$ μm) lasers. For weak linear absorption, stimulated Brillouin scattering (SBS) and stimulated Raman scattering (SRS) were usually observed, and for stronger linear absorption – stimulated thermal scattering caused by the heating due to linear absorption (linear STS-2).

In the first experimental studies of SBS with near-ir pump radiation [7–10], the unshifted spectral components were expected to be the pump spectral lines. But under the experimental conditions of [7–10], the pump spectral lines could not be distinguished from slightly-shifted components corresponding, for instance, to linear STS-2.

Multiphoton absorption could not influence the experiments because $5 \div 10$ near-ir photons with energies $1 \div 2$ eV would be required to obtain the nearest electron resonance with an energy about 10 eV.

Theoretical studies of SS have mostly relied on experimental results obtained for the near-ir region, and the modern SS theory applies only to linearly absorbing media [1–5,11,12]. The theory of stimulated thermal scattering (STS) proposed in [13,14] incorporates linear absorption only.

Reliable near-ultraviolet (near-uv) radiation sources (discharge XeF, XeCl, KrF, and ArF excimer lasers) became available considerably later than the solid-state near-ir lasers. When experimentalists in the 1980-s had to deal with the PC via SS driven by excimer laser beams [15–22], the SS theory developed for the near-ir was applied to the near-uv spectral region.

2. Previous studies of stimulated scattering and phase conjugation in the near-ultraviolet region

The first studies concerning PC via SS in liquids (hexane, heptane, and others) were reported in [15] (XeF, $\lambda = 351$ nm) [18], (XeCl, $\lambda = 308$ nm) [16,19], (KrF, $\lambda = 248$ nm), and [17] (ArF, $\lambda = 193$ nm). In the above and subsequent studies [20,21], the experimental SS spectrum comprised a single shifted line, which was attributed to "SBS". Note that the frequency shift of the "SBS" line in [17–19] was comparable to the laser system spectral resolution.

The reflection coefficient of the "Brillouin" mirror measured in [19] gradually decreased with increasing pump intensity I_L from 25% at the threshold ($I_L^{THR} \approx 10^{10}$ W/cm^2) to 10% at $I_L \approx 10^{11}$ W/cm^2. Note that in this experiment the decrease in the reflection coefficient was due to the decrease in PC fidelity for the "Brillouin" mirror.

In [15,16,18,20] the PC fidelity for the "Brillouin" mirror was found to degrade with increasing linear absorption coefficient α of the nonlinear liquid.

In [22] the experimental SS spectrum obtained in hexane by using KrF laser radiation also comprised a single line, which was attributed to "linear STS-2".

The linear absorption coefficient varied from $\alpha = 0.02$ to 0.1 cm^{-1} in the studies of "SBS" [15–21] and amounted to $\alpha = 0.22$ cm^{-1} in the investigation of "linear STS-2" [22].

In order to increase the pump intensities in [15–22], the amplified laser beams were focused by lenses with focal lengths $F = 5 \div 10$ cm. The focal caustics corresponded to the volumes of the nonlinear interaction, and their lengths (see Section 6.2) were $L \leqslant 0.1$ cm. A considerable intensity attenuation due to the linear absorption over such distances occurs when $\alpha > 1$ cm^{-1}, which exceeds the values mentioned above.

The pump pulse durations in [15–22] were $\tau_0 = 5 \div 10$ ns.

Table 1 summarizes the results gained from the previous studies of stimulated backscattering in hexane for near-uv pump radiation. The first column presents a reference to the previous study; the second and third columns – the pump wavelength λ and intensity I_L; the fourth column – is the experimentally measured frequency shift Ω; the last column – is the physical mechanism, that, the authors of the reference believed to be responsible for the observed SS.

3. Inconsistency between previous experimental results and the existing theory of stimulated scattering

3.1. "SBS" frequency shift

No one in the previous studies of "SBS" [15–21] calculated the theoretically predicted frequency shift to compare it with the experimentally measured one.

Table 1
Previous studies of the stimulated backscattering in hexane for the near-uv pump radiation generated by ArF (193 nm), KrF (248 nm), XeCl (308 nm), and XeF (351 nm) excimer lasers

Reference	Pump wavelength λ nm	Pump intensity I_L, W/cm^2	Experimentally measured frequency shift in hexane Ω cm^{-1}	Physical mechanism of SS suggested by authors of the reference
[17]	193	$\approx 10^{10}$	≈ 0.2	SBS
[16]	248	$> 2 \times 10^{10}$	≈ 0.1	SBS
[19]	248	$> 10^{10}$	≈ 0.1	SBS
[18]	308	$> 10^{11}$	< 0.15	SBS
[21]	308	$> 10^{12}$	0.24	SBS
[15]	351	$> 5 \times 10^{9}$	0.2	SBS
[22]	248	$> 10^{11}$	< 0.02	Linear STS-2

Table 2
Theoretically predicted backward ($\theta = \pi$) SBS frequency shift Ω_B in hexane for the pump wavelengths listed in Table 1

Pump wavelength λ nm	Theoretically predicted SBS frequency shift in hexane $\Omega_B,\ cm^{-1}$
193	0.49
248	0.41
308	0.33
351	0.30

In accordance with the existing theory [1–5], the SBS frequency shift Ω_B depends on the pump frequency ω_L (the pump wavelength λ) and the scattering angle θ (see Eq. (13) below). Table 2 shows the values of Ω_B calculated for hexane, $\theta = \pi$, and the pump wavelengths listed in Table 1 (for the material data see Section 6.3). It is clear that for the same λ the predicted values (Table 2) disagree with the measured values attributed to "SBS" (Table 1). The disagreement, which is too large to be entirely caused by experimental errors, emerges for pump wavelengths ranging from $\lambda = 193$ to 351 nm.

3.2. Phase conjugation fidelity for "brillouin" mirror

The decrease in PC fidelity for increased the pump intensity above its threshold value detected in [19] is not dependent on SBS, because, in accordance with existing theory [4,11], strong pump saturation improves the discrimination of noise sources.

3.3. Emergence of "Linear STS-2" Component and Disappearance of "SBS" Component

Emergence of the "linear STS-2" component in [22] was explained by the increase in the linear absorption coefficient from $\alpha = 0.02 \div 0.1$ cm^{-1} mentioned in [15–21], to $\alpha = 0.22$ cm^{-1}. But it was not explained how such an increase in α could cause the suppression of "SBS" in [22]. Indeed, the "SBS" component has been observed in [15–21] for practically the same experimental conditions as in this paper.

4. Experimental setup

The problem concerns the understanding of both the temporal and the spatial behavior of the back-reflected pulses manifested in the frequency shift and the PC fidelity, respectively. The abnormal "SBS"

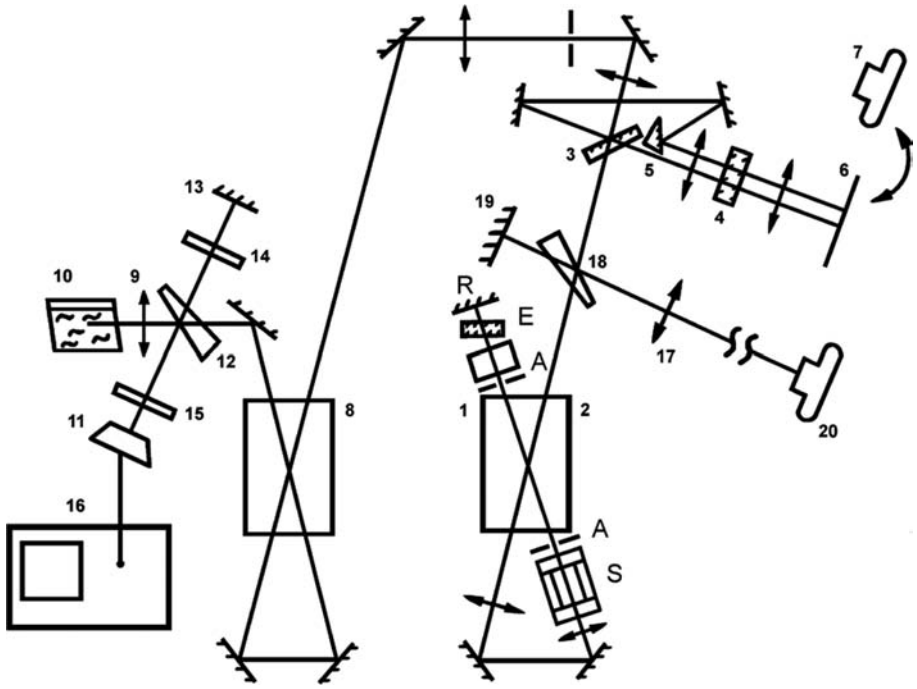

Fig. 1. Experimental setup for the investigation of the stimulated backscattering of a XeCl excimer laser beam in hexane: (1) the master oscillator and (2) the preamplifier based on the first ELI-91 XeCl laser; (3, 12, 18) beamsplitters; (4) the Fabry-Perot etalon and (5) the prism of the spectrum analyzer; (6) the luminescent screen; (7, 20) cameras; (8) the two-pass amplifier based on the second ELI-91 XeCl laser; (9) the lens with one of three possible focal lengths $F = 11$, or 50, or 100 cm; (10) the cell filled with hexane; (11) the FEK-29KPU photodiode and (16) the S7-19 oscilloscope of the time-domain analyzer; (13, 19) back-reflecting mirrors; (14, 15) the neutral filters; (17) the divergence analyzing lens with the focal length $f_1 = 3$ m.

was detected in a variety of studies conducted by a number of laboratories for nearly a decade [15–21], which rules out accidental experimental errors. This problem may be resolved by examining the fundamental physical mechanisms responsible for SS.

To investigate the physical mechanisms responsible for stimulated backscattering of nanosecond near-uv pulses, we constructed the experimental setup (Fig. 1) based on two commercially available ELI-91 XeCl excimer lasers ($\lambda = 308$ nm). The setup was designed as a master-oscillator-power-amplifier (MOPA) system. Hexane was used as the nonlinear liquid.

4.1. Master oscillator

The master oscillator generates a weak narrow-bandwidth beam, whose diffraction-limited divergence was created by two apertures A of radius $r_0 = 0.8$ mm mounted one on each side of the MO active cell.

The bandwidth was narrowed by means of a cavity consisting of a nontransparent mirror R at one end and a mode selector S at the other. The selector operates as an interference filter with a frequency-dependent reflection coefficient. Originally [23], a selector of this kind was used in a Nd:glass laser characterized by a spontaneous lifetime close to 1 μs. The spontaneous lifetime for a XeCl laser is about 20 ns. For a 1 m- long cavity, this yields six round trips which is not sufficient to select a single longitudinal mode. The optical system proposed in [23] is useless when applied to the XeCl laser. However, a single longitudinal mode was selected by using an extra Fabry-Perot etalon E placed inside the MO cavity.

Table 3
Laser parameters

Parameter	Commercially available ELI-91 laser	Master oscillator	Amplified beam
Bandwidth, cm^{-1}	15	5×10^{-3}	5×10^{-3}
Aperture	10 mm × 20 mm	$\emptyset$ 1.6 mm	8 mm × 10 mm
Divergence, rad	10^{-2}	6×10^{-4}	3×10^{-4}
Pulse duration (FWHM), ns	20	8	8
Pulse energy, mJ	50	5×10^{-2}	3
Wavelength, nm	308	308	308

The MO output characteristics are presented in the third column of Table 3; the characteristics of a commercially available ELI-91 laser are listed in the second column.

4.2. Experimental technique

The beam generated by MO 1 was expanded by a telescope and preamplified in the same active volume 2 of the first ELI-91 XeCl laser to approximately 1 mJ. After going twice through the amplifier 8 using the second ELI-91 XeCl laser head, the pulse achieved a nearly Gaussian temporal shape of 8-ns duration [full width at half maximum (FWHM)], 3-mJ energy, and $5 \times 10^{-3} cm^{-1}$ bandwidth. Characteristics of the amplified beam are specified in the last column of Table 3.

The amplified beam was focused by lens 9 into cell 10 filled with hexane. The nonlinear interaction took place in the focal caustic of lens 9. The backscattered wave traveled back through the system and was amplified in 8.

Beamsplitter 12 was used to guide both forward- and backward-propagating beams into the time-domain analyzer. The temporal power profiles were measured by means of the FEK-29KPU photodiode 11 (the resolution being equal to 200 ps) and S7-19 oscilloscope 16 (the bandwidth being equal to 5 GHz). The phase-conjugation mirror reflectivity was determined as the ratio of the backscattered beam to the amplified beam peak power.

Beamsplitter 3 was used to guide both forward- and backward-propagating beams into the spectrum analyzer (Fabry-Perot etalon 4 with a variable dispersion-free region combined with prism 5), which produced the composite temporal spectrum of both the pump wave and the stimulated backscattered wave simultaneously on luminescent screen 6 or camera 7. This facilitated the measurement of the relative frequency shift. The temporal spectra were not changed by amplification in 8.

Beamsplitter 18 was used to guide both forward- and backward-propagating beams into the divergence analyzer. For each beam, camera 20 created a photographic image of the focal spot produced by lens 17 with the focal length $f_1 = 3$ m. This photographic image carries only the amplitude information. Since the phase modulation gets transformed into an amplitude modulation in the focal region as in the far field, the beam divergence θ_L can be calculated from the relation $\theta_L \approx \frac{d}{f_1}$, where d is the focal spot diameter. In order to measure the amplified beam divergence the divergence analyzer was placed downstream of amplifier 8.

4.3. Nonlinear liquids and cells

In the previous experiments [15–22], the amplified beams were focused by lenses with the focal lengths $F = 5 \div 10$ cm into about 5 cm – long cells filled with nonlinear liquids. Organic solvents utilized in uv chromatography, such as hexane, heptane, and ethanol, were used as the nonlinear liquids. Similar results were obtained for different liquids. Since hexane (C_6H_{14}) was investigated in almost all of these studies (see Table 1), we also chose it.

In our experiments, the amplified beam was focused by lens 9 into the center of cylindrical glass cell 10 with internal diameter 40 mm, filled with hexane. We used 5 cm – long cells in combination with lens 9 having $F = 11$ cm and 30 cm – long cells in combination with lens 9 having $F = 50$, and 100 cm. Each cell was sealed by two fused-silica input-output windows inclined at the angle of 5^0 to avoid parasitic reflections.

We used the high-performance liquid chromatography grade hexane produced by Oldrich Chemical Co., Milwaukee, WI, and chemically pure hexane from Russian suppliers. Their linear absorption coefficients measured at $\lambda = 308$ nm were $\alpha = (0.01 \pm 0.003)$ and $\alpha = (0.046 \pm 0.003)$ cm^{-1}, respectively.

We added extremely small amounts of acetone to the hexane to slightly increase the linear absorption coefficient, so that the liquids used in our cells were characterized by $\alpha = 0.01$, 0.046, 0.08, 0.17 cm^{-1} at $\lambda = 308$ nm.

The refractive index of hexane at $\lambda = 308$ nm and its temperature derivative at constant pressure are [2] $n \approx 1.4$, $\left(\frac{\partial n}{\partial T}\right)_p = -53 \times 10^{-5}$ K^{-1}. The corresponding permittivity and its derivative are $\varepsilon = n^2 \approx 2$, $\left(\frac{\partial \varepsilon}{\partial T}\right)_p = \frac{\partial \varepsilon}{\partial n}\left(\frac{\partial n}{\partial T}\right)_p = 2n\left(\frac{\partial n}{\partial T}\right)_p \approx -1.5 \times 10^{-3}$K^{-1}.

5. Experimental results

5.1. *Experiment 1: The dependence of the temporal stimulated backscattering spectrum on the pump intensity*

When constant parameters of the amplified beam (see Table 3) are maintained, the pump intensity in cell 10 (see Fig. 1) can be varied by means of neutral filters or by changing the focal length of lens 9. The SS was close to its threshold for any lens 9 employed. Therefore, we could not use neutral filters, which reduce the amplified beam power. The pump intensity I_L was varied only by changing the focal length F of lens 9.

Three different lenses 9 with $F = 11$, 50, and 100 cm were used. For each lens ($F = $ const), the temporal spectrum was obtained by the spectrum analyzer described above with the Fabry-Perot etalon 4 having a dispersion-free region of 0.66 cm^{-1}. Only the chromatography-grade hexane ($\alpha = 0.01$ cm^{-1}) was used.

Figure 2 shows three images corresponding to the three values of F. Each photograph comprises two parts: the pump spectrum (right) and the stimulated backscattered spectrum (left). The stimulated backscattered spectrum has a single unshifted component when $F = 11$ cm (Fig. 2a); two components when $F = 50$ cm: an unshifted one and a Stokes one shifted by 0.33 cm^{-1} (Fig. 2b); and a single Stokes component shifted by 0.33 cm^{-1} when $F = 100$ cm (Fig. 2c).

5.2. *Experiment 2: The dependence of the temporal stimulated backscattering spectrum on the linear absorption coefficient*

We used all cells having $\alpha = 0.01$, 0.046, 0.08, 0.17 cm^{-1}. For each $\alpha = $ const we examined the dependence of the stimulated backscattering spectrum on the pump intensity, which was controlled by changing the focal length of lens 9. The dependence on F for $\alpha = 0.046$, 0.08 cm^{-1} was similar to that for $\alpha = 0.01$ cm^{-1} illustrated by Figs 2a–2c. Each stimulated backscattering spectrum obtained for $\alpha = 0.17$ cm^{-1} contained a single unshifted component (as in Fig. 2a).

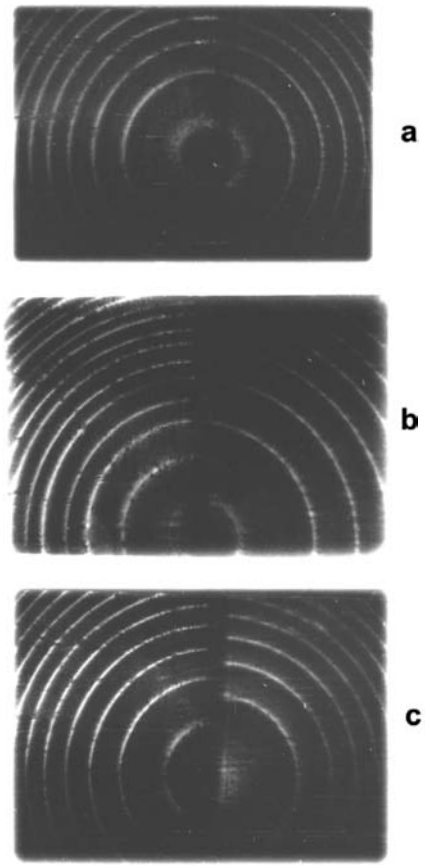

Fig. 2. Results of Experiments 1 and 2: three temporal spectra obtained by the spectrum analyzer with Fabry-Perot etalon 4 having the dispersion-free region of 0.66 cm^{-1}. Each photograph comprises two parts: the pump spectrum (right) and the stimulated backscattered spectrum (left) in hexane at a constant linear absorption coefficient α for three focal lengths of lens 9: $F = (a)$ 11, (b) 50, (c) 100 cm. The dependence of the stimulated backscattering spectrum on F is similar for $\alpha = 0.01$, 0.046, 0.08 cm^{-1}.

5.3. Experiment 3: The dependence of the phase-conjugation fidelity on the pump intensity

When the forward-propagating beam passes amplifier 8, its divergence increases by a factor of 3. We measured the divergences of forward- and backward-propagating beams at the location of beamsplitter 18 with the help of the divergence analyzer described above. We examined the dependence of the backward-propagating beam divergence on the pump intensity, which was controlled by changing the focal length of lens 9. We used only the chromatography-grade hexane ($\alpha = 0.01$ cm^{-1}) to avoid the thermal self-action caused by linear absorption. The experiment provided information on the phase-conjugation fidelity: when the PC fidelity is "high", the forward and the backward aberrations must compensate each other.

Figure 3 shows three photographic images created by camera 20. The resulting divergences are: $\theta_L \approx 3 \times 10^{-4}$rad for the forward-propagating beam (Fig. 3a); $\theta_L \approx 3 \times 10^{-4}$rad for the "high" phase-conjugation fidelity backscattered beam obtained with $F = 100$ cm (Fig. 3b); and $\theta_L \approx 2 \times 10^{-3}$rad for the "poor" phase-conjugation fidelity backscattered beam obtained with $F = 11$ cm (Fig. 3c).

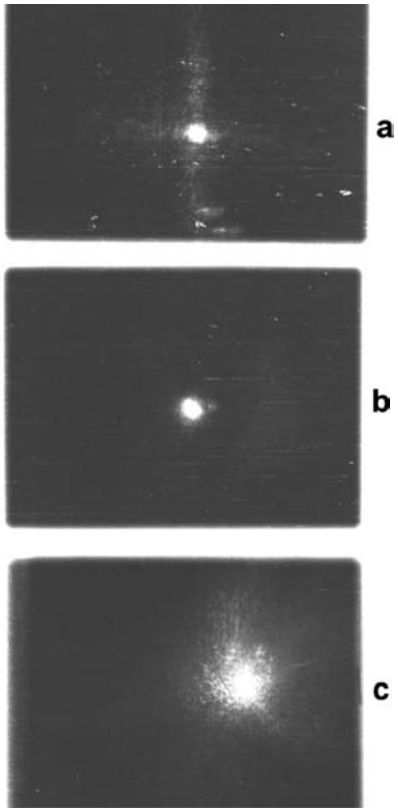

Fig. 3. Results of Experiment 3: three focal spots obtained by the divergence analyzer for (a) the forward-propagating beam; (b) the backward-propagating beam ($F = 100\ cm$, "high" phase-conjugation fidelity); (c) the backward-propagating beam ($F = 11\ cm$, "poor" phase-conjugation fidelity). Images (b) and (c) were obtained for hexane with $\alpha = 0.01\ cm^{-1}$.

5.4. Experiment 4: The temporal power profiles and the phase-conjugation mirror reflectivity

The analysis of the temporal evolution of the pulses with the time-domain analyzer described above is important, because the nonlinear mirror may change their amplitudes, durations, and shapes. All the liquids used had $\alpha = 0.01$, 0.046, 0.08, 0.17 cm^{-1}.

The backscattered temporal power profile was found to have a nearly Gaussian shape and the duration (FWHM) of approximately 7 ns. The slightly shorter duration as compared to that of the pump (see Table 3) can be attributed to the threshold nature of SS.

The phase-conjugation mirror reflectivity reached 20% for $\alpha = 0.01$ cm^{-1} and gradually decreased with increasing α. The reflectivity increased as the focal caustic of lens 9 was shifted from the center toward the input window of cell 10.

6. Analysis and interpretation of experimental results

6.1. Results of experiments which require theoretical analysis

The observations in our Experiments 1–4 on stimulated backscattering in hexane for different values of α and F that require further theoretical analysis can be summarized as follows.

1. The dependence of the backscattering spectrum on F obtained for $\alpha = 0.01 \div 0.08$ cm^{-1}:
   (1.1) the presence of two components when $F = 50$ cm: an unshifted one (with the experimental error 0.02 cm^{-1}) and the Stokes one shifted by 0.33 cm^{-1} (Fig. 2b);
   (1.2) the disappearance of the unshifted component when F is increased from 50 to 100 cm (Figs 2b and 2c);
   (1.3) the disappearance of the shifted component when F is reduced from 50 to 11 cm (Figs 2a and 2b).
2. The dependence of the backscattering spectrum when α is varied from $0.01 \div 0.08$ to 0.17 cm^{-1}:
   (2.1) the disappearance of the shifted component when $F = 50$, 100 cm;
   (2.2) the appearance of the unshifted component when $F = 100$ cm.
3. The substantial decrease in the phase-conjugation fidelity obtained when at $\alpha = 0.01$ cm^{-1}F is reduced from 100 to 11 cm (Figs 3b and 3c).

6.2. The specific features of the stimulated scattering in our experiments

At the initial stage of the SS process, a weak scattered wave is generated as a result of the spontaneous scattering of the pump wave. In the resulting steady state without considerable pump saturation, the scattered wave intensity I_S is expressed as [1–5]:

$$I_S(L) = I_S(0)\ \exp(I_L G L), \tag{1}$$

where I_S (0) is the spontaneously scattered intensity, I_L is the pump intensity, G is the gain factor, and L is the nonlinear interaction length. The threshold condition for SS is

$$(I_L G L)^{THR} \approx 30. \tag{2}$$

If the total gain $(I_L G L)$ for a certain SS mechanism is below the threshold (2), the mechanism does not contribute to the overall SS pattern observed in an experiment.

Unfortunately, three-dimensional calculations of the real beam focal caustic are problematic even for vacuum. For organic liquids, only rough approximations can be used. Fortunately, in contrast to the near-ir, for the near-uv due to the fluorescence of hexane a blue track of the focused laser beam was simply observed through a thin transparent glass wall of the cell (of course, in a dark laboratory). The focal caustic geometry was measured and successively compared with the values calculated below.

The length of a light pulse with duration 8 ns is $L_P \approx 2.4$ m. The amplified beam with duration $\tau_0 \approx$ 8 ns, divergence $\theta_L \approx 3 \times 10^{-4}$ rad, and radius $R_L \approx 0.5$ cm (Table 3) was focused by lens 9. In accordance with Eq. (5), the length L of the focal caustic varied from $L_{MIN} \approx 0.6$ mm for $F = 11$ cm to $L_{MID} \approx 1.5$ cm for $F = 50$ cm and $L_{MAX} \approx 6$ cm for $F = 100$ cm. The long-pulse condition $L_P >> L$ is met for the entire range of values of F. At any moment of time, the pump power W_L can be treated as constant over the caustic length L, which is approximately equal to the length of the area where the nonlinear interaction occurs. To simplify the analysis, we assume that the pump intensity I_L is uniformly distributed over a cylindrical focal caustic of diameter d_f and length L.

It should be noted that such a technique is frequently met in nonlinear optical studies. For instance, the impact of the focal caustic dimensions upon the optical breakdown threshold has been studied in [24]. Ruby laser pulses were focused by lenses of focal lengths $F = 1 \div 13$ cm into gases. The focal caustics were supposed to have cylindrical shapes, but their dimensions were not measured. The transition from

the focal length to the focal spot diameter was performed with the help of the equation $d_f \approx F\theta_L$, where θ_L is the laser beam divergence. In contrast to [24], long-focal-length lenses with $F \geqslant 11$ cm were used in our experimental conditions. Moreover, due to the fluorescence of hexane, the focal caustics were seen with the naked eye, and for $F = 50$ and 100 cm their lengths could be measured with a ruler.

When a laser beam with power W_L, radius R_L, and divergence θ_L is focused by a lens, the product $(I_L L)$ is independent of the focal length F of this lens. Indeed,

$$I_L \approx \frac{W_L}{S_f}, \tag{3}$$

$$S_f = \frac{\pi d_f^2}{4} \approx \frac{\pi \left(F\theta_L\right)^2}{4}, \tag{4}$$

$$L \approx \frac{d_f}{\theta_0/2} \approx \frac{F\theta_L}{R_L/F} = \frac{F^2\theta_L}{R_L}, \tag{5}$$

where W_L, R_L, θ_L are independent of F; $d_f \approx F\theta_L$; S_f is the cross-sectional area of the focal caustic; $\theta_0 \approx 2R_L/F$ is the convergence angle of the beam after the lens. We obtain

$$I_L \propto F^{-2}, \quad L \propto F^2 \quad \Rightarrow \quad (I_L L) \approx \text{ const.} \tag{6}$$

The full expression is

$$(I_L L) \approx \frac{4W_L}{\pi\, \theta_L R_L} \approx \frac{4U_L}{\pi\, \theta_L R_L \tau_0}, \tag{7}$$

where U_L and τ_0 are the energy of the pulse and its duration, respectively. For the parameters of the amplified beam presented in Table 3, Eq. (7) yields $(I_L L) \approx 3 \times 10^3$ MW/cm. The amplified beam energy 3 mJ (Table 3) corresponds to the absence of diagnostic equipment and reflects the maximum possible value for this laser system before cell 10. Due to the diagnostic and other energy losses between the exit of amplifier 2 and the focal caustic of lens 9, the real on-target energy is $U_L \approx 1.5$ mJ. Accordingly, we have $(I_L L) \approx 1.5 \times 10^3$ MW/cm.

There are two varying parameters in our experiments – α and F. As far as the variation of F is concerned, Eq. (6) shows that the value

$$(I_L L) \approx 1.5 \times 10^3 \text{ MW/cm} \tag{8}$$

is constant. Since $(I_L L) \approx const$, the only parameter that may affect the left part of Eq. (2) via G is α. If the SS process does not involve heating due to linear absorption, G is independent of α, and the total gain $(I_L G L)$ does not change in our experiments.

The diameter of the amplified beam incident on lens 9 is $D_L \approx 1$ cm (Table 3). The focal length of lens 9 is $F > 10$ cm. Therefore, $D_L/F < 0.1$, and the focal caustics were not distorted by spherical aberrations of lens 9 or by a jump in the refractive index across the air-cell boundary.

6.3. The parameters of SBS and linear STS-2 for our experimental conditions

Since SBS and linear STS-2 were considered responsible for the observed SS in the previous studies (see Table 1), we should calculate their parameters for our experimental conditions.

6.3.1. Properties of SBS

According to the SBS model [1–5], the modulated electrostrictive force amplifies a hypersonic wave with wave vector $q = k_L - k_S$ and frequency

$$\Omega_B = |q|\, v, \tag{9}$$

where ω_L, k_L and ω_S, k_S denote the frequencies and the wave vectors of the pump and scattered waves; v is the speed of sound. The steady-state gain factor near the Stokes resonance peak is

$$G_B = \frac{\rho^2 \left(\partial\varepsilon/\partial\rho\right)^2}{1 + \left(\omega_L - \omega_S - \Omega_B\right)^2 / \Gamma_B^2} \cdot \frac{\omega_S \mathrm{q}^2}{4\Omega_B \Gamma_B \rho n^2 c^2}, \tag{10}$$

where ρ is the density, c is the speed of light, and n is the unperturbed refractive index. The decay rate Γ_B is related to the decay time τ_B:

$$\Gamma_B\,(q) = A\,|q|^2\,, \quad \tau_B \approx \Gamma_B^{-1}. \tag{11}$$

For liquids, $A = \frac{2\eta_1}{3\rho}$, where η_1 is the shear viscosity. The highest gain factor Eq. (10) is achieved when $\omega_L - \omega_S = \Omega_B$. When the scattered wave propagates at an angle θ relative to the pump wave,

$$q = |q| = |k_L - k_S| \approx 2\,|k_L|\ \sin\left(\theta\ /\ 2\right) = 2\left(\omega_L n/c\right)\ \sin\left(\theta\ /\ 2\right). \tag{12}$$

Accordingly, the SBS frequency shift is

$$\Omega_B = q\ v = 2\omega_L n\left(v/c\right)\ \sin\left(\theta\ /\ 2\right). \tag{13}$$

6.3.2. Properties of linear STS-2

According to the linear STS-2 model [1–4,13], the modulated heating amplifies a thermal wave with wave vector $q = k_L - k_S$. The steady-state gain factor is

$$G_T \approx \frac{\omega_S \alpha}{cn\rho\ c_p \Gamma_T} \left(\frac{\partial\varepsilon}{\partial T}\right) \frac{\left(\omega_L - \omega_S\right)/\Gamma_T}{1 + \left(\omega_L - \omega_S\right)^2 / \Gamma_T^2}, \tag{14}$$

where α is the linear absorption coefficient, c_p is the specific heat, and $\chi =$ is the thermal diffusivity. The decay rate Γ_T is related to the decay time τ_T:

$$\Gamma_T = \chi\,|q|^2\,, \quad \tau_T \approx \Gamma_T^{-1}. \tag{15}$$

Since $\frac{\partial\varepsilon}{\partial T}$ is negative for most substances, a positive gain corresponds to an anti-Stokes frequency shift $(\omega_L - \omega_S) < 0$. The highest gain factor (14) is achieved when $(\omega_L - \omega_S) = \Omega_T = -\Gamma_T$.

6.3.3. The predicted values of the SBS and linear STS-2 parameters for our experiments

Under our experimental conditions, the following numerical values [2,5,25] should be substituted into Eqs (9)–(15):

$$\lambda = 308\ \text{nm}\ ,\ \theta = \pi\ ,\ \rho \approx 0.66\ \frac{\mathrm{g}}{\mathrm{cm}^3},\ n \approx 1.4\ ,\ \eta_1 \approx 3.2 \times 10^{-3} P \approx 3.2 \times 10^{-3} \frac{\mathrm{g}}{\mathrm{cm}\ s},$$
$$v \approx 10^5 \frac{\mathrm{cm}}{s},\ c \approx 3 \times 10^{10} \frac{\mathrm{cm}}{s},\ \rho \left(\frac{\partial\varepsilon}{\partial\rho}\right)_T \approx 1\ ,\ \ \frac{\omega_S}{2\pi} \approx \frac{\omega_L}{2\pi} \approx 10^{15}\mathrm{Hz}\ ,\ \chi \approx 10^{-3}\ \frac{\mathrm{cm}^2}{s},$$
$$\left(\frac{\partial n}{\partial T}\right)_P \approx -53 \times 10^{-5}\ K^{-1},\ \left(\frac{\partial\varepsilon}{\partial T}\right)_P \approx -1.5 \times 10^{-3}\ K^{-1},\ c_P \approx 2.3\ \frac{J}{g\ K}\ ,\ \delta = \frac{c_P}{c_V} \approx 1.3.$$

Table 4
Gain factors G_T, G_B and total gains $(I_L G_T L)$, $(I_L G_B L)$ for linear STS-2 and SBS calculated for various values of α, but for constant $(I_L L) \approx 1.5 \times 10^3$ MW/cm (as in our experiments)

α, cm^{-1}	Linear STS-2		SBS	
	$G_T,\ cm/MW$	$(I_L G_T L)$	$G_B,\ cm/MW$	$(I_L G_B L)$
0.01	0.002	3	0.07	105
0.046	0.009	14	0.07	105
0.1	0.02	30	0.07	105

The predicted SBS frequency shift is $\Omega_B = 0.33$ cm^{-1} (see Table 2). The hypersonic grating decay time is $\tau_B \approx 1$ ns. Since this time is shorter than the pump duration by a factor of 8, the steady-state model can be used. The frequency-optimized SBS gain factor (10) is expressed as

$$G_B = \frac{\omega_S \mathrm{q}^2}{4\Omega_B \Gamma_B \rho n^2 c^2} = \frac{3}{16 n^3 c v \eta_1} \approx 0.07\ \frac{\mathrm{cm}}{\mathrm{MW}}. \tag{16}$$

The predicted linear STS-2 frequency shift is $\Omega_T \approx -\Gamma_T \approx -0.01$ cm^{-1}. The thermal grating decay time is $\tau_T \approx 3$ ns. Even though it is shorter than the pump duration by almost a factor of 3, we can not reliably use the steady-state model. Since we explore the possibility of the emergence of linear STS-2 in an experiment rather than attempting to maximize its efficiency, we do use the steady-state model to simplify the further analysis. The thermal-grating wavelength Λ_T associated with the backscattering is

$$\Lambda_T = \frac{2\pi}{q} \approx \frac{2\pi}{2k_L} = \frac{\lambda}{2n} \approx 10^{-7}\ \mathrm{m}. \tag{17}$$

The time of the pressure relaxation over Λ_T is

$$\tau_{pr} = \frac{\Lambda_T}{v} \approx 10^{-10}\ \mathrm{s}. \tag{18}$$

Since $\tau_{pr} << \tau_0$, G_T can be obtained by using the permittivity temperature derivative at constant pressure. The frequency-optimized linear STS-2 gain factor (14) is expressed as

$$G_T = \frac{\omega_S \alpha}{2cn\rho c_P \Gamma_T} \left(\frac{\partial \varepsilon}{\partial T}\right)_P = \frac{\alpha\ c}{8\omega_L n^3 \rho\ c_P \chi} \left(\frac{\partial \varepsilon}{\partial T}\right)_P \approx 0.2\ \alpha\ \frac{\mathrm{cm}^2}{\mathrm{MW}}. \tag{19}$$

The frequency-optimized gain factors and total gains for linear STS-2 and SBS calculated for various values of α, but for constant $(I_L L) \approx 1.5 \times 10^3$ MW/cm, as in our experiments, are listed in Table 4. The first column of the table shows the linear absorption coefficient α; the second and fourth columns, the gain factors G_T and G_B; the third and the last columns, the total gains $(I_L G_T L)$ and $(I_L G_B L)$.

The theoretical estimates presented in Table 4 lead to the following conclusions.

Linear STS-2. The total gain (depending on α via G_T) is much lower than the threshold given by Eq. (2) both for the "chemically pure" ($\alpha = 0.046$ cm^{-1}), and a fortiori for the chromatography-grade ($\alpha = 0.01$ cm^{-1}) hexane. The threshold is reached when $\alpha = \alpha_{STS}^{THR} \approx 0.1$ cm^{-1}.

SBS. The total gain (independent of α) is higher than the threshold given by Eq. (2).

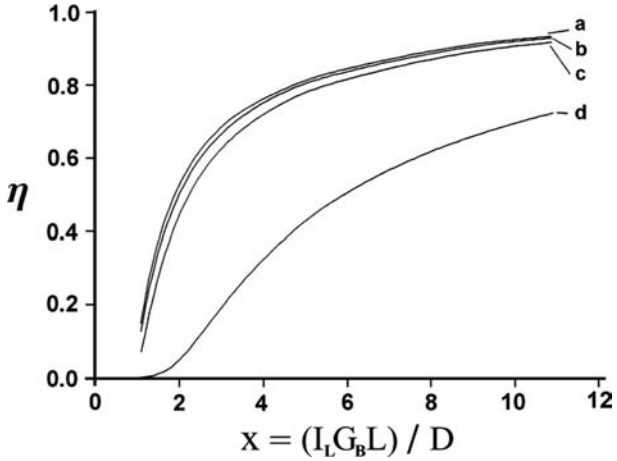

Fig. 4. Predicted SBS conversion efficiency η vs. the total gain normalized to the threshold value $D \approx 30$ for hexane, for $\lambda =$ 308 nm and $\alpha = (a)\ 0.0001,\ (b)\ 0.03,\ (c)\ 0.05,\ (d)$ 0.1 cm^{-1}.

6.4. The emergence and disappearance of the spectral components in accordance with the existing theory

6.4.1. The shifted component of the stimulated backscattering spectrum

Since the total gain $(I_L G_B L)$ (Table 4) exceeds the threshold (2) and the measured value of the frequency shift 0.33 cm^{-1} (Figs 2b and 2c) agrees with Eq. (13) (Table 2), the shifted component should be attributed to SBS.

To explain the absence of the shifted component in Fig. 2a, we explore the possibility of SBS breakdown. The only mechanism that can suppress SBS under our conditions is phase mismatch [11, 12]. When the permittivity of the medium changes with time due to the weak uniform heating caused by linear absorption with the coefficient α, the wavelengths of the pump and scattered waves vary. Since the acoustic wave has a finite response time, the phase matching conditions are violated. If $I_L\,(L)$ is the input pump intensity and $I_S\,(L)$ is the output backscattered intensity, then the SBS conversion efficiency over the length L of nonlinear interaction is $\eta = \frac{I_S(L)}{I_L(L)}$. The dependence of η on $I_L\,(L)$ is given by the relation [11,12]:

$$h\,(D + \ln\,\eta) = \Gamma_B G_B\ arctg\,\{\ I_L\,(L)\,(1-\eta)\ \ L\ h/\Gamma_B\}\,, \tag{20}$$

where $D \approx 30$, G_B is the peak backward SBS gain factor defined by Eq. (16), and

$$h = \frac{\alpha\ \omega_L}{2cn\rho c_p}\left(\frac{\partial\varepsilon}{\partial T}\right)_P .$$

Figure 4 shows the SBS conversion efficiency η as a function of the total gain normalized by its threshold value $x = \frac{(I_L G_B L)}{D}$, evaluated numerically by using the relation Eq. (20) for hexane, for $\lambda = 308$ nm, and for several values of α. The critical value corresponding to curve "d" is $\alpha_{CR} \approx 0.1$ cm^{-1}. For $\alpha =$ 0.01, 0.046, 0.08 cm^{-1}, no SBS suppression due to phase mismatch should be expected.

6.4.2. The unshifted component of the stimulated backscattering spectrum

PC via SS can be caused by mechanisms other than SBS [1,3,4]. Since the measured frequency shift does not exceed 0.02 cm^{-1} (the experimental error), we should consider stimulated thermal scattering

caused by heating due to the electrocaloric effect (STS-1), linear STS-2, and stimulated Rayleigh wing scattering (SRWS).

First, consider SRWS. Since the molecular anisotropy of liquid hexane is weak [26], the excitation of SRWS is impossible. Normally, the SRWS gain factor for liquids does not exceed $G_{RW} \approx 10^{-3}$ cm/MW [1]. For our condition Eq. (8) the SRWS total gain does not exceed $(I_L G_{RW} L) \approx 1.5$, which is much lower than the threshold Eq. (2).

Now consider STS-1. According to [1], the STS-1 to SBS gain factor ratio is

$$\frac{G_{RL}}{G_B} = \frac{(\delta - 1)\ c\Gamma_B}{4\pi\ v\omega_S}. \tag{21}$$

For our experimental conditions, $\frac{G_{RL}}{G_B} \leqslant 10^{-2}$. From the value of $(I_L G_B L)$ in the last column of Table 4, the STS-1 total gain is $(I_L G_{RL} L) \leqslant 1$, which is much lower than the threshold Eq. (2).

The processes of SRWS and STS-1 do not involve heating due to absorption of the radiation, and their total gains do not change in our experiments as long as $(I_L L)$ is constant (see Section 6.2). The emergence of SRWS and STS-1 components under our experimental conditions is impossible.

Now consider linear STS-2. The predicted frequency shift $\Omega_T \approx -0.01$ cm^{-1} (see Section 6.3.3) agrees with the measured one. Indeed, the absolute value of the latter is less than 0.02 cm^{-1} (the experimental error). Heating due to absorption of the radiation is involved in the linear STS-2 process, and its total gain varies with α while $(I_L L)$ is constant. The emergence of the linear STS-2 component under our experimental conditions (Table 4) is possible only when $\alpha \geqslant 0.1$ cm^{-1}.

6.5. Decrease in phase-conjugation fidelity in accordance with the existing theory

The only mechanism that can cause a decrease in the PC fidelity (Figs 3b and 3c) under our experimental conditions is phase self-modulation [11,12]. Consider the following cylindrically symmetric problem in coordinates $(R,\ z,\ t)$. A wave with a plane front and a spatially nonuniform intensity $I_L\,(R,t)$ enters a nonlinear medium at $t = 0$ across a boundary located at $z = 0$ and propagates towards a boundary located at $z = L$. The medium is characterized by the linear absorption coefficient α. Heat conduction does not contribute in the transverse coordinate R. The temperature increment over time t is

$$\delta T\,(R,t) = \frac{1}{\rho\ c_P} \int\limits_0^t \alpha\ I_L\,(R,\tau)\ d\tau = \frac{\alpha}{\rho\ c_P} \int\limits_0^t I_L\,(R,\tau)\ d\tau. \tag{22}$$

The refractive index depends on temperature, $n = n_0 + \delta n\,(T)$, where the nonlinear term is

$$\delta n\,(R,t) = \left(\frac{\partial n}{\partial T}\right)\ \delta T\,(R,t) = \left(\frac{\partial n}{\partial T}\right) \frac{\alpha}{\rho\ c_P} \int\limits_0^t I_L\,(R,\tau)\ d\tau\ . \tag{23}$$

The wave vector is $k\,(R,t) \approx e_z k\,(R,t)$, where $k = k_0 + \delta k = \frac{\omega}{c}\,(n_0 + \delta n)$.

The nonlinear phase increment over the distance L is

$$\begin{aligned} &\delta\Phi\,(R,t) = \delta k\ L = \tfrac{\omega L}{c}\delta n\,(R,t) = \tfrac{\omega L}{c}\left(\tfrac{\partial n}{\partial T}\right)\tfrac{\alpha}{\rho\ c_P} \int\limits_0^t I_L\,(R,\tau)\ d\tau\ = \\ &= \tfrac{\omega}{c}\left(\tfrac{\partial n}{\partial T}\right)\tfrac{\alpha}{\rho\ c_P} \int\limits_0^t I_L\,(R,\tau,F)\ L\,(F)\ d\tau. \end{aligned} \tag{24}$$

A wave with a plane front at $z = 0$ will have a radially nonuniform front at $z = L$. The front distortion is zero at $t = 0$ and maximal at the end of the pulse.

Due to the phase self-modulation of the pump wave, the backscattered wave gets coupled to the dynamically distorted beam. Taking into account the finite nonlinearity decay time, this effect may cause a decrease in PC fidelity.

It must be noted that lenses 9 as well as cells 10 (see Fig. 1) were changed only in the intervals between separate sets of experiments. The SS of a great number of pump pulses was studied in every set. That is why F is a parameter in the final form of expression (24), which remains invariant over the pump duration. For pump pulses from different sets of experiments, at any instant τ the product $(I_L L)$ contained in (24) does not depend on F, as shown by Eq. (6). Therefore, $\delta\Phi\,(R,t)$ does not depend on F, and heating with $\alpha = const$ can not explain the decrease in the PC fidelity when F is reduced from 100 to 11 cm.

Let's make numerical evaluations of $\delta\Phi$ for our experimental conditions:

$$\delta\Phi = \frac{\omega}{c}\left(\frac{\partial n}{\partial T}\right)\frac{\alpha}{\rho\, c_P}\int\limits_0^t (I_L\ L)\ d\tau \approx \frac{\omega}{c}\left(\frac{\partial n}{\partial T}\right)_P \frac{\alpha}{\rho\, c_P}\,(I_L\ L)\ \tau_0 \approx -\alpha\,[cm^{-1}] \times 10^3 \text{rad.} \quad (24a)$$

For $\alpha = 10^{-2}$ cm^{-1} we obtain $|\delta\Phi| \approx 10$ rad. Such a large value confirms strong effect of the phase self-modulation. Equation (24a) expresses the upper limit of the $\delta\Phi$ estimation. Indeed, first, the value of $\left(\frac{\partial n}{\partial T}\right)$ at constant pressure was used, but the pressure stabilization over the focal caustic requires time. Second, our model was developed for weak heating. For strong one the heat conduction should be taken into account.

6.6. The implication of two-photon absorption in the theory of stimulated scattering

The existing SS theory developed for linearly absorbing media cannot explain our experimental results. First, since the linear absorption with $\alpha < 0.1$ cm^{-1} is not sufficiently strong to give rise to linear STS-2, the physical mechanism responsible for the unshifted component observed for $\alpha = 0.01 \div 0.08$ cm^{-1} (Figs 2a and 2b) remains unclear. Second, since the linear absorption with $\alpha < 0.1$ cm^{-1} is not strong enough to suppress SBS via phase mismatch, the disappearance of the SBS component when F is reduced from 50 to 11 cm (Figs 2a and 2b) observed for $\alpha = 0.01 \div 0.08$ cm^{-1} is yet to be explained. Third, the linear absorption with $\alpha = 0.01$ cm^{-1} = const cannot explain the substantial decrease in the PC fidelity caused by the decrease in F from 100 to 11 cm (Figs 3b and 3c).

Two-photon absorption should be expected in hexane for $\lambda < 400$ nm [27]. Suppose that our experiments were strongly affected by the two-photon absorption. More specifically, assume that the unshifted component corresponds to the STS-2 process associated with the heating caused by two-photon absorption. We call this mechanism the two-photon STS-2, as distinct from the previously known mechanism induced by linear (single-photon) absorption, i.e., linear STS-2.

The intensity $I\,(z)$ of the radiation propagating along the z axis is governed by the following equation [1, 28]

$$\frac{dI}{dz} = -\gamma I^2, \quad (25)$$

where γ is the two-photon absorption coefficient. Its solution is

$$I\,(z) = \frac{I_0}{1 + I_0\gamma z}, \quad (26)$$

where $I_0 = I(0)$. For weak two-photon absorption ($I_0\gamma_z << 1$), this solution gets reduced to

$$I(z) = I_0(1 - I_0\gamma z). \tag{27}$$

In our experiments, we have the condition (8) and $\gamma \approx 10^{-4}$ cm/MW (see Section 6.7). Thus, $(I_L\gamma L) \approx 0.15$ and Eq. (27) can be used.

The weak linear absorption with coefficient α is described by the equation

$$I(z) = I_0(1 - \alpha_z). \tag{28}$$

It follows from Eqs (27) and (28) that in our experiments $(I_L\gamma)$ plays the role of α. We can define the total absorption coefficient as

$$\alpha_\Sigma = \alpha + (I_L\gamma), \tag{29}$$

where $(I_L\gamma)$ is the two-photon contribution. The equivalence should be understood in a quantitative sense. The linear (single-photon) and the two-photon absorption can be treated as similar processes only with respect to the final result of the resonant light-matter interaction, i.e., the irreversible dissipation of electromagnetic into thermal energy. Linear and two-photon absorption are different in terms of quantum mechanical schemes and expressions for the absorption cross-section.

The physical mechanisms of linear STS-2 and two-photon STS-2 are essentially different, being roughly similar with respect to transformation of temperature fluctuations into permittivity ones.

6.6.1. Why is I_0 replaced by I_L in Eqs (27)–(29)?

Due to the complexity of the theoretical task, including several connected linear and nonlinear effects, we made the approximation that our pump intensity does not change along the nonlinear interaction length. In accordance with this approximation, we replaced the input intensity I_0 with the pump intensity I_L in Eqs (27)–(29). This approximation is based on the following considerations. The amplified beam parameters provided conditions for SS very close to its threshold, so that strong pump saturation does not take place. As follows from the title of this paper, there are two main objectives of this study: first, to obtain a pure two-photon STS-2 spectral line, and second, to obtain a pure SBS spectral line. The two-photon STS-2 mechanism should dominate for focusing as hard as possible with linear absorption as weak as possible, i.e. for $F = 11$ cm and $\alpha_{MIN} = 0.01$ cm^{-1}. The caustic length is $L_{MIN} = 0.06$ cm. Even for $\alpha_{MAX} = 0.17$ cm^{-1}, $\alpha_{MAX}L_{MIN} = 0.01$, and $\exp(-0.01) = 0.99$. The linear absorption is negligible. The SBS mechanism should dominate for as soft as possible focusing with as weak as possible linear absorption, i.e. for $F = 100$ cm and $\alpha_{MIN} = 0.01$ cm^{-1}. The caustic length is $L_{MAX} =$ 6 cm, $\alpha_{MIN}L_{MAX} = 0.06$, and $\exp(-0.06) = 0.94$. The linear absorption is also negligible.

The observation of linear STS-2 in the previous study [22] is not clear (see Section 3.3). Therefore, linear STS-2 also calls for further investigation. For $\alpha_{STS}^{THR} \approx 0.1$ cm^{-1}, $\alpha_{STS}^{THR}L_{MAX} = 0.6$ and $\exp(-0.6) = 0.55$. The linear absorption becomes considerable only for $F = 100$ cm (i.e., $L = L_{MAX}$) and $\alpha \geqslant \alpha_{STS}^{THR} \approx 0.1$ cm^{-1}.

Under our experimental conditions, the two-photon absorption is constant and equal to $(I_L\gamma_L) \approx 0.15$ (see Section 6.6), and $\exp(-0.15) = 0.86$. The two-photon absorption is weak.

Table 5
The two-photon contribution $(I_L\gamma)$ to the total absorption coefficient (29) of hexane at $\lambda = 308$ nm for pump intensities I_L corresponding to the three focal lengths F of lens 9 used in our experiments

$F,\ cm$	$I_L, W/cm^2$	$(I_L\gamma)\ ,\ cm^{-1}$
11	$\geqslant 10^{10}$	$\geqslant 1.0$
50	10^9	≈ 0.1 (experiment)
100	2.5×10^8	≈ 0.025

6.7. The calculation of two-photon absorption cross-section from the threshold pump intensity for two-photon STS-2

When $(I_L L) = \text{const}$, linear STS-2 occurs if $\alpha \geqslant \alpha_{STS}^{THR}$. The two-photon STS-2 must also exhibit threshold behavior, but with respect to $(I_L\gamma)$ rather than α. When the material properties α and γ are kept constant, an increase in I_L caused by a decrease in F leads to different consequences for the total gain $(I_L G_T L)$. It remains invariant for linear STS-2 and increases for two-photon STS-2, because $G_T \propto \alpha = const$ (see Eq. (14)) in the former case and $G_T \propto (I_L\gamma) \propto I_L$ in the latter.

The linear and two-photon STS-2 can be distinguished experimentally. If the medium with α and γ such that $\alpha,\ (I_L\gamma) << \alpha_{STS}^{THR}$ is used and I_L is gradually increased while $(I_L L)$ is kept constant, the pure two-photon STS-2 component must appear in the spectrum when $(I_L\gamma) \approx \alpha_{STS}^{THR}$.

Let us find $(I_L\gamma)$. The total gain for STS-2 caused both by the linear and the two-photon absorption (29) reaches the threshold (2) when $\alpha_\Sigma^{THR} \approx \alpha_{STS}^{THR} \approx 0.1$ cm^{-1} (Table 4). For $\alpha = 0.01$ cm^{-1}, an unshifted component appears in the backscattering spectrum when $I_L^{THR} \approx 10^9$ W/cm^2 ($F = 50$ cm) (Fig. 2b). When $I_L \approx 2.5 \times 10^8$ W/cm^2 ($F = 100$ cm) there is no unshifted component (Fig. 2c), i.e., the threshold is not reached. Since $\alpha = 0.01$ cm^{-1} $<< \alpha_{STS}^{THR} \approx 0.1$ cm^{-1}, the unshifted component must be attributed to the pure two-photon STS-2 mechanism. The threshold pump intensity $I_L^{THR} \approx 10^9$ W/cm^2 can be used to obtain the estimate

$$\alpha_\Sigma^{THR} = \alpha + \left(I_L^{THR}\gamma\right) \approx \left(I_L^{THR}\gamma\right) \approx \alpha_{STS}^{THR} \approx 0.1 \text{ cm}^{-1}. \tag{30}$$

For a particular pump wavelength (for $\lambda = 308$ nm in our case) the coefficient γ describes a property of the medium (of the chromatography-grade hexane in our case). If $(I_L\gamma)$ is known for one value of I_L (for I_L^{THR} in our case), then it can readily be calculated for other values of I_L. The first column of Table 5 gives the three focal lengths F of lens 9 used in our experiments; the second column, the three corresponding pump intensities I_L; and the last column, the two-photon contribution $(I_L\gamma)$ to the total absorption coefficient (29).

From $\left(I_L^{THR}\gamma\right) \approx 0.1$ cm^{-1} and $I_L^{THR} \approx 10^9$ W/cm^2, we can calculate the two-photon absorption coefficient γ and the cross-section σ_2. Indeed,

$$\gamma = \frac{I_L^{THR}\gamma}{I_L^{THR}} \approx \frac{0.1\ \ \left[cm^{-1}\right]}{10^9\ \ [W/cm^2]} \approx 10^{-10}\,[cm/W] \approx 10^{-4}\,[cm/MW]\,, \tag{31}$$

$$(I_L\gamma) = \sigma_2 N \frac{I_L}{\hbar\omega}, \tag{32}$$

where $\frac{I_L}{\hbar\omega}$ is the pump intensity in units of $[photons \times cm^{-2} \times s^{-1}]$, and $N = \frac{\rho}{M}$ is the molecular density (M is the molecular mass). For hexane (C_6H_{14}) $N \approx 4 \times 10^{21}$ cm^{-3}. The photon energy corresponding to $\lambda = 308$ nm is $\hbar\omega \approx 4$ eV $\approx 6.4 \times 10^{-19}$ J. We have

$$\sigma_2 = \frac{\hbar\omega \left(I_L^{THR}\gamma\right)}{I_L^{THR}\, N} \approx (2 \pm 1) \times 10^{-50} cm^4 s. \tag{33}$$

The accuracy is estimated as

$$\frac{\delta\sigma_2}{\sigma_2} \approx \frac{\delta\alpha^{THR}}{\alpha^{THR}} + \frac{\delta I_L}{I_L} \approx 0.2 + 0.3 \approx 0.5, \tag{34}$$

where α^{THR} is the experimental threshold value for the linear STS-2.

For comparison, consider the two-photon nonresonant ionization of a many-electron atom at a moderate electric field strength, which does not involve near-threshold absorption, multiple ionization, and perturbation of the atomic spectra. A typical cross-section of this process is $\sigma_2^i \approx 10^{-49} \div 10^{-48}$ cm^{4}s [29, 30]. Normally, σ_2^i is smaller than the cross-section for the two-photon bound-bound transition at the absorption-line center. The value (33) extracted from the experimental data is smaller than σ_2^i. This substantiates our assumption that the main contribution to the STS-2 gain is made by the two-photon absorption. The relatively small value of σ_2 may be explained by the fact that the two-photon absorption scheme ($\lambda/2 = 154$ nm, hexane) corresponds to a wing of the absorption line.

6.8. Phase mismatch for SBS caused by two-photon heating

The relationship between I_L, $(I_L\gamma)$ and F (see Table 5) explains why the SBS component is not observed for $\alpha = 0.01$ cm^{-1} when $F = 11$ cm (Fig. 2a). Indeed, in this case $I_L \geqslant 10^{10}$ W/cm^2, and the total absorption coefficient $\alpha_\Sigma = \alpha + (I_L\gamma) \approx (I_L\gamma) \geqslant 1.0$ cm^{-1} is much larger than the critical value $\alpha_{CR} \approx 0.1$ cm^{-1} corresponding to phase mismatch (Fig. 4). The heating due to the two-photon absorption is sufficiently strong to cause SBS breakdown.

6.9. The phase self-modulation and the decrease in phase-conjugation fidelity caused by two-photon heating

We consider only the case of Fig. 3 ($\alpha = 0.01$ cm^{-1} = const), when linear absorption (Table 5) and linear STS-2 (Table 4) do not contribute. The case of heating due to linear absorption was discussed in [11,12].

Assuming that the two-photon absorption plays the dominant role, we replace α with $(I_L\gamma)$ in Eqs (22)–(24), and the nonlinear phase increment over distance L becomes

$$\delta\Phi\,(R,t,F) = \delta k\; L = \frac{\omega}{c}\left(\frac{\partial n}{\partial T}\right)\frac{\gamma}{\rho\; c_P}\int\limits_0^t I_L^2\,(R,\tau,F)\;\; L\,(F)\;\; d\tau. \tag{35}$$

The quantity $\left(I_L^2 L\right) = I_L\,(I_L L)$ in Eq. (35) increases with I_L as $(I_L L) = const$, i.e. $\delta\Phi\,(R,t,F)$ depends on F. The two-photon heating explains the increase in the phase self-modulation of the pump wave when F is reduced from 100 to 11 cm.

Table 6
Physical mechanisms of the stimulated backscattering of XeCl ($\lambda = 308$ nm) laser pulses with duration $\tau_0 \approx 8$ ns in hexane characterized by two typical values of the linear absorption coefficient α, for pump intensities I_L corresponding to the three focal lengths F of lens 9, and $(I_L L) \approx 1.5 \times 10^3$ MW/cm (L is the nonlinear interaction length)

F, cm	I_L, W/cm^2	Physical mechanisms of stimulated backscattering	
		$\alpha = 0.01 \div 0.08$ cm^{-1}	$\alpha = 0.17$ cm^{-1}
100	2.5×10^8	SBS	Linear STS-2
50	10^9	SBS + Two-photon STS-2	Linear STS-2 + Two-photon STS-2
11	$\geqslant 10^{10}$	Two-photon STS-2	

The hypersonic grating decay time $\tau_B \approx 1$ ns (see Section 6.3.3) is shorter than the pump duration by a factor of 8. The phase hologram adjusts to the dynamic variations of the pump field caused by the phase self-modulation due to the two-photon heating. The SBS ensures a high PC fidelity.

The thermal grating decay time $\tau_T \approx 3\ ns$ (see Section 6.3.3) is shorter than the pump duration by a factor of 3. The phase hologram cannot keep pace with the dynamic variations of the pump field caused by the phase self-modulation due to two-photon heating. Since the pump wave is scattered by a retarded hologram, the PC fidelity for two-photon STS-2 loses quality.

6.10. Stimulated scattering mechanisms consistent with the present studies

Table 6 summarizes our experimental and theoretical studies of stimulated backscattering of XeCl ($\lambda = 308$ nm) laser pulses with the duration $\tau_0 \approx 8$ ns in liquid hexane. The first two columns show the three focal lengths F of lens 9 used in our experiments and the corresponding pump intensities I_L. The last two columns list the revealed physical mechanisms of the stimulated backscattering in hexane characterized by two typical values of the linear absorption coefficient $\alpha = 0.01 \div 0.08$ cm^{-1} and $\alpha = 0.17$ cm^{-1}. Since the nonlinear region is the focal caustic of length L, the quantity $(I_L L) \approx 1.5 \times 10^3$ MW/cm remains unchanged for our experiments.

An analysis of the case $I_L \approx 2.5 \times 10^8$ W/cm^2 ($F = 100$ cm) where the two-photon absorption is insignificant (see Table 5), leads to the following conclusions.

1. The presence of linear STS-2 for $\alpha = 0.17$ cm^{-1} and its absence for $\alpha = 0.01 \div 0.08$ cm^{-1} agree with the estimated threshold value $\alpha_{STS}^{THR} \approx 0.1$ cm^{-1} (see Table 4).
2. The absence of SBS for $\alpha = 0.17$ cm^{-1} and its presence for $\alpha = 0.01 \div 0.08$ cm^{-1} are consistent with the theoretical critical value for the phase mismatch $\alpha_{CR} \approx 0.1$ cm^{-1} (see Fig. 4).
3. The absence of the SBS + linear STS-2 combination is explained by the fact that $\alpha_{STS}^{THR} \approx 0.1$ cm^{-1} is close to $\alpha_{CR} \approx 0.1$ cm^{-1}, while the step of the variation of α from 0.08 to 0.17 cm^{-1} in our experiments is not sufficiently small to observe both these mechanisms simultaneously.

The presence of the SBS + two-photon STS-2 combination indicates that the step of the variation of $\alpha_\Sigma = \alpha + (I_L \gamma)$ in our experiments is sufficient for a simultaneous observation of both mechanisms.

The presence of the linear STS-2 + two-photon STS-2 combination is yet to be substantiated. These two mechanisms are virtually impossible to separate in our experimental spectra. Our theoretical analysis shows that neither linear STS-2 nor two-photon STS-2 can be singled out as the dominant mechanism when $\alpha \geqslant 0.1$ cm^{-1} and $I_L \geqslant 10^9$ W/cm^2.

6.11. Experimental observation of a genuine SBS line in the near-ultraviolet region

According to the existing theory, which takes into account linear absorption (see Table 4 and Fig. 4), only SBS can play a role in our experiments when $\alpha < 0.1$ cm^{-1}, while only linear STS-2 can contribute

when $\alpha > 0.1$ cm^{-1} (in view of phase mismatch for SBS). It is not surprising that these two mechanisms are listed in the last column of Table 1 as those suggested in the previous studies.

Both SBS and linear STS-2 in Table 1 are incorrect. Indeed, it follows from the third column of Table 1 that $I_L \geqslant 10^{10}$ W/cm^2 in all the previous studies. However, according to Table 6, for $I_L \geqslant 10^{10}$ W/cm^2, either two-photon STS-2 or the linear STS-2 + two-photon STS-2 combination should be observed in hexane when $\alpha < 0.1$ cm^{-1} and $\alpha > 0.1$ cm^{-1}, respectively. Therefore SBS should be replaced by two-photon STS-2 in all rows of Table 1 with the exception of the last one, while the linear STS-2 should be replaced with the linear STS-2 + two-photon STS-2 combination in the last row. This consideration is corroborated by the fact that the measured frequency shift Ω in the fourth column of Table 1 is much smaller than the Brillouin shift Ω_B predicted theoretically for the same λ (Table 2). It can be concluded that the genuine SBS line has not been observed in previous studies of the stimulated scattering in the near-uv region.

In our experiments the stimulated scattering of near-uv ($\lambda = 308$ nm) laser radiation in hexane was studied, and a SBS line with frequency shift equal to 0.33 cm^{-1} (see Figs 2b and 2c) in full agreement with the theory (see Table 2), was observed. To observe the genuine SBS line we had to reduce the pump intensity from $I_L \geqslant 10^{10}$ W/cm^2 (Fig. 2a) as in previous studies (Table 1) to $I_L \leqslant 10^9$ W/cm^2 (Figs 2b and 2c), while keeping the total gain for SBS (Table 4) invariant. This made it possible to reduce the two-photon contribution to the total absorption coefficient (Table 5) and to weaken the effect of the SBS phase mismatch due to two-photon heating.

6.12. Effects of self-focusing and plasma formation on stimulated scattering

All light-producing phenomena were inspected visually through a thin transparent glass wall of the cell.

First, consider self-focusing. There are two mechanisms responsible for self-focusing – the Kerr-effect and electrostriction [31]. The relaxation time for the Kerr-effect is $\tau_K \approx 10^{-11}$ s. The relaxation time for electrostriction is approximately equal to the time for the acoustic wave to pass through the focal caustic diameter. The minimal value for this time under our experimental conditions is $\tau_{STR}^{MIN} \approx \frac{F_{MIN}\theta}{v} \approx \frac{(11\text{ cm})\,(3\times10^{-4}\text{rad})}{10^5\text{ cm/s}} \approx 3 \times 10^{-8}$ s $= 30$ ns, which is considerably more than the pump pulse duration $\tau_0 \approx 8$ ns. Therefore, as well as in [32,33], under our experimental conditions only the Kerr-effect should be taken into account. The self-focusing is characterized by the critical power [34]

$$P_{CR} = \frac{(1.22\ \lambda)^2\, 4\pi\ c}{128\ c\ n\ n_2} = \frac{\pi\ (1.22\ \lambda)^2}{32\ n\ n_2} \approx 8 \times 10^5 \text{W},$$

where $n_2 \approx 4 \times 10^{-13}\ [ESU] \approx 1.2 \times 10^{-12}\ \left[\text{cm}^2/\text{kW}\right]$ is a Kerr constant of hexane [26]. Our pump power is

$$W_L \approx \frac{1.5\text{ mJ}}{8\text{ ns}} \approx 2 \times 10^5\text{ W} \approx 0.25\ P_{CR}.$$

For the input power $P < 0.273\ P_{CR}$ self-focusing does not develop [34]. Hence, self-focusing should not affect our experiments. Usually, self-focusing in liquids is followed by thin channels of light [35] and by increase in the divergence angle of the radiation passing through the cell in the forward direction. A visual inspection of the nonlinear liquid and the radiation did not show these signs of self-focusing.

Second, consider plasma formation. The acoustic wave generated as a result of SBS is supposed to be the reason for optical destruction in solids [7,36]. The dynamics of internal optical destruction in solids

was studied in [37]. During the course of the laser pulse, the destruction has the form of a thread placed along the focal caustic. The pace of thread development is much higher than the speed of a shock wave. The thread diameter is considerably smaller than the focal caustic diameter. Subsequent to the laser pulse the destruction grows in the transverse direction and possesses the form of disks. The SBS can not completely provide the energy transformation. Preference is given to the destruction mechanisms associated with self-focusing and multi-photon ionization.

A theory of the optical breakdown in liquids does not exist, because not much is known about it [1, 34]. For $\hbar\omega = 4$ eV fast three-photon-ionization of hexane provides the initial electrons. The breakdown threshold depends on the electron multiplication rate. Different approaches (classical or quantum) are used to describe how the electron gains energy, depending on the relation between the photon energy $\hbar\omega$ and the average electron energy increment during a single collision, $\Delta\varepsilon$ [38]. If $\Delta\varepsilon >> \hbar\omega$, the classical kinetic equation can be used. If $\hbar\omega \mathfrak{e} \Delta\varepsilon$, the quantum kinetic equation containing finite-difference expressions should be used. For our moderate pump intensity $I_L < 10^{11} W/cm^2$, we have $\Delta\varepsilon \approx 1\ eV$. Taking into account $\hbar\omega = 4\ eV > \Delta\varepsilon \approx 1\ eV$, the quantum kinetic equation should be solved.

As a rough approximation, a liquid could be considered as a gas under ultrahigh pressure of thousands of atmospheres. For the noble gases under thousands of atmospheres [38,39] the optical breakdown threshold reaches $E \approx 10^6$ V/cm, $I \approx$ (E/20)$^2 \approx 2.5 \times 104^9$ W/cm^2. For molecular gases [38,40] the thresholds are hundred-folds higher than for single-atom gases, because it is more difficult for the electron to pass the "dangerous" region between excitation and ionization.

Usually, the optical breakdown in a liquid is followed by a flash of light [35] and bubbles. That was not detected by visual inspection. It is possible, that for organic liquids like hexane the electromagnetic energy is transmitted to the hydrodynamic perturbations instead of an avalanche. The emergence of SBS and STS-2 in our experiments confirms this supposition.

7. Summary

The present study focuses on the stimulated scattering of nanosecond (5 ÷ 10 ns) near-uv ($\lambda = 193 \div 351$ nm) laser pulses in liquids (hexane, heptane, and others). Some experimental results gained from previous studies concerning the frequency shift and phase-conjugation fidelity disagree with the existing theory of SS, which was developed for the near-ir ($\lambda = 0.69 \div 1.06\ \mu$m) spectral region and takes into account only linear (single-photon) light absorption.

To resolve the inconsistency, SS of XeCl excimer laser radiation ($\lambda = 308$ nm) with the duration 8 ns in liquid hexane for various values of the linear absorption coefficient α and the pump intensity I_L was investigated experimentally.

In contrast to the previous near-uv studies, we managed to create a new master oscillator, running in a single longitudinal mode. As is well-known, this mode of operation is characterized not only by a small spectrum, but also by a near-Gaussian temporal behavior without uncontrolled intensity peaks (mode interference). So our estimates of the pump intensity were much more reliable than previous ones. Due to the smaller bandwidth, we had less amplified beam energy and limited experimental possibilities as compared to the previous studies (we could not use neutral filters to control the pump intensity). We also managed to create a spectrum analyzer, which monitored the temporal spectra of two counter-propagating pulses in different but close enough fields. It allowed us to be sure that the right field involves only a pump spectrum, and the left field – only a backscattered spectrum. Without such an analyzer, any slightly-shifted backscattered spectral line may be simply confused with the spectral line of the pump radiation.

When the product $(I_L L) \approx 1.5 \times 10^3$ MW/cm (L is the nonlinear interaction length) remains invariant, the experimental SS spectrum depends not only on α, but also on I_L. For $\alpha < 0.1$ cm^{-1} and $I_L \geqslant 10^{10}$ W/cm^2, the spectrum includes a line corresponding to the mechanism of stimulated thermal scattering induced by the heating due to two-photon absorption. For $\alpha < 0.1$ cm^{-1} and $I_L \leqslant 10^9$ W/cm^2, the spectrum includes a line in the near-uv region, which corresponds to genuine stimulated Brillouin scattering and is characterized by the frequency shift $\Omega_B = 0.33$ cm^{-1}, in full agreement with the theory. For $\alpha > 0.1$ cm^{-1} or $I_L \geqslant 10^{10}$ W/cm^2, SBS is suppressed by phase mismatch due to heating caused by the linear or two-photon absorption, respectively. To detect the genuine SBS line for $\alpha < 0.1$ cm^{-1}, we had to reduce the pump intensity while keeping constant the total gain for SBS and thus weaken the phase mismatch due to the two-photon heating.

When two-photon STS-2 is used for phase-conjugation, the PC fidelity is lower than that achieved by using SBS because of the two-photon thermal phase self-modulation.

The molecular cross-section for the two-photon absorption of hexane at $\lambda = 308$ nm, $\sigma_2 \approx (2 \pm 1) \times 10^{-50}$ cm^4 s, is found from the experimental threshold pump intensity for two-photon STS-2.

The SBS lines observed in previous studies have frequency shifts much smaller than those predicted by the theory and must be interpreted as two-photon STS-2 lines. The physical mechanisms of linear STS-2 and two-photon STS-2 are essentially different and their lines can readily be distinguished in the spectrum. The total inconsistency between the experimental behavior of two-photon and linear STS-2 lines explains why the two-photon STS-2 lines observed in the previous studies were attributed to SBS for almost a decade.

The physical mechanism of two-photon STS-2 is not specific for the near-uv spectral region.

References

[1] Y.R. Shen, The Principles of Nonlinear Optics (Wiley-Interscience, New York, 1984; Nauka, Moscow, 1989; Wiley-Interscience, Hoboken, NJ, 2003).
[2] S. Kielich, Molecular Nonlinear Optics (PWN, Warsaw, 1977; Nauka, Moscow, 1981) [J.R.Lalanne, A.Ducasse, and S.Kielich, Laser Molecule Interaction: Laser Physics and Molecular Nonlinear Optics (Wiley, New York, 1996)].
[3] V.G. Dmitriev, Nonlinear Optics and Phase Conjugation (Fizmatlit, Moscow, 2003) [in Russian].
[4] B.Ya. Zeldovich, N.F. Pilipetsky and V.V. Shkunov, Principles of Phase Conjugation (Nauka, Moscow, 1985; Springer-Verlag, Berlin, 1985).
[5] I.L. Fabelinskii, Molecular Scattering of Light (Nauka, Moscow, 1965; Plenum, New York, 1968).
[6] B.Ya. Zeldovich, V.I. Popovichev, V.V. Ragulskii and F.S. Faizullov, *Zh Eksp Teor Fiz Pis'ma Red* **15** (1972), 160, [JETP Lett. **15** (1972), 109].
[7] R.Y. Chiao, C.H. Townes and B.P. Stoicheff, *Phys Rev Lett* **12** (1964), 592.
[8] E. Garmire and C.H. Townes, *Appl Phys Lett* **5** (1964), 84.
[9] R.G. Brewer and K.E. Rieckhoff, *Phys Rev Lett* **13** (1964), 334.
[10] R.G. Brewer, *Appl Phys Lett* **5** (1964), 127.
[11] V.V. Kuzmin, Tr. Fiz. Inst. P.N.Lebedeva, Akad. Nauk SSSR **207**, 3 (Nauka, Moscow, 1991) [Non-Linear Optics and Molecular Light Scattering, edited by N.G. Basov and I.L. Fabelinskii, Proc. P.N.Lebedev Phys. Inst., Vol. **207**] [in Russian].
[12] S.F. Grigoriev, O.P. Zaskalko and V.V. Kuzmin, *Zh Eksp Teor Fiz* **92** (1987), 1246 [*JETP* **65** (1987), 697].
[13] V.S. Starunov, *Zh Eksp Teor Fiz* **57** (1969), 1012 [*JETP* **30** (1970), 553].
[14] V.S. Starunov and I.L. Fabelinskii, *Usp Fiz Nauk* **98** (1969), 441; [*Sov Phys Usp* **12** (1970), 463].
[15] M. Statkine, I.J. Bijio, B.J. Feldman and R.A. Fisher, *Opt Lett* **7** (1982), 108.
[16] M.C. Gower, *Opt Lett* **7** (1982), 423.
[17] M.C. Gower, *Opt Lett* **8** (1983), 70.
[18] E. Armandillo and D. Proch, *Opt Lett* **8** (1983), 523.
[19] M.C. Gower and R.G. Caro, *Opt Lett* **7** (1982), 162.
[20] G.M. Davis and M.C. Gower, *IEEE J Quantum Electron* **27** (1991), 496.

[21] S.S. Alimpiev, V.S. Bukreev, S.K. Vartapetov, I.A. Veselovskii, V.S. Nersisian, A.Z. Obidin and A.M. Prokhorov, *Kratk Soobshch Fiz* **11**(12) (1989), [*Sov Phys-Lebedev Inst Rep* **11** (1989), 12].
[22] S.S. Alimpiev, V.S. Bukreev, S.K. Vartapetov, I.A. Veselovskii, B.I. Kusakin, S.V. Lihanckii and A.Z. Obidin, *Kvantovaya Elektron* (*Moscow*) **18** (1991), 89; [*Sov J Quantum Electron* **21** (1991), 80].
[23] A.L. Egorov, V.V. Korobkin and R.V. Serov, *Kvantovaya Elektron* (*Moscow*) **2** (1975), 513; [*Sov J Quantum Electron* **5** (1975), 291].
[24] A.J. Alcock, C.De. Michelis and M.C. Richardson, *IEEE J Quantum Electron* **6** (1970), 622.
[25] V.F. Nozdrev, The Use of Ultrasonics in Molecular Physics (Fizmathlit, Moscow, 1958; Pergamon Press, Oxford, 1965).
[26] P.P. Ho and R.R. Alfano, *Phys Rev A* **20** (1979), 2170.
[27] A.J. Gordon and R.A. Ford, The Chemist's Companion (Wiley, Ney York, 1972).
[28] Yu.N. Karamzin, A.P. Sukhorukov and V.A. Trofimov, Mathematical Modeling in Nonlinear Optics (Moscow State University Press, Moscow, 1989) [in Russian].
[29] M. Ammosov, N. Delone, M. Ivanov, I. Bondar and A. Masalov, *Adv At Mol Opt Phys* **29** (1992), 34.
[30] N.B. Delone and V.P. Krainov, Fundamentals of Nonlinear Optics of Atomic Gases (Nauka, Moscow, 1986; Wiley, New York, 1988).
[31] R.Y. Chiao, E. Garmire and C.H. Townes, *Phys Rev Lett* **13** (1964), 479.
[32] Y.R. Shen, *Phys Lett* **20** (1966), 378.
[33] P. Lallemand and N. Blombergen, *Phys Rev Lett* **15** (1965), 1010.
[34] J.F. Reintjes, Nonlinear Optical Parametric Processes in Liquids and Gases (Academic Press, New York, 1984; Mir, Moscow, 1987).
[35] R.G. Brewer and J.R. Lifsits, *Phys Lett* **23** (1966), 79.
[36] C.R. Giuliano, *Appl Phys Lett* **5** (1964), 137.
[37] J.P. Budin, *J Raffy, Appl Phys Lett* **9** (1966), 291.
[38] Yu.P. Raizer, Laser-Induced Discharge Phenomena. (Nauka, Moscow, 1974; Consultants Bureau, New York, 1977).
[39] D.H. Gili and A.A. Dougal, *Phys Rev Lett* **15** (1965), 845.
[40] Yu.B. Afanasiev, Ye.M. Belenov and I.A. Poluektov, *Zh Eksp Teor Fiz Pis'ma Red* **15** (1972), 60; [*JETP Lett* **15** (1972), 41].

Journal of Computational Methods in Sciences and Engineering 10 (2010) 411–423
DOI 10.3233/JCM-2010-0330
IOS Press

Modulation of stimulated Brillouin scattering and stimulated temperature scattering spectral components by two-photon heating

V.B. Karpov* and V.V. Korobkin
Coherent and Nonlinear Optics Department, A.M.Prokhorov General Physics Institute, Russian Academy of Sciences, Vavilov Street 38, 119991 Moscow, Russia

Abstract. The effects of linear (single-photon) and two-photon heating to the thin structures of the stokes and anti-stokes spectral components of stimulated Brillouin scattering (SBS) and stimulated temperature scattering (STS) are compared. The thin structures of the linear and two-photon STS-2 possess the same shapes. For the Fabry-Perot etalon based spectrum analyzer the linear and two-photon STS-2 components are experimentally indistinguishable not only from one another, but also from the STS-1 component. To reach the higher spectral resolution methods of heterodyning and intensity fluctuations correlation should be used. In contrast to a linear (single-photon) case for two-photon heating a stokes SBS component exhibits the spectral shift depending on the pump intensity. Emergence of the anti-stokes SBS component is possible when the pump intensity is sufficiently high so that the positive two-photon thermal gain may compensate the negative electrostrictive gain.

1. Introduction

For high enough light intensity and coherence the well-known spontaneous Brillouin-Rayleigh triplet [1,2] manifests itself as the doublet of a slightly anti-stokes shifted stimulated temperature scattering caused by linear or two-photon absorption (linear or two-photon STS-2) line and a stokes-shifted stimulated Brillouin scattering (SBS) line. For the near-ir spectral region (the pump wavelength is $\lambda_1 = 0.69 \div 1.06$ μm) this effect has been observed in [3,4]. For the near-uv spectral region ($\lambda_1 = 193 \div 351$ nm) this effect has been observed in [5], Fig. 2. Indeed, in the previous near-uv studies [6–13] the two-photon STS-2 lines have been associated mistakenly with the SBS and linear STS-2 lines [5].

SBS is the unique converter of a powerful coherent light wave into a powerful coherent hyperacoustical wave. SBS is the nonlinear-optical mechanism providing phase conjugation (PC) of the best quality [14, 15]. There are two physical mechanisms responsible for the acoustical wave amplification during an SBS process [1,2,4,16,17]. One of these mechanisms (hereinafter called the conventional SBS) is due to an electrostrictive variation of pressure [18–21]. The other one (hereinafter called the thermal SBS) is attributed to a pressure variation caused by the thermal expansion. For the linear (single-photon) light absorption the thermal SBS (hereinafter called the linear thermal SBS) has been discussed in [22–24].

It should be noted that the SBS analysis in [5], Section 6.3.1 is based on the purely conventional mechanism. Even the effect of the linear thermal SBS was ignored. This is a quite typical approximation, used for instance in the study of the PC provided by SBS [14].

*Corresponding author. E-mail: karpov@kapella.gpi.ru; korobkin@kapella.gpi.ru.

In this paper, a contribution of the two-photon heating to the thermal SBS mechanism (hereinafter called the two-photon thermal SBS) modifying the thin structures of the stokes [5], Fig. 2 and anti-stokes (not at all observed in [5]) components is analyzed.

The unshifted lines in the left sides of [5], Fig. 2 (relative to the pump ones in the right sides) correspond to the linear and two-photon STS-2 mechanisms. The shifted lines correspond to the SBS mechanism. The observation of the thin structures of these lines including the pump ones is restricted by the Fabry-Perot etalon based spectrum analyzer [5]. The spectral resolution of a Fabry-Perot etalon is limited by several MHz (or 10^{-3} cm^{-1}) [25]. To reach the higher spectral resolution methods of heterodyning and intensity fluctuations correlation should be used. Thus, the experimental high-resolution spectral profile of a Brillouin line exhibiting antisymmetrical behavior is given in [26].

In analysis, instead of a linear absorption coefficient α [1,2,4,16,17,22,24], a total absorption coefficient [5]

$$\alpha_\Sigma = \alpha + (I_L\gamma)\,, \tag{1}$$

where $(I_L\gamma)$ is the two-photon effect (I_L is the pump intensity and γ is a two-photon absorption coefficient), should be used. In [23] an effective linear absorption coefficient $\alpha_{eff}(\omega)$ has been introduced for gases to describe the thermalization processes of the absorbed electromagnetic energy.

2. Mass (bulk) and serface forces

The theory of the coupling of light and elastic waves is based on the Lagrange equation [18,19]. In [18] a linearized system for small perturbations has been solved. The photoelastic coupling of a longitudinal acoustic wave in an isotropic medium was studied in [19], and the nonlinear system from [18] taking into account a saturation effect has been solved.

The Lagrange equation [27] describes the dynamics of discrete particles. It takes into account only the mass (bulk) forces and ignores the surface ones. For a continuous media both mass and surface forces should be incorporated [28] and the Navier-Stokes equation should be used instead of the Lagrange one. Indeed, any plane acoustic wave propagating in a continuous media provides shear motion leading to the attenuation due to viscosity [29].

3. Material equations

Interaction of a light wave, characterized by a total electrical field vector E, with an isotropic dielectric medium is described by the hydrodynamic equations linearized with respect to the small deviations of density $\Delta\rho$, temperature ΔT, pressure ΔP and a velocity vector V from the equilibrium values ρ_0, T_0, P_0 and $V = 0$ [1,2,4,16,30]:

$$\begin{aligned}\rho_0\frac{\partial V}{\partial\, t} + \frac{v^2}{\delta}grad\,(\Delta\rho) + \frac{v^2\beta\rho_0}{\delta}grad\,(\Delta T) - \eta\nabla^2 V = \\ = \frac{\gamma^e}{8\pi}grad\left(E^2\right),\end{aligned} \tag{2}$$

$$\frac{\partial}{\partial\, t}(\Delta\rho) + \rho_0 div(V) = 0, \tag{3}$$

$$\left(\rho_0 C_V \frac{\partial}{\partial\, t} - \lambda_{\,T}\nabla^2\right)(\Delta T) - \frac{C_V\,(\delta-1)}{\beta}\frac{\partial}{\partial\, t}\,(\Delta\rho) = \\ = \frac{nc\alpha_\Sigma}{4\pi}\left(E^2\right) - \frac{1}{8\pi}\left(\frac{\partial\varepsilon}{\partial T}\right)_p\left(T_0\frac{\partial}{\partial\, t}\left(E^2\right)\right). \tag{4}$$

Here $v = \sqrt{\frac{1}{\rho_0\beta_S}}$ is the speed of sound in a medium with adiabatic compressibility β_S, c is the speed of light in vacuum, $\delta = \frac{C_P}{C_V}$ is the ratio of specific heats (a frequently used symbol γ in Eq. (1) provides the logical connection with [5]), $\beta = -\frac{1}{\rho_0}\left(\frac{\partial\rho}{\partial T}\right)_P$ is a volumetric thermal expansion coefficient at constant pressure, $\gamma^e = \rho_0\left(\frac{\partial\varepsilon}{\partial\rho}\right)_T$ is an electrostriction coefficient, η is viscosity, λ_T is thermal conductivity, ε is permittivity, n is a refractive index, and α_Σ is defined above in Eq. (1).

In the Navier-Stokes Eq. (2) the pressure deviation is expressed as [22,23,31–33]:

$$\Delta P = \frac{v^2}{\delta}\ \ (\Delta\rho) + \frac{v^2}{\delta}\rho_0\beta\,(\Delta T)\,, \tag{5}$$

and its gradient is moved into the left-hand side. The right-hand side of Eq. (2) represents an electrostrictive force [34]. The first and second right-hand side terms of the heat Eq. (4) represent the heating due to light absorption and due to an electrocaloric effect [1,34], respectively.

Equations (2) and (3) can be combined into one by eliminating the velocity vector V:

$$\left(-\frac{\partial^2}{\partial\, t^2} + \frac{v^2}{\delta}\nabla^2 + \frac{\eta}{\rho_0}\frac{\partial}{\partial\, t}\nabla^2\right)(\Delta\rho) + \frac{v^2\beta\rho_0}{\delta}\nabla^2\,(\Delta T) = \\ = \frac{\gamma^e}{8\pi}\nabla^2\left(E^2\right). \tag{6}$$

A permittivity variation may be expressed as

$$\Delta\varepsilon = \left(\frac{\partial\varepsilon}{\partial\rho}\right)_T\Delta\rho + \left(\frac{\partial\varepsilon}{\partial T}\right)_\rho\Delta T. \tag{7}$$

Usually [1,2,16,30]

$$\left|\left(\frac{\partial\varepsilon}{\partial\rho}\right)_T\Delta\rho\right| >> \left|\left(\frac{\partial\varepsilon}{\partial T}\right)_\rho\Delta T\right|, \tag{8}$$

$$\left(\frac{\partial\varepsilon}{\partial T}\right)_P \approx -\beta\left(\rho_0\frac{\partial\varepsilon}{\partial\rho}\right)_T. \tag{9}$$

The task has been provided by the material Eqs (4) and (6) involving two independent hydrodynamical variables $\Delta\rho$ and ΔT.

4. SBS and STS gain parameters

Consider two counterpropagating linearly polarized plane electromagnetic waves, a pump wave and a backscattered wave, characterized by electrical field vectors $\boldsymbol{E}_L$ and $\boldsymbol{E}_S$:

$$\boldsymbol{E}_L = \frac{1}{2}\boldsymbol{e}\ \left\{\ E_1\,(z,t)\ \exp\left(ik_1 z - i\omega_1 t\right) + c.c.\right\}, \tag{10}$$

$$\boldsymbol{E}_S = \frac{1}{2}\boldsymbol{e}\ \{\ E_2\left(z,t\right)\ \exp\left(-ik_2 z - i\omega_2 t\right) + c.c.\}\,. \tag{11}$$

Here, $\boldsymbol{e}$ is a polarization vector; $E_1\left(z,t\right)$ and $E_2\left(z,t\right)$ are complex amplitudes; ω_1, ω_2 and k_1, k_2 are temporal and spatial frequencies, respectively. A total electric field vector is $\boldsymbol{E} = \boldsymbol{E}_L + \boldsymbol{E}_S$. The waves are controlled by diffraction, linear and nonlinear polarizations, and are coupled by the electrodynamical Eqs [1,2,16,30]

$$\left[\nabla^2 - \frac{\varepsilon}{c^2}\frac{\partial^2}{\partial\, t^2}\right]\boldsymbol{E}_L = \frac{4\pi}{c^2}\frac{\partial^2}{\partial\, t^2}\boldsymbol{P}^{NL}_{\omega_1}, \tag{12}$$

$$\left[\nabla^2 - \frac{\varepsilon}{c^2}\frac{\partial^2}{\partial\, t^2}\right]\boldsymbol{E}_S = \frac{4\pi}{c^2}\frac{\partial^2}{\partial\, t^2}\boldsymbol{P}^{NL}_{\omega_2}, \tag{13}$$

with the right-hand sides representing the nonlinear sources oscillating with the frequencies ω_1 and ω_2. For the plane waves diffraction is absent. Following Eqs (7) and (8), a nonlinear polarization vector is

$$\boldsymbol{P}^{NL}\left(z,t\right) = \frac{1}{4\pi}\Delta\varepsilon\left(\mathrm{z,t}\right)\boldsymbol{E}\left(\mathrm{z,t}\right) \cong \frac{1}{4\pi}\left(\frac{\partial\varepsilon}{\partial\rho}\right)_T \Delta\rho\left(z,t\right)\boldsymbol{E}\left(\mathrm{z,t}\right). \tag{14}$$

According to the material Eqs (4) and (6), the nonlinearity of a dipole vector function (14) is due to the dependence of $\Delta\rho$ and ΔT on a scalar function $\boldsymbol{E}^2$. We seek the steady-state solution based on the slowly oscillating part of $\boldsymbol{E}^2$

$$\begin{array}{l}\left\langle \boldsymbol{E}^2\right\rangle = \left\langle \left(\boldsymbol{E}_L + \boldsymbol{E}_S\right)^2\right\rangle = \left\langle 2\boldsymbol{E}_L\boldsymbol{E}_S\right\rangle = \\ = \frac{1}{2}\left\{E_1\left(z\right)E_2^*\left(z\right)\ \exp\left[-i\left(\omega_1-\omega_2\right)\ t + i\left(k_1+k_2\right)\ z\right] + c.c.\ \right\}\ ,\end{array} \tag{15}$$

and the appropriate approximations for $\Delta\rho$ and ΔT

$$\Delta\rho\left(z,\ t\right) = \frac{1}{2}\ \{\ \rho_a\left(z\right)\ \exp\left[-i\left(\omega_1-\omega_2\right)\ t + i\left(k_1+k_2\right)\ z\right]\ + c.c.\}\,, \tag{16}$$

$$\Delta T\left(z,\ t\right) = \frac{1}{2}\ \{\ T_a\left(z\right)\ \exp\left[-i\left(\omega_1-\omega_2\right)\ t + i\left(k_1+k_2\right)\ z\right]\ + c.c.\}\,. \tag{17}$$

On substitution of Eqs (9), (15)–(17) into Eqs (4) and (6), a linear system for the complex amplitudes $\rho_a\left(z\right),\ T_a\left(z\right),$ and $E_1\left(z\right)E_2^*\left(z\right)$ is obtained

$$\left(-\Omega^2 + \frac{v^2}{\delta}q^2 + i\frac{\eta}{\rho_0}q^2\Omega\right)\rho_a + \frac{v^2\beta\rho_0}{\delta}q^2 T_a = \frac{1}{8\pi}\left(\rho_0\frac{\partial\varepsilon}{\partial\rho}\right)_T q^2 E_1 E_2^*, \tag{18}$$

$$i\Omega\frac{c_V\left(\delta-1\right)}{\beta}\rho_a + \left(-i\rho_0 c_V\Omega + \lambda_T q^2\right)T_a = \frac{1}{4\pi}nc\alpha_\Sigma E_1 E_2^* - \frac{1}{8\pi}\left(\rho_0\frac{\partial\varepsilon}{\partial\rho}\right)_T \beta T_0\Omega E_1 E_2^*, \tag{19}$$

where $q = |\boldsymbol{q}| = k_1 + k_2$, $\Omega = \omega_1 - \omega_2$.

Following Eqs (18)–(19) the steady-state density and temperature amplitudes are ρ_a, $T_a \propto E_1 E_2^*$. In terms of a cubic nonlinear susceptibility the nonlinear polarization vectors appearing in Eqs (12)–(13) are

$$(\boldsymbol{P}^{NL}_{\omega_1})_i = \chi^{(3)}_{ijkl}(\omega_1)(\boldsymbol{E}_L)_j(\boldsymbol{E}_S)_k(\boldsymbol{E}_S)_l, \tag{20}$$

$$(\boldsymbol{P}_{\omega_2}^{NL})_i = \chi_{ijkl}^{(3)}(\omega_2)(\boldsymbol{E}_L)_j(\boldsymbol{E}_L)_k(\boldsymbol{E}_S)_l. \tag{21}$$

Solving Eq. (18) for T_a, and inserting the result into Eq. (19) we obtain $\rho_a \propto \chi^{(3)} E_1 E_2^*$. On substitution the expression for $\Delta\rho$ from Eq. (16) into Eq. (14) we derive in accordance with Eq. (21):

$$\begin{aligned}\chi^{(3)}(\omega_2) = \frac{1}{4\pi D}\left(\rho_0\frac{\partial\varepsilon}{\partial\rho}\right)_T \frac{1}{16\pi\rho_0}\left\{-2\beta nc\alpha_\Sigma\rho_0\frac{v^2q^2}{\delta} + \left(\rho_0\frac{\partial\varepsilon}{\partial\rho}\right)_T q^2\times\right.\\ \left.[\lambda_T q^2 - i\rho_0 c_V\Omega + i\left(1-\frac{1}{\delta}\right)\rho_0 c_P\Omega]\right\}\times\left\{[-\Omega^2 + \frac{v^2q^2}{\delta} + i\frac{\eta^2q^2}{\rho_0}\Omega]\times\right.\\ \left.[\lambda_T q^2 - i\rho_0 c_V\Omega] - i\left(1-\frac{1}{\delta}\right)\rho_0 c_V\Omega v^2q^2\right\}^{-1}.\end{aligned} \tag{22}$$

In our case $D = 3$. The cubic nonlinear susceptibility defined by Eq. (22) exhibits resonances at $\Omega = 0$ and $\Omega_B = qv = (k_1 + k_2)\,v$. For $\Omega \approx 0,\ |\Omega| << \Omega_B$ Eq. (22) incorporates electrocaloric and absorptive terms:

$$\chi^{(3)R} \approx \chi^{(3)R1} + \chi^{(3)R2}, \tag{23}$$

where

$$\chi^{(3)R1} = -\frac{1}{32\pi^2 D}\left(\rho_0\frac{\partial\varepsilon}{\partial\rho}\right)_T^2 \beta_S\,(\delta-1)\left[\frac{2-\delta}{2\,(\delta-1)} + \frac{i\Gamma_R}{\Omega + i\Gamma_R}\right], \tag{24}$$

$$\chi^{(3)R2} = \frac{1}{64\pi^2 D}\left(\rho_0\frac{\partial\varepsilon}{\partial\rho}\right)_T^{\frac{\alpha_\Sigma cn\beta}{\Gamma_R c_P\rho_0}} \frac{i\Gamma_R}{\Omega + i\Gamma_R}, \tag{25}$$

$$\Gamma_R = \frac{\lambda_T q^2}{\rho_0 c_P}.$$

The correspondent imaginary parts are

$$\begin{aligned}Im\chi^{(3)R1} &= -\frac{1}{32\pi^2 D}\left(\rho_0\frac{\partial\varepsilon}{\partial\rho}\right)_T^2 \beta_S\,(\delta-1)\,\frac{\Gamma_R\Omega}{\Omega^2+\Gamma_R^2} = \\ &= -\frac{1}{32\pi^2 D}\left(\rho_0\frac{\partial\varepsilon}{\partial\rho}\right)_T^2 \beta_S\,(\delta-1)\,\frac{\Omega/\Gamma_R}{(\Omega/\Gamma_R)^2+1},\end{aligned} \tag{26}$$

$$\begin{aligned}Im\chi^{(3)R2} &= \frac{1}{64\pi^2 D}\left(\rho_0\frac{\partial\varepsilon}{\partial\rho}\right)_T^{\frac{\alpha_\Sigma cn\beta}{\Gamma_R c_P\rho_0}} \frac{\Gamma_R\Omega}{\Omega^2+\Gamma_R^2} = \\ &= \frac{1}{64\pi^2 D}\left(\rho_0\frac{\partial\varepsilon}{\partial\rho}\right)_T^{\frac{\alpha_\Sigma cn\beta}{\Gamma_R c_P\rho_0}} \frac{\Omega/\Gamma_R}{(\Omega/\Gamma_R)^2+1}.\end{aligned} \tag{27}$$

For $\Omega \approx \pm\Omega_B$ Eq. (22) incorporates electrostrictive and absorptive terms:

$$\chi^{(3)B} \approx \chi^{(3)B1} + \chi^{(3)B2}, \tag{28}$$

where

$$\chi^{(3)B1} = \frac{1}{64\pi^2 D}\left(\rho_0\frac{\partial\varepsilon}{\partial\rho}\right)_T^2 \beta_S\,(2-\delta)\,\frac{\rho_0 v}{\eta q}\,\frac{\Gamma_B/2}{|\Omega|-\Omega_B \pm i\Gamma_B/2}, \tag{29}$$

$$\chi^{(3)B2} = \mp\frac{i}{32\pi^2 D}\left(\rho_0\frac{\partial\varepsilon}{\partial\rho}\right)_T^{\frac{\alpha_\Sigma cn\beta}{\Gamma_B c_P\rho_0}}\,\frac{\Gamma_B/2}{|\Omega|-\Omega_B \pm i\Gamma_B/2}, \tag{30}$$

$$\Gamma_B = \frac{\eta q^2}{\rho_0}.$$

The bottom signs in Eqs (29)–(30) correspond to the stokes ($\omega_1 > \omega_2, \Omega > 0$) and the top sings - to the anti-stokes ($\omega_1 < \omega_2, \Omega < 0$) spectral regions, respectively. Consider the imaginary part of Eq. (29).

$$\begin{aligned} Im\chi^{(3)B1} &= \pm\frac{1}{64\pi^2 D}\left(\rho_0\frac{\partial\varepsilon}{\partial\rho}\right)_T^2 \beta_S\,(2-\delta)\,\frac{\rho_0 v}{\eta q}\,\frac{\Gamma_B^2/4}{\left(|\Omega|-\Omega_B\right)^2+\ \Gamma_B^2/4} = \\ &= \pm\frac{1}{64\pi^2 D}\left(\rho_0\frac{\partial\varepsilon}{\partial\rho}\right)_T^2 \beta_S\,(2-\delta)\,\frac{\rho_0 v}{\eta q}\,\frac{1}{\left[2\left(|\Omega|-\Omega_B\right)/\Gamma_B\right]^2+\ 1}. \end{aligned} \tag{31}$$

The maximum and minimum values of the electrostrictive term defined by Eq. (31), appearing for $(|\Omega|-\Omega_B)\approx 0$, are equal to

$$Im\chi^{(3)B1}_{MAX} = \frac{1}{64\pi^2 D}\left(\rho_0\frac{\partial\varepsilon}{\partial\rho}\right)_T^2 \beta_S\,(2-\delta)\,\frac{\rho_0 v}{\eta q} = \frac{\beta_S\,(2-\delta)\,\Omega_B}{64\pi^2 D\Gamma_B}\left(\rho_0\frac{\partial\varepsilon}{\partial\rho}\right)_T^2. \tag{32}$$

Consider the imaginary part of Eq. (30).

$$\begin{aligned} Im\chi^{(3)B2} &= \mp\frac{1}{32\pi^2 D}\left(\rho_0\frac{\partial\varepsilon}{\partial\rho}\right)_T^{\frac{\alpha_\Sigma cn\beta}{\Gamma_B c_P\rho_0}}\,\frac{\left(|\Omega|-\Omega_B\right)\ \Gamma_B/2}{\left(|\Omega|-\Omega_B\right)^2+\Gamma_B^2/4} = \\ &= \mp\frac{1}{32\pi^2 D}\left(\rho_0\frac{\partial\varepsilon}{\partial\rho}\right)_T^{\frac{\alpha_\Sigma cn\beta}{\Gamma_B c_P\rho_0}}\,\frac{2\left(|\Omega|-\Omega_B\right)/\Gamma_B}{\left[2\left(|\Omega|-\Omega_B\right)/\Gamma_B\right]^2+\ 1}. \end{aligned} \tag{33}$$

The maximum and minimum values of the absorptive term defined by Eq. (33), appearing for $(|\Omega|-\Omega_B)\approx \pm\Gamma_B/2$, are equal to

$$\begin{aligned} Im\chi^{(3)B2}_{MAX} &= \frac{1}{32\pi^2 D}\left(\rho_0\frac{\partial\varepsilon}{\partial\rho}\right)_T \frac{\alpha_\Sigma cn\beta}{\Gamma_B c_P\rho_0}\,\frac{\Gamma_B^2/4}{\Gamma_B^2/4+\Gamma_B^2/4} = \\ &= \frac{\alpha_\Sigma cn\beta}{64\pi^2 D\Gamma_B c_P\rho_0}\left(\rho_0\frac{\partial\varepsilon}{\partial\rho}\right)_T. \end{aligned} \tag{34}$$

The ratio of Eqs (34) and (32) provides the relative contribution of the absorptive and electrostrictive mechanisms into SBS gain (see Section 7).

$$\frac{Im\chi^{(3)B2}_{MAX}}{Im\chi^{(3)B1}_{MAX}} = \left(\frac{\alpha_\Sigma cn\beta}{64\pi^2 D\Gamma_B c_P\rho_0}\left(\rho_0\frac{\partial\varepsilon}{\partial\rho}\right)_T\right)\ \left(\frac{64\pi^2 D\Gamma_B}{\beta_S\,(2-\delta)\,\Omega_B}\left(\rho_0\frac{\partial\varepsilon}{\partial\rho}\right)_T^{-2}\right) =$$

$$= \frac{\alpha_\Sigma cn\beta}{c_P\rho_0\beta_S\left(2-\delta\right)\Omega_B}\left(\rho_0\frac{\partial\varepsilon}{\partial\rho}\right)_T^{-1} = \frac{\left(\delta-1\right)}{\left(2-\delta\right)}\frac{\alpha_\Sigma cn}{\beta T_0\Omega_B}\left(\rho_0\frac{\partial\varepsilon}{\partial\rho}\right)_T^{-1} = \tag{35}$$

$$= \frac{\left(\delta-1\right)}{\left(2-\delta\right)}\frac{\alpha_\Sigma\lambda_1}{4\pi\beta T_0}\frac{c/v}{sin\left(\theta/2\right)}\left(\rho_0\frac{\partial\varepsilon}{\partial\rho}\right)_T^{-1},$$

where

$$\frac{\beta}{\beta_S} = \frac{\rho_0 c_P\left(\delta-1\right)}{\beta T_0}, \quad \lambda_1 = \frac{2\pi c}{\omega_1}, \quad k_1 = \frac{2\pi n}{\lambda_1},$$

$$\Omega_B = qv = 2k_1 v\ sin\left(\theta/2\right) = \frac{4\pi\ v\ n}{\lambda_1} sin\left(\theta/2\right),$$

λ_1 is the pump wavelength and θ is the angle of scattering.

On substitution of the resulting expression for P^{NL} into Eqs (12)–(13) we derive a system [16]:

$$\left(\frac{\partial}{\partial z}+\alpha_\Sigma\right)\left|E_1\left(z\right)\right|^2 = -G\ \left|E_1\left(z\right)\right|^2\left|E_2\left(z\right)\right|^2, \tag{36}$$

$$\left(\frac{\partial}{\partial z}-\alpha_\Sigma\right)\left|E_2\left(z\right)\right|^2 = -G\ \left|E_1\left(z\right)\right|^2\left|E_2\left(z\right)\right|^2. \tag{37}$$

Following Eq. (37), when the pump intensity $I_L\left(z\right)\propto\left|E_1\left(z\right)\right|^2$ is treated as constant over the length L of nonlinear interaction, the scattered wave intensity $I_S\left(z\right)\propto\left|E_2\left(z\right)\right|^2$ exponentially increases along z with a gain coefficient

$$g = G\left|E_1\right|^2-\alpha_\Sigma,$$

where $G\propto Im\chi^{(3)}(\omega_2)$ is a gain parameter. The general formula for G is [16] (See Eqs (26), (27), (31), and (33))

$$G\left(\Omega\right) = \pm\beta_B^e\frac{1}{1+\left(2\Delta\Omega/\Gamma_B\right)^2}\pm\beta_B^a\frac{2\Delta\Omega/\Gamma_B}{1+\left(2\Delta\Omega/\Gamma_B\right)^2}+\left(\beta_R^e-\beta_R^a\right)\frac{\Omega/\Gamma_R}{1+\left(\Omega/\Gamma_R\right)^2}, \tag{38}$$

where

$$\Omega=\omega_1-\omega_2, \quad \Delta\Omega=\left|\Omega\right|-\Omega_B, \quad \Omega_B=\left(k_1+k_2\right)v, \tag{39}$$

$$\Gamma_B = \frac{\eta\left(k_1+k_2\right)^2}{\rho_0}, \quad \Gamma_R = \frac{\lambda_T\left(k_1+k_2\right)^2}{\rho_0 C_P}. \tag{40}$$

In the first two expressions of Eq. (38) signs "$+$" and "$-$" correspond to the stokes ($\omega_1>\omega_2,\Omega>0$) and anti-stokes ($\omega_1<\omega_2,\Omega<0$) spectral regions, respectively. The material parameters $\beta_B^e,\beta_B^a,\beta_R^e$ and β_R^a are positive.

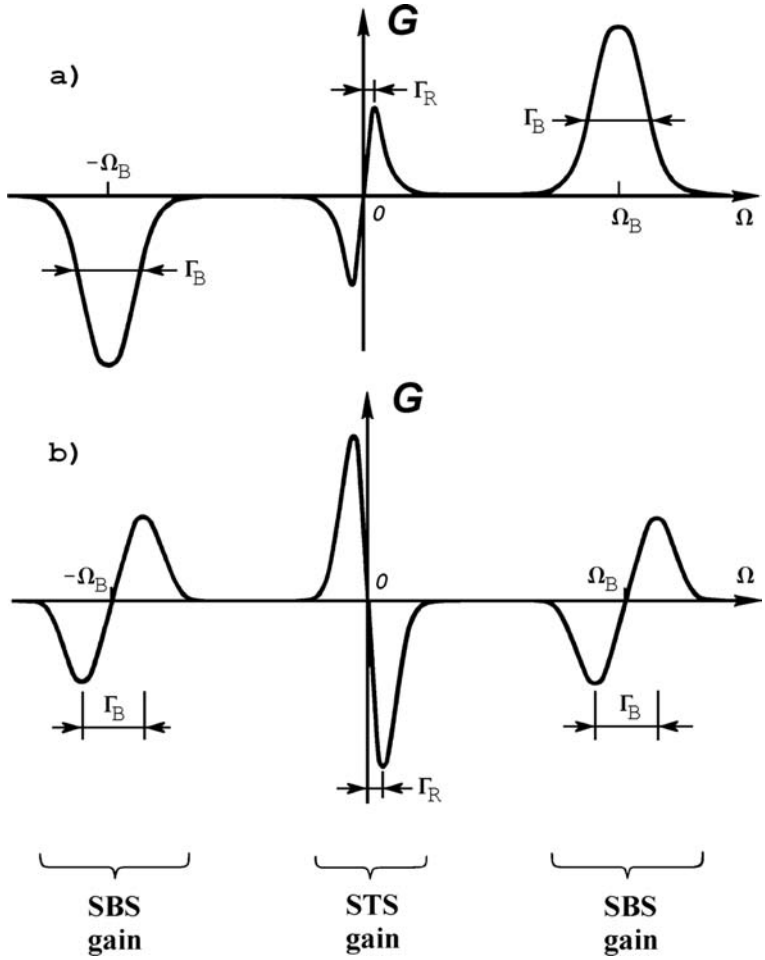

Fig. 1. The gain parameter $G(\Omega)$ defined by Eq. (38) for the SBS and STS mechanisms: (a) conventional SBS and STS-1; (b) thermal SBS and STS-2.

5. SBS and STS spectral components for linear absorption

Figure 1 shows the spectral profiles of $G(\Omega)$ for the SBS and STS mechanisms. For linear absorption such curves can be found in [2,17]. A couple of the SBS curves in the vicinity of the stokes resonance can be found in [4,16]. Excitation of an anti-stokes SBS component was not considered there.

The term proportional to β_B^e in Eq. (38) represents the conventional SBS. The spectral profile (Fig. 1a) possesses positive stokes and negative anti-stokes values. The widths (FWHM) of resonance peaks are approximately equal to Γ_B.

The term proportional to $\beta_B^a \propto \alpha$ represents the linear thermal SBS. The spectral profile (Fig. 1b) possesses positive and negative values in both stokes and anti-stokes regions. The widths (FWHM) of resonance peaks are approximately equal to $\Gamma_B/2$.

The term proportional to $\beta_R^a \propto \alpha$ represents the STS due to linear absorption (the linear STS-2). The spectral profile (Fig. 1b) possesses positive anti-stokes and negative stokes values. The widths (FWHM) of resonance peaks are approximately equal to Γ_R.

The term proportional to β_R^e represents the STS due to an electrocaloric effect (the STS-1). The spectral profile (Fig. 1a) is mirror symmetric to that of the linear STS-2.

6. SBS and STS spectral components for two-photon absorption

Single-photon and two-photon transitions provide complementary spectroscopic data [16]. In analysis [5] linear (single-photon) absorption switches to two-photon one by replacing α with γI_L. In particular, β_R^a, $\beta_B^a \propto \gamma I_L$.

Being essentially different [5], the mechanisms of the linear STS-2 and two-photon STS-2 are characterized by the common gain curve (Fig. 1b). The shifts and widths of its resonance peaks are close to Γ_R, which is less than the spectral resolution of the typical experimental setup [5]. In this respect, the linear and two-photon STS-2 spectral components are experimentally indistinguishable not only from one another, but also from the STS-1 one, characterized by the mirror symmetric gain curve (Fig. 1a).

SBS contains the experimentally distinguishable [16] conventional and thermal components. In the stokes region the conventional SBS component must be shifted by the thermal SBS component. For linear absorption this shift depends on α. For two-photon absorption this shift depends on γI_L (see Section 7). In the anti-stokes region the positive two-photon thermal values, being proportional to $\beta_B^a \propto I_L$, are added to the negative conventional values, being proportional to $\beta_B^e = \text{const}$, and the positive overall SBS gain can be achieved when I_L is sufficiently high.

7. Overall stokes SBS gain

Denoting the stokes SBS part of Eq. (38) by β_B and dividing it by β_B^e, we obtain

$$(\beta_B/\beta_B^e) = \frac{1}{1+(2\Delta\Omega/\Gamma_B)^2} + (\beta_B^a/\beta_B^e)\,\frac{2\Delta\Omega/\Gamma_B}{1+(2\Delta\Omega/\Gamma_B)^2}. \tag{41}$$

Setting

$$(\beta_B/\beta_B^e) \equiv Z, \quad (\beta_B^a/\beta_B^e) \equiv Y, \quad (2\Delta\Omega/\Gamma_B) \equiv X,$$

we rewrite Eq. (41) as

$$Z\,(X,Y) = \frac{1}{1+X^2} + Y\frac{X}{1+X^2}. \tag{42}$$

The symmetric (1) and antisymmetric (2) curves in Fig. 2 represent the normalized right-hand side terms of Eq. (42), respectively, in the case of $Y = 1$.

The parameters β_B^a, β_B^e, and Γ_B are independent of $\Delta\Omega$. A variable X describes the frequency shift $\Delta\Omega$. When $X = 1$, the shift is $\Delta\Omega = \Gamma_B/2$. A variable $Y \geqslant 0$ expresses a relative contribution of the thermal and conventional SBS mechanisms. $Y < 1$ is the realistic case of the strong conventional and weak thermal mechanisms; and $Y > 1$ is the unrealistic case because of the self-action and phase mismatch due to heating [5]. For linear absorption [2,4] (see Eq. (35))

$$Y = \frac{\beta_B^a}{\beta_B^e} = \frac{\delta-1}{2-\delta}\,\frac{\alpha\lambda_1}{4\pi\beta T_0}\,\frac{c/v}{sin\,(\theta/2)\,\rho_0\,(\partial\varepsilon/\partial\rho)_T}, \tag{43}$$

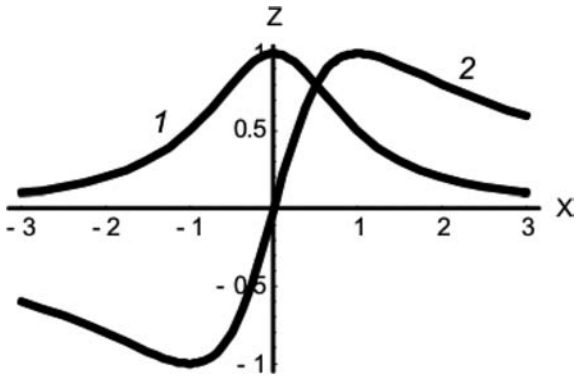

Fig. 2. Normalized spectral curves of the gain parameter for: (1) the conventional SBS; (2) the thermal SBS.

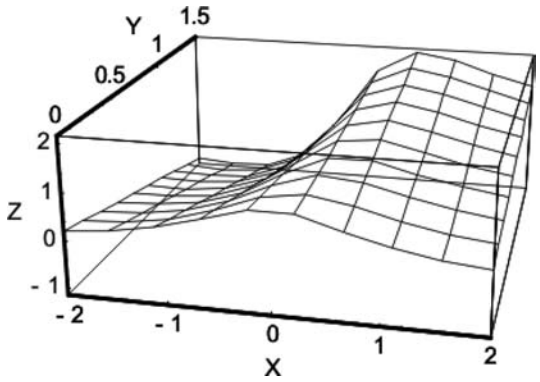

Fig. 3. A three-dimensional plot of the overall stokes SBS gain parameter for the conventional and thermal mechanisms.

where $\theta = \pi$ for the backscattering. Thus,

$$Y = (\text{const}) \times \alpha. \tag{44}$$

For two-photon absorption α is substituted by γI_L in Eq. (43), and

$$Y = (\text{const}) \times (\gamma I_L)\,. \tag{45}$$

According to Eqs (44) and (45), when the material properties are held constant ($\alpha, \gamma = \text{const}$), a change in I_L can cause a change in Y for the two-photon thermal SBS, only.

A function $Z\,(X,\ Y)$ can be treated as a dependence const $\times\, \beta_B\,(X)$ at different values of Y. Figure 3 shows a three-dimensional plot of $Z = Z\,(X,\ Y)$ for Y varying from 0 to 1.5. The intersection of $Z\,(X,\ Y)$ with the plane $Y = 0$ is the even function of X corresponding to the conventional SBS. The contour plot in Fig. 4 demonstrates the shift more clearly.

The experimentally observed stimulated scattering spectral components are 5-times narrower [14] than the gain curves in Figs 3 and 4. Hence, in an experiment the extra shift must be more pronounced.

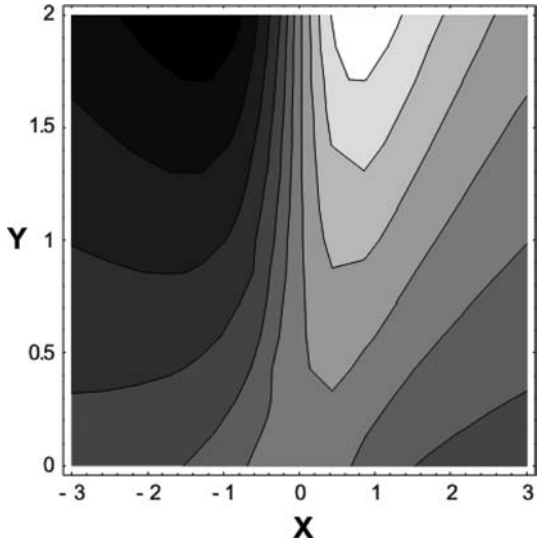

Fig. 4. The contour plot corresponding to Fig. 3. The gray-scale legend is evident from Fig. 3

8. Numerical estimates for spectral shift

According to the relaxation theory developed by Mandelstam and Leontovich, attenuation of a hypersonic wave in a liquid is dominated by shear viscosity [20,32,33,35]. Therefore,

$$\eta \approx \frac{2\eta_1}{3}, \quad k_1 + k_2 \approx 2k_1 = \frac{4\pi n}{\lambda_1}, \tag{46}$$

where η_1 is a shear viscosity coefficient. From Eq. (40) we obtain

$$\Gamma_B = \frac{2\eta_1}{3\rho_0}\left(\frac{4\pi n}{\lambda_1}\right)^2 = \frac{32\pi^2 n^2 \eta_1}{3\rho_0 \lambda_1^2}. \tag{47}$$

Following [5], we perform estimates for liquid hexane (C_6H_{14}), $\lambda_1 = 308$ nm, and the material parameters [1,20,35,36]:

$$\lambda_1 \approx 3\times 10^{-5}\ cm\ ,\ \theta = \pi\ ,\ \rho_0 \approx 0.66\ \tfrac{g}{cm^3},\ n \approx 1.4\ ,\ \eta_1 \approx 3.2\times 10^{-3} P \approx 3.2\times 10^{-3}\tfrac{g}{cm\ s},$$
$$\beta \approx 1.4\times 10^{-3} K^{-1},\ T_0 \approx 300\ K,\ v \approx 10^5 \tfrac{cm}{s},\ c \approx 3\times 10^{10}\tfrac{cm}{s},\ \rho_0\left(\tfrac{\partial \varepsilon}{\partial \rho}\right)_T \approx 1\ ,\ \delta = \tfrac{C_P}{C_V} \approx 1.3.$$

Then Eq. (47) yields

$$\Gamma_B \approx 1.1\times 10^9 Hz \approx 0.03\ \text{cm}^{-1}.$$

Eq. (43) gives

$$Y = \frac{\beta_B^a}{\beta_B^e} \approx 0.73\times\alpha, \tag{48}$$

where α is measured in cm^{-1}. $Y = 1$ corresponds to $\alpha = 1.37\ \text{cm}^{-1}$.

Table 1
Two-photon contribution γI_L to the total absorption coefficient at $\lambda_1 =$ 308 nm in hexane for the three values of the pump intensity I_L

I_L W/cm^2	γI_L, cm^{-1}
$\geqslant 10^{10}$	$\geqslant 1.0$
10^9	≈ 0.1
2.5×10^8	≈ 0.025

For two-photon absorption α is substituted by γI_L in Eq. (48), and

$$Y = 0.73 \times (\gamma I_L)\,. \tag{49}$$

Table 1 borrowed from [5] lists the two-photon contribution γI_L obtained for the three experimental values of I_L. The maximum value is $(\gamma I_L^{\max}) \approx 1$ cm^{-1} and

$$Y^{\max} = 0.73 \times (\gamma I_L^{\max}) \approx 0.73.$$

Due to losses and saturation the stimulated scattering is generated near the top of the curve in Fig. 3. Hence, from Fig. 4 $Y \approx 0.73$ corresponds to $X \approx 0.5$, and the frequency shift is

$$\Delta\Omega \approx \frac{\Gamma_B}{4} \approx 0.007 \text{ cm}^{-1}.$$

It should be noted that the SBS component was suppressed in [5] at $I_L^{\max}$ because of the phase mismatch associated with the two-photon heating. For $I_L \approx 10^9$ W/cm^2 we have $(\gamma I_L) \approx 0.1$ cm^{-1} (see Table 1) and $Y \approx 0.07$ (see Eq. (49)). The appropriate shift (see Fig. 4) is too small, to be detected under the experimental conditions of [5]. This is not surprising because the analysis presented in [5] was focused on other issues.

9. Summary

The basic equations describing stimulated Brillouin scattering (SBS) and stimulated temperature scattering (STS) are used to determine the spectral profile of the gain parameter for the stokes and anti-stokes spectral regions. The cases of the linear (single-photon) and two-photon absorption are compared.

For the Fabry-Perot etalon based spectrum analyzer the linear STS-2 and two-photon STS-2 components are experimentally indistinguishable not only from one another, but also from the STS-1 component.

In the stokes region the conventional SBS component is shifted by the thermal SBS component. In contrast to linear absorption, for two-photon absorption this shift depends on the pump intensity I_L. In the anti-stokes region the positive two-photon thermal gain, being proportional to I_L, is added to the negative conventional gain, and the positive overall SBS gain can be achieved when I_L is sufficiently high. Estimates made for liquid hexane and a pump wavelength 308 nm show that the typical extra shift of the stokes SBS component is 0.007 cm^{-1}.

The spectral resolution of a Fabry-Perot etalon is limited by several MHz (or 10^{-3} cm^{-1}). To reach the higher spectral resolution the methods of heterodyning and intensity fluctuations correlation should be used.

References

[1] S. Kielich, Molecular Nonlinear Optics (PWN, Warsaw, 1977/Nauka, Moscow, 1981); J.R. Lalanne, A. Ducasse and S. Kielich, Laser – Molecule Interaction: Laser Physics and Molecular Nonlinear Optics (Wiley, New York, 1996).
[2] S.A. Akhmanov and N.I. Koroteev, Methods of Nonlinear Optics in Spectroscopy of Light Scattering (Nauka, Moscow, 1981) (in Russian).
[3] D.H. Rank, C.W. Cho, N.D. Foltz and T.A. Wiggins, *Phys Rev Lett* **19** (1967), 828.
[4] V.S. Starunov and I.L. Fabelinskii, *Usp Fiz Nauk* **98** (1969), 441; [*Sov Phys Usp* **12** (1970), 463].
[5] V.B. Karpov and V.V. Korobkin, *Phys Rev A* **77**(063812) (2008), 1–14.
[6] M. Statkine, I.J. Bijio, B.J. Feldman and R.A. Fisher, *Optics Letters* **7**(3) (1982), 108.
[7] M.C. Gower, *Optics Letters* **7**(9) (1982), 423.
[8] M.C. Gower, *Optics Letters* **8**(2) (1983), 70.
[9] E. Armandillo and D. Proch, *Optics Letters* **8**(10) (1983), 523.
[10] M.C. Gower and R.G. Caro, *Optics Letters* **7**(4) (1982), 162.
[11] G.M. Davis and M.C. Gower, *IEEE J Quant Electron* **27**(3) (1991), 496.
[12] S.S. Alimpiev, V.S. Bukreev, S.K. Vartapetov, I.A. Veselovskii, V.S. Nersisian, A.Z. Obidin and A.M. Prokhorov, *Kratk Soobshch Fiz* (12) (1989), 11; [*Sov Phys-Lebedev Inst Reports* (12) (1989), 12].
[13] S.S. Alimpiev, V.S. Bukreev, S.K. Vartapetov, I.A. Veselovskii, B.I. Kusakin, S.V. Lihanckii and A.Z. Obidin, *Kvant Elektron* (*Moscow*) **18** (1991), 89; [*Quant Electron* **21** (1991), 80].
[14] B.Ya. Zeldovich, N.F. Pilipetsky and V.V. Shkunov, Principles of Phase Conjugation (Nauka, Moscow, 1985/Springer-Verlag, Berlin, 1985).
[15] V.G. Dmitriev, Nonlinear Optics and Phase Conjugation (Fizmatlit, Moscow, 2003) [in Russian].
[16] Y.R. Shen, The Principles of Nonlinear Optics (Wiley-Interscience, New York, 1984/Nauka, Moscow, 1989/Wiley-Interscience, Hoboken, NJ, 2003).
[17] B.Ya. Zeldovich and I.I. Sobelman, *Usp Fiz Nauk* **101** (1970), 3; [*Sov Phys Usp* **13** (1970), 307].
[18] N.M. Kroll, *J Appl Phys* **36** (1965), 34.
[19] C.L. Tang, *J Appl Phys* **37** (1966), 2945.
[20] I.L. Fabelinskii, Molecular Scattering of Light (Nauka, Moscow, 1965/Plenum, New York, 1968).
[21] N. Bloembergen, Nonlinear Optics (W.A.Benjamin Inc., New York, 1965/Mir, Moscow, 1966).
[22] R.M. Herman and M.A. Gray, *Phys Rev Lett* **19** (1967), 824.
[23] M.A. Gray and R.M. Herman, *Phys Rev* **181** (1969), 374.
[24] R.N. Enns and I.P. Batra, *Phys Rev* **180** (1969), 227.
[25] J.M. Vaughan, in Photon Correlation and Light Beating Spectroscopy, Ed. by H.Z. Cummins and E.R. Pike, (Plenum, New York, 1974/Mir, Moscow, 1978).
[26] E.R. Pike, in Photon Correlation and Light Beating Spectroscopy, Ed. by H.Z. Cummins and E.R. Pike (Plenum, New York, 1974/Mir, Moscow, 1978).
[27] L.D. Landau and E.M. Lifshitz, *Course of Theoretical Physics*, Vol. 1: Mechanics (Nauka, Moscow, 1988/Pergamon, Oxford, 1960).
[28] L.G. Loitsianskii, Mechanics of Liquids and Gases (Drofa, Moscow, 2003/Pergamon, Oxford, 1966).
[29] J. Lamb, in Physical Acoustics Principles and Methods, Ed. by W.P. Mason, Vol. II Part A, Properties of Gases, Liquids and Solutions (Academic Press, New York, 1965/Mir, Moscow, 1968).
[30] Nonlinear Spectroscopy, Ed. by N. Bloembergen (Societa Italiana di Fisica, Bologna, 1977/North-Holland Publ. Comp., Amsterdam, 1977/Mir, Moscow, 1979).
[31] V.E. Gusev and A.A. Karabutov, Laser Optical Acoustics (Nauka, Moscow, 1991) (in Russian).
[32] I.G. Mikhailov, V.A. Solov'ev and Yu.P. Syrnikov, Fundamentals of Molecular Acoustics (Nauka, Moscow, 1964) (in Russian).
[33] L.D. Landau and E.M. Lifshitz, *Course of Theoretical Physics*, Vol. 6: Hydrodynamics (Nauka, Moscow, 1986/Pergamon, Oxford, 1984).
[34] L.D. Landau and E.M. Lifshitz, *Course of Theoretical Physics*, Vol. 8: Electrodynamics of Continuous Media (Nauka, Moscow, 1982/Pergamon, Oxford, 1984).
[35] V.F. Nozdrev, The Use of Ultrasonics in Molecular Physics (Fizmathlit, Moscow, 1958/Pergamon, Oxford, 1965).
[36] M.I. Shakhparonov, Methods for Studying Heat Motion of Molecules and Structure of Liquids (Moscow State University Press, Moscow, 1963) (in Russian).

Journal of Computational Methods in Sciences and Engineering 10 (2010) 425–431
DOI 10.3233/JCM-2010-0331
IOS Press

Exciting field phase effect on the entanglement death and birth phenomena for nonlinear coupler system

A. Kowalewska-Kudłaszyk[a,*] and W. Leoński[b]
[a]*Nonlinear Optics Division, Department of Physics, Adam Mickiewicz University, Umultowska 85, 61-614 Poznań, Poland*
[b]*Institute of Physics, University of Zielona Góra Prof.Z.Szafrana 4a, 65-516 Zielona Góra, Poland*

Abstract. We consider time-evolution of the disentanglement process of once generated entangled qubit pair as a result of the phase variation of the pumping field. As a source of maximally entangled states we use the nonlinear coupler (two oscillators with Kerr-like nonlinearities) with nonlinear internal interactions. The coupler prepared in a maximally entangled state interacts afterwards with external reservoir of thermal character and pumping field as well. We show that the fact of the coupling with additional state (which can create additional entanglement with one of the 2-qubit system's previously entangled states) is an origin of interesting entanglement decay behaviour. We can observe shortening of both: entanglement death-time and entanglement birth caused by changing the phase of an external driving field.

1. Introduction

The main subjects of interest of nonlinear optics at its early stage were connected with interactions of classically treated light and matter. Practically attainable strong optical fields made it possible to discover the new, nonlinear properties of molecules and atoms which can be revealed in such interactions. Many papers by professor S.Kielich have been devoted to these problems – see the comprehensive list of his papers concerning for instance Kerr and Cotton-Mouton effects in dielectric liquids, light scattering and others in [1]. Gradualy investigation of nonlinear optical processes gave rise to development of nonlinear quantum optics dealing with the quantum properties of optical fields. In particular, among others, problems concerning photon statistics or obtaining squeezed states of light were widely discussed [1]. They were also thoroughly investigated with references to the systems described by Kerr nonlinearities (see for example [2–4]). It should be also pointed out that many other physical aspects of such systems (as classically or quantum chaotic dynamics, generation of one photon states) were also considered in the group founded by Prof. Kielich – see for example [5,6].

In modern quantum optics problems related to quantum entanglement belong to those of the greatest interest and attract a lot of attention. They are closely related to quantum information theory. In this domain of research of great current importance the role of nonlinear media is also essential. The systems with nonlinearities of the Kerr type turned out to be useful in quantum informatics – one of the areas

*Corresponding author. E-mail: e-mail:annakow@amu.edu.pl.

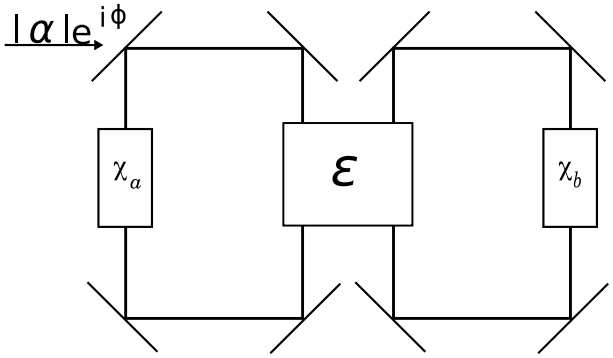

Fig. 1. The model of a nonlinear coupler with external pumping by the coherent field of the amplitude $|\alpha|$ and phase ϕ.

of quantum theory – as a potential source of maximally entangled states. The processes of generation of such states in a system composed of two nonlinear systems (described by nonlinearities of the Kerr type) interacting with each other in a linear or a nonlinear way were mentioned in [7,8] and in [9]. Such systems, called in literature nonlinear couplers (or in quantum information theory papers *nonlinear quantum scissors*), have been also investigated from the point of view of the properties of light generated in these processes.

From the practical point of view, the problems concerning the decay of entanglement in a real environment are of special interest. The system-environment interactions lead to the entanglement losses but they are not always of the same character. In several recent years many papers have been devoted to the so called *sudden death* [10,11] or even *sudden birth of entanglement* [12,13]. Various types of entangled pair's environments lead to diverse types of decay – an entanglement once generated may not only unexpectedly disappear in a finite time (we observe a *sudden death* effect) but also sometimes its reappearance is possible (*sudden birth*) in spite of the fact that within the entangled pair there are no direct interactions.

In this context a nonlinear coupler has also its important place in the studies of the disentanglement processes. We have dealt with this problem for example in [14], where the thermal reservoir was the reason for sudden death of entanglement generated by the coupler or death and birth events appearing one after another.

In the present considerations we would like to concentrate on the problem of the influence of the phase of the external coherent field exciting one of the couplers modes on the entanglement decay in an external reservoir.

2. The model

We model the nonlinear coupler via two anharmonic oscillators (described by the Kerr-like nonlinearities χ_a and χ_b) with nonlinear interaction between them of the strength ϵ. Moreover, we assume that the system is externally driven and this pump strength is characterized by the complex parameter $\alpha = |\alpha|e^{i\phi}$. In fact, the system is described by the following Hamiltonian:

$$\hat{H} = \frac{\chi_a}{2}(\hat{a}^\dagger)^2\hat{a}^2 + \frac{\chi_b}{2}(\hat{b}^\dagger)^2\hat{b}^2 + \epsilon(\hat{a}^\dagger)^2\hat{b}^2 + \epsilon^\star(\hat{b}^\dagger)^2\hat{a}^2 + \alpha\hat{a}^\dagger + \alpha^\star\hat{a} \tag{1}$$

where $\hat{a}(\hat{a}^\dagger)$ and $\hat{b}(\hat{b}^\dagger)$ are the usual photon annihilation (creation) operators in the oscillators modes a and b, respectively. The exemplary scheme of such a coupler can be depicted as in Fig. 1.

It has been already shown that the system we deal with can be treated as *nonlinear quantum scissors* (NQS) device – under some assumptions, the system cuts off the whole space of the two mode number states and leaves the system's dynamic between just the three of them:

$$|\psi(t)\rangle_{cut} = c_{2,0}(t)\,|2\rangle_a\,|0\rangle_b + c_{1,2}(t)\,|1\rangle_a\,|2\rangle_b + c_{0,2}(t)\,|0\rangle_a\,|2\rangle_b\,. \tag{2}$$

Moreover, it can be a source of maximally entangled states (MES) [9]. MES states generated by the nonlinear Kerr-like coupler with nonlinear interaction between the oscillators are the following:

$$\begin{aligned}
|B_1\rangle &= \frac{1}{\sqrt{2}}\left(|2\rangle_a\,|0\rangle_b + i\;|0\rangle_a\,|2\rangle_b\right),\\
|B_2\rangle &= \frac{1}{\sqrt{2}}\left(|2\rangle_a\,|0\rangle_b - i\;|0\rangle_a\,|2\rangle_b\right),\\
|B_3\rangle &= \frac{1}{\sqrt{2}}\left(|2\rangle_a\,|0\rangle_b + i\;|1\rangle_a\,|2\rangle_b\right)
\end{aligned} \tag{3}$$

and in fact are the *Bell-like* states. Our system can be treated from the quantum information theory point of view as a qutrit-qubit one since the dynamics in the mode a is restricted to the three states $\{|0\rangle, |1\rangle, |2\rangle\}$, whereas for the mode b to the two states $\{|0\rangle, |2\rangle\}$.

3. Decay of entanglement – interaction with external reservoir

The main aim of this paper is to examine the influence of phase ϕ of the parameter of interaction with the pumping field α on the process of disentanglement resulting from the interaction with external reservoir. Therefore, we prepare our system to be initially in one of the maximally entangled states (in our case $|B_1\rangle$ state) and after that we allow the system to interact with the external environment. We consider the zero-temperature as well as thermal reservoirs and model the interactions via the master equation in the standard Born and Markov approximations. This equation can be written as

$$\begin{aligned}
\frac{d\hat{\rho}}{dt} = &-\frac{1}{i}\left(\hat{\rho}\hat{H} - \hat{H}\hat{\rho}\right) + \sum_{k\in\{a,b\}}\left[\hat{C}_k\hat{\rho}\hat{C}_k^\dagger - \frac{1}{2}\left(\hat{C}_k^\dagger\hat{C}_k\hat{\rho} + \hat{\rho}\hat{C}_k^\dagger\hat{C}_k\right)\right]\\
&+ 2\sum_{k\in\{a,b\}}\left[\hat{C}_{k_n}^\dagger\hat{\rho}\hat{C}_{k_n} + \hat{C}_{k_n}\hat{\rho}\hat{C}_{k_n}^\dagger - \hat{C}_{k_n}^\dagger\hat{C}_{k_n}\hat{\rho} - \hat{\rho}\hat{C}_{k_n}\hat{C}_{k_n}^\dagger\right],
\end{aligned} \tag{4}$$

where the operators $\hat{C}_a$ and $\hat{C}_b$ are responsible for the damping in both the oscillator modes a and b, whereas $\hat{C}_{a_n}$ and $\hat{C}_{b_n}$ describe the interaction with thermal bath. These operators are defined as:

$$\hat{C}_k = \sqrt{2\gamma_k}\,\hat{k}, \hat{C}_{k_n} = \sqrt{\gamma_k n_k}\,\hat{k} \tag{5}$$

where $k \in \{a, b\}$.

As a measure of entanglement degree we choose the concurrence, proposed by Wooters in [15]. However, it is defined for the $2 \otimes 2$ systems, whereas in our case the system is of $3 \otimes 2$ dimension. Therefore, in further considerations we focus on the entanglement obtained within the 2-qubit subsystem of the whole one. Our system can be treated as a 2-qubit one only when the external pumping is absent.

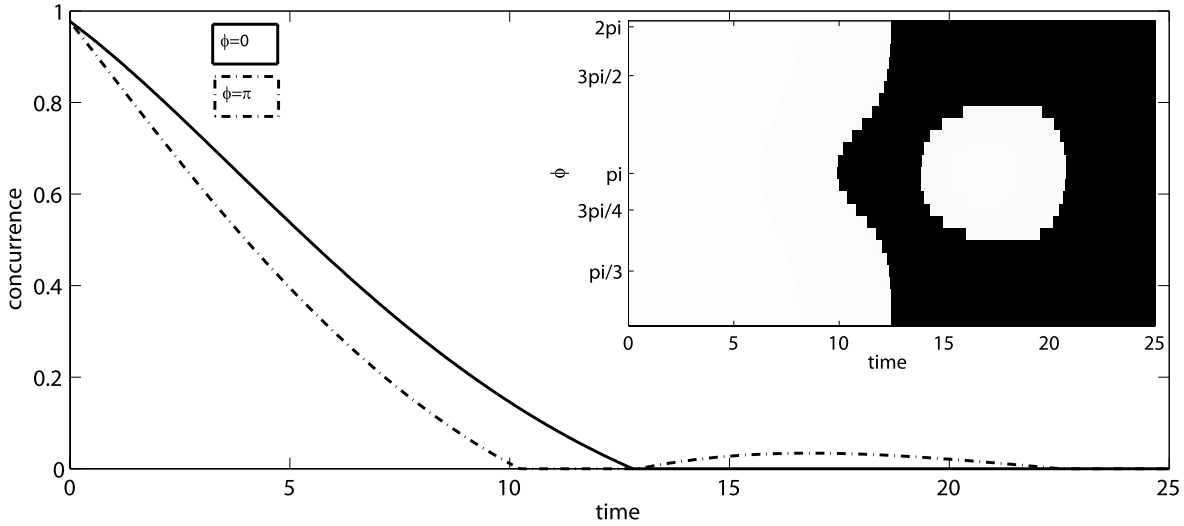

Fig. 2. Concurrence versus time for the two-qubit subsystem for various values of phase ϕ of external pumping. A coupler is initially prepared in a MES state and later left inside the zero-temperature reservoir. We assume that $|\alpha| = \pi/\chi$, $\gamma_a = \gamma_b = 0.01$, $n_a = 0$, $n_b = 1$ and $\epsilon = 0$. The parameters $\chi_a = \chi_b = \chi = 25$ and time are scaled in units of $1/\chi$.The inset – the map of $C(t)$ for various values of ϕ. The black areas are for $C(t) = 0$, whereas white ones for $C(t) > 0$.

In general, due to the presence of α the third entangled state is created ($|B_3\rangle$), and hence the entanglement can be periodically transferred out from the $2 \otimes 2$ subsystem during evolution.

For the system inside the reservoir, the character of entanglement decay depends on the presence (or absence) of internal coupling (ϵ) and the strength of external pumping $|\alpha|$. The decay of entanglement for such system, but without the ϕ dependence, was considered in [14]. It was shown that it is possible to observe not only the oscillating character of entanglement decay for $\epsilon \neq 0$, when the reservoir is in zero-temperature state, but sequences of entanglement deaths and births can be also seen as the reservoir is characterized by a different from zero mean number of photons. In the absence of $|\alpha|$, such a decay character is a consequence of interactions between both oscillators and the states of the reservoir (states of the oscillators and reservoir are described by number states). Different from zero values of $|\alpha|$ enables temporal transfer of the entanglement out from the subsystem considered, which may additionally enhance the death effect (shorten the time after which death appears), or increase the time after which entanglement birth occurs.

In this paper we would like to show that by varying the phase of external pumping field one can change the character of entanglement decay in a significant way. It is visible for thermal reservoirs as well as for zero-temperature ones that the oscillating character of decay (the same for $\epsilon \neq 0$ and for $\epsilon = 0$) does not change for various ϕ values. The only difference is that for the system evolution the completely separable state ($C = 0$) is not generated periodically. In consequence, the system remains entangled to a greater or lesser degree before it achieves the final disentangled state.

The more pronounced variations in the system dynamics can be observed for thermal reservoirs cases. As we will show, the decay of entanglement in thermal environment can lead to such phenomena as *entanglement sudden death* often followed by the *entanglement sudden birth*. It is sufficient that one of the reservoir modes is characterized by the average number of photons equal to one, to observe variations in the entanglement dynamics as the phase of external coupling changes, Fig. 2.

For further analysis we assume that the damping processes originating from the interaction with the reservoir are weak (if we compare damping constants with the nonlinearities) because we need to avoid

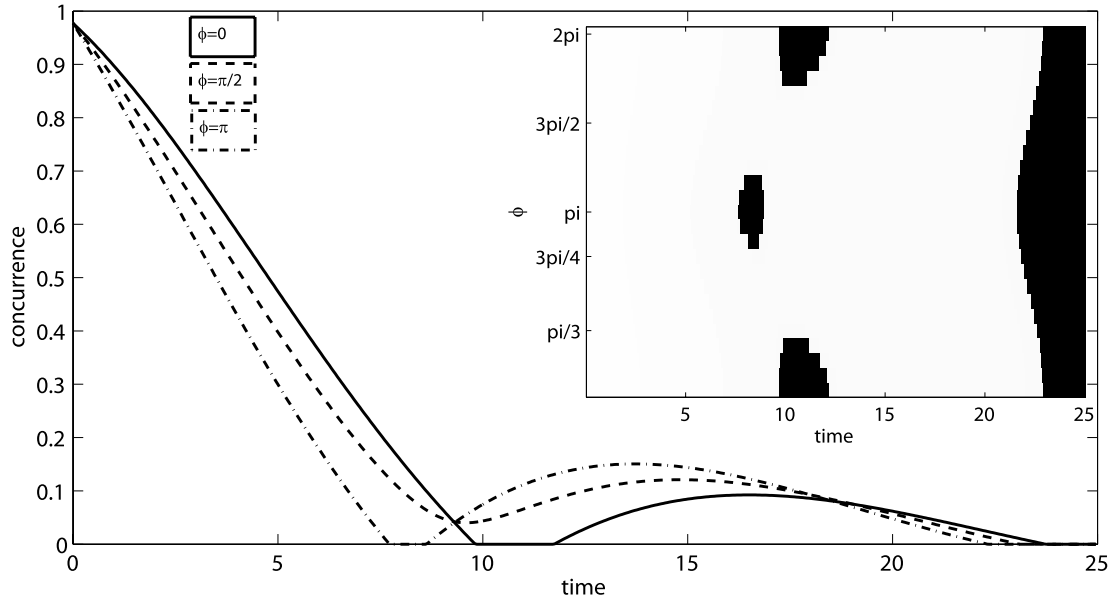

Fig. 3. The same as in Fig.2 but for nonzero internal coupler coupling – $\epsilon = 0.02$.

too rapid disentanglement processes in our system. However, one should keep in mind that the damping considered in the model is strong enough to generate visible effects introduced by the environment anyway.

Thus, in general, we observe some possibility of shortening the time after which the sudden death of entanglement occurs in some ranges of phase ϕ. This effect is more pronounced when the strength of coupling ϵ between the oscillators within the coupler is small. Moreover, this effect is even visible when oscillators do not mutually interact during the disentanglement process, compare Fig. 2 for $\epsilon = 0$ and Fig. 3 for $\epsilon \neq 0$.

In particular, the external pumping α is responsible for population of the $|1\rangle_a |2\rangle_b$ state and from this state the population may decay to one of the states ($|0\rangle_a |2\rangle_b$) involved in the 2-qubit subsystem we deal with. This mechanism enables the entanglement to reappear in the system, despite of the fact that qubits do not interact with each other any more. It is of course more pronounced for greater values of α, as the amount of population which may return to the 2-qubit subsystem has to be sufficiently large to compensate the damping process. Moreover, it is interesting that changes in the value of ϕ may cause the rebirth of entanglement without changing the intensity of external pumping. This fact is easily visible from Fig. 2. To understand this feature we should mention that the change in the phase ϕ may cause faster growth of the $|1\rangle_a |2\rangle_b$ state population (and faster decay of $|0\rangle_a |2\rangle_b$ state). In consequence, the population transfer between these two states takes place earlier than for the case when the phase $\phi = 0$ and therefore, the states engaged in the 2-qubit system gain enough population to rebuild some amount of entanglement. As a result *sudden birth* of entanglement can be observed.

It should be stressed out that in fact the two features (shorten the period of time when the death of the entanglement is observed and entanglement rebirth) occur for the same values of ϕ. Moreover, the maximal shortening of the time mentioned takes place for the same ϕ for which the maximal value of reborn entanglement is observed. In addition, for the same value of ϕ the reborn entanglement remain visible for the longest period of time. The physical origin of this phenomenon is the same as for the

entanglement rebirth. Faster (if we compare it with $\phi = 0$ case) decay of one of the states of the 2-qubit system results in faster decay of entanglement and earlier appearance of entanglement sudden death.

Inclusion of the interaction within the coupler ($\epsilon \neq 0$) preserves the shortening of the time when death starts to be visible, see Fig. 3. However, it is not possible for this case to observe the situation when the entanglement vanishes totally after reaching its first minimum (or zero). We can explain this feature by the fact that even small interaction between the oscillators makes return the entanglement to the system possible, so that even for $\phi = 0$ a rebirth of entanglement is present. Moreover, due to this interaction it is also possible to preserve the system from temporaly disentanglement (obtaining separable state) and for some phases (see the inset of Fig. 3) the concurrence does not reach zero value before the moment the final disentanglement takes place.

4. Conclusions

We have analysed one of the wide spectrum of aspects concerning the entanglement obtaining and entanglement evolution in external environment under various side conditions, that is the influence of external pumping phase on the entanglement decay. The system under consideration consists of a nonlinear coupler (two mutually interacting anharmonic oscillators with Kerr-like nonlinearities) interacting with external reservoir and pumping field as well. We have used this system's ability to produce maximally entangled state and focused on disentanglement process evolution inside the thermal reservoir. Moreover, although the system can be treated as a qutrit-qubit one, we have analysed the entanglement within its 2-qubit subsystem. We have discussed the changes in disentanglement process as a result of variations of the of external driving field, showing that even for relatively small values of driving field amplitude α, despite of the fact that there is no interactions between once entangled oscillators, it is possible to obtain return of entanglement to the subsystem considered as a result of changing the phase ϕ. Moreover, this effect arises simultaneously with shortening of the time when the first entanglement sudden death becomes visible.

At this point we can draw the conclusion of rather general nature. Nonlinear optical systems seem to be promising in one of the branches of modern quantum optics – quantum information theory, giving hope for further applications in this quickly developing area. This fact strengthens our belief that the importance of the contribution of Professor Stanisław Kielich and ideas inspired by them cannot be overestimated when we look at the modern trends in physics development.

References

[1] http://zon8.physd.amu.edu.pl/historia/kielich-art.html.
[2] R. Tanaś and S. Kielich, *Quantum Optics* **2** (1990), 23.
[3] R. Tanaś, S. Kielich, *J Modern Optics* **37** (1990), 1935.
[4] S. Kielich, R. Tanaś and R. Zawodny, in: *Modern Nonlinear Optics*, M. Evans and S. Kielich, eds, *Adv Chem Phys* **85**(I), 541 (Wiley, New York, 1993).
[5] P. Szlachetka, K. Grygiel and J. Bajer, *Phys Rev E* **48** (1993), 101.
[6] W. Leoński and R. Tanaś, *Phys Rev A* **49** (1994), R20.
[7] W. Leoński and A. Miranowicz, *J Optics B* **6** (2004), S37–S42.
[8] W. Leoński and A. Miranowicz, *J Optics B* **6** (2004), S43–S46.
[9] A. Kowalewska-Kudłaszyk and W. Leoński, *Phys Rev A* **73** (2006), 042318.
[10] K. Zyczkowski, P. Horodecki, M. Horodecki and R. Horodecki, *Phys Rev A* **65** (2001), 012101.
[11] T.Yu and J.H. Eberly, *Phys Rev Lett* **93** (2004), 140404.
[12] Z. Ficek and R. Tanaś, *Phys Rev A* **74** (2006), 024304.

[13] Z. Ficek and R. Tanaś, *Phys Rev A* **74** (2008), 054301.
[14] A. Kowalewska-Kudłaszyk and W. Leoński, *JOSA B* **73** (2009), 042318.
[15] W.K. Wootters, *Phys Rev Lett* **80** (1998), 2245.

Journal of Computational Methods in Sciences and Engineering 10 (2010) 433–449
DOI 10.3233/JCM-2010-0332
IOS Press

Temperature effect on the optical spectra of Iron(III) metal complexes exhibiting spin crossover and potential nonlinear optical properties

Jean François Lamère[a], Viviane Peyrou[a], Isabelle Sasaki[a], Pascal G. Lacroix[a,*], Laure Vendier[a] and Marie Laure Boillot[b]
[a]*CNRS; LCC (Laboratoire de Chimie de Coordination); 205 route de Narbonne, F-31077 Toulouse, France*
[b]*ICMMO, Equipe de Chimie Inorganique, (UMR 8182), Univ Paris-Sud, 91405 Orsay, France*

Abstract. Two complexes of formula [Fe^{III}(salten)(DEAS)](BPh$_4$) and [Fe^{III}(salten)(MPS)](BPh$_4$) are reported in which H_2 salten is the 4-azaheptamethylene-1,7-bis(salicylideneiminate) quinquadentate Schiff base ligand, DEAS is 4'-diethylamino-stilbazole, and MPS is 4'-[2-(methoxymethyl)pyrrolidinyl]-stilbazole. Both complexes exhibit a partial S = 5/2 → 1/2 spin crossover behaviour on cooling down to low temperature. Additionally, DEAS exhibits potential nonlinear optical (NLO) properties in relation to an intense $\pi - \pi^*$ charge transfer transition between the amine and the pyridine moieties. The temperature dependence of the optical spectra of [Fe^{III}(salten)(DEAS)]$^+$ is compared to that of 4'-diethylamino-1-methylstilbazolium (DEAMS$^+$), a cation related to [Fe^{III}(salten)(DEAS)]$^+$, in which the NLO active DEAS ligand is linked to a methyl instead of an iron complex, and therefore exhibits no magnetic behaviour. The occurrence of a red shift upon cooling down is discussed in relation with the spin equilibrium, on the basis of the ZINDO calculated spectra. A similar shift is observed between [Fe^{III}(salten)(mepepy)]$^+$ complex (mepepy = 1-(pyridin-4-yl)-2-(N-methylpyrrol-2-yl)-ethane) and Me-mepepy$^+$, N-methylated form of mepepy. The potential effect of these behaviours on the NLO properties is discussed, in a perspective of molecular materials with interacting electronic capabilities.

Keywords: Spin crossover, nonlinear optics, ZINDO, semi-empirical methods, UV-vis spectra

1. Introduction

Since the report by Davydov et al. that substituted benzene ring could exhibit strong second harmonic generation (SHG) [1], molecular materials have gradually been recognized to possess enhanced quadratic nonlinear optical (NLO) properties [2,3] *versus* those of the commercially available ferroelectric crystals (e.g. $LiNbO_3$ or KH_2PO_4) [4], by virtue of their large quadratic hyperpolarizabilities (β). Furthermore, the versatility of molecular chemistry offers a unique opportunity to meet additional challenges, such as designing multi-property materials, which could attract much interest, in relation to the emerging concept of molecular switch [5,6]. Nevertheless, the possibility of achieving a switch in the NLO response has

*Corresponding author. Tel.: +33 561333188; Fax: +33 561553003; E-mail: pascal@lcc-toulouse.fr.

been considered only recently [7]. Until now, the most convincing NLO switch seems to be that reported by Coe et al. [8] who have used coordination chemistry to design ruthenium(II) complexes in which drastic β reduction is observed upon $Ru^{II} \rightarrow Ru^{III}$ oxidation.

Metal complexes exhibit structural and electronic features of greater complexity than those of the first generation of "push-pull" organic molecules previously investigated, such as unusual topologies (e.g. octupolar symmetries) [9,10], unique photochemical and electrochemical properties [11], and a variety of potential magnetic behaviours [12]. Along this line, the design of paramagnetic [13] or magnetically coupled [14] metal complexes with NLO response has been envisioned. However, the possibility for an interplay between magnetic and NLO properties in these molecules remains somewhat speculative, and up to date has never been observed.

Few years ago, we have reported on a computational approach aimed at investigating a possible quadratic NLO modulation achieved upon spin transition in an iron(II) Schiff base complex [15]. This possibility has also been envisioned by Létard et al. [17], and by Nakano et al. [18], at the level of the cubic NLO response. The spin transition is a well investigated behaviour, first observed by Cambi et al. [19]. Numerous studies have been devoted to this intriguing phenomenon [20], which leads to a modification of the electron configuration and a modulation of the coordination sphere of the metal center, both effects which have the potential to affect the value of the molecular hyperpolarizability (β). Nevertheless, to date, and despite various experimental efforts, no real success in actual systems has been obtained, and the observation of an interplay between spin transition and nonlinear optics remains a challenging target.

As a new step in the search of multi-property molecular units combining NLO capabilities and magnetic behaviour, we have been interested in the influence of the spin transition phenomenon on the electronic spectra of complexes built up from "push-pull" π-conjugated ligands. A recent report by Real et al. [21] has shown that spin crossover behaviours can take place in iron(II) complexes built up from "push-pull" substituted stilbazole ligands. To continue along this line, and on the occasion of a special celebration of the carrier of Prof. Kielich, who was interested in both magnetic and NLO phenomenon at the border line of experimental and theoretical investigations, we wish to report on another investigation of the relationship between magnetic and charge transfer properties in three iron(III) complexes, [Fe^{III}(salten)(DEAS)](BPh_4), [Fe^{III}(salten)(MPS)](BPh_4), and [Fe^{III}(salten)(mepepy)](BPh_4) (H_2salten = 4-azaheptamethylene-1,7-bis(salicylideneiminate); DEAS = 4'-diethylaminostilbazole; MPS = 4'-[2-(methoxymethyl)pyrrolidinyl]-stilbazole; mepepy = 1-(pyridin-4-yl)-2-(N-methylpyrrol-2-yl)-ethane (Scheme)). The temperature dependence of the optical spectra of [Fe^{III}(salten)(DEAS)]$^+$ and [Fe^{III}(salten)(mepepy)]$^+$ will be compared to those of $DEAMS^+$ (4'-diethylamino-1-methylstilbazolium) and Me-$mepepy^+$ (N-methylated form of mepepy), respectively. These systems provide two sets of related chromophores in which the electronic spectra are dominated by intense $\pi \rightarrow \pi$* transitions having charge transfer character, between an amino substituent and the pyridine moieties, which behaves as a strong acceptor unit after alkylation or metal complexation. These electronic features have long been recognized to bring about the benchmarks stilbazolium-like units with extremely large NLO responses, which have been widely investigated since the 80's, in Langmuir Blodgett films [22], self-assembled multilayers [23], intercalated NLO materials [24], or single crystals [25], with SHG efficiencies up to 1000 times that of urea in some cases [24a]. Additionally, the metal complexes belong to a family of well known iron(III) derivatives built up from the parent [Fe^{III}(salten)(pyridine)]$^+$ ion, all of them exhibiting a gradual and partial S = 5/2 to 1/2 spin crossover upon cooling down to low temperature [26]. Therefore, these molecular units offer a unique opportunity to investigate the temperature dependence of NLO chromophore spectra, in the presence of a magnetic phenomenon.

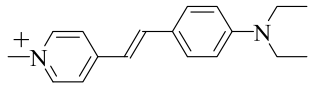

DEAMS$^+$

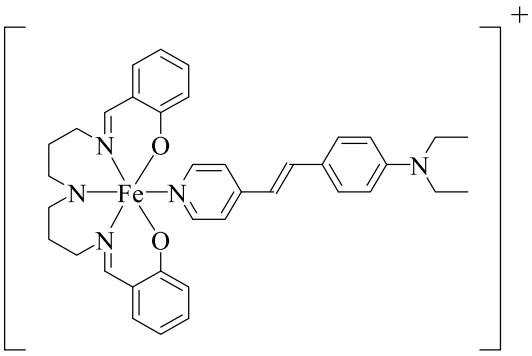

$[Fe^{III}(salten)(DEAS)]^+$

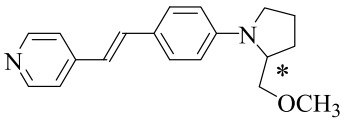

MPS

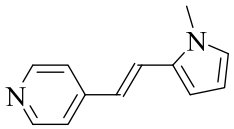

mepepy

Scheme

After the observation of a pronounced red shift at low temperature in the electronic spectrum of the iron (III) complexes, together with the observation of a gradual spin crossover, the charge transfer behaviours will be discussed within the INDO semi-empirical approach, to rationalize the origin of the optical modulation. The effect of this behaviour in term of potential NLO modulation will be tentatively evaluated in the last section.

2. Experimental section

2.1. Starting materials and equipment

The starting materials and solvents were used without further purification, except for DMF, which was distilled on barium oxide. 4'-dimethylamino-1-methylstilbazolium iodide (DAMS$^+$I$^-$) [27], 4'-diethylamino-1-methylstilbazolium iodide (DEAMS$^+$I$^-$) [27], 4-[2-(methoxymethyl)pyrrolidinyl] benzaldehyde [28], [Fe^{III}(salten)(Cl)] [25a], and [Fe^{III}(salten)(mepepy)](BPh$_4$) [25c], were synthesized as previously described. Elemental analysis were performed by the "Service de Microanalyses du Laboratoire de Chimie de Coordination", in Toulouse. The NMR spectra were registered on a Bruker AM 250 spectrometer. UV-visible absorption measurements were performed on a Varian CARY 5E double-beam

spectrophotometer, equipped with an APD Cryogenics closed-cycle helium cryogenic system including a DMX-1E cryostat and a DE-202 expander instrument. The thin films samples for UV-visible measurements were poly (methyl methacrylate) (PMMA) containing 5% of chromophore. In a typical procedure, 114 mg of PMMA and 5.8 mg of iron complex were dissolved in 0.6 mL of chloroform and were used to prepare thin films by using the spin coating technique (Karlsuss CT62). Solid state sample were KBr pressed pellets (13 mm diameter, 100 mg), with 1 wt. -% NLO material.

2.2. Synthesis

2.2.1. 4'-Diethylaminostilbazole (*DEAS*)

4-chloroaniline (1.280 g, 10^{-2} mol) and 4-diethylaminobenzaldehyde (1.77 g, 10^{-2} mol) were dissolved at 40°C in 12.5 mL of absolute ethanol. After addition of two drops of sulphuric acid, the reaction mixture was stirred at room temperature for 15 minutes. N-(4'-diethylaminobenzylidene) 4-chloroaniline was obtained as an orange solid by precipitation after one night at low temperature, filtered off, washed with absolute ethanol, and dried under vacuum. Yield 2.29 g (80%). ^{1}H NMR ($CDCl_3$)δ 8.245 (s, 1H), 7.715 (d, $J = 8.8$ Hz, 2H), 7.300 (d, $J = 8.6$ Hz, 2H), 7.099 (d, $J = 8.6$ Hz, 2H), 6.680 (d, $J = 8.8$ Hz, 2H), 3.413 (q, $J = 7.0$ Hz, 4H), 1.195 (t, $J = 7.0$ Hz, 6H). In a second step, one part of this compound (1.49 g, 5.2 10^{-3} mol) was dissolved in 25 mL of DMF, with powdered KOH (1.2 g, 2.1 10^{-2} mol). After addition of 4-picoline (0.53 mL, 5.4 10^{-3} mol), the reaction mixture was heated at 90°C for 1 hr 30. After cooling down, 50 mL of methanol were added, and the mixture was abandoned overnight at 0°C, which allowed the precipitation of a yellow compound. After filtration, the solid was washed with water and methanol and finally dried under vacuum. Yield 930 mg (71%). Elemental analysis. Found: C, 80.8; H, 7.9; N, 10.9%. Calc. for $C_{17}H_{20}N_2$: C, 80.9; H, 8.0; N, 11.1%. ^{1}H NMR ($CDCl_3$)δ 8,499 (d, $J = 6.2$ Hz, 2H), 7.410 (d, $J = 8.9$ Hz, 2H), 7.291 (d, $J = 6.2$ Hz, 2H), 7.228 (d, $J = 16.2$ Hz, 1H), 6.764 (d, $J = 16.2$ Hz, 1H), 6.664 (d, $J = 8.9$ Hz, 2H), 3.398 (q, $J = 7.0$ Hz, 4H), 1.191 (t, $J = 7.0$ Hz, 6H).

2.2.2. [Fe^{III} (salten)(DEAS)](BPh$_4$)

A solution of [Fe^{III}(salten)(Cl)] (0.856 g, 2 10^{-3} mol) and DEAS (0.506 g, 2 10^{-3} mol) in methanol (50 mL) was heated at 60°C for one hour, then was filtered hot. The filtrate was added to a solution of $NaBPh_4$ (684 mg, 2 10^{-3} mol) in 20 mL of methanol. The mixture was heated at 60°C for 5 min and stood overnight at 0°C, to allow the formation of a dark precipitate. The solid was filtered, washed with methanol and ether, then dried under vacuum. Yield 1.56 g (87%). Elemental analysis. Found: C, 75.7; H, 6.5; N, 7.1%. Calc. for $C_{61}H_{63}BFeN_5O_2$: C, 75.9; H, 6.6; N, 7.3%.

2.2.3. 4'-[2-(methoxymethyl)pyrrolidinyl]-stilbazole (*MPS*)

A mixture of 4-picoline (3.2 mL, 5.5 10^{-2} mol) and NaH (1.32 g, 5.5 10^{-2} mol) in 10 mL of DMF was heated for 2 hours at 60°C. Then, 4-[2-(methoxymethyl)pyrrolidinyl] benzaldehyde (7.2 g, 5.5 10^{-2} mol) diluted in 10 mL of DMF was added and the reaction mixture was heated for 7 more hours at 60°C. After cooling, the resulting mixture was poured into 300 mL of water, which leads to a red precipitate. The solid was filtered off, washed with water, and dried under vacuum. The crude product was then dissolved in hot heptane, filtered hot, evaporated to dryness, and finally purified by chromatography on SiO_2 (60Å 70–200 μm) using heptane-AcOEt (7/3). Yield: 12.79 g (78%) of MPS as a bright yellow solid. ^{1}H NMR ($CDCl_3$)δ 8.488 (d, $J = 5.8$ Hz, 2H), 7.295 (d, $J = 6.0$ Hz, 2H), 7.405 (d, $J = 8.8$ Hz, 2H), 7.222 (d, $J = 16.2$ Hz, 1H), 6,764 (d, $J = 16.2$ Hz, 1H), 6,630 (d, $J = 8.8$ Hz, 2H), 3.918 (m, 1H), 3.42–3.53 (m, 2H), 3.373 (s, 3H), 3.199 (t, $J = 8.9$ Hz, 2H), 1.72–2.09 (m, 4H).

2.2.4. [Fe^{III} (salten)(MPS)](BPh$_4$)

A solution of [Fe^{III}(salten)(Cl)] (360 mg, 8.4 10^{-4} mol) and MPS (320 mg, 1.09 10^{-3} mol) in methanol (18 mL) was heated at 60°C for one hour, then was filtered hot. After addition of NaBPh$_4$ (288 mg, 8.4 10^{-4} mol) to the filtrate, and an additional heating for 5 min at 60°C, the reaction mixture was stood overnight at room temperature, which led to a dark precipitate, which was filtered, washed with methanol then ether. Yield 0.635 g (75%). Elemental analysis. Found: C, 74.7; H, 6.4; N, 7.0%. Calc. for $C_{63}H_{65}BFeN_5O_3$: C, 75.1; H, 6.5; N, 7.0%.

2.2.5. Me-mepepy$^+I^-$

Following the general procedure of Kung [27], 4-picoline (930 mg, 10^{-2} mol) and methyliodide (1.42 g, 10^{-2} mol) were readily reacted, which afforded 4-picolinium iodide as a pale yellow solid. The resulting solid was dissolved in 15 mL of 2-propanol, with 1.1 g (10^{-2} mol) of N-methylpyrole-2-carboxaldehyde and 3 drops of piperidine. The solution was refluxed for 20 hours, which led to a large amount of an orange precipitate. After cooling down to room temperature, the product was filtered, washed with propanol and dried under vacuum. Yield 2.642 g (80%). Elemental analysis. Found: C, 47.9; H, 4.2; N, 8.4%. Calc. for $C_{13}H_{15}IN_2$: C, 47.9; H, 4.6; N, 8.6%. ^{1}H NMR (DMSO-d_6)δ 8.685 (d, $J = 6.8$ Hz, 2H), 8.098 (d, $J = 6.9$ Hz, 2H), 7.907 (d, $J = 15.9$ Hz, 1H), 7.090 (m, 1H), 7.057 (d, $J = 16.1$ Hz, 1H), 6.878 (dd, $J =$ 3,9 and 1.3 Hz, 1H), 6.211 (dd, $J = 3.8$ and 2.6 Hz, 1H), 4.170 (s, 3H), 3.800 (s, 3H). The compound was then turned to the hexafluorophosphate salt by metathesis, using NH_4PF_6 aqueous solution. Single crystals were obtained by slow diffusion of diethyl ether in a solution of Me-mepepy$^+$(PF_6)$^-$ in acetonitrile.

2.3. Crystallographic studies

Single crystals of DAMS$^+$I$^-$ were obtained by slow evaporation in ethanol. X-ray data for DAMS$^+$I$^-$ and Me-mepepy$^+$(PF_6)$^-$ were collected at room temperature and 180 K, on a Xcalibur Oxford Diffraction diffractometer using a graphite-monochromated Mo-Kα radiation ($\lambda = 0.71073$Å) and equipped with an Oxford Cryosystems Cryostream Cooler Device. The crystallographic data are summarized in Table 1. The final unit cell parameters have been obtained by means of a least-squares refinement performed on a set of 5000 well measured reflections. Empirical absorption corrections were applied: $T_{min} = 0.6557$, $T_{max} = 0.8456$ for DAMS$^+$I$^-$ [29]; $T_{min} = 0.945$, $T_{max} = 0.971$ for Me-mepepy$^+$(PF_6)$^-$ [30]. The structures have been solved by Direct Methods using SIR92 [31], and refined by means of least-squares procedures on a F^2 with the aid of the program SHELXL97 [32] included in the software package WinGX version 1.63 [33]. The Atomic Scattering Factors were taken from International tables for X-Ray Crystallography [34]. All hydrogens atoms were located on a difference Fourier maps, and refined by using a rigid model. All non-hydrogens atoms were anisotropically refined, and in the last cycles of refinement a weighting scheme was used, where weights are calculated from the following formula: $w = 1/[\sigma^2(Fo^2)+(aP)^2+bP]$ where $P = (Fo^2+2Fc^2)/3$. Drawing of molecule is performed with the program ORTEP32 [35] with 50% probability displacement ellipsoids for non-hydrogen atoms.

In the structure of Me-mepepy$^+$(PF_6)$^-$, a disorder was solved on the anion, with occupancy of 0.50/0.50 for each fluorine atoms at room temperature and 0.80/0.20 at 180 K. Crystallographic data have been deposited with the Cambridge Crystallographic Data Center.

2.4. Computational methods

The all-valence INDO (intermediate neglect of differential overlap) method [36] was employed for the calculation of the optical spectra of the chromophores at room temperature and at 180 K. Calculations

Table 1
Crystal Data for $DAMS^+I^-$ and $(Me\text{-}mepepy)^+(PF_6)^-$ at High and Low Temperature

	$DAMS^+I^-$		$(Me\text{-}mepepy)^+(PF_6)^-$	
	293 K	180 K	298 K	180 K
crystal data				
chemical formula	$C_{16}H_{19}IN_2$	$C_{16}H_{19}IN_2$	$C_{13}H_{15}F_6N_2P$	$C_{13}H_{15}F_6N_2P$
mol.wt.	366.23	366.23	344.24	344.24
crystal size (mm)	0.2 × 0.15 × 0.08	0.2 × 0.15 × 0.08	0.25 × 0.17 × 0.1	0.25 × 0.17 × 0.1
crystal system	monoclinic	monoclinic	triclinic	triclinic
space group	$P2_1/c$	$P2_1/c$	P-1	P-1
a (Å)	6.326(2)	6.3060(6)	8.517(1)	8.424(1)
b (Å)	7.712(3)	7.6273(8)	9.295(2)	9.236(1)
c (Å)	32.068(11)	32.083(3)	10.612(2)	10.547(1)
α (°)	90	90	72.02(2)	71.49(1)
β (°)	90.36(3)	90.361(8)	71.25(2)	70.39(1)
γ (°)	90	90	73.74(2)	74.17(1)
V (Å^3)	1564.4(9)	1543.1(3)	741.3(2)	720.2(2)
P_{calc} (Mg/m^3)	1.555	1.576	1.542	1.587
μ (MoKα) (cm^{-1})	0.2037	0.2065	0.247	0.255
data collection				
radiation (MoKα) (Å)	0.71073	0.71073	0.71073	0.71073
scan mode	ω and ϕ	ω and ϕ	ω and ϕ	ω and ϕ
θ range (°)	2.93–26.30	2.96–32.15	2.99–25.63	3.54–25.63
no. of reflections				
measured	11688	16105	5397	5284
unique	3189	5077	2804	2723
used	3189	5077	2804	2723
refinement				
refinement on	F^2	F^2	F^2	F^2
no. of variables	175	175	262	262
H-atom treatment	calculated	calculated	calculated	calculated
R [I>2sigma(I)]	0.0389	0.0353	0.0677	0.0459
wR	0.0457	0.0448	0.1588	0.1059
$\Delta\rho_{max}$ (e Å^{-3})	0.456	0.664	0.369	0.409
$\Delta\rho_{min}$ (e Å^{-3})	−0.331	−0.774	−0.779	−0.315
GOF	0.826	0.793	0.951	0.931

were performed using the INDO/1 Hamiltonian incorporated in the commercially available MSI software package ZINDO [37]. The monoexcited configuration interaction (MECI) approximation was employed to describe the excited states. The 100 lowest energy transitions between the 10 highest occupied molecular orbitals and the 10 lowest unoccupied ones were chosen to undergo CI mixing.

For $Me\text{-}mepepy^+$, the calculations were performed on the present crystal structures. No crystal data being available for $DEAMS^+$, metrical parameters used for the calculations were taken from the present X-ray structures of $DAMS^+$. Metrical parameters used for $[Fe^{III}(salten)(mepepy)]^+$, were those of the previously reported structure of $[Fe^{III}(salten)(mepepy)]^+([Pd(dmit)_2]_2)^-$, available at 280 and 180 K [38]. As no crystal data are available for $[Fe^{III}(salten)(DEAS)]^+$, the molecular structures were built up from the X-ray structures of $[Fe^{III}(salten)(mepepy)]^+([Pd(dmit)_2]_2)^-$ and $DAMS^+I^-$, at both high and low temperatures. It is justified by the fact that variations of the coordination cores derive from the spin crossover processes, which, in this temperature range, are of comparable magnitude in both complexes (*vide infra*). Therefore, the modification of the metal-pyridine (Fe-N) bond lengths were assumed to be the same in any iron(III)-based complexes and equal to 0.06 Å (averaged value provided by the X-ray data available) [38].

The pseudo-centrosymmetric electronic environment of the [Fe^{III}(salten)] core and the absence of strong donor acceptor character on the salten fragment leads to the suggestion (eventually verified by ZINDO) that the metal center is not involved in the dominant charge transfer process, which is located on the DEAS and mepepy moieties. Therefore, the calculations performed at both S = 1/2 and 5/2 spin states were found to lead to very similar (energy, intensity) charge transfer features. In order to simplify the discussion, the results presented here will be those obtained with S = 1/2, which lead to a more simple description of the electronic properties at the molecular level.

2.5. Magnetic measurements

Magnetic susceptibility data for the iron complexes were recorded using a SQUID-based magnetometer on a QUANTUM Design Model MPMS instrument. All data were corrected for diamagnetism estimated from Pascal's constant [39] (-587×10^{-6} cm^3 mol^{-1} and -610×10^{-6} cm^3 mol^{-1}, for [Fe^{III}(salten)(DEAS)](BPh$_4$) and [Fe^{III}(salten)(MPS)](BPh$_4$), respectively). The magnetic data for [Fe^{III}(salten)(mepepy)](BPh$_4$) have been previously reported [25c].

3. Results

3.1. Synthesis and characterization

Although 4'-diethylaminostilbazole has been previously reported in the literature [40,41], we provide a new synthetic route, which implies the reaction of 4-picoline with N-(4'-diethylaminobenzylidene) 4-chloroaniline in the presence of dimethylformamide and potassium hydroxide ("anil synthesis") [42]. This convenient method has then been extended to the synthesis of numerous o, m, p-styrylpyridines [43]. The organic compounds are readily characterized by ^{1}H NMR spectroscopy. The double bond linkages were confirmed to be trans by ^{1}H NMR analysis, based on the value of the $J_{CH=CH}$ coupling constant (c.a. 16 Hz). The spectrum of Me-mepepy$^+$I$^-$ is complicated by the fact that the signal of the hydrogen linked to carbon C12 ($\delta = 7.090$ ppm) is hidden by the signal of an ethylenic hydrogen ($\delta = 7.06$ ppm). However, the integration proves without any ambiguity the presence of the hydrogen atom.

[Fe^{III}(salten)(DEAS)](BPh$_4$) and [Fe^{III}(salten)(MPS)](BPh$_4$) were readily obtained by the procedure reported previously for various [Fe^{III}(salten)(X-py)]$^+$ derivatives [25a], which implies the synthesis of [Fe^{III}(salten)(Cl)] and the appropriate substituted pyridine. 4'-Diethylaminostilbazole (DEAS) was used instead of the parent and more traditionally used 4'-dimethylaminostilbazole (DAS) which is not soluble enough. Indeed, all our attempts to obtain [Fe^{III}(salten)(DAS)](BPh$_4$) failed. We have observed that in the present [Fe^{III}(salten)(X-py)](BPh$_4$) series, concentrations less than 10^{-2} mol L^{-1} may lead to a partial decoordination of the substituted pyridine [44]. In the case of DAS the poor solubility hampered the formation of the suitable complex, whereas the higher solubility of DEAS allows the obtention of the desired complex in excellent yield.

4'-[2-(Methoxymethyl)pyrrolidinyl]-stilbazole (MPS) is a chiral parent of DEAS, selected in relation to the need for noncentrosymmetric crystals, which would have guarantied some SHG signal in solid state. Indeed pyrrolidinyl-based chromophores have been observed to exhibit large crystal efficiencies in some cases [45]. In the case of [Fe^{III}(salten)(MPS)]$^+$, this would have allowed a direct and easy measurement of the temperature dependence of the NLO response performed on powdered sample. Nevertheless, although the iron complex was obtained in good yield, this compound turned out to be completely amorphous, and therefore SHG silent.

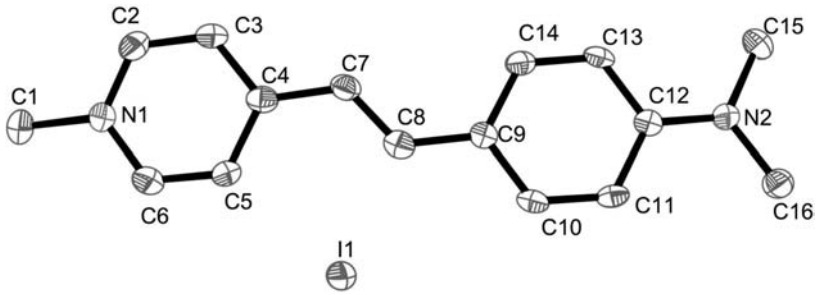

Fig. 1. Atom labelling scheme for $DAMS^+I^-$. The ellipsoids are drawn at the 30% probability level. Hydrogen atoms are omitted for clarity.

3.2. Description of the structures

It is important to point out that although several crystal structures containing the $DAMS^+$ chromophore have been reported in the literature, for example with TsO^- [24b], $[Ni(dmit)_2]^-$ [46], $La(NO_3)_6$ [47], $PbBr_6^-$ [48], and also I^- [49], none of these reports have focussed on the effect of temperature on the molecular geometry, which is essential for the present investigation.

$DAMS^+I^-$ crystallizes in the monoclinic $P2_1/c$ space group. On cooling down from 293 to 180 K, the contraction of the cell parameters is more pronounced (around 1%) along the *b*axis, which roughly corresponds to the packing direction. Figure 1 illustrates the $DAMS^+I^-$ molecule with the atomic numbering scheme. Although $DAMS^+$ appears planar, the molecule is slightly bent with an angle equal to 11.09° between the aromatic rings at 293 K (10.92° at 180 K). At room temperature, the largest deviation from the molecular mean plan is equal to 0.385(4) and 0.351(4) Å at the C(15) and C(1) atoms, respectively. These values move to 0.377(3) and 0.388(3) Å at 180 K. The degree of planarity is approximately the same at both temperature, with Rms deviation of 18 fitted atoms (N(1), N(2), C(1) to C(16)) equal to 0.1765 and 0.1833 Å, at 293 and 180 K, respectively. A careful comparison of the modulation of the intra-molecular bond lengths (Table 2) does not reveal any significant modification in the molecular structures. In particular, the averaged bond lengths are equal to 1.400(4) Å at both temperatures. Moreover, only four bond lengths modifications are larger than 1%, the largest change of 1.7% being observed at the C(4)-C(5) bond.

$(Me\text{-}mepepy)^+(PF_6)^-$ crystallizes in the triclinic P-1 space group. On cooling down from 298 to 180 K, the main contaction of the cell (around 1%) is observed along the a axis. The asymmetric unit cell is shown in Fig. 2, with the atomic numbering scheme. The Me-mepepy$^+$ cation is roughly planar, with an angle of 9.05° between the two aromatic rings at 298 K (9.25° at 180 K). At room temperature, the largest deviation from the π-conjugated mean plane is equal to 0.119 Å, at C(10) (0.126 Å, at 180 K). The comparison of the intra-molecular bond-lengths (Table 2) reveals no significant modification between high and low temperature, with averaged values of 1.385(6) and 1.388(3) Å, at 298 and 180 K, respectively. This difference which falls in the range of the esd's uncertainty is not significant, taking into account the modest quality of the structure recorded at room temperature. The only bond lengths modification larger than 1% is equal to 1.5%, at the C(4)–C(5) bond.

Finally, it must be concluded that the temperature has no major effect on the overall molecular geometry of the organic cations. In particular, the methyl-pyridine distance (C(1)-N(1) bond) is not modified, within the range of uncertainty, which strongly contrast with the 0.12 to 0.15 Å bond lengths reduction observed in iron(III) Schiff base complexes with a complete spin crossover [50]. Nevertheless, the possibility that subtle modifications can lead to observable optical change will be considered in the next section.

Table 2
Bond Lengths (in Å) for $DAMS^+ I^-$ and Me-$mepepy^+ (PF_6)^-$ at High and Low Temperature, Esd's in Parantheses Refer to the Last Significant Digit

	$DAMS^+ I^-$		Me-$mepepy^+ (PF_6)^-$	
	293 K	180 K	298 K	180 K
C(1)-N(1)	1.470(5)	1.469(3)	1.471(5)	1.466(3)
C(2)-N(1)	1.337(5)	1.351(3)	1.334(5)	1.345(3)
C(2)-C(3)	1.371(5)	1.355(4)	1.352(6)	1.349(3)
C(3)-C(4)	1.406(5)	1.407(4)	1.396(5)	1.398(3)
C(4)-C(5)	1.384(5)	1.408(4)	1.391(6)	1.412(3)
C(4)-C(7)	1.444(5)	1.444(4)	1.435(5)	1.434(3)
C(5)-C(6)	1.367(5)	1.361(4)	1.350(6)	1.353(4)
C(6)-N(1)	1.348(5)	1.356(3)	1.342(5)	1.347(3)
C(7)-C(8)	1.351(5)	1.343(4)	1.328(6)	1.336(3)
C(8)-C(9)	1.455(5)	1.448(4)	1.423(5)	1.429(3)
C(9)-C(14)	1.399(5)	1.411(4)		
C(9)-C(10)	1.405(5)	1.401(4)	1.396(5)	1.389(3)
C(10)-C(11)	1.375(5)	1.376(4)	1.389(6)	1.385(3)
C(11)-C(12)	1.412(5)	1.421(4)	1.361(6)	1.374(4)
C(12)-N(2)	1.374(5)	1.363(3)	1.356(5)	1.346(3)
C(12)-C(13)	1.411(5)	1.417(4)		
C(13)-C(14)	1.381(5)	1.363(4)		
C(15)-N(2)	1.444(5)	1.462(3)		
C(16)-N(2)	1.462(5)	1.452(3)		
C(9)-N(2)			1.382(5)	1.381(3)
C(13)-N(2)			1.456(6)	1.461(3)

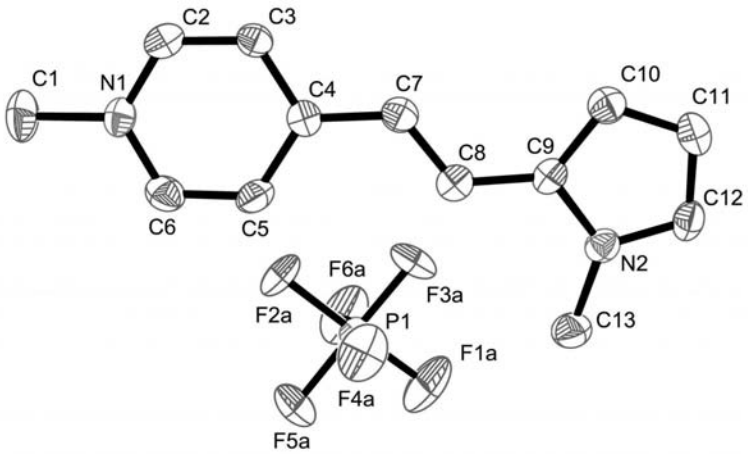

Fig. 2. Atom labelling scheme for Me-$(mepepy)^+ (PF_6)^-$. The ellipsoids are drawn at the 30% probability level. Hydrogen atoms are omitted for clarity.

3.3. Optical spectra

$[Fe^{III}(salten)(DEAS)]^+$, and $DEAMS^+$ are a set of related chromophores which possess the same general NLO features: (*i*) a diethylamino substituent as a strong electron donor; (*ii*) a stilbazole skeleton as an conjugated pathway; (*iii*) a pyridine moieties, turned into an efficient withdrawing fragment either by alkylation ($DEAMS^+$) or by metal complexation ($[Fe^{III}(salten)(DEAS)]^+$). Furthermore, they possess

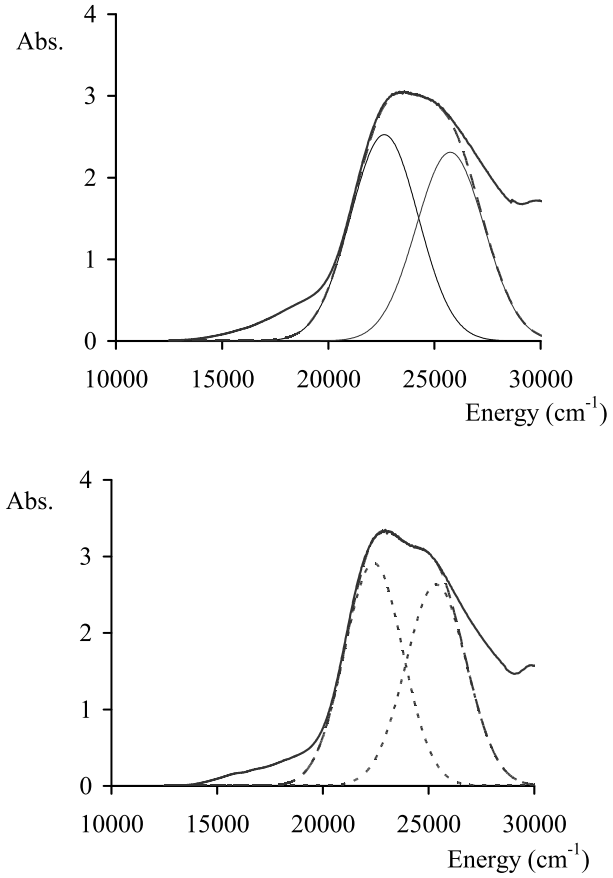

Fig. 3. Optical spectra recorded in PMMA matrix (plain lines) for $[Fe^{III}(salten)(DEAS)]^{+}(BPh_4)^{-}$ at 350 K (top) and 10 K (bottom). The dotted lines are the simulated spectra, arising from the contribution of two single components.

the same 1+ charge. It is therefore relevant to compare their electronic spectra, which should exhibit closely related features. These similarities can be transposed to the set of $[Fe^{III}(salten)(mepepy)]^{+}$, and Me-mepepy^{+} chromophores, with the slight difference that the donating capabilities of methyl pyrrole is reduced *versus* that of the diethylaminophenyl group.

The optical spectra were first recorded in polymeric matrix at 353 and 10 K, for $[Fe^{III}(salten)(DEAS)](BPh_4)$. They are shown in Fig. 3. Weak bands are observed in the 15000–20000 cm^{-1} energy range, and are ascribed to phenol $\rightarrow$ iron(III) charge transfer transitions. Decreasing the temperature from 353 to 10 K leads to the appearance of a weak LMCT absorption band located in the low energy range (ca. 15500 cm^{-1} in the 10 K spectrum), the concomitant disappearance of the HS LMCT band (ca. 18500 cm^{-1} at 353 K). These observations which compare well with those previously reported for this set of iron(III) complexes [51] support the occurrence of a very smooth spin equilibrium of $[Fe^{III}(salten)(DEAS)](BPh_4)$ embedded in the PMMA matrix. These electronic features result in a pseudo centrosymmetric contribution to the overall charge transfer process. More importantly, the spectra reveal a large and intense DEAS-based band in the 20000–28000 cm^{-1} energy range. This band is found to exhibit an energy shift of several hundreds of cm^{-1} on cooling down to low temperature. However, the observation that it is built up from two components in both cases (Fig. 3) rises the question of the full reliability of the origin and quantification of the observed behaviour. The dominant low lying

Table 3
Experimental Transition Energies (in cm^{-1}) for the Iron(III) Complexes and the Methylpyridinium Related Molecules, Recorded in KBr at High and Low Temperature, with Experimental and ZINDO Energy Shift (in cm^{-1})

chromophore	energies (temperature/K)		energy shifts between high and low temperature	
			experimental	calculated
$[Fe^{III}(salten)(DEAS)]^+$	22940 (298)	22350 (47)	−590 (± 50)	−738
$DEAMS^+$	19750 (298)	19650 (48)	−100 (± 50)	−310
$[Fe^{III}(salten)(mepepy)]^+$	24930 (293)	24470 (48)	−460 (± 50)	−581
Me-$mepepy^+$	22200 (292)	22350 (48)	+150 (± 100)	−193

component (22640 cm^{-1}) is likely ascribable to the $\pi \rightarrow \pi^*$ transition in the DEAS moieties in the complex. The origin of the side-transition observed at higher energy (25740 cm^{-1}) is not perfectly clear, but is observed in any cases for iron complexes dispersed in thin film materials. One might tentatively associate it to vibronic transitions. However, such features which are usually well resolved at low temperature in free stilbazole ligands, are not observed here in DEAS and $DEAMS^+I^-$, in polymer matrix. It seems therefore more relevant to attribute this side transition to some amount of decoordinated DEAS ligand, or partially decoordinated complex in the matrix. This unexpected observation suggests that, the ultimate quantification of the optical (and hence NLO) behaviour of the iron complexes may not be fully reliable in polymer matrices. Therefore, this route was abandoned.

In an alternative approach, the spectra were recorded on powdered samples dispersed in KBr pellets. This provides a crystal state comparison with the magnetic and computed optical data, which are based on powder measurements, and X-ray data, respectively (see experimental section). The absorption maxima are presented in Table 3 at high and low temperature. The data indicate a general trend for lower transition energies at low temperature, except in the case of Me-$mepepy^+$, were the shift cannot be determined precisely, due to the presence of shoulders, but however remains weak. More importantly, a 590 cm^{-1} energy shift is observed in the absorption maxima of $[Fe^{III}(salten)(DEAS)](BPh_4)$, which does not find its counterpart in the related $DEAMS^+$ cation. This effect, further confirmed in the set of mepepy-based chromophores suggests an enhancement of the withdrawing effect of the metal-pyridine fragments, at low temperature. Assuming that $DEAMS^+$ is a non magnetic model for $[Fe^{III}(salten)(DEAS)]^+$, the issue of a magnetic effect on the optical shift becomes naturally addressed.

3.4. Magnetic properties

As previously mentioned, the iron (III) complexes described in the present investigation belong to a family of spin crossover derivatives based on the general formula $[Fe^{III}(salten)(X\text{-}py)]^+$ [26]. The temperature dependence of the magnetic data expressed as the $\chi \times T$ product (χ being the molar magnetic susceptibility, and T, the temperature) are showed in Fig. 4 for $[Fe^{III}(salten)(DEAS)](BPh_4)$ and $[Fe^{III}(salten)(MPS)](BPh_4)$. The $\chi \times T$ product shows a gradual decrease on cooling down ascribable to a partial S = 5/2 to 1/2 crossover of iron(III) ions. Theoretically, a pure S = 5/2 spin state is associated with a $\chi \times T$ product of 4.375 cm^3 mol^{-1} K (assuming $\chi \times T \sim (g^2 \times S(S+1))/8$ and g ∼ 2) [52]. Accordingly, the S = 1/2 spin state is associated with a $\chi \times T$ product of 0.375 cm^3 mol^{-1} K. In the case of $[Fe^{III}(salten)(DEAS)](BPh_4)$, the $\chi \times T$ product is equal to 2.28 and 0.63 cm^3 mol^{-1} K at 300 and 30 K, respectively, which indicates a lowering of the high spin fraction from 50% to 6%. In the case of $[Fe^{III}(salten)(MPS)](BPh_4)$, $\chi \times T$ drops from 2.96 to 1.14 cm^3 mol^{-1} K between 300 and 30 K, which correspond to 75 and 19% of high spin fractions, respectively. In both cases, it is important

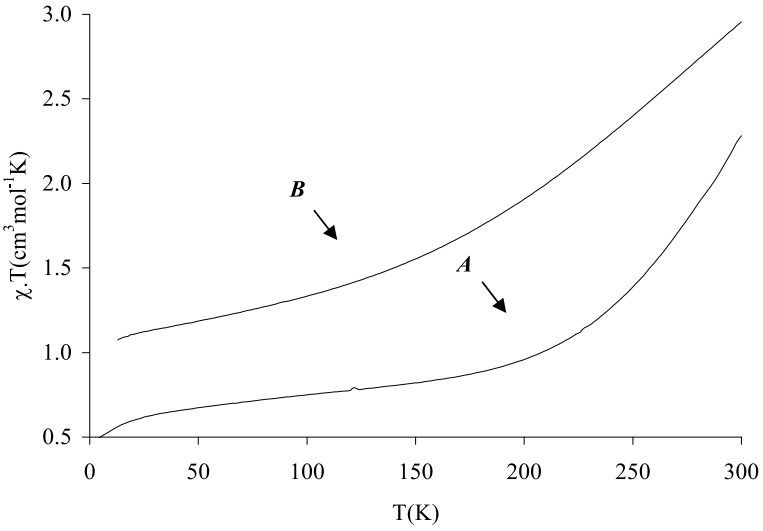

Fig. 4. Temperature dependence of the $\chi \times T$ product of $[Fe^{III}(salten)(DEAS)]^{+}(Bph_4)^{-}$ (*A*), and $[Fe^{III}$ (salten) $(MPS)]^{+}(BPh_4)^{-}$ (*B*).

to point out that the spin crossover is far from being complete, and appears more gradual in the case of $[Fe^{III}(salten)(MPS)]$ (BPh_4), an effect which may be related to the amorphous character of the MPS containing sample.

The magnetic properties of $[Fe^{III}(salten)(mepepy)](BPh_4)$ have previously been reported [25c], and therefore will not be discussed here. However, they are found to be closely related to those of $[Fe^{III}(salten)(DEAS)](BPh_4)$. Finally, the overall magnetic behaviours of the three iron(III) complexes are similar to those of the various $[Fe^{III}(salten)(L)](BPh_4)$, previously reported materials, for example with L = pyridine [25a], 3-methylpyridine [25a], and stilbazole [25e].

4. Discussion

The dominant and low-lying optical transitions of two cations, $DEAMS^{+}$, and $[Fe^{III}(salten)(DEAS)]^{+}$ have been investigated, and at first were found roughly similar. However, in the case of $[Fe^{III}$ $(salten)(DEAS)]^{+}$, the transition reveals a shift of 590 cm^{-1} on cooling down, which finds a very modest (100 cm^{-1}) counterpart in $DEAMS^{+}$. Similar observations were made on the set of Me-mepepy^{+} and $[Fe^{III}(salten)(mepepy)]^{+}$ cations. Therefore, and for simplification, the discussion will focus on the $DEAMS^{+}$, and $[Fe^{III}(salten)(DEAS)]^{+}$ systems, only.

In order to provide additional evidences for (*i*) the origin of the transition in the cations, and (*ii*) the occurrence of a larger shift at low temperature for the iron complexes, the calculated spectra (Table 4) have to be discussed, and compared to the experimental data (Table 3).

The calculated spectra are dominated at room temperature by a single and very intense intra-ligand transition located at 21140 and 25510 cm^{-1} for $DEAMS^{+}$ and $[Fe^{III}(salten)(DEAS)]^{+}$, respectively, which have to be compared to the experimental 19750 and 22940 cm^{-1} values. We have frequently observed a tendency for overestimated energies calculated by ZINDO in Schiff base complexes containing paramagnetic species [14a,15]. The slight discrepancy observed in the present case falls in the range of uncertainty of the ZINDO approach, and therefore the calculated prediction can be further analysed at

Table 4
ZINDO Data (λ_{max} in nm, E in cm^{-1}, and Composition of the First Excited State) for the Intense Charge Transfer Transition of $DEAMS^+$ and $[Fe^{III}(salten)(DEAS)]^+$

	transition	λ_{max} (E)	composition of CI expansion[1]
$DEAMS^+$			
T = 293 K	$1 \rightarrow 2$	473 (21140)	0.939 $\chi_{46\rightarrow47}$
T = 180 K	$1 \rightarrow 2$	480 (20830)	0.944 $\chi_{46\rightarrow47}$
$[Fe^{III}(salten)(DEAS)]^+$			
T = 293 K	$1 \rightarrow 7$	390 (25655)	0.937 $\chi_{111\rightarrow113}$
T = 180 K	$1 \rightarrow 7$	401 (24917)	0.939 $\chi_{111\rightarrow113}$
Me-mepepy$^+$			
T = 293 K	$1 \rightarrow 2$	456 (21941)	0.931 $\chi_{38\rightarrow39}$
T = 180 K	$1 \rightarrow 2$	460 (21748)	0.931 $\chi_{38\rightarrow39}$
$[Fe^{III}(salten)(mepepy)]^+$			
280 K	$1 \rightarrow 7$	385 (25980) 0.933	$\chi_{103\rightarrow105}$
160 K	$1 \rightarrow 7$	394 (25399) 0.912	$\chi_{103\rightarrow105}$

[1]Orbitals 46 (47) are the HOMO (LUMO) in $DEAMS^+$. Orbitals 111 (113) are the HOMO -1 (LUMO) in $[Fe^{III}(salten)(DEAS)]^+$. Orbitals 38 (39) are the HOMO (LUMO) in Me-mepepy$^+$. Orbitals 103 (105) are the HOMO -1 (LUMO) in $[Fe^{III}(salten)(mepepy)]^+$.

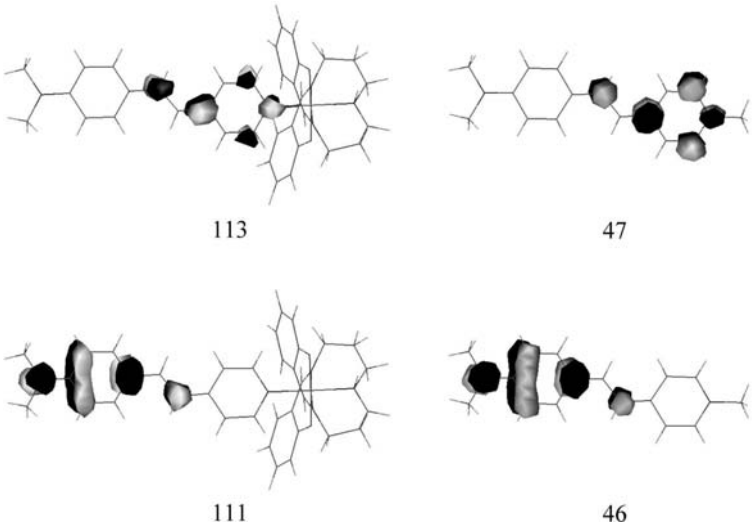

Fig. 5. ZINDO Calculated Occupied (bottom) and Unoccupied (top) Orbitals Involved in the Intense Optical Transition of $[Fe^{III}(salten)(DEAS)]^+$ (left) and $DEAMS^+$ (right).

the orbital level. Interestingly, both transitions are based on a single component (46→47 and 111→113, for $DEAMS^+$, and $[Fe^{III}(salten)(DEAS)]^+$, respectively). These orbitals are shown in Fig. 5. It must be emphasized that the orbitals are essentially the same in both cations. In particular, the $[Fe^{III}(salten)]$ core does not contribute significantly to orbital 113 of the complex (e.g. 0.2% of the electron density on the metal atom), which indicates that the low lying transition remains a "stilbazolium-like" behaviour. These similarities confirm that the coordination of a metal fragment increases the withdrawing character of the pyridine, which becomes almost as strong as that of the methylpyridinium. This effect of metal coordination is a general trend, reported for example, in the case of tungsten [53], rhodium and iridium [54], zinc and mercury [55], boron [56], and in the well investigated series of polypyridine

ruthenium complexes [57]. It offers a route for a potential correlation between optical and magnetic properties.

Besides the simple temperature effect, and contrary to the situation encountered in DEAMS$^+$, where the methyl-pyridine distance is constant, a shortening of the Fe^{III}-N bond induced by the spin crossover phenomenon has widely been reported [50,58] and is assumed to be equal to 0.06 Å in the present case, according to the averaged X-ray data available [38]. The anticipated enhancement of the withdrawing character of the pyridine, leads to a calculated switch equal to 738 and 310 cm^{-1}, for [Fe^{III}(salten)(DEAS)]$^+$ and DEAMS$^+$, respectively (Table 4). These values have to be compared to the experimental 590 ($\pm$ 50) and 100 ($\pm$ 50) cm^{-1} values (Table 3). Certainly, the agreement is not excellent. Nevertheless, the trend for larger shift expected in the case of spin cross over phenomenon is confirmed.

With the observation of a red shift in the intra-ligand charge transfer transition of a complex subjected to a spin crossover phenomenon, the intriguing issue of a possible interplay between magnetism and nonlinear optics is naturally addressed. Indeed, the low lying electronic transition of "push-pull" stilbazolium derivatives is responsible for their large NLO response, according to a "two-level" model, which relates β to a ground (g) and an excited (e) state having charge transfer character, in relation to the energy of the transition (E_{ge}), its oscillator strength (f_{ge}), and the difference between ground and excited state dipole moment ($\Delta\mu_{ge}$) through the following equation [60]:

$$\beta = \frac{3e^2\hbar^2 f_{ge}(\Delta\mu)_{ge}}{2mE_{ge}^3} \times \frac{E_{ge}^4}{\left(E_{ge}^2 - (2\hbar\omega)^2\right)\left(E_{ge}^2 - (\hbar\omega)^2\right)}$$

in which $\hbar\omega$ is the energy of the incident laser beam. Additional transitions may participate to the β expression (above equation) depending on their intensity (f) and push-pull character ($\Delta\mu$), in particular the LMCT transition, which are strongly spin dependent. However, it is clear in the present case that their low intensity and pseudo centrosymmetric character hampered their contribution to be relevant in term of NLO capabilities. According to the two-level model, and at the typical Nd:YAG laser wavelength of 1.064 μm, the experimental observation of a shift of 590 cm^{-1} in [Fe^{III}(salten)(DEAS)](BPh$_4$) should therefore correspond to a sizeable β enhancement of 29%.

Nevertheless, the present approach is based on the traditional description, which assumes that the interaction of a medium with light is regarded within the framework of a dielectric subjected to an electric field [61]. In this case, no magnetic effect will interfere with the NLO response. At a deeper theoretical level, the framework should be enlarged to encompass both electric and magnetic dipole transitions, leading to generalized mixed electric and magnetic contribution to the NLO tensor [62]. Although our ambition is not to establish here the thorough magnetic-NLO property relationship in spin crossover iron complexes, the present investigation provides insights towards an approach of molecular materials in which both magnetic and NLO responses could be engaged in a real interplay.

5. Conclusion

DEAMS$^+$ and [Fe^{III}(salten)(DEAS)]$^+$ are cationic chromophores built up from the "push-pull" stilbazolium core responsible for large optical nonlinearities. Both of them exhibit closely related intense and low-lying charge transfer transitions, in which the [Fe^{III}(salten)] core is not engaged. Besides a temperature effect, the dominant transition of [Fe^{III}(salten)(DEAS)](BPh$_4$) exhibits a significant red shift on cooling down. Structural and computational investigations suggest that this behaviour derives from the shortening of the iron-pyridine distance occurring upon spin crossover, which enhances the withdrawing character of the pyridine, and finally the charge transfer process. These observations provide a route for a potential interplay in molecular materials combining magnetic and NLO properties.

Acknowledgment

The authors thank Dr. A. Mari for his aid with the magnetic measurements.

References

[1] B.L. Davidov, L.D. Derkacheva, V.V. Dunina, M.E. Zhabotinskii, V.K. Zolin, L.G. Kreneva and M.A. Samokhina, *JEPT Lett* **12** (1970), 16–17.
[2] Special Issue on Optical Nonlinearities in Chemistry, *Chem Rev* **1** (1994), 94.
[3] (a) Nonlinear Optical Properties of Organic Molecules and Crystals; J. Zyss and D.S. Chemla, eds, Academic Press: Orlando, FL, 1987.
(b) Molecular Nonlinear Optics; J. Zyss; Academic Press: San Diego, CA, 1994.
(c) Nonlinear Optics of Organic Molecules and Polymers; H. S. Nalwa and S. Miyata, Eds.; CRC Press: Boca Raton, FL, 1996.
[4] S.K. Kurtz, in Nonlinear Optical Materials – Laser Handbook, F.T. Arecchi and E.O. Schultz-Dubois, eds, North-Holland, *Amsterdam* **1** (1972), 923.
[5] J.M. Lehn, Supramolecular Chemistry-Concepts and Perspectives; VCH, Weinheim, 1995.
[6] M.D. Ward, *Chem Soc Rev* **24** (1995), 121–134.
[7] B.J. Coe, *Chem Eur J* **5** (1999), 2464–2471.
[8] B.J. Coe, S. Houbrechts, I. Asselberghs and A. Persoons, *Ang Chem Int Ed* **38** (1999), 366–369.
[9] For a general introduction of nonlinear optics in octupolar geometry see: J. Zyss and I. Ledoux, *Chem Rev* **94** (1994), 77–105.
[10] For more recent reports to illustrate this approach, see for example: (a) R. Kannan, G.S. He, T.-C. Lin, P.N. Prasad, R.A. Vaia and L.-S. Tan, *Chem Mater* **6** (2004), 185–194.
(b) J. Brunel, O. Mongin, A. Jutand, I. Ledoux, J. Zyss and M. Blanchard-Desce, *Chem Mater* **15** (2003), 4139–4148; and references herein.
(c) H. Le Bozec, T. Le Bouder, O. Maury, I. Ledoux and J. Zyss, *J Opt A: Pure Appl Opt* **4** (2002), S189–S196.
[11] (a) G.L. Geoffroy and M.S. Wrighton, *Organometallic Photochemistry*, Academic Press: New York, 1979.
(b) J.P. Collman and L.S. Hegedus, *Principles and Applications of Organotransition Metal Chemistry*, University Science Books: Mill Valley, CA, 1987.
[12] O. Kahn, *Molecular Magnetism*, VCH Publishers : New York, 1993.
[13] S. Di Bella, I. Fragalà, I. Ledoux and T.J. Marks, *J Am Chem Soc* **117** (1995), 9481–9485.
[14] (a) F. Averseng, P.G. Lacroix, I. Malfant, N. Périssé, C. Lepetit and K. Nakatani, *Inorg Chem* **40** (2001), 3797–3804.
(b) O. Margeat, P.G. Lacroix, J.P. Costes, B. Donnadieu, C. Lepetit and K. Nakatani, *Inorg Chem* **43** (2004), 4743–4750.
[15] F. Averseng, C. Lepetit, P.G. Lacroix and J.P. Tuchagues, *Chem Mater* **12** (2000), 2225–2229.
[16] (a) J.F. Létard, S. Montant, P. Guionneau, P. Martin, A. Le Calvez, E. Freysz, D. Chasseau, R. Lapouyade and O. Kahn, *Chem Commun* (1997), 745–746.
[17] (b) J.F. Létard, L. Capes, G. Chastanet, N. Moliner, S. Létard, J.A. Real and O. Kahn, *Chem Phys Lett* **313** (1999), 115–120.
[18] (a) M. Nakano, R. Kishi, N. Nakagawa, S. Ohta, H. Takahashi, S.-I. Furukawa, K. Kamada, K. Ohta, B. Champagne, E. Botek, S. Yamada and K. Yamaguchi, *J Phys Chem A* **110** (2006), 4238–4243.
(b) M. Nakano, R. Kishi, S. Ohta, H. Takahashi, T. Kubo, K. Kamada, K. Ohta, E. Botek and B. Champagne, *Phys Rev Lett* **99** (2007), 033001(1)–033001(4).
[19] L. Cambi and L. Szegö, *Ber Dtsch Chem Ges* **64** (1931), 259–264.
[20] For recent reviews devoted to the spin transition phenomenon, see: (a) "Topics in Current Chemistry", Spin Crossover in Transtion Metal Compounds I.-III; P. Gütlich and H.A. Goodwin, eds, 2004, vol. 233–235.
(b) A. Bousseksou, G. Molnar and G. Matouzenko, *Eur J Inorg Chem* (2004), 4353.
(c) A.B. Gaspar, V. Ksenofontov, M. Seredyuk and P. Gütlich, *Coord Chem Rev* **249** (2005), 2661–2676.
[21] G. Agusti, A.B. Gaspar, M. Carmen Munoz, P.G. Lacroix and A. Real, *Aust J Chem* **62** (2009), in press.
[22] See for example: (a) G.J. Ashwell, P.D. Jackson and W.A. Crossland, *Nature* **368** (1994), 438–440.
(b) K.Z. Wang, C.H. Huang, G.X. Xu, Y. Xu, Q. Liu, D.B. Zhu, X.S. Zhao, X.M. Xie and N.Z. Wu, *Chem Mater* **6** (1994), 1986–1989.
[23] (a) T.J. Marks and M.A. Ratner, *Angew Chem Int Ed Engl* **34** (1995), 155.
(b) D. Li, M.A. Ratner, T.J. Marks, C. Zhang, J Yang and K.G. Wong, *J Am Chem Soc* **112** (1990), 7389–7390.
[24] P.G. Lacroix, R. Clément, K. Nakatani, J. Zyss and I. Ledoux, *Science* **263** (1994), 658–660.
[25] (a) S.R. Marder, J.W. Perry and W.P. Schaefer, *Sciences* **245** (1989), 626–628.

(b) S.R. Marder, J.W. Perry and C.P. Yakymyshyn, *Chem Mater* **6** (1994), 1137–1147 and references therein.
(c) B.J. Coe, J.A. Harris, I. Asselberghs, K. Wostyn, K. Clays, A. Persoons, B.S. Brunschwig, S.J. Coles, T. Gelbrich, M.E. Light, M.B. Hurthouse and K. Nakatani, *Adv Funct Mater* **13** (2003), 347–357.
[26] (a) N. Matsumoto, S. Ohta, Y. Ohyoshi, A. Ohyoshi, S. Kohata, H. Okawa and Y. Maeda, *J Chem Soc Dalton Trans* (1985), 2575–2584.
(b) S. Ohta, C. Yoshimura, N. Matsumoto, H. Okawa and A. Ohyoshi, *Bull Chem Soc Jpn* **59** (1986), 155–159.
(c) A. Sour, M.L. Boillot, E. Rivière and Ph. Lesot, *Eur J Inorg Chem* (1999), 2117–2119.
(d) R. Boca, Y. Fukuda, M. Gembicky, R. Herchel, R. Jarosciak, W. Linert, F. Renz and J. Yuzurihara, *Chem Phys Lett* **325** (2000), 411–419.
(e) S. Hirose, S. Hayami and Y. Maeda, *Bull Chem Soc Jpn* **73** (2000), 2059–2066.
(f) S. Hayami, Y. Hosokoshi, K. Inoue, Y. Einaga, O. Sato and Y. Maeda, *Bull Chem Soc Jpn* **74** (2001), 2361–2368.
[27] T.K. Kung, *J Chin Chem Soc* **25** (1978), 131–139.
[28] R. Andreu, I. Malfant, P.G. Lacroix, H. Gornitzka and K. Nakatani, *Chem Mater* **11** (1999), 840–848.
[29] R.H. Blessing, *Acta Cryst A* **51** (1995), 33–38.
[30] N. Walker and D. Stuart, *Acta Cryst A* **39** (1983), 158–166.
[31] SIR92 – A program for crystal structure solution. A. Altomare, G. Cascarano, C. Giacovazzo and A. Guagliardi, *J Appl Crystallogr* **26** (1993), 343–350.
[32] SHELX97 [Includes SHELXS97, SHELXL97, CIFTAB] – Programs for Crystal Structure Analysis (Release 97–92). G. M. Sheldrick, Institüt für Anorganische Chemie der Universität, Tammanstrasse 4, D-3400 Göttingen, Germany, 1998.
[33] WINGX – 1.63 Integrated System of Windows Programs for the Solution, Refinement and Analysis of Single Crystal X-Ray Diffraction Data. L.J. Farrugia, *J Appl Crystallogr* **32** (1999), 837–848.
[34] INTERNATIONAL tables for X-Ray crystallography, 1974, Vol IV, Kynoch press, Birmingham, England.
[35] ORTEP3 for Windows – L.J. Farrugia, *J Appl Crystallogr* **30** (1997), 565.
[36] (a) M.C. Zerner, G. Loew, R. Kirchner and U. Mueller-Westerhoff, *J Am Chem Soc* **102** (1980), 589–599.
(b) W.P. Anderson, D. Edwards and M.C. Zerner, *Inorg Chem* **25** (1986), 2728–2732.
[37] ZINDO, release 96.0, Molecular Simulations Inc., Cambridge, U. K., 1996.
[38] C. Faulmann, S. Dorbes, B. Garreau de Bonneval, G. Molnar, A. Bousseksou, C.J. Gomez-Garcia, E. Coronado and L. Valade, *Eur J Inorg Chem* (2005), 3261–3270.
[39] A. Earnshaw, *Introduction to Magnetochemistry*, Academic Press: London, 1968.
[40] E.D. Parker and A. Furst, *J Org Chem* **23** (1958), 201–203.
[41] A.K. Sheinkman, A.N. Kost, V.I. Sheichenko and A.N. Rozenberg, *Ukr Khim Zhu* **33** (1967), 941–946.
[42] G.R. Newkome and J.M. Robinson, *Tetrahedron Lett* **15** (1974), 691–694.
[43] A.E. Siegrist, H.R. Meyer, P. Gassmann and S. Moss, *Helv Chim Acta* **63** (1980), 1311–1334.
[44] This effect is observed on UV-visible spectra recorded at room temperature in the range of concentration 10^{-2}–10^{-4} mol L^{-1}, and is more pronounced at lower concentrations. (M.L. Boillot, *unpublished observation*).
[45] J. Zyss, J.F. Nicoud and M. Coquillay, *J Chem Phys* **81** (1984), 4160–4167.
[46] I. Malfant, R. Andreu, P.G. Lacroix, C. Faulmann and P. Cassoux, *Inorg Chem* **37** (1998), 3361–3370.
[47] J. Huanwang, W. Xin, H. Zijie, C. Shuying and L. Du, *Polyhedron* **13** (1994), 1035–1038.
[48] G.C. Papavissiliou, G.A. Mousdis, A. Terzis, C.P. Raptopoulou and Z. Naturforsch, *B: Chem Sci* **58** (2003), 815–816.
[49] (a) T.H. Lu, T.J. Lee and K.T. Kuo, *J Chin Chem Soc* **26** (1979), 53–56.
(b) A. Mishra, R.K. Behera, F.R. Fronczek, M. Vidyasagar and G.B. Behera, *Indian J Chem, Sect B* **38** (1999), 982–985.
[50] From the structural data obtained with ferric Schiff base complexes, the average of the metal ligand bond lengths of LS (HS) species is expected to vary as <Fe-O> = 1.879–1.895 (1.908–1.939) Å; <Fe- Nimine> = 1.930–1.944 (2.081–2.125) Å; and <Fe-Namine> = 1.999–2.046 (2.173–2.215) Å. These variations span over the range reported for the Schiff base ferric complexes undergoing a spin crossover in the following reports: (a) P.G. Sim, E. Sinn, R.H. Petty, C.L. Merill and L. Wilson, *J Inorg Chem* **20** (1981), 1213–1222.
(b) M.D. Timken, D.N. Hendrickson and E. Sinn, *Inorg Chem* **24** (1985), 3947–3955.
(c) Y. Nishida, K. Kino and S. Kida, *J Chem Soc Dalton Trans* (1987), 1957–1961.
(d) H. Oshio, K. Toriumi, Y. Maeda and Y. Takashima, *Inorg Chem* **30** (1991), 4252–4260.
(e) Y. Maeda, H. Oshio, K. Toriumi and Y. Takashima, *J Chem Soc Dalton Trans* (1991), 1227–1235.
(f) Y. Maeda, Y. Noda, H. Oshio and Y. Takashima, *Bull Chem Soc Jpn* **65** (1992), 1825–1831.
(g) A.J. Conti, R.K. Chadha, K.M. Sena, A.L. Rheinhold and D.N. Hendrickson, *Inorg Chem* **32** (1993), 2670–2680.
[51] see for example: A. Ohyoshi, J. Hondo, N. Matsumoto, S. Ohta and S. Sakamoto, *Bull Chem Soc Jpn* **59** (1986), 1611–1613.
[52] in ref. 12, Chap. 2, pp. 9–29.
[53] D.R. Kanis, P.G. Lacroix, M.A. Ratner and T.J. Marks, *J Am Chem Soc* **116** (1994), 10089–10102.
[54] D.W. Bruce, D.A. Dunmur, E. Lalinde, P.M. Maitlis and P. Styring, *Liq Cryst* **3** (1988), 385–395.

[55] M. Bourgault, C. Mountassir, H. Le Bozec, I. Ledoux, G. Pucetti and J. Zyss, *J Chem Soc, Chem Commun* (1993), 1623–1624.
[56] M.J.G. Lesley, A. Woodward, N.J. Taylor, T.B. Marder, I. Cazenobe, I. Ledoux, J. Zyss, A. Thornton and D.W. Bruce, *Chem Mater* **10** (1998), 1355–1365.
[57] H. Le Bozec and T. Renouard, *Eur J Inorg Chem* (2000), 229–239.
[58] (a) E. König, *Prog Inorg Chem* **35** (1987), 527–622.
(b) E. König, Structure and Bonding, Springer–Verlag, *Berlin* **76** (1991), 53–152.
[59] (a) J.L. Oudar and J. Chemla, *J Chem Phys* **66** (1977), 2664–2668.
[60] (b) J.L. Oudar, *J Chem Phys* **67** (1977), 446–457.
[61] N.P. Prasad and D.J. Williams, Introduction to Nonlinear Optical Effects in Molecules and Polymers; Wiley: New York, 1991.
[62] G.H. Wagniere, Linear and Nonlinear Optical Properties of Molecules; VCH: New York, 1993.

Journal of Computational Methods in Sciences and Engineering 10 (2010) 451–458
DOI 10.3233/JCM-2010-0333
IOS Press

Dynamics of collapse of optical pulses in Kerr medium

V. Cao Long[a], W. Leoński[a] and H. Nguyen Viet[b]
[a]*Institute of Physics, Zielona Góra University, ul. Prof. Szafrana 4a, 65-516 Zielona Góra, Poland*
[b]*Soltan Institute for Nuclear Studies, Hoża 69, 00-681 Warsaw, Poland*

Abstract. We consider the propagation of optical pulses in Kerr medium in the presence of a harmonic potential for 2D case in framework of Variational Approximation (VA). We will use two types of trial function: gaussian and hyperbolic secant ones. We will show that if the value of the nonlinearity parameter reaches a certain critical value the pulse collapses. This collapse corresponds to the physical situation when the self-focusing effect dominates over the dispersion and diffraction. We show that our analytical results are confirmed by several numerical calculations which are in excellent agreement with those of the VA predictions. By the analogy between the propagation equation and Gross-Pitajevski equation for Bose-Einstein condensates (BECs) we can transfer obtained results to the case of BEC placed in a external harmonic potential. It follows that in both of cases the wave collapse can appear.

1. Introduction

This paper is dedicated to the memory of prof. Stanisław Kielich, an outstanding polish physicist, a foundator and the leader of "Poznań School of Nonlinear Optics". His achievements in Quantum and Nonlinear Optics are well-known to the world [1,2]. One of us (W.L.), his "scientific grandson", has had a great honour of collaborating with him for a long time. An another one (C.L.V) met him at Conference EKON (Quantum Electronics and Nonlinear Optics) in 1980 and greating admired his genius of organization. It is worth to note that the first papers of Poznan' School were, among other things, concerning Kerr effects and light propagation in Kerr media [3]. At this point, we should also mention an other series of Kielich's papers dealing with such aspects of the interaction of nonlinear media with quantum optical field as bunching and antibunching effects (for instance *see:* [4]) or squeezing [5, 6]. Another problem which has been intensively considered by Poznań School was the laser induced autoionization [7].

In our paper we shall concentrate on one aspect of light propagation in nonlinear medium, in particular, the propagation of so-called solitons in Kerr medium. Consideration of the self-focusing effect in nonlinear propagation of light is interesting both theoretically and practically. Theoretically, because sometimes we can see dramatic concurrence between different nonlinear effects of the pulse propagation in the nonlinear medium. When the self-focusing effect dominates over the other effects as the dispersion, diffraction etc. the amplitude of the optical pulse (soliton) increases drastically. From other hand, if we reach a critical point the pulse completely collapses. In practice, this phenomenon is very dangerous as it usually destroys the optical material.

In this paper, we use an analogy between nonlinear optics in Kerr media and the Bose-Einstein condensate (BEC) system [8]. A common ground here is the nonlinear Schrödinger equation, which

with the proper substitution of variables describes both types of phenomena. In nonlinear optics it is a light propagation equation that relates the signal at the end of the nonlinear crystal to the signal at the input face of the medium. In the Bose-Einstein condensate dynamics it is the called Gross-Pitajevski equation. Hence, all results of this consideration can be transferred into the BEC systems. Thus, for some values of the nonlinear coupling constant we can have the collapse and the explosion of the BEC [9]. Such collapse of the self-focusing waves described by the nonlinear Schrödinger equation (NLSE) in nonlinear optics and plasma turbulence has been reviewed in [14]. In this paper we use the variational approximation (VA) and we will predict the critical point in which the optical pulse collapses. One should keep in mind that when we apply the VA the choice of the trial functions becomes essential. In practice, we shall concentrate on two cases that correspond to the Gaussian Ansatz (GA) and the Secant Ansatz (SA). We also have performed variational calculations for these two types of the trial functions. Moreover, to confirm our analytical predictions numerically we use time imaginary method [11]. One could see that the secant trial function is more proper.

2. Variational approximation

In the paper [10], using a method based on a consistent and mathematically rigorous expansion of the linear dispersion relation with included nonlinear optical response of the medium, we derived a general propagation equation for light pulse in an arbitrary dispersive nonlinear medium which is called Generalized Nonlinear Schrödinger Equation (GNLSE). In the case of Kerr media we have a well-known cubic nonlinearity which leads to the well-known Nonlinear Schrödinger Equation (NLS). In this paper we concentrate on the model of two-dimensional (2D) NLS. this model describes the propagation of the pulse in a Kerr medium in the presence of a harmonic potential [8]:

$$i\Psi_t = -\frac{1}{2}(\Psi_{xx} + \Psi_{yy}) + \frac{\omega^2 x^2}{2}\Psi - g|\Psi|^2\Psi \tag{1}$$

where g is a nonlinear coefficient. Our notations are chosen for easy transfer of the results to the case of Bose-Einstein condensates. This is a special case of the transformed NLS equation, so-called TNLS equation considered by Berge' [14] (see equation (152) in this paper). Generally, GNLSE has a very complicated form and looking for its solutions is usually a very difficult task. Analytical methods to solve this equation are effective only for some special cases [13]. For this reason several methods of finding approximate solutions are used. One of them is the powerful variational method based on choosing a proper trial function. This trial function should, of course, remain compatible with the main invariants and conservation laws of the original NLS equation. It is well known that a great deal of the physical processes involved in a given nonlinear problem can be understood in terms of the formation of spatial, temporal or spatio-temporal localized structures or solitons. To find soliton solutions of equation given above, corresponding to the propagation of the pulse on the xy plane we use the following (SA) in two directions x and y:

$$\Psi(x,y,t) = A(t)\ \text{sech}\left(\frac{x}{W(t)}\right)\ \text{sech}\left(\frac{y}{V(t)}\right)\ \exp\{i(\phi(t) + \frac{1}{2}(b(t)x^2 + \beta(t)y^2))\} \tag{2}$$

where the variational parameters $A(t)$, $\phi(t)$, $b(t)$, $\beta(t)$, $W(t)$ and $V(t)$ stand for the amplitude, total phase, spatial chirp coefficients, transverse widths along x and y directions, respectively. Moreover, in VA scheme we use the Lagrange function in the following form [12]:

$$L = \frac{1}{2}\int_{-\infty}^{\infty}\int_{-\infty}^{\infty} \mathrm{d}x\mathrm{d}y\left[i(\Psi_t\Psi^* - \Psi_t^*\Psi) - |\Psi_x|^2 - |\Psi_y|^2 - \omega^2 x^2|\Psi|^2 + g|\Psi|^4\right]. \tag{3}$$

In consequence, we apply our ansatz to the above Lagrange function and integrate the result over spatial variables x and y. Finally, we obtain the following function:

$$L = 4A^2WV\left[\frac{2gA^2}{9} - \phi^{'} - \frac{1}{6}\left(\frac{1}{W^2} + \frac{1}{V^2}\right) - \frac{\pi^2}{24}(V^2(\beta^{'} + \beta^2) + W^2(b^{'} + b^2 + \omega^2))\right]. \quad (4)$$

At this point we are in the position to derive Euler-Lagrange equations for our parameters (treated as dynamical variables) in the form of the following system of differential equations:

$$b = \frac{W^{'}}{W}, \quad (5)$$

$$\beta = \frac{V^{'}}{V}, \quad (6)$$

$$W^{''} = \frac{4}{\pi^2 W^3} - \frac{2g}{3\pi^2 VW^2} - \omega^2 W, \quad (7)$$

$$V^{''} = \frac{4}{\pi^2 V^3} - \frac{2g}{3\pi^2 WV^2}, \quad (8)$$

$$\phi^{'} = \frac{g}{9WV} - \frac{1}{6}\left[\frac{1}{V^2} + \frac{1}{W^2} + \frac{\pi^2}{4}(\omega^2 W^2 + WW^{''} + VV^{''})\right], \quad (9)$$

and

$$A^2WV = const. \quad (10)$$

Moreover, since for our ansatz we have

$$\int_{-\infty}^{\infty}\int_{-\infty}^{\infty} |\Psi|^2 \, \mathrm{d}x\mathrm{d}y = 4A^2WV, \quad (11)$$

we can derive that

$$4A^2WV = 1. \quad (12)$$

At this point we shall concentrate on the stationary regime. Therefore, for the above differential equations we set $W^{'} = W^{''} = 0$ and $V^{'} = V^{''} = 0$. In consequence, we obtain the following solutions for our parameters:

$$\beta = b = 0, \quad (13)$$

$$V = \frac{6}{g}W, \quad (14)$$

$$W = \sqrt[4]{\frac{36 - g^2}{9\pi^2\omega^2}}. \quad (15)$$

One can see that the form of the last formula leads to the necessary condition for the existence of solitons: the value of nonlinearity parameter g should satisfy the inequality $g < 6$. Therefore, we treat the value

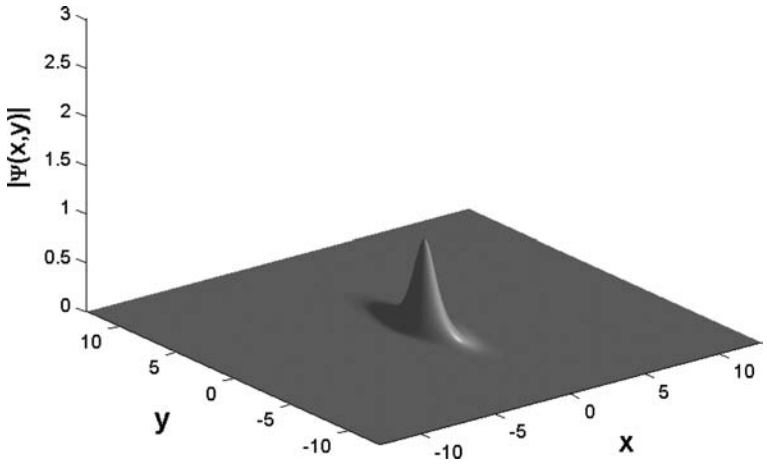

Fig. 1. Soliton solution corresponding to the value of nonlinearity parameter which is below the critical value ($g = 3$). The parameter $\omega = 4$.

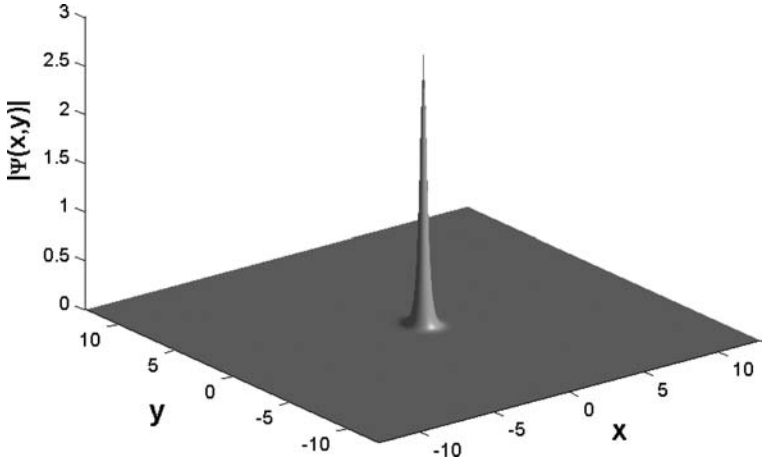

Fig. 2. The same as in Fig. 1 but for g close to its critical value ($g = 5.9$).

$g_c = 6$ as a critical one, and when the value of g becomes greater than g_c, the collapse of soliton occurs. In such case, the pulse becomes very narrow and its amplitude tends to infinity.

To confirm these analytical results we apply by using direct numerical time imaginary method introduced in [11]. The numerical results are shown in Fig. 1, where we assumed that $g = 3$, $\omega = 4$ and in Fig. 2 for $g = 5.9$ and $\omega = 4$. We see that when the value nonlinear coefficient becomes closed to its critical value (Fig. 2), the pulse becomes very sharp and narrow, contrary to the situation depicted in Fig. 1 – the pulse amplitude tends to infinity when the nonlinear coefficient approaches the critical value.

3. Optical chemical potential

At this point we come back to the soliton solution of our problem. This solution can be expressed as:

$$\Psi(x, y, t) = e^{-i\mu_{2D}t}\Phi(x, y), \tag{16}$$

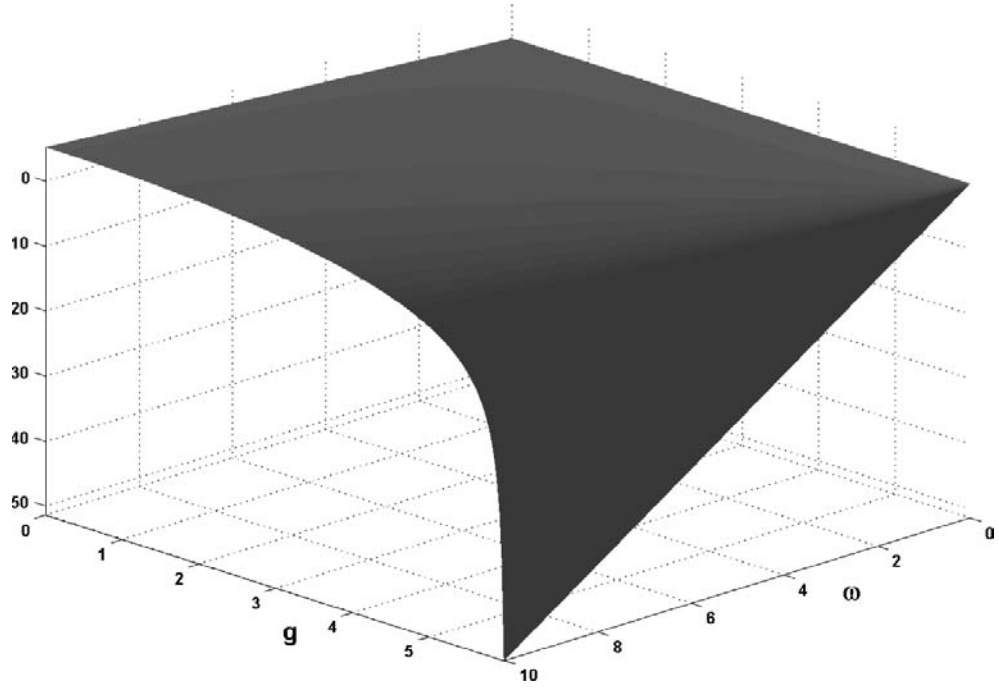

Fig. 3. Chemical potential obtained from VA as a function of g and ω.

μ_{2D} is an *optical chemical potential* (OCP) which is strictly related to the energy of the pulse. Moreover, we assume that $\Phi(x, y)$ is a real function of spatial variables x and y.

In particular, for the functions discussed here, we substitute expressions (14), (15) determining the widths of the soliton to the Eq. (9) for $\phi^{'}$ and we obtain:

$$\phi^{'} = -\frac{\pi\omega}{18}\frac{18 - g^2}{\sqrt{36 - g^2}}. \tag{17}$$

Hence the phase of soliton can be expressed as:

$$\phi(t) = \int \phi^{'} dt = -\frac{\pi\omega t}{18}\frac{18 - g^2}{\sqrt{36 - g^2}}. \tag{18}$$

From above definition of the optical chemical potential (16), after comparison it with our ansatz, we can easily conclude that

$$\phi(t) = -\mu_{2D} t \tag{19}$$

and therefore, we can write that

$$\mu_{2D} = \frac{\pi\omega}{18}\frac{18 - g^2}{\sqrt{36 - g^2}}. \tag{20}$$

The dependence of OCP on g and ω is displayed in Fig. 3. We see that its value decreases rapidly as g goes to 6, and moreover, as ω becomes greater and greater such decrease becomes more pronounced for values of g smaler than 6.

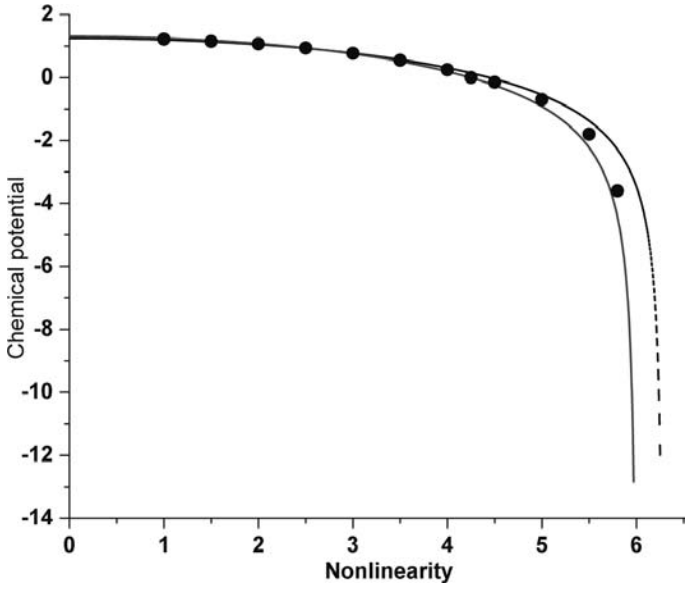

Fig. 4. Chemical potential as a function of the nonlinearity parameter g for $\omega = 2.5$.

In the next step we derive expression for the OCP corresponding to GA. For that purpose we apply the results presented in [12]. Thus, the formula for μ_{2D} can be written in the following form:

$$\mu_{2D} = \frac{\omega}{2\pi} \frac{2\pi^2 - g^2}{\sqrt{4\pi^2 - g^2}}. \tag{21}$$

It is easily seen that for the case discussed here the critical value of nonlinearity $g_c = 2\pi$.

Now, we shall again confirm our analytical results using numerical calculations. Thus, Fig. 4 shows the values of OCP as a function of g with the assumption that the value of ω is fixed $\omega = 2.5$ calculated numerically (circle marks) and derived from our analytical formulas (lines). The dashed line corresponds to GA, whereas the continuous line to the SA. We can observe that the the continuous line fits better to the numerical results than its dashed counterpart, so we can conclude that the trial secant function gives more accurate results than the gaussian one.

4. Dynamics of the collapse

In this section we shall concentrate on the collapse phenomenon. In particular, we will discuss the case when $g \geqslant 6$. In this regime we have:

$$V = \frac{6}{g} W \simeq W. \tag{22}$$

At this point we need to assume that our system has cylindrical symmetry. If we drop the harmonic term, we can write down that

$$W'' = \frac{4}{\pi^2 W^3} - \frac{2g}{3\pi^2 W^3} = \frac{(12 - 2g)}{3\pi^2 W^3}. \tag{23}$$

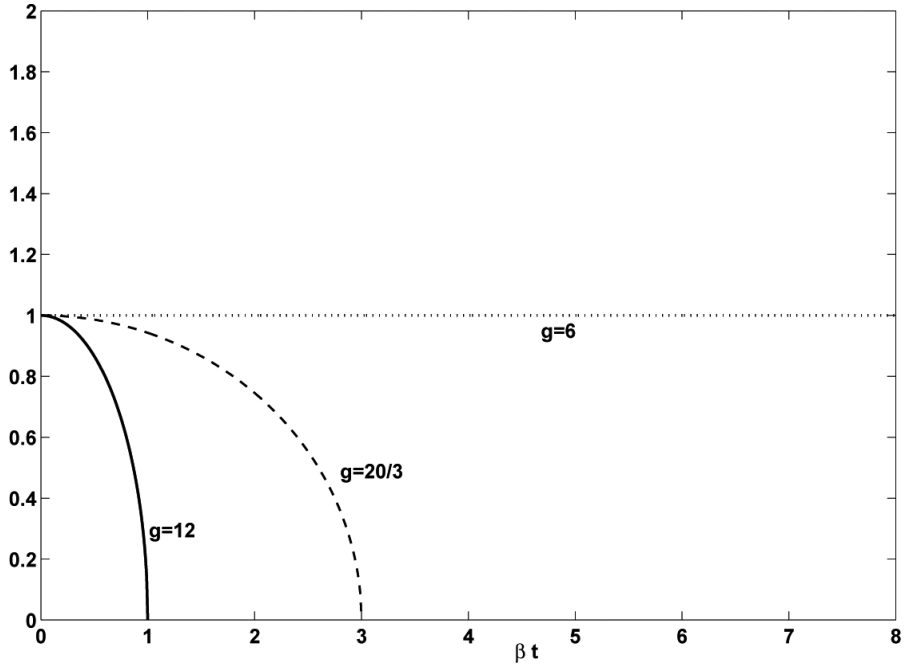

Fig. 5. The time-dependence of the pulse width $W(t)$ for various values of g for the case of collapses. The time t is scaled in the units of β ($\beta = \frac{2}{\pi W_0^2}$).

Next, if we set that

$$\lambda = \frac{2(g-6)}{3\pi^2} > 0. \tag{24}$$

we get the following ordinary differential equation determining the width $W(t)$:

$$W'' = -\frac{\lambda}{W^3}. \tag{25}$$

We can easily solve this equation assuming that $W(0) = W_0$, $W'(0) = 0$ (for stationary solution), where the parameter W_0 is a certain value of the initial width of the pulse.

Thus, after integrating the Eq. (25) we obtain the solution

$$W(t) = W_0\sqrt{1 - \frac{\lambda t^2}{W_0^4}} \tag{26}$$

and we introduce the time of collapse t_{col} by demanding:

$$W(t_{col}) = W_0\sqrt{1 - \frac{\lambda t_{col}^2}{W_0^4}} = 0. \tag{27}$$

In consequence we can write that

$$t_{col} = \frac{W_0^2}{\sqrt{\lambda}}. \tag{28}$$

Figure 5 shows the change of the pulse width for the case when the collapse occurs. We see that this width decreases to zero for shorter times as the value of the parameter g increases. Moreover, we see that the situation depicted in Fig. 5 agrees with that shown in the Fig. 2 on the page 304 of [14].

5. Conclusions

In our paper we have considered TNLS equation by concentrating on the special case that describes the wave collapses effect. In particular, this equation has been applied to describe light pulse propagation in a Kerr medium. Employing the variational scheme, we have shown that for the two cases discussed (both for the secant ansatz and for gaussian one) the wave collapse can appear. Moreover, it was proved that the secant trial function is more proper than its Gaussian counterpart. This fact is quite understandable because the "non-perturbed" solution is the secant hyperbolic solution. It should be stressed out that by the analogy between the propagation equation and Gross-Pitajevski equation for Bose-Einstein condensates we can transfer obtained results to the case of BECs placed in a external harmonic potential.

Acknowledgment

We would like to thank prof. Marek Trippenbach for some suggestions and fruitful discussions.

References

[1] S. Kielich, Molekularna optyka nieliniowa, PWN Warszawa 1978.
[2] Modern Nonlinear Optics, Vol. 85 of Advances in Chemical Physics, edited by M. Evans and S. Kielich, Wiley, New York 1993.
[3] R. Tanas and S. Kielich, *Opt Commun* **46** (1983), 23.
[4] S. Kielich, M. Kozierowski and R. Tanaś, Antibunching in light harmonics generation from field quantisation in "Coherence and Quantum Optics IV" (Plenum, New York, 1978), pp. 511–515.
[5] M. Kozierowski and S. Kielich, *Physics Letters A* **94** (1983), 213.
[6] R. Tanaś and S. Kielich, *Optics Communications* **45** (1983), 351.
[7] W. Leonski, R. Tanas and S. Kielich, *J Opt Soc Am* **B4** (1987), 72.
[8] C.L. Van, D.X. Khoa and M. Trippenbach, *Introduction to Nonlinear Optics*, Vinh 2003.
[9] E.A. Donley et al., *Nature* **412** (2001), 295.
[10] V.C. Long, H. Nguyen Viet, M. Trippenbach and K. Dinh Xuan, Propagation Technique for Ultrashort Pulses I, *Computational Methods in Science and Technology* **14**(1) (2008), 5.
[11] C.L. Van, D.X. Khoa, N.V. Hung and M. Trippenbach, Application of the time imaginary method in the quest for soliton solutions, paper presented on the 32th National Theoretical Symposium, Da Nang, Vietnam 2008.
[12] C.L. Van, D.X. Khoa, N.V. Hung and M. Trippenbach, Reduction of 2D problem of Bose – Einstein condensate trapped in a harmonic potential to the 1D problem, paper presented on the 32th National Theoretical Symposium, Da Nang, Vietnam 2008.
[13] C.L. Van and P.P. Goldstein, A Concise Course in Nonlinear Partial Differential Equations, University of Zielona Gora 2008 (Poland).
[14] L. Bergé, *Phys Rep* **303** (1998), 259.

Journal of Computational Methods in Sciences and Engineering 10 (2010) 459–467
DOI 10.3233/JCM-2010-0312
IOS Press

Elongation-CIS method: Describing excited states of large molecular systems in regionally localized molecular orbital basis

Marcin Makowski[a,*], Feng Long Gu[b,c] and Yuriko Aoki[a,c]
[a]*Department of Molecular and Material Sciences, Kyushu University, 6-1 Kasuga-Park, Fukuoka, 816-8580, Japan*
[b]*Center for Computational Quantum Chemistry, South China Normal University, Guangzhou, 510006 China*
[c]*CREST, Japan Science and Technology Agency* (*JST*), *Kawaguchi Center Building, Honcho 4-1-8, Kawaguchi, Saitama, 332-0012, Japan*

Abstract. The elongation methodology is extended towards description of excited states through the *ab initio* CIS expansions in regionally localized molecular orbital basis. The formalism and implementation of the elongation-CIS method are presented. The expected accuracy of the method in comparison to the conventional CIS approach is illustrated by the results of calculations for model systems.

Keywords: Elongation method, excited states, configuration interaction

1. Introduction

Providing computational tools that would be capable to describe electronic structure of large molecular systems with good accuracy while keeping demand on computer resources at reasonable level constitutes one of the major goals of the current computational chemistry. In the past, only semiempirical methods were applicable for quantitative treatment of huge systems. Nowadays, also *ab initio* methods are gaining more and more practical value for studying systems considered important in the fields of biochemistry and material science.

The efforts in the development of low cost-scaling *ab initio* methods has been mainly focused on the ground state properties. The progress in this area brought brilliant results both when regarding the size of the systems tractable [1,2] and the level of accuracy achievable [3–5]. Nonetheless, for the applications in the fields of photochemistry and photophysics the problem of efficient description of electronically excited states must be also addressed. One of the possible approaches towards this issue is to combine well established fragmentation/localization techniques for exploiting nearsightedness of the ground state electronic structure with the approximations introducing the similar concept of locality into

*Corresponding author: Department of Theoretical Chemistry, Jagiellonian University, Ingardena 3, Kraków, 30-060 Poland. E-mail: makowskm@chemia.uj.edu.pl.

excitation space treatment. The latter can be justified by taking into account that usually only relatively small, energetically low-lying subset of all excited states is crucial for the explanation of the interesting experimental phenomena. Further, in many complex systems these states arise due to the presence of the limited number of photoactive constituents (chromophores), while the influence of the remaining parts of the moiety on spectral characteristics of the whole system can be treated as small perturbation only.

If our ground state computations provide us with localized molecular orbitals, we may translate the above assumptions into an approximate computational procedure for the purpose of excited states calculations. The approximation we may try is to restrict the configuration space of a given standard quantum-chemical method (CIS, TDDFT, MCSCF . . .) to the set of excitations engaging only the orbitals that are localized in the preselected regions of the molecular system. As the examples of successful computational schemes built in this manner, the CIS and TDDFT extensions of the Fragment Molecular Orbital methodology [6,7] may be revoked. Here, we present the elongation-CIS method which is another approach of similar flavour. It relies on the elongation method to obtain the ground state description within HF approximation and subsequently employs regionally localized molecular orbitals (RLMOs) produced in the elongation-HF procedure to construct the excitation space for CIS method.

The article is organized as follows. We first briefly review basic ideas and capabilities of the elongation method. Then we proceed to the presentation of elongation-CIS formalism and implementation. In the next section we examine the accuracy of the elongation-CIS method on the basis of calculations for a few model systems. We conclude with a short summary including the future directions of development.

2. Elongation method

The elongation method has been proposed by Imamura et al. [8] as a tool for the calculations of electronic structure of large quasi-one-dimensional systems. It treats the system under study as a polymer chain whose electronic structure is constructed iteratively through adding monomer units one by one to the initial oligomer (starting cluster). This procedure may be considered as a simple theoretical analogue of the experimental polymerization/copolymerization synthetic mechanism. The computational advantages originate from the fact that before each subsequent addition, a set of localized molecular orbitals (LMO) is constructed. The subset of LMOs, localized on regions far from the current reaction site, is kept frozen during the subsequent steps.

To present the computational flow of the elongation procedure let us assume that the SCF equations have been solved for the starting cluster and the full transformation matrix from atomic orbital (AO) basis to canonical molecular orbitals (CMOs) basis has been evaluated. In the initial step the system is divided into two fragments: A_1 and B_1. Specifically, the fragment A_1 consists of AOs (atoms) that are far from the chain propagation site, the fragment B_1 extends over the remaining part of the system with the current reaction center included. The set of AOs taken from both fragments is used in the localization procedure [9] to make the transformation of canonical orbitals into two sets of RLMOs assigned to the fragments A_1 and B_1 separately.

After the localization is performed, one can proceed to the first elongation step. The system is extended by adding a monomer unit M_1 as a set of AOs and initially guessed MOs. At this point the whole system may be represented as $S = (A_1|B_1M_1) = (A_1|S_1)$, where the solid line separates the current frozen and active parts. Hartree-Fock (Kohn-Sham) equations are solved in a self-consistent way after the transformation of pseudoeigenvalue problem to the LMO basis set. The SCF problem is limited to the active space S_1, while the orbitals assigned to A_1 fragment are kept frozen. The propagation step can be followed by another localization that partitions S_1 into new frozen (A_2) and new active region (B_2).

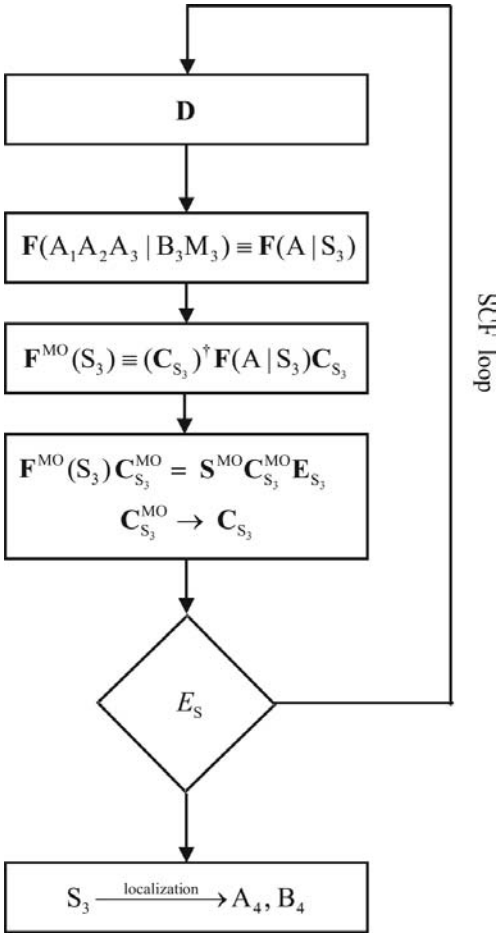

Fig. 1. Flowchart of the elongation computational procedure as applied for the third elongation step. Matrices marked with MO superscript are represented in MO (LMO) basis, the others in AO basis.

The propagation/localization cycle is repeated until the final system is constructed, in Fig. 1 we present its schematic flowchart for the hypothetical third elongation step.

The number of the variational degrees of freedom in the SCF procedure is kept practically constant during the elongation process. This feature effectively removes the diagonalization bottleneck that plagues standard HF/KS calculations for very large systems. Nevertheless, to fulfill the whole potential of the elongation method for favourable cost-scaling, one must also reduce the computational workload attached to the construction of the AO-based Fock matrix in each elongation step. For this purpose we use the cut-off technique [10] combined with the quantum fast multipole method and the linearly-scaling exchange matrix construction algorithm [11].

In its current state, the elongation method can be applied to the semiempirical, HF and DFT calculations with geometry optimization included [12] and to the semiempirical CIS calculations [13,14]. Recently, the extension of elongation methodology towards description of dynamic correlation effects in the framework of MP2 formalism has also been formulated [15]. The elongation method has been employed for a variety of applications including calculations of band structure [16], non-linear optical properties [17] or electronic structure of large biomolecules [18], to name a few recent. The main de-

velopments that are required to make the methodology universal are the efficient generalization to two- and three-dimensional systems, extension towards coupled clusters methods and enabling an efficient description of not only the ground, but also the excited states in *ab initio* framework. The work is under progress in our group to provide satisfactory solutions for the first two issues, the last one we have addressed in relatively the simplest fashion by the elongation-CIS approach presented here.

3. Elongation-CIS

The CIS method is in principle the simplest approach to address the problem of calculating the electronic structure of excited states. Its limitations are both of qualitative and quantitative nature.

First, it can account properly only for the states that are dominated by single excitations from the wavefunction structure point of view. Although the states that belong to the main domain of interest for spectroscopists are usually of such nature, the exceptions are not so rare with the lowest excited singlet state of polyenes serving as probably the most famous example.

Second, even if the description of the state is qualitatively correct, still the CIS calculations may be expected to overestimate excitation energies by roughly 1–2 eV comparing to experimental values. This discrepancy can be partly remedied by the CIS(D) correction as developed by Head-Gordon [19]. Another quite cost efficient alternative, which nowadays become the de facto standard as a quantitative method, is TDDFT approach [20]. While its only semi-quantitative character should be kept in mind, still the CIS method can be treated as a valuable first step in the analysis of excited states of large systems.

The CIS formulation as used for the elongation-based formalism is summarized below. For the closed-shell reference ground state it is useful to employ in calculations CSF-type basis set instead of determinant basis, which allows for the separate treatment of singlet and triplet states. In such a basis the elements of CIS Hamiltonian matrices for singlet and triplet can be evaluated respectively, as

$$^1H_{ia,jb} = \delta_{ij}\delta_{ab}E_0 + 2(ia|jb) - (ij|ab) + \delta_{ij}F_{ab} - \delta_{ab}F_{ij} \tag{1}$$

$$^3H_{ia,jb} = \delta_{ij}\delta_{ab}E_0 - (ij|ab) + \delta_{ij}F_{ab} - \delta_{ab}F_{ij}, \tag{2}$$

where the two-electron integrals are written in the Mulliken convention with i, j denoting doubly occupied MOs while a, b used for virtual MOs, F_{ij} and F_{ab} denote MO-based Fock matrix elements and E_0 represents the ground state energy. In canonical MO basis, non-diagonal elements of Fock matrix disappear and the formulas reduce to a well-known form including orbital energies [21]

$$^1H_{ia,jb} = \delta_{ij}\delta_{ab}E_0 + 2(ia|jb) - (ij|ab) + \delta_{ij}\delta_{ab}(\epsilon_a - \epsilon_i) \tag{3}$$

$$^3H_{ia,jb} = \delta_{ij}\delta_{ab}E_0 - (ij|ab) + \delta_{ij}\delta_{ab}(\epsilon_a - \epsilon_i). \tag{4}$$

In case of the elongation-CIS our molecular orbital basis consists of RLMOs, which are not canonical in full space. Due to this the more general expressions (1, 2) are used.

The diagonalization of Hamiltonian matrices provides the energies of the excited states as eigenvalues and the excited state vectors as eigenvectors. It may be noted that E_0 term occurs along the diagonal of the entire Hamiltonian matrix. This means that it can be subtracted before diagonalization and added it back later to each of the eigenvalues – now representing just excitation energies. In practice, we are usually interested in the low-lying excited states and only the small subset of the lowest eigenvalues and

corresponding eigenvectors are required. For such a case an iterative scheme can be used instead of full diagonalization. During the iterative procedure [22], the so-called sigma vectors

$$\sigma_{ia}^{\lambda} = \sum_{jb} H_{ia,jb} T_{jb}^{\lambda} \tag{5}$$

are repeatedly calculated from the Hamiltonian matrix and the trial CIS vectors labeled by λ. To evaluate them we employ the procedure developed by Foresman et al. [21] and Maurice et al. [23] that allows for an efficient construction of sigma vectors directly from AO-based two electron integrals avoiding the four-index transformation to the MO basis. The procedure consists of three steps, which we describe below for the singlet case.

First, the pseudo-density matrices for each λ are constructed from the MO coefficients and trial vectors

$${}^1P_{rs}^{\lambda} = \sum_{jb} C_{rj}\, {}^1T_{jb}^{\lambda} C_{sb}. \tag{6}$$

Then pseudo-Fock matrices are built in an integral-driven fashion

$${}^1F_{pq}^{\lambda} = \sum_{rs} [2(pq|rs) - (pr|qs)]\, {}^1P_{rs}^{\lambda}. \tag{7}$$

When the contraction of AO integrals is finished, the pseudo-Fock matrices are transformed-back to MO basis and Fock-matrix terms are added to complete sigma vectors evaluation

$${}^1\sigma_{ia}^{\lambda} = \sum_{pq} C_{pa}\, {}^1F_{pq}^{\lambda} C_{qi} + \sum_{jb} {}^1T_{jb}^{\lambda} F_{ab}\delta_{ij} - \sum_{jb} {}^1T_{jb}^{\lambda} F_{ij}\delta_{ab} \tag{8}$$

For the purpose of elongation-CIS calculations we restrict our CIS Hamiltonian basis to the subset of more or less local excitations. Moreover, the local character of RLMOs employed reflects in the sparsity of molecular orbital coefficients matrix. These factors gives rise to the potential efficiency advantage over the conventional CIS method. We take them into account in our actual implementation by replacing the dense transformations (6, 8) by operations over sparse structures and by adding, on the top of Schwarz inequalities, the additional prescreening during pseudo-Fock matrices formation to avoid calculation of contributions not needed in the back-transformation step. In addition to excitation energies, also transition dipole moments between the ground and excited states are computed by the elongation-CIS procedure through the construction of transition densities from the eigenvectors.

4. Benchmark calculations

The elongation-CIS routines has been linked to the implementation of the elongation method present in GAMESS package [24]. For benchmarking purposes we present the results of calculations for a few selected model-type systems. The simplest of them is a linear cluster of hydrogen molecules, the other two contain benzene chromophoric units. The first of them is 1,36-diphenylhexatriacontane (DPHT) which consists of a pair of chromophores linked by inactive chain. The second is a stack of 21 benzene molecules representing the system of chromophoric units coupled through space. The schematic structure of the systems considered is presented in Fig. 2.

The division into fragments for the elongation method purposes was done as following. For hydrogen molecules chain each fragment consisted of 4 molecules. In DPHT molecule each benzene ring has

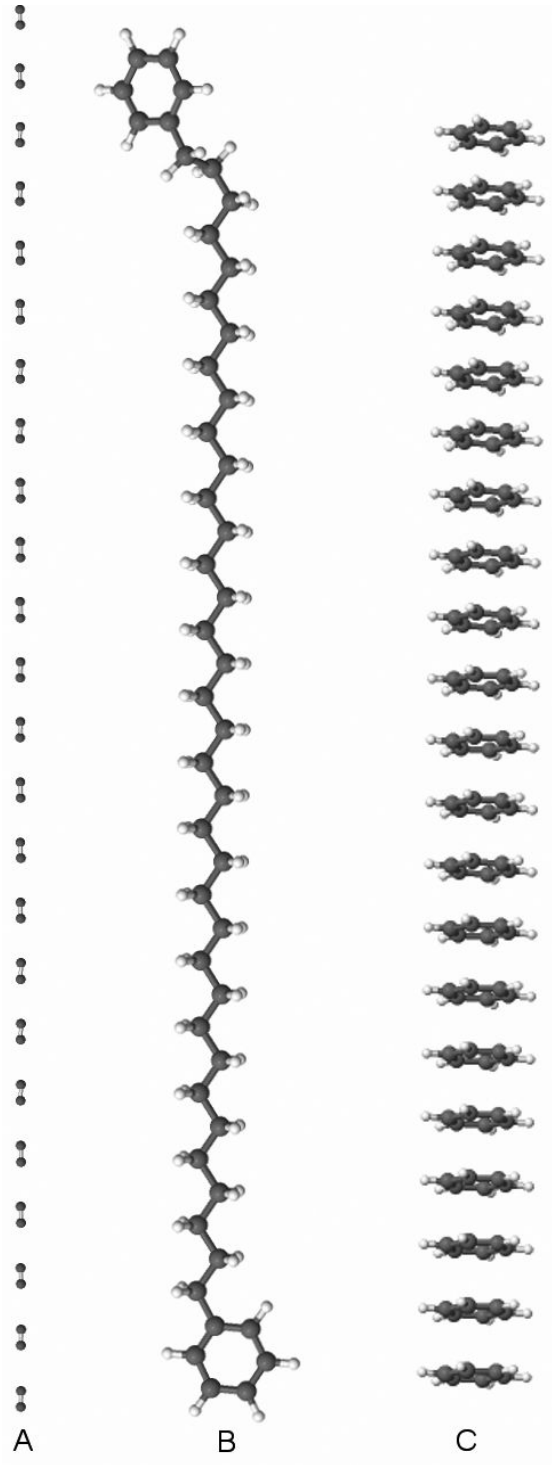

Fig. 2. Model systems considered: A – 24-unit linear chain of hydrogen molecules, B – 1, 36-diphenylhexatriacontane, C – stack of 21 benzene molecules.

Table 1
The four lowest singlet excited states of the linear cluster of 24 hydrogen molecules as calculated using cc-pVDZ basis set. Excitation energies given in eV, in parentheses the non-zero component of transition dipole moment (in a.u.)

	conventional CIS	elongation-CIS
S_1	11.7634 (6.3089)	11.7634 (6.3089)
S_2	11.8374 (0.00000)	11.8374 (0.00002)
S_3	11.9405 (1.9219)	11.9405 (1.9220)
S_4	12.0652 (0.00000)	12.0652 (0.00007)
Number of configurations	5184	2304

Table 2
The four lowest singlet and triplet excited states of DPHT molecule as calculated using 6-31G basis set. Excitation energies given in eV, in parentheses oscillatory strengths corresponding to the transitions.

	conventional CIS	elongation-CIS
S_1	6.1473 (0.00309)	6.1473 (0.00308)
S_2	6.4219 (0.00599)	6.4219 (0.00596)
S_3	6.6157 (0.01848)	6.6158 (0.01832)
S_4	6.6181 (0.01166)	6.6182 (0.01159)
T_1	3.4253	3.4253
T_2	3.4302	3.4302
T_3	5.1741	5.1742
T_4	5.1770	5.1771
Number of configurations	76035	22011

been treated as a separate fragment while alkane chain has been divided into three fragments equal in size. For benzene stack a single fragment consisted of 3 benzene molecules. In each case the starting cluster for the elongation-HF calculation included two fragments combined and in each elongation step one fragment was added and one simultanously frozen. In the intermediate steps of the elongation procedure for DPHT molecule the terminal hydrogen atoms were used as caps for broken bonds. In the elongation-CIS calculations, the nearest-neighbour approximation for the construction of excitation space has been employed. Namely, only the excitations from an occupied orbital assigned to a given fragment to a virtual orbitals assigned to the same or neighbouring fragment were included. In case of DPHT molecule calculations, additionally the central fragment of alkane chain was excluded completely from excitation space construction. The conventional CIS calculations were done using the routines included in GAMESS package. The convergence threshold for residue norm in Davidson procedure has been set to 10^{-5} for both the conventional and elongation-CIS calculations. The threshold for MO coefficients in sparse elongation-CIS transformations has been set to 10^{-6}.

We gathered in Tables 1–3 the results of calculations performed for the lowest excited states of the systems studied.

Energetics of the lowest singlet states is reproduced with the accuracy of order of 0.0001 eV, which should be considered as sufficient for all practical purposes. The similar conclusion holds for the energies of triplet states (see Table 2). Also transition dipole moments (oscillatory strengths) that can be translated directly into absorption intensities agree very well between the elongation and conventional calculations. It is worth to note that in all the cases using a local approximation for the excitation space led to the number of configurations significantly lower than considered in full CIS conventional calculations.

We checked also what accuracy can be expected for properties less directly connected to the CIS spectra. For this purpose we calculated longitudinal static polarizability of the hydrogen molecules

Table 3
The lowest singlet excited states of stacked benzene molecules system as calculated using 6-31G* basis set. Excitation energies given in eV, in parentheses oscillatory strengths corresponding to the transitions

	conventional CIS	elongation-CIS
S_1	4.046 ($< 10^{-6}$)	4.047 ($< 10^{-6}$)
S_2	4.057 ($< 10^{-6}$)	4.058 ($< 10^{-6}$)
S_3	4.078 ($< 10^{-6}$)	4.079 ($< 10^{-6}$)
S_4	4.085 ($< 10^{-6}$)	4.087 ($< 10^{-6}$)
Number of configurations	750141	290871

Table 4
The longitudinal static polarizability (in a.u.) of 24-unit hydrogen molecules cluster as calculated using cc-pVDZ basis set

CPHF	FF-HF	SOS-CIS	SOS-elongation-CIS
215.01	215.01	218.00	218.73

cluster by the usage of sum-over-states (SOS) method. For both conventional and elongation approaches the summation was restricted to 100 lowest excited singlets. The elongation-CIS density of states was substantially different from the conventional one in high-energy range, which is easy to understand as neglected non-local excitations become there of importance. Nonetheless, the polarizability was reproduced with the error of only a few promilles (see Table 4) and agreed also quite well with the values obtained in CPHF and finite field HF calculations.

5. Summary

We showed on the basis of calculations for a few model systems that elongation-CIS method can be a reliable substitution of conventional CIS approach. While the method is accurate when comparing to the conventional calculations, it may constitute an attractive alternative due to efficiency reasons which are of dual nature. First, the elongation approach towards calculation of HF reference ground state removes the diagonalization bottleneck and allows for the treatment of large systems with linearly-scaling cost. Second, the elongation method provides, in a natural way, the regionally localized molecular orbitals that can be used to restrict excited configurations space. Obviously, inherent CIS approach deficiencies limits the applicability of the method for the fully quantitative investigations. We are currently working on the improvement in this area by the implementation of the elongation-TDDFT scheme.

References

[1] E. Rudberg, E.H. Rubensson and P. Sałek, *J Chem Phys* **128** (2008), 184106.
[2] T. Ijegami, T. Ishida, D.G. Fedorov, K. Kitaura, Y. Inadomi, H. Umeda, M. Yokokawa and S. Sekiguchi, Proceedings of Supercomputing, 2005, *IEEE Computer Society*, Seatle, WA, 2005, 10.
[3] S. Saebo and P. Pulay, *Annu Rev Phys Chem* **44** (1993), 213.
[4] F.R. Manby, H.-J. Werner, T. Adler and A.J. May, *J Chem Phys* **124** (2006), 94103.
[5] M. Schütz and F.R. Manby, *Phys Chem Chem Phys* **5** (2003), 3349.
[6] Y. Mochizuki, S. Koikegami, S. Amari, K. Segawa, K. Kitaura and T. Nakano, *Chem Phys Lett* **406** (2005), 283.
[7] M. Chiba, D.G. Fedorov and K. Kitaura, *J Chem Phys* **127** (2007), 104108.

[8] A. Imamura, Y. Aoki and K. Maekawa, *J Chem Phys* **94** (1991), 5419.
[9] F.L. Gu, Y. Aoki, J. Korchowiec, A. Imamura and B. Kirtman, *J Chem Phys* **121** (2004), 10385.
[10] J. Korchowiec, F.L. Gu, A. Imamura, B. Kirtman and Y. Aoki, *Int J Quant Chem* **102** (2005), 785.
[11] J. Korchowiec, J. Lewandowski, M. Makowski, F.L. Gu and Y. Aoki, *J Comput Chem* **30** (2009), 2515.
[12] M. Makowski, J. Korchowiec, F.L. Gu and Y. Aoki, *J Comput Chem* **27** (2006), 1603.
[13] Y. Kurihara, Y. Aoki and A. Imamura, *J Chem Phys* **108** (1998), 10303.
[14] V. Pomogaev, F.L. Gu, A. Pomogaeva and Y. Aoki, *Int J Quant Chem* **109** (2009), 1328.
[15] M. Makowski, J. Korchowiec, F.L. Gu and Y. Aoki, *J Comput Chem* **31** (2010), 1733.
[16] A. Pomogaeva, M. Springborg, B. Kirtman, F.L. Gu and Y. Aoki, *J Chem Phys* **130** (2009), 194106.
[17] A. Pomogaeva, F.L. Gu, A. Imamura and Y. Aoki, *Theo Chem Acc* **125** (2010), 453.
[18] Y. Orimoto, F.L. Gu, A. Imamura and Y. Aoki, *J Chem Phys* **126** (2007), 215104.
[19] M. Head-Gordon, R.J. Rico, M. Oumi and T.J. Lee, *Chem Phys Lett* **219** (1994), 21.
[20] M.E. Casida, *Recent advances in density functional methods*, World Scientific, Singapore, 1995, 155.
[21] J.B. Foresman, M. Head-Gordon, J.A. Pople and M.J. Frisch, *J Phys Chem* **96** (1992), 135.
[22] E.R. Davidson, *J Comp Phys* **17** (1975), 87.
[23] D. Maurice and M. Head-Gordon, *Int J Quant Chem Symp* **29** (1995), 361.
[24] M.W. Schmidt, K.K. Baldridge, J.A. Boatz, S.T. Elbert, M.S. Gordon, J.H. Jensen, S. Koseki, N. Matsunaga, K.A. Nguyen, S. Su, T.L. Windus, M. Dupuis and J.A. Montgomery, *J Comput Chem* **14** (1993), 1347.

Journal of Computational Methods in Sciences and Engineering 10 (2010) 469–474
DOI 10.3233/JCM-2010-0336
IOS Press

On magnetic field of ring current

M. M. Mestechkin*
12773 Seabreeze Farms Dr. # 33 San Diego, CA 92130, USA

Abstract. The explicit expression for magnetic induction vector of a ring current at arbitrary point in toroidal coordinates is presented in terms of the full elliptic integral of the first kind and its derivative over integral modulus. There is a conjugated point for any observation point: it is an image of the latter in a sphere with the ring current as its equator. The conjugated point lies on the same vector and has the same integral modulus as the initial point.

Keywords: Ring current, magnetic induction vector, full elliptic integral, toroidal coordinates

PACS: 41.20 Gz

1. Introduction

The formula for the magnetic induction produced by a ring current in the symmetry axes is well known from the initial standard course of physics. However, it is difficult to find a similar formula for the magnetic induction vector outside of the axes even in monographs on a magnetostatics. Meanwhile a detail picture of this field would be useful for design of various NMR devices for physics and medicine purposes and even for tokamaks construction. It is worthwhile to mention that the courses of math-analysis, e.g. [1], which are studied simultaneously, include all what is necessary for derivation of such formula. The purpose of this short note is to fill the gap.

2. Magnetic induction vector of ring current

The spherical coordinates of the observation point A (Fig. 1) are (R, θ, $\pi/2-\varphi$), the radius of the ring current is a, the coordinate origin is in the centre of the ring, and the plane of the ring is *xy*. Due to the cylindrical symmetry point A is possible to place into the plane yz without loss of generality. The current flows counterclockwise; the vector element of the ring arc is $d\boldsymbol{l} = ad\varphi(-\cos\varphi\mathbf{i} + \mathbf{j}\sin\varphi)$, and position of the observation point relative to it is given by $\boldsymbol{r} = -a\sin\varphi\mathbf{i} + (-a\cos\varphi)\mathbf{j} + z\mathbf{k}$. Then $[d\boldsymbol{l}, \boldsymbol{r}] = azd\varphi\sin\varphi\mathbf{i} + azd\varphi\cos\varphi\mathbf{j} + (a^2 - a\cos\varphi)d\varphi\mathbf{k}$. Now it is possible to write the expression of the magnetic induction vector, produced by this element of current according to the Biot – Savart law (in SI units):

$$\begin{aligned} d\mathbf{B} &= \mu I[d\mathbf{l}, \mathbf{r}]/4\pi r^3 = \mu I a(\mathbf{i}z\sin\varphi + \mathbf{j}z\cos\varphi + (a - y\cos\varphi)\mathbf{k})d\varphi/4\pi r^3, \\ r^2 &= a^2 + z^2 + y^2 - 2y\cos\varphi = a^2 + R^2 - 2Ra\sin\theta\cos\varphi, \end{aligned} \tag{1}$$

*Corresponding author. E-mail: mestechkinmm@gmail.com.

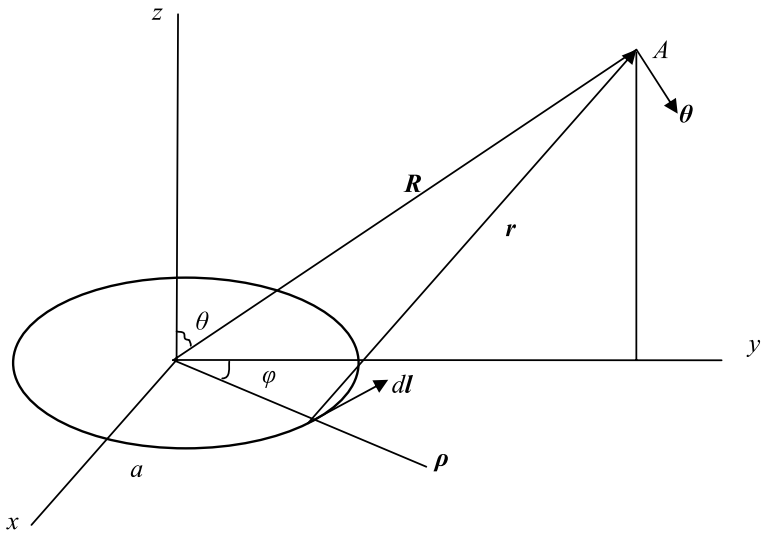

Fig. 1. Position of the observation point.

where $\boldsymbol{R}$ is the vector of A relative to the ring centre. To find the total value of $\boldsymbol{B}$ the expression (1) should be integrated over all circle. Integration is simplified if the integrand is put in the form $1-2p\cos\varphi+p^2$, and notation $2Ra\sin\theta/(a^2+R^2)\equiv q$ is introduced:

$$\begin{aligned} &a^2+R^2-2Ra\sin\theta\cos\varphi = d^2(1-2p\cos\varphi+p^2)/(1+p^2),\ 2p/(1+p^2)=q,\\ &q=\sin\theta/\xi,\ \xi=(R/a+a/R)/2\geqslant 1,\ p=q/(1\pm\sqrt{1-q^2}),\ d^2=a^2+R^2. \end{aligned} \tag{2}$$

The final formula has no peculiarities on the symmetry axes, where $q=0$, if we choose the upper sign. Then $p=0$ for $q=0$, and $p=1$ for $q=1$. The domain of θ is $0\leqslant\theta\leqslant\pi$, and that of p and q is [0,1]. The x-component of *B* is absent since sinφ is odd, and in accordance with the cylindrical symmetry:

$$\begin{aligned} &\mathbf{B}=\frac{\mu Ia}{4\pi d^3}(1+p^2)^{3/2}(RJ\cos\theta\mathbf{j}+(aH-RJ\sin\theta)\mathbf{k});\\ &J=\int_0^{2\pi}(1-2p\cos\varphi+p^2)^{-3/2}\cos\varphi d\varphi,\ H=\int_0^{2\pi}(1-2p\cos\varphi+p^2)^{-3/2}d\varphi \end{aligned} \tag{3}$$

Parameters $p=q=0$ in the symmetry axes that results in the simplest formula $\boldsymbol{B}=\boldsymbol{k}\mu Ia^2/2d^3$ since $J=0$, $H=2\pi$ in the axes. The periodicity, parity and substitution of φ by $\pi-\varphi$ demonstrate that integrals do not depend on the sign of p. The equalities

$$\frac{\cos\varphi-p}{(1-2p\cos\varphi+p^2)^{3/2}}=\frac{d}{dp}(1-2p\cos\varphi+p^2)^{-1/2};$$

$$(1-2p\cos\varphi+p^2)^{-1/2}-(1-2p\cos\varphi+p^2)^{-3/2}=\frac{p^2-2p\cos\varphi}{(1-2p\cos\varphi+p^2)^{3/2}}$$

allow to reduce J and H to the complete elliptic integral K of the first kind

$$\int_0^{\pi} (1 - 2p\cos\varphi + p^2)^{-1/2} d\varphi = 2\mathrm{K}$$

(p. 106 of Ref. [1]). Namely, the substitution: $1-\cos\varphi = 2\sin^2\alpha$ and subsequent Gauss-Landen transformation (p. 165 [1]) give $2\mathrm{K}(2\sqrt{p}/(1+p))/(1+p) = 2\mathrm{K}(p)$ that leads to the following connections between functions J and H and the elliptic integral and its derivative K′ over p, and to the final formula for the magnetic induction

$$\begin{aligned} J - pH = 4K', 4K - H = p^2H - 2pJ;\ J = 4(pK + (1+p^2)K')/(1-p^2), \\ H = 4(K + 2pK')/(1-p^2). \end{aligned} \tag{4}$$

$$\mathbf{B} = \frac{\mu I a}{\pi d^3}(1+p^2)^{3/2}[\boldsymbol{\theta} R(pK + (1+p^2)K') + \mathbf{k}(a(K + 2pK')]/(1-p^2) \tag{5}$$

The unit vector $\boldsymbol{\theta} = \mathbf{j}\cos\theta - \mathbf{k}\sin\theta$ corresponds to the angle θ. Thus, the induction vector components depend on the distance d from the ends of perpendicular ring diameter as the field in the symmetry axes. The dependence on the polar angle θ comes only through the integral modulus p Eq. (2).

3. Conjugated and related field points

Let us consider the image, C, of the observation point A in an enveloping sphere, which has the current ring as its equator. The image C is situated in the same vector *R* as A, but inside the sphere so that $\mathrm{OC}\cdot R = a^2$. It is clear after substitution of the expression of R through OC into formula (2) for q that q as well as p is identical for both points A and C and that $a\xi$ from Eq. (2) is the distance from O to the middle of segment AC. These points, A and C, can be mentioned as the conjugated points. Thus, there is a point inside of the enveloping sphere, which is characterized by the same coefficients at the field components, depending on p, as the conjugated point, lying on the same vector outside the sphere.

Such pairs of points are not unique. There are many other relative points with the same integral modulus. The latter depends only on q and is the same in the surface, described by the equation $q(R^2+a^2) = 2aR\sin\theta$ in the spherical coordinates R, θ with fixed q. This is the equation of torus of radius $OT = a(1+p^2)/2p$ with the common centre O with the ring, and its internal radius $LT = a(1-p^2)/2p$. The torus is symmetric relative to *xy*-plane, and its section by the plane $x = 0$ is shown in Fig. 2. The current ring is situated inside this torus (the bold line QP) on the distance $PT = a(1-p)^2/2p$ from its central circle (point T in Fig. 2). All scalar parameters (besides R and d) in Eq. (5) are identical for all points on the torus surface.

To build the torus we draw the tangent *AB* to the enveloping sphere (in $x = 0$ plane), passing through the point A, and drop a perpendicular onto the radius-vector *R* of A and obtain the conjugated point C. Using these two points, it is easy to find in the ring plane the centre T of the circle (T) of relative points. The intersection point L of the circle with *xy*-plane, the closest to the ring centre, has the distance $OL = ap$ from that centre and submits the parameter p (the furthest intersection point S gives $1/p$, which may be used for verification). Then from the table of elliptic integrals [2] (or from the Table below), both field components in an arbitrary point A and in all relative points on the torus surface can be calculated by means of Eq. (5).

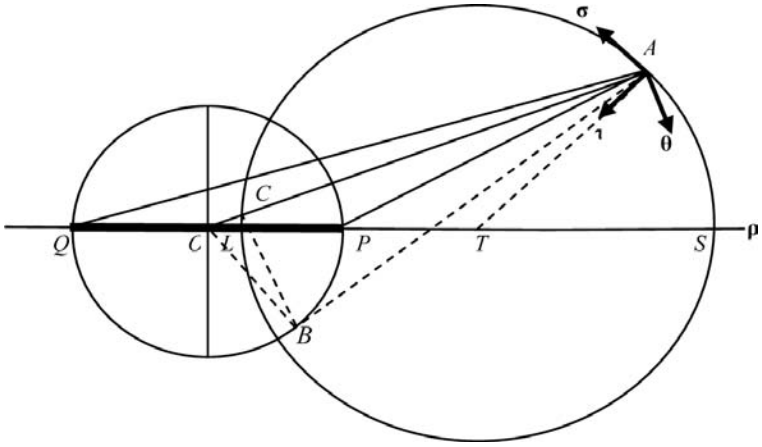

Fig. 2. Construction of the set of relative points.

4. Field components in toroidal coordinates

The above results look naturally in toroidal coordinates (σ, τ, φ), $0\leqslant \sigma < \pi$, $0\leqslant \tau < \infty$, $0\leqslant \varphi < 2\pi$:

$$\begin{aligned} &\rho = (a\mathrm{sh}\tau)/u,\ z = (a\sin\sigma)/u,\ u = \mathrm{ch}\tau - \cos\sigma;\ x = a\mathrm{sh}\tau\sin\varphi/u,\ y = a\mathrm{sh}\tau\cos\varphi/u,\\ &\quad \rho^2 = x^2 + y^2,\\ &ds^2 = d\rho^2 + \rho^2 d\varphi^2 + dz^2 = a^2(d\sigma^2 + d\tau^2 + \mathrm{sh}^2\tau d\varphi^2)/u^2;\ \mathrm{tg}\theta = \mathrm{sh}\tau/\sin\sigma,\\ &R^2 = \rho^2 + z^2 = a^2(\mathrm{ch}\tau + \cos\sigma)/u. \end{aligned} \tag{6}$$

The parameters from Eq. (5) are on account of Eq. (2)

$$q = \mathrm{th}\tau,\ p = \mathrm{th}(\tau/2),\ d^2 = 2a^2\mathrm{ch}\tau/u,\ 1 - p^2 = 1/\mathrm{ch}^2(\tau/2),\ 1 + p^2 = \mathrm{ch}\tau\,/\mathrm{ch}^2(\tau/2). \tag{7}$$

The circle T is a σ-coordinate line, and two circles, passing trough points P, Q and the observation point A with centres on the symmetry axes, form together a τ-coordinate line (not shown in Fig. 2; vector σ points at its centre according to Eqs (8, 10) below). Each of the last two circles is orthogonal to the circle T in the intersection point. The radii of these two circles are a/sinσ, and the intersection points with the z-axes are $\pm a$tg(σ/2). The equations of both circles and the T-circle are

$$\rho^2 + (z \mp a\mathrm{ctg}\sigma)^2 = a^2/\sin^2\sigma,\ (\rho - a\mathrm{cth}\tau)^2 + z^2 = a^2/\mathrm{sh}^2\tau \tag{8}$$

Equation (8) agree with the intersections of the T-circle with the horizontal axes ρ in points S and L, which coordinates are ath(τ/2)= a/p and ath(τ/2)= ap, and the position of its centre is $a\mathrm{th}\tau = a/q$. The product of distances *AP* and *AQ* is $2a^2/u$. Therefore the comparison of two expressions: 1/2*AP*·*AQ*·sin($\perp PAQ$) and az of the ΔPAQ area shows that the coordinate $\sigma = \perp PAQ$. Thus, the τ-coordinate line is a circle, from any point of which the diameter of the ring circle is seen under a constant angle σ.

The connection of unit vectors of toroidal and cylindrical systems at point A, shown in Fig. 2, is

$$\begin{aligned} &\boldsymbol{\sigma} = \boldsymbol{\rho}\cos\alpha + \mathbf{k}\sin\alpha,\ \boldsymbol{\tau} = -\boldsymbol{\rho}\sin\alpha + \mathbf{k}\cos\alpha;\\ &\boldsymbol{\rho} = \boldsymbol{\sigma}\cos\alpha - \boldsymbol{\tau}\sin\alpha,\ \mathbf{k} = \boldsymbol{\sigma}\sin\alpha + \boldsymbol{\tau}\cos\alpha;\ \boldsymbol{\theta} = \boldsymbol{\sigma}\cos(\alpha+\theta) - \boldsymbol{\tau}\sin(\alpha+\theta). \end{aligned} \tag{9}$$

The unit vector $\boldsymbol{\tau}$ is directed inside the circle T and orthogonal to it, α is the angle between the tangent to the circle in point A and the axes $\boldsymbol{\rho}$. Vectors $\boldsymbol{\sigma}$, $\boldsymbol{\tau}$, $\boldsymbol{\varphi}$ form the right orthogonal system, which is confirmed by the equations for tangents, z'_τ, z'_σ, of τ- and σ- lines, following from definitions (6),

$$\begin{aligned} z'_\tau &= dz/d\rho|_{\sigma=\text{const}} = \partial z/\partial\tau : \partial\rho/\partial\tau = \sin\sigma\text{sh}\tau/(\cos\sigma\text{ch}\tau - 1), \\ &\cos\alpha = \text{sh}\tau\sin\sigma/u, \\ z'_\sigma &= \text{tg}\alpha = dz/d\rho|_{\sigma=\text{const}} = \partial z/\partial\sigma : \partial\rho/\partial\sigma = (1-\cos\sigma\text{ch}\tau)/\sin\sigma\text{sh}\tau, \\ &\sin\alpha = (1-\text{ch}\tau\cos\sigma)/u. \end{aligned} \tag{10}$$

The conjugated point C is the second intersection point of τ- and σ-circles, which cylindrical coordinates according to Eq. (7) are $\rho = a\text{sh}\tau/(\text{ch}\tau+\cos\sigma)$, $z = -a\sin\sigma/(\text{ch}\tau+\cos\sigma)$.

The field expression (5) can be written now in toroidal coordinates if parameters are inserted from Eq. (7). It is before convenient to take into account connections, which follow from Eqs (6) and (10):

$$\begin{aligned} &\sin\theta = \text{sh}\tau/r,\ \ \cos\theta = \text{sin}\sigma/r,\ \ r = (\text{ch}^2\tau - \cos^2\sigma)^{1/2}; \\ &\sin(\alpha+\theta) = \text{ch}\tau\sin\sigma/r,\ \ \cos(\alpha+\theta) = \text{sh}\tau\text{ccos}\sigma/r \end{aligned} \tag{11}$$

After that the induction vector can be presented as

$$\mathbf{B}{=}B_\uparrow(u/2)^{1/2}[r\boldsymbol{\theta}(sh(\tau/2)K + ch\tau/\text{ch}(\tau/2)K') + u\mathbf{k}(\text{ch}(\tau/2)K + 2sh(\tau/2)K')]/\text{ch}^2(\tau/2). \tag{12}$$

The value of coefficient $B_\uparrow$ depends on the chosen units:

$$B_\uparrow = \mu I/2\pi a = 2\mu I/ca \tag{13}$$

The first expression is valid in SI, the second in Gaussian system, where $\mu_0 = 1$. The nonorthogonality of unit vectors in Eq. (12) and the presence of $K' = \partial K/\partial p$ (while the modulus of elliptic integral is th(τ/2) now) make this formula somewhat inconvenient.

This shortcoming disappears after using the unit vectors of toroidal system σ and τ using Eqs (9–11)

$$\begin{aligned} \mathbf{B}(\sigma,\tau) = B_\uparrow &\left(\frac{\text{ch}\tau-\text{cos}\sigma}{1+\text{ch}\tau}\right)^{1/2} \\ &[2\boldsymbol{\sigma}(\text{K}\sin^2(\sigma/2) + \text{sh}\tau\partial\text{K}/\partial\tau) + \tau\sin\sigma(\text{th}(\tau/2)\text{K} - 2\partial\text{K}/\partial\tau)]\ . \end{aligned} \tag{14}$$

Both functions, K and ∂K/$\partial\tau$, which enter this rather simple formula, increase monotonously in the interval $0 < p < 1$ and can be taken from the Table below. Equation (14) gives a complete picture of field distribution, in particular, it allows to find the field gradient, which determines the space change of local absorption of radiation in magnetic resonance devices, using the gradient expression in toroidal coordinates: $\partial/\partial\mathbf{r} = (u/a)(\boldsymbol{\sigma}\partial/\partial\sigma + \boldsymbol{\tau}\partial/\partial\tau + \boldsymbol{\varphi}\partial/\text{sh}\tau\partial\varphi)$ and other necessary characteristics.

5. Conclusion

The explicit equation for magnetic induction vector of a ring current in an arbitrary point is presented by the simple formula (14) through the full elliptic integral and its derivative.

Table 1
Functions of toroidal coordinate τ from Eq. (14)

N[a]	τ	p	K	$dK/d\tau$	N	τ	p	K	$dK/d\tau$	N	τ	p	K	$dK/d\tau$
0	0.0000	0.0000	1.5708	0.0000	30	1.0986	0.5000	1.6858	0.2031	60	2.6339	0.8660	2.1565	0.3880
1	0.0349	0.0175	1.5709	0.0069	31	1.1391	0.5150	1.6941	0.2097	61	2.7048	0.8746	2.1842	0.3934
2	0.0698	0.0349	1.5713	0.0137	32	1.1801	0.5299	1.7028	0.2163	62	2.7780	0.8829	2.2132	0.3988
3	0.1048	0.0523	1.5719	0.0206	33	1.2215	0.5446	1.7119	0.2229	63	2.8536	0.8910	2.2435	0.4041
4	0.1397	0.0698	1.5727	0.0274	34	1.2633	0.5592	1.7214	0.2294	64	2.9318	0.8988	2.2754	0.4094
5	0.1748	0.0872	1.5738	0.0343	35	1.3057	0.5736	1.7312	0.2359	65	3.0129	0.9063	2.3088	0.4146
6	0.2098	0.1045	1.5751	0.0411	36	1.3486	0.5878	1.7415	0.2424	66	3.0971	0.9135	2.3439	0.4196
7	0.2450	0.1219	1.5767	0.0479	37	1.3920	0.6018	1.7522	0.2488	67	3.1846	0.9205	2.3809	0.4247
8	0.2802	0.1392	1.5785	0.0548	38	1.4360	0.6157	1.7633	0.2553	68	3.2759	0.9272	2.4198	0.4296
9	0.3155	0.1564	1.5805	0.0616	39	1.4806	0.6293	1.7748	0.2617	69	3.3711	0.9336	2.4610	0.4344
10	0.3509	0.1736	1.5828	0.0685	40	1.5258	0.6428	1.7868	0.2680	70	3.4708	0.9397	2.5046	0.4392
11	0.3864	0.1908	1.5854	0.0753	41	1.5717	0.6561	1.7992	0.2744	71	3.5754	0.9455	2.5507	0.4438
12	0.4220	0.2079	1.5882	0.0821	42	1.6183	0.6691	1.8122	0.2807	72	3.6855	0.9511	2.5998	0.4484
13	0.4577	0.2250	1.5913	0.0889	43	1.6657	0.6820	1.8256	0.2870	73	3.8016	0.9563	2.6521	0.4528
14	0.4936	0.2419	1.5946	0.0957	44	1.7138	0.6947	1.8396	0.2932	74	3.9245	0.9613	2.7081	0.4570
15	0.5297	0.2588	1.5981	0.1025	45	1.7627	0.7071	1.8541	0.2995	75	4.0552	0.9659	2.7681	0.4612
16	0.5659	0.2756	1.6020	0.1093	46	1.8126	0.7193	1.8691	0.3057	76	4.1946	0.9703	2.8327	0.4652
17	0.6023	0.2924	1.6061	0.1161	47	1.8633	0.7314	1.8848	0.3119	77	4.3442	0.9744	2.9026	0.4691
18	0.6389	0.3090	1.6105	0.1229	48	1.9149	0.7431	1.9011	0.3180	78	4.5056	0.9781	2.9786	0.4729
19	0.6757	0.3256	1.6151	0.1296	49	1.9676	0.7547	1.9180	0.3241	79	4.6808	0.9816	3.0617	0.4764
20	0.7128	0.3420	1.6200	0.1364	50	2.0214	0.7660	1.9356	0.3301	80	4.8725	0.9848	3.1534	0.4798
21	0.7500	0.3584	1.6252	0.1431	51	2.0762	0.7771	1.9539	0.3361	81	5.0842	0.9877	3.2553	0.4830
22	0.7875	0.3746	1.6307	0.1498	52	2.1323	0.7880	1.9729	0.3421	82	5.3206	0.9903	3.3699	0.4860
23	0.8253	0.3907	1.6365	0.1566	53	2.1897	0.7986	1.9927	0.3480	83	5.5884	0.9925	3.5004	0.4888
24	0.8634	0.4067	1.6426	0.1633	54	2.2484	0.8090	2.0133	0.3538	84	5.8974	0.9945	3.6519	0.4913
25	0.9018	0.4226	1.6490	0.1699	55	2.3085	0.8192	2.0347	0.3597	85	6.2626	0.9962	3.8317	0.4937
26	0.9404	0.4384	1.6557	0.1766	56	2.3701	0.8290	2.0571	0.3655	86	6.7093	0.9976	4.0528	0.4956
27	0.9794	0.4540	1.6627	0.1833	57	2.4333	0.8387	2.0804	0.3712	87	7.2851	0.9986	4.3387	0.4974
28	1.0188	0.4695	1.6701	0.1899	58	2.4983	0.8480	2.1047	0.3768	88	8.0963	0.9994	4.7427	0.4987
29	1.0585	0.4848	1.6777	0.1965	59	2.5651	0.8572	2.1300	0.3824	89	9.4827	0.9998	5.4349	0.4996

[a]The row number is simultaneously the modulus of the elliptic integral in angle degrees.

Acknowledgment

The author expresses his deep gratitude to Professor G. Maroulis for this opportunity to pay tribute to Professor S. Kielich, whose books on nonlinear electrical and optical properties of matter had influence on the research in this field of his Soviet colleagues, especially in the theory of mixed electrical and magnetic nonlinear properties.

References

[1] Г.М.Фихтенгольц; Курс дифференциального и интегрального исчисления, т.2, ГИТТЛ, М-Л, 1951.
[2] W.H. Beyer, CRC Standard mathematical tables, Florida, 1981.

Journal of Computational Methods in Sciences and Engineering 10 (2010) 475–485
DOI 10.3233/JCM-2010-0337
IOS Press

Nonlinear optical properties of solvated molecules

Kurt V. Mikkelsen
Department of Chemistry, University of Copenhagen, Universitetsparken 5, DK-2100 Copenhagen Ø, Denmark
E-mail: kmi@kemi.ku.du

Abstract. Homogeneous dielectric media models are considered when calculating nonlinaer optical molecular porperties using correlated electronic structure response methods.

Keywords: Homogeneous dielectric media, correlated electronic structure, response methods, nonlinear optical properties

1. Introduction

The focus of this presentation is on the theoretical background of homogeneous solvation models for calculating nonlinear optical molecular properties of solvated molecules described by correlated electronic structure response methods [1–35]. Historically, methods within this area of research have been addressing the effects of solvation on the electronic wave function of solvated molecules and the focus has primarily been on uncorrelated electronic structure methods [1–11,14–18]. Only within the last two decades methods based on correlated electronic structure descriptions have appeared for the calculation of the electronic wave function of a solvated molecule using the second order Møller-Plesset (MP2) method [27,29], the multiconfigurational self-consistent reaction field (MCSCRF) level [12,19] and the coupled-cluster self-consistent reaction field (CCSCRF) level [35].

In order to investigate theoretically time-dependent molecular properties of solvated molecules, we utilize solvent response theory for correlated electronic structure methods [44–46,23,20]. Solvent response theory is conveniently derived by the ultilization of modern response theory [36–43]. Presently, we consider general electronic states of solvated molecules and are not limited to closed shell molecular compounds. In the case of closed shell molecular systems we refer to methods utilizing closed shell coupled cluster electronic structure and closed shell density functional theory for the electronic structure of the solvated system [48–61]. The present focus is on the electronic structure of molecular systems interacting with an outer solvent where the electronic subsystem is described by a correlated electronic structure wave function. Based on solvent response theory we are able to calculate different molecular properties of solvated molecules such as:

- frequency-dependent second hyperpolarizabilities (γ),
- three-photon absorptions,
- two-photon absorption between excited states,
- frequency-dependent polarizabilities of excited states,

– frequency dependent first hyperpolarizability tensors,
– two-photon matrix elements.
– frequency dependent polarizabilities
– excitation and deexcitation energies along with their corresponding transition moments.

The paper is organized such that the initial section describes response theory, followed by a section on the energy functional and a section on solvent response theory.

The energy functionals for the homogeneous dielectric media are covered and generally the basic idea is to divide a large system into two subsystems. The subsystem of principal interest is described by quantum mechanics, whereas the other subsystem is treated by a much coarser method such as classical electrostatics [1–32,18]. We represent the interactions between the quantum subsystem and the outer solvent by the induced polarization in the outer solvent and the electric field due to the charge distribution of the solvated quantum mechanical subsystem [1–17]. The quantum mechanical and classical subsystems are coupled by an effective interaction operator and thereby one obtains a modified quantum mechanical equation for finding the quantum mechanical electronic wave function of the solvated molecule [1–12,14–16,18,23,25,27–32].

2. Response theory

The Ehrenfest equation provides the time evolution of the molecular state

$$\frac{d}{dt}\langle\tilde{0}|\tilde{\mathbf{T}}^{\dagger}|\tilde{0}\rangle = \langle\tilde{0}|\frac{d}{dt}\tilde{\mathbf{T}}^{\dagger}|\tilde{0}\rangle - i\langle\tilde{0}|[\tilde{\mathbf{T}}^{\dagger}, H]|\tilde{0}\rangle \tag{1}$$

and the Ehrenfest equation has to be fulfilled for the following set of operators;

$$\mathbf{T} = (\mathbf{q}^{\dagger}, \mathbf{R}^{\dagger}, \mathbf{q}, \mathbf{R}) \tag{2}$$

which are defined according to:

$$\begin{aligned} R_n^{\dagger} &= |n\rangle\langle 0| \\ q_{pq}^{\dagger} &= E_{pq} = \sum_{\sigma} a_{p\sigma}^{\dagger} a_{q\sigma} \end{aligned} \tag{3}$$

The function of these operators is to determine effectively the time evolution of the multi configurational self-consistent field (MCSCF) state

$$|\tilde{0}\rangle = e^{i\kappa(t)} e^{iS(t)} |0\rangle \tag{4}$$

and for mathematical convenience we provide these as their time transformed counterparts in Eq. (1):

$$\begin{aligned} \tilde{q}_{pq}^{\dagger} &= e^{i\kappa(t)} q_{pq}^{\dagger} e^{-i\kappa(t)} \\ \tilde{q}_{pq} &= e^{i\kappa(t)} q_{pq} e^{-i\kappa(t)} \\ \tilde{R}_n^{\dagger} &= e^{i\kappa(t)} e^{iS(t)} R_n^{\dagger} e^{-i\kappa(t)} e^{-iS(t)} \\ \tilde{R}_n &= e^{i\kappa(t)} e^{iS(t)} R_n e^{-i\kappa(t)} e^{-iS(t)} \end{aligned} \tag{5}$$

The propagators $e^{i\kappa(t)}$ and $e^{iS(t)}$ are written as

$$\kappa(t) = \sum_{q\rangle p} \left\{ \kappa_{pq}(t) E_{pq} + \kappa^*_{qp}(t) E_{qp} \right\} \tag{6}$$

and

$$S(t) = \sum_{n} \left\{ S_n(t) R^\dagger_n + S^*_n(t) R_n \right\} \tag{7}$$

Furthermore, we are able to write the amplitudes as a vector

$$\boldsymbol{\beta} = \begin{pmatrix} \boldsymbol{\kappa} \\ \mathbf{S} \\ \boldsymbol{\kappa}^* \\ \mathbf{S}^* \end{pmatrix} \tag{8}$$

which following a transformation to the more general operator basis [64], $\{\mathbf{O}\}$, provides a partition into an orbital and a configurational part

$$\kappa(t) + S(t) = \mathbf{T}\,\boldsymbol{\beta} = \mathbf{O}\,\boldsymbol{\alpha} \tag{9}$$

$$O_j = O_{oj} + O_{cj} \tag{10}$$

Finally, the corresponding amplitude of $(\kappa(t) + S(t))$ in this basis can be written as

$$\begin{aligned} \kappa(t) &= \sum_j \alpha_j O_{oj} \\ S(t) &= \sum_j \alpha_j O_{cj} \end{aligned} \tag{11}$$

and we find that the Ehrenfest equation in this basis becomes

$$\frac{d}{dt}\langle\tilde{0}|\tilde{\mathbf{O}}^\dagger|\tilde{0}\rangle = \langle\tilde{0}|\frac{d}{dt}\tilde{\mathbf{O}}^\dagger|\tilde{0}\rangle - i\langle\tilde{0}|[\tilde{\mathbf{O}}^\dagger, H]|\tilde{0}\rangle \tag{12}$$

and the time transformed operators, $\left\{\tilde{\mathbf{O}}\right\}$, are defined in analogy with Eq. (6).

We consider a molecular system interacting with a time-dependent perturbation due to a time-dependent electromagnetic field and the Hamiltonian of the total system is given as

$$H = H_0 + W_{sol} + V(t) \tag{13}$$

with the condition that $V(t \to -\infty) = 0$. For this limit the generalized Brillouin condition is given by

$$\langle 0|[\lambda, H_0 + W_{sol}]|0\rangle = 0 \tag{14}$$

where λ designates variational parameters in orbital and configuration space.

3. Homogeneous dielectric medium model

For this model, a solvated molecular system interacts with a time-dependent electromagnetic field and the molecular system is either interacting with an equilibrium or a nonequilibrium solvation state. The solute molecule is placed within a cavity surrounded by a linear, homogeneous and isotropic dielectric medium and the molecular charge distribution is obtained by using the multi configurational self-consistent field (MCSCF) procedure. The charge distribution of the solute induces a polarization field in the dielectric medium and the induced polarization field is partitioned into optical and inertial polarization vectors and is coupled self-consistently to the MCSCF procedure. During sudden processes, only the optical polarization field is allowed to equilibrate with the solute state whereas the inertial polarization field remains unchanged. Thereby, the inertial polarization field reflects the initial charge distribution of the solute and this results in a nonequilibrium solvent configuration.

The nonequilibrium solvation for a molecular state is described using the following interaction operator between the outer dielectric medium and the molecular system [23]

$$\tilde{W}_{sol} = \sum_{lm} g_l(\epsilon_{op})(T^n_{lm})^2 + \sum_{lm} g_l(\epsilon_{st},\epsilon_{op})(T^n_{lm})^2 + \tilde{T}_g(\epsilon_{st},\epsilon_{op}) \tag{15}$$

where the nuclear charge moment operators T^n_{lm} is

$$T^n_{lm} = \sum_g Z_g t^{lm}(\mathbf{R}_g) \tag{16}$$

Here Z_g is the nuclear charge on atom g, $\mathbf{R}_g$ its position and t^{lm} the real spherical harmonics and we have that the reaction field factors are given by

$$\begin{aligned} g_l(\epsilon) &= -\frac{1}{2} R_{cav}^{-(2l+1)} \frac{(l+1)(\epsilon-1)}{l+\epsilon(l+1)} \\ g_l(\epsilon_{st},\epsilon_{op}) &= g_l(\epsilon_{st}) - g_l(\epsilon_{op}) \end{aligned} \tag{17}$$

where R_{cav} is the cavity radius and l the order of the multipole expansion. The third term within the interaction operator is given by a sum

$$\tilde{T}_g(\epsilon_{st},\epsilon_{op}) = g^{(a)}_{sol} + \tilde{g}^{(b)}_{sol} + g^{(c)}_{sol}, \tag{18}$$

where:

$$\begin{aligned} g^{(a)}_{sol} &= -2\sum_{lm} g_l(\epsilon_{op}) T^n_{lm} T^e_{lm} \\ \tilde{g}^{(b)}_{sol} &= 2\sum_{lm} g_l(\epsilon_{op}) T^e_{lm} \langle \tilde{0}|T^e_{lm}|\tilde{0}\rangle \\ g^{(c)}_{sol} &= -2\sum_{lm} g_l(\epsilon_{st},\epsilon_{op}) \langle T_{lm}(\rho_i)\rangle T^e_{lm}. \end{aligned} \tag{19}$$

The electronic charge moment operators are defined as;

$$T^e_{lm} = \sum_{pq} t^{lm}_{pq} E_{pq} = \sum_{pq} \langle \phi_p | t^{lm}(\mathbf{r}) | \phi_q \rangle E_{pq} \tag{20}$$

The creation and annihilation operators for an electron in spin-orbital $\phi_{p\sigma}$ are denoted $a^\dagger_{p\sigma}$ and $a_{p\sigma}$. The spin-free operator E_{pq} (summation over the spin quantum number σ) is represented as

$$E_{pq} = \sum_\sigma a^\dagger_{p\sigma} a_{q\sigma} \tag{21}$$

and the expectation value appearing in $g^{(c)}_{sol}$ is given by $\langle T_{lm}\rangle = T^n_{lm} - \langle T^e_{lm}\rangle$.

The three terms in Eq.(18) represent the following

- that the term $g^{(a)}_{sol}$ is due to the optical polarization, induced by the nuclear charge distribution, interacting with the solute electronic charge distribution.
- The corresponding polarization interaction due to the electronic charge distribution is given by the term $\tilde{g}^{(b)}_{sol}$. This operator describes the instantaneous coupling between the molecular state and the optical polarization state in the dielectric medium.
- The third term, $g^{(c)}_{sol}$, describes the interaction of the inertial polarization vector with the electronic charge distribution and the inertial polarization is due to the initial solute charge distribution $\langle T_{lm}\rangle = T^n_{lm} - \langle T^e_{lm}(\rho_i)\rangle$.

We find that the evolution of the electronic wave function of the molecular system is determined by the following Ehrenfest equation

$$\frac{d}{dt}\langle\tilde{0}|\tilde{\mathbf{O}}^\dagger|\tilde{0}\rangle = \langle\tilde{0}|\frac{d}{dt}\tilde{\mathbf{O}}^\dagger|\tilde{0}\rangle - i\langle\tilde{0}|[\tilde{\mathbf{O}}^\dagger, H_0 + V(t) + \tilde{W}_{sol}]|\tilde{0}\rangle \tag{22}$$

We focus on the electronic part of $\tilde{W}_{sol}$ since the first two terms of $\tilde{W}_{sol}$ do not contribute to Eq.(22)

$$\tilde{W} = \left\{g^{(a)}_{sol} + g^{(c)}_{sol}\right\} + \tilde{g}^{(b)}_{sol} = g^{(a+c)}_{sol} + \sum_{lm} A^{lm}\langle\tilde{0}|B^{lm}|\tilde{0}\rangle \tag{23}$$

with $A^{lm} = 2g_l(\epsilon_{op})T^e_{lm}$ and $B^{lm} = T^e_{lm}$. For the limit $t \to -\infty$, $\tilde{W}$ reduces to:

$$W = g^{(a+c)}_{sol} + \sum_{lm} A^{lm}\langle 0|B^{lm}|0\rangle \tag{24}$$

Thereby, we have the following expression for the Ehrenfest equation (Eq.(22))

$$\begin{aligned}\frac{d}{dt}\langle\tilde{0}|\tilde{\mathbf{O}}^\dagger|\tilde{0}\rangle = {} & \langle\tilde{0}|\frac{d}{dt}\tilde{\mathbf{O}}^\dagger|\tilde{0}\rangle - i\langle\tilde{0}|[\tilde{\mathbf{O}}^\dagger, H_0 + V(t)]|\tilde{0}\rangle \\ & - i\langle\tilde{0}|[\tilde{\mathbf{O}}^\dagger, g^{(a+c)}_{sol}]|\tilde{0}\rangle - i\sum_{lm}\langle\tilde{0}|[\tilde{\mathbf{O}}^\dagger, A^{lm}]|\tilde{0}\rangle\langle\tilde{0}|B^{lm}|\tilde{0}\rangle\end{aligned} \tag{25}$$

where the vacuum part of Eq. (25) has been derived for all but the solvent contribution by Olsen et al. [64] and the matrix representation of the solvent modifications to the response equations is found by expanding the last two terms. We have that the solvent contributions have the following structure

$$\langle\tilde{0}|[\tilde{\mathbf{O}}^\dagger, A\langle\tilde{0}|B|\tilde{0}\rangle]|\tilde{0}\rangle = \langle\tilde{0}|[\tilde{\mathbf{O}}^\dagger, A]|\tilde{0}\rangle\langle\tilde{0}|B|\tilde{0}\rangle, \tag{26}$$

where A and B are time-independent operators. Expanding $\langle\tilde{0}|B|\tilde{0}\rangle$ as a normal expectation value, we find that the matrix representation of Eq.(25) becomes:

$$\sum_{n=1}^{\infty}(i)^n S^{[n+1]}_{j,l_1,l_2,\ldots l_n}\dot{\alpha}_{l_1}(t)\prod_{\mu=2}^{n}\alpha_{l_\mu}(t) =$$

$$
\begin{aligned}
&-\sum_{n=0}^{\infty}(i)^{n+1}\left\{E^{[n+1]}_{j,l_1,l_2,\ldots l_n}+V^{t[n+1]}_{j,l_1,l_2,\ldots l_n}\right\}\prod_{\mu=1}^{n}\alpha_{l_\mu}(t)\\
&-\sum_{n=0}^{\infty}(i)^{n+1}\left\{C^{[n+1]}_{j,l_1,l_2,\ldots l_n}+\sum_{k=0}^{n}\sum_{lm}A^{lm[n-k+1]}_{j,l_{(k+1)}\ldots l_n}B^{lm[k]}_{l_1,l_2,\ldots l_k}\right\}\prod_{\mu=1}^{n}\alpha_{l_\mu}(t)
\end{aligned}
\tag{27}
$$

where we utilize the definitions of $S^{[n+1]}_{j,l_1,l_2,\ldots l_n}$ and $V^{t[n+1]}_{j,l_1,l_2,\ldots l_n}$ from Ref. [64]. Furthermore, we have

$$
B^{lm[n]}_{l_1 l_2\ldots l_n}=\sum_{k=0}^{n}\frac{(-1)^n}{k!(n-k)!}\langle 0|\prod_{\mu=1}^{k}\hat{O}_{cl_\mu}\prod_{\mu=k+1}^{n}\hat{O}_{ol_\mu}B^{lm}|0\rangle,
\tag{28}
$$

and

$$
\begin{aligned}
X^{[n+1]}_{j,l_1,l_2,\ldots l_n}=&\\
&+\sum_{k=0}^{n}\frac{(-1)^n}{k!(n-k)!}(\langle 0|[O^{\dagger}_{cj},\prod_{\mu=1}^{k}\hat{O}_{cl_\mu}\prod_{\mu=k+1}^{n}\hat{O}_{ol_\mu}X]|0\rangle\\
&+\langle 0|\prod_{\mu=1}^{k}\hat{O}_{cl_\mu}[O^{\dagger}_{oj},\prod_{\mu=k+1}^{n}\hat{O}_{ol_\mu}X]|0\rangle),
\end{aligned}
\tag{29}
$$

where X is to be replace by either of

$$
\begin{aligned}
H_0 &\rightarrow E^{[n+1]}_{j,l_1,l_2,\ldots l_n}\\
g^{(a+c)}_{sol} &\rightarrow C^{[n+1]}_{j,l_1,l_2,\ldots l_n}\\
A^{lm} &\rightarrow A^{lm[n+1]}_{j,l_1,l_2,\ldots l_n}.
\end{aligned}
\tag{30}
$$

4. The quadratic solvent response functions

We obtain the terms for the solvent modifications of the quadratic response functions, denoted $W^{[3]}_{jkl}$, by collecting all terms for $n=2$ in Eq. (27)

$$
\begin{aligned}
&W^{[3]}_{jl_1l_2}\alpha_{l_1}\alpha_{l_2}=iC^{[3]}_{j,l_1l_2}\alpha_{l_1}\alpha_{l_2}+\\
&i\sum_{lm}\left\{B^{lm[2]}_{l_1l_2}A^{lm[1]}_{j}+B^{lm[1]}_{l_1}A^{lm[2]}_{j,l_1}+B^{lm[0]}A^{lm[3]}_{j,l_1l_2}\right\}\alpha_{l_1}\alpha_{l_2}.
\end{aligned}
\tag{31}
$$

In order to achieve efficient and compact expressions we define the following solvent operators

$$
T=2\sum_{lm}g_l(\epsilon_{op})\langle 0|T^e_{lm}|0\rangle T^e_{lm}
\tag{32}
$$

$$
W=T-2\sum_{lm}\left\{g_l(\epsilon_{op})T^n_{lm}+g_l(\epsilon_{st},\epsilon_{op})\langle T(\rho_i)\rangle\right\}T^e_{lm}
\tag{33}
$$

$$A^1 = \sum_{lm} g_l(\epsilon_{op}) \left\{ \langle 0|T^e_{lm}({}^1\kappa)|0\rangle + \langle 0^{1L}|T^e_{lm}|0\rangle + \langle 0|T^e_{lm}|0^{1R}\rangle \right\} T^e_{lm} \tag{34}$$

$$\begin{aligned} A^{12} = \sum_{lm} & g_l(\epsilon_{op})(\langle 0|T^e_{lm}({}^1\kappa,\, {}^2\kappa)|0\rangle + 2(\langle 0^{1L}|T^e_{lm}({}^2\kappa)|0\rangle + \langle 0|T^e_{lm}({}^2\kappa)|0^{1R}\rangle) \\ & +(\langle 0^{1L}|T^e_{lm}|0^{2R}\rangle + \langle 0^{2L}|T^e_{lm}|0^{1R}\rangle))T^e_{lm} \end{aligned} \tag{35}$$

and finally, the solvent contributions to the response equations can be written as

$$\begin{aligned} & W^{[3]}_{j(kl)} N^1_k N^2_l = \\ & \frac{1}{2}P(1,2) \begin{pmatrix} \langle 0|[q_j, W({}^1\kappa,\, {}^2\kappa) + 2A^{12} + 4A^1({}^2\kappa)]|0\rangle \\ \langle j|W({}^1\kappa,\, {}^2\kappa) + 2A^{12} + 4A^1({}^2\kappa)|0\rangle \\ \langle 0|[q^\dagger_j, W({}^1\kappa,\, {}^2\kappa) + 2A^{12} + 4A^1({}^2\kappa)]|0\rangle \\ -\langle 0|W({}^1\kappa,\, {}^2\kappa) + 2A^{12} + 4A^1({}^2\kappa)|j\rangle \end{pmatrix} \\ & + \; P(1,2) \begin{pmatrix} \langle 0|[q_j, W({}^2\kappa) + 2A^2]|0^{1R}\rangle + \langle 0^{1L}|[q_j, W({}^2\kappa) + 2A^2]|0\rangle \\ \langle j|W({}^2\kappa) + 2A^2|0^{1R}\rangle \\ \langle 0|[q^\dagger_j, W({}^2\kappa) + 2A^2]|0^{1R}\rangle + \langle 0^{1L}|[q^\dagger_j, W({}^2\kappa) + 2A^2]|0\rangle \\ -\langle 0^{1L}|W({}^2\kappa) + 2A^2|j\rangle \end{pmatrix} \\ & + \; \frac{1}{2}P(1,2) \begin{pmatrix} \langle 0^{1L}|[q_j, W]|0^{2R}\rangle + \langle 0^{2L}|[q_j, W]|0^{1R}\rangle \\ 0 \\ \langle 0^{1L}|[q^\dagger_j, W]|0^{2R}\rangle + \langle 0^{2L}|[q^\dagger_j, W]|0^{1R}\rangle \\ 0 \end{pmatrix} \\ & + \; 2P(1,2)\langle 0|A^2|0\rangle \begin{pmatrix} 0 \\ {}^1S_j \\ 0 \\ {}^1S^{'}_j \end{pmatrix} \\ & + \; P(1,2)\, {}^1S_n\, {}^2S^{'}_n \begin{pmatrix} \langle 0|[q_j, T]|0\rangle \\ \langle j|T|0\rangle \\ \langle 0|[q^\dagger_j, T]|0\rangle \\ -\langle 0|T|j\rangle \end{pmatrix}. \end{aligned} \tag{36}$$

5. The cubic solvent response functions

We obtain the contributions to the cubic response functions arising from the interactions between the solvent and the solute. The solvent modifications to the cubic response theory are obtained by adding the third order solvent contributions to the corresponding vacuum equations and we have from Eq. (27)

$$O^3(-i\langle\tilde{0}|[\tilde{\mathbf{O}}^\dagger, \tilde{W}]|\tilde{0}\rangle) = iG^{[4]}_{j,h_1h_2h_3}\alpha_{h_1}\alpha_{h_2}\alpha_{h_3} + \tag{37}$$

$$i\sum_{lm}\left\{D^{lm[3]}_{h_1h_2h_3}C^{lm[1]}_{j}+D^{lm[2]}_{h_1h_2}C^{lm[2]}_{j,h_2}+D^{lm[1]}_{h_1}C^{lm[3]}_{j,h_1h_2}+D^{lm[0]}C^{lm[4]}_{j,h_1h_2h_3}\right\}\alpha_{h_1}\alpha_{h_2}\alpha_{h_3}.$$

Compact and efficient expressions are obtained by constructing the following effective solvent operators:

$$A=\sum_{lm}C^{lm}\langle 0|D^{lm}|0\rangle=2\sum_{lm}g_l(\epsilon_{op})\langle 0|T^e_{lm}|0\rangle T^e_{lm}, \tag{38}$$

$$W=A+g^{(a+c)}_{sol}=A-2\sum_{lm}\left\{g_l(\epsilon_{op})T^n_{lm}+g_l(\epsilon_{st},\epsilon_{op})\langle T(\rho_i)\rangle\right\}T^e_{lm}, \tag{39}$$

$$A^1=2\sum_{lm}g_l(\epsilon_{op})\left\{\langle 0|T^e_{lm}({}^1\kappa)|0\rangle+\langle 0^{1L}|T^e_{lm}|0\rangle+\langle 0|T^e_{lm}|0^{1R}\rangle\right\}T^e_{lm}, \tag{40}$$

$$B^1=-\frac{2}{3}\sum_{lm}g_l(\epsilon_{op})\left\{\langle 0|T^e_{lm}|0^{1R}\rangle+\langle 0^{1L}|T^e_{lm}|0\rangle\right\}T^e_{lm}, \tag{41}$$

$$\begin{aligned}A^{12}=&\sum_{lm}g_l(\epsilon_{op})(\langle 0|T^e_{lm}({}^1\kappa,\,{}^2\kappa)|0\rangle+2(\langle 0^{1L}|T^e_{lm}({}^2\kappa)|0\rangle+\langle 0|T^e_{lm}({}^2\kappa)|0^{1R}\rangle),\\&+(\langle 0^{1L}|T^e_{lm}|0^{2R}\rangle+\langle 0^{2L}|T^e_{lm}|0^{1R}\rangle))T^e_{lm},\end{aligned} \tag{42}$$

$$\begin{aligned}A^{123}=&\sum_{lm}g_l(\epsilon_{op})(\frac{1}{3}\langle 0|T^e_{lm}({}^1\kappa,\,{}^2\kappa,\,{}^3\kappa)|0\rangle+(\langle 0^{1L}|T^e_{lm}({}^2\kappa,\,{}^3\kappa))|0\rangle+\langle 0|T^e_{lm}({}^2\kappa,\,{}^3\kappa))|0^{1R}\rangle),\\&+(\langle 0^{1L}|T^e_{lm}({}^3\kappa)|0^{2R}\rangle+\langle 0^{2L}|T^e_{lm}({}^3\kappa)|0^{1R}\rangle))T^e_{lm}.\end{aligned} \tag{43}$$

$$\tag{44}$$

In Eq. (38)–Eq. (44) we have utilized the following transformed states

$$\begin{aligned}|0^R\rangle&=-\sum_n S_n|n\rangle\\\langle 0^L|&=\sum_n S^*_n\langle n|,\end{aligned} \tag{45}$$

and index transformed solvent integrals

$$\begin{aligned}Y({}^1\kappa)&=[{}^1\kappa(t),Y]\\Y({}^1\kappa,\,{}^2\kappa)&=[{}^2\kappa(t),[{}^1\kappa(t),Y]]\\Y({}^1\kappa,\,{}^2\kappa,\,{}^3\kappa)&=[{}^3\kappa(t),[{}^2\kappa(t),[{}^1\kappa(t),Y]]]\end{aligned} \tag{46}$$

Thereby, we are able to write the solvent modifications to, $E^{[4]}N^1N^2N^3$, the cubic solvent response equations as

$$-W^{[4]}_{j(klm)}N^1_kN^2_lN^3_m=P(1,2,3)(\tag{47}$$

$$
+\left(\frac{1}{2}\langle 0^{2L}|W|0^{3R}\rangle+\frac{2}{3}\langle 0|W+\frac{3}{2}A|0\rangle\,{}^2S_n\,{}^3S_n^{'}\right)\begin{pmatrix} O \\ {}^1S_j \\ 0 \\ {}^1S_j^{'}\end{pmatrix}
$$

$$
+\ {}^2S_n\,{}^3S_n^{'}\begin{pmatrix} \frac{2}{3}(\langle 0^{1L}|[q_j,W+\frac{3}{2}A]|0\rangle+\langle 0|[q_j,W+\frac{3}{2}A]|0^{1R}\rangle) \\ \frac{1}{6}\langle j|W+\frac{3}{2}A|0^{1R}\rangle \\ \frac{2}{3}(\langle 0^{1L}|[q_j^{\dagger},W+\frac{3}{2}A]|0\rangle+\langle 0|[q_j^{\dagger},W+\frac{3}{2}A]|0^{1R}\rangle) \\ -\frac{1}{6}\langle 0^{1L}|W+\frac{3}{2}A|j\rangle\end{pmatrix}
$$

$$
+\frac{1}{2}\begin{pmatrix} \langle 0^{1L}|[q_j,W({}^3\kappa)+A^3]|0^{2R}\rangle+\langle 0^{2L}|[q_j,W({}^3\kappa)+A^3]|0^{1R}\rangle \\ 0 \\ \langle 0^{1L}|[q_j^{\dagger},W({}^3\kappa)+A^3]|0^{2R}\rangle+\langle 0^{2L}|[q_j^{\dagger},W({}^3\kappa)+A^3]|0^{1R}\rangle \\ 0\end{pmatrix}
$$

$$
+\begin{pmatrix} 0 \\ (\frac{1}{2}\langle 0^{2L}|W({}^3\kappa)+A^3|0\rangle+\langle 0|W({}^3\kappa)+A^3|0^{2R}\rangle)\,{}^1S_j \\ 0 \\ (\langle 0^{2L}|W({}^3\kappa)+A^3|0\rangle+\frac{1}{2}\langle 0|W({}^3\kappa)+A^3|0^{2R}\rangle)\,{}^1S_j^{'}\end{pmatrix}
$$

$$
+\ {}^1S_n\,{}^2S_n^{'}\begin{pmatrix} \langle 0|[q_j,W({}^3\kappa)+A({}^3\kappa)+2A^3+B^3]|0\rangle \\ \frac{1}{2}\langle j|W({}^3\kappa)+A({}^3\kappa)+2A^3+B^3|0\rangle \\ \langle 0|[q_j^{\dagger},W({}^3\kappa)+A({}^3\kappa)+2A^3+B^3]|0\rangle \\ -\frac{1}{2}\langle 0|W({}^3\kappa)+A({}^3\kappa)+2A^3+B^3|j\rangle\end{pmatrix}
$$

$$
+\frac{1}{2}\begin{pmatrix} \langle 0^{1L}|[q_j,W({}^2\kappa,\,{}^3\kappa)+2A^{23}+2A^2({}^3\kappa)]|0\rangle+\langle 0|[q_j,W({}^2\kappa,\,{}^3\kappa)+2A^{23}+2A^2({}^3\kappa)]|0^{1R}\rangle) \\ \langle j|W({}^2\kappa,\,{}^3\kappa)+2A^{23}+2A^2({}^3\kappa)|0^{1R}\rangle \\ \langle 0^{1L}|[q_j^{\dagger},W({}^2\kappa,\,{}^3\kappa)+2A^{23}+2A^2({}^3\kappa)]|0\rangle+\langle 0|[q_j^{\dagger},W({}^2\kappa,\,{}^3\kappa)+2A^{23}+2A^2({}^3\kappa)]|0^{1R}\rangle) \\ -\langle 0^{1L}|W({}^2\kappa,\,{}^3\kappa)+2A^{23}+2A^2({}^3\kappa)|j\rangle\end{pmatrix}
$$

$$
+\frac{1}{2}\langle 0|W({}^2\kappa,\,{}^3\kappa)+2A^{23}+2A^2({}^3\kappa)|0\rangle\begin{pmatrix} 0 \\ {}^1S_j \\ 0 \\ {}^1S_j^{'}\end{pmatrix}
$$

$$
+\frac{1}{6}\begin{pmatrix} \langle 0|[q_j,W({}^1\kappa,\,{}^2\kappa,\,{}^3\kappa)+6A^{123}+6A^{12}({}^3\kappa)+3A^1({}^2\kappa,\,{}^3\kappa)]|0\rangle \\ \langle j|W({}^1\kappa,\,{}^2\kappa,\,{}^3\kappa)+6A^{123}+6A^{12}({}^3\kappa)+3A^1({}^2\kappa,\,{}^3\kappa)|0\rangle \\ \langle 0|[q_j^{\dagger},W({}^1\kappa,\,{}^2\kappa,\,{}^3\kappa)+6A^{123}+6A^{12}({}^3\kappa)+3A^1({}^2\kappa,\,{}^3\kappa)]|0\rangle \\ -\langle 0|W({}^1\kappa,\,{}^2\kappa,\,{}^3\kappa)+6A^{123}+6A^{12}({}^3\kappa)+3A^1({}^2\kappa,\,{}^3\kappa)|j\rangle\end{pmatrix}
$$

$$
+\frac{3}{4}\,{}^2S_n\,{}^3S_n^{'}\begin{pmatrix} 0 \\ \langle j|A|0^{1R}\rangle \\ 0 \\ -\langle 0^{1L}|A|j\rangle\end{pmatrix}
$$

$$+\frac{1}{2}\,{}^2S_n\,{}^3S'_n \begin{pmatrix} 0 \\ \langle j|A({}^3\kappa)+A^3+B^3|0\rangle \\ 0 \\ -\langle 0|A({}^3\kappa)+A^3+B^3|j\rangle \end{pmatrix})$$

where $P(1,2,3)$ is the permutation operator.

6. Conclusion

Generally, we observe that the modifications to the response method when coupling a molecular system to a dielectric media are represented by constructing effective one-electron operators that represent the induced optical and inertial polarizations in the dielectric media.

Acknowledgments

K.V.M. thanks Statens Naturvidenskabelige Forskningsråd, Statens Tekniske Videnskabelige Forskningsråd, the Danish Center for Scientific Computing and the EU-network NANOQUANT for support.

References

[1] M.D. Newton, *J Phys Chem* **79** (1975), 2795.
[2] J.O. Noell and K. Morokuma, *Chem Phys Lett* **36** (1975), 465.
[3] D.L. Beveridge and G.W. Schnuelle, *J Phys Chem* **79** (1975), 2562.
[4] J.Hylton, R.E. Christoffersen and G.G. Hall, *Chem Phys Lett* **24** (1974), 501.
[5] R. Contreras and A. Aizman, *Int J Quant Chem* **27** (1985), 193.
[6] H. Hoshi, M. Sakurai, Y. Inone and R. Chujo, *J Chem Phys* **87** (1987), 1107.
[7] O. Tapia, *Molecular Interactions*, by H. Ratajczak and W.J. Orville-Thomas, Wiley, New York, 1980.
[8] A. Warshel, *Chem Phys Lett* **55** (1978), 454.
[9] E. Sanchez-Marcos, B. Terryn and J.L Rivail, *J Phys Chem* **87** (1985), 4695.
[10] D. Rinaldi, *Comput Chem* **6** (1982), 155.
[11] O. Tapia, *Quantum Theory of Chemical Reactions*, by R. Daudel, A. Pullman, L. Salem and A. Veillard, (vol. 3), 25, Wiley, Dordrecht, 1980.
[12] G. Karlström, *J Phys Chem* **93** (1989), 4952.
[13] M. Karelson and M. Zerner, *J Am Chem Soc* **112** (1990), 9405.
[14] P.N. Day, J.H. Jensen, M.S. Gordon, S.P. Webb, W.J. Stevens, M. Krauss, D. Garmer, H. Basch and D. Cohen, *J Chem Phys* **105** (1996), 1968.
[15] W. Chen and M.S. Gordon, *J Chem Phys* **105** (1996), 11081.
[16] C.J. Cramer and D.G. Truhlar, *J Am Chem Soc* **113** (1991), 8305.
[17] C.J. Cramer and D.G. Truhlar, *Science* **256** (1992), 213.
[18] K.V. Mikkelsen, E. Dalgaard and P. Svanstøm, *J Phys Chem* **91** (1987), 3081.
[19] K.V. Mikkelsen, H. Ågren, H.J.Aa. Jensen and T. Helgaker, *J Chem Phys* **89** (1988), 3086.
[20] K.V. Mikkelsen, P. Jørgensen and H.J.Aa. Jensen, *J Chem Phys* **100** (1994), 6597–6607.
[21] K.V. Mikkelsen, Y. Luo, H. Ågren and P. Jørgensen, *J Chem Phys* **100** (1994), 8240.
[22] K.V. Mikkelsen, Y. Luo, H. Ågren and P. Jørgensen, *J Chem Phys* **102** (1995), 9362.
[23] K.V. Mikkelsen and K.O. Sylvester-Hvid, *J Phys Chem* **100** (1996), 9116.
[24] S. Di Bella, T.J. Marks and M.A. Ratner, *J Am Chem Soc* **116** (1994), 4440.
[25] J. Yu and M.C. Zerner, *J Chem Phys* **100** (1994), 7487.
[26] R. Cammi, M. Cossi, B. Mennucci and J. Tomasi, *J Chem Phys* **105** (1996), 10556.
[27] A. Willetts and J.E. Rice, *J Chem Phys* **99** (1993), 1993.
[28] R. Cammi, M. Cossi and J. Tomasi, *J Chem Phys* **104** (1996), 4611.

[29] M.W. Wong, M.J. Frisch and K.B. Wiberg, *J Am Chem Soc* **113** (1991), 4776.
[30] J.G. Angyan, *Chem Phys Lett* **241** (1995), 51.
[31] F.J. Olivares del Valle and J. Tomasi, *Chem Phys* **150** (1991), 139.
[32] C. Chipot, D. Rinaldi and J.L. Rivail, *Chem Phys Lett* **191** (1991), 287.
[33] C.J. Cramer and D.G. Truhlar, *Chem Rev* **99** (1999), 2161.
[34] J. Tomasi, R. Cammi and B. Mennucci, *Int J Quant Chem* **75** (1999), 783.
[35] O. Christiansen and K.V. Mikkelsen, *J Chem Phys* **110** (1999), 1365.
[36] D.M. Bishop, *Adv Quant Chem* **25** (1994), 1.
[37] D.P. Shelton and J.E. Rice, *Chem Rev* **94** (1994), 195.
[38] D.R. Kanis, M.A. Ratner and T.J. Marks, *Chem Rev* **94** (1994), 195.
[39] B.L. Hammond and J.E. Rice, *J Chem Phys* **97** (1992), 1138.
[40] S.P. Karna, G.B. Talapatra, W.M.K.P. Wijekoon and P.N. Prasad, *Phys Rev A* **45** (1992), 2763.
[41] H. Sekino and R.J. Bartlett, *J Chem Phys* **98** (1993), 3022.
[42] D. Jonsson, P. Norman, Y. Luo and H. Ågren, *J Chem Phys* **105** (1996), 581.
[43] D. Jonsson, P. Norman and H. Ågren, *J Chem Phys* **105** (1996), 6401.
[44] O. Christiansen and K.V. Mikkelsen, *J Chem Phys* **110** (1999), 8348.
[45] D. Jonsson, P. Norman, H. Ågren, Y. Luo, K.O. Sylvester-Hvid and K.V. Mikkelsen, *J Chem Phys* **109** (1998), 6351.
[46] K.O. Sylvester-Hvid, K.V. Mikkelsen, D. Jonsson, P. Norman and H. Ågren, *J Chem Phys* **109** (1998), 5576.
[47] K.O. Sylvester-Hvid, K.V. Mikkelsen, D. Jonsson, P. Norman and H. Ågren, *J Phys Chem A* **103** (1999), 8375.
[48] J. Kongsted, A. Osted, K.V. Mikkelsen, P.-O. Åstrand and O. Christiansen, *J Chem Phys* **121** (2004), 8435.
[49] K. Aidas, J. Kongsted, A. Osted, K.V. Mikkelsen and O. Christiansen, Accepted for publication in *J Phys Chem A* (2005).
[50] J. Kongsted, A. Osted, K.V. Mikkelsen and O. Christiansen, *J Phys Chem A* **107** (2003), 2578.
[51] J. Kongsted, A. Osted, K.V. Mikkelsen and O. Christiansen, *J Chem Phys* **118** (2003), 1620.
[52] J. Kongsted, A. Osted, K.V. Mikkelsen and O. Christiansen, *J Chem Phys* **119** (2003), 10519.
[53] J. Kongsted, A. Osted, K.V. Mikkelsen and O. Christiansen, *J Chem Phys* **120** (2004), 3787.
[54] J. Kongsted, A. Osted, K.V. Mikkelsen and O. Christiansen, *Mol Phys* **100** (2002), 1813.
[55] A. Osted, J. Kongsted, K.V. Mikkelsen and O. Christiansen, *J Phys Chem A* **108** (2004), 8646.
[56] A. Osted, J. Kongsted, K.V. Mikkelsen and O. Christiansen, *Mol Phys* **101** (2003), 2055.
[57] L. Jensen, P.Th. van Duijnen and J.G. Snijders, *J Chem Phys* **118** (2003), 514.
[58] L. Jensen, P. Th van Duijnen and J.G. Snijders, *J Chem Phys* **119** (2003), 3800.
[59] L. Jensen, M. Swart and P. Th. van Duijnen, *J Chem Phys* **122** (2005), 034103.
[60] L. Jensen and P. Th. van Duijnen, *Int J Quantum Chem* **102** (2005), 612.
[61] P. Th. van Duijnen, A.H. de Vries, M. Swart and F. Grozema, *J Chem Phys* **117** (2002), 8442.
[62] Y. Luo, H. Ågren, K.V. Mikkelsen and P. Jørgensen, *Adv Quant Chem* **26** (1995), 165.
[63] K.V. Mikkelsen, A. Cesar, H. Ågren and H.J. Aa Jensen, *J Chem Phys* **103** (1995), 9010–9023.
[64] J. Olsen and P. Jørgensen, *J Chem Phys* **82** (1985), 3235.
[65] P. Jørgensen, H.J.Aa. Jensen and J. Olsen, *J Chem Phys* **89** (1988), 3654.
[66] J. Olsen, H.J.Aa. Jensen and P. Jørgensen, *J Comput Phys* **74** (1988), 265.
[67] H. Hettema, H.J.Aa. Jensen, J. Olsen and P. Jørgensen, *J Chem Phys* **97** (1992), 1174.
[68] K.O. Sylvester-Hvid, K.V. Mikkelsen, D. Jonsson, P. Norman and H. Ågren, *J Chem Phys* **109** (1998), 5576–5584.

Journal of Computational Methods in Sciences and Engineering 10 (2010) 487–498
DOI 10.3233/JCM-2010-0338
IOS Press

Paradoxes of measures of quantum entanglement and Bell's inequality violation in two-qubit systems

Adam Miranowicz, Bohdan Horst and Andrzej Koper
Faculty of Physics, Adam Mickiewicz University, 61-614 Poznań, Poland

Abstract. We review some counterintuitive properties of standard measures describing quantum entanglement and violation of Bell's inequality (often referred to as "nonlocality") in two-qubit systems. By comparing the nonlocality, negativity, concurrence, and relative entropy of entanglement, we show: (i) ambiguity in ordering states with the entanglement measures, (ii) ambiguity of robustness of entanglement in lossy systems and (iii) existence of two-qubit mixed states more entangled than pure states having the same negativity or nonlocality. To support our conclusions, we performed a Monte Carlo simulation of 10^6 two-qubit states and calculated all the entanglement measures for them. Our demonstration of the relativity of entanglement measures implies also how desirable is to properly use an operationally-defined entanglement measure rather than to apply formally-defined standard measures. In fact, the problem of estimating the degree of entanglement of a bipartite system cannot be analyzed separately from the measurement process that changes the system and from the intended application of the generated entanglement.

1. Introduction

Quantum entanglement [1,2], being at heart of Bell's theorem [3], is considered to be an essential resource for quantum engineering, quantum communication, quantum computation, and quantum information [4]. There were proposed various entanglement measures and criteria to detect entanglement. Nevertheless, despite the impressive progress in understanding this phenomenon (see a recent comprehensive review by Horodecki et al. [5] and references therein), a complete theory of quantum entanglement has not been developed yet.

It is a commonly accepted fact that the entropy of entanglement of two systems, which is defined to be the von Neumann entropy of one of the systems, is the unique entanglement measure for bipartite systems in a pure state [6]. However, in the case of two systems in a mixed state, there is no unique entanglement measure. In order to describe properties of quantum entanglement of bipartite systems various measures have been proposed. Examples include [5]: entanglement of formation, distillable entanglement, entanglement cost, PPT entanglement cost, relative entropy of entanglement, or geometrical measures of entanglement.

It should be stressed that classification of entanglement measures of mixed states and effective methods of calculation of such measures are among the most important but still underdeveloped (with a few exceptions) problems of quantum information [7].

Here, we shortly review counterintuitive properties of some entanglement measures in the simplest non-trivial case of entanglement of two qubits.

2. Measures of quantum entanglement

We will study quantum entanglement and closely related violation of Bell's inequality for two qubits in mixed states according to some standard measures:

(i) To describe the entanglement of formation [8] of a given two-qubit state $\hat{\rho}$, we apply the Wootters concurrence [9] defined as

$$C(\hat{\rho}) = \max\left(0, 2\max_i \lambda_i - \sum_i \lambda_i\right) \tag{1}$$

in terms of λ_i's, which are the square roots of the eigenvalues of $\hat{\rho}(\hat{\sigma}_2 \otimes \hat{\sigma}_2)\hat{\rho}^*(\hat{\sigma}_2 \otimes \hat{\sigma}_2)$, where σ_2 is the Pauli spin matrix and asterisk stands for complex conjugation. The concurrence $C(\hat{\rho})$ is related to the entanglement of formation, $E_F(\hat{\rho})$, as follows [9]:

$$E_F(\hat{\rho}) = \mathcal{W}[C(\hat{\rho})], \quad \text{where} \quad \mathcal{W}(x) \equiv h\left(\frac{1}{2}[1+\sqrt{1-x^2}]\right), \tag{2}$$

and $h(y) = -y\lg y - (1-y)\lg(1-y)$ is binary entropy.

(ii) The PPT entanglement cost, which is the entanglement cost [5] under operations preserving positivity of the partial transposition (PPT), can be given as [10,11]:

$$E_{\rm PPT}(\hat{\rho}) = \lg[N(\hat{\rho})+1] \tag{3}$$

in terms of the negativity:

$$N(\hat{\rho}) = 2\sum_j \max(0, -\mu_j). \tag{4}$$

These measures are related to the Peres-Horodecki criterion [12,13]. In Eq. (4), μ_j are the eigenvalues of the partial transpose $\hat{\rho}^\Gamma$.

(iii) The relative entropy of entanglement (REE) [14,15] is a measure of entanglement corresponding to a "distance" of an entangled state from separable states. Precisely, the REE can be defined as the minimum of the relative quantum entropy

$$S(\hat{\rho}||\hat{\rho}_{\rm sep}) = {\rm Tr}\,(\hat{\rho}\lg\hat{\rho} - \hat{\rho}\lg\hat{\rho}_{\rm sep}) \tag{5}$$

in the set $\mathcal{D}$ of all separable states $\hat{\rho}_{\rm sep}$, i.e.,

$$E_R(\hat{\rho}) = \min_{\hat{\rho}_{\rm sep}\in\mathcal{D}} S(\hat{\rho}||\hat{\rho}_{\rm sep}) \equiv S(\hat{\rho}||\hat{\rho}_{\rm css}), \tag{6}$$

where $\hat{\rho}_{\rm css}$ denotes the closest separable state (CSS) to $\hat{\rho}$. Numerical problems to calculate the REE are shortly discussed in Appendix A.

(iv) To describe a degree of violation of Bell's inequality [3] due to Clauser, Horne, Shimony and Holt (CHSH) [16], we use the modified Horodecki measure [17,19]:

$$B(\hat{\rho}) \equiv \sqrt{\max\left[0, \max_{j<k}\,(u_j+u_k) - 1\right]}, \tag{7}$$

which is given in terms of the eigenvalues u_j $(j=1,2,3)$ of $U_{\hat{\rho}} = T_{\hat{\rho}}^T T_{\hat{\rho}}$, where $T_{\hat{\rho}}$ is a real matrix with elements $t_{nm} = {\rm Tr}\,[\hat{\rho}\,(\hat{\sigma}_n \otimes \hat{\sigma}_m)]$, $T_{\hat{\rho}}^T$ is the transposition of $T_{\hat{\rho}}$ and $\hat{\sigma}_n$ $(n=1,2,3)$ are Pauli's spin matrices. For short, we refer to B as "nonlocality" (measure).

For any two-qubit pure state $|\psi\rangle$, the nonlocality B is equal to the entanglement measures C and N:

$$B(|\psi\rangle) = C(|\psi\rangle) = N(|\psi\rangle). \tag{8}$$

It is seen that for this case the measures B, C and N correspond to the relative entropy of entanglement E_R and von Neumann's entropy:

$$\mathcal{W}[B(|\psi\rangle)] = \mathcal{W}[C(|\psi\rangle)] = \mathcal{W}[N(|\psi\rangle)] = E_R(|\psi\rangle) = E_{\mathrm{Neumann}}(|\psi\rangle), \tag{9}$$

where $\mathcal{W}$ is given in Eq. (2).

In the following we describe somewhat surprising properties of the entanglement measures for two-qubits in *mixed* states. For brevity, by referring to the entanglement measures, we also mean the nonlocality B.

3. Ambiguity in ordering states with entanglement measures

Our problem can be posed as follows:

Problem 1. *Two measures of entanglement, say $\mathcal{E}'$ and $\mathcal{E}''$, imply the same ordering of states if the condition [18]*

$$\mathcal{E}'(\hat{\rho}_1) < \mathcal{E}'(\hat{\rho}_2) \Leftrightarrow \mathcal{E}''(\hat{\rho}_1) < \mathcal{E}''(\hat{\rho}_2) \tag{10}$$

is satisfied for arbitrary states $\hat{\rho}_1$ and $\hat{\rho}_2$. The question is whether this condition is fulfilled for all "good" entanglement measures.

In early fundamental works on quantum information, it is often claimed that good entanglement measures should fulfill this condition. For example, in Ref. [14] it was stated that: "For consistency, it is only important that if $\hat{\rho}_1$ is more entangled then $\hat{\rho}_2$ for one measure than it also must be for all other measures."

For qubits in pure states, condition (10) is always fulfilled, since all good measures are equivalent. However, standard measures can imply different ordering of mixed states even for only two qubits. This was first shown numerically by Eisert and Plenio [18] by analyzing their results of Monte Carlo simulations of two-qubit states. The problem was then analyzed by others [19–28].

To our knowledge, the first analytical examples of two-qubit states violating condition (10) were given in Refs. [19,23]. In Ref. [24], to find analytical examples of extreme violation of Eq. (10), we applied the results of Verstraete et al. [29] concerning allowed values of the negativity N for a given value of the concurrence C.

Note that the violation of condition (10) cannot be observed for pure states of two-qubit systems. By contrast, for three-level systems (the so-called qutrits), analytical examples of violation of the condition are known even for pure states [20–22].

The property that ordering of states depends on the applied entanglement measure sounds counter-intuitive. Nevertheless, it is physically sound since states, which are differently ordered according to two measures, cannot be transformed into each other with 100% efficiency by applying local quantum operations and classical communication (LOCC) only. Virmani and Plenio [21] proved in general terms that all good asymptotic entanglement measures are either identical or have to imply different ordering on some quantum states.

In Ref. [25], the three measures (the negativity, concurrence, and REE) were compared and found analytical examples of states (say $\hat{\rho}'$ and $\hat{\rho}''$) for which one measure implies state ordering opposite to that implied by the other two measures:

$$\begin{aligned} &C(\hat{\rho}') < C(\hat{\rho}''), \quad N(\hat{\rho}') < N(\hat{\rho}''), \quad E_R(\hat{\rho}') > E_R(\hat{\rho}''); \\ &C(\hat{\rho}') < C(\hat{\rho}''), \quad N(\hat{\rho}') > N(\hat{\rho}''), \quad E_R(\hat{\rho}') < E_R(\hat{\rho}''); \\ &C(\hat{\rho}') > C(\hat{\rho}''), \quad N(\hat{\rho}') < N(\hat{\rho}''), \quad E_R(\hat{\rho}') < E_R(\hat{\rho}''). \end{aligned} \tag{11}$$

There can be found other analytical examples of states exhibiting even more peculiar ordering of states according to these three measures. Examples include pairs of states for which a degree of entanglement is preserved according to one or two measures but it is different according to the other measures, e.g.:

$$\begin{aligned} &C(\hat{\rho}') = C(\hat{\rho}''), \quad N(\hat{\rho}') < N(\hat{\rho}''), \quad E_R(\hat{\rho}') > E_R(\hat{\rho}''); \\ &C(\hat{\rho}') < C(\hat{\rho}''), \quad N(\hat{\rho}') = N(\hat{\rho}''), \quad E_R(\hat{\rho}') > E_R(\hat{\rho}''); \\ &C(\hat{\rho}') < C(\hat{\rho}''), \quad N(\hat{\rho}') > N(\hat{\rho}''), \quad E_R(\hat{\rho}') = E_R(\hat{\rho}''). \end{aligned} \tag{12}$$

and

$$\begin{aligned} &C(\hat{\rho}') = C(\hat{\rho}''), \quad N(\hat{\rho}') = N(\hat{\rho}''), \quad E_R(\hat{\rho}') < E_R(\hat{\rho}''); \\ &C(\hat{\rho}') = C(\hat{\rho}''), \quad N(\hat{\rho}') < N(\hat{\rho}''), \quad E_R(\hat{\rho}') = E_R(\hat{\rho}''); \\ &C(\hat{\rho}') < C(\hat{\rho}''), \quad N(\hat{\rho}') = N(\hat{\rho}''), \quad E_R(\hat{\rho}') = E_R(\hat{\rho}''). \end{aligned} \tag{13}$$

The comparative analyses presented in Refs. [19,23–25] are not only related to a mathematical problem of classification of states according to various entanglement measures. They could also enable a deeper understanding of some physical aspects of entanglement.

3.1. Nonequivalent states with the same entanglement according to E_R, C and N

Problem 2. *Find analytical examples of *nonequivalent* two-qubit states $\hat{\rho}'$ and $\hat{\rho}''$ exhibiting the same entanglement of formation [$C(\hat{\rho}') = C(\hat{\rho}'')$], the same PPT entanglement cost [$N(\hat{\rho}') = N(\hat{\rho}'')$], and the same relative entropy of entanglement [$E_R(\hat{\rho}') = E_R(\hat{\rho}'')$]?*

As a first attempt to find such an example, let us compare two different pure states:

$$\begin{aligned} |\psi'\rangle &= c'_{00}|00\rangle + c'_{01}|01\rangle + c'_{10}|10\rangle + c'_{11}|11\rangle, \\ |\psi''\rangle &= c''_{00}|00\rangle + c''_{01}|01\rangle + c''_{10}|10\rangle + c''_{11}|11\rangle, \end{aligned} \tag{14}$$

fulfilling the condition

$$|c'_{00}c'_{11} - c'_{01}c'_{10}| = |c''_{00}c''_{11} - c''_{01}c''_{10}|, \tag{15}$$

which guarantees the same degree of entanglement according to the measures C, N and E_R. However, states $|\psi'\rangle$ and $|\psi''\rangle$ can be transformed into each other by local operations. Namely, by applying local rotations, $|\psi\rangle$ can be converted into ($p = p', p''$)

$$|\tilde{\psi}(p)\rangle = \sqrt{p}|01\rangle + \sqrt{1-p}|10\rangle \tag{16}$$

for which the negativity and concurrence are equal to $2\sqrt{p(1-p)}$. The same value is obtained also for $|\tilde{\psi}(1-p)\rangle$, but this state can be transformed into $|\tilde{\psi}(p)\rangle$ by applying the NOT gate to each of the qubits. This shows that pure states are *not* a good example of states satisfying the conditions specified in Problem 2.

As a second attempt, let us compare two Bell diagonal states described by $\hat{\rho}'_B$ and $\hat{\rho}''_B$ with the same maximum eigenvalue $\max_i \lambda_i > 1/2$. These states have the same entanglement according to the measures C, N and E_R. However, as shown in Ref. [25], states $\hat{\rho}'_B$ and $\hat{\rho}''_B$ exhibit different nonlocality, i.e., violate Bell's inequality to different degree. Specifically, the nonlocality B for a Bell diagonal state is given by [25]:

$$B(\hat{\rho}_B) = \sqrt{\max\{0, 2\max_{(i,j,k)}[(\lambda_i-\lambda_j)^2+(\lambda_k-\lambda_4)^2]-1\}}, \tag{17}$$

where subscripts (i,j,k) correspond to cyclic permutations of $(1,2,3)$. It is seen that the violation of Bell's inequality depends on all values of λ_i, while the entanglement measures E_R, C, and N depend only on the largest value $\max_i \lambda_i > 1/2$. Thus, states $\hat{\rho}'_B$ and $\hat{\rho}''_B$, fulfilling the conditions $\mathrm{eig}(\hat{\rho}'_B) \neq \mathrm{eig}(\hat{\rho}''_B)$ and $\max\{\mathrm{eig}(\hat{\rho}'_B)\} = \max\{\mathrm{eig}(\hat{\rho}''_B)\} > 1/2$, have the same entanglement measures: $E_R(\hat{\rho}'_B) = E_R(\hat{\rho}''_B)$, $C(\hat{\rho}'_B) = C(\hat{\rho}''_B)$ and $N(\hat{\rho}'_B) = N(\hat{\rho}''_B)$, but the states are not equivalent as they exhibit different nonlocality, $B(\hat{\rho}'_B) \neq B(\hat{\rho}''_B)$.

4. Ambiguity of robustness of entanglement

4.1. Maximally entangled pure states in lossy cavities

Let us analyze the following problem:

Problem 3. *Which maximally entangled pure states are the most fragile or robust to decoherence of two qubits in lossy cavities?*

This problem was addressed in Refs. [19,23] by analyzing decoherence of optical photon-number qubits stored initially in the following three maximally entangled (pure) states (MES):

$$|\Psi_1\rangle = \frac{1}{\sqrt{2}}(|01\rangle - |10\rangle), \quad |\Psi_2\rangle = \frac{1}{\sqrt{2}}(|00\rangle + |11\rangle), \tag{18}$$

$$|\Psi_3\rangle = \frac{1}{2}(|00\rangle + |01\rangle + |10\rangle - |11\rangle) \equiv \frac{1}{\sqrt{2}}(|0,+\rangle + |1,-\rangle), \tag{19}$$

where $|\pm\rangle = (|0\rangle \pm |1\rangle)/\sqrt{2}$. State $|\Psi_3\rangle$ can be obtained from $|\Psi_2\rangle$ by applying Hadamard's gate to the second qubit.

To address Problem 3, let us analyze two entangled qubits in a superposition of vacuum and single-photon states (so-called photon-number qubits) in a lossy cavity (or, equivalently, in two cavities). Then, one can apply the standard master-equation approach to describe the effect of radiative decay of cavities (i.e., zero-temperature reservoirs) on entanglement of two qubits according to the concurrence $C_k(t)$, negativity $N_k(t)$, and nonlocality $B_k(t)$ [19]. In Fig. 1, it is assumed that the qubits are initially in the

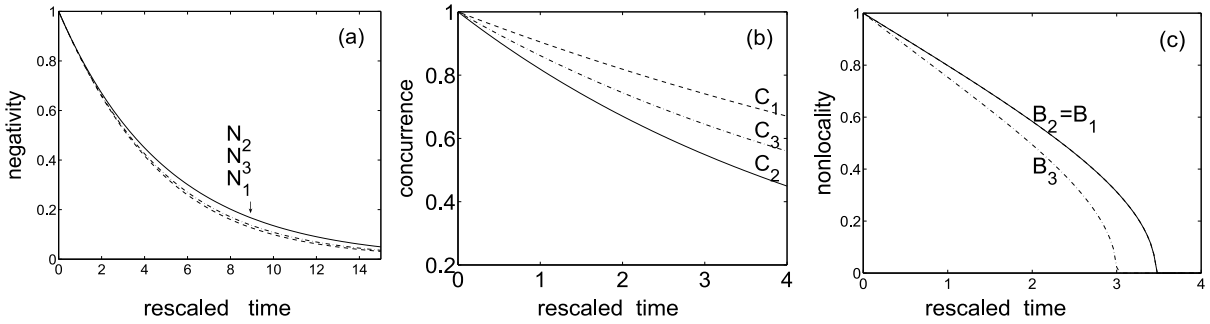

Fig. 1. Decay of entanglement between two qubits initially in the maximally entangled states $|\Psi_k\rangle$ (for k = 1,2,3) in lossy cavities with damping rates $\gamma = 0.1$ described by: (a) the negativity N, (b) the concurrence C, and (c) the nonlocality B. It is seen that there is no simple answer to the question which of the initial states $|\Psi_k\rangle$ is the most fragile (or robust) to decoherence. In the discussed model of dissipation, the fastest decoherence exhibits: $|\Psi_1\rangle$ according to N, $|\Psi_2\rangle$ according to C, and $|\Psi_3\rangle$ according to B.

MES $|\Psi_k\rangle$ for k = 1,2,3 and the cavity damping rate is $\gamma = 0.1$. By analyzing Fig. 1, one can conclude that entanglement decays in this model fulfill the inequalities:

$$\begin{aligned} N_2(t) &\geqslant N_3(t) \;\geqslant\; N_1(t), \\ B_1(t) = B_2(t) &\;\geqslant\; B_3(t), \\ C_1(t) &\geqslant C_3(t) \;\geqslant\; C_2(t). \end{aligned} \tag{20}$$

It is worth noting that due to the Markov approximation assumed in the derivation of the master equation, our conclusions are valid for evolution times t short in comparison to reservoir decay time γ^{-1}, and much longer than correlation time τ_c of reservoir(s), i.e., $\tau_c \ll t - t_0 \ll \gamma_j^{-1}$, where t_0 is the initial evolution time. Thus, in this specific dissipation model, the most fragile to dissipation is $|\Psi_1\rangle$ according to the negativity N, $|\Psi_2\rangle$ according to the concurrence C, and $|\Psi_3\rangle$ according to the nonlocality B. The results seem to be contradicting, but it should be remembered that measures C, N and B describe different aspects of mixed states even if for pure states they coincide $C = N = B$. Results of Refs. [19,23] clearly confirm the relativity of state ordering by C, N and B. This example of Ref. [19] was probably the first demonstration of this property in a real physical process.

4.2. Maximally entangled mixed states in lossy cavities

Here, we analyze decay of Werner's state, which can be defined for $p \in \langle 0, 1\rangle$ as [31]:

$$\hat{\rho}_1^{(p)}(0) = p|\Psi_1\rangle\langle\Psi_1| + \tfrac{1-p}{4}\,\hat{I}\otimes\hat{I}, \tag{21}$$

which is a mixture of the singlet state, $|\Psi_1\rangle$, and maximally mixed state, given by $\hat{I}\otimes\hat{I}$, where $\hat{I}$ is identity operator. Original Werner's state can be generalized for mixtures of other Bell states with $\hat{I}\otimes\hat{I}$. Thus, one can define Werner-type state as follows ($k = 2, 3$):

$$\hat{\rho}_k^{(p)}(0) = p|\Psi_k\rangle\langle\Psi_k| + \tfrac{1-p}{4}\,\hat{I}\otimes\hat{I}, \tag{22}$$

where $|\Psi_2\rangle$ and $|\Psi_3\rangle$ are given by Eqs (18) and (19), respectively.

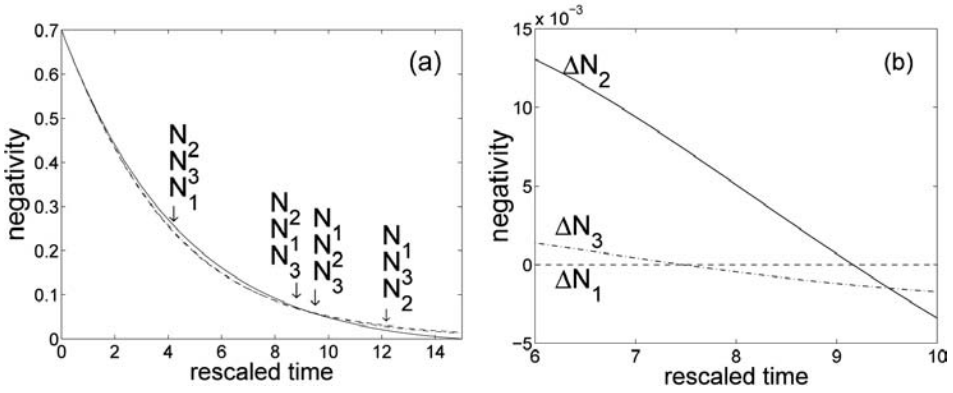

Fig. 2. Decay of entanglement of two photon-number qubits in a lossy cavity. Entanglement is measured by the negativity (a) N_k and (b) $\Delta N_k = N_k - N_1$ for qubits initially in Werner's states $\hat{\rho}_k^{(p)}(0)$ for $k = 1,2,3$ and $p = 0.8$. The cavities damping rate is $\gamma = 0.1$. For clarity, the scale of figure (b) is enlarged in comparison to figure (a).

Werner's states can be considered as *maximally entangled mixed states* (MEMS) of two qubits since the amount of entanglement of these states cannot be increased by any unitary transformation [32] and they are maximally entangled (according to the concurrence) for a given value of linear entropy [33].

Let us ask more specific question related to Problem 3:

Problem 4. *Which MEMS are the most robust to dissipation in the discussed model of lossy cavities?*

Even for such formulated question there is no simple answer. To show this we analyze the same model of decaying photon-number qubits in a lossy cavity (or cavities) as studied in Sect. 4.1, but for qubits initially in Werner's states $\hat{\rho}_k^{(p)}(0)$ for $k = 1,2,3$ and $p = 0.8$. Let us compare the decays of the negativity as shown in Fig. 2 and also described in detail in Table I in Ref. [19]. It is seen that a given Werner state can be more robust to decay than another Werner's state at short evolution times but, in turn, less robust at longer times. The differences between the negativity values for various states shown in Fig. 2 are not very large but still distinct.

5. Mixed states more entangled than pure states

Problem 5. *Can two-qubit *mixed* states be more entangled than *pure* states according to some entanglement measure $\mathcal{E}'$ at a fixed value of another entanglement measure $\mathcal{E}''$ assuming $\mathcal{E}'(\hat{\rho}) \leqslant \mathcal{E}''(\hat{\rho})$ for any state $\hat{\rho}$?*

It can be shown analytically that pure states are the upper bound for the negativity for a given value of the concurrence [29], as shown in Fig. 3(a), and the upper bound for the REE as a function of the concurrence [15], as presented in Fig. 3(b). Similar conclusions can be drawn for, e.g., the nonlocality for a given value of the concurrence [see Fig. 3(c)], and the nonlocality as a function of the negativity.

Thus, it is reasonable to conjecture that pure states are the upper bound also for the REE, e.g., for a given value of the negativity. But it was shown in Refs. [25,28] that this conjecture is wrong [see Fig. 3(e)]. This property can be demonstrated analytically on the example of, e.g., the Horodecki state [5] defined as a mixture of the maximally entangled state [e.g., the singlet state $|\Psi_1\rangle$] and a separable state

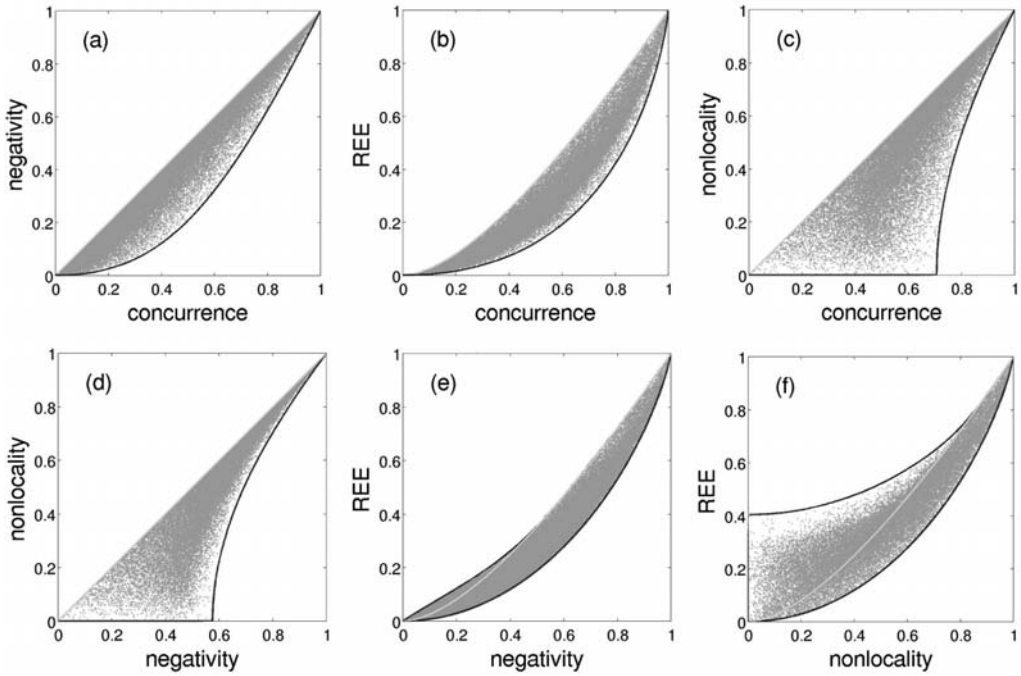

Fig. 3. (Color online) Entanglement and nonlocality measures for 10^6 two-qubit states $\hat{\rho}$ generated by a Monte Carlo simulation. Green curves correspond to pure states, and blue curves show the upper and lower bounds of a one measure $\mathcal{E}'(\hat{\rho})$ as a function of another $\mathcal{E}''(\hat{\rho})$. It is seen that pure states $|\psi\rangle$ lie for the whole range of abscissa at the upper bound of: (a) the negativity $N(\hat{\rho})$ for a given value of the concurrence $C(\hat{\rho})$ (b) the REE $E_R(\hat{\rho})$ vs $C(\hat{\rho})$, (c) the nonlocality $B(\hat{\rho})$ vs $C(\hat{\rho})$, and (d) $B(\hat{\rho})$ vs $N(\hat{\rho})$. However, for (e) $E_R(\hat{\rho})$ vs $N(\hat{\rho})$ and (e) $E_R(\hat{\rho})$ vs $B(\hat{\rho})$ pure states are at the upper bound for abscissa values close to one only. Thus, in the cases (e) and (f), the entanglement of mixed states can exceed that of pure states for abscissa values close to zero.

orthogonal to it (e.g., $|00\rangle$):

$$\hat{\rho}^{(H)} = p|\Psi_1\rangle\langle\Psi_1| + (1-p)|00\rangle\langle 00|, \tag{23}$$

where $p \in \langle 0, 1\rangle$. The negativity and REE for the Horodecki state are equal to

$$N(\hat{\rho}^{(H)}) = \sqrt{(1-p)^2 + p^2} - (1-p), \tag{24}$$

$$E_R(\hat{\rho}^{(H)}) \equiv E_R^{(H)}(N) = 2h(1-p/2) - h(p) - p, \tag{25}$$

respectively, where $p = \sqrt{2N(1+N)} - N$ and $h(x)$ is binary entropy. By comparing the REEs for Horodecki's state and for pure states, it can be shown that [25,28]:

$$E_R^{(H)}(N) > E_R^{(P)}(N) \quad \text{for } 0 < N < N_Y, \tag{26}$$

$$E_R^{(H)}(N) < E_R^{(P)}(N) \quad \text{for } N_Y < N < 1, \tag{27}$$

where $N_Y = 0.3770\cdots$ and $E_R^{(H)}(N_Y) = E_R^{(P)}(N_Y) = 0.2279\cdots$, which corresponds to point Y in Fig. 4. These inequalities were shown analytically by expending $E_R^{(H)}(N)$ and $E_R^{(P)}(N)$ in power series of $N = \epsilon$ ($N = 1 - \epsilon$) for values close to 0 (1). Moreover, mixed states corresponding to blue region

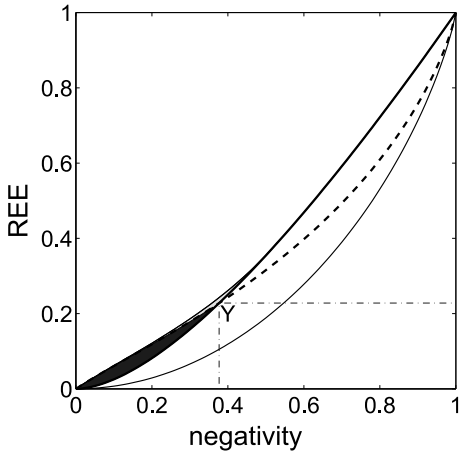

Fig. 4. (Color online) The relative entropy of entanglement (REE), $E_R(\hat{\rho})$, as a function of the negativity, $N(\hat{\rho})$, for pure states (thick solid curve), Horodecki states (dashed curve) and Bell diagonal states (thin solid curve). Blue and yellow regions correspond to mixed states with the REE higher than that for pure states for a given value the negativity. States in blue region are described in the text.

in Fig. 4, for which the inequality in Eq. (26) holds, can be obtained by mixing the Horodecki state $\hat{\rho}_H$ with a separable state $\hat{\rho}_{\rm css}^{(H)}$ closest to $\hat{\rho}_H$ [25]:

$$\hat{\rho}^{(H')}(p,N) = (1-x)\hat{\rho}^{(H)} + x\hat{\rho}_{\rm css}^{(H)}, \tag{28}$$

where $N \in \langle 0,1\rangle$, $p \in \langle\sqrt{2N(1+N)} - N, 1\rangle$ and $x = [(N+p)^2 - 2N(1+N)]/[p^2(1+N)]$. The closest separable state $\hat{\rho}_{\rm css}^{(H)}$ is given by ($q = p/2$):

$$\hat{\rho}_{\rm css}^{(H)}(p) = q(1-q)\sum_{j,k=0}^{1}(-1)^{j-k}|j,1-j\rangle\langle k,1-k| + (1-q)^2|00\rangle\langle 00| + q^2|11\rangle\langle 11|. \tag{29}$$

By applying Vedral-Plenio's theorem [15], the REE can be found as follows [25]:

$$E_R(\hat{\rho}^{(H')}) \equiv E_R^{(H')}(p,N) = q^2 x\lg x + 2qy_1\lg\left(\frac{y_1}{1-q}\right) + y_2\lg\left(\frac{y_2}{(1-q)^2}\right), \tag{30}$$

where $y_1 = 1 - qx$ and $y_2 = 1 - 2q + q^2x$. With this choice of x, parameter N is just the negativity of $\hat{\rho}^{(H')}(p,N)$. States corresponding to blue region in Fig. 4 can be obtained as special cases of state $\hat{\rho}^{(H')}(p,N)$ for N in the range $0 < N < N_Y$ and proper values of p. Thus, it is seen that there are mixed states for which the REE is greater than that for pure states at least in the range $N \in (0, N_Y)$. Later, in Ref. [28], it was shown that the generalized Horodecki states exhibit this property in slightly larger range as shown by yellow region in Fig. 4. There is some evidence [28] that the upper bound of the REE as a function of the negativity is likely to be given by these states.

Recently, we also analytically demonstrated [30] that the entanglement REE for a given nonlocality for mixed states exceeds that for pure states [see Fig. 3(f)]. Moreover, this effect occurs in the larger range of abscissa values in comparison to the dependence of the REE on the negativity, as seen by comparing Figs 3(e) and 3(f).

6. Conclusion

In this short review, we presented a few intriguing properties of some standard entanglement measures for two qubits. Our examples include a comparison of the negativity corresponding to the Peres-Horodecki criterion [12,13], the Wootters concurrence [9], and the relative entropy of entanglement of Vedral et al. [14]. Moreover, the predictions of these measures were also compared with the Horodecki measure [17] of the violation of Bell's inequality, referred here to as "nonlocality".

We discussed the following three counterintuitive properties of entanglement measures: (i) entangled states *cannot* be ordered uniquely with the entanglement measures, which also implies that (ii) fragility or robustness of entanglement of dissipative systems *cannot* be uniquely classified by entanglement measures, and (iii) there are two-qubit mixed states, which are more entangled (according to the REE) than pure states for a given negativity or nonlocality.

It is well known that there is no unique entanglement measure for mixed states. But the relativity of entanglement measures and its implications are more counterintuitive. Our demonstration might indicate that operational approaches to the quantum entanglement problem are more meaningful rather than standard approaches based on formally-defined measures. We find the problem of defining operational entanglement measures analogous to operational approaches to the quantum phase problem [1] posed by Noh et al. [34,35]. The idea is to define entanglement (or phase) measures in terms of what actually is, or can be, measured.

We hope that the discussed problem of non-unique ordering of states according to formally-defined entanglement measures can stimulate investigations of operationally-defined measures oriented for some specific experiments.

Acknowledgements

The work was supported by the Polish Ministry of Science and Higher Education under Grant No. N N202 261938.

Appendix A: Notes on the calculation of the REE

The concurrence, negativity and nonlocality can be calculated easily. By contrast, there has not yet been proposed an efficient method to calculate the REE for arbitrary mixed states even in the case of two qubits [36]. Analytical formulas for the REE are known only for some special sets of states with high symmetry (see [5,37] and references therein). Thus, usually, numerical methods for calculating the REE have to be applied [15,38,39].

It is a long-standing problem, posed by Eisert [36], of obtaining an analytical compact formula for the REE for two qubits. The problem is equivalent to finding the closest separable state $\hat{\rho}_{\rm css}$ for a given entangled state $\hat{\rho}$. In Ref. [37], a few arguments were given indicating that this problem, probably, cannot

[1] Noh et al. in Ref. [35] wrote: "There has been a good deal of discussion in the past of the most appropriate dynamical variable to represent the phase of a quantum field, and many candidates have been studied. Our analysis suggests that this question may not have a general answer with respect to the measured phase operators, because different measurement schemes lead to different operators. As in many other quantum-mechanical problems, it seems that questions about the value of a dynamical variable cannot be divorced from the measurement process that generates the ensemble."

be solved analytically for arbitrary states. Nevertheless, there exists a solution to the inverse problem of finding an analytical formula for $\hat{\rho}$ for a given closest separable state $\hat{\rho}_{\rm css}$ as derived by Ishizaka et al. [40,37].

The complexity of the problem can be explained (see, e.g., Ref. [15]) by virtue of Caratheodory's theorem, which implies that any separable two-qubit state can be decomposed as

$$\hat{\rho}_{\rm sep} = \sum_{j=1}^{16} p_j^2 |\psi_j^{(1)}\rangle\langle\psi_j^{(1)}| \otimes |\psi_j^{(2)}\rangle\langle\psi_j^{(2)}|, \tag{A1}$$

where the kth ($k = 1, 2$) qubit pure states can be parametrized, e.g., as follows

$$|\psi_j^{(k)}\rangle = \cos\alpha_j^{(k)}|0\rangle + \exp(i\eta_j^{(k)})\cos\alpha_j^{(k)}|1\rangle, \tag{A2}$$

and $p_j = \sin\phi_{j-1}\prod_{i=j}^{15}\cos\phi_i$ with $\phi_0 = \pi/2$. Thus, the minimalization of the quantum relative entropy $S(\hat{\rho}||\hat{\rho}_{\rm sep})$, given by Eq. (5), with $\hat{\rho}_{\rm sep}$ described by Eq. (A1), should be performed over $16 \times 4 + 15 = 79$ real parameters. Usually (see, e.g., Refs. [15,38]), gradient-type algorithms are applied to perform the minimalization. Řeháček and Hradil [38] proposed a method resembling a state reconstruction based on the maximum likelihood principle. Doherty et al. [39] designed a hierarchy of more and more complex operational separability criteria for which convex optimization methods (known as semidefinite programs) can be applied efficiently. One can also use an iterative method based on Ishizaka formula [40, 37] for the closest entangled state for a given separable state in order to find the closest separable state for a given entangled state. Our algorithms for calculating the REE are based either on the latter method or on a simplex search method without using numerical or analytic gradients.

References

[1] E. Schrödinger, *Naturwissenschaften* **23** (1935), 807, 823, 844.
[2] A. Einstein, B. Podolsky and N. Rosen, *Phys Rev* **47** (1935), 777.
[3] J.S. Bell, *Speakable and Unspeakable in Quantum Mechanics* (Cambridge University Press, Cambridge, UK, 1987).
[4] M.A. Nielsen and I.L. Chuang, *Quantum Computation and Quantum Information* (Cambridge University Press, Cambridge, UK, 2000).
[5] R. Horodecki, P. Horodecki, M. Horodecki and K. Horodecki, *Rev Mod Phys* **81** (2009), 865.
[6] S. Popescu, *Phys Rev Lett* **72** (1994), 797.
[7] O. Krueger and R.F. Werner, eds, *Some Open Problems in Quantum Information Theory*, e-print arXiv:quant-ph/0504166v1.
[8] C.H. Bennett, D.P. DiVincenzo, J.A. Smolin and W.K. Wootters, *Phys Rev A* **54** (1996), 3824.
[9] W.K. Wootters, *Phys Rev Lett* **80** (1998), 2245.
[10] K. Audenaert, M.B. Plenio and J. Eisert, *Phys Rev Lett* **90** (2003), 27901.
[11] S. Ishizaka, *Phys Rev A* **69** (2004), 020301.
[12] A. Peres, *Phys Rev Lett* **77** (1996), 1413.
[13] M. Horodecki, P. Horodecki and R. Horodecki, *Phys Lett A* **223** (1996), 1.
[14] V. Vedral, M.B. Plenio, M.A. Rippin and P.L. Knight, *Phys Rev Lett* **78** (1997), 2275.
[15] V. Vedral and M.B. Plenio, *Phys Rev A* **57** (1998), 1619.
[16] J.F. Clauser, M.A. Horne, A. Shimony and R.A. Holt, *Phys Rev Lett* **23** (1969), 880.
[17] R. Horodecki, P. Horodecki and M. Horodecki, *Phys Lett A* **200** (1995), 340.
[18] J. Eisert and M. Plenio, *J Mod Opt* **46** (1999), 145.
[19] A. Miranowicz, *Phys Lett A* **327** (2004), 272.
[20] K. Zyczkowski, *Phys Rev A* **60** (1999), 3496; K. Zyczkowski and I. Bengtsson, *Ann Phys* (*N.Y.*) **295** (2002), 115.
[21] S. Virmani and M.B. Plenio, *Phys Lett A* **268** (2000), 31.
[22] T.C. Wei, K. Nemoto, P.M. Goldbart, P.G. Kwiat, W.J. Munro and Frank Verstraete, *Phys Rev A* **67** (2003), 022110; T.C. Wei and P.M. Goldbart, *ibid* **68** (2003), 042307.

[23] A. Miranowicz, *J Phys A* **37** (2004), 7909.
[24] A. Miranowicz and A. Grudka, *Phys Rev A* **70** (2004), 032326.
[25] A. Miranowicz and A. Grudka, *J Opt B* **6** (2004), 542.
[26] M. Ziman and V. Bužek, *Phys Rev A* **73** (2006), 012312.
[27] Y. Kinoshita, R. Namiki, T. Yamamoto, M. Koashi and N. Imoto, *Phys Rev A* **75** (2007), 032307.
[28] A. Miranowicz, S. Ishizaka, B. Horst and A. Grudka, *Phys Rev A* **78** (2008), 052308.
[29] F. Verstraete, K.M.R. Audenaert, J. Dehaene and B. De Moor, *J Phys A* **34** (2001), 10327.
[30] B. Horst, S. Ishizaka, A. Koper and Miranowicz, in preparation.
[31] R.F. Werner, *Phys Rev A* **40** (1989), 4277.
[32] S. Ishizaka and T. Hiroshima, *Phys Rev A* **62** (2000), 022310.
[33] W.J. Munro, D.F.V. James, A.G. White and P.G. Kwiat, *Phys Rev A* **64** (2001), 030302(R).
[34] J.W. Noh, A. Fougères, and L. Mandel, *Phys Rev Lett* **67** (1991), 1426; *ibid* **71** (1993), 2579.
[35] J.W. Noh, A. Fougères and L. Mandel, *Phys Rev A* **45** (1992), 424.
[36] J. Eisert, *Problem 8: Qubit formula for relative entropy of entanglement*, in Ref. [7].
[37] A. Miranowicz and S. Ishizaka, *Phys Rev A* **78** (2008), 032310.
[38] J. Řeháček and Z. Hradil, *Phys Rev Lett* **90** (2003), 127904.
[39] A.C. Doherty, P.A. Parrilo and F.M. Spedalieri, *Phys Rev Lett* **88** (2002), 187904.
[40] S. Ishizaka, *Phys Rev A* **67** (2003), 060301.

Journal of Computational Methods in Sciences and Engineering 10 (2010) 499–519
DOI 10.3233/JCM-2010-0339
IOS Press

Comparative study between ONIOM, ab initio and DFT methods, application: α and β L-fucopyranose

Sofiane Moussi and Ourida Ouamerali
Laboratory of Physico-Chimie Théorique et Chimie Informatique, Faculty of Chemistry, U. S. T. H. B University, 16111 Algiers, Algeria

Abstract. The ONIOM method was used to reproduce geometrical parameters, atomic charges, dipole moment for α and β L-Fucopyranose which are biological interest molecules. The results of ONIOM(MP2/HF) and ONIOM(B3LYP/HF) calculations were compared to the values obtained by means of its corresponding theoretical levels MP2, DFT and RHF with 6-31G* bases set, using GAUSSIAN 98 software.

1. Introduction

The biological importance of L-fucose appears owing to the fact that it occurs as a component of serum protein [1], blood group substance [2,3], bacterial polysaccharides [4,5], and as a constituent of macromolecules in a variety of animal and plant tissue [1,6]. Fucose is also implicated in neuronal communication that underlies long-term memory storage [7–10].

L-fucose is characterized by the lack of a hydroxyl on the methyl group. This reduces considerably the conformational space due to the rotation of the hydroxyls groups. Compared to glucose which have 729 [11,12] possible conformations, Fucose manifest 81 (see Fig. 1) Conformations in chair forms, this pyranoses forms is preferential for most simple sugar in solution such as L-fucopyranose [11].

Many theoretical studies of sugar show that the hydrogen bond (HO. . .H) has an important impact on the stability of those molecules [11–13]. Indeed, Imre G. Csizmadia and collaborators [14] carried out a conformational study for α-L-fucopyranose and confirm that the orientations of the hydroxyl groups are not independent of each other. In the most stable rotamers, the number of possible OH. . . O (hydrogen bond) interactions is maximal, leading to the formation of an intra-molecular chain of hydroxyl groups [14]. As mentioned above, α-L-fucose and β-L-fucose exist in pyranose form; in this form we distinguish two chair conformations:

1. The first is the $^4C_1$: for the α-L-fucopyranose (α-LF) it corresponds to an anomeric hydroxyl group (noted OH (a)) in equatorial position (eq), whereas for the β-L-fucopyranose (β-LF) OH(a) is in axial position (ax).
2. The second is $^1C_4$: It is exactly the reverse of the $^4C_1$. OH(a) of the α-LF will be in axial position and that of the β-LF will be equatorial. (See Fig. 2)

We consider only the most stable rotamers for the α-LF and β-LF, which correspond to the conformations with a maximal HO. . . H interaction. We obtained one most stable rotamers for $^4C_1\alpha$-LF and one most stable rotamers for $^1C_4\alpha$-LF, Idem for $^4C_1\beta$-Lf and $^1C_4\beta$-Lf.

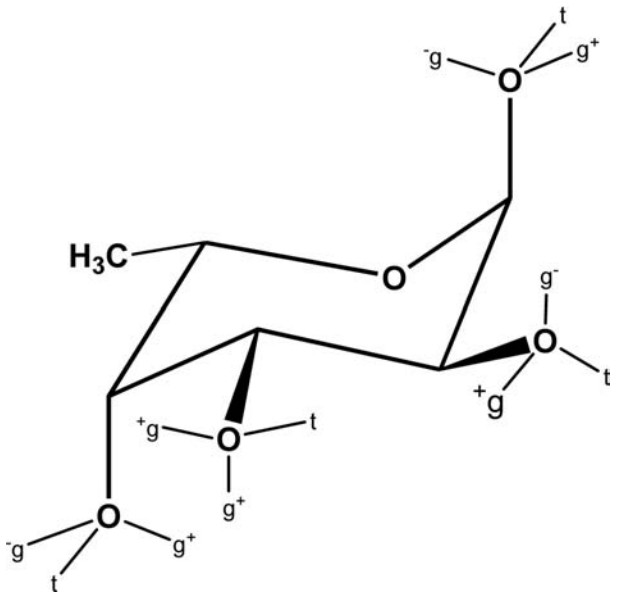

Fig. 1. Schematic representation of 81 possible minimum energy rotamers of $^{1}C_{4}\alpha$-L-fucopyranose [14]. The idealised C (x+1)-Cx-O-H torsions are denoted by g+, t, and g- for gauche clockwise (60°), anti (180°) and gauche counter clockwise (−60°), respectively where $x = 1, 2, 3, 4$.

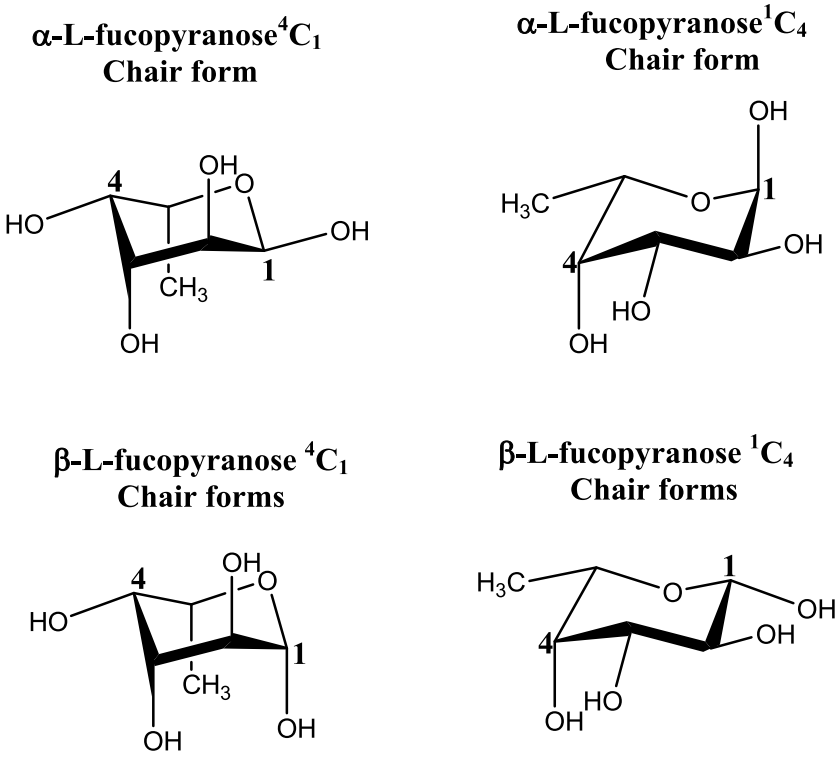

Fig. 2. graphical representation of $^{4}C_{1}$ and $^{1}C_{4}$ chair forms for α and β L-fucopyranose.

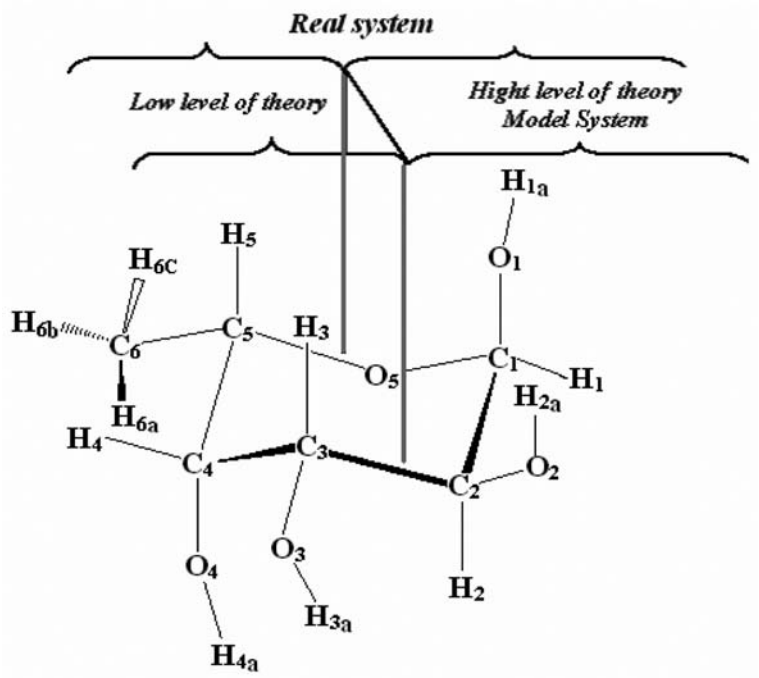

Fig. 3. Two-layered ONIOM partition of α-L-fucopyranose and β-L-fucopyranoe.

2. ONIOM methodologies

ONIOM (Own N-layer Integrated molecular Orbital molecular Mechanics) is a hybrid computational method developed by Morokuma and collaborators [15–23] that allows different levels of theory to be applied to different parts of a molecular system. This approach considering both the IMOMM [16] and IMOMO[17] models which combine layers of different levels of Molecular Orbital theory and molecular-mechanics force fields to achieve an optimal cost performance strategy in obtaining structural and energetic information. In the two-layered ONIOM method, the molecular system under study is divided into an inner and an outer layer. The inner layer consists of the most critical elements of the system, and the rest of the system comprises the outer layer.

In the terminology of Morokuma and collaborators, the full system is called "real" and is treated with a low theoretical level. The inner layer is termed "model" and is treated with both the low and high levels of theory. For our molecules (α-LF and β-LF), we use a two-layered ONIOM scheme (See Fig. 3).

In GAUSSIAN 98 software [24], ONIOM method can divide molecules in two or three layers. The basic idea of ONIOM approach can be easily understood when it is considered as an extrapolation scheme in two-dimensional space spanned by the size of the system in one axes and the level of theory on the other axes [17] (See Fig. 4).

In The case of two-layer, the extrapolated energy E_{ONIOM2} is defined as [16,17]:

$$E_{ONIOM2} = E(\text{low, real}) - E(\text{low, model}) + E(\text{high, model}) = E_3 - E_1 + E_2$$

Where E_3 is the energy of the entire system calculated at the low level of theory and E_1, E_2 are the energies of the model system determined at the low and high level of theory, respectively.

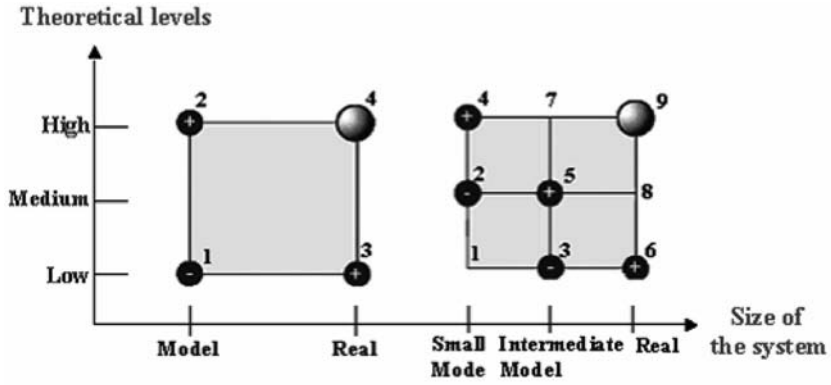

Fig. 4. Schematic representation of two-layer (left) and three-layer (right) ONIOM extrapolation schemes. E_4 and E_9 represent respectively the true energy of the real system for the two-layered and three-layered ONIOM scheme [16,17].

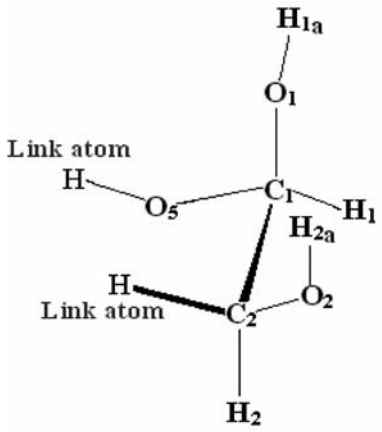

Fig. 5. Cutting covalent bond and link atom treatment for $\alpha-$L-fucopyranose.

If on the partitioning system a covalent bond has to be cut like in our case (Fig. 3), ONIOM scheme implemented in Gaussian98 treat the frontier between the two levels of theory by link atom. It consists of adding a monovalent atom along this covalent bond to fill the valency of the inner layer (model system). See Fig. 5.

In Gaussian 98 implementation the link atom is a hydrogen atom, they are only present in the model system and its treatment differs in the different implementations that have been published.

2.1. Computational aspect

The aim of this work is to study the behavior of ONIOM method for the pyranic cycle of the oses and to determine the influence of the cutting effects on the covalent bonds of our molecules and the effects of the link atoms added along those covalent bonds to the relative energy, geometrical parameters (bond length, valence angles, dihedral angels, and hydrogen bond), Mulliken charges, dipole moment, especially to see if the anomeric behavior of the molecules is affected. To confirm the results for the pyranosic form we chose two oses, which are α-L-fucopyranose and β-L-fucopyranose in chair conformation.

Table 1
The relative energy (kcal /mol) between the various conformations calculated by B3LYP, MP2 and RHF methods with 6-31G* bases set

ΔE (kcal/mol)	B3LYP	MP2	HF
$^4\mathbf{C}_1\alpha$-$^4\mathbf{C}_1\beta$	3.78	0.15	4.14
$^1\mathbf{C}_4\alpha$-$^4\mathbf{C}_1\alpha$	2.89	3.23	3.07
$^1\mathbf{C}_4\beta$-$^1\mathbf{C}_4\alpha$	1.67	1.67	1.93
$^1\mathbf{C}_4\beta$-$^4\mathbf{C}_1\alpha$	4.56	4.90	5.00
$^1\mathbf{C}_4\beta$-$^4\mathbf{C}_1\beta$	8.34	5.05	9.14

In order to define the most stable chair forms between $^4\mathrm{C}_1\alpha$-LF and $^1\mathrm{C}_4\alpha$-LF and between $^4\mathrm{C}_1\beta$-Lf and $^1\mathrm{C}_4$ β-Lf, we performed an ab-initio calculations: second order moller plesset (MP2) Method [25], Hatree Fock (RHF) method and Density functional theory (DFT) using B3LYP hybrid method [26]. This functional was first implemented into GAUSSIAN 92/DFT [27] program. It is a logical extension of Becke's three-parameter concept using LYP correlation function [28]); according to the 6-31G* bases set using GAUSSIAN (98) software [24]. The 6-31G* are sufficient bases set to reproduce the physical and chemical properties of sugars [11–14]. The results were compared to the experimental values obtained by RX [29–32].

Once obtained the most stable conformation for α-LF and β-LF, which corresponds to the $^1\mathrm{C}_4$ chair form, we carried out the two-layered ONIOM calculation according to GASSIAN98 software. In this two layered ONIOM calculations we integrate two molecular orbital methods using ONIOM(MP2/6-31G*:HF/6-31G*), ONIOM(B3LYP/6-31G*: HF/6-31G*) and ONIOM(HF/6-311G*:HF/6-31G*). Then we compare the resulting relative energy, time calculations, geometrical parameters, Mulliken atomic charges and dipole moment with those obtained by means of the non integrated molecular orbital methods such as MP2, DFT and RHF.

3. Results and discussion

The results of energy according to Table 1 shows that the $^1\mathbf{C}_4$ chair forms are the most stable for both α-LF (axial C1-OH) and β-LF (equatorial C1-OH). It is also noted that the order of stability of the fourth conformations is the same for the B3LYP, MP2, and RHF methods (Fig. 3).

This order of stability for which $^1\mathrm{C}_4$ β-LF is more stable than $^1\mathrm{C}_4$ α-LF, and $^1\mathrm{C}_4$ α-LF is more stable than the $^4\mathrm{C}_1$ α-LF and the least stable are the $^4\mathrm{C}_1$ β-LF, is confirmed by experience [32]. The difference in energy between the $^4\mathrm{C}_1$ α-LF and the $^4\mathrm{C}_1$ β-LF calculated by MP2 method is very small compared to that obtained by B3LYP and RHF.

The relative energy between $^4\mathrm{C}_1$ α-LF and $^1\mathrm{C}_4$ α-LF conformations is estimated by experience approximately 5 Kcal /mol [32], this energy is underestimated by B3LYP, MP2, and RHF methods of approximately 2 kcal/mol.

We carried out the two-layered ONIOM calculation for the most stable rotamers $^1\mathbf{C}_4$ αLf and $^1\mathbf{C}_4\beta$Lf according to GASSIAN98 software. In this tow layered ONIOM calculations we integrate two molecular orbital methods using ONIOM(MP2/6-31G*:HF/6-31G*), ONIOM(B3LYP/6-31G*: HF/6-31G*) and ONIOM(HF/6-311G*:HF/6-31G*).

Like it is mentioned above, this method consists in dividing our molecule into two regions, the interesting part is studied by a high theoretical level (B3LYP, MP2) and the other part by a low theoretical

Table 2
ΔS values (hartree) for $^1C_4 - \alpha$-L-Fucopyranose $^1C_4 - \beta$-L-Fucopyranose obtained by MP2, B3LYP and RHF, the value between brackets design the error of extrapolation ΔD for the ONIOM(MP2/B3LYP) and ONIOM(MP2/HF) scheme and those between hook is the ΔD for ONIOM(B3LYP/HF) scheme

Level	$^1C_4\alpha$-L-Fucopyranose	$^1C_4\beta$-L-Fucopyranose
MP2	-305.566 (0.000)	-305.573 (0.000)
B3LYP	-306.478 (0.912)	-306.486 (0.913)
RHF	-304.696 (-0.870) [1.782]	-304.697 (-0876) [1.78]

level (RHF) (see Fig. 3). The atoms implied in the high theoretical level are those numbered (C1, C 2, O1, O2, O5, H1, H2, H1a, H2a). The remainder will belong to the low theoretical level.

This integration of different levels is confirmed by a Substituent-value (S-value) calculation, which is a potential indicator to know how to select the methods to be combined, and how to partition the system into high and low level.

ΔS^{level}= ΔE(level, real)–ΔE(level, model)

Using the ΔSvalues, the error D of the ONIOM extrapolation $\Delta E^{\mathrm{ONIOM}}$, compared to the target calculation ΔE^{high}_{real}, can be written as [17]:

$\Delta D = \Delta$E(high, real) -ΔE^{ONIOM}

= [ΔE(high, real) – ΔE(high, model)] –[ΔE(low, real –ΔE(low, model)]

= ΔS^{high}– ΔS^{low}

In Table 2, we present the S-value results calculation for the $^1\mathbf{C}_4$ αLf and $^1\mathbf{C}_4$ βLf. The geometry for this molecule is optimized by RMP2/ 6-31G* level which is the target level calculation.

The S-values obtained by B3LYP and RHF calculations for $^1\mathbf{C}_4$ αLf and $^1\mathbf{C}_4$ βLf are all quite close to the target value of -305.5666 hartree and -305.5734 hartree respectively. Table 2 also show that the difference between the S-value for the target and the low level of theory are constant for both $^1\mathbf{C}_4$ αLf and $^1\mathbf{C}_4$ βLf (0.912 $\pm$ 0.001 Hartree for (RMP2:B3LYP), 0.870 $\pm$ 0.006 Hartree for (RMP2:RHF) and 1.782 $\pm$ 0.007 Hartree for (B3lyp:RHF)), which indicates that the error of extrapolation is constant. So, we would conclude that both (MP2:B3LYP) and (MP2:RHF) integrations are justified but we could simply choose the cheapest method as the low level in ONIOM2 calculations. For this, and like it mentioned above, we choose to perform ONIOM(MP2:RHF) and ONIOM(B3LYP:RHF) calculation to compare the MP2 and B3LYP correlation effects for the high level of theory.

In order to determine the effects of the change of bases set on the low level to the energy calculation, we carried out an ONIOM calculations with B3LYP(6-31G*) at the high level, with various bases set (STO-3G*, 3-21G*, 6-311G*) at the low level for $^1C_4$ α-LF, the results were compared to ONIOM(B3LYP/6-31G*:HF/6-31G*) and B3LYP/6-31G* calculations (see Table 3).

It is noted that the resulting energy from ONIOM(B3LYP/6-31G*:HF/6-31G*) and ONIOM(B3LYP/6-31G*:HF/6-311G*) calculations are relatively close to B3LYP/6-31G* energy value, whereas ONIOM(B3LYP/6-31G*:HF/STO-3G*) and (B3LYP/6-31G*:HF/3-21G*) are with a higher energy. to conclude that the bases set 6-31G* is sufficient to use for both high and low levels of theory, we determined the geometrical parameters obtained by the preceding ONIOM calculations (Table 4), and

Table 3
$^1C_4$ α-L-Fucopyranose, Relative energy values to B3LYP/6-31+G* calculation obtained by ONIOM methods with different bases set in the low level

Methods	Relative energy (Hartree) for B3LYP/6-31G-*
ONIOM(B3LYP/6-31G*:HF/6-31G*)	1.788601
ONIOM(B3LYP/6-31G*:HF/STO-3G*)	5.6282
ONIOM(B3LYP/6-31G*:HF/3-21G*)	3.465501
ONIOM(B3LYP/6-31G*:HF/6-311G*)	1.7210
B3LYP/6-31G*	−611.946836

Table 4
Bases set effects of ONIOM(B3LYP:HF) for results of geometrical parameters in low-level calculations for $\alpha-$L-fucopyranose

α-L-fucopyranose		B3LYP 6-31G*	ONIOM (B3lyp/6-31G* :HF/STO-3G*)	ONIOM (B3lyp6-31G* :HF/3-21G*)	ONIOM (B3lyp/6-31G* :HF/6-311G*)	ONIOM (B3LYP/6-31G* :HF/6-31G*)
Bond lengths						
C1-C2	(R1)	1.529	1.524	1.520	1.532	1.531
C2-C3	(R2)	1.530	1.575	1.533	1.532	1.534
C3-C4	(R3)	1.531	1.556	1.517	1.521	1.522
C4-C5	(R4)	1.534	1.562	1.526	1.522	1.524
C5-C6	(R5)	1.521	1.544	1.521	1.513	1.516
C1-O1	(R6)	1.424	1.417	1.425	1.428	1.427
C1-O5	(R7)	1.401	1.412	1.397	1.393	1.395
C2-O2	(R8)	1.424	1.415	1.422	1.424	1.424
C3-O3	(R9)	1.425	1.433	1.440	1.401	1.402
C4-O4	(R10)	1.418	1.433	1.434	1.396	1.398
C5-O5	(R11)	1.444	1.422	1.467	1.457	1.447
Valence angles						
O5-C1-C2	(A1)	111.9	111.9	111.6	112.6	112.4
O5-C1-O1	(A2)	113.2	113.1	112.7	113.3	113.1
C2-C1-O1	(A3)	105.7	105.9	105.1	105.4	105.5
C1-C2-C3	(A4)	110.5	110.0	109.4	110.4	110.4
C1-C2-O2	(A5)	112.2	112.1	113.2	111.7	111.9
O2-C2-C3	(A6)	110.8	110.9	109.3	111.0	110.8
C2-C3-C4	(A7)	110.1	109.5	109.2	110.4	110.2
C2-C3-O3	(A8)	110.1	111.0	108.8	110.6	110.5
O3-C3-C4	(A9)	107.7	107.1	106.4	107.7	107.7
C3-C4-C5	(A10)	109.8	109.3	110.8	110.1	110.0
C3-C4-O4	(A11)	109.9	110.5	108.1	110.7	110.5
O4-C4-C5	(A12)	110.1	109.5	108.8	109.8	109.6
C4-C5-O5	(A13)	112.1	112.2	111.6	111.3	111.3
C4-C5-C6	(A14)	113.1	111.7	112.2	113.7	113.5
C6-C5-O5	(A15)	106.2	106.7	105.2	106.1	106.2
C1-O5-C5	(A16)	116.1	116.2	115.6	115.8	116.2

carried out a comparison of geometrical parameters between those calculated by ONIOM and those resulting of DFT method according to B3LYP/ 6-31G*. The comparison between the results of bond length and valence angles is illustrated in Figs 6 and 7 respectively.

Figures 6 and 7 show that the results of the geometrical parameters (bond length, valence angles) obtained by ONIOM (B3LYP/6-31G*: HF/6-311G*) and ONIOM(B3LYP/6-31G*:HF/6-31G*) are almost confused with the straight lines, which represents the values of the parameters calculated by B3LYP/6-31G*, this is not the case of the other calculations. This makes it possible to validate this

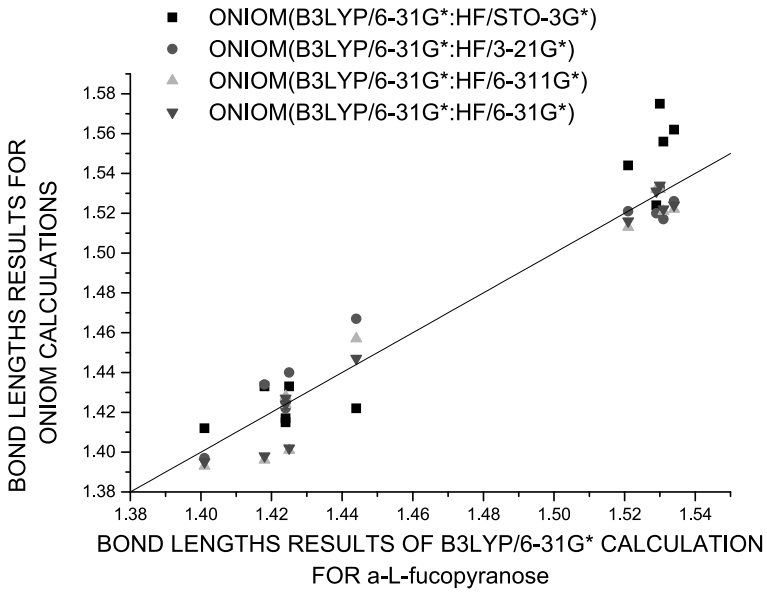

Fig. 6. Comparison between the resulting bond lengths by ONIOM(B3LYP/HF) calculations and B3LYP(6-31G*) for $\alpha-$L-Fucopyranose.

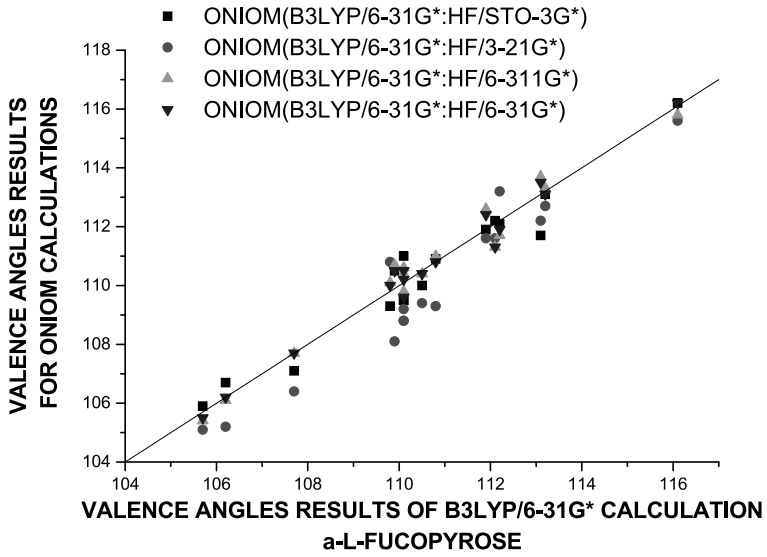

Fig. 7. Comparison between the resulting valence angles by ONIOM(B3LYP/HF) calculations and B3LYP(6-31G*) for $\alpha-$L-Fucopyranose.

bases set and to preserve it for next stages. This also shows that the ONIOM method is sensitive to the bases set. Indeed, the change of bases set on the part treated by HF in ONIOM calculations influence the geometrical results of the part treated by B3LYP of our molecule. According to the preceding table, the C1-C2, C1-O1, C2-O2 and C1-O5 inter atomic distances vary from an ONIOM calculation to another. The relative bond lengths for those obtained by B3LYP/6-31G* calculation are in Table 5.

This table shows that the C-H and O-H distances do not vary with the change of bases set in the part

Table 5
The relative bond length to B3LYP/6-31G* obtained by ONIOM calculations with different bases set in the low theoretical part

^{1}**C$_4\alpha$-LF**	B3LYP 6-31G*	ONIOM (B3lyp/6-31G* :HF/STO-3G*)	ONIOM (B3lyp6-31G* :HF/3-21G*)	ONIOM (B3lyp/6-31G* :HF/6-311G*)	ONIOM (B3LYP/6-31G* :HF/6-31G*)
C1-C2	1.530	0.006	0.1	0.002	0.001
C1-O1	1.424	0.007	0.001	0.004	0.003
C2-O2	1.424	0.009	0.003	0.000	0.000
C1-O5	1.405	0.007	0.008	0.012	0.01
C1-H1	1.096	0.000	0.002	0.001	0.000
O1-H1a	0.970	0.000	0.000	0.000	0.000
C2-H2	1.093	0.001	0.002	0.000	0.000
O2-H2a	0.973	0.001	0.000	0.001	0.000

Tables 6 and 7
The calculations results of relative energy (Hartree), the dipole moments (Debye) and the computing times for ONIOM, ab-initio and DFT methods for α-LF and β-LF

α-L-fucopyranose	Energie (Hartree)	Dipole moment (Debye)
MP2/6-31G*	$-610.\ 150$	2.84
HF/6-31G*	1.672	2.60
ONIOM(MP2/HF)	0.87	2.61
B3lyp/6-31G*	$-611.\ 940$	2.55
HF/6-31G*	3.462	2.60
ONIOM(b3lyp/HF)	1.782	3.78
HF/6-311G*	-608.628	2.67
HF/6-31G*	0.15	2.60
ONIOM(HF/HF)	0.068	2.60

β-L-fucopyranose	Energie (Hartree)	Dipole moment (Debye)
MP2/6-31G*	-610.152	0.76
HF/6-31G*	1.67	0.69
ONIOM(MP2/HF)	0.876	0.72
B3lyp/6-31G*	-611.943	0.71
HF/6-31G*	3.461	0.69
ONIOM(b3lyp/HF)	1.752	1.01
HF/6-311G*	-608.625	0.73
HF/6-31G*	0.143	0.69
ONIOM(HF/HF)	0.068	0.70

treated by HF calculation. This indicates that the treatment by link atoms does not influence the result of geometrical parameters of the atoms which are far from the border between different theoretical levels of ONIOM calculations. But the bond length, which is adjacent to the frontiers, was influenced by the change of the bases set in the low theoretical level.

Once the bases set 6-31G* was validate, we carried out calculations on $^1C_4$ βLF and $^1C_4$ αLF using MP2/6-31G*, B3LYP/6-31G*, HF/6-311G*, HF/6-31G*, ONIOM(MP2/6-31G*:HF/6-31G*), ONIOM(B3LYP/6-31G*:HF/6-31G*) and ONIOM(HF/6-311G*:HF/6-31G*) methods. We have compared the results of the values of energies, the dipole moments and the computing times (Table 6 for

$^1C_4$ α-LF and 7 for $^1C_4$ β-LF).

Tables 6 and 7, show an improvement on the value of energies compared to HF/6-31G* method, due to the partial correlation energies introduced into the ONIOM(MP2:RHF) and ONIOM(B3LYP:RHF) calculations in high level part, on one hand, and due to the improvement of the bases set on highs level region of the molecule for ONIOM(HF/HF) with different base.

The computing times are considerably reduced by ONIOM method compared to B3LYP and MP2 methods. Moreover, compared to MP2 calculation the reducing time are more than 60%. This reduction of the computing times represents one of this method interests.

The dipole moments are well evaluated by ONIOM method except those resulting from ONIOM(B3LYP/HF) which are overestimated.

The comparison between different geometrical parameters, bond length, valence angles, intra-cyclic and extra-cyclic dihedral angles, is represented in Table 8 for the $^1C_4\alpha$-LF and Table 9 for $^1C_4$ β-LF.

3.1. Geometrical results and discussion for $^1C_4$ α-L-fucopyranose

According to Table 8, MP2, B3LYP and RHF calculations shows that the distance C1-O5 is smaller than the distance O5-C5, these results are on agreement with the experimental results (X-ray [31]), which indicates that C1-O5 and O5-C5 bond length are respectively 1.411A° and 1.480A°. However the experimental results also shows that the distance C1-O5 is larger than C1-O1 (1,381 A°), whereas the different theoretical methods do not reproduce this result. The deviation for the experimental data is due to the fact that the comparison between calculated and crystal structure is not straightforward because the ring of the hydroxyl groups orientate them selves differently in the gaze phase than in the crystalline phase. The intermolecular O. . . H dominate in crystals [30,31,33]. We also notice that various ONIOM calculations have the same behavior as the other theoretical method for the bond lengths mentioned above.

The first comparisons between the ab-initio and DFT method with the experimental results will be presented, and then we do another comparison between the results of ONIOM methods and that of the experimental data. (See respectively; Fig. 8 (A) and 8 (B)).

According to Fig. 8 (A), MP2 and relatively DFT methods give a good results which are close to the experimental data compared to RHF method for the C-O bond length, expect the C1-O1 distance (anomeric region) which is over estimated by MP2 and B3LYP. HF gives close results to the experiment one (Table 7). For C-C bond length MP2 and RHF methods gives practically a same results which is too close to the experimental data than B3LYP method which gives an C-C average value equal to 1.529 A° compared to 1.519A° for MP2, 1.522A° for RHF/6-31G* and 1.520A° for experience [31].

The average value of the angles of the pyranic cycle other than that of the C5-O5-C1 is 109.6° for the experimental data, 110.68° for MP2, 110.88 for B3LYP and 111.70 for HF/6-31G* calculations.

The resulting average value of this angles for ONIOM(MP2:RHF) and ONIOM(B3LYP/HF) calculations are respectively 110.84 and 110.86. This indicates that the value obtained by RHF calculation are corrected and improved.

In Fig. 8 (B), one notices that the results of bond lengths obtained by ONIOM method are conclusive compared with those resulting from the experiment. It is noted that the ONIOM results of the C-C bond lengths such as R3, R4 and R5 (see Table 8) are very close to the experimental one. R1 and R2 values are overestimated respectively by ONIOM(B3LYP:RHF) and both ONIOM(B3LYP:RHF), ONIOM(MP2:RHF) calculations. Related to C-O bond lengths, the results obtained by ONIOM(MP2:RHF) and ONIOM(B3LYP:RHF) are conclusive for R7 and R8 whereas R6 is

Table 8
Geometrical parameters resulting of X-rays [30], MP2, DFT, HF, ONIOM(MP2;HF), ONIOM(B3LYP:HF) for α-L-fucopyranose

α-L-fucopyranose		RX	MP2 6-31G*	B3LYP 6-31G*	HF 6-311G*	HF 6-31G*	ONIOM (MP2/HF)	ONIOM (B3LYP/HF)	ONIOM (HF/HF)
Bond length									
C1-C2	(R1)	1.523	1.519	1.529	1.521	1.522	1.521	1.531	1.520
C2-C3	(R2)	1.520	1.519	1.530	1.521	1.522	1.531	1.534	1.523
C3-C4	(R3)	1.519	1.520	1.531	1.522	1.524	1.523	1.522	1.524
C4-C5	(R4)	1.526	1.524	1.534	1.525	1.526	1.524	1.524	1.527
C5-C6	(R5)	1.510	1.514	1.521	1.515	1.517	1.516	1.516	1.517
C1-O1	(R6)	1.381	1.425	1.424	1.398	1.399	1.427	1.427	1.397
C1-O5	(R7)	1.411	1.405	1.401	1.378	1.381	1.398	1.395	1.380
C2-O2	(R8)	1.433	1.428	1.424	1.401	1.402	1.428	1.424	1.400
C3-O3	(R9)	1.444	1.429	1.425	1.402	1.403	1.403	1.402	1.403
C4-O4	(R10)	1.430	1.422	1.418	1.396	1.398	1.397	1.398	1.398
C5-O5	(R11)	1.480	1.445	1.444	1.417	1.418	1.450	1.447	1.409
Valence angle									
O5-C1-C2	(A1)	109.7	111.9	111.9	111.9	111.6	112.3	112.4	111.7
O5-C1-O1	(A2)	112.3	112.9	113.2	112.4	112.4	113.0	113.1	112.3
C2-C1-O1	(A3)	108.4	105.2	105.7	106.6	106.6	105.2	105.5	106.6
C1-C2-C3	(A4)	109.8	110.0	110.5	110.5	110.6	110.5	110.4	110.5
C1-C2-O2	(A5)	109.4	112.0	112.2	111.8	111.8	111.4	111.9	111.8
O2-C2-C3	(A6)	110.7	110.5	110.8	110.8	110.9	110.9	110.8	110.7
C2-C3-C4	(A7)	109.8	109.8	110.1	110.3	110.2	110.1	110.2	110.2
C2-C3-O3	(A8)	111.0	109.9	110.1	110.7	110.6	110.5	110.5	110.5
O3-C3-C4	(A9)	109.4	107.4	107.7	107.7	107.8	107.7	107.7	107.8
C3-C4-C5	(A10)	108.7	110.1	109.8	109.7	109.7	110.0	110.0	109.6
C3-C4-O4	(A11)	108.5	109.5	109.9	110.5	110.3	110.4	110.5	110.3
O4-C4-C5	(A12)	111.6	109.0	110.1	109.7	109.5	109.6	109.6	109.5
C4-C5-O5	(A13)	110.1	111.6	112.1	111.5	111.4	111.3	111.3	111.5
C4-C5-C6	(A14)	112.6	112.7	113.1	113.3	113.2	113.5	113.5	113.1
C6-C5-O5	(A15)	106.3	105.7	106.2	106.8	106.7	106.2	106.2	106.8
C1-O5-C5	(A16)	114.2	114.7	116.1	117.3	117.2	115.8	116.2	117.7
Dihedral angle Intra-cyclic									
O5-C1-C2-C3	(D1)	−56.54	−55.51	−54.02	−52.45	−52.76	−53.00	−52.20	−52.33
C1-C2C3-C4	(D2)	57.51	55.32	54.74	53.51	53.70	53.86	53.48	53.70
C2-C3-C4-C5	(D3)	−57.39	−54.70	−53.92	−53.70	−53.80	−54.60	−54.78	−53.79
C3-C4-C5-O5	(D4)	56.86	53.47	52.27	52.62	52.80	53.75	53.88	52.59
C4-C5-O5-C1	(D5)	−59.29	−55.0	−53.91	−54.93	−55.2	−54.91	−54.88	−54.88
C5-O5-C1-C2	(D6)	58.58	55.87	54.33	54.48	54.84	54.39	53.89	54.41
Dihedral angle Extra-cyclic									
O1-C1-C2-O2	(E1)	−55.30	−55.82	−54.47	−53.17	−53.63	−53.45	−52.40	−53.24
O1-C1-C2-C3	(E2)	66.35	67.56	69.75	70.78	70.38	70.4	71.52	70.63
O2-C2-C3-O3	(E3)	−60.55	−62.45	−61.49	−62.86	−62.72	−63.01	−62.96	−62.71
O2-C2-C3-C4	(E4)	−181.63	179.56	179.78	178.00	178.23	177.97	178.03	178.23
O3-C3-C4-O4	(E5)	−57.91	−54.27	−52.87	−53.58	−53.81	−54.13	−54.31	−53.87
O3-C3-C4-C5	(E6)	−179.41	−174.19	−174.09	−174.60	−174.52	−175.24	−175.44	−174.49
O4-C4-C5-C6	(E7)	57.76	52.07	51.21	51.58	51.82	51.83	51.95	51.88
O4-C4-C5-O5	(E8)	−62.71	−66.714	−68.86	−68.88	−68.39	−67.87	−67.77	−68.496
C5-O5-C1-O1	(E9)	−62.01	−62.65	−65.12	−65.40	−64.96	−64.51	−65.473	−65.29
C6-C5-O5-C1	(E10)	−181.56	−177.91	−177.90	−179.13	−179.25	−178.91	−178.87	−178.91

Table 9
Geometrical parameters resulting of MP2, DFT, HF, ONIOM(MP2;HF), ONIOM(B3LYP:HF) for β-L-fucopyranose

β-L-fucopyranose		MP2 6-31G*	B3LYP 6-31G*	HF 6-311G*	HF 6-31G*	ONIOM (MP2/HF)	ONIOM (B3LYP/HF)	ONIOM (HF/HF)
Bond length								
C1-C2	(R1)	1.519	1.531	1.520	1.521	1.520	1.531	1.519
C2-C3	(R2)	1.511	1.522	1.514	1.517	1.524	1.526	1.517
C3-C4	(R3)	1.522	1.533	1.523	1.525	1.525	1.525	1.525
C4-C5	(R4)	1.527	1.539	1.527	1.529	1.527	1.527	1.530
C5-C6	(R5)	1.514	1.521	1.514	1.517	1.515	1.515	1.517
C1-O1	(R6)	1.406	1.403	1.382	1.383	1.406	1.403	1.382
C1-O5	(R7)	1.413	1.410	1.385	1.387	1.408	1.406	1.387
C2-O2	(R8)	1.425	1.421	1.400	1.402	1.426	1.422	1.400
C3-O3	(R9)	1.428	1.425	1.400	1.402	1.400	1.400	1.401
C4-O4	(R10)	1.421	1.417	1.396	1.400	1.397	1.397	1.397
C5-O5	(R11)	1.439	1.437	1.412	1.413	1.443	1.440	1.404
Valence angle								
O5-C1-C2	(A1)	109.5	109.7	109.8	109.7	109.7	109.9	109.7
O5-C1-O1	(A2)	108.3	108.6	108.5	108.6	108.4	108.8	108.4
C2-C1-O1	(A3)	110.7	110.9	110.8	110.9	110.6	110.9	111.0
C1-C2-C3	(A4)	110.1	110.2	110.0	110.0	110.3	110.0	110.0
C1-C2-O2	(A5)	111.5	111.8	111.5	111.4	111.1	111.6	111.5
O2-C2-C3	(A6)	107.1	107.6	107.5	107.5	107.6	107.5	107.4
C2-C3-C4	(A7)	109.4	109.8	110.0	109.9	109.7	109.9	109.9
C2-C3-O3	(A8)	111.0	111.3	111.6	111.5	111.4	111.4	111.5
O3-C3-C4	(A9)	107.3	107.4	107.7	107.8	107.7	107.7	107.8
C3-C4-C5	(A10)	110.2	110.2	109.9	109.8	110.2	110.2	109.8
C3-C4-O4	(A11)	109.6	109.9	110.5	110.4	110.4	110.4	110.3
O4-C4-C5	(A12)	108.8	109.8	109.4	109.3	109.4	109.4	109.3
C4-C5-O5	(A13)	111.7	112.2	111.4	111.2	111.3	111.4	111.3
C4-C5-C6	(A14)	112.7	113.0	113.3	113.3	113.5	113.5	113.2
C6-C5-O5	(A15)	106.2	106.8	107.3	107.2	106.7	106.7	107.3
C1-O5-C5	(A16)	112.9	114.2	115.4	115.4	114.0	114.3	115.8
Dihedral angle Intra-cyclic								
O5-C1-C2-C3	(D1)	−60.04	−59.08	−57.44	−57.50	−58.37	−57.76	−57.20
C1-C2C3-C4	(D2)	56.39	55.86	54.80	55.00	55.47	55.21	55.00
C2-C3-C4-C5	(D3)	−52.65	−51.74	−51.96	−52.20	−52.61	−52.87	−52.14
C3-C4-C5-O5	(D4)	52.99	51.40	52.05	52.30	52.92	53.04	52.08
C4-C5-O5-C1	(D5)	−58.19	−56.90	−58.09	−58.30	−58.10	−58.03	−58.04
C5-O5-C1-C2	(D6)	60.94	59.88	60.18	60.30	60.18	59.79	60.05
Dihedral angle Extra-cyclic								
O1-C1-C2-O2	(E1)	61.76	61.20	63.55	63.50	62.86	62.64	63.95
O1-C1-C2-C3	(E2)	−179.49	−179.13	−177.30	−177.45	−177.92	−178.06	−176.98
O2-C2-C3-O3	(E3)	−63.84	−63.10	−64.04	−64.11	−63.94	−63.70	−63.98
O2-C2-C3-C4	(E4)	177.84	178.08	176.41	176.43	176.78	177.02	176.54
O3-C3-C4-O4	(E5)	−53.44	−51.67	−52.94	−53.30	−53.19	−53.38	−53.30
O3-C3-C4-C5	(E6)	−173.25	−172.88	−173.82	−173.88	−174.12	−174.36	−173.80
O4-C4-C5-C6	(E7)	52.22	50.85	51.66	51.94	51.76	51.87	51.96
O4-C4-C5-O5	(E8)	−67.31	−69.90	−69.46	−68.94	−68.63	−68.56	−69.06
C5-O5-C1-O1	(E9)	−178.15	−178.65	−178.54	−178.32	−178.97	−178.62	−178.57
C6-C5-O5-C1	(E10)	178.50	178.83	177.34	177.31	177.54	177.58	177.55

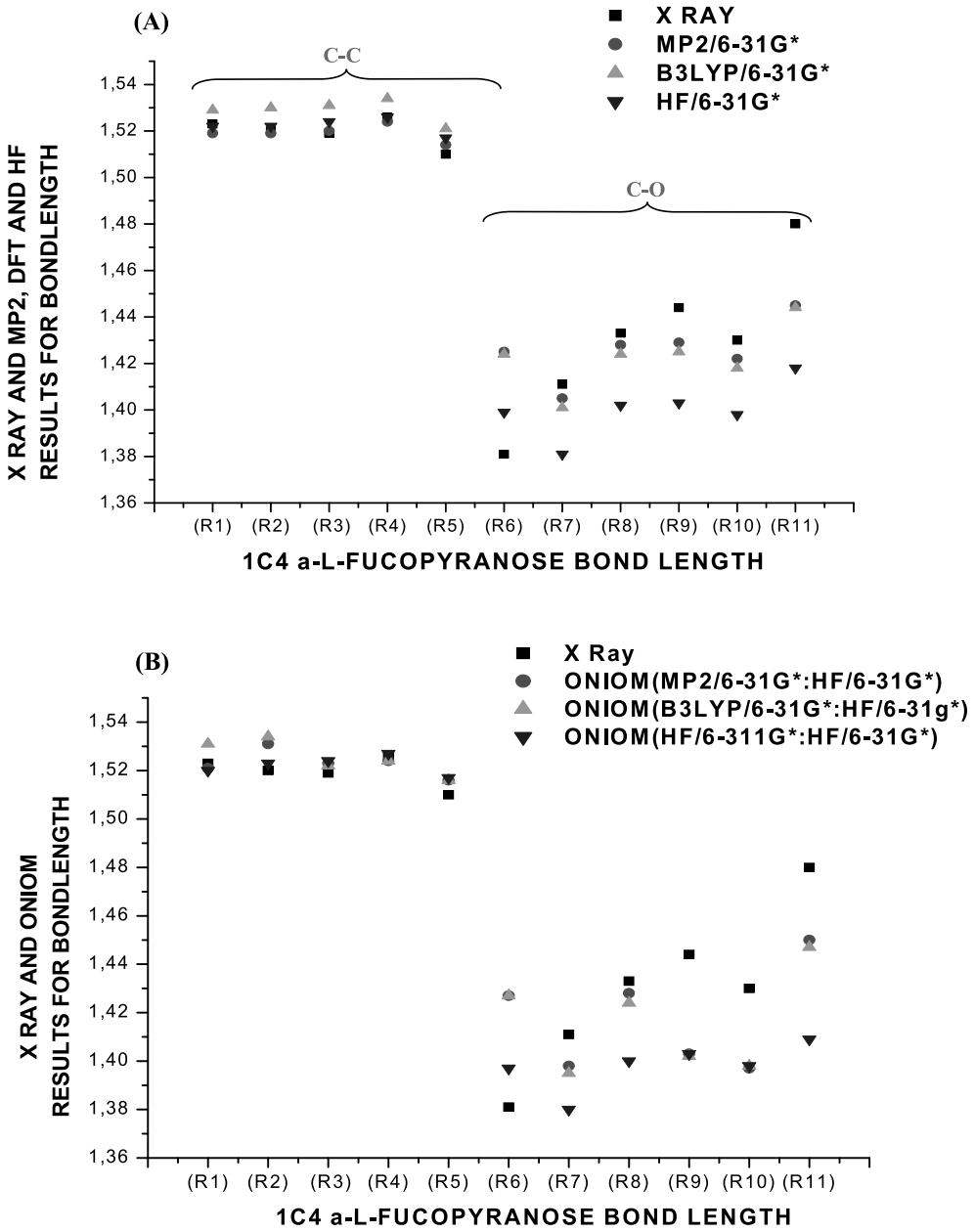

Fig. 8. Bond length Comparison between X Ray, MP2, B3LYP and RHF calculations for (**A**) using 6-31G* and between X ray [30], ONIOM(MP2/HF), ONIOM(B3LYP/HF), ONIOM(HF/6-311G*:HF6-31G*) for (**B**) .

on evaluated. We also announce that bond lengths C5-O5 (R11) and C2-C3 (R2) belonging to the border between the two theoretical levels applied to our molecule, according to selected cutting (Fig. 3), are longer than the average value. That is due to the link atom introduced by ONIOM method between these two pairs of atoms.

If we compare Fig. 8 (A) with Fig. 8 (B), we distinguishes a clear improvement from the results of bond lengths R3, R4 and R5 obtained by ONIOM(B3LYP:RHF) calculation than for those obtained by

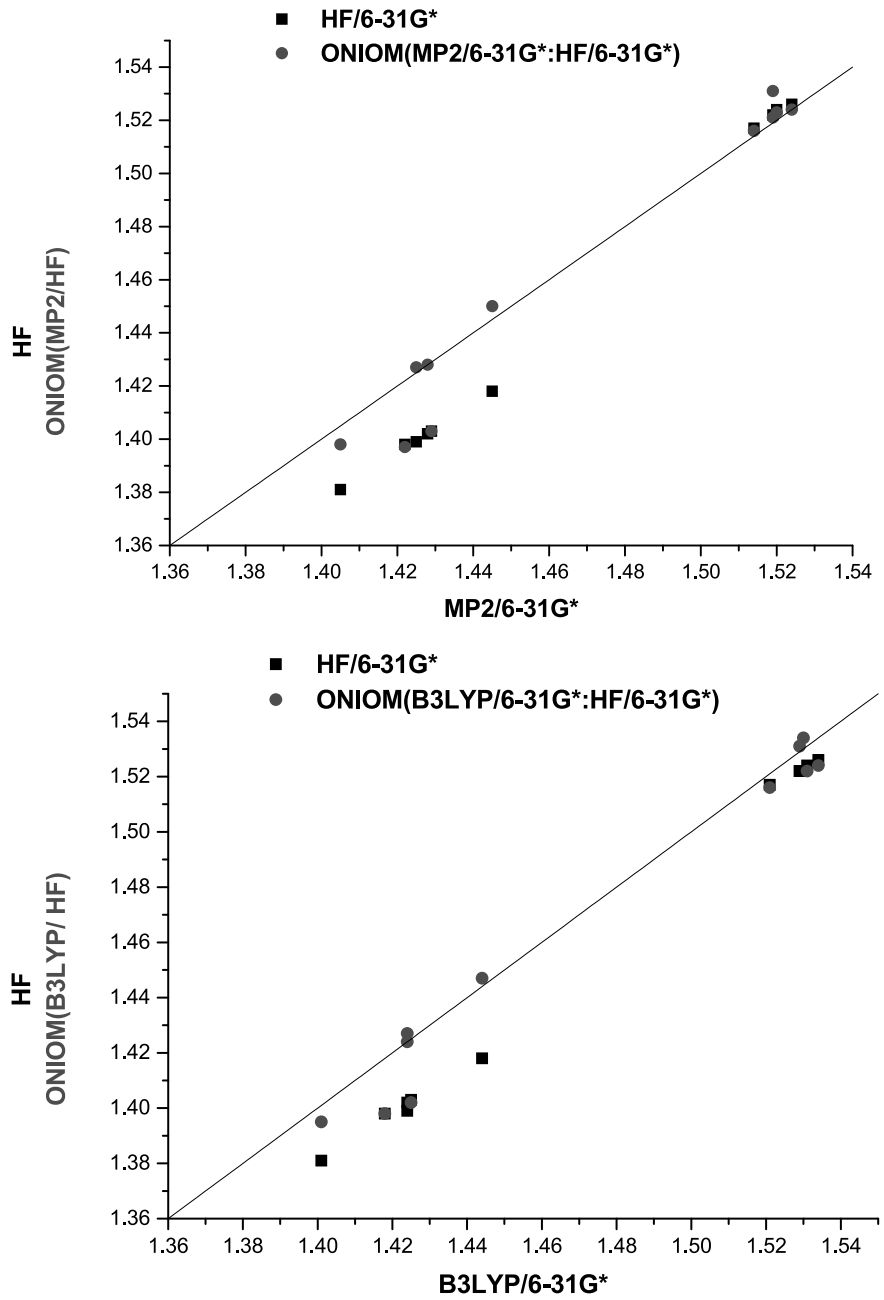

Fig. 9. α-LF, Comparison between the resulting bond length for ONIOM(MP2/HF), ONIOM(B3LYP/HF) and its corresponding non integrated theoretical levels calculations.

B3lyp/6-31G*. The precision of MP2 calculation are preserved while using ONIOM(MP2:RHF) for C-C bonds.

The C-O bonds C1-O1 (R6), C1-O5 (R7) and C2-O2 (R8) obtained by ONIOM(MP2:RHF) and ONIOM(B3LYP:RHF) are very close to the results obtained respectively by MP2 and B3LYP calculation,

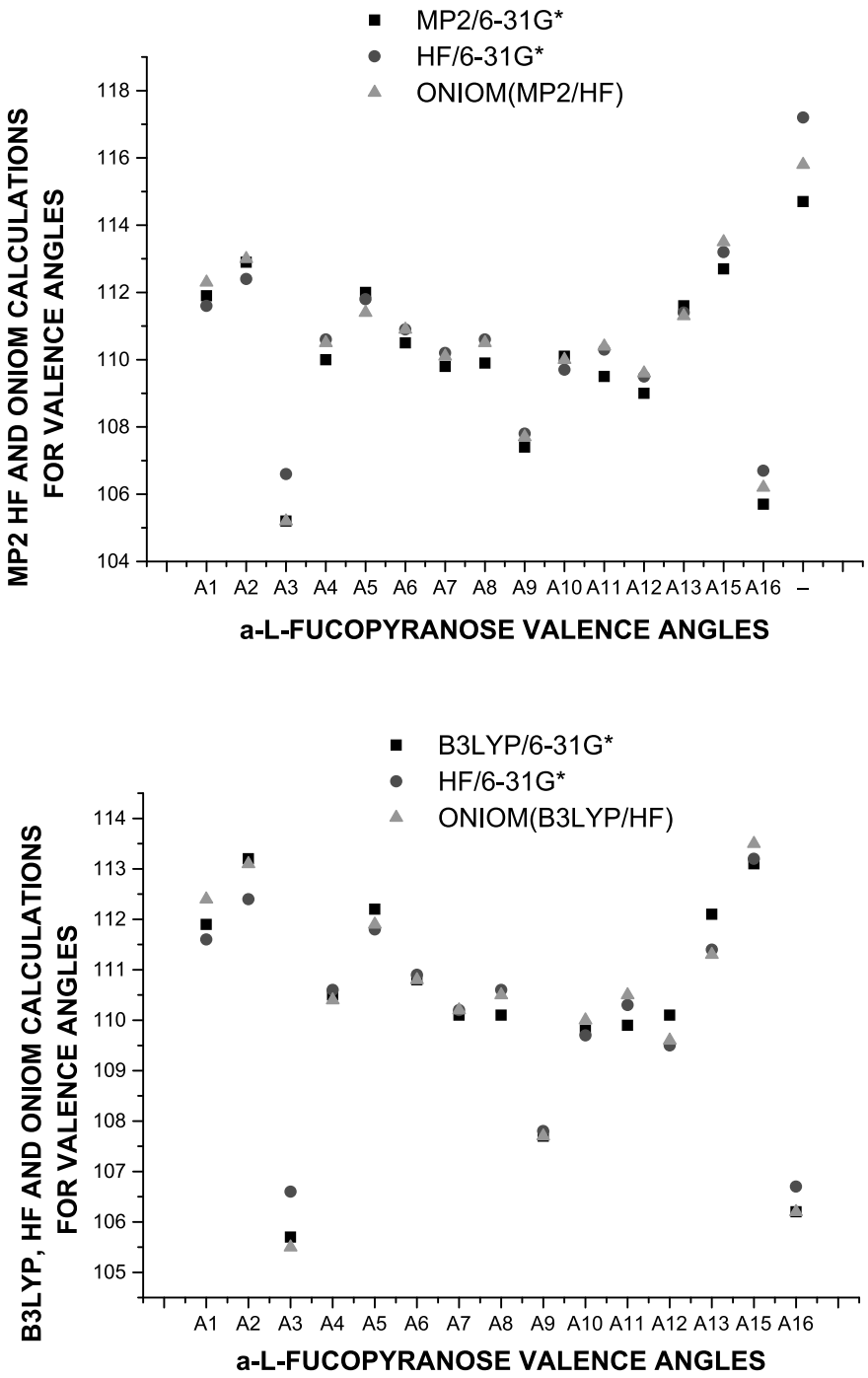

Fig. 10. α-LF, Comparison between the resulting valence angles for ONIOM(MP2/HF), ONIOM(B3LYP/HF) and its corresponding non integrated theoretical levels calculations.

whereas the results obtained for R9 and R10 are very close to those obtained by the HF method. This behavior of ONIOM method obtained for the bond lengths is the same one for the angle of valence and the dihedral angles.

To make on evidence this behavior, we used a graphic illustration (Figs 9 and 10).

Figure 9 indicate that the MP2 and RHF calculations gives approximately the same C-C bond lengths but diverge for the C-O.

The ONIOM calculation merge with the line indicating that the resulting bond lengths are very close to the values obtained by MP2/6-31G*. These observations are proved for B3LYP calculations.

For the angles calculations (Fig. 10, ONIOM methods gives a good results compared to HF/6-31G* and the results are very close to MP2 and DFT methods.

3.2. Geometrical results and discussion for $^1C_4\beta$-L-fucopyranose

According to Table 9, the C2-C3 bond length calculated on HF (1.517 A°) and MP2 (1.511 A°) levels with 6-31G* base set is relatively shorter than the average value of C-C bond (1.520 A°) in sugars, whereas the C4-C5 distance obtained in HF(1.529 A°) and MP2(1.527 A°) is longer. Let us recall that B3LYP over-estimates the C-C bond lengths. The ONIOM(MP2:RHF) method gives an acceptable C-C bond lengths compared to those given by MP2 and HF (See Fig. 11). We also announce that the C2-C3 distance was corrected by ONIOM(MP:RHF) calculation it passes from 1.511 A° (MP2) to 1.524 A°, this is due to the fact that C2-C3 represents the border between the two theoretical levels (MP2 and HF) corresponding to ONIOM(MP2:HF) calculation.

The resulting C4-C5 distance obtained by ONIOM(MP2:RHF) and HF/6-31G * was very close. This is due to the fact that the two atoms C4 and C5 belong to the part of the molecule treated by the low theoretical level which corresponds to HF/6-31G *, this means that distance C4-C5 value will be close to HF result. Relate to the ONIOM(B3LYP:RHF) results, distance C1-C2 and C2-C3 have the same behavior as B3LYP/6-31G * whereas C3-C4, C4-C5 and C5-C6 distances follow the behavior of HF/6-31G *.

Contrary to the α-LF, the MP2 and B3LYP methods applied to β-LF, give C1-O1 bond smaller than C1-O5 bond; this is in agreement with the anomeric effects.

For the valence angle and the intra and extra cyclic dihedral angle, the ONIOM results Compared to its corresponding non-integrated methods have the same behavior as mentioned to α-LF. (See Fig. 12).

The ONIOM calculations carried out on the part treated by a high theoretical level give similar results to it corresponding non integrated theoretical calculation (MP2, B3LYP) whereas the region treated in low theoretical level (RHF) has a same behavior of purely HF calculations.

For both α-LF and β-LF, there is a considerable improvement of the geometrical results obtained by ONIOM compared to the HF level that is due to the introduction of a partial electronic correlation from the treatment of a part of the molecule by MP2 or B3LYP. So the ONIOM calculations can compete with a high calculations method to reproduce geometrical parameters with reduced times for small molecules.

Van den Enden et al. [34] classified the O. . . H non-bonded interactions into three major groups: p-, *sp*3-, and s-type interaction. The idealized values for the out-of plane angle between an Ox . . . Hy vector and the Cx–Ox–H plane would be 90°, 125°, and 180°, respectively. The *sp*3-type interaction seems to be energetically favorable, and hydrogen atoms are trying to maintain this angle as much as possible.

For O. . . H interactions we used the O . . . H distance and one angle (e.g. O. . . H-O or R-O-C. . . H out of plane angle [34]). The O. . .H-O angle is not discussed here, because the linearity and non-linearity of the O. . .H-O angle is extensively discussed in the literature [35] and this parameter is completely insensitive

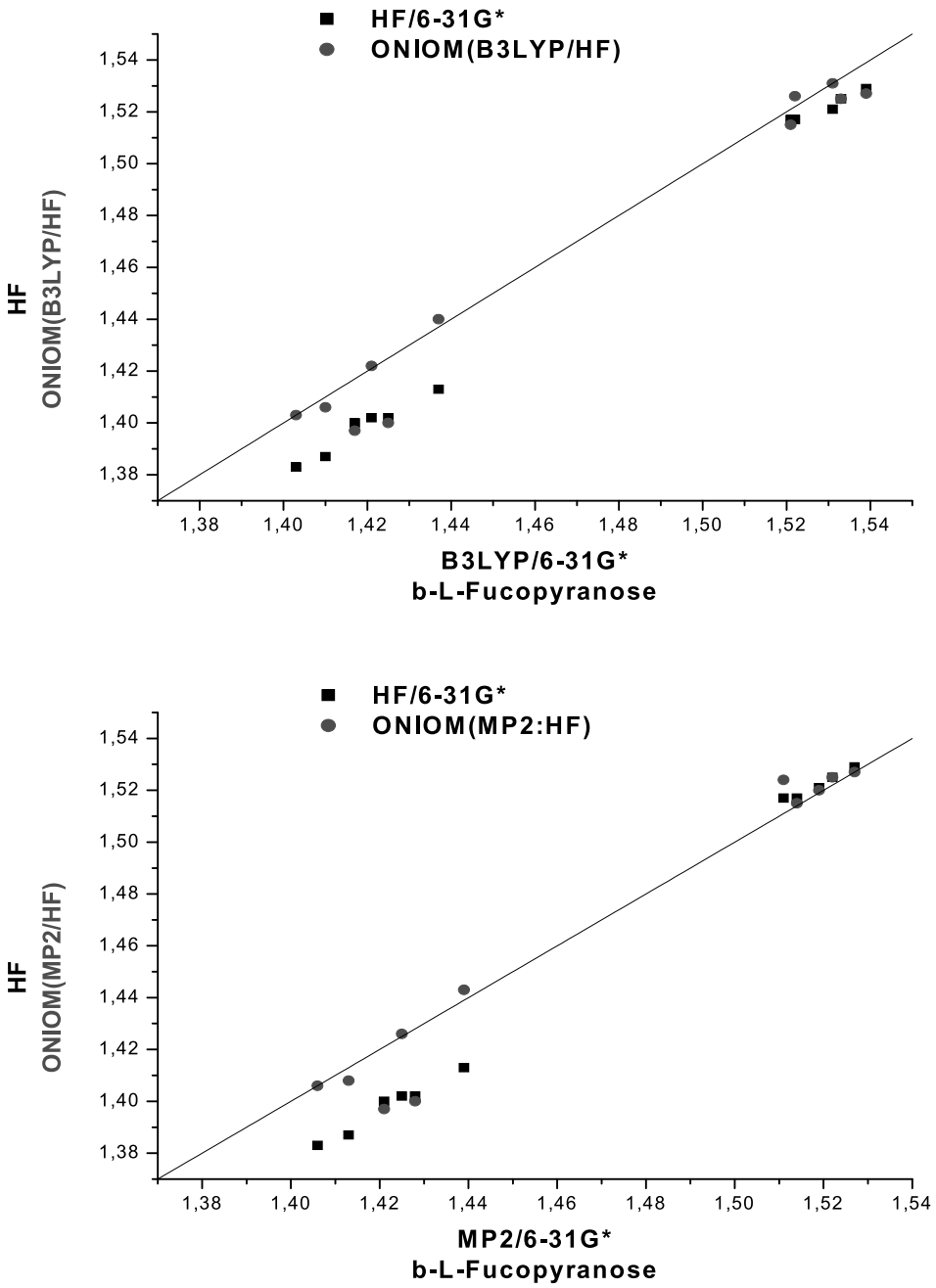

Fig. 11. β-LF, Comparison between the resulting bond length for ONIOM(B3LYP/HF), ONIOM(MP2/HF) and its corresponding non integrated theoretical levels calculations.

to the spatial arrangement of the oxygen lone pairs [36]. Also in sugars this angle is determined by other geometrical constraints and it deviates considerably from 180°. Alternatively, the O. . . H interactions for non-symmetric cases can be characterized in a polar coordinate system centered on the O atom by three coordinates that provide the exact position of the H atom: the O. . . H distance, the C-O. . . H angle

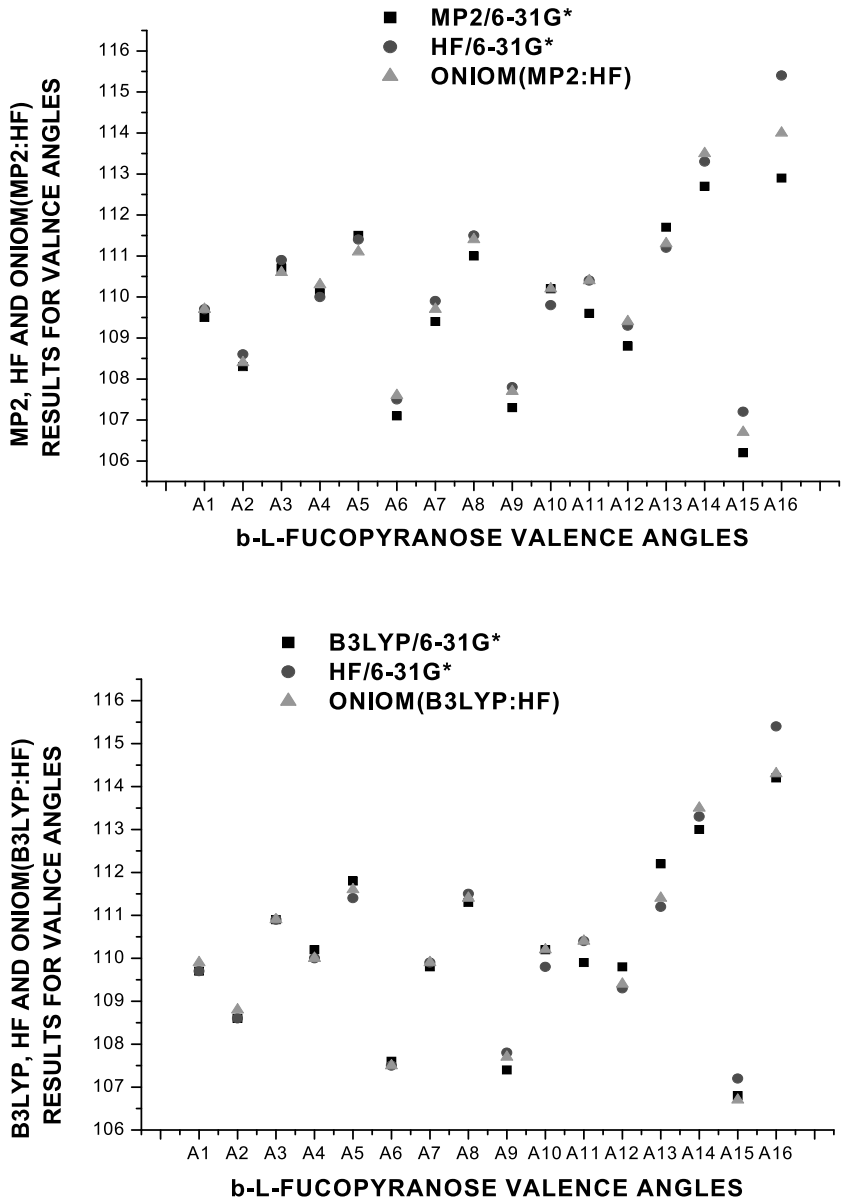

Fig. 12. β-LF, Comparison between the resulting valence angles for ONIOM(MP2/HF), ONIOM(B3LYP/HF) and its corresponding non integrated theoretical levels calculations.

and the R-O-C. . . H dihedral angle [36].

The deviation of the C-C-O-H to its ideal value can be an indicator for the power of the Hydrogen bond.

Table 10 show that for α-LF, the values of the O. . .H distance are well estimated by B3LYP method, whereas the ONIOM(MP2:RHF) and ONIOM(B3LYP/HF) calculations gives a longer H3. . .O2 and H4. . .O3 distances who are respectively 2.445 A° and 2.256 A° for ONIOM(MP2/HF) and 2.615 A° and 2.256 A° for ONIOM(B3LYP:RHF). Those methods give too long values for the distance H3. . .O2 to

Table 10
The geometrical parameters (nuclear distance and angle) implicated on the hydrogen bond for α-L-Fucopyranose obtained by MP2, B3LYP, HF, ONIOM(MP2/HF), ONIOM(B3LYP/HF) calculations using 6-31G* bases set

$\alpha-$LF	MP2	B3LYP	HF	MP2/HF	B3lLYP/HF
H2...O1	2.223	2.239	2.256	2.169	2.250
H3...O2	2.345	2.356	2.422	2.443	2.615
H4...O3	2.166	2.173	2.251	2.257	2.266
C1-O1...H2	82.0	82.0	81.8	82.6	80.4
C2-O2...H3	74.8	74.8	74.8	74.0	68.0
C3-O3...H4	80.8	80.8	81.1	81.0	81.0
H1-O1-C1...H2	143.6	143.8	146.0	143.6	143.0
H2-O2-C2...H3	-112.9	-113.8	-113.0	-114.8	-116.2
H3-O3-C3...H4	131.8	135.2	138.0	138.4	1387

Table 11
The geometrical parameters (nuclear distance and angle) implicated on the hydrogen bond for α-L-Fucopyranose obtained by MP2, B3LYP, HF, ONIOM(MP2/HF), ONIOM(B3LYP/HF) calculations using 6-31G* bases set

β-LF	MP2	B3LYP	HF	MP2/HF	B3lLYP/HF
H2...O1	2.443	2.458	2.516	2.437	2.466
H3...O2	2.339	2.355	2.409	2.421	2.416
H4...O3	2.158	2.153	2.248	2.248	2.250
C1-O1...H2	76.4	76.3	75.7	76.1	68.8
C2-O2...H3	76.9	76.7	76.9	76.3	71.2
C3-O3...H4	81.2	81.5	81.3	81.4	80.8
H1-O1-C1...H2	108.1	106.9	114.1	109.9	108.0
H2-O2-C2...H3	151.0	151.8	148.8	152.9	153.8
H3-O3-C3...H4	135.0	137.9	142.2	142.0	142.0

constitute an hydrogen bond. It is announced that for these bonds the ONIOM(MP2:RHF) has the same behavior as that of pure HF results.

The valence angles results are close to the MP2 calculations except that to ONIOM(B3LYP:RHF) for C2-O2-H3 valence angle which is under-estimated of 6.8°. Concerning the dihedrals angles, the ONIOM results for angle H1-O1-C1...H2 are close to results MP2, while the two other angles, approach the values obtained by HF calculations. For the β-LF (Table 11), ONIOM(B3LYP:RHF) calculations have the same behavior as that observed for the α-LF whereas the results ONIOM(MP2:RHF) are better than those of HF calculations.

We also carried out a comparison between the results of Mulliken charges calculated by these various methods for α-LF and β-LF (Tables 12 and 13). The replacement of 6-31G* bases set by 6-311G* in RHF calculations affect the results of MULLIKEN charges, although their behavior on all atoms is the same one.

For α-LF, according to Table 12, the carbon C1 and oxygen O5 carry charge respectively of $+0.285$ and -0.482 calculated by HF/6-311G* and respectively $+0.427$ and -0.656 by HF/6-31G *. The results of the charges obtained by HF/6-31G* are very close to the MP2, whereas the computed values by HF/6-311G* approaches more the B3LYP/6-31G* calculations. B3LYP and HF/6-311G* indicates that the charges carried by the atom O5 (-0.487 for B3LYP and -0.482 for HF/6-311G *) are much smaller than that carried by the atom O1 (-0.638 for B3LYP and -0.716 for HF/6-311G *), while calculations makes by MP2 and HF/6-31G * for these two atoms are closer. It is also noted that the atoms C2 according to B3LYP calculations and HF/6-311G * is practically not charged whereas MP2 and HF/6-31G * gives an average values of $+0.126$. Although the results of the charges obtained by HF/6-31G* is close to those

Table 12
The resulting Mulliken charges for α-L fucopyranose

α-L fucopyranose	Mulliken charges						
Methods	MP2	B3LYP	HF	HF	ONIOM	ONIOM	ONIOM
Atoms	6-31G*	6-31G*	6-311G*	6-31G*	(MP2/HF)	(B3LYP/HF)	(HF/HF)
C1	0.422	0.303	0.285	0.427	0.422	0.342	0.385
O5	−0.662	−0.487	−0.482	−0.656	−0.756	−0.714	−0.799
O1	−0.779	−0.638	−0.716	−0.774	−0.774	−0.755	−0.774
H1	0.192	0.141	0.220	0.185	0.185	0.264	0.205
H1a	0.456	0.405	0.436	0.456	0.455	0.460	0.460
C2	0.125	0.087	0.030	0.127	0.127	0.283	0.335
O2	−0.783	−0.647	−0.700	−0.780	−0.780	−0.668	−0.619
H2	0.215	0.162	0.244	0.209	0.209	0.287	0.293
H2a	0.462	0.406	0.435	0.461	0.461	0.501	0.514

Table 13
The resulting Mulliken charges for β-L fucopyranose

β-L fucopyranose	Mulliken charges						
Methods	MP2	B3LYP	HF	HF	ONIOM	ONIOM	ONIOM
Atoms	6-31G*	6-31G*	6-311G*	6-31G*	(MP2/HF)	(B3LYP/HF)	(HF/HF)
C1	0.470	0.328	0.297	0.481	0.434	0.336	0.385
O5	−0.669	−0.495	−0.484	−0.664	−0.766	−0.613	−0.785
O1	−0.759	−0.620	−0.677	−0.759	−0.739	−0.679	−0.705
H1	0.172	0.129	0.200	0.163	0.174	0.188	0.167
H1a	0.450	0.399	0.422	0.452	0.448	0.432	0.446
C2	0.119	0.097	0.080	0.120	−0.006	0.295	0.398
O2	−0.787	−0.654	−0.719	−0.782	−0.747	−0.718	−0.694
H2	0.180	0.125	0.206	0.174	0.144	0.250	0.264
H2a	0.462	0.406	0.439	0.460	0.441	0.500	0.523

of MP2, the ONIOM(MP2:RHF) results are very close to those of HF/6-31G*. Whereas for ONIOM (B3LYP:RHF) calculation, the charge carried by O5 passes from −0.487 (B3LYP) to −0.714. According to the results ONIOM(B3LYP:RHF) diverge compared to those of B3LYP and HF/6-31G*. The same behavior is to be announced for the β-LF.

However, since RHF/6-311G * calculations reproduced well the Mulliken charges results of B3LYP/6-31G*, it is perhaps preferable to use ONIOM(B3LYP/6-31G* :HF/6-311G *) integration.

References

[1] R.J. Winzler, *Method Biochem Anal* **2** (1955), 294.
[2] E.A. Kabat, *The Blood Orouv Substances*, Academic Press. New'York, 1956.
[3] M. Heidelberger, *Annu Rev Biochem* **26** (1956), 641.
[4] O. Westphal, F. Kaufman, O. Luderitz and Z. Stierlin, *Zentralbl Bakteriol parasitenk* **179** (1960), 336
[5] W.F. Dudman and J.F. Wilkinson, *Biochem J* **62** (1956), 289.
[6] T. Mori, *Advance Carbohyd Chem* **8** (1953), 315.
[7] (**a**) R. Jork, J. Potter, S. Bullock, G. Grecksch, H. Matthies, S.P.R. Rose, *Neurosci Res Commun* **5** (1989), 105–110. (**b**) S. Bullock, J. Potter and S.P.R. Rose, *J Neurochem* **54** (1990), 135–142.
[8] (**a**) S.P.R. Rose and R. Jork, *BehaV Neural Biol* **48** (1987), 246–258. (**b**) M. Krug, R. Jork, K. Reymann, M. Wagner and H. Matthies, *Brain Res* **540** (1991), 237–242. (**c**) C.G.A. Lorenzini, E. Baldi, C. Bucherelli, B. Sacchetti and G. Tassoni, *Neurobiol Learn Mem* **68** (1997), 317–324. (**d**) A.A. Tiunova, K.V. Anokhin and S.P.R. Rose, *Learn Mem* **4** (1998), 401–410.
[9] (**a**) H. Matthies, S. Staak and M. Krug, *Brain Res* **725** (1996), 276–280.
(**b**)M. Krug, M. Wagner, S. Staak and K.H. Smalla, *Brain Res* **643** (1994), 130–135.

[10] L. Hsieh-Wilson, The Tangled Web: Unraveling the Molecular Basis for Communication In The Brain, *Engineering & Science* **2** (2001), 14–23.
[11] C.J. Cramer and D.G. Truhlar, *J Am Chem Soc* **115** (1993), 5745.
[12] G.I. Csonka, I. Kolossvary, P. Csaszar, K. Elias and I.G. Csizmadia, *J Mol Struct* (*THEOCHEM*), in press.
[13] G.I. Csonka, K. Elias and I.G. Csizmadia, *Chem Phys Lett* **257** (1996), 49.
[14] –[13] G.I. Csonka, K. Elias and I.G. Csizmadia, *J Comput Chem* **18** (1996), 330, 03.
[15] S. Dapprich, I. Komaromi, K.S. Byun, K. Morokuma and M.J. Frisch, *J Mol Struct* **462** (1999), 1–21.
[16] S. Humbel, S. Sieber and K. Morokuma, *J Chem Phys* **105** (1996), 1959–1967.
[17] M. Kuno, S. Hannongbua and K. Morokuma, *Chem Phys Lett* **380** (2003), 456–463.
[18] F. Maseras and K.J. Morokuma, *Comput Chem* **16** (1995), 1170–1179.
[19] M. Svensson, S. Humbel, R.D.J. Froese, T. Matsubara, S. Sieber and K. Morokuma, *J Phys Chem* **100** (1996), 19357–19363.
[20] M. Svensson, S. Humbel and K. Morokuma, *J Chem Phys* **105** (1996), 3654–3661.
[21] T. Vreven and K. Morokuma, *J Comput Chem* **21** (2000), 1419–1432.
[22] T. Vreven, B. Mennucci, C.O. da Silva, K. Morokuma and J. Tomasi, *J Chem Phys* **115** (2001), 62–72.
[23] T. Vreven, K. Morokuma, O. Farkas, H.B. Schlegel and M.J. Frisch, *J Comput Chem* **24** (2003), 760–769.
[24] M.J. Frisch, G.W. Trucks, H.B. Schlegel, G.E. Scuseria, M.A. Robb, J.R. Cheeseman et al., Gaussian 98, rev. A.9. Pittsburgh, PA: Gaussian, Inc, 1998.
[25] C. Moller and M.S. Plesset, *Phys Rev* **46** (1934), 618.
[26] A.D. Becke, Density-functional thermochemistry. III. The roleof exact exchange, *J Chem Phys* **98**(7) (1993), 5648–5652.
[27] M.J. Frisch, G.W. Trucks, M. Head-Gordon, P.M.W. Gill, M.W. Wong, J.B. Foresman, B.G. Johnson, H.B. Schlegel, M.A. Robb, E.S. Replogle, R. Gomperts, J.L. Andres, K. Raghavachari, J.S. Binkley, C. Gonzalez, R.L. Martin, D.J. Fox, D.J. DeFrees, J. Baker, J.J.P. Stewart and J.A. Pople, GAUSSIAN 92/DFF, Revision G (Gaussian, Inc., Pittsburgh, PA, 1993).
[28] C. Lee, W. Yang and R.G. Parr, *Phys Rev B* **37** (1988), 785.
[29] J.L. Asensio and J. Jimenez-Barbero, *Biopolymers* **35** (1995), 55.
[30] D. Lamba, A.L. Segre, G. Fabrizi and G. Matsuhiro, *Carbo-hydr Res* **243** (1993), 217 and references cited therein.
[31] F. Longchambon and H. Giller-Pandraud, *Acta Cryst* **B33** (1977), 2094.
[32] D.B. Berkowitz and S.A. Banner, *American Chemical Society* **26** (1987), 2606.
[33] U. Salzner and P.v.R. Schleyer, *J Org Chem* **59** (1994), 2138.
[34] L. Van den Enden, C. Van Alsenoy, J.N. Scarsdale and L. Shafer, *J Mol Struct* (*Theochem*) **104** (1983), 471.
[35] S. Sheiner, in: *Reviews in Computational Chemistry*, (Vol Ii), K.B. Lipkowitz and D.B. Boyd, eds, (VCH, New York, 1991) p. 165 and references cited therein.
[36] M.J. Frisch, J.E. Del Bene, J.S. Binkley and H.F. Schaefer III, *J Chem Phys* **84** (1986), 2279.

Journal of Computational Methods in Sciences and Engineering 10 (2010) 521–529
DOI 10.3233/JCM-2010-0340
IOS Press

Assessment of the performace of the functional density theory to compute molecular polarizabilities using molecular polarization maps

Lurdes Roset and Juan J. Perez*
Department of Chemical Engineering, Technical University of Catalonia ETS d'Enginyeria Industrial, Av. Diagonal, 647, 08028 Barcelona, Spain

Abstract. In the present report we analyze the performance of DFT to compute molecular polarizabilities through the analysis of molecular polarization potential that can be used as a tool to understand their spatial effects in the calculation of molecular polarizabilities. This is done in the present report through the results obtained for three reference molecules: hydrogen cyanide, formaldehyde and urea. Calculations were carried out at the density functional theory using the BLYP and B3LYP functionals. The results of the polarization maps reveal similar trends observed with the calculation of the different components of the polarizability tensor. However, the use of the maps permits to understand spatial effects specific for each level of calculation and each basis set.

1. Introduction

Dipole polarizability accounts for the linear contribution to the induced dipole of a charge distribution in the presence of an electric field [1]. The polarizability is an important magnitude involved in the description of molecular interactions with a determining role in some cases [2,3]. Since its experimental determination is not straightforward, computational methods provide a reasonable alternative to obtain estimates of this property [4]. Indeed, polarizability can routinely be calculated from the molecular electron density through either the computation of the analytical derivative of the dipole moment or computing the second derivative of the energy versus the electric field [5]. Alternatively, the Finite field theory (FFT) can also be used for this purpose; however it requires a careful choice of electric field to be in the position to disregard higher order contributions [6]. At the Hartree-Fock level this procedure is equivalent to use the perturbation theory known as the couple Hartree-Fock method (CPHF) [7].

The effect of the polarizability in molecular interactions and its distribution in space can be rationalized using the Molecular Polarization Potential (MPP) maps. They represent an interesting way to look at polarizabilities accounting for the spatial distribution of the deformability of the molecular electron density as a correction to the Molecular Electrostatic Potential (MEP) maps [8–11]. Indeed, the MEP represents the first order (coulombic) contribution of the interaction energy between a point charge and a

*Corresponding author. Tel.: +34 934016679; Fax: +34 934017150; E-mail: juan.jesus.perez@upc.edu.

molecule, whereas the MPP represents the second order (induced) contribution to the interaction energy of a molecule in the same conditions. However, MPP maps can also be used as a tool to provide a quantitative measure of how the spatial distribution of the electron density affects the calculation of the polarizability [12], providing new insights into the understanding of the effect of the extension of the basis sets and/or the deficiencies for describing the induced moments of alternative procedures to compute the electron density [12–18].

The purpose of this report is to analyze the performance of the DFT method to compute molecular polarizabilities. In this work we report the results of calculations using two different commonly used exchange functionals. DFT results reported in this work show an overestimation of polarizability estimates as had been previously published in the literature [19]. Furthermore, in order to understand the origin of such a behavior we carried out a comparative analysis of the MPP maps using the calculations computed at the MP4 level using a 6-311++(2d,2p) basis set as reference [20]. In the present work benchmark calculations have been performed on three small molecules: hydrogen cyanide, formaldehyde and urea.

2. Methods

The polarizability tensor was calculated from the second derivative of the energy on the optimized geometries within each computational method. For the computation of the MPP maps, molecules were placed on the XZ plane and the maps computed on the plane y $=$ 4 bohr above the molecular plane. Grid points were computed every bohr and extended approximately 6 bohr beyond the van der Waals molecular surface. Since the molecules selected have a symmetry plane only one half of the points of the grid were computed. The total number of points calculated was 231 points for hydrogen cyanide, 242 for formaldehyde and 312 for urea.

The polarization was computed at each point of the grid by subtracting the coulomb contribution to the interaction energy (ΔE) computed using a probe charge of 0.1 a.u. The coulomb contribution (eV) was computed from the corresponding molecular electrostatic potential map. The polarization potential (P) can easily be obtained from the following expression:

$$\Delta E(r) = eV(r) + e^2 P(r)$$

Calculations at the DFT level were carried out with the BLYP [21] and B3LYP [22] functionals, using a 6-311++(2d,2p) [20] basis set that includes two sets of polarization functions as well as diffuse functions. Calculations were also carried out at the SCF and MP2 and MP4 level with the same basis set to be used as reference. All the calculations reported in this work were performed with the Gaussian94 package [23].

3. Results and discussion

Estimates of the polarizability tensor for the three molecules studied in the present work are listed in Table 1 together with the available experimental results. Inspection of the Table shows that whereas the MP4 improves systematically both, SCF and MP2 results by less than a 5%, the DFT method tends to overestimate polarizability calculations beyond MP4 results. However, the two functionals used in the present work exhibit a differential behavior, with the B3LYP providing closer values to MP4 estimates.

Table 1
Estimates of the polarizability tensor molecules reported in the present work computed with the 6-311++(2d,2p) basis set. Values correspond to the different tensor components (α_{xx}, α_{yy}, α_{zz}) followed by the average value $< \alpha >$ (in bold), computed as $< \alpha >= (\alpha_{xx}, +\alpha_{yy} + \alpha_{zz})/3$. All values are in atomic units ($1e^2a_0^2E_h^{-1} = 1.648778 \times 10^{-41}C^2.m^2.J^{-1}$). Experimental values available are also listed

		RHF	MP2	MP4	BLYP	B3LYP	Exper. value $< \alpha >$
Hydrogen	xx	11.36	11.51	11.44	12.22	11.88	
cyanide	yy	11.36	11.51	11.44	12.22	11.88	
	zz	26.12	26.34	26.99	27.01	26.49	
	$< \alpha >$	**16.28**	**16.45**	**16.62**	**17.15**	**16.75**	**17.5**
Formaldehyde	xx	15.23	15.24	16.54	17.90	16.96	
	yy	10.48	10.71	10.86	11.17	10.99	
	zz	21.51	21.56	22.09	23.58	22.72	
	$< \alpha >$	**15.74**	**15.89**	**16.50**	**17.55**	**16.87**	**16.5**
Urea	xx	32.47	33.45	34.50	40.77	38.01	
	yy	22.61	25.14	25.17	26.45	25.13	
	zz	35.37	36.72	36.98	42.10	39.91	
	$< \alpha >$	**30.15**	**31.77**	**32.22**	**36.44**	**34.35**	**31.9**

Specifically, for formaldehyde and hydrogen cyanide the results are very similar to MP4 estimates, whereas for the case of urea estimates are about 5% above. In contrast, the BLYP exhibits a poorer behavior with deviations of about 5% for formaldehyde and hydrogen cyanide and even a 10% for urea.

Some insight of the performance of the DFT method can be obtained from the analysis of the MPP maps, however, more interesting the MPP themselves are the maps of the deviations of the polarization from a reference that can provide information about systematic differences between the different methods of calculation. Figures 1–3 show the polarization difference maps (in percentage), with the MP4 calculation being taken as reference. As can be seen, difference maps of the Hartree-Fock and MP2 calculations are smooth; the improvement is continuous, whereas the maps of the DFT calculations are rough with values underestimated in the neighborhood of the atoms and values overestimated in the outer-most regions of the molecule.

In the case of the hydrogen cyanide the largest differences between the Hartree-Fock calculations and the MP4 are around the nitrogen lone pair (Fig. 1a), with underestimations around 15%, whereas for the rest of the molecule these difference goes down to a 4%. Clearly the MP2 calculation is closer to the reference MP4 calculations (Fig. 1b), with deviations of around a 2% in the neighborhood of the nitrogen lone pair. This behavior clearly reflects the continuous improvement in the evaluation of the polarizability when the correlation energy is included. In contrast, in the case of the DFT calculations difference maps are uneven with zones where the polarization is overestimated and regions where it is underestimated (Figs 1c and 1d). The two functionals exhibit a similar behavior with an underestimation of the polarization in the neighborhood of the nuclei with peaks that reach a 10% around the nitrogen lone pair and an overestimation of the polarization of around a 4% in the outer-most regions of the molecule in the case of the BLYP functional and around a 8% for the B3LYP functional. Thus, although both maps show an uneven topography the B3LYP surface exhibits larger differences between lows and highs.

Similar results are obtained after the analysis performed to the formaldehyde molecule. The Hartree-Fock procedure underestimates the polarization in regard to the MP4 calculations up to 25% in the areas close to the oxygen lone pairs (Fig. 2a). This effect is reduced with differences up to 4% when the correlation energy is included at the MP2 level (Fig. 2b). In regard to the DFT calculations, the

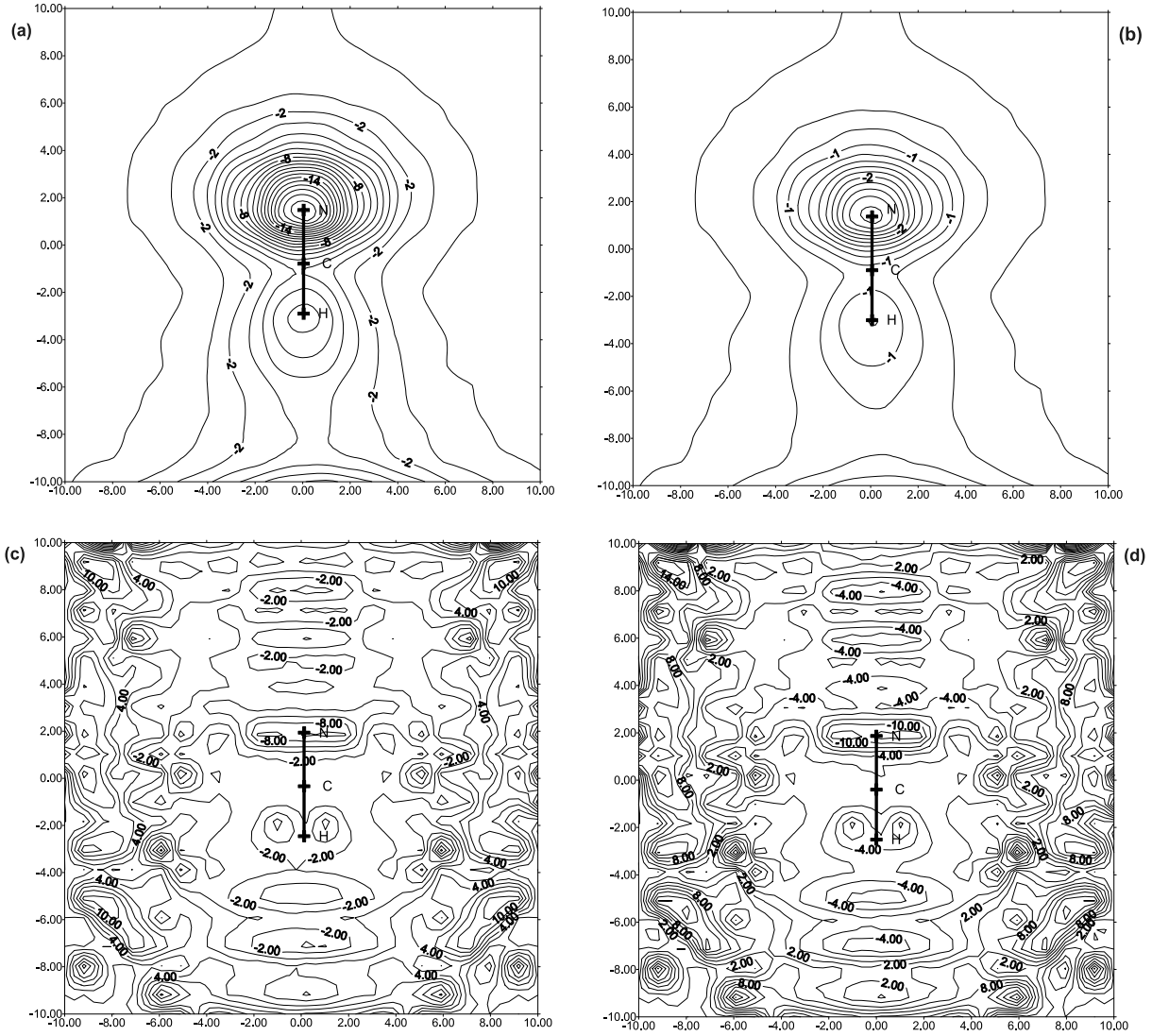

Fig. 1. Molecular polarization difference maps (in percentage) for HCN at different levels of the theory using the MP4 calculation as reference. (a) RHF/MP4 (b) MP2/MP4 (c) BLYP/MP4 (d) B3LYP/MP4.

two functionals overestimate the polarizability, although values computed with the B3LYP are closer to those obtained with the MP4 method. Difference maps reveal an uneven distribution of the polarization with underestimations in regions close to the nuclei and overestimations in the outer-most regions of the molecule (Figs 2c and 2d).

In regard to urea, Figs 3a–3d show the polarization difference maps taking the MP4 calculation as reference. The same trends as described above can be observed: whereas the SCF and MP2 maps are smooth, the DFT maps are uneven. Thus, the SCF calculation underestimates the polarization about a 25% (Fig. 3a) whereas the MP2 calculation only around 2% (Fig. 3b). On other hand, DFT calculations exhibit underestimations up to 50% close to the nuclei (Figs 3c and 3d) and overestimations of around 20% in the outer-most regions.

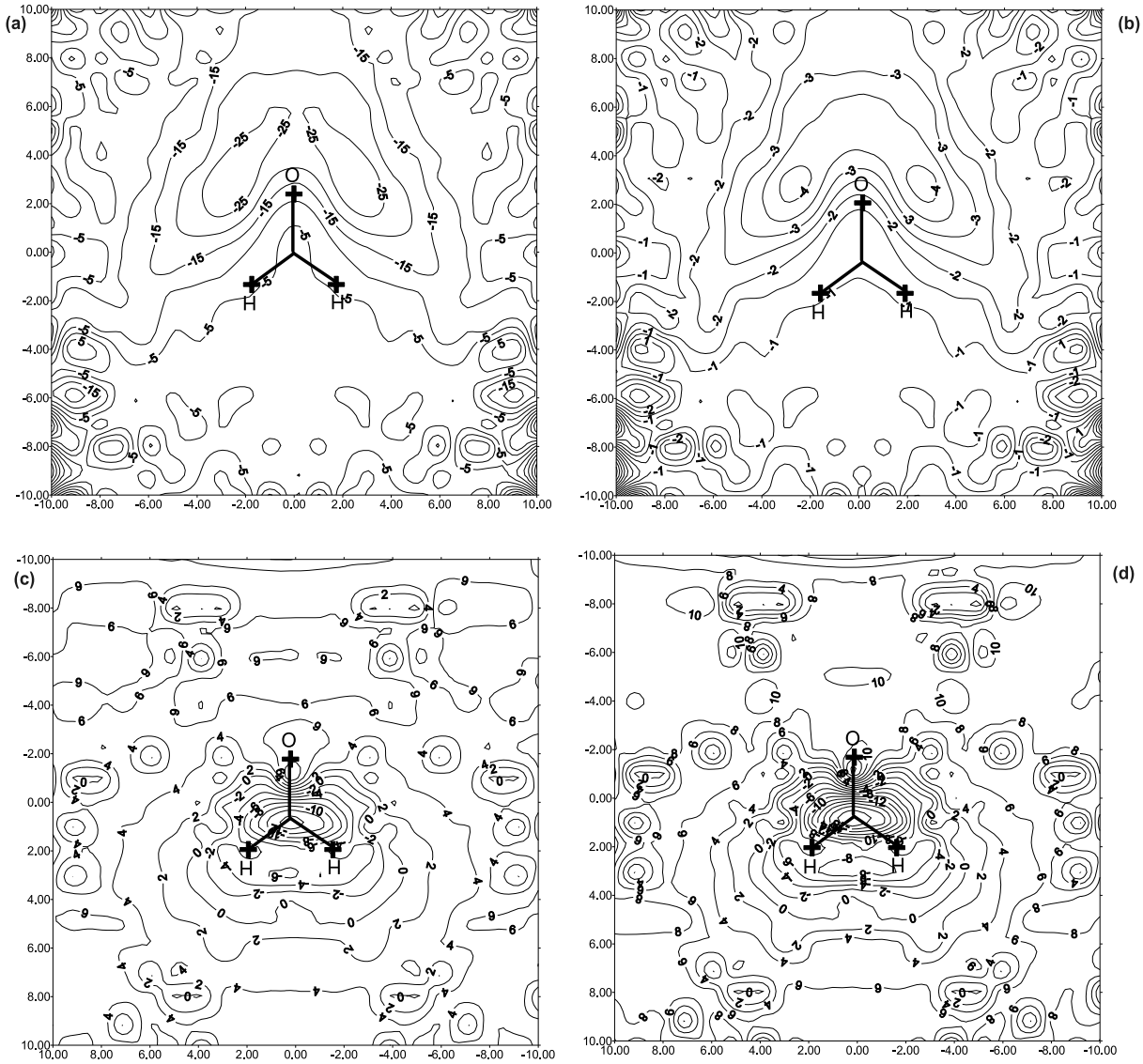

Fig. 2. Molecular polarization difference maps (in percentage) for formaldehyde at different levels of the theory, using the MP4 calculation as reference. (a) RHF/MP4 (b) MP2/MP4 (c) BLYP/MP4 (d) B3LYP/MP4.

A good description of the electronic density in the outer-most regions of the molecules is critical for good values of the polarizability. This is supported by the need to use extended basis sets including diffused functions to get good estimates [12]. Accordingly, comparison of the polarization maps may suggest that the overestimation of the polarizability obtained when using the DFT method in contrast to the Hartee-Fock and MP procedures must be due to the overestimation of the polarization in these regions. This effects is more remarkable in the perpendicular components.

Figures 4–6 show the correlations between the values of the polarization computed with different methods and the MP4. As expected, the correlation between points computed at the SCF, MP2 versus the MP4 method is good, being the fit better for points of lower polarization. In contrast, the correlation

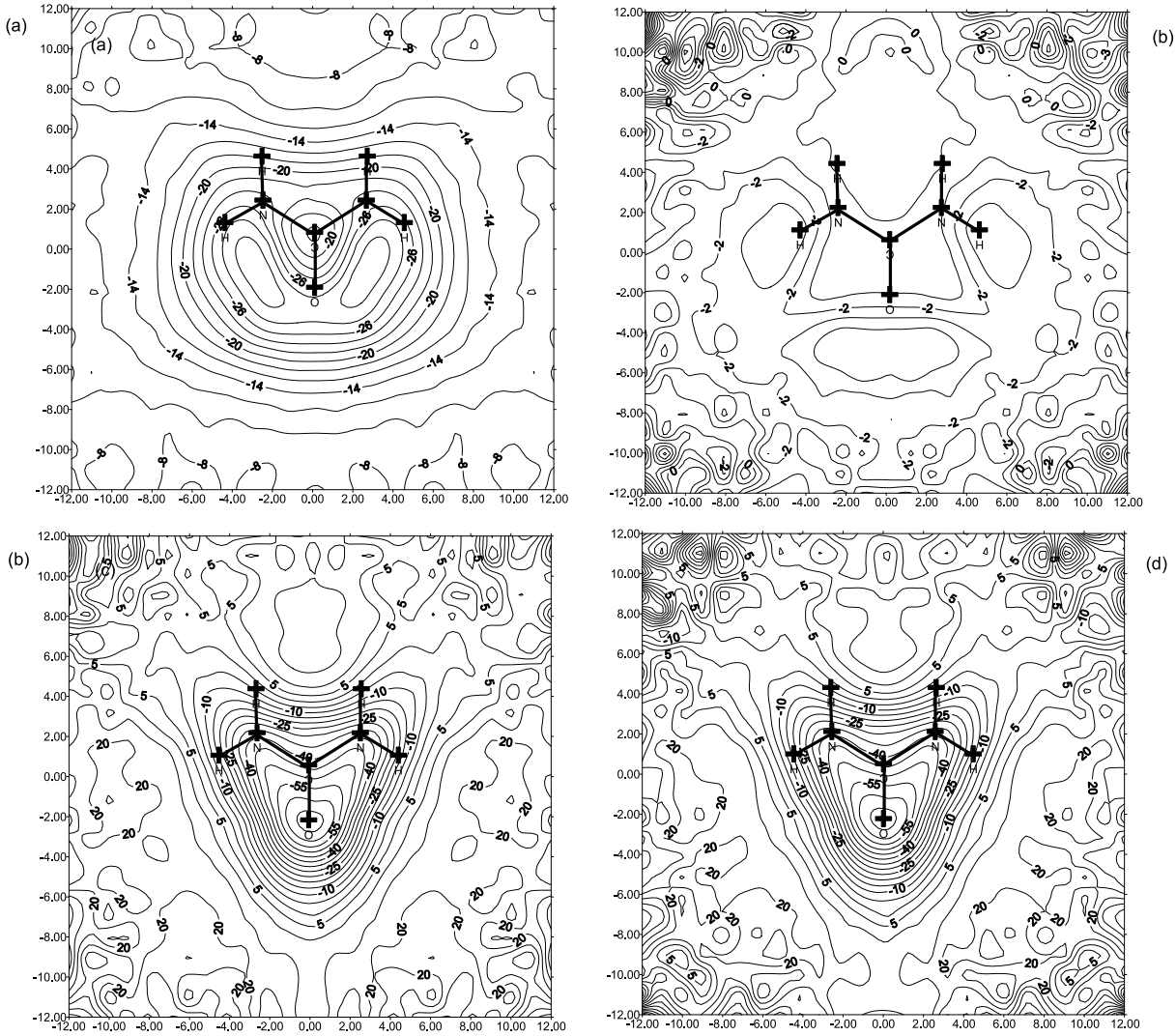

Fig. 3. Molecular polarization difference maps (in percentage) for urea at different levels of the theory using the MP4 calculation as reference. (a) RHF/MP4 (b) MP2/MP4 (c) BLYP/MP4 (d) B3LYP/MP4.

is worse in the DFT calculations. As can be seen there are points poorly computed, even some of then have the sign changed. However, most of these outsiders correspond to small values of polarization and are due to the lack of accuracy of the density function.

4. Conclusions

The aim of the present report is to assess the spatial distribution of the effects observed when using different basis sets and at different levels of the theory for the computation of molecular polarizabilities. For this purpose, we computed the molecular polarization potential of three small molecules: hydrogen cyanide, formaldehyde and urea. The results show that the DFT method overestimates the values of he polarization in the outer-most regions of the molecule, being this the reason for the overestimation of

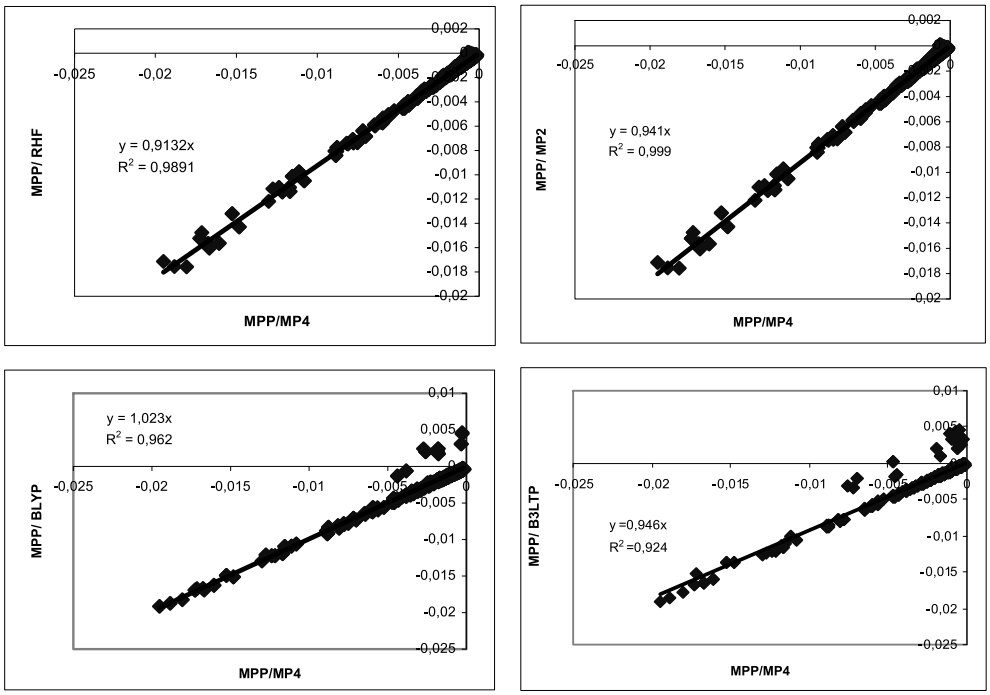

Fig. 4. Molecular polarization maps correlation plots of HCN computed at different levels using the MP4 level as reference. All the results are in a.u.

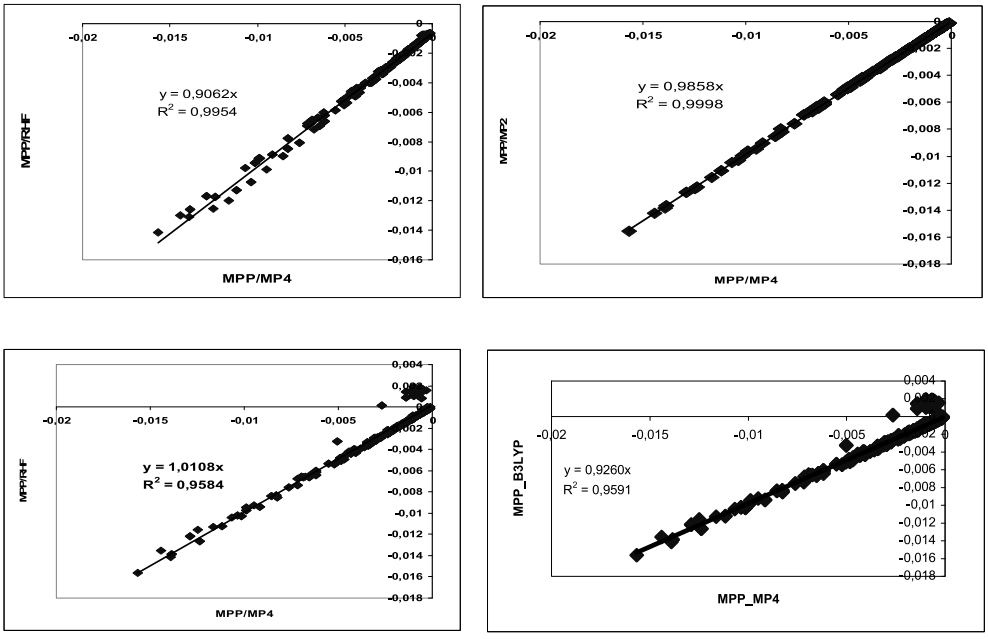

Fig. 5. Molecular polarization maps correlation plots of formaldehyde computed at different levels using the MP4 level as reference. All the results are in a.u.

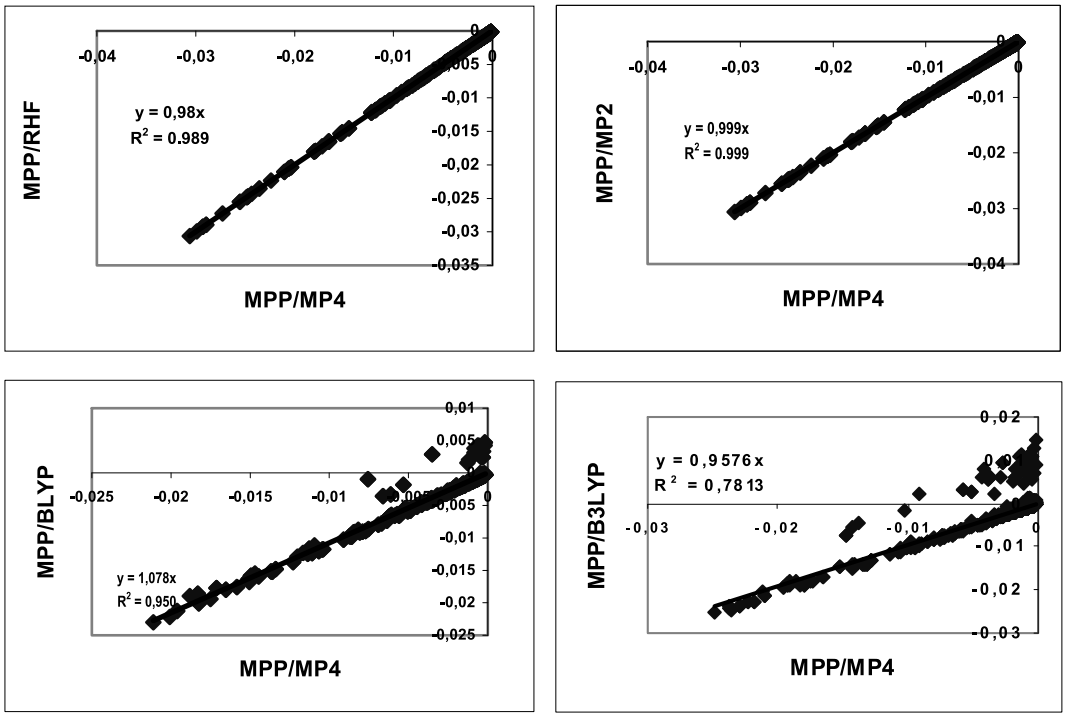

Fig. 6. Molecular polarization maps correlation plots of urea computed at different levels using the MP4 level as reference. All the results are in a.u.

polarizability estimates. Moreover, calculations carried out at the DFT level exhibit a poor correlation compared to MP4 calculations, with the BLYP functional exhibiting a better behavior. Interestingly, points outside of the correlation correspond to small values of the polarization and even there are some values with the sign changed suggesting that the accuracy of the density function is small for the electric field used in the calculations.

Acknowledgement

The Barcelona Supercomputer Center is acknowledged for a generous allocation of computer time. The Spanish Ministry of Science of Science and innovation supported this work through the project SAF2008-04943-C02-01.

References

[1] A.D. Buckingham, *Quart Rev* **13** (1959), 183.
[2] C. Hansch, W.E. Steinmetz, A.J. Leo, S.B. Mekapati, A. Kurup and D. Hoekman, *J Chem Inf Comput Sci* **43** (2003), 120.
[3] A. Grossfield, P. Ren and J.W. Ponder, *J Am Chem Soc* **125** (2003), 15671.
[4] A. Chelkowski, *Dielectric Physics*, Studies in physical and theoretical chemistry, Elsevier, Amsterdam, The Netherlands.
[5] J.E. Rice, R.D. Amos, S.M. Colwell, N.C. Handy and J. Sanz, *J Chem Phys* **93** (1990), 8828.
[6] H.D. Cohen and C.C.J. Roothaan, *J Chem Phys* **43** (1965), S34.
[7] H. Hinchliffe and D.G. Bounds, in: *Theoretical Chemistry, A Specialists Periodical Report*, R.N. Dixon and C. Thomson, eds, The Chemical Society. Bartholomeus Press, Dorking, United Kingdom, 1978.

[8] E. Scrocco and J. Tomasi, in: *Topics in Current Chemistry*, (Vol 42), Springer-Verlag, Berlin, 1973.
[9] H. Weinstein, *Int J Quantum Chem* **QBS2** (1975), 5969.
[10] P. Politzer and J.S. Murray, in: *Reviews of Computational Chemistry*, (Vol. 2), K.B. Lipskowitz, D.B. Boyd, eds, VCH Publishers, New York, 1991.
[11] A. Hinchliffe, *Modelling Molecular Structures*, John Wiley and Sons Ltd, Chichester, 1996.
[12] L. Roset, J. Rubio-Martinez and J.J. Perez, *Theor Chem Acc* (2009).
[13] R. Bonaccorsi, E. Scrocco and J. Tomasi, *Theor Chim Acta* **43** (1976), 63.
[14] M.M. Francl, *J Phys Chem* **89** (1985), 428.
[15] I. Alkorta, J.J. Perez and H.O. Villar, *J Mol Graph* **12** (1994), 3.
[16] I. Alkorta, H.O. Villar and J.J. Perez, *J Phys Chem* **97** (1993), 9113.
[17] I. Alkorta and J.J. Perez, *Int J Quantum Chem* **57** (1996), 123.
[18] I. Alkorta and J.J. Perez, *Elec J Theor Chem* **1** (1995), 26.
[19] A. Hinchliffe, J.J. Perez and H.J. Soscun Machado, *Elec J Theor Chem* **2** (1997), 325.
[20] T. Clark, J. Chandrasekhar, G.W. Spitznagel and P.R. Schleyer, *J Comp Chem* **4** (1983), 294.
[21] A.D. Becke, *Phys Rev* **A38** (1988), 3098.
[22] A.D. Becke, *J Chem Phys* **98** (1993), 5648.
[23] M.J. Frisch, G.W. Trucks, H.B. Schlegel, P.M.W. Gill, B.G. Johnson, M.A. Robb, J.R. Cheeseman, T. Keith, G.A. Peterson, J.A. Montgomery, K. Raghavachari, M.A. Al-Laham, V.G. Zakrzewski, J.V. Ortiz , J.B. Foresman, C.Y. Peng, P.Y. Ayala, W. Chen, M.W. Wong, J.L. Andres, E.S. Replogle, R. Gomperts, R.L. Martin, J. Fox, J.S. Binkley, D.J. Defrees, J. Baker, J.J.P. Stewart, M. Head-Gordon, C. Gonzales and J.A. Pople, Gaussian94, Revision B 2; Gaussian Inc Pittsburgh PA, 1995.
[24] A.L. McClellan, *Tables of Experimental Dipole Moments*, Freeman. San Francisco, 1963.
[25] Landolt-Bornstein, Atom und Molecularphysik, Springer Verlag, Berlin, Vol1 part 3, 1951.
[26] J. Applequist, J.R. Carl and K.K. Fung, *J Am Chem Soc* **94** (1972), 2953.

Journal of Computational Methods in Sciences and Engineering 10 (2010) 531–543
DOI 10.3233/JCM-2010-0341
IOS Press

Nonlinear optical properties of functionalized DNA

I. Rau[a], O. Krupka[b], J.G. Grote[c], F. Kajzar[a,d] and B. Sahraoui[d,*]
[a]*POLITEHNICA University of Bucharest, Faculty of Applied Chemistry and Materials Science, Str. Polizu nr. 1, Bucharest, Romania*
[b]*Kiev National Taras Shevchenko University, Macromolecular Chemistry Department, Volodymyrska street, 64, 01033 Kiev, Ukraine*
[c]*Air Force Research Laboratory Materials & Manufacturing Directorate, Wright-Patterson Air Force Base, 3005 Hobson Way, Dayton, OH 45433-7707, USA*
[d]*Institute of sciences and molecular technologies of Angers MOLTECH Anjou - UMR CNRS 6200 Molecular interaction nonlinear optics and structuring MINOS, 2 Bd. Lavoisier, 49045, France*

Abstract. Third-order nonlinear optical properties of functionalized deoxyribonucleic acid (DNA) are studied by optical third harmonic generation at 1 0642 nm fundamental wavelength. The studies were performed on thin films of DNA-CTMA and DNA-CTMA doped with a charge transfer molecules DR1 and with a cobalt phthalocyanine. They show that DNA, similarly as synthetic polymers, can be used as matrix for highly active NLO chromophores.

Keywords: DNA, DNA-CTMA, doped DNA-CTMA, third harmonic generation, NLO susceptibility

1. Introduction

Since the discovery of its double helice structure by J. Watson and F. Crick in 1953 [1] the deoxyribonucleic acid (DNA) became a center of interest for biologists and biochemists. It is commonly known how important role plays this supramolecule in biological life of living species. Indeed, all genetic information is encoded in the sequences of nucleobases, basic structural elements of DNA. It determines the life of living species from the very beginning. Because of their important biological role the nucleic acids and their derivatives attract a lot of attention of researchers due to their chemical structure [2–5].

Since a few years DNA attracts also an increasing interest as a potential material for applications in photonics and in electronics [6–24]. Composed from four bases, with a relatively weak π electron conjugation in phenyl rings only, DNA exhibits a large transparency range, the cut off wavelength being determined by the absorption of conjugated π electrons in phenyl rings.

One of the problems limiting practical application of pure DNA is its poor temperature stability and solubility. Pure DNA is soluble in water only. It has a characteristic, double stranded chiral structure. At about 90 centigrades the double stranded structure changes to a single stranded spiral. The pure solubility and thermal stability limited obviously its practical application, despite its great

*Corresponding author: Prof. B. Sahraoui, E-mail: bouchta.sahraoui@univ-angers.fr.

interest because of abundance in nature and biodegradability. In fact DNA is an ionic compound, with DNA charged negatively and Na^+ as counterion. K. Tanaka and Y. Okahata [6] as well as Timura et al. [7] have shown recently that the counterion Na^+ can be substituted by an amphiphile cation, leading to a more stable compound, soluble in polar organic solvents. Also its temperature stability is highly improved. DNA functionalized with hexadecyltrimetylammonium chloride (CTMA) is thermally stable up to around 230 centigrades. It shows also excellent film formation properties. Excellent light propagation properties, with propagation losses of 0.2 dB/cm was obtained. Thin films of DNA-CTMA have been successfully used as buffer layers in organic electro-optic modulators (EOM). Due to the controlled conductivity a better distribution of electric field through the EOM structure is obtained, with larger field on the EO polymer active layer. DNA-CTMA systems was also used in other kind of applications such as field effect transistors (FET's), biopolymer based organic light emitting diodes (BIOLED's) [25]. and for solar energy conversion.

However one of the problems encountered in practical application of DNA and DNA-CTMA is the already mentioned large optical gap. For applications in nonlinear optics a large π electron conjugation is required. Similarly as in synthetic polymers, this can be obtained by functionalizing DNA or DNA-CTMA systems with active NLO molecules, whose choice will depend on targeted applications.

In this paper we describe some results obtained on nonlinear optical properties of DNA-CTMA system alone, and doped with two kinds of molecules:

(i) quasi 1D charge transfer molecule
(ii) molecule with 2D π electton conjugation

in view of their application in third-order NLO optics.

2. Chemical synthesis and material processing

DNA used in our studies was provided by Chitose Institute of Science and Technology (CIST, Japan). It was obtained from salmon food waste and separated from other constituents present in. The procedure leading to obtaining pure DNA includes homogenization, enzyme treatment, protein elimination, carbon treatment, freeze drying and purification exhibits a large molecular weight. Its direct use for thin film fabrication leads to thin films with large propagation losses and inhomogeneous thickness, because of high solution viscosity. The two most prevalent techniques for molecular weight reduction of DNA are chemical treatment with enzymes and mechanical shearing. Enzyme treatment requires a precise knowledge of the DNA structure and base sequence to determine which enzyme will cut the DNA in the precise location. This technique is valuable for biologists who are studying the structure of single DNA molecules in very low quantities. However, using DNA in optoelectronic device applications requires the use of bulk material processing techniques [26]. In order to decrease the viscosity of DNA solutions the ultrasonic procedure was used [27]. After sonication the DNA aqueous solution is filtered through a nylon filter (0.45 μm) and used in next steps. Figure 1 shows the distribution of molecular weights after different time of sonication process based on measurements of the hydrodynamic volume. The chemical structure of DNA is shown (without Na^+ counterion) in Fig. 2.

As already mentioned, pure DNA is soluble only in water. In order to obtain a compound soluble in another solvent it is functionalized with a surfactant. Cationic surfactants having longer ($>$16) alkyl chains are water insoluble, and chains shorter than C16 might induce poor mechanical property of materials. DNA complexes made with longer alkyl chains might damage the double helix structure of

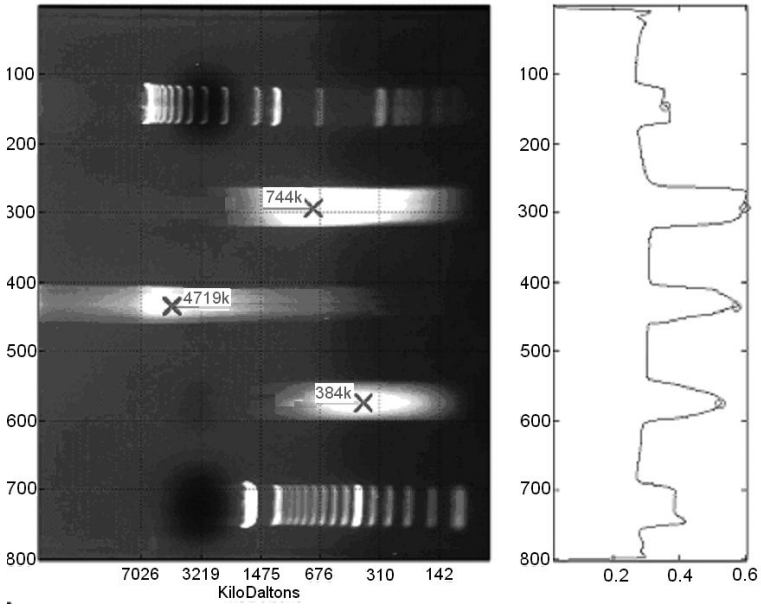

Fig. 1. Molecular weights distribution of DNA.

DNA as the strong association and aggregation among alkyl chains might break the hydrogen bonds of the nucleobase pairs [13].

The DNA-CTMA system was obtained in the following way (cf. Fig. 2). A 6 g/L solution of DNA in 18 MΩ cm deionized water at 20°C, was obtained by using a magnetic stirrer during the night. The CTMA surfactant (cf. Fig. 2), with a slightly higher concentration (6.2 g/L), was dissolved in the same conditions in 18 MΩcm deionized water. One litre of the aqueous DNA- Na^+ solution was added dropwise to 1 L of aqueous solution of cationic amphiphiles and mixed at room temperature during 6 hours. The precipitate DNA-CTMA surfactant complex was collected by vacuum filtration through a 0.4 μm nylon filter, washed with 18 MΩ cm deionized water and then dried in vacuum at 35°C.

The obtained in this way DNA-CTMA complex is insoluble in water, but soluble in such organic solvents as chloroform, benzene and a large number of alcohols including isopropanol, methanol, ethanol and butanol. These solvents are more convenient in thin film processing and device fabrication than water.

As already mentioned the DNA molecule is highly transparent with limited π electron conjugation (phenyl rings) that is why not large $\chi^{(3)}$ susceptibility is expected. Therefore to increase its NLO response we have doped DNA-CTMA with two dopants, known for the π electron delocalisation:

1. Cobalt phthalocyanine (CoPc) with an in-plane π electron delocalization
2. N-Ethyl-N-(2-hydroxyethyl)-4-(4-nitrophenylazo)aniline (Disperse Red 1, DR1)

Their chemical structures are shown in Fig. 3

Purified CoPc powders were purchased from Sigma Aldrich Co. The CoPc powders were dissolved in tetrahydrofuran (THF). Solvent (THF) was dried by distillation from purple sodium benzophenone ketyl under argon. The solvent did not produce any signal under the experimental conditions.

N,N-dimethylformamide (DMF) was vacuum-distilled off from calcium hydride just prior to use. Chlorobenzene was dried by distillation under argon.

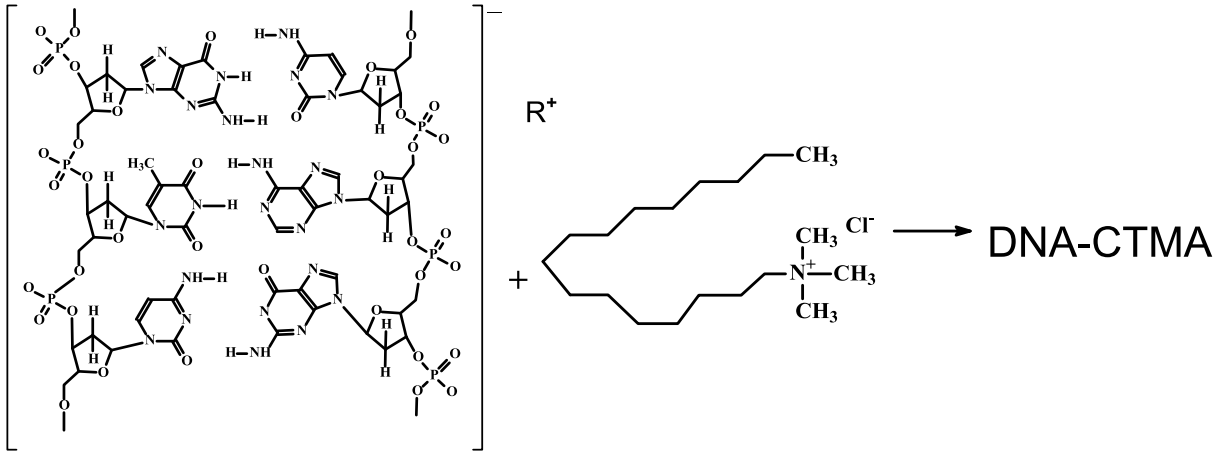

Fig. 2. Chemical structure of a DNA segment and surfactant CTMA.

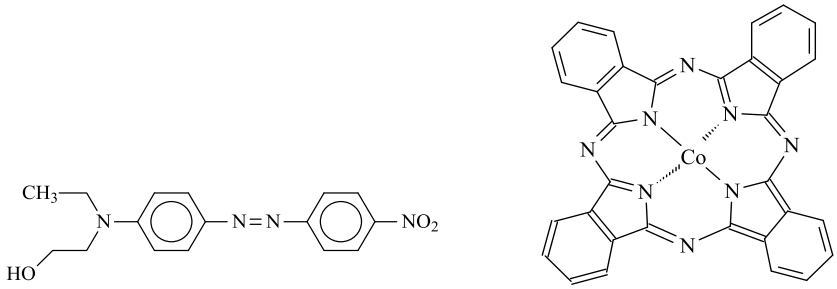

DR1 **CoPc**

Fig. 3. Chemical structure of DR1 and of CoPc.

The second chromophore, N-Ethyl-N-(2-hydroxyethyl)-4-(4-nitrophenylazo)aniline (DR1), purchased from Aldrich, was purified by a double recrystallization from an absolute methanol solution.

3. Thin film processing

For thin film fabrication solutions of DNA-CTMA and DNA-CTMA-Dye were filtered through a 0.2 μm nylon filter before the thin film deposition. The glass substrates used were carefully cleaned in a commercial surfactant using ultrasounds and then washed several times in deionized water. The cleaning procedure was ended by baking in an oven at 200°C for one hour.

On such cleaned glass substrates the spin-coating technique was used to make thin films of DNA-CTMA and DNA-CTMA doped with organic dye with controlled thickness. Immediately after the deposition the thin films were cured in oven at 80°C for one hour in order to eliminate the remaining solvent.

In preparation of functional-dye-doped DNA-CTMA films the same concentration of DNA-CTMA 80 g/L in solvent was used. For DNA-CTMA-CoPc a 2:1 chloroform:butanol solvent mixture was used and sole butanol for DNA-CTMA-DR1. Films with weight concentrations of 5%, 10%, 15% dyes in DNA-CTMA films were prepared for NLO properties studies.

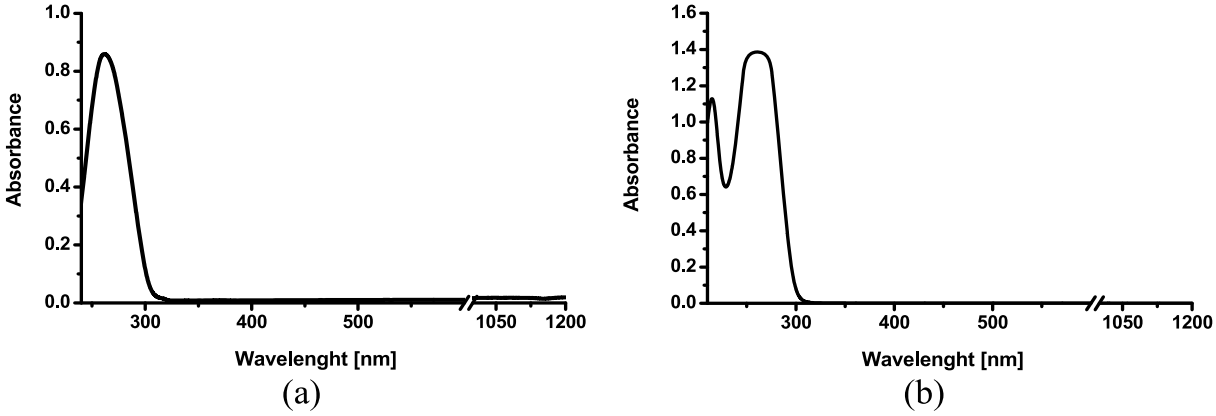

Fig. 4. Absorption spectra of pure DNA in buffer Ac (a) and of DNA-CTMA complex (b) in butanol.

4. Thin film spectroscopy

The spectroscopic UV-VIS-NIR in spectral region 210–1200 nm on solutions kept in a quartz cuve (C $= 10^{-5}$ mol/L) and on thin films deposited on BK7 glass plates were performed at room temperature with a Perkin Elmer UV/VIS/NIR Lambda 19 spectrometer.

The UV absorption spectrum of DNA is an important property for determining whether the π–π stacking of nucleobases occurs. The DNA double helix in aqueous solution has a specific absorption band extending from 220 to 300 nm with the maximum absorption wavelength $\lambda_{\max}$ of 260 nm, characteristic for phenyl rings as seen in Fig. 4. The DNA-surfactant complex exhibits the same absorption, with $\lambda_{\max}$ at 260 nm, assigned as the characteristic absorption of the nucleobases in DNA. However, our data indicate that the absorption coefficient is not the same as compared to the aqueous DNA. The absorption coefficient for all the DNA-surfactant complexes is larger than that of the aqueous DNA solution. It indicates possible changes, to some degree, in the π–π stacking structure of the DNA strands. Also a little modification of the absorption band is observed, most likely due to the different environment.

Figure 5 shows solution absorption spectra of DNA-CTMA and DNA-CTMA-DR1 (5% DR1 concentration) and DR1 alone. DR1 is a well known as 1D charge transfer molecule, with electron donating (CH_3) and electron accepting (NO_2) end groups, separated by a π electron transmitter, composed of two phenyl rings and –N=N– segment (cf. Fig. 3). It is particularly used for second order NLO effects, but because of the strong π electron conjugation it is also interesting for third order NLO effects. The UV absorption of nucleobases at around 260 nm is clearly seen in the first two absorption spectra (curves 1 and 2 in Fig. 5). As already mentioned, this strong absorption band corresponds to the $\pi - \pi^*$ transition of electrons of C = C bond of DNA bases. The second absorption band at around 490 nm in DNA-CTMA-DR1 (2) is similar to that of pure DR1 (spectrum 3) showing very similar solvent influence.

The chemical structure of another doping molecule used, i.e. the cobalt phthalocyanine CoPc ($C_{32}H_{16}N_8Co$) is also shown in Fig. 3. It is a planar molecule with two-dimensional (2D) π electron conjugation. As discussed by Kajzar [28] such molecules exhibit smaller cubic susceptibilities compared to those with 1D π electron delocalization. The central metal atom (Co) is connected with four ligands (the benzene ring plus the pyrrole ring) by nitrogen bridges. In CoPc there are 18 π electrons surrounding the central metal atom characterized by a large delocalization, as it is seen from the value of the optical gap. The UV-VIS-NIR absorption spectra of DMF solutions of CoPc (1), DNA-CTMA complex (2) and of a guest-host system DNA-CTMA-CoPc (3) are displayed in Fig. 6. We notice that

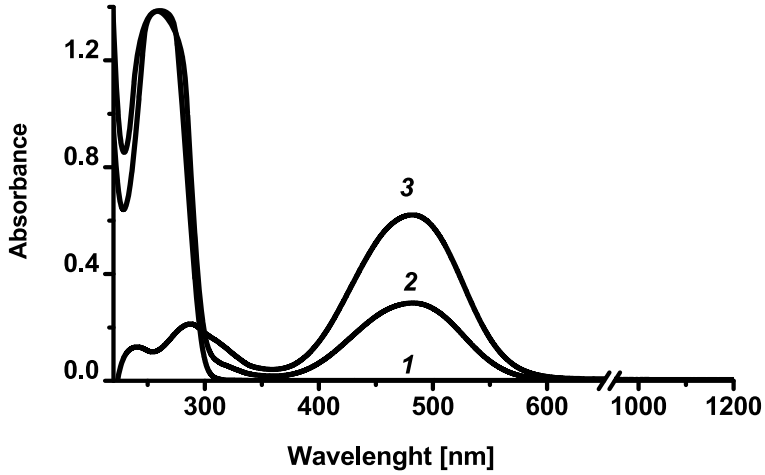

Fig. 5. Absorption spectra of DNA-CTMA (curve 1), DNA-CTMA-DR1 (5%) (curve 2) and DR1 alone (curve 3) in solution.

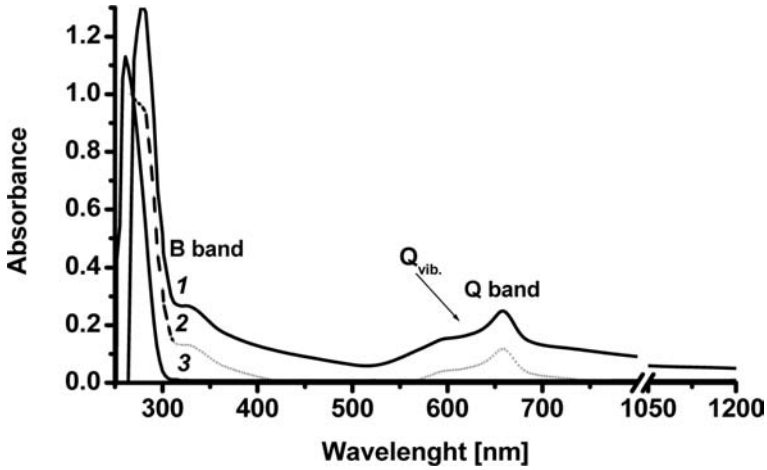

Fig. 6. Absorption spectra of CoPc (curve 1), DNA-CTMA-CoPc (curve 2) and DNA-CTMA (curve 3) in DMF.

the optical absorption spectra of CoPc exhibit two major absorption regions called Q and B bands. The single, sharp absorption peak (near 657 nm) in the visible region (CoPc solution) is associated with the Q band. The small absorption peak in Q band of CoPc is assigned as a vibrational component [29] and marked Q_{vib}.

The strongly broadened peak near 300 nm in CoPc solution spectrum is due to both a_{2u} to e_g (B_1) and b_{2u} to e_g (B_2) transitions and corresponds to the B (Soret) band transition. Due to overlapping the width of the B band is significantly greater than that of Q band. Both B and Q bands are due to the $\pi - \pi$* transitions [4,30–34]. In the spectral region of 400–600 nm, the ground-state absorption of CoPc is very weak. However at this wavelength range the metal phthalocyanines exhibits a quite important excited state absorption, exploited in optical power limiting [35,36]. The maximum of the excited-state absorption is located at the wavelength of around 500 nm, which is just the location of the minimum of the ground-state absorption [8,37]. The absorption peak of DNA-CTMA-CoPc at 278 nm is blueshifted with respect to DNA-CTMA and exhibits a small shoulder (near 308 nm), which comes from the B-band

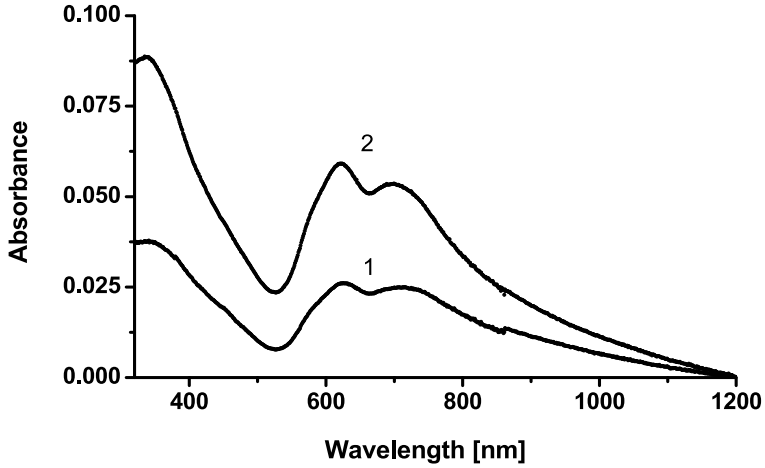

Fig. 7. Absorption spectra of DNA-CTMA-CoPc deposited on glass substrates and doped with 5% (1) and 10% (2) of CoPc.

of CoPc. Apparently it is interaction effect with the DNA matrix.

The absorption spectra of thin films of DNA-CTMA, doped with 5% and 10% of CoPc, deposited on glass substrates, are shown in Fig. 7. Due to the interaction with the matrix a significant broadening of the Q and B bands is observed. The intensity of vibronic Q bands is even reversed, as compared to the solution case. It shows that the linear spectroscopic properties of DNA-CTMA-CoPc depend on the intermolecular interactions of CoPc molecules with the matrix. These interactions are influenced by the peripheral substituent in DNA-CTMA [38].

5. Nonlinear optical properties

The nonlinear optical properties studies of pure and doped DNA-CTMA systems were performed by using the optical third harmonic generation (THG). This technique allows to measure the fast, electronic part of cubic susceptibility $\chi^{(3)}(-3\omega;\omega,\omega,\omega)$ where ω is the fundamental beam frequency. The measurements were done using a Q switched Nd:YAG laser, operating at 1 064 nm fundamental wavelength with 13 ns pulse duration and 10 Hz operation rate. The studied films, deposited on BK7 glass substrates, were mounted on a rotation stage, kept in vacuum in order to avoid air contribution [39] and the harmonic intensities were collected as function of the incidence angle, when rotating thin film around an axis perpendicular to the beam propagation direction and coinciding with it.

The experimental setup used is shown schematically in Fig. 8. The fast Si photodiode, located just behind the mirror of laser cavity, is used for triggering boxcar and for correction of fundamental beam intensity fluctuations. The half wave plate ($\lambda/2$) was used to change easily the fundamental beam polarization. As the measured samples are isotropic vertical (s) polarization was used for both incident fundamental and the outcome harmonic beams. Filter F1 transmits fundamental beam whereas filter F2 the harmonic one.

The THG intensities were calibrated with THG measurements on a high purity silica slab done at the same conditions. The THG intensity from a system: substrate + thin film is given by [40].

$$I_{3\omega}(\theta) = \frac{64\pi^4}{c^2}\left|\frac{\chi^{(3)}}{\Delta\varepsilon}\right|_f^2 \left| e^{i(\varphi_\omega^s+\varphi_{3\omega}^f)}\left[T_1\left(1-e^{-i\Delta\varphi_s}\right)+\rho T_2 e^{i\Phi}\left(e^{i\Delta\varphi_f}-1\right)\right]\right|^2 I_\omega^3 \tag{1}$$

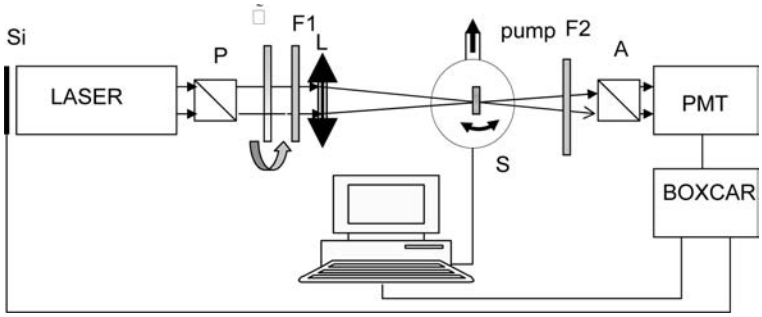

Fig. 8. Schematic presentation of THG experimental setup. LASER – Nd:YAG, 13 ns, 10 Hz, 1064 nm, $\lambda/2$ –half wave plate, P – polarizer, L – convergent lens, F1, F2 – filters (with selective filter: 355 nm), S – rotating sample stage, Si – fast Si photodiode for triggering and laser power control, PMT – photomultiplier tube.

where the bulk susceptibility $\chi^{(3)}(-3\omega;\omega,\omega,\omega)$ is related to the molecular hyperpolarizability $\gamma(-3\omega;\omega,\omega,\omega)$ through the following relation

$$\chi^{(3)}(-3\omega;\omega,\omega,\omega) = NF\gamma(-3\omega;\omega,\omega,\omega) \tag{2}$$

with N being the molecules number density

$$N = \frac{dN_A}{M} \tag{3}$$

and d is the material density. In Eq. (3) N_A is the Avogadro's number and M is the molecular mass, respectively.

In Eq. (2) F is the global local field factor, which for a THG process is given by

$$F = f_{3\omega}(f_\omega)^3 \tag{4}$$

The factors $f_{\omega,3\omega}$ in Eq. (4) take account of the screening of external AC optical field with fundamental (ω) or harmonic (3ω) frequency by the molecular field. It depends on the symmetry of the molecule under consideration. For molecules with a spherical symmetry it is given by

$$f_{\omega,3\omega} = \frac{n^2_{\omega,3\omega} + 3}{2} \tag{5}$$

where $n_{\omega,3\omega}$ is the medium index of refraction at $\omega(3\omega)$ requency.

$\Delta\varepsilon$ in Eq. (1) is the dielectric constant dispersion of the medium

$$(\Delta\varepsilon)_{s,f} = \varepsilon^{s,f}_{3\omega} - \varepsilon^{s,f}_{\omega} \tag{6}$$

with $\varepsilon = n^2$. The superscripts s and f refer to the substrate (s) and the thin film (f), respectively

The phases appearing in Eq. (1) are given by

$$\varphi^{s,f}_{\omega,3\omega} = \frac{6\pi l}{\lambda} n^{s,f}_{\omega,3\omega} \cos\theta^{s,f}_{\omega,3\omega} \tag{7}$$

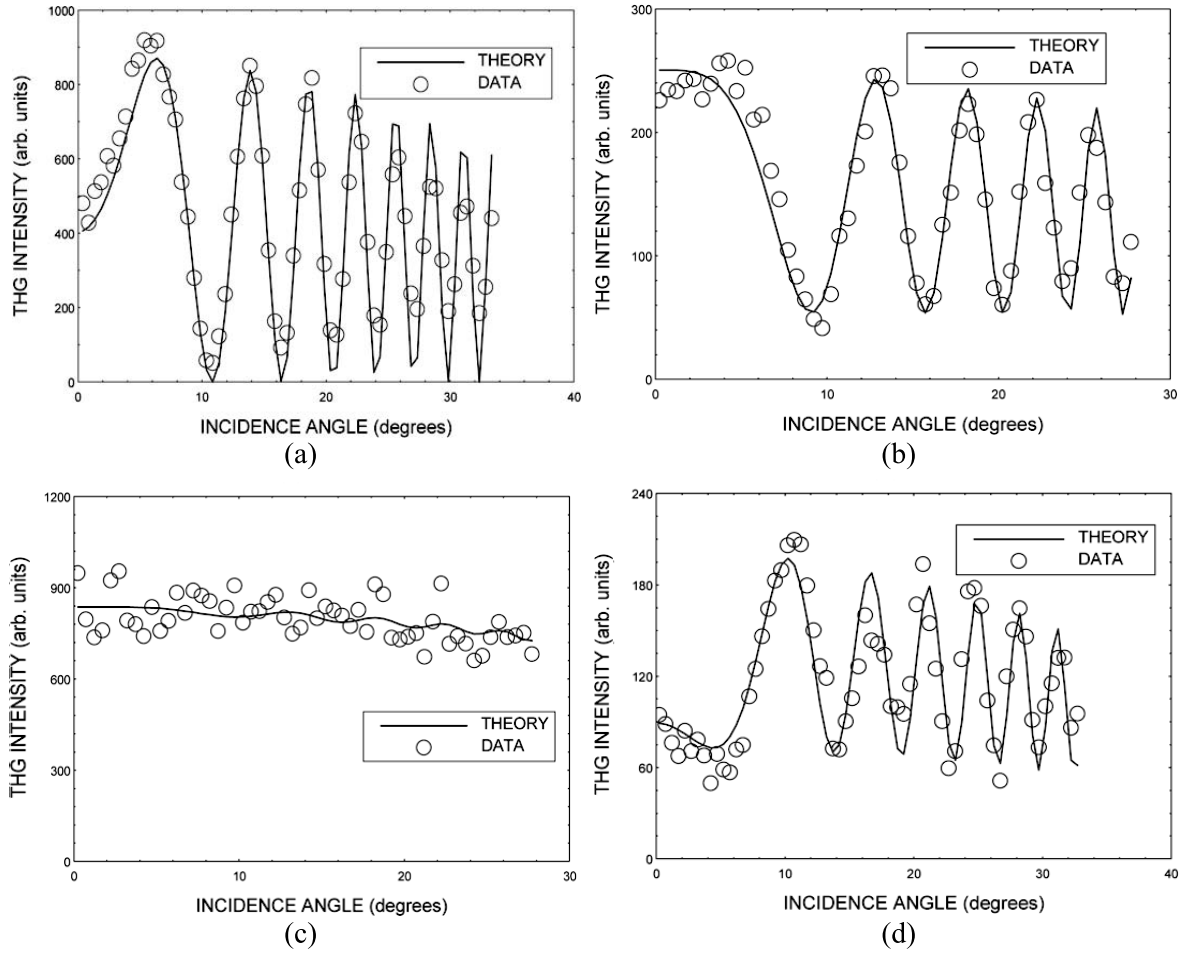

Fig. 9. Measured (open circles) and calculated (solid lines) THG intensities for the glass substrate (a), deposited thin films on glass substrates of: DNA-CTMA (b), DNA-CTMA-DR1 (5%) (c) and DNA-CTMA-CoPc (5%) (d). The intensities don't match with actual THG responses as they are not corrected here for the fundamental beam attenuation by used filters.

for waves with frequency ω or 3ω in medium s or f, respectively. $\theta^{s,f}_{\omega,3\omega}$ are propagation angles in the given (s or f) medium and for waves with ω, 3ω of requencies and l is the medium thickness. T_1 and T_2 in Eq. (1) are factors arising from transmission and boundary conditions (cf. Ref. [41]).

$$\rho = \left\{ \frac{\chi^{(3)}}{\Delta\varepsilon} \right\}_f \Big/ \left\{ \frac{\chi^{(3)}}{\Delta\varepsilon} \right\}_s \tag{8}$$

Φ is the phase of the thin film susceptibility (or difference with that of substrate if not zero), I_ω is the fundamental beam intensity and the phase mismatches $\Delta\varphi$ are given by

$$\Delta\varphi_{s,f} = \varphi^{s,f}_{\omega} - \varphi^{s,f}_{3\omega} \tag{9}$$

with $\varphi^{s,f}_{\omega,3\omega}$ given by Eq. (7).

The collected incidence angle dependent third harmonic intensities were least – square fitted with Eq. (1). Figure 9 displays the measured (open circles) and the fitted (continuous line) THG intensities

Table 1
Thin film thicknesses (in μm), refractive indices, coherence lengths and third order nonlinear optical susceptibilities $\chi^{(3)}(-3\omega;\omega,\omega,\omega)$ of studied materials

Sample	Thickness [μm]	Refractive index n_ω	Coherence length [μm]	$\chi^{(3)}(-3\omega;\omega;\omega;\omega)$ in 10^{-14} [esu]
DNA-CTMA	0.367	1.488[a]	7.4[a]	11.5 ± 0.1
DNA-CTMA-DR1 (5%)	3.484	1.488[b]	7.4	155 ± 16
DNA-CTMA-DR1 (10%)	4.060	1.488	7.4	69 ± 7
DNA-CTMA-DR1 (15%)	3.484	1.488	7.4	85 ± 9
DNA-CTMA-CoPc (5%)	0.149	1.488	7.4	30 ± 3
DNA-CTMA-CoPc (10%)	0.162	1.488	7.4	19 ± 2
DNA-CTMA-CoPc (15%)	0.168	1.488	7.4	17 ± 2
Glass plate	1041	1.50664	5.62	2.1 ± 0.2
silica	1010	1.44967	6.71	1.43 ± 0.14[c]
PMMA		1.4795[d]	8.28[d]	3.2[d,e]

[a] Grote et al. [42].
[b] assumed (see text).
[c] Gubler and Bosshard [43].
[d] Morichere et al. [45].

from the glass plate alone (a), glass plate with DNA-CTMA (b), glass plate with DNA-CTMA-DR1 (c) and DNA-CTMA-CoPc (d) thin films. A good agreement is observed between the calculated and measured THG intensities. For the glass substrate alone, the Maker fringes, due to the interference of the free and bound waves in the glass slab, can be seen. This is due to the fact that the glass slab thickness (1 040 nm) is much larger than the coherence length for this material (5.62 μm). In Figs 9.b, 9.c and 9.d we can see a monotonically varying, with incidence angle, contribution from thin films of DNA-CTMA, DNA-CTMA-DR1 and DNA-CTMA-CoPc to that of substrate. In all cases these contributions are decreasing with the incidence angle due to the envelope function (less light coupled into thin film when increasing the incidence angle). This behaviour is due to the fact that the thin film thickness is smaller than the coherence length. It is also seen that in the case of DR1 and CoPc doped films (Figs 9.c, 6.29.d) the thin film contribution is more important than in the case of undoped film (Fig. 9.b).

In the fitting procedure, the values of the refractive index for DNA-CTMA, reported by Grote et al. [42] were used. For doped films we used the same refractive indices as for DNA-CTMA. Indeed, for the relatively low dopant concentration we do not expect a significant change of the refractive index in the doped film. Also, in the case of THG in thin films, the harmonic intensities do not depend on the difference of refractive indices, but on their sum. A correction for the absorption at the harmonic wavelength in doped films was taken into account by introducing a complex index of refraction in the calculations, with imaginary part calculated from the optical absorption spectrum. For silica and BK7 glass the tabulated values for the refractive indices were used and the slab thickness was determined from the fit. Independent THG measurements on a clean glass slab were also performed to calibrate the data with the THG measurements on a silica slab.

The values of third order $\chi^{(3)}(-3\omega;\omega,\omega,\omega)$ susceptibility of the investigated materials derived from THG measurements are listed in Table 1 and compared with those of silica, BK7 glass and of a common synthetic polymer which is polymethyl metacrylate (PMMA).

For the calibration with silica we used the value reported recently by Gubler and Bosshard [43] ($\chi^{(3)}(-3\omega;\omega,\omega,\omega) = 1.43 \pm 0.14 \times 10^{-14}$ esu), which is about two times smaller than the previously reported one [44]. In the case of DNA-CTMA films we observe the value of THG susceptibility about one order of magnitude larger than that for silica. It is also larger as for the other commonly used

polymer PMMA [45] (cf. Table 1.). This difference may be well accounted for by the presence of highly polarizable conjugated π electrons in DNA.

A significant increase of $\chi^{(3)}(-3\omega;\omega,\omega,\omega)$ susceptibility is observed for DNA-CTMA-DR1 system. The largest, relative increase (with respect to the number of doping molecules) is observed at 5% doping level. Similar behaviour at low doping level is observed also in the case of DNA-CTMA-CoPc system. The largest value is obtained for films doped with 5% of CoPc, although the increase is much less significant than in the case of doping with DR1. The $\chi^{(3)}(-3\omega;\omega,\omega,\omega)$ value of DNA-CTMA-DR1 (5%) is almost five times larger than for DNA-CTMA-CoPc (5%). In the case of both studied systems we observe a decrease of NLO susceptibility for higher dopant concentration (10% and 15%), although still significantly larger values than for undoped systems. Possible explanations of these effects are:

(i) interaction with matrix (DC Stark effect)
(ii) large local field factor

We note here that the fact we observe the same effect at low doping level for both dopants (DR1 and CoPc) shows that it isn't an experimental artifact. The fact that we observe largest value of cubic susceptibility for DNA-CTMA-DR1 than for DNA-CTMA-CoPc, at the same doping level may be well accounted for by the dimensionality aspects of π electron delocalization, resulting in smaller molecular hyperpolarizability γ of CoPc (2D π electron delocalization) with respect to DR1 (1D π electron delocalization) [28] and by a possible two photon resonance contributions to $\chi^{(3)}(-3\omega;\omega,\omega,\omega)$ susceptibility in both dopants.

6. Conclusions

The present study shows that the used biopolymer DNA, and particularly the DNA-CTMA system is an interesting counterpart of synthetic polymers for application in photonics. Similarly as synthetic polymers it can be functionalized to get an active NLO material. The recent study shows that the chemical stability of doping molecules is better in DNA matrix than in synthetic polymer. A one order of magnitude smaller kinetic decay were observed [46]. An important advantage of this polymer is its biodegradability. Due to the peculiar chiral structure of DNA two types of doping are possible:

(i) intercalation (inside the helix),
(ii) doping outside the helix.

Intercalation takes place at low doping level [47], whereas when the space inside the helices is filled doping molecules will be located in intermolecular space. Obviously the chemical environment is different in these two cases, so consequently both the local field factor and the electronic structure of doping molecules may be different at low and higher doping levels what can explain the observed behaviour of $\chi^{(3)}(-3\omega;\omega,\omega,\omega)$ susceptibility at low doping concentration in case of both dopants used: DR1 and CoPc. In favour of the existence of specific environment in DNA based biopolymers is the observed three orders of magnitude faster refractive index grating formation as compared to synthetic polymers [48].

Other studies could subject of interesting investigation is the *fonctionalisation of DNA with octopolar molecules [49]* and the mixtures of DNA with p – *Conjugation Across the tetrathiafulvalene Core for NLO applications [50]*.

Acknowledgments

The authors would like to thank the US Air Force European Office for Aerospace Research and Development (London) for the financial support of this research.

References

[1] J.D. Watson and F.H.C. Crick, *Nature* **171** (1953), 737.
[2] X. Dou, T. Takama, Y. Yamaguchi, K. Hirai, H. Yamamoto, S. Doi and Y. Ozaki, *Appl Opt* **37** (1998), 759.
[3] S. Asayama, A. Maruyama, Ch.-S. Cho and T. Akaike, *Bioconjugate Chem* **8** (1997), 833.
[4] J.P. Jacobsen, J.B. Pedersen and D.E. Wemmer, *Nucleic Acid Research* **23** (1995), 753.
[5] L.F. Hansen, L.K. Jensen and J.P. Jacobsen, *Nucleic Acid Research* **24** (1996), 859.
[6] K. Tanaka and Y. Okahata, *J Am Chem Soc* **118** (1996), 10679.
[7] H. Kimura, S. Machida, K. Hone and Y. Okahata, *Polymer Journal* **30** (1998), 708.
[8] A. Watanuki, J. Yoshida, S. Kobayashi, H. Ikeda and N. Ogata, *Proc SPIE* **5724** (2005), 234.
[9] L. Wang, G. Zhang, S. Horinouchi, J. Yoshida and N. Ogata, *Nonl Opt* **24** (2000), 63.
[10] Y. Kawabe, L. Wang, T. Koyama, S. Horinouchi and N. Ogata, *Proc SPIE* **4106** (2000), 369.
[11] Y. Kawabe, L. Wang, S. Horinouchi and N. Ogata, *Adv Mater* **12** (2000), 1281.
[12] T. Koyama, Y. Kawabe and N. Ogata, *Proc SPIE* **4464** (2002), 248.
[13] L. Wang, J. Yoshida, N. Ogata, S. Sasaki and T. Kamiyama, *Chem Mater* **13** (2001), 1273.
[14] L. Wang, G. Zhang, S. Horinouchi, J. Yoshida and N. Ogata, *Nonl Opt* **24** (2000), 63.
[15] L. Wang, M. Fukushima, J. Yoshida and N. Ogata, *Nanotechnology toward the organic photonics*, GooTech Ltd., Chitose-shi, Japan, 2002, pp. 379–384.
[16] J. Yoshida, L. Wang, S. Kobayashi, G. Zhang, H. Ikeda and N. Ogata, *Proc SPIE* **5351**, (2004), 260.
[17] L. Wang, K. Ishihara, H. Izumi, M. Wada, G. Zhang, T. Ishikawa, A. Watanabe, S. Horinouchi and N. Ogata, *Proc SPIE* **4905** (2002), 143.
[18] H.-W. Fink, H. Schmid, E. Ermantraut and T. Schulz, *J Opt Soc Am* **A 14**, (1997), 2168.
[19] H.A. Wagenknecht, *Chemie in Unserer Zeit* **36** (2002), 318.
[20] L. Tang, Z. Sun, J. Guo and Z. Wang, *Chinese Opt Letters* **4** (2006), 101.
[21] G. Zhang, H. Takahashi, L. Wang, J. Yoshida, S. Kobayashi, S. Horinouchi and N. Ogata, *Proc SPIE* **4905** (2002), 375.
[22] J.G. Grote, N. Ogata, D.E. Diggs and F.K. Hopkins, *Proc SPIE* **4991** (2003), 621.
[23] P. Gupta, P.P. Markowicz, K. Baba, J. O'Reilly, M. Samoc, P.N. Prasad and J.G. Grote, *J Appl Phys Lett* **88** (2006), 213109.
[24] A.J. Steckl, *Nature Photonics* **1** (2006), 3.
[25] P.P. Yaney, E.M. Heckman and J.G. Grote, *Proc SPIE* **6646** (2007), 664601.
[26] J.G. Grote, J.A. Hagen, J.S. Zetts, R.L. Nelson, D.E. Diggs, M.O. Stone, P.P. Yaney, E. Heckman, C. Zhang, W.H. Steier, A.K.-Y. Jen, L.R. Dalton, N. Ogata, M.J. Curley, S.J. Clarson and F.K. Hopkins, *J Phys Chem B* **108** (2004), 8584.
[27] E. Heckman, J. Hagen, P. Yaney, J. Grote and F. Hopkins, *Appl Phys Lett* **87** (2005), 211115.
[28] F. Kajzar, *Nonl Optics* **5** (1993), 329.
[29] D.R. Tackley, G. Dent and W.E. Smith, *Phys Chem Chem Phys* **3** (2001), 1419.
[30] S. Senthilarasu, R. Sathyamoorthy, S. Lalitha, A. Subbarayan and K. Natarajan, 82, (2004), 179.
[31] M.M. El-Nahass, H.M. Zeyada, M.S. Azis and N.A. El-Ghamaz, *Opt Mat* **27** (2004), 491.
[32] C.C. Leznoff and A.B. P. Lever, Phthalocyanines, Properties and Applications, *VCH Publishers, Inc* (1989).
[33] B. Derkowska, M. Wojdyła, R. Czaplicki, Z. Sofiani, W. Bała and B. Sahraoui, *Opt Commun* **274** (2007), 206.
[34] M. Wojdyła, M. Rębarz, P. Dalasiński, W. Bała, Z. Łukasiak, B. Derkowska and B. Sahraoui, Optical properties of metallophthalocyanines, Alq3 and perylene derivatives investigated by photoluminescence, absorption, reflection, and photomodulated spectroscopy, *Trends In Optical Materials Research, chapter 1*, pp. 1–54, Editor: Owen G. Gardens, Nova Science Publisher Inc. 2006.
[35] L.W. Tutt and T.F. Boggess, *Prog Quant Electron* **17** (1993), 299.
[36] J.D. Swalen and F. Kajzar, *Nonl Optics* **27** (2001), 13.
[37] C. Li, L. Zhang, M. Yang, H. Wang and Y. Wg, *Phys Rev A* **49** (1994), 1149.
[38] B. Derkowska, K. Jaworowicz, O. Krupka, M. Karpierz, M. Wojdyła, W. Bała, F. Kajzar and B. Sahraoui, *J Appl Phys* **101** (2007), 083112.
[39] F. Kajzar and J. Messier, *Phys Rev A* **32** (1985), 2352.
[40] F. Kajzar, J. Messier and C. Rosilio, *J Appl Phys* **60** (1986), 3040.

[41] F. Kajzar, Third Harmonic Generation, in: *Characterization Techniques and Tabulations for Organic Nonlinear Optical Materials*, M. Kuzyk and C. Dirk, eds, Marcel Dekker, Inc., New York 1998, pp. 767–839.
[42] J. Grote, D. Diggs, R. Nelson, J. Zetts, F. Hopkins, N. Ogata, J. Hagen, E. Heckman, P. Yaney, M. Stone and L. Dalton, *Mol Cryst Liq Cryst* **426** (2005), 3.
[43] U. Gubler and C. Bosshard, *Phys Rev B* **61** (2000), 10702.
[44] B. Buchalter and G.R. Meredith, *Appl Opt* **21** (1982), 3221.
[45] D. Morichere, M. Dumont, Y. Levy, G. Gadret and F. Kajzar, *Proc SPIE* **1560** (1991), 214.
[46] M. Moldoveanu, A. Meghea, R. Popescu, J.G. Grote, F. Kajzar and I. Rau, *Mol Cryst Liq Cryst* in print.
[47] G. Pawlik, A.C. Mitus, J. Mysliwiec, A. Miniewicz and J.G. Grote, *Chemical Physics Letters* **484** (2010), 321.
[48] A. Miniewicz, A. Kochalska, J. Mysliwiec, A. Samoc, M. Samoc and J.G. Grote, *Appl Phys Lett* **91** (2007), 04118.
[49] B. Derkowska, J.C. Mulatier, I. Fuks, B. Sahraoui, X. Nguyen Phu and C. Andraud, *Journal of Optical American Society of America B* **18**(5) (2001), 610–616.
[50] N. Terkia-Derdra, R. Andreu, M. Sallé, E. Levillain, J. Orduna, J. Garin, E. Orti, R. Viruela, R. Pou-Amérigo, B. Sahraoui, A. Gorgues, J.-F. Favard and A. Riou, *Chemistry – A European Journal* **6**(7) (2000), 1199–1223.

Journal of Computational Methods in Sciences and Engineering 10 (2010) 545–553
DOI 10.3233/JCM-2010-0342
IOS Press

Effect of magnetic dipole coupling on optical binding energies between molecules

A. Salam*
Department of Chemistry, Wake Forest University, Winston-Salem, NC 27109-7486, USA

Abstract. Within the framework of molecular quantum electrodynamics, the method of induced multipole moments is used to compute the laser-induced intermolecular energy shift between an electric dipole polarizable molecule and a magnetic dipole susceptible molecule, and between two magnetic dipole polarizable molecules. The physical viewpoint adopted in the calculation is one in which an applied electromagnetic field induces molecular multipole moments in each entity, which couple via the retarded resonant multipole-multipole interaction tensors. Expectation values taken over the ground electronic states of the material system, and a radiation field state containing n photons, leads directly to the coupling energy. Results are obtained for external radiation in a fixed orientation relative to the internuclear axis, with a thorough polarization analysis being carried out for linearly and circularly polarized radiation propagating in directions parallel and perpendicular to the separation distance vector, as well as for a freely tumbling molecular pair. Comparison is made with field-induced discriminatory energy shifts occurring between optically active molecules – which also involve coupling of electric and magnetic dipole moments, and the leading contribution to optical binding forces arising within the electric dipole approximation.

1. Introduction

The late Professor Stanislaw Kielich made many seminal contributions to the study of light scattering by molecules, and intermolecular interactions, inspiring numerous workers in these fields [1,2]. His legacy continues today, especially with the continuing advances in the generation of coherent sources of laser light, which have led to ever more novel nonlinear and quantum optical phenomena being proposed and/or detected [3–5].

An interesting recent process that has been much studied both theoretically and experimentally is the modification of the energy shift between a pair of coupled molecules by an intense beam of laser radiation – often more commonly known as the optical binding energy [6–10]. An early calculation of this effect within the framework of molecular quantum electrodynamics [11,12] was carried out by Thirunamachandran [6]. For a pair of interacting neutral electric dipole polarizable molecules subject to an external electric field, the change in energy shift was evaluated using fourth-order diagrammatic perturbation theory, and found to be

$$\Delta E_{dyn} = \frac{I}{\varepsilon_0 c}\bar{e}_i^{(\lambda)}(\vec{k})e_j^{(\lambda)}(\vec{k})\alpha(A;k)\alpha(B;k)ReV_{ij}(k,\vec{R})\cos(\vec{k}\cdot\vec{R}), \tag{1}$$

where $I = n\hbar c^2 k/V$ is the irradiance of the incident beam, which contains n photons of mode $(\vec{k},\lambda)$, where $\vec{k}$ is the wavevector, and λ is the polarization index, whose unit electric vector is $\bar{e}^{(\lambda)}(\vec{k})$, V is

*Corresponding author. E-mail: salama@wfu.edu.

the volume of quantization, and Latin subscripts denote Cartesian tensor components, with an implied summation convention for repeated indices. The quantity $\alpha(\xi;k)$ is the isotropic dynamic electric dipole polarizability of species $\xi = A,\, B$

$$\alpha(\xi;k) = \frac{2}{3}\sum_r \frac{|\vec{\mu}^{0r}(\xi)|^2}{E_{r0}^2 - (\hbar ck)^2}, \tag{2}$$

where $\vec{\mu}^{0r}(\xi)$ is the transition electric dipole moment matrix element of molecule ξ between ground electronic state $|0>$ and excited state $|r>$, and $E_{r0} = E_r - E_0$ is the energy difference between these two states. Intermolecular coupling is clearly personified by the presence in expression (1) of the retarded resonant dipole-dipole interaction tensor $V_{ij}(k,\vec{R})$,

$$V_{ij}(k,\vec{R}) = \frac{1}{4\pi\varepsilon_0 R^3}[(\delta_{ij} - 3\hat{R}_i\hat{R}_j)(1-ikR) - (\delta_{ij} - \hat{R}_i\hat{R}_j)k^2R^2]e^{ikR}, \tag{3}$$

in which $k = E_{r0}/\hbar c$, and the intermolecular separation distance vector is $\vec{R} = \vec{R}_B - \vec{R}_A$. The result (1) is interpreted as arising from the scattering of a real incident photon at different molecular centres, and the exchange of a virtual photon between the pair. Initially, both molecules are in their ground electronic states, as is also the case finally, with electric dipole allowed transitions occurring to intermediate electronic states $|r>$ and $|s>$ in species A and B, respectively, with corresponding unit increases or decreases in the number of real and virtual photons, whose initial and final states are represented by $|n(\vec{k},\lambda);0(\vec{p},\varepsilon)>$, where $(\vec{p},\varepsilon)$ denotes the mode characteristics of the virtual photon. Since a finite amount of energy is relayed between the two sites, the contribution (1) has been termed the "dynamic" one, and is seen to be directly proportional to the product of electric dipole polarizabilities of each molecule.

If both molecules are polar, however, Bradshaw and Andrews [9] showed that there is an additional term that contributes to the optical binding energy. It is also of fourth order, and arises when the real incident photon is emitted and absorbed, or absorbed and emitted, by the same site, either molecule A or molecule B, with a single virtual photon again propagating between the pair. It takes the form

$$\Delta E_{stat} = \frac{I}{2\varepsilon_0 c} e_i^{(\lambda)}(\vec{k})\bar{e}_l^{(\lambda)}(\vec{k})[\beta_{ijl}(A;k)\mu_k^{00}(B) + \mu_k^{00}(A)\beta_{ijl}(B;k)]V_{jk}(0,\vec{R}), \tag{4}$$

where $\vec{\mu}^{00}(\xi)$ is the ground state static electric dipole moment of molecule $\xi = A,\, B$, and $\beta_{ijk}(\xi;k)$ is the corresponding molecular first hyperpolarizability tensor. This contribution is termed the "static" one since no real energy is transferred between centres [9,13]. This is confirmed by the appearance in result (4) of the static dipolar coupling potential $V_{ij}(0,\vec{R})$,

$$V_{ij}(0,\vec{R}) = \frac{(\delta_{ij} - 3\hat{R}_i\hat{R}_j)}{4\pi\varepsilon_0 R^3}, \tag{5}$$

which is simply the zero-frequency limit of $V_{ij}(k,\vec{R})$ Eq. (3). The total energy shift is given by the sum of Eqs (1) and (4). As expressed, both of these terms apply to the situation in which the incoming laser polarization is in a fixed orientation relative to the internuclear separation distance vector, $\vec{R}$. For a freely tumbling molecular pair, ΔE_{stat} is found to vanish, while the dynamic term becomes

$$\begin{aligned}\Delta E_{dyn} = &-\frac{I}{8\pi\varepsilon_0^2 cR^3}\alpha(A;k)\alpha(B;k) \\ &\left[kR\sin 2kR + 2\cos 2kR - \frac{5\sin 2kR}{kR} - \frac{6\cos 2kR}{k^2R^2} + \frac{3\sin 2kR}{k^3R^3}\right],\end{aligned} \tag{6}$$

and which is linearly proportional to the laser irradiance. Near- and far-zone asymptotic limits are readily calculable from Eq. (6), and exhibit inverse and modulated inverse square dependence on R, respectively.

While results for both mechanisms may be obtained straightforwardly using standard techniques of diagrammatic time-dependent perturbation theory, a fair amount of labour is involved since each contribution requires summation over forty-eight time-ordered diagrams. An alternative physical viewpoint and calculational method allows these results to be obtained in a more facile manner, however. The approach entails the coupling of permanent and transition electric dipole moments induced at each centre by fluctuations of the electromagnetic field, to the resonant retarded or static dipolar coupling potential [13–15]. Evaluating the expectation value over the ground state of both molecules with the radiation field containing $n(\vec{k},\lambda)$ photons readily yields the interaction energy. The method has also successfully been applied to the interactions in the presence of an external field occurring between pure electric dipole polarizable molecules of arbitrary multipole order [15], as well as to the leading discriminatory term taking place between two chiral molecules [16]. This last contribution necessitates the inclusion of magnetic dipole coupling, with each species being electric-magnetic dipole polarizable.

It is the purpose of this paper to investigate other contributions to the field-induced intermolecular interaction energy involving the magnetic dipole interaction term that are of a similar order to the energy shift between optically active molecules. Due to the computational simplicity of the induced moment method, this approach will be employed for the calculation of the interaction energy when one or both species are magnetic dipole polarizable. A complete polarization analysis will also be carried out for light that is linearly or circularly polarized propagating in directions parallel and perpendicular to the intermolecular join.

2. Laser-induced energy shift: One magnetic susceptible molecule

The field induced intermolecular energy shift when one or both molecules are paramagnetically susceptible is now calculated via the fluctuating multipole moment method outlined at the end of the previous Section. Let A be an electric dipole polarizable molecule and B be a magnetic dipole susceptible one, located at $\vec{R}_A$ and $\vec{R}_B$, respectively, with their relative separation $\vec{R}$ defined as before. Further, let both molecules be subject to the action of an intense electromagnetic field. Hence to leading order, the electric displacement field induces an electric dipole moment, $\vec{\mu}(A)$ in species A, while the magnetic field causes a magnetic dipole moment to be induced in species B, $\vec{m}(B)$. Explicitly,

$$\mu_i^{ind}(A) = \varepsilon_0^{-1}\alpha_{ij}(A;k)d_j^{\perp}(\vec{k},\vec{R}_A), \tag{7}$$

and

$$m_i^{ind}(B) = \chi_{ij}(B;k)b_j(\vec{k},\vec{R}_B). \tag{8}$$

In expression (7), $\alpha_{ij}(A;k)$ is the frequency-dependent electric dipole polarizability tensor, whose isotropic form, was given by formula (2). $d_j^{\perp}(\vec{k},\vec{r})$ is the j-th component of the transverse electric displacement field, whose second quantized form for a specific $(\vec{k},\lambda)$-mode of the radiation field is given by

$$d_j^{\perp}(\vec{k},\vec{r}) = i\left(\frac{\hbar ck\varepsilon_0}{2V}\right)^{1/2}[e_j^{(\lambda)}(\vec{k})a^{(\lambda)}(\vec{k})e^{i\vec{k}\cdot\vec{r}} - \bar{e}_j^{(\lambda)}(\vec{k})a^{\dagger(\lambda)}(\vec{k})e^{-i\vec{k}\cdot\vec{r}}], \tag{9}$$

where $a^{(\lambda)}(\vec{k})$ and $a^{\dagger(\lambda)}(\vec{k})$ are annihilation and creation operators for a photon whose index of polarization is λ, and direction of propagation is $\vec{k}$. In relation (8), $b_j(\vec{k},\vec{r})$ is the magnetic analogue of formula (9)

$$b_j(\vec{k},\vec{r}) = i\left(\frac{\hbar k}{2\varepsilon_0 cV}\right)^{1/2}[b_j^{(\lambda)}(\vec{k})a^{(\lambda)}(\vec{k})e^{i\vec{k}\cdot\vec{r}} - \bar{b}_j^{(\lambda)}(\vec{k})a^{\dagger(\lambda)}(\vec{k})e^{-i\vec{k}\cdot\vec{r}}], \tag{10}$$

with $\vec{b}^{(\lambda)}(\vec{k}) = \hat{k}\times\vec{e}^{(\lambda)}(\vec{k})$ the unit magnetic polarization vector. The magnetic dipole analogue of the electric dipole polarizability is the magnetic susceptibility tensor

$$\chi_{ij}(B;k) = \sum_s \left\{\frac{m_i^{0s}(B)m_j^{s0}(B)}{E_{s0}-\hbar ck} + \frac{m_j^{0s}(B)m_i^{s0}(B)}{E_{s0}+\hbar ck}\right\}, \tag{11}$$

and which is written in terms of the transition magnetic dipole moment operator between ground $|0>$ and excited state $|s>$ of molecule B, $m_i^{0s}(B) = -\frac{e}{2m}\varepsilon_{ijk} < 0|q_j(B)p_k(B)|s>$, where p_k is the k-th component of the linear momentum operator of an electron located at q_j, and ε_{ijk} is the third-rank skew-symmetric tensor.

The electric and magnetic dipole moments induced at each centre Eqs (7) and (8) couple via the retarded resonant electric-magnetic dipole interaction tensor $U_{ij}(k,\vec{R})$ [17],

$$U_{ij}(k,\vec{R}) = \frac{1}{4\pi\varepsilon_0 R^3}\varepsilon_{ijk}\hat{R}_k[ikR + k^2R^2]e^{ikR}, \tag{12}$$

giving rise to an interaction energy

$$\Delta E = Im\mu_i^{ind}(A)m_j^{ind}(B)U_{ij}(k,\vec{R}), \tag{13}$$

where *Im* denotes the imaginary part, which is taken since for real wavefunctions, the transition electric dipole moment is real and its magnetic counterpart is pure imaginary. A formula for the energy shift expressed explicitly in terms of the response tensors of each molecule may be obtained on substituting for the induced dipole moments from Eqs (7) and (8), yielding

$$\Delta E = Im\varepsilon_0^{-1}\alpha_{ik}(A;k)\chi_{jl}(B;k)d_k^{\perp}(\vec{k},\vec{R}_A)b_l(\vec{k},\vec{R}_B)U_{ij}(k,\vec{R}). \tag{14}$$

Hence the field modified intermolecular interaction energy is obtained from formula (14) on taking the expectation value over the product molecule-field state $|E_0^A, E_0^B; n(\vec{k},\lambda)>$, corresponding to both molecules in the ground electronic state $E_0^{\xi},\ \xi = A, B$ and the incident field containing $n(\vec{k},\lambda)$ photons. The expectation value of the molecular factor is elementary, producing the ground state electric dipole polarizability and magnetic dipole susceptibility. The electromagnetic field factor, however, corresponds to the average value of the product of the electric displacement and magnetic fields at two spatially separated points, being a field-field spatial correlation function. It is easily evaluated using the forms for the field operators Eqs (9) and (10), giving

$$\begin{aligned} &< n(\vec{k},\lambda)|d_k^{\perp}(\vec{R}_A)b_l(\vec{R}_B)|n(\vec{k},\lambda)> = \left(\frac{\hbar k}{2V}\right) \\ &\quad [(n+1)e_k^{(\lambda)}(\vec{k})\bar{b}_l^{(\lambda)}(\vec{k})e^{-i\vec{k}\cdot\vec{R}} + n\bar{e}_k^{(\lambda)}(\vec{k})b_l^{(\lambda)}(\vec{k})e^{i\vec{k}\cdot\vec{R}}]. \end{aligned} \tag{15}$$

It is common to make the approximation $n+1 \approx n$ in Eq. (15), which is appropriate for an intense beam of laser light. Hence the two terms are then complex conjugates of each other, enabling twice the real part to be taken, allowing Eq. (15) to be written as

$$\left(\frac{n\hbar k}{2V}\right) e_k^{(\lambda)}(\vec{k})\bar{b}_l^{(\lambda)}(\vec{k})\cos(\vec{k}\cdot\vec{R}). \tag{16}$$

For a pair of isotropic molecules, a rotational average may be carried out using the result [18]

$$< \alpha_{ik}(A;k)\chi_{jl}(B;k) >=< \alpha_{ik}(A;k) >< \chi_{jl}(B;k) >= \delta_{ik}\delta_{jl}\alpha(A;k)\chi(B;k), \tag{17}$$

where the angular brackets denote an orientational average, and a factor of 1/3 has been subsumed into each of the isotropic susceptibility tensors. Substituting (16) and (17) into (14), and contracting tensors, produces the following expression for the change in energy shift between an electric dipole polarizable molecule and a magnetic dipole susceptible body caused by an applied radiation field,

$$\Delta E = \left(\frac{n\hbar k}{\varepsilon_0 V}\right)\alpha(A;k)\chi(B;k)e_i^{(\lambda)}(\vec{k})\bar{b}_j^{(\lambda)}(\vec{k})ImU_{ij}(k,\vec{R})\cos(\vec{k}\cdot\vec{R}). \tag{18}$$

The result above applies to the case where the two coupled molecules have a fixed orientation with respect to the direction of propagation of the incident laser beam. Before going on to calculate the interaction energy for a freely tumbling pair, a polarization analysis is carried out in the next Section.

3. Polarization analysis

In this Section the energy shift (18) is examined for incoming radiation that is either linearly or circularly polarized and propagating either parallel ($||$) or perpendicular ($\perp$) to the internuclear axis.

3.1. Linearly polarized radiation

First consider a linearly polarized electromagnetic field propagating in a direction parallel to $\vec{R}$, that is, $\hat{k}||\hat{R}$ and $\vec{b}\perp\hat{R}$, where the circumflex designates a unit vector, so that $\cos(\vec{k}\cdot\vec{R}) = \cos kR$. Writing $\bar{b}_j^{(\lambda)}(\vec{k}) = \varepsilon_{jmn}\hat{k}_m\bar{e}_n^{(\lambda)}(\vec{k})$, and substituting for $U_{ij}(k,\vec{R})$, the energy shift (18) becomes

$$\begin{aligned}\Delta E_{lin}^{||} = {} & \frac{n\hbar k}{4\pi\varepsilon_0^2 cR^3 V}\alpha(A;k)\chi(B;k)\varepsilon_{ijk}\varepsilon_{jmn}e_i^{(\lambda)}(\vec{k})\bar{e}_n^{(\lambda)}(\vec{k})\hat{k}_m\hat{R}_k \\ & (kR\cos kR + k^2R^2\sin kR)\cos kR.\end{aligned} \tag{19}$$

Since $\varepsilon_{ijk}\varepsilon_{jmn}e_i^{(\lambda)}(\vec{k})\bar{e}_n^{(\lambda)}(\vec{k})\hat{k}_m\hat{R}_k = 1$ for this particular configuration, Eq. (19) simplifies to

$$\Delta E_{lin}^{||} = \tfrac{I}{4\pi\varepsilon_0^2 c^3 R^3}\alpha(A;k)\chi(B;k)(kR\cos^2 kR + k^2R^2\sin kR\cos kR), \tag{20}$$

when written in terms of the irradiance.

For perpendicular incident propagation, that is $\hat{k}\perp\hat{R}$ and $\vec{b}||\hat{R}$, $\vec{k}\cdot\vec{R} = 0$ and $\cos(\vec{k}\cdot\vec{R}) = 1$. Thus Eq. (18) becomes

$$\Delta E_{lin}^{\perp} = \tfrac{n\hbar k}{4\pi\varepsilon_0^2 cR^3 V}\alpha(A;k)\chi(B;k)\varepsilon_{ijk}\varepsilon_{jmn}e_i^{(\lambda)}(\vec{k})\bar{e}_n^{(\lambda)}(\vec{k})\hat{k}_m\hat{R}_k(kR\cos kR + k^2R^2\sin kR). \tag{21}$$

Now $\varepsilon_{ijk}\varepsilon_{jmn}e_i^{(\lambda)}(\vec{k})\bar{e}_n^{(\lambda)}(\vec{k})\hat{k}_m\hat{R}_k = 0$ so that the energy shift vanishes,

$$\Delta E_{lin}^{\perp} = 0. \tag{22}$$

3.2. Circularly polarized radiation

To help facilitate the analysis of the energy shift when circularly polarized light is selected, use is made of the identity

$$e_i^{(L/R)}(\vec{k})\bar{b}_j^{(L/R)}(\vec{k}) = \frac{1}{2}[\pm i(\delta_{ij} - \hat{k}_i\hat{k}_j) + \varepsilon_{ijk}\hat{k}_k]. \tag{23}$$

For parallel propagation, on inserting Eq. (23) and the imaginary part of Eq. (12) into Eq. (18) gives for the interaction energy,

$$\begin{aligned}\Delta E_{L/R}^{||} = &\frac{n\hbar k}{8\pi\varepsilon_0^2 cR^3V}\alpha(A;k)\chi(B;k)\varepsilon_{ijl}\hat{R}_l[\pm i(\delta_{ij} - \hat{k}_i\hat{k}_j) + \varepsilon_{ijk}\hat{k}_k] \\ &(kR\cos kR + k^2R^2\sin kR)\cos kR.\end{aligned} \tag{24}$$

Only the anti-symmetric part of the polarization factor remains as the symmetric part is zero. With $\varepsilon_{ijk}\varepsilon_{ijl}\hat{k}_k\hat{R}_l = 2$, Eq. (24) simplifies to

$$\Delta E_{L/R}^{||} = \frac{I}{4\pi\varepsilon_0^2 c^3R^3}\alpha(A;k)\chi(B;k)(kR\cos kR + k^2R^2\sin kR)\cos kR. \tag{25}$$

For perpendicular propagation, substituting (23) and (12) into (18) produces

$$\begin{aligned}\Delta E_{L/R}^{\perp} = &\frac{n\hbar k}{8\pi\varepsilon_0^2 cR^3V}\alpha(A;k)\chi(B;k)\varepsilon_{ijl}\hat{R}_l[\pm i(\delta_{ij} - \hat{k}_i\hat{k}_j) + \varepsilon_{ijk}\hat{k}_k] \\ &(kR\cos kR + k^2R^2\sin kR) = 0,\end{aligned} \tag{26}$$

which vanishes since $\varepsilon_{ijk}\varepsilon_{ijl}\hat{k}_k\hat{R}_l = 0$. It is interesting to note that $\Delta E_{L/R}^{||} = \Delta E_{lin}^{||}$, and that $\Delta E_{L/R}^{\perp} = \Delta E_{lin}^{\perp} = 0$.

Asymptotically limiting forms for the identical non-vanishing energy shifts Eqs (20) and (25) at short and long pair separation distances are obtained straightforwardly. In the former distance regime, $kR << 1$, and McLaurin series expansions of the trigonometric factor result in the near-zone limiting form

$$\Delta E_{lin}^{||}(NZ) = \Delta E_{L/R}^{||}(NZ) = \tfrac{Ik}{4\pi\varepsilon_0^2 c^3R^2}\alpha(A;k)\chi(B;k), \tag{27}$$

which exhibits inverse square dependence on R. At the opposite extreme, $kR >> 1$, and the far-zone limit is

$$\Delta E_{lin}^{||}(FZ) = \Delta E_{L/R}^{||}(FZ) = \frac{Ik^2}{4\pi\varepsilon_0^2 c^3R}\alpha(A;k)\chi(B;k)\sin kR\cos kR, \tag{28}$$

which displays a modulated inverse dependence on R.

4. Freely tumbling molecular pair

Often the molecular pair is freely tumbling, which means that all orientations of $\vec{R}$ relative to $\vec{k}$ are allowed. An exact expression for the energy shift may be obtained in this case on assuming that all directions are equally likely, corresponding to an unweighted average. Returning to formula (14), and inserting expression (15) for circularly polarized light, produces

$$\Delta E = \left(\frac{\hbar k}{2\varepsilon_0 V}\right) Im\alpha_{ik}(A;k)\chi_{jl}(B;k) \\ [(n+1)e_k^{(L/R)}(\vec{k})\bar{b}_l^{(L/R)}(\vec{k})e^{-i\vec{k}\cdot\vec{R}} + n\bar{e}_k^{(L/R)}(\vec{k})b_l^{(L/R)}(\vec{k})e^{i\vec{k}\cdot\vec{R}}]U_{ij}(k,\vec{R}). \tag{29}$$

Substituting identity Eq. (23) and rotational averaging then gives

$$\Delta E = \frac{1}{2}\left(\frac{\hbar k}{2\varepsilon_0 V}\right) Im\alpha(A;k)\chi(B;k)[\{\pm i(\delta_{ij} - \hat{k}_i\hat{k}_j) + \varepsilon_{ijs}\hat{k}_s\}(n+1)e^{-i\vec{k}\cdot\vec{R}} \\ +\{\mp i(\delta_{ij} - \hat{k}_i\hat{k}_j) - \varepsilon_{ijs}\hat{k}_s\}ne^{i\vec{k}\cdot\vec{R}}]U_{ij}(k,\vec{R}). \tag{30}$$

On making use of the antisymmetric property of the $U_{ij}(k,\vec{R})$ tensor, the symmetric terms appearing in Eq. (30) may then be discarded. The tumbling average is computed via

$$< \hat{k}_k e^{\pm i\vec{k}\cdot\vec{R}} >= \frac{1}{4\pi}\int d\Omega \hat{k}_k e^{\pm i\vec{k}\cdot\vec{R}} = \mp i\left(\frac{\cos kR}{kR} - \frac{\sin kR}{k^2R^2}\right)\hat{R}_k, \tag{31}$$

so that the energy shift Eq. (30) becomes

$$\Delta E = \frac{\hbar k}{16\pi\varepsilon_0^2 cR^3 V}(2n+1)\alpha(A;k)\chi(B;k)\varepsilon_{ijk}\varepsilon_{ijs}\hat{R}_k\hat{R}_s\left(\frac{\cos kR}{kR} - \frac{\sin kR}{k^2R^2}\right) \\ (kR\cos kR + k^2R^2\sin kR), \tag{32}$$

after substituting for $U_{ij}(k,\vec{R})$ and simplifying. Noting that $\varepsilon_{ijk}\varepsilon_{ijs}\hat{R}_k\hat{R}_s = 2$, and defining the incident beam intensity as $I = (2n+1)\hbar c^2 k/V$, results in

$$\Delta E = \frac{I}{16\pi\varepsilon_0^2 c^3 R^3}\alpha(A;k)\chi(B;k)\left(kR\sin 2kR + 2\cos 2kR - \frac{\sin 2kR}{kR}\right), \tag{33}$$

which holds for isotropic A and B, and for all directions of the incoming field relative to $\vec{R}$, and is repulsive. Near- and far-zone limiting forms readily follow from expression (33). In the first case, *kR* $<<$ 1 and

$$\Delta E(NZ) = -\frac{Ik^2}{24\pi\varepsilon_0^2 c^3 R}\alpha(A;k)\chi(B;k), \tag{34}$$

exhibiting attractive, and inverse R behaviour. The far-zone asymptote is

$$\Delta E(FZ) = \frac{Ik}{16\pi\varepsilon_0^2 c^3 R^2}\alpha(A;k)\chi(B;k)\sin 2kR, \tag{35}$$

which has modulated inverse square dependence.

5. Laser-induced energy shift: Two magnetic susceptible molecules

It is a straightforward extension of the method presented in Section 2 to compute the laser-induced shift in intermolecular interaction energy between two magnetic dipole polarizable molecules. With an identical expression to Eq. (8) for the magnetic dipole moment induced in body A by the magnetic field, the energy shift is

$$\Delta E = m_i^{ind}(A) m_j^{ind}(B) Re V_{ij}(k,\vec{R}) = \chi_{ik}(A;k)\chi_{jl}(B;k) b_k(\vec{k},\vec{R}_A) b_l(\vec{k},\vec{R}_B) Re V_{ij}(k,\vec{R}), \quad (36)$$

with the retarded resonant coupling tensor given by Eq. (3), and familiar from the matrix element for the resonant transfer of energy between two electric or two magnetic dipoles. Taking the expectation value of the right-hand side of Eq. (36) over the ground electronic state of both molecules, and a non-vanishing number state of the field, with the latter given by

$$\begin{aligned} &< n(\vec{k},\lambda)|b_k(\vec{R}_A) b_l(\vec{R}_B)|n(\vec{k},\lambda) >= \left(\frac{\hbar k}{2\varepsilon_0 c V}\right) \\ &\quad [(n+1) b_k^{(\lambda)}(\vec{k}) \bar{b}_l^{(\lambda)}(\vec{k}) e^{-i\vec{k}\cdot\vec{R}} + n \bar{b}_k^{(\lambda)}(\vec{k}) b_l^{(\lambda)}(\vec{k}) e^{i\vec{k}\cdot\vec{R}}], \end{aligned} \quad (37)$$

on using the magnetic field Eq. (10), the energy shift becomes

$$\Delta E = \left(\frac{n\hbar k}{\varepsilon_0 c V}\right) \chi(A;k)\chi(B;k) b_i^{(\lambda)}(\vec{k}) \bar{b}_j^{(\lambda)}(\vec{k}) Re V_{ij}(k,\vec{R}) \cos(\vec{k}\cdot\vec{R}), \quad (38)$$

on approximating $n+1$ by n, and after performing a rotational average on molecules A and B. Expression (38) is seen to be identical in form to result Eq. (1), the dynamic contribution to the field-induced interaction between two electric dipole polarizable molecules on substituting for the irradiance of the laser field and replacing $\frac{1}{c} m_i^{0r}(A)$ by $\mu_i^{0r}(A)$, $\frac{1}{c} m_j^{0s}(B)$ by $\mu_j^{0s}(B)$, and the magnetic polarization vectors by their electric counterparts. Since

$$e_i^{(L/R)}(\vec{k}) \bar{e}_j^{(L/R)}(\vec{k}) = b_i^{(L/R)}(\vec{k}) \bar{b}_j^{(L/R)}(\vec{k}) = \frac{1}{2}[(\delta_{ij} - \hat{k}_i \hat{k}_j) \mp i\varepsilon_{ijk}\hat{k}_k], \quad (39)$$

identical results are obtained on analyzing the polarization characteristics, in addition to the freely tumbling averaged pair interaction energy, with the latter given by formula (6) subject to the substitutions mentioned above, as well as for the corresponding asymptotic limits.

6. Summary

In this paper it has been shown how the induced multipole moment method may be employed to calculate in a facile way higher multipole moment contributions to the radiation-induced intermolecular interaction energy shift, in particular those interactions involving one or two magnetically susceptible molecules. The physical viewpoint of the approach is based on electric and magnetic multipole moments being induced in a polarizable body by an applied electromagnetic field. The moments induced at each centre are coupled via the appropriate retarded resonant multipole-multipole coupling tensor. Explicit results have been obtained for the field-induced interaction energy between an electric dipole polarizable molecule and a magnetic dipole polarizable molecule, and between two magnetically susceptible bodies. Not only are the expressions obtained valid for freely tumbling isotropic molecules, but also for the

incoming beam in a fixed relative orientation to the molecular separation distance vector. A complete polarization analysis was also carried out for linearly and circularly polarized light propagating in parallel or perpendicular directions to $\vec{R}$.

It should be remarked that the interaction between an electric dipole polarizable molecule and a magnetic dipole susceptible one is the leading higher-order correction term that is non-vanishing for isotropic systems when going beyond the electric dipole approximation [19]; it is also non-discriminatory. Since the magnetic dipole moment is about 10^3 times smaller in magnitude than the electric dipole moment, the magnetic dipole-magnetic dipole field induced energy shift will be very small for most species, and can be neglected in a first treatment. There is, however, another interaction that is of a similar order to the $\alpha(A) - \chi(B)$ interaction energy, which survives orientational averaging [16]. It is a discriminatory energy shift induced by an applied field occurring between two optically active molecules, each characterized by isotropic electric-magnetic dipole polarizability $G(\xi)$, $\xi = A$, B, with

$$G(\xi;k) = \sum_r \frac{2}{3}\frac{|\vec{\mu}^{0r}(\xi)\cdot\vec{m}^{r0}(\xi)|\hbar ck}{E_{r0}^2 - (\hbar ck)^2}, \tag{40}$$

and is given by [16]

$$\Delta E(disc) = \frac{I}{8\pi\varepsilon_0^2 c^3 R^3} G(A;k)G(B;k)\left[4\frac{\sin 2kR}{kR} + 6\frac{\cos 2kR}{k^2R^2} - 3\frac{\sin 2kR}{k^3R^3}\right]. \tag{41}$$

Replacing one enantiomer by its mirror image form changes the sign of ΔE in Eq. (41) since the response tensor $G(\xi;k)$ is a pseudoscalar function of $\vec{\mu}^{0r}(\xi)$ and $\vec{m}^{0r}(\xi)$. Like limit Eq. (34), the near-zone asymptote of Eq. (41) exhibits inverse dependence on R, while in the far-zone, a weaker modulated R^{-4} behaviour is predicted. Interaction energy (41) dominates in the case of interacting chiral molecules.

References

[1] J.R. Lalanne, A. Ducasse and S. Kielich, *Laser-Molecule Interaction: Laser Physics and Molecular Nonlinear Optics*, Wiley, New York, 1996.
[2] M. Evans and S. Kielich, Eds, *Modern Nonlinear Optics*, (Vols I-III), Wiley, New York, 1993.
[3] S. Mukamel, *Principles of Nonlinear Optical Spectroscopy*, Oxford University Press, New York, 1995.
[4] D.L. Andrews and P. Allcock, *Optical Harmonics in Molecular Systems*, Wiley-VCH, Weinheim, 2002.
[5] D.L. Andrews, *Structured Light and Its Applications*, Academic Press, London, 2008.
[6] T. Thirunamachandran, *Mol Phys* **40** (1980), 393.
[7] M.M. Burns, J.-M. Fournier and J.A. Golovchenko, *Phys Rev Lett* **63** (1989), 1233.
[8] S.A. Tatarkova, A.E. Carruthers and K. Dholakia, *Phys Rev Lett* **89** (2002), 283901.
[9] D.S. Bradshaw and D.L. Andrews, *Phys Rev A* **72** (2005), 033816.
[10] J. Rodriguez and D.L. Andrews, *Phys Rev A* **79** (2009), 022106.
[11] D.P. Craig and T. Thirunamachandran, *Molecular Quantum Electrodynamics*, Dover, New York, 1998.
[12] A. Salam, *Molecular Quantum Electrodynamics*, Wiley, Hoboken, New Jersey, 2010.
[13] A. Salam, *Phys Rev A* **76** (2007), 063402.
[14] D.P. Craig and T. Thirunamachandran, *Theo Chem Acc* **102** (1999), 112.
[15] A. Salam, *Phys Rev A* **73** (2006), 013402.
[16] A. Salam, *J Chem Phys* **124** (2006), 014302.
[17] G.J. Daniels, R.D. Jenkins, D.S. Bradshaw and D.L. Andrews, *J Chem Phys* **119** (2003), 2264.
[18] D.L. Andrews and T. Thirunamachandran, *J Chem Phys* **67** (1977), 5026.
[19] L.C. Dávila Romero, J. Rodriguez and D.L. Andrews, *Opt Comm* **281** (2008), 865.

Journal of Computational Methods in Sciences and Engineering 10 (2010) 561–572
DOI 10.3233/JCM-2010-0327
IOS Press

An apparent critical point in binary mixtures of nitrotoluene with alkanes: Experimental and simulation study

Blazej Ratajczak[a], Malgorzata Sliwinska-Bartkowiak[a,*], Tomasz Koziol[a], Benoit Coasne[b] and Keith E. Gubbins[c]
[a]*Faculty of Physics, Adam Mickiewicz University, Umultowska 85, 61-614 Poznań, Poland*
[b]*Department of Chemical Physics, University of Montpellier, Mont.2, France*
[c]*Department of Chemical & Biomolecular Eng., North Carolina State University, Raleigh, NC, USA*

Abstract. We report an experimental and simulation study of binary mixtures of o- and m-nitrotoluene with decane and hexadecane. Mixtures of o-nitrotoluene with alkanes form a classical critical mixtures, but m-nitrotoluene / n – alkane mixtures show an apparent critical point, which lies in a metastable, experimentally inaccessible state, below the melting point, affecting physical and chemical properties of this systems in the stable liquid phase. The presence of the apparent critical point in this mixture has been experimentally observed by Nonlinear Dielectric Effect (NDE) measurements as an anomalous increase in the NDE values typical of critical concentrations. The phase diagram of this mixture shows evidence that the system freezes in the homogenous phase and its melting point is higher than its critical temperature [1–3]. For such a system, we performed Monte Carlo simulations aimed at analysing the kind of phase transitions observed, and the conditions of their occurrence in a nonpolar/dipolar mixture. We perform studies for classical critical systems of o-nitrotoluene with decane and hexadecane The enthalpy, configurational energy and radial distribution function have been estimated by the MC simulation method in the NPT system. Immiscibility conditions according to Schoen and Hoheisel [4] approach are also discussed.

Keywords: Metastable mixtures, MC simulations, near critical point, nonlinear dielectric effect

1. Introduction

The presence of the apparent critical point has now been established for a large group of liquid mixtures having a positive mixing enthalpy [1,2,5–10]. The melting point of these mixtures is higher than their critical point. Their critical point falls in the range of metastable states, and direct experimental determination of the critical point in such systems is usually impossible because of the problem with reaching the desired overcooled state. The presence of such a point affects the physico-chemical properties of the system in the stable liquid phase and is the reason for anomalous behaviour of many physical quantities sensitive to the inhomogeneity of the medium. Critical fluctuations appearing in such a system at temperatures well above the critical are frozen *in statu nascendi* forming separate molecular

*Corresponding author. E-mail: msb@amu.edu.pl.

structures in the solid phase. In classical critical mixtures [11] in which the phase separation is observed, the density correlation range is described by the exponential law:

$$\xi = \xi_0 \left(\frac{T - T_C}{T_C} \right)^{-\nu} \tag{1}$$

where the mean range of molecular interactions correlation for the liquids of small molecules is $\xi_0 \sim$ 0.2 nm. The critical range in which large density fluctuations lead to formation of two phases from the single homogeneous phase is characterised by a correlation range of 10^2 nm, which tends to infinity at the critical point. At temperatures much higher than Tc, the value of ξ decreases according to Eq. (1). In mixtures exhibiting apparent critical point behavior, the increase in the correlation range ceases on freezing, and the value of ξ remains finite.

The methods allowing monitoring of the increase in the correlation range in critical systems are able to detect inhomogeneities in the structure of the mixture at temperatures well above Tc, and are good detectors of pre-critical phenomena. One of such method is that based on the phenomenon of Nonlinear Dielectric Effect (NDE), defined as a change in the electric permittivity induced by a strong electric field E:

$$\frac{\Delta\varepsilon}{E^2} = \frac{\varepsilon^E - \varepsilon^0}{E^2} \tag{2}$$

where ε^E is the permittivity in the field E, and ε^0 that in its absence. The sign and magnitude of NDE of a liquid depends on the kind of inter- and intramolecular interactions and their energies. The NDE method has been applied in the investigation of interdipolar interactions, intermolecular rotation, formation of hydrogen bonds and molecular associations [12–17]. Since NDE is sensitive to inhomogeneities of the medium, it has been applied to study mixtures with limited miscibility and a critical point [17–25]. The earliest investigation carried out by Piekara [18,19], proved that in the vicinity of the critical point the NDE takes high positive values, increasing as the temperature approaches Tc. Later, using the droplet model of phase transitions [26,27], Goulon & Greffe [28,29] have shown that the fluctuation in NDE is described by the critical exponent Φ, according to:

$$\left(\frac{\Delta\varepsilon}{E^2} \right)_{fl} = \left(\frac{\Delta\varepsilon}{E^2} \right) - \left(\frac{\Delta\varepsilon}{E^2} \right)_b = A \left(\frac{T - T_C}{T_C} \right)^{-\phi} \tag{3}$$

where: $(\Delta\varepsilon/E^2)$ – is the measured effect of NDE, and $(\Delta\varepsilon/E^2)_b$ is the background effect, for the mixture in absence of critical fluctuations, A is the amplitude, T_C – the critical temperature and the critical exponent Φ is defined by the relation:

$$\Phi = \gamma - 2\beta = (2 - \eta)\,\nu - 2\beta \tag{4}$$

where γ and β are the usual critical exponents for the isothermal compressibility and density difference between the two phases respectively, and η and ν are the critical exponents of the total correlation function g(r) and the correlation length ξ. An increase in NDE in the vicinity of critical concentrations has been observed even at temperatures 20-50K above Tc [17,22,23]. The anomalous increase in NDE near the phase transition point has been attributed to the increasing intensity of molecular fluctuations in the region of critical concentrations when the temperature approaches its critical value. NDE investigations have proved that mixtures of o-nitrotoluene and n-alkanes are classical critical mixtures, whereas mixtures of m-nitrotoluene and n-alkanes and o- and m-nitrotoluene with cycloalkanes are characterised by an

NDE typical of critical mixtures, but solidify in the homogeneous phase [1,5–7,30]. An attempt has been made at interpreting the phenomena taking place in the two types of mixtures by assuming the same mechanism in both cases. The attempt was justified by the fact that for both types of mixtures, the temperature dependence of NDE related to critical fluctuations is described by a power law with the same values of the critical exponents [2,6]. On the other hand, analysis of the phase diagrams (T,x)p showing the melting points as functions of concentrations x of the m-nitrotoluene – alkane mixtures under atmospheric pressure, proved that in the concentration range in which NDE anomalies were observed, there exists two kinds of molecular clusters: one richer and the other poorer in the polar component [7]. These clusters, unstable in the liquid phase, remain distinct in the solid phase. Interpreted as molecular clusters characteristic of a precritical state, they point to the possibility of freezing of the critical fluctuations of the system. The hypothetical critical temperatures of these mixtures estimated from analysis of the second virial coefficients [10], fell in the range of temperatures below their melting points, corresponding to a metastable, experimentally inaccessible state. The results of these studies have proved that mixtures of m-nitrotoluene with alkanes, as well as o- and m-nitrotoluene with cycloalkanes and 1,3-dimethoxybenzene with alkanes, in their metastable state below their melting point show an apparent critical point affecting physical and chemical properties of these systems in the stable liquid phase. In this paper we report the results of Monte Carlo simulations performed for a simple model of mixtures of o- and m-nitrotoluene with n – decane and n – hexadecane, aimed at analysing the kinds of phase transitions observed, and the conditions of their occurrence in Lennard-Jones mixtures. The enthalpy, configurational energy and radial distribution functions have been estimated using the MC simulation method in the NPT ensemble. Immiscibility conditions according to the Schoen and Hoheisel [4] approach are also discussed.

2. Simulation method

A model of the mixtures of m- and o-nitrotoluene with decane and hexadecane [10] were studied by Monte Carlo simulations in the (N,P,T) ensemble (where the number of particles, N, is fixed, and both pressure, P, and temperature T, are constant). The molecules were contained in a cubic box with periodic boundary conditions in all 3 dimensions. The systems studied are a mixtures of dipolar and non-dipolar molecules. For such systems we can apply the potential:

$$u\left(r_{ij}\right) = 4\varepsilon_{\alpha}\left[\left(\frac{\sigma_{\alpha}}{r_{\alpha}}\right)^{12} - \left(\frac{\sigma_{\alpha}}{r_{\alpha}}\right)^{6}\right] - \frac{\alpha\mu^{2}}{r_{\alpha}^{6}} \tag{5}$$

This model has been successfully applied to a mixture nitrobenzene – cyclododecane, showing similar properties [31]. This potential takes into regard the dipolar moment of the dipolar molecule (μ) and polarizability (α). In the mixtures studied there are three possible types of interactions: nonpolar molecule – nonpolar molecule (u_{11}), dipolar molecule – dipolar molecule (u_{22}) and nonpolar molecule – dipolar molecule (u_{12}). For the first type interactions u_{11}: $\mu = 0$, and Eq. (5) takes the form of the L- J potential.

For the interactions u_{22} and u_{12} Eq. (5) can also be expressed in the form of the Lennard-Jones potential [10]:

$$u\left(r_{ij}\right) = 4\,\varepsilon_{\alpha}\left[\left(\frac{\sigma_{\alpha}}{r_{ij}}\right)^{12} - \left(\frac{\sigma_{\alpha}}{r_{ij}}\right)^{6}\right] \tag{6}$$

Table 1
ε_{12}/k and σ_{12} values for studied mixtures

mixture	m-nitrotoluene – decane	m-nitrotoluene – hexadecane	o-nitrotoluene – decane	o-nitrotoluene – hexadecane
ε_{12}k	591,19[K]	580,82[K]	649,58[K]	
σ_{12}	6,383[A]	6,973[A]	6,387[A]	6,976[A]

These two transformations require a conversion of the parameters ε and σ. For u_{22} ($\alpha = 22$) the values of ε and σ were taken after [10], while for u_{12} ($\alpha = 12$) we have:

$$\sigma_{12} = \xi^{-\frac{1}{6}} \left(\frac{\sigma_{11} + \sigma_{22}}{2} \right) \tag{7}$$

$$\varepsilon_{12} = \xi^2 \sqrt{\varepsilon_{11}\varepsilon_{22}} \tag{8}$$

where:

$$\xi = 1 + \frac{\alpha_1 \mu_2^2}{4\sigma_{11}^3} \sqrt{\frac{\varepsilon_{22}}{\varepsilon_{11}}} \tag{9}$$

The values of ε_{22}/k and σ_{22} for o- and m-nitrotoluene are: 625,41[K]; 5,660[A] and 639,33[K]; 5,660[A] respectively and for ndecane and nhexadecane: ε_{11}/k and σ_{11} are 513,07[K]; 7,140[A] and 645,32[K]; 7,140[A], ε_{12}/k and σ_{12} values for studied mixtures are presented in Table 1 [10].

The values of σ_{12} and ε_{12} in mixtures relative to the values calculated from the Lorentz – Berthelot relations:

$$\sigma_{12LB} = \frac{\sigma_{11} + \sigma_{22}}{2} \tag{10}$$

$$\varepsilon_{12LB} = \sqrt{\varepsilon_{11}\varepsilon_{22}} \tag{11}$$

are: $\sigma_{12} = 0.997^*\sigma_{12LB}$, $\varepsilon_{12} = 1.032^*\varepsilon_{11LB}$ (m-nitrotoluene – decane), $\sigma_{12} = 0.998^*\sigma_{12LB}$, $\varepsilon_{12} = 1.029^*\varepsilon_{11LB}$ (m-nitrotoluene – n-hexadecane) $\sigma_{12} = 0.998^*\sigma_{12LB}$, $\varepsilon_{12} = 1.025^*\varepsilon_{11LB}$ (o-nitrotoluene – n-decane), $\sigma_{12} = 0.998^*\sigma_{12LB}$, $\varepsilon_{12} = 1.022^*\varepsilon_{11LB}$ (o-nitrotoluene – n-hexadecane).

It is evident that the parameter ξ modifies the Lorentz–Berthelot relation mainly for the parameter ε^{eff}, the σ^{eff} parameter is practically the same as the LJ σ parameter. The dipolar moment of nitrotoluene enhances the u_{12}type interactions. The dipolar moment of m-nitrotoluene (13.6^*10^{-30} Cm) is larger than dipolar moment of o-nitrotoluene (12.3^*10^{-30} Cm), maling the $\varepsilon_{12}^{\text{eff}}$ parameter stronger for m-nitrotoluene mixtures than for o-nitrotoluene.

All simulations were performed for $N = 500$ molecules for concentrations in the range for $x_2 = 0.20$ to $x_2 = 0.80$. For each value of concentration the study was performed for 16 temperatures from $T^* = 0.3$ to $T^* = 0.6$ (where $T^* = kT/\varepsilon_{22}$), corresponding to 192 K–384 K for m-nitrotoluene- mixtures and 188 K–375 K for o-nitrotoluene- mixtures. The pressure was assumed to be $p^* = 2{,}081^*10^{-3}$ for m-nitrotoluene- mixtures and $p^* = 2{,}127^*10^{-3}$ for o-nitrotoluene- mixtures (where $p^* = p\sigma_{22}^3/\varepsilon_{22}$) which corresponds to 1 Atm. We performed 10^5 Monte Carlo Steps to equilibrate the system, followed by 10^5 steps to sample the data. However, at the selected temperature and Lennard-Jones interaction parameters we performed 10^7 steps to verify the quality of equilibration and sampling.

For each concentration, the temperature dependencies of the volume, enthalpy and configurational energy of the system were analysed. Moreover the angular functions [32] were recorded as expressed by:

$$Q_l = \sqrt{\frac{4\pi}{2l+1}\sum_{m=-l}^{l}\left|\bar{Q}_{lm}\right|^2} \tag{12}$$

where:

$$\bar{Q}_{lm} = \frac{1}{N_b}\sum Y_{lm}\left(\theta\left(r\right),\phi\left(r\right)\right) \tag{13}$$

In the above formula N_b is the number of nearest neighbours and Y_{lm} is the spherical harmonic. The nearest neighbours were assumed to be the molecules at a distance shorter than 1.3σ. The angular functions were calculated for $l = 4$ and $l = 6$ (the functions Q_4 and Q_6). Analysis of these functions allows identification of the crystalline structure [32]. The shape of the radial distribution functions (g_{11}, g_{12}, g_{22}) were recorded for each T values, and the g parameter was found:

$$g = \frac{g_{11\,\max} + g_{22\,\max}}{2g_{12\,\max}} \tag{14}$$

The parameters $g_{11\,\max}$, $g_{22\,\max}$ and $g_{12\,\max}$ correspond to the first maxima of g_{11}, g_{22} and $g_{12,}$ respectively. According to the Schoen and Hoheisel postulates [4] the value of the parameter g indicates if the system tends to phase separate. If no clusters are formed in the system then $g = 1$, but when cluster formation starts $g > 1$. Moreover, the value of g is proportional to the size of the clusters formed.

3. Simulation results

The model of the systems m- and o-nitrotoluene withn n- decane and n-hexadecane was studied by MPT-MC simulations for the temperature range T* = 0.3 to T* = 0.6 and different values of x_2.

Figure 1 presents the calculated values of reduced volume (V* in σ_{22}^3) for m-nitrotoluene – n-decane (a) and o-nitrotoluene – n-decane (c) and reduced enthalpy (H* in kt/ε_{22}) for m-nitrotoluene – n-decane [33], (b) and o-nitrotoluene – n-decane (d), for their pre-critical and critical concentrations x_2 (for more details see Figs 5 and 7). For both mixtures in the vicinity of T*≈0.39 a jumpwise change in the functions H*(T*) (Fig. 1b and 1d) and V*(T*) (Fig. 1a and 1c) was observed, indicating a first order phase transition [34]. For temperatures T* > 0.39 the mixtures are in the liquid phase. $T^*_S = 0.39$ is the freezing point of the mixtures. Interestingly, the angular functions Q_4 and Q_6 Eq. (12) calculated for T* < 0.39 do not indicate the presence of any of the structures: fcc, hcp, bcc, sc in the solid phase. The same result is obtained for each concentration x_2 for these mixtures. The freezing temperatures in reduced units are the same for m- and o-nitrotoluene mixtures but m-nitrotoluene and o-nitrotoluene have different ε_{22} values, it being larger for m-nitrotoluene (Table 1). The relation between reduced temperature and absolute temperature is T* = kT/ε_{22} and T* = 0.39 (solidification of m- or o-nitrotoluene – n-decane mixtures) corresponds to T = 249K for m-nitrotoluene – n-decane and to T = 244K for o-nitrotoluene – n-decane.

In Fig. 2. are presented the calculated values of reduced volume and enthalpy for m- and o-nitrotoluene with hexadecane. The results are similar to those for m- and o-nitrotoluene – decane mixtures (Fig. 1)

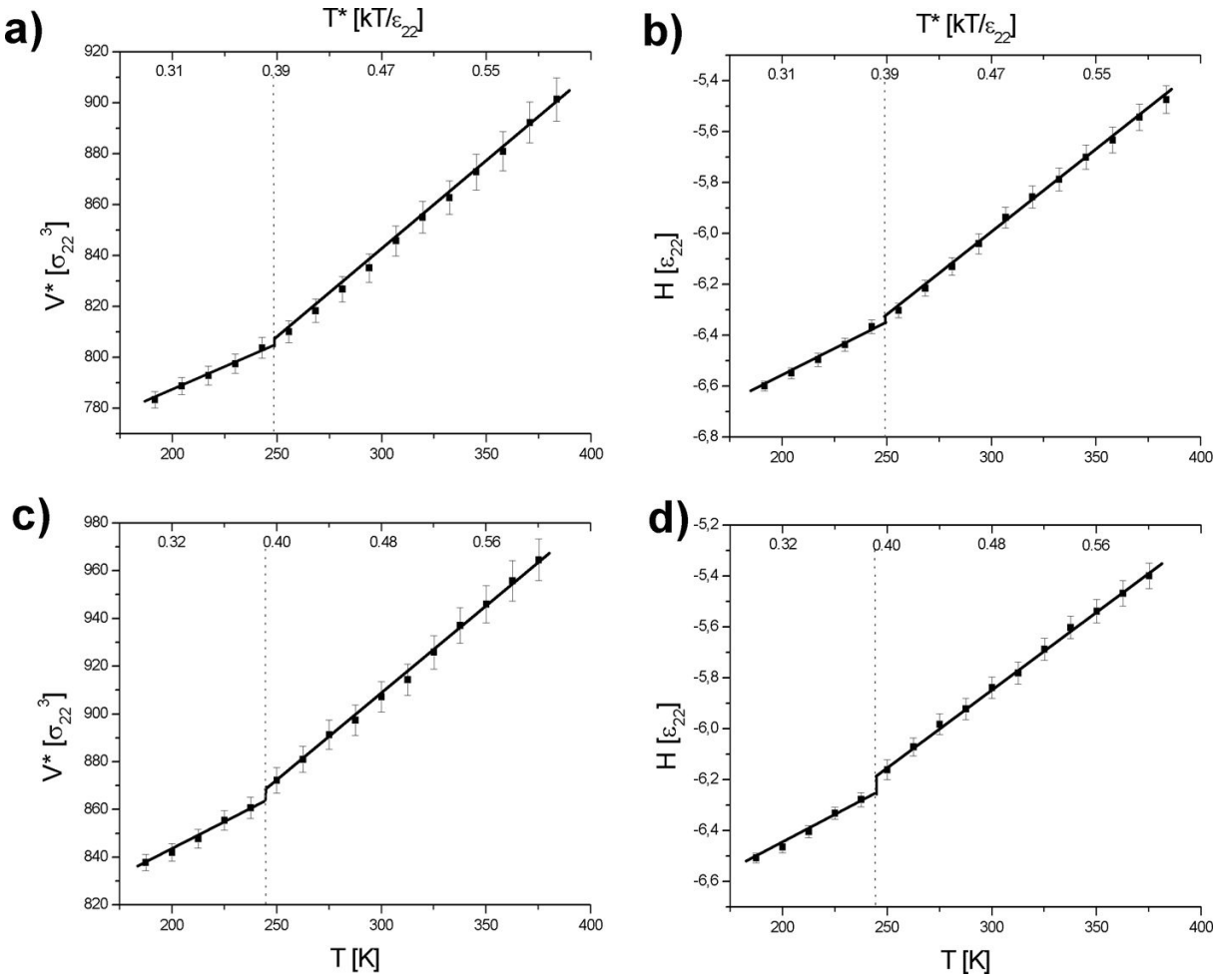

Fig. 1. Temperature dependence of reduced volume (V*) and reduced enthalpy (H*) for the systems: a) and b) m-nitrotoluene – decane, and c) and d) o-nitrotoluene – decane for their pre-critical and critical concentrations x_2. (for m-nitrotoluene – decane $x_2 = 0.49$, for o-nitrotoluene – decane $x_2 = 0.38$ – for more details see Figs 5 and 7).

but in this case the freezing temperature $T^*_S \approx 0.41$, which corresponds to $T_S = 263$ K for the m-nitrotoluene – n-hexadecane and $T_S = 256$ K to o-nitrotoluene – n-hexadecane systems. The freezing temperatures of these systems are higher than for the mixtures of these dipolar liquids with n-decane (Fig. 1). These results clearly show that the freezing temperature of the systems studied depends on the ε parameteters; ε_{11} for n-decane is lower than for n-hexadecane and freezing temperatures of the mixtures of dipolar liquids with n-decane are lower than with n-hexadecane. Also, regarding freezing temperature of the mixtures of o-and m-nitrotoluene with the same alkane, we observe that for higher ε_{22} value (m-nitrotoluene) the freezing temperature of the mixture is higher than for mixtures with lower value of ε_{22} (o-nitrotoluene).

Figure 3 presents the temperature dependence of the g parameter Eq. (14) for the pre-critical concentrations for m-nitrotoluene – n-decane and m-nitrotoluene – n-hexadecane. The g parameter can give information on the growth of clusters in the system studied. For both mixtures, with decreasing temperature the g value increases but the increase ceases at the freezing point ($T^* = 0.39$ for m-nitrotoluene –

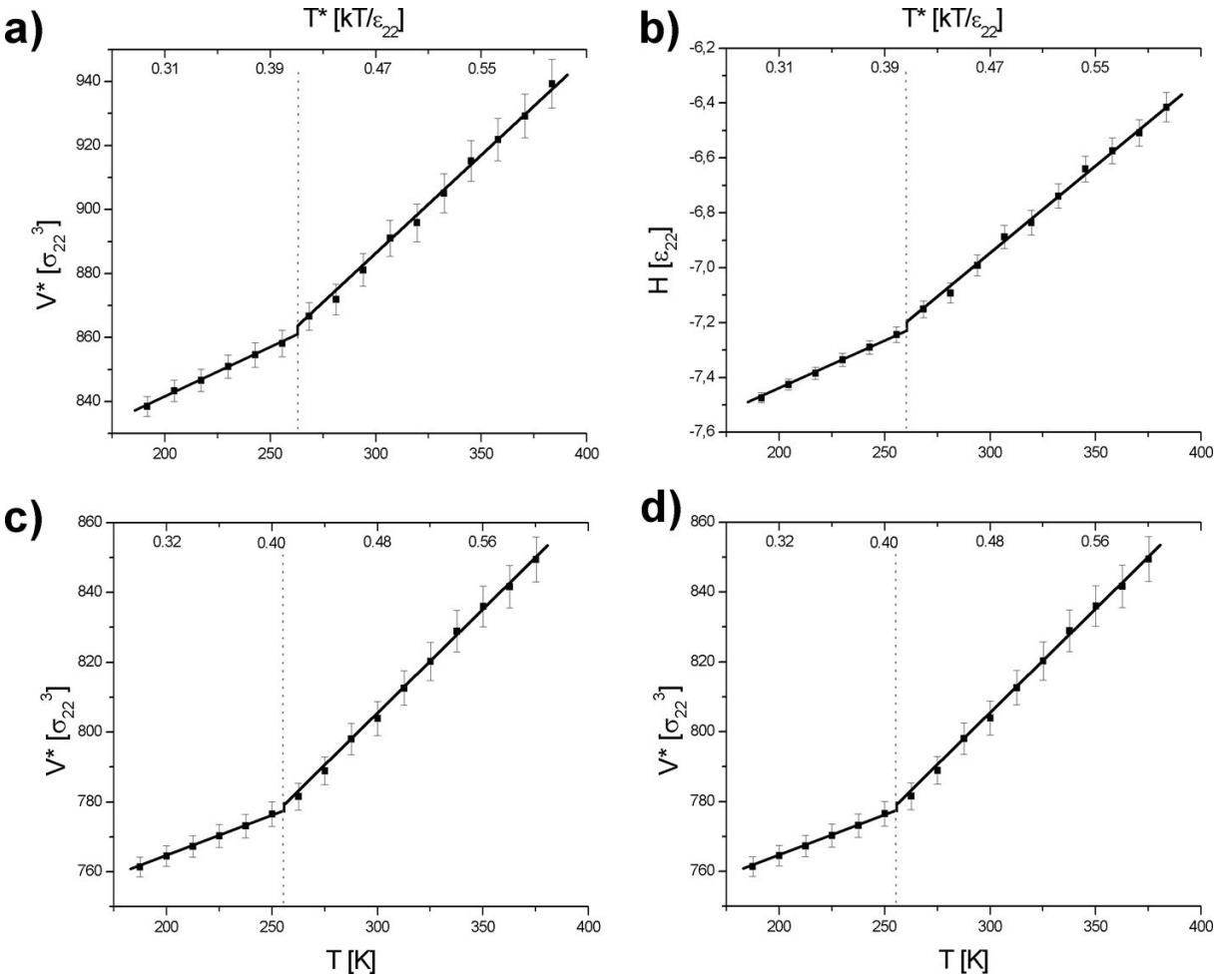

Fig. 2. Temperature dependence of of reduced volume (V*) and reduced enthalpy (H*) for the systems: a) and b) m-nitrotoluene – n-hexadecane,) and c) and d) o-nitrotoluene – n- hexadecane for their pre-critical and critical concentrations x_2. (for m-nitrotoluene – n-hexadecane $x_2 = 0.66$, for o-nitrotoluene – n-hexadecane $x_2 = 0.70$ – for more details see Figs 5 and 7).

n-decane and at T* = 0.41 for m-nitrotoluene – n-hexadecane). This observation suggests that the growth of clusters in the system has been stopped by the freezing but with incomplete phase separation. Therefore, the hypothetical critical point of this mixture is lower than the freezing point.

Figure 4 presents the temperature dependence of the g parameter for the critical concentrations for o-nitrotoluene – n-decane (Fig. 4a) and o-nitrotoluene – n-hexadecane (Fig. 4b) mixtures. At the same temperature T* we observe the solidification of the systems, but the g values before solidification are much larger than for the mixtures of m-nitrotoluene with the same alkane. This shows that pre-critical clusters for the o-nitrotoluene mixtures are much larger than for m-nitrotoluene and the o-nitrotoluene systems are very close to their critical temperature. From experiment it is known that o-nitrotoluene-mixtures show a classical critical point at a temperature higher than their melting point, but those results clearly explain the stronger tendency for cluster formation for o-nitrotoluene mixtures than for m-nitrotoluene with alkanes.

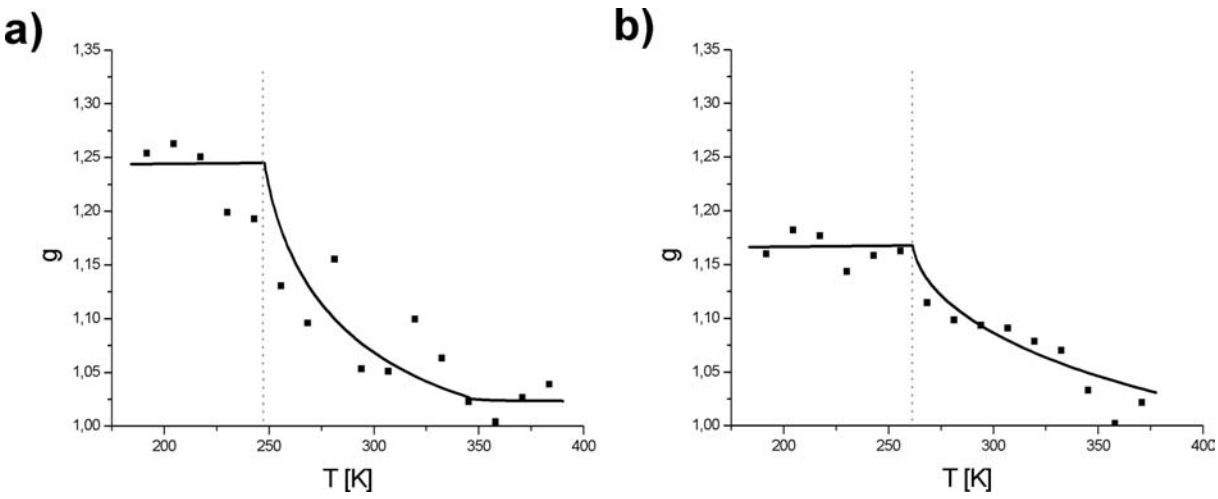

Fig. 3. Temperature dependence of g parameter for a) m-nitrotoluene – n-decane for $x_2 = 0.49$ and b) m-nitrotoluene – n-hexadecane for $x_2 = 0.66$. With decreasing temperature g increases until the freezing point of the mixture is reached.

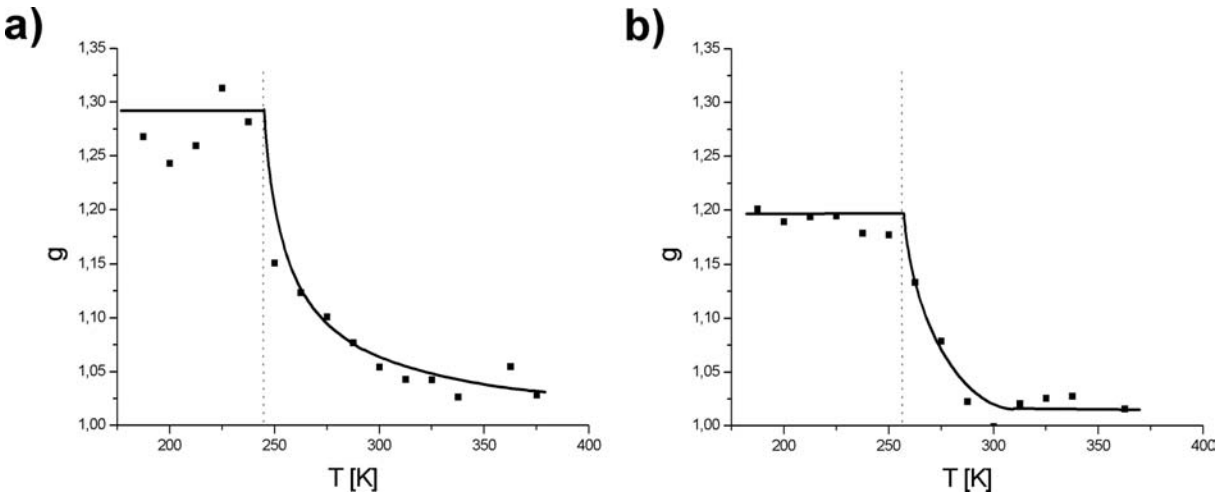

Fig. 4. Temperature dependence of g parameter for a) o-nitrotoluene – n-decane for $x_2 = 0.38$ and b) o-nitrotoluene – n-hexadecane for $x_2 = 0.70$.

In Fig. 5 we present the concentration dependence of the g parameters at a temperature just below $T_{s,}$ for the systems m-nitrotoluene with n-decane and n-hexadecane. Near the concentrations: $x_2 = 0.49$ (m-nitrotoluene – n-decane) and $x_2 = 0.66$ (m-nitrotoluene – n-hexadecane) the $g(x_2)$ functions show a clear peak, showing that for this concentrations the clusters grow to their largest size. Therefore these values of x_2 must be pre-critical concentrations of these mixtures. Such results of molecular simulations describe the experimentally observed behaviour of the mixture of m-nitrotoluene with n-decane and n-hexadecane relatively well.

Figure 6 presents the NDE (x_2) functions for these systems at various temperatures [1]. The concentration dependence of NDE for different temperatures has revealed the greatest NDE increase at about $x_2 = 0.54$ and $x_2 = 0.68$ for mixtures of m-nitrotoluene with n-decane and n-hexadecane respectively. The anomalous increase in NDE with decreasing temperature for this systems of these concentrations

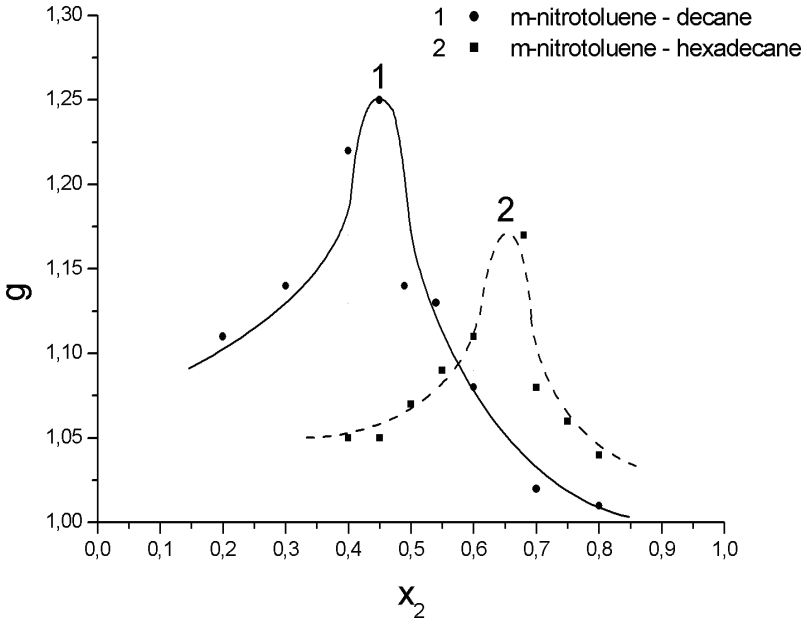

Fig. 5. Parameter g as a function of concentration x_2 for $T < T_S$ for 1: m-nitrotoluene – n-decane, 2: m-nitrotoluene – n-hexadecane. A distinct peak appears at $x_2 = 0.49$ and $x_2 = 0.66$ respectively.

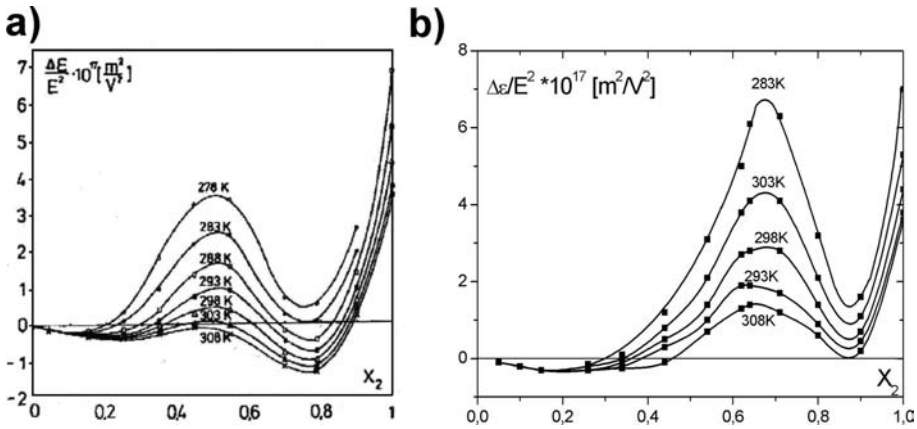

Fig. 6. The NDE vs. x_2 for a) m-nitrotoluene – decane and b) m-nitrotoluene – hexadecane at various temperatures.

is related to the increase in the range of correlation of the density fluctuations typical of pre-critical systems.

In Fig. 7 we present the concentration dependences of the g parameter at a temperature below T_s, for the systems o-nitrotoluene with n-decane and n-hexadecane. Near the concentrations: $x_2 = 0.38$ (o-nitrotoluene – n-decane) and $x_2 = 0.70$ (o-nitrotoluene – n-hexadecane) the $g(x_2)$ function has a peaks, showing that for this concentrations the clusters grow to the largest size. For these systems these are critical concentrations, as is experimentally confirmed by the results of NDE.

Figure 8 presents typical NDE vs. concentration results for critical o-nitrotoluene with n-decane [1] and n-hexadecane [35] systems at various temperatures. An anomalous increase of NDE near the critical

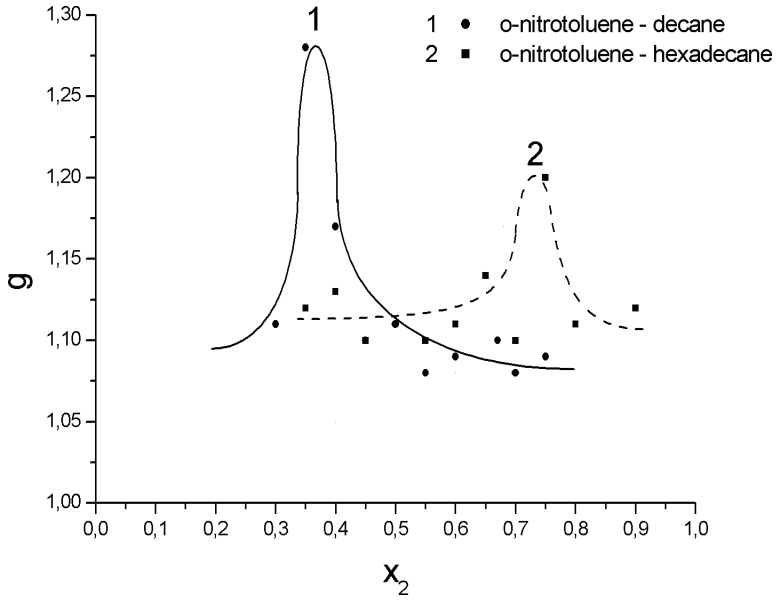

Fig. 7. Parameter g as a function of concentration x_2 for $T < T_S$ for 1: o-nitrotoluene – n-decane, 2: o-nitrotoluene – n-hexadecane. A distinct peak appears at $x_2 = 0.38$ and $x_2 = 0.70$ respectively.

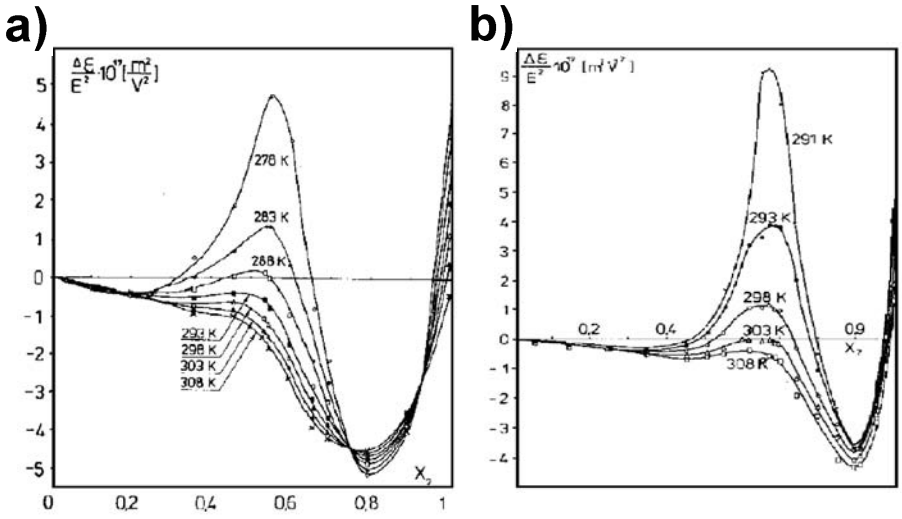

Fig. 8. The NDE vs. x_2 for a) o-nitrotoluene – n-decane and b) o-nitrotoluene – n-hexadecane systems at various temperatures [2].

concentration is observed. The critical concentrations shown in Fig. 8 are very close to the concentrations of the maxima of the $g(x_2)$ functions (Fig. 7).

Figure 9 presents experimental values of critical (for the mixtures of o-nitrotoluene with n-alkanes) and pre-critical (for the mixtures of m-nitrotoluene with n-alkanes) concentrations x_C, vs. number of carbon atoms n in alkanes [10]. The value of critical concentration increases with the number of C atoms and so with increasing molecular volume of n-alkanes. The same values of x_c and precritical values of $x_c^{'}$ for the same alkane are related with the similar molecular volume of o- and m-nitrotoluene [10].

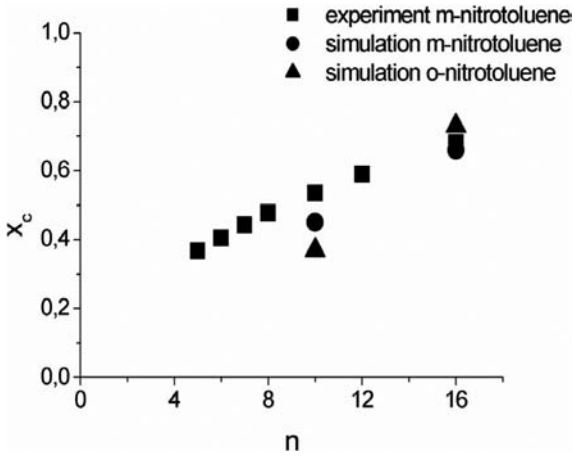

Fig. 9. Experimental and simulation results of critical concentration x_C vs. number of carbon atoms n in n-alkane. For large alkanes the critical concentration is larger than for small alkanes.

The values obtained from the simulations are very close to the experimental results. For longer alkanes the critical concentrations are larger relative to the shorter alkanes, and is related to the increase of σ_{11} parameter of alkanes.

4. Conclusions

The aim of the study was to show that for some critical mixtures of m- nitrotoluene with alkanes, a elevated melting point leads to an apparent critical point in the metastable phase of the system, below its melting point. NDE studies for these mixtures have indicated that the systems show a far pre-critical effect without phase separation, because the effect is inhibited by the system's freezing. The results of the simulations presented show that the use of an effective potential of Lennard – Jones form, taking into account dipolar forces, allows us to describe the thermodynamics of the systems studied relatively well, and to observe the apparent critical point. A comparison of the behavior of m-nitrotoluene – n-alkane systems with classical critical systems (o-nitrotoluene with n-alkanes) shows the influence of the ε_{22} parameter on the freezing temperature of these mixtures and clearly show the tendency to phase separate in both types of mixture. Similar studies are planned for a group of a mixture showing a similar pre-critical effect.

Acknowledgment

This work is supported by Polish Ministry of Science and High Education, grant MNiSW No. N N202 73 03 33.

References

[1] M. Sliwinska-Bartkowiak, B. Szurkowski and T. Hilczer, *Chem Phys Lett* **94** (1983), 609.
[2] M. Sliwinska-Bartkowiak, *Ber Bunsengess Phys Chem* **94** (1990), 64.

[3] M. Sliwinska-Bartkowiak, *Phys Lett A* **128** (1988), 84.
[4] M. Schoen and C. Hoheisel, *Mol Phys* **57** (1986), 65.
[5] M. Sliwinska-Bartkowiak, *Chem Phys Lett* **112** (1984), 237.
[6] M. Sliwinska-Bartkowiak and L. Radojewska, *Ber Bunsenges Phys Chem* **99** (1990), 1187.
[7] M. Sliwinska-Bartkowiak, *Phys Lett A* **128** (1988), 84.
[8] M. Sliwinska-Bartkowiak, *Phys Lett* **89** (1982), 465.
[9] M. Sliwinska-Bartkowiak, B. Szurkowski and T. Hilczer, *Phase Tran* **18** (1989), 77.
[10] M. Sliwinska-Bartkowiak and J. Phys, *Condens Matter* **5** (1993), 407.
[11] H.E. Stanley, *Introduction to Phase Transitions and Critical Phenomena*, Clarendon Press, Oxford, 1971.
[12] A. Piekara, *Acta Phys Polon* **10** (1950), 37.
[13] A. Chelkowski, *Acta Phys Polon* **24 165** (1963).
[14] J. Malecki, *J Chem Soc Faraday II* **72** (1976), 104.
[15] J. Nowak, J. Malecki, J.M. Thiebaut, J.M. Rivail and J. Chem, *Soc Faraday II* **76** (1980), 179.
[16] M. Dutkiewicz, *Chem Phys Lett* **121** (1985), 73.
[17] A. Chelkowski, *Dielectric Physics, Elsevier/North/Holland*, Inc., New York, 1980.
[18] A. Piekara, *Phys Rev* **42** (1936), 448.
[19] A. Piekara, Nonlinear Behaviour of Molecules, in: *Atoms and Ions in Electric, Magnetic and Electromagnetic Fields*, L. Neel, ed., North-Holland, Amsterdam, 1979, p. 336.
[20] K. Zboinski, *Chem Phys Lett* **39** (1976), 336.
[21] W. Pyzuk and K. Zboinski, *Chem Phys Lett* **52** (1977), 557.
[22] J. Malecki and J. Ziolo, *Chem Phys* **35** (1978), 187.
[23] K. Zboinski, H. Opiola and L. Piekara-Sady, *Chem Phys* **40** (1979), 77.
[24] S.J. Rzoska and J. Chrapec, *J Ziolo, Physica A* **139** (1986), 569.
[25] S.J. Rzoska anb J. Chrapec, *Phase Transitions* **15** (1989), 1.
[26] D.W. Oxtoby and H. Methiu, *Phys Rev Lett* **36** (1976), 1092.
[27] D.W. Oxtoby, *Phys Rev A* **15** (1977), 1251.
[28] J. Goulon, J.L. Greffe and D.W. Oxtoby, *J Chem Phys* **70** (1979), 4742.
[29] J. Goulon, D.W. Oxtoby, J.M. Thiebaut and J.L. Greffe, Nonlinear Behaviour of Molecules, in: *Atoms and Ions in Electric, Magnetic and Electromagnetic Fields*, L. Neel, ed., North-Holland, Amsterdam, 1979, p. 343.
[30] H. Buchowski, *Chemia Fizyczna*, PWN, Warszawa, 1980.
[31] M. Sliwinska-Bartkowiak, B. Ratajczak, L. Golibrocki and M. Banaszak, *J Chem Phys* (2006), 124.
[32] J.S. van Duijneveldt and D. Frenkel, *J Chem Phys* (1992), 96.
[33] B. Ratajczak, M. Sliwinska-Bartkowiak, B. Coasne and K.E. Gubbins, *J Non-Cryst Solids* (accepted).
[34] P.G. Debenedetti and F.H. Stillinger, *Nature* **410** (2001), 259.
[35] M. Sliwinska-Bartkowail, *Chem Phys Lett* **112** (1984), 237.

Journal of Computational Methods in Sciences and Engineering 10 (2010) 573–583
DOI 10.3233/JCM-2010-0345
IOS Press

Ab initio and DFT study of the static dipole (hyper)polarizabilities of benzaldehyde and thio-benzaldehyde molecules in gas phase

Humberto Soscún[a,b,*]
[a]*Centro Nacional de Tecnología Química CNTQ, Complejo Tecnológico Simón Rodríguez CTSR, La Carlota, Caracas, Venezuela*
[b]*Laboratorio de Química Inorgánica Teórica, Departamento de Química, Facultad Experimental de Ciencias, La Universidad del Zulia, Ap. 526, Grano de Oro, Maracaibo, Venezuela*

Abstract. The results of *ab initio* and density functional theory DFT calculations of dipole moments and electronic contributions to static dipole (hyper)polarizabilities of benzaldehyde and thiobenzaldehyde molecules in gas phase are presented. These properties were evaluated at the SCF, MP2, MP4 and DFT (B3LYP) levels of theory with a selection of basis sets that include polarization and diffuse functions on the C, O, S and H atoms: 6-31+G(d,p) (A), 6-311++G(3d,3p) (B), 6-31+G(d*,p) (C) and the Sadlej (D) basis sets, using HF/A, MP2/A and B3LYP/A optimized geometries under the Cs symmetry restriction. The C basis set has been optimized in terms of the maxima second hyperpolarizability at HF level. Both MP2 and MP4 methods, performed at full electron configuration, have shown to perform well in the calculation of such properties.

Considering the basis sets effects, the impact of the electron correlation in the (hyper)polarizabilities of these molecules is analyzed systematically in terms of the differences between MP2 and MP4 perturbation theory and those from DFT(B3LYP) methods.

The effects of substitution of the C = S fragment by the C = O group in the benzaldehyde molecule, giving the formation of thiobenzaldehyde, lead to enhanced results of nonlinear optical properties in terms of their first (β) and second hyperpolarizability (γ), that shown to be higher than those for *para*-Nitroaniline molecules. In fact, thiobenzaldehyde exhibit significant values of nonlinear optical properties which make this chromophore a prospective building block for nonlinear optical materials.

Keywords: Hyperpolarizabilities, HF, MP2, MP4, DFT, benzaldehyde, thiobenzaldehyde

1. Introduction

The search for new materials with enhanced nonlinear optical (NLO) properties is currently an active area of experimental and theoretical research due to their potential technologic applications in the photonic field [1–4]. In this context, organic NLO materials have shown great promise in the area of photonics and molecular electronic due to their useful physical and optical properties. These compounds can be easily synthesized and their properties can be evaluated by different NLO techniques in gas phase, solution, condense phase or processed into optical-quality thin films [5,6]. Additionally, these properties can be theoretically determined by modelling the electronic, optical, and NLO properties using either ab initio or semiempiric techniques [7,8]. This strategy eliminates the high costs associated with the synthetic and characterization process approach. Furthermore, it offers the possibility of testing the potential usefulness of a material.

*Corresponding author. E-mail: hsoscun@mct.gob.ve; hsoscun@cntq.gob.ve.

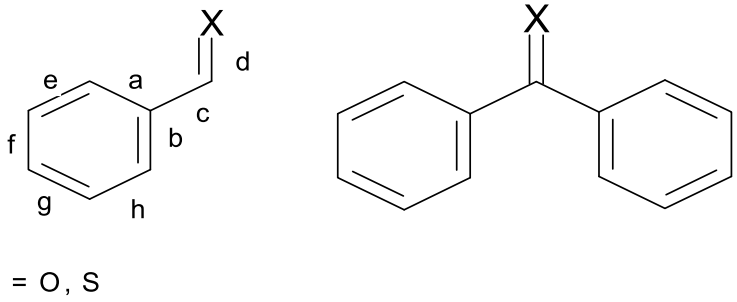

Fig. 1. Atomic labels, geometric parameters and axis orientation of benzaldehyde, thio-benzaldehyde and benzophenone molecules with Cs symmetry.

The C = O group is a chromophore that can be found in many organic and organometallic compounds and it determines an electronic driving force for conjugation within a molecule when is bonded to a resonant structure such as benzene and benzene derivatives [9]. This feature makes C = O group a polar moiety that can induce important polarizable effects in the electronic structure of a conjugated molecule. The representative aromatic compounds that contain the C = O group in the form of tri-substituted carbon atom are the benzaldehyde and dibenzophenone compounds, which are shown in Fig. 1.

In the present work, we have studied theoretically at different levels of theory and basis sets for the first time the electronic contribution to the dipole moment μ, static dipole polarizability (α) and (hyper) polarizabilities (first hyperpolarizability β and second hyperpolarizability γ) of benzaldehyde and thiobenzaldehyde molecules in gas phase, which are prototype aromatic compounds, to understand the effect of the S atom in the aldehyde moiety chemically bonded to a phenyl ring. Results for dibenzophenone will be published in a separate paper.

2. Theory and computational method

In the model of polarization of Buckingham, the interaction between the electronic density of a molecular system and an static external electric field induces a dipole moment μ, that is expressed as a Taylor series in terms of the electric field $\Im$ as [10]:

$$\mu_i(\Im) = \mu_i(0) + \alpha_{ij}\Im_j + \frac{1}{2}\beta_{ijk}\Im_j\Im_k + \frac{1}{6}\gamma_{ijkl}\Im_j\Im_k\Im_l + \quad (1)$$

where μ_i (0) is the static dipole moment component of the isolated molecule and the α_{ij}, β_{ijk} and γ_{ijkl} coefficients are the components of the tensors of the static dipole polarizability, first hyperpolarizability and second hyperpolarizability, respectively. In Eq. (1), the i, j, k, l indexes correspond to the Cartesian x, y, z axis and the Einstein summation convention is satisfied. Similar to the Eq. (1), an expression for the $\mathrm{E}(\Im)$ energy of the molecular system is defined in terms of the electric field $\Im$

$$\mathrm{E}(\Im) = \mathrm{E}(0) - \mu_i\Im_i - \frac{1}{2}\alpha_{ij}\Im_i\Im_j - \frac{1}{6}\beta_{ijk}\Im_i\Im_j\Im_k - \frac{1}{24}\gamma_{ijkl}\Im_i\Im_j\Im_k\Im_l + \quad (2)$$

where E (0) is the total energy of the free molecular system. Formally, the α_{ij}, β_{ijk} and γ_{ijkl} properties can be obtained by successive differentiation of the Eq. (1) with respect to the electric field $\Im$. For low intensity electric fields $\Im$, the main response is the dipole polarizability α_{ij} that governs the linear optical phenomena, whereas for intense $\Im$ fields appear the nonlinear optical phenomena that are determined

by $\beta_{ijk}$and γ_{ijkl} hyperpolarizabilities, which are referred as nonlinear optical NLO properties. These properties are called static for electric fields at zero frequency ($\omega = 0$) and dynamic for oscillating fields $\Im(\omega)$ ($\omega \neq 0$). The invariant properties associated to α_{ij}, β_{ijk} and γ_{ijkl} tensors, employed in this work, are the average dipole polarizability $\bar{\alpha}$ and the anisotropy of the polarizability $\Delta\alpha$, and the $\bar{\beta}_t$ and $\bar{\gamma}$ mean values. These properties are obtained from the independent components of the (hyper) polarizability tensors and can be written as

$$\bar{\alpha} = \frac{1}{3}\sum_{i=1}^{3}\alpha_{ii} \tag{3}$$

$$\Delta\alpha = \sqrt{\frac{\left[(\alpha_{xx}-\alpha_{yy})^2 + (\alpha_{xx}-\alpha_{zz})^2 + (\alpha_{yy}-\alpha_{zz})^2 + 6(\alpha_{xy}^2+\alpha_{yz}^2+\alpha_{xz}^2)\right]}{2}} \tag{4}$$

$$\bar{\beta}_t = \sqrt{\sum_{i=1}^{3}\beta_i^2} \tag{5}$$

and

$$\bar{\gamma} = \frac{1}{5}\sum_{i,j=x,y,z}^{\gamma_{iijj}} \tag{6}$$

where $\beta_i = (\beta_{iii} + \beta_{ijj} + \beta_{ikk})$, μ_i ($i = x, y, z$) is the *i-th* component of dipole moment μ with $(i, j, k, l) = (x, y, z)$. In the present work, we have evaluated the independent components of the static dipole (hyper)polarizabilities of the title molecules within the finite field approach [11] by using the Gaussian 98 [12] software coupled to Fortran 77 FFIELD [13] program at different levels of theory. FFIELD employ the finite field equations of Kurtz et al. that consider perturbations until double finite electric fields [14] in terms of the Eq. (2) and electric field intensities of 0.005 au. The numeric stabilities of the results obtained with this methodology have been reported elsewhere.

In the present study, the static (hyper)polarizabilities of the benzaldehyde and thiobenzaldehyde molecules were calculated using *ab initio* HF, MP2 [15] and MP4 [16] methods and the *density functional theory* B3LYP [17] hybrid approach, in conjunction with the standard 6-31+G(d,p) (A) [18], the extended 6-311++G(3d,3p) (B) [19], the optimized 6-31+G(d*,p) (C) [20] and the specialized Sadlej (D) [21] basis sets, where C basis set has been optimized in terms of the maxima second hyperpolarizability at HF level. It is important to note that the A, B, C and D basis sets are augmented with d polarizations and sp diffuse functions for C and O atoms and, additionally, p polarization functions for H atoms, as well. These extensions are considered as significant features for the good performance of basis sets in NLO calculations. We expect that these basis sets, in conjunction with the MP2, MP4 and DFT methods, are a good starting point to give accurate estimated values for the studied properties of benzaldehyde and thiobenzaldehyde molecules in vacuum. It is worth to mention that recently it has been reported that the MP4/B, MP4/D and B3LYP/B methodologies give good performance for molecular (hyper)polarizabilities of para-Nitroaniline in gas phase [22], which results are comparable to more sophisticated and accurate methods, such as CCSD/aug-cc-pVTZ applications [23].

All the calculations have been carried out by using fully Cs optimized geometries of the benzaldehyde and thiobenzaldehyde molecules at HF, MP2 and B3LYP methods with the standard A = 6-31+G(d, p)

Table 1
Optimized geometric parameters of benzaldehyde and thiobenzaldehyde with the HF, MP2 and B3LYP methods and the standard 6-31+G(d,p) basis set (A). Bond lengths Rij en Angstroms and bond angles <ijk in degrees °

	X = O; Benzaldehyde			X = S; Thiobenzaldehyde		
	HF/A	MP2/A	B3LYP/A	HF/A	MP2/A	B3LYP/A
Rij/Angstroms						
C_1-C_2	1.3937	1.4016	1.4050	1.3979	1.4049	1.4103
C_2-C_3	1.3824	1.3924	1.3922	1.3810	1.3912	1.3903
C_3-C_4	1.3916	1.4003	1.4017	1.3916	1.4003	1.4021
C_4-C_5	1.3858	1.3968	1.3978	1.3858	1.3964	1.3978
C_5-C_6	1.3878	1.3955	1.3959	1.3860	1.3948	1.3940
C_6-C_1	1.3889	1.4000 (1.397)[a]	1.4025	1.3953	1.4050	1.4101
C_1-C_7	1.4338	1.4783 (1.479)[a]	1.4807	1.4668	1.4654	1.4610
C_7-X_8	1.1918	1.2290 (1.212)[a]	1.2187	1.6165	1.6263	1.6401
C_2-H_{10}	1.0743	1.0821	1.0855	1.0736	1.0822	1.0854
C_3-H_{11}	1.0752	1.0821	1.0860	1.0751	1.0823	1.0860
C_4-H_{12}	1.0757	1.0822	1.0863	1.0756	1.0823	1.0862
C_5-H_{13}	1.0751	1.0820	1.0858	1.0750	1.0822	1.0858
C_6-H_{14}	1.0769	1.0840 (1.095)[a]	1.0877	1.0762	1.0839	1.0871
C_7-H_9	1.0951	1.1043	1.1116	1.0805	1.0905	1.0943
<ijk/°						
C_1-C_2-C_3	119.9	119.5	119.9	120.2	120.1	120.3
C_2-C_3-C_4	119.0	120.2	120.1	120.2	120.4	120.3
C_3-C_4-C_5	120.4	120.2	120.3	120.2	119.8	120.1
C_4-C_5-C_6	119.6	119.8	119.7	119.6	120.0	119.8
C_5-C_6-C_1	120.2	119.9	120.21	120.7	120.5	120.8
C_1-X_7-O_8	124.6	124.5	125.0	128.6	127.5	128.3
C_2-C_1-C_7	120.5	120.5	120.8	122.6	122.3	122.6
C_1-C_7-H_9	115.1	115.2	114.8	113.5	113.9	113.6
X_8-C_7-H_9	120.3	120.3	120.3	117.9	118.6	118.1
C_1-C_2-H_{10}	119.1	119.0	118.7	119.3	119.1	118.7
C_2-C_3-H_{11}	120.1	120.1	120.0	119.9	119.7	119.9
C_3-C_4-H_{12}	119.8	119.9	119.8	119.9	120.1	119.9
C_4-C_5-H_{13}	120.2	120.1	120.2	120.3	120.1	120.2
C_5-C_6-H_{14}	119.9	120.4	120.2	119.7	120.1	119.0

a) Average experimental results from electron diffraction. Ref. [24].

basis set, considering planar equilibrium structures as reported for the gas-phase electron diffraction and MP2(FC)/6-31G* investigation of the aromatic aldehyde [24].

The reference of the coordinate system assumes that the molecules lie in the *yz* plane with the z axis being the perpendicular one.

3. Results and discussions

3.1. Geometry optimizations

Benzaldehyde is an important organic molecule, which framework is present in a large variety of derivatives of different natural and synthetic compounds, with multiple organic, inorganic, and organometallic applications. Thiobenzaldehyde molecule is constructed by substitution of the O atom by S one in the C = X moiety. The relevant optimized geometric parameters, obtained in the present study for these molecules, considered as Cs symmetry as shown in Fig. 1, calculated by using HF, MP2 and B3LYP

Table 2
Total energy E_T/au, HOMO and LUMO energies/au, dipole moments μ/Debyes and dipole polarizability α/au of benzaldehyde and thiobenzaldehyde with the HF, MP2 and B3LYP methods and the 6-31+G(d,p) (A), 6-311++G(3d,3p) (B), 6-31+G(d*,p) (C) and Sadlej (D) basis sets

	HF/A	MP2/A	MP4/A	B3LYP/A	B3LYP/B	B3LYP/C	B3LYP/D
				X = O; Benzaldehyde			
-E_T	343.45449	344.59379		345.59797			
E_{HOMO}	−0.3534	−0.3531					
E_{LUMO}	0.0640	0.0573					
μ_x	0.000	0.000	0.000	0.000	0.000	0.000	0.000
μ_y	−0.594	−0.605	−0.924	−0.700	−0.692	−0.702	−0.690
μ_z	1.297	1.163	0.912	1.238	1.219	1.293	1.216
μ	1.427	1.311	1.298	1.422	1.402	1.471	1.398 (1.377)[a] (1.263)[b] (1.10)[c]
α_{xx}	49,87	49.10	48.75	49.87	53.85	45.92	54.62
α_{xy}	−13.88	−12.52	−12.41	−13.38	−13.32		−13.44
α_{yy}	110.68	105.86	105.05	110.69	114.62	104.50	116.57
α_{yz}	5.17	5.04	4.89	5.17	4.88		4.12
α_{zz}	93.03	89.76	89.22	91.77	94.06	101.75	96.80
α_{zx}	−7.65	−7.42	−7.35	−7.65	−7.34		−7.49
α_{ave}	84.53	81.57	81.01	84.11	87.51	84.06	89.33 (86.25)[a] (87.73)[c]
$\Delta\alpha$	86.36	80.98	80.31	86.01	85.22	90.97	86.78
				X = S; Thiobenzaldehyde			
-E_T	666.08786	667.18561		668.55328			
E_{HOMO}	−0.3336	−0.3320					
E_{LUMO}	0.0229	0.0021					
μ_x	0.000	0.000	0.000	0.000	0.000	0.000	0.000
μ_y	0.043	0.022	0.007	0.103	0.099	0.082	0.099
μ_z	−1.478	−1.088	−1.078	−1.409	−1.358	−1.472	−1.372
μ	1.479	1.089	1.078	1.413	1.362	1.474	1.375
α_{xx}	56.20	55.31	55.30	56.21	62.62	56.55	63.57
α_{xy}	4.28	2.67	2.59	4.28	4.05		4.02
α_{yy}	109.9	106.72	106.17	109.90	113.10	103.93	113.77
α_{yz}	23.17	20.46	19.26	23.17	22.12		21.83
α_{zz}	160.73	149.71	147.76	160.73	166.27	165.83	166.76
α_{zx}	9.41	6.56	6.39	9.41	9.30		9.25
α_{ave}	100.92	103.49	103.08	108.95	114.00	108.77	114.70
$\Delta\alpha$	142.32	127.34	124.01	124.31	140.26	134.23	139.45

a) B3LYP/6-311+G(3df,2p). NIST databases;
b) Experimental Gas phase. Ref. [26];
c) Experimental Liquid phase (Neat). Ref. [5].

methods with the standard 6-31+G(d,p) basis sets are displayed in Table 1. Additional experimental geometric parameters from electron diffraction [24] are also included in Table 1 for comparison. There is excellent agreement between the present geometry results for benzaldehyde and those from experimental determinations. Energy values of the optimized structures and the corresponding HOMO and LUMO energies of both studied molecules are reported in Table 2. Additional calculated properties, displayed in Table 2 and subsequent Tables are analyzed in the next sections.

3.2. Dipole moments μ

The dipole moment μ of benzaldehyde has been accurately determined by using Stark effect techniques measured at conditions of supersonic expansion [25], with uncertainty of 0.1% level, where the orientation of the components (from negative to positive) were assumed on the basis of MP2/6-31G(d,p) and DFT(B3LYP)/6-31G(d,p) calculations. The measured μ value is of 1.235 au, which is comparable to previously reported gas-phase total dipole moment of 1.263 Debyes [26]. Additionally, experimental μ

value of 1.10 Debyes has been reported for liquid benzaldehyde [25]. In this work, in doing the NLO property evaluations of benzaldehyde and thiobenzaldehyde calculations, theoretical determinations of this property were automatically performed by using MP2, MP4 and B3LYP methods with the selection of basis sets indicated in the section of Methods. The corresponding results obtained here for μ of benzaldehyde range 1.298 Debyes – 1.471 Debyes, where the lower reported experimental value corresponds to the gas phase one of 1.263 Debyes, which is in good correspondence with the μ calculated at MP4 level (1.298 Debyes). The μ DFT values tend to be higher than those from MP2 and MP4 methods.

The μ dipole moment of the thiobenzaldhyde calculated at different levels of theory and a variety of basis sets, it is also reported in Table 2. For this compound there is not reference about experimental determination or theoretical estimation of this property. The μ results obtained here show greater discrepancies between the methods and basis sets than those for benzaldehyde, being the lowers for the MP2/A (1.098 Debyes) and MP4/A (1.078 Debyes) methods. The corresponding μ DFT values are similar between both molecules, which oscillate from 1.362 Debyes (B3LYP/B) to 1.474 Debyes (B3LYP/6-31+G(d*,p)). If the μ MP4 value is taken as reference, thiobenzaldehyde molecule is in gas phase much less polar than benzaldehyde one.

3.3. Static dipole polarizabilities α_{ij}, α_{ave}, $\Delta\alpha$

The α_{ij} components, average polarizability α_{ave} and polarizability anisotropy $\Delta\alpha$ results obtained in this work for benzaldehyde and thiobenzaldehyde with different models and basis sets are displayed in Table 2. The α_{ij}terms are reported for record purposes. The experimental dipole polarizability α_{ave} of liquid benzaldehyde has been reported and the corresponding value of 87.73 au [5] is shown in Table 2. Additionally, the NIST Computational chemistry databases report a series of α_{ave} results for this property calculated by using different theoretical models and basis sets. For instance, a value of $\alpha_{ave} = 86.25$ au, calculated at B3LYP/6-311G(3df,2p) level, reported there in is also shown in Table 2 for comparison purposes. The analysis of the present calculations, indicate that DFT α_{ave} results are consistent with both, experimental and theoretical values reported from the literature. However, MP2 and MP4 dipole polarizability values for benzaldehyde displayed in Table 2 are almost 10% less than the experimental one. Considering that we are only taking in account for these calculations the electronic part of the dipole polarizability, and dynamic and vibrational effects are neglected, the correspondence between DFT results and the experimental can be considered as casual. We expect, that MP4 method reflects the real electronic contribution of this property for the macroscopic static dipole polarizability of benzaldehyde molecule. How there are no reports in the literature about the $\Delta\alpha$ anisotropy for the title molecules, the results presented in this work are of predictive nature. It is important to note that the corresponding results for the α tensor at B3LYP/6-31+G(d*,p) level were calculated in the principal axis system of the molecular polarizability where the crossing terms are zero.

Table 2 also contains the present results for the static α_{ij}components, α_{ave} and $\Delta\alpha$ for thiobenzaldehyde molecule in gas phase, where no reports about optical properties of this S aromatic compound have been published so far in the literature. The important features of these calculations is that MP2, MP4 and DFT α_{ave} results show that substitution of the S atom by the O one in the C = X bond of the carbonyl function of the aldehyde group induce significant changes in the internal electronic rearrangements of thiobenzaldehyde molecule, which are reflected and enhanced in the presence of a electric field. Independently of the employed methodology, the α_{ave} dipole polarizability increases more than 20% due to the presence of the S atom in relation to the compound with the oxygen one. The anisotropy in thiobenzaldehyde is much larger than in benzaldehyde molecule.

The observed electronic effects due to the presence of the S atom on the optical properties of conjugated organic compounds are long recognized, where one of the theoretical pioneer works is due to the Eckard and Sadlej groups [27]. For example, the observed variations in the dipole moments of cyclic ketones and thio-ketones were rationalized in terms of the conjugation, intermolecular electron transfer, and differences in the electronegativities of the oxygen and sulphur atoms. Whereas, the dipole polarizability changes can be understood in terms of the extent of the p-electron conjugation, were the replacement of oxygen by sulphur leads to a significant increase of the dipole polarizability which parallels the differences between atomic polarizabilities of oxygen and sulphur [27]. In this study, Eckard and Sadlej groups [27] have found that despite of the complicated multiconfiguration structure of the ground state wave function of cyclic ketones and thioketones molecules, the single reference MP2 method is able to perform in a similar way as a single reference CC, CASSCF and CASPT2 methods, where a congruence between MP2 and higher theory level was found for electric property calculations. In this context, we are confidents in the semi-quantitative reliability of the present (hyper)polarizability MP2 and MP4 results of the studied molecules.

3.4. Static dipole First Hyperpolarizabilities β_{ijj}, β_i and β_t

We report for the first time a systematic and accurate theoretical investigation about the static first hyperpolarizabities β of benzaldehyde and thiobenzaldehyde molecules, were the effect of the change of the S by O atom is explored at different levels of theory and basis sets for this property. The calculated components of the β tensor, β_{ijj}, β_i and β_t of these molecules are displayed in Table 3. Additionally, it is reported for comparison purposes the experimental β value of benzaldehyde, measured using solution-phase dc electric field induced second-harmonic generation (EFISH) [5].

It is worth to mention, that we have calculated the static β_t property for *para*-Nitroaniline PNA molecule in gas phase at the MP4/A level of theory for comparison, which results are also included in Table 3. The β_t results for benzaldehyde shown in Table 3 goes from 235 au (B3lYP/6-31+G(d,p)) to 292 au (B3LYP/6-31+G(d*,p)) at DFT level, whereas for MP2 and MP4 levels of theory, the corresponding results are 314.6 au and 371.2 au, respectively. In this case, the electron correlation at the perturbation level increases the property in relation to DFT calculations. These values are much higher than the experimental EFISH first dipole polarizability β_t for this molecule in solution, which value is 96.2 au. With respect to the theoretical β_t value of 1808.0 au for PNA (See Table 3), benzaldehyde shows a lower first hyperpolarizability, which results are in correspondence with the shorter conjugation and lower push pull mechanisms that occurs in this molecule with respect to those in PNA.

The results obtained here for the first hyperpolarizability of thiobenzaldehyde are displayed in Table 3. The presence of the S in atom in thiobenzaldehyde instead of the O one in benzaldehyde, induces strong electronic effects on the first hyperpolarizability, where there is a factor of 4.4 for the ratio $\beta_v =$ (MP4, thiobenzaldehyde)/β_v (MP4, benzaldehyde). Additionally, the MP2 and MP4 electron correlation effects are, for the first hyperpolarizability of this molecule, larger than those from DFT ones in more than 50%. At this point it is important to mention that thiobenzaldehyde, according to results of Table 3, shows a first hyperpolarizability that is almost similar to that of PNA molecule, at the same level of calculations.

3.5. Static dipole second hyperpolarizabilities γ_{iijj}, γ_{ave}

Table 4 display the present results of the components and the average second hyperpolarizability γ of benzaldehyde and thiobenzaldehyde molecules calculated at the different levels of theory and basis sets. For comparison are reported the experimental γ values of benzaldehyde, determined in solution at both,

Table 3
The first dipole hyperpolarizability β/au of benzaldehyde and thiobenzaldehyde with the HF, MP2 and B3LYP methods and the 6-31+G(d,p) (A), 6-311++G(3d,3p) (B), 6-31+G(d*,p) (C) and Sadlej (D) basis sets

	HF/A	MP2/A	MP4/A	B3LYP/A	B3LYP/B	B3LYP/C	B3LYP/D
			X = O Benzaldehyde				
β_{yxx}	33.5	35.2	36.2	38.3	29.8	28.6	28.2
β_{yyy}	−129.8	−217.1	−353.1	−212.5	−196.6	−222.1	−184.6
β_{yzz}	−41.1	−114.4	−54.3	−87.6	−79.1	−97.5	−78.6
β_{zxx}	−36.7	−38.2	−24.88	−42.3	−38.8	−41.7	−54.9
β_{zyy}	63.3	106.0	75.7	96.8	85.8	105.5	87.2
β_{zzz}	−52.6	−38.1	−52.2	−45.0	−50.7	−38.8	−34.1
β_x	0.0	0.0	0.0	0.0	0.0	0.0	0.0
β_y	−137.4	−296.3	−371.2	−261.8	−246.0	−291.0	−235.0
β_z	−26.0	105.8	−1.38	9.5	−1.7	25.0	−1.7
β_t	139.8	314.6	371.2 (92.6)[a]	262.0	246.0	292.0	235.0
			X = S Thiobenzaldehyde				
β_{xxx}	0.0	0.0	0.0	0.0	0.0	0.0	0.0
β_{xyy}	0.0	0.0	0.0	0.0	0.0	0.0	0.0
β_{xzz}	0.0	0.0	0.0	0.0	0.0	0.0	0.0
β_{yxx}	24.4	21.5	20.9	20.4	20.5	26.9	14.2
β_{yyy}	−579.6	−1427.4	−1465.4	−810.5	−753.3	−761.8	−743.6
β_{yzz}	−121.5	−118.7	−139.0	−128.6	−119.7	−153.7	−140.4
β_{zxx}	−1.7	−3.8	−3.6	−5.5	−9.1	−33.9	−39.0
β_{zyy}	303.5	307.0	351.9	337.9	305.5	337.7	317.2
β_{zzz}	23.0	44.2	42.6	30.7	15.2	2.0	0.0
β_x	0.0	0.0	0.0	0.0	0.0	0.0	0.0
β_y	−676.7	−1524.6	−1582.5	−918.7	−882.0	−949.3	−922.9
β_z	324.8	347.5	390.9	363.2	314.7	366.5	330.4
β_t	750.6	1563.7	1630.1 (1808.0) PNA	987.9	936.5	1017.6	980.3

a) Experimental Liquid phase (Neat). Ref. [5].

third harmonic generation THG and electric field induced second harmonic DC-EFISH techniques [5]. At HF/A level, the γ_{ave} value for the aromatic O aldehyde is relatively low, of about 13000 au. When the electron correlation EC is taken in account at MP2/A level, the γ_{ave} for this molecule increases in about 38 % giving a value of 17901 au. The inclusion of higher level of EC to this property such as MP4/A, a higher value is obtained of about 20290 au that corresponds to a 56 % with respect to HF and 13.3 % in relation to MP2 one. Additionally, the consideration of EC with the DFT (B3LYP) approach is dependent of the selected basis sets, how can be seen from results of Table 4. In fact, the EC at the B3LYP/A are higher than with MP2/A in relation to HF/A γ_{ave} values. The higher EC effects are observed with the Sadlej basis sets that give the highest value of γ_{ave} for benzaldehyde (23290 au). However, the B3LYP/6-31+G(d*,p) methodology is able to reproduce a γ_{ave} value for this molecule that is close to the MP4/A calculated property. In order to have a clear picture of these values, we have performed specific calculations of second hyperpolarizability for *para*-Nitroaniline PNA molecule in gas phase at the MP4/A level and MP2/A optimized geometry, where the corresponding value is of 34810 au. These results represent indeed the low ability of third order polarization of benzaldehyde molecule, which is much lower than in PNA one, and can be explained in terms of the structural differences in both molecules, where benzaldehyde is characterized by one substituted acceptor group to the aromatic ring, while PNA is dominated by a push-pull polarization mechanism, that induce enhanced second and third order polarizabilities.

We consider that the best representative theoretical results from those of Table 4 for benzaldehyde

Table 4
Second dipole hyperpolarizability γ/au of benzaldehyde and thiobenzaldehyde with the HF, MP2 and B3LYP methods and 6-31+G(d,p) (A), 6-311++G(3d,3p) (B), 6-31+G(d*,p) (C) and Sadlej (D) basis sets

	HF/A	MP2/A	MP4/A	B3LYP/A	B3LYP/B	B3LYP/C	B3LYP/D
			X = O Benzaldehyde				
γ_{xxxx}	11360	12409	14594	12823	10331	12768	12830
γ_{yyyy}	15604	24569	38401	26410	25782	31888	29098
γ_{zzzz}	7850	12399	12749	14608	14665	19199	18170
γ_{xxyy}	4294	5247	6934	5479	5155	6922	6836
γ_{xxzz}	4494	5337	5736	5583	5178	7225	6271
γ_{yyzz}	6148	9480	5182	10023	9703	12151	11049
γ_{ave}	12937	17901	20290	19202	18170	23290	21502
			(10522)[a] (29384)[b]				
			X = S Thiobenzaldehyde				
γ_{xxxx}	14833	21137	24840	25768	24032	31260	27566
γ_{yyyy}	56352	109993	130610	76120	70181	78200	77227
γ_{zzzz}	15161	16066	16647	17165	13603	15024	17154
γ_{xxyy}	13815	17146	19436	18507	17028	22645	20305
γ_{xxzz}	7809	9718	10464	10370	9730	10236	12600
γ_{yyzz}	5147	6452	6688	6781	6447		8801
γ_{ave}	27977	42765	49055	38073	34845	44767	41072
			(34810) PNA				

a) Experimental Liquid phase (Neat, THG). Ref. [5].
b) Experimental Liquid phase (Neat, EFISHG). Ref. [5].

correspond to γ_{ave} at MP4/A level, which value is of 20290 au. This result is in the same order of magnitude of the THG (10522 au) and EFISHG (29384 au) experimental γ_{ave} measurements for this molecule in solution, which are also shown in Table 4. In this sense, we have performed TD-DFT(B3LYP)/6-31+G(d,p) calculations for benzaldehye at the frequency of 1064 nm for THG and EFISHG processes, and the corresponding results for these optical processes are 36561.7 au and 28244.7 au, respectively. At this level of theory, the benzaldehyde experimental EFISHG γ_{ave} value is very well reproduced for our theoretical calculations, while the THG process is not. We are aware that further research is necessary in this context of NLO optical prediction of conjugated molecules.

Results of Table 4 show that substitution of the C = O by C = S group, that give the formation of thiobenzaldehyde molecule, induces strong changes in the response of the electronic distribution in presence of intense electric fields. In fact, the third order hyperpolarizabilities γ_{ave} of thiobenzaldehyde are more than twice that corresponding value for the oxygenated compound. Furthermore, the sulphur compound is able to give higher response than PNA molecule in similar conditions, where the MP4/A results are γ_{ave} (benzaldehyde) = 49055 au $>$ γ_{ave} (PNA) = 34810 au. The results of PNA were specifically calculated in this work for comparison purposes. These results show the ability of the S atom to construct positive conjugation in an aromatic system, without belong to a push-pull model such as in PNA molecule, where the system Acceptor/Donor groups are linked by a conjugated π-bridge. The results of these electronic properties indicate that organic conjugated systems based in thiobenzaldehyde frames could be seriously considered as potential or attractive networks to construct materials for NLO applications in different technologic areas.

4. Conclusions

In the present study we investigated the dipole moments μ, dipole polarizabilities α, and first β and second γ hyperpolarizabilities of benzaldehyde and thiobenzaldehyde molecules in vacuum. The

basis set saturation, including s and *sp* diffuse functions, multiple d and p polarization functions, Sadlej specialized d optimized basis sets, and the electron correlation contribution at MP2, MP4 and DFT=B3LYP approaches has been extensively investigated for the electronic contribution of the static μ, α, β and γ properties. Despite, DFT methods in conjunction with extended and specialized basis sets are able to give a reasonable representation for the static electric properties of aromatic compounds, we have found that MP4 in conjunction with a standard 6-31+G(d,p) basis set is appropriate high-level correlated methodology for accurate calculations of dipole moments, and dipole (hyper)polarizabilities of benzaldehyde and thiobenzaldehyde. The calculated properties for benzaldehyde have been compared with the experimental results obtained from THG and EFISHG techniques, where the concordances and differences have been discussed. To rationalize the present results, we have performed specific calculations for *para*-nitroaniline molecule and their results are also discussed. The electron correlation contribution to the (hyper)polarizabilities has been analyzed, and it has been found, however, that despite of most of the electron correlation contribution is accounted for at the level of the MP2 approximation, the MP4 effects need to be taken in account.

Despite of the polarizability differences between the studied molecules, their effects on the (hyper)polarizability calculations lead to an enhancement in such properties when the O is changed by S in the C=X moiety of the aromatic aldehyde structures. Further research is being carried out in our laboratory in order to characterize in a formal way the higher order electric properties of benzaldehyde and thiobenzaldehyde molecules and its push-pull derivatives, taking in account high level electron correlation, solvent effects and dynamic dependence of the optical processes.

We expect to extend these results to similar systems with two o more aromatic rings and increasing the substitution of donor/acceptor groups in positions where the conjugation path can be effective for enhancing the NLO properties.

References

[1] J.A. Delaire and K. Naakatani, *Chem Rev* **100** (2000), 1817–1845.
[2] J.L. Bredas, C. Adant, P. Tackx, A. Persoons and B.M. Pierce, *Chem Rev* **94** (1994), 243–278.
[3] *Nonlinear Optical and Electroactive Properties of Polymers*, edited by P.N. Prasad and D.R. Ulrich ∼Plenum, New York, 1988.
[4] *Nonlinear Optical Properties of Organic Molecules and Crystals*, edited by D.S. Chemla and J. Zyss ∼Academic, New York, 1987, Vols. I and II; *Principles and Applications of Non-linear Optical Materials*, edited by R.W. Munn and C.N. Ironside ∼Chapman and Hall, London, 1993; *Nonlinear Optical Properties of Polymers*, A.J. Heeger, J. Orenstein, D.R. Ulrich, eds, Materials Research Society Symp. Proc. Vol. 109; MRS: Pittsburgh, **1987**; *Nonlinear Optical and Electroactive Polymers*; P.N. Prasad and D.R. Ulrich, eds, Plenum: New York, 1988.
[5] L.T. Cheng, W. Tam, S.H. Stevenson, G.R. Meredith, G. Rikken and S.-R. Marder, *J Phys Chem* **95** (1991), 10631–10643.
[6] D.P. Shelton and J.E. Rice, *Chem Rev* **94** (1994), 3–29; D.R. Kanis, M.A. Ratner and T.J. Marks, **94** (1994), 195–242.
[7] B. Beck and U.W. Grummt, *J Phys Chem B* **102**(4) (1998), 664–670.
[8] M.S. Sucarrat, M. Duran, J.M. Luis and B. Kirtman, *J Chem Phys* **118** (2003), 711.
[9] http://www.chemguide.co.uk/organicprops/
[10] A.D. Buckingham, *Adv Chem Phys* **12** (1967), 107.
[11] H.D. Cohen and C.C.J. Roothaan, *J Chem Phys* **43** (1965), S34–S39.
[12] Gaussian 98, Revision A.9, M.J. Frisch, G.W. Trucks, H.B. Schlegel, G.E. Scuseria, M.A. Robb, J.R. Cheeseman, V.G. Zakrzewski, J.A. Montgomery, Jr., R.E. Stratmann, J.C. Burant, S. Dapprich, J.M. Millam, A.D. Daniels, K.N. Kudin, M.C. Strain, O. Farkas, J. Tomasi, V. Barone, M. Cossi, R. Cammi, B. Mennucci, C. Pomelli, C. Adamo, S. Clifford, J. Ochterski, G.A. Petersson, P.Y. Ayala, Q. Cui, K. Morokuma, D.K. Malick, A.D. Rabuck, K. Raghavachari, J.B. Foresman, J. Cioslowski, J.V. Ortiz, A.G. Baboul, B.B. Stefanov, G. Liu, A. Liashenko, P. Piskorz, I. Komaromi, R. Gomperts, R.L. Martin, D.J. Fox, T. Keith, M.A. Al-Laham, C.Y. Peng, A. Nanayakkara, M. Challacombe, P.M.W. Gill, B. Johnson, W. Chen, M.W. Wong, J.L. Andres, C. Gonzalez, M. Head-Gordon, E.S. Replogle and J.A. Pople, Gaussian, Inc., Pittsburgh PA, 1998.

[13] The Kurtz equations were codified in the fortran 77 FFIELD software, designed and developed at the Laboratory of Theoretical and Inorganic Chemistry of La Universidad del Zulia, as interface for the Gaussian 98 and Gaussian 03 computational programs, to allow the evaluation of energies at different electric field components at Hartre-Fock and post-Hartree-Fock theory levels, using internal and external basis sets, to calculate the energy numeric derivatives and obtaining the components of microscopic linear and nonlinear optical property tensors of the considered molecules. This procedure is able to calculate the NLO properties in gas phase and in solution.
[14] H.A. Kurtz, J.P. Stewart and K.M. Dieter, *J Comp Chem* **11** (1990), 82–87.
[15] M.H. Gordon, J.A. Pople and M.J. Frisch, *Chem Phys Lett* **153** (1988), 503–506.
[16] R. Krishnan and J.A. Pople, *Int J Quant Chem* **14** (1978), 91–100, G.W. Trucks, J.D. Watts, E.A. Salter and R.J. Bartlett, *Chem Phys Lett* **153** (1988), 490–495.
[17] A.D. Becke, *Phys Rev A* **38** (1988), 3098, J.W. Yang and R.G. Parr, *Phys Rev B* **37** (1988), 785, A.D. Becke, *J Chem Phys* **98** (1993), 5648–5662.
[18] M.J. Frisco, J.A. Pople and J.S. Binkley, *J Chem Phys* **80** (1984), 3265–3269.
[19] M.J. Frisco, J.A. Pople, J.S. Binkley, *J Chem Phys* **80** (1984), 3265–3269.
[20] H. Soscún, O. Castellano, Y. Bermúdez, C. Toro, N. Cubillán, A. Hinchliffe and X. Nguyen-Phu, *Int J Quantum Chem* **106** (2006), 1130–1137.
[21] A. Sadlej, *Collect Czech Chem Commun* **53** (1988), 1995–2016; A.J. Sadlej, *Urban M Theochem* **234** (1991), 147–171; A. Sadlej, *Theo Chim Acta* **79** (1991), 123–140, I. Cernusak, V. Kello and J. Sadlej, *Collect Czech Chem Commun* **68** (2003), 211–239.
[22] J. Urdaneta, Y. Bermúdez, F. Arrieta, M. Rosales, N. Cubillán, J. Hernández, O. Castellano and H. Soscún, *Theoret Chem Acc*, Published online 18 November 2009. http://www.springerlink.com/content/1026283715m28m13/.
[23] J.R. Hammond and K.J. Kowalski, *Chem Phys* **130** (2009), 194108.
[24] K.B. Borisenko, C.W. Bock and I. Hargittai, *J Phys Chem* **100**(18) (1996), 7426–7434.
[25] O. Desyatnyk, L. Pszczokowski, S. Thorwirth, T.M. Krygowskid and Z. Kisiel, *Phys Chem Chem Phys* **7** (2005), 1708–1715.
[26] Y. Kawashima and K. Kozima, *Bull Chem Soc Jpn* **47** (1974), 2879.
[27] U. Eckart, M.P. Fulscher, L. Serrano-Andres and A.J. Sadlej, *J Chem Phys* **113**(15) (2000), 6235–6244.

Journal of Computational Methods in Sciences and Engineering 10 (2010) 585–594
DOI 10.3233/JCM-2010-0346
IOS Press

Noble gas broadening calculation for fundamental bands of H_2S

Starikov Vitaly Ivanovich*
Tomsk State University of Control Systems and Radioelectronics, Tomsk, 634050, Russia

Abstract. The results of calculations of He-, Ne-, Ar-, Kr-, and Xe- broadening coefficients of ν_1, ν_2 and ν_3 ro-vibrational lines of H_2S molecule are presented and discussed. The calculations were performed in the framework of the Robert-Bonamy method, in which the exact trajectory model was incorporated. Parameters of the interaction potentials, chosen in the form of atom-atom potentials, were optimized to give the best agreement with the existing experimental data. With the exception of the some data the agreement between the calculated and experimentally measured broadening coefficients γ is satisfactory for the ν_1 and ν_3 bands of H_2S for all collisional partners. The measured strong $J-$dependence of helium broadening in the ν_2 band did not appear in the calculation. Besides, it was found that an interaction potential for H_2S- He system is ambiguously determined. The optimal set of the parameters for H_2S- He interaction potential was used in the calculation of the helium broadening coefficients for the ν_1 band of H_2S ($J \leqslant 15$, 100 K $\leqslant T \leqslant$ 1000K) and then for their analytical representation.

Keywords: Noble gas broadening, H_2S, intermolecular potential, semi-classical impact method, analytical formula for half-widths

1. Introduction

The rovibrational spectrum of the H_2S molecule is the subject of intensive theoretical and experimental investigations because this molecule is the important atmospheric pollutant produced by natural as well as by industrial sources. For an atmospheric application it is necessary to know the self- and air-broadening coefficients of H_2S. The quantum number dependence of these coefficients was investigated in Refs [1–3] for the ν_2, ν_1, ν_3 and $2\nu_2$ bands.

The pressure-induced shift and broadening of H_2S absorption lines in the ν_2 band due to collisions between H_2S molecules and quadrupole molecules, such as N_2, O_2, D_2, H_2 and CO were experimentally studied in detail in Ref. [4]. The results of calculation of the corresponding broadening coefficients were reported in different papers; see, for example [5,6].

Only little information is available about the noble gas broadening of H_2S absorption lines. In Ref. [1] the helium broadening coefficients γ were measured for 8 lines of the ν_2 band at room temperature. In Ref. [7] the He-, Ne-, Ar-, and Kr, and Xe- broadening coefficients were determined for 23 lines from the ν_1, ν_3 and ν_2 band of H_2S; they are listed in Tables 1–2. From the transitions under study the pronounced J dependence of the broadening coefficients γ was observed. The largest change in γ from values of about 0.1 to 0.013 cm^{-1}/atm was obtained for collisions with argon and krypton. The shift and broadening coefficients of two H_2S lines in the ν_2 band due to collisions of H_2S molecules and neon and krypton were determined in Ref. [8].

*Corresponding author. E-mail: vstarikov@yandex.ru.

Table 1
Experimental [7] and calculated helium and neon broadening coefficients in fundamental bands of H_2S, $T = 296$ K

								H_2S-He			H_2S-Ne	
ν, cm^{-1}	Band	J_f	K_{af}	K_{cf}	J_i	K_{ai}	K_{ci}	exp	Cal.	γ(sur)	exp	Cal.
2693.2838	ν_1	4	4	0	3	3	1	0.045	0.041	0.043	0.0305	0.041
2740.9751	ν_1	5	3	3	4	0	4	0.049	0.043	0.044	0.0553	0.042
2713.8530	ν_1	5	4	1	4	3	2	0.043	0.042	0.043	0.0382	0.043
2740.0321	ν_1	6	4	2	5	3	3	0.040	0.041	0.043	0.0329	0.043
2717.9659	ν_1	6	5	2	5	4	1	0.0378	0.039	0.042	0.0330	0.041
2740.9150	ν_1	7	6	2	6	5	1	0.0309	0.037	0.040	0.0324	0.038
2716.0085	ν_1	8	4	5	7	3	4	0.040	0.038	0.041	0.0342	0.037
2715.0784	ν_1	8	3	5	7	4	4	0.0437	0.038	0.041	0.0400	0.036
2741.7631	ν_1	8	6	3	7	5	2	0.035	0.037	0.040	0.0580	0.040
2762.5175	ν_1	8	7	1	7	6	2	0.0356	0.036	0.038	0.0381	0.036
2714.2992	ν_1	9	3	7	8	2	6	0.0359	0.037	0.039	0.0252	0.033
2714.2885	ν_1	9	2	7	8	3	6	0.0371	0.037	0.040	0.0300	0.033
2761.4825	ν_1	9	7	3	8	6	2	0.0400	0.033	0.038	0.0374	0.036
2739.3810	ν_1	10	5	6	9	4	5	0.0520	0.036	0.039	0.0349	0.034
2761.4458	ν_1	12	6	7	11	5	6	0.0383	0.034	0.036	0.0323	0.031
742.40910	ν_1	15	0	15	14	1	14	0.0302	0.028	0.027	0.0195	0.022
2714.5480	ν_3	4	3	1	3	1	2	0.0580	0.049		0.0390	0.038
2717.3082	ν_3	6	5	1	5	5	0	0.0393	0.044		0.0267	0.032
2741.7315	ν_3	8	4	4	7	4	3	0.0470	0.045		0.0370	0.032
2740.1501	ν_3	8	7	2	7	7	1	0.0590	0.040		0.0220	0.026
2741.5120	ν_3	8	7	1	7	7	0	0.0318	0.041		0.0240	0.027
1293.2192	ν_2	5	4	1	4	3	2	0.0370	0.042		0.0317	0.036
1295.0949[a]	ν_2	12	1	12	11	0	11				0.0197	0.019

[a] γ (exp) is taken from [8].

Two pure rotational transitions $1_{10} \leftarrow 1_{01}$ and $2_{20} \leftarrow 2_{11}$ of H_2S in the H_2S-He system in the temperature region between 4.3 and 1.8K and 1–600K were investigated in Refs [9,10]. A good agreement between the calculated and measured collisional cross-sections over the temperature region 20–600K was achieved in Ref. [10]. The *ab initio* potential energy surface (PES) for the H_2S- He collision system was used in these calculations.

The aim of this work is to perform the calculations of the noble gas broadening of H_2S absorption lines for the extended in comparison with Refs [1,7,8] set of rotational quantum numbers J, K_a and in the case of H_2S-He system for the extended temperature interval.

2. Method of calculation

The calculations were performed in the framework of *RBET* method, based on the semi-classical formalism of Robert and Bonamy (*RB*) [11], in which only the resonance functions obtained for the exact trajectories (*ET*) [12] were incorporated. According to the *RB* formalism for the transition $i \rightarrow f$ in the H_2S molecule perturbed by the pressure of monoatomic gases, the broadening, γ_{if}, and shifting, δ_{if}, coefficients may be calculated as

$$\gamma_{if} + i\delta_{if} = \frac{n}{c} \int_0^\infty \mathrm{v} F(\mathrm{v}) d\mathrm{v} \int_{r0}^\infty Dr_c dr_c [1 - \exp(-iS_1 - S_{2,i}^{outer} - S_{2,f}^{outer^*} - S_2^{middle''})], \qquad (1)$$

Table 2
Experimental [7] and calculated argon-, krypton,- and xenon- broadening coefficients in fundamental bands of H_2S, $T = 296$ K

								H_2S-Ar		H_2S-Kr		H_2S-Xe	
ν, cm^{-1}	Band	J	K_{ai}	K_{ci}	J_f	K_{af}	K_{cf}	exp	Cal.	exp	Cal.	exp	Cal
2693.2838	ν_1	4	4	0	3	3	1	0.0604	0.055	0.0723	0.063	0.0553	0.066
2740.9751	ν_1	5	3	3	4	0	4	0.0850	0.055	0.0960	0.056	0.0819	0.067
2713.8530	ν_1	5	4	1	4	3	2	0.0590	0.056	0.0680	0.056	0.0670	0.069
2740.0321	ν_1	6	4	2	5	3	3	0.0500	0.054	0.0690	0.050	0.0870	0.067
2717.9659	ν_1	6	5	2	5	4	1	0.0472	0.052	0.0640	0.051	0.0610	0.065
2740.9150	ν_1	7	6	2	6	5	1	0.0500	0.049	0.0610	0.063	0.0640	0.061
2716.0085	ν_1	8	4	5	7	3	4	0.0510	0.051	0.0630	0.056	0.0620	0.062
2715.0784	ν_1	8	3	5	7	4	4	0.0536	0.051	0.0720	0.056	0.0634	0.062
2741.7631	ν_1	8	6	3	7	5	2	0.0700	0.049	0.0910	0.050	0.0920	0.062
2762.5175	ν_1	8	7	1	7	6	2	0.0480	0.047	0.0632	0.051	0.0630	0.059
2714.2992	ν_1	9	3	7	8	2	6	0.0440	0.049	0.0470	0.063	0.0530	0.060
2714.2885	ν_1	9	2	7	8	3	6	0.0420	0.049	0.0570	0.056	0.0530	0.060
2761.4825	ν_1	9	7	3	8	6	2	0.0571	0.046	0.0640	0.056	0.0750	0.060
2739.3810	ν_1	10	5	6	9	4	5	0.0450	0.049	0.0680	0.050	0.0590	0.060
2761.4458	ν_1	12	6	7	11	5	6	0.0520	0.047	0.0510	0.051	0.0560	0.059
2742.4091	ν_1	15	0	15	14	1	14	0.0268	0.035	0.0370	0.063	0.0356	0.041
2714.5480	ν_3	4	3	1	3	1	2	0.0690	0.061	0.0850	0.064	0.0710	0.074
2717.3082	ν_3	6	5	1	5	5	0	0.0503	0.056	0.0667	0.059	0.0613	0.065
2741.7315	ν_3	8	4	4	7	4	3	0.0560	0.056	0.0690	0.059	0.0650	0.064
2740.1501	ν_3	8	7	2	7	7	1	0.0570	0.051	0.0410	0.055	0.0630	0.056
2741.5120	ν_3	8	7	1	7	7	0	0.0460	0.052	0.0521	0.056	0.0540	0.059
1293.2192	ν_2	5	4	1	4	3	2	0.0540	0.055	0.0820	0.061	0.0880	0.072
1295.0949[a]	ν_2	6	4	2	5	3	3			0.0567	0.060		

[a] γ(exp) is taken from [8].

Here, n is the density of the buffer gas; c is the speed of light; v is the relative velocity of interacting particles; and r_c is the closest approach distance between them. The formulas for the interruption functions of the first and second orders, $S_1(b)$ and $S_2(b)$, respectively, the parameter r_0, the Jacobian D of the transition from the variable (b, v) (b is the impact parameter) to the variable (r_c, v) are presented in [11]. To calculate the functions $S_1(b)$ and $S_2(b)$ it is necessary to specify the intermolecular interaction potential. This potential was defined as the sum of pair-wise Lennard-Jones 6–12 interactions between atoms of H_2S molecule and noble gas atom

$$V = V_{1,2}^{aa} = \sum_{i=1}^{3} \left(\frac{d_{i2}}{r_{i2}^{12}} - \frac{e_{i2}}{r_{i2}^{6}} \right), \tag{2}$$

The subscripts i and 2 refer to the $i-$th atom of H_2S molecule and noble gas atom, respectively, d_{i2} and e_{i2} are the atomic pair energy parameters. When expressed in terms of rotational matrix $D^{l_1}_{mm_1}(\Omega_1)$, the potential (2) is written as [13].

$$V_{1,2}^{aa} = \sum_{q=0}^{4} \sum_{l_1=0}^{2} \sum_{m_1,m=-l_1}^{l_1} \left[{}^{|m_1|}_{|m|} b_q^{l_1} \frac{^{|m_1|}D^{l_1}_{12+q}}{r^{12+q}} - {}^{|m_1|}_{|m|} c_q^{l_1} \frac{^{|m_1|}E^{l_1}_{6+q}}{r^{6+q}} \right] D^{l_1}_{mm_1}(\Omega_1). \tag{3}$$

Here r is the center of mass separation, D and E are the analytic functions of the parameters e_{i2}, d_{i2}, r_H, r_S and β, where r_H and r_S are the H-G and S-G distances, respectively, G is the center of the mass of H_2S molecule and 2β is the angle HGH. The expressions for D and Eas well as numerical constants

b and c are given in Refs [13,14]. The atom-atom potential (3) contains an isotropic part ($l_1 = 0$) which was approximated by the Lennard-Jones 6–12 potential

$$V_{isot} = 4\varepsilon_{12}\left\{-\frac{\sigma_{12}^6}{r^6} + \frac{\sigma_{12}^{12}}{r^{12}}\right\}, \tag{4}$$

in which the subscript 1 refers to H_2S molecule. This potential was used in the trajectory calculation according to the scheme from Ref. [12]. Usually the Lennard-Jones parameters ε_{12} and σ_{12} are constructed by the "combination" rules [15]

$$\varepsilon_{12} = \sqrt{\varepsilon_1 \cdot \varepsilon_2},$$
$$\sigma_{12} = \frac{1}{2}(\sigma_1 + \sigma_2) \tag{5}$$

The values of ε_2 and σ_2 for the discussed noble gas atoms are given Ref. [15]. According to Ref. [16] for H_2S gas $\varepsilon_1/k_B \equiv \varepsilon_{H2S-H2S}/k_B = 309.6$ K and $\sigma_2 \equiv \sigma_{H2S-H2S} = 3.509$ Å. The atomic pair energy parameters d_{H2} and e_{H2} may be calculated according to the rules (5) from the known values for $\varepsilon_{H-H}/k_B = 11.2544$K and $\sigma_{H-H} = 2.68259$Å [17]. No available data exist for the e_{S2} and d_{S2}. These parameters as well as ε_{12} and σ_{12} were optimized in the calculations to give the best agreement between the calculated and measured coefficients γ for H_2S lines perturbed by the noble gas atoms He, Ne, Ar, Kr and Xe.

The rovibratioinal wave functions required in the calculations of the broadening coefficients were obtained in the fitting of an effective Hamiltonian, written in terms of generating functions [6], to the known experimental energy levels and frequencies of the transitions [18,19].

3. Helium broadening

For H_2S-He system there is an *ab initio* potential surface (PES) presented in Ref. [10]. In order to obtain the set of the parameters for the potential (3) the least-squares fitting procedure was applied to fit Eq. (3) to the potential values at 17 different angular configurations given in Table II of Ref. [10] (DESP calculation). Those parameters which determine the angular dependence of the potential (3) were found to be poorly determined. Besides, the configurations with the distances $r = 4.5$; 5.0 bohr (1 bohr = 0.529177Å) were omitted because they give a bad result of the fitting. Thus only parameters of isotropic potential $\varepsilon_{12}/k_B = (9.7 \pm 1.8)$K and $\sigma_{12} = (3.57 \pm 0.32)$ Å were determined (the well depth of the H_2S-He *ab initio* potential [10] is about 22K). From these parameters $e_{12} = e_{S2}$ +2$e_{H2} = 1.1 \cdot 10^{-11}$ erg $\cdot$ Å^6 and $d_{12} = d_{S2}$ +2$d_{H2} = 2.3 \cdot 10^{-8}$ erg $\cdot$ Å^{12} were calculated. Parameters $e_{H2} = 0.0$ and $d_{H2} = 0.8 \cdot 10^{-9}$ erg $\cdot$Å^{12} were estimated from the combination rules (5). An obtained set of the parameters ε_{12}, σ_{12}, e_{H2}, d_{H2}, $e_{S2} = e_{12}$ -2e_{H2}, and $d_{S2} = d_{12}$ -2d_{H2} was used in the first step of the calculation of helium broadening coefficients γ for the ν_1 band of H_2S. The comparison between $N = 16$ ($J_i \leqslant 15$) calculated (cal.1) and measured γ is shown in Fig. 1 where the coefficients γ are located according to Table 1. The quality of calculations was characterized by the quantity

$$rms = \left\{\sum_{i=1}^{N} [\gamma_i(\exp) - \gamma_i(cal)]^2/N\right\}^{1/2} \tag{6}$$

Table 3
Optimal sets of the parameters for the interactions potential (3) which give a minimum of *rms* (6) for the ν_1 band of H_2S

	H_2S-He		H_2S-Ne	H_2S-Ar	H_2S-Kr	H_2S-Xe
$\varepsilon_{12}k_B$, K	10.0	56.	104.8	192.	230.	260.
σ_{12}, Å	3.57	3.07	3.17	3.5	3.60	3.85
e_{12}	0.11	0.25	0.585	1.94	2.74	4.66
d_{12}	0.243	0.217	0.595	3.55	5.9	15.0
e_{H-A}	0.0	0.0	0.005	0.18	0.26	0.46
e_{S-A}	0.11	0.25	0.58	1.58	2.22	3.54
d_{H-A}	0.014	0.0075	0.021	0.24	0.5	1.2
d_{S-A}	0.215	0.202	0.553	3.07	4.9	12.6

Parameters e and d are given in 10^{-10} egr $\cdot$ Å^6 and 10^{-7}erg $\cdot$ Å^{12}, respectively.

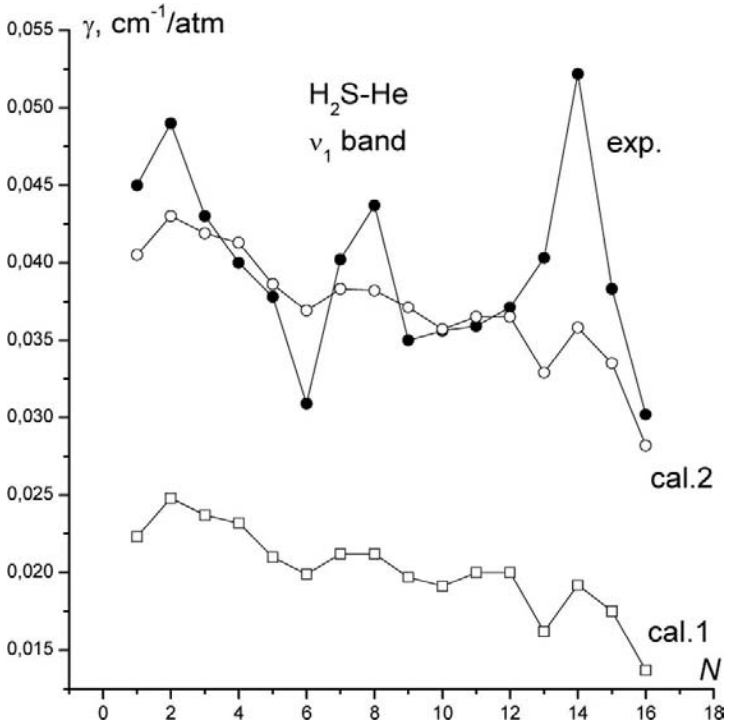

Fig. 1. Comparison of experimentally measured (solid circles) [7] and calculated (open circles and squares) helium broadening coefficients for the ν_1 band of H_2S. Cal.1 and cal.2 correspond to the initial ($d_{S2} = 0.237$) and the optimal ($d_{S2} = 0.215$) value of the parameters d_{S2} (in 10^{-7} erg $\cdot$ Å^{12}), respectively, for the potential, presented in the second column of Table 3.

For the discussed set of parameters *rms* $= 4.0 \cdot 10^{-4}$ cm^{-1}/atm. In the second step of calculation the parameter d_{S2} was adjusted to give the best agreement between γ(exp) and γ(*cal*). The comparison between γ(exp) and γ(*cal*) is shown in Table 1 and in Fig. 1 (cal.2). The optimal set of the parameters, which leads to the best agreement, is presented in the second column of Table 3. For this set of parameters *rms* $= 3.0 \cdot 10^{-5}$cm^{-1}/atm.

Note that the obtained Lennard-Jones parameters ε_{12} and σ_{12} for V_{isot} (4) differ significantly from those, which are given by the Eqs (5). According to these equations $\varepsilon_{12}/k_B = 56.0$ K and $\sigma_{12} = 3.07$ Å.

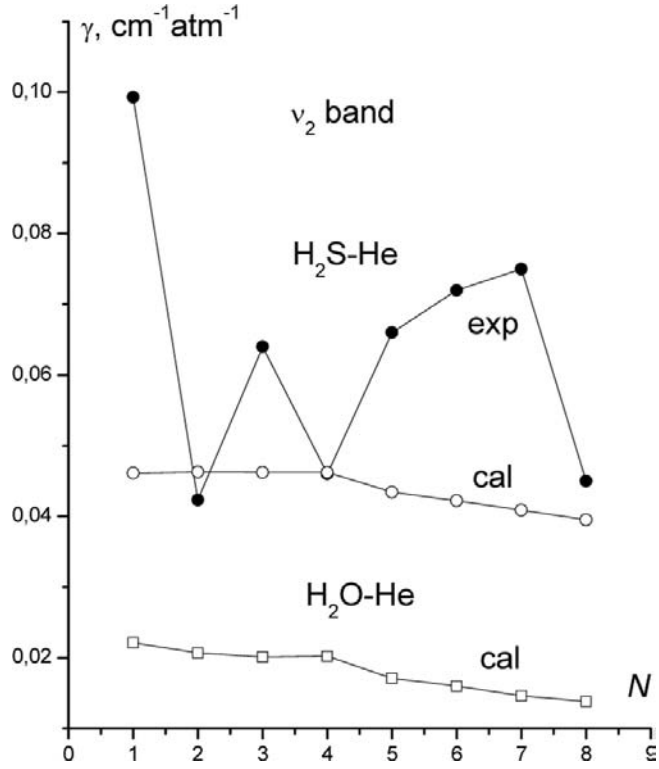

Fig. 2. Comparison of experimentally measured [1] (solid circles) and calculated (open circles and squares) helium broadening coefficients for the same lines of ν_2 band of H_2S and H_2O molecules.

Again starting with these parameters we obtained a new optimal set of parameters for the potential (3) which gives approximately the same *rms* $= 3.2 \cdot 10^{-5}$ cm^{-1}/atm. This set of parameters is shown in the third column of Table 2.

Thus, there are at least two optimal potential parameters (3), which give the same *rms* of the calculation for the helium-broadening coefficients for ν_1 lines of H_2S. Two optimal sets of parameters were tested in the calculations of the cross section σ for the rotational transitions $1_{10} \leftarrow 1_{01}$ and $2_{20} \leftarrow 2_{11}$ at 100K. For the first set we obtained $\sigma = 20.8$ Å^2 and $\sigma = 20.4$ Å^2 for these two transitions, respectively, and for the second set $\sigma = 30.0$ Å^2 and $\sigma = 30.4$ Å^2. The comparison with the experimentally measured cross sections presented in Figs 12 and 13 of Ref. [10] shows that the first optimal set of potential parameters gives better agreement with them than the second set.

The calculation of helium – broadening coefficients for the ν_3 band of H_2S with the first optimal set of potential parameters showed that their variation may significantly (with a factor of 1.8) decrease the *rms* of the calculation. The broadening coefficients γ presented in the 5-th column of Table 1, were calculated with $d_{H2} = 1.7 \cdot 10^{-9}$ erg $\cdot$ Å^{12}.

The optimal sets of potential parameters from the second and third columns of Table 3 were used in the calculation of the broadening coefficients for the ν_2 band of H_2S. The comparison with the existing measured γ [1] ($J_i \leqslant 7$, $K_{ai} \leqslant 4$) is given in Fig. 2. The coefficients γ are located according to Table 1 of Ref. [1]. The strong $J-$ dependence of calculated γ was not obtained. To verify the results of calculations we performed the calculations oh helium- broadening coefficients for the same transitions $[J_i K_{ai} K_{ci}\ ] \rightarrow [J_f K_{af} K_{cf}]$ of the ν_2 band but for H_2O molecule. The potential parameters for the

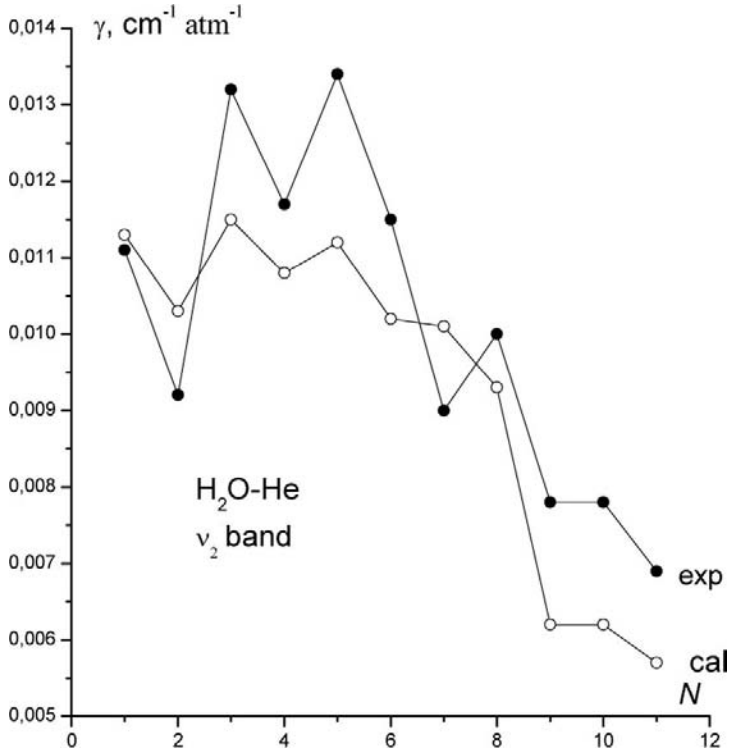

Fig. 3. Comparison of experimentally measured [22] and calculated (solid and open circles, respectively) helium broadening coefficients for the ν_2 band of H_2O molecules.

H_2O-He system may be considered as good established [20] and they give a rather good agreement between calculated and existing measured γ for this band [20,21]. This may be seen from Fig. 3 where the comparison between the calculated and measured [22] γ for the ν_2 band of H_2O is presented. Here γ are located according to Table 2 of Ref. [22]. For the studied in [22] transitions $8 \leqslant J_i \leqslant 16$, $0 \leqslant K_{ai} \leqslant 6$ and the ratio $\gamma_{maximal}/\gamma_{minimal}$ is about 2.0. This variation of γ appeared also in the calculation. But for the lines with $1 \leqslant \quad J_i \leqslant 7$, $0 \leqslant K_{ai} \leqslant 4$ such large variation of γ is absent as it is shown in Fig. 2.

Thus in the framework of the used calculation method and interaction potential (3) the strong J-dependence in measured [1] helium broadening coefficients for the ν_2 band of H_2S can not be explained.

4. Neon-, argon-, krypton,-and xenon – broadening

In the first stage of the calculation the Lennard-Jones parameters ε_{12}, σ_{12} of isotropic potential (4) for the system H_2S-A (A = Ne, Ar, Kr, and Xe) and parameters e_{HA} and d_{HA} were calculated according to the "combination" rules (5). Then ε_{12}, σ_{12} were used in the calculations $e_{1A} = e_{SA}$ +$2e_{HA}$ and $d_{1A} = d_{SA}$ +$2d_{HA}$. Then the parameter d_{SA} was optimized to give the minimum of *rms* (6) for the lines of ν_1 band. As a consequence the parameter d_{HA} changed so that the calculated d_{1A} remained constant. Obtained in this way the optimal values of the potential parameters are presented in the corresponding column of Table 4 and calculated broadening coefficients and their comparison with the experimental data are given in Tables 1 and 2. These sets of the parameters don't give the minimum *rms* (6) for the ν_3 band of H_2S in the systems H_2S-Ne and H_2S-Ar. These minimums were achieved for $d_{SA} = 0.563$ and

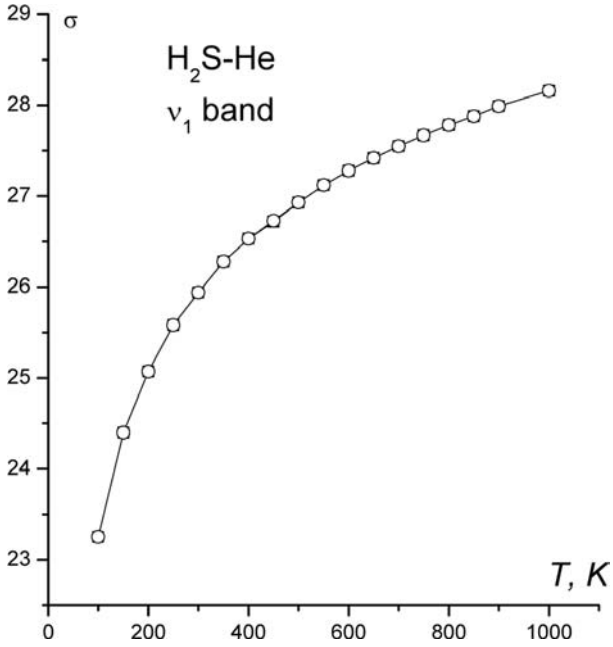

Fig. 4. Calculated cross-sections σ (in Å^2) as a function of temperature for the $1_{10} \leftarrow 1_{01}$ (open circles) and $2_{20} \leftarrow 2_{11}$ (open squares) transitions of ν_1 band of H_2S.

2.99 (in 10^{-7} erg $\cdot$ Å^{12}) in the case of Ne and Ar broadening, respectively. The results of calculation γ for the ν_2 band were obtained with the parameters from Table 4.

Thus similar to helium broadening the best agreements between γ(exp) [7] and γ(*cal*) for different vibrational bands were achieved with different optimal potential parameters.

5. Analytical representation of helium broadening coefficients of H_2 S for the ν_1 band

The optimal set of the potential parameters for H_2S-He system from the second column of Table 3 was used for the calculation of helium broadening coefficients of ν_1 H_2S lines with $J_i, J_f \leqslant 15$, $\Delta K = |K_{a,I} - K_{af}| \leqslant 3$ for the temperature interval 100 K$\leqslant T \leqslant$ 1200 K. For the analytical representation of these calculated coefficients γ the analytical expression [23]

$$\gamma_{if} \equiv \gamma(sur) = x_1 + \frac{x_2(J_i,J_f)Ch[\alpha_2(J_i,J_f)(K_i-K_f)(K_i+K_f)]}{Ch[\alpha_1(J_i,J_f)(K_i-x_{e1}(J_i,J_f)]Ch[\alpha_1(J_i,J_f)(K_f-x_{e1}(J_i,J_f)]} \tag{7}$$

was applied. In this expression

$$\begin{aligned} x_k(J_i,J_f) &= x_{k0} + x_{k1}(J_i+J_f) + \ldots \\ x_{el}(J_i,J_f) &= x_{el0} + x_{el1}(J_i+J_f) + \ldots \\ \alpha_l(J_i,J_f) &= \alpha_{l0} + \alpha_{l1}(J_i+J_f) + \ldots, \end{aligned} \tag{8}$$

Table 4
Parameters of γ(*sur*) (7)–(9) for helium-broadening coefficients of ν_1 band of H_2S^* ($x_3 = \alpha_1, x_4 = x_{e1}, x_5 = \alpha_2$)

x_{20}	$(0.5090 \pm 0.0015) \cdot 10^{-1}$	x_{50}	$(0.10089 \pm 0.0078) \cdot 10^{-1}$
x_{21}	$-(0.6413 \pm 0.0070) \cdot 10^{-3}$	x_{51}	$-(0.1400 \pm 0.0299) \cdot 10^{-3}$
x_{30}	-0.1042 ± 0.0043	n_{20}	-0.4520 ± 0.0005
x_{31}	$(0.1452 \pm 0.0166) \cdot 10^{-2}$	n_{21}	-0.9601 ± 0.0017
x_{40}	-1.2365 ± 0.1313	$n_{30} = n_{31}$	-0.4912 ± 0.0040
x_{41}	0.2879 ± 0.0057	$n_{40} = n_{41}$	-0.13355 ± 0.00239
		$n_{50} = n_{51}$	-0.3417 ± 0.0101

*Parameters x_{20} and x_{21} are in cm^{-1}/ atm; other parameters are dimensionless.

and x_{k0}, ... α_{l1} are adjustable parameters and k, l = 1,2. The temperature dependence of γ was described through the temperature dependence of the these parameters, for example,

$$x_{kl}(T) = x_{kl}(T_0) \cdot \left(\frac{T}{T_0}\right)^{n_{kl}} \tag{9}$$

Here $T_0 = 296$K. Parameters x_{k0}, ... α_{l1} as well as n_{kl} were obtained in the fitting of Eqs (7)–(9) to the calculated γ. They are presented in Table 4. The comparison between the calculated γ(*sur*) and γ(exp) is given in the seventh column of Table 1. As an example the calculated temperature dependence of the cross sections σ for two transitions $1_{10} \leftarrow 1_{01}$ and $2_{20} \leftarrow 2_{11}$ is shown in Fig. 4. According to Figs 12 and 13 of Ref. [10] experimentally measured $\sigma \approx 20 \cdot$ Å^2 at 100K for the pure rotational transition $1_{10} \leftarrow 1_{01}$ and $2_{20} \leftarrow 2_{11}$. That is in good agreements with the calculated σ.

6. Conclusion

In this paper the results of calculations of He-, Ne-, Ar,-Kr-, and Xe broadening coefficients in fundamental bands of H_2S are presented and discussed. It was found that for H_2S-He, H_2S-Ne, and H_2S-Ar systems the optimal potentials are different for different vibrational bands. Besides, we could not describe the experimentally measured in Ref. [1] strong J – dependence of helium broadening of H_2S lines in the ν_2 band. The source of the large discrepancies between measured and calculated γ for the ν_2 band of H_2S may be connected with the strong vibrational dependence of the collisional potential or with the used calculation scheme. Note that some different sets of potential parameters for H_2S-He system give approximately the same quality of fitting of measured coefficients γ.

Presented in Table 3 optimal sets of potential parameters can not be considered as well established. For their determination it is desirable to know the experimentally measured broadening (and shifting) coefficients γ and δ for the extended set of rotational quantum numbers $J$and K_a.

References

[1] J. Waschull, F. Kuhnemann and B. Sumpf, *J Mol Spectrosc* **165** (1994), 150–158.
[2] B. Sumpf, I. Meusel and H.-D. Kronfeldt, *J Mol Spectrosc* **177** (1996), 143–145.
[3] B. Sumpf, *J Mol Spectrosc* **181** (1997), 160–167.
[4] A. Kissel, B. Sumpf, H.-D. Kronfeldt, B.A. Tikhomirov and Yu.N. Ponomarev, *J Mol Spectrosc* **216** (2002), 1–10.
[5] G.D. Tejwani and E.S. Yeung, *J Quant Spectrosc Radiat Transfer* **17** (1997), 323–326.
[6] V.I. Starikov and A.E. Protasevich, *Optics and Spectroscopy* **101** (2006), 523–531.
[7] B. Sumpf, I. Meusel and H.-D. Kronfeldt, *J Mol Spectrosc* **184** (1997), 51–55.

[8] A. Kissel, H.-D. Kronfeldt, B. Sumpf, Yu.N. Ponomarev, I.V. Ptashnik and B.A. Tichomirov, *Spectrochimica Acta, Part A* **55** (1999), 2007–2013.
[9] D.R. Willey, D.N. Bittner and F.C.De Lucia, *J Mol Spectrosc* **134** (1989), 240–242.
[10] C.D. Ball, M. Mengel, F.C.De Lucia and D.E. Woon, *J Chem Phys* **111** (1999), 8893–8903.
[11] D. Robert and J. Bonamy, *J de Physique* **40**(10) (1979), 923–943.
[12] N.N. Lavrentieva and V.I. Starikov, *Molecular Physics* **104** (2006), 2759–2766.
[13] B. Labani, J. Bonamy, D. Robert, J.M. Hartmann and J. Taine, *J Chem Phys* **84** (1986), 4256–4267.
[14] S.P. Neshyba and R.R. Gamache, *J Quant Spectrosc Radiat Transfer* **50** (1993), 443–453.
[15] J.O. Hirschfelder, C.F.Curtiss and R.B. Bird, *Molecular Theory of Gases and Liquids*, Wiley, New York, 1967.
[16] L. Monchick and E.A. Mason, *J Chem Phys* **35** (1961), 1676–1697.
[17] J.-P. Bouanich, *J Quant Spectrosc Radiat Transfer* **47** (1992), 243–250.
[18] O.N. Ulenikov, A.B. Malikova, M. Koivusaari, S. Alanko and R. Anttila, *J Mol Spectrosc* **176** (1996), 229–235.
[19] A.D. Bykov, O.V. Naumenko, M.A. Smirnov, L.N. Sinitsa, L.R. Brown, J. Crisp and D. Crisp, *Can J Phys* **72** (1994), 89–1000.
[20] V.I. Starikov and N.N. Lavrentieva, Collisional broadening and shifting of spectral lines of atmospheric molecules, IAO SB RAS, Tomsk, 2006, 308 P [in Russian].
[21] A.M. Solodov and V.I. Starikov, *Optics and Spectroscopy* **105** (2008), 14–20.
[22] C. Claveau, A. Henry, D. Hurtmans and A. Valentin, *J Quant Spectrosc Radiat Transfer* **68** (2001), 273–298.
[23] V.I. Starikov and A.E. Protasevich, *Optics and Spectroscopy* **98** (2005), 368–373.

Journal of Computational Methods in Sciences and Engineering 10 (2010) 595–614
DOI 10.3233/JCM-2010-0325
IOS Press

Optically induced static magnetization due to molecular reorientational processes in dc electric field

S. Woźniak*
Nonlinear Optics Division, Department of Physics, A.Mickiewicz University, Umultowska 85, 61-614 Poznań, Poland

Abstract. The molecular theory of optically induced static magnetization is extended to systems acted on with a dc electric field. The two effects, the invers Faraday effect and invers magnetochiral birefringence, are analysed for their dependence on an electric field perpendicular or parallel to the propagation direction of the incident light beam. The mechanisms responsible for the effects are described in terms of linear and nonlinear multipole polarizability tensors as well as molecular reorientation functions defined by the generalized Langevin-Kielich functions. The effects at electric saturation are a source of information concerning the tensor components of electric dipole, magnetic dipole and electric quadrupole polarizability.

Keywords: Invers Faraday effect, Invers magnetochiral birefringence, Nonlinear polarizabilitiesv, Generalized Langevin-Kielich functions

PACS numbers: 33.15Kr, 33.57+c, 42.65.-k, 78.20.Ls.

1. Introduction

It is very well know that an isotropic molecular medium without any external field does not exhibit any birefringence exept circular birefringence if the system is composed of chiral molecules. The multipolar theory of electromagnetic polarization states that the optical properties of a molecular system undergo modification when an external electric or magnetic field is applied [1–4]. One of the effects of a static magnetic field $\mathbf{B}^0$ acting on a medium in which a linearly polarized beam of monochromatic light propagates in the direction of $\mathbf{B}^0$ consists in the rotation of the plane of polarization discovered by Faraday. Extensive lists of the papers on the Faraday effect in nonconducting liquid and gaseous media may be found in the reviews by Buckingham and Stephens [5] and by Palik and Henvis [6].

Van der Ziel, Pershan and Malmstrom [7] have shown experimentally that circularly polarized light induces in a medium a static magnetization. They have measured the effect in a few glasses and liquids and have called this the inverse Faraday effect. The effect has been investigated theoretically [8–13] and measured in terbium gallium garnet [14], Tb-droped aluminium-boron-silicate glass [15] and in plasmas [16–18]. Some interesting applications of the inverse Faraday effect have been also proposed [19–22].

A static magnetic field applied along the propagation direction of circularly polarized light in a molecular medium possessing natural optical activity induces a linear magnetorefractive effect [23–25]. The

*Corresponding author. Fax: +48 61 825 7758; E-mail: wozniak@amu.edu.pl.

molecular theory of this effect has been formulated for molecules with a nondegenerate or degenerate electronic ground state [26]. It has been shown in [26,27] that the change in refractive index and in absorption coefficient in the presence of a static magnetic field applied along the direction of light propagation is not a circular differential effect, and that it can occur in optically active media for circularly, linearly and unpolarized light, leading to magnetochiral birefringence and magnetochiral dichroism [28, 29]. The molecular theory of these effects has been extended to the case of additional external static electric [30] or optical [31] fields for media composed of diamagnetic as well as paramagnetic molecules [32]. The effects has been also discussed theoretically in [33,34]. Magnetochiral birefringence has been first measured by Kleindienst and Wagnière [35] and then by Kalugin et al. [36] and Vallet et al. [37].

Wagnière has shown [38] that a coherent beam of light of arbitrary polarization traveling in a medium composed of randomly oriented chiral molecules induces a static magnetization parallel or antiparallel to the direction of light propagation. The sign of the magnetization depends on the direction of propagation of the light as well as on the particular enantiomer of the chiral molecules, and changes by either reversing the propagation direction or replacing the chiral molecules by their enantiomers. This nonlinear optical effect, in analogy to the inverse Faraday efect (IFE), is named inverse magnetochiral birefringence (IMCHB). The role of molecular symmetry in IMCHB in nonabsorbing molecular systems has been discussed in [11], whereas the effect for molecular systems near their optical resonances – in [39].

In the present paper we discuss the influence of molecular reorientational processes, forced by a dc electric field, on optically induced static magnetization: the invers Faraday effect and inverse magnetochiral birefringence.

2. Fundamentals

We consider an arbitrary nondissipative system of volume V containing N uncorrelated atoms or molecules in homogeneous dc magnetic and electric fields, $\mathbf{B}^0$ and $\mathbf{E}^0$, on which a light wave with electric vector

$$\mathbf{E}(\mathbf{r},t) = \mathbf{E}(\omega,\mathbf{k})\exp(-i\omega t) \; + \mathbf{E}^*(\omega,\mathbf{k})\exp(i\omega t) \tag{1}$$

is incident, where $\mathbf{E}(\omega,\mathbf{k}) = \mathbf{E}(\omega)\exp(i\mathbf{k}\cdot\mathbf{r})$.

The interaction between macroscopic nondissipative media and time-varying electromagnetic field can be described by time-averaged potential function, the free energy density [40]. In our case the effective free energy density has the following form:

$$\begin{aligned}\Delta F = -\rho\Big\{ & \frac{1}{2} < {}^{e}\alpha^{e}_{ij}(-\omega;\omega) >_{E^0,B^0} E^*_i E_j + < {}^{e}\alpha^{m}_{ij}(-\omega;\omega) >_{E^0,B^0} E^*_i B_j \\ & + \frac{1}{3} < {}^{e}\alpha^{q}_{i(jl)}(-\omega;\omega) >_{E^0,B^0} E^*_i E_{lj} \\ & + \Big[\frac{1}{2} < {}^{e}\alpha^{em}_{ijp}(-\omega;\omega,0) >_{E^0,B^0} E^*_i E_j + < {}^{e}\alpha^{mm}_{ijp}(-\omega;\omega,0) >_{E^0,B^0} E^*_i B_j \\ & + \frac{1}{3} < {}^{e}\alpha^{qm}_{i(jl)p}(-\omega;\omega,0) >_{E^0,B^0} E^*_i E_{lj}\Big] B^0_p + c.c.\Big\},\end{aligned} \tag{2}$$

where $E_i \equiv E_i(\omega,k)$, $E_{lj} \equiv \nabla_l E_j$, $\rho = N/V$, $\mathbf{B}$ is the magnetic vector of the light wave, $< \cdots >_{E^0,B^0}$ stands for the statistical average in the presence of the external fields $\mathbf{B}^0$ and $\mathbf{E}^0$, and ( )

denotes symmetry in respective pair of indices. Moreover, we have

$$({}^{A}\boldsymbol{\alpha}^{B})^{*} = {}^{B}\boldsymbol{\alpha}^{A} \tag{3}$$

for $A, B = e,\ m,\ q$.

In Eqs (2) and (3) the polarizabilities ${}^{e}\boldsymbol{\alpha}^{e}(-\omega;\omega)$, ${}^{e}\boldsymbol{\alpha}^{m}(-\omega;\omega)$ and ${}^{e}\boldsymbol{\alpha}^{q}(-\omega;\omega)$ are the electric-dipole polarizabilities related to dipolar-electric, dipolar-magnetic and quadrupolar-electric transitions, respectively; ${}^{m}\boldsymbol{\alpha}^{e}(-\omega;\omega)$ is the magnetic-dipole and ${}^{q}\boldsymbol{\alpha}^{e}(-\omega;\omega)$ – the electric-quadrupole polarizability, both related to dipolar-electric transitions. The quantum mechanical form of these tensors can be found in [1,41]. Moreover, in Eq. (2) there are tensors ${}^{e}\boldsymbol{\alpha}^{em}(-\omega;\omega,0)$, ${}^{e}\boldsymbol{\alpha}^{mm}(-\omega;\omega,0)$ and ${}^{e}\boldsymbol{\alpha}^{qm}(-\omega;\omega,0)$ which are connected with variation of multipolar polarizabilities in the presence of the field $\mathbf{B}^0$; their quantum mechanical forms can be derived applying stationary perturbation calculus [4, 26,42].

Applying the classical Boltzmann average with $U = -\boldsymbol{\mu}^{m}\cdot\boldsymbol{B}^{0}$, the potential energy of the molecule in the field $\mathbf{B}^0$ with $\boldsymbol{\mu}^{m}$ being its permanent magnetic dipole moment, we have:

$$\begin{aligned}
\Delta F = &-\rho\Big\{\frac{1}{2} < {}^{e}\alpha^{e}_{ij} >_{E^0} E^{*}_{i}E_{j} + < {}^{e}\alpha^{m}_{ij} >_{E^0} E^{*}_{i}B_{j} + \frac{1}{3} < {}^{e}\alpha^{q}_{i(jl)} >_{E^0} E^{*}_{i}E_{lj}\Big\} \\
&-\rho\Big\{\frac{1}{2}\Big[< {}^{e}\alpha^{em}_{ijp} >_{E^0} + \frac{1}{k_BT} < {}^{e}\alpha^{e}_{ij}\mu^{m}_{p} >_{E^0} \Big]E^{*}_{i}E_{j} \\
&+\Big[< {}^{e}\alpha^{mm}_{ijp} >_{E^0} + \frac{1}{k_BT} < {}^{e}\alpha^{m}_{ij}\mu^{m}_{p} >_{E^0} \Big]E^{*}_{i}B_{j} \\
&+\frac{1}{3}\Big[< {}^{e}\alpha^{qm}_{i(jl)p} >_{E^0} + \frac{1}{k_BT} < {}^{e}\alpha^{q}_{i(jl)}\mu^{m}_{p} >_{E^0} \Big]E^{*}_{i}E_{lj}\Big\}B^{0}_{p} + c.c..
\end{aligned} \tag{4}$$

For simplicity we omit in Eq. (4) frequency ω writing ${}^{e}\alpha^{e}_{ij}$ instead of ${}^{e}\alpha^{e}_{ij}(-\omega;\omega)$, ${}^{e}\alpha^{mm}_{ijp}$ instead of ${}^{e}\alpha^{mm}_{ijp}(-\omega;\omega,0)$ and so on.

The polarizabilities in Eq. (4) can be expressed in the following form [26]:

$${}^{e}\alpha^{e}_{ij} = {}^{e}\beta^{e}_{(ij)} + i\,{}^{e}\gamma^{e}_{[ij]},\quad {}^{e}\alpha^{m}_{ij} = {}^{e}\beta^{m}_{ij} + i\,{}^{e}\gamma^{m}_{ij},\quad {}^{e}\alpha^{q}_{i(jl)} = {}^{e}\beta^{q}_{i(jl)} + i\,{}^{e}\gamma^{q}_{i(jl)}, \tag{5}$$

$${}^{e}\alpha^{em}_{ijp} = {}^{e}\beta^{em}_{(ij)p} + i\,{}^{e}\gamma^{em}_{[ij]p},\quad {}^{e}\alpha^{mm}_{ijp} = {}^{e}\beta^{mm}_{ijp} + i\,{}^{e}\gamma^{mm}_{ijp},\quad {}^{e}\alpha^{qm}_{i(jl)p} = {}^{e}\beta^{qm}_{i(jl)p} + i\,{}^{e}\gamma^{qm}_{i(jl)p}, \tag{6}$$

where the tensors ${}^{e}\boldsymbol{\beta}^{e}$, ${}^{e}\boldsymbol{\gamma}^{m}$, ${}^{e}\boldsymbol{\beta}^{q}$, ${}^{e}\boldsymbol{\gamma}^{em}$, ${}^{e}\boldsymbol{\beta}^{mm}$ and ${}^{e}\boldsymbol{\gamma}^{qm}$ are symmetric with respect to time inversion (i – tensors), whereas ${}^{e}\boldsymbol{\gamma}^{e}$, ${}^{e}\boldsymbol{\beta}^{m}$, ${}^{e}\boldsymbol{\gamma}^{q}$, ${}^{e}\boldsymbol{\beta}^{em}$, ${}^{e}\boldsymbol{\gamma}^{mm}$ and ${}^{e}\boldsymbol{\beta}^{qm}$ are antisymmetric with respect to time inversion (c – tensors) and components of all tensors $\boldsymbol{\beta}$ and $\boldsymbol{\gamma}$ are real in the absence of absorption; [ ] denotes antisymmetry in the enclosed indices. Non-zero components of these tensors, for all molecular symmetries, can be found in [43]

Since the static magnetization $\boldsymbol{M}$ is given by [44]

$$M_p = -\partial\Delta F/\partial B^{0}_{p}, \tag{7}$$

taking into consideration the relations (5), (6) and $E_{lj} = iE_jk_l$, we have

$$M_p = M^{(1)}_{p} + M^{(2)}_{p} + M^{(3)}_{p}, \tag{8}$$

where

$$M_p^{(1)} = \frac{1}{2}\rho\Big[< {}^e\gamma^{em}_{[ij]p} >_{E^0} + \frac{1}{k_BT} < {}^e\gamma^{e}_{[ij]}\mu^m_p >_{E^0} \Big] iE^*_i E_j + c.c.. \tag{9}$$

$$M_p^{(2)} = \rho\Big[< {}^e\beta^{mm}_{ijp} >_{E^0} + \frac{1}{k_BT} < {}^e\beta^{m}_{ij}\mu^m_p >_{E^0} \Big] E^*_i B_j + c.c., \tag{10}$$

$$M_p^{(3)} = -\frac{1}{3}\rho\Big[< {}^e\gamma^{qm}_{i(jl)p} >_{E^0} + \frac{1}{k_BT} < {}^e\gamma^{q}_{i(jl)}\mu^m_p >_{E^0} \Big] E^*_i E_j k_l + c.c.. \tag{11}$$

If the incident light beam propagates in the direction of the Z-axis of the laboratory coordinate system $\{XYZ\}$ we have for the component M_z of the static magnetization

$$M_z^{(1)} = \rho\Big[< {}^e\gamma^{em}_{[xy]z} >_{E^0} + \frac{1}{k_BT} < {}^e\gamma^{e}_{[xy]}\mu^m_z >_{E^0} \Big] (E^*_x E_y - E_x E^*_y), \tag{12}$$

$$M_z^{(2)} = \frac{\rho}{c}\Big[< {}^e\beta^{mm}_{xyz} - {}^e\beta^{mm}_{yxz} >_{E^0} + \frac{1}{k_BT} < ({}^e\beta^{m}_{xy} - {}^e\beta^{m}_{yx})\mu^m_z >_{E^0} \Big] (|E_x|^2 + |E_y|^2), \tag{13}$$

$$\begin{aligned} M_z^{(3)} = -\frac{\rho\omega}{3c}\Big[& < {}^e\gamma^{qm}_{x(xz)z} + {}^e\gamma^{qm}_{y(yz)z} >_{E^0} \\ & + \frac{1}{k_BT} < ({}^e\gamma^{q}_{x(xz)} + {}^e\gamma^{q}_{y(yz)})\mu^m_z >_{E^0} \Big] (|E_x|^2 + |E_y|^2). \end{aligned} \tag{14}$$

Introducing the intensity of left (-) and right (+) circularly polarized light

$$I^{\pm} = \frac{1}{2}\varepsilon_0 cn |E^{\pm}|^2 \tag{15}$$

with the electric field

$$E^{\pm} = \sqrt{2}/2 (E_x \mp iE_y), \tag{16}$$

and the intensity I of unpolarized (or arbitrarily polarized light)

$$I = \frac{1}{2}\varepsilon_0 cn |\boldsymbol{E}|^2, \tag{17}$$

where n is the refractive index of the medium, c – velocity of light in vacuum, we have

$$M_z^{(1)} = \frac{2\rho}{\varepsilon_0\, cn}\Big[< {}^e\gamma^{em}_{[xy]z} >_{E^0} + \frac{1}{k_BT} < {}^e\gamma^{e}_{[xy]}\mu^m_z >_{E^0} \Big] (I^- - I^+) \tag{18}$$

$$M_z^{(2)} = \frac{2\rho}{\varepsilon_0\, c^2 n}\Big[< {}^e\beta^{mm}_{xyz} - {}^e\beta^{mm}_{yxz} >_{E^0} + \frac{1}{k_BT} < ({}^e\beta^{m}_{xy} - {}^e\beta^{m}_{yx})\mu^m_z >_{E^0} \Big] I, \tag{19}$$

$$M_z^{(3)} = -\frac{2\rho\omega}{3\varepsilon_0\, c^2 n}\Big[< {}^e\gamma^{qm}_{x(xz)z} + {}^e\gamma^{qm}_{y(yz)z} >_{E^0} + \frac{1}{k_BT} < ({}^e\gamma^{q}_{x(xz)} + {}^e\gamma^{q}_{y(yz)})\mu^m_z >_{E^0} \Big] I. \tag{20}$$

Eq. (18) describes a static magnetization induced by circularly polarized light and this effect is named the inverse Faraday effect [7]. The expressions $M_z^{(2)}$ and $M_z^{(3)}$ describe a static magnetization induced by unpolarized (or arbitrarily polarized light) and this effect is named inverse magnetochiral birefringence [10].

For molecules of very low symmetry for which the tensor of linear electric polarizability ($\omega = 0$) possesses three different components ${}^e\beta^e_{11}(0) \neq {}^e\beta^e_{22}(0) \neq {}^e\beta^e_{33}(0)$, the averaging procedure (18)- (20) leads to result of a high degree of complication. Accordingly here, we shall consider molecules for which the tensor components ${}^e\beta^e_{\alpha\beta}(0)$ fulfil the relation

$$ {}^e\beta^e_{11}(0) = {}^e\beta^e_{22}(0) \neq {}^e\beta^e_{33}(0), \tag{21}$$

where the subscripts 1, 2 and 3 refer to the molecular system of coordinates $\{1, 2, 3\}$.

The relation (21) occurs for molecules of 67 magnetic point group symmetries among of them molecules of 16 point groups are dipolar with an intrinsic electric dipole moment μ directed along of 3-axis of the molecular system of coordinates [43].

In our case, the distribution function applied to the averaging of the individual terms of Eqs (18)–(20) has the form [3,45,46]:

$$ f(\theta, E_i^0) = \frac{exp(p\cos\theta \pm q\cos^2\theta)}{4\pi^2 \int\limits_0^\pi exp(p\cos\theta \pm q\cos^2\theta)\sin\theta d\theta} \tag{22}$$

involving the dimensionless permanent electric dipole reorientation parameter p and polarizability ellipsoid reorientation parameter q of the molecule

$$ p = \frac{\mu E_i^0}{k_B T}, \tag{23}$$

$$ q = \frac{|{}^e\delta^e(0)|}{2k_B T}\,(E_i^0)^2, \tag{24}$$

with ${}^e\delta^e(0) = {}^e\beta^e_{33}(0) - {}^e\beta^e_{11}(0)$ – the anisotropy of electric polarizability ${}^e\boldsymbol{\beta}^e(0)$; E_i^0 represents E_y^0 or E_z^0, a dc electric field applied perpendicular or parallel to the direction of the light propagation, respectively. The signs "$+$" and "$-$" in Eq. (22) refer, respectively, to molecules with positive and negative anisotropy ${}^e\delta^e(0)$ and θ is the angle between the field $\mathbf{E}^0$ and 3–axis of the molecule in the molecular coordinate system. The distribution function (22) being independent of the other two Euler angles φ and ψ ($0 \leqslant \varphi \leqslant 2\pi,\ 0 \leqslant \psi \leqslant 2\pi,\ 0 \leqslant \theta \leqslant \pi$), when going over with the multipole polarizability tensor components (18)–(20) to molecular coordinates, the averaging over these two angles reduces to isotropic averaging [3,47]:

$$ <\cos^n\varphi> = <\cos^n\psi> = <\sin^n\varphi> = <\sin^n\psi> = \begin{cases} \frac{(2t-1)!!}{2^t t!}, & \text{for } n = 2t, \\ 0, & \text{for } n = 2t+1. \end{cases} \tag{25}$$

For nondipolar molecules averaging in Eqs (18)–(20) is carried out with the distribution function (22) at $p = 0$.

3. Inverse Faraday effect

3.1. Absence of the field $\mathbf{E}^0$

In the absence of an external dc electric field $\mathbf{E}^0$, the statistical average $< \cdots >_{E_0}$ in Eq. (18) becomes the isotropic average $< \cdots >$ giving [11]

$$M_z^{(1)}(0) = \frac{\rho}{3\varepsilon_0\, c\, n}\, \varepsilon_{\alpha\beta\gamma} \Big[{}^e\gamma^{em}_{[\alpha\beta]\gamma} + \frac{1}{k_B T}\, {}^e\gamma^{e}_{[\alpha\beta]} \mu^m_\gamma \Big] (I^- - I^+), \tag{26}$$

where $\varepsilon_{\alpha\beta\gamma}$ is the Levi-Civita third-rank antisymmetric unit tensor and the components ${}^e\gamma^{em}_{[\alpha\beta]\gamma}$, ${}^e\gamma^{e}_{[\alpha\beta]}$ and μ^m_γ are given in the molecular frame of coordinates $\{1, 2, 3\}$.

The above equation describes the static magnetization induced by circularly polarized light and is equivalent to expressions which have been derived by Atkins and Miller [9] and Wagnière [10]. This effect occurs in any molecular system.

For paramagnetic molecules which fulfil the relation (21) (23 magnetic point group symmetries) we have [11]

$$M_z^{(1)}(0) = \frac{2\rho}{3\varepsilon_0\, c\, n} \Big[{}^e\gamma^{em}_{123} + 2\, {}^e\gamma^{em}_{231} + \frac{1}{k_B T}\, {}^e\gamma^{e}_{12}\, \mu^m_3 \Big] (I^- - I^+), \tag{27}$$

and for diamagnetic ones (44 magnetic point group symmetries)

$$M_z^{(1)}(0) = \frac{2\rho}{3\varepsilon_0\, c\, n} \Big[{}^e\gamma^{em}_{123} + 2\, {}^e\gamma^{em}_{231} \Big] (I^- - I^+). \tag{28}$$

3.2. DC electric field $\mathbf{E}^0$ *perpendicular to the incident light beam* $(\mathbf{E}^0 \perp \mathbf{k})$

Assume a molecular medium to be acted on additionally with a dc electric field E^0_y applied along the Y- axis of the laboratory system of coordinates.

3.2.1. Diamagnetic molecules

On carring out statistical averaging in Eq. (18) for diamagnetic dipolar molecules we obtain

$$M_z^{(1)\perp} = \frac{2\rho}{3\varepsilon_0\, c\, n} \Big[{}^e\gamma^{em}_{123} + 2\, {}^e\gamma^{em}_{231} - ({}^e\gamma^{em}_{123} - {}^e\gamma^{em}_{231}) \Phi_1(p, \pm q) \Big] (I^- - I^+), \tag{29}$$

where the molecular reorientation function

$$\Phi_1(p, \pm q) = \frac{1}{2} \{ 3 L_2(p, \pm q) - 1 \} \tag{30}$$

is given by the generalized Langevin-Kielich function $L_2(p, \pm q)$ with [45]

$$L_n(p, \pm q) = \frac{\int\limits_0^\pi \cos^n\theta\, exp(p\cos\theta \pm q\cos^2\theta) \sin\theta d\theta}{4\pi^2 \int\limits_0^\pi exp(p\cos\theta \pm q\cos^2\theta) \sin\theta d\theta}; \tag{31}$$

the superscript $\perp$ in Eq. (29) stands for the configuration $(\mathbf{E}^0 \perp \mathbf{k})$.

In the case of weak molecular reorientation ($p \ll 1$, $q \ll 1$), the function $\Phi_1(p, \pm q)$ can be expressed as follows

$$\Phi_1(p, \pm q) = \frac{p^2}{15} \pm \frac{2q}{15} + \cdots \tag{32}$$

whence Eq. (29) have the form

$$M_z^{(1)\perp} = \frac{2\rho}{45\varepsilon_0\, c\, n} \Big\{ 15({}^e\gamma_{123}^{em} + 2\,{}^e\gamma_{231}^{em}) - ({}^e\gamma_{123}^{em} - {}^e\gamma_{231}^{em}) \Big[\Big(\frac{\mu}{k_B T} \Big)^2 + \frac{{}^e\delta^e(0)}{k_B T} \Big] (E_y^0)^2 \Big\} (I^- - I^+). \tag{33}$$

If the field E_y^0 increases, the parameters p and q increas as well, and the function $\Phi_1(p, +q)$ increases monotonously being always positive, contrary to the function $\Phi_1(p, -q)$ which has the positive maximum and then tends to negative value [45,46]. In the case of very strong molecular reorientation ($p \to \infty$, $q \to \infty$)

$$\Phi_1(\infty, +\infty) = 1, \tag{34}$$

$$\Phi_1(\infty, -\infty) = -\frac{1}{2}, \tag{35}$$

and for diamagnetic dipolar molecules with positive anisotropy ${}^e\delta^e(0)$ of relevance here

$$M_z^{(1)\perp}(+\infty) = \frac{2\rho}{\varepsilon_0\, c\, n}\, {}^e\gamma_{231}^{em}\, (I^- - I^+), \tag{36}$$

whereas for molecules with ${}^e\delta^e(0) < 0$

$$M_z^{(1)\perp}(-\infty) = \frac{\rho}{\varepsilon_0\, c\, n}\, ({}^e\gamma_{123}^{em} + {}^e\gamma_{231}^{em})(I^- - I^+). \tag{37}$$

For diamagnetic nondipolar molecules Eq. (29) contains $\Phi_1(\pm q)$ in place of $\Phi_1(p, \pm q)$ and $\mu = 0$ in Eq. (33). The value of the function $\Phi_1(+q)$ increases monotonously (being always positive) with increasing the parameter q on contrary to the value of the function $\Phi_1(-q)$ which decreases monotonously (being always negative) with increasing q. If molecular ordering attains saturation ($q \to \infty$) then

$$\Phi_1(+\infty) = 1, \tag{38}$$

$$\Phi_1(-\infty) = -\frac{1}{2}, \tag{39}$$

and for diamagnetic nondipolar molecules with positive or negative anisotropy ${}^e\delta^e(0)$ we have $M_z^{(1)\perp}(+\infty)$ or $M_z^{(1)\perp}(-\infty)$ given by Eqs (36) or (37), respectively.

The function $\Phi_1(p, \pm q)$ describes, as well, the reorientation process of Kerr's effect in a strong electric field [48], light scattering in solutions of biomacromolecules in an electric or magnetic field [46] and occurrs in description of second-harmonic generation by isotropic media in a dc electric field [3,45]. The functions $\Phi_1(\pm q)$ is also involved, for instance, in Rayleigh [49,50] and Raman [51] light scattering.

3.2.2. Paramagnetic molecules

On calculating the mean values of Eq. (18) with distribution function (22) for paramagnetic dipolar molecules we obtain

$$M_z^{(1)\perp} = \frac{2\rho}{3\varepsilon_0\, c\, n}\Big[{}^e\gamma_{123}^{em} + 2\,{}^e\gamma_{231}^{em} + \frac{1}{k_BT}\,{}^e\gamma_{12}^{e}\,\mu_3^m - \Big({}^e\gamma_{123}^{em} - {}^e\gamma_{231}^{em} + \frac{1}{k_BT}\,{}^e\gamma_{12}^{e}\,\mu_3^m\Big)\Phi_1(p,\pm q)\Big](I^- - I^+). \tag{40}$$

In the case of weak molecular reorientation the static magnetization $M_z^{(1)}$ is given by the following expression

$$M_z^{(1)\perp} = \frac{2\rho}{45\varepsilon_0\, c\, n}\Big\{15({}^e\gamma_{123}^{em} + 2\,{}^e\gamma_{231}^{em} + \frac{1}{k_BT}\,{}^e\gamma_{12}^{e}\,\mu_3^m) - ({}^e\gamma_{123}^{em} - {}^e\gamma_{231}^{em} + \frac{1}{k_BT}\,{}^e\gamma_{12}^{e}\,\mu_3^m)\Big[\Big(\frac{\mu}{k_BT}\Big)^2 + \frac{{}^e\delta^e(0)}{k_BT}\Big](E_y^0)^2\Big\}(I^- - I^+). \tag{41}$$

At molecular ordering saturation

$$M_z^{(1)\perp}(+\infty) = \frac{2\rho}{\varepsilon_0\, c\, n}\;{}^e\gamma_{231}^{em}\,(I^- - I^+), \tag{42}$$

for molecules with ${}^e\delta^e(0) > 0$ and

$$M_z^{(1)\perp}(-\infty) = \frac{\rho}{\varepsilon_0\, c\, n}\,({}^e\gamma_{123}^{em} + {}^e\gamma_{231}^{em} + \frac{1}{k_BT}\,{}^e\gamma_{12}^{e}\,\mu_3^m)(I^- - I^+). \tag{43}$$

for molecules with ${}^e\delta^e(0) < 0$.

For paramagnetic nondipolar molecules the static magnetization is described by Eq. (40) with $\Phi_1(\pm q)$ instead of $\Phi_1(p,\pm q)$ and, at weak molecular reorientation, we have Eq. (41) with $\mu = 0$.

It is noteworthy that, at electric saturation of molecules with positive anisotropy ${}^e\delta^e(0)$, there is no pure paramagnetic contribution to the inverse Faraday effect considered above (see Eqs (36) and (42)). Moreover, the effect is dependent on but one polarizablity tensor component ${}^e\gamma_{231}^{em}$. Thus, it can be determined directly by the measurement of the inverse Faraday effect at electric suturation discussed above.

3.3. DC electric field $\mathbf{E}^0$ *parallel to the incident light beam* ($\mathbf{E}^0 \parallel \mathbf{k}$)

Assume now a molecular system to be acted on additionally with a dc electric field E_z^0 applied parallel to the direction of the light propagation (Z-axis of the laboratory frame of coordinates). In this case the distribution function $f(\theta, E_z^0)$ used for calculating the mean values of Eq. (18) has the form (22) with $E_i^0 = E_z^0$.

3.3.1. Diamagnetic molecules

In this experimental configuration the inverse Faraday effect induced in madia composed of diamagnetic dipolar molecules is described by the expression

$$M_z^{(1)\parallel} = \frac{2\rho}{3\varepsilon_0\, c\, n}\Big[{}^e\gamma_{123}^{em} + 2\,{}^e\gamma_{231}^{em} + 2({}^e\gamma_{123}^{em} - {}^e\gamma_{231}^{em})\Phi_1(p,\pm q)\Big](I^- - I^+), \tag{44}$$

with the molecular reorientation function $\Phi_1(p,\pm q)$ given by Eq. (30); the superscript $\|$ stands for the configuration $\mathbf{E}^0 \parallel \mathbf{k}$.

In the case of weak molecular reorientation due to the field E_z^0

$$M_z^{(1)\|} = \frac{2\rho}{45\varepsilon_0\, c\, n}\Big\{ 15({}^e\gamma_{123}^{em} + 2\,{}^e\gamma_{231}^{em}) + 2({}^e\gamma_{123}^{em} - {}^e\gamma_{231}^{em})\Big[\Big(\frac{\mu}{k_BT}\Big)^2 + \frac{{}^e\delta^e(0)}{k_BT}\Big](E_z^0)^2\Big\}(I^- - I^+). \tag{45}$$

If the electric field E_z^0 leads to molecular ordering saturation described, for molecules with positive and negative anisotropy ${}^e\delta^e(0)$, by the functions $\Phi_1(+\infty,+\infty)$ and $\Phi_1(+\infty,-\infty)$ (Eqs (34) and (35)), respectively, we have

$$M_z^{(1)\|}(+\infty) = \frac{2\rho}{\varepsilon_0\, c\, n}\ {}^e\gamma_{123}^{em}\,(I^- - I^+), \tag{46}$$

for ${}^e\delta^e(0) > 0$, and

$$M_z^{(1)\|}(-\infty) = \frac{2\rho}{\varepsilon_0\, c\, n}\ {}^e\gamma_{231}^{em}\,(I^- - I^+), \tag{47}$$

for ${}^e\delta^e(0) < 0$.

For diamagnetic nondipolar molecules we have Eq. (44) with the function $\Phi_1(\pm q)$ instead of $\Phi_1(p,\pm q)$ and Eq. (45) with $\mu = 0$. Moreover, Eqs (46) and (47) are fulfilled for nondipolar molecules as well.

Eqs (46) and (47) show that in the case of very strong molecular reorientation only one polarizability tensor component mediates the effect: ${}^e\gamma_{123}^{em}$ for molecules with ${}^e\delta^e(0) > 0$ and ${}^e\gamma_{231}^{em}$ for ones with ${}^e\delta^e(0) < 0$. Thus, these components can be determined directly from the measurement of the inverse Faraday effect at electric saturation.

3.3.2. Paramagnetic molecules

Applying the above procedure for paramagnetic dipolar molecules we get

$$M_z^{(1)\|} = \frac{2\rho}{3\varepsilon_0\, c\, n}\Big[{}^e\gamma_{123}^{em} + 2\,{}^e\gamma_{231}^{em} + \frac{1}{k_BT}\,{}^e\gamma_{12}^{e}\,\mu_3^m + 2({}^e\gamma_{123}^{em} - {}^e\gamma_{231}^{em} + \frac{1}{k_BT}\,{}^e\gamma_{12}^{e}\,\mu_3^m)\Phi_1(p,\pm q)\Big](I^- - I^+). \tag{48}$$

If the dimensionless reorientation parameters p and q fulfil the relations $p \ll 1$ and $q \ll 1$, the magnetization $M_z^{(1)\|}$ can be expressed in the form:

$$M_z^{(1)\|} = \frac{2\rho}{45\varepsilon_0\, c\, n}\Big\{ 15({}^e\gamma_{123}^{em} + 2\,{}^e\gamma_{231}^{em} + \frac{1}{k_BT}\,{}^e\gamma_{12}^{e}\,\mu_3^m) + 2({}^e\gamma_{123}^{em} - {}^e\gamma_{231}^{em} + \frac{1}{k_BT}\,{}^e\gamma_{12}^{e}\,\mu_3^m)\Big[\Big(\frac{\mu}{k_BT}\Big)^2 + \frac{{}^e\delta^e(0)}{k_BT}\Big](E_z^0)^2\Big\}(I^- - I^+). \tag{49}$$

On the other hand, if the field E_z^0 is strong enough to forced molecular ordering saturation, then

$$M_z^{(1)\|}(+\infty) = \frac{2\rho}{\varepsilon_0\, c\, n}\ \Big({}^e\gamma_{123}^{em} + \frac{1}{k_BT}\,{}^e\gamma_{12}^{e}\,\mu_3^m\Big)(I^- - I^+), \tag{50}$$

for ${}^{e}\delta^{e}(0) > 0$, and

$$M_z^{(1)\parallel}(-\infty) = \frac{2\rho}{\varepsilon_0\, c\, n}\ {}^{e}\gamma_{231}^{em}\ (I^- - I^+), \tag{51}$$

for ${}^{e}\delta^{e}(0) < 0$.

In the case of paramagnetic nondipolar molecules we have Eq. (48) with $\Phi_1(\pm q)$ instead of $\Phi_1(p, \pm q)$, Eq. (49) with $\mu = 0$ and, at electric saturation, Eqs (50) and (51). It results from Eq. (51) that there is no paramagnetic contribution to the effect for molecules with negative anisotropy ${}^{e}\delta^{e}(0)$ at molecular ordering saturation forced by the field E_z^0. Eqs (47) and (51) show that the polarizability tensor component ${}^{e}\gamma_{231}^{em}$ of dia- and paramagnetic molecules (dipolar and nondipolar) with the negative anisotropy ${}^{e}\delta^{e}(0)$ can be determined by the measurement of the inverse Faraday effect at longitudinal electric saturation. Moreover, in the system composed of molecules with the positive anisotropy ${}^{e}\delta^{e}(0)$, the paramagnetic contribution to the effect is 3 times larger at saturation than at the absence of the field E_z^0.

4. Inverse magnetochiral birefringence

Inverse magnetochiral birefringence is the effect in which the static magnetization is induced in a medium by unpolarized or arbitrarily polarized light. In a molecular system it is described by Eqs (19) and (20). For futher consideration it is convenient to rewrite these equations in the forms

$$M_z^{(2)} = {}^{D}M_z^{(2)} + {}^{P}M_z^{(2)} \tag{52}$$

with

$${}^{D}M_z^{(2)} = \frac{2\rho}{\varepsilon_0\, c^2 n} < {}^{e}\beta_{xyz}^{mm} - {}^{e}\beta_{yxz}^{mm} >_{E^0}\ I \tag{53}$$

$${}^{P}M_z^{(2)} = \frac{2\rho}{\varepsilon_0\, c^2 n k_B T} < ({}^{e}\beta_{xy}^{m} - {}^{e}\beta_{yx}^{m})\mu_z^m >_{E^0}\ I, \tag{54}$$

and

$$M_z^{(3)} = {}^{D}M_z^{(3)} + {}^{P}M_z^{(3)} \tag{55}$$

with

$${}^{D}M_z^{(3)} = -\frac{2\rho\omega}{3\varepsilon_0\, c^2 n} < {}^{e}\gamma_{x(xz)z}^{qm} + {}^{e}\gamma_{y(yz)z}^{qm} >_{E^0}\ I, \tag{56}$$

$${}^{P}M_z^{(3)} = -\frac{2\rho\omega}{3\varepsilon_0\, c^2 n k_B T} < ({}^{e}\gamma_{x(xz)}^{q} + {}^{e}\gamma_{y(yz)}^{q})\mu_z^m >_{E^0}\ I, \tag{57}$$

where the superscripts D and P stand for diamagnetic and paramagnetic contributions.

4.1. Absence of the external field $\mathbf{E}^0$

In this case the statistical average $< \cdots >_{E^0}$ in Eqs (19) and (20) becomes isotropic space average $< \cdots >$ leading to [11]

$$ {}^{D}M_z^{(2)}(0) = \frac{2\rho}{3\varepsilon_0\, c^2\, n}\, \varepsilon_{\alpha\beta\gamma}\, {}^{e}\beta^{mm}_{\alpha\beta\gamma}\, I, \tag{58} $$

$$ {}^{P}M_z^{(2)}(0) = \frac{2\rho}{3\varepsilon_0\, c^2\, nk_BT}\, \varepsilon_{\alpha\beta\gamma}\, {}^{e}\beta^{m}_{\alpha\beta}\, \mu^m_\gamma\, I, \tag{59} $$

$$ {}^{D}M_z^{(3)}(0) = -\frac{4\rho\omega}{3\varepsilon_0\, c^2 n} X_{\alpha\beta\gamma\delta}\, {}^{e}\gamma^{qm}_{\alpha(\beta\gamma)\delta}\, I, \tag{60} $$

$$ {}^{P}M_z^{(3)}(0) = -\frac{4\rho\omega}{3\varepsilon_0\, c^2 nk_BT} X_{\alpha\beta\gamma\delta}\, {}^{e}\gamma^{q}_{\alpha(\beta\gamma)} \mu^m_z\, I, \tag{61} $$

where

$$ X_{\alpha\beta\gamma\delta} = \frac{1}{30}(\delta_{\alpha\beta}\delta_{\gamma\delta} - \delta_{\alpha\gamma}\delta_{\beta\delta} - \delta_{\alpha\delta}\delta_{\beta\gamma}) \tag{62} $$

with $\delta_{\alpha\beta}$ being second-rank unit tensors (Kronecker deltas).

The static magnetization described by Eqs (58)–(62) is non-zero in molecular systems composed of chiral molecules of 24 magnetic points group symmetries [11,43]. However, in the present paper we are interested in molecules which fulfil the relation (21) and this restriction leaves us with the symmetries 3, 4, 6, ∞, $4\underline{2}2$, $3\underline{2}$ and $6\underline{2}2$ for paramagnetic molecules, and the symmetries $\underline{4}$, $\underline{6}$, 422, $\underline{4}2\underline{2}$, 32, 622 and $\underline{6}2\underline{2}$ for diamagnetic ones [11]. For paramagnetic molecules possessing these symmetries we have

$$ {}^{D}M_z^{(2)}(0) = \frac{4\rho}{3\varepsilon_0\, c^2\, n}\, ({}^{e}\beta^{mm}_{123} + {}^{e}\beta^{mm}_{231} + {}^{e}\beta^{mm}_{312})\, I, \tag{63} $$

$$ {}^{P}M_z^{(2)}(0) = \frac{4\rho}{3\varepsilon_0\, c^2\, nk_BT}\, {}^{e}\beta^{m}_{12}\, \mu^m_3\, I, \tag{64} $$

$$ {}^{D}M_z^{(3)}(0) = -\frac{2\rho\omega}{15\varepsilon_0\, c^2 n}\Big[{}^{e}\gamma^{qm}_{3333} + 2({}^{e}\gamma^{qm}_{1111} + {}^{e}\gamma^{qm}_{1122} + {}^{e}\gamma^{qm}_{1133} + {}^{e}\gamma^{qm}_{3311})\Big]\, I, \tag{65} $$

$$ {}^{P}M_z^{(3)}(0) = -\frac{2\rho\omega}{15\varepsilon_0\, c^2 nk_BT}\, ({}^{e}\gamma^{q}_{333} + 2\,{}^{e}\gamma^{q}_{113})\mu^m_3\, I. \tag{66} $$

For diamagnetic molecules with the above symmetries we have only Eqs (63) and (65).

4.2. DC electric field $\mathbf{E}^0$ *perpendicular to the incident light beam* ($\mathbf{E}^0 \perp \mathbf{k}$)

4.2.1. Diamagnetic molecules

The infuence of pure reorientational processes on inverse magnetochiral birefringence in isotropic media composed of diamagnetic molecules is described by Eqs (53) and (56). On averaging with the distribution function (22) we get for diamagnetic dipolar molecules having the symmetries $\underline{4}$, $\underline{6}$

$$
\begin{aligned}
{}^{D}M_z^{(2)\perp} = \frac{2\rho}{3\varepsilon_0\, c^2\, n} \Big[& 2({}^{e}\beta_{123}^{mm} + {}^{e}\beta_{231}^{mm} + {}^{e}\beta_{312}^{mm}) \\
& + ({}^{e}\beta_{231}^{mm} + {}^{e}\beta_{312}^{mm} - 2\,{}^{e}\beta_{123}^{mm})\, \Phi_1(p, \pm q) \Big] I,
\end{aligned} \tag{67}
$$

$$
\begin{aligned}
{}^{D}M_z^{(3)\perp} = -\frac{\rho\omega}{30\varepsilon_0\, c^2 n} \Big[& 4\,{}^{e}\gamma_{3333}^{qm} + 8({}^{e}\gamma_{1111}^{qm} + {}^{e}\gamma_{1122}^{qm} + {}^{e}\gamma_{1133}^{qm} + {}^{e}\gamma_{3311}^{qm}) - 4\,{}^{e}\gamma_{3333}^{qm}\, \Phi_2(p, \pm q) \\
& + 2({}^{e}\gamma_{1111}^{qm} + {}^{e}\gamma_{1122}^{qm} - 4\,{}^{e}\gamma_{1133}^{qm})\, \Phi_3(p, \pm q) + 5\,{}^{e}\gamma_{1331}^{qm}\, \Phi_4(p, \pm q) \\
& + 12\,{}^{e}\gamma_{3311}^{qm}\, \Phi_5(p, \pm q)) \Big]\, I,
\end{aligned} \tag{68}
$$

where $\Phi_1(p, \pm q)$ is given by Eq. (30) and

$$
\Phi_2(p, \pm q) = \frac{1}{16}\, \{45 L_4(p, \pm q) - 30 L_2(p, \pm q) + 1\}, \tag{69}
$$

$$
\Phi_3(p, \pm q) = \frac{1}{8}\, \{30 L_2(p, \pm q) - 15 L_4(p, \pm q) - 7\}, \tag{70}
$$

$$
\Phi_4(p, \pm q) = \frac{1}{8}\, \{15 L_4(p, \pm q) - 6 L_2(p, \pm q) - 1\}, \tag{71}
$$

$$
\Phi_5(p, \pm q) = \frac{1}{4}\, \{5 L_4(p, \pm q) - 1\} \tag{72}
$$

are determined by the generalized Langevin-Kielich functions (31).

For diamagnetic nondipolar molecules (symmetries 422, $\underline{42}\underline{2}$, 32, 622, $\underline{62}\underline{2}$) the functions $\Phi_n(p, \pm q)$ in Eqs (67) and (68) have to be replaced by functions $\Phi_n(\pm q)$.
If molecular ordering attains saturation ($p \to \infty$, $q \to \infty$) then

$$
\Phi_n(\infty, +\infty) = 1, \quad \Phi_n(+\infty) = 1, \tag{73}
$$

$$
\Phi_2(\infty, -\infty) = \Phi_2(-\infty) = \frac{1}{16}, \quad \Phi_3(\infty, -\infty) = \Phi_3(-\infty) = -\frac{7}{8}, \tag{74}
$$

$$
\Phi_4(\infty, -\infty) = \Phi_4(-\infty) = -\frac{1}{8}, \quad \Phi_5(\infty, -\infty) = \Phi_5(-\infty) = -\frac{1}{4}, \tag{75}
$$

and for dipolar and nondipolar molecules with positive anisotropy ${}^{e}\delta^{e}(0)$

$$
{}^{D}M_z^{(2)\perp}(+\infty) = \frac{2\rho}{\varepsilon_0\, c^2\, n}\, ({}^{e}\beta_{231}^{mm} + {}^{e}\beta_{312}^{mm})\, I, \tag{76}
$$

whereas ${}^{D}M_z^{(3)}$ for molecules with the symmetries $\underline{4}$, 422, $\underline{42}\underline{2}$ becomes

$$ {}^{D}M_z^{(3)\perp}(+\infty) = -\frac{\rho\omega}{6\varepsilon_0\, c^2 n}(2\,{}^{e}\gamma^{qm}_{1111} + 2\,{}^{e}\gamma^{qm}_{1122} + 4\,{}^{e}\gamma^{qm}_{3311} + {}^{e}\gamma^{qm}_{1331})\, I, \tag{77} $$

and for the symmetries $\underline{6}$, 32, 622, $\underline{6}\underline{22}$

$$ {}^{D}M_z^{(3)\perp}(+\infty) = -\frac{\rho\omega}{3\varepsilon_0\, c^2 n}({}^{e}\gamma^{qm}_{1111} + 2\,{}^{e}\gamma^{qm}_{3311} - {}^{e}\gamma^{qm}_{1221}) I. \tag{78} $$

For molecules with negative anisotropy ${}^{e}\delta^{e}(0)$

$$ {}^{D}M_z^{(2)\perp}(-\infty) = \frac{\rho}{\varepsilon_0\, c^2\, n}\,(2\,{}^{e}\beta^{mm}_{123} + {}^{e}\beta^{mm}_{231} + {}^{e}\beta^{mm}_{312})\, I, \tag{79} $$

$$ \begin{aligned} {}^{D}M_z^{(3)\perp}(-\infty) = -\frac{\rho\omega}{48\varepsilon_0\, c^2 n}&(10\,{}^{e}\gamma^{qm}_{1111} + 6\,{}^{e}\gamma^{qm}_{3333} + 10\,{}^{e}\gamma^{qm}_{1122} \\ &+ 24\,{}^{e}\gamma^{qm}_{3311} + 8\,{}^{e}\gamma^{qm}_{3322} - {}^{e}\gamma^{qm}_{1331}) I. \end{aligned} \tag{80} $$

It is noteworthy that, at electric saturation, the effect under consideration is determined by a lesser number tensor components ${}^{e}\beta^{mm}_{\alpha\beta\gamma}$ and ${}^{e}\gamma^{qm}_{\alpha(\beta\gamma)\delta}$ than in the field-less case. The functions $\Phi_1(p,\pm q)$, $\Phi_2(p,\pm q)$ and $\Phi_3(p,\pm q)$ jointly describe, as well, light scattering by solution of macromolecules in external electric and magnetic fields [46] (the function $Q(p,\pm q)$ of [46] fulfils the relation $Q(p,\pm q) = 2\Phi_2(p,\pm q) - \Phi_3(p,\pm q)$) and the function $\Phi_2(p,\pm q)$ is involved in description of the circular intensity difference light scattering by optically active madia in dc electric field [52]. The functions $\Phi_1(\pm q)$, $\Phi_2(\pm q)$ and $\Phi_3(\pm q)$ describe, for instance, laser optical saturation of molecular reorientation in Rayleigh [49, 50] and Raman [51] light scattering (the functions $R_1(\pm q)$ and $R_4(\pm q)$ of [51] fulfil the relations $R_1(\pm q) = 4\Phi_2(\pm q) - 3\Phi_3(p,\pm q)$ and $R_4(\pm q) = 2\Phi_2(\pm q) - \Phi_3(p,\pm q)$).

4.2.2. Paramagnetic molecules

Inverse magnetochiral birefringence in isotropic media composed of paramagnetic molecules is described by Eqs (52)–(57) which present diamagnetic (Eqs (53) and (56)) as well as paramagnetic (Eqs (54) and (57)) contributions to the effect. For paramagnetic dipolar molecules (the symmetries 3, 4, 6, ∞) we have Eqs (67) and (68) whereas for nondipolar ones (the symmetries $4\underline{22}$, $3\underline{2}$, $6\underline{22}$) the functions $\Phi_n(p,\pm q)$ in Eqs (67) and (68) have to be replaced by functions $\Phi_n(\pm q)$. Moreover, for paramagnetic dipolar and nondipolar molecules we have Eqs (76), (79) and (80), whereas Eq. (77) is now for the symmetries $\underline{4}$ and $4\underline{22}$, and Eq. (78) for the symmetries 3, 6, ∞, $3\underline{2}$ and $6\underline{22}$.

Carring out the statistical averaging in Eqs (54) and (57) for paramagnetic dipolar molecules (the symmetries 3, 4, 6, ∞) we have

$$ {}^{P}M_z^{(2)\perp} = \frac{4\rho}{3\varepsilon_0\, c^2\, nk_BT}\; {}^{e}\beta^{m}_{12}\,\mu^{m}_{3}\left[1 - \Phi_1(p,\pm q)\right] I, \tag{81} $$

$$ {}^{P}M_z^{(3)\perp} = -\frac{2\rho\omega}{15\varepsilon_0\, c^2 nk_BT}\,\mu^{m}_{3}\left\{ {}^{e}\gamma^{q}_{333}\left[1 - \Phi_2(p,\pm q)\right] + 2\,{}^{e}\gamma^{q}_{113}\left[1 - \Phi_3(p,\pm q)\right]\right\} I \tag{82} $$

with the molecular reorientation functions $\Phi_1(p,\pm q)$, $\Phi_2(p,\pm q)$ and $\Phi_3(p,\pm q)$ given by Eqs (30), (69) and (70). For a medium composed of paramagnetic molecules without an intrinsic electric dipole moment

(molecules possessing the symmetries $4\underline{22}$, $3\underline{2}$, $6\underline{22}$) the functions $\Phi_n(p,\pm q)$ of Eqs (81) and (82) have to be replaced by the functions $\Phi_n(\pm q)$.
In the case of very strong molecular reorientation ($p\to\infty$, $q\to\infty$), we have (35),(39), (73) and (74) and for molecules with electric anisotropy ${}^e\delta^e(0)>0$

$$ {}^PM_z^{(2)\perp}(+\infty) = {}^PM_z^{(3)\perp}(+\infty) = 0, \tag{83}$$

whereas for ones with ${}^e\delta^e(0)<0$

$$ {}^PM_z^{(2)\perp}(-\infty) = \frac{2\rho}{\varepsilon_0\, c^2\, nk_BT}\; {}^e\beta^m_{12}\,\mu^m_3\, I, \tag{84}$$

$$ {}^PM_z^{(3)\perp}(-\infty) = -\frac{\rho\omega}{8\varepsilon_0\, c^2 nk_BT}\,({}^e\gamma^q_{333} + 4\,{}^e\gamma^q_{113})\,\mu^m_3\, I. \tag{85}$$

The magnetization ${}^PM_z^{(2)\perp}(-\infty)$ at electric saturation of molecules with ${}^e\delta^e(0)<0$ is 1.5 times greater than the magnetization ${}^PM_z^{(2)}(0)$ in the absence of the external field $\mathbf{E}^0$.

4.3. DC electric field $\mathbf{E}^0$ parallel to the incident light beam ($\mathbf{E}^0 \parallel \mathbf{k}$)

Asume, as in the Subsection 3.3, an isotropic medium to be acted on additionally with a dc electric field E^0_z ($\mathbf{E}^0 \parallel \mathbf{k}$).

4.3.1. Diamagnetic molecules

On calculating the mean values of Eqs (53) and (56) with distribution function (22) for optically active diamagnetic dipolar molecules (the symmetries $\underline{4}$, $\underline{6}$), we obtain

$$ {}^DM_z^{(2)\parallel} = \frac{4\rho}{3\varepsilon_0\, c^2\, n}\Big[\,{}^e\beta^{mm}_{123} + {}^e\beta^{mm}_{231} + {}^e\beta^{mm}_{312} + (2\,{}^e\beta^{mm}_{123} - {}^e\beta^{mm}_{231} - {}^e\beta^{mm}_{312})\,\Phi_1(p,\pm q)\Big] I, \tag{86}$$

$$\begin{aligned} {}^DM_z^{(3)\parallel} = -\frac{2\rho\omega}{15\varepsilon_0\, c^2 n}\Big\{ & {}^e\gamma^{qm}_{3333} + 2({}^e\gamma^{qm}_{1111} + {}^e\gamma^{qm}_{1122} + {}^e\gamma^{qm}_{1133} + {}^e\gamma^{qm}_{3311}) \\ & - 5\,{}^e\gamma^{qm}_{1331}\,\Phi_1(p,\pm q) + (8\,{}^e\gamma^{qm}_{1133} + 5\,{}^e\gamma^{qm}_{1331} - 2\,{}^e\gamma^{qm}_{1122} - 2\,{}^e\gamma^{qm}_{1111})\,\Phi_5(p,\pm q) \\ & - {}^e\gamma^{qm}_{3333}\,\Phi_6(p,\pm q) - 2\,{}^e\gamma^{qm}_{3311}\,\Phi_7(p,\pm q))\Big\}\, I \end{aligned} \tag{87}$$

with

$$ \Phi_6(p,\pm q) = \frac{1}{2}\,\{15L_4(p,\pm q) - 15L_2(p,\pm q) + 2\}, \tag{88}$$

$$ \Phi_7(p,\pm q) = \frac{1}{2}\,\{15L_2(p,\pm q) - 10L_4(p,\pm q) - 3\}, \tag{89}$$

whereas $\Phi_1(p,\pm q)$ and $\Phi_5(p,\pm q)$ are given by Eqs (30) ang (72), respectively.

For nondipolar molecules (symmetries 422, $\underline{42}\underline{2}$, 32, 622, $\underline{62}\underline{2}$) the effect is described by Eqs (86) and (87) with the functions $\Phi_n(\pm q)$ instead of $\Phi_n(p,\pm q)$.

The influence of reorientation processes in a dc electric field should be well apparent for parameters $p \geqslant 1$ and $q \geqslant 1$. Since

$$\Phi_6(\infty, +\infty) = \Phi_6(+\infty) = 1, \quad \Phi_7(\infty, +\infty) = \Phi_7(+\infty) = 1, \tag{90}$$

$$\Phi_6(\infty, -\infty) = \Phi_6(-\infty) = 1, \quad \Phi_7(\infty, -\infty) = \Phi_7(-\infty) = -\frac{3}{2}, \tag{91}$$

we obtain an interesting result for electric saturation, when for dipolar and nondipolar molecules with positive anisotropy ${}^e\delta^e(0)$ we get

$${}^D M_z^{(2)\parallel}(+\infty) = \frac{4\rho}{\varepsilon_0\, c^2\, n}\ {}^e\beta_{123}^{mm}\, I, \tag{92}$$

$${}^D M_z^{(3)\parallel}(+\infty) = -\frac{4\rho\omega}{3\varepsilon_0\, c^2 n}\ {}^e\gamma_{1133}^{qm}\, I\,; \tag{93}$$

for molecules with negative anisotropy ${}^e\delta^e(0)$

$${}^D M_z^{(2)\parallel}(-\infty) = \frac{2\rho}{\varepsilon_0\, c^2\, n}\ ({}^e\beta_{231}^{mm} + {}^e\beta_{312}^{mm})\, I, \tag{94}$$

whereas ${}^D M_z^{(3)\parallel}(-\infty)$ for molecules with the symmetries $\underline{4}$, 422 and $\underline{42}\underline{2}$ amounts to

$${}^D M_z^{(3)\parallel}(-\infty) = -\frac{\rho\omega}{6\varepsilon_0\, c^2 n}\,(2\,{}^e\gamma_{1111}^{qm} + 2\,{}^e\gamma_{1122}^{qm} + 4\,{}^e\gamma_{3311}^{qm} + {}^e\gamma_{1331}^{qm})I, \tag{95}$$

and for the symmetries $\underline{6}$, 32, 622 and $\underline{6}\underline{22}$ to

$${}^D M_z^{(3)\parallel}(-\infty) = -\frac{\rho\omega}{3\varepsilon_0\, c^2 n}\,({}^e\gamma_{1111}^{qm} + 2\,{}^e\gamma_{3311}^{qm} - {}^e\gamma_{1221}^{qm})I. \tag{96}$$

The functions $\Phi_5(p, \pm q)$, $\Phi_6(p, \pm q)$ and $\Phi_7(p, \pm q)$ describe also reorientational processes in Rayleigh light scattering in the presence of external dc fields [46] (the function $T(p, \pm q)$ of [46] fulfils the relation $4T(p, \pm q) = 2\Phi_7(p, \pm q) + \Phi_5(p, \pm q)$), $\Phi_6(p, \pm q)$ describes, as well, the circular intensity difference light scattering by optically active madia in a dc electric field [52] and the functions $\Phi_5(\pm q)$, $\Phi_6(\pm q)$ and $\Phi_7(\pm q)$ are involed in description of the influence of an intense laser beam on Rayleigh [49,50] and Raman [51] light scattering.

4.3.2. Paramagnetic molecules

In substances containing of paramagnetic molecules the effect of inverse magnetochiral birefringence contains, as in Section 4.2.2, diamagnetic as well as paramagnetic contributions. For paramagnetic dipolar molecules (the symmetries 3, 4, 6, ∞) we have Eqs (86) and (87) whereas for nondipolar ones (the symmetries $4\underline{22}$, $3\underline{2}$, $6\underline{22}$) the functions $\Phi_n(p, \pm q)$ in Eqs (86) and (87) have to be replaced by functions $\Phi_n(\pm q)$. Moreover, for paramagnetic dipolar and nondipolar molecules we have Eqs (92), (93) and (94), whereas Eq. (95) is now for the symmetries $\underline{4}$ and $4\underline{22}$, and Eq. (96) for the symmetries 3, 6, ∞, $3\underline{2}$ and $6\underline{22}$.

For the field configuration considered now, the pure paramagnetic contributions to the static magnetization (Eqs (54) and (57)) have the following form:

$$ {}^{P}M_z^{(2)\parallel} = \frac{4\rho}{3\varepsilon_0\, c^2\, nk_BT}\; {}^{e}\beta^{m}_{12}\, \mu^{m}_{3}\, \Big[1 + 2\,\Phi_1(p,\pm q)\Big] I, \tag{97} $$

$$ {}^{P}M_z^{(3)\parallel} = -\frac{2\rho\omega}{15\varepsilon_0\, c^2 nk_BT}\, \mu^{m}_{3}\, \Big\{ {}^{e}\gamma^{q}_{333}\Big[1 - \Phi_6(p,\pm q)\Big] + 2\, {}^{e}\gamma^{q}_{113}\, \Big[1 + 4\Phi_5(p,\pm q)\Big]\Big\}\; I \tag{98} $$

with the molecular reorientation functions $\Phi_1(p,\pm q)$, $\Phi_5(p,\pm q)$ and $\Phi_6(p,\pm q)$ given by Eqs (30), (72) and (88). For paramagnetic molecules with no intrinsic electric dipole moment the functions $\Phi_n(p,\pm q)$ of Eqs (97) and (98) have to be replaced by $\Phi_n(\pm q)$.

The result are of especial interest in the case of longitudinal electric saturation. For dipolar and nondipolar molecules with ${}^{e}\delta^{e}(0) > 0$ we then have

$$ {}^{P}M_z^{(2)\parallel}(+\infty) = \frac{4\rho}{\varepsilon_0\, c^2\, nk_BT}\; {}^{e}\beta^{m}_{12}\, \mu^{m}_{3}\, I, \tag{99} $$

$$ {}^{P}M_z^{(3)\parallel}(+\infty) = -\frac{4\rho\omega}{3\varepsilon_0\, c^2 nk_BT}\, {}^{e}\gamma^{q}_{113}\, \mu^{m}_{3}\, I, \tag{100} $$

whereas for ones with ${}^{e}\delta^{e}(0) < 0$

$$ {}^{P}M_z^{(2)\parallel}(-\infty) = {}^{P}M_z^{(3)\parallel}(-\infty) = 0. \tag{101} $$

Thus we note that, contrary to the configuration $\mathbf{E}^0 \perp \mathbf{k}$, for which the paramagnetic magnetization terms ${}^{P}M_z^{(2)\perp}(-\infty)$ and ${}^{P}M_z^{(3)\perp}(-\infty)$ are non-zero for molecules with ${}^{e}\delta^{e}(0) < 0$, the paramagnetic terms at longitudinal electric ($\mathbf{E}^0 \parallel \mathbf{k}$) saturation are non-zero for molecules with ${}^{e}\delta^{e}(0) > 0$. Moreover, it is noteworthy that the magnetization ${}^{P}M_z^{(2)\parallel}(+\infty)$ is 3 times greater than the zero-field magnetization ${}^{P}M_z^{(2)}(0)$, and that ${}^{P}M_z^{(3)\parallel}(+\infty)$ is dependent on but one component ${}^{e}\gamma^{q}_{113}$ of the electric-quadrupole polarizability ${}^{e}\gamma^{q}_{\alpha(\beta\gamma)}(\omega)$.

5. Discussion and conclusions

Our present considerations regarding the inverse Faraday effect and inverse magnetochiral birefringence are an extension of the theory of these effects over the molecular reorientation processes forced by an external dc electric field $\mathbf{E}^0$ and are valid for molecules possessing axial symmetry (given by Eq. (21)) for any degree of ordering, including electric saturation (i.e. complete alignment). In the case of polar molecules with positive anisotropy ${}^{e}\delta^{e}(0)$ the intrinsic electric dipole moments as well as induced ones tend concordantly to orient themselves into the electric field direction, so that with growing field intensity E^0 the generalized Langevin-Kielich functions $L_n(p,+q)$ tend to the limiting value 1, which defines the state of complite electric saturation of molecular reorientation. In consequence the functions $\Phi_n(p,+q)$ and $\Phi_n(+q)$ tend to 1 as well and we have $\Phi_n(\infty,+\infty) = \Phi_n(+\infty) = 1$. For molecules with negative anisotropy ${}^{e}\delta^{e}(0)$, the picture is entirely different. If the intrinsic electric dipole moment $\boldsymbol{\mu}$ lies along the symmetry axis, the electric polarizability ${}^{e}\beta^{e}_{33}(0)$ parallel to the latter is less than the polarizabillity ${}^{e}\beta^{e}_{11}(0)$ perpendicular thereto. Consequently, whereas the torque of the intrinsic electric

dipole tends to align the molecule parallel to the applied electric field direction, the torque due to the induced electric dipole tends to orient it perpendicular to the field $\mathbf{E}^0$. With growing field intensity E^0, increasing the induced electric dipole parameter q, the molecule goes over from parallel to perpendicular orientation with respect to $\mathbf{E}^0$. As a result of this reorientation, the generalized Langevin-Kielich functions $L_n(p,-q)$ decrease with growing E^0 tending to zero as q grows [3]. In the limit, when the field E^0 is very strong causing total alignment of the molecules, the reorientation functions $\Phi_n(\infty,-\infty)$ and $\Phi_n(-\infty)$ are given by Eqs (35), (39), (74), (75) and (91). In consequence the measurements of the static magnetization in the inverse Faraday effect or inverse magnetochiral birefringence in the absence of the external field $\mathbf{E}^0$ and at electric saturation are a sorce of information concerning the multipole polarizability tensor components mediating the effects.

5.1. Invers Faraday effect

5.1.1. Configuration $\mathbf{E}^0 \perp \mathbf{k}$

It follows from Sections 3.1 and 3.2 that two polarizability components, ${}^e\gamma^{em}_{231}$ and ${}^e\gamma^{em}_{123}$, involved in the inverse Faraday effect can be determined from the measurement of the static magnetizations $M_z^{(1)}(0)$, $M_z^{(1)\perp}(+\infty)$ and $M_z^{(1)\perp}(-\infty)$, namely:

(a) for dia- and paramagnetic molecules with ${}^e\delta^e(0) > 0$

$$ {}^e\gamma^{em}_{231} = \frac{\varepsilon_0\, c\, n}{2\rho(I^- - I^+)}\, M_z^{(1)\perp}(+\infty), \tag{102} $$

(b) for diamagnetic molecules with ${}^e\delta^e(0) > 0$

$$ {}^e\gamma^{em}_{123} = \frac{\varepsilon_0\, c\, n}{2\rho(I^- - I^+)} \Big[3M_z^{(1)}(0) - 2M_z^{(1)\perp}(+\infty)\Big], \tag{103} $$

(c) for diamagnetic molecules having ${}^e\delta^e(0) < 0$

$$ {}^e\gamma^{em}_{231} = \frac{\varepsilon_0\, c\, n}{2\rho(I^- - I^+)} \Big[3M_z^{(1)}(0) - 2M_z^{(1)\perp}(-\infty)\Big], \tag{104} $$

$$ {}^e\gamma^{em}_{123} = \frac{\varepsilon_0\, c\, n}{2\rho(I^- - I^+)} \Big[4M_z^{(1)\perp}(-\infty) - 3M_z^{(1)}(0)\Big]. \tag{105} $$

5.1.2. Configuration $\mathbf{E}^0 \parallel \mathbf{k}$

In this experimental configuration two components, ${}^e\gamma^{em}_{231}$ and ${}^e\gamma^{em}_{123}$, can be obtained from the measurement the static magnetizations $M_z^{(1)}(0)$, $M_z^{(1)\parallel}(+\infty)$ and $M_z^{(1)\parallel}(-\infty)$, namely:

(a) for dia - and paramagnetic molecules with ${}^e\delta^e(0) < 0$

$$ {}^e\gamma^{em}_{231} = \frac{\varepsilon_0\, c\, n}{2\rho(I^- - I^+)}\, M_z^{(1)\parallel}(-\infty), \tag{106} $$

(b) for diamagnetic molecules with ${}^e\delta^e(0) > 0$

$$ {}^e\gamma^{em}_{123} = \frac{\varepsilon_0\, c\, n}{2\rho(I^- - I^+)}\, M_z^{(1)\parallel}(+\infty), \tag{107} $$

$$ {}^e\gamma^{em}_{231} = \frac{\varepsilon_0\, c\, n}{4\rho(I^- - I^+)} \Big[3M_z^{(1)}(0) - M_z^{(1)\parallel}(+\infty)\Big], \tag{108} $$

(c) for diamagnetic ones with ${}^{e}\delta^{e}(0) < 0$

$$ {}^{e}\gamma^{em}_{123} = \frac{\varepsilon_0\, c\, n}{2\rho(I^- - I^+)} \Big[3M_z^{(1)}(0) - 2M_z^{(1)\parallel}(-\infty)\Big]. \tag{109} $$

The polarizability tensor component ${}^{e}\gamma^{e}_{12}$ of paramagnetic molecules having ${}^{e}\delta^{e}(0) > 0$ can be determined by the measurement of the magnetizations $M_z^{(1)}(0)$, $M_z^{(1)\perp}(+\infty)$ and $M_z^{(1)\parallel}(+\infty)$:

$$ {}^{e}\gamma^{e}_{12} = \frac{\varepsilon_0\, c\, n k_B T}{2\rho\mu_3^m(I^- - I^+)} \Big[3M_z^{(1)}(0) - M_z^{(1)\parallel}(+\infty) - 2M_z^{(1)\perp}(+\infty)\Big]. \tag{110} $$

Moreover, the following relations are fulfilled for diamagnetic as well as paramagnetic molecules:

$$ 3M_z^{(1)}(0) = 2M_z^{(1)\perp}(+\infty) + M_z^{(1)\parallel}(+\infty) \tag{111} $$

for molecules with ${}^{e}\delta^{e}(0) > 0$ and

$$ 3M_z^{(1)}(0) = 2M_z^{(1)\perp}(-\infty) + M_z^{(1)\parallel}(-\infty) \tag{112} $$

for ones with ${}^{e}\delta^{e}(0) < 0$.

5.2. Inverse magnetochiral birefringence

The static magnetization of inverse magnetochiral birefringence is mediated by the polarizability tensors related with dipolar-magnetic transitions (${}^{e}\boldsymbol{\beta}^{m}$, ${}^{e}\boldsymbol{\beta}^{mm}$) and quadrupolar-electric transitions (${}^{e}\boldsymbol{\gamma}^{q}$, ${}^{e}\boldsymbol{\gamma}^{qm}$). If the probability of dipolar-magnetic transitions are much larger than the probability of quadrupolar-electric ones, then ${}^{D}M_z^{(2)} \gg {}^{D}M_z^{(3)}$. In this case the polarizability tensor component ${}^{e}\beta^{mm}_{123}$ of diamagnetic molecules can be determined from the measurement of the magnetizations in the absence of an external field and at electric saturation in the configuration $\mathbf{E}^0 \perp \mathbf{k}$, when for molecules with ${}^{e}\delta^{e}(0) > 0$ we have

$$ {}^{e}\beta^{mm}_{123} = \frac{\varepsilon_0\, c^2\, n}{4\rho I} \Big[3\,{}^{D}M_z^{(2)}(0) - 2\,{}^{D}M_z^{(2)\perp}(+\infty)\Big], \tag{113} $$

and for ones with ${}^{e}\delta^{e}(0) < 0$

$$ {}^{e}\beta^{mm}_{123} = \frac{\varepsilon_0\, c^2\, n}{4\rho I} \Big[4\,{}^{D}M_z^{(2)\perp}(-\infty) - 3\,{}^{D}M_z^{(2)}(0)\Big], \tag{114} $$

or from the measurement of the static magnetization at electric saturation in the configuration $\mathbf{E}^0 \parallel \mathbf{k}$, when for molecules having ${}^{e}\delta^{e}(0) > 0$ we get

$$ {}^{e}\beta^{mm}_{123} = \frac{\varepsilon_0\, c^2\, n}{4\rho I}\ {}^{D}M_z^{(2)\parallel}(+\infty), \tag{115} $$

whereas for ones with ${}^{e}\delta^{e}(0) < 0$

$$ {}^{e}\beta^{mm}_{123} = \frac{\varepsilon_0\, c^2\, n}{4\rho I} \Big[3\,{}^{D}M_z^{(2)}(0) - 2\,{}^{D}M_z^{(2)\parallel}(-\infty)\Big]. \tag{116} $$

However, if ${}^{D}M_z^{(3)} \gg {}^{D}M_z^{(2)}$, then the component ${}^{e}\gamma_{1133}^{qm}$ of diamagnetic molecules with ${}^{e}\delta^{e}(0) > 0$ can be determined directly from ${}^{D}M_z^{(3)\parallel}(+\infty)$:

$$ {}^{e}\gamma_{1133}^{qm} = -\frac{3\varepsilon_0\, c^2\, n}{4\rho\omega I}\ {}^{D}M_z^{(3)\parallel}(+\infty). \tag{117}$$

Moreover, the diamagnetic and paramagnetic terms of the static magnetization fulfil the following relations:

$$ 3\,{}^{D}M_z^{(2)}(0) = 2\,{}^{D}M_z^{(2)\perp}(+\infty) + {}^{D}M_z^{(2)\parallel}(+\infty) = 2\,{}^{D}M_z^{(2)\perp}(-\infty) + {}^{D}M_z^{(2)\parallel}(-\infty), \tag{118}$$

$$ 3\,{}^{P}M_z^{(2)}(0) = {}^{P}M_z^{(2)\parallel}(+\infty) = 2\,{}^{P}M_z^{(2)\perp}(-\infty). \tag{119}$$

It is noteworthy that, at electric saturation in the configuration $\mathbf{E}^0 \perp \mathbf{k}$, the paramagnetic terms ${}^{P}M_z^{(2)\perp}(+\infty)$ and ${}^{P}M_z^{(3)\perp}(+\infty)$ are equal to zero for molecules with positive anisotropy ${}^{e}\delta^{e}(0)$ contrary to the configuration $\mathbf{E}^0 \parallel \mathbf{k}$ in which there is no paramagnetic contribution to inverse magnetochiral birefringence for molecules possessing negative anisotropy ${}^{e}\delta^{e}(0)$.

The possibilities of observing in experiment the influence of reorientational processes on optically induced static magnetization in isotropic madia hinge on the feasibility of producing sufficiently intense electric field as well as on the electric properties of the molecules. For molecules with $p \ll 1$ and $q \ll 1$ the effect of molecular reorientation is negligible. This is the case for molecules with an intrinsic electric dipole moment $\mu \sim 10^{-29}$ Cm in a field $E^0 \sim 10^6 \mathrm{Vm}^{-1}$ at room temperature, when $p \sim 10^{-2}$.

The influence of molecular reorientation on the above effects should become apparent at $p \sim 1$ or $q \sim 1$. This can be achieved for macromolecules having an intrinsic electric dipole moment $\mu \sim 10^{-28} \div 10^{-27}$Cm in an electric field $E^0 \sim 10^6 \div 10^7 \mathrm{Vm}^{-1}$, when $p > 1$ and electric saturation can be attained [47,53–55], as e.g. in solutions of polybenzyl-L-glutamate (PBLG) in dioxane [53] and in solutions of polystyrene in benzene and carbontetrachloride [55]. In this case the influence of molecular reorientation on optically induced static magnetization is of the same order of magnitude as the field-less effect.

References

[1] S. Kielich, *Acta Phys Pol* **29** (1966), 875.
[2] A.D. Buckingham, *Adv Chem Phys* **12** (1967), 107.
[3] S. Kielich, *Nonlinear Molecular Optics*, Nauka, Moscow, 1981 (in Russian).
[4] L.D. Barron, *Molecular Light Scattering and Optical Activity*, Cambridge University, Cambridge, 1982.
[5] A.D. Buckingham and P.J. Stephens, *Ann Rev Phys Chem* **17** (1966), 38.
[6] E.D. Palik and B.W. Henvis, *Appl Opt* **6** (1967), 603.
[7] J.P. Van der Ziel, P.S. Pershan and L.D. Malmstrom, *Phys Rev Lett* **15** (1965), 190.
[8] P.S. Pershan, J.P. Van der Ziel and L.D. Malmstrom, *Phys Rev* **143** (1966), 575.
[9] P.W. Atkins and M.H. Miller, *Mol Phys* **15** (1971), 503.
[10] G. Wagnière, *Phys Rev A* **40** (1989), 2437.
[11] S. Woźniak, G. Wagnière and R. Zawodny, *Phys Lett A* **154** (1991), 259.
[12] S. Woźniak, M.W. Evans and G. Wagnière, *Mol Phys* **75** (1992), 81.
[13] P.V. Volkov and M.A. Novikov, *Crystallography Reports* **47** (2002), 824.
[14] M.Y.A. Raja, D. Allen and W. Sisk, *Appl Phys Lett* **67** (1995), 2123.
[15] N.G. Kalugin and G. Wagnière, *J. Opt.* B: *Quantum Semiclass Opt* **3** (2001), 189.
[16] J. Dechamps, M. Fitaire and M. Lagoutte, *Phys Rev Lett* **25** (1970), 1330.

[17] Y. Horovitz, S. Eliezer, A. Ludmirsky, Z. Henis, E. Moshe, R. Shpitalnik and B. Arad, *Phys Rev Lett* **78** (1997), 1707; Y. Horovitz, S. Eliezer, Z. Henis, Y. Paiss, E. Moshe, A. Ludmirsky, M. Werdiger, B. Arad and A. Zigler, *Phys Lett A* **246** (1998), 329.
[18] Z. Najmudin, M. Tatarakis, A. Pukhov, E.L. Clark, R.J. Clarke, A.E. Dangor, J. Faure, V. Malka, D. Neely, M.I.K. Santala and K. Krushelnick, *Phys Rev Lett* **87** (2001), 215004.
[19] A.V. Kimel, A. Kirilyuk, P.A. Usachev, R.V. Pisarev, A.M. Balbashov and Th. Rasing, *Nature* **435** (2005), 655.
[20] V.V. Kruglyuk and M.E. Portnoi, *Tech Phys Lett* **31** (2005), 1047.
[21] C.A. Perroni and A. Liebsch, *J Phys: Condens Matter* **18** (2006), 7063.
[22] V.V. Kruglyuk, M.E. Portnoi and R.J. Hicken, *J Nanophotonics* **1** (2007), 1.
[23] M.P. Groenewege, *Mol Phys* **5** (1962), 541.
[24] N.B. Baranova, Yu.V. Bogdanov and B.Y. Zel'dovich, *Optics Commun* **22** (1977), 242.
[25] N.B. Baranova and B.Y. Zel'dovich, *Mol Phys* **38** (1979), 1085.
[26] S. Woźniak and R. Zawodny, *Phys Lett A* **85** (1981), 111; *Acta Phys Pol A* **61** (1982), 175; *Acta Phys Pol A* **68** (1985), 675.
[27] G. Wagnière and A. Meier, *Chem Phys Lett* **93** (1982), 78.
[28] G. Wagnière, *Z Naturf* **39a** (1984), 254.
[29] L.D. Barron and J. Vrbancich, *Mol Phys* **51** (1984), 715.
[30] S. Woźniak, *Mol Phys* **59** (1986), 421; *Phys Lett A* **119** (1986), 256.
[31] S. Woźniak, *J Chem Phys* **85** (1986), 4217.
[32] S. Woźniak, *Acta Phys Pol A* **72** (1987), 779.
[33] S. Coriani, M. Pecul, A. Rizzo, P. Jörgensen and M. Jaszuński, *J Chem Phys* **117** (2002), 6417.
[34] A. Rizzo and S. Coriani, *J Chem Phys* **119** (2003), 11064.
[35] P. Kleindienst and G. Wagnière, *Chem Phys Lett* **288** (1998), 89.
[36] N.K. Kalugin, P. Kleindienst and G. Wagnière, *Chem Phys* **248** (1999), 105.
[37] M. Vallet, R. Ghosh, A. Le Floch, T. Ruchon, F, Bretenaker and J.-Y. Thépot, *Phys Rev Lett* **87** (2001), 183003.
[38] G. Wagnière, *Z Phys D* **8** (1988), 229.
[39] S. Woźniak, M.W. Evans and G. Wagnière, *Mol Phys* **75** (1992), 99.
[40] P.S. Persham, *Phys Rev* **130** (1963), 919.
[41] S. Kielich, *Proc Phys Soc* **86** (1965), 709.
[42] A. Messiah, *Quantum mechanics*, North-Holland, Amsterdam, 1964.
[43] R. Zawodny, *Thesis*, A. Mickiewicz University, Poznań, 1977; S. Woźniak, R. Zawodny and B. Linder, *J Physique* **44** (1983), 403.
[44] Y.R. Shen, *The principles of nonlinear optics*, Wiley, New York, 1984.
[45] S. Kielich, *J Opto-Electron* **2** (1970), 5.
[46] S. Kielich, *Acta Phys Pol A* **37** (1970), 447.
[47] S. Kielich, in: *Dielectric and Related Molecular Processes*, M. Davis, ed., Chemical Society of London, London, 1972, Vol.1, p. 192.
[48] C.T O'Konski, K. Yoshioka and W.H. Orttung, J Chem Phys **63** (1959), 1558; K. Yoshioka and C.T O'Konski, *Biopolimers* **4** (1966), 499.
[49] S. Kielich, *Acta Phys Pol A* **37** (1970), 719.
[50] S. Kielich, *J Colloid Interface Sci* **34** (1970), 228.
[51] S. Kielich, Z. Ozgo and L. Wołejko, *J Raman Spectrosc* **3** (1975), 313.
[52] S. Woźniak and S. Kielich, *J Chem Phys* **94** (1991), 7588.
[53] G.P. Jones, M. Gregson and M. Davies, *Chem Phys Lett* **4** (1969), 33.
[54] M. Gregson, G.P. Jones and M. Davies, *Trans Faraday Soc* **67** (1971), 1630.
[55] S. Kielich, Z. Przeniczny, *Chem Phys Lett* **6** (1970), 72.